UNCLASSIFIED

AD NUMBER
AD488480
LIMITATION CHANGES
TO: **Approved for public release; distribution is unlimited.**
FROM: **Distribution authorized to U.S. Gov't. agencies and their contractors; Critical Technology; JUL 1966. Other requests shall be referred to Air Force Rocket Propulsion Laboratory, Attn: RPRP, Edward, CA 93523. This document contains export-controlled technical data.**
AUTHORITY
AFRPL ltr, 22 Mar 1973

THIS PAGE IS UNCLASSIFIED

F14571
179
67-0254

1967.0254

POPPET AND SEAT DESIGN DATA FOR AEROSPACE VALVES

Technical Report AFRPL-TR-66-147

July 1966

CPIA
NOV 10 1966
RECEIVED

Air Force Rocket Propulsion Laboratory
Research and Technology Division
Air Force Systems Command
Edwards, California

Project No. 6753, Task No. 675304

(Prepared under Contract No. AF04(611)-9712 by Rocketdyne Division of North American Aviation, Inc., Canoga Park, California. G. F. Tellier, Author)

~~This document is subject to special export controls and each transmittal to foreign governments or foreign nationals may be made only with prior approval of AFRPL (RPRP), Edwards, California 93523.~~

Distribution Statement A:
Approved for public release;
distribution is unlimited.

AD 488 480

F14571

NOTICES

Qualified users may obtain copies of this report from the Defense Documentation Center.

Defense Documentation Center release to the Office of Technical Services is not authorized.

When U.S. Government drawings, specifications, or other data are used for any purpose other than a definitely related Government procurement operation, the Government thereby incurs no responsibility or any obligation whatsoever, and the fact that the Government may have formulated, furnished, or in any way supplied the said drawings, specifications, or other data, is not to be regarded by implication or otherwise, or in any manner licensing the holder or any other person or corporation, or conveying any rights or permission to manufacture, use, or sell any patented invention that may in any way be related thereto.

If this copy is not needed, return to AFRPL (RPRPD), Edwards, California.

Private STINET

Home | Collections

View Saved Searches | View Shopping Cart | View Orders

Add to Shopping Cart

Other items on page 1 of your search results: 1

View XML

Citation Format: Full Citation (1F)

Accession Number:
AD0488480
Citation Status:
Active
Citation Classification:
Unclassified
Fields and Groups:
131100 - Pumps, Filters, Pipes, Tubing, Fittings & Vlvs
Corporate Author:
ROCKETDYNE CANOGA PARK CA
Unclassified Title:
(U) POPPET AND SEAT DESIGN DATA FOR AEROSPACE VALVES.
Title Classification:
Unclassified
Descriptive Note:
Final rept. Apr 64-Feb 66,
Personal Author(s):
Tellier, G F
Report Date:
Jul 1966
Media Count:
761 Page(s)
Cost:
$44.60
Contract Number:
AF 04(611)-9712
Report Number(s):
R-6472
AFRPL-TR-66-147
Project Number:
AF-6753
Task Number:
675304
Monitor Acronym:
AFRPL
Monitor Series:
TR-66-147
Report Classification:
Unclassified
Descriptors:
(U) *VALVES, SEALS(STOPPERS), LIQUID PROPELLANT ROCKET ENGINES, TAPER, DAMAGE, FINISHES, GRINDING, LEAKAGE(FLUID), TURBULENCE, LAMINAR FLOW, DEFORMATION, SURFACE PROPERTIES, MOMENTUM, SPRINGS, PRESSURE, GASES, CONICAL BODIES, TUNGSTEN COMPOUNDS, CARBIDES, SPHERES

Identifiers:
(U) POPPET VALVES, VALVE SEATS.
Identifier Classification:
Unclassified
Abstract:

(U) Presented herein is a description of the work accomplished in providing fundamental sealing data on metal-to-metal seat and poppet valving elements. The reported effort supplements and updates initial results published as Technical Documentary Report No. RPL-TDR-64-68, Rocket Engine Valve Poppet and Seat Design, dated May 1964. The program involved experimental and analytical studies of the detailed aspects of valve seating. Flat, conical, and spherical test models were fabricated with particular emphasis placed on documentation of fabrication methods and description of the resultant surfaces. Model stress-leakage characteristics, as a function of surface texture, geometry, coatings, and material variations, were experimentally investigated. The resulting information is presented in graphical form supported by inspection evidence from which test surface condition and features were deduced. Mathematical models relating surface texture and resulting deformation characteristics are formulated to provide understanding of the leakage path closure mechanism and extrapolation of experimental stress-leakage data. Additionally, cyclic effects on model sealing capabilities were investigated. A simplified analysis relating tester and model configuration with anticipated dynamic loading characteristics is developed and further extended by digital programming techniques. A high degree of correlation was obtained between the analytical predictions and the test results.

Abstract Classification:
Unclassified
Distribution Limitation(s):
01 - APPROVED FOR PUBLIC RELEASE
Source Serial:
F
Source Code:
308000
Document Location:
DTIC AND NTIS
Change Authority:
ST-A AFRPL LTR, 22 MAR 73

Privacy & Security Notice | Web Accessibility

private-stinet@dtic.mil

POPPET AND SEAT DESIGN DATA FOR AEROSPACE VALVES

Technical Report AFRPL-TR-66-147

July 1966

Air Force Rocket Propulsion Laboratory
Research and Technology Division
Air Force Systems Command
Edwards, California

Project No. 6753, Task No. 675304

(Prepared under Contract No. AF04(611)-9712 by Rocketdyne Division of North American Aviation, Inc., Canoga Park, California, G. F. Tellier, Author)

This document is subject ~~to special~~ export controls and each ~~transmittal~~ to foreign ~~governments~~ or foreign nationals may be ~~made only~~ with prior approval ~~of AFRPL~~ (RPRP), Edwards, California ~~93523~~.

FOREWORD

This final report was prepared in compliance with Contract AF04(611)-9712, Project No. 6753, Task No. 675304, covering a period of performance from April 1964 through February 1966.

Principal Rocketdyne investigators were T. Caywood and J. W. Lewellen, with G. F. Tellier as Project Engineer. The test fixture digital computer program was developed by J. G. Absalom. Analysis of the "dubbed-seat" contact stress distribution was prepared by Dr. S. B. Roberts. Program Managers were R. A. Byron and W. A. Anderson. The report was compiled by Messrs. Tellier and Lewellen.

Air Force administration of the program was by the Air Force Rocket Propulsion Laboratory, Edwards Air Force Base, with J. R. Lawrence as Project Engineer.

Specialized fabrication and preparation of test models and fixtures was contracted with L. A. Gauge Co., Inc., Sun Valley, California, whose cooperation and interest is gratefully acknowledged.

This report was given Rocketdyne Report No. R-6472.

This technical report has been reviewed and is approved.

J. R. LAWRENCE
Project Engineer

ABSTRACT

Presented herein is a description of the work accomplished in providing fundamental sealing data on metal-to-metal seat and poppet valving elements. The reported effort supplements and updates initial results published as Technical Documentary Report No. RPL-TDR-64-68, "Rocket Engine Valve Poppet and Seat Design Data," dated May 1964.

The program involved experimental and analytical studies of the detailed aspects of valve seating. Flat, conical, and spherical test models were fabricated with particular emphasis placed on documentation of fabrication methods and description of the resultant surfaces. Model stress-leakage characteristics, as a function of surface texture, geometry, coatings, and material variations were experimentally investigated. The resulting information is presented in graphical form supported by inspection evidence from which test surface condition and features were deduced. Mathematical models relating surface texture and resulting deformation characteristics are formulated to provide understanding of the leakage path closure mechanism and extrapolation of experimental stress-leakage data.

Additionally, cyclic effects on model sealing capabilities were investigated. A simplified analysis relating tester and model configuration with anticipated dynamic loading characteristics is developed and further extended by digital programming techniques.

A high degree of correlation was obtained between the analytical predictions and the test results. From cycle tests of representative models at various impact levels, corrosion fretting was determined to be a fundamental mode of surface degradation and, from these results, an optimum seating configuration evolved.

CONTENTS

Appendix A

Appendix B

ILLUSTRATIONS

TABLES

INTRODUCTION

Poppet and seat design is largely an individual effort in which the designer draws upon experience, ingenuity, and a repertory of personal and company design data. Because the aerospace valve business is highly competitive, there is seldom ample time or finances to undertake lengthy analyses or fundamental experimental evaluations. Often, too much time is spent probing the test failure rather than studying the successful component. Furthermore, since most worthwhile test-correlated design information is considered proprietary and thus not disseminated, attendant advances in the state of the art have been slow with new developments obscured and often not pursued. Consequently, most new rocket engine valves require extensive evolutionary development effort directed toward correcting design deficiencies just to achieve a status quo condition.

An initial program was accomplished by Rocketdyne under Contract AF04(611)-8392 to provide fundamental information on valve seating and leakage. The program was a two-phase effort that summarized current valve design technology and provided basic metal-to-metal seating characteristic design data. Phase I was a survey of pertinent patents, technical literature, and industry data to determine current technology levels and indicate specific areas where information was lacking or obsolete. Notable in the results of the survey was the lack of data applicable to the mechanism of seating or the correlation between theoretical and actual characteristics. Consequently, Phase II was devoted to a detailed analytical and experimental investigation of metal surfaces, their measurement, and a definition of the governing leakage equations. The experimental effort was confined to simple, flat poppet and seat models. These were fabricated and tested so that individual variables could be controlled, measured, and analytically correlated with seating equations describing leakage, seat land pressure distribution, and surface deformations with load. Where correlation was not possible, the detail definition of the material and geometric surface properties interpreted from included raw data provided a frame of reference for design purposes. The results of this program are reported in "Rocket Engine Valve Poppet and Seat Design Data," RPL-TDR-64-68.

The purpose of the follow-on program was to extend the range of information established in the initial effort with a more detailed investigation of metal surfaces, their interaction, and wear effects on the closure mechanism. Like the initial program, this effort consisted of two basic phases. The first phase was an extensive evaluation of surface texture effects on seating characteristics. For this investigation, 25 flat poppet and seat models with lathe-turned, ground, and lapped seating surfaces were fabricated and tested to establish basic stress-leakage performance characteristics. As an adjunct to surface texture studies, 12 conical and spherical models were also fabricated for investigation of basic seating geometry parameters for a single surface texture. Additionally, 21 model configurations were utilized in evaluating the effects of common seating errors and various surface treatments on previously established stress-leakage characteristics.

As a prelude to model preparation, a survey of available manufacturing and processing literature was performed which indicated that little information relating a finishing process with the resultant surface characteristics has been published. Thus, a reasonable documentation of the pertinent manufacturing parameters involved in model fabrication has been included in this report. In addition to a listing of dimensions and characteristics interpreted from inspection of model surfaces, the actual raw inspection data are included. This description of process and the resulting surface features may be employed for additional study and correlation beyond that covered herein.

A basic tenet established for model testing and inspection was the multiple measurement-multiple test philosophy. Whenever possible, cross checks of measured parameters were made with supplemental or redundant instrumentation. Rarely was one set of test results allowed to suffice without repeated verification. Furthermore, test and inspection methods, procedures, accuracy, and limitations have been thoroughly documented. It is believed the results obtained, while analytical correlation was not always possible, are of an accuracy level sufficient to be used as a reference standard.

Analytical support of surface texture and seating geometry investigations included refinements to analyses introduced during the initial effort and additional studies occasioned by the variety of surfaces fabricated for follow-on work. Among the latter are analytical flow path description and stress-leakage equations for circular lay surface texture, contact loading and pressure distribution relationships for curvilinear and dubbed flat seating configurations, and definition of conical and spherical seating geometry. Correlation between analyses and model test results was performed as permitted by the accuracy of the test model.

The second phase involved dynamic loading of representative seating configurations. This effort was conducted to investigate the parameters limiting valve closure endurance and determine the relationships between seating degradation and cyclic frequency intensity. To pursue these investigations, a cycle tester was constructed that is unique in its precision and minimal influence on model test results. Analysis of tester operational characteristics led to simplified equations relating velocity impact parameters potentially applicable to valve design. A digital program, formulated to support basic analyses and describe dynamic loading characteristics of test models, yielded extremely close correlation with actual instrumented results. The digital program, reproduced herein along with correlative data, may be used as a guide for further impact analytical considerations.

Nine flat and one each conical and spherical models were cycle tested with impact stress levels ranging from 2300 to 159,000 psi. Most models were cycled 10,000 times, but two configurations were each subjected to 1,000,000 cycles. In general, because of fixed-position testing, a leakage reduction with cycles was noted. However, surface degradation in the form of varying degrees of corrosion fretting occurred on most models. From these tests, an optimum geometry (minimum degradation) of crowned contact with identical poppet and seat land widths evolved.

The results of the follow-on program have proved even more conclusively than the initial effort that the complexities of the real surface defy explicit definition and correlation to the level demanded by current specifications. However, the surface descriptions of 69 models, and data from 134 stress-leakage tests, acting as a frame of reference and combined with an understanding of the configuration and deformation characteristics of these surfaces, should provide a base from which more meaningful design decisions may be made.

SURFACE STUDIES

Valve seating is the basic process of closing off an opening to effect a cessation of flow. Since the ideal closure has never been achieved for fabricated engineering surfaces, it must be concluded that: (1) a no-load gap exists between contacting faces, and (2) the gap is created by various geometrical errors. The study of surfaces containing these errors has been a part of considerable research accomplished in recent years to explain and define the phenomena of friction and wear. Optical and mechanical instruments have been developed to observe and measure both the overall geometry and the minute structure of surfaces. Contact theories have evolved from numerous experimental research programs which have synthesized models of surface asperities amenable to an analytical treatment. Evaluation of the accumulated results of many researchers, combined with a knowledge of the detail surface inspection and finishing methods, will support analysis of the mechanism of valve seat leakage.

SURFACE TERMINOLOGY AND REPRESENTATION

Included in this section are definitions of terms relating to the subject, as well as parameters which generally describe the average surface. The following definitions have been extracted from Ref. 1.

Surface Texture

Surface texture is concerned with the geometric irregularities of solid surfaces produced by the various machining and finishing processes. It is the repetitive or random deviations from the nominal surface which form the pattern of the surface. Surface texture includes roughness, waviness, lay, and flaws.

Nominal Surface. Nominal surface is the intended surface contour, the shape and extent of which is usually shown and dimensioned on a drawing or descriptive specification.

Profile. The profile is the contour of a surface in a plane perpendicular to the surface, unless some other angle is specified.

Centerline (Median Line). The centerline is the line about which roughness is measured, and is the line parallel to the general direction of the profile within the limits of the roughness-width cutoff, such that the sums of the areas contained between it and those parts of the profile which lie on either side of it are equal.

Roughness. Roughness consists of the finer irregularities in the surface texture usually including those irregularities which result from the inherent action of the production process. These are considered to include traverse feed marks and other irregularities within the limits of the roughness-width cutoff.

Roughness Height. Roughness height usually is rated as the arithmetical average devision expressed in microinches measured normal to the centerline. It may also be expressed as a root-mean-square technique which had much usage in the past.

Roughness Width. Roughness width is the distance parallel to the nominal surface between successive peaks or ridges which constitute the predominant pattern of the roughness. Roughness width is rated in inches.

Roughness-Width Cutoff (Sampling Length). The roughness-width cutoff is the greatest spacing of repetitive surface irregularities to be included in the measurement of average roughness height. Roughness-width cutoff must always be greater than the roughness width to obtain the total roughness height rating. In most electrical averaging instruments, the roughness-width cutoff can be selected. It is a characteristic of the instrument rather than that of the surface being measured. In selecting the roughness-width cutoff, care must be taken to choose a value which will include all of the surface irregularities which it is desired to assess. Roughness-width cutoff is rated in inches, and standard values include 0.003, 0.010, 0.030, and 0.100.

Waviness. Waviness is the usually widely spaced component of surface texture and is generally of wider spacing than the roughness-width cutoff. Waviness may result from such factors as deflections, vibration, chatter, heat treatment, or warping strains. Roughness may be considered as superimposed on a wavy surface.

Waviness Height. Waviness height is rated in inches as the peak-to-valley distance.

Waviness Width. Waviness width is rated in inches as the spacing of successive wave peaks or successive wave valleys.

Lay. The lay is the direction of the predominant surface pattern ordinarily determined by the production method used.

Flaws. Flaws are irregularities which occur at one place, or at relatively infrequent or widely varying intervals in a surface. Flaws include such defects as cracks, blow holes, checks, ridges, and scratches. Unless otherwise specified, the effect of flaws is not included in the roughness height measurements.

Surface Symbols

The symbol used to designate surface irregularities is the check mark with the horizontal extension (Fig. 1).

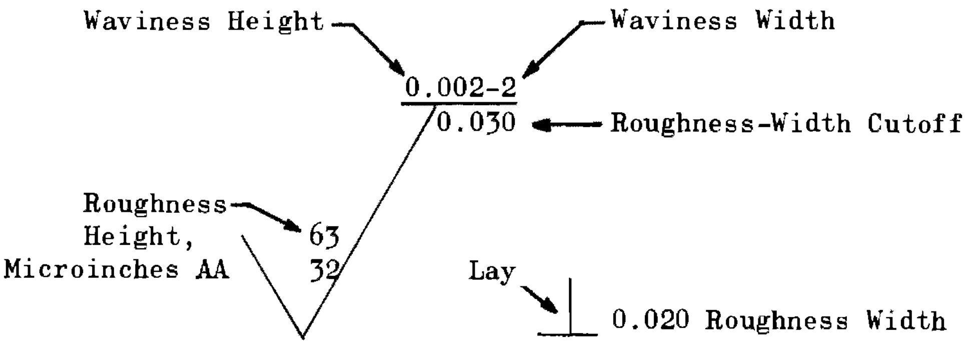

Figure 1. Standard Surface Symbol With Representative Surface Characteristics

Arithmetical Average

The arithmetical average deviation from the centerline is described by the following integral:

$$AA = \frac{1}{\ell} \int_{x=0}^{x=\ell} |Y| \, dx$$

where

Y = ordinate of the curve of the measured profile

ℓ = length over which the average is taken

An approximation of the average roughness may be found by adding the absolute value of the Y-increments and dividing the sum by the number of increments taken (Fig. 2).

$$AA = \frac{Y_a + Y_b + Y_c \ldots\ldots + Y_n}{n}$$

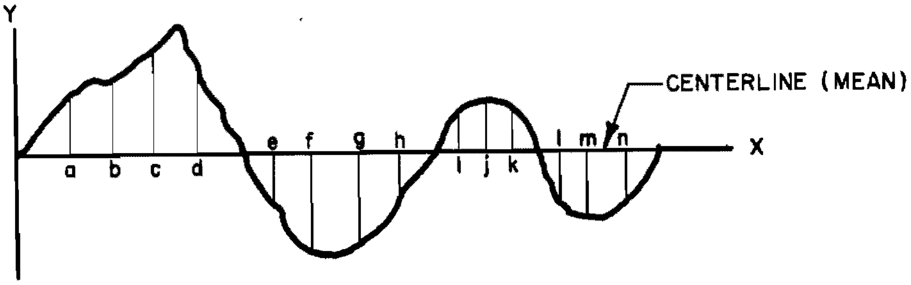

Figure 2. Incremental Division of Theoretical Surface Profile

Root Mean Square

Root-mean-square centerline deviation is defined by the following integral:

$$\text{rms} = \left[\frac{1}{\ell} \int_{x=0}^{x=\ell} Y^2 dx \right]^{1/2}$$

As with the approximate method for AA above, rms may be found by squaring each value of the Y-increment, summing and dividing by the number of increments, and then taking the square root. The effect is to weight the larger heights. Instruments designed for rms roughness values read somewhat higher (Fig. 2) than those calibrated for arithmetical average when compared on a given surface. The arithmetical average method has replaced the rms technique as an index of surface quality.

Peak-to-Valley Measurement Proposal

Interest has been increasing in the desirability of specifying surface quality by peak-to-valley measurements rather than arithmetical average roughness. This would be most applicable in situations requiring extremely smooth finishes and where specifications of scratches were important. Reliable measurement can best be made with the interference microscope (microinterferometer), noting that very smooth surfaces, as those produced by lapping, usually have more or less uniform irregularities with few deeper scratches.

Specifications. The following specifications for peak-to-valley parameters are being considered by the ASA (Ref. 2) for inclusion in a future standard:

1. Peak-to-valley height of general (average) surface texture shall not exceed XX microinches in XX inch.
2. Peak-to-valley height of individual irregularities shall not exceed XX microinches, and there shall be no more than X irregularities per X inch.
3. Pitting or voids contained in XX sq in. are acceptable.

The tentative standard is being prepared which will involve measuring the surface texture by optical methods.

Symbols for Optical Measurement. A proposal has been made to the ASA standards committee (Ref. 2) suggesting the surface finish symbol shown in Fig. 3 for surfaces requiring optical measurement.

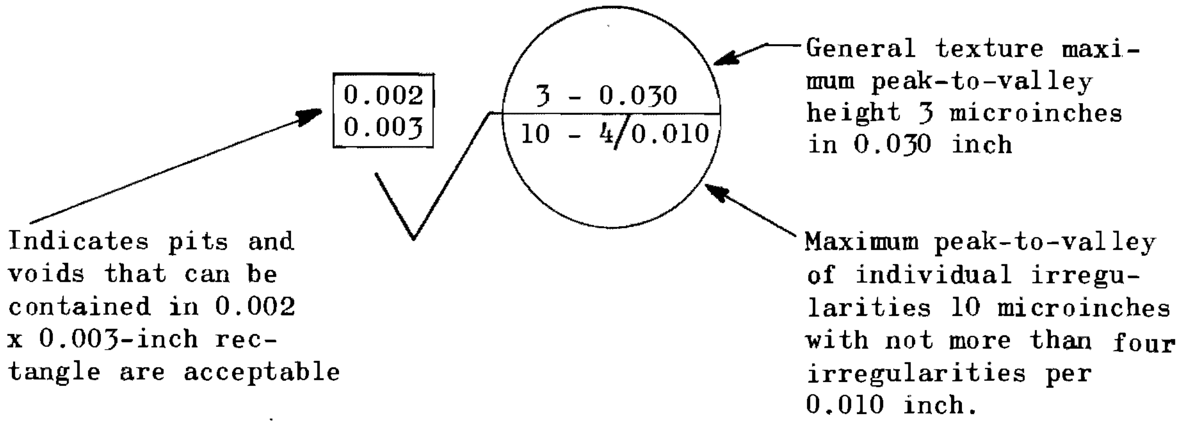

Indicates pits and voids that can be contained in 0.002 x 0.003-inch rectangle are acceptable

General texture maximum peak-to-valley height 3 microinches in 0.030 inch

Maximum peak-to-valley of individual irregularities 10 microinches with not more than four irregularities per 0.010 inch.

Figure 3. Surface Symbol for Optical Measurement

Errors of Form

These errors refer to deviation of the nominal surface from perfect geometry and do not include surface texture. Definitions for tolerances of form are given in MIL-STD-8C.

MEASURING METHODS AND DEVICES

A brief review of surface measuring devices will include only instruments capable of measuring at the level significant to this study.

Stylus Instruments

The most common method of measuring surface roughness is by moving a cone-shaped diamond stylus over the surface and translating its vertical motion to a value of average deviation from the mean. Factors which affect the resulting reading include the radius of the stylus, its force upon the surface, and the reference surface or skid upon which the tracer is supported. Error may be introduced because of mechanical vibration and electrical limitations. The almost universally used devices use stylus tracers with electrical amplification and may be grouped as follows.

Continuously Averaging Instantaneous Readout. This is a tracer-type instrument using either the standard 0.0005-inch radius stylus or the 0.0001-inch stylus for fine finishes. Vertical movements of the stylus are converted into voltage and amplified to actuate a direct-reading dial. These readings are in rms or arithmetical average with the lower limit of surface discrimination down to about 1 microinch. This device shows variations in average roughness height but does not indicate asperity configuration or wavelength greater than the set cutoff value.

Permanent Record. This is an electromechanical stylus instrument for measuring and recording roundness, flatness, roughness, scratches, flaws, and total profiles. For a linear reference, a precision flat is employed;

for round surfaces, an ultra-precision spindle is used. Magnified readings or traces are recorded on a chart with vertical magnifications of up to 50,000 times, enabling discriminate study of geometry and minute surface variations including waviness and asperity angle.

Probably the most important factor contributing to misinterpretation of surface roughness is the stylus tip radius size. It is obvious that some valleys and cracks cannot be reached by stylus tips of 0.0005- and 0.0001-inch radius found in most instruments. Also, these instruments evaluate the roughness along a thin line which undermines accuracy because the three-dimensional aspect is not taken into account. This situation might be minimized by traversing in various directions and also by having knowledge of the distribution of the irregularities.

Interesting comparisons have been made of various tip radii effects on similar surfaces(Ref. 3). Results showed that, for a turned surface, the 0.001-inch stylus read 53-microinch AA finish while the 0.0001-inch stylus gave a reading of 52-microinch AA, hardly a significant difference. But in three ground surfaces, the blunter instrument could not bottom consistently, therefore giving smaller measurements. For these surfaces, the 0.001-inch radius tip measured 1.6-microinch AA for the first, 5.5 for the second, and 22 for the third. The 0.0001-inch tip measured 1.8-, 7-, and 31-microinch AA, respectively. The difference in stylus effect is more pronounced in the rougher finishes for those ground surfaces.

The precision of stylus instruments was tested by comparison with standards which were constructed and measured optically by Bickel (Ref. 4). One observation was the effect of the tracer radius in interpreting sharp corners as being rounded (Fig. 4).

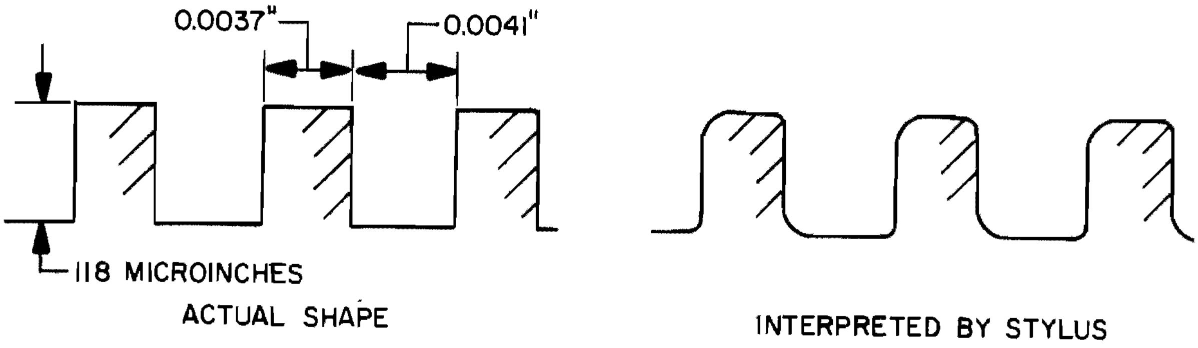

Figure 4. Stylus Interpretation of a Rectangular Shape

While profiles of simple sine wave shapes could be accurately followed by the stylus, the combined form of rectangular shapes upon a sine wave (Fig. 5) could not be contoured satisfactorily.

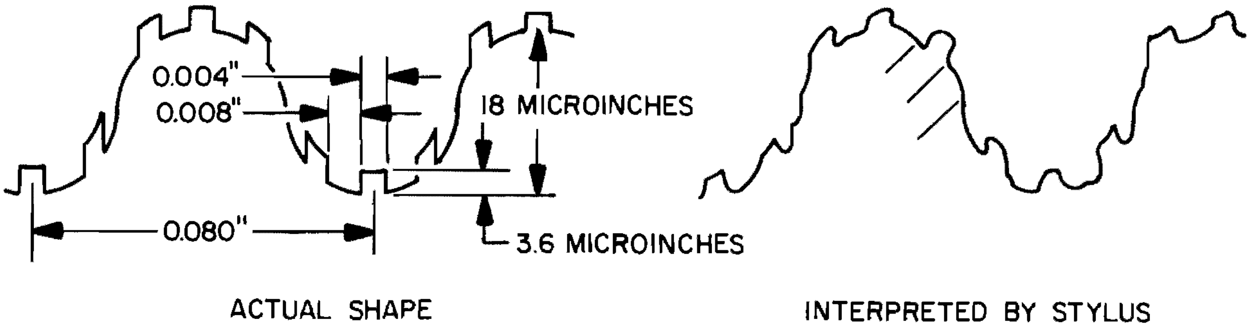

Figure 5. Stylus Interpretation of a Combination Shape

Table 1 indicates the results obtained by Bickel in a comparison of three stylus instruments (set at the cutoff values noted) while measuring rectangular profiles similar to those shown in Fig. 4.

TABLE 1

COMPARISON OF ARITHMETICAL AVERAGING INSTRUMENTS (MICROINCHES AA)

Calculated	Instrument A, 0.030 inch	Instrument B, 0.060 inch	Instrument C, 0.030 inch
2.7	2.6	2.36	3.2
25.0	25.6	26.4	30.0
58.0	57.0	53.3	68.0
120.0	124.0	128.0	136.0

A calculated curve which relates the stylus radius error with the average roughness height of precision reference specimens used to calibrate these instruments is found in Appendix C of Ref. 1. The reference specimen profile is made up of a series of known sizes of peaks and valleys having included angles of 150 degrees. For example, use of stylus tips having 0.0005- and 0.0001-inch radii for a reference specimen of a 4-microinch AA results in errors of 77 and 12 percent, respectively, indicating the relative capability of each tip radius to bottom the 150-degree included angle.

In measuring errors of form, the precision spindle electromechanical stylus instrument providing a profile record has generally replaced the more simple two and three point comparitor methods. (See Ref. 5 for a comprehensive collection of papers on roundness measurement.) Where lobing and nonsymmetrical errors exist, this is the only technique which will give valid results. However, as with all measuring methods, familiarity with potential errors and correct interpretation of the profile is necessary to obtain accurate and repeatable results. Of particular importance is the proper alignment of the basic reference of the part being measured with respect to the measuring datum. In the case of flat parts, the nominal surface must be parallel with a plane perpendicular to the spindle axis so that recorded deviations are totally from the part and not from setup errors. The mean axis of cylindrical parts must be coincident with the axis of the spindle or an error in roundness will be superimposed upon the profile. For example, a perfectly round part will present a sine wave linear trace when located eccentrically from the spindle axis. Furthermore, interpretation of numerical values can be geometrically misleading due to high vertical magnification (5×10^4). Dips in the profile trace of round surfaces are significant only of a small change in radius and not actual depressions in the surface (neglecting surface texture).

Taper Sectioning

Taper sectioning is a method whereby the surface roughness is magnified by slicing (grinding and lapping) the surface at an oblique angle. The magnification of the surface asperities of a taper section is a function of the taper angle, e.g., if the section is cut at 2.3 degrees, the vertical dimension would be 25 times the horizontal. Most materials require hard surface electroplating to prevent damage when cutting. This method of surface study is most accurate when the irregularities are wedge-shaped or produced by unidirectional processes. When ground surfaces of this type are viewed, they appear as jagged, sharp peaks with an irregular pattern. Lapped multidirectional surfaces are very difficult to evaluate because they include pits, gouges, and material that appears to be floating on the surface. Evidently, what is seen considering various sized cones as the surface makeup will depend on the sectioning angle and at what point it cuts each cone.

Excellent taper sectioning can be seen in Plate I of Ref. 6 and pages 191 and 192 of Ref. 7. These microphotographs show the irregular contour of various finishes on metal surfaces. One particular photo (Ref. 7) shows a 1.6-microinch-rms surface whose vertical dimensions are optically magnified to 10,000X. The surface appears to be less jagged than other photos of higher rms values. A taper section microphotograph (Ref. 7) shows a surface finished by loose-abrasive lapping. It is unique in that no definite trace can be observed, rather what is seen are outlines of cones or "mountains" of various sizes superimposed and scattered throughout. Analysis of such surfaces would be difficult even though the surface can be microscopically resolved to 1 microinch.

Optical Interference

The use of the principle of light wave interference makes it possible to measure surface finishes to a high degree of precision. Monochromatic light is directed through a transparent material with an accurate flat side which lies on the surface being inspected (Fig. 6). The two surfaces are separated by a thin "wedge" of air. Light waves are reflected from the work piece and the optical flat surfaces so that waves in phase produce bands of light and, conversely, when they are out of phase the waves interfere, producing dark bands. Alternate bands of light and dark approximately the same width appear at right angles to the direction of the air wedge. The bands give the effect of a contour map, decreasing in width and increasing in number as the wedge separation distance increases. Conversely, on a flat surface the bands will appear straight and parallel. The distance from a point on one band to the next band is equal to 1/2 of the wave length of the light used. The waviness and jaggedness of the interference bands are an indication of the surface irregularity and can be measured.

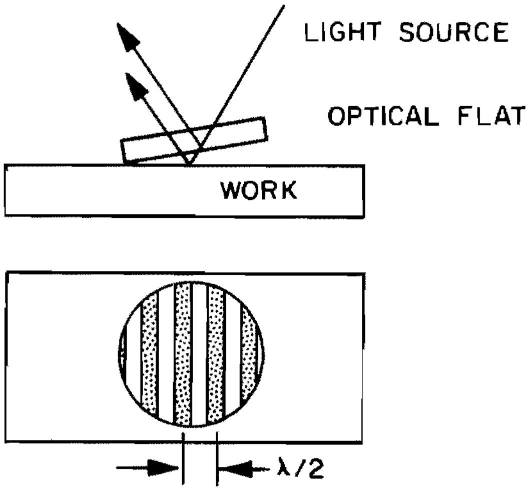

Figure 6. Light Interference With an Optical Flat

Optical Flats. Optical flats are precision glass or quartz plates that are flat to less than 0.000001 inch, and utilize optical interference between the specimen and the optical flat as shown in Fig. 6. Normally, a source of monochromatic light is used. Some of the light sources available are white light with a wave length (λ) of approximately 20 microinches, yellow-orange light at 23.2 microinches, and green light at 21.5 microinches.

Microinterferometry. Microinterferometry is the use of the optical flat and monochromatic light source with a microscope, which gives a very sensitive method of measuring surface roughness. The instruments incorporating this principle are known as interference microscopes or microinterferometers. The Zeiss instrument (Ref. 8), with magnification lenses of 80X, 200X, and 480X, uses a reference mirror on one side of the optical flat and two light beams. Various reflecting powers are available so the brightness of the test piece can be matched, giving sharp fringes.

This type of equipment is best applied on highly finished or glossy surfaces where the deviation of surface heights is within a few light wave lengths. Coarse surfaces cause the contour lines to become very close together and interpretation very difficult.

Multiple-Beam Interferometry. Most of the advances toward the high degree of sensitivity of the multiple-beam interferometry method of measuring surface contour have been made recently. Surfaces of the optical flat and the specimen (if nonreflective) are coated with silver having a high reflecting coefficient and also a high transmission coefficient so that incident light will be reflected back and forth resulting in an interference pattern of all these beams (Ref. 9 and 10). The relatively wide bands usually observed in other optical methods are reduced to thin lines which are able to reveal fine detail down to 0.02 microinch when sufficient horizontal resolution is available.

Electron Microscope

The high resolving power of the electron microscope makes it useful for the determination of fine finishes. Its main difficulty is that the electrons must pass through the specimen before striking a photographic plate, thereby limiting its use to thin sections. Another drawback is the necessity of using high vacuum and strong electron beams which can cause physical changes in certain specimens (Ref. 11).

The surface roughness is estimated by light and dark areas on the photographic plate. Electrons hitting high spots have a longer path to travel so that a smaller portion of them will pass through. The relative density on the photo plate is an indication of the variation of surface height.

In certain instances (thick sections), it is impractical to use the actual specimen so plastic replicas of the surface are used. The surface is coated with a film which is then stripped off and examined. In practice, resolution down to 0.2 microinch or magnification of 10,000 diameters (Ref.12) is usual, although linear magnification of 50,000 is possible with this type of instrument under optimum conditions. Excellent microphotographs of polished surfaces obtained by this technique can be seen on pages 188 and 189 of Ref. 11.

The disadvantages of the replica technique can be avoided by the electron reflection method where the surface is viewed obliquely and the surface protuberances are seen in profile. This method, studied by Halliday (Ref. 13), is shown to be particularly suitable for the examination of surfaces on which the irregularities are small; therefore, ground, lapped, finely abraded and polished surfaces can be studied.

Profile or Light Section Microscope

This simple optical method gives a detail picture of the surface but only of a very thin plane. The light source provided through a narrow slit falls on the specimen at an angle of 45 degrees to the surface of the specimen. Seen in the optical system is a cross section of local irregularities made by a line of light following the surface contour (Fig. 7).

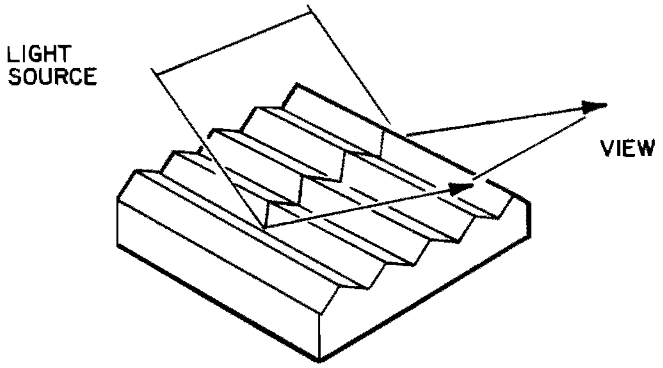

Figure 7. Principle of the Light Section Microscope

The smallest irregularity visible is on the order of the wave length of light or microinches (Ref.11). Sensitivity of this method is between 20 and 1600 microinches in deviation from the plane surface. It is considerably less sensitive than interferometry, being based on simple magnification rather than interference.

CHARACTERISTICS OF REAL SURFACES

To visualize real surfaces properly requires the ability to think small coupled with first-hand experience. There are many variations possible in ground and lapped surfaces because of the complexity of even the most regular fine finishes. Some idea of the scope of the topography can be obtained with the analogy of a plowed field or a mountainous terrain. Metal surface asperities undergo transformations similar to erosion as the surface is made smooth. Peaks are removed, and the remaining slopes become less steep.

Dimensions

Real surface dimensions are measured normally in microinches or millionths of an inch with nearly 40 microinches to the micron (10^{-6} meters) and 250 Angstrom units to the microinch. Metal valve seats are normally finished to less than 16 microinches AA by grinding and lapping, which places the upper peak-to-valley measurement at less than 100 microinches (0.0001 inch). At the other end of the spectrum, the lower limit of interest is in the vicinity of 1 microinch based on current-day achievements.

To describe the surface geometry more completely, an angle is often associated with surface asperities. This angle is the slope of individual undulations relative to the nominal surface. Except for machine-induced regularities, the asperity slope has wide variation from minute fraction of a degree to approaching the vertical, depending upon the scale of roughness viewed. As with mountainous terrain, large-scale undulations have shallow angles, and range from a gross flat characteristic of one gradual curve to periodic waviness. Superimposed upon the larger undulations are smaller and smaller facets (analogous to individual mountain peaks), and the smaller the facet viewed, the larger the slope angle may be.

A detailed examination of ground, lapped, and abraded surfaces was undertaken by Halliday (Ref. 13) using reflection-electron microscopy. Micrographs of aluminum, copper, mild steel, and hardened tool steel show asperity slope angles and heights from 0.1 degree and 0.4 microinch for electropolished aluminum to 30 degrees and 70 microinches for ground, hardened steel. Finer surfaces of approximately a 10-microinch height had corresponding asperity angles of about 1 to 2 degrees. This places the base dimensions of these asperities between 100 and 1000 microinches.

Rabinowicz (Ref. 14) describes results of absorption methods used for deducing real surface area. It is noted that relatively smooth surfaces obtained by rolling or electropolishing have real areas only slightly greater than projected; however, a metal surface obtained by an abrasion process has a total area nearly three times its projected area. The significance is that for the latter surface the angular inclines would have to be quite large, the average slope angle being 70 degrees.

Configuration

It has often been assumed that the irregularities or asperities of finishes that have been ground or lapped multidirectionally are generally cone shaped. They begin in the shape of wedges, scratches, etc., but are slowly rounded as cuts are taken radially. Examining any one irregularity microscopically would show smaller irregularities pointing to a situation of flatness not being possible in an absolute sense.

Bowden and Taber (Ref. 6) describe investigations of yield pressure as a function of the included angle or a single, cone-shaped asperity in an analysis of the plasticity characteristics of the cone.

Other surface investigators in various experiments concluded that meaningful results are possible when assuming conical asperity shapes (Ref. 15, 16, 17, and 18). Archard (Ref. 15) discussed some interesting data of an experiment by Halliday who, by reflection-electron microscopy, measured the slopes of surface irregularities of various steel and copper cylinders that were rough-etched and rolled against each other with contact force high enough to cause plastic flow. The resultant maximum slope angle measured 1.2 degrees, and the minimum 0.8 degree. Archard's conclusions suggested that asperities of angles more than some calculable amount will plastically yield until they reach the shallow, low, wide-base shapes measured above. These asperities of small slope will elastically deform into the surface until sufficient bearing area is developed to support the applied load.

Many of the approximations of the conical shape and size can be applied to the pyramidal shape. This shape can be assumed to result if a surface is finished by a process involving abrasion or cutting in two directions normal to each other. In unidirectional processes such as turning or superfinishing the wedge-shape irregularity results. Scratches fall into this category. As the wedge shapes become shorter in length as in grinding, they approach more closely the pyramidal shapes.

The geometry of spherical-shaped asperities has been assumed by Archard (Ref. 15), Kragelsky (Ref. 19), and Bowden and Tabor (Ref. 6) in contact analyses where this idealized configuration lessened the mathematical difficulties involved. It is probable that,among the various shapes suggested, the spherical one is most unlikely to occur except in unique cases. However, with a situation of worn, broken,or deformed peak points, almost any shape asperity may approximate the sphere if only at its tip.

There is little information on the statistical distribution of asperities of fine surfaces. The surface of the most finely finished material can be described as irregular if very sensitive instruments are used to examine it. Indications are that all surfaces contain random irregularities of various sizes with scratches, cracks, and intermittent flaws. Application of distribution laws can only be done theoretically with approximation as the result.

A paper by Reason (Ref. 20) shows profile charts of two actual surfaces whose profiles do not appear congruent but having similar AA values. These inconsistencies have been recognized by researchers in the field (Ref. 4, 21 and 7) in considering the multitudinous variables affecting surface geometry; it has been suggested by Reason (Ref. 20) that, for some surfaces, the process of manufacturing may need to be specified with the AA used as a simple controlling measure. This approach is obviously applicable to many critical valve sealing surfaces.

Visual Appearance

In describing real surfaces, a great deal of importance is often placed on visual effects and what is assumed from them. At best, the resolving power of optical microscopes is 6.7 microinches*, and no configurations smaller than this dimension can be clearly seen. Matte surfaces contain irregularities smaller than 40 microinches set at random angles so as to scatter the majority of light. The darker the surface the more scattered

---

*1/3 wave length of maximum intensity

the light and, thus, rougher the surface. Conversely, polished surfaces have broad areas which reflect a great deal of light similar to a mirror; however, in normal terms of peak-to-valley roughness, both surfaces can have the same average value.

Attempting to judge surface texture on a purely visual basis is generally misleading. Matte surfaces will tend to hide defects and scratches. However, a smooth appearing, mirror-like surface may contain relatively large undulations.

Composition

The surface layer is composed of a mixture of absorbed gases, metallic oxides, and various other contaminants in amounts depending upon past history. It is these contaminants which maintain sufficient separation between mating surfaces to preclude welding. Bowden and Tabor (Ref. 6) indicate that freshly lapped or ground metals (iron, nickel, chromium, and aluminum) will acquire a layer of oxide between 10 and 100 Angstroms thick in about 5 minutes or less. It is the breakdown of these oxides and other films which lead to wear and galling or seizure.

Because of the work-hardening nature of the finishing process, the hardness of the surface layer will be greater than the base metal. Soft, work-hardenable materials will have a larger increase than hardened steels. In addition, hardness within the crystalline grain structure of metals may vary considerably. This can induce roughness between contacting surfaces under loaded conditions.

CONTACT AREA AND LOADING EFFECTS

If two relatively smooth surfaces are brought together, contact will take place only in isolated spots. The irregular nature of the surfaces will permit stable touching at three points of contact until increased load causes a combination of plastic flow of the initially contacted asperities and elastic deformation of the supporting base material.

Gross areas of contact may be completely defined when the contact is curvilinear as in bearings and curved rollers, etc. The Hertz theory of elastic contacts (Ref. 22) describes a contact stress distribution which allows computation of gross bearing area, maximum stress, and deformation. Nominally flat surfaces, which are not perfectly flat, do not have well-defined regions of gross contact until loads are such as to bring the geometric total of the bearing surfaces in intimate contact. Even then the real contact area is only a relatively small percentage of the gross or apparent bearing area because of surface roughness.

In their study of friction and lubrication, Bowden and Tabor (Ref. 6) have evolved contact theories to describe the real contact area between metal surfaces. These are based upon observed evidence that: (1) real contact area increases in direct proportion to applied load, and (2) friction force, while independent of apparent area, is a function of the real area of contact. If the contacting asperities are assumed in a state of full plasticity and welded at contact, the force required to shear the welds would be the friction force. The real area of contact is defined by the plastic flow pressure (P_m), or stress, of the surface asperities and load (W), so that:

$$A_r = \frac{W}{P_m}$$

The plastic flow pressure has been evaluated for pyramidal and spherical shapes and, for the shallow slope angles normal for asperities, is related to the elastic limit (Y) by a constant. It is, therefore, independent of the applied load; for fully work-hardened metal:

$$P_m \cong 2.8Y$$

The real area of contact is also defined by the material shear strength (S) and friction force (f) as

$$A_r = \frac{f}{S}$$

and it follows that the friction coefficient:

$$\mu = \frac{f}{W} = \frac{A_r S}{A_r P_m} = \frac{S}{P_m}$$

This relationship has been experimentally correlated for a number of different materials. Considering that valve seats normally work well below the yield strength, it is apparent that the real areas of contact computed from the above equation would result in a very small percentage of the apparent area in real contact. If it can be assumed that the apparent contact area (A_a) is defined, the ratio of real to apparent area is equal to the ratio of apparent stress (S_a) to plastic flow pressure (P_m), or:

$$\frac{A_r}{A_a} = \frac{W/P_m}{W/S_a} = \frac{S_a}{P_m} = \frac{S_a}{2.8Y}$$

A typical hardened valve seat (Y = 250,000 psi) operating at 10,000-psi apparent stress would then have a real contact area equal to 1.4 percent of the apparent contact seating area.

In flat surface experiments (Ref. 6), two steel surfaces (lapped flat within a few fringes) of 0.124 and 3.25 sq in. were brought together under various loads, and the electrical resistance between them was measured to determine the real contact area. Results for the 3.25-sq in. pair are duplicated as follows:

Load, pounds	Apparent Stress, psi	n Contacts	Diameter of Each Contact, inches	Fraction of Area in Contact	R, 10^{-5} ohms
4.4	1.35	3	0.004	1/100,000	50.0
11.0	3.38	5	0.005	1/40,000	25.0
44.0	11.4	9	0.007	1/10,000	9.0
220.0	68.0	22	0.009	1/2,000	2.5
1100.0	338.0	35	0.017	1/400	0.9

The results indicate real area proportional to load. However, the range of apparent stress is far below valve seat stresses.

Through analysis of wear experiments, Archard (Ref. 15) has concluded that real surfaces support their loads predominantly in an elastic manner with only a small percentage of the contacts undergoing plastic flow. Friction between real surfaces has been experimentally proved to be proportional to the real area of contact. Archard has examined mathematical models of spherical surface protuberances pressing on a flat plate and has shown that real contact area is a power function of the load or

$$A \propto W^n$$

where n = 2/3 for a single protuberance (Hertz) and approaches unity for numerous protuberances. This conclusion was also reached by Kragelsky (Ref.19). Consequently, it was concluded (Ref. 15) that surface welding was a consequence of singular encounters occurring infrequently, and the more typical event is an elastic contact in which protuberances separate without damage. The elastic event thus determines friction and not welding as concluded by Bowden and Tabor.

In substantiation of his views, Archard describes the results of reflection electron microscopic examination (Ref. 13) of some metal surfaces (aluminum, copper, iron, nickel, steel, etc.) pressed flat (base metal plastically flowed) by a carefully polished, hardened-steel anvil. It was shown that the resulting slopes of the asperities were in all cases less than 1.2 degrees and, following compression, were entirely elastic in that the asperities could be pressed just flat without plastic flow. Moreover, in experiments involving phase contrast microscopy observation of nominally flat, ground, polished, and lapped specimens against a metallized gloss surface, Dyson and Hirst (Ref. 23) concluded that the bearing area may be comprised of considerably more points of contact than noted by Bowden and Tabor. Instead of 9 contacts at a 0.007-inch diameter and 44 pounds, they measured many contacts of only a "few microns" (0.0001 to 0.0002 inch) under similar conditions. This evidence supports Archard's hypothesis of bearing area increasing directly with load through an increase in number of contacts.

The elastic theory would suggest that low slopes of irregularities of the fine finishes being considered applicable to valve seats would preclude the occurrence of plastic flow. The significance here is important when considering the effect of removing the load which allows, in this reversible process, a return to the original state of the surface.

Further substantiation of Archard's views of elastic behavior of surface asperities are provided by O'Connor (Ref. 24) in examining the role of asperities in transmitting tangential forces. An idealized surface with a sinusoidal profile is assumed in contact with a flat surface of the same material under an average pressure. For purely elastic deformation, the Hertz theory indicates real to apparent area of contact

$$\frac{A_r}{A_a} = 0.684 \left(\frac{P}{E} \frac{\lambda}{h} \right)^{1/2}$$

with

$$\frac{\lambda}{h} > 1.27 \frac{EP}{Y^2}$$

as required microgeometry for elastic behavior

where

A_a = apparent area

A_r = real area

E = elastic modulus

h = peak-to-valley height of surface asperities

P = average Hertz contact pressure

Y = yield strength

λ = wave length of surface asperities

For full plasticity, the required load is approximately 75 times that re-required for initial yield; therefore, the criterion for fully plastic behavior is:

$$\frac{\lambda}{h} < 0.017 \frac{EP}{Y^2}$$

Microscopic examination of several surfaces varying from rough-and-soft (λ/h of 5 and DPH* 145) to smooth-and-hard (λ/h of 30 and DPH 700) indicated a general correlation with the above analysis, i.e., the asperities of the soft material yielded plastically while the hard surface indicated no signs of yielding, either directly or with profile records. These experiments were performed using a normal load of 13,440 pounds between two surfaces, one of which was flat and the finish varied, and the other curved to a 30-inch radius with the surface hard and polished. The high, normal load resulted in elastic contact circles of approximately a 1/2-inch diameter and maximum contact pressures for the hard and soft materials of 83,000 and 53,000 psi, respectively. Although the asperities of the soft material yielded, its real area of contact was only slightly larger than the harder specimen. The A_r/A_a values for the soft metal that were calculated and microscopically measured was 0.28 at the center or maximum pressure area, whereas the calculated value for the harder material was 0.20.

The paper concludes that the majority of surface irregularities of typical engineering surfaces are deformed elastically, or at least do not reach the condition of full plasticity. Under these conditions, the area of real contact is determined by the surface topograph (λ/h) as well as hardness of the material, and is appreciably greater than a purely plastic analysis would suggest.

Generally supporting the theory that surfaces deform under load in a predominantly elastic mode is a significant collection of papers from the Soviet Union (Ref. 23), summarizing the results of studies on contact area. Of particular importance was the conclusion that real bearing area

---

*DPH = Vickers diamond pyramid hardness number increases with load as a function of increasing number of contacting asperities with the growth of individual asperity contacts contributing little to the total area. (It should be noted, however, that when the real bearing area becomes an appreciable fraction of the apparent area, the concept of individual contacting asperities fails and real area must increase with increase in the size of individually contacted asperities.)

The above concepts are generally supported by Greenwood (Ref. 26) who examined the influence of asperity distribution statistics upon contact area and compliance between rough surfaces and flats. He proposes a "plasticity index" for surfaces with spherical asperities which predicts elastic contact at heaviest loads for "polished and well run-in" surfaces. (This index is much the same as that of O'Conner's previously presented.)

SURFACE DAMAGE AND WEAR

The vast literature on friction and wear attests to the complexity of this subject. The purpose of this section is not to summarize the literature which has been accomplished by recognized authorities (Ref. 6, 27, 14 and 28), but to present a synopsis of related data which might lead toward an understanding of cyclic seating effects upon the closure geometry and leakage.

Elastic theory has shown that, for direct normal contact, material failure initially occurs below the surface. As tangential forces are applied, the maximum shearing stress moves up toward the surface (Ref. 29) and, with sufficient friction, exists at the surface. Overcoming frictional forces, interfacial slip with wear results.

For most valve seats, a period of cyclic service usually results in some change in the leakage characteristic. When leakage decreases with cycles, a "run or wear-in" process is thought of and for the converse, a "wear-out." A change in the leakage characteristic certainly denotes a change in the seating compliance (since seat loads are fixed) and, in the absence of changing external forces, a change in the surface profile. The converse assumption of constant leakage representing constant surface profile is not likely because the probable interplay between surface roughness, macroelastic and plastic strains due to contaminants and edge contacts, and wear from interfacial shear.

Plastic Strains

Substrate plastic strains with attendant change of geometrical form are a complex function of the impulse load and its distribution. Valve seating members having errors of form (taper, out-of-roundness, or parallelism) or which are imperfectly guided may be subject to such deformations depending upon the amount of error. Because of the geometrical complexity of most valve seating errors, a theoretical treatment for stress distribution which might allow an elastic design approach is generally not available (see Seating Analysis section for treatment of this subject).

Where initial impacts cause plastic deformation, subsequent cycles under like conditions will produce predominantly elastic deformation since the material has been deformed and strengthened to an equilibrium state. Interfacial compliance will be affected in proportion to the amount and location of plastically displaced material because this material must henceforth be elastically deformed by the fixed seat load. If the displaced material is above the plane of seating, leakage will be increased. Conversely, if material has been pressed into the seating plane, a decrease in leakage will result.

Experience has shown that, for functional valves, leakage is generally reduced with cycles up to some point, holds constant, and then increases. This characteristic involves a combination of plastic strain of the surface asperities and supporting substrate along with a wear process. The amount of leakage change and corresponding cycles is related to the surface profile and roughness, seating errors, material properties, and impact energy.

Valve seats undergoing plastic flow with each cycle ("brute-force" approach) generally have a relatively low cyclic capacity due to work hardening of the interface material. With work hardening and a fixed seat load, leakage might be expected to increase with cycles, ending in abrupt failure from surface fatigue. This is not to say such valves do not seal well. Indeed, many industrial valves hold very low leakage levels but at the expense of weight, heavy seat loads and short life.

Other valves employing liquid metal as interfacial material have been investigated (Ref. 30) and found to be capable of holding molecular leakage levels. However, many severe technological problems need to be overcome before a reliable cyclic capability is developed.

Wear

Because of the above complexities and the difficulties of measuring the minute dimensions associated with even large leakage changes, very little factually correlated experimental data on the mechanism of valve failures have been documented. Consequently, the many descriptions and hypotheses of seating mechanisms and subsequent failure modes are largely conjectural (including some of the preceding discussion). This leaves little from which to draw any conclusion as to the predominant wear process in seating.

A review of the literature has indicated that,while the laws of friction have been fairly well substantiated, there are no satisfactory laws for wear. As a result, the design of equipment considering wear must be based upon direct experimental evidence and guided by the documented test data of many researchers.

Rabinowicz (Ref. 14) describes four basic types of wear as:

1. Adhesive wear. This is the most common form of wear. Junctions are formed between sliding surfaces which subsequently shear in either of the two metals or at the interface, depending upon relative strengths.

2. Abrasive wear. Surfaces are worn by the plowing action of hard particles.

3. Corrosive wear. Surface films formed by a corrosive environment are worn away so that corrosion continues.

4. Surface fatigue wear. Repeated high contact loads induce surface and subsurface cracks which eventually break up the surface leaving relatively large pits.

Wear has also been more generally divided into its most predominant forms by Tabor (Ref. 28) as mild and severe wear. Below a certain load, it has been observed that interfacial shear occurs and wear is small (mild wear); above this load, wear rises catastrophically to values that may be many times greater (severe wear). In severe wear, the loss of material is mainly due to subsurface shearing of the weaker metal.

When wear is due mainly to the shearing of junctions (i.e., adhesive wear), an empirical relation for the value of wear per unit distance of travel is:

$$Z = \frac{KW}{3p}$$

where (K) represents the percent of friction junctions producing wear, (W) is the applied load, and (p) is the hardness of the wearing surface. Tabulated values for (K) show that the wear rate between two surfaces is reduced by: (1) use of hard materials, and (2) use of materials with low interaction, i.e., unlike materials of low solubility.

The above relationship does not, however, provide any information about the change in surface texture with wear. Rabinowicz (Ref. 14) has shown that, in some cases, wear particle sizes can be predicted on the basis of elastic surface energy and hardness properties. Considerable data have been abstracted from the literature and combined with experimental results in application of this theory to sliding metallic seals (Ref. 31). While the theory has been correlated for experiments using soft metals, no data are given for the various combinations of harder metals known to have the best wear characteristics.

Fretting. In many cases, wear takes place in various combinations and degrees. One of these which has received considerable attention is fretting, or more commonly, fretting corrosion. A thorough summary of fretting prepared by Harry Diamond Laboratories (Ref. 32) describes the test methods, results, and conclusions from over 200 reports obtained from the English literature.

Fretting is caused by small oscillatory tangential motions between two materials. The process normally involves relatively large numbers of cycles, occurs over a wide range of loads, and is usually accompanied by a formation of corrosion products which are a function of material and environment. The mechanism of fretting appears to be a wear process involving adhesion that is further accelerated by corrosion and abrasive wear from the corrosion products. However, fretting has been produced in literally all material combinations and various atmospheres (including a vacuum); therefore, corrosion is not necessarily a part of the process. Fretting corrosion factors (Ref. 32) of potential significance to poppet and seat design are listed below:

1. Load. As load on the test part is increased without changing other factors, relative slip gradually decreases. Weight loss (due to wear) has corresponding increase, reaches a maximum, and then decreases to zero when the parts are sufficiently loaded to preclude slip.
2. Slip Amplitude. Fretting is generally recognized to occur from oscillating motions between 5×10^{-8} and 10^{-2} inches. In general, the wear rate is proportional to the slip amplitude.
3. Slip Frequency and Duration. While fretting wear is not greatly dependent upon the frequency of oscillations, it is proportional to the total number of oscillations. Therefore, parts subject to the higher frequencies would be expected to suffer the greatest wear (assuming constant slip amplitude).
4. Temperature. Fretting increases with lower temperatures with the worst condition reported for steel in air at -240 F. Fretting has also been produced at -300 F. Between 32 and 300 F, fretting

was almost constant. It would appear that high surface temperatures do not generally occur due to fretting (see bibliography in Ref. 32 for specific materials).

5. Atmosphere. Oxidation is an important consideration in determining the amount of damage; hence, the presence of oxygen and water vapor affect the rate of fretting. For ferrous materials, it is essentially the controlling factor in the damage process. Increases in wear of from 3 to 10 times have been observed for changes in atmosphere from nitrogen to air. However, tests made in a vacuum indicate that even though oxidation is suppressed, damage may be increased. Tests in a helium atmosphere indicate damage is caused almost entirely by metal transfer.

6. Materials. In general, softer materials fret more than hard materials. Metals which form hard, abrasive oxides (such as aluminum, chromium, and tin) are particularly susceptible. Aluminum and stainless steel form hard oxide debris (Al_2O_3 and Cr_2O_3), and also very rapidly oxidize and absorb oxygen upon exposure to fresh air. Stainless steel is reported as being the most susceptible of all materials to fretting. (While literally all materials fret to some degree, even with lubrication, it would appear that the extent must be determined for a specific application, choosing materials most suitable.)

7. Surface Roughness. In general, the finer the surface the more susceptible to fretting wear. No data have been reported on terminal surface roughnesses produced by fretting.

In the case of curved contact surfaces such as bearings, it has been shown that fretting can result from small tangential loads, even though there is no gross slipping (Ref. 24, 33, 34 and 35). Because of the elliptical pressure distribution under normal load between curved surfaces, a small annular area at the edge of contact exists in which any externally applied tangential force must exceed the frictional restraining force. This is caused by the elastic lateral deformation in the higher loaded central area of the contact which governs the total motion between the contacting parts. Thus, as the contact pressure diminishes to zero toward the contact edge, a point is reached where the frictional force from local normal load is exceeded by the tractive force. Tractive forces between curved surfaces can be applied externally as a straight tangential load or couple.

Another more subtle source of interfacial tractive forces occurs when materials are pressed together which do not deform laterally in like fashion due to either unlike configuration or different elastic properties (shear modulus and Poisson's ratio). Goodman (Ref. 36) has described analytically the second case occurring between normally loaded, perfectly rough spheres.

Even when like materials were used in cyclic normal loading between spheres, fretting has been observed (Ref. 33). However, this was attributed to the likely possibility that the vibration within the cycling apparatus caused small tangential forces to be applied to the contact area.

Contamination

For the most part, the stringent weight and performance requirements for rocket engine control valves has precluded the brute force approach to seating. The survey of numerous valve designs in the initial program effort (Ref. 37) and other component development and test programs (Ref. 38, 39 and 66) has shown the need for hard poppets and seats with light seat loads and close guidance of moving members. The consequence is a requirement for finer surfaces, narrower seat lands with an attendant increased sensitivity to contamination.

Reference 41 presents a comprehensive summary of contamination, its nature, externally viewed effects (sticking poppets, leakage, etc.), cleaning and control methods, and considerations in design. Review of this and other literature will show that little has been accomplished in quantitatively defining either the source/volume of contaminants or their effect on valve seating. Consequently, filtration and cleaning requirements are based upon generalization of contamination sensitivity and availability of commercial products rather than detailed knowledge of the real problem. This is manifest in numerous failure reports citing contamination as the cause of malfunction.

SURFACE-FINISHING METHODS

Surface-finishing methods capable of generating surface quality and precision applicable to rocket engine control valve seating are turning, grinding, lapping, and polishing. While turning and grinding may not generally be associated with the very smooth surfaces, roughness as low as 2-microinch AA for turning, and 1-microinch AA for grinding is possible (Ref. 1).

A survey of the literature indicates that little information relating a specific finishing operation with the resultant surface texture has been published. This is particularly true for surfaces commensurate with precision valve sealing, i.e., less than 16-microinch AA. It is suspected that considerable unpublished information exists but is not disseminated for proprietary (competitive) reasons.

Most researchers consider the noted operations from a production basis and are concerned with the economical removal of metal. However, the literature does document operation fundamentals, theories of the metal cutting mechanism and some process effects on the workpiece and general surface texture-metal removal relationships.

Turning

To produce a precision-turned surface the machine tool must be in excellent condition. However, even the best conventional machines are inadequate for some purposes. The duPont Company, for instance, has applied the hydrostatic gas-lubricated bearing principle to several machine tools. One, with a design target of producing 4-inch-diameter hemispheres true within ±25 microinches has turned aluminum parts of this type round within approximately 1-microinch with a 2-microinch rms roughness (Ref. 42).

Other considerations regarding the turned surface are:

1. In general, the higher the cutting speed, the smaller the roughness (Ref. 43).
2. Lapped cutting tools have a sharper, more uniform cutting edge (Ref. 44). (It follows that improved surface roughness results.)
3. For a given cutting condition, improved surface roughness will result with successive changes from high-speed steel, to carbide to ceramic and diamond tools (Ref. 45).
4. The conglomerate of welded chip particles forming on the cutting tool face called "bue" (built-up edge) is detrimental to surface texture. Increased cutting speeds reduce this formation and its detrimental effect (Ref. 45 and 46).
5. Surface temperature at the tool tip is quite high with observed values greater than 500 F and increases with cutting speed. Tool wear and surface texture deterioration are accelerated with temperature increases (Ref. 47, 48, and 49). (This implies that workpiece surface metallurgical transformations are likely.)

Grinding

In the grinding process, metal is removed in chip form although very brittle materials may disintegrate into dust particles. Three distinct actions are involved: (1) rubbing, where some abrasive grains do little more than elastically deform the surface, (2) plowing, when there is insufficient interference between grain and work, and the metal is simply plastically pushed aside, and (3) cutting or chip removal (Ref. 50 and 51).

Grinding as a mechanical process is almost unique in the creation of very high interface temperatures. The heat, however, is conducted more quickly into the workpiece than through the interface between the work and grinding fluid. Thus, all the fluid can do is remove the heat from the workpiece after it has produced whatever change it can induce. While plastic deformation produces residual compressive stresses, the heating action results in tensile stresses. Furthermore, hard metals may be tempered to a lesser hardness or increased hardness may be caused by transformation of austenite to martensite or by cold-working the austenite. Thus, the properties of the metal surface may be radically different from the unaffected substrata. The temperature present during the cutting action cannot be deduced from the spark stream or surface discolorations. Since wheel trailing edge cutting may remove oxides, the absence of an oxide film does not necessarily mean that excessive temperatures were not generated (Ref. 50).

The two principal ingredients of a grinding wheel are the abrasive grains and the bond which holds them together. The three abrasive grains most commonly used are aluminum oxide, silicon carbide, and diamond, which are available in several varieties differing primarily in friability, a measure of fracturing ease to provide new cutting elements. Wheel bonds employed are vitrified clay (most commonly used), organic materials, and metal (Ref. 50). From the recommended uses and applications (Ref. 43), it would appear that, for hard valve sealing surfaces, a soft organic bond such as shellac with diamond grit (minimal wear, hence, consistent cutting) might provide an optimum cutting combination. However, no references were noted relating grinding process and specific wheel to the roughness produced.

Lapping

Lapping is an abrasion process used to establish size, geometry, or fine texture at extremely small tolerance levels. In the production flat lapping operation, surface roughness of 2- to 3-microinch AA is usually achieved using close-grained cast-iron laps. While it is commonly believed that the lap should be softer than the workpiece, production lapping of soft steels and nonferrous metals such as aluminum and copper with cast-iron laps is successfully accomplished (Ref. 44).

The soft-lap philosophy presumes the lapping action is performed by embedded abrasive. However, some question as to the exact cutting mechanism exists. Hawxhurst (Ref. 44) indicates that the amount of embedded abrasive is negligible, does little cutting, and is removed by subsequent cleaning. This theory suggests the lapping action to be one of occasional cutting by rolling or suspended abrasive particles.

In another experiment (Ref. 52) the amount of abrasive embedded in the lapped workpiece was measured by radiation techniques. It was found, for example, that tool steel lapped with 11- to 28-micron silicon carbide having a vehicle-to-abrasive ratio of 18:1 on a cast-iron plate and following a 3-minute scrub under running water, retained approximately 24,000 abrasive particles/sq in. Although not measured, it was concluded that the cast-iron lap employed had also retained a significant amount of abrasive.

True chips are formed in the lapping process until the abrasive particle size approaches the 8-micron dimension. With smaller sizes, it is believed that the process is limited to plastic deformation without chip formation (Ref. 53). However, recent experiments (Ref. 54 and 55) suggest a mechanism for cutting at this level.

The most commonly used abrasives are manufactured silicon carbide and aluminum oxide which are preferred over natural abrasives since they have low impurity level and exhibit definite hardness, toughness, and friability properties. Aluminum oxide, for instance, is available in as many as five types varying in the noted properties. Other natural abrasives predominantly used are corundum, emery, and garnet (Ref. 43).

In the lapping process, the abrasive is suspended in a carrying agent or vehicle which is designed to suspend the abrasive particles, cool the working surfaces, float or lubricate the workpiece, and carry off spent abrasive and chips produced by the operation. The vehicle is generally a petroleum base of low viscosity with additives which increase body, strength, and cohesion to keep the abrasive in suspension. Water-soluble vehicles are also used (Ref. 44).

Abrasive size grading is based on National Bureau of Standards criteria and specified by a number which represents the approximate number of openings per linear inch in the screen or mesh used for grading. Grades smaller than 400-mesh size are specified in micron ranges (Ref. 44). (An elutriation process is used for smaller size grading where mesh straining or sieving is impractical. Diamond compound, for instance, is available in the 0- to 0.1-micron range. Shape grading is apparently a function of industry competition.) An indication of potential surface roughness and the relationship of grain size and grade for diamond abrasive is shown below (Ref. 56):

Grade No.	Grain Size, micron	Grit Size Mesh, equivalent	Microinch AA	
			Metal Lap	Soft Lap
	(For fast stock removal)			
60	35 to 85	230	20 to 25	3 to 4
45	30 to 60	325	10 to 15	2 to 3
30	20 to 40	600	6 to 8	1 to 1.5
	(General purpose)			
15	8 to 22	1,200	4 to 5	0.5 to 0.75
9	6 to 12	2,000	3 to 4	0.5
6	4 to 8	3,000	3	0.4
	(Finest select work)			
3	1 to 5	8,000	2	0.2
1	0 to 2	14,500	1	0.0+
1/2	0 to 1	50,000	0.5	0.00

Polishing

It is common practice to brighten metal surfaces by rubbing them against a series of successively finer abrasives, generally by machine operations. The resultant surface, however, depends largely upon the way the abrasive is used. If the abrasive is firmly bonded to a cloth, paper, or similar backing, a surface containing obvious scratches which diffuse light, causing a somewhat dull appearance, is generally produced; this is considered an abraded surface. If, however, the same abrasive is used as an unbonded slurry on a soft cloth pad, it may produce a bright mirrorlike appearance on the polished surface (Ref. 54 and 55).

The nature of the polished surface and the mechanism of producing it is still subject to discussion. Beilby postulated that material was smeared over the surface to fill in the pre-existing irregularities, leaving a surface covered with an amorphous-like layer. This Beilby layer theory has for some time been the accepted mechanism of polishing. Bowden and Hughes refined the theory by proposing a thermally activated process where asperities are locally melted and deposited in adjacent depressions, thus gradually filling them and leveling the surface.

Samuels (Ref. 54 and 55) in reporting these developments, however, suggests that new evidence indicates polishing is primarily a cutting mechanism. This theory considers plastic shearing of surface layers, gradually cutting away the irregularities, and replacing them by a set of much finer ones. The resultant surface is compression-plastically deformed and fully crystalline; a Beilby layer is not formed.

It should be noted that, while polishing with soft-cloth pads can improve a metal surface, unlike lapping on a precision flat surface, it will not correct errors of form.

LEAKAGE FLOW ANALYSIS

DEFINING PARAMETERS

In considering the leakage and flow across a valve seat, a number of equations must be taken into account. These range from the nozzle equation which generally applies to the wide open valve to the viscous and molecular flow equations applicable under seated conditions. The equations derived in this section are presented for compressible and noncompressible fluids for flow through parallel plates. The equations are equally applicable to flat, conical, and spherical valve configurations because the near and on-seated passage configurations approximate the parallel plate model. Because of the importance of the laminar flow regime, the special case of taper in the direction of flow is also considered.

A specific example of nitrogen flow through a model valve seat is presented which shows how each flow regime blends into the next to build the overall flow-leakage characteristic curve. As the flow regime boundries are not sharply defined, the example additionally illustrates the range over which the various equations may be applied.

Nozzle Flow

The compressible and incompressible flow equations derive from the basic Euler momentum relationship. The Euler equation gives the following relationship between velocity, pressure, and density:*

$$\frac{V^2}{2g} + \int \frac{dP}{\rho} = \text{constant}$$

---

*See pages 61 and 62 for nomenclature.

For the incompressible consideration, density (ρ) is constant, and the resultant relationship is known as the Bernoulli equation. If the inlet velocity is neglected, the following equation evolves for flow of an incompressible fluid through a nozzle:

$$\omega = CA\sqrt{2\ g\ \rho\ (P_1 - P_2)}$$

This equation requires a discharge coefficient (C) to correct the ideal frictionless flow to the actual case. The discharge coefficient is a function of the specific configuration being considered, therefore, it is derived from emperical data.

For the specific application of this equation to a valve configuration, area (A) is the minimum flow opening expressed as a function of the stroke height (h_p) and the minimum seat perimeter. This substitution can be made in the nozzle and the turbulent channel equations. For circular valve seats where the radial land width (L) is small with respect to the ID, it is convenient to assume a mean seat perimeter $W = \pi D_s$, where (D_s) is the mean seat diameter.

With compressible flow, the density is not constant and therefore the integral of dP/ρ must be evaluated for specific assumptions. For an adiabatic, frictionless process considering a perfect gas, the following equation is derived:

$$\omega = \frac{CAP_1}{\sqrt{RT_1}}\sqrt{gk\left(\frac{2}{k+1}\right)^{\frac{k+1}{k-1}}}$$

As in the case of the incompressible flow, a discharge coefficient is required to account for the irreversibility of flow. The above equation further assumes that choked or sonic flow exists across the nozzle.

In practice, leakage is most often expressed in terms of a volumetric flow. For compressible fluids, where density is a variable function of pressure and temperature, standard conditions (P_s, T_s, ρ_s) must be defined. The conversion relationship for all fluids is :

$$Q = \frac{\omega}{\rho_s} = \omega \frac{RT_s}{P_s}$$

Therefore, for both incompressible and compressible flow at standard conditions, the weight and volumetric flows differ by a constant.

The nozzle equations can be applied to a poppet valve configuration (similar to an orifice) from the wide open condition to the near-seated position. When the valve closure height has decreased to the position where wall friction at the seating surface (and thus land length) is significant, the nozzle regime terminates and turbulent channel flow commences. There is no precise point at which nozzle flow terminates, the transition being a complex function of the particular channel geometry and Reynolds number. However, in general, if the length to height ratio is 10 or greater, channel flow is imminent.

Turbulent Channel Flow

In this flow regime, the same basic continuity and momentum considerations hold with the addition of a term for the effects of friction. In the case of an incompressible fluid, the basic Bernoulli equation is modified to the form

$$\Delta P = \frac{fL}{D} \frac{\rho V^2}{2g}$$

where flow is defined by continuity as

$$\omega = \rho A V$$

The first equation expresses differential pressure as a function of friction factor (f) and velocity (V). The friction factor is related to velocity through emperical parametric curves of friction vs Reynolds number and wall roughness (Moody diagram Ref. 57). The solution to these equations is by trial and error.

The equations for flow in the turbulent channel regime were developed for flow-through circular tubes. To apply the equations to other channel configurations, the tube diameter in these equations must be expressed in terms of hydraulic diameter (D). Hydraulic diameter is defined as four times the ratio of the cross-sectional area to the wetted perimeter. For parallel plates, the hydraulic diameter is equal to twice the plate spacing ($2h_p$).

The equations used to compute compressible fluid flow in this regime are obtained from Shapiro (Ref. 58). They assume an adiabatic constant-area flow and include the effects of internal fluid and wall friction and fluid momentum. To compute the weight flowrate, two equations are required. The first is a relationship between entrance mach number (M) and friction factor (f) for the condition of choked flow at the exit of the valve seat channel (M=1)

$$\frac{fL}{D} = \frac{1-M^2}{kM^2} + \frac{k+1}{2k} \ln \frac{(k+1)\, M^2}{2\left(1+\frac{k-1}{2} M^2\right)}$$

As in the incompressible case, the solution of this equation is by trial and error. Shapiro's text gives considerable assistance in the solution of this equation by tabulating fL/D vs Mach number, thus permitting interpolation of desired information. For the subsonic solution, reference is made to Shapiro's text.

Once the entrance Mach number and density are determined, they are used in the continuity equation to compute the weight flowrate based on the inlet conditions

$$\omega = \rho\, AM \sqrt{k\ g\ RT}$$

The equations in this section are confined to the turbulent flow regime, i.e., Reynold numbers greater than 2000. However, these equations can be extended into the initial portion of the laminar flow regime where fluid momentum is still an important consideration. In this case, the friction factor is a linear function of Reynolds number and is given for the parallel plate consideration as

$$f = 96/Re \qquad \text{and} \qquad Re > 500$$

The defining equation for Reynolds number is:

$$Re = \frac{VD\rho}{\mu g}$$

As before, (D) refers to the hydraulic diameter for other than round configurations. For the parallel plate consideration of a circular valve seat, this equation may be reduced to:

$$Re = \frac{2\omega}{W\mu g}$$

Laminar Flow

The analysis of fluid flow in this regime assumes that the temperature is constant (isothermal), that the fluid momentum effects are negligible, and that viscous shear forces govern the flow, i.e., Reynolds number less than 500. These assumptions result in the Poiseuille equation for flow through stationary flat plates (Ref. 59):

$$-\frac{dP}{dX} = \frac{12\,\mu\, V_{average}}{h^2}$$

By using the continuity equation, the relationship is reduced to express the viscous flow through flat plates:

$$\omega = \frac{\rho\, W h_p^{\,3}\,(P_1 - P_2)}{12\mu\, L}$$

For a compressible gas, thermal effects are present; however, the assumption of isothermal condition can be made because of the small channel thickness and low velocity. The compressible version of the Poiseuille equation is obtained by assuming an average density across the seat land and a perfect gas; therefore,

$$\omega = \frac{Wh_p^3 (P_1^2 - P_2^2)}{24\mu \, LRT}$$

This same basic relationship can be derived for flow between circular flat plates. This equation contains the natural log of the radius ratio which accounts for radial divergence of the flow and is as follows:

$$\omega = \frac{\pi h_p^3}{12\mu \ln \frac{R_o}{R_i}} \left(\frac{P_1^2 - P_2^2}{RT} \right)$$

Normally, this divergence can be neglected as the R_o/R_i ratio is close to unity.

For the special case where convergent or divergent taper exists between seating surfaces, the equivalent parallel plate separation becomes

$$h_e = \frac{2h_p^2 (h_o + h_p)^2}{h_o + 2h_p}$$

where (h_p) is the separation at the narrow end of the land (L) and $(h_o + h_p)$ the separation at the wide end. Thus, for $h_o = 0$, $h_e^3 = h_p^3$. (See Seating Analysis section for further discussion and data on taper flow.)

Transition and Molecular Flow

The determination of molecular flow involves the application of the kinetic theory of gases. A flow equation derived (Ref. 60) for the molecular regime is as follows

$$Q = \frac{4}{3} \frac{V_a}{\int_o^L \frac{H}{A^2} \, dL} (P_1 - P_2)$$

This equation relates the flow (Q) to the mean molecular speed (V_a), differential pressure $(P_1 - P_2)$, and geometry where (H) is the channel perimeter. When this basic relationship is applied to parallel planes, the equation has the form:

$$\omega = \frac{4}{3} \sqrt{\frac{2}{\pi}} \frac{W h_p^2}{L} \frac{(P_1 - P_2)}{\sqrt{\frac{RT}{g}}}$$

There exists a transition region where both molecular and laminar (viscous) flow effects are operating. The limits of these regions are approximately defined by the ratio of mean free path of the molecule (λ') to the characteristic dimension of the channel (h_p) when:

$\lambda'/h_p < 0.01$, flow is viscous

λ'/h_p is 0.01 to 1.0, transitional flow exists

$\lambda'/h_p > 1.0$, flow is molecular

From kinetic theory of gases, the mean free path of gas molecules is given as

$$\lambda' \cong \frac{\delta\mu\sqrt{RTg}}{P}$$

where δ is a constant. At atmospheric pressure and 70 F, the computed value of δ is nearly constant (~1.8) for nitrogen, helium, argon, and hydrogen gases. Assuming at high pressures that $\bar{P}$ is the mean channel pressure, the average mean free path reduces to:

$$\bar{\lambda}' \cong \frac{3.6\,\mu\sqrt{RTg}}{P_1 + P_2}$$

The separation at midtransition flow may be found by equating the molecular and laminar flow equations and is given by:

$$h_p = \frac{25.5\,\mu\sqrt{RTg}}{P_1 + P_2}$$

The corresponding ratio of $\bar{\lambda}'/h_p$ is 0.14. A modified equation proposed for flow in the transition region is:

$$\omega_{total} = \omega_{viscous} + \epsilon\omega_{molecular}$$

The molecular flow factor (ϵ) is generally close to unity. It takes into consideration such items as the difference in gases and physical properties of the passage walls. For simplicity and in lieu of explicit test data, (ϵ) has been assumed as unity.

Throughout the entire range of laminar and molecular flow, the flowrate computed from each of the specific equations will predominate in its applicable regime of flow. Thus, the summation equation above may be used without regard to regime boundary since the flow computed for the regime outside of its range will be negligible (see Sample Computation).

STATIC PRESSURE DISTRIBUTIONS

Static pressure distribution across a valve seat is of interest to the valve designer in determining the forces associated with a particular configuration. These forces determine such external performance parameters as cracking and reseat in relief valves or influence stability in the case of regulators. The theoretical aspects of pressure distribution for the various flow regimes are discussed in the subsequent paragraphs.

Nozzle Flow Regime

There has been a considerable amount of analytical work conducted on converging nozzles, particularly for compressible flow. However, the particular model under investigation has essentially constant cross section along the flow path; therefore the model is analogous to a short-tube orifice. The pressure profile along this orifice configuration is similar to the converging nozzle because the flow separates from the walls after entering the seating separation and exits with the stream contracted (vena contracta). Unfortunately, this analysis is basically qualitative, and the determination of the pressure profile in this configuration must be determined experimentally.

Turbulent Channel Flow Regime

For the incompressible fluid, the pressure drop is a direct function of the length of the path; therefore, the pressure profile is a straight line across the seat land. This results in an effective seat diameter location at the land midpoint.

The pressure distribution for the compressible gas consideration is somewhat more complex. Shapiro's equation discussed previously is based upon sonic exit velocity and that the corresponding length computed is for a specific inlet velocity. By assuming various channel lengths and computing the inlet conditions, the pressure profile can be determined for the complete channel. In general, the pressure profile along the channel approximates a straight line for the higher Reynolds numbers. However, as the valve model closes (corresponding to a decrease in h_p and Reynolds number), the pressure profile progressively approaches the parabolic shape found in the laminar flow regime.

Laminar Flow Regime

Unlike the analysis of pressure distribution in the nozzle and turbulent channel regimes, the laminar consideration is straightforward. A general equation for pressure profile may be derived from the laminar flow equation. For parallel and tapered plates, the pressure at any point across the seat land is:

$$P = P_1 \left\{ 1 - \beta \left[1 - \left(\frac{P_2}{P_1} \right)^n \right] \right\}^{1/n}$$

For incompressible flow, n = 1; for compressible flow, n = 2. Equations for β are:

1. Parallel Plates

$$\beta_P = \frac{X}{L}$$

2. Convergent Plates

$$\beta = \frac{X}{L} \; \frac{\left[2\left(1 + \frac{h_p}{h_o}\right) - \frac{X}{L} \right] \left(\frac{h_p}{h_o} \right)^2}{\left[2\left(1 + \frac{h_p}{h_o}\right) - 1 \right] \left(1 + \frac{h_p}{h_o} - \frac{X}{L} \right)^2} = \beta_c$$

3. Divergent Plates

$$\beta = \frac{X}{L} \; \frac{\left(2\frac{h_p}{h_o} + \frac{X}{L} \right) \left(1 + \frac{h_p}{h_o} \right)^2}{\left(2\frac{h_p}{h_o} + 1 \right) \left(\frac{h_p}{h_o} + \frac{X}{L} \right)^2} = \beta_d$$

The profile described by the parallel plate equation is linear for incompressible flow and parabolic for compressible flow. Seat land taper causes the profile to be biased in the direction of the narrow opening as shown on the following page.

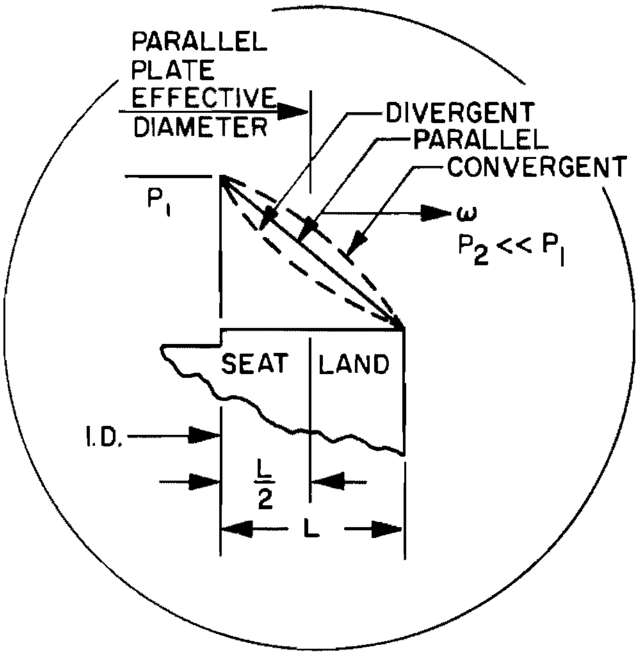

INCOMPRESSIBLE FLUID

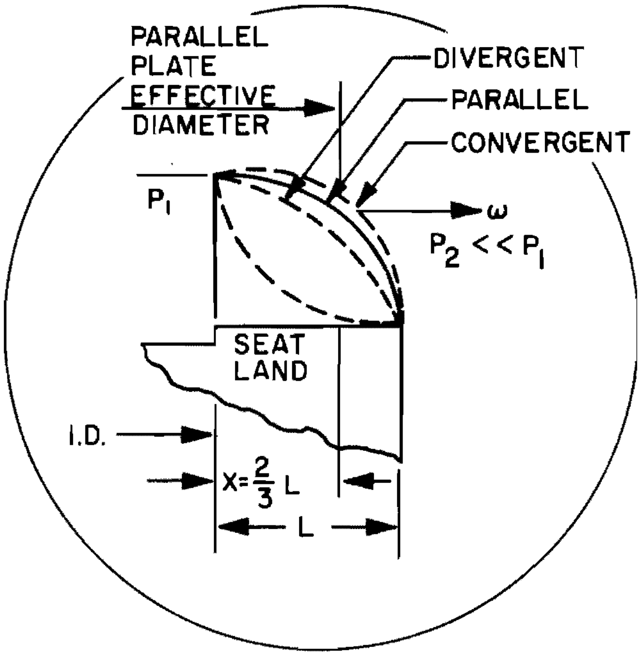

COMPRESSIBLE FLUID

Integration of the parallel plate profile equation for average pressure gives the following for incompressible flow:

$$\overline{P}_i = \frac{P_1 + P_2}{2}$$

for compressible flow:

$$\overline{P}_c = \frac{2}{3} \frac{P_1^3 - P_2^3}{P_1^2 - P_2^3}$$

For high-pressure valves leaking to atmosphere, (P_2) may be neglected, thus the average pressure reduces to:

$$\overline{P}_i \cong \frac{P_1}{2} \quad \text{and} \quad \overline{P}_c \cong \frac{2}{3} P_1$$

It follows that for (L) small relative to the ID, the effective seat diameter for laminar flow compressible media is located at 2/3 the distance across the seat land and the effective diameter is given by:

$$D_e = D_s + \frac{1}{3} L$$

For most valve seats, the land is relatively narrow and the ID circumference is very nearly equal to the OD circumference. Thus, the effect of radially spreading flow (divergence) may be neglected and the above equations are applicable. When the seat land width becomes sufficiently large with respect to the ID, radial divergence must be considered. Hence, for parallel plates:

$$\beta = \frac{\ell n \frac{R}{R_i}}{\ell n \frac{R_o}{R_i}} \qquad (R = R_i + x)$$

The effect of radial divergence is to straighten out the parabolic curve and, for the extreme case, reverse the curve so that the effective diameter is less than the land midpoint.

Detail consideration was not given to the transition and molecular pressure distributions because these flow regimes almost always occur under highly stressed seating conditions; therefore, the force resulting from small differences in the effective seat area is negligible relative to the total seat force.

SAMPLE COMPUTATION

To illustrate how the previously developed flow equations are used, the following sample computation is presented. The seat model selected is the 1-inch configuration used in the off-seat leakage tests. A cross section of this seat configuration is shown in Fig. 8. Flow is from the

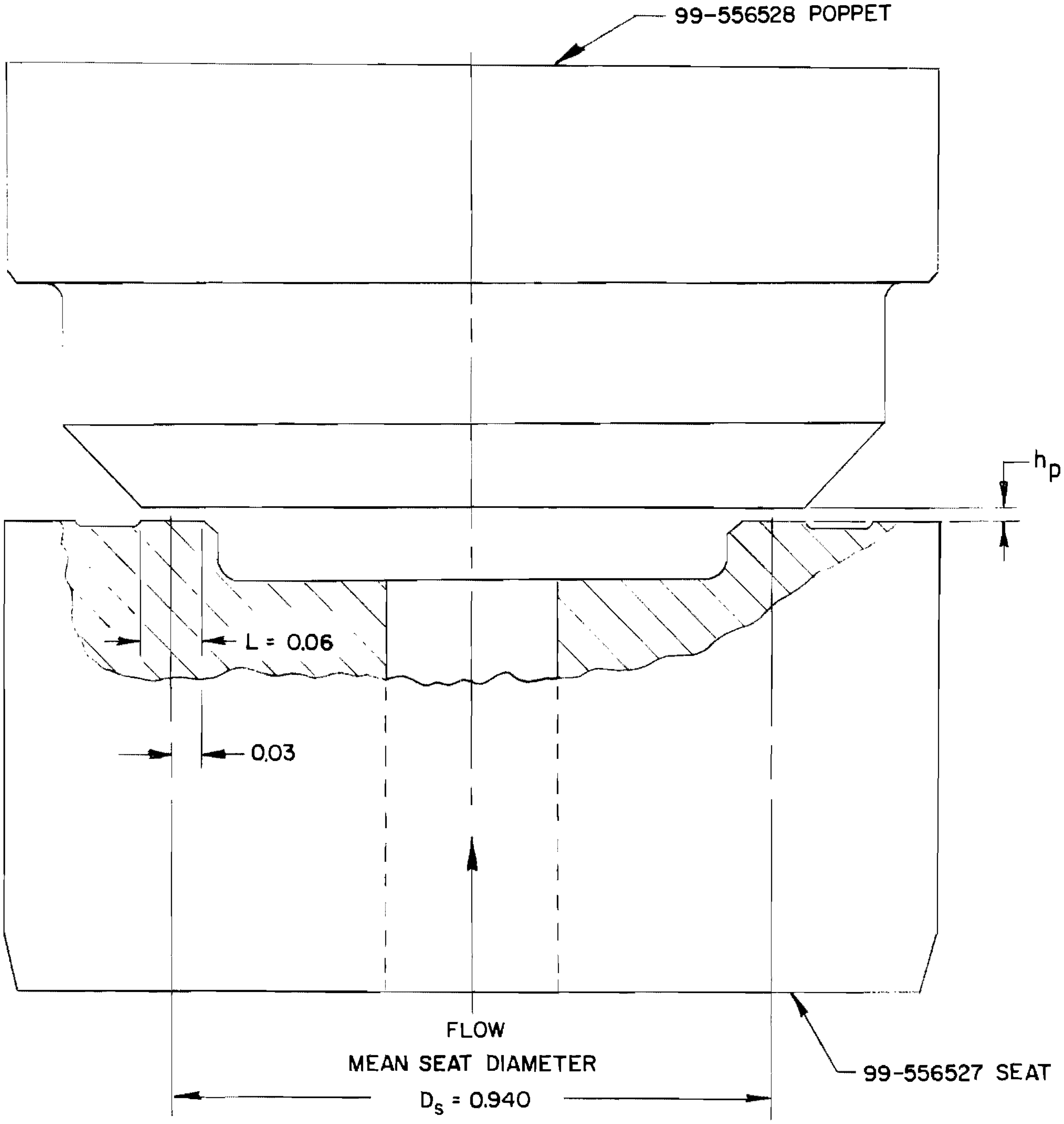

Figure 8. Typical 1.0-Inch Poppet and Seat Model

inside (ID) to the outside (OD) of the 0.060-inch flat seat land. Leakage has been computed for nitrogen gas at a 100-psig inlet pressure, a 70 F inlet gas temperature, and a 14.7-psia outlet pressure.

Figure 9 presents the leakage spectrum for the sample computation. The various flow regimes, i.e., nozzle, turbulent channel, laminar, transitional, and molecular are identified on the curve. Also, the limits of each regime are shown. A range of theoretical parametric data has been computed for various pressures and gases and is presented with the test data in the Experimental Test Program section.

The following parameters are known values for this seat configuration and are used in the flow equations to compute the noted leakage characteristics.

Discharge coefficient	$C = 0.95$
Gravitational acceleration constant	$g = 1.39 \times 10^6$ in./min^2
Specific heat ratio	$k = 1.4$
Channel length or land width	$L = 0.060$ inch
Inlet pressure	$P_1 = 114.7$ psia
Discharge pressure	$P_2 = P_s = 14.7$ psia
Gas constant	$R = 663$ in./R
Absolute temperature	$T_1 = T_s = 530$ R
Channel perimeter (πD_s)	$W = 2.95$ inches
Absolute viscosity	$\mu = 4.40 \times 10^{-11}$ lb-min/in.^{2}

Nozzle Flow

For a compressible fluid flowing sonically the following equation is used:

$$Q = \frac{RT_s}{P_s}\left[\frac{C\,Wh_p\,P_1}{\sqrt{RT_1}}\sqrt{gK\left(\frac{2}{k+1}\right)^{\frac{k+1}{k-1}}}\right]$$

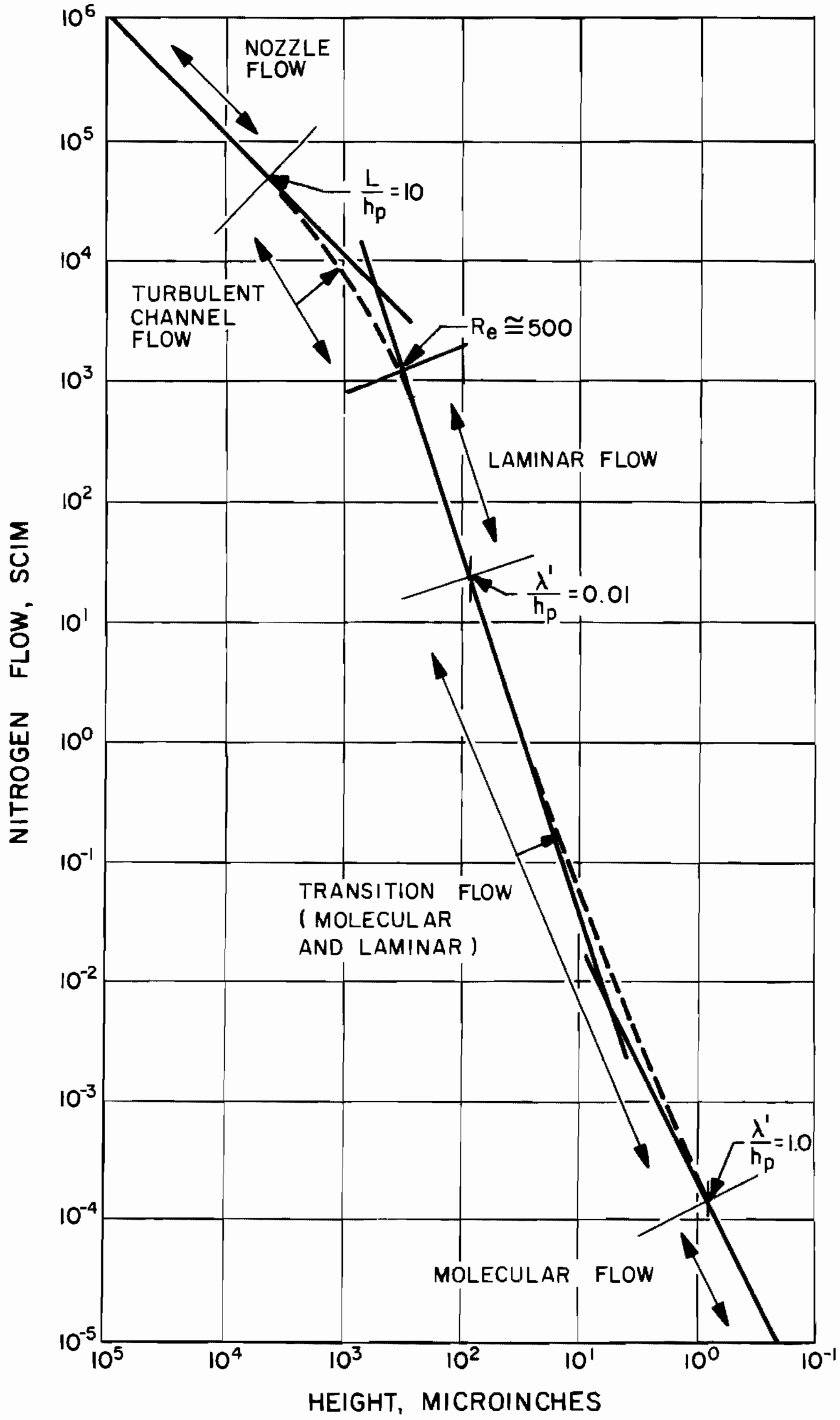

Figure 9. Theoretical Nitrogen Flow Through the Valve Model Shown in Fig. 8.

Using the assumptions and data outlined:

$$Q = 1.045 \times 10^7 h_p$$

The orifice flow ceases, and turbulent channel flow commences at a height (h_p) of approximately 6×10^3 microinches (Fig. 9). The land width is 0.060 inch giving an L/h_p ratio of 10 for the break point.

Turbulent Channel Flow

Flow in this regime is defined by a curve on log-log paper; therefore, a sample calculation of one point will illustrate the method used. Leakage is computed for a stroke height (h_p) of 0.001 inch in the following steps:

1. Hydraulic diameter, $D = 2h_p = 0.002$ inch
2. A friction coefficient (f) is estimated at 0.040. This is the starting point for the trial and error solution; (f) will be verified at the conclusion of this computation.
3. Compute $fL/D = \frac{fL}{2h_p} = 1.20$
4. Using Table B-4, Ref. 58 and the equation

$$\frac{fL}{D} = \frac{1 - M^2}{kM} + \frac{k+1}{2k} \ln \frac{(k+1)\, M^2}{2\left(1 + \frac{k-1}{2} M^2\right)}$$

   yields entrance Mach number $(M_1) = 0.49$.

5. Assuming an isentropic entrance condition, entrance static presure (P_1) can be computed from the following equation (Ref.58) where P_o is the stagnation (total) pressure of 114.7 psia, and M is the entrance Mach number

$$\frac{P_o}{P_1} = \left(1 + \frac{k-1}{2} M^2\right)^{k/k-1}$$

   therefore, static entrance pressure, $(P_1) = 97.3$ psia.

6. Again, assuming isentropic conditions, the entrance static temperature (T_1) is computed from the following equation for a total temperature (T_o) of 530 R.

$$\frac{T_o}{T_1} = 1 + \frac{k-1}{2} M^2$$

therefore, static temperature (T_1) = 506 R

7. The following series of equations are used to compute the flow (Q) in the channel

$$V_1 = M \sqrt{kg\ RT_1}$$

$$\rho_1 = \frac{P_1}{RT_1}$$

$$A = Wh_p$$

$$\omega = \rho_1 AV_1$$

$$Q = \omega \frac{RT_s}{P_s}$$

from which the flow, Q = 8090 scim

8. To prove the flow computation, the originally estimated friction coefficient (f) is checked. Reynolds number is first computed:

$$Re = \frac{DV_1\rho_1}{\mu g} = 3.76 \times 10^3$$

Using the computed value for Reynolds number, a friction coefficient is determined from the Moody diagram. The friction coefficient determined from this curve is close enough to the original estimate of 0.040 so that a recomputation is not necessary.

The curve plotted from this and other data points is shown as a dashed line in Fig. 9. This flow regime extends into the initial portion of laminar flow, i.e., Re below 2000 where fluid momentum is still an important consideration.

Laminar Flow

Laminar flow for nitrogen gas is computed from the Poiseuille equation in the following form:

$$Q = \frac{RT_s}{P_s}\left[\frac{Wh_p^3 (P_1^2 - P_2^2)}{24 \mu L RT}\right]$$

Using the assumptions and data outlined:

$$Q = 4.08 \times 10^{13}\left(h_p^3\right)$$

This flow regime continues until molecular flow can be detected and the transition flow (laminar + molecular) begins.

Transition and Molecular Flow

The equation used to compute leakage in the molecular regime is as follows:

$$Q = \frac{RT_s}{P_s}\left[\frac{4}{3}\sqrt{\frac{2}{\pi}}\,\frac{Wh_p^2 (P_1 - P_2)}{L\sqrt{RT/g}}\right]$$

Using the assumptions and data outlined:

$$Q = 2.49 \times 10^{8}\left(h_p^2\right)$$

This flow regime is plotted on the lower right of Fig. 9. The dashed line connecting the laminar and molecular flow regimes is simply the sum of the two leakage values. Therefore, the transition equation is

$$Q_{Transition} = Q_{Laminar} + Q_{Molecular}$$

The boundaries of this transition regime are defined by the following limits

$$\overline{\lambda}'/h_p = 0.01 \text{ to } 1.0$$

The molecular mean free path (λ') is 3.61 microinches for nitrogen at standard conditions (70 F and 14.7 psia). For a mean pressure of 50 psig, $\overline{\lambda}' = 0.82$ microinch.

The corresponding height limitation of the transition regime is between 0.82 and 82 microinches with the point of equal laminar-molecular flow at 6.05 microinches (Fig. 9).

NOMENCLATURE

A = area, sq in.

C = discharge coefficient

D = hydraulic diameter, inches

D_e = effective pressure balance diameter

D_s = mean seat diameter

f = friction coefficient

g = gravitational acceleration constant, 1.39×10^6 in./min^2

h_o = taper height, inches

h_e = equivalent parallel plate channel height, inches

h_p = parallel plate channel height, inches

k = ratio of specific heats

L or X = channel length, inches

M = entrance Mach number

P = static pressure, psia

Q = volumetric flow at standard conditions of temperature (T_s) and pressure (P_s), in.^{3}/min or for compressible flow, scim

R_i = inside diameter, inches

R_o = outside diameter, inches

R = gas constant, in./R

Re = Reynolds number

T = static temperature, R

V = velocity, in./min

W = channel width or perimeter, inches

Greek Symbols

ω = weight flowrate, lb/min

μ = viscosity, lb-min/in.^{2}

ρ = density, lb/in.^{3}

λ' = mean molecular free path, inches

β = pressure profile factor

Subscripts

1 = inlet or entrance conditions

2 = outlet or discharge conditions

o = stagnation conditions

s = standard conditions

i = incompressible

c = compressible

SEATING ANALYSIS

The flow analysis has shown that leakage per unit length of seal (perimeter) is a function of two basic geometrical parameters--poppet-to-seat gap and radial land width. Experience has proved that for any real configuration, leakage is inversely proportional to the applied load. The purpose of this analysis is to (1) provide means for numerically describing the constituents of seating surfaces which create the leakage gap, and (2) to derive equations relating seat load to leakage. In some cases these relationships will be based upon simple, imperfect models. In many cases no analysis exists or could be made due to the complexity of the problem. Therefore, it is to be expected that experimental correlation will be necessary to reveal the real situation. However, the understanding provided by these relationships in the comparitive sense will assist in the pursuit of advanced designs.

GEOMETRY OF VALVE SEATING

The performance of a metal-to-metal valve seat is intimately related to the geometrical configuration of the seating surfaces. While a large variety of configurations are employed, the fundamental flat, conical, and spherical geometries can be identified in most cases. This stems from the simplicity of these shapes which are attendant with natural fabrication processes. The three configurations are shown in Fig. 10 with the parameters and equations combining basic geometry and load for the definition of apparent seat stress (S).

Superimposed upon real valve seating surfaces is a variety of other smaller geometries which often have a greater influence on the closure than the more obvious gross configuration. Most apparent is surface texture which includes the machining errors of roughness, waviness, pits, nodules, and scratches. However, often overlooked and of more subtle influence is the geometry of the seat land. While a seat land may be specified by engineering drawing or fabrication process, perfect conformability of mating surfaces is impossible and deviations are difficult to define or prove

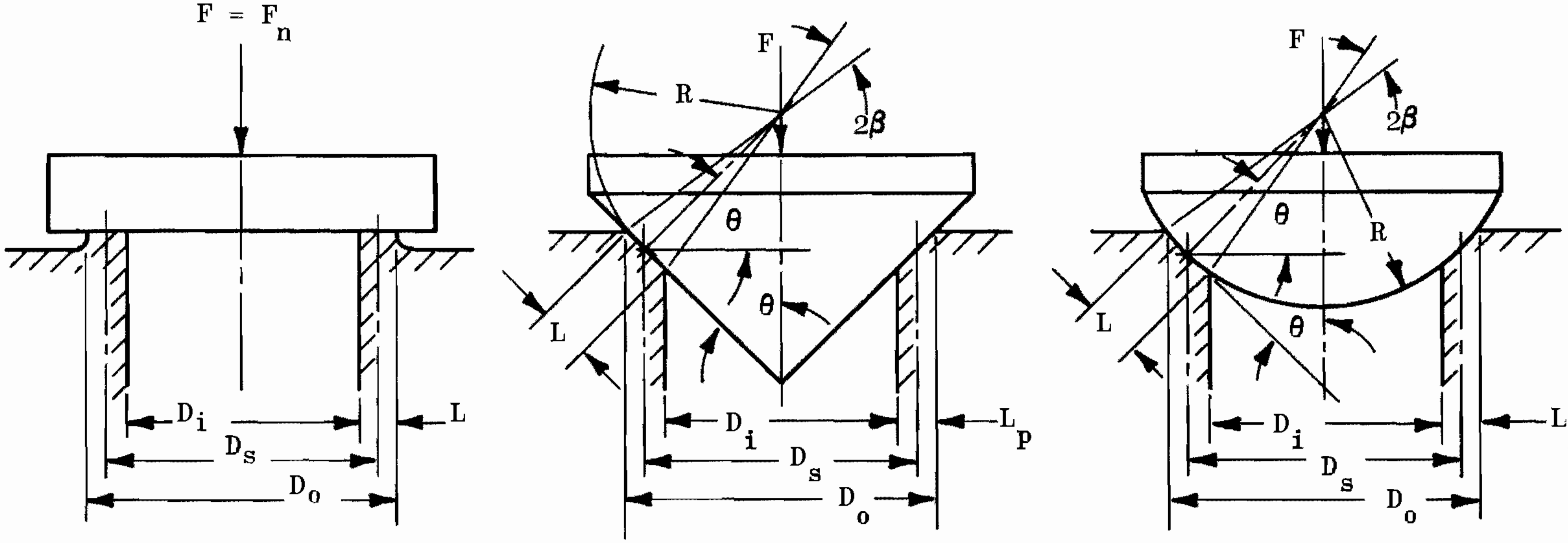

$$L = 1/2\ (D_o - D_i)$$

$$D_s = 1/2\ (D_o + D_i) = D_i + L$$

$$A_s = \pi D_s L$$

$$S \equiv \frac{F}{A_s} \equiv \frac{F}{\pi D_s L}$$

$$L_p = 1/2\ (D_o - D_i) = L \sin \theta$$

$$L = 2R \tan \beta \cong 2\beta R$$

$$D_s = D_i + L_p$$

$$A_s = \pi D_s L$$

$$A_{sp} = \pi D_s L_p$$

$$F_n = F/\sin \theta$$

$$F_r = F/\tan \theta$$

$$S \equiv \frac{F}{A_{sp}} \equiv \frac{F_n}{A_s}$$

$$L = 2\beta R$$

$$L_p = 1/2\ (D_o - D_i) \cong L \sin \theta$$

$$D_s = 2R \cos \theta$$

$$A_s = \pi D_s L$$

$$A_{sp} = \pi D_s L_p$$

$$S \equiv \frac{F_n}{A_s} \equiv \frac{F}{A_{sp}}$$

Figure 10. Flat, Conical, and Spherical Seating Equations

precisely; hence, the actual contact dimensions may be quite different than planned and also may change with seat load. Because leakage is inversely dependent upon real contact land dimensions it follows that variation of these dimensions will also have an effect on leakage.

In many cases of valve design, the final geometry of seating is unspecified, being controlled by shop practices to meet initial leakage requirements and ultimately the potentially plastic effects of cycling. Considering the variety of seating land geometries possible, this practice results in poor predictability of performance from valve to valve through any period of use. Therefore, it is necessary that each part of the contact land be considered and defined within reasonable limits. While these limits will vary with performance requirements and shop capability, the analyses presented herein combined with dimensional analysis of the experimental models (see Experimental Program section) should serve as a design guide.

Land geometry is identical in cross section for the flat and conical configurations. For spherical seating, the only difference is the definition of a land width on a curved surface which is usually narrow; thus, except for this one difference, the seat land is the same for all three configurations. The land, which may be on the seat, poppet or both, is composed of the three basic parts as illustrated below:

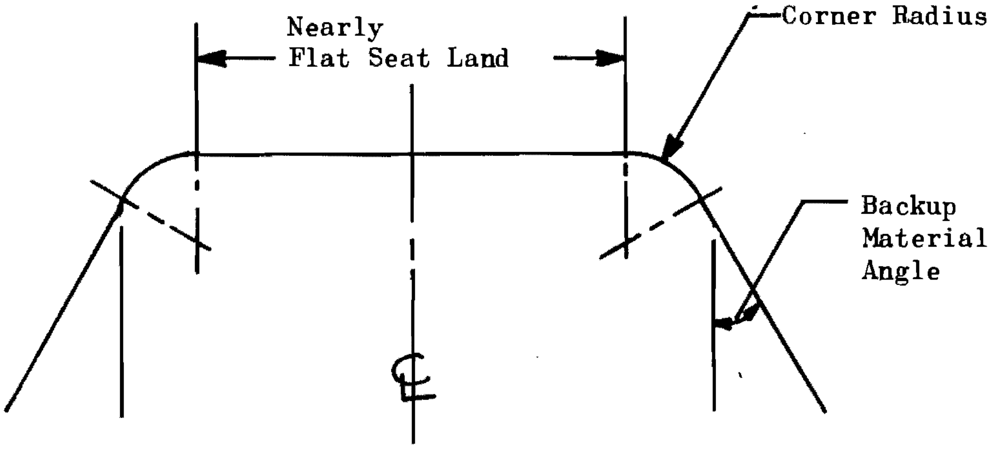

Each of these parts may take many forms and combinations too numerous to depict. The backup material angle on most flat seats is zero (but may approach 90 degrees) whereas for 45-degree conical or spherical seating, it is normally 45 degrees (but also may approach 90 degrees). The "flat land" may be flat, concave, or convex with symmetry near its own centerline or to the seat diameter. Corner radii also vary over a considerable range from a mere ragged discontinuity formed by intersecting surface roughnesses to the opposite extreme of a complete sphere (ball in cone).

SEATING GAP

The seating gap under a no-load condition is a result of variation in the above land geometry combined with dimensional and positional errors. In many cases, the real length of land contact is a complex function of the load, being formed elastically with each contact. The seat land may have been developed through plastic flow of an initially sharp edge with subsequent deformations predominantly elastic. Where the land is plastically formed, the resultant contact shape is largely indeterminate. With defined simple curved shapes, however, a Hertz stress analysis may be used to predict the elastically loaded configuration. In any case, a definite land length does exist under the slightest load, and the term "sharp seat" is a relative generalization.

Dimensional errors result in deviations from true form and nonconformity between poppet and seat lands. Symmetrical errors may create only a taper gap with full contact at the roughness level around the periphery; however, errors of roundness always result in a through-gap. Even with symmetrical errors, as exemplified by differential radii in spherical seating, a finite load must be applied to establish a minimal land for adequate sealing or else leakage could be in the nozzle regime and, thus, much greater than for the laminar condition.

It is notable that unlike the flat poppet and seat (for which it is relatively simple to obtain near-perfect conformity), the conical and spherical designs necessitate a match of physical dimensions, i.e., the included angle for the cone and radius for the sphere. As a result, these configurations will almost always have a taper gap from a few microinches to thousandths of an inch, depending upon size and fabrication and measurement precision. For constrained flat and conical seats, parallelism and axis tilt are usual positional errors. Freedom from this error is the advantage of the spherical seat.

Superimposed upon the seat land, and causing gaps which may only be reduced but never closed, are the surface textural errors of roughness, waviness, modules, pits, and scratches. Thus, a variety of geometrical errors cause conformal gaps in seating which must be reduced through load deformation of the "high" material.

EQUIVALENT FLOW PATHS FOR SURFACE DEVIATIONS

The deviations of seating geometry that result in leakage may be broadly divided into the following:

1. Gross abnormalities of geometry such as out-of-parallel plates; broad curvatures measured as a deviation from a flat plane; and spherical, out-of-round, or tapered mating surfaces
2. Parameters of surface texture, i.e., roughness, waviness, nodules, pits, and scratches

The leakage flow through these various surface deviations may be indirectly approximated by computing the equivalent flow path of each deviation for that portion of the seating surface it occupies. As previously shown, valve seat leakage takes place mainly in the laminar and, to a lesser extent, in the molecular flow regimes. In laminar flow between parallel plates, the defining parameters are the channel length or the radial land width (L), peripheral width ($W = \pi D_s$), and separation height cubed (h^3). The same conditions hold for molecular flow except the separation height is squared (h^2).

Because the surface deviations considered herein are very close approximations of parallel plates, the flow may be imagined to travel through discrete radial channels of varying height which may be integrated to arrive at an equivalent parallel plate separation (h_e).

In these calculations, advantage is taken of the fact that the majority of flow occurs through the larger spaces so that small nonradial flows may be neglected. It has also been assumed that the seat land width is sufficiently narrow with respect to the ID to neglect radial flow divergence.

Simplified Chordal Equations

In analyses of various curved geometries the expression for the chordal height often occurs as shown below:

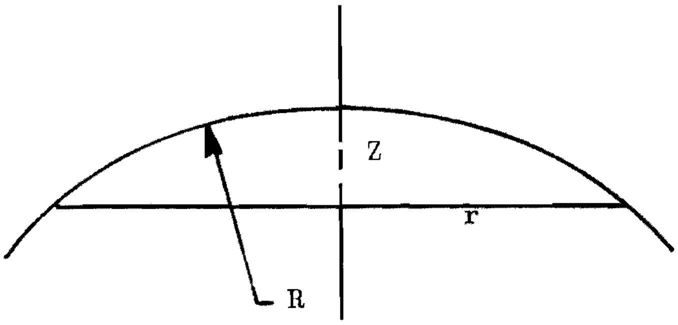

The equation defining this geometry is:*

$$r = \sqrt{2RZ - Z^2} \cong \sqrt{2RZ}$$

$$Z \cong \frac{r^2}{2R}$$

For most analyses herein, R is much larger than Z; therefore, the approximate relation may be used with small error as shown below:

R/Z	Error, percent
25.4	1.0
5.4	5.0
2.9	10.0

---

*See pages 149 through 152 for nomenclature.

Gross Geometry Deviations

Valve seat leakage caused by gross separations in the interface is mainly laminar, but may be turbulent channel or nozzle flow. Although there may, in unusual instances, be significant molecular flow, the addition of this component will be reserved for consideration of flow through surface roughness. While a large number of surface deviations are possible, there is a great similarity between the various gap shapes which allows the consideration of maximum gap and equivalent height to be reduced to a reasonable few. These may often be superimposed to obtain approximate results for composite shapes. In the case of taper gaps (h_0), a physical separation of the seating surfaces (h_p) is assumed to exist due to surface texture or other errors.

Out-of-Parallel Flat Poppet and Seat. For this case, the seating surfaces are assumed perfectly smooth and flat with flow perfectly radial. The flow may be imagined to follow a large but finite number of radial stream channels which may be summed to obtain the total flow through the gap. Because laminar flow varies as the height cubed, it follows that the predominate flow path is through the widest gap. The analytical model and describing equations are shown below:

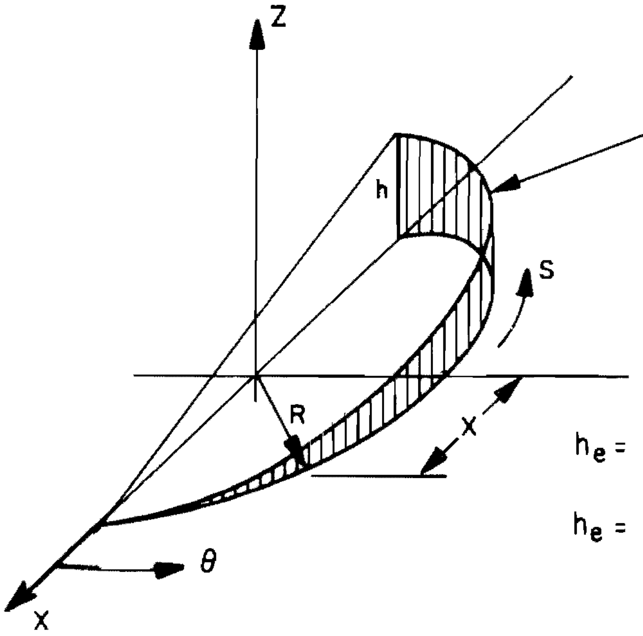

$$Z = \frac{h}{2}\left(1 - \frac{X}{R}\right)$$

$$S = R\,\theta$$

$$X = R\cos\theta$$

$$h_e = \left[\frac{1}{\pi R}\int_{R}^{-R}\left[Z(S)\right]^3 dS\right]^{1/3}$$

$$h_e = \left(\frac{5}{16}\right)^{1/3} h$$

As curve Z is one-half of a sine wave when unwrapped, the same result is obtained by integrating Z over the length πR. It can be shown for this model that the assumption of perfect radial flow results in small error because more than 90 percent of the total flow discharges from the wide 180 degrees of the periphery, leaving less than 10 percent of the flow involved in the contact regions where the flow is partially circumferential.

Sinusoidal Gap Separations. The flat poppet and seat having one or both surfaces cylindrically out-of-flat (egg-shaped poppet) and also, out-of-round conical, and spherical seating surfaces all have gaps which are basically sinusoidal regardless of the number of lobes. Consequently, integration of these shapes yields the same results obtained for the flat out-of-parallel case above, i.e.:

$$h_e = \left(\frac{5}{16}\right)^{1/3} h$$

where h is the maximum gap.

Axially Symmetrical Tapered Seating. Taper between poppet and seat is usual for nearly all forms of seating involving matching surfaces. It results in flat seating from customary convex (or to a lesser extent concave) machining errors as schematically shown below:

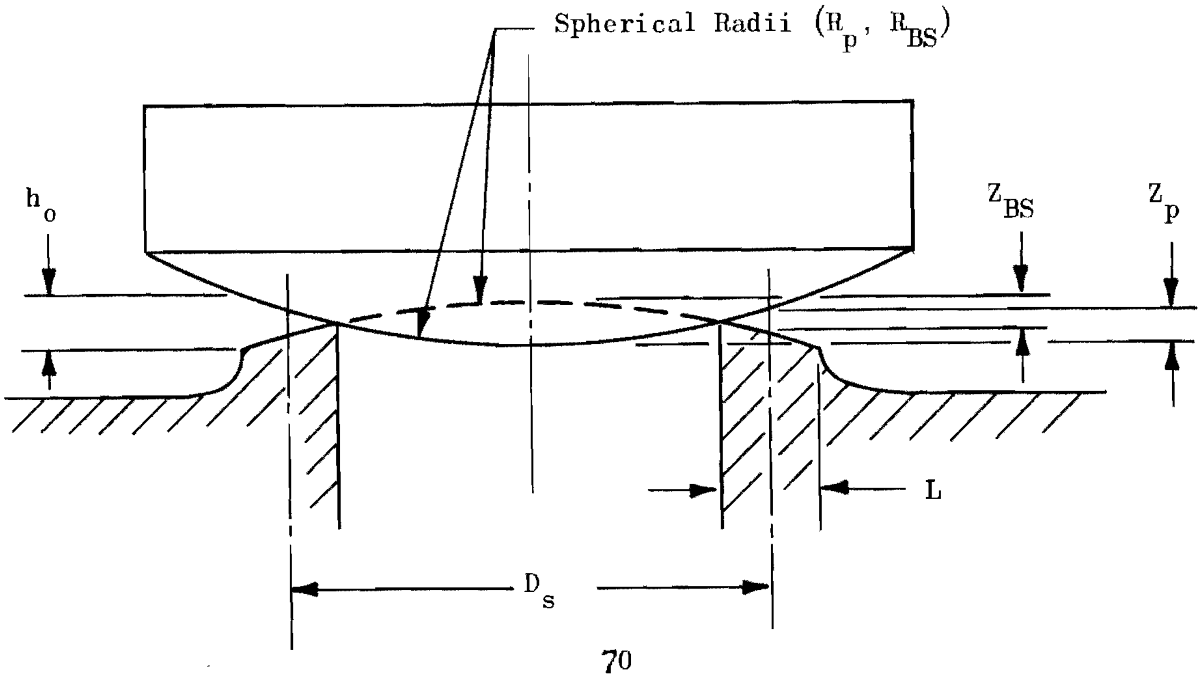

For flatness errors (Z_1 and Z_2) measured nominally at the mean seat diameter (D_s), the taper gap (h_o) is derived from the simplified chordal equation as

$$h_o \cong \frac{4L}{D_s} (Z_p + Z_{BS})$$

with the appropriate sign applied to Z for concave or convex conditions.

A more unusal symmetrical form error is the crowned surface which might occur from excessive polishing of a flat, conical, or even spherical seat, thus dubbing the edges. Although the actual shape is often elliptical, the geometry may be approximately described by the chordal equation. A similar seating configuration occurring naturally is the ball in a wide conical seat (elastic contact only). Taper gaps from these configurations are shown below:

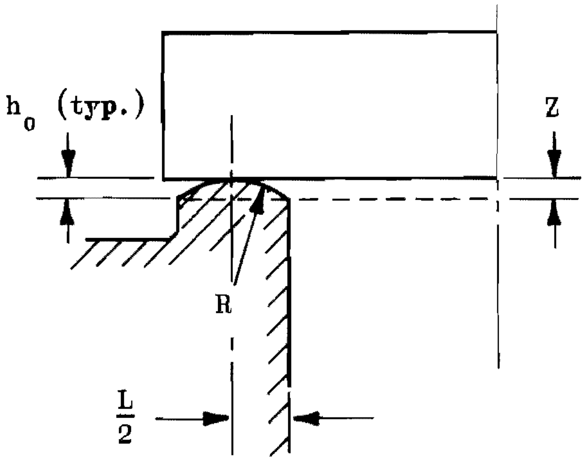

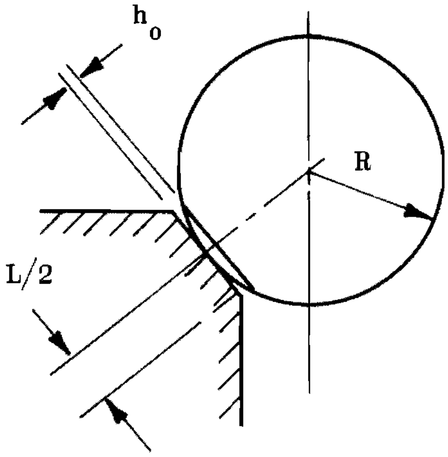

$$h_o = Z \cong \frac{(L/2)^2}{2R} \cong \frac{L^2}{8R}$$

As previously noted, a more serious problem exists for the conical and spherical surfaces because of the conformal dependence upon physical dimensions (see Model Fabrication section). For conical seating, the seat gap is a function of the land width (L) and differential seating or half angle ($\Delta\theta$) between poppet and seat; thus $h_o \cong \Delta\theta L$.

With sperical seating, the taper gap is related to the differential (ΔR) between the poppet (R_p) and ball seat (R_{BS}) spherical radii. The exact equation is cumbersome in that small differences necessitate a computer solution. However, simplification is possible for seating half angle (θ) between 15 and 75 degrees, and land width (L) small with respect to the basic spherical radius (R). Applicable terms are shown in the following sketch for the case where (R_{BS}) is greater than (R_p). The approximate solution for (h_o) is derived from the sine law with (L) assumed a straight line.

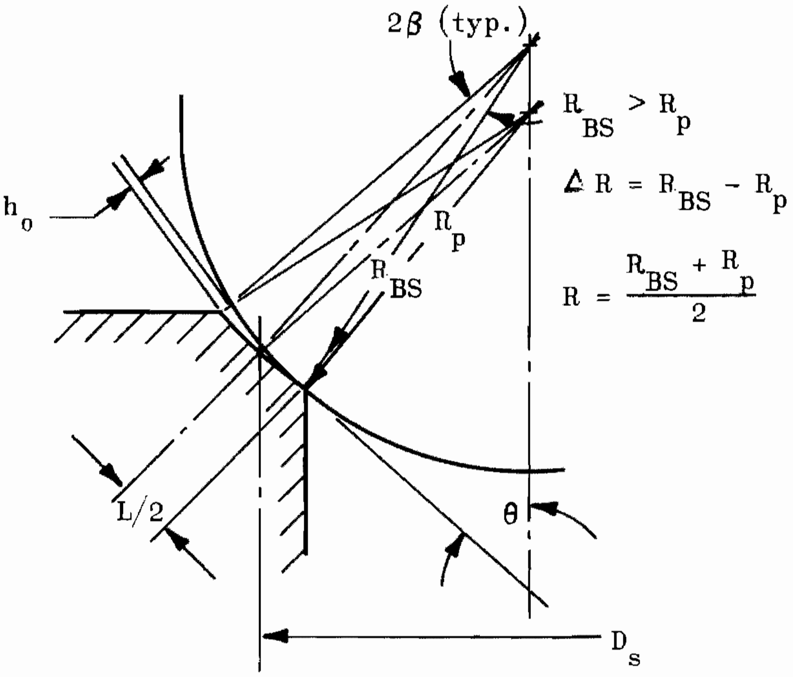

$$h_o \cong \frac{\Delta RL}{R_p \tan(\theta \pm \beta)} = \frac{\Delta DL}{D \tan(\theta \pm \beta)}$$

$$\beta \cong \frac{L}{2R} : (+) \text{ for } R_{BS} > R_p; \ (-) \text{ for } R_p > R_{BS}$$

$$\theta = \text{arc cos } \frac{D_s}{2R}$$

In terms of the differential between ball and seat spherical diameters (ΔD) and mean seat diameter (D_s):

$$h_o \cong \frac{\Delta DL \cos \theta}{D_s \tan(\theta \pm \beta)} \cong \Delta \theta L$$

Taper gap data are plotted in Fig. 11 in terms of the taper angle ($\Delta \theta$). Consideration of experimental data has shown that the usual tolerance angular differential of 1/2 to 1.0 degree would, in most cases, result in unacceptably large taper gaps.

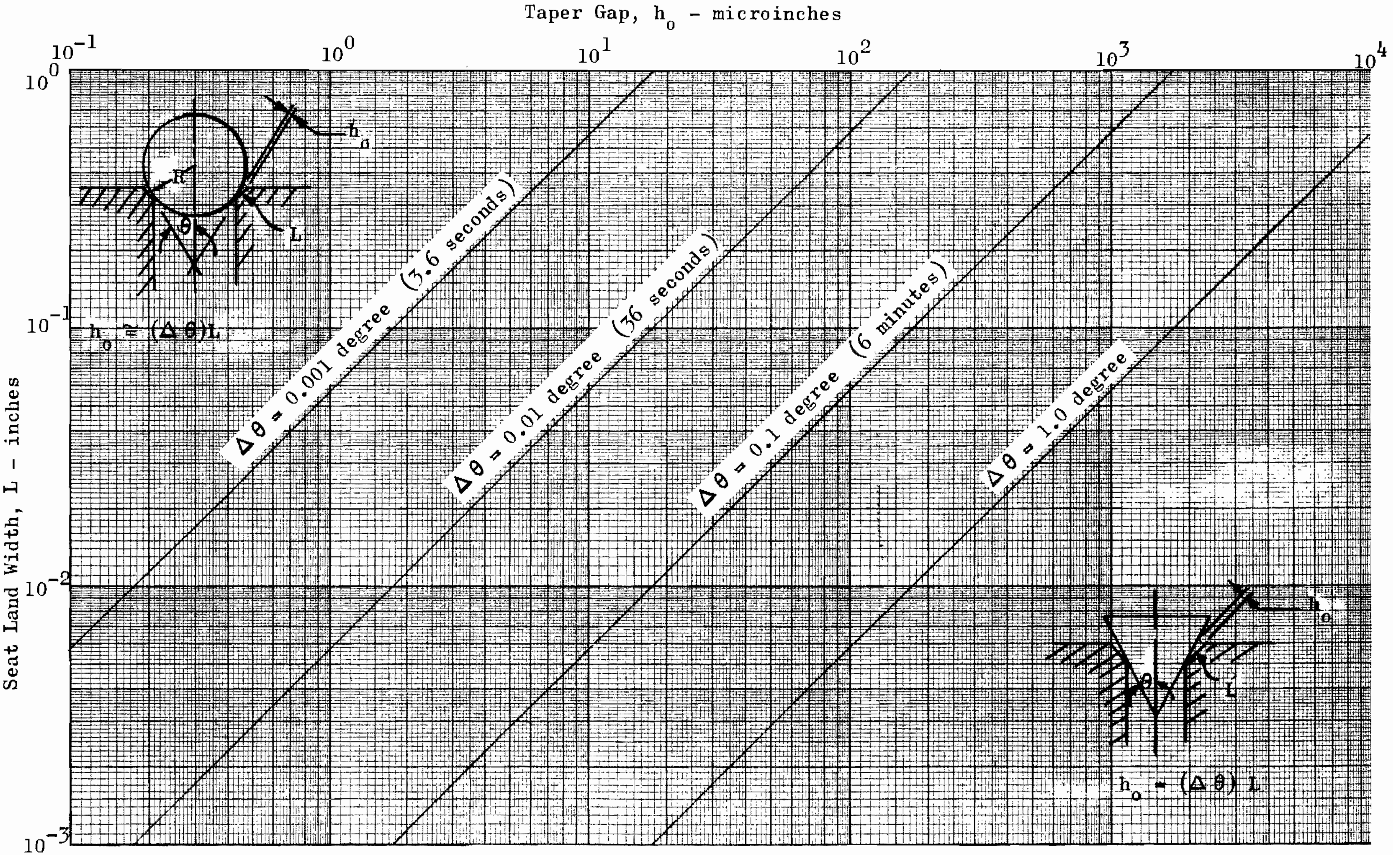

Figure 11. Taper Gap for Flat, Conical, and Spherical Seating

The problem now is to describe the taper gap (h_o) in leakage parameter terms. For the ideal case of perfectly smooth flat or round surfaces, there would be no leakage. Roughness and/or geometry errors do, however, casue a separation which, due to the very narrow contact land, may be assumed to offer negligible resistance to flow (unless the taper gap is very large in which case the leakage would result from a nozzle flow condition). With some gap, the problem is resolved to one of simple tapered flow. The equivalent separation for this case has been presented in the Leakage Flow Analysis section. The simple integration averaging process may not be used for channel height varying along the flow direction. Comparison of laminar flow factors is illustrated in Fig. 12 for two cases noted as "linear" and "taper" flow. For the linear case, h does not vary in the direction of land width (L), and the cubical average (h_e) is obtained as previously shown. For taper flow, the basic flow equation must be integrated with L to obtain an equivalent path height. There is a small difference between the two flow factors at (h_p/h_o) ratios greater than one; thus, the more universal M_L factor may be used to approximate complex surface geometry. Below this value, however, taper flow should be considered as the defining parameter and N_L used to compute the flow.

Tilted Conical Poppet. Tilting a conical poppet in its seat results in an elliptical out-of-roundness between the poppet and seat. Because righting moments are nil near axial coincidence and, for most cases, tilt is caused by eccentrically applied seating forces, this is a natural error for the conical configuration. The problem is to determine the relationship between tilt angle and maximum seat gap from whence an equivalent flow path may be obtained.

The geometry of the tilted cone is shown in Fig. 13. The intersection between seat and poppet axes is at point (0) for all angles of tilt (Y). From this construction, the analysis follows.

The point of maximum out-of-roundness, and thus gap, is located approximately 90 degrees removed along the line joining the contact points between poppet and seat (point q). The gap generated in this plane results

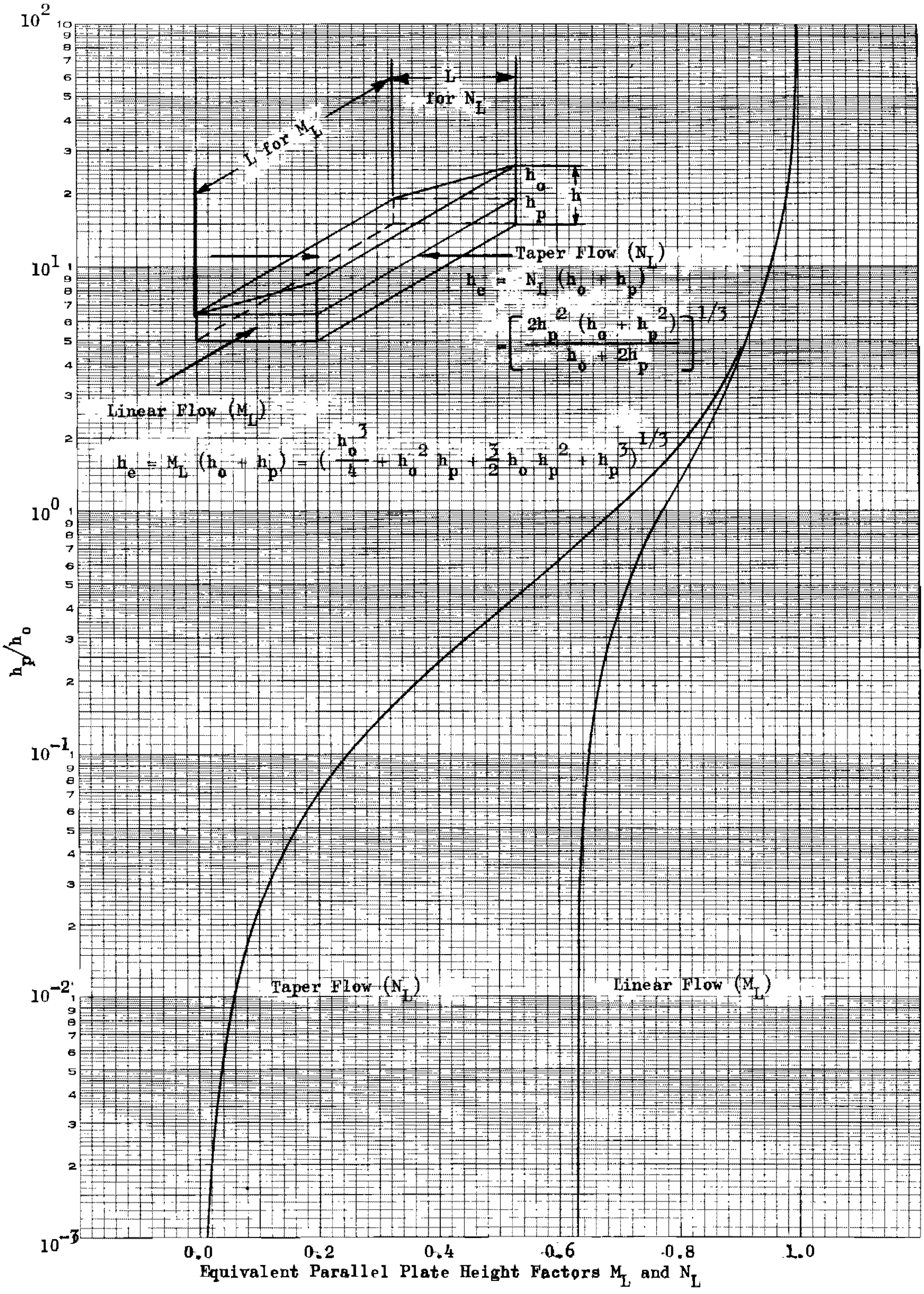

Figure 12. Laminar Flow Factors

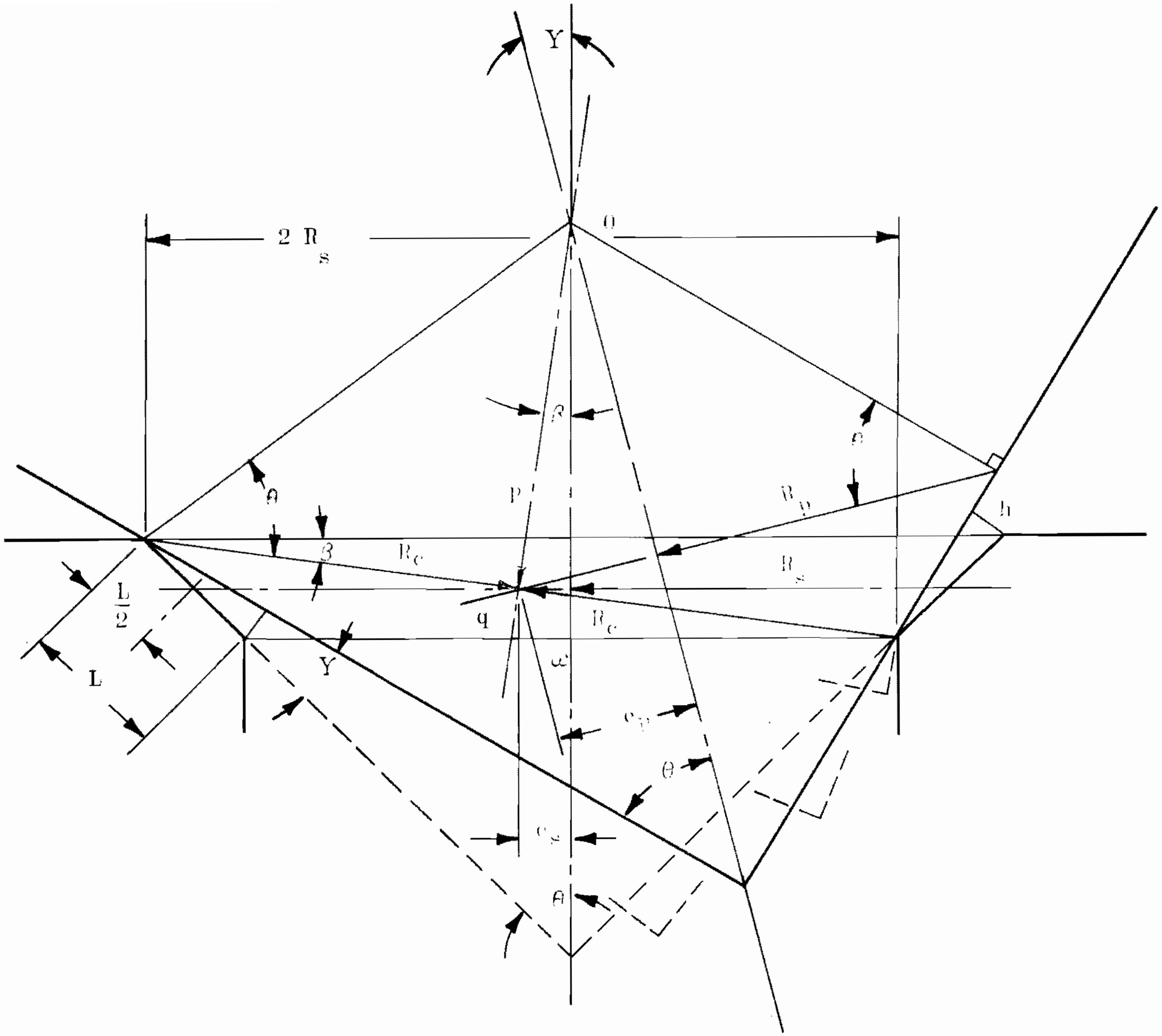

Figure 13. Tilted Conical Poppet Geometry

from two ellipses having major semiaxes (R_c) and minor semiaxes reduced from circular radii (R_p) and (R_s) by eccentricities (e_p) and (e_s). This is shown below in the section through plane R_c.

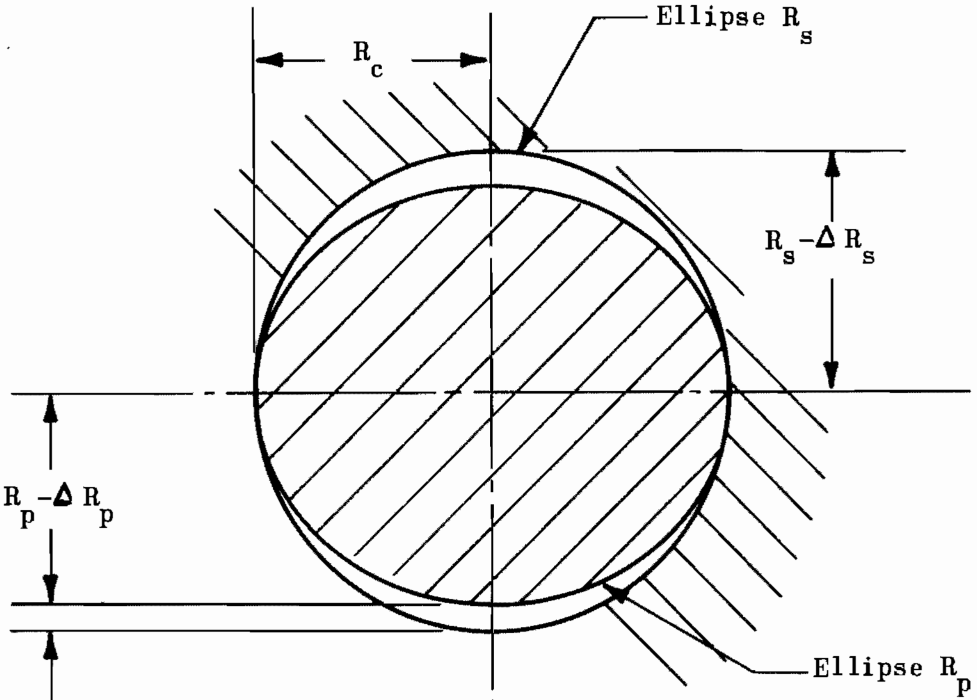

Section Through R_c

The equation for maximum gap (q) which lies in the plane (R_c) is:

$$q = (R_s - \Delta R_s) - (R_p - \Delta R_p)$$

where the elliptical change in radii are obtained from circular sections through lines (R_s) and (R_p) as illustrated below:

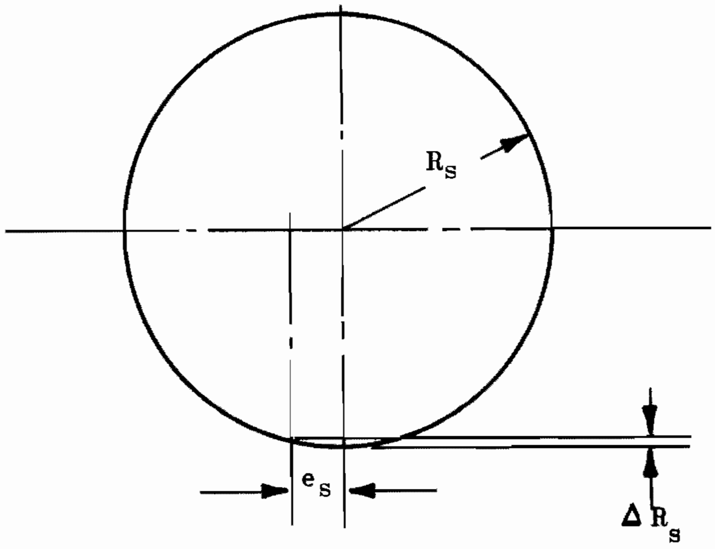

Section Through R_c

From the preceding sketch:

$$\Delta R_s \cong \frac{e_s^2}{2R_s} \quad \text{and} \quad \Delta R_p \cong \frac{e_p^2}{2R_p}$$

Solving for R_p:

$$R_p = \frac{P \cos (\Upsilon + \beta)}{\tan \theta}$$

$$P = R_c \tan \theta; \; R_c = \frac{R_s}{\cos \beta}$$

$$P = \frac{R_s \tan \theta}{\cos \beta}$$

$$R_p = \frac{R_s \cos (\Upsilon + \beta)}{\cos \beta}$$

Solving for e_s:

$$e_s = P \sin \beta = \frac{R_s \tan \theta \sin \beta}{\cos \beta}$$

$$e_s = R_s \tan \theta \tan \beta$$

Solving for e_p:

$$e_p = P \sin (\Upsilon + \beta)$$

$$e_p = \frac{R_s \tan \theta \sin (\Upsilon + \beta)}{\cos \beta}$$

Solving for q:

$$q = R_s - \Delta R_s - (R_p - \Delta R_p)$$

$$\Delta R_s = \frac{1}{2} R_s \tan^2 \theta \tan^2 \beta$$

$$\Delta R_p = \frac{R_s \tan^2 \theta \sin^2 (\Upsilon + \beta)}{2 \cos \beta \cos (\Upsilon + \beta)}$$

$$q = R_s \left\{ 1 - \frac{\cos (\Upsilon + \beta)}{\cos \beta} + \frac{1}{2} \tan^2 \theta \left[\frac{\sin^2 (\Upsilon + \beta)}{\cos \beta \cos (\Upsilon + \beta)} - \tan^2 \beta \right] \right\}$$

where

$$\beta = \text{arc sin} \frac{L \cos \theta}{2 R_s}$$

For small angles (< 4 degrees) of (Υ) and (β), the above equations may be simplified to the following form:

$$q \cong \frac{\Upsilon}{2 \cos \theta} \left(L + \frac{R_s \Upsilon}{\cos \theta} \right)$$

The perpendicular gap at q is:

$$h_q = q \cos \theta$$

$$h_q \cong \frac{1}{2} \; L \, \Upsilon + \frac{D_s \Upsilon^2}{4 \cos \theta} \quad ;$$

whereas the perpendicular gap at the two contact points is $h = L\Upsilon$, or the same gap as obtained with symmetrical taper ($\Upsilon = \Delta \theta$).

The first term in the equation for h_q represents the taper gap, and the second term the elliptical gap. The significance of these two terms is shown in Fig. 14 where h_q is plotted for L equal zero, and the family of conical angles experimentally investigated. The value of h for a range of land widths is also shown. Except for narrow land widths and large tilt angles, these parameters show that the elliptical term is usually negligible (this was the case for the experimental models). Accordingly, the gap valume may be approximated by the sinusoidal shape illustrated in Fig. 15. As shown, the circumferential ID and OD lengths are nearly the same because L is small with respect to D_s. Clearly, the flow path is

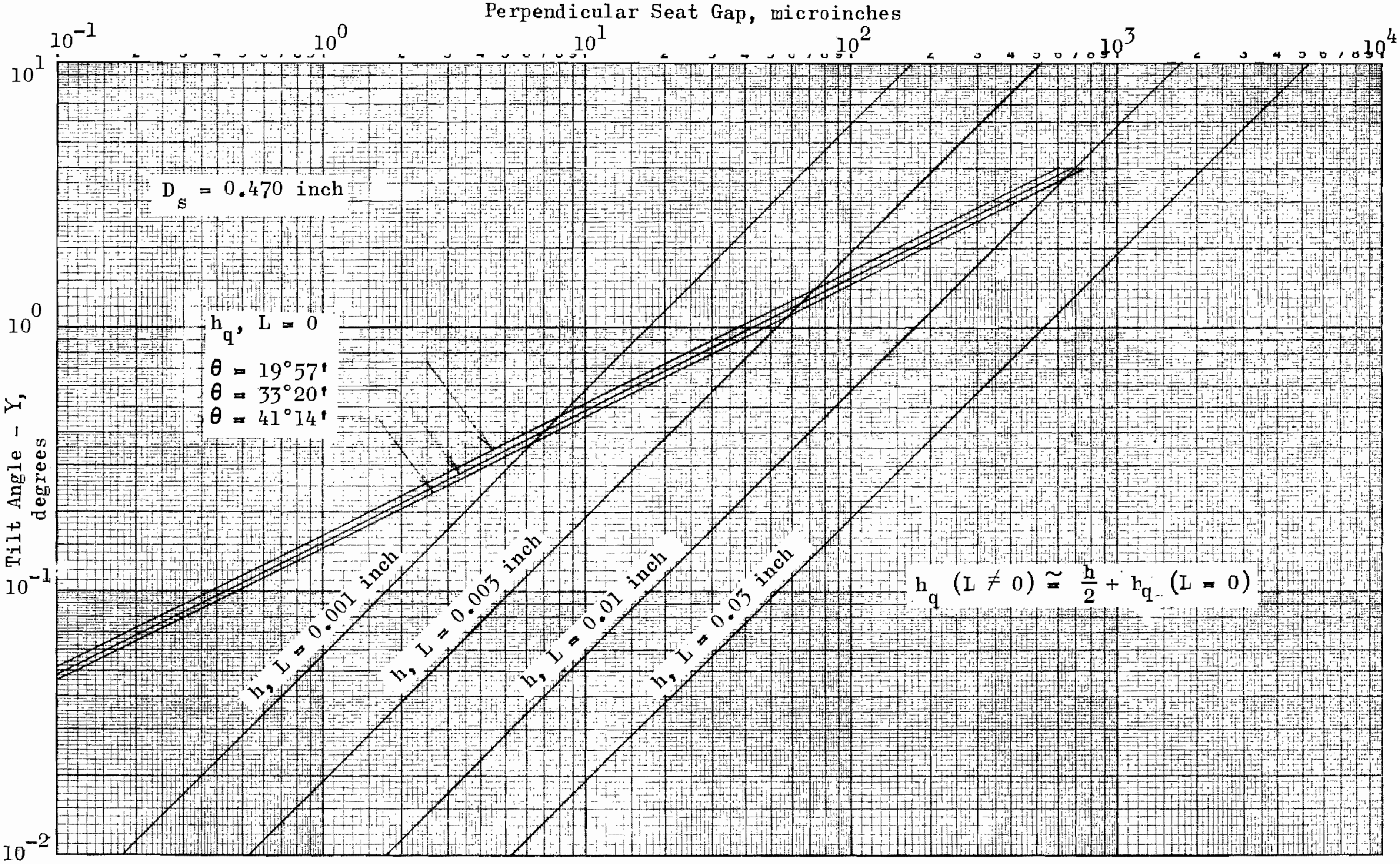

Figure 14. Tilted Conical Poppet-Seat Gap

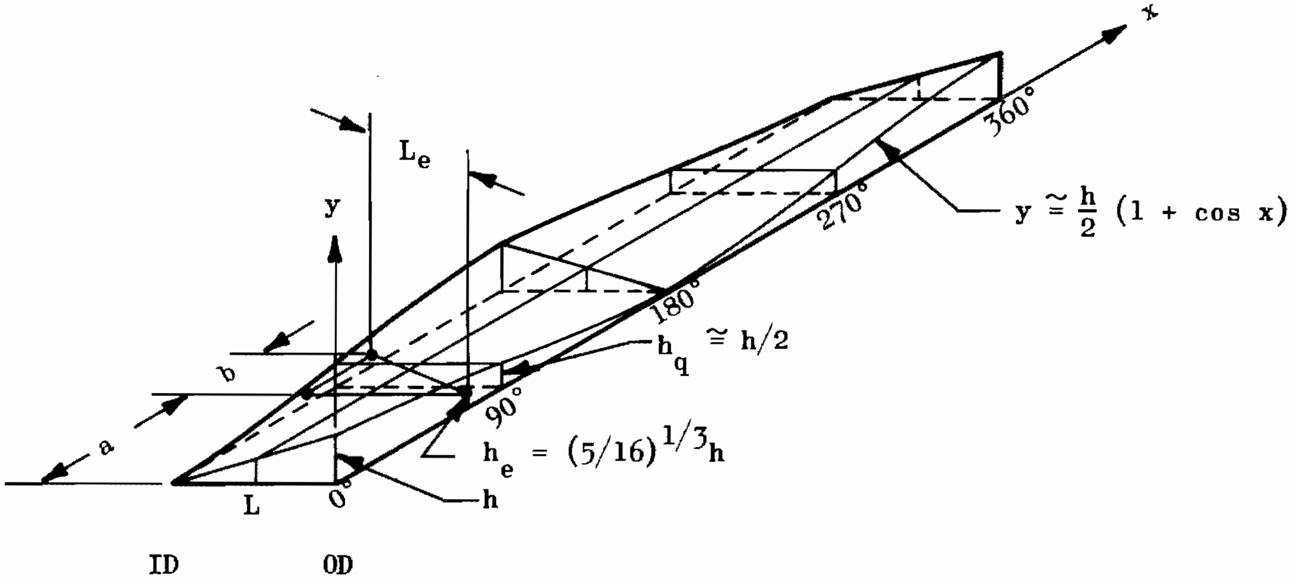

Figure 15. Seat Gap Volume From a Tilted Conical Poppet

partially circumferential with flow entering at the greatest gap (h), splitting into two parts and recombining at the exit.

To arrive at an equivalent parallel plate height (h_e) and flow path based upon the previous parameter, the following assumptions are made:

1. The convergent-divergent flow height ratio (h_p/h_o, Fig. 12) is nominally one; therefore, the cubically averaged laminar flow factor (M_L) may be used to determine (h_e). Based upon the sine wave shape:

$$h_e = \left(\frac{5}{16}\right)^{1/3} h$$

2. The effective length of flow path (L_e) is determined by the entrance and exit heights equal to (h_e) as shown in Fig. 15. The resultant equation for (L_e) is:

$$L_e \cong \sqrt{L^2 + b^2}$$

where

$$b \cong \frac{\pi D_s}{2} - 2a$$

thus

$$L_e \cong \sqrt{L^2 + 0.132\ D_s^2}$$

Generally the L^2 term above can be neglected (e.g., $D_s/L > 10$, error <4 percent), and L_e is reduced to approximately 0.363 D_s. Thus, the flow path is circular for about 10 percent of the seat circumference. Introduction of (L_e) and (h_e) into the laminar flow equation shows the general relationship between geometry and leakage, i.e.:

$$Q \propto L^3\ Y^3$$

with leakage independent of seat diameter. This explains why narrow land widths are desirable for conical seated valves where tilt cannot be accurately controlled. It may be shown that for usual valve designs the tilt angle is sufficiently controlled (normally less than 1 degree) to preclude nozzle flow (i.e., $L_e/h_e > 10$).

Surface Texture Deviations

Except in rare instances, loaded on-seat leakage will be laminar and, for gases, may reach molecular levels. The basic leak path is through the interstices formed by contacting waviness and/or roughness. Additional leakage components of possible significance may be through nodule created gaps, radial scratches, or a density of interconnecting pits. As with gross geometry deviations, weighted averages of the maximum spacing height (h) can be computed for various regular geometric wave forms.

Surface Roughness and Waviness.

The geometrical terms and equations used to describe model surfaces are summarized in the sinusoidal representation shown in Fig. 16. The height (h) and wave length (λ), can be assumed to represent various other wave forms and exist as waviness or roughness, or a combination of both. For example, a sinusoidal curve of smaller (h) and (λ) can be superimposed upon the sine wave shown. In addition, these waves can be imagined to be either linear into the paper or undulating in a similar fashion as that indicated resulting in a three-dimensional series of "hills and valleys" which contain a smaller version of the same. For the fine surfaces under consideration (h = 0.5 to 20 microinches), the average asperity angle (Φ) will seldom exceed 4 degrees, and sharp lapping scratches do not have slope angles much greater than 10 degrees.

Various averages have been computed from the equations shown in Fig. 16 for a number of regular geometric wave forms (Fig. 17). These factors may be used to estimate the variations between surfaces and the possible effects on leakage performance.

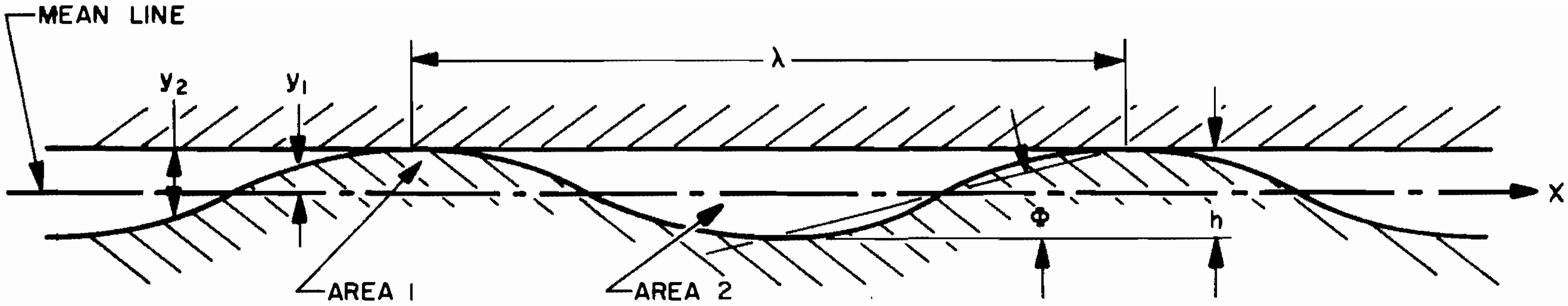

$$AA = \frac{1}{\lambda}\int_0^{\lambda} |y_1|\, dx \ ; \quad rms = \left[\frac{1}{\lambda}\int_0^{\lambda} y_1^2\, dx\right]^{1/2}$$

$$h_{eL} = \left[\frac{1}{\lambda}\int_0^{\lambda} y_2^3\, dx\right]^{1/3} \ ; \quad h_{eM} = \left[\frac{1}{\lambda}\int_0^{\lambda} y_2^2\, dx\right]^{1/2}$$

Average Asperity Angle $\Phi \cong \frac{2h}{\lambda}$

Location of Mean Line Defined by Area 1 = Area 2

Figure 16. Model Surface Geometry With Defining Equations

WAVE FORM: h = 1		M_L*	M_M*	AA	rms	$\frac{h}{AA}$	$\frac{h}{rms}$	$\frac{G}{h}$	$\frac{G}{AA}$	$\frac{rms}{AA}$
UNIFORMLY RANDOM	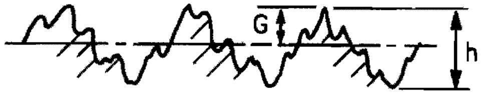	---	---	0.2	0.25	5.0	4.0	0.5	2.5	1.25
ROUND CRESTED PARABOLIC	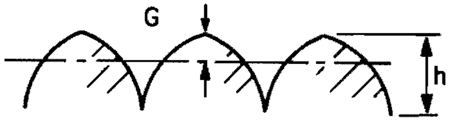	0.523	---	0.256	0.298	3.91	3.36	0.333	1.29	1.16
SHARP CRESTED PARABOLIC	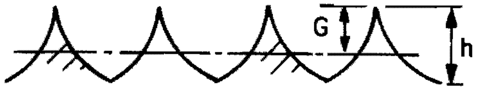	0.770	---	0.256	0.298	3.91	3.36	0.667	2.60	1.16
SINUSOIDAL	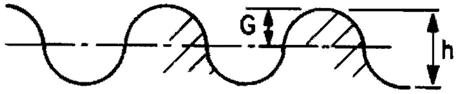	0.678	0.612	0.318	0.353	3.14	2.83	0.5	1.57	1.11
SAW TOOTH	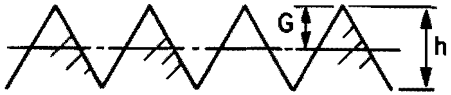	0.630	0.578	0.25	0.289	4.0	3.46	0.5	2.0	1.16
SQUARE	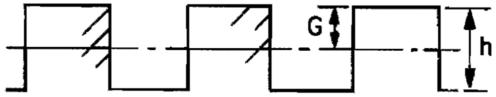	1.0	1.0	0.5	0.5	2.0	2.0	0.5	1.0	1.0

*$h_{eL} = M_L h$; $h_{eM} = M_M h$

Figure 17. Average Height Values for Various Wave Forms

Scratches. The remaining surface defects pertinent to valve seating are scratches, nodules, and pits in decreasing significance. Because of the difficulty associated with defining these defects, they take on a much greater importance than is commensurate with their usual contribution to leakage. Of particular significance in this respect are scratches. The definition of the relative effect of scratches (and other defects) upon leakage may be estimated through comparison of their size-number contribution to total leakage as compared with other deviations.

The analytical model considered is the seat land having one radial scratch as shown below:

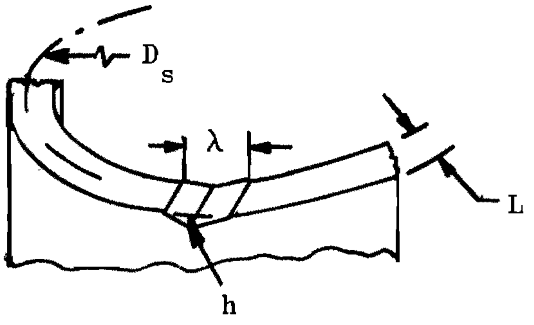

The equivalent height for the sawtooth configuration from Fig. 17 is:

$$h_{eL} = 0.63\ h \quad \text{and} \quad h_{eM} = 0.58\ h$$

Scratch density (β_s) relates the one-radial-scratch-model to the usual case of many radial scratches; thus

$$\beta_s \equiv \frac{n\,\lambda}{\pi\,D_s} \quad \text{or} \quad n = \frac{\pi\,D_s\beta_s}{\lambda}$$

where Q for many scratches of average width (λ) equals (n) times (Q_s) for one scratch. Scratch leakage, computed for later correlation with experimental data, is shown in Fig. 18 with the reduced flow equation and applicable data.

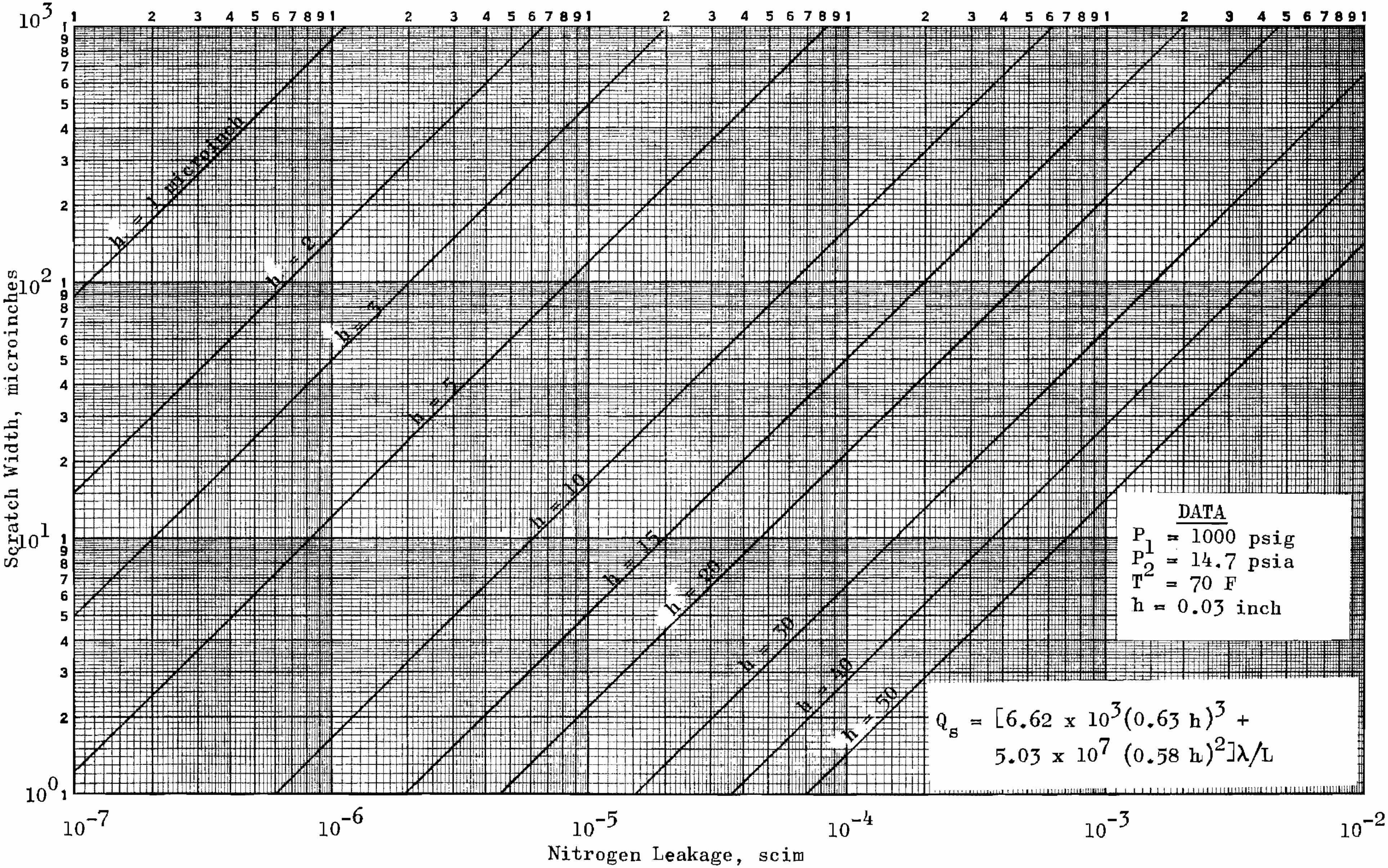

Figure 18. Single Scratch Leakage, Q_s

Nodules. Contaminants and nodules have a highly load sensitive effect on leakage due to their usually small contact area. Uniformly dispersed over the seating area, the separation height is merely the parallel plate configuration. However, one nodule will cause the out-of-parallel positional error previously discussed. In this case, contact will occur at the roughness height of the two surfaces and the equivalent height must be determined for the combined gaps (i.e., M_L in Fig. 12 where h_p is the equivalent combined roughness height, and h_0 the out-of-parallel gap).

Pits. Few localized pits not bridging the seat land will have little effect on leakage. A uniform distribution of pits will tend to reduce the effective land width since they offer negligible flow resistance (large relative h).

SURFACE DEFORMATION AND LEAKAGE

No analysis exists which accurately describes the deformation of real surfaces. Approximation analyses are either extremely complex (see Ref. 25, and 40) or limited to specific configurations and materials which restrict their application. Because leakage results from some separation between contacting interfaces, it is the change in this gap with load that is of interest, i.e.,

$$Q \propto (h - \delta)^3$$

where (δ) is the deformation of contacting geometry. From this equation, it may be seen that as (δ) approaches (h), the variability of Q must increase greatly because of test model differences or analytical inaccuracies. Consequently, the deformation and leakage analyses of simplified model surfaces will serve mainly for comparison with experimental data to assist in understanding the mechanism of seating. This concept will be exemplified in later discussions of test model stress-leakage characteristics where the inspection, test, and analytical inputs will be combined to support explanations of notable phenomena.

The deformation of simplified model surfaces is based on the assumption of total elasticity of the interfacial contacts and substrata with uniform unit loading over the seating land. The nominal plastic deformations that take place in real contacts will be neglected as contributing little to the load required to effect a shutoff. Each model defect will be treated separately, and it is assumed that loads may be superimposed to arrive at a final solution. Therefore, the load to depress nodules into the waviness will be added to the load required to flatten waviness which in turn, will be added to the load necessary for compressing the roughness component. No simple analysis exists which describes the characteristics of scratches or shallow v grooves in a compressed surface; therefore, the results of model tests must be reviewed to arrive at some quantitative evaluation. Additionally, it is assumed that the deformations of one defect do not affect another. This is not actually the case because all defects are an integral part of the surface. However, the incurred error is assumed negligible because the relative stiffness of nodule tips or wave crests is generally small compared with the substrata. This assumption becomes increasingly invalid as the protuberance spreads out and approaches the general plane comprised of the average roughness.

Analysis of the deformations is based upon Hertz equations for curvilinear contacts. These equations have been reduced to a relatively simple form in Roark (Ref. 61) for a variety of singular contacts. Included are sphere-on-plate, sphere-on-sphere, cylinder-on-plate, cylinder-on-cylinder, crossed cylinders, etc. From these geometrical shapes and the previous data on model surfaces, a variety of models may be set up for analysis. The primary difference between each of these configurations is the spring rate, or the load to achieve a given deflection, and the load that the contact can support before plastic flow results. For example, the sphere-on-sphere is considerably more deformable than the cylinder-on-cylinder.

General Waviness and Roughness Model

Consideration of the various types of surfaces fabricated in the test program resulting from turning,grinding, lapping, and polishing has indicated that the most general model configuration is one which is multidirectional. (The special case of eccentric circular lay is considered in subsequent sections.)

Real surface contacts consist of combinations of crossed ridges and contacting spherical protuberances or nodules, interlaced with scratches. A loose abrasive lapped surface of general matte appearance has an extremely nodular structure, generally termed homogenous or multidirectional, which is interspersed with numerous nicks and scratches lying below the general terrain. The diamond lapped surface generally has a definite lay, either unidirectional or criss-crossed, caused by scratches which may have raised ridges along their lips or edges. Even in unidirectional diamond lapping these scratches criss-cross each other in angles of a few degrees, breaking ridge continuity. Thus, mating of unidirectional surfaces results essentially in a multidirectional gap configuration.

From these observations and those noted in the literature (see Surface Studies), the model selected for analysis and data correlation is the sinusoidal surface in one direction mating with a similar surface rotated 90 degrees. The result is a multiplicity of crossed-rods contacts. This model has the advantage that the wave lengths and heights of each surface may be varied independently without destroying the model concept; also, resultant deflections are very near that obtained for spherical contacts.

Of primary concern is what happens to the displaced metal as the surfaces are loaded. Under an elastic condition, a change in volume of the stressed members will occur, and one assumption might be that the depressed metal simply disappears. It is more likely that,for the extremely shallow hills and valleys of most seating surfaces, the valleys rise as the hills are depressed.

A second consideration is that, as the surface asperities are compressed, a point is eventually reached when the assumed model is not the controlling characteristic, and deformation has rendered the model invalid. This transition is not fully understood but it is assumed that it is gradual and will tend to cause a general stiffening of the surface so that more load will be required to decrease leakage than the analysis predicts. However, the primary objective of the analysis is to place the controlling variables in proper perspective with test data used to establish a reference datum.

Deformation Equations. The variation of the average leakage path (h_e) with load (or gross seat stress) can be established from Fig. 19. The approach of the two sinusoidal surfaces shown is approximated by the Hertz equation for the deformation of two cylinders modified by a factor (ϵ) which may be assumed to vary from 1 to 2. If $\epsilon = 1$, the displaced material is assumed to disappear into the surface. If $\epsilon = 2$, the valleys are assumed to rise in proportion to the deformation of the peaks. The deformation in terms of the periodic surfaces shown is

$$\delta = 2C \left[\frac{S^2}{a^2} \left(h_1 \lambda_2^2 + h_2 \lambda_1^2 \right) \right]^{1/3}$$

where

$$S \equiv \frac{F}{\pi D_s L}, \quad R_r \cong \frac{\lambda^2}{16h}$$

and

a = elastic constant for two contacting surfaces, psi

$$a = \frac{E_1}{1 - \nu_1^2} + \frac{E_2}{1 - \nu_2^2}$$

C = function of λ and h

D_s = mean seat diameter, inches

E = elastic modulus, psi

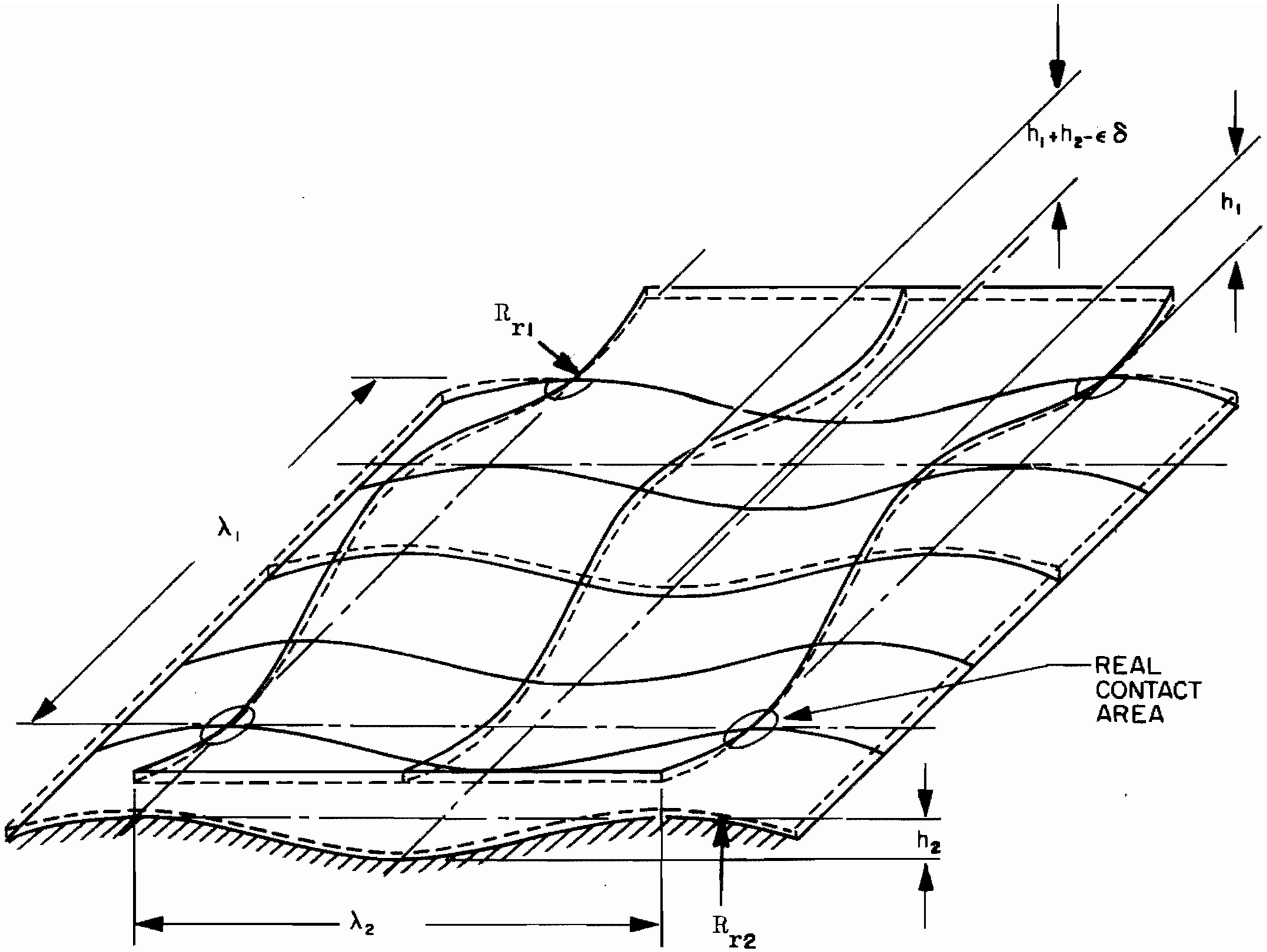

Figure 19. Sinusoidal Model Surfaces

F = total seat load, pounds

h = peak-to-valley height, inches

L = seat land width, inches

R_r = sinusoidal model roughness radius, inches

S = apparent contact stress (also equal to individual contact load divided by $\lambda_1 \times \lambda_2$), psi

λ = wavelength, inches

δ = contact deformation defined by the approach of points remote from the contact, inches

ν = Poisson ratio

The maximum allowable seat load, or apparent stress, is based upon metal failure from subsurface shear which is assumed equal to one-half the yield strength of the material in normal tension. The maximum shear stress is equal to one-third the maximum contact stress. Relating these terms results in an expression for maximum allowable apparent stress based on geometry and yield strength

$$S_m = \left(\frac{\pi}{4} A^{1/2} B Y\right)^3 \frac{\alpha^2 \lambda_1^{3} \lambda_2^{3}}{(\lambda_1^{2} h_2 + \lambda_2^{2} h_1)^2}$$

where

$$S_m = \frac{F_m}{\pi D_s L}$$

and

A and B = functions of λ and h

F_m = maximum seat load, pounds

S_m = maximum apparent contact stress, psi

Y = yield strength, psi

α = elastic constant for two contacting surfaces, 1/psi

$$\alpha = \frac{1 - \nu_1^2}{E_1} + \frac{1 - \nu_2^2}{E_2}$$

Values of Variables A, B, and C

$\dfrac{\lambda_1^2/h_1}{\lambda_2^2/h_2}$	1	2	3	4	6	10
A	0.91	1.2	1.4	1.5	1.8	2.2
B	1	0.63	0.48	0.40	0.31	0.22
C	2.08	2.0	2.0	1.9	1.8	1.6

Combining the deformation equation with the relation for the averaged heights (h_{eL} and h_{eM}) results in an expression relating the apparent seat stress to the equivalent leakage path in terms of the surface microgeometry and material properties. The general expression is

$$H_e = M \; (H - \epsilon \; \delta)$$

where

$H = h_1 + h_2$

M = either the laminar or molecular factors of Fig. 17

Simplification for Identical Surfaces. The previous equations have been derived so that surfaces of different roughness and wave lengths may be evaluated. Where the two seating surfaces differ appreciably, the deflections must be computed from these equations. In general, however, the techniques used to finish a poppet are also used on the seat, and the resulting surfaces are quite similar, if not identical. Considerable mathematical simplification of the previous equations is afforded if the two surfaces are treated as identical. In most cases, nominal differences can be simply averaged. Assuming $\epsilon = 3/2$ (valleys rise 1/2 the peak deformation) the equations are reduced as follows:

$$\delta = \left(\frac{36\,\alpha^2\,S^2\,h^3}{\Phi^2}\right)^{1/3} = \left(\frac{4.5\,\alpha^2\,S^2\,H^3}{\Phi^2}\right)^{1/3}$$

$$\Phi \cong \frac{2h}{\lambda} = \frac{H}{\lambda}$$

$$S_m = \frac{0.42\,\alpha^2\,Y^3}{\Phi^2}$$

$$H_{eL} = 0.68\,(H - \frac{3}{2}\,\delta) = 1.36\,(h - \frac{3}{4}\,\delta)$$

$$H_{eM} = 0.61\,(H - \frac{3}{2}\,\delta) = 1.22\,(h - \frac{3}{4}\,\delta)$$

The flattening stress (S_f) may be obtained by letting $\delta = 4/3\ h$; H_e is zero, and theoretically, leakage is zero. Although flattening stress is only hypothetical (because of model breakdown and real surface defects), it results in a valuable criterion of surface deformability. The flattening stress for the assumed model is

$$S_f = \frac{0.257\,\Phi}{\alpha}$$

which indicates that for any elastic material, the apparent stress to achieve a given deformation is dependent upon only the average asperity angle. The analogy of the corrugated tin roof helps visualize this relation. It is apparent that increasing the number of corrugations per foot will increase the stiffness of the structure and vice versa.

The relative importance between waviness and roughness can be obtained by computing the ratio of the waviness to roughness flattening loads; therefore,

$$\frac{S_{f_w}}{S_{f_r}} = \frac{\Phi_w}{\Phi_r}$$

In most cases, the roughness will not be flattened; therefore, the above criterion should be determined using the actual apparent stress applied.

Deformation of Nodules

The treatment of nodular deformations is the same as for roughness except for the introduction of a density function (β_n) and a slightly different model assumption. Because most nodular contacts are more round than elongated and quite larger than opposing roughness, the assumed model is a sphere on flat.

Comparison between contact deformation and the substrate deflection where the contact load is assumed uniformly distributed over the nodule base area indicates that for the shallow angles of the nodules considered herein substrate deflection can be neglected. As with the roughness model, though, deformation approaching (h_n) results in a breakdown of the assumed model and real flattening loads will be considerably greater than calculated. Referring to Fig. 20, the derived equations are

$$\beta_n = \frac{d}{\lambda_n}, \quad R_n = \frac{d^2}{8h_n}$$

$$\delta_n = \left(\frac{18\,\alpha^2\, S_n^{\,2}\, h_n^{\,3}}{\beta_n^4\, \Phi_n^{\,2}} \right)^{1/3}$$

$$S_{mn} = \frac{1.1\, \beta_n^{\,2}\, \alpha^2\, Y^3}{\Phi_n^{\,2}}$$

$$S_{fn} = \frac{0.236\, \beta_n^2\, \Phi_n}{\alpha}$$

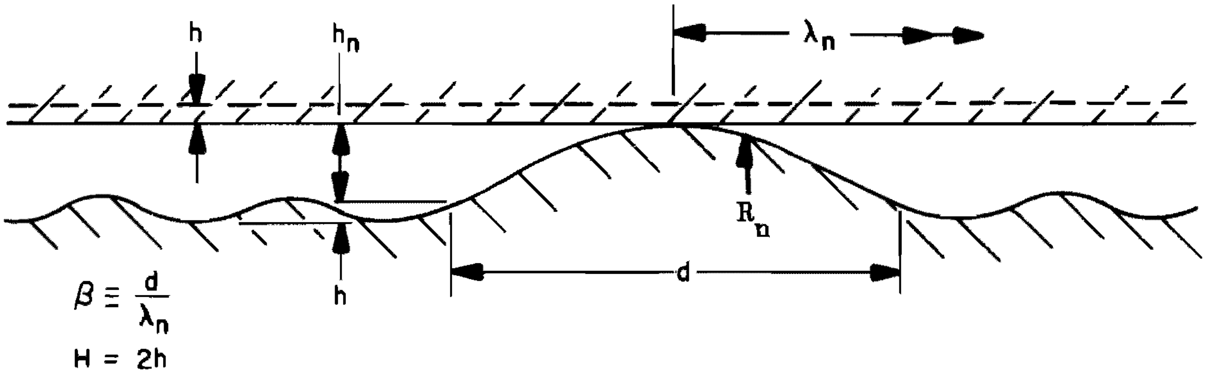

Figure 20. Model of Hemispherical Nodule

If $\beta_n = 1$, these equations represent a flat surface contacting a surface comprised entirely of spherical caps. Ratios of these equations with those of the previous models for surfaces of equal height and wavelength give the following results:

$$\frac{\delta_n}{\delta} = \left(\frac{18}{4.5}\right)^{1/3} = 1.6$$

$$\frac{S_{mn}}{S_m} = \frac{1.1}{0.42} = 2.6$$

$$\frac{S_{fn}}{S_f} = \frac{0.236}{0.257} = 0.92$$

These ratios indicate that the nodular surface is not only more compliant than the crossed rods model but is also more capable of supporting a given load elastically. The load to flatten is nearly the same for both models. The reason for the greater compliance and strength of the entirely nodular surface is because it is not sinusoidal; therefore, it has more effective contact area per wavelength (λ).

Of primary concern in this analysis is the flattening stress because, in most cases, fully separated seat leakage would be quite high. As with waviness, the ratio of nodule-to-roughness flattening stresses will allow an estimation of the relative importance of nodules

$$\frac{S_{fn}}{S_{fr}} = \frac{\beta_n^2 \Phi_n}{\Phi_r}$$

If the seat load is insufficient to flatten nodules, the equivalent height may be approximated by adding the nodular space to the equivalent heights for the asperities of both surfaces; therefore, the general expression is

$$H_{en} = h_n - \delta_n + M H$$

The load to flatten nodules or waviness subtracts from the total load so the roughness deformation expression is modified accordingly

$$\delta_r = \left[\frac{36\,\alpha^2\, h^3\, (S - S_n - S_w)^2}{\Phi^2}\right]^{1/3}$$

Stress-Leakage Equations

The deformation and leakage flow equations previously developed may be combined to obtain a composite equation relating all of the known variables. While such an expression is exceedingly cumbersome and is better handled in parts, it does allow at one viewing a consideration of all variables.

Assumptions. The assumptions leading to the final equations are as follows:

1. Leakage flow is described by the laminar and molecular flow equations for parallel plates. Total flow is the sum of molecular and laminar flow.
2. Appropriately weighted averaging factors may be used to obtain equivalent parallel plate heights for calculating leakage.
3. Seat load is uniformly applied and is uniformly distributed across the seat land (L).
4. Mating surfaces are sinusoidal in one direction, cross-layed at 90 degrees, and have the same peak-to-valley height and wave length (there are no superimposed nodules or waviness).
5. Surface deformation equations are valid up to 3/2 of the yield strength based on Vicker's hardness tests.
6. Hertz theory is valid for peak deformation to define the decrease in (h) up to some value to be determined by test.

Equations.

$$S_m = \frac{0.42\ \alpha^2\ Y^3}{\Phi^2}$$

$$S_f = \frac{0.257\ \Phi}{\alpha}$$

$$\delta = \left(\frac{4.5\ \alpha^2\ S^2\ H^3}{\Phi^2}\right)^{1/3}$$

$$H_{eL} = 0.68\ (H - 3/2\ \delta)$$

$$H_{eM} = 0.61\ (H - 3/2\ \delta)$$

$$H = h_1 + h_2$$

$$\omega_L = \frac{\pi\ D_s\ H_{eL}^3\ (P_1^2 - P_2^2)}{24\ \mu\ L\ RT}$$

NOTE: $RT = \frac{P}{\rho}$

$$\omega_M = \frac{4}{3}\ \sqrt{2\ \pi}\ \ \frac{D_s\ H_{eM}^2\ (P_1 - P_2)}{L\ \sqrt{RT/g}}$$

$$Q = \frac{\omega}{\rho} = \omega \frac{RT_s}{P_s}$$

For

$P_s = 14.7$ psia

$T_s = 70$ F $= 530$ R

$g = 32.2$ ft/sec^2 $= 1.39 \times 10^6$ in./min^2

$$Q_L = \frac{4.71\ D_s\ H_{eL}^{3}\ (P_1^{2} - P_2^{2})}{\mu\ LT}$$

$$Q_M = \frac{1.42 \times 10^{5}\ D_s\ H_{eM}^{2}\ (P_1 - P_2)}{L} \sqrt{\frac{R}{T}}$$

$$Q = Q_L + Q_M$$

Composite Equation.

$$Q = \frac{4.71\ D_s\ (P_1^{2} - P_2^{2})}{\mu\ LT} \left[M_L\ (H - \epsilon\ \delta)\right]^{3} + \frac{1.42 \times 10^{5}\ D_s\ (P_1 - P_2)}{L} \sqrt{\frac{R}{T}} \left[M_M\ (H - \epsilon\ \delta)\right]^{2}$$

Parametric Stress-Leakage Data

Parametric data have been computed from the previous equations in support of the experimental test program. The poppet and seat model design is shown in Fig. 21 with appropriate dimensions. Test and configuration constants and parameterized variables are summarized below with the reduced equations.

Test and Configuration Constants. The test and configuration constants are as follows:

Mean seat diameter	$D_S = 0.470$ inch
Seat land width	$L = 0.03$ inch
Inlet pressure	$P_1 = 1015$ psia
Outlet pressure	$P_2 = 14.7$ psia
Gas temperature	$T = 70$ F $= 530$ R
Gas constant	$R = 663$ in./R (nitrogen)
Gas viscosity	$\mu = 4.4 \times 10^{-11}$ lb-min/in.^{2} (nitrogen)

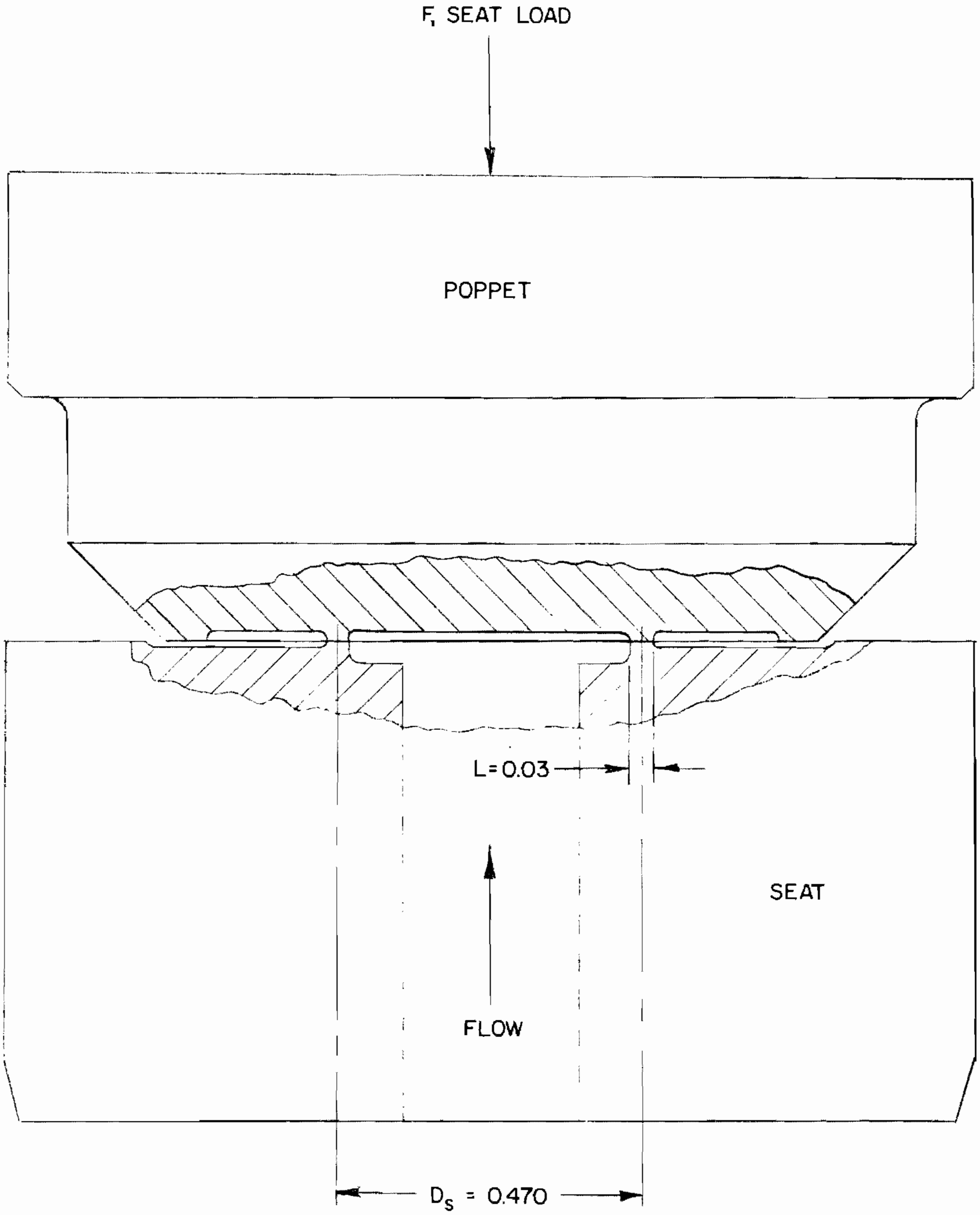

Figure 21. Typical 1/2-Inch Poppet and Seat Model

Reduced Equations for 1/2-Inch Model Seat. The reduced equations are as follows:

$$Q_L = 3.26 \times 10^{15} H_{eL}^{\ 3}$$

$$Q_M = 2.49 \times 10^{9} H_{eM}^{\ 2}$$

$$Q_L = 3.26 \times 10^{15} \left\{ 1.36 \left[h - \frac{3}{4} \left(\frac{36\, \alpha^2 s^2 h^3}{\Phi^2} \right)^{1/3} \right] \right\}^3$$

$$Q_M = 2.49 \times 10^{9} \left\{ 1.22 \left[h - \frac{3}{4} \left(\frac{36\, \alpha^2 s^2 h^3}{\Phi^2} \right)^{1/3} \right] \right\}^2$$

$$Q = Q_L + Q_M$$

Material Parameters. The following lists the material parameters.

Material	Vickers Hardness Number kg/mm^2	Yield Strength Criterion, psi	Elastic Constant,* 1/psi	Elastic Modulus, psi
440C Stainless Steel	800	610,000	0.0607×10^{-6}	30×10^{6}
6061-T651 Aluminum	123	93,800	0.182×10^{-6}	10×10^{6}
Tungsten Carbide	1330	1,000,000	0.0202×10^{-6}	90×10^{6}

*Poisson's ratio, $\nu \cong 0.3$

Surface Profile Parameters. The surface profile parameters are:

1. Peak-to-valley height for one surface (second surface identical), $h = 1, 1.5, 2, 3, 4.5, 6, 9, 12$ and 18×10^{-6} inches

   NOTE: These h values correspond to approximate AA values of 1/3, 1/2, 2/3, 1.0, 1.5, 2.0, 3.0, 4.0, and 6.0 microinches examined in the experimental program.

2. Average asperity angle, $\Phi = 1/16, 1/4, 1$ and 4 degrees (must be in radians for use in equations).

The parametric curves of leakage vs apparent seat stress are shown in Fig. 22 through 24 for the constants and variables noted above. The curves cover a span of 10^7 scim for seat stress from 100 to 100,000 psi. The basic parameter for each family of curves is h (e.g., $h = 1.0$ microinch) with variations of Φ showing the span from typical waviness to roughness. An evaluation of these curves shows the effect of h, Φ, and α on leakage.

Interpreting the curves requires certain precautions and observations. Multicycle log-log paper can be very misleading because of the great span of data. For example, consider the scope of data in the first cycle (100 to 1000 psi) in relationship with the second, then the third. Also, the curves represent deformation of a uniform surface and not the more complex model of knobs on knobs on knobs proposed by Archard (see Surface Studies). The effect of waviness superimposed on roughness (a beginning of Archard's model) can be evaluated by subtracting the apparent stress to flatten waviness from the total available apparent stress to arrive at a final leakage value. To find the leakage of both waviness and roughness when waviness is not eliminated, the waviness leakage is added to the roughness leakage obtained at the 100-psi (essentially zero) stress level.

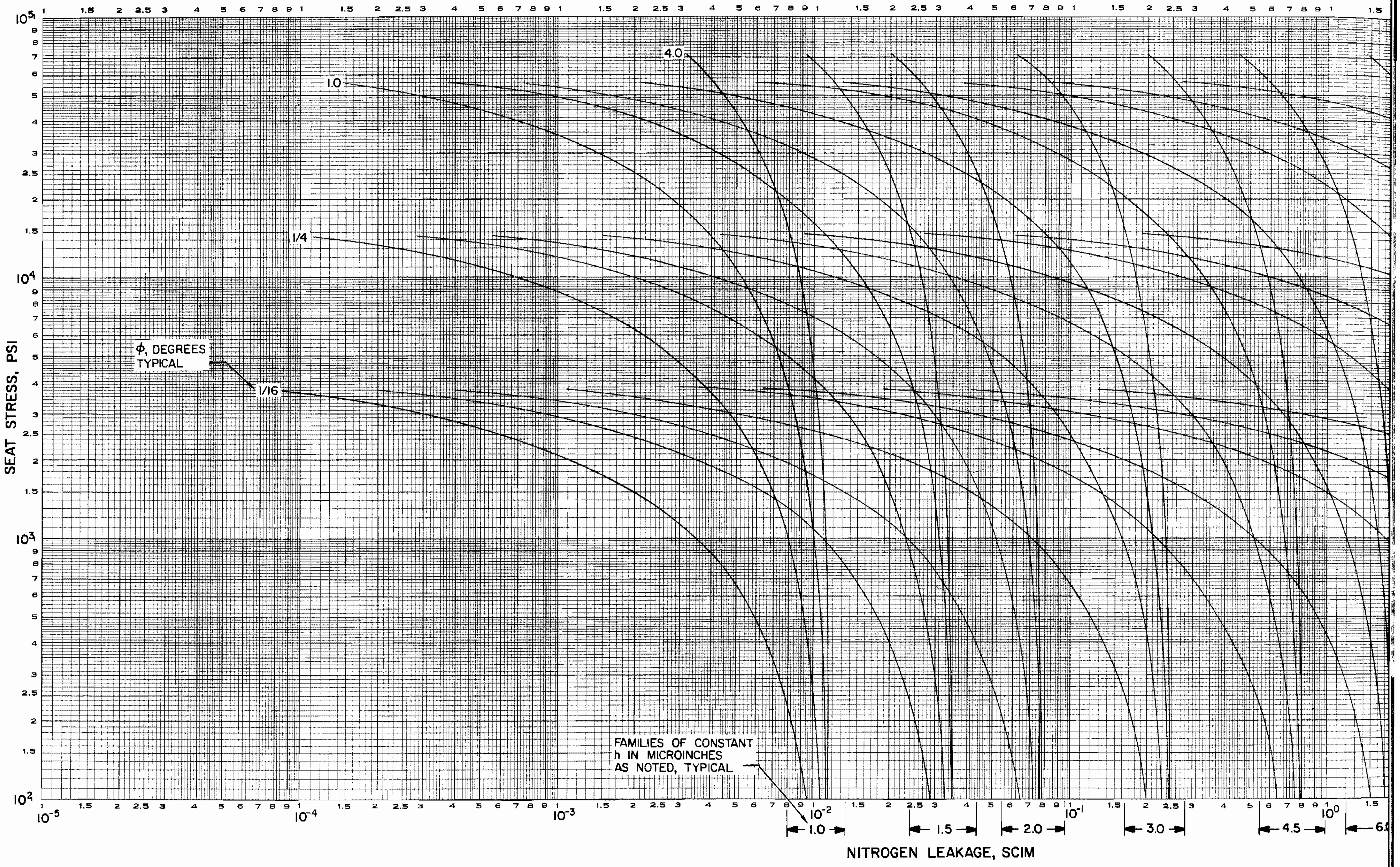
SEAT STRESS, PSI
NITROGEN LEAKAGE, SCIM
10^5
10^4
10^3
10^2
10^{-5}
10^{-4}
10^{-3}
10^{-2}
10^{-1}
10^0
4.0
1.0
1/4
1/16
φ, DEGREES
TYPICAL
FAMILIES OF CONSTANT
h IN MICROINCHES
AS NOTED, TYPICAL
1.0
1.5
2.0
3.0
4.5
6.

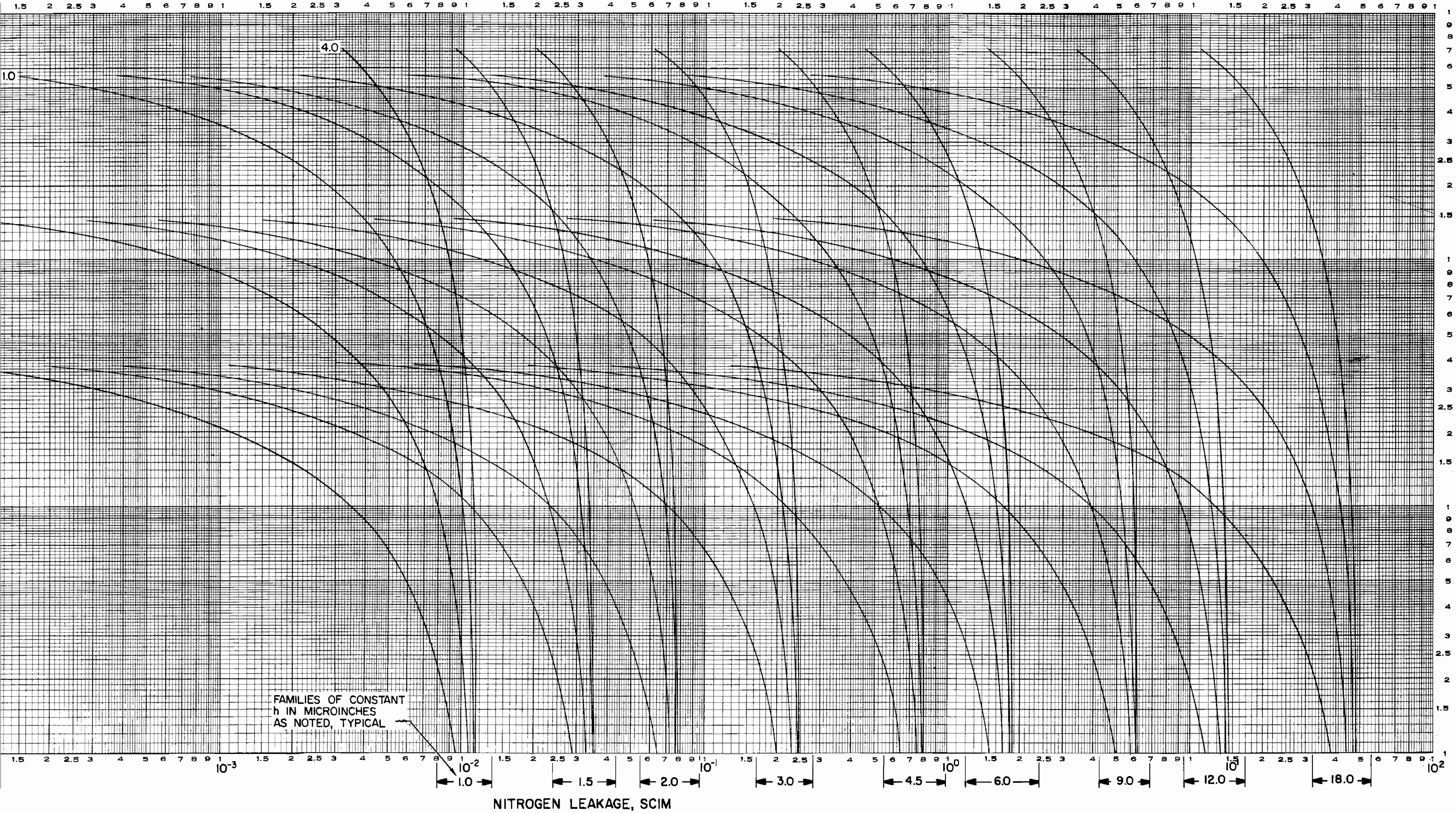

Figure 22. Theoretical Parametric Stress vs Leakage Curves for Steel

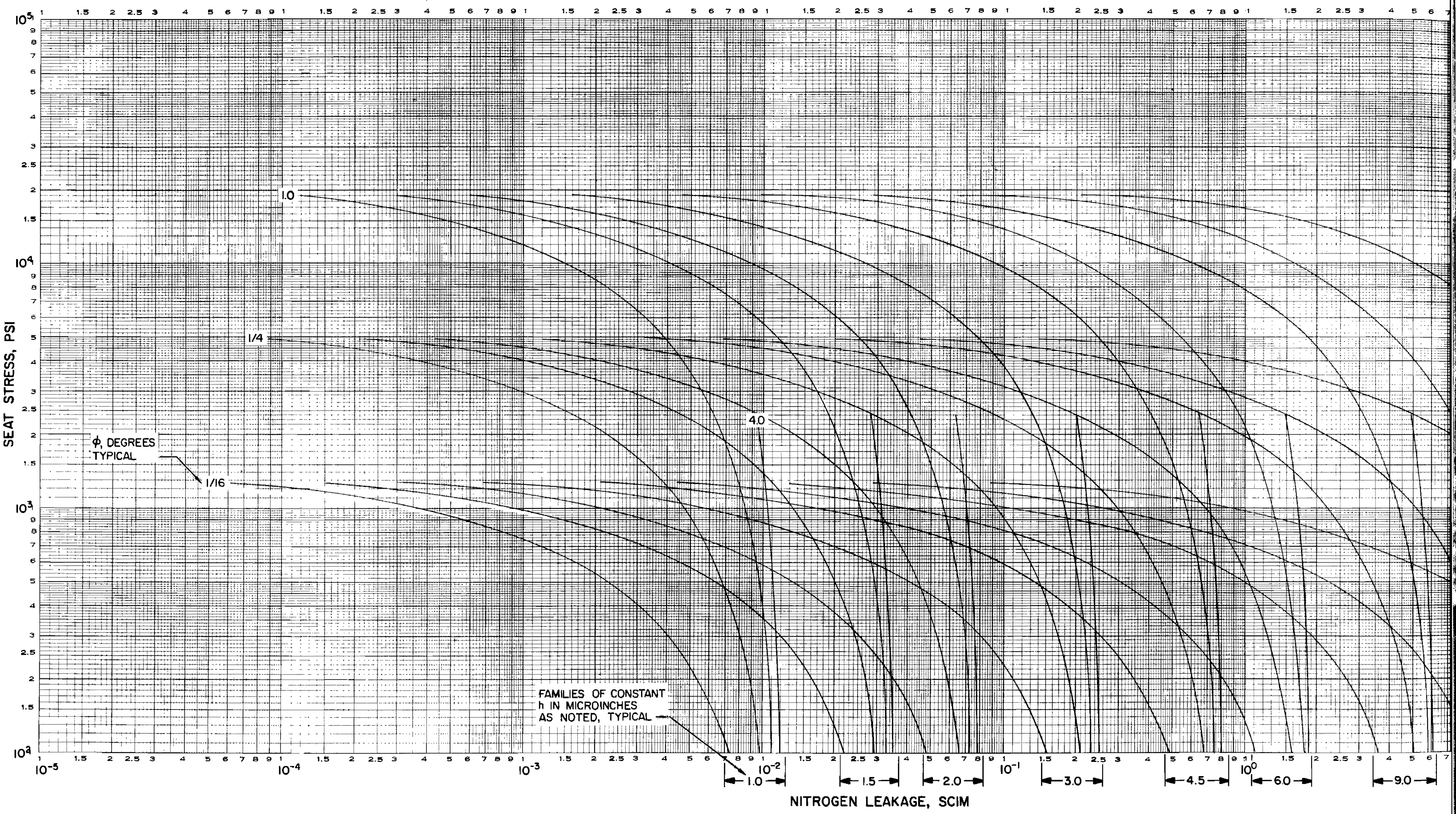
SEAT STRESS, PSI
NITROGEN LEAKAGE, SCIM
10^5
10^4
10^3
10^2
10^-5
10^-4
10^-3
10^-2
10^-1
10^0
1.0
1/4
1/16
4.0
φ, DEGREES TYPICAL
FAMILIES OF CONSTANT h IN MICROINCHES AS NOTED, TYPICAL
1.0
1.5
2.0
3.0
4.5
6.0
9.0

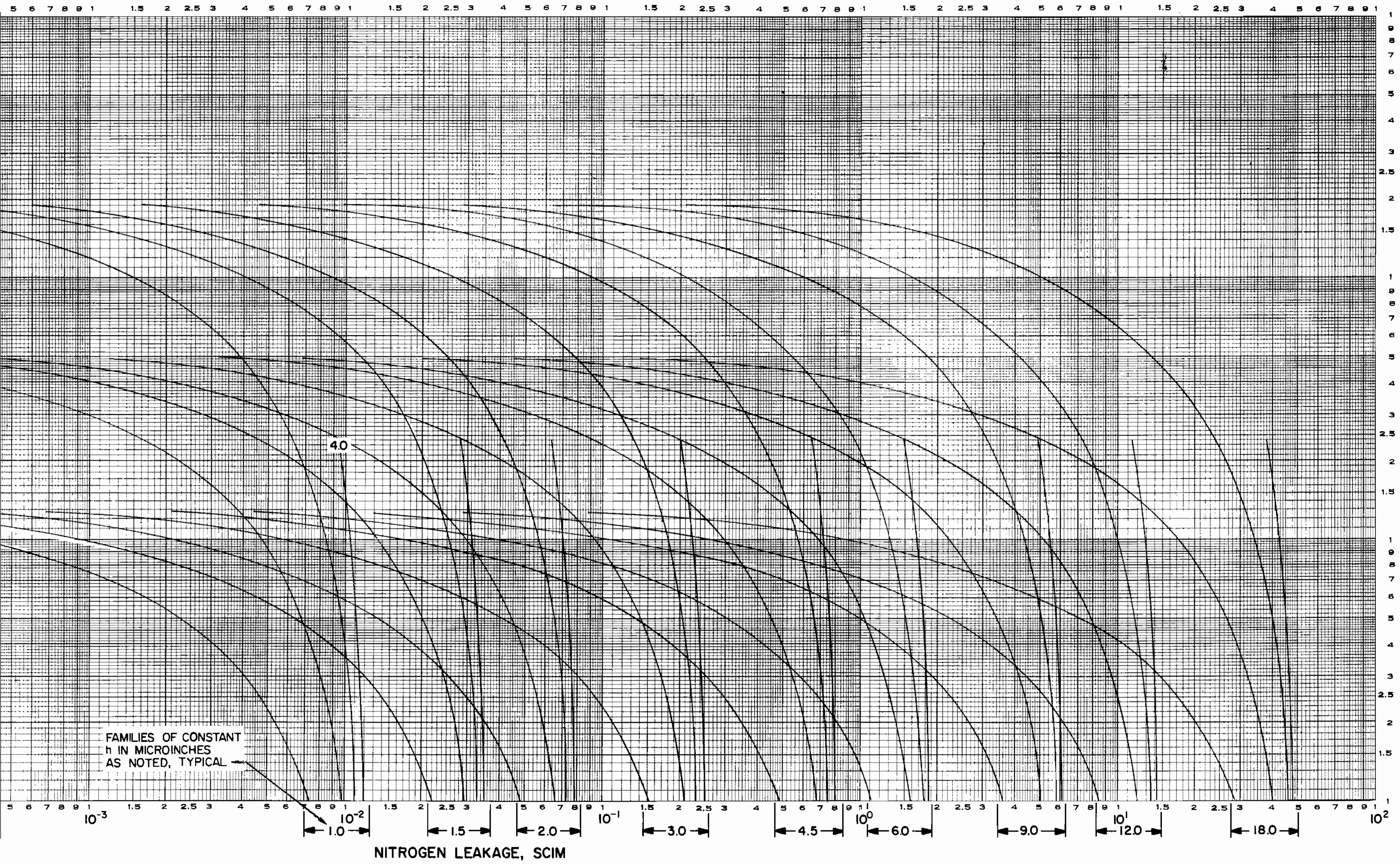

Figure 23. Theoretical Parametric Stress vs Leakage Curves for Aluminum

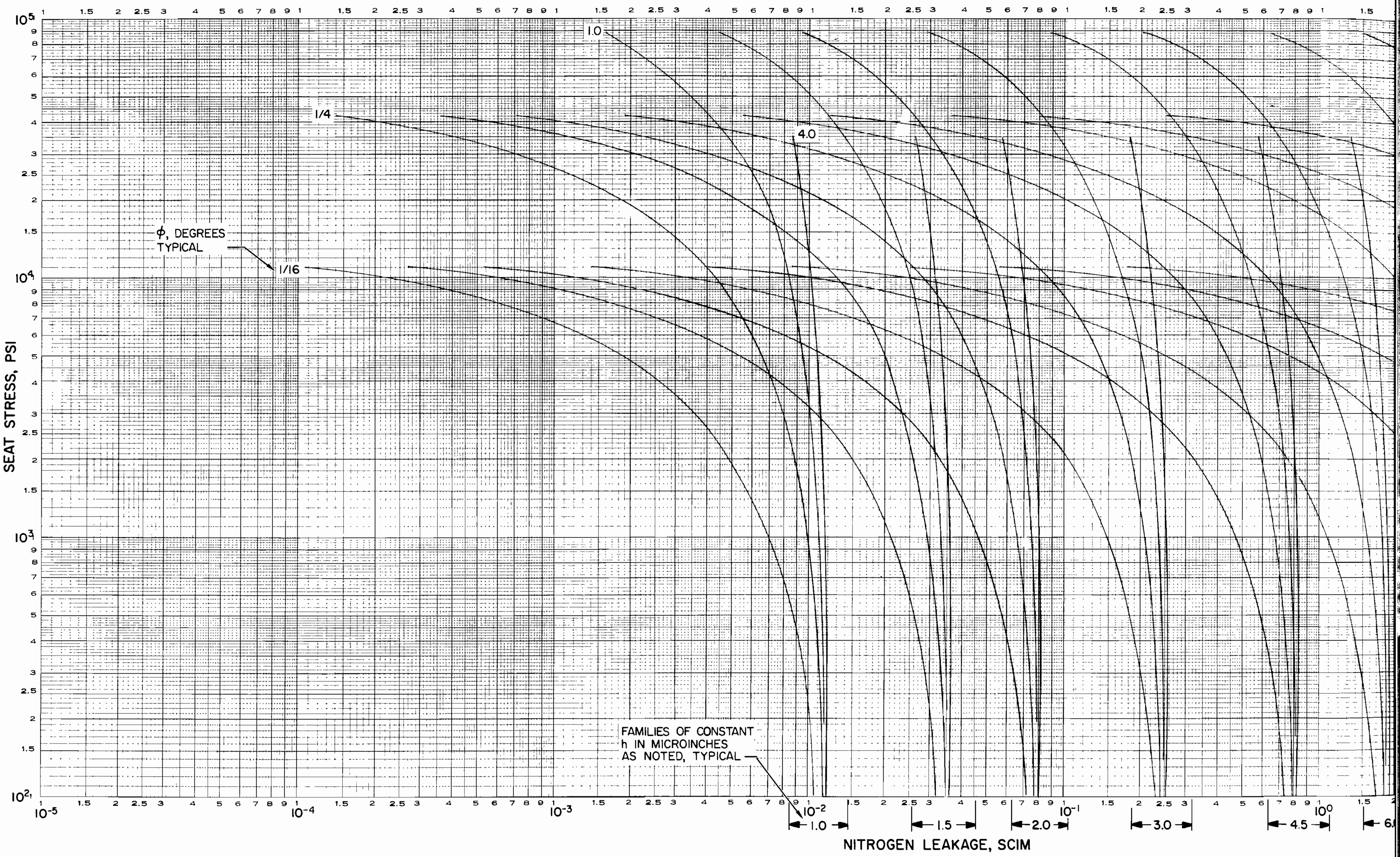
SEAT STRESS, PSI
NITROGEN LEAKAGE, SCIM
10⁵
10⁴
10³
10²
10⁻⁵
10⁻⁴
10⁻³
10⁻²
10⁻¹
10⁰
φ, DEGREES TYPICAL
1/16
1/4
1.0
4.0
FAMILIES OF CONSTANT h IN MICROINCHES AS NOTED, TYPICAL
1.0
1.5
2.0
3.0
4.5

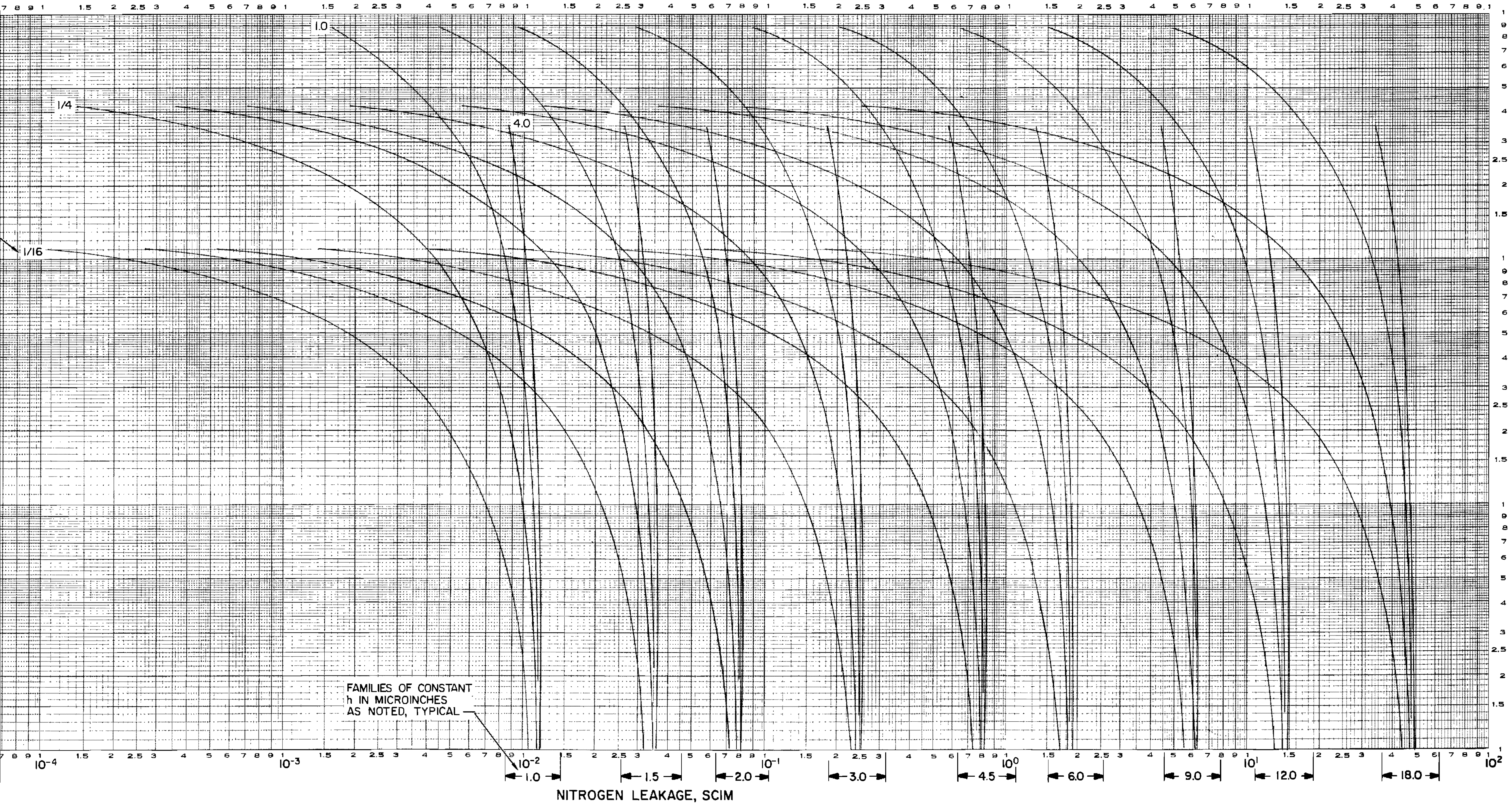

Figure 24. Theoretical Parametric Stress vs Leakage Curves for Tungsten Carbide

Stress-leakage data for other test conditions and valve seat configurations may be obtained by applying appropriate ratios of the variable parameters to the governing equations. Because the total leakage described by these curves is a combination of laminar and molecular flow, the division of this flow must first be determined so that the ratios may be applied separately to each term of the total flow equation $(Q = Q_L + Q_M)$. Figure 25 plots the ratios of Q_M/Q and Q_L/Q in percent for the parametric data curves of Fig. 22 through 24; i.e., for the specific model at a 1000-psig inlet pressure.

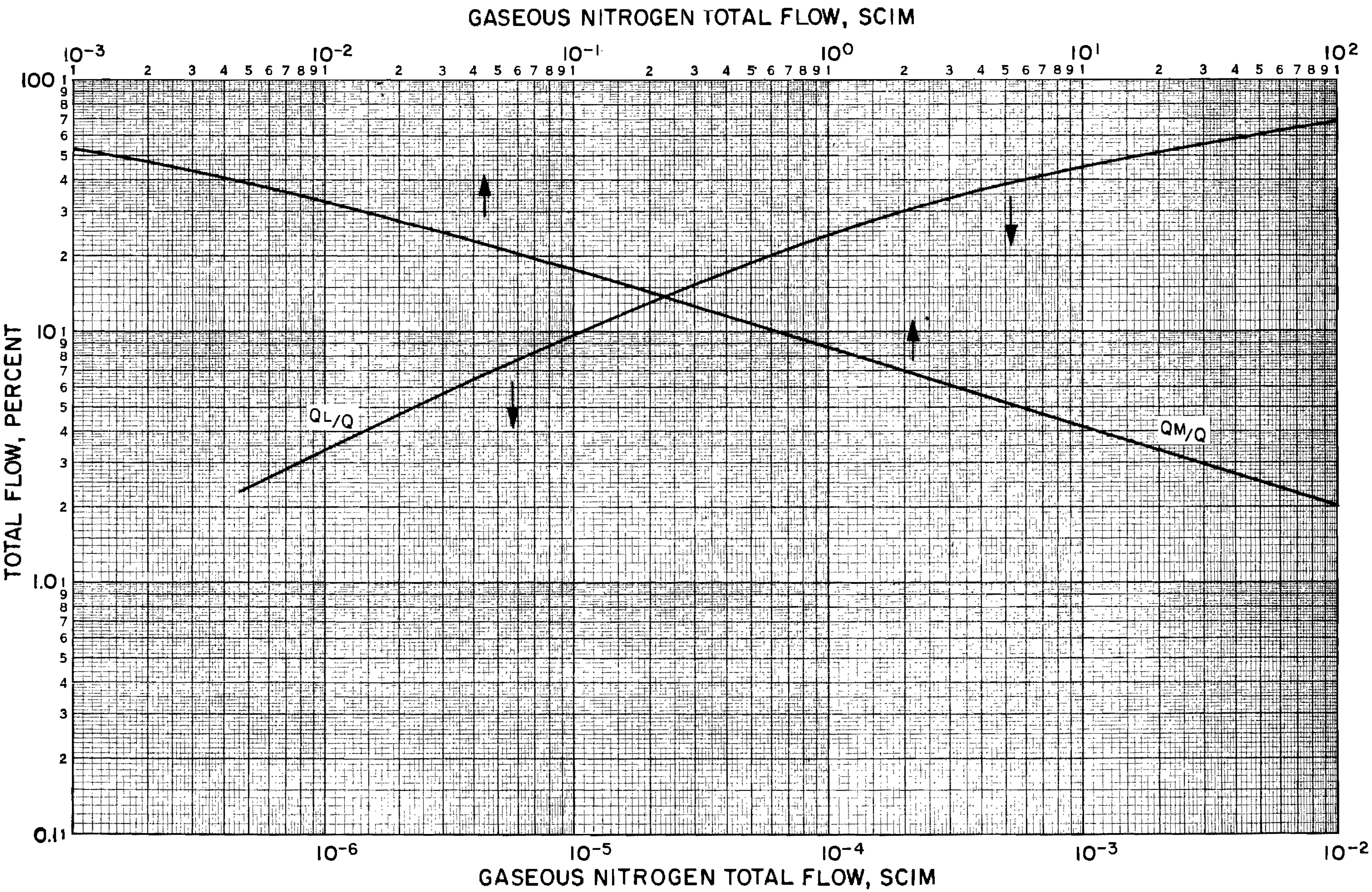

Figure 25. Division of Total Flow in Fig. 22 Through 24

CIRCULAR LAY SURFACE DEFORMATION AND LEAKAGE

The improved sealability of circular lay surfaces is widely recognized. However, little data exist for specification and control of the geometric circular parameters affecting leakage. Evaluation of finishing methods and experimental poppet and seat models has shown that the ideal case of perfectly circular and concentric poppet and seat roughness lays is quite unlikely. As roughness with lay is much less than across lay, the leakage near crest contact is relatively negligible. Therefore, the significant leakage paths will result from the eccentric contact of circular lay surfaces.

Unlike multidirectional surfaces having a nearly uniform flow path, the mating of circular lay poppets and seats results in very complex geometry which has been demonstrated from leakage tests to be extremely load sensitive. The purpose of this analysis is to first examine the geometry of a simplified circular lay model to define the probable leakage path, and second to analytically describe the change in this path resulting from an applied load.

As with the previous analysis, the assumption of a sinusoidal surface characteristics serves to represent the roughness with Hertz equations describing contact deformation and stress. Both surfaces are assumed to be identical with sinusoidal crest and troughs perfectly circular.

Circular Lay Model

The schematic model of eccentric circular lay surfaces is shown in Fig. 26. This eccentric overlay of two sets of concentric circles represents the crests of the circular waves. Each intersection signifies a real contact point. From the indicated constructions, the contact angle (ψ_N) and the number of contacts per wave length in one quadrant (N_{90}) may be determined as follows.

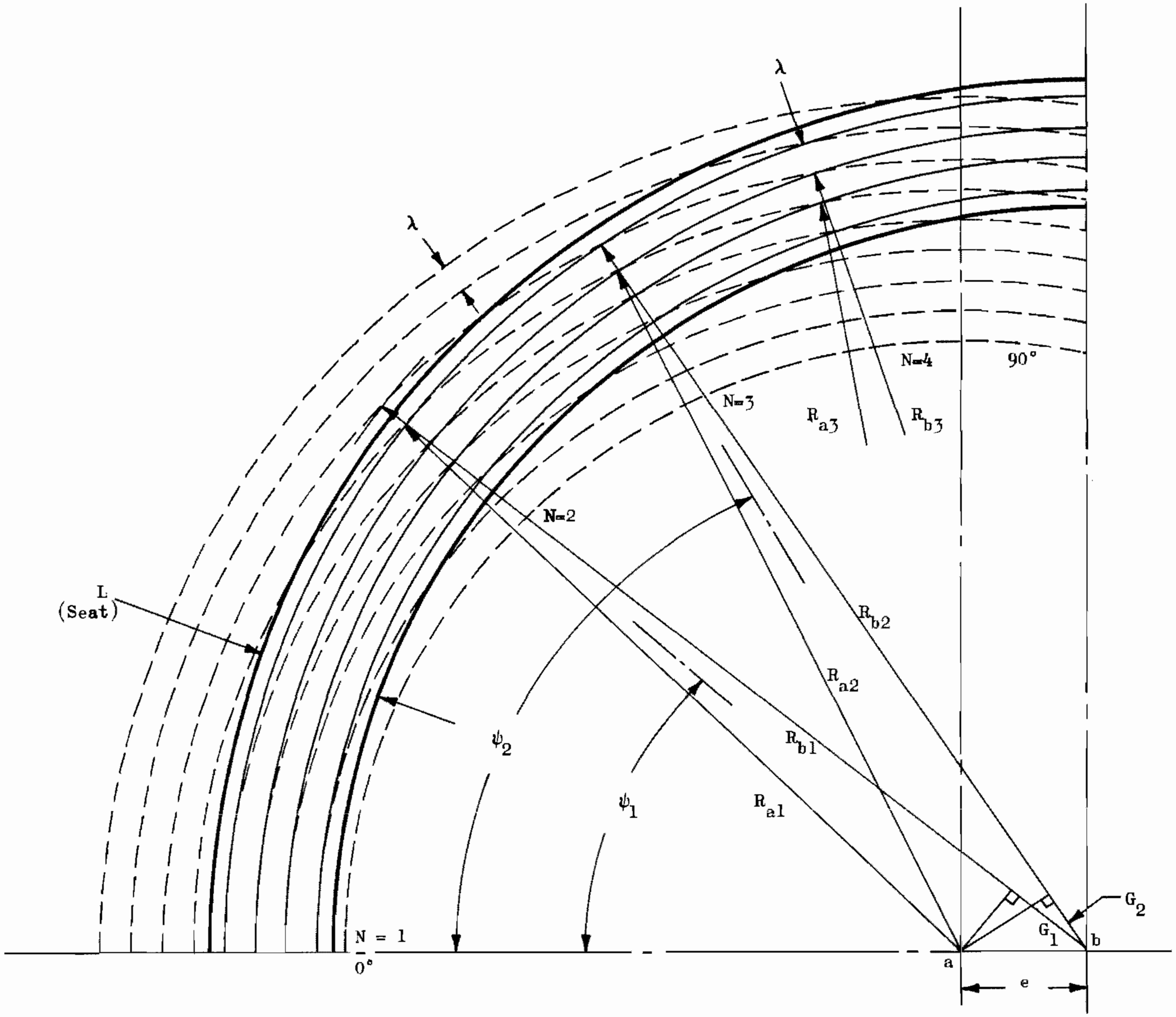

Figure 26. Model of Eccentric Circular Lay Surfaces

$$G_N = e \cos \psi; \qquad R_{a1} = R_{a2} = R_{a3}$$

$$R_{b1} = R_{bN} + (N-1)\,\lambda; \qquad e = R_{b1} = R_{a1}$$

$$\psi_N = \text{arc cos}\left(1 - \frac{N\,\lambda}{e}\right)$$

$$N_{90} = \frac{e}{\lambda}\ ; \qquad e \geqq \lambda$$

where (N) signifies the specific contact. For land width (L) small with respect to seat diameter (D_s), the mean length of each intersection is:

$$\ell_N = \frac{D_s}{2}\,(\Delta\,\psi_N)$$

$$\Delta\,\psi_N = \psi_N - \psi_{N-1} \text{ (radians)}$$

Note that $\Sigma\,\Delta\,\psi_N = \pi/2$, or 90 degrees. It can be seen in Fig. 26 that e/λ is (4) and there are (4) intersections (N_{90}) in each quadrant per (radial) wavelength. Moreover, the distribution of contacts, while regular, is not uniform over the seat area, as (ℓ_1) is much greater than (ℓ_4). The equation for the ratio of (ℓ_1/ℓ_4) is:

$$\frac{\ell_1}{\ell_{90}} = \frac{\text{arc cos}\left(1 - \frac{\lambda}{e}\right)}{\text{arc sin}\ \frac{\lambda}{e}}$$

The variability of this ratio is shown below:

$\frac{\lambda}{e}$	1	$\frac{1}{4}$	$\frac{1}{10}$	$\frac{1}{100}$
N_{90}	1	4	10	100
$\frac{\ell_1}{\ell_{N_{90}}}$	1	2.86	4.43	143.0

Leakage Path

The leakage flow path formed by the model surfaces is shown in Fig. 27. With no applied load, each surface will contact at wave crests resulting in a variable sinusoidal gap equal, at the maximum spacing between contacts, to the sum of the peak-to-valley height of each surface. The flow space along contacts (from point a to b) varies as shown by line C. As the predominant flow path will follow the maximum gap, it would seem that some circumferential flow is inevitable; however, the circumferential length of path is very long compared with (L) and, from Fig. 27 radial flow is unrestricted since a space varying at contact from zero to (2h) and between contacts at a constant (h) does exist. For this analysis, it is assumed that the flow path may be approximated by the appropriate average of the space described by line C, thus neglecting the total gap height (2h); equivalent parallel plate heights based on the sinusoidal shape are:

$$H_{eL} = 0.68\ h; \qquad H_{eM} = 0.61\ h$$

Mechanism of Closure

From the previous analysis, several facts become apparent which partially explain the high closure rate of the circular lay surface. Comparison with the unidirectional model shows that the circular lay model will usually have considerably fewer real contacts. The number of circular lay contacts (N_c) is

$$N_c = \frac{4eL}{\lambda^2}, \qquad (e \geqq \lambda)$$

whereas the number of contacts for the crossed unidirectional lay model is given by:

$$N_u = \frac{A_s}{\lambda^2} = \frac{\pi D_s L}{\lambda^2}$$

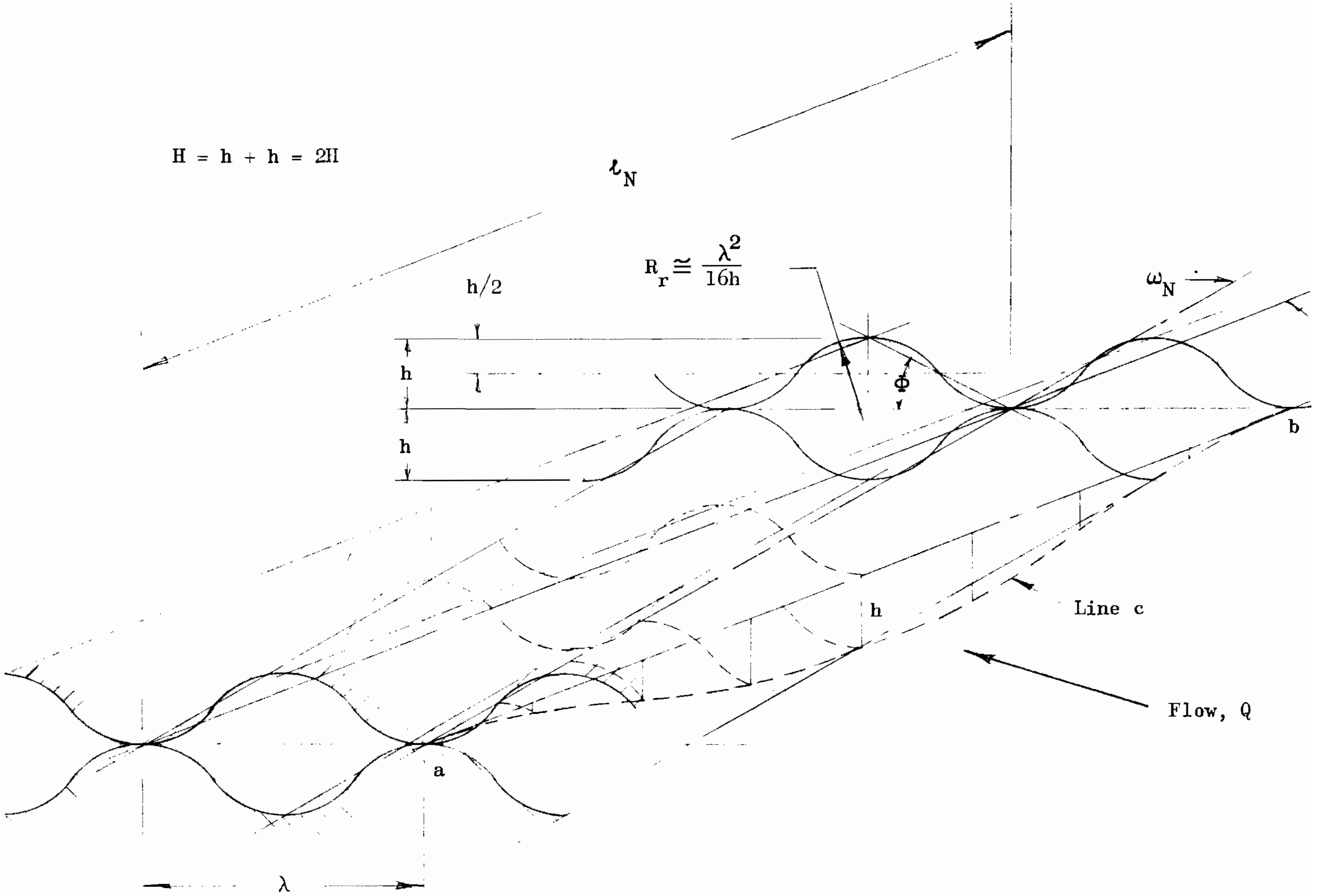

Figure 27. Flow Path of Eccentric Circular Lay Surfaces

Thus

$$\frac{N_u}{N_c} = \frac{\pi D_s}{4e}$$

As (D_s) is much greater than (e), the real contacts of the circular lay surface will be loaded proportionately more and accordingly will have greater deformation than the unidirectional model.

Of greater significance is the amount of deformation required by these model surfaces to effect full closure. For the assumptions made, the circular lay surfaces must only deform one-half of the peak-to-valley space (h at line C, Fig. 27) while the unidirectional surfaces must deform some definitely larger amount (assumed 3/2 h).

From these observations, it is apparent why circular lay surfaces have a higher leakage shutoff rate than even smoother unidirectional lay surfaces.

Of further consideration is the effect of load upon contact geometry. From the study of nodules, it was shown reasonable to assume small substrate deformation under a contact compared with contact deformation because of relative stiffnesses. This indicates that deflection is uniform over the seating surface, but due to the nonlinear distribution of contacts and their varying contact geometry, the load will be distributed according to the dictates of deformation and contact geometry.

Deformation Equations

The solution for the load deformation, elliptical contact area, and stress is based upon equations presented in Ref. 61, 28, and 29. These indefinite equations are complex, involving elliptical integrals. Because of the extremely small contact intersection angle (ω_N), some simplifications may be made; however, the solution for apparent stress and load involving a summation of individual contact loads must be obtained by trial and error by assuming a deformation and solving for the parameters of each contact.

The elliptical contact area and orientation is shown in the sketch below with the equation for intersection angle (ω_N):

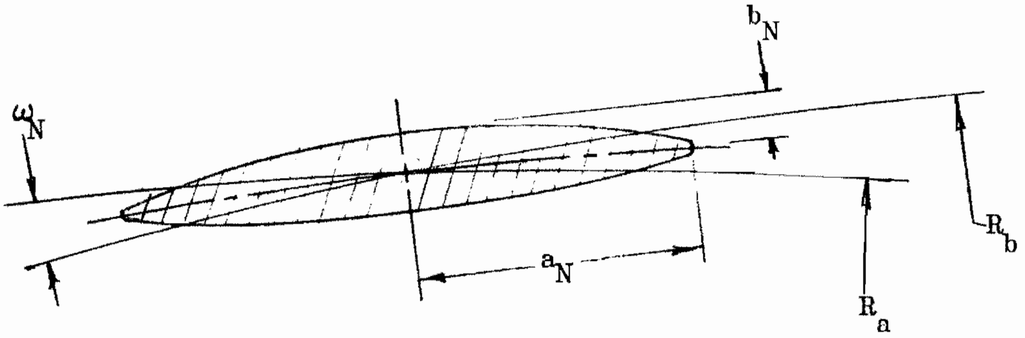

$$\omega_N = \text{arc tan}\,\frac{\lambda}{\ell_N} \cong \frac{\lambda}{\ell_N} \cong \frac{2\lambda}{D_s\,\Delta\psi_N}$$

The shape of the contact ellipse depends upon the wave contact radii (R_r, Fig. 27) and the angle (ω_N). These parameters are related by the expression:

$$\frac{A}{B} = \frac{(1 - k^2)\,(K - E)}{E - (1 - k^2)\,K}$$

where (K) and (E) are complete elliptic integrals formed with modulus (k) and, further:

$$\left(\frac{A}{B}\right)_N = \frac{\omega_N^{\,2}/4R_r}{1/R_r} = \frac{\omega_N^{\,2}}{4} = \left(\frac{\lambda}{2\ell_N}\right)^2 = \left(\frac{\lambda}{D_s\,\Delta\psi_N}\right)^2$$

Examination of these functions has shown that for arc sin $k > 82$ degrees, the above function may be accurately represented by an empirical logrithmic (base 10) equation, since (k) and (E) are very close to one. Thus, for values of $A/B < 0.044$ ($K > 3.4$), the above equation may be reduced to:

$$\log\left(\frac{3.95\,D_s\,\Delta\psi_N}{\lambda}\right)^2 = 0.868\,K_N - \log\,(K_N - 1) = G_N$$

For limited solutions additional simplification results; thus:

$4 > K_N < 100$

$$K_N = 1.396\ G_N^{0.961}$$

$$K_N = 2.72 \left(\log \frac{3.95\ D_s\ \Delta \psi_N}{\lambda} \right)^{0.961}$$

$4 > K_N < 20$

$$K_N = 1.293\ G_N$$

$$K_N = 2.586 \log \frac{3.95\ D_s\ \Delta \psi_N}{\lambda}$$

Semimajor and semiminor axes of the contact ellipse are found from:

$$a_N = \left[\frac{3\ D_s^{\ 2}\ \Delta \psi_N^{\ 2}\ P_N\ \alpha\ (K_N - 1)}{32\ \pi\ h} \right]^{1/3}$$

$$b_N = \frac{\lambda\ a_N}{D_s\ \Delta \psi_N \sqrt{K_N - 1}}$$

Individual contact load (P_N) corresponding to a given deflection (δ) is given by:

$$P_N = \frac{2\ \pi\ a_N\ \delta}{3\ K_N\ \alpha}$$

$$P_N = \frac{\pi\ D_s\ \Delta \psi_N}{6\alpha} \sqrt{\frac{\delta^3\ (K_N - 1)}{h\ K_N^{\ 3}}}$$

Average contact stress is the load divided by contact area. Based on the Hertz normal stress distribution, the maximum contact stress occurring in the contact center is 3/2 times the average, or:

$$\sigma_{CN} = \frac{3}{2} \frac{P_N}{\pi a_N b_N}$$

$$\sigma_{CN} = \frac{4}{\alpha\lambda} \sqrt{\frac{\delta h}{K_N}}$$

Therefore, for any given deflection, the maximum contact stress is nearly the same for all contacts (since K_N does not vary appreciably). The maximum allowable individual contact stress is based (as before) upon the relationship between subsurface shear and yield strength (Y) in normal tension with maximum allowable individual contact load given as:

$$\frac{3}{2} \frac{P_{Nm}}{\pi a_N b_N} \cong \frac{3}{2} Y$$

$$P_{Nm} \cong \pi a_N b_N Y$$

$$P_{Nm} \cong \frac{D_s \Delta\psi_N \alpha^2 \lambda^3 Y^3 \sqrt{K_N - 1}}{36.2 h^2}$$

Contact stress 90 degrees from the lay tangent point is maximum; therefore, (P_{Nm}) should be computed for this point.

Although the assumed model breaks down for deflections approaching (h/2), the theoretical load to flatten is of interest for evaluation of significant variables and comparison with the unidirectional lay model. Because of the relatively large circular separation between contacts, it will be assumed that (δ) must **equal** (h) for complete flattening; individual contact load is given by:

$$P_{Nf} = P_N \left(\frac{h}{\delta}\right)^{3/2}$$

As the load increases, the contact semimajor axes (a_N) increase to close off the radial flow path. It is coincident with gap closure $(\delta = h)$ that adjacent lengths nearly contact. This relationship is shown by the following ratio:

$$\left(\frac{a}{\ell/2}\right)_N = \sqrt{\frac{\delta\ (K_N - 1)}{h\ K_N}}$$

Thus, for $(\delta = h)$, the ratio is very nearly one for all contacts. For $a \cong \ell/2$:

$$b_N = \frac{\lambda}{4\sqrt{K_N - 1}}$$

This indicates the contact width $(2b_N)$ will usually be less than 1/10 of the wave length (λ). The contact geometry near closure is illustrated by Fig. 28 where the ellipse geometry is shown undistorted by adjacent material. Actually, the deformed contact geometry would be biased to follow line C of Fig. 27.

Figure 28 shows that the load has both a significant effect on the radial length of flow path and the entrance openings available for the effluent to enter the seat land. At zero load, the entire circumferential land length $(\sim \pi D_s)$ is available; however, as (a_N) increases with load, the entrance will be proportionately reduced, and the flow will be forced to zig-zag circumferentially in moving radially across the land (L). The effective land length (W_e) may be idealized as the differential between the mean diametral length (πD_s) and the summation of the contact lengths. Because the ratio $(2a/\ell)$ does not vary appreciably with (N), the nominal effective width is given by:

$$W_e \cong \pi D_s \left(1 - \frac{2a}{\ell}\right)$$

$$W_e \cong \pi D_s \left(1 - \sqrt{\frac{\delta\ (K - 1)}{hK}}\right)$$

where an average value for K may be used.

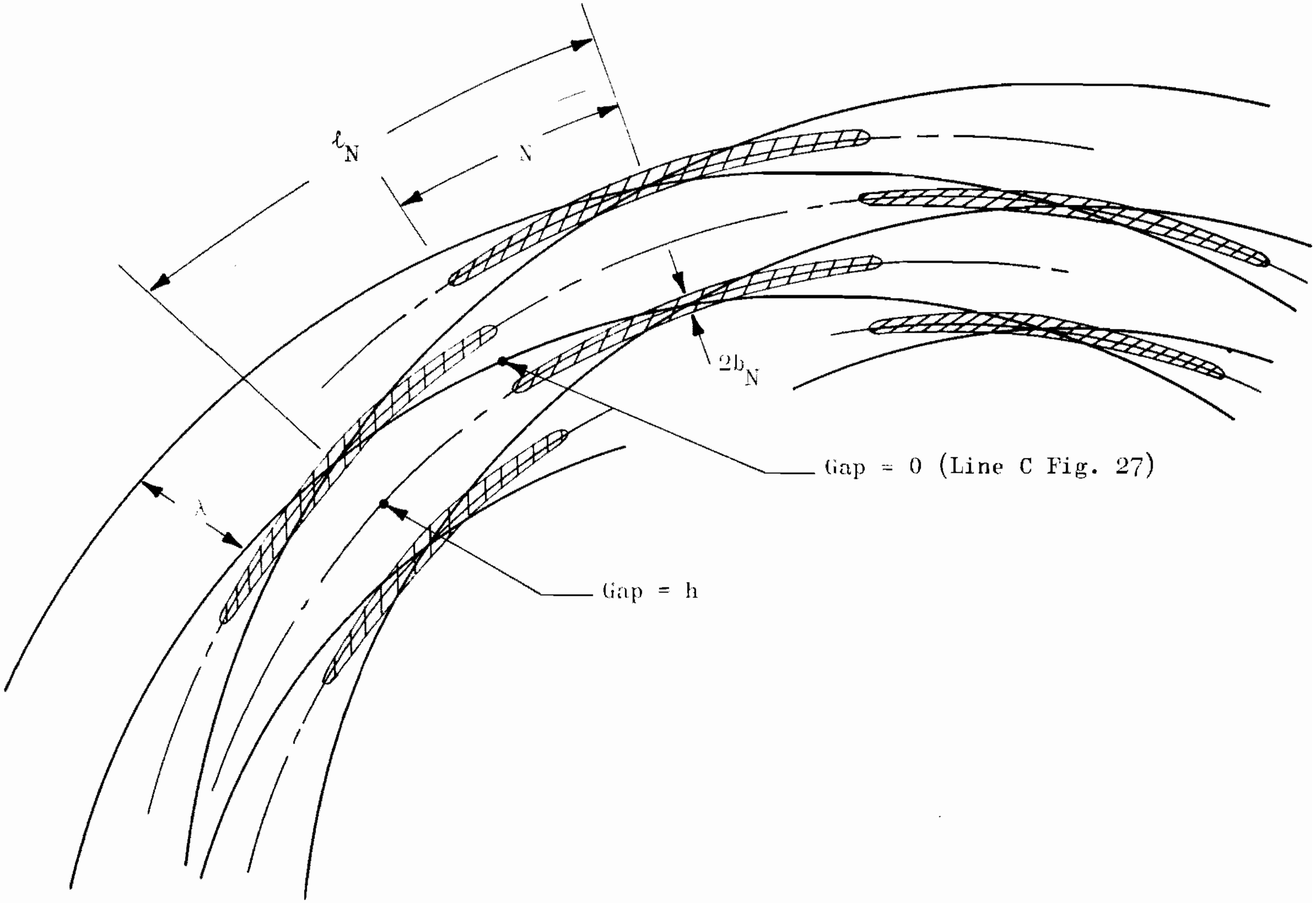

Figure 28. Circular Lay Surface Contact at Closure

Apparent Seat Stress

Total load is found by:

$$F = 4 \left(\frac{L}{\lambda}\right) \Sigma P_N$$

Apparent stress for circular lay is defined as:

$$S_c = \frac{F}{A_s} = \frac{4 \left(\frac{L}{\lambda}\right) \Sigma P_N}{\pi D_s L} = \frac{4 \Sigma P_N}{\pi D_s \lambda}$$

Apparent flattening stress is given by:

$$S_{cf} = S_c \left(\frac{h}{\delta}\right)^{3/2}$$

Comparison of Unidirectional and Circular Lay Deformation

Circular Lay Parameters. The following circular lay parameters are assumed for a single common data point computation with the basic test and configuration constants previously presented for the unidirectional lay model unchanged:

Peak-to-valley height	$h = 1.0 \times 10^{-6}$ inch
Wavelength	$\lambda = 50.0 \times 10^{-6}$ inch
Deflection	$\delta = 0.1253 \times 10^{-6}$ inch
Lay Eccentricity	$e = 0.0005$ inch

From this and previous input data, the following parameters are determined:

1. Average roughness angle:

$$\Phi = \frac{2h}{\lambda} = 0.04 \text{ radians} = 2.29 \text{ degrees}$$

2. Circular lay contacts:

$$N_{90} = \frac{e}{\lambda} = 10$$

$$N_c = \frac{4eL}{\lambda^2} = 2.4 \times 10^4$$

3. Maximum allowable individual contact load for contact (N = 10) is:

$$P_{10m} = 0.391 \text{ pound}$$

Additional parameters computed for each contact (N = 1 at tangent point to N = 10) are shown in Table 2. The basic variable reflected by this data is the contact intersection angle (ω_N), which is inversely proportional to ($\Delta \psi_N$). The smaller the intersection angle, the stiffer the contact becomes, thus requiring a greater load for a given deformation.

From the tabulated data, the final parameters controlling leakage may be determined.

$$\text{Total load, } F_c = 4 \left(\frac{L}{\lambda}\right) \Sigma P_N = 64.8 \text{ pounds}$$

$$\text{Apparent stress, } S_c = \frac{F}{\pi D_s L} = 1462 \text{ psi}$$

The flattening load at N = 10 (point of maximum stress) is

$$P_{10f} = P_{10} \left(\frac{h}{\delta}\right)^{3/2} = 22.4 \ (1.84 \times 10^{-3}) = 0.041 \text{ pound}$$

or considerably under the maximum allowable load, therefore well within the elastic limit. Apparent flattening stress is:

$$S_{cf} = 22.5 \ S_c = 32{,}900 \text{ psi}$$

Reduction in flow width will be the nominal 33.5 percent reflected by the $2a/\ell$ ratio of Table 2.

TABLE 2

COMPUTED CIRCULAR LAY DEFORMATION PARAMETERS

N	1	2	3	4	5	6	7	8	9	10
ω, degrees	0.0270	0.0634	0.0803	0.0925	0.1016	0.1086	0.1146	0.1180	0.1203	0.1215
$\Delta\psi$, degrees	25.9	11.02	8.70	7.56	6.87	6.43	6.11	5.92	5.79	5.75
ℓ, inches	0.106	0.0452	0.0357	0.0310	0.0282	0.0264	0.0250	0.0243	0.0238	0.0236
K	10.93	9.96	9.69	9.54	9.43	9.35	9.30	9.26	9.24	9.23
P, pounds x 10^3	7.04	3.28	2.66	2.35	2.16	2.03	1.936	1.888	1.850	1.840
a, inch x 10^3	17.8	7.57	5.97	5.19	4.71	4.38	4.17	4.04	3.96	3.94
b, inch x 10^6	1.333	1.400	1.421	1.431	1.436	1.436	1.446	1.446	1.450	1.455
σ_c, psi x 10^{-5}	1.410	1.473	1.494	1.508	1.515	1.522	1.526	1.530	1.531	1.532
$2a/\ell$	0.337	0.336	0.335	0.335	0.335	0.335	0.335	0.335	0.335	0.335

Unidirectional Lay Parameters. The number of contacts within the apparent contact area is given by

$$N_u = \frac{\pi D_s L}{\lambda^2} = 1.77 \times 10^7$$

or 738 times the number obtained for the circular lay model.

From the unidirectional lay analysis, the deflection corresponding to $(S_c = S_u)$ is given as

$$\delta_u = \left(\frac{36\, \alpha^2\, S_u^{\;2}\, h^3}{\Phi^2} \right)^{1/3} = 0.0562 \times 10^{-6} \text{ inch}$$

or about one-half that obtained for the circular lay model.

Flattening stress for the unidirectional surfaces is based upon $(\delta = 3/4\ h)$ and is

$$S_{uf} = \frac{0.257\Phi}{\alpha} = 169{,}000 \text{ psi}$$

or over five times that required for the circular lay surface. It should be noted that the previous assumption of rising valleys have little effect on the above result since closure for the unidirectional model based upon $(\delta_u = h)$ results in a flattening stress of

$$S_{uf} = \frac{\Phi}{6\,\alpha} = 111{,}000 \text{ psi}$$

which is still significantly larger than (S_{cf}). It is thus apparent that from only a deformation view, the circular lay model will experience a greater reduction of leakage than its unidirectional lay counterpart.

Laminar Leakage Comparison. For the circular case, the ratio of unloaded to loaded leakage is given by:

$$\left(\frac{Q \text{ @ } S = 1462 \text{ psi}}{Q \text{ @ } S = 0 \;.}\right) = \left(\frac{h}{h - \delta_c}\right)^3 \frac{W}{W_e} = 2.26$$

For the unidirectional case

$$\left(\frac{Q \text{ @ } S = 1462 \text{ psi}}{Q \text{ @ } S = 0}\right) = \left(\frac{h}{h - \frac{3}{4}\delta_u}\right)^3 = 1.14$$

which shows the circular lay surface to be a more effective closure configuration.

SEAT LAND CONTACT STRESS DISTRIBUTION AND DEFORMATION

For the previous analyses, the flat total land widths of equal width (L) resulted in a nearly uniform distribution of the axial load radially across the land. Each real contact (for the assumed model) could thus be expected to deform equally. In many cases of valve seating, this condition will not exist. The contact stress distribution will be nonlinear and, hence, may be a controlling factor in the definition of effective land contact width (L) and/or profile deformation. With simple curved land shapes, the Hertz analysis provides equations for stresses and deformation. However, more complex contacts which have not been analytically defined must be evaluated through comparative estimates based on simplified analyses and experiment.

Contact stress distribution and deformation equations for defined cases are summarized in the following paragraphs. These equations have been extracted from Ref. 61 and 28. Special cases of complex contacts have also been evaluated to ascertain the degrees of difficulty associated in effecting a solution. For one of these, prevalent in seating, the equations for contact stress and length have been derived.

Sharp Corner Seat Land

The valve seat having sharp corners mating with a wider poppet land may be idealized as a flat, rigid block on flat plate. Although the normal contact stress distribution is based upon an inelastic block with zero friction, it does provide insight into the real case wherein corner stresses become very large, often resulting in plastic deformation of both members and seat corner fracturing. The contact schematic and equations are shown below:

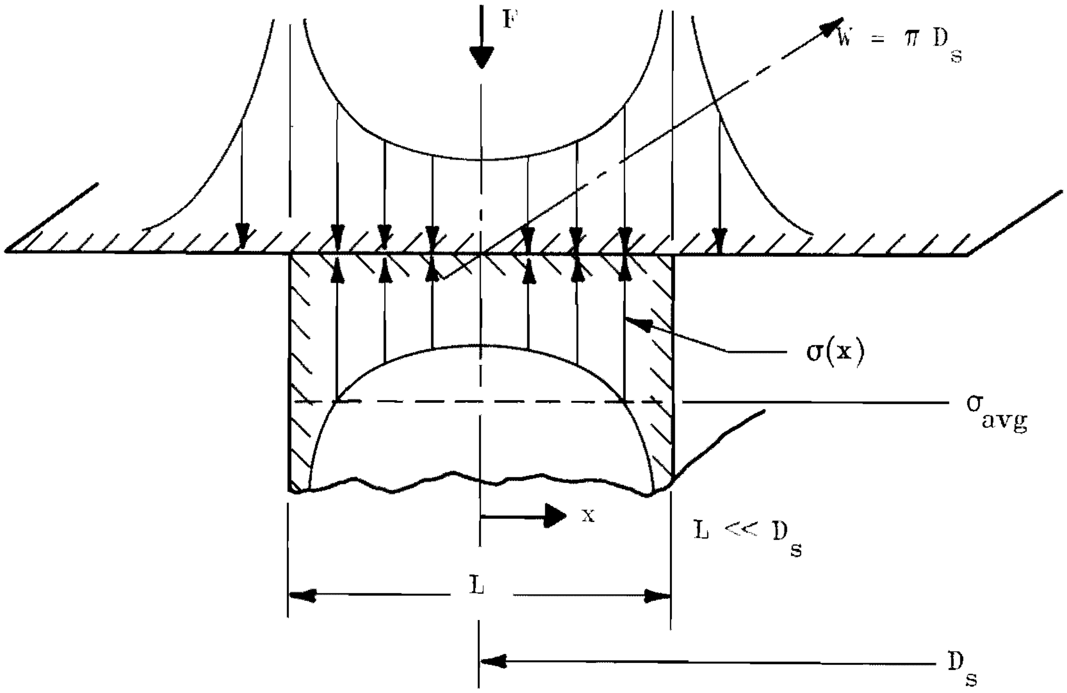

$$\sigma(x) = \frac{F}{\pi W \sqrt{(L/2)^2 - x^2}}$$

$$\sigma_{max} \; (x \rightarrow L/2) \rightarrow \infty$$

$$\sigma_{min} \; (x = 0) = \frac{2F}{\pi WL}$$

$$\sigma_{avg} = \frac{F}{WL} = \frac{F}{\pi D_s L} = S$$

For the real case, it is apparent that plastic flow or fracturing with brittle materials would relieve the high corner stress which would result in a more uniform pressure distribution across the seat land. Nevertheless, the contact stress near the edge could be many times greater than the apparent stress (S). This would result in a greater asperity deformation at the seat ID and OD which may, therefore, be the primary sealing areas. The net effect would be to cause a central channel into which leakage could gain entrance and exit through flaws or scratches on both sides of the seat land but which do not necessarily bridge the land. Where corner conditions are neglected, this could be the significant leakage path.

Crowned Poppet and Seat

This case occurs when either or both poppet and seat are fully crowned and is idealized by mating toroid sections. It is assumed that the contact width (across L) is small with respect to the seat diameter. The seat and contact stress distribution schematic with applicable equations are shown below:

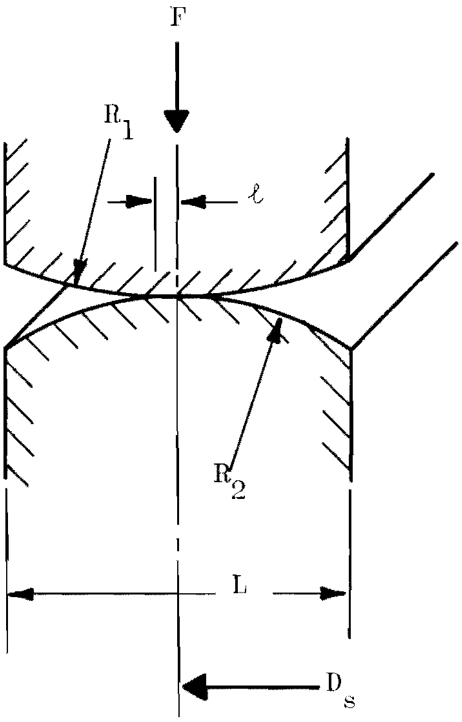

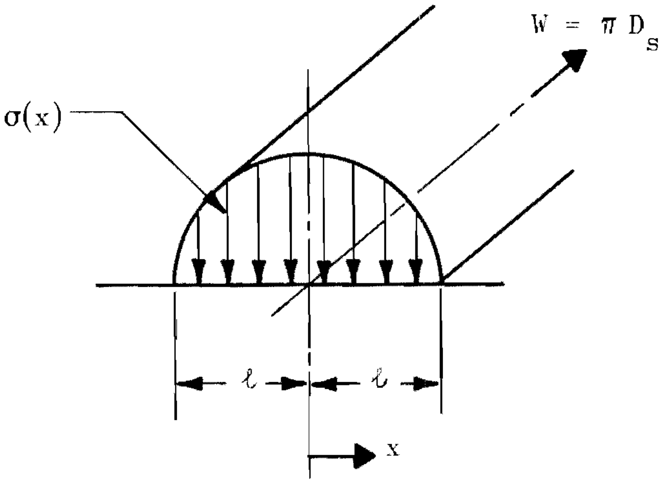

$L \ll D_s$

$2\ell \ll L$

$$\sigma(x) = \frac{2F}{\pi \ell W} \sqrt{1 - \left(\frac{x}{\ell}\right)^2}$$

$$\sigma_{max}\,(x = 0) = \sigma_c = \frac{2\,F}{\pi \ell W} = \frac{2F}{\pi^2 D_s \ell}$$

$$\sigma_{min}\,(x = \ell) = 0$$

$$\sigma_{avg} = \frac{F}{2\ell W} = \frac{F}{2\pi D_s \ell} = \frac{\pi}{4} \sigma_c$$

$$\ell = \sqrt{\frac{4 F \alpha}{\pi^2 D_s \left(\frac{1}{R_1} + \frac{1}{R_2}\right)}}$$

$$\sigma_{avg} = \sqrt{\frac{F\left(\frac{1}{R_1} + \frac{1}{R_2}\right)}{16 \alpha D_s}}$$

$$\frac{\sigma_{avg}}{2\ell} = \frac{\pi\left(\frac{1}{R_1} + \frac{1}{R_2}\right)}{16 \alpha}$$

As before, the maximum allowable contact stress is assumed as 3/2 the normal tension yield strength. Therefore, maximum allowable load is:

$$F_m = \frac{9 \pi^2 \alpha D_s Y^2}{4\left(\frac{1}{R_1} + \frac{1}{R_2}\right)}$$

where Y is the weaker material yield strength.

For minimum leakage, the maximum land contact length is necessary. However, to preclude the potentially damaging edge contacts indicated in the rigid block case, the real contact length (2ℓ) should be somewhat less than (L) under maximum loading. As (2ℓ) approaches (L) under load, the unconstrained edges will result in greater width (2ℓ) than predicted. Nevertheless, the load flattening to reach this point does provide a design limit. Unless stresses are near the elastic limit, it is assumed that corner radii and elasticity in both surfaces will be adequate to compensate this error. The load to flatten crowned surfaces is given by

$$F_f = \frac{\pi^2 D_s L^2 \left(\frac{1}{R_1} + \frac{1}{R_2}\right)}{16 \alpha}$$

or, since full land contact is assumed, the (apparent) flattening stress is:

$$S_f = \frac{F}{\pi D_s L} = \frac{\pi L\left(\frac{1}{R_1} + \frac{1}{R_2}\right)}{16\,\alpha} = \sigma_{avg}$$

By allowing one of the radii to become very large, the preceding equations are reduced to the case of a cylinder on flat plate.

Dubbed Seat

In practice, the preceding two cases rarely occur. Corner radii, edge roll or duboff, and land taper are usually present to some degree. Since equations describing these complex conditions are not available in the literature, their derivation was undertaken. Because of the difficulty of solution, only the case of the "dubbed" seat land was completed. To supplement the analytic solution, the feasibility of photoelastic techniques was also examined. The results of this study are presented following the derivation.

The analytical model considered is illustrated below:

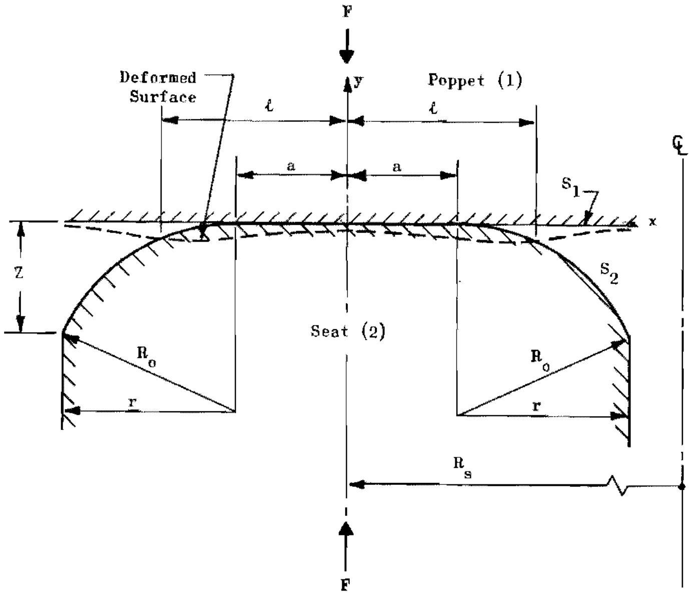

Assumptions applicable to this model are:

1. The materials composing poppet and seat are homogeneous, isotropic, and linearly elastic.
2. The physical problem can be considered as a two-dimensional plane-stress problem, provided:

   $2\ (a + r) \ll R_s$

3. The length of the contact surface is such that:

   $\ell \ll (a + r)$

4. The contact surfaces are perfectly smooth and frictionless.

The following solution is based upon the work of N. I. Muskhelishvili (Ref. 62). The surfaces 1 and 2 can be represented mathematically as follows.

Surface 1 (S_1).

$$y_1 = 0 \qquad ; -\infty \leqq x \leqq \infty$$

Surface 2 (S_2).

$$y_2 = \sqrt{R_o^{\,2} - (x + a)^2} - R_o; \quad (-\ell - r) \leqq x \leqq -\ell$$

$$y_2 = 0 \qquad -\ell \leqq x \leqq \ell$$

$$y_2 = \sqrt{R_o^{\,2} - (x - a)^2} - R_o; \quad \ell \leqq x \leqq (\ell + r)$$

Representation of S_2 outside the above range is not considered. Differentiating these equations gives:

$$y_1' = \frac{dy_1}{dx} = 0 \qquad ; -\infty \leqq x \leqq \infty \tag{1}$$

$$y_2' = \frac{dy_2}{dx} = \frac{-(x + a)}{\left[R_o^2 - (x + a)^2\right]^{1/2}} \;; \qquad (-\ell - r) \leqq x \leqq -\ell$$

$$= 0 \;; \qquad -\ell \leqq x \leqq \ell$$

$$= \frac{-(x - a)}{\left[R_o^2 - (x - a)^2\right]^{1/2}} \;; \qquad \ell \leqq x \leqq (\ell + r) \qquad (2)$$

The following quantity is defined with $f(x)$ an even function:

$$f(x) \equiv y_1 - y_2. \qquad (3)$$

Contact Length. For this case, the length (2ℓ) of the contact surface, is given by the following relationship:

$$\int_a^{\ell} \frac{x f'(x)\, dx}{\sqrt{\ell^2 - x^2}} = \frac{\alpha F}{\pi D_s} \qquad (4)$$

Substituting Eq. 1, 2, and 3 into 4 yields:

$$\frac{\alpha F}{\pi D_s} = \int_a^{\ell} \frac{x\,(x - a)\, dx}{\left[R_o^2 - (x - a)^2\right]^{1/2} \left[\ell^2 - x^2\right]^{1/2}} \qquad (5)$$

where $a \leqq \ell \leqq (a + r)$.

Now,

$$\frac{1}{\left[R_o^2 - (x - a)^2\right]^{1/2}} = \frac{1}{R_o \left[1 - \left(\frac{x - a}{R_o}\right)^2\right]^{1/2}}$$

$$\cong \frac{1}{R_o} \left[1 + \frac{1}{2} \left(\frac{x - a}{R_o}\right)^2\right]$$

Substitute this into the above integral to obtain:

$$\frac{\alpha F R_o}{\pi D_s} \int_a^{\ell} \frac{x\,(x - a)\left[1 + \frac{1}{2}\left(\frac{x - a}{R_o}\right)^2\right] dx}{\left[\ell^2 - x^2\right]^{1/2}}$$

$$= \int_a^{\ell} \frac{1}{(\ell^2 - x^2)^{1/2}} \left[\frac{x^4}{2R_o^2} - \frac{3ax^3}{2R_o^2} + x^2\left(1 + \frac{3a^2}{2R_o^2}\right) - x\left(a + \frac{a^3}{2R_o^2}\right)\right] dx \qquad (6)$$

which when integrated and simplified yields:

$$\frac{\alpha F R_o}{\pi D_s} = \frac{\pi \ell^2}{4}\left[1 + \frac{3}{2R_o^2}\left(\frac{\ell^2}{2} + a^2\right)\right] +$$

$$-(\ell^2 - a^2)^{1/2}\,\frac{a}{2}\left[1 + \frac{5}{8}\,\frac{\ell^2}{R_o^2} + \frac{1}{2}\,\frac{a^2}{R_o^2}\right] +$$

$$-\sin^{-1}\left(\frac{a}{\ell}\right)\left[\frac{\ell^2}{2}\left(1 + \frac{3a^2}{2R_o^2} + \frac{3\,\ell^2}{8R_o^2}\right)\right] \qquad (7)$$

For the special case, a = 0, Eq. 7 reduces to:

$$\frac{\alpha F R_o}{\pi D_s} = \frac{\pi \ell^2}{4}\left[1 + \frac{3\,\ell^2}{4R_o^2}\right]$$

This corresponds to the problem of a cylinder in contact with a flat plate. In the classical solution to this problem, it is assumed that $\ell/R_o \ll 1$; thus,

$$\frac{\alpha F R_o}{\pi D_s} \cong \frac{\pi\,\ell^2}{4}$$

or

$$\ell = \sqrt{\frac{4\alpha F R_o}{\pi^2 D_s}}$$

corresponding to the previous solution for $R_1 = \infty$.

Returning to Eq. 7, dividing both sides by a^2, and letting

$$\Omega \equiv \frac{2\alpha F R_o}{\pi D_s a^2}$$

$$\tau \equiv \frac{\ell}{a}$$

and

$$\rho \equiv \frac{R_o}{a}$$

gives

$$\Omega = \frac{\pi\tau^2}{2}\left[1 + \frac{3}{2\rho^2}\left(\frac{\tau^2}{2} + 1\right)\right] - (\tau^2 - 1)^{1/2}\left[1 + \frac{5}{8}\frac{\tau^2}{\rho^2} + \frac{1}{2\rho^2}\right] + -\sin^{-1}\left(\frac{1}{\tau}\right)\left[\tau^2\left(1 + \frac{3}{2\rho^2} + \frac{3\tau^2}{8\rho^2}\right)\right] \quad (8)$$

For sufficiently large ρ, and assuming τ is near (1), then

$$\Omega \cong \frac{\pi\tau^2}{2} - (\tau^2 - 1)^{1/2} - \tau^2 \sin^{-1}\left(\frac{1}{\tau}\right) \quad (9)$$

Contact Stress Distribution. The stress distribution at the contact surface is given by the relationship:

$$\sigma(x) = \frac{\sqrt{\ell^2 - x^2}}{2\pi\alpha} \int_{-\ell}^{\ell} \frac{f'(t)\,dt}{(t - x)\sqrt{\ell^2 - t^2}} \tag{12}$$

This formula appears incorrectly in Muskhelishvili's book (Ref. 62, p. 493). Since $f'(t)$ is odd, $-f'(-t) = f'(t)$, and $f'(t) = 0$, $|x| < a$, thus:

$$\sigma(x) = \frac{\sqrt{\ell^2 - x^2}}{2\pi\alpha} \int_{a}^{\ell} \frac{f'(t)}{\sqrt{\ell^2 - t^2}} \left[\frac{1}{t + x} + \frac{1}{t - x}\right] dt$$

Approximating $f'(t)$, $a \le t \le \ell$, by $f'(t) = \frac{t - a}{R_o}$ gives:

$$\sigma(x) \cong \frac{\sqrt{\ell^2 - x^2}}{2\pi R_o \alpha} \int_{a}^{\ell} \frac{(t - a)}{\sqrt{\ell^2 - t^2}} \left[\frac{1}{t + x} + \frac{1}{t - x}\right] dt$$

or

$$\frac{2\pi R_o \alpha\, \sigma(x)}{\sqrt{\ell^2 - x^2}} = \Lambda(a, \ell, x) + \Lambda(a, \ell, -x) \tag{13}$$

where

$$\Lambda(a, \ell, x) \equiv \int_{a}^{\ell} \frac{(t - a)\,dt}{\sqrt{\ell^2 - t^2}\,(t - x)}$$

From (Ref. 63), the following integrals are recorded after letting $v = t - x$, $c = \ell^2 - x^2$, $b = -2x$ and $d = -1$:

$$I_1 = \int \frac{dv}{[c + bv + dv^2]^{1/2}} = -\sin^{-1}\left[\frac{2d\,v + b}{(b^2 - 4dc)^{1/2}}\right] = \sin^{-1}\left(\frac{v + x}{\ell}\right)$$

provided,

1. $b^2 > 4dc$ implies that $4x^2 > -4\,\ell^2 + 4x^2$ or $0 > -4\,\ell^2$

   (This is always satisfied since (ℓ) is real.)

2. $\left|2dv + b\right| < (b^2 - 4dc)^{1/2}$

   $\left|v + x\right| < \ell$

   or $t < \ell$ (This is satisfied at all points in the interval (a, ℓ) except at the end point where $t = \ell$ and $\sin^{-1}(1) = \pi/2$.)

$$I_2 = \int \frac{dv}{v\,[c + bv + dv^2]^{1/2}} = -\frac{1}{c}\,\ell n \left| \frac{2(cV)^{1/2}}{v} + \frac{2c}{v} + b \right|$$

where

$c > 0$ implies that $x^2 < \ell^2$

$V = c + bv + dv^2$

Substitute I_1 and L_2 into Eq. 13 and obtain:

$$\Lambda\,(a, \ell, x) = \left[+\sin^{-1}\frac{v + x}{\ell} + \frac{(a - x)}{c}\,\ell n \left| \frac{2(cV)^{1/2}}{v} + \frac{2c}{v} - 2x \right.\right]_{a-x}^{\ell-x} \tag{14}$$

Now,

$$(cV)^{1/2} = \left[(\ell^2 - x^2)^2 - 2x\,(\ell^2 - x^2)\,v - v^2\,(\ell^2 - x^2)\right]^{1/2},$$

$$(cV)^{1/2}\Big|_{\ell-x} = \left[(\ell^2 - x^2)^2 - 2x\,(\ell^2 - x^2)\,(\ell-x) - (\ell-x)^2\,(\ell^2 - x^2)\right]^{1/2}$$

$$= 0 \tag{15a}$$

and

$$(cV)^{1/2}\Big|_{a-x} = \left[(\ell^2 - x^2)^2 - 2x\ (\ell^2 - x^2)\ (a-x) - (a-x)^2\ (\ell^2 - x^2)\right]^{1/2}$$

$$= \left[(\ell^2 - x^2)\ (\ell^2 - a^2)\right]^{1/2} \qquad (15b)$$

Substitute Eq. 15 into Eq. 14 to obtain:

$$\Lambda\ (a,\ \ell,\ x) = \sin^{-1}(1) - \sin^{-1}\left(\frac{a}{\ell}\right) + \frac{a-x}{(\ell^2-x^2)^{1/2}}$$

$$\left[\ell n\ \left|\frac{2\ (\ell^2-x^2)}{\ell-x}\ -2x\right| \quad - \ell n\left|\frac{2[(\ell^2-x^2)(\ell^2-a^2)]^{1/2}}{a-x} + \frac{2(\ell^2-x^2)}{a-x}\ -2x\right|\right]$$

$$= \frac{\pi}{2} - \sin^{-1}\left(\frac{a}{\ell}\right) + \frac{a-x}{(\ell^2-x^2)^{1/2}}\ \left[\ell n\ 2\ell\ + \right.$$

$$\left. - \ell n\left|\frac{2\ [(\ell^2-x^2)(\ell^2-a^2)]^{1/2} + 2\ (\ell^2-x^2)\ -2x\ (a-x)}{a-x}\right|\right]$$

$$= \frac{\pi}{2} - \sin^{-1}\ \left(\frac{a}{\ell}\right) + \frac{a-x}{(\ell^2-x^2)^{1/2}}\left[\ell n\left|\frac{(a-x)}{[(\ell^2-x^2)(\ell^2-a^2)]^{1/2} + \ell^2-ax}\right|\right] \qquad (16)$$

with $\Lambda\ (a,\ \ell,\ -x)$ found similarily. Introducing Eq. 16 into Eq. 13 and using nondimensional parameters ($\gamma = x/a$) and ($\tau = \ell/a$), the contact stress distribution is given as:

$$\frac{\pi R_o \alpha}{a}\ \sigma(\gamma) \equiv Q(\gamma) = \sqrt{\tau^2-\gamma^2}\left(\frac{\pi}{2}\ - \sin^{-1}\ \frac{1}{\tau}\right) +$$

$$\left(\frac{1-\gamma}{2}\right)\ell n\left|\frac{\tau(1-\gamma)}{\sqrt{(\tau^2-\gamma^2)(\tau^2-1)} + \tau^2-\gamma}\right| + \left(\frac{1+\gamma}{2}\right)\ell n\ \left[\frac{\tau(1+\gamma)}{\sqrt{(\tau^2-\gamma^2)(\tau^2-1)} + \tau^2+\gamma}\right|$$

For the following special cases, $Q(\gamma)$ becomes

$$Q(0) = \frac{\pi\tau}{2} - \tau \sin^{-1} \left(\frac{1}{\tau}\right) - \ell n \left| (\tau^2 - 1)^{1/2} + \tau \right|$$

$$Q(1) = \left[\pi - 2 \sin^{-1} \left(\frac{1}{\tau}\right) - \frac{2}{\tau^2 - 1} \ell n \, \tau \right] \sqrt{\tau^2 - 1}$$

and

$$Q(\tau) = 0$$

For a = 0 (i.e., cylinder on flat plate) the stress distribution becomes

$$\pi R_o \alpha \, \sigma(x) = \frac{\pi}{2} \sqrt{\ell^2 - x^2}$$

or

$$\sigma(x) = \frac{\sqrt{\ell^2 - x^2}}{2\alpha R_o}$$

But, for a = 0, it was shown that

$$\ell^2 = \frac{4\alpha F R_o}{\pi^2 D_s}$$

Therefore,

$$\sigma(x) = \frac{\sqrt{\frac{4\alpha F R_o}{\pi^2 D_s} - x^2}}{2 \alpha R_o}$$

and

$$\sigma(0) = \sigma_{max} = \sigma_c = \sqrt{\frac{F}{\pi^2 \alpha R_o D_s}}$$

which checks with the previous solution with $R_1 = \infty$

Parametric Results. The previous analysis permits the determination of the deformed contact surface length (2ℓ) and corresponding stress distribution $\sigma(\gamma)$. A limited range of parametric data has been computed and is presented in Fig. 29 and 30. The following steps are taken to solve a specific problem:

1. Calculate $\Omega = \dfrac{2\alpha F R_o}{\pi D_s a^2}$
2. Solve for (τ) by trial, or enter Fig. 29 with Ω and read τ to obtain $\ell = a\tau$
3. Using the value of τ, locate appropriate distribution of $Q(\gamma)$ in Fig. 30.
4. To find $\sigma(\gamma)$, read $Q(\gamma)$ at any value (γ) from 0 to τ and multiply by $a/\pi R_0 \alpha$
5. If only $\sigma_{max} = \sigma_c$ or σ_{min} is desired, enter Fig. 29 with value of (τ) and proceed as in step 4

From Fig. 30, it is apparent that local stresses near the contact edge can be much greater than at the center depending upon the geometry. Furthermore, the range of stress distribution shapes will vary in between those presented for the previous two cases (flat block and cylinder). Therefore, effective sealing will generally be achieved in locations of greatest contact stress, however, this is not without due regard to necessary contact length.

Photoelastic Feasibility Study. To supplement the analytic solution, a feasibility study was undertaken to determine if photoelastic techniques could be applied to the contact problem. The goals of this study were as follows:

1. Determine if stress concentrations caused by surface roughness would prevent accurate fringe order readings in the vicinity of the contact surface

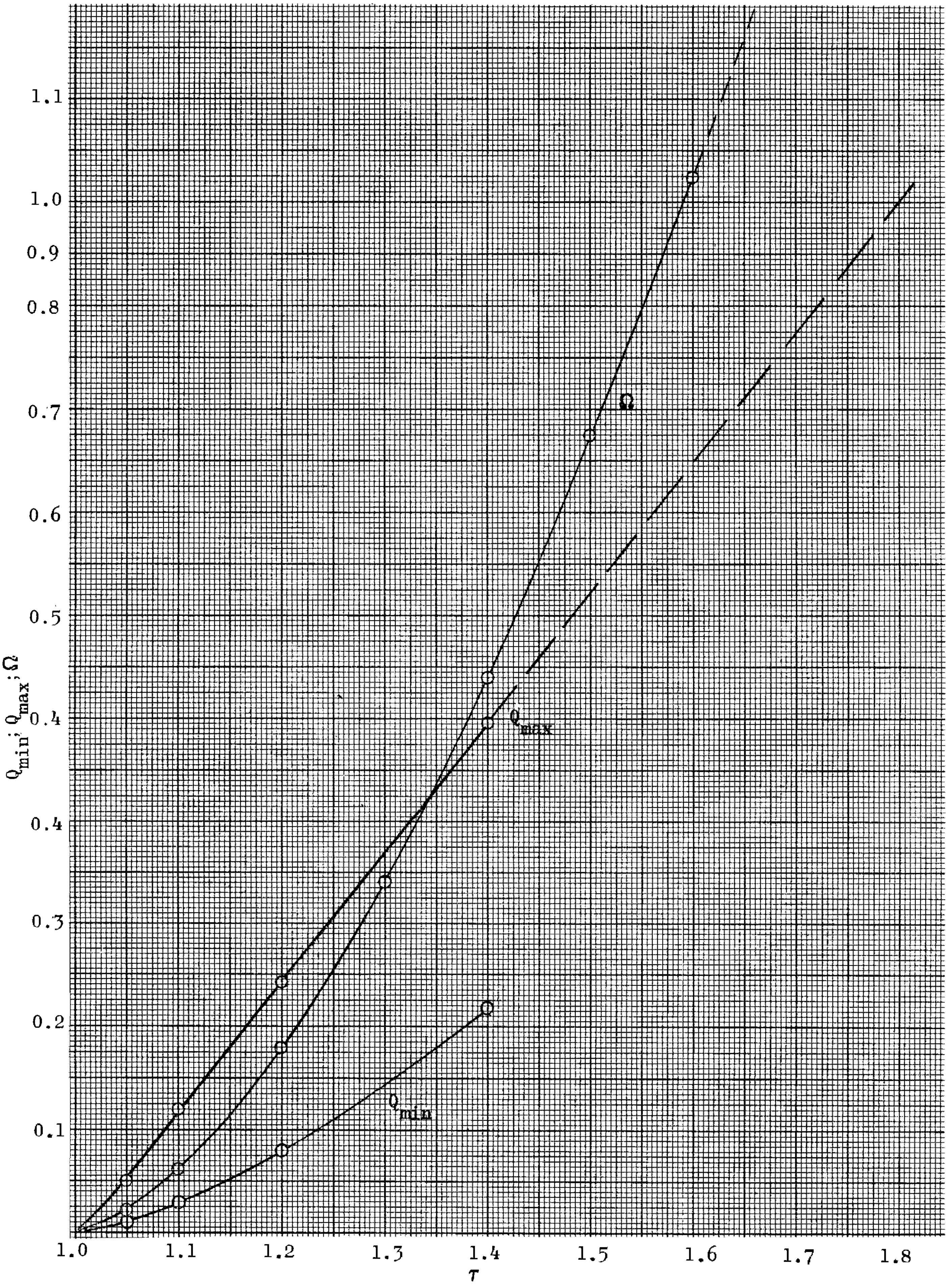

Figure 29. Contact Stress Function for Dubbed Seat

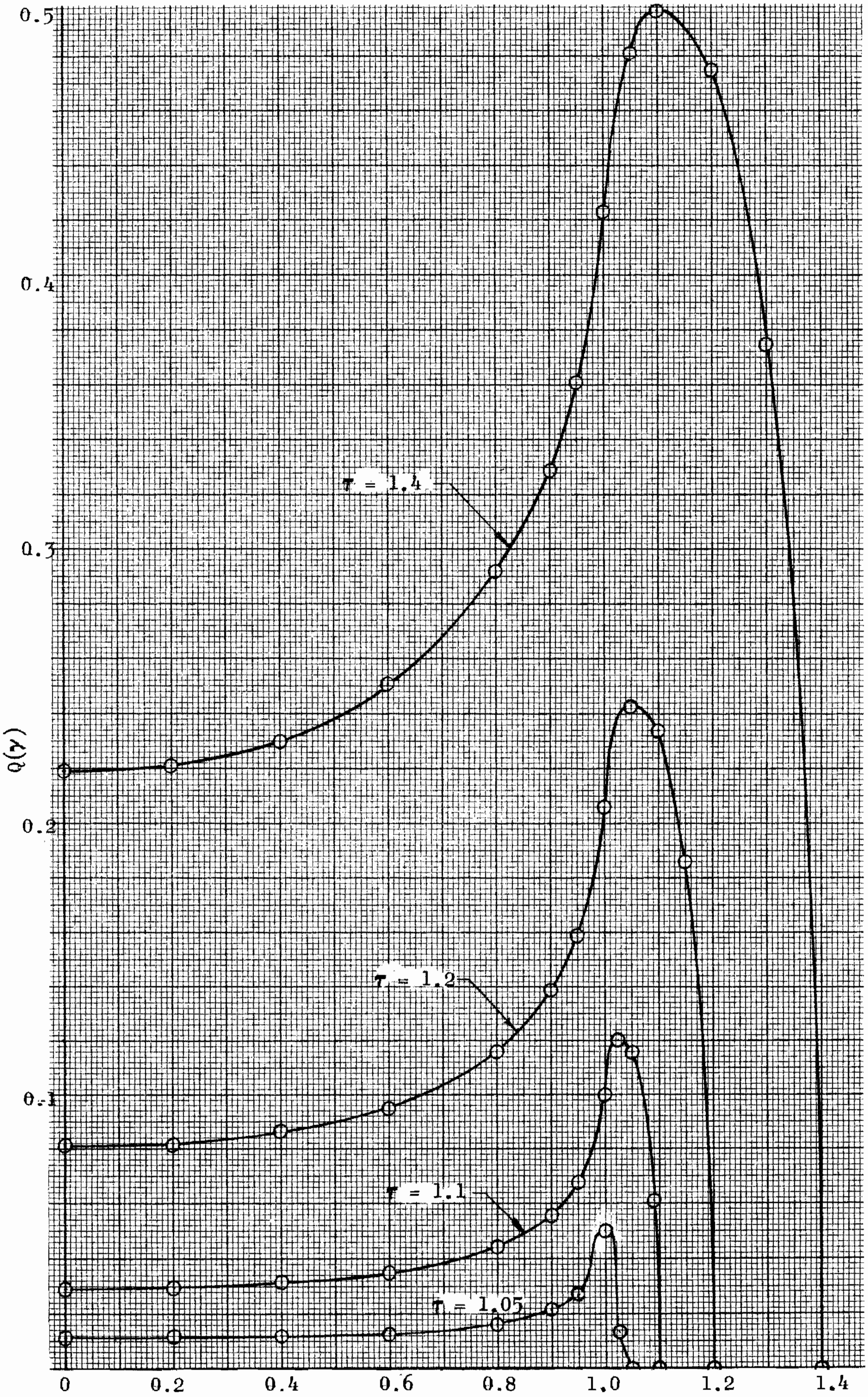

Figure 30. Contact Stress Distribution for Dubbed Seat

2. Determine if the model could be properly loaded in existing fixtures

3. Verify stress distribution predicted by analysis

4. Determine whether photoelastic techniques can be employed in the the study of more complex poppet valve contact problems, such as those illustrated below:

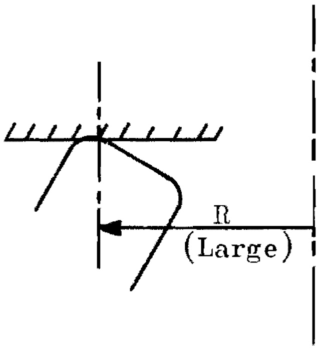

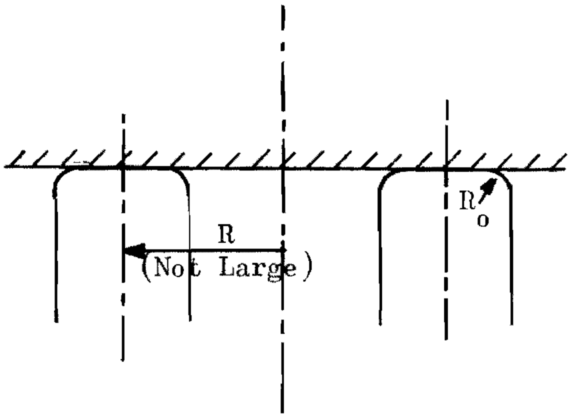

Procedure. A model consisting of a flat plate and probe simulating the seat and poppet respectively, was constructed from 3/8 inch C.R. -39, photoelastic plastic. The probe had a 1-inch flat machined onto a 4-inch radius cylindrical surface as shown below:

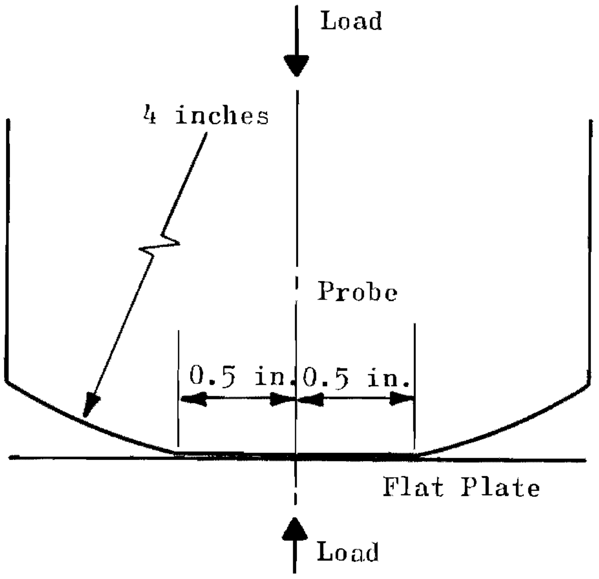

The geometry of the photoelastic model did not coincide with the mathematical model used in the analysis, i.e., the center of curvature of the photoelastic model is on the axis of symmetry, whereas in the mathematical model, it is displaced a distance (a), parallel to the seat. The limited scope of this feasibility study did not permit the construction of a more refined model. A photograph of the photoelastic model is shown in Fig. 31.

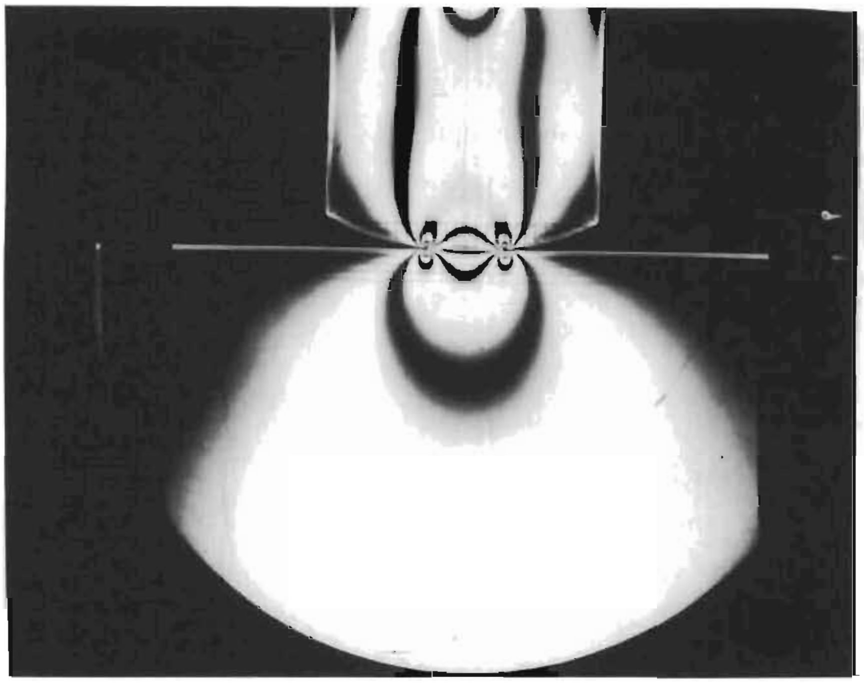

Figure 31. Photoelastic Model Showing Isochromatic Fringes

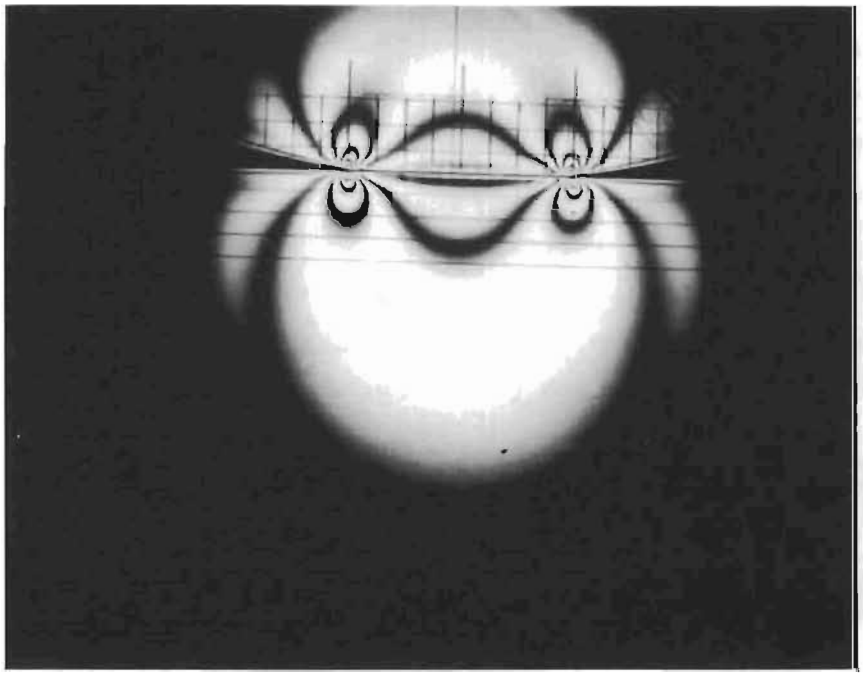

Figure 32. Magnified View of Isochromatics Near Contact Surface

Results and Discussion. Figure 32 is a magnified view of the loaded model, showing the isochromatic fringes in the neighborhood of the contact surface. The straight lines which appear in the photograph are a gridwork which was lightly scratched onto the surface of the unloaded model. Inspection of this photograph reveals that local disturbances on the contact surface did not perturb the fringe pattern and the fringe order could be read as close as 1/2 of a grid spacing (0.05 inch) from the contact surface.

The existing loading fixtures in the photoelastic laboratory were found to be adequate for studying models of this type. However, it was found that the alignment of the model in a plane perpendicular to the line of sight of the polariscope was very important in achieving a stress state that was invariant through the model thickness. Slight variations in alignment resulted in indistinct isoclinics and consequently inaccurate principal stress directions.

The fringe order and principal stress directions were evaluated at each gridpoint along the first and second gridlines located 0.10 and 0.21 inch from the contact surface. The method of shear-differences was used to calculate the stress distribution $\sigma(\gamma)$ along the first gridline. A plot of this stress distribution is shown in Fig. 33. A comparison of the shape of this pressure distribution, and the one, analytically determined at the contact surface (see Fig. 30, $\tau = 1.10$) shows good agreement. The maximum occurs near the intersection of the flat and radius, and the minimum occurs on the axis of symmetry. Because of the difficulty discussed in the previous paragraph, and the fact that the photoelastic and analytical models are not identical, no comparison of numerical values is made.

In general, it can be concluded that photoelastic methods can be of substantial aid in the analysis of valve seating contact stresses.

Model Seat Parametric Data

Comparative data for the crowned and dubbed seat lands are shown in Fig. 34 and 35. The model schematically illustrated on each graph is the same as previously described for support of the experimental program. For the

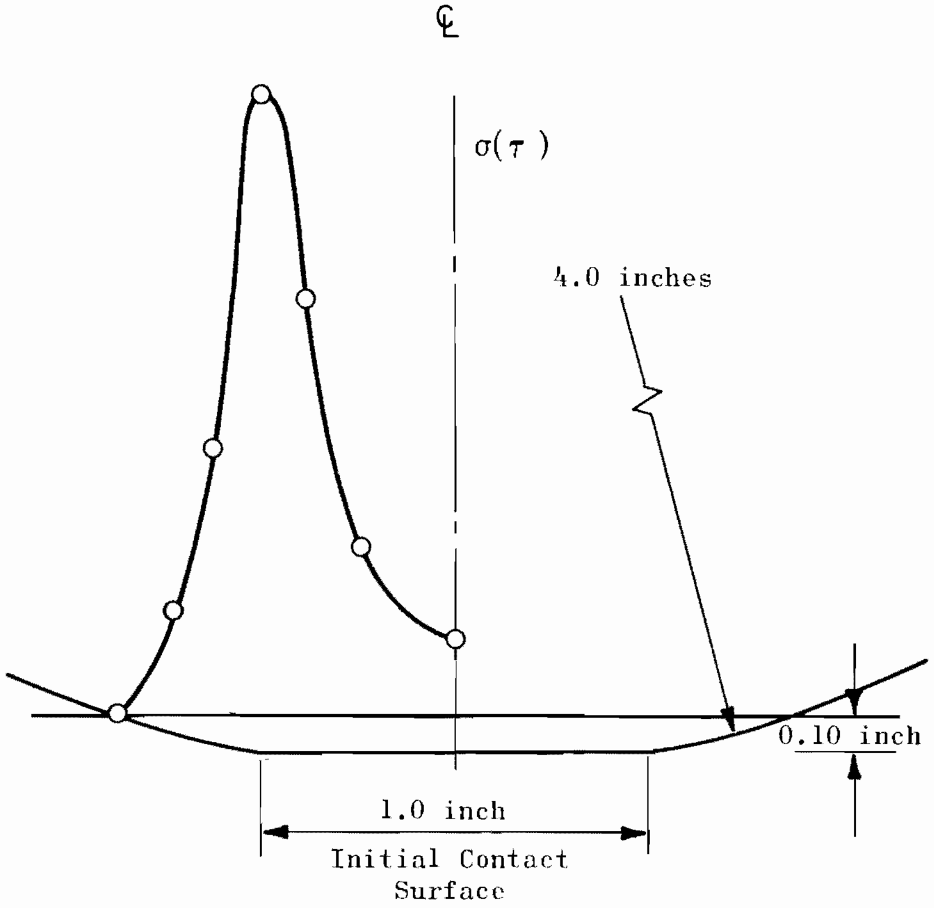

Figure 33. Normal Stress on Gridline 0.10-Inch From Initial Contact Surface

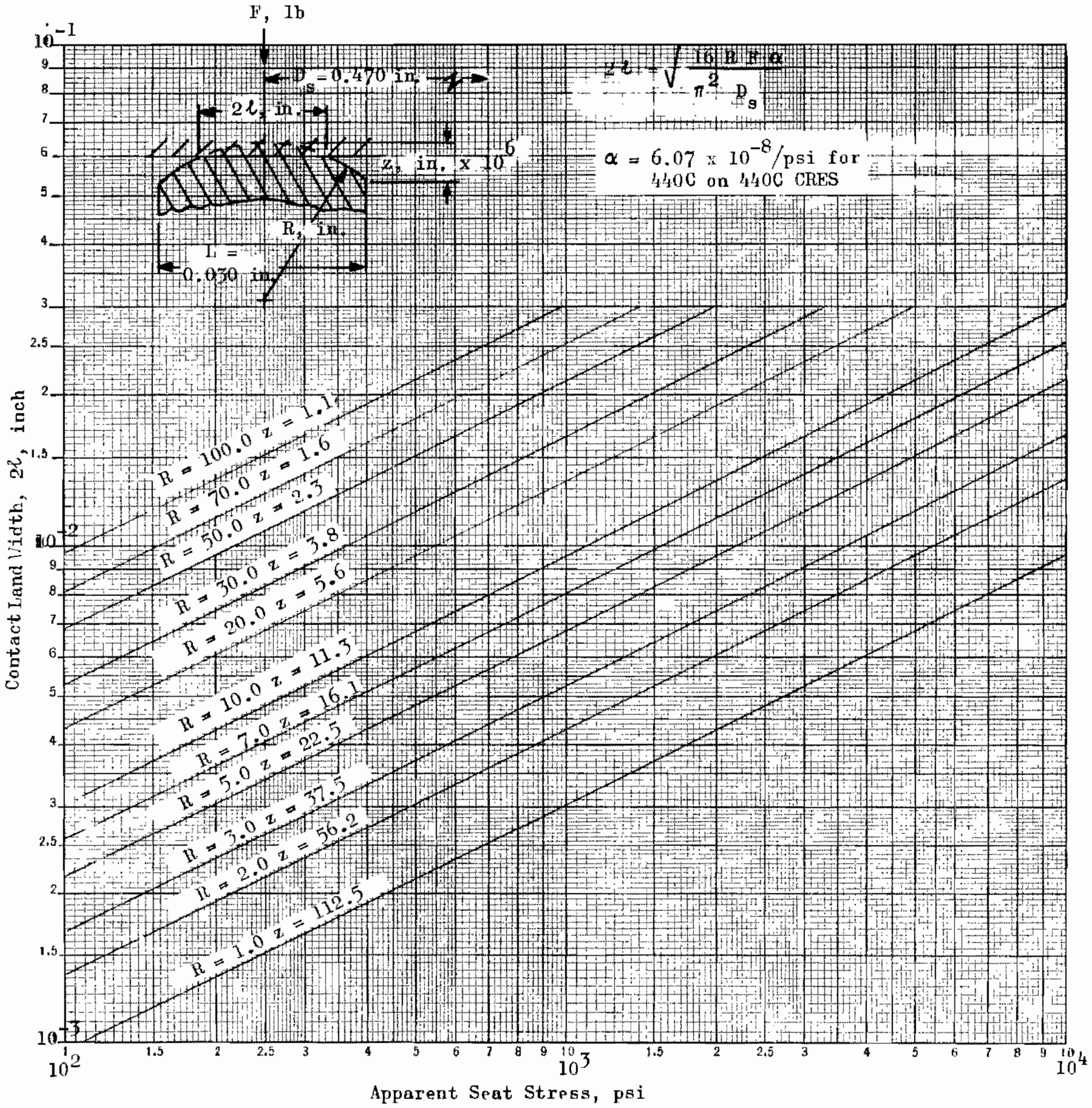

Figure 34. Crowned Seat Contact Land Width vs Apparent Seat Stress

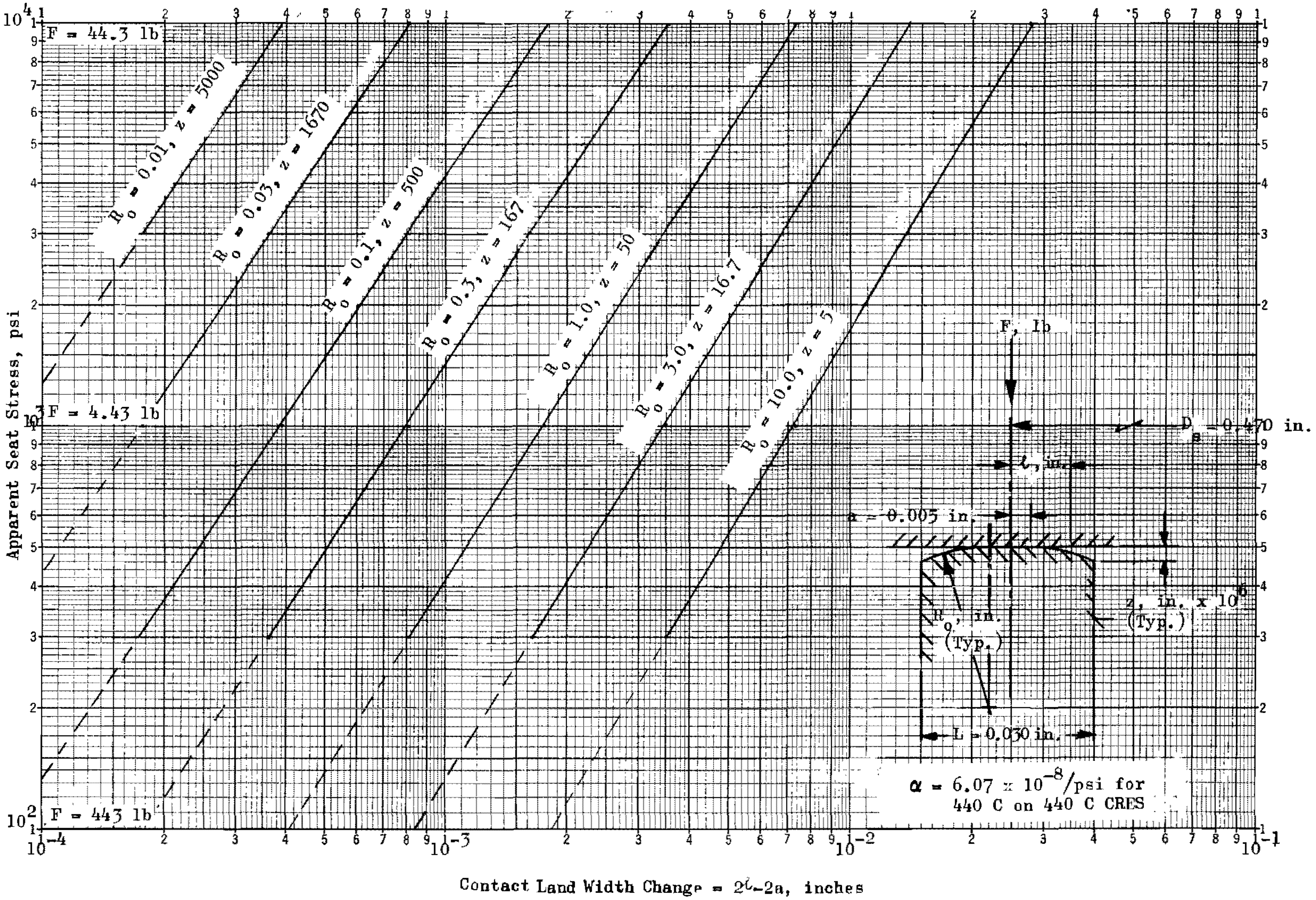

Figure 35. Dubbed Seat Contact Land Width Change vs Apparent Seat Stress

crowned seat, contact land width (2ℓ) is plotted vs apparent seat stress ($F/\pi D_s L$) with the crown radius (R) and duboff height (Z) as parameters. Seat contact land width change (2ℓ - 2a) for a = 0.005 inch is shown vs apparent seat stress for the dubbed configuration.

For each of these configurations, contact stresses over the contact area defined by (2ℓ) are much greater than apparent stress. For example, at R = 3 inches (Z = 37.5 microinches), the crowned seat land width at 3000-psi apparent stress is 0.0091 inch; average and maximum contact stresses are:

$$\sigma_{avg} = 3000 \left(\frac{0.03}{0.0091}\right) = 9890 \text{ psi}$$

$$\sigma_c = \frac{4}{\pi} \sigma_{avg} = 12,600 \text{ psi}$$

At 3000-psi apparent seat stress, the dubbed seat land width change for R_0 = 3 inches (Z = 16.7 microinches) is 0.0067 inch (2ℓ = 0.0167), resulting in the following stresses:

$$\sigma_{avg} = 3000 \left(\frac{0.03}{0.0167}\right) = 5400 \text{ psi}$$

$$\sigma_{max} = 7420 \text{ psi}$$

Reducing R_0 increases the maximum stress σ_c, e.g., with the same conditions above (S = 3000 psi) except (R_0) reduced to 0.01 inch, land width (2ℓ) becomes 0.01017 for an increase of only 0.00017 inch and (σ_c) is increased to 39,300 psi. Thus, what might seem a generous corner radius actually causes a dangerously high contact stress which, if augmented by impact loads and tangential forces, will cause plastic flow or fracturing in many materials.

NOMENCLATURE

The nomenclature listed below represents only those variables and parameters of basic importance in final derived equations. Notations employed in developing solutions and which may be duplicated but with different meaning are defined in text. A pound, inch, minute system of units has been used in all analyses.

AA = arithmetic average, microinch

a = radial half width of initial

a_N = circular lay semimajor contact ellipse axis, inches

A_s = $\pi D_s L$, apparent seat land contact area, sq in.

A_{sp} = $\pi D_s L_p$, apparent seat land normal projected contact area, sq in.

b_N = circular lay semiminor contact ellipse axis, inches

d = nodule base diameter, inches

D = spherical or cylindrical diameter, inches

ΔD = differential between spherical or cylindrical diameter, inches

D_s = mean seat diameter, inches

e = eccentricity of circular lay surfaces, inches

E = elastic modulus, psi

F = total normal seat load, pounds

g = gravitational acceleration constant, 1.39×10^6 in./min^2

h = maximum flow height (gap) between smooth surfaces or peak-to-valley height for one surface, inches

h_e = equivalent parallel plate height between smooth surfaces or for one surface, inches

h_o = $h - h_p$, out-of-parallel height, inches

h_p = smooth parallel plate height, inches

h_q = perpendicular seating gap 90 degrees from contact for tilted conical poppet, inches

H = maximum peak-to-valley height for two contacting sinusoidal surfaces, inches

H_e = equivalent parallel plate height for two contacting sinusoidal surface, inches

K = elliptic integral, circular lay contact

ℓ = contact half width (radial) for crowned or dubbed seat land, inches

ℓ_N = circumferential length between circular lay contacts, inches

L = total radial seat land width, inches

L_e = effective seat land width for tilted conical poppet, inches

L_p = total radial projected seat land width, inches

M = h_e/h, laminar or molecular flow maximum height weighting factor

N = circular lay model contact number

N_{90} = number of circular lay contacts in one quadrant

N_c = number of circular lay contacts

N_u = number of unidirectional lay contacts

N_L = laminar taper flow weighting factor

P = pressure, psia

P_N = specific circular lay contact load, pounds

q = out-of-round gap for tilted conical poppet, inches

$Q(\gamma)$ = contact stress distribution parameter for dubbed seat

Q = flow, cubic inches per minute at 14.7 psia and 70 F, scim

r = chord radius, inches

R = spherical or cylindrical radius, inches; or specific gas constant, in./R

ΔR = differential between spherical or cylindrical radii, inches

R_o = roll-off radius for dubbed seat, inches

R_s = mean seat radius, inches

S = total normal apparent seat contact stress, psi

S_f = apparent seat stress to flatten, psi

S_m = maximum allowable apparent seat stress based upon real contact yield strength, psi

T = temperature, R

W = πD_s, mean circumferential seat land length, inches

W_e = effective circumferential land length for circular lay surfaces, inches

x = independent distance variable, inches

Y = surface yield strength, psi

Z = chordal height, inches

Greek Symbols

α = elastic constant for two contacting surfaces, 1/psi

β = density function or angle, radians

γ = x/a

δ = surface deformation, inches

ϵ = surface deformation factor

θ = poppet and seat included half (seating) angle, radians

$\Delta\theta$ = differential seating angle (i.e., taper angle), radians

λ = wave length, inches

μ = viscosity, lb-min/sq in.

ν = Poisson's ratio

π = 3.1416. . .

ρ = gas density, lb/cu in.

$\sigma(x)$, $\sigma(\gamma)$ = contact stress distribution, psi

σ_c = maximum contact stress, psi

τ = ℓ/a

Υ = (tilt) angle between conical poppet and seat axes, radians

Φ = $2h/\lambda$, average sinusoidal slope, radians

$\Delta\psi_N$ = sector angle between circular lay contacts, radians

ω = weight flowrate, lb/min

Ω = load parameter for dubbed seat

Subscripts

1 = inlet conditions or surface (1)

2 = outlet conditions or surface (2)

BS = ball seat

c = circular or compressible

e = equivalent or effective

f = flattening

i = incompressible

L = laminar factor or flow

m = maximum allowable

M = molecular factor or flow

n = nodule

N = specific circular lay contact

p = poppet

r = roughness

s = scratch

u = unidirectional

w = waviness

TEST FIXTURES

The stages of operation in poppet-type valves are full open, partially open, just contacting, and fully closed or loaded. Additionally, the normal valve must undergo these stages of operation for numerous cycles (100 to more than 1,000,000). Thus, the investigation of valving operation must involve a test fixture capable of functioning like a valve while permitting accurate measurements of position, loads, pressures, leakage, and other pertinent parameters. In consideration of these requirements, test fixtures were designed to provide the following evaluation capabilities:

1. Near-seated flow and resultant forces
2. On-seat leakage as a function of pressure, load, surface texture, and basic geometry
3. Cycling in a controlled manner with measurements of impact loads

All design considerations were predicated on the fundamental requirement that test fixtures used to investigate these parameters should have minimal influence on the data so obtained. The indicated accuracy and precision ultimately attained, particularly for the load-leakage parameter, was such as to be considered a reference datum. Thus, similar to the use of gage blocks as a measurement standard, the resultant seating data form a basis of comparison for performance of like surfaces in actual valving applications.

Two fixtures were employed in the test program. The initially fabricated unit was utilized for off-seat and initial load cycle on-seat testing and is subsequently called the static tester. The second fixture (cycle tester) provided the tool for cyclic performance investigations. The following paragraphs describe pertinent design features, certain fabrication and development procedures, basic capabilities, and cycle tester design analyses.

TEST FIXTURE DESCRIPTION

Both testers have similar load application and measurement, test model retention, and basic operational characteristics. The static tester built for the initial program effort (Ref. 37), formed the development tool from which design refinements were established and subsequently incorporated in the cycle version. Although details of static tester design, fabrication, and development are presented in Ref. 37, pertinent information is reiterated to permit comparative discussion of both test fixtures. Detail drawings for both units in their final version are presented as Fig. 36 and 37.

Loading Method

The first design feature to be established was that the test model poppet be loaded by a pneumatically pressurized piston. Primary advantages of such a method are system simplicity and cleanliness, availability of high-pressure gases and necessary control components, and ease of control for both static and dynamic testing.

Selection of piston size represented a compromise influenced by such considerations as reasonable pressurization levels required to produce sufficient stress in the model seat land and a length-to-diameter (L/D) ratio large enough to minimize poppet-seat parallelism deviation. A nominal piston diameter of 1.5 inches (loading area of 1.767 sq in.) was selected having an 0.0001- to 0.0002-inch piston-bore diametral clearance and an L/D ratio of approximately 5. Assuming a minimum bottle supply pressure of 1500 psig, the resultant maximum seat load is 2650 pounds, corresponding to a seat stress of approximately 60,000 psi for a 0.500-inch OD, 0.03-inch land width seat. (The selection of seat dimensions also involved compromise and was based on a diameter and land width representative of actual valves, amenable to fabrication and inspection. Furthermore, in conjunction with loading piston design, these dimensions must make possible the establishment of stress levels encompassing typical rocket engine poppets and seats.)

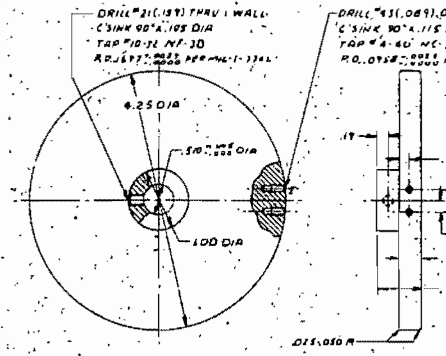

(-43) INDEX WHEEL (A13)

MAT'L: 6061-T6 AL ALLOY BAR QQ-A-325, 4½ DIA X.81

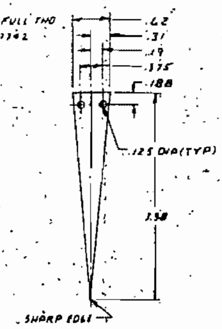

(-45) POINTER (A15)

MAT'L: 1095 STL SHEET, SPRING TEMP MIL-S-7947, .025 X.69 X3.5

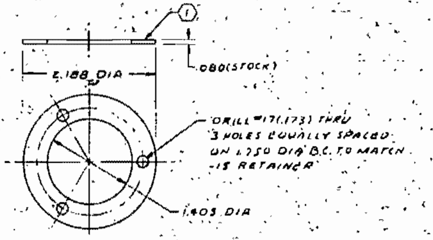

(-27) PLATE - SPRING RETAINER

2. PASSIVATE PER RA0110-018
1. MAT'L: 302 CRES, MIL-S-5059, COMP 302, COND A, .080 X 2.31 X 2.31 SHEET
NOTES: -27 PLATE

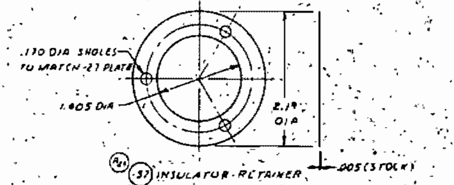

(A21) (-37) INSULATOR - RETAINER

1. MAT'L: ACETATE SHEET .005 X2.25 X2.25
NOTES: -55 INSULATOR

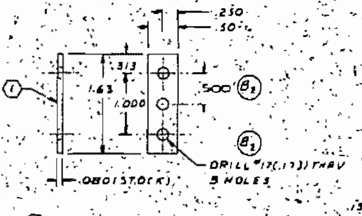

(-31) PLATE - SPRING RETAINER

2. PASSIVATE PER RA0110-018
1. MAT'L: 302 CRES, MIL-S-5059, COMP 302, COND A, .080 X .56 X 1.75
NOTES: -31 PLATE

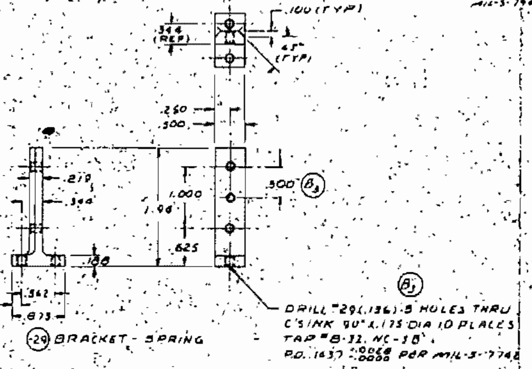

(-29) BRACKET - SPRING

3. .093 FILLET RADII
2. PASSIVATE PER RA0110-018
1. MAT'L: 303 CRES, MIL-S-7720, COMP 303, COND A, 1" X 1" X 2.0" BAR
NOTES: -29 BRACKET

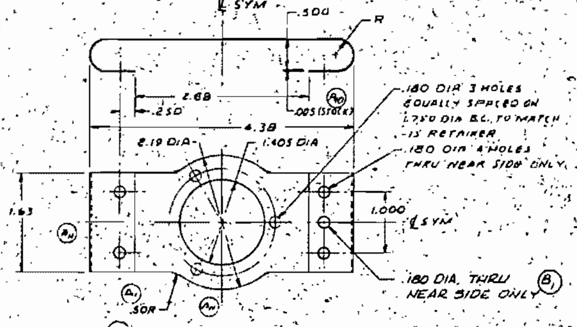

(-13) SPRING - POPPET RETAINER

2. PASSIVATE PER RA0110-018
(A9) 1. MAT'L: 302 CRES, MIL-S-5059, COMP 302, COND A, .005 X 2.31 X 5.75 SHEET
NOTES: -13 SPRING

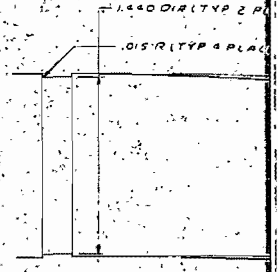

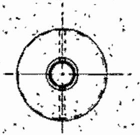

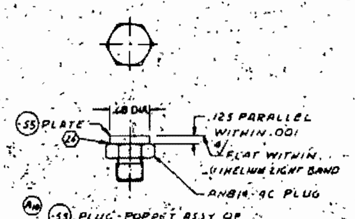

(A16) (-53) PLUG - POPPET, ASSY OF

(26) 2. INSTALL WITH SCOTCH #400 DOUBLE FACE TAPE (MINN. MINING & MFG. CO, ST. PAUL, MINN.)
1. MAT'L: -55 440C CRES, QQ-S-763, CLASS 440C, COND A, ¾ DIA X .19 BAR
NOTES: -53 PLUG

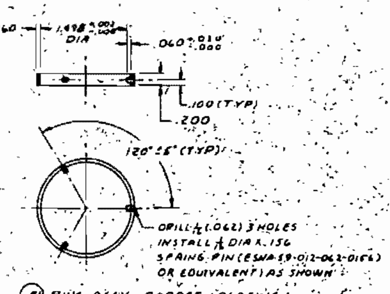

(-51) RING ASSY - POPPET LOCATING

(A5) 3. 63 ALL SURFACES
2. PASSIVATE PER RA0110-018
1. MAT'L: 303 CRES, MIL-S-7720, COMP 303, COND A, 1¾ DIA X .25 BAR
NOTES: -51 RING ASSY

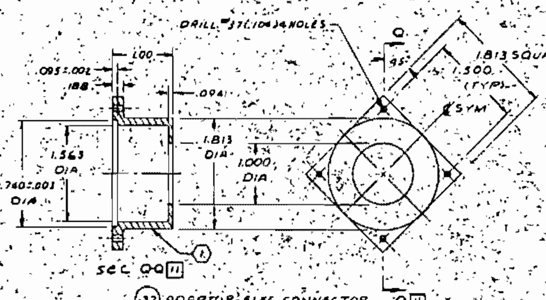

(-37) ADAPTOR - ELEC. CONNECTOR

3. ANODIZE PER MIL-A-8625, TYPE I (RA0109-003)
2. .030 FILLET RADII
1. MAT'L: 2024-T351 AL ALLOY, QQ-A-268, COND T351, 2"X2" X 1.12 BAR
NOTES: -37 ADAPTOR

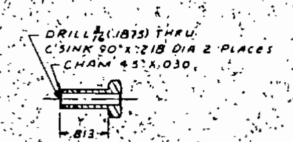

(-35) BOLT - SEAT RETAINING

2. PASSIVATE PER RA0110-018
1. MAKE FROM NAS1005-8A BOLT (A-286 CRES OR DISCALOY, 160,000 PSI MIN)
NOTES: -35 BOLT

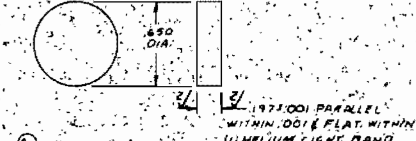

(A14) (-49) SPACER
SCALE: 2 TIMES

1. MAT'L: TUNGSTEN CARBIDE ROCKWELL A 90 MIN
NOTES: -49 SPACER

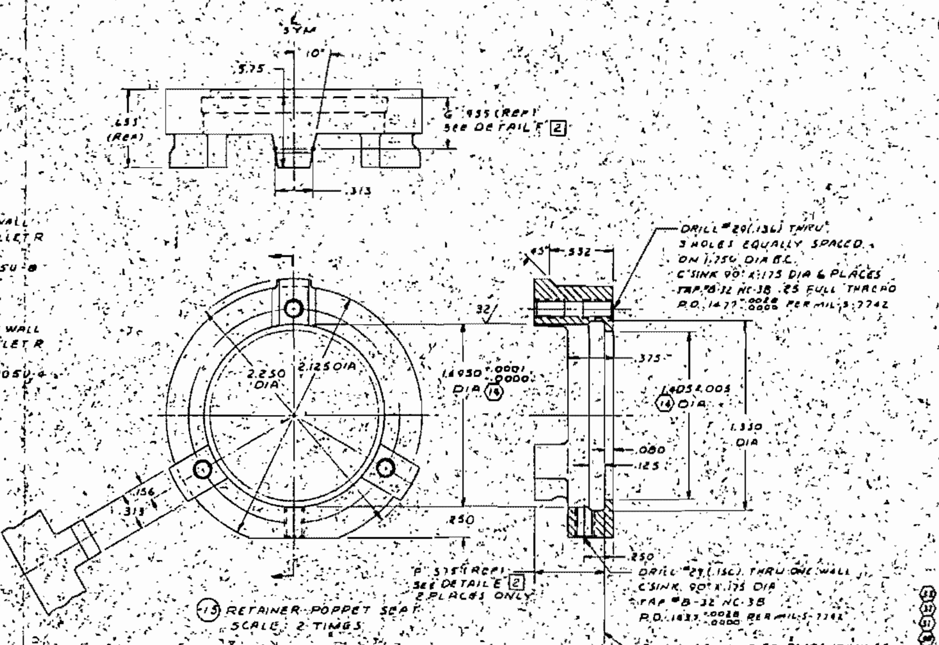

(-15) RETAINER - POPPET SEAT
SCALE: 2 TIMES

6. 63 ALL SURFACES
(14) 5. CONCENTRIC WITHIN .005 TIR
4. .030 FILLET RADII
3. PASSIVATE PER RA0110-018
2. HEAT TREAT 58-60 ROCKWELL 'C' PER MIL-H-6875 (RA0105-14)
1. MAT'L: 440C CRES, QQ-S-763, CLASS 440C, COND A, 2½ DIA X .75
NOTES: -15 RETAINER

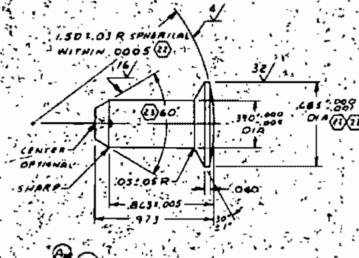

(A22) (-47) PIN - CENTERING
SCALE: 2 TIMES

5. 63 UNLESS OTHERWISE NOTED
(21)(22) 4. CONCENTRIC WITHIN .001
3. PASSIVATE PER RA0110-018
2. HEAT TREAT 58-60 R_C PER MIL-H-6875 (RA0105-14)
1. MAT'L: 440C CRES, QQ-S-763, CLASS 440C, COND A, ¾ DIA X 1.06 BAR
NOTES: -47 PIN

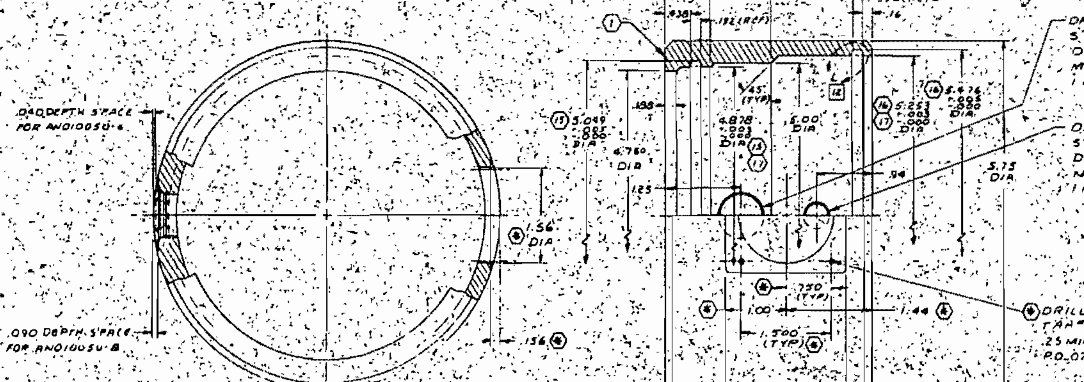

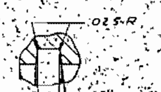

DETAIL C 11
TYP 2 PLACES
SCALE 2 TIMES

(-33) RING - COVER
(-330)

5. DIMENSIONS CODED ✱ DO NOT APPLY TO -330
(12)(16)(15) 4. CONCENTRIC WITHIN .003 TIR
3. ANODIZE PER MIL-A-8625 TYPE I (RA0109-003)
2. .06 FILLET RADII
1. MAT'L: 2024-T351 AL ALLOY, QQ-A-268, COND T351, 6" DIA X 4.0" BAR
NOTES: -33 RING

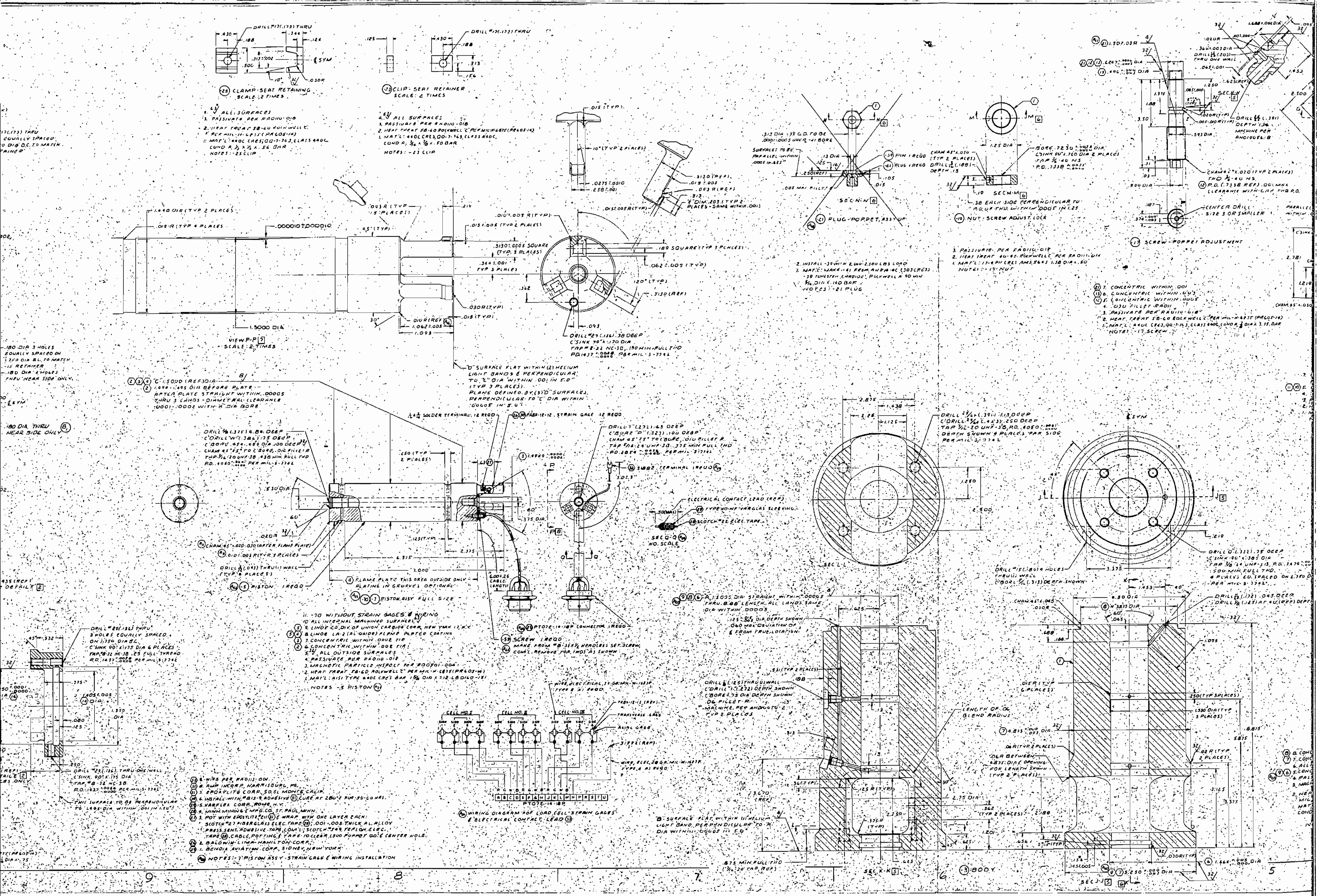
-25 CLAMP-SEAT RETAINING SCALE: 2 TIMES
-23 CLIP-SEAT RETAINER SCALE: 2 TIMES
VIEW P-P
SCALE: 2 TIMES
-21 PLUG-POPPET, ASSY OP
SEC N-N
SEC M-M
-19 NUT-SCREW ADJUST. LOCK
-17 SCREW-POPPET ADJUSTMENT
SEC H-H
-10 -7 PISTON ASSY FULL SIZE
-5 PISTON 1 REQD
SEC Q-Q NO SCALE
SEC L-L
SEC K-K
SEC J-J
-3 BODY
WIRING DIAGRAM FOR LOAD CELL STRAIN GAGES & ELECTRICAL CONTACT LEAD
CELL NO. I
CELL NO. II
CELL NO. III
PT07E-14-18P
9
8
7
6
5

1. 63 ALL SURFACES
3. PASSIVATE PER RA0110-018
2. HEAT TREAT 58-60 ROCKWELL C PER MIL-H-6875 (PRC05-14)
1. MAT'L: 440C CRES, QQ-7-763, CLASS 440C COND A, ½ x ⅝ x .56 BAR

NOTES: -25 CLIP

4. 63 ALL SURFACES
3. PASSIVATE PER RA0110-018
2. HEAT TREAT 58-60 ROCKWELL C PER MIL-H-6875 (PRC05-14)
1. MAT'L: 440C CRES, QQ-7-763, CLASS 440C, COND A, 3/16 x ⅜ x .50 BAR

NOTES: -23 CLIP

2. INSTALL -39 WITH 2,000-2,500 LBS LOAD
1. MAT'L: MAKE -41 FROM AN DIA 4C (303 CRES) -39 TUNGSTEN CARBIDE, ROCKWELL A 90 MIN 5/16 DIA X .140 BAR

NOTES: -21 PLUG

3. PASSIVATE PER RA0110-018
2. HEAT TREAT 40-45 ROCKWELL C PER RA0111-014
1. MAT'L: 17-4 PH CRES AMS 5643 1.38 DIA x .50

NOTES: -19 NUT

7. CONCENTRIC WITHIN .001
6. CONCENTRIC WITHIN .003
5. CONCENTRIC WITHIN .0005
4. .030 FILLET RADII
3. PASSIVATE PER RA0110-018
2. HEAT TREAT 58-60 ROCKWELL C PER MIL-H-6875 (PRC05-14)
1. MAT'L: 440C CRES, QQ-7-763, CLASS 440C, COND A, ⅞ DIA X 3.75 BAR

NOTES: -17 SCREW

11. -70 WITHOUT STRAIN GAGES & WIRING
10. ALL INTERNAL MACHINED SURFACES 32
9. LINDE CO. DIV. OF UNION CARBIDE CORP. NEW YORK 17, N.Y.
8. LINDE LA-2 (AL OXIDE) FLAME PLATED COATING
7. CONCENTRIC WITHIN .0002 TIR
6. CONCENTRIC WITHIN .002 TIR
5. 32 ALL OUTSIDE SURFACES
4. PASSIVATE PER RA0110-018
3. MAGNETIC PARTICLE INSPECT PER R00501-004
2. HEAT TREAT 58-60 ROCKWELL C PER MIL-H-6875 (PRC05-14)
1. MAT'L: AISI TYPE 440C CRES BAR 1⅝ DIA X 7.12 LB0160-151

NOTES -5 PISTON

9. WIRE PER RA0113-001
8. AMP INCORP. HARRISBURG, PA.
7. EPOXYLITE CORP. SO. EL MONTE, CALIF.
6. INSTALL WITH #815-9 ADHESIVE (31), CURE AT 280°F FOR 50-60 HRS.
5. VARFLEX CORP., ROME, N.Y.
4. MINN. MINING & MFG. CO. ST. PAUL, MINN.
3. POT WITH EPOXYLITE #211 (31) & WRAP WITH ONE LAYER EACH: SCOTCH #27 FIBERGLASS ELEC. TAPE (28); .001-.003 THICK AL. ALLOY PRESS. SENS. ADHESIVE TAPE, COM'L; SCOTCH #549 TEFLON ELEC. TAPE (28). CABLE, POTTING & TAPE TO CLEAR 1.500 POPPET OD & CENTER HOLE.
2. BALDWIN-LIMA-HAMILTON CORP.
1. BENDIX AVIATION CORP., SIDNEY, NEW YORK

NOTES: -7 PISTON ASSY-STRAIN GAGE & WIRING INSTALLATION

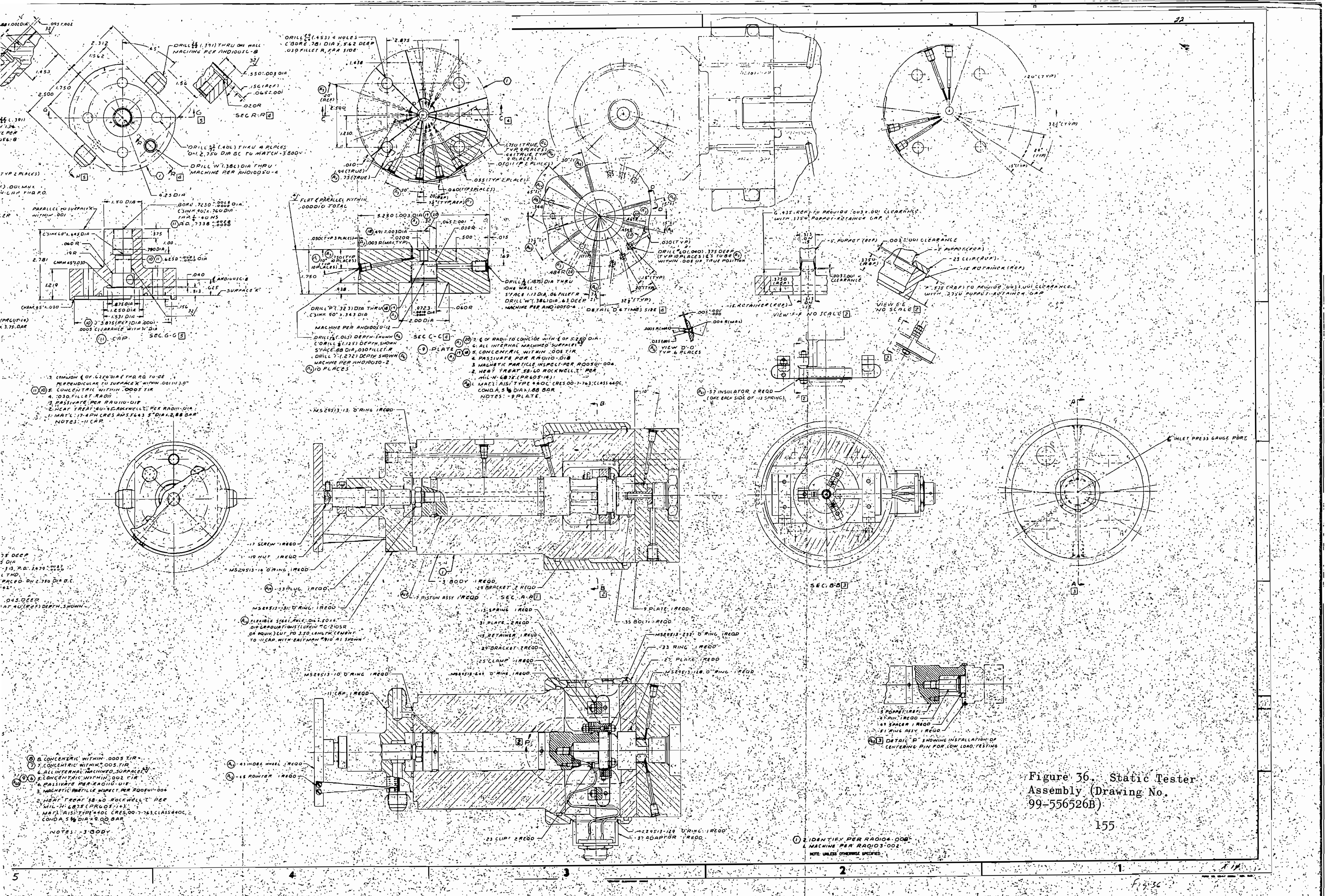

Figure 36. Static Tester Assembly (Drawing No. 99-556526B)

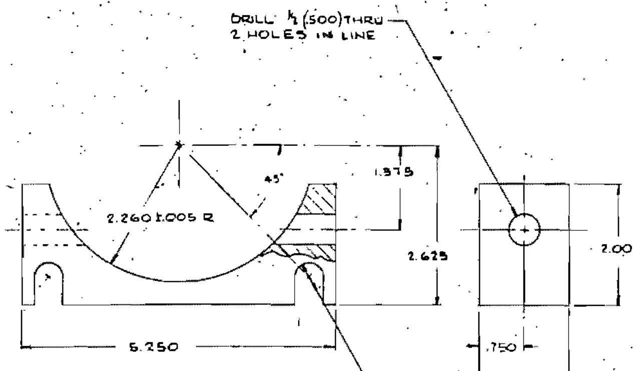

(-65) SADDLE

NOTES

1. MAT'L 6061-T651 AL ALLOY PL
   QQ-A-327, COND T 1½ x 2.25 x 5.37

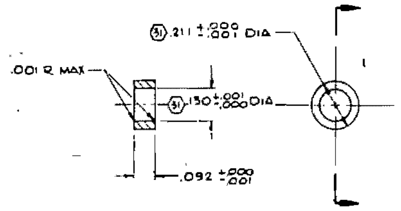
(31) $.211^{+.000}_{-.001}$ DIA
.001 R MAX
(31) $.130^{+.001}_{-.000}$ DIA
$.092^{+.000}_{-.001}$

SECTION
SCALE 4/1

(-57) GUIDE

NOTES

1. MAT'L 17-4 PH CRES BAR
   AMS 5643, COND A ¼ DIA x .12
2. HEAT TREAT PER RA0111-016
   COND H900 (R_c 40-47)
3. (31) CONCENTRIC WITHIN .001 TIR
4. PASSIVATE PER RA0110-018
5. ALL MACHINED SURFACES 63√

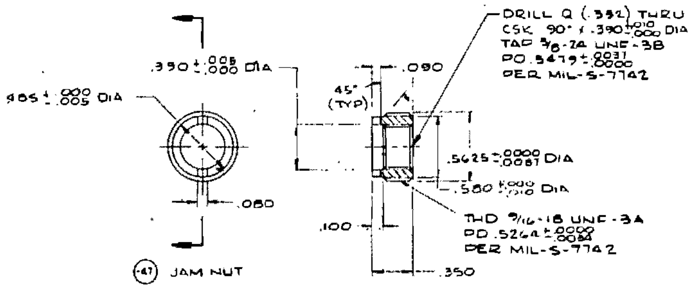
$.685^{+.000}_{-.005}$ DIA
$.390^{+.005}_{-.000}$ DIA
.080
45° (TYP)
.090
DRILL Q (.332) THRU
CSK 90° x $.390^{+.010}_{-.000}$ DIA
TAP ⅜-24 UNF-3B
PD $.3479^{+.0031}_{-.0000}$
PER MIL-S-7742
$.5625^{+.0000}_{-.0081}$ DIA
$.580^{+.000}_{-.010}$ DIA
THD 9/16-18 UNF-3A
PD $.5264^{+.0000}_{-.0034}$
PER MIL-S-7742
.100
.350

(-47) JAM NUT

SECTION
SCALE: 2/1

NOTES

1. MATL 17-4 PH CRES BAR, AMS5643
   COND A, ¾ DIA x .50
2. HEAT TREAT PER RA0111-016
   COND H900 (R_c 40-47)
3. PASSIVATE PER RA0110-018
4. ALL MACHINED SURFACES 63√

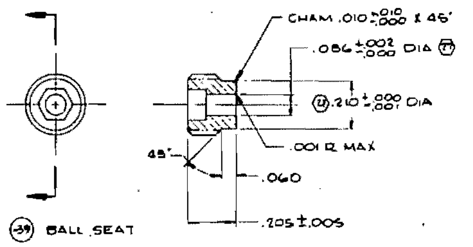
CHAM $.010^{+.010}_{-.000}$ x 45°
$.086^{+.002}_{-.000}$ DIA (77)
(27) $.210^{+.000}_{-.001}$ DIA
.001 R MAX
45°
.060
.205±.005

(-39) BALL SEAT

SECTION
SCALE: 4/1

NOTES

1. MAKE FROM HOLO-KROME
   HEADLESS SET SCREW
   ¼-28 x .25 Lg
2. (77) CONCENTRIC TO THD PD
   WITHIN .003 TIR

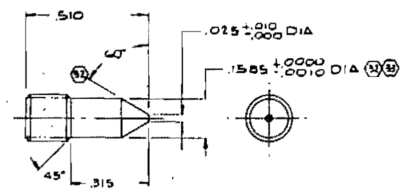
.510
60°
(32)
$.025^{+.010}_{-.000}$ DIA
$.1585^{+.0000}_{-.0010}$ DIA (32)(33)
45°
.315

(-59) LOCK PIN
SCALE: 4/1

NOTES

1. MAKE FROM HOLO-KROME
   HEADLESS SET SCREW
   10-32 x .62
2. (32) CONCENTRIC WITHIN .001 TIR
3. (33) CONCENTRIC WITHIN .003 TIR
   TO THREAD PD

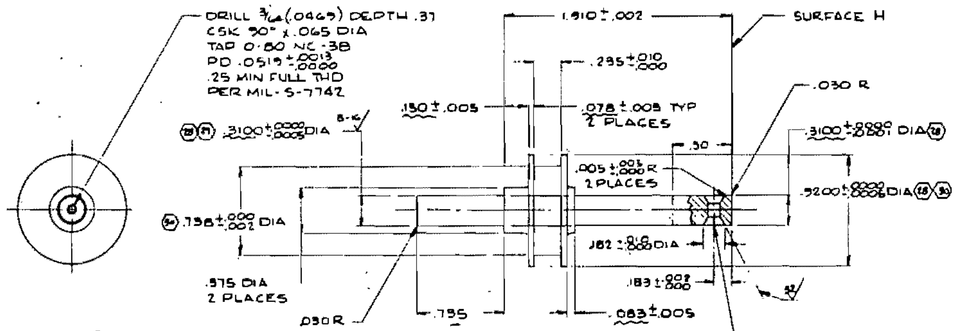

(-49) PLUNGER
SCALE: 2/1

NOTES

1. MAT'L 17-4 PH CRES BAR
   AMS 5643, COND A
   1.0 DIA x 2.75
2. HEAT TREAT PER RA0111-016
   COND H900 R_c 40-47
3. PASSIVATE PER RA0110-018
4. ALL MACHINED SURFACES 63√
5. ALL FILLET RADII $.005^{+.010}_{-.000}$
6. BREAK CORNERS $.005^{+.005}_{-.000}$
7. (28) CONCENTRIC WITHIN .0002 TIR
8. (77) NORMAL TO SURFACE H
   WITHIN .001 TOTAL
9. (30) CONCENTRIC WITHIN .002 TIR

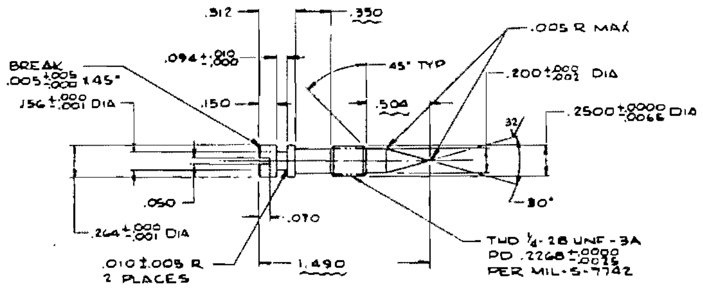
.312
.350
$.094^{+.010}_{-.000}$
BREAK
$.005^{+.005}_{-.000}$ x 45°
$.156^{+.000}_{-.001}$ DIA
.150
45° TYP
.504
.005 R MAX
$.200^{+.000}_{-.002}$ DIA
$.2500^{+.0000}_{-.0066}$ DIA
32
30°
.050
.070
$.264^{+.000}_{-.001}$ DIA
.010±.005 R
2 PLACES
1.490
THD ¼-28 UNF-3A
PD $.2268^{+.0000}_{-.0025}$
PER MIL-S-7742

(-43) NEEDLE VALVE
SCALE: 2/1

NOTES

1. MAT'L 17-4 PH CRES BAR, AMS 5643
   COND A, 5/16 DIA x 1.50
2. HEAT TREAT PER RA0111-016
   COND H900 (R_c 40-47)
3. PASSIVATE PER RA0110-018
4. ALL MACHINED SURFACES 63√
5. ALL DIAMETERS CONCENTRIC
   WITHIN .003 TIR

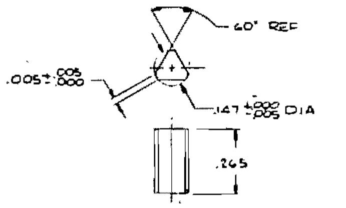

(-63) PIN
SCALE: 4/1

NOTES

1. MAT'L 303 S or SE CRES BAR
   QQ-S-763 COND A CL 303
   3/16 DIA x .270
2. PASSIVATE PER RA0110-018

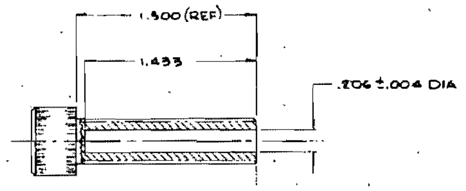

(-55) REGULATOR SCREW
SCALE: 2/1

NOTES

1. MAKE FROM HOLO-KROME
   SOCKET HEAD CAP SCREW
   ⅜-24 x 1½ Lg

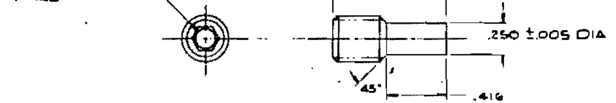

(-53) LOCK SCREW
SCALE: 2/1

NOTES

1. MAKE FROM HOLO-KROME
   HEADLESS SETSCREW
   ⅜-24 x 1.0 Lg

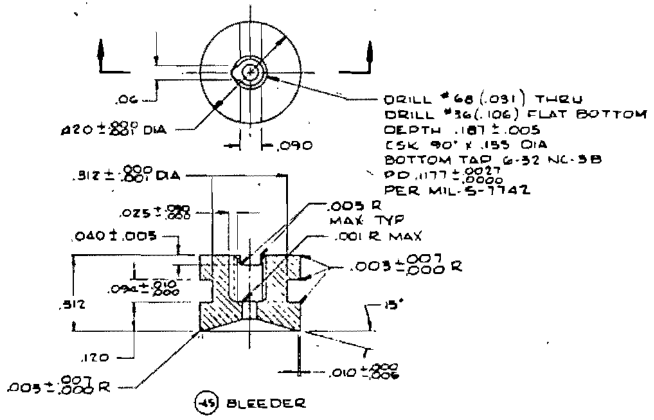

(-45) BLEEDER

SECTION
SCALE: 4/1

NOTES

1. MAT'L 17-4 PH CRES BAR, AMS 5643,
   COND A, ½ DIA x .25
2. HEAT TREAT PER RA0111-016
   COND H1150 (R_c 28-37)
3. PASSIVATE PER RA0110-018
4. ALL MACHINED SURFACES 63√
5. ALL DIAMETERS CONCENTRIC
   WITHIN .003 TIR

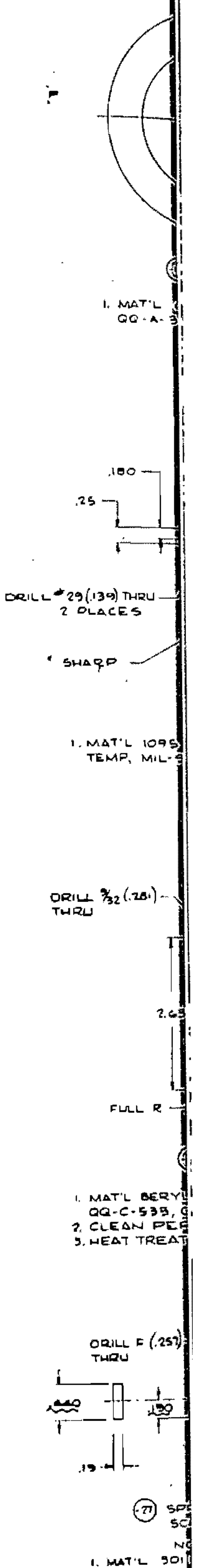

1. MAT'L
   QQ-A-3

1. MAT'L 1095
   TEMP, MIL-S

1. MAT'L BERYL
   QQ-C-533,
2. CLEAN PE
3. HEAT TREAT

(-77) SP
SC
N
1. MAT'L 301
   COMP 301
2. PASSIVAT

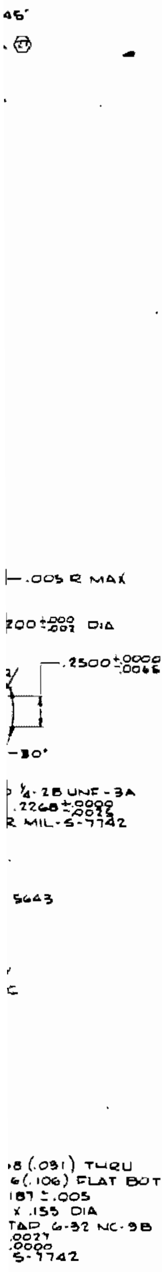

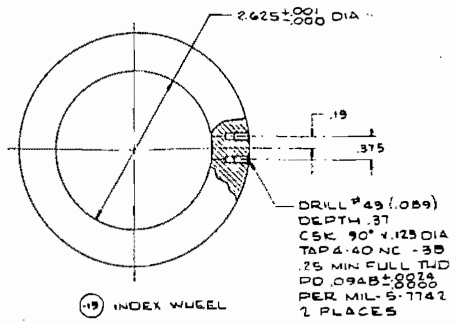

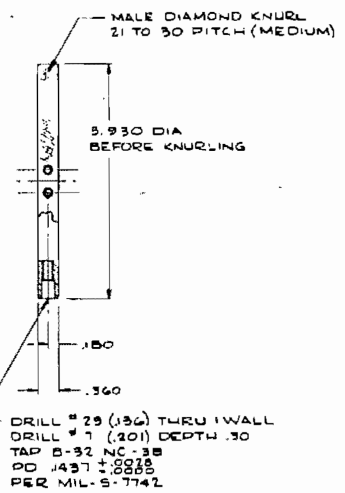

(-19) INDEX WHEEL

NOTES

1. MAT'L 6061-T651 AL ALLOY BAR QQ-A-325, 4 DIA X .43

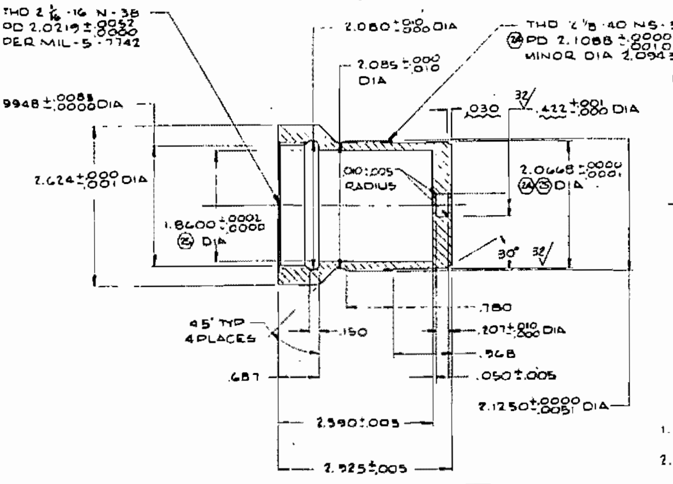

SECTION K-K 9

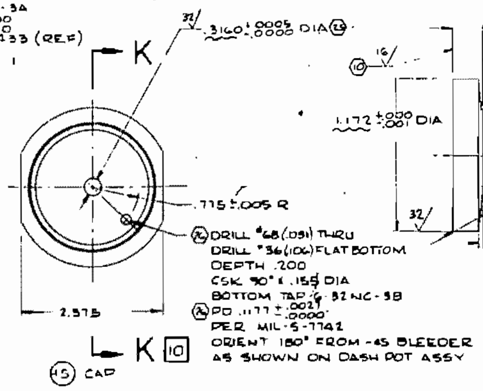
K
32
.3160 +.0005 -.0000 DIA (26)
.715 ±.005 R
(26) DRILL #68 (.031) THRU
DRILL #36 (.106) FLAT BOTTOM
DEPTH .200
CSK 90° X .155 DIA
BOTTOM TAP 6-32 NC-3B
(26) PD .1177 +.0027 -.0000
PER MIL-S-7742
ORIENT 180° FROM -45 BLEEDER
AS SHOWN ON DASH POT ASSY
2.575
K 10

(-15) CAP

NOTES

1. MAT'L 17-4PH CRES BAR AMS 5643, COND A, 2 3/4 DIA X 3.00
2. HEAT TREAT PER RA0111-016 COND H900 (RC 40-47)
3. PASSIVATE PER RA0110-018
4. ALL MACHINED SURFACES 63
5. ALL FILLET RADII .030
(24) 6. CONCENTRIC WITHIN .0005 TIR
(25) 7. CONCENTRIC WITHIN .0002 TIR
(26) 8 CONCENTRIC WITHIN .003 TIR

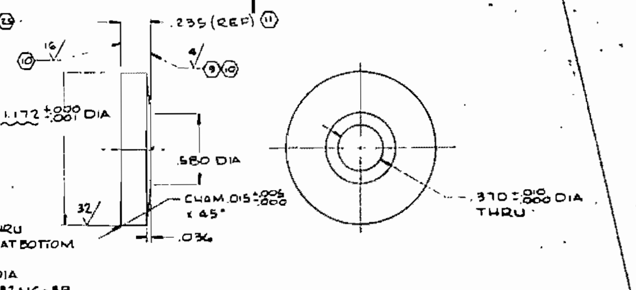

(-18) GUIDE
SCALE: 2/1

NOTES

1. MAT'L 440 C CRES BAR, QQ-S-763, COND A, CL 440C, 1 1/4 DIA X .30
(9) 2. FLAT WITHIN 2 BANDS OF HELIUM LIGHT
(10) 3. PARALLEL WITHIN .00005 TOTAL
4. PASSIVATE PER RA0110-018
(11) 5. MATCH AT ASSEMBLY TO OBTAIN .015 ±.001 DIMENSION IN DASHPOT SECTION

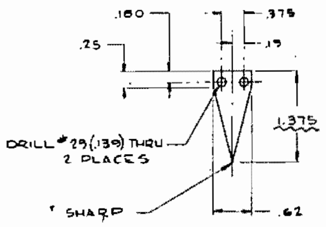

(-23) POINTER

NOTES

1. MAT'L 1095 STL SHEET, SPRING TEMP, MIL-S-7947, .010 X .69 X 1.50

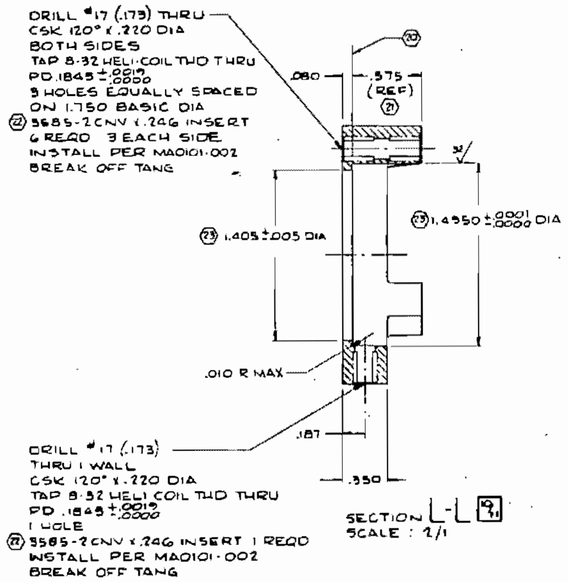

SECTION L-L 9/11
SCALE: 2/1

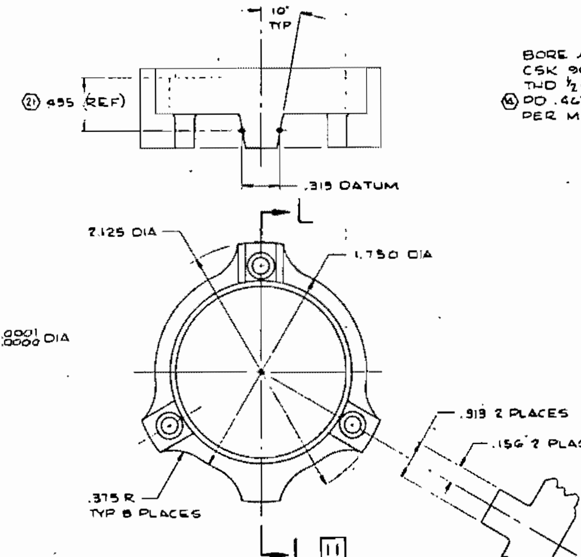

(-17) RETAINER

NOTES

1. MAT'L 6061-T651 AL ALLOY BAR QQ-A-325, 2 1/2 DIA X .75
(20) 2. NORMAL TO 1.4950 DIA WITHIN .0001 TIR
3. ALL MACHINED SURFACES 63
(21) 4. THIS DIMENSION TO MATCH DIMENSION ON 99-556526-15
(22) 5. HELI-COIL CORP., DANBURY, CONN
(23) 6. CONCENTRIC WITHIN .005 TIR

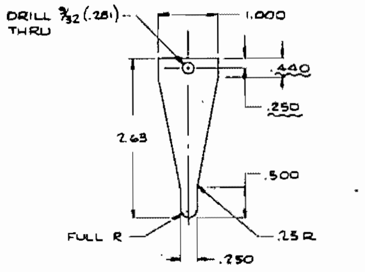

(-25) SPRING

NOTES

1. MAT'L BERYLLIUM COPPER STRIP QQ-C-533, COND 1/4 H, .040 X 1.05 X 2.75
2. CLEAN PER PRI-6
3. HEAT TREAT PER LA0111-011

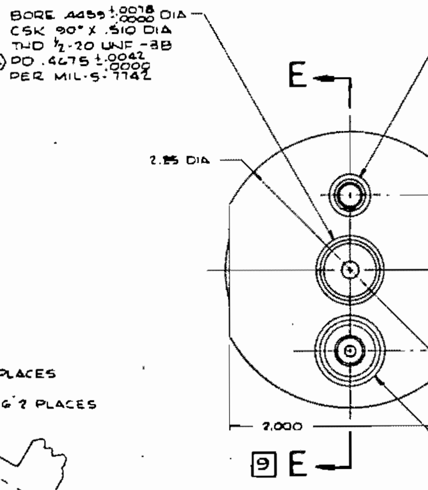

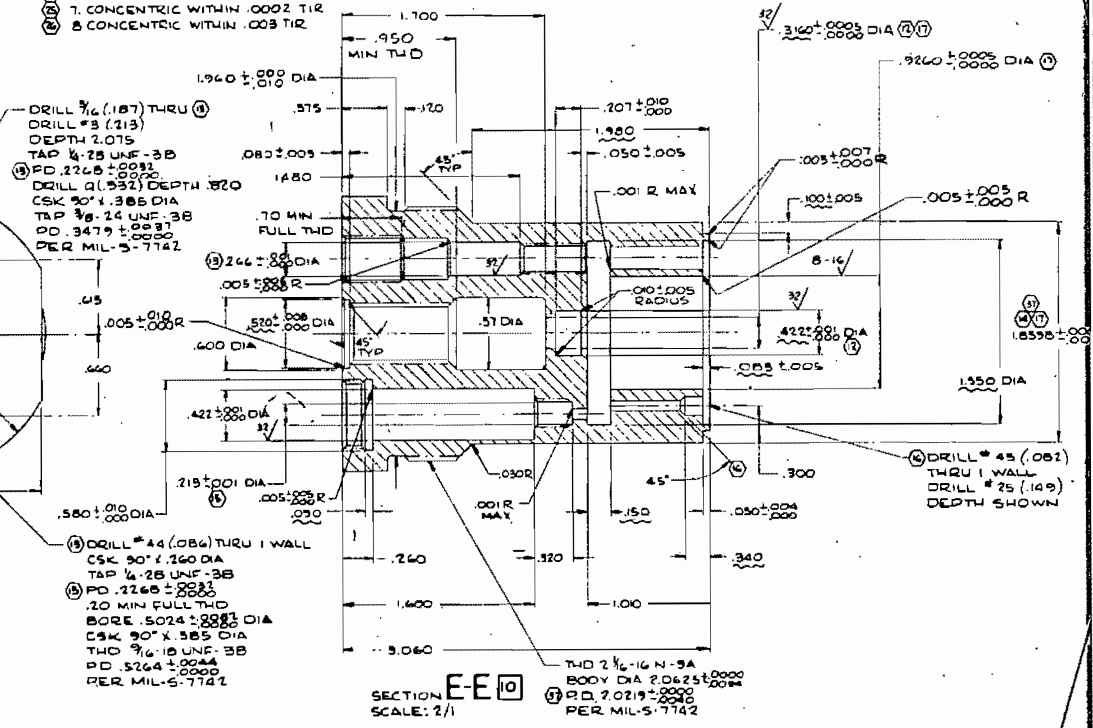

SECTION E-E 10
SCALE: 2/1

(-9) DASH POT

NOTES

1. MAT'L 17-4 PH CRES BAR AMS 5643, COND A, 2 7/8 X 3.12
2. HEAT TREAT PER RA0111-016 COND H1075 (RC 51-57)
3. PASSIVATE PER RA0110-018
4. ALL MACHINED SURFACES 63
(37)(16)(15)(14)(13)(12) 5. CONCENTRIC WITHIN .002 TIR
(17) 6. CONCENTRIC WITHIN .0002 TIR

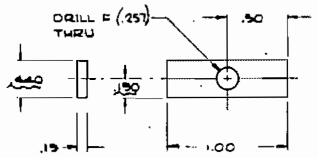

(-27) SPRING CLAMP
SCALE: 2/1

NOTES

1. MAT'L 301 CRES SHT, MIL-S-5059 COMP 301 .19 X .37 X 1.06
2. PASSIVATE PER RA0110-018

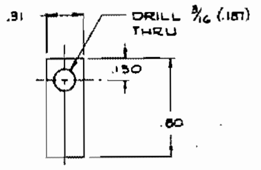

(-29) SWITCH
SCALE: 2/1

NOTES

1. MAT'L BERYLLIUM COPPER STRIP QQ-C-533, COND 1/4 H, .020 X .37 X 1.00
2. CLEAN PER PRI-6

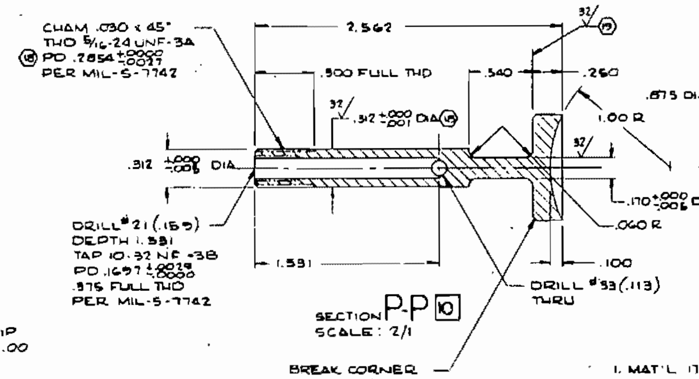

SECTION P-P 10
SCALE: 2/1

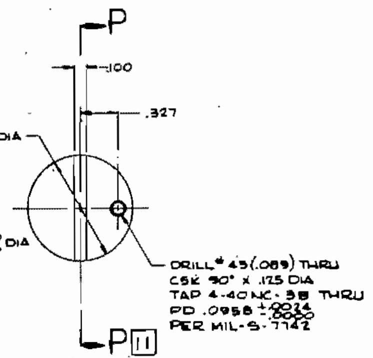

(-33) BOLT

NOTES

1. MAT'L 17-4PH CRES BAR, AMS 5643 COND A, 1.0 DIA X 2.75
2. HEAT TREAT PER RA0111-016 RC 40-47 180,000 - 215,000 PSI
3. PASSIVATE PER RA0110-018
4. ALL MACHINED SURFACES 63
(18) 5. CONCENTRIC WITHIN .001 TIR
(19) 6. NORMAL TO 5/16 THD PD WITHIN .001 TOTAL

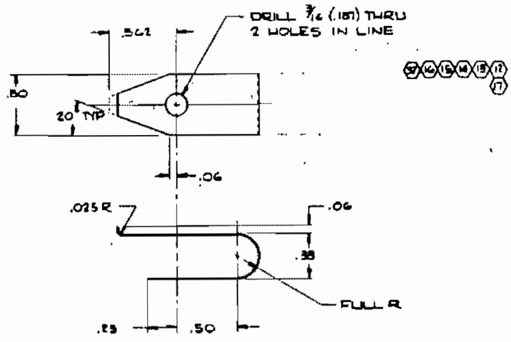

(-45) SWITCH SPRING
SCALE: 2/1

NOTES

1. MAT'L BERYLLIUM COPPER STRIP QQ-C-533, COND 1/4 H, .010 X .62 X 2.50
2. CLEAN PER PRI-6
3. DETAIL SHOWN IN THE INSTALLED POSITION

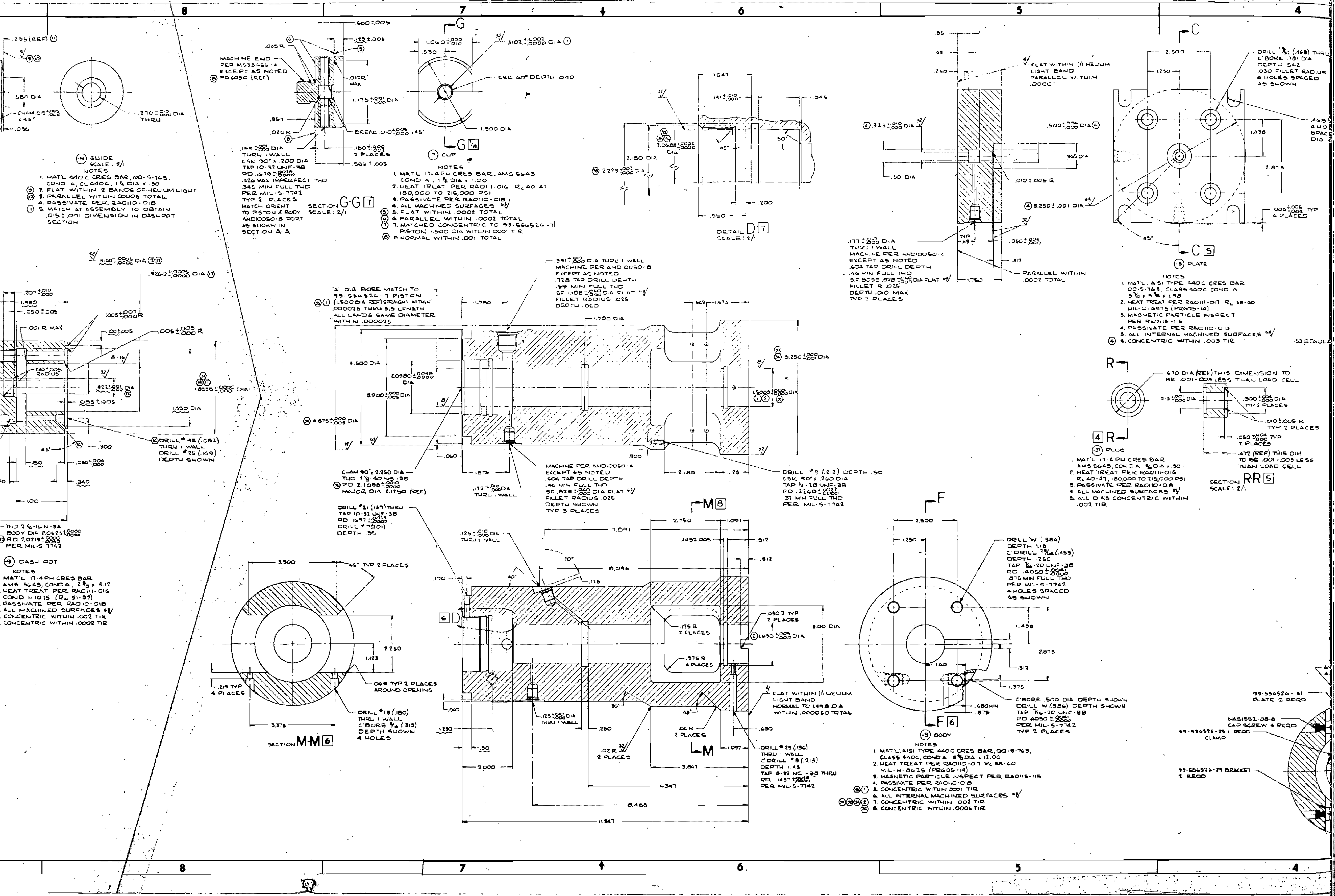

8
7
6
5
4
.235 (REF) (11)
.580 DIA
CHAM .015 +.005 -.000 x 45°
.036
.370 +.010 -.000 DIA THRU
MACHINE END PER MS33656-4 EXCEPT AS NOTED
(8) PD .6050 (REF)
.600 ±.005
.125 ±.005
.010R MAX
1.175 +.001 -.000 DIA
.557
.020 R
BREAK .010 +.005 -.000 x 45°
.180 +.000 -.002 2 PLACES
.566 ± .005
.159 +.001 -.000 DIA THRU 1 WALL CSK 90° x .200 DIA TAP 10-32 UNF-3B PD .1679 +.0029 -.0000 .426 MAX IMPERFECT THD .345 MIN FULL THD PER MIL-S-7742 TYP 2 PLACES MATCH ORIENT TO PISTON & BODY AND10050-8 PORT AS SHOWN IN SECTION A-A
SECTION G-G 7
SCALE: 2/1
G
1.060 +.000 -.010
.530
.3102 +.0002 -.0000 DIA (7)
CSK 60° DEPTH .040
1.500 DIA
G 1/8
(-7) CUP
1.047
.141 +.010 -.000
.045
7.0688 +.002 -.0000 DIA
2.180 DIA
(36) 2.229 +.002 -.000 DIA
45°
30°
.200
.550
DETAIL D 7
SCALE: 2/1
.85
.45
.250
FLAT WITHIN (1) HELIUM LIGHT BAND PARALLEL WITHIN .00001
(4) .323 +.010 -.000 DIA
.500 +.006 -.000 DIA (4)
.50 DIA
.945 DIA
.010 ±.005 R
(4) 5.250 ±.001 DIA
TYP .69
.050 +.004 -.000
.512
1.750
PARALLEL WITHIN .0002 TOTAL
.177 +.010 -.000 DIA THRU 1 WALL MACHINE PER AND10050-4 EXCEPT AS NOTED .604 TAP DRILL DEPTH .46 MIN FULL THD S.F. BOSS .828 +.010 -.000 DIA FLAT FILLET R .015 DEPTH .010 MAX TYP 2 PLACES
C
2.500
1.250
DRILL 15/32 (.468) THRU C'BORE .781 DIA DEPTH .562 .030 FILLET RADIUS 4 HOLES SPACED AS SHOWN
1.438
2.875
.005 +.005 -.004 TYP 4 PLACES
45°
C 5
.3160 +.0005 -.0000 DIA (12)(17)
.9260 +.0005 -.0000 DIA (17)
.207 +.010 -.000
1.980
.050 ±.005
.003 +.007 -.000 R
.001 R MAX
.100 ±.005
.005 +.005 -.000 R
.010 ±.005 RADIUS
.422 +.001 -.000 DIA (12)
.085 ±.005
1.8330 +.0000 -.0001 DIA
1.550 DIA
45°
.300
.150
.030 +.004 -.000
.340
1.010
(6) DRILL #43 (.082) THRU 1 WALL DRILL #25 (.149) DEPTH SHOWN
THD 2 1/16-16 N-3A BODY DIA 2.0625 +.0000 -.0094 PD 2.0219 +.0000 -.0040 PER MIL-S-7742
'A' DIA BORE MATCH TO 99-556526-7 PISTON (1.500 DIA REF) STRAIGHT WITHIN .000025 THRU 3.5 LENGTH ALL LANDS SAME DIAMETER WITHIN .000025
1.780
.391 +.010 -.000 DIA THRU 1 WALL MACHINE PER AND10050-8 EXCEPT AS NOTED .728 TAP DRILL DEPTH .59 MIN FULL THD SF 1.188 +.010 -.000 DIA FLAT FILLET RADIUS .025 DEPTH .060
1.780 DIA
.542
1.473
4.500 DIA
2.0980 +.0048 -.0000 DIA
3.900 +.000 -.005 DIA
(36) 4.875 +.000 -.005 DIA
5.250 +.000 -.001 DIA
1.5000 +.0001 -.0000 DIA (1)(2)
.060
.500
1.875
2.188
1.128
CHAM 30° x 2.250 DIA THD 2 1/8-40 NS-3B PD 2.1088 +.0010 -.0000 MAJOR DIA 2.1250 (REF)
.172 +.010 -.000 DIA THRU 1 WALL
MACHINE PER AND10050-4 EXCEPT AS NOTED .604 TAP DRILL DEPTH .46 MIN FULL THD SF .828 +.010 -.000 DIA FLAT FILLET RADIUS .025 DEPTH SHOWN TYP 3 PLACES
DRILL #3 (.213) DEPTH .50 CSK 90° x .260 DIA TAP 1/4-28 UNF-3B PD .2268 +.0032 -.0000 .37 MIN FULL THD PER MIL-S-7742
.670 DIA (REF) THIS DIMENSION TO BE .001-.003 LESS THAN LOAD CELL
.513 +.001 -.000 DIA
.500 +.004 -.000 DIA TYP 2 PLACES
.010 ±.005 R TYP 2 PLACES
.050 +.004 -.000 TYP 2 PLACES
.472 (REF) THIS DIM TO BE .001-.003 LESS THAN LOAD CELL
R
4 R
SECTION R-R 5
SCALE: 2/1
-53 REGULA
DRILL #21 (.159) THRU TAP 10-32 UNF-3B PD .1697 +.0019 -.0000 DRILL #7 (.201) DEPTH .35
.125 +.010 -.000 DIA THRU 1 WALL
M 8
2.750
1.097
.145 ±.005
.812
.512
7.891
8.096
70°
40°
.125
.190
3.500
45° TYP 2 PLACES
2.250
1.125
.219 TYP 4 PLACES
3.375
.06R TYP 2 PLACES AROUND OPENING
DRILL #19 (.180) THRU 1 WALL C'BORE 5/16 (.313) DEPTH SHOWN 4 HOLES
SECTION M-M 6
6 D
.030R TYP 2 PLACES
.175 R 2 PLACES
3.00 DIA
(2) 1.650 +.003 -.000 DIA
.375 R 4 PLACES
FLAT WITHIN (1) HELIUM LIGHT BAND NORMAL TO 1.498 DIA WITHIN .000050 TOTAL
.060
1.250
.125 +.010 -.000 DIA THRU 1 WALL
.250
.02 R 2 PLACES
50°
45°
.06 R 2 PLACES
.650
1.097
DRILL #29 (.136) THRU 1 WALL C'DRILL #3 (.213) DEPTH 1.43 TAP 8-32 NC-3B THRU PD .1437 +.0030 -.0000 PER MIL-S-7742
.30
2.000
3.847
6.347
8.463
11.347
M
F
2.800
1.250
DRILL 'W' (.386) DEPTH 1.13 C'DRILL 29/64 (.453) DEPTH .250 TAP 7/16-20 UNF-3B PD .4050 +.0041 -.0000 .875 MIN FULL THD PER MIL-S-7742 4 HOLES SPACED AS SHOWN
1.438
2.875
1.60
.312
1.375
C'BORE .500 DIA DEPTH SHOWN DRILL W (.386) DEPTH SHOWN TAP 7/16-20 UNF-3B PD .4050 +.0041 -.0000 PER MIL-S-7742 TYP 2 PLACES
.680 MIN
.875
F 6
99-556526-31 PLATE 2 REQD
NAS1352-08-8 CAP SCREW 4 REQD
99-556526-25 1 REQD CLAMP
99-556526-29 BRACKET 2 REQD

(-15) GUIDE
SCALE: 2/1

NOTES
1. MAT'L 440C CRES BAR, QQ-S-763, COND A, CL 440C, 1 1/4 DIA x .30
(9) 2. FLAT WITHIN 2 BANDS OF HELIUM LIGHT
(10) 3. PARALLEL WITHIN .00005 TOTAL
4. PASSIVATE PER RA0110-018
(11) 5. MATCH AT ASSEMBLY TO OBTAIN .015 ± .001 DIMENSION IN DASHPOT SECTION

(-7) CUP

NOTES
1. MAT'L 17-4PH CRES BAR, AMS 5643 COND A, 1 1/2 DIA x 1.00
2. HEAT TREAT PER RA0111-016 R_c 40-47 180,000 TO 215,000 PSI
3. PASSIVATE PER RA0110-018
4. ALL MACHINED SURFACES 63/
(5) 5. FLAT WITHIN .0002 TOTAL
(6) 6. PARALLEL WITHIN .0002 TOTAL
(7) 7. MATCHED CONCENTRIC TO 99-556526-7 PISTON 1.500 DIA WITHIN .0001 TIR
(8) 8. NORMAL WITHIN .001 TOTAL

(-8) PLATE

NOTES
1. MAT'L AISI TYPE 440C CRES BAR QQ-S-763, CLASS 440C COND A 5 3/8 x 5 3/8 x 1.88
2. HEAT TREAT PER RA0111-017 R_c 58-60 MIL-H-6875 (PR605-14)
3. MAGNETIC PARTICLE INSPECT PER RA0115-115
4. PASSIVATE PER RA0110-018
5. ALL INTERNAL MACHINED SURFACES 63/
(4) 6. CONCENTRIC WITHIN .003 TIR

(-37) PLUG
1. MAT'L 17-4 PH CRES BAR AMS 5643, COND A, 3/4 DIA x .30
2. HEAT TREAT PER RA0111-016 R_c 40-47, 180,000 TO 215,000 PSI
3. PASSIVATE PER RA0110-018
4. ALL MACHINED SURFACES 32/
5. ALL DIA'S CONCENTRIC WITHIN .002 TIR

(-9) DASH POT

NOTES
MAT'L 17-4PH CRES BAR AMS 5643, COND A, 2 5/8 x 3.12
HEAT TREAT PER RA0111-016 COND H1075 (R_c 31-37)
PASSIVATE PER RA0110-018
ALL MACHINED SURFACES 63/
CONCENTRIC WITHIN .002 TIR
CONCENTRIC WITHIN .0002 TIR

(-3) BODY

NOTES
1. MAT'L: AISI TYPE 440C CRES BAR, QQ-S-763, CLASS 440C, COND A, 5 5/8 DIA x 12.00
2. HEAT TREAT PER RA0110-017 R_c 58-60 MIL-H-8625 (PR605-14)
3. MAGNETIC PARTICLE INSPECT PER RA0115-115
4. PASSIVATE PER RA0110-018
(35)(1) 5. CONCENTRIC WITHIN .0001 TIR
6. ALL INTERNAL MACHINED SURFACES 8/
(37)(38)(34)(2) 7. CONCENTRIC WITHIN .002 TIR
(36) 8. CONCENTRIC WITHIN .0005 TIR

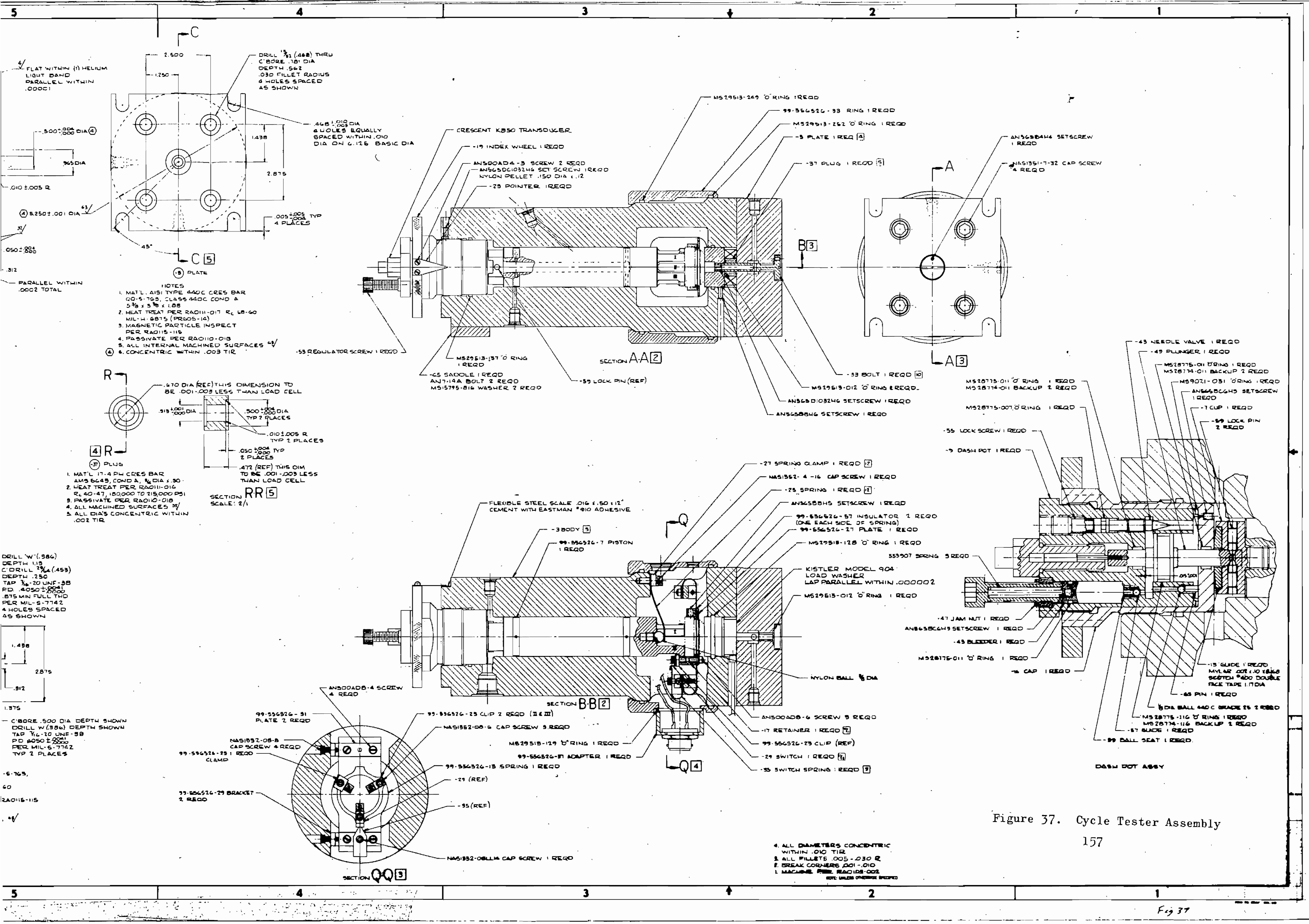
SECTION A-A 2
SECTION B-B 2
SECTION Q-Q 3
SECTION RR 5
SCALE: 2/1
C 5
-9 PLATE
-37 PLUG
CRESCENT KB50 TRANSDUCER
-19 INDEX WHEEL 1 REQD
AN500AD4-3 SCREW 2 REQD
-29 POINTER 1 REQD
MS29513-249 'O' RING 1 REQD
99-556526-33 RING 1 REQD
MS29513-262 'O' RING 1 REQD
-5 PLATE 1 REQ
-37 PLUG 1 REQD
AN565B4H4 SETSCREW 1 REQD
NAS1351-7-32 CAP SCREW 4 REQD
-53 REGULATOR SCREW 1 REQD
MS29513-137 'O' RING 1 REQD
-45 SADDLE 1 REQD
AN7-14A BOLT 2 REQD
MS15795-816 WASHER 2 REQD
-59 LOCK PIN (REF)
-33 BOLT 1 REQD
MS29513-012 'O' RING 2 REQD
AN565B8H6 SETSCREW 1 REQD
-43 NEEDLE VALVE 1 REQD
-49 PLUNGER 1 REQD
-7 CUP 1 REQD
-55 LOCK SCREW 1 REQD
-9 DASH POT 1 REQD
-47 JAM NUT 1 REQD
-43 BLEEDER 1 REQD
-15 GUIDE 1 REQD
-63 PIN 1 REQD
-57 GUIDE 1 REQD
-99 BALL SEAT 1 REQD
DASH POT ASSY
FLEXIBLE STEEL SCALE .016 x .50 x 12" CEMENT WITH EASTMAN #910 ADHESIVE
-3 BODY 5
99-556526-7 PISTON 1 REQD
-27 SPRING CLAMP 1 REQD
NAS1352-4-16 CAP SCREW 1 REQD
-25 SPRING 1 REQD
AN565B8H5 SETSCREW 1 REQD
99-556526-57 INSULATOR 2 REQD (ONE EACH SIDE OF SPRING)
99-556526-27 PLATE 1 REQD
MS29513-128 'O' RING 1 REQD
553907 SPRING 5 REQD
KISTLER MODEL 904 LOAD WASHER LAP PARALLEL WITHIN .000002
MS29513-012 'O' RING 1 REQD
NYLON BALL 1/8 DIA
AN500AD8-6 SCREW 5 REQD
-17 RETAINER 1 REQD
99-556526-23 CLIP (REF)
-21 SWITCH 1 REQD
-35 SWITCH SPRING 1 REQD
AN500AD8-4 SCREW 4 REQD
99-556526-31 PLATE 2 REQD
NAS1352-08-8 CAP SCREW 4 REQD
99-556526-25 1 REQD CLAMP
99-556526-29 BRACKET 2 REQD
99-556526-23 CLIP 2 REQD
NAS1352-08-6 CAP SCREW 5 REQD
MS29513-129 'O' RING 1 REQD
99-556526-11 ADAPTER 1 REQD
99-556526-13 SPRING 1 REQD
-21 (REF)
-35 (REF)
NAS1352-08LL16 CAP SCREW 1 REQD
NOTES
1. MAT'L AISI TYPE 440C CRES BAR
2. HEAT TREAT PER RA0111-017
3. MAGNETIC PARTICLE INSPECT PER RA0115-115
4. PASSIVATE PER RA0110-018
5. ALL INTERNAL MACHINED SURFACES
6. CONCENTRIC WITHIN .003 TIR
-37 PLUG
1. MAT'L 17-4 PH CRES BAR
2. HEAT TREAT PER RA0111-016
3. PASSIVATE PER RA0110-018
4. ALL MACHINED SURFACES
5. ALL DIA'S CONCENTRIC WITHIN .002 TIR
4. ALL DIAMETERS CONCENTRIC WITHIN .010 TIR
3. ALL FILLETS .005-.030 R
2. BREAK CORNERS .001-.010
1. MACHINE FINISH RA0109-002
NOTE: UNLESS OTHERWISE SPECIFIED
5
4
3
2
1
Fig 37

Figure 37. Cycle Tester Assembly

Load Measurement Instrumentation

Model poppet and seat loads were measured by a pressure-loaded piston and electronic devices. These independent methods provided a variety of data and also means for cross correlation.

Pressure-Area Method. The relationship of accurately applied control pressure and the precisely known piston area provided a convenient method of determining model loading. It was used exclusively for stress-leakage tests in both static and cycle testers and for strain gage resistor and piezoelectric load cell static calibration. For initial contract load-distribution tests, the pressure area load measurements served as supporting correlation for strain-gage load cell readings (Ref. 37).

Strain-Gage Load Cells. This system, initially employed in static tester development and correlation of pressure-area load data, used a Baldwin-Lima-Hamilton type SR-4 etched constantan foil strain gage (P/N FABX-12-12). This unit consisted of two identical gages with strain axes 90 degrees opposed, one mounted directly on the other with a bakelite backing. Each piston leg (load cell) used four of these gages mounted with one element of each parallel and the other perpendicular to the piston centerline. This provided four active elements wired in series to amplify input strain with four dummy elements providing temperature compensation. Each load cell comprised the active leg of a bridge circuit, used a separate amplifier, and through suitable switching, the output could be individually displayed. Load cell range was 3000 pounds maximum per cell.

The units were attached to the tester piston legs with a heat-curing epoxy bond after initial lapping. (Final piston lapping was accomplished after strain-gage installation, checkout, and calibration.) During preliminary testing, hysteresis appeared to be a problem but was virtually eliminated by curing the load cell epoxy bond for 2-1/2 days at 300 F.

A Consolidated Electrodynamics Corp. (CEC) high-frequency power supply was used for the 10-volt, 3-kilocycle reference voltage and a CEC 113-B system for amplification and demodulation of the load cell output signal. The information was displayed on a Leeds and Northrup direct-inking chart recorder.

As reported in Ref. 37 each load cell was initially calibrated with a dead weight system to 100 pounds load. Higher load calibration was performed on an Instron testing machine. Calibration resistors were established for full-scale readings of 30, 100, 300, 1000, and 3000 pounds. Net system accuracy was well within 5 percent of the applied load and load changes of 0.3 percent of full scale (0.1 pound at the 30-pound range) could be detected.

As noted in subsequent paragraphs, the instrumented piston was transferred to the cycle tester for follow-on effort dynamic load measurement. The aforementioned 3-kilocycle system had inadequate response characteristics and was replaced for these later tests by d-c energization and amplification equipment. This arrangement used a Microdot, Inc., power supply with a Dynamics Instrument Co. d-c amplifier. Output data were displayed on a Tektronix dual-beam oscilloscope with Polaroid camera attachment. The initially made calibration resistors were satisfactorily rechecked and used in the dynamic system. Supplemental periodic resistor calibration checks were performed with the piston pressure-area loading method.

Piezoelectric Load Cell. In addition to the piston-mounted strain gages, a piezoelectric load cell (0- to 20,000-pound range) was installed in the cycle tester. This unit, a quartz crystal device shaped like a thick washer, was made by the Kistler Instrument Corp. Used with a Kistler electrostatic charge amplifier and oscilloscope output display, it provided stable, wide-range, high-frequency response dynamic load data.

Normally, such devices are somewhat temperature sensitive. As installed, however, the load cell was wrung to the tester baseplate and, in turn, covered by the test model seat as shown in Fig. 37. The intimate contact with relatively massive cycle tester parts and isolation from ambient air currents permitted drift-free static as well as dynamic measurements. Although the unit had a 20,000-pound maximum range, it produced a remarkably pure d-c signal such that, with suitable charge amplifier and oscilloscope amplification, load levels as low as 50 pounds were accurately measured.

The piezoelectric load cell system could be calibrated either by direct loading or insertion of a reference d-c signal through the amplifier. The additional complications of the latter method were undesirable so the piston pressure-area method of calibration loading was used. System integrity and the previously noted isolation from thermal gradients resulted in extremely stable operation. Calibration settings could be maintained for days without adjustment. As with the dynamic application of the strain-gage system, piezoelectric load cell output was displayed on the Tektronix oscilloscope screen.

Hydrostatic Bearing

A system for centering the piston in the body during testing was employed to eliminate friction and rigidly support the piston. The design was based on the radial forces acting on a piston when axial flow through the clearance between piston and cylinder exists. With flow through a diverging or converging clearance of an eccentric piston, an asymmetrical pressure distribution is set up which will develop a radial force acting to either force the piston against the cylinder (diverging flow) or center it in the cylinder (converging flow). The former condition often produces, in piston-type control valves, a condition called "hydraulic lock" (Ref. 64). An application of the latter case was used in both testers to create a type of hydrostatic bearing. To minimize wear, provide electrical insulation, and good antiseizure characteristics when unpressurized or contaminated, both pistons were aluminum oxide flame plated (Linde process).

As initially designed (Ref. 37), the static tester piston was tapered at each end such that a condition of reducing diametral clearance from top and bottom land grooves to a center land existed. Pressurization (film pressure) at the outer ends would then cause a converging flow toward the piston center with a resultant self-centering effect. To preclude gaseous leakage past the outer lands into the control pressure and leak collection cavities, SAE-70 oil was initially used as the film fluid with a nitrogen gas pressurant. Experiments indicated, however, that out-of-round or waviness discrepancies on the test poppet end of the piston (bottom) created a force which cocked the piston at this end (hydraulic lock). Interconnecting passages were therefore blocked and, with the piston pressurized at the top end only, the problem was eliminated.

It was further noted, that with flow toward the piston center, a relatively short righting or centering moment was created. If the taper direction had been reversed and the piston pressurized such that film pressure flow was directed from piston center to each end, a larger moment, and hence, more effective centering force would have resulted. However, top taper pressurization proved adequate for initial (static) tests which were completed without further experimentation or rework. When, for follow-on effort, a separate cycle test unit was required, hydrostatic bearing design improvements were incorporated in both testers.

In the redesigned configuration, fabricated tapers were eliminated. Analysis indicated that simply by center pressurization, the body and piston would elastically deform (the piston constricting and the body expanding) sufficiently to form the desired tapered flow passages outward to each piston end. From the results of static tester development tests, it appeared that the success of this scheme depended upon better control of piston-bore roundness and straightness deviations.

Two pistons had been made during initial static tester fabrication. The first was used for early development tests but geometrical discrepancies of the lapped tapers resulted in poor centering characteristics. The aluminum oxide was completely ground from this piston which was then replated and prelap ground (oversize) at the close of the initial program.

The second piston, used with tapers for initial static tests, was instrumented with strain-gage load cells. To provide additional dynamic load measurement capabilities, this piston was allocated for cycle tester use while the first was reworked to fit the static tester.

The static tester piston was lapped to a 120- to 130-microinch body diametral clearance, straight within 15 microinches. End lands were 50 microinches smaller than the center section to preclude edge contact in the maximum cocked position. The body was not reworked but remeasurement indicated the bore central section was 1.500075-inch diameter instead of 1.500120 inch as reported in Ref. 37. (It should be noted that diametral measurement values quoted involved use of both air gage and mechanical comparator instruments and represent averages of a finite number of data points. Because all portions of a given diameter were not lapped simultaneously and both setup and basic measurement instrument accuracy must be considered, net diametral clearances are estimated accurate to ±20 microinches.)

Tests using piston center pressurization with gaseous nitrogen indicated the static tester piston, as reworked, would "float" as a near-frictionless bearing at 350 psig. At 450 psig, the piston withstood a 105 in.-lb moment (about the piston center) without diametral contact. Similarly, at film pressures of 700 and 1100 psig, cocking moments of 210 and 310 in.-lb, respectively, could be accommodated. This represented a considerable improvement over the initial tester (approximately 60 in.-lb moment resistance at 1000 psig) and all further static tests were performed with this configuration using a more than adequate 600-psig film pressure.

Because of potential damage to the installed strain gage load cells, the piston to be used in the cycle tester was not recoated. Instead, the OD was lapped to remove existing tapers. Final piston diameter was 1.498000 with the end lands 10 to 20 microinches smaller. (This accounts for the difference in static-cycle tester piston areas noted in the Experimental Test Program section.) The cycle tester body bore was matched to this diameter and, by multiple straight-rod lapping, was made round and straight enough to achieve hydrostatic bearing action with only 50 microinches nominal diametral clearance.

Performance tests with center piston pressurization indicated the piston floated with only 100-psig film pressure. At 300 psig, resistance to a cocking moment in excess of 150 in.-lb was demonstrated. To ensure a safe-operating margin with such a small diametral clearance, however, operating pressure was established at 600 psig. It is interesting to note that, with the noted clearance, gas consumption was quite low. For example, at the 600-psig film-pressure level, a total flowrate of only 35-scim nitrogen was measured.

Model Position Measurement

As shown in Fig. 36 and 37, both testers utilized 40-pitch (micrometer) screw threads for axial test poppet positioning. An indicator lapped to a sharp point was attached to the screw thread handwheel while a machinist's steel scale with 0.01-inch graduations was epoxy glued to the tester body or endcap. With known thread pitch and scale circumference, the relationship between screw axial and rotational motion could be precisely determined and indicated by pointer-scale incremental changes. To aid scale-reading resolution a 5-power lens was mounted over the scale, making possible interpolation to ±0.001 inch (scale), or approximately ±2 microinches axial travel.

For dynamic displacement measurement, a Model KB50 (Crescent Engineering and Research Co.) variable reluctance position transducer was used. As shown in Fig. 37, the unit was mounted in the dashpot with the moving slug threaded into the dashpot piston shaft. The transducer was powered by a CEC Model 127, 20-kilocycle carrier-amplifier, a self-contained power supply, demodulator, and amplifier system.

The static tester, used for all precision off-seat tests, employed a lapped and polished 1.5-inch-radius ball joint between screw thread and piston. In this manner, a nearly perfect geometric contact was achieved and the effect of thread abnormalities and contact area waviness on axial displacement (as interpreted by rotary motion) was rendered insignificant. Dashpot geometrical considerations precluded use of the same type joint on the cycle tester. Axial displacement accuracy in this tester was not critical, however, and the dashpot-piston joint was essentially used as a thrust bearing.

During initial evaluation tests, it was noted that the 17-4 PH (R_c45) dashpot cap had galled in turning on the 440C (R_c60) guide. The galled area was polished and a Mylar washer inserted between the two surfaces. (This also served to electrically isolate the piston from the dashpot body). Although the loading bearing of both testers was lubricated with centerpoint lube, only the cycle tester exhibited a galling problem.

Repeatability of linear measurements and an accurate reference datum was provided by an electrical contact system. The aluminum oxide plating on both pistons provided electrical insulation from the tester body. Additional insulation in the flexure poppet mounting system and at other potential contact points effectively isolated test poppet from seat. A flashlight battery, resistor, and microammeter connected in series with the poppet and seat permitted indication of no-load contact between the two.

Model Position Control

To achieve angular and radial position repeatability in case of model disassembly and retest, the poppets were provided with a V-groove which was located to the piston through a retaining ring with a set screw. The piston, in turn, was oriented to the tester body through the retaining ring with a flexure device which prevented rotary motion while offering insignificant axial force. The test seats and tester body base were witness marked permitting orientation within 0.003 inch at the 1.5-inch OD. Concentricity and clearances of the fixture details were controlled to maintain less than 0.0008-inch total eccentricity between the poppet and seat guide diameters.

Basic parallelism control was established by lapping the piston leg bearing surfaces (feet) parallel to the baseplate. This procedure involved several operations. First, the baseplates were lapped parallel within 3 microinches over the 0.50-inch nominal seating diameter. (In the case of the cycle tester, this parallelism was measured between the attached piezoelectric load cell face and baseplate bottom.) The baseplate, body, and piston were assembled, film (centering) pressure applied, and the tester set upright on a granite surface plate. Individual piston feet were then indicated relative to the surface plate and lapped to match. Final net parallelism deviation between piston feet and the surface to which test model seats were mounted (baseplate or load cell) did not exceed 6 microinches over the nominal 0.50-inch seating diameter.

For the majority of surface evaluation tests where seating compliance only was critical and repeated poppet-seat separation (hence positive retention) not a factor, a ball joint loading system was used. This arrangement (shown in Fig. 36, detail P) nullifies tester and model parallelism deviations and permits free-floating surface mating. Surfaces so tested were uniform and a slight radial shift was noncritical. Similarly, rotary positioning to the degree afforded by the flexure system was not essential.

Leakage Collection

Both testers employed an O-ring sealed cover which could be slipped down over the test cavity for leak collection pruposes. Instrumentation cables were also passed through this cover with sealed receptacles. This leak collection method, however, was used only for relatively large flow, i.e., in excess of approximately 3.5 scim. For smaller flowrates, a volume-reducing arrangement was employed as described in the Experimental Test Program section.

Velocity Control

The cycle tester incorporated a variable-orifice (needle valve) hydraulic dashpot for impact velocity control (Fig. 37). This unit was provided with a spring-piston pressurized reservoir to form a "stiff" system and replenish fluid lost through O-ring seal leakage. Dashpot piston and shaft bearing area clearances were designed such that metal-to-metal contact could not occur even under worst eccentricity, abnormality, or diametral tolerances. The shaft was thus electrically isolated (a necessity for electrical contact tests) and could not form wear particles. MIL-H-5606 hydraulic fluid was used.

The dashpot was an integral part of the precision screw thread used for piston positioning and formed a housing for the position transducer. It could be separated from the tester piston by removal of two lock screws accessible through adjacent pressure ports.

TEST FIXTURE ASSEMBLY PROBLEMS

As reported in Ref. 37 static tester assembly problems were minimal. The major setbacks encountered were in the piston centering arrangement and establishment of an adequate strain gage load cell system. Functionally, the cycle tester was almost trouble-free but a severe assembly galling problem occurred. An undesirable effect of surface texture on mating parts assembly dimensions also was detected during static and cycle tester assembly and parallelism measurements.

Cycle Tester Galling

During initial assembly checkout, the lanolin-lubricated dashpot cap (Fig. 37, -15 detail) seized when threaded into the body. Approximately 400 ft-lb torque failed to unthread the galled member and only by packing the cap with dry ice was removal effected. Minor polishing and lapping rework failed to improve significantly the threading action and more positive measures were undertaken which ultimately resulted in satisfactory performance.

The cap was reworked by removing 0.001 inch from the pilot diameter and 0.002 to 0.003 inch from the thread crest. Its pilot diameter and 40-pitch threads were liquid honed and both threads and pilot diameter were coated with two layers of dry film lubricant (molybdenum disulfide in resin base). The body pilot diameter was honed to remove high spots then highly polished with special emphasis on all corner radii. An additional lubrication of extreme pressure moly-lithium grease was applied to the cap pilot diameter while its threads were treated with EP air-drill bearing oil.

During reassembly, the dashpot body (Fig. 37, -9 detail) seized in the cap and could not be removed. Fortunately, all subassembly details had been installed and it was possible to oil fill and bleed the unit. The bypass 1/8-inch ball valve had been assembled so that free-flow return of the plunger was allowed. Although a redesigned cap was fabricated, the dashpot remained operable throughout the test program and replacement was not necessary. The galling problems noted may be attributed to the combination of design and fabrication-assembly errors enumerated below:

1. Long thread and pilot diameter engagement should have been avoided where possible. When galling occurred, the affected area had to traverse an excessive distance during removal with attendant additional damage. A point on the dashpot cap, for instance, from a nominal bottomed condition would move more than 16 linear feet before threads were disengaged. Even the dashpot body with coarse threads would traverse more than 3 feet.
2. Material choice, though differential hardness existed, was improper. The 17-4 PH steel is susceptible to contamination caused metal upset with subsequent galling. With the redesigned dashpot cap, hard chrome plate would have been utilized as an antiseize measure.
3. The specified detail parts surface roughness was not commensurate with the clearances involved. The use of lapped and polished surfaces instead of as-ground 16-microinch AA finish (undoubtedly with typical grinding waves) would have been a deterrent to galling.
4. Tester body and dashpot cap threads were independently ground without benefit of the match lapping operation practiced with the static tester. (In the latter unit, the male thread was made first and the female counterpart successively tapped and

lapped to match. Larger thread size and tester body bulk made this approach impractical in the case of the cycle tester.) Though not proved, it is suspected that a thread-pilot diameter axis abnormality existed in the cycle tester body which caused rubbing of the dashpot cap pilot diameter and thus contributed to the gall problem.

5. Finally, the use of lanolin and other similar lubricants with poor antigall properties during initial assembly attempts was incorrect and may have precipitated the problem.

Surface Texture of Mating Parts

Prior to cycle tester assembly, the baseplate, piezoelectric load cell, and seat were lapped parallel within a few microinches. Individual part parallelism deviation was measured and recorded. When the three pieces were wrung together, the net parallelism deviation did not reasonably agree with the sum of individual measurements. It was determined that the aluminum oxide wet slurry lapped surfaces (about 2-microinch AA) were covered with 10- to 20-microinch high nodules characteristic of this lapping process. While not detected by stylus instrument parallelism checks, the nodules (acting like springs) prevented intimate contact, hence the noted stackup discrepancy. The surfaces concerned were then diamond lapped to remove protuberances, separately inspected, and reassembled. This time the net stackup measurement correlated with individual values.

When the effectiveness of the diamond-lapped surface was proved, all bearing areas were similarly reworked using 1- to 5-micron diamond compound. The resulting surface was equivalent to approximately 1-microinch AA, although no attempt to eliminate noncritical deep scratches was made.

Both static and cycle tester baseplates (top and bottom), piston feet pads, and piezoelectric load cell (both sides) were so refinished. In addition, the loading faces (side opposite sealing surface) of all follow-on test poppets and seats were similarly reworked.

CYCLE TESTER DYNAMIC ANALYSIS

With suitable instrumentation, the impulse delivered externally to model poppets and seats may be measured accurately. However, the capability of a valve seat to withstand cycling loading is a function of the impact loads seen by contacting interfaces. Test data must, therefore, be supplemented with additional information to define the peak impact load experienced by the poppet and seat interfaces. To this end, a dynamic analysis of the cycle tester has been performed. In the first part, explicit equations are developed from simple mass-energy concepts to describe the peak load, natural frequency, and load period experienced by an impacted poppet and seat. The second analysis, based upon the same concepts, considers the entire dynamics of the cycle tester from initiation of control pressure buildup through impact and multiple bouncing to the conclusion of damped vibration. For this analysis, a 7094 IBM digital computer is used to solve iteratively the dynamic equations of force and motion.

By correlating computer and experimental output data for the two tester load cell systems, an accurate estimate of the impact loads experienced by the poppet and seat interfaces may be deduced. Moreover, correlation of the simplified analysis and digital program outputs with test data will provide a foundation for the analysis and prediction of impact loads in other valve configurations.

Introduction of Analytical Concepts

Equations describing the dynamics of the tester configuration are obtained by the summation of forces on the various free bodies in the system. This description of impact is based on Newton's second law of motion. However, some information can also be obtained by the application of energy and momentum concepts. The following paragraphs discuss the energy and momentum equations as applicable to the tester configuration.

Energy Concept. One of the most straightforward approaches to the study of impact is to assume that no energy is dissipated in friction, thus 100 percent of the input energy is transmitted to the impacted body. By using the energy equations and assuming a weight (W) falling from a height (h) on a spring of rate (K), the equations for the total deflection can be derived.

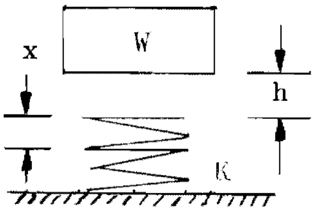

Body Potential Energy = W(h+x)

Spring Potential Energy = 1/2 K x^2

Since there is no energy loss:

$$W(h + x) - 1/2\ K\ x^2 = 0$$

Rearranging, substituting x_{static} for W/K and solving by the quadratic formula yields the following equation for maximum deflection:

$$x_{max} = x_{static} + \left[(x_{static})^2 + 2(x_{static})\ h \right]^{1/2}$$

Two limiting cases which illustrate the effects of a suddenly applied load and the impact of a moving body are of interest.

Suddenly Applied Load. If the h term approaches zero, the energy equation is reduced to:

$$x_{max} = 2\ x_{static}$$

and

$$F_{max} = K\ x_{max} = 2\ F_{static}$$

Impact of a Moving Body. For the other limiting case where (h) is very large compared to the static deflection the equation reduces to:

$$x_{max} = \left[2\ (x_{static})\ h \right]^{1/2}$$

Equating the potential energy term (h) to the equivalent kinetic energy term ($V^2/2g$) and substituting W/K for x_{static} results in:

$$x_{max} = V\left(\frac{W}{g\,K}\right)^{1/2} = V\left(\frac{m}{K}\right)^{1/2} = \frac{V}{\omega_n}$$

where (ω_n) is the system natural frequency and (V) the impact velocity. The maximum spring force can now be computed as:

$$F_{max} = K\,x_{max} = V(K\,m)^{1/2} = \frac{K\,V}{\omega_n}$$

This shows that the maximum force is a function of the impact velocity, spring rate, and body mass (m).

The energy concept has provided means for determining the maximum deflection (or force) but has given no indication of the time duration over which it acts. Subsequent analysis will show the time-dependent relations and be correlated with the maximum deflection computations.

Momentum Concept. The fundamental equation used to define the kinetics of bodies is Newton's second law of motion, which is:

$$\Sigma F_x = m\,a_x = \frac{d}{dt}(m\,V_x)$$

The principle of impulse and momentum is given as:

$$\int_{t_1}^{t_2} \Sigma\,F_x\,dt = \int_{V_{x1}}^{V_{x2}} d(m\,V_x) = m\,V_{x2} - m\,V_{x1}$$

$$\text{or} \quad \text{impulse}_x \equiv \Delta\,(\text{momentum})_x$$

From this, it can be seen that the impulse is the product of a changing force over the time interval in which it acts and the change in momentum is mass times the change in velocity of the body. The term impact is often associated with impulse and is loosely defined as a sudden impulse such as the collision of two bodies.

To illustrate the use of the momentum concept, this equation will be applied to the model used in the energy analysis and a comparison made of the resulting maximum force on the spring. To evaluate the impulse integral, the force term must be expressed as a function of a time. From vibration analysis, the sinusoidal function will be assumed where:

$$F(t) = F_{max} \sin(\omega_n t)$$

This equation expresses the time dependent force oscillations, $F(t)$, as a function of the system natural frequency, and the maximum force, F_{max} and will be integrated in the impulse equation from 0 to $\pi/2$ where all of the momentum has been converted to spring deflection.

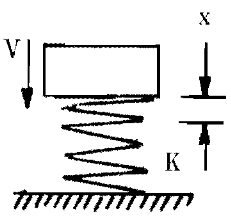

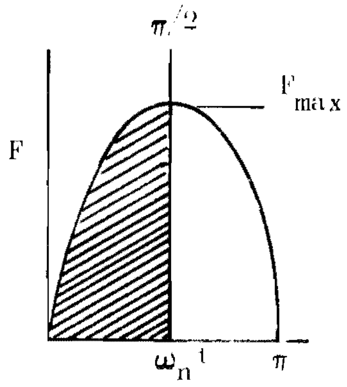

$$m V \int_{t_1}^{t_2} F(t)\,dt = F_{max} \int_0^{\pi/2} \sin \omega_n t \, dt$$

$$\text{or } F_{max} = m V \omega_n$$

Substituting $[K/M]^{1/2}$ for ω_n and

rearranging gives $F_{max} = \dfrac{KV}{\omega_n}$

This value for F_{max} is identical to the kinetic energy derivation for the impact of a moving body thus showing agreement between the two solutions when the sinusoidal oscillation is assumed.

Analytical Model

The cycle tester shown in Fig. 37 is a composite of many springs, masses, friction, pressure, and damping forces that must be identified, grouped, and reduced to a significant few suitable for analytical description. Figure 38 is a schematic of the tester in which the assumed significant parameters are identified. The values for fixed and variable parameters used in impact computations are described below (also included are applicable computer program symbols).

Weights.

W_1 = W1 = piston assembly, as shown in Fig. 37 (neglecting dashpot plunger weight), less weight of one of the three load cells legs, 2.98 pounds

W_2 = W2 = flat 440C poppet with associated clamp ring assembly plus weight of one leg of three load cells, 0.476 pound

W_3 = W3 = flat 440C seat plus 2/3 weight of piezoelectric load cell, 0.432 pound

W_4 = WB = body weight, 65 pounds

Spring Rates.

YDASH = dashpot spring rate due to material elasticity. Computed from the dimensions given in Fig. 37 for stretch in -15 cap, belling in -15 cap base, stretch in -49 plunger, and oil bulk compression, 1.55×10^5 lb/in.

K_1 = YS1 = strain gage load cells consisting of three series rates per leg, i.e., root spring, column spring, and foot to poppet bearing spring, reciprocally added gives 1.68×10^6 lb/in., or a total, 5.04×10^6 lb/in.

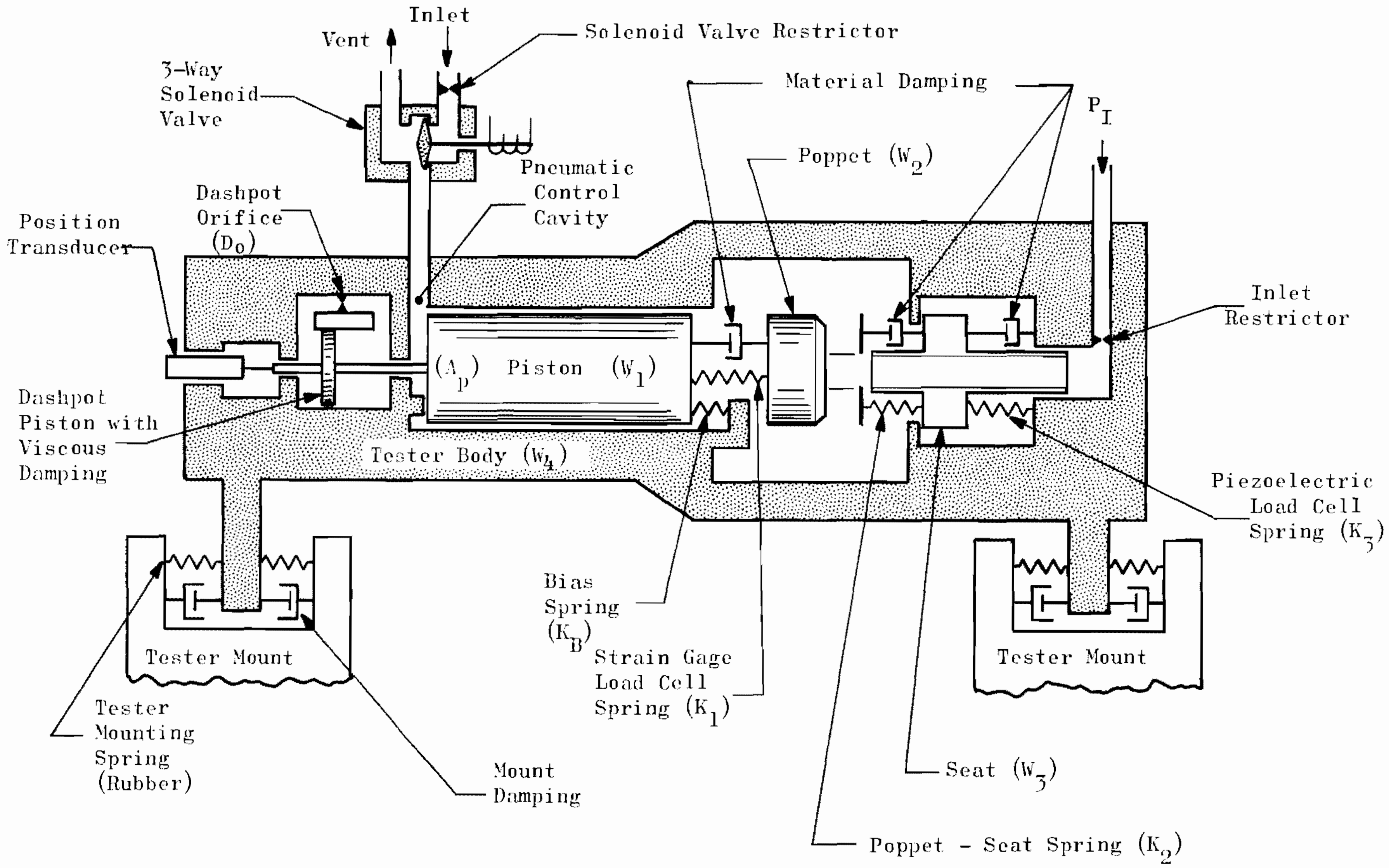

Figure 38. Cycle Tester Schematic

K_2 = YS2 = poppet to seat interface spring rate determined from load-deflection test of 1/2-inch OD, 0.03-inch land 440C flat poppet and seat (similar to Model Y_f), 7.0×10^6 lb/in.

K_3 = YS3 = piezoelectric load cell and base spring rate. Load cell = 40×10^6 lb/in.; base plate bearing ≅ 37.3×10^6 lb/in.; reciprocally added, 19.3×10^6 lb/in.

K_4 = YRP0S = YRNEG = rubber mount spring, 1000 lb/in.

K_B = YSB = piston bias spring (installed at 13.0 pounds with poppet contacting the seat), 31.4 lb/in.

Damping Coefficients. For internal material damping, these coefficients are obtained from the preceding values using the equation below with an assumed damping ratio (δ) of 0.03 for steel and 0.1 for rubber:

$$r = 2\delta \sqrt{\frac{K\,W}{g}}$$

where

g = 386 in./sec^2

DAMP1 = piston-load cells, 12.0 lb-sec/in.

DAMP2 = poppet-seat interface, 5.57 lb-sec/in.

DAMP3 = seat-piezoelectric load cell, 7.15 lb-sec/in.

DP0SB = DNEGB = rubber mounts, 3.68 lb-sec/in.

DAMPD = dashpot viscous damping used primarily to dampen computer-derived piston oscillations up to impact; assumed, 5 lb-sec/in.

Additional parameters used in the computer program are defined in the program and input data listings presented later.

Simplified Tester Analysis

The purpose of this analysis is to view the cycle tester in its most simplified form to obtain a preliminary approximation of the impact curve shape. Because the impact (or impulse) curve is the time integral of force, the solution must contain time-dependent equations. Therefore, the basic approach will be to consider only the significant spring mass systems and sum the forces according to Newton's basic law.

Development of Simplified Model. The first step in simplifying the tester analytical model is to assume that the piston and poppet have just contacted the seat with an initial velocity $\dot{x}(o)$, and a holding force (F) due to the pneumatic driving pressure on the piston. These two initial inputs are respectively analogous to the idealized impulse function and step input commonly used in servo-analysis theory. The first simplification of the tester configuration results in the schematic system shown below.

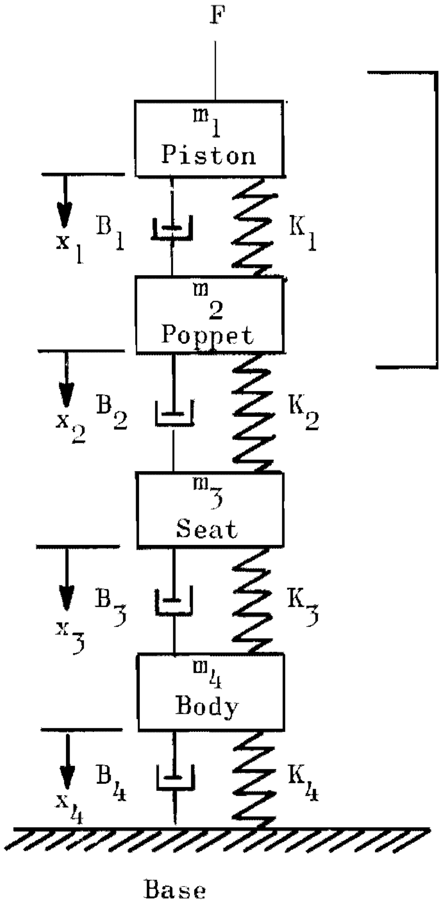

Input: F, $\dot{x}_1(o)$, $\dot{x}_2(o)$

where:

F = step input

$\dot{x}_1(o)$, $\dot{x}_2(o)$ are defined as initial velocities of positions x_1 and x_2 only

Summing the forces on each mass results in the following equations:

$$\Sigma F_1 = F - m_1\ddot{x}_1 - B_1(\dot{x}_1-\dot{x}_2) - K_1(x_1-x_2) = 0$$

$$\Sigma F_2 = B_1(\dot{x}_1-\dot{x}_2) + K_1(x_1-x_2) - m_2\ddot{x}_2 - B_2(\dot{x}_2-\dot{x}_3) - K_2(x_2-x_3) = 0$$

$$\Sigma F_3 = B_2(\dot{x}_2-\dot{x}_3) + K_2(x_2-x_3) - m_3\ddot{x}_3 - B_3(\dot{x}_3-\dot{x}_4) - K_3(x_3-x_4) = 0$$

$$\Sigma F_4 = B_3(\dot{x}_3-\dot{x}_4) + K_3(x_3-x_4) - m_4\ddot{x}_4 - B_4\dot{x}_4 - K_4x_4 = 0$$

These equations can be numerically solved by the Laplace technique to obtain a position vs time curve for each of the four positions. The greatest limitation to this approach is that only specific solutions for a given set of input conditions are provided. This makes the solution of the four spring-mass system a rather laborious task. To simplify the mathematical model further, the following assumptions are made.

Assumption 1. Because the body mass (m_4) and the load cell spring rate (K_3) are about one order of magnitude greater than related parameters, the model is assumed to be rigid at (m_3).

Assumption 2. Empirical data have shown that the internal damping in steel structures is small, thus the first overshoot will be approximated by the undamped consideration.

These two assumptions permit reduction of the mathematical model to an undamped dual spring-mass system. Further simplification may be made by assuming there is little phase lag or attenuation between the piston load cell spring and the seat spring; this leads to the final assumption.

Assumption 3. The two positions $(x_1$ and $x_2)$ have the following fixed relationship in the dual spring-mass system.

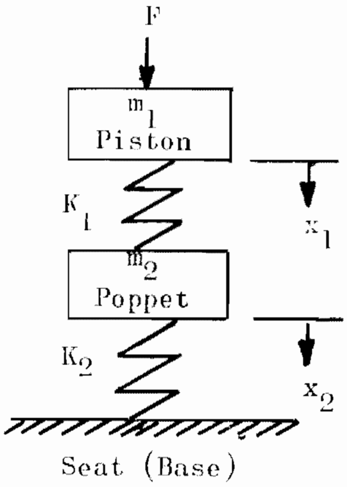

$$F_1 = F_2$$

$$K_1(x_1-x_2) = K_2x_2$$

$$x_2 = \frac{K_1}{K_1+K_2}\;x_1$$

$$\Sigma F_1 = F - m_1\ddot{x}_1 - K_1(x_1-x_2) = 0$$

$$\Sigma F_2 = K_1(x_1-x_2) - m_2\ddot{x}_2 - K_2x_2 = 0$$

Based on the above three assumptions, the dual spring-mass system may now be reduced to an equivalent single spring-mass system. Solving for (x_1) utilizing the fixed relationship for $(x_1$ and $x_2)$ results in:

$$\left[m_1 + \frac{K_1}{K_1+K_2}\;m_2\right]\ddot{x}_1 + \left[\frac{K_1\;K_2}{K_1+K_2}\right]x_1 = F$$

where:

Equivalent mass $(m_E) = m_1 + \dfrac{K_1}{K_1+K_2}\;m_2$

Equivalent spring rate $(K_E) = \dfrac{K_1\;K_2}{K_1+K_2}$

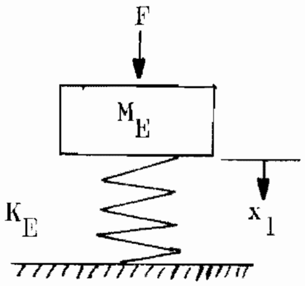

Inputs: F, $\dot{x}_1(o)$

Solution of Spring-Mass System by Laplace Technique. The previously developed differential equation is now written in Laplace notation including the initial velocity $\dot{x}(o)$ and letting $x(o) = 0$. For convenience, the subscripts E and 1 have been dropped.

$$m\, s^2\, \bar{x}\,(s) - m\, \dot{x}(o) + K\, \bar{x}\,(s) = \frac{F}{s}$$

Solving for $\bar{x}\,(s)$ and reducing the equation into partial fractions results in:

$$\bar{x}\,(s) = \frac{F/ms + \dot{x}(o)}{s^2 + K/m}$$

$$\bar{x}\,(s) = \frac{F/K}{s} - \frac{(F/K)\, s}{s^2 + K/m} + \frac{\dot{x}(o)}{s^2 + K/m}$$

Inverting the equation gives the displacement (x) as a function of time (t):

$$x(t) = F/K - F/K \cos\, (K/m)^{1/2}\, t + \frac{\dot{x}(o)}{(K/m)^{1/2}} \sin\, (K/m)^{1/2}\, t$$

Rewriting the equation to show the time-dependent impact force, $F(t)$, where $F(t) = K\, x(t)$ and noting that the system natural frequency, $\omega_n = (K/m)^{1/2}$ yields:

$$F(t) = F\,(1 - \cos\, \omega_n\, t) + \frac{K\, \dot{x}(o)}{\omega_n} \sin\, \omega_n\, t$$

This equation states that the impact force is the sum of the transient component force due to sudden application of the static force plus the transient force of the velocity impact. To define further the impact curve, the time to reach maximum force is determined by differentiating $F(t)$ and equating to zero.

$$\frac{dF(t)}{dt} = 0 + F\, \omega_n\, \sin\, \omega_n t + K\, \dot{x}(o)\, \cos\, \omega_n t = 0$$

$$\omega_n t\ (\text{ at } F_{max}) = \tan^{-1} \left[- \frac{\frac{K\, \dot{x}(o)}{\omega_n}}{F} \right]$$

This equation shows that the time to reach maximum force is a function of the relative maximum amplitudes of the two transient forces; thus, an evaluation of the system constants is required to determine $\omega_n t$.

To view the boundaries of $\omega_n t$, the two limiting cases for the amplitude ratio will be considered.

Case 1. $F \longrightarrow 0$

$$\left[\frac{\frac{K\,\dot{x}(o)}{\omega_n}}{F}\right] \longrightarrow \infty$$

$$\mathrm{Tan}^{-1}\left[\frac{\frac{K\,\dot{x}(o)}{\omega_n}}{F}\right] = \omega_n t \longrightarrow \frac{\pi}{2}$$

Inserting these values into the F(t) equation results in the maximum force for a velocity (impulse) input only:

$$F_{max} = \frac{K\,\dot{x}(o)}{\omega_n} \quad (\text{ at } \omega_n t = \frac{\pi}{2})$$

Case 2. $\dot{x}(o) \longrightarrow 0$

$$\left[\frac{\frac{K\,\dot{x}(o)}{\omega_n}}{F}\right] \longrightarrow 0$$

$$\omega_n t \longrightarrow \pi$$

$$F_{max} = 2F$$

To clarify further the meaning of the equations, the following graphical representation is presented where $\frac{K\,\dot{x}(o)}{\omega_n}$ is arbitrarily set equal to F thus:

$$\omega_n t \text{ (at } F_{max}) = \tan^{-1}(-1) = \frac{3\pi}{4}$$

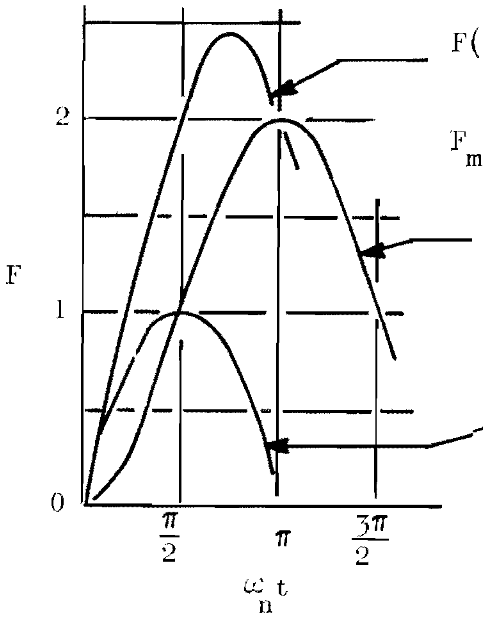

$$F(t) = F(1 - \cos \omega_n t) + \frac{K\,\dot{x}(o)}{\omega_n} \sin \omega_n t$$

$$F_{max} = 2.414\ F \ (\text{ at } \omega_n t = \frac{3\pi}{4})$$

$$F(t) = F(1 - \cos \omega_n t)$$

$$F_{max} = 2F \ (\text{ at } \omega_n t = \pi)$$

$$F(t) = \frac{K\,\dot{x}(o)}{\omega_n} \sin \omega_n t$$

$$F_{max} = F(\text{ at } \omega_n t = \frac{\pi}{2})$$

Dashpot Consideration. The preceding equations give a simplified view of the tester dynamics. Given the impact velocity and the unbalanced forces acting on the piston just before impact, the maximum initial impact force can be approximately determined.

With the use of an orificed hydraulic dashpot for velocity control (constant control pressure), the forces acting on the moving piston will be balanced at impact. However, elastic energy stored by the dashpot container, rod, and oil will be delivered to the impacted surfaces as a time variable, dependent upon the decay rate of dashpot pressure (which, in turn, is a function of the dashpot orifice opening). The equations describing the time dependent and steady-state dashpot functions are as follows:

$$P_D = P_c \frac{A_P}{A_D}$$

$$CA_o = A_C \ V_P \sqrt{\frac{\rho}{2g\,P_{Di}}}$$

$$P_D = P_{Di} \left(1 - \frac{K\ t\ V_P}{2\ A_D\ P_{Di}} \right)$$

$$F_s = P_{Di}\ A_D \left[1 - \left(1 - \frac{K\ t\ V_P}{2\ A_C\ P_{Di}} \right)^2 \right]$$

$$t_f = \frac{2\ P_{Di}\ A_D}{K\ V_P}$$

$$K = \frac{P_{Di}\ A_D^{\ 2}}{\Delta V}$$

where

A_D = net dashpot plunger area, 0.598 in.^{2}

A_o = variable orifice area, in.^{2}

A_p = net control piston area, 1.687 in.^{2}

C = orifice coefficient, 0.67

F_s = seat force, pounds

g = 386 in./sec^2

K = spring rate, 1.55×10^5 lb/in.

P_c = steady-state control pressure, psig

P_D = dashpot pressure, psig

P_{Di} = initial dashpot pressure ($2.82\ P_c$), psig

t = time, seconds

t_f = total or final time, seconds

V_D = dashpot plunger velocity, in./sec

ΔV = dashpot volume change, in.^{3}

ρ = oil density, 0.0313 lb/in.^{3}

These equations describe a parabolic relationship for the decay of (P_D) and thus buildup of (F_s). Consequently, the effect of the dashpot is not as a suddenly applied load from control pressure as might be assumed. Furthermore, the phase relationship between (1) seat force buildup due to dashpot pressure decay, and (2) the velocity impact will determine their additive effect in arriving at peak impact load.

For low impact velocities where the dashpot orifice is nearly closed, (t_f) above will be long with respect to the system (piston, poppet and seat) natural frequency and thus, impulse time. As a result, the initial impact force will contain little of the potential load to be delivered by the decay of dashpot pressure. Subsequent impulses due to bounding will experience a rising "effective" (P_c) as (P_D) decays; therefore, these bounces may result in greater peak loads if this effect is a significant portion of the impulse load.

With high impact velocities (t_f near natural frequency), the energy stored in the dashpot may be dumped more nearly as a suddenly applied load. However, this assumes the piston and poppet velocities instantly drop to zero upon contact. Because a velocity decay period is required in which the piston decelerates to zero and the impulse load peaks, the attached dashpot piston also is in motion and decelerating. These complex interrelated effects cannot be described explicitly, but as will be later shown, with higher velocities the contribution of suddenly applied load is small with respect to the impulse load and thus can be neglected.

As employed in the digital computer program described below, the definition of the dashpot orifice area required for a given steady-state impact velocity is derived from the balance of forces acting on the piston. Including the bias spring force (F_b) and a dashpot plunger viscous drag force $(r\ V_D)$ neglected in the above equations, the orifice size is given as:

$$A_o = \left[\frac{A_D^3\ V_D^2\ \rho}{2\ g\ C^2 (P_c\ A_P - F_b - r\ V_P)} \right]^{1/2}$$

where (r) is the damping coefficient in lb-sec/in. and D_o = DOD.

Digital Computer Program

An IBM 7094 digital computer program, written in FORTRAN II coding, was developed for analysis of the cycle tester dynamics. The program was used initially for design studies in predicting cycle tester performance with alternate design features and in establishing design criteria. The program was then refined in obtaining detailed correlation between computer run results and test results. Better correlation was obtained when an idealized liquid dashpot description, used for design studies, was replaced by a dashpot description which included dashpot elasticity, as noted above, and internal damping.

A schematic of the cycle tester, as used for the computer mathematical model, with identifying nomenclature appears in Fig. 39. A complete listing of the FORTRAN program and sample data output (described later) appears in Appendix A.

Program Description. The program listing includes general notes and alphabetically ordered nomenclature as an introduction. Comment statements are interspersed throughout the listing for word descriptions of each phase of the computations. The comment statements serve as a flow diagram for the program. In general, the computation procedure is as follows:

1. Read input data from data cards
2. Print input data tabulation
3. Set initial conditions for program variables
4. Compute program constants
5. Set initial conditions for CRT and printout routines
6. Enter iterative computation loop

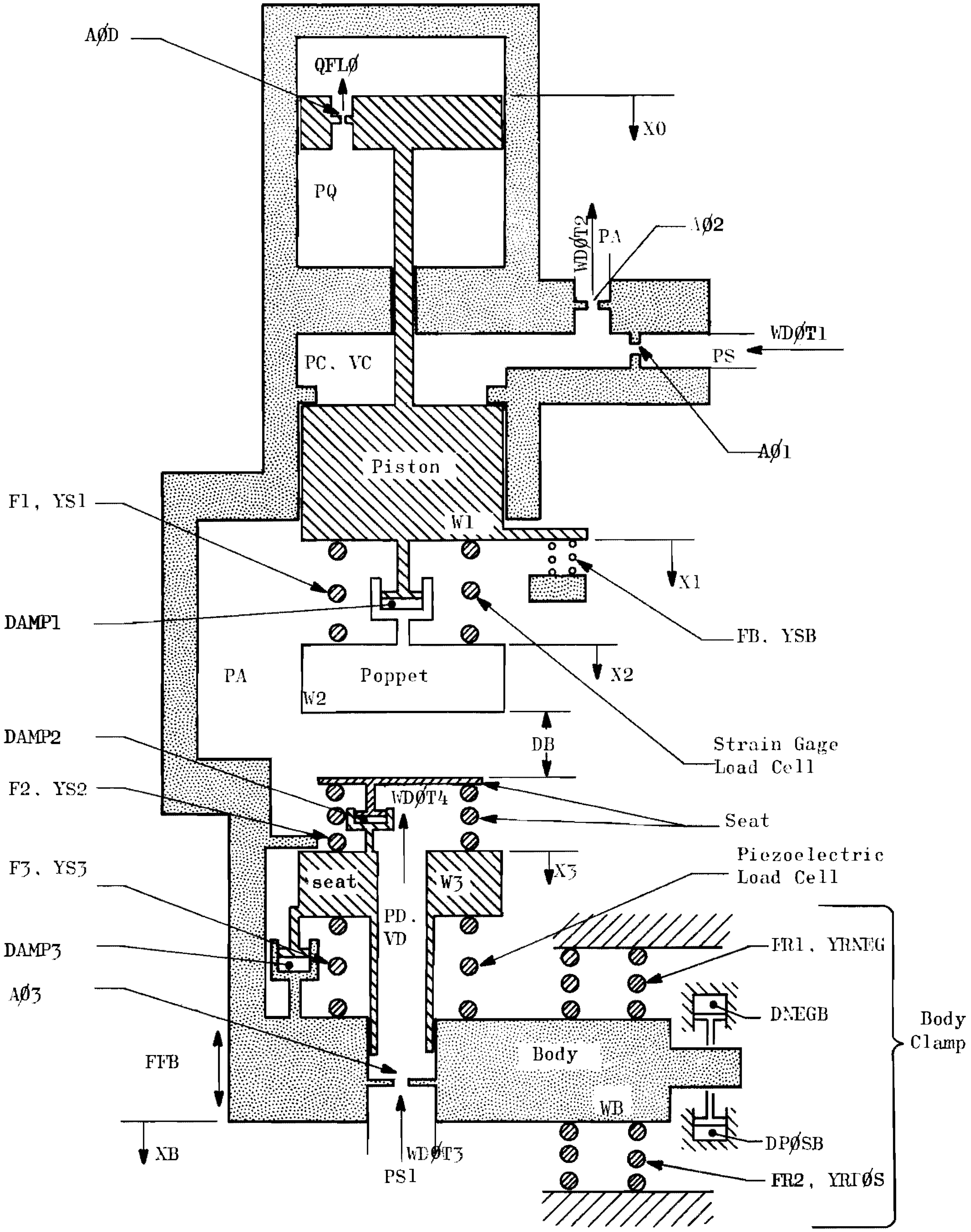

Figure 39. Cycle Test Fixture Digital Computer Mathematical Model

7. Compute gas flowrates. To compute each gas weight flowrate term call subprogram FLØW with numerical values for the upstream pressure, the downstream pressure, and the effective flow area. (One subprogram, FLØW, listed in Appendix A, serves for computing all flow terms, using nozzle equations for sonic or subsonic flow in either direction.)

8. Compute pneumatic pressurizing coefficients

9. Compute rates of change of pressures (Rates of change of pressures are functions of flow in, flow out, volume, and rate of change of volume.)

10. Compute pressures (Numerical integration of rates of change of pressures)

11. Compute combined piston and poppet acceleration, velocity, and displacement. If poppet is more than 0.0005 inch from initial contact with seat, go to 12. If within 0.0005 inch, reset time increment to 10^{-7} second and go to 13. Instantaneous acceleration is the sum of the forces divided by the mass. Velocity is obtained by numerical integration of acceleration. Displacement is the integral of velocity.

12. Compute dashpot flow, pressure, and force; go to 20

13. Compute piston acceleration, velocity, and displacement

14. Compute dashpot flow, pressure, and force

15. Compute spring forces

16. Compute poppet acceleration, velocity, and displacement

17. Compute spring forces

18. Compute seat acceleration, velocity, and displacement

19. Compute spring forces

20. Compute body acceleration, velocity, and displacement

21. Compute miscellaneous variables

22. Compute poppet velocity relative to body

23. Reidentify and store velocity and acceleration values

24. Increase TIME by one increment of time

25. Store and print computed output data

26. If TIME is less than FINIS, go to 7; if equal, go to 27

27. Call subprogram CRT for graphic display of selected output data. The CRT program listing appears in Appendix A.

The basic equations used in formulating the mathematical model are:

1. $P \cdot V = W \cdot R \cdot TEMP$

2. $dP/dt = dW/dt \cdot R \cdot TEMP/V + dX/dt \cdot P \cdot A/V$

3. $P = \int dP/dt \cdot dt$

4. $dW/dt = C \cdot A \cdot P \cdot S/\sqrt{R \cdot TEMP}$

5. $d^2X/dt^2 = F/m$

6. $dX/dt = \int d^2X/dt^2 \cdot dt$

7. $X = \int dX/dt \cdot dt$

Equation 1 is the perfect gas equation of state.

Equation 2 is the derivative of Eq. 1, substituting $dV/dt = A(dX/dt)$, and describes the time rate of change of pressure caused by gas mass entering or discharging from a volume, and includes a pumping term if the volume is changing with time. The temperature derivative is assumed negligible.

Equation 3 is the integral of Eq. 2.

Equation 4 is the nozzle isentropic flow equation, corrected for an orifice description.

Equation 5 is Newton's second law of motion. Equations 6 and 7 are the integrals of Eq. 5.

The programming of these equations for iterative numerical computations follows the 27-step outline, with details listed in Appendix A.

Spring-mass resonant frequencies greater than 30,000 cps were encountered and it was necessary to reduce the computation time increment to 0.1 microsecond for smooth output data.

To conserve computer time, each computation run begins with the piston and poppet lumped as a single mass with no interconnecting spring and with a time increment of 5 microseconds. As the pneumatically powered piston and poppet approach seat contact, the computation time interval is reduced to the smaller value and all springs and masses are then considered as discrete items. The smaller time increment is thereby used only for the time period during which the fast transients accompanying seat contact and rebound occur. The required computer time is thereby minimized.

One item of input data (XTIME), typically 0.0015 second, terminates the computer run when XTIME seconds of real time have elapsed beyond the switching point at which the smaller time increment of 1/10 microsecond is used. The time for a computer run is therefore whatever time is required for displacement of the poppet and piston from the off-seat stop to 0.0005 inch from seat contact plus XTIME. One item of input data, FINIS (in seconds), limits the real time duration of a computer run in the event that incorrect data are supplied to the program.

Computed output data are presented in tabular form for every hundredth computed point, and in photographic reproductions of cathode ray tube displays for each tenth computed point. Two separate printouts of tabulated data provide enough columns of data to permit examination of all variables of interest in the system. One column for TIME (real time in seconds) is common to both tabulations. Two graphical displays are produced, one showing poppet and body displacements as time functions and one showing forces as time functions. The force display shows seat contact force and two force transducer outputs. The displacement display covers the entire real time duration for a run. The force display has an expanded time scale for that portion of the run which occurs with the smaller (1/10 microsecond) computation time increment. The graphical force display, with its time scale starting just prior to initial seat contact can be compared with test data oscilloscope photographs with their time scale starting at the time of initial contact.

The digital computer program describes the cycle tester dynamics independently of the numerical values of system inputs such as supply pressures, orifice sizes, damping coefficients, spring rates, etc. The program reads in data from an input data deck for each computer run, with no changes required in the program itself. The program prints out a tabulation of its input data for each run, as shown in Appendix A.

A detailed discussion of the analytic techniques employed and the methods used in the computer programming are presented in Ref. 65.

Data Output. Program output has been prepared covering the range of experimental data investigated. Rather than generate data for nominal conditions, the output is presented for several specific impact velocities obtained in test. Therefore, it has been included with the discussion of cycle test calibration (following) for direct comparison with instrumentation output data.

CYCLE TEST CALIBRATION

Prior to model cycle testing, it was necessary to establish the dynamic characteristics and limits of the cycle tester and associated instrumentation. With this information, model tests could be performed recording a minimum of data, based upon velocity and impact load repeatability and correlation. Some 10,000 cycles accumulated under impact velocities from 2 to 36 in./sec proved the capabilities of the tester, and it was further shown that impact velocity and load were closely repeatable.

For the calibration series, a flat 440C poppet and seat served as a typical model (similar to Y_f; see Experimental Test section where the cycle test setup is discussed along with instrumentation accuracies and general model assembly and test procedures). The poppet and seat were installed in the tester as shown in Fig. 37, each with about 100 pounds preload.

Dashpot assembly was made with the bypass check valve allowed to open fully. This condition, coupled with plunger seal clearance, resulted in piston rebound damping from viscous friction only.

As will be seen, the significant forces acting at constant velocity impact are derived from control and dashpot pressures (PC and PQ) and impact velocity of the poppet relative to the body (XDOT2B). Seat inlet pressure did not significantly influence impact or stabilized forces because of low setting (psi = 5 psig) and small inlet orifice (D03 = 0.014 inch) relative to seat orifice (D04 = 0.440 inch). Static seat force (stress) was governed by the balance of forces at stabilization (see Experimental Test section).

Two basic series of tests were performed for calibration. The first, using the dashpot, investigated tester characteristics for a range of impact velocities at a static (seat) stress of approximately 5000 psi. For these tests, solenoid valve supply pressure (PS = PC) was set at 141.0 psig and stroke equal to 0.1000 inch. The influence of increased control pressure was also evaluated for one test with (PS) set at 272 psig (10,000-psi seat stress).

The second series of tests was performed to investigate the tester impact characteristics without the dashpot. This was accomplished by dropping the vertically positioned piston and poppet on the seat from precisely known heights. The impact velocity was computed based upon the height compensating for the known flexure spring characteristic. Reduced data from these tests are included with the correlation of all test data at the end of this section.

Test and Computer Data

Representative dashpot controlled test data are presented in Fig. 40 through 51 for analytical correlation. These data are oscilloscope photos of the position, strain gage load cells, and piezoelectric load cell transducer outputs. Scale factors are given in each figure title in units per lined division with vertical input first and horizontal (time, running right to left), second.

Corresponding computer output data are shown in Fig. 52 through 59. Computer inputs are as previously defined and further enumerated in Appendix A for the 1.87 in./sec run (also includes tabulated output through 0.00598 seconds). Input variations from this example are defined in the output plot figure titles as dashpot orifice diameter (D0D) and supply pressure (PS). Two time base plots are presented for each test condition:

1. Displacements from solenoid valve energization through XTIME
    - a. Poppet relative to body (DB-X2RB), dots
    - b. Body relative to fixed mount (XB), X's

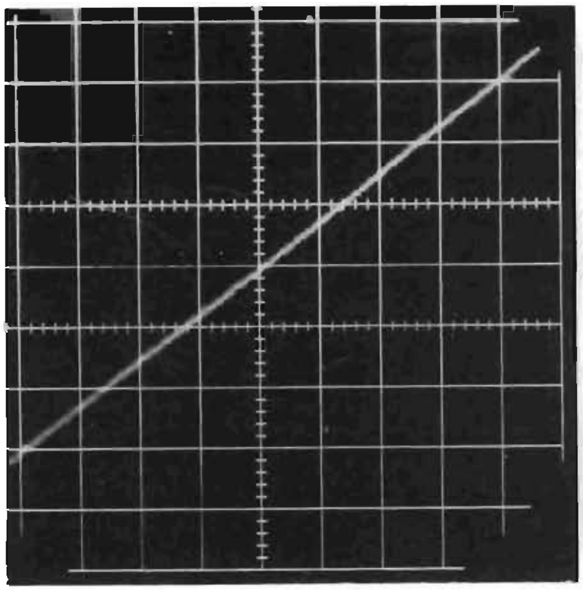

Figure 40. Position, 1.87 in./sec Impact Velocity, PS=141 psig (0.0125 in./div; 0.005 sec/div)

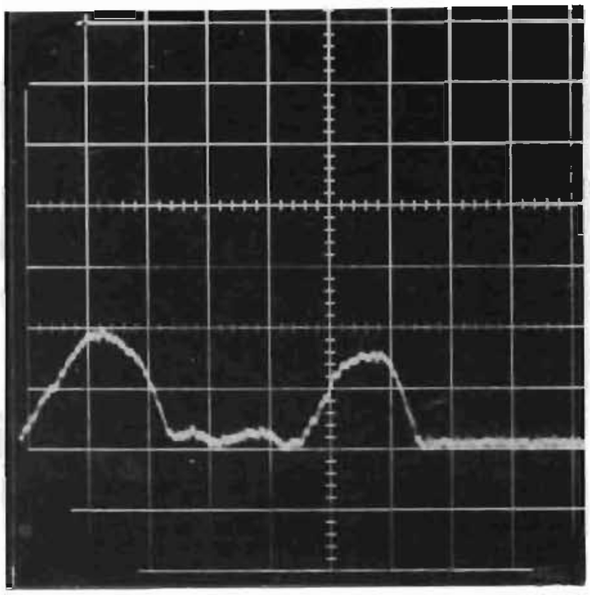

Figure 41. Strain Gage Load Cell No. 1 1.87 in./sec Impact Velocity, PS=141 psig (50 lb/div; 0.0001 sec/div)

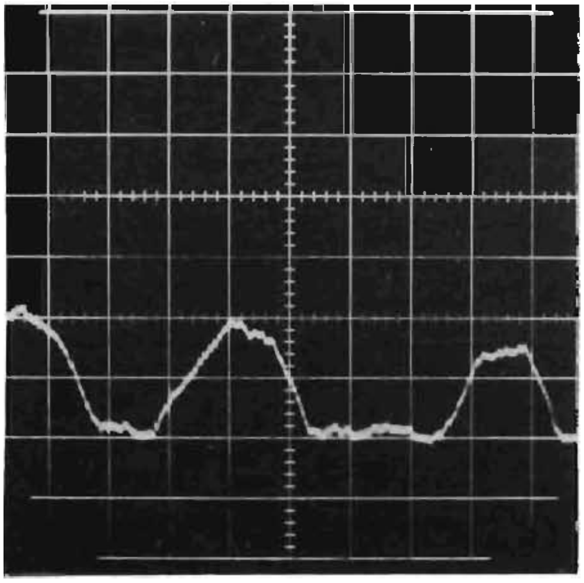

Figure 42. Strain Gage Load Cell No. 2, 1.87 in./sec Impact Velocity, PS=141 psig (50 lb/div; 0.0001 sec/div)

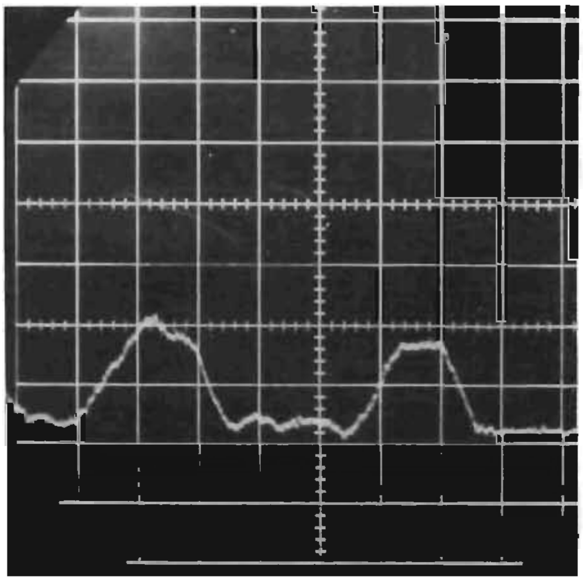

Figure 43. Strain Gage Load Cell No. 3, 1.87 in./sec Impact Velocity, PS=141 psig (50 lb/div; 0.0001 sec/div)

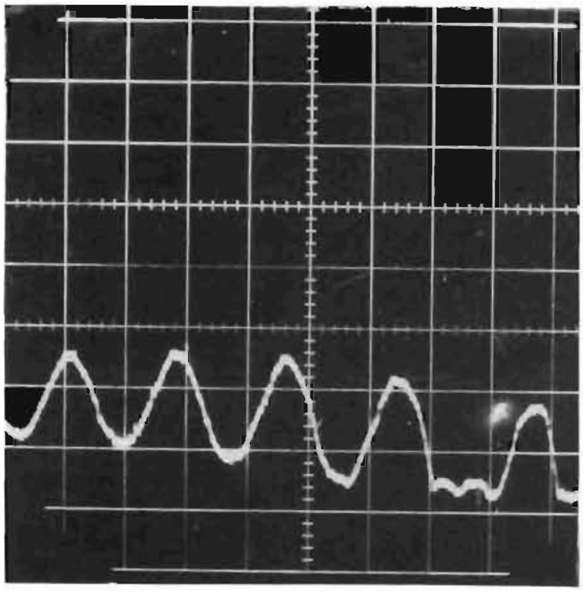

Figure 44. Strain Gage Load Cell No. 1, 1.87 in./sec Impact Velocity, PS = 141 psig (50 lb/div; 0.0002 sec/div)

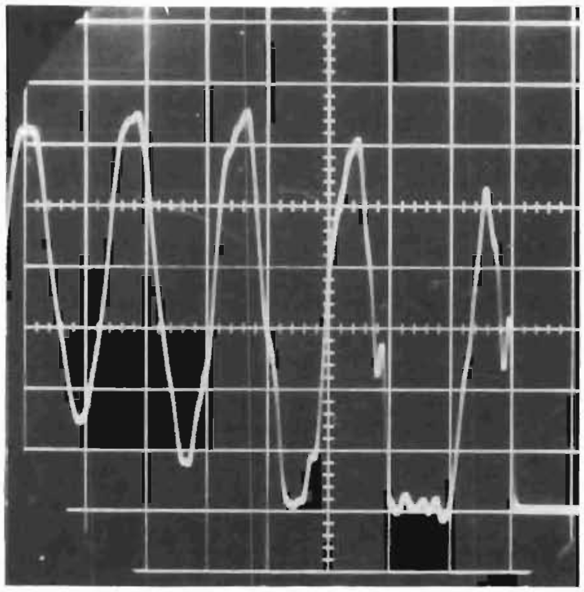

Figure 45. Piezoelectric Load Cell, 1.87 in./sec Impact Velocity, PS = 141 psig (50 lb/div; 0.0002 sec/div)

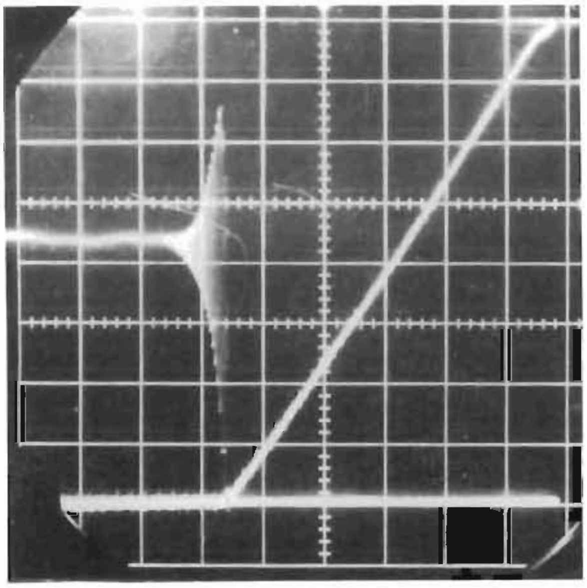

Figure 46. Piezoelectric Load Cell and Position, 1.87 in./sec Impact Velocity, PS = 141 psig (50 lb/div and 0.0125 in./div; 0.01 sec/div)

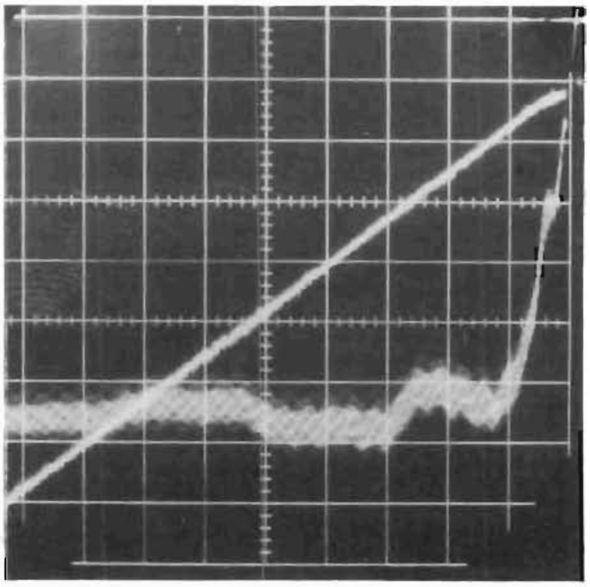

Figure 47. Control Pressure (PC) and Position, 1.87 in./sec Impact Velocity, PS = 141 psig (20 psi/div and 0.0125 in./div; 0.005 sec/div)

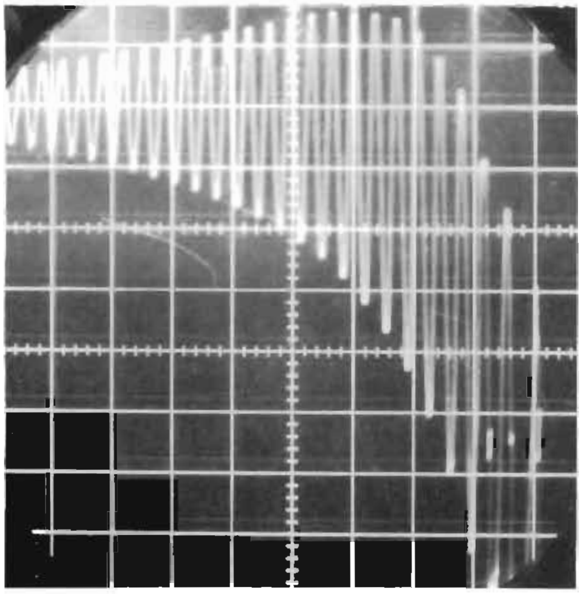

Figure 48. Piezoelectric Load Cell, 1.77 in./sec Impact Velocity, PS = 272 psig (50 lb/div; 0.001 sec/div)

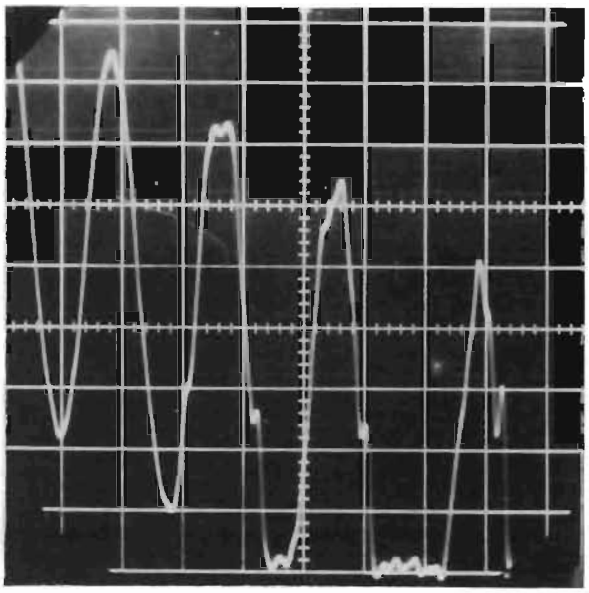

Figure 49. Piezoelectric Load Cell, 1.77 in./sec Impact Velocity, PS = 272 psig (50 lb/div; 0.0002 sec/div)

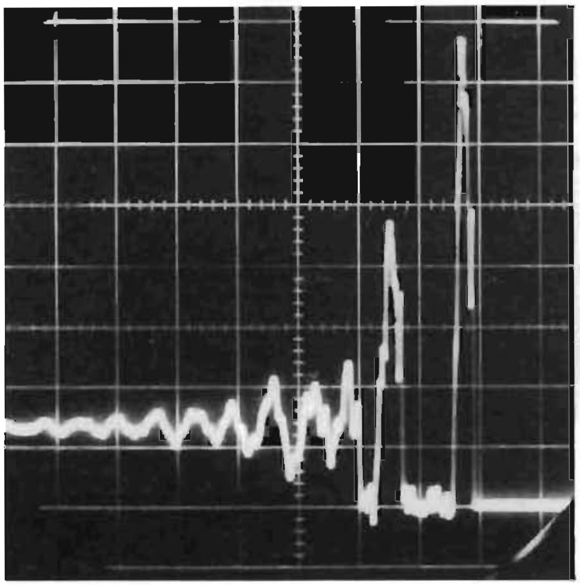

Figure 50. Piezoelectric Load Cell, 8.46 in./sec Impact Velocity, PS = 141 psig (162.5 lb/div; 0.0005 sec/div)

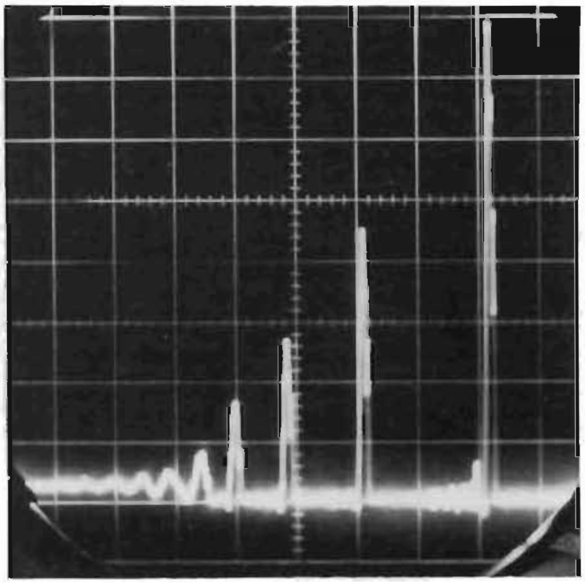

Figure 51. Piezoelectric Load Cell, 35.6 in./sec Impact Velocity, PS = 141 psig (750 lb/div; 0.001 sec/div)

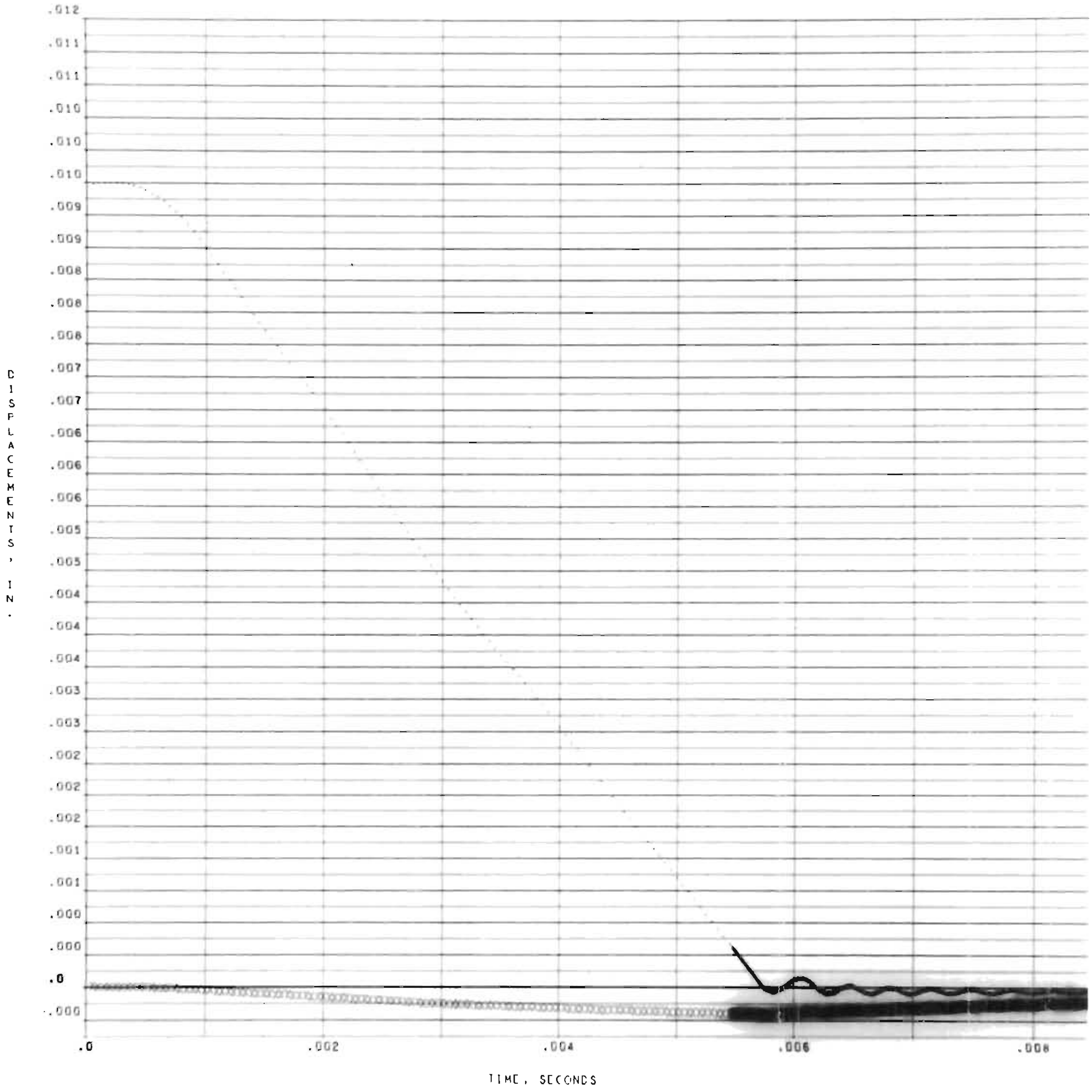

Figure 52. Computed Poppet (·) and Body (x) Displacements, 1.87 in./sec Impact Velocity, PS = 156 psia, DØD = 0.0266 in.

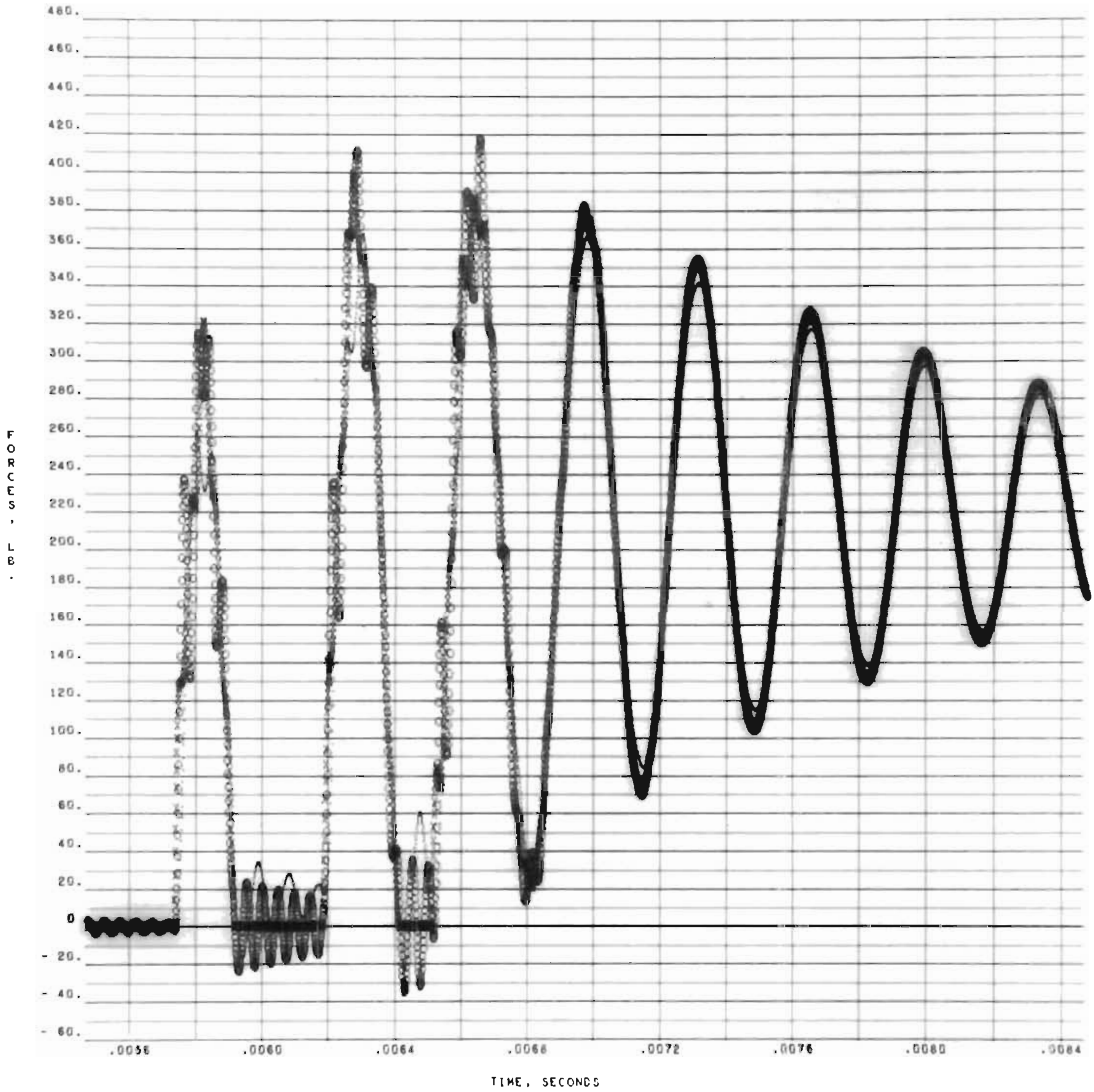

Figure 53. Computed Spring Forces, F1 (·), F2 (x), F3 (o), 1.87 in./sec Impact Velocity, PS = 156 psia, DØD = 0.0266 in.

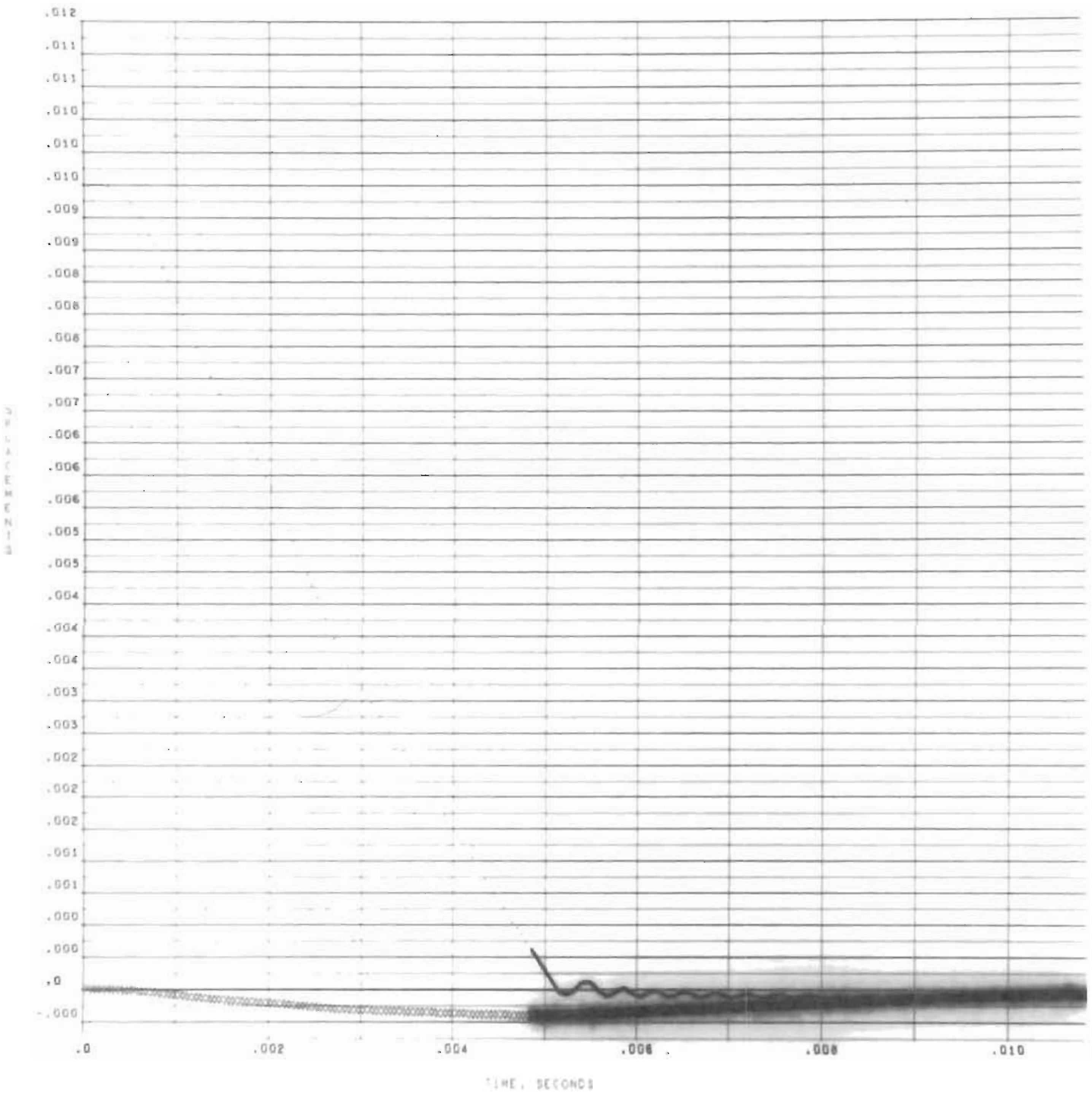

Figure 54. Computed Poppet (·) and Body (x) Displacements, 1.77 in./sec Impact Velocity, PS = 287 psia, DØD = 0.0217 in.

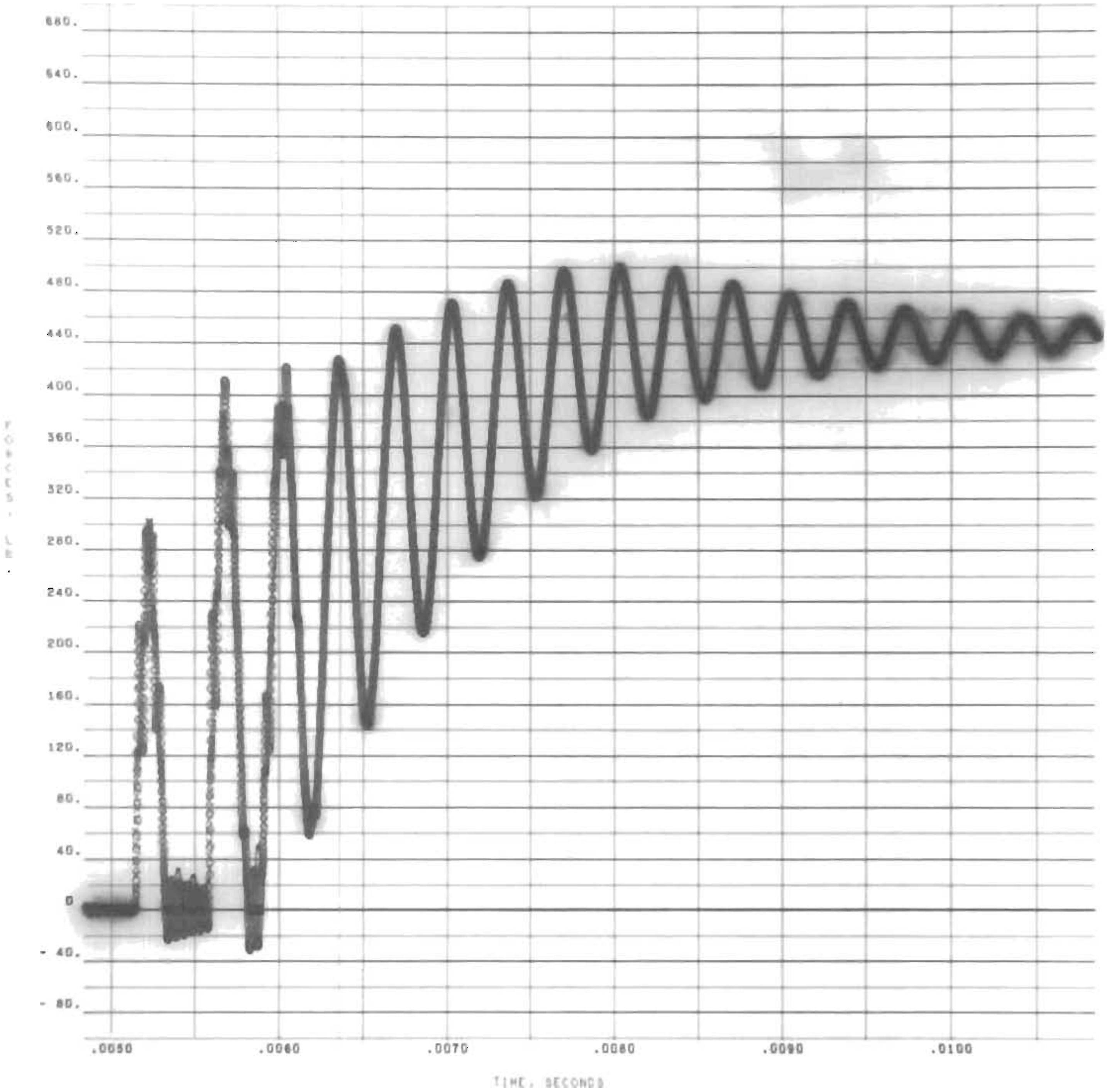

Figure 55. Computed Spring Forces, F1 (·), F2 (x), F3 (o), 1.77 in./sec Impact Velocity, PS = 287 psia DØD = 0.0217 in.

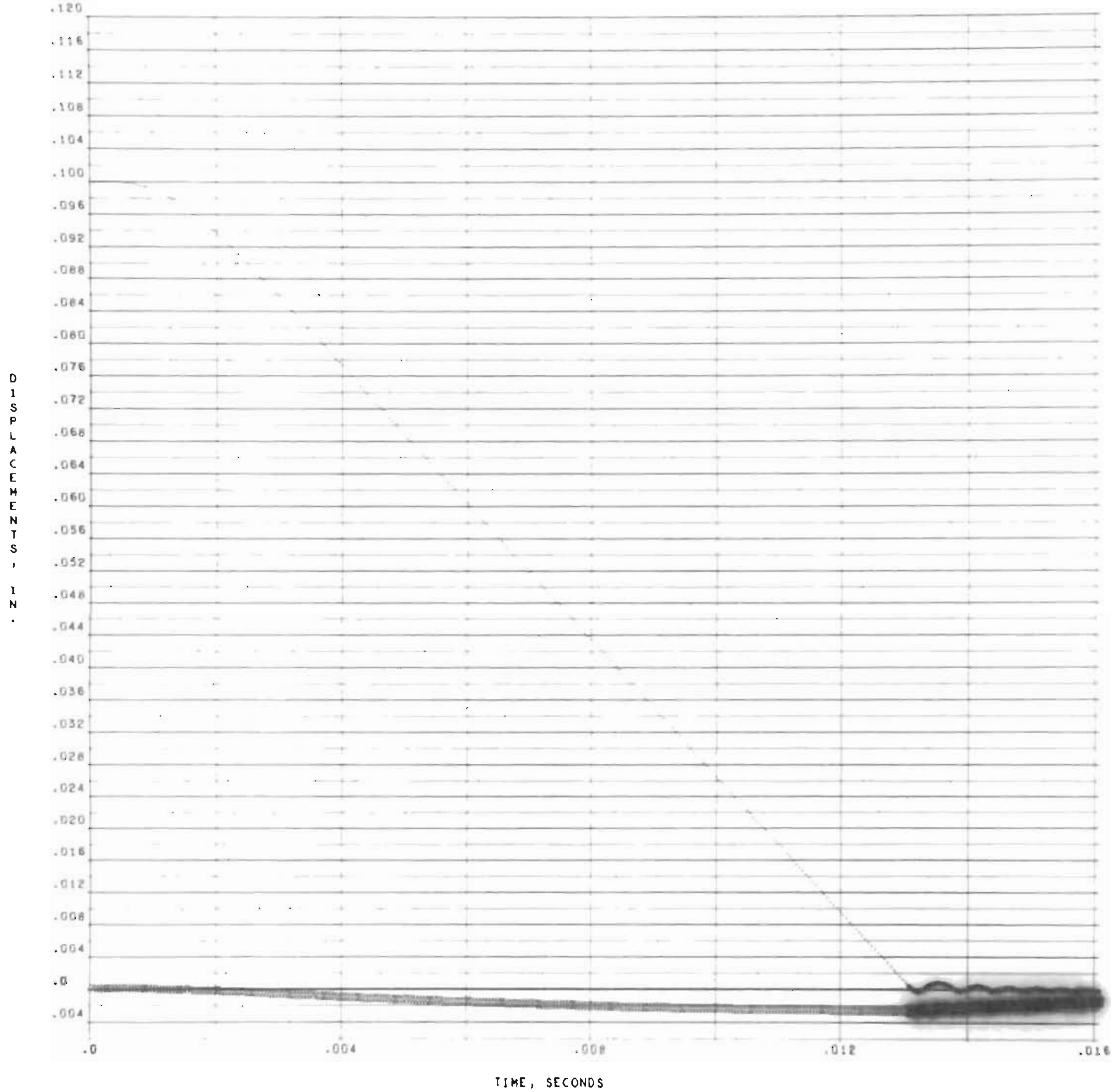

Figure 56. Computed Poppet (·) and Body (x) Displacements, 8.46 in./sec Impact Velocity, PS = 156 psia, D0D = 0.0591 in.

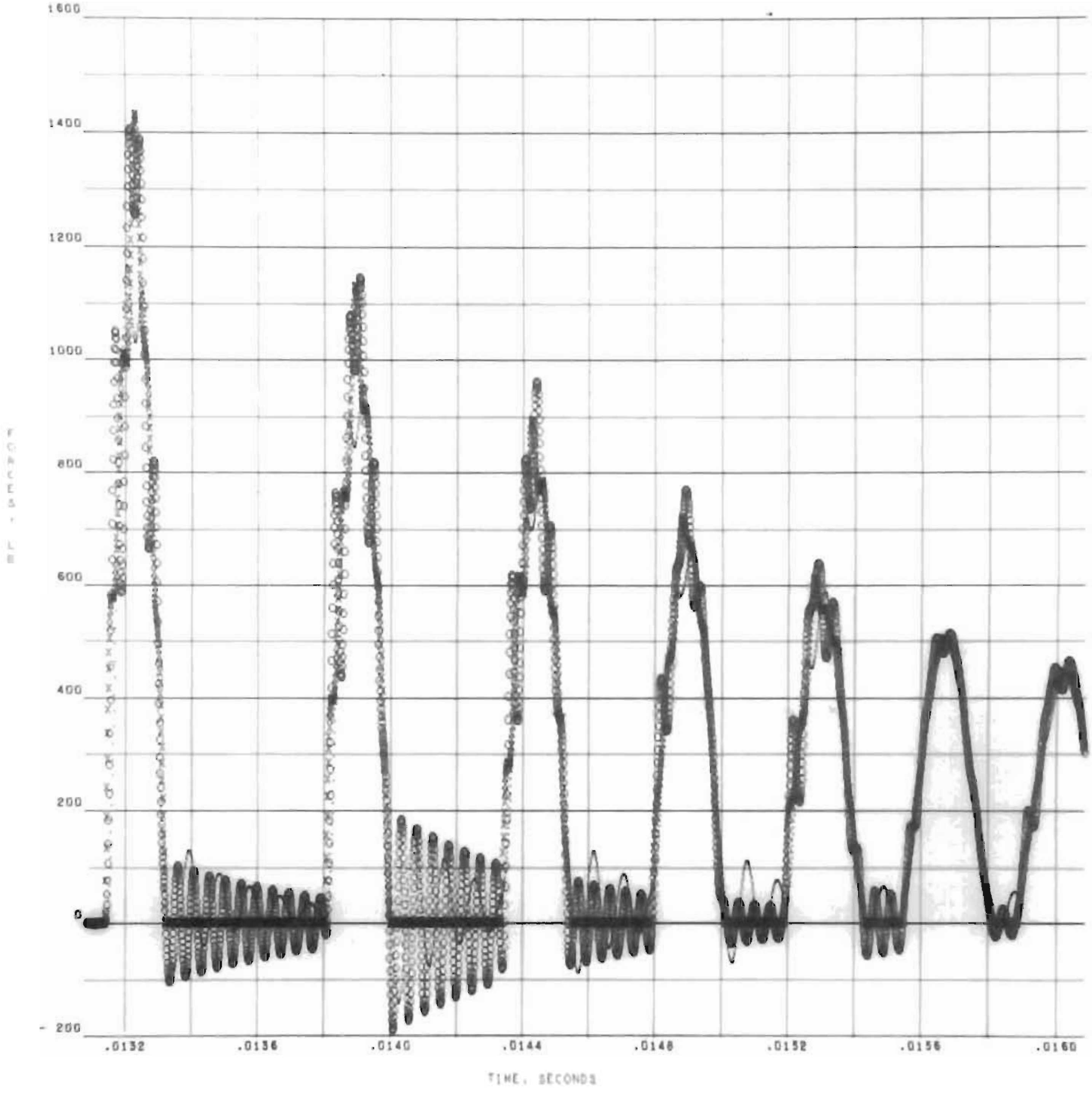

Figure 57. Computed Spring Forces, F1 (·), F2 (x), F3 (o), 8.46 in./sec Impact Velocity, PS = 156 psia, DØD = 0.0591 in.

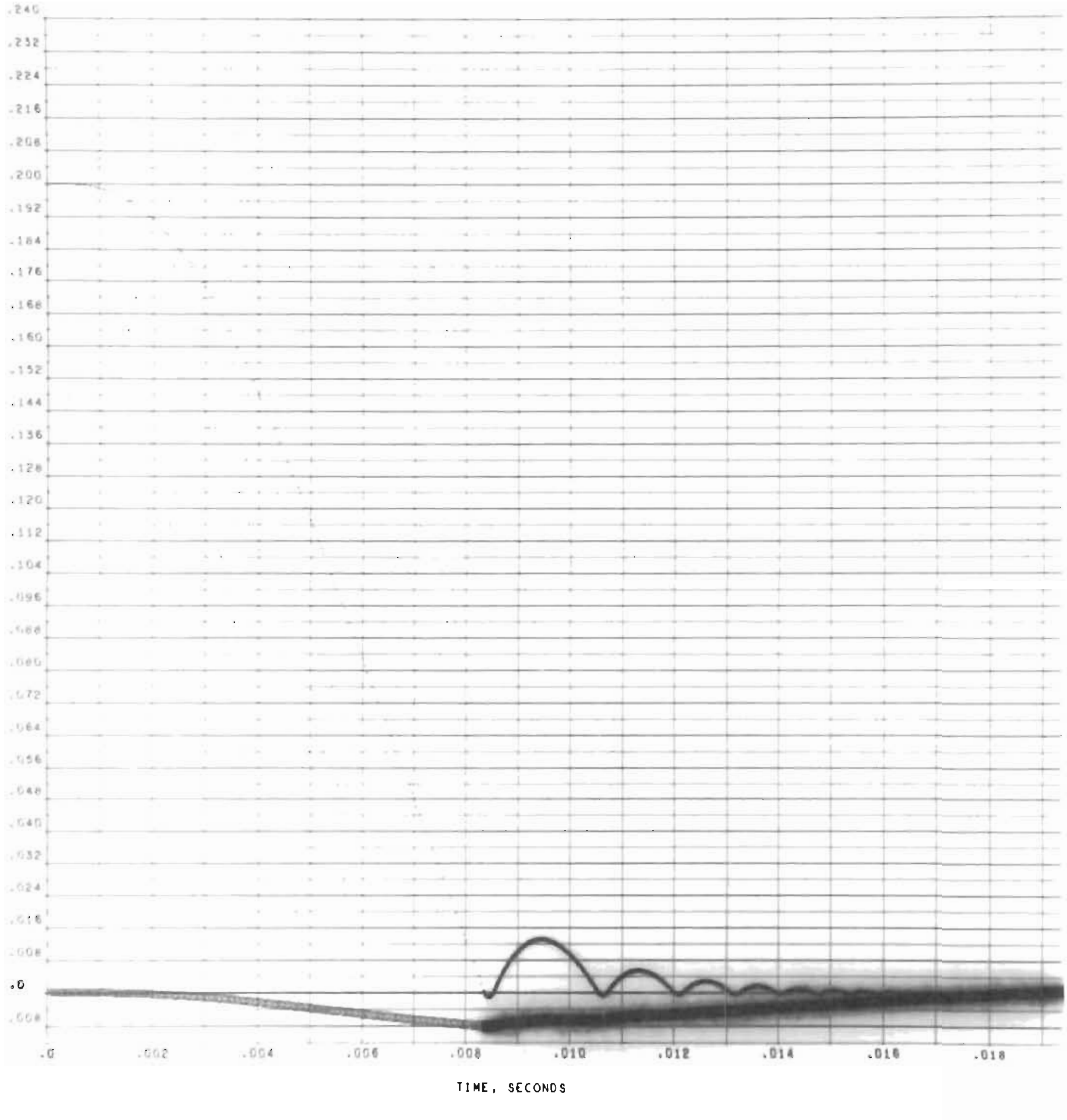

Figure 58. Computed Poppet (·) and Body (x) Displacements, 35.6 in./sec Impact Velocity, PS = 156 psia, DØD = 0.1702 in.

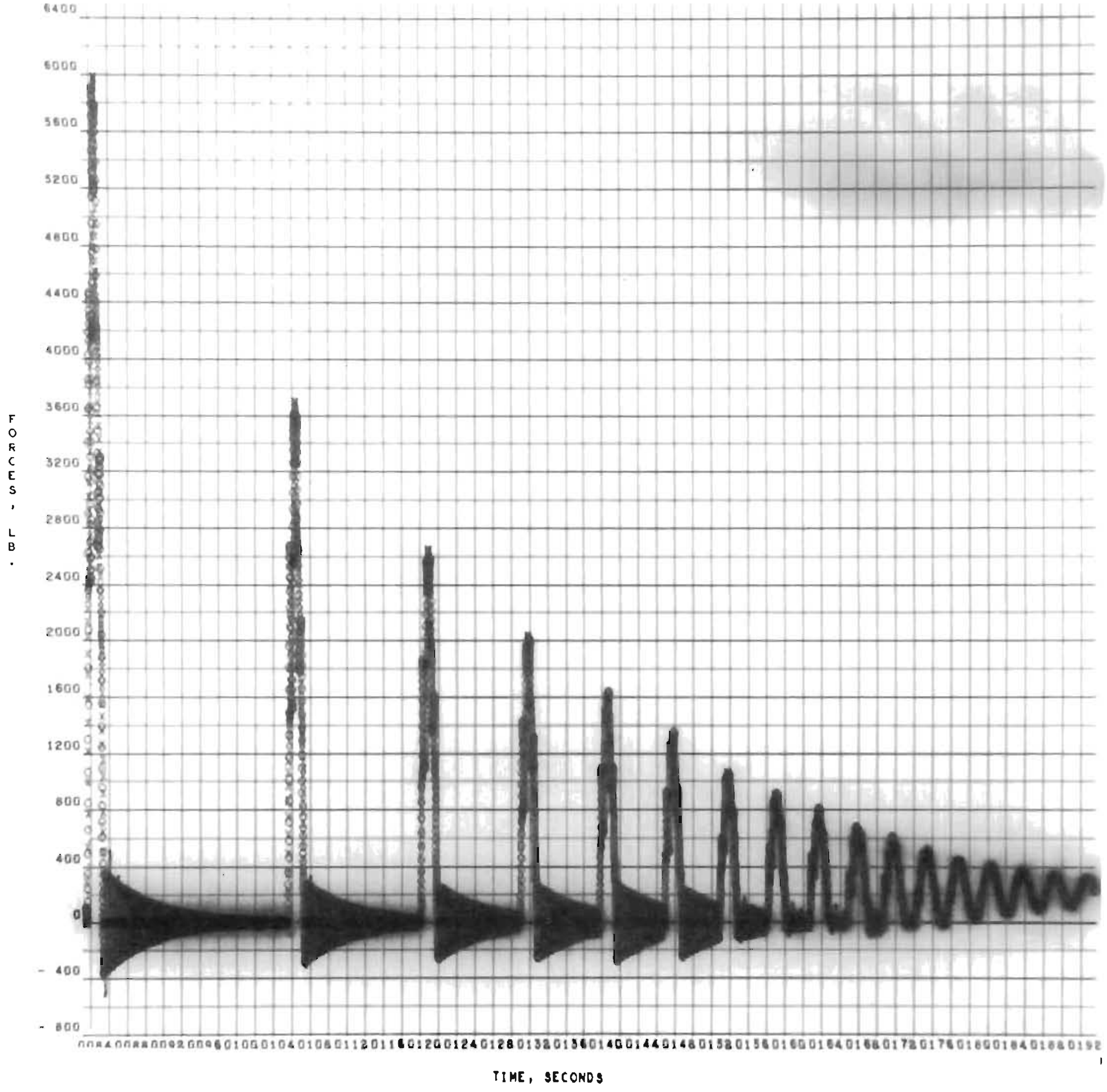

Figure 59. Computed Spring Forces, F1 (·), F2 (x), F3 (o), 35.6 in./sec Impact Velocity, PS = 156 psia, DØD = 0.1702 in.

2. Spring forces for XTIME

   a. Strain gage load cells summed as one output (F1), dots

   b. Poppet-seat interface
      (F2), X's

   c. Piezoelectric load cell
      (F3), circles

<u>1.87-in./sec Impact Velocity, 5000-psi Static Stress</u>. This test initiated the dynamic calibration series and was nominally the lowest velocity considered. It was performed four times, twice as a tester operation and data acquisition learning period, a third time to obtain "final" data, and lastly as a recheck of instrumentation capabilities after inadvertent seat impact loading to approximately 8300 pounds (piezoelectric cell). These tests demonstrated dashpot action repeatability for a given setting as velocity remained constant with cycles and time. For example, between the beginning of test two and end of test three, some 1100 cycles and an 11-day downtime period elapsed; velocity varied from 1.85 to 1.88 in./sec. Similarly, both strain-gage and piezoelectric load cell values were repeatable within data reduction resolution.

The position trace shown in Fig. 40 is typical of the traces used to calculate impact velocity. For the test stroke of 0.1000 inch, the trace runs from the ninth to first division line.

Impact loads for the three strain gage load cells corresponding to the above position trace are shown in Fig. 41, 42, and 43. An additional trace from cell No. 1 with an increased time base illustrates initial impact, one bounce and on-seat vibration (Fig. 44). The necessity for maximum gain rendered the output from these transducers susceptible to ground noise; therefore, most of the impact data were provided by the piezoelectric load cell. Output from this cell is illustrated in Fig. 45 for initial and peak impulses at the noted impact velocity. Two impacts are shown with cell ringing indicated by the high-frequency oscillations between impacts.

A composite trace of position and load is shown in Fig. 46. Control pressure and position are similarly shown in Fig. 47 where the pressure trace is initiated on the ninth division line. For the 141-psig (PS) input, control pressure (PC) rises at about 17,400 psi/sec with 90 percent of steady state (PC) reached at 0.0125-inch stroke. The steady-state pressure shown in Fig. 47 reflects the isentropic drop in (PS) due to the sudden additive of 1.55-cu in. cylinder volume (VC) to the 100-cu in. feed system volume. Consequently, the steady-state load shown in Fig. 46 (215 pounds) has not quite reached its maximum value of 221 pounds (5000-psi seat stress).

Computer program output data corresponding to the previous test conditions are shown in Fig. 52 and 53. The sample input and tabulated output data contained in Appendix A are for this run. Figure 52 illustrates the relative displacements of poppet and body. Because of the large body mass and mount restraints, it undergoes little movement.

As shown in the tabulted output of Appendix A, dashpot pressure (PQ) has decayed only 15 psi at the time of initial impulse peak load (about 0.00582 second). Thus initial peak loads are primarily due to impact velocity. Although impulse characteristics agree reasonably with test data, greater peak loads are predicted. This is attributed to the influence of low-rate springs at the poppet, seat and piezoelectric load cell interfaces, and main piston (as a spring) not considered in the program. It is significant, however, that piezoelectric load cell and seat spring initial impulse forces follow closely and are greater than the strain-gage peak force by about 20 percent, or almost exactly the difference indicated by test data.

1.77-in./sec Impact Velocity, 10,000-psi Static Stress. This test illustrates the time-dependent dashpot forces delivered to the seat. By increasing (PS) to 272 psig, it was necessary to reduce the dashpot orifice opening to maintain the same velocity. This increased the dashpot force delivery time by increasing (PQ) decay time. As shown in the load cell output (Fig. 48 and 49, zero load on first line), nine load cycles were required to reach maximum load with only one bounce after the initial impulse.

Computer output data shown in Fig. 54 and 55 agree very closely with test data, i.e., one bounce and nine cycles to peak load. As before, initial impact is greater than obtained from test data; however, peak loads are nearly the same.

8.46- and 35.6-in./sec Impact Velocities, 5000-psi Static Stress. These higher velocities are representative of those employed in model cycle testing. Because of the relatively high velocity loads, pressure forces are largely submerged. This is indicated by the impact traces of Fig. 50 and 51.

Although test initial impact loads agree with computer data reasonably well (Fig. 57 and 59) at the noted velocities (Fig. 56 and 58), it is apparent from comparison of bounce decays that test damping exceeds the computer model damping. Examination of test parts after cycle testing indicated poppet and seat clamp face separation as evidenced by bearing area fretting wear. Considering the light(100 pounds) preload and computer data, it is reasonably certain that separation did occur. However, separation of bearing surfaces is not included in the tester computer description and, therefore, might partially account for discrepancies noted between computed and test data.

Correlation of Analyses and Test Data

A summary of data reduced from all calibration tests is presented in Table 3. The significance of these data is the consistency of impact force-velocity ratios above 2 in./sec where dashpot forces do not significantly influence impact forces. This is further shown by the drop

TABLE 3

CYCLE TEST CALIBRATION PARAMETERS

Test Condition	Impact Velocity, V, in./sec	Control Pressure, psig	Poppet Stroke, inch	Strain Gage Sum, Fl, pounds	Piezo-electric Cell, F3, pounds	Initial Impulse Time, milli-seconds	No. of Impacts	On-Seat Frequency, cps	F3/V, $\frac{\text{lb-sec}}{\text{in.}}$
Dashpot Controlled	1.85	141	0.1000	220*	259	0.211	2	2840	140
↓	1.87	↓	↓	220**	255	0.209	↓	2840	136
↓	4.04	↓	↓	--	597	0.203	↓	3010	148
↓	4.26	↓	↓	--	630	--	↓	—	148
↓	6.40	↓	↓	--	1016	0.188	↓	3050	159
↓	7.53	↓	↓	--	1155	0.185	↓	3020	153
↓	8.46	↓	↓	--	1247	0.179	↓	~3100	147
↓	17.3	↓	↓	--	2680	0.178	3	~3100	155
↓	35.6	↓	↓	--	5950	0.173	4 to 5	~3100	167
↓	1.77	272	↓	--	249	0.203	2	2890	141
Drop Tests	1.69	0	0.00370	--	247	0.198	>10	~2900	146
↓	3.33	0	0.0142	404***	480	0.185	>10	~3000	144
↓	6.83	0	0.057	832****	990	0.175	>10	~3100	145

*F1 = $\Sigma F_1 + F_2 + F_3$

= 72.5 + 74.5 + 72.5 = 220; F3/F1 = 1.18

**F1 = 74.0 + 75.0 + 70.5 = 220; F3/F1 = 1.16

***F1 = 132 + 138 + 134 = 404; F3/F1 = 1.19

****F1 = 274 + 281 + 277 = 832; F3/F1 = 1.19

tests in which the F/V ratio is constant at 146 lb-sec/in. from 1.69 to 6.83 in./sec which is comparable with higher velocity dashpot tests.

Although not significantly affecting the initial impact loads, the dashpot did, however, provide a considerable control on the number of bounces. With only material internal damping, the drop tests indicated more than ten significant impacts compared with two for most dashpot controlled tests.

Reduction of significant data from the computer and test runs is compared, along with data computed from the simplified equations below:

	Natural Frequency, cps					
Data Source	Strain Gage Load Cells	Piezoelectric Load Cell	System, On-Seat	Initial Impulse Time, milliseconds	Initial Impact Piezoelectric-Velocity Ratio F3/V, $\frac{\text{lb-sec}}{\text{in.}}$	F3/F1
Test	~10,100	~21,000	2840 to 3100	0.17 to 0.20	136 to 167	1.16 to 1.19
Computer Analysis	11,000	20,700	2970	0.180	~166	1.20
Simplified Analysis	10,200	20,900	3000	0.167	155	——

Considering the cycle tester complexity, computed data and test results correlate reasonably well. This is particularly evident in the ratio of piezoelectric and strain gage load cell outputs (F3/F1). This correlation and the close agreement between computed seat and piezoelectric load cell spring forces (F2 and F3) lead to the conclusion that the actual seat impact force may be obtained directly from the piezoelectric load cell output. Furthermore, the close agreement given by the simplified analysis indicates that this technique may be used for design extrapolation when supported by defining test data.

Of overall significance to seating design, this analysis has shown that the number of impacts incurred per real cycle is variable and depends to a great degree on the system spring rates, weights, impact velocity, and damping. It is reasonably certain that most metal-seated valves without viscous damping experience several significant impacts per cycle. From the analysis it is also apparent that seat impact forces can be reduced by employing low velocities and moving weights along with low-rate contact springs.

MODEL FABRICATION AND SURFACE PREPARATION

One of the basic purposes of the program research effort was to produce design data relating the sealing surface with performance. For these data to be meaningful, however, they should be reproducible. Thus, not only should the surface be defined, but the method which produced it must be sufficiently well described to permit reasonable reproduction. The following paragraphs delineate the known fabrication factors contributing to specific model surface preparation and ultimate performance.

Three basic model configurations were designed--flat, conical, and spherical. Flat models for the initial contract effort were made to the no-change drawing requirements of Fig. 60 through 62. These models were modified as required for follow-on testing. Additional flat models for the follow-on program were fabricated from the A-change drawings of Fig. 63 and 64.

Conical models with three basic angles, nominally 20, 33, and 41 degrees, were made for the follow-on effort of seating geometry evaluation tests. Details of these models are shown in Fig. 65 and 66. To permit investigation of misaligned cone axis performance, a series of tapered spacers was also fabricated (Fig. 67). Typical conical model assembly with and without tilting spacer showing installation of a volume-reducing leak collector ring (Fig. 68) is shown in Fig. 69.

Similarly, for seating geometry evaluation purposes, spherical models with the same nominal seating angles as the conical versions were also fabricated. The spherical poppets (Fig. 70) were epoxy-set in retainers after machining (Fig. 71) to form a semipermanent assembly as shown in Fig. 72. Figure 73 illustrates the spherical seats.

As noted in the Test Fixture section, the initially made flat seat dimensions were determined in conjunction with loading piston size. The subsequently made conical and spherical models were designed such that the

0.030-inch land width and 0.470-inch mean seating diameter dimensions established for the flat models was maintained. Thus, varied configuration performance could be compared on a common basis.

While conical and spherical seating angles of 15, 30, and 45 degrees were desired, it will be noted that the parts were made with somewhat-different fractional angles. This relationship was dictated by the 0.470-inch-mean-diameter requirement, and the resultant angles represent the best approximation possible with the standard ball sizes available.

As some of the initially fabricated models were reworked to the later change, basic configuration is denoted by drawing-change letter in the applicable test model section. Additionally, all parts were serialized as also noted in the Test section. Rework of a previously tested configuration is indicated by the serial number suffix (RW), followed by the rework sequence number. Model designations for initial contract models reiterated herein is by single letter exactly as in Ref. 37. Additional models fabricated for the follow-on effort carry subscripts--f (flat), c (conical), and s (spherical).

All of the test models presented above are complete except for final finishing of the back* and seating surfaces. Experimental finishing investigations and detail model surface preparation procedures are presented in the following paragraphs. Description and evaluation of the resultant dimensions and surfaces is discussed generally in the Model Inspection Equipment, Procedures, and Data section and more specifically for each model in applicable test model sections.

FLAT-TURNED MODELS

Lathe-turned models to be evaluated included both rough (~ 16AA) and finer (~ 4AA) surfaces on hardened 17-4 PH stainless steel (R_c 45) and 6061-T651 aluminum alloy. As previously mentioned, the literature survey

---

*As noted in the Test Fixture section, to ensure model assembly accuracy, the backfaces of all follow-on poppets and seats were unidirectional diamond lapped to about 1-microinch AA using 1- to 5-micron diamond, as described herein.

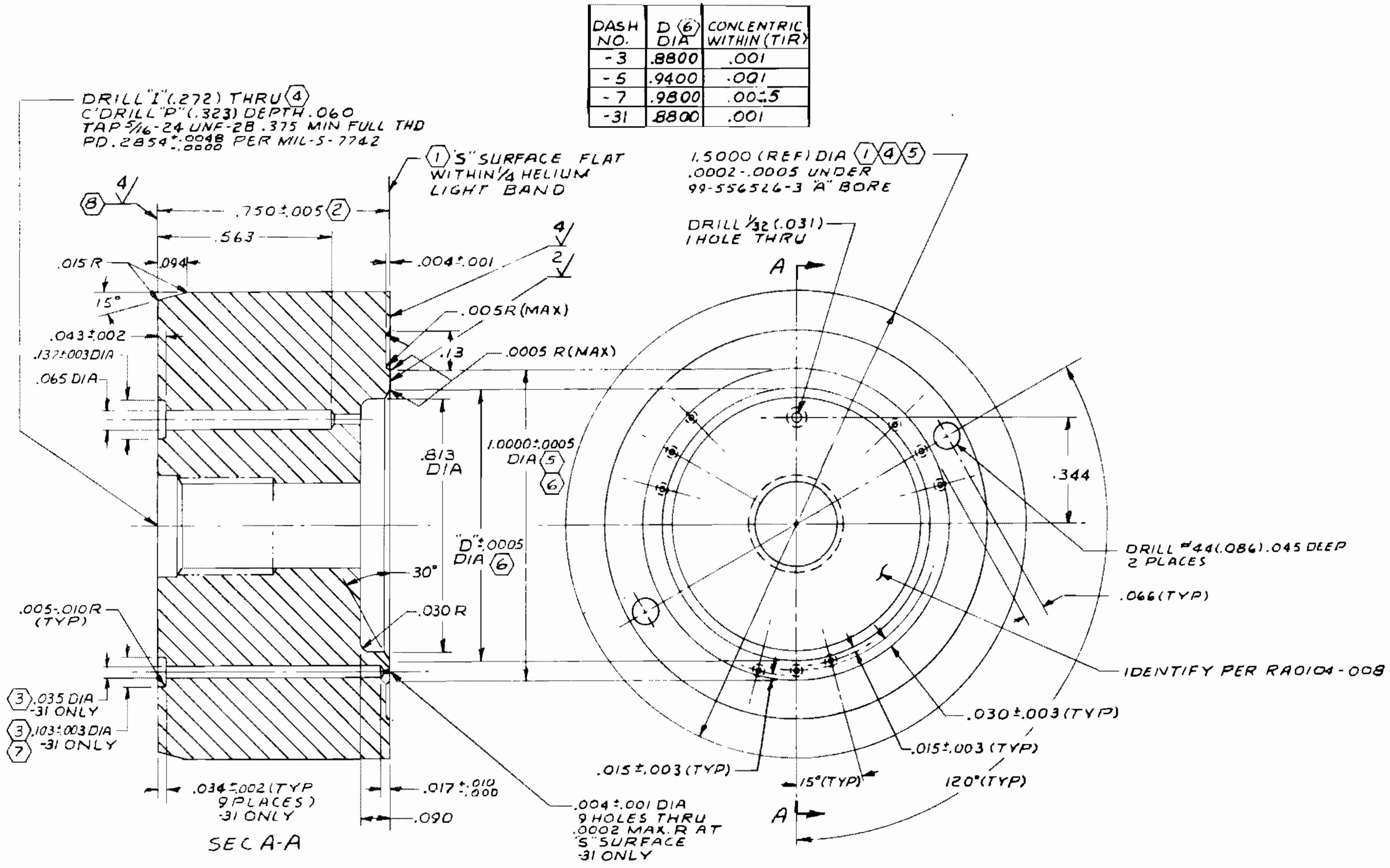
DRILL "I" (.272) THRU ⟨4⟩
C'DRILL "P" (.323) DEPTH .060
TAP 5/16-24 UNF-2B .375 MIN FULL THD
PD .2854 +.0048 -.0000 PER MIL-S-7742
⟨1⟩ "S" SURFACE FLAT WITHIN 1/4 HELIUM LIGHT BAND
⟨8⟩
4
.750±.005 ⟨2⟩
.563
.015 R
.094
.004±.001
4
2
15°
.005R (MAX)
.043±.002
.137±.003 DIA
.13
.0005 R (MAX)
.065 DIA
.813 DIA
1.0000±.0005 DIA ⟨5⟩ ⟨6⟩
"D"±.0005 DIA ⟨6⟩
30°
.030 R
.005-.010R (TYP)
⟨3⟩ .035 DIA -31 ONLY
⟨3⟩ .103±.003 DIA ⟨7⟩ -31 ONLY
.034±.002 (TYP 9 PLACES) -31 ONLY
.017 +.010 -.000
.090
SEC A-A
1.5000 (REF) DIA ⟨1⟩⟨4⟩⟨5⟩ .0002-.0005 UNDER 99-556526-3 "A" BORE
DRILL 1/32 (.031) 1 HOLE THRU
A
.344
DRILL #44 (.086) .045 DEEP 2 PLACES
.066 (TYP)
IDENTIFY PER RA0104-008
.030±.003 (TYP)
.015±.003 (TYP)
120° (TYP)
.015±.003 (TYP)
15° (TYP)
A
.004±.001 DIA 9 HOLES THRU .0002 MAX. R AT "S" SURFACE -31 ONLY

DASH NO.	D ⟨6⟩ DIA	CONCENTRIC WITHIN (TIR)
-3	.8800	.001
-5	.9400	.001
-7	.9800	.0015
-31	.8800	.001

⟨8⟩ 8. FLAT WITHIN ONE HELIUM LIGHT BAND.
⟨7⟩ 7. ℄ OF .103 DIA'S TO MATCH ℄'S OF 99-556526-9 #60 DRILL HOLE PATTERN WITHIN .005
⟨5⟩ 5. CONCENTRIC WITHIN .001 TIR
⟨4⟩⟨3⟩ 4. CONCENTRIC WITHIN .005 TIR
⟨2⟩ 3. PARALLEL WITHIN .000010
⟨1⟩ 2. PERPENDICULAR TO 1.5000 DIA WITHIN .0003 IN 1.5"
1. 32√ ALL SURFACES EXCEPT HOLES 63√
NOTE: UNLESS OTHERWISE SPECIFIED

HEAT TREAT	58-60 ROCKWELL "C" PER MIL-H-6875 (PR605-14)
FINISH	PASSIVATE PER RA0110-018
MAT'L	AISI TYPE 440C CRES LB0160-151 1 5/8 DIA x .88 BAR

Figure 60. 1.0-Inch Model Seat (Drawing No. 99-556527)

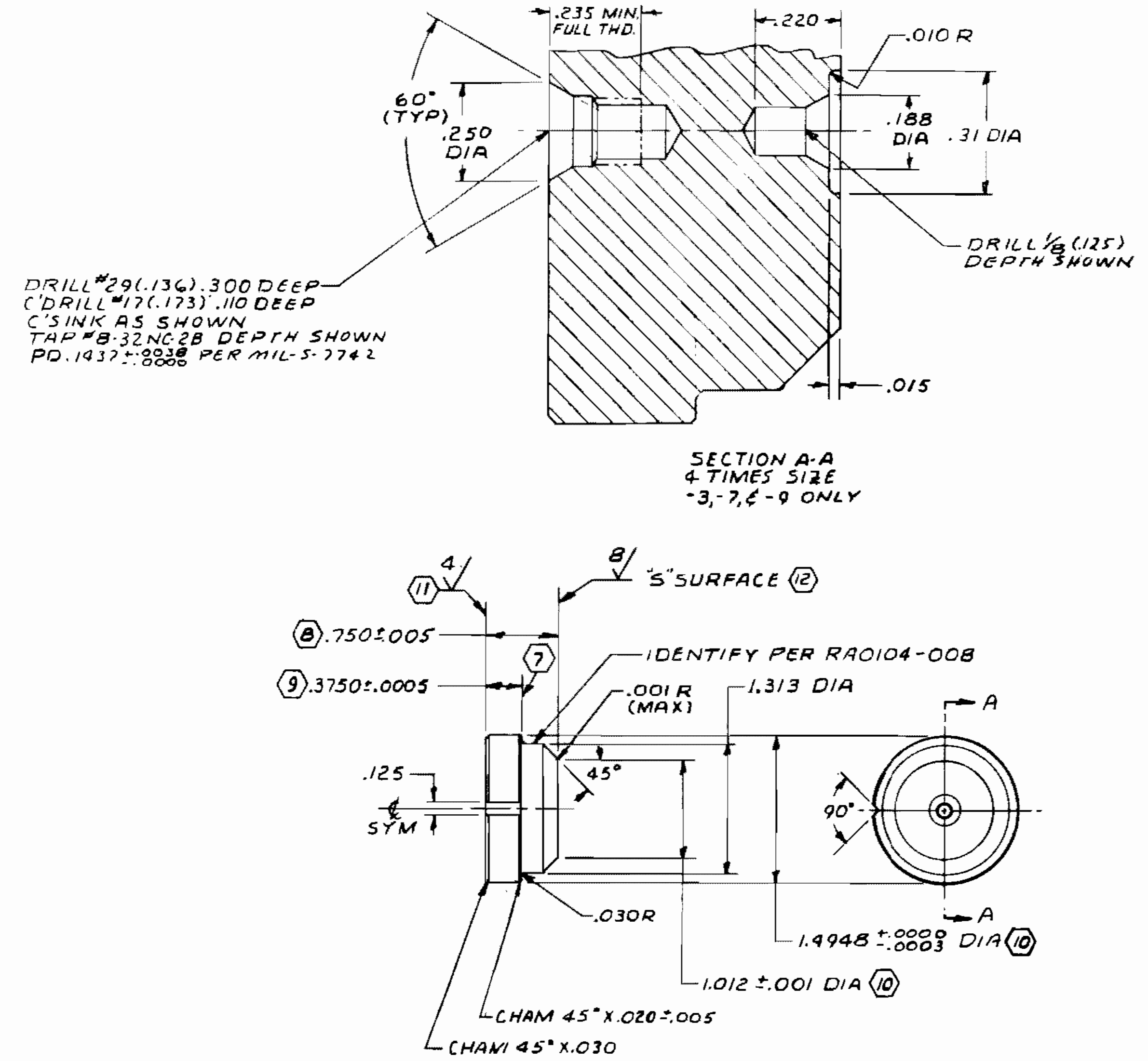

⑫ 13. "S" SURFACE LEFT "AS GROUND"
⑪ 12. FLAT WITHIN ONE HELIUM LIGHT BAND
⑩ 11. CONCENTRIC WITHIN .002 TIR
⑨ 10. PARALLEL WITHIN .0003
⑧ 9. PARALLEL WITHIN .000050
⑦ 8. PERPENDICULAR TO 1.4948 DIA WITHIN .0003 IN 1.5"
⑥ 7. -7 HEAT TREAT 40-45 ROCKWELL "C"
PER RA0111-014
⑤ 6 -3 HEAT TREAT 58-60 ROCKWELL "C"
PER MIL-H-6875 (PR605-14)
④ 5. -9 6061-T651 AL ALLOY, QQ-A-325, TEMP T651
1 3/4 X .88 BAR
③ 4. -7 17-4 PH CRES AMS 5643 1 5/8 DIA X .88 BAR
② 3. -5 TUNGSTEN CARBIDE ROCKWELL "A" 90-93
1 1/2 DIA X .88 BAR
① 2 -3 AISI TYPE 440C LB0160-151 1 5/8 DIA X .88 BAR
1 32√ ALL SURFACES EXCEPT HOLE 63√
NOTE: UNLESS OTHERWISE SPECIFIED

HEAT TREAT -5 & -9 NONE
-3 NOTED ⑤
-7 NOTED ⑥

FINISH -5 & -9 NONE
-3 & -7 PASSIVATE
PER RA0110-018

MAT'L
NOTED ①②③④

Figure 61. Model Poppet
(Drawing No. 99-556528)

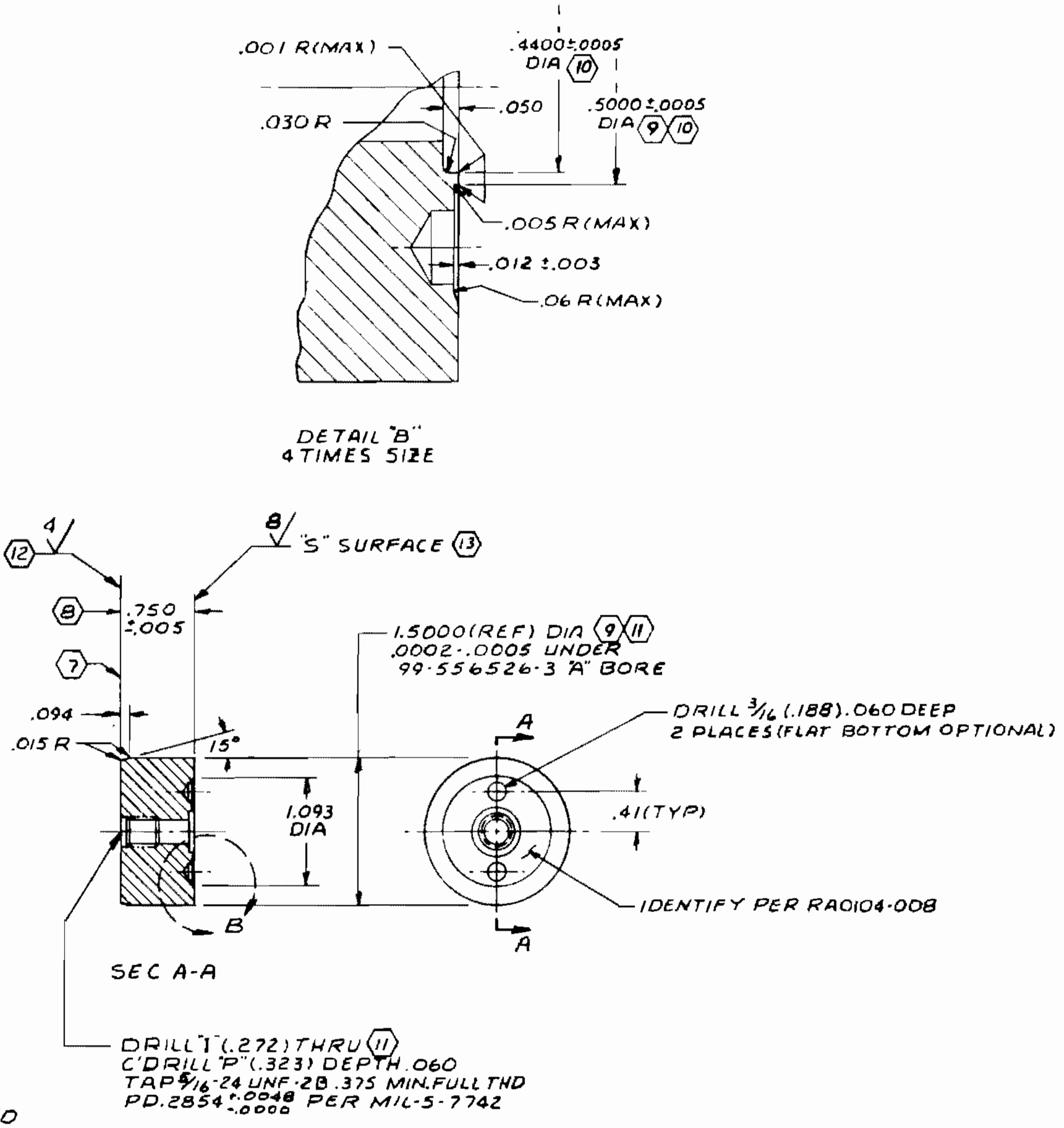

⟨13⟩ 13. "S" SURFACE LEFT "AS GROUND"
⟨12⟩ 12. FLAT WITHIN ONE HELIUM LIGHT BAND
⟨11⟩ 11. CONCENTRIC WITHIN .005 TIR
⟨10⟩⟨9⟩ 10. CONCENTRIC WITHIN .001 TIR
⟨8⟩ 9. PARALLEL WITHIN .000050
⟨7⟩ 8. PERPENDICULAR TO 1.5000 DIA WITHIN .0003 IN 1.5"
⟨6⟩ 7. -7 HEAT TREAT 40-45 ROCKWELL "C" PER RA0111-014
⟨5⟩ 6. -3 HEAT TREAT 58-60 ROCKWELL "C" PER MIL-H-6875 (PR605-14)
⟨4⟩ 5. -9 6061-T651 AL. ALLOY, QQ-A-325, TEMP T651 1 3/4 X .88 BAR
⟨3⟩ 4. -7 17-4 PH CRES AMS5643 1 5/8 DIA X .88 BAR
⟨2⟩ 3. -5 TUNGSTEN CARBIDE ROCKWELL "A" 90-93 1 1/2 DIA X .88 BAR
⟨1⟩ 2. -3 AISI TYPE 440C LB0160-151 1 5/8 DIA X .88 BAR
1. 32√ ALL SURFACES EXCEPT HOLE 63√

NOTE: UNLESS OTHERWISE SPECIFIED

HEAT TREAT -5 ¢ -9 NONE -3 NOTED ⟨5⟩ -7 NOTED ⟨6⟩
FINISH -5 ¢ -9 NONE -3 ¢ -7 PASSIVATE PER RA0110-018
MAT'L NOTED ⟨1⟩⟨2⟩⟨3⟩⟨4⟩

Figure 62. 0.5-Inch Model Seat
(Drawing No. 99-556529)

(12) 12. FLAT WITHIN ONE HELIUM LIGHT BAND
(11) 11. CONCENTRIC WITHIN .005 TIR
(10)(9) 10. CONCENTRIC WITHIN .0005 TIR
(8) 9. PARALLEL WITHIN .000025
(7) 8. PERPENDICULAR TO 1.5000 DIA WITHIN .0003 IN 1.5"
(6) 7. -7 HEAT TREAT 40-45 ROCKWELL "C"
PER RA0111-014
(5) 6. -3 HEAT TREAT PER PR605-14 EXCEPT FINAL TEMPER
TO PRODUCE R_C 58-62. MIN FINAL TEMPER 350°F
(4) 5. -9 6061-T651 AL. ALLOY, QQ-A-325, TEMP T651
$1\frac{3}{4}$ X .88 BAR
(3) 4 -7 17-4 PH CRES AMS 5643 $1\frac{5}{8}$ DIA X .88 BAR
(2) 3. -5 TUNGSTEN CARBIDE ROCKWELL "A" 90-93
$1\frac{1}{2}$ DIA X .88 BAR
(1) 2. -3 AISI TYPE 440C 180160-151 $1\frac{5}{8}$ DIA X .88 BAR
1. 32√ ALL SURFACES EXCEPT HOLE 63√

HEAT TREAT -5 & -9 NONE -3 NOTED (5) -7 NOTED (6)
FINISH -5 & -9 NONE -3 & -7 PASSIVATE PER RA0110-018
MAT'L NOTED (1)(2)(3)(4)

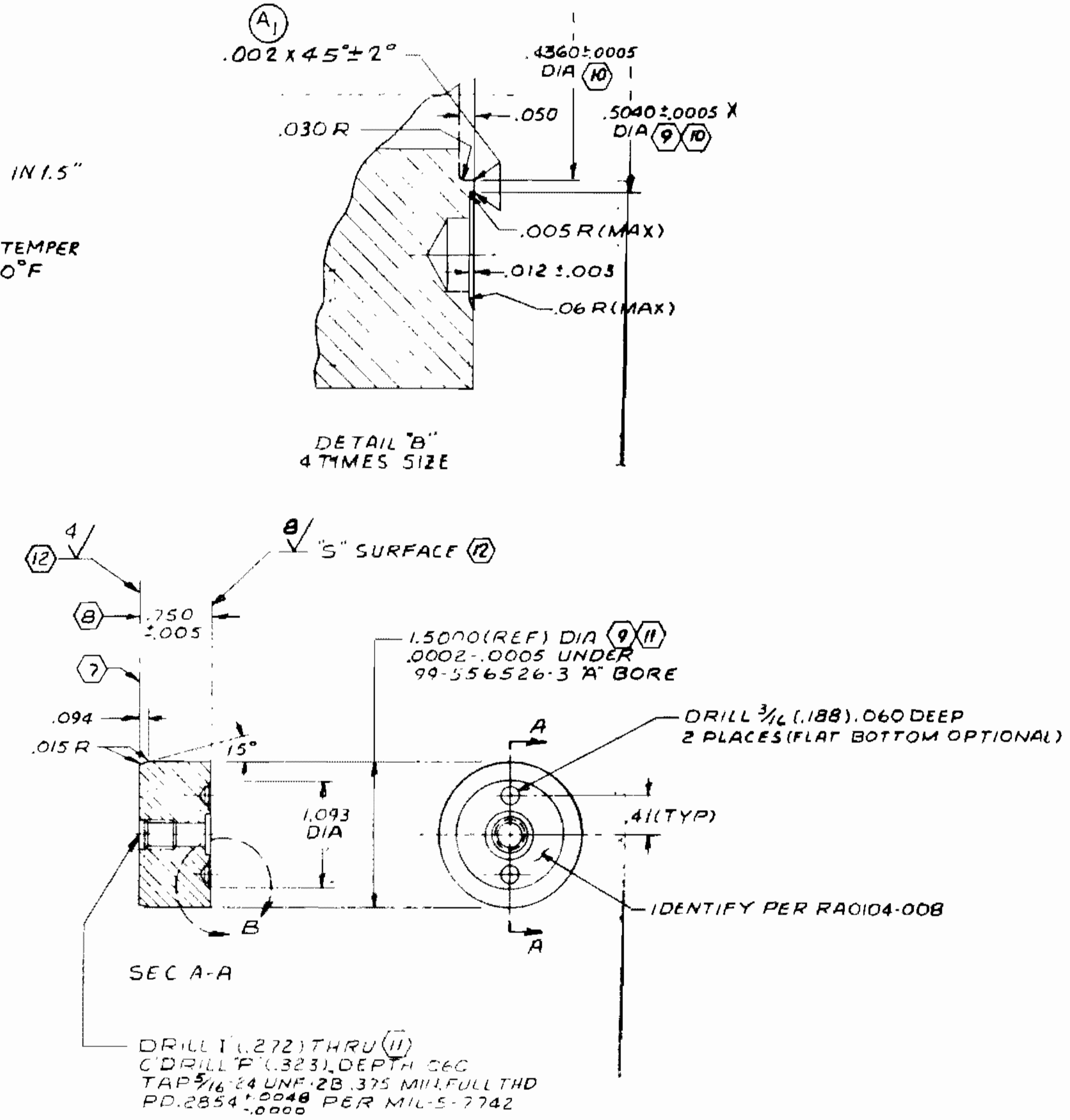

Figure 63. 0.5-Inch Model Seat (Drawing No. 99-556529A)

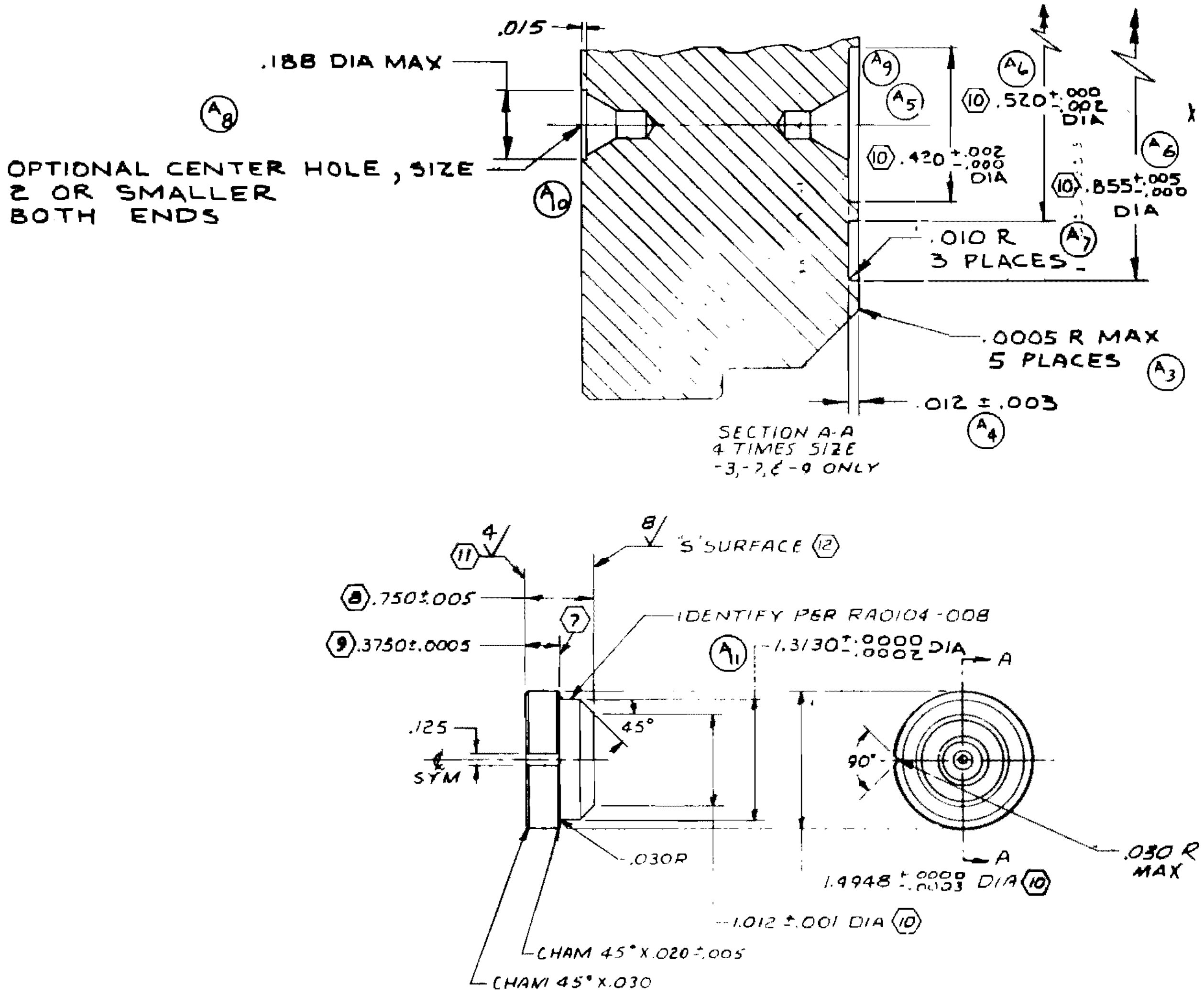

⟨12⟩ 13. "S" SURFACE LEFT AS GROUND"
⟨11⟩ 12. FLAT WITHIN ONE HELIUM LIGHT BAND
⟨10⟩ 11. CONCENTRIC WITHIN .001 TIR
⟨9⟩ 10. PARALLEL WITHIN .0003
⟨8⟩ 9. PARALLEL WITHIN .000050
⟨7⟩ 8. PERPENDICULAR TO 1.4948 DIA WITHIN .0003 IN 1.5"
⟨6⟩ 7. -7 HEAT TREAT 40-45 ROCKWELL "C" PER RA0111-014
⟨5⟩ 6 -3 HEAT TREAT PER PR605-14 EXCEPT FINAL TEMPER TO PRODUCE R_C 58-62. MIN FINAL TEMPER 350°F
⟨4⟩ 5 -9 6061-T651 AL ALLOY, QQ-A-325, TEMP T651 1 3/4 x .88 BAR
⟨3⟩ 4. -7 17-4 PH CRES AMS 5643 1 5/8 DIA x .88 BAR
⟨2⟩ 3 -5 TUNGSTEN CARBIDE ROCKWELL "A" 90-93 1 1/2 DIA x .88 BAR
⟨1⟩ 2 -3 AISI TYPE 440C LB0160-151 1 5/8 DIA x .88 BAR
1 32√ ALL SURFACES EXCEPT HOLE 63√

HEAT TREAT -5 & -9 NONE -3 NOTED ⟨5⟩ -7 NOTED ⟨6⟩
FINISH -5 & -9 NONE -3 & -7 PASSIVATE PER RA0110-018
MAT'L NOTED ⟨1⟩⟨2⟩⟨3⟩⟨4⟩

Figure 64. Model Poppet (Drawing No. 99-556528A)

DASH Nº	"A" DIA	"B" DIA	"C" ANGLE	"L" DIM (REF)
-1	.4683	.4717	39°54′	.005
-2	.4598	.4802	39°54′	.030
-3	.4673	.4727	66°40′	.005
-4	.4535	.4865	66°40′	.030
-5	.4667	.4733	82°28′	.005
-6	.4502	.4898	82°28′	.030

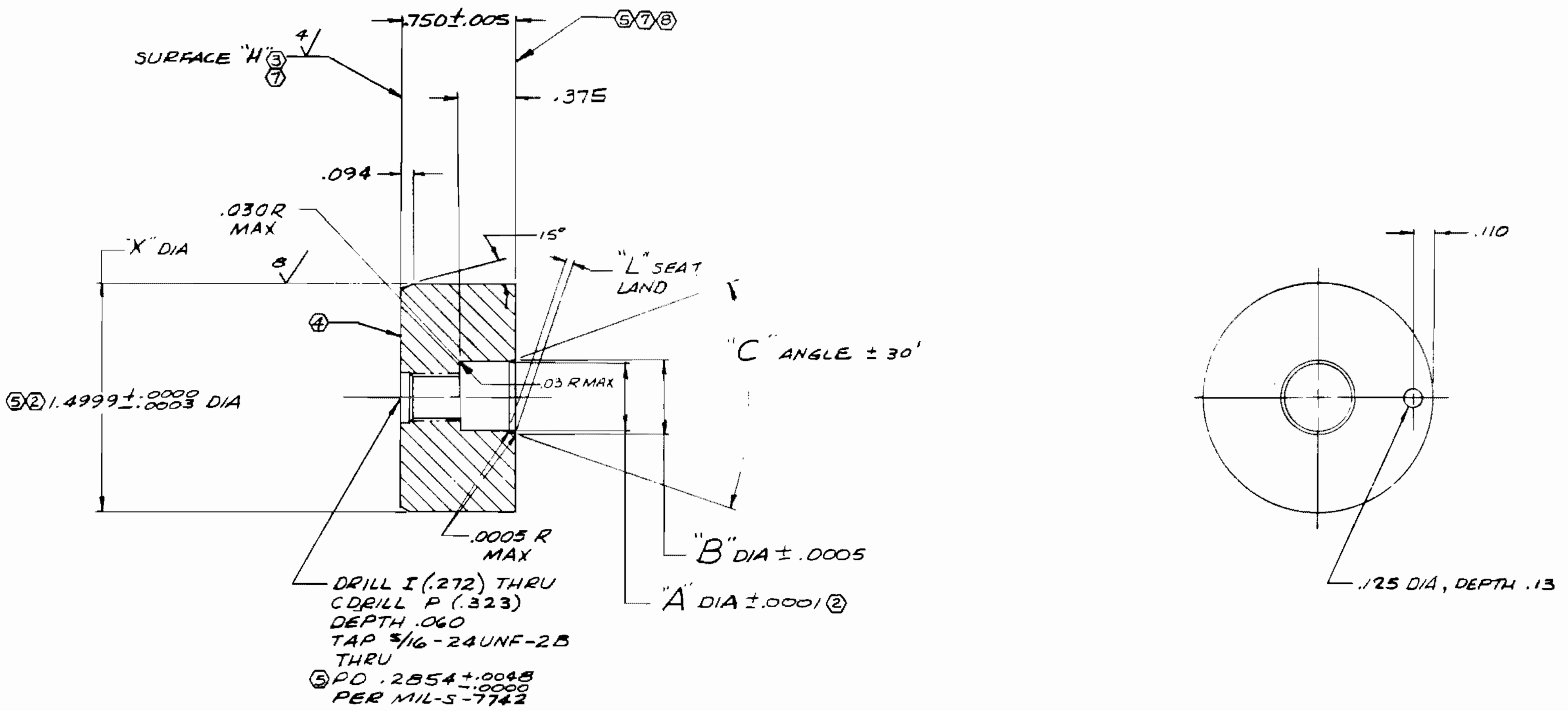

⑧ 9. NORMAL TO "A" DIA WITHIN .0001 TOTAL
⑦ 8. FLAT WITHIN .000010
⑥ 7. CONCENTRIC WITHIN .005 T.I.R.
⑤ 6. PARALLEL TO SURFACE H WITHIN .0001 TOTAL.
④ 5. IDENTIFY PER RA0104-008.
4. MACHINE PER RA0103-002.
③ 3. NORMAL TO "X" DIA WITHIN .0003 TOTAL
② 2. CONCENTRIC WITHIN .0002 T.I.R.
① 1. HEAT TREAT PER PR605-14 EXCEPT FINAL TEMPER TO PRODUCE R_c 58-62. MINIMUM FINAL TEMPER 350 °F.

NOTE: UNLESS OTHERWISE SPECIFIED

Figure 66. Conical Model Seat (Drawing No. 99-557781)

DASH Nº	"A" DIM	"B" ANGLE (REF)
-8	.0083 ±.0003	0° 19.2′
-10	.0158 ±.0005	0° 36.6′
-12	.0290 ±.0010	1° 7.2′

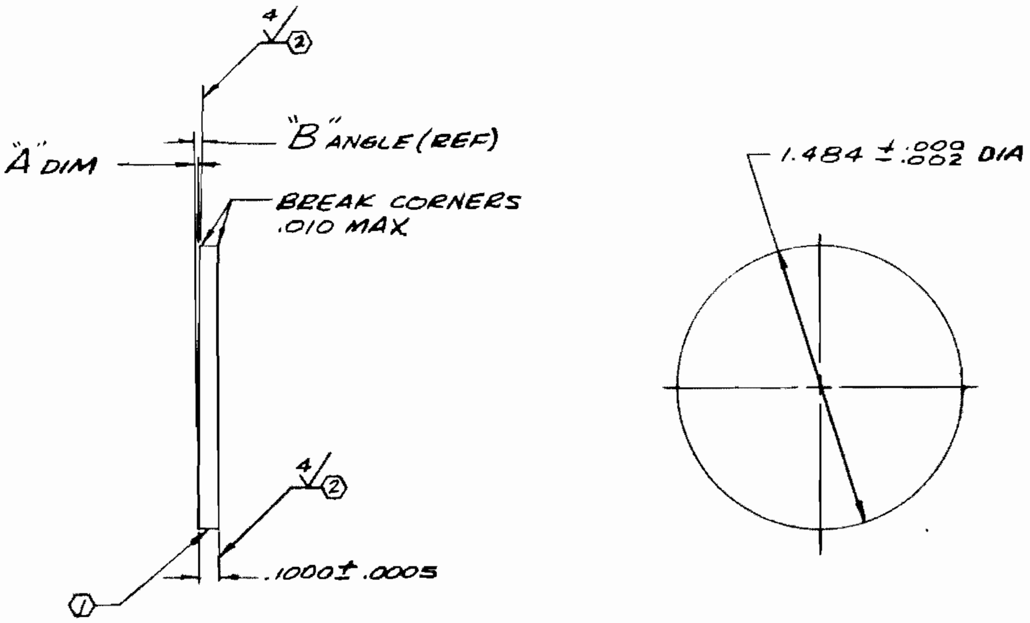

③ 4. HEAT TREAT PER PR 605-14 EXCEPT FINAL TEMPER TO PRODUCE R_c 58-62 MINIMUM FINAL TEMPER 350 F

② 3. FLAT WITHIN .000010 INCHES TOTAL.

① 2. IDENTIFY PER RA0104-008.

1. MACHINE PER RA0103-002.

HEAT TREAT	③
FINISH	VAPOR DEGREASE
MAT'L	440C CRES BAR 1½ DIA x .18 LB0160-151

Figure 67. Conical Poppet Tilting Spacer (Drawing No. 99-557784)

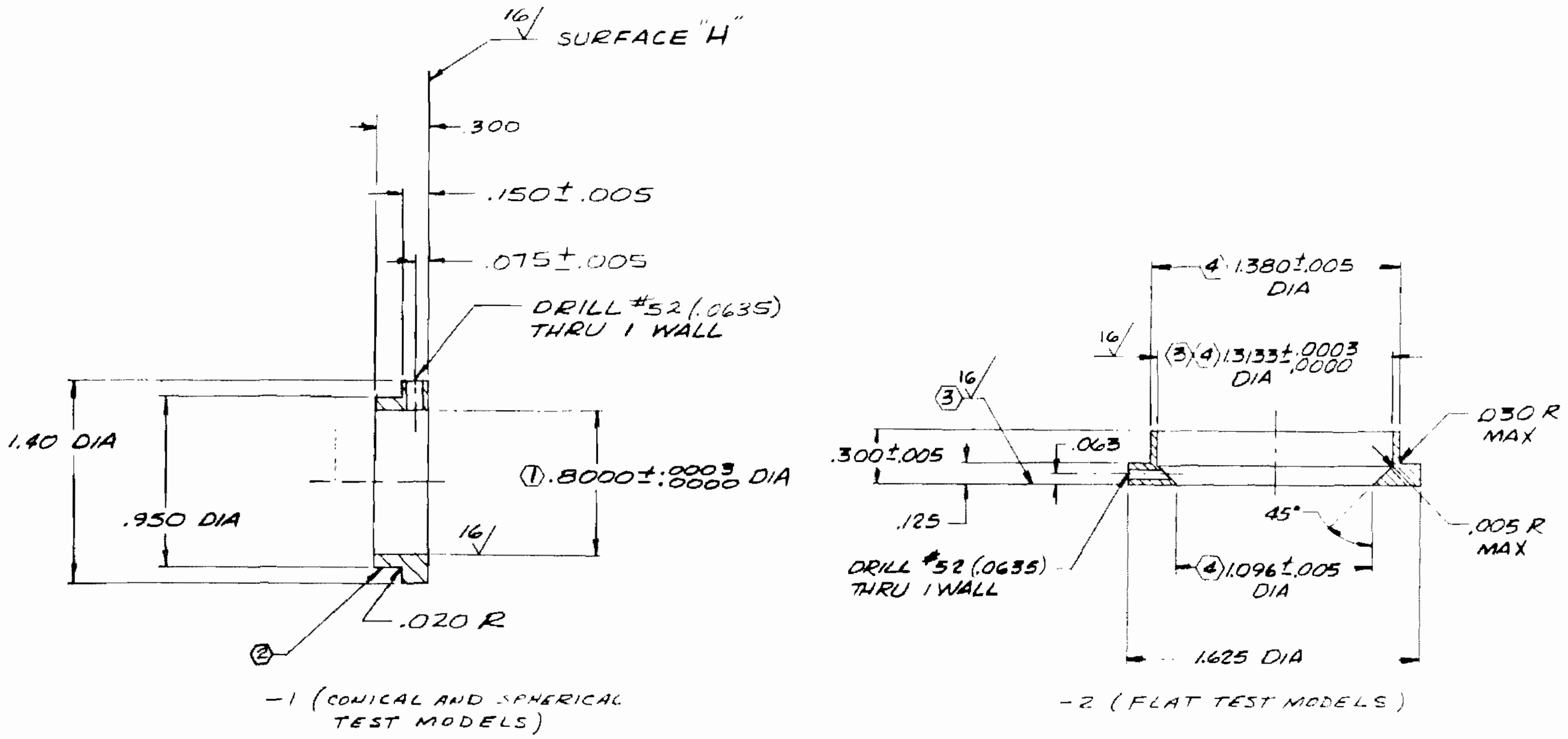

−1 (CONICAL AND SPHERICAL TEST MODELS)

−2 (FLAT TEST MODELS)

(4) 6. CONCENTRIC WITHIN .003 TOTAL
(3) 5. NORMAL WITHIN .0003 TOTAL
② 4. IDENTIFY PER RA0104-008.
3. MACHINE PER RA0103-002.
2. BREAK CORNERS .001 $^{+.009}_{-.000}$
① 1. NORMAL TO SURFACE "H" WITHIN .0005 TOTAL.

HEAT TREAT	
FINISH	VAPOR DEGREASE
MAT'L	7075-T651 AL ALLOY BAR 1⅜ DIA × .56 QQ-A-282

Figure 68. Leak Volume Reducing Ring (Drawing No. 99-557779)

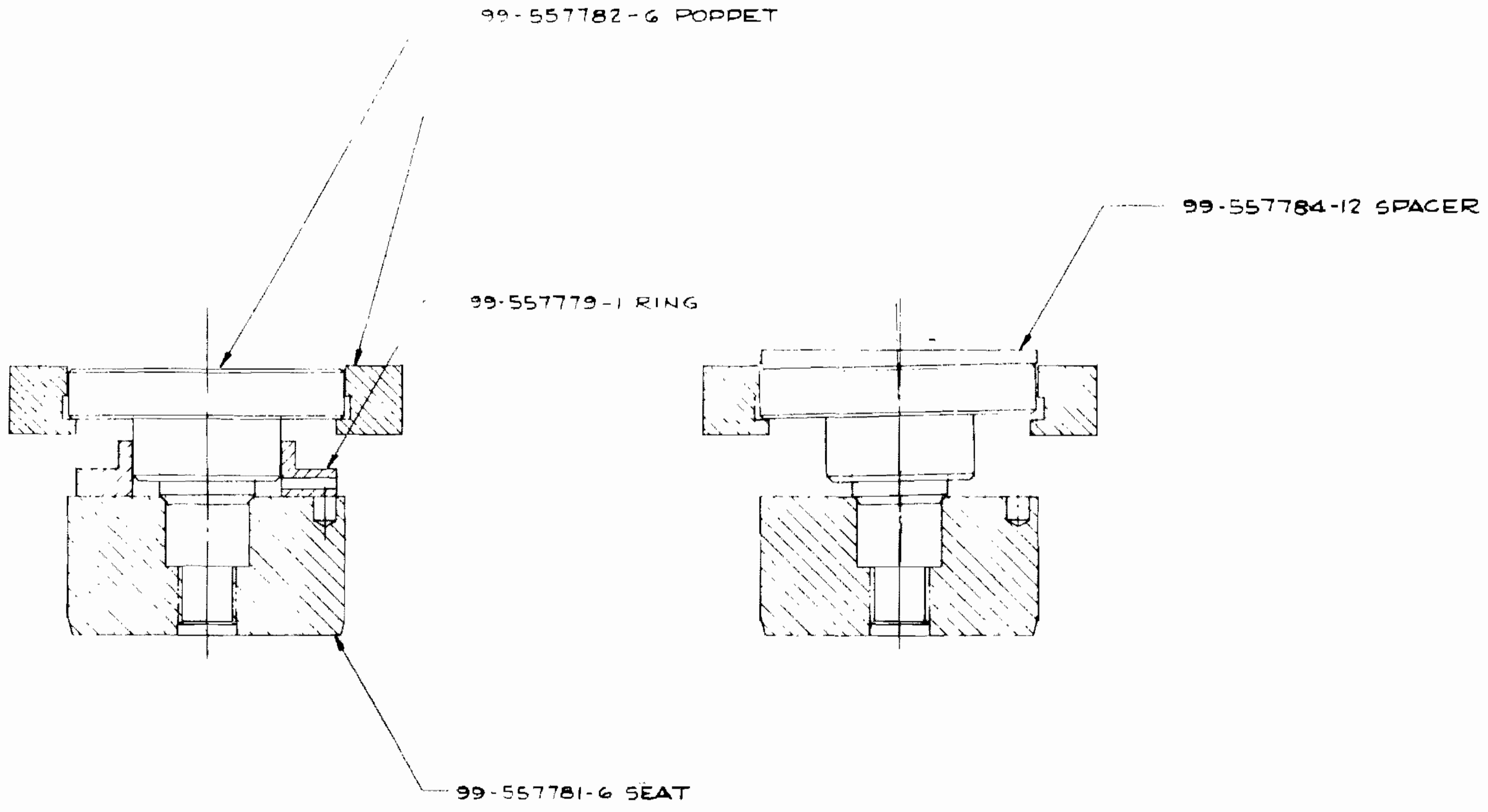

Figure 69. Conical Poppet and Seat Assembly

DASH Nº	"A" DIM	① "B" DIA	(REF) FOR USE WITH SEAT ANGLE	SPHERICITY
- 2	.426	$\frac{1}{2}$(.500)	39°54'	.000010
- 4	.453	$\frac{9}{16}$(.5625)	66°40'	.000010
- 6	.560	$\frac{5}{8}$(.625)	82°28'	.000010
- 8	.560	$\frac{5}{8}$(.625)	82°28'	.000050
- 10	.560	$\frac{5}{8}$(.625)	82°28'	.000100
- 12	.560	$\frac{5}{8}$(.625	82°28'	.000200

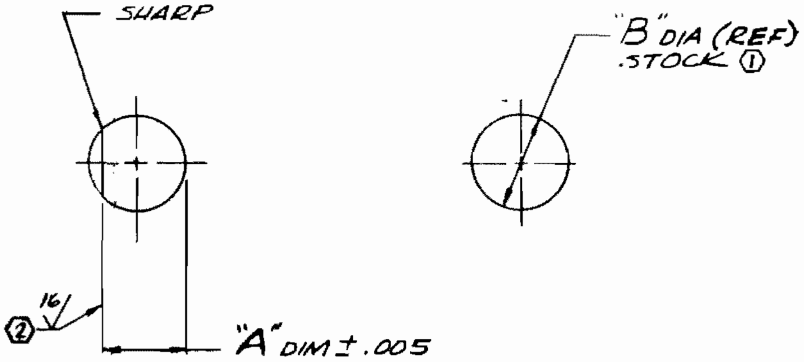

② 2. FLAT WITHIN .000050 TOTAL
1. MACHINE PER RA0103-002

HEAT TREAT	
FINISH	VAPOR DEGREASE
MAT'L	MAKE FROM COML 440C BALLS ①

Figure 70. Spherical Poppet (Drawing No. 99-557778)

DASH N°	"A" DIA	"B" DIM	(REF) FOR USE WITH SEAT ANGLE	"C" DIM
-2	.5003	.200	39° 54'	.704
-4	.5628	.250	66°40'	.727
-6	.6253	.400	82°28'	.770

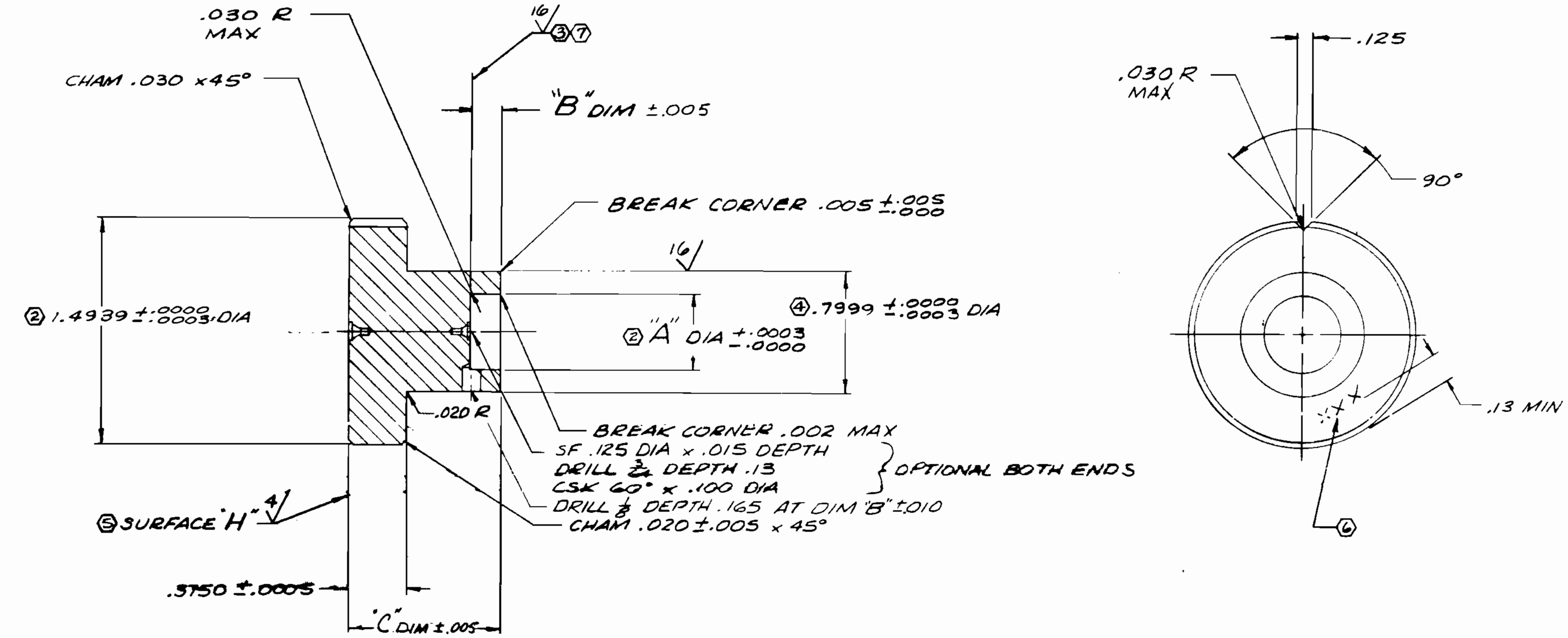

⑦ 8. FLAT WITHIN .0001 TOTAL
⑥ 7. IDENTIFY PER RA0104-008
⑤ 6. FLAT WITHIN .000010
④ 5. NORMAL TO SURFACE "H" WITHIN .0005 TOTAL.
4. MACHINE PER RA0103-002.
③ 3. PARALLEL TO SURFACE "H" WITHIN .001 TOTAL.
② 2. CONCENTRIC WITHIN .0002 T.I.R.
① 1. HEAT TREAT PER PR605-14 EXCEPT FINAL TEMPER TO PRODUCE Rc 58-62. MINIMUM FINAL TEMPER 350 °F

LESS OTHERWISE SPECIFIED

HEAT TREAT	①
FINISH	
MAT'L	440C CRES BAR 1 5/8 DIA x 1.12 LB0160-151

Figure 71. Spherical Poppet Retainer (Drawing No. 99-557780)

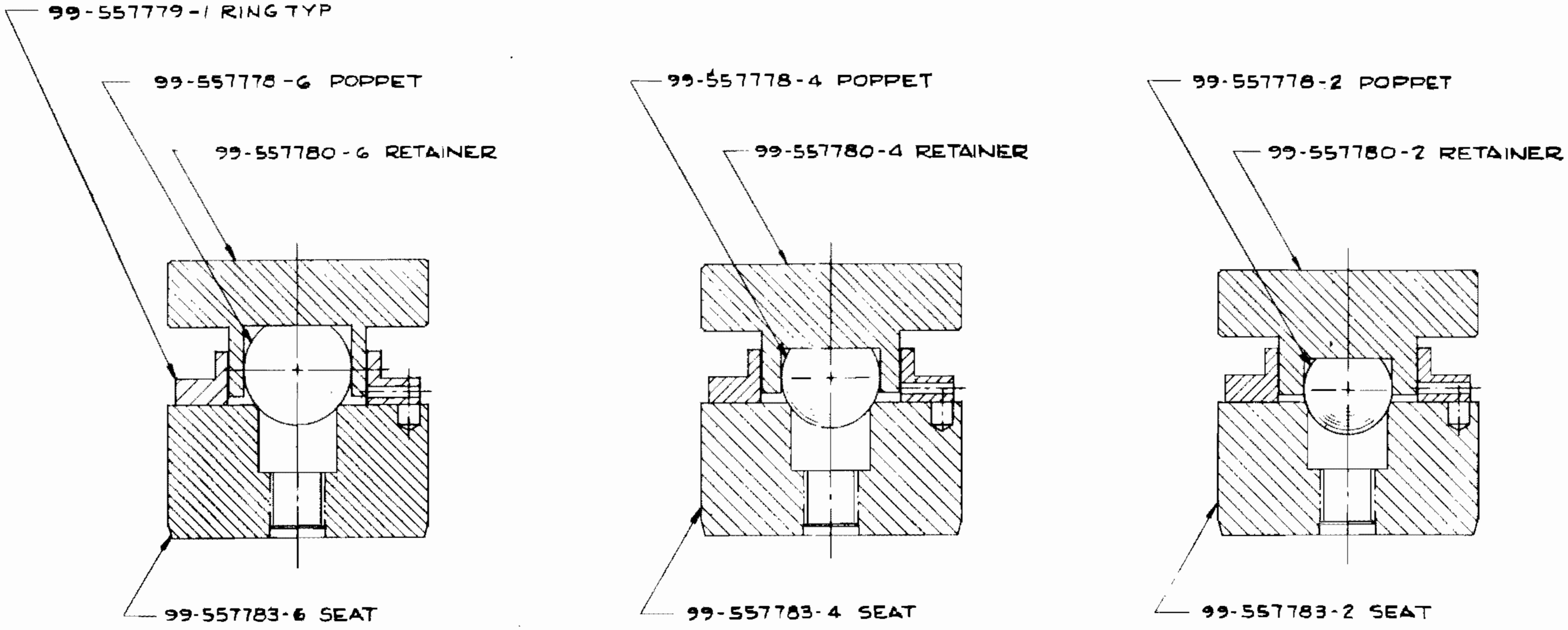

Figure 72. Spherical Poppet and Seat Assembly

DASH No	"A" DIA	"B" DIA (REF)	"C" BALL DIA	"D" DIM	"E" ANGLE (REF)	SEAT LAND "L" (REF)
-1	.4683	.4717	$\frac{1}{2}$(.500)	.3330	39°54′	.005
-2	.4589	.4794	$\frac{1}{2}$(.500)	.3211	39°54′	.030
-3	.4672	4727	$\frac{9}{16}$(.5625)	.4337	66°40′	.005
-4	.4531	.4858	$\frac{9}{16}$(.5625)	.4231	66°40′	.030
-5	.4667	.4733	$\frac{5}{8}$(.625)	.5166	82°28′	.005
-6	.4500	.4892	$\frac{5}{8}$(.625)	.5070	82°28′	.030

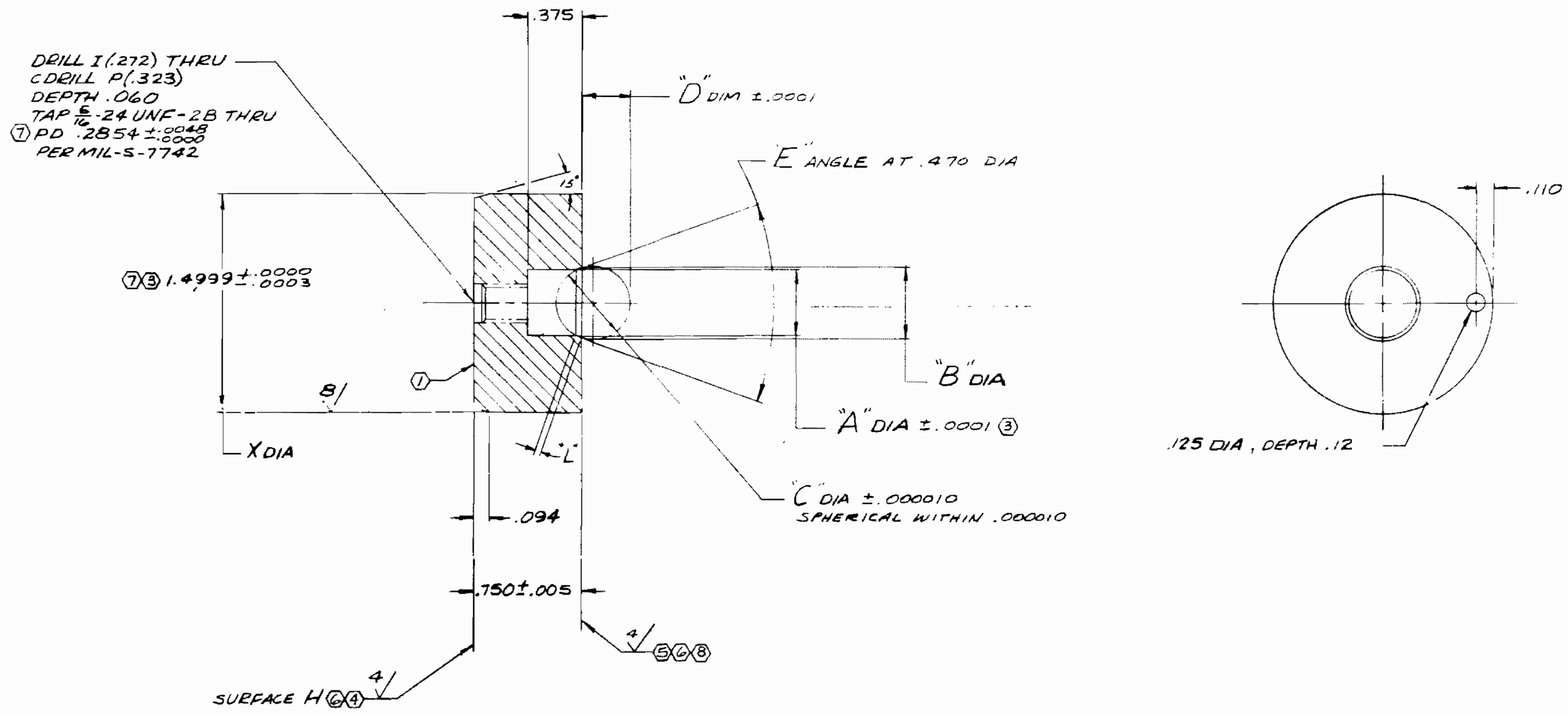

⑧ 9. NORMAL TO "A" DIA WITHIN .0001 TOTAL
⑦ 8. CONCENTRIC WITHIN .005 T.I.R.
⑥ 7. FLAT WITHIN .000010
⑤ 6. PARALLEL TO SURFACE H WITHIN .00010 TOTAL.
④ 5. NORMAL TO X DIA WITHIN .0003 TOTAL.
③ 4. CONCENTRIC WITHIN .0002 T.I.R.
② 3. HEAT TREAT PER PR605-14 EXCEPT FINAL TEMPER TO PRODUCE R_c 58-62. MINIMUM FINAL TEMPER 350°F.
① 2. IDENTIFY PER RA0104-008.
1. MACHINE PER RA0103-002.

NOTE: UNLESS OTHERWISE SPECIFIED

HEAT TREAT	②
FINISH	VAPOR DEGREASE
MAT'L	440C CRES BAR 1$\frac{5}{8}$ DIA x .81 LB0160-151

Figure 73. Spherical Seat (Drawing No. 99-557783)

yielded little information relating the turning operation with the resultant surface texture. Discussion with Rocketdyne production manufacturing personnel indicated that turned surfaces under 16-microinch AA were impractical and that, in general, grinding would be employed when lesser roughness levels were specified. This, apparently, is the common production approach.

The problem was then taken to the basic (machinist) level. Discussion with two experienced precision mechanics elicited the following information, particularly about turning 17-4 PH steel:

1. For fine finishing, a precision lathe is necessary. At their shop, Hardinge lathes were used.
2. The lathe must be limited to finish-cutting operations as precision degradation will occur if deep roughing cuts are frequently taken.
3. While they had not attempted lower levels, hardened 17-4 PH was commonly cut to about 10-microinch AA.
4. Although diamond tooling was employed for harder materials (for instance R_c 60 440C stainless steel) carbide tools were used on 17-4 PH. (High-speed steel tooling was used for aluminum parts.)
5. Cutting tool and condition. Here opinions diverged. One man advocated lapped preformed nose radii with high surface speed, while the second preferred dead sharp tooling (with self-generated radius following several cuts) and relatively slow speed.
6. Depth of cut should be kept to a minimum with 0.005-inch preliminary and 0.002- to 0.001-inch final cuts. Because of tool and workpiece springback, depth of cut less than 0.001-inch usually results in a nonuniform skipping or burnishing action.
7. Coolant or cutting aids. It was generally agreed that dry cutting was to be avoided, but opinions varied as to the use of commercial compounds vs such fluids as benzene and kerosene.

To investigate these claims and establish procedures for fabrication of test models, a brief experimental program was undertaken. Because the specific recommendations of expert machinists were being followed, these experiments do not represent a methodical investigation of individual parameters.

Turning Experiments, 17-4 PH Steel

Sample parts were used in these experiments, approximately 1.305-inch OD with a 0.125-inch land. A 3/8-inch, right-hand, no-side-cutting edge angle Carboloy No. 883 tungsten carbide tool was employed. The tool was diamond-ground to a near dead sharp edge and corner conditions and mounted normal to the sample face, on center. Cutting direction was from ID to OD. All experimental and final model machining was performed on a Hardinge Model HLV-H lathe.

With this tool, a 0.005-inch preliminary and 0.002-inch final cut was turned. Without tool change, three 0.005-inch and no 0.002-inch cuts were taken on a second sample. Workpiece speed was 370 rpm (~ 126 sfm) with a tool feed of ~0.00049 in./rev. A commercial cutting fluid, "Meyers Miracle" (Micronite Finish, Inc., Chicago, Illinois), was used.

Both sample parts exhibited a fairly uniform, 10-microinch PTV surface with the second somewhat better overall than the first. Cutting tool condition before and after these cuts is shown in Fig. 74 through 77. Little evidence of bue was noted, and the nose radius generated was less than 0.001 inch.

In considering the formed radius approach, a tool of the same type was lapped on all faces and a 0.014/0.015-inch nose radius formed. A cut taken at 1100 rpm (~ 376 sfm) with a 0.0014-in./rev feed produced a rougher surface than that of the self-generated radius tool. Inspection of this second tool (shown in Fig. 78) indicated approximately 0.0005-inch bue.

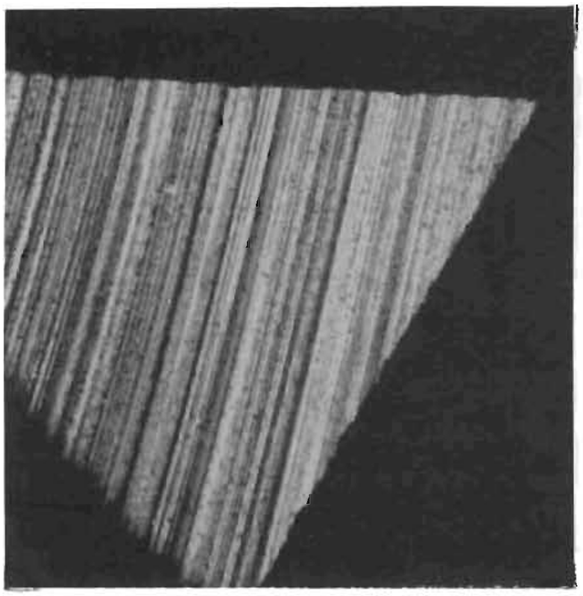

Figure 74. Sample 17-4 PH Cutting Tool No. 1, 0.033- x 0.033-Inch Plain Photo Showing Top Face As-Ground

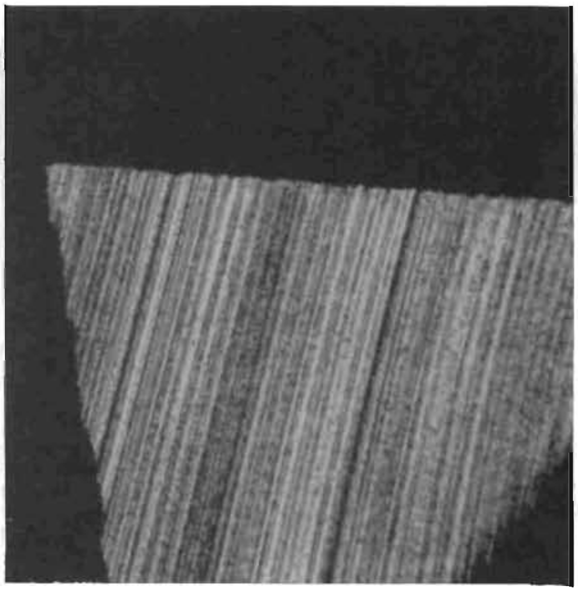

Figure 75. Sample 17-4 PH Cutting Tool No. 1, 0.033- x 0.033-Inch Plain Photo Showing Side Cutting Face As-Ground

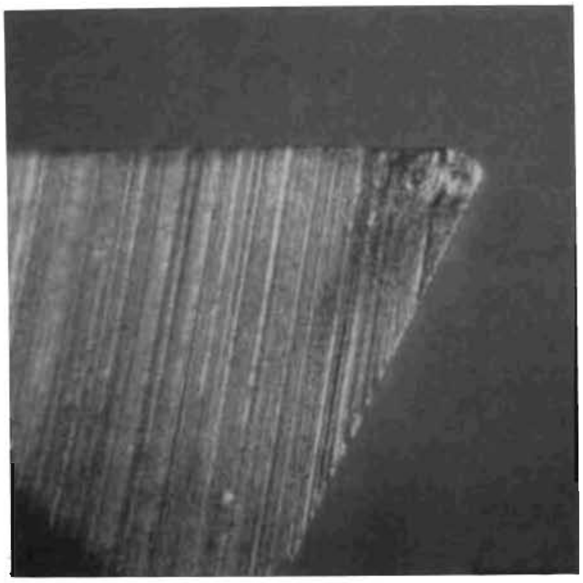

Figure 76. Sample 17-4 PH Cutting Tool No. 1, 0.033- x 0.033-Inch Plain Photo Showing Top Face After Turning Two Samples

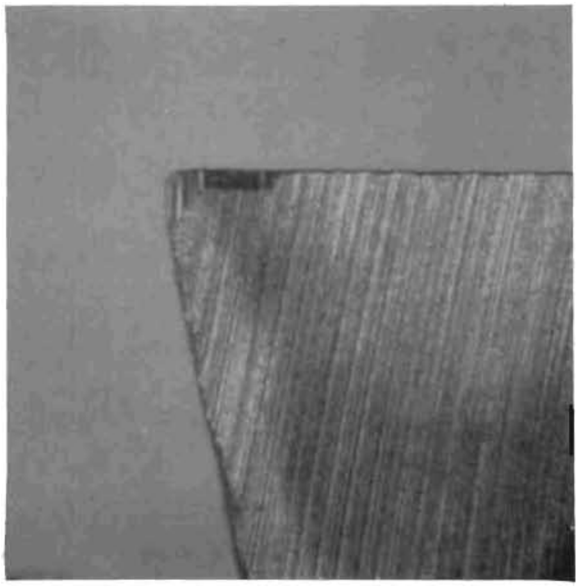

Figure 77. Sample 17-4 PH Cutting Tool No. 1, 0.033- x 0.033-Inch Plain Photo Showing Side Cutting Face After Turning Two Samples

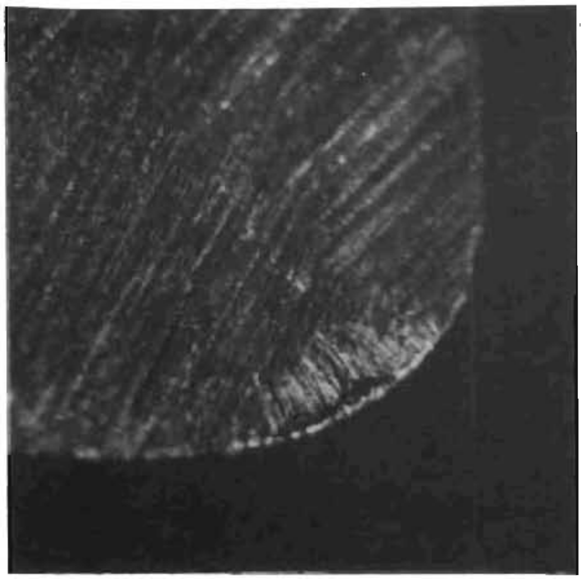

Figure 78. Formed Radius Sample 17.4 PH Cutting Tool, 0.033- x 0.033-Inch Plain Photo Showing Top Face After Sample Turning

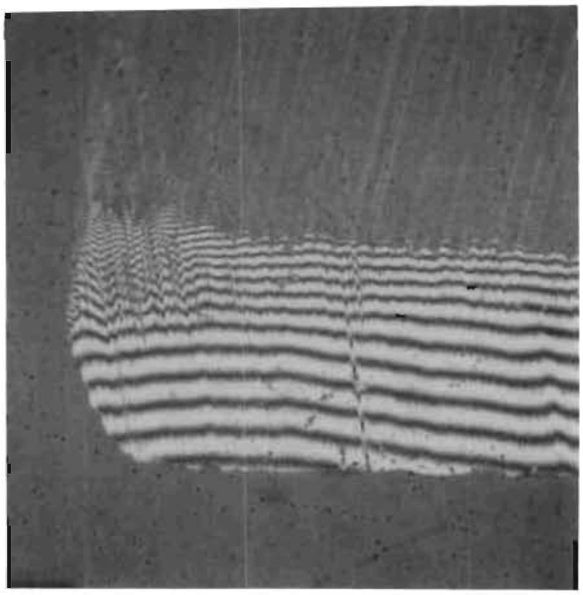

Figure 79. Formed Radius Sample 17.4 PH Cutting Tool, 0.033-x 0.033-Inch Interference Photo Showing Top Face Prior to Sample Turning

A third tool, still of the same type, was lapped and a ~ 0.012-inch radius formed as shown in Fig. 79. Using a noncritical roughing tool to take a 0.005-inch preparatory cut, the formed tool followed with a 0.002-inch cut, taken dry but under the same feed and speed conditions as the self-generated radius parts. There appeared to be negligible tool wear and, while the sample part looked nearly the same as the first samples, it was slightly rougher and more wavy as evidenced by Profilometer readings.

Part	Profilometer Surface Roughness Arithmetic Average, Microinch, 0.0005-Inch Stylus Tip Radius					
	Cutoff, inches					
	Cross Lay			With Lay		
	0.03	0.01	0.003	0.03	0.01	0.003
Sample, self-generated tool radius	2.4	1.9	1.9	2.5	1.5	0.8
Sample, formed tool radius	3.7	3.5	2.9	2.5	1.9	1.5

At this point, it was decided that the self-generating radius approach was more likely to produce the desired surfaces and no further experimentation was performed.

Turning Experiments, Aluminum

Turning fine surface roughness aluminum parts proved to involve no major problems and minimal experimental effort was expended. While detail procedures are reported in the specific model description, the following general requirements evolved:

1. Tool: high-speed steel with chip breaker and fairly sharp nose radius
2. Speed: approximately 150 sfm
3. Feed: approximately 0.0003 in./rev
4. Final depth of cut: 0.005 inch
5. Lubricant: kerosene

Model Fabrication

Although fabricated to the general no-change drawing requirements of Fig. 61 and 62, certain seating land changes were necessary when turned model surfaces were cut. To provide a positive land for inspection purposes, a relief groove was cut into the poppet face. It was found, however, that a simple diametral plunge cut at the land OD raised a burr on the edge of the seating surface. Therefore, all poppets were machined from the ID and, when the desired OD was attained, the tool was fed into the work to form the relief groove in a continuous cutting operation. The seats, although having basic fabricated relief grooves, were cut in the same fashion. The outer lapped land was not cut. Setup concentricity on poppets and seats was held to 0.000050 TIR. Specific surface fabrication data are tabulated below.

Model	Average Cutting Speed, sfm	Nominal Feed, in./rev	Final Cut Depth, inch	Cutting Fluid
Q_f	45.5	0.00069	0.0030	Meyers Miracle
N_f	56.5	0.00029	0.0020	Meyers Miracle
R_f	115.5	0.00031	0.0050	Kerosene
S_f	166.0	0.00029	0.0050	Kerosene

FLAT-GROUND MODELS

To permit evaluation of surface texture resulting from grinding operations, two representative models were made; one with unidirectional lay, the second having nearly circular lay. These model surfaces were fabricated on a linear reciprocating surface grinder with rotary table attachment capabilities. A perfect circular lay is not possible with this machine as the grinding wheel turns at high speed in a plane normal and tangential to the surface of the relatively slowly rotating workpiece producing a series of short tangential cuts.

The almost infinite combinations of feed rates and wheel type precluded extensive experimentation. The recommendations of experienced precision grinding machinists were evaluated in the fabrication of several sample parts. Inspection indicated these surfaces would be suitable for test, and the model surfaces were prepared in the same manner.

Both model surfaces were fabricated on a Model 612 Boyer-Schultz linear reciprocating surface grinder. Although this machine required manually operated feeds, its bearings were in better condition than available automatic machines. A fine-grit, aluminum-oxide vitrified bond wheel (38A80-J5VBE), turning at 2850 rpm (3820 sfm), was used with Richfield D.O. soluble oil grinding fluid.

For fabrication of circular lay surfaces, parts were mounted on a portable rotating table attached to the grinder bed. The part was set up to rotate concentrically within 0.001-inch TIR and wheel-workpiece centers were aligned within 0.001 inch. At the point of contact, grinding wheel and workpiece rotated in opposite directions with the wheel turning at 2850 rpm and the table at 73 rpm.

The model surfaces were fabricated as follows with the final passes made at zero depth of cut to a sparkout condition:

Model and Lay	Workpiece Speed Relative to Wheel Contact Point, sfm	Workpiece Feed		Depth of Cut, inch
		in./rev	in./pass	
Model D_f Unidirectional	6.5	---	0.005 to 0.010	0.0001
Model A_f Circular	9.0	0.00045	---	0.0002

PROCESSED MODELS

Except for the anodized aluminum models, the noted processes were applied to previously fabricated and tested surfaces to evaluate and compare the process effect on sealing capabilities.

Liquid Honed

Many static sealing surfaces are liquid honed to improve basic fabrication-caused roughness. The resultant surface is generally quite uniform in appearance and is sometimes referred to as a satin finish. One test model was made to investigate the surface and sealing characteristics of this process.

The liquid-hone process employs a slurry of water and abrasive pumped to a pressurized gas-fed nozzle and directed at the workpiece. The extent to which the surface is changed is dependent upon nozzle-workpiece spacing, pressure, abrasive, and exposure time variations.

Sample 440C stainless-steel surfaces were unidirectional diamond lapped to approximately 1-microinch AA and subjected to various combinations of process time and particle velocity using 320-grit, aluminum-oxide abrasive. The fine-base surface was chosen to ensure that a terminal finish (the best to be attained with the abrasive used) would be produced.

These experiments indicated that, with the workpiece 6 inches from the nozzle and a supply pressure of 25 psig, near 100-percent surface change (process density) was achieved after 20 seconds exposure time. Appropriately masked to provide an unhoned comparison surface outside the seating area, Model I_f was processed in this manner.

In the course of abrasive blasting experiments, the glass bead buffing process was investigated briefly also. This concept considers that the workpiece is peened to improve the existing surface and base metal is not removed or "appreciably" disrupted. This may be true for rougher or softer material surfaces. It was found, however, that in both wet and dry systems using 0.001- to 0.003-inch-diameter beads, when pressures and exposure time of sufficient magnitude to cause discernible change in the 440C sample surface were used, the beads shattered on impact, cutting the test surface. To achieve 100-percent process density, the surface was so degraded as to be nearly identical to the liquid-honed samples and no further investigations were performed.

Passivated

Many rocket engine valve parts are passivated as a routine matter of course. The process is generally considered to perform two functions: (1) supercleaning where embedded metal chips and fabrication residue are removed, thus rendering the surface "passive" to corrosive attack, and (2) the formation of an extremely thin protective oxide film.

Test Model J_f, with 1-microinch AA unidirectional lapped poppet and seat surfaces, was subjected to a standard passivation process (Rocketdyne Process Specification RA0110-018) consisting of cleaning, immersion in a solution of 20- to 55-percent (by volume) nitric acid and deionized water at 135 F for 30 minutes and subsequent hot-water rinse.

Anodized

Although 6061 aluminum alloy is often not anodized, tests of untreated models resulted in gross surface plastic deformation. To provide a more stable surface, Model U_f and V_f seats were chromic acid-anodized (after geometrical surface preparation) per Rocketdyne Process Specification RA0109-021 (MIL-A-8625).

Gold Plated

The use of gold plate as a soft interfacial sealant was investigated by plating the model seat member only. One conical and two flat models were processed to evaluate thick (40 to 60 microinches) and thin (10 to 20 microinches) coatings. A standard electrolytic plating process was used (Rocketdyne Process Specification RA0109-005). Because all parts were made of 440C stainless steel, a 5- to 7-microinch nickel strike was required prior to plating to ensure proper adhesion.

FLAT-LAPPED MODELS

The flat-lapped models constituted the majority of model surfaces investigated. This stemmed from established process and techniques which have proved to be the simplest for producing precision surfaces. Furthermore, many rocket engine valves utilize flat lapped seating surfaces.

Because of the subjectivity (art) associated with the lapping process, little specific data were available for the initial contract effort to produce the desired variety of surface textures (0.5 to 8 AA). As a result, available commercial lapping methods were employed. These models (reiterated herein), constitute the rougher surface textures investigated and also do not have the refinements incorporated in later follow-on models.

The mechanism of lapping is not a well-understood process. Theories for the surface textures produced herein have resulted from a study of those surfaces in conjunction with the load-leakage test which has proved to be a more accurate measure of overall geometry than any instrument utilized in the program. While the models fabricated for the initial effort were lapped by experienced mechanics, all flat lapped follow-on models were finished by the program project engineer, thus allowing first-hand experience in the process definition and also means for trial and error advancement of techniques.

Correlation of inspection and test data with fabrication methods proved to be a powerful tool in directing the overall experimental fabrication approach. This led to progressive improvements reflected by the follow-on models. These are reported in the Experimental Test Program section in near-chronological order.

General methods for surface finishing the flat lapped models are described in the following paragraphs. Features peculiar to any one model are identified in the surface description given in the specific test model sections.

Loose Abrasive (Wet) Lapped

In loose abrasive lapping, rolling particles wear the workpiece (and lap) by occasional cutting. The abrasives are held in suspension by a special compound which is diluted as necessary with kerosene or similar hydrocarbons to maintain a wet slurry of abrasive and carrying agent. Because of the relatively large amount of compound required, inexpensive grits such as aluminum oxide are most often used. A feature of many abrasive grits is that they wear or break down readily into smaller crystals so that a progressively finer surface finish is obtained with continued use. Unfortunately. this breakdown is not uniform and deep scratches often occur.

The texture produced from wet lapping is a multidirectional matte appearing surface composed of a distribution of hills and valleys. This is caused by the changing path of the workpiece on the lap. Deeper pits and scratches caused by larger particles are generally not visible due to the overlay of smaller texture (near light wave length in dimension) within these larger defects that results in their visual merger with the general texture. (Many sealing surfaces are being produced with the erroneous concept that the matte texture provides the best sealing characteristic, primarily due to the obvious scratches and flaws evident with more reflective surface finishes. A little polishing generally suffices to brighten matte surfaces and reveal otherwise hidden defects.)

Figure 80 shows a test part being lapped. While unused compound is nearly white, the mixture is rapidly turned black from the myriad of metallic lapping chips. This is one measure of the metal removal rate.

The goal of the initial contract effort was to vary the surface roughness from 1/2 to 8 AA in incremental steps while keeping the other surface parameters constant. The action of a variety of compounds on 440C steel

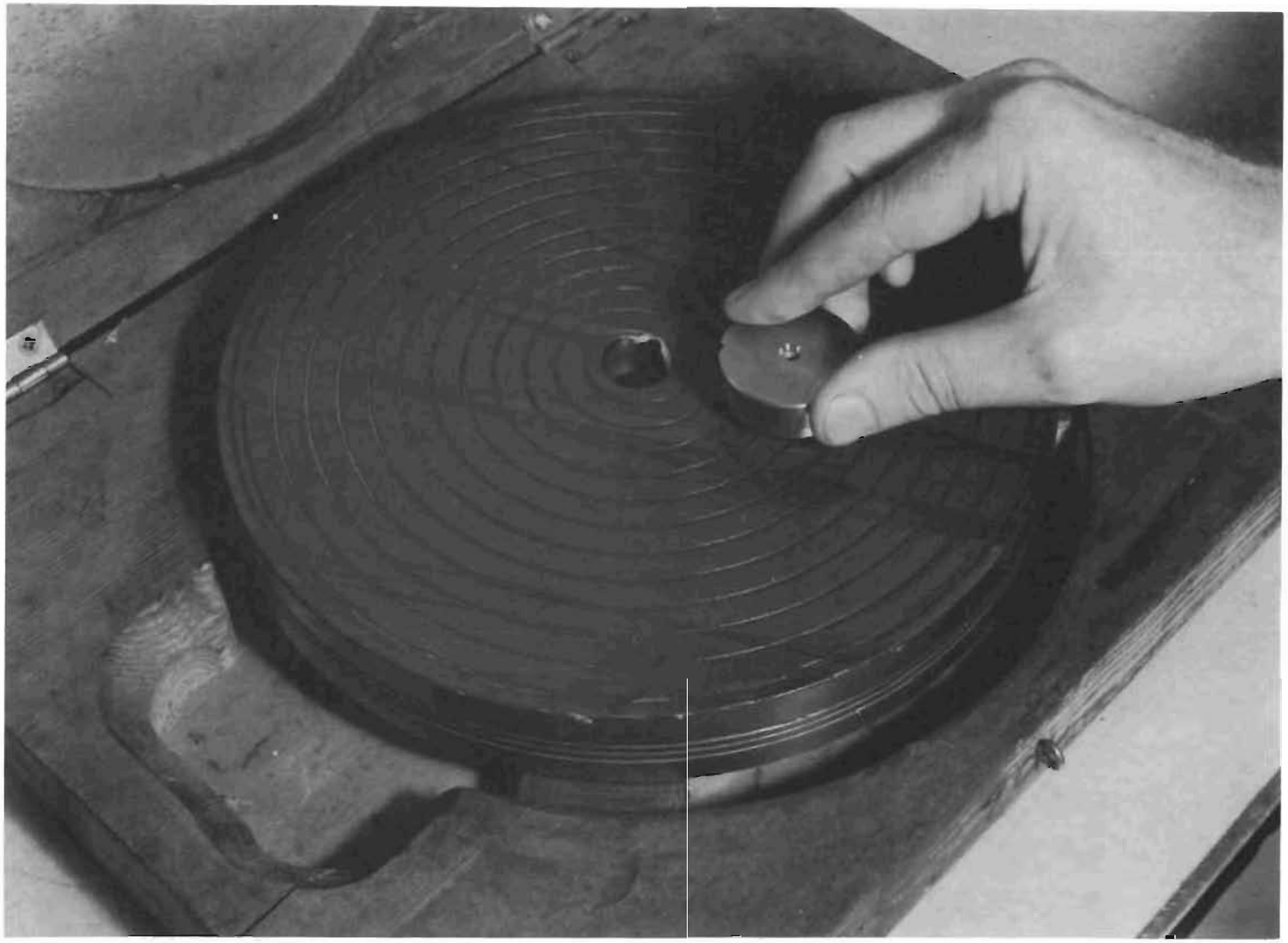

5AJ81-9/17/63-C1A

Figure 80. Test Part Being Lapped

test parts was investigated before defining a final-finishing method; these included aluminum oxide, silicon carbide, and corundum. The normal surface roughness on a production lapped part was 2- to 3-microinch AA (0.03-inch cutoff) as lapped with a 900-grit aluminum oxide compound (Models A, seat only, and B). Unfortunately, semiuniform surfaces above this roughness level were very difficult to achieve. The major problems with the rougher surfaces were severe scratches and edge rounding (or duboff). By trial and error, nearly uniform surfaces of 4 (Model C) and 6 (Model D) microinches AA were achieved using 280-grit corundum compound. Both surfaces were obtained with the same compound but at different stages of compound breakdown.

The test parts used for the evaluation of material properties (J and K) and gross geometry errors (H and I) were prepared with the 900-grit aluminum oxide compound to a nominal 2-microinch AA roughness.

Inspection of the surface texture under the interference microscope required a reasonable degree of reflectivity; therefore, most of the test poppets and seats having a matte texture were lightly polished. The exceptions were the 4- and 6-microinch AA surfaces (Models C and D) where a rough texture was of interest. Polishing of these surfaces to a reasonable degree of reflectivity would have reduced the roughness by as much as 50 percent.

The polishing operation realigns the surface texture, leaving shallow, smooth-sided troughs made up of facets inclined at small angles. Realignment of these facets at nearly the same angle produces a highly reflective configuration which is the visual characteristic of a polished metal surface.

The compounds used for polishing are generally very fine. For the test poppets and seats, 1200-grit aluminum oxide compound was used. Bond writing paper taped to a precision flat granite surface plate provided the necessary resilient lap to retain the compound.

Diamond Lapped

Diamond lapping is usually performed with much less compound (in some cases almost dry) than the loose abrasive process previously described. This is due primarily to the high cost of diamond compounds. The theory of cutting is that the diamond particles are embedded into the lapping plate with a myriad of minute cutting edges protruding above the compound film to shear material from the workpiece. Actually, the characteristically pitted surface produced by rolling compound grits may be obtained by using a thick film or, as previously described, a wet slurry of compound and a thinning agent such as oil or kerosene.

The surface obtained with very thin films of compound (including aluminum oxide, etc.) is basically composed of a continuous series of scratches. Because of the relatively long lengths of the scratches with respect to light wavelength, diamond lapped surfaces are relatively mirrorlike. With specular surfaces, scratches down to only 1-microinch deep may be discerned without magnification by proper orientation of the surface toward a bright light.

All of the 440C follow-on models were diamond lapped. Considerable experimentation was performed to produce suitable models of different geometry for comparison of the surface roughness parameter. Consequently, lapping methods were developed to produce several extremely fine surface textures. It is emphasized, however, that such methods were aimed at producing only a few models and, therefore, do not represent the evolvement of any production technique.

Meehanite cast iron was employed for the basic lapping plates. These plates were 6 inches in diameter with 0.06-inch concentric circular grooves spaced at 1-inch diametral intervals. The plate surface was initially prepared by machine flat lapping with 900-grit aluminum oxide compound to a 10- to 20-microinch, full-crown (convex) condition. This allowed for lap wear while maintaining poppets and seats flat within 2 microinches over the 1/2-inch seat diameter.

The surface was then ultrasonically cleaned followed by hand lapping with a hardened steel part using the final grit-size diamond. This adequately removed the softer 900-grit compound. Paste compounds of "Pressure-Tested"* diamond grits having a medium concentration were used with the above plates for all diamond lapping.

Wear of the lapping plates from use was quite variable and depended primarily upon the amount of lapping performed with loose compound. Wear was considerably less when lapping with a fixed thin film which did not coat the workpiece. Continuous inspection with an optical flat allowed the plates to be kept in a reasonably flat condition by distributing the wear. However, reconditioning was required after about 3 hours use.

Preliminary preparation of the test models before diamond lapping consisted of a multidirectional lapping of both faces to about a 2-microinch AA roughness. Parallelism across the 1/2-inch seating diameter was held to within 10 microinches.

Unidirectional Lay. Test models A (poppet), F, and G, fabricated for the initial effort, were hand lapped using a 4- to 8-micron diamond. The final surfaces, however, bear little resemblance to the as-lapped condition because of a variable amount of polishing (see model inspection data).

Models G_f, X_f, Y_f, I_f, J_f, T_f, W_f, and P_f, finished for follow-on contract tests, represented the basic standard from which other variables were studied. These models were all lapped to a nominal 0.7-microinch AA roughness as follows:

1. A 6-inch plate was coated by distributing light spots of 1- to 5-micron compound at 1-inch intervals over the plate and then smearing with the finger.

---

*Diamond Tool Research Co., Inc.

2. The plate was then run-in with a hardened steel cylinder to create a uniform film. Benzene was used, as required, to thin the film so that a uniform thickness could be obtained.

3. The run-in part was then checked to ensure proper plate condition and the plate cleaned and recharged.

4. Poppets and seats were finished by alternately lapping at right angles to remove entirely the previous texture. As this is represented by the deepest scratch, up to 20 microinches was removed, depending upon film thickness and pressure.

   Thin film (light gray) and high pressure (> 3 psi) resulted in deep scratches and rougher finish. Thick film (heavy black) coated the workpiece and caused rolling grit and thus undesirable pits. The optimum film thickness, obtained by trial and error, was found to be just enough to support the workpiece and grit without coating the lapped surface. Too much benzene thinning necessitated recharging the plate. With proper film thickness, the plate appeared almost dry with a gray-black color. With this film, a uniform surface texture was obtained on the 440C models in as few as ten 4-inch strokes removing about 10 to 15 microinches of material. During stroking (about 4 in./sec), the part was made to glide freely (float) without viscous drag. This was accomplished with lapping pressure less than 1 psi. The final peak-to-valley roughness was primarily a function of film thickness and lapping pressure.

Model L_f represented an unsuccessful attempt to obtain scratch-free unidirectional seating surfaces having a peak-to-valley roughness of less than 1 microinch. After considerable experimentation, it was concluded that due to the extremely low material removal rate (about 1 microinch for 400 inches of lapping), the probability of lapping out a 5-microinch-deep scratch without causing another one was remote. Consequently, model L_f was finished to a nominal 0.3-microinch AA with approximately 60 scratches about 30 microinches wide and less than 3 microinches deep.

The procedure followed for lapping model L_f consisted of:

1. Poppet and seat were diamond lapped to 1-microinch AA as noted above.
2. A 6-inch plate was charged with 0- to 1-micron water-soluble lapping compound.
3. As before, development of the correct lapping film was necessary to ensure minimum scratching. With this compound, the film was obtained by alternately spraying (sparingly) with benzene and lightly wiping with a Kimwipe tissue to distribute and remove excess compound. The workpiece was then gently laid on the lap and unidirectionally stroked to develop further the final film thickness. If the correct amount of compound was on the lap, this occurred within several strokes and the part was then alternately right-angle lapped to remove previous textures.

The point at which to stop lapping and accept the results of the above procedure is a matter of personal judgment. Many times during the course of refinishing various models, additional strokes were taken to make slight improvements only to have the surface ruined (at least for use as a test model) by deep scratches. It should be noted, however, that one or a few deep scratches may contribute an insignificant amount of leakage under a given loading. Knowing the desired loaded leakage of a typical model, the scratch leakage may be computed from the equations and curves presented in the Seating Analysis section.

Tungsten carbide poppets of models R_s and S_s were finished as above. Because of the extreme hardness of carbide, scratching was minimal and very uniform texture was obtained in considerably less time than the 440C models.

Circular Lay. Circular lay as applied to most surfaces is a misnomer. The American Standard (Ref. 1) defines lay as "the direction of the predominant surface pattern, ordinarily determined by the production method used." Because most drawings do not specify production methods, the parameters of lay circularity are undefined.

Initial attempts at hand diamond lapping circular lay surfaces proved unsatisfactory. While pleasing to the eye, microinterferometric inspection revealed the surface texture to consist of a criss-crossing of scratches which would tend to decrease the efficacy of this technique.

A series of experiments was undertaken utilizing a lathe for turning the model while machine feeding a small lap across the seating face. The setup for lathe lapping is shown in Fig. 81. The fixture for loading and positioning the lap consisted of a spring-loaded plunger with a 3/16-inch steel ball socketed in centerpoint holes provided in the plunger end and backface of the lap. The self-aligning lap was restrained from turning with the workpiece by guide ears on the plunger holder (Fig. 82).

To maintain flat surfaces, it was necessary for the lap load to be distributed between the wider outer land and the seating surface. It was also found that the entire seat diameter could not be enclosed by the lap (Fig. 82) as the lapped surfaces had to be kept barely wet with benzene to avoid sticking. This requirement precipitated the rework of the relieved poppet land as shown in Fig. 64.

Detail procedures and requirements which evolved for lathe lapping are summarized below:

1. The lap (consisting of a rectangular block of Meehanite, 5/8 x 15/16 x 0.30 inch, containing a 45-degree crossing of 1/16-inch-wide grooves on 3/16-inch centers) was conditioned flat within 2 microinches convex using the final diamond grit and then cleaned.
2. A thin smear of diamond compound was spread on the lap and an even film distributed by running-in a small steel block.

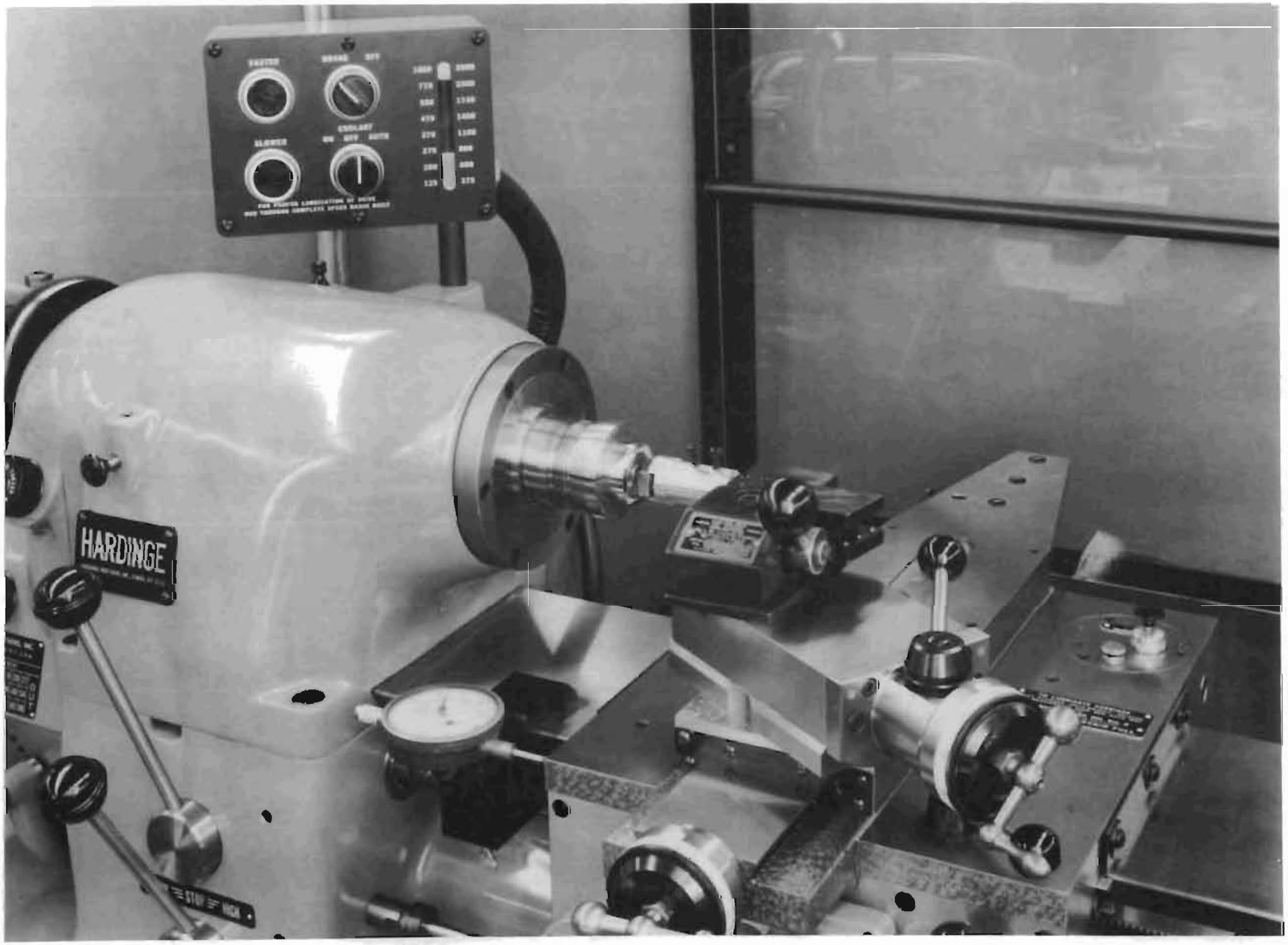

6AD41-3/16/66-C1F

Figure 81. Lathe Setup for Circular Lay Lapping Flat Surfaces

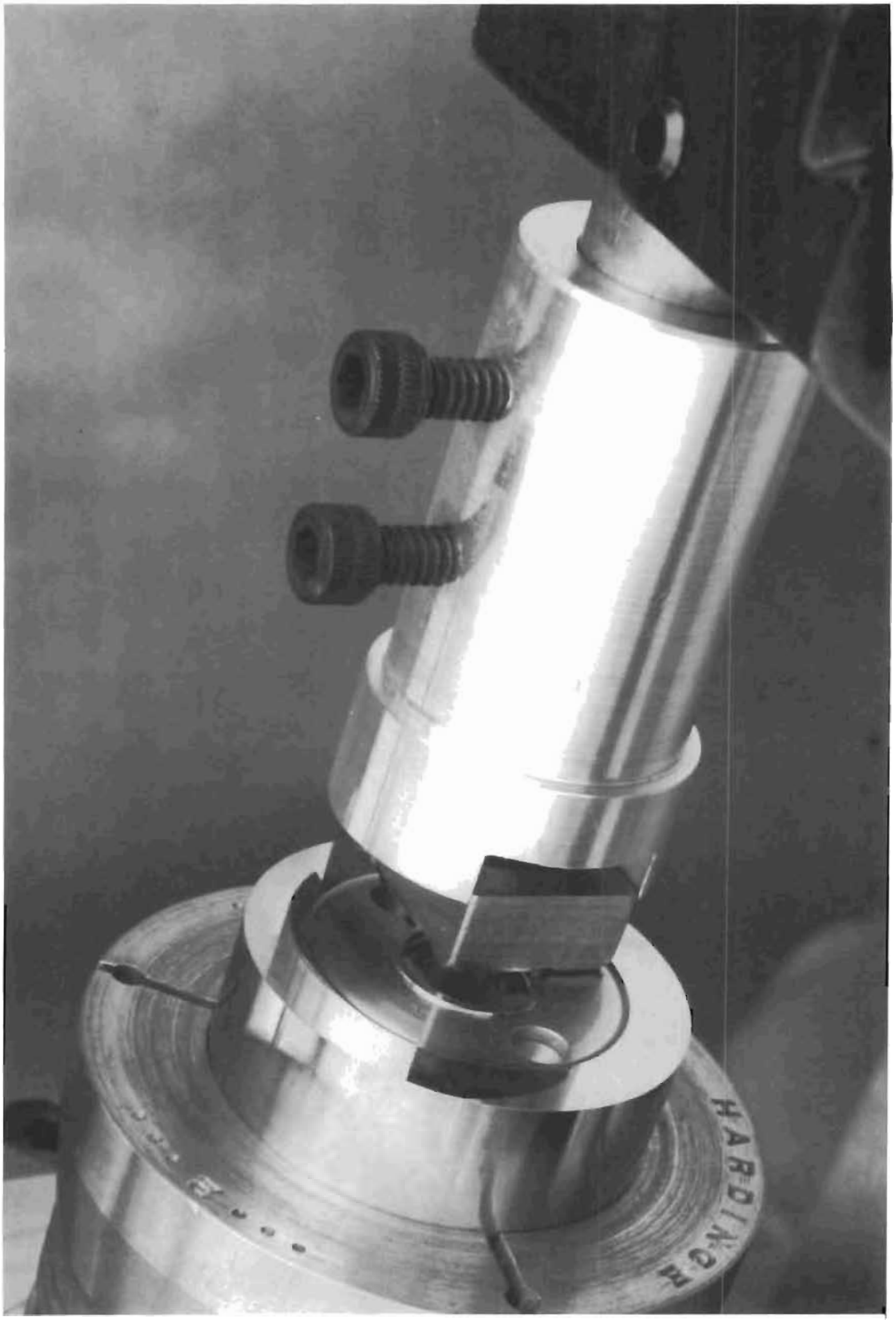

6AD41-3/16/66-C1E

Figure 82. Circular Lay Lapping Fixture

3. With the lathe running at 250 rpm and 0.005 in./rev (compound) feed, the seating face was wet with benzene and immediately followed by loading of the lap to the seat with 0.3-pound force (about 4-psi contact pressure for the actual bearing area). Crossfeed was alternately reversed (without stopping lathe) so that lap load was balanced between the seat and outer lap land.

4. The seat face was periodically sprayed with benzene to maintain a barely wet interface between lap and seat. Black deposits at the lap edge were indicative of cutting.

5. To eliminate most radial scratches a part was run about 5 to 50 minutes, depending upon prefinish,with intermediate lap recharging. While deep radial scratches (10 microinches) caused long running time, wide scratches (> 100 microinches) or flaws could not be removed by too fine a compound as the tendency was to lap inside the scratch. Consequently, the prelap finish consisted of about the same roughness level as the final nominal circular lay roughness.

To compare with previous unidirectional finishes, circular lapped models were prepared using 1 to 5 (B_f) and 0 to 1 (H_f and CC_f, including tungsten carbide poppet) micron diamond compounds.

Corner Duboff and Crowning. During the test effort (later described) it was found that sharp corners (< 0.0001-inch radius) were being fractured. Corner breaks were therefore provided on additional model seats (S/N's 009 through 012) as shown in Fig. 63. While the added land edge backup material precluded further fractures, a corner discontinuity still resulted from flat lapping which caused high contact stresses at these locations. During fabrication of early models, it was found that corner duboff was a natural result of lapping on a resilient surface (such as bond paper on a granite flat). Moreover, by varying lap time, amount of compound, and pressure, the dubbing could be varied from a small edge roll to almost a full land crown radius.

All flat diamond lapped models were lightly polished using a completely wiped-in film of 1200-grit aluminum oxide compound on bond paper. This consisted of about five swirling rubs which improved reflectivity but did not noticeably dub the corners. Later models, however, were intentionally predubbed before final finishing (see models Y_f, G_{f1}, H_f, T_f, W_f, and P_f) to provide a more uniform seating stress.

The development of the dubbed land led to the improved circular lay, full-crowned seats of models M_f, AA_f, and Z_f (poppet also). These crowned models were finished in the following steps.

1. The seating surfaces were unidirectional lapped with 1- to 5-micron diamond compound followed by polish dubbing. Too-heavy polish caused enlargement of minute flaws or pits.
2. The seat was then set up on the lathe as before, except the lap and ball joint axes were made coincident with that of the seat. For a resilient lap, a piece of 3/8- x 5/8-inch micarta (3/8-inch depth) with a polished flat lapping surface was used. This was charged with a thin film of 1- to 5-micron diamond compound using a small steel block.
3. With the lathe running (as before) the seat surface was wet with benzene immediately followed by loading of the lap to the seat with about 2 pounds of force. Depending upon charge, predub and scratches to be removed, 1 to 5 minutes were required to finish a seat. Benzene was used, as necessary, to keep the lapping surfaces barely wet.

CONICAL MODELS

With conical models, the basic fabrication problem is to match the included angles of poppet and seat. For a given leakage requirement, the maximum differential for good design (i.e., low peak contact stress) is a complex function of the loading and surface roughness since these factors are interrelated with the load variable land width. Some insight into the problem may be gained by comparison with the crowned land geometry. For a crowned seat of 10.0-inch radius ($Z = 11.3$ microinches) the apparent flattening stress (Fig. 34) for a 0.03-inch land is about 10,000 psi. Neglecting the edge effects which will lower this value, the maximum contact stress (σ_c) is 12,700 psi ($4/\pi \times 10,000$).

A tapered land of the same gap would have nearly the same geometry and volume of metal to be displaced in developing a full land width. Because of the higher contact stress at the contacting taper edge, the flattening load should be something less than that of the crowned model. It would seem reasonable, therefore, that the taper gap for model valve seats being considered should not exceed, say, 15 microinches for a working apparent contact stress of 5000 to 20,000 psi. Below 5000 psi, land width is likely to be low, whereas above 20,000 psi, the peak contact stress could cause plastic deformation of the mating surface for many material combinations. (A possible solution to this might be the use of a poppet suitably harder than the seat. However, this is no assurance that the poppet will not be plastically deformed as concentrated contact pressure in constrained areas may be many times greater than unrestrained plastic flow pressures which are nominally three times yield strength.)

As might be expected, holding taper differential to 15 microinches over a 0.03-inch land proved quite difficult. The corresponding differential half angle, $\Delta\theta = h/L = 0.0286$ degree = 1.72 minutes, required a match setup in a Hardinge lathe. To establish a normal reference plane, the lathe faceplate was turned in place.

Prefinishing of the seats (A_c, B_c, C_c, and D_c) consisted of diamond turning the seating land from a sharp corner on the lathe (after heat treat) at a predetermined compound angle. The cone was then cast-iron form lapped at 250 rpm, followed by hand cast-iron stick lapping with 0- to 2-micron diamond compound to produce a nominal 1-microinch AA roughness.

The poppets matched to the above seats were made the same except conical geometry was initially obtained by grinding, followed by diamond turning with form lapping ommitted. By locking the lathe compound in one position for a basic angle, differential angle between cone axes (tilt) was maintained below 5 microinches over the 0.03-inch seating land. This was monitored by using the compound ways as a reference plane in conjunction with an electronic gage.

While the conical models produced were probably better than most conical valve seats, they contained serious errors of form. Most serious was a waviness out-of-round condition on the poppets generated in grinding and elastically followed by the diamond tool in turning. These deviations were missed during fabrication but were readily apparent from Proficorder traces (see inspection data). A second error resulted from hand stick lapping in which natural rocking caused corner dubbing and seat crowning. Although crowning was accepted as a desirable condition, these models did not meet requirements for comparison with the flat models. Furthermore, because of the number of superimposed errors, assessment of performance characteristics was difficult. Consequently, additional 41-degree models were made to preclude these errors.

Models E_c, F_c, and G_c were fabricated as above except both poppet and seat were form lapped to ensure reasonable roundness. To obtain near-flat seating surfaces, a small wooden bob was used in a rotary tool to lap the land concave. This compensated for the convex tendency of the final stick lapping which was performed with 0- to 1-micron diamond compound at 250 rpm.

Conical lapping proved to be more time consuming and difficult than any other process used. It is likely that a production-oriented setup could be devised in which a pair of aligned precision spindles are employed to fabricate and position multiple conical laps and thus eliminate hand-lapping errors. Multiple laps would be necessary as they are not self-correcting like flats or spheres.

It is also possible that slight lapping of these poppets and seats together would have resulted in more comformable geometry.

SPHERICAL MODELS

As with conical seating, land taper poses the most serious geometric seating error. An obvious advantage of the spherical geometry, however, is the self-alignment feature inherent in a ball seat.

Land taper is caused by differences between the poppet and seat spherical diameters (ΔD). This difference arises from differential between poppet and lapping ball diameters with the latter effectively increased some amount, depending upon lapping compound film thickness.

Lap Ball Analysis

In fabricating models A_s, B_s, C_s, and D_s, taper was controlled by selecting matching poppet and lapping ball diameters. This was based upon an analysis of the probable film thickness (t) and its variation with lapping. This procedure was necessary because, once lapped, the final seat radii cannot be determined with sufficient accuracy to predict the resultant differential and, thus, taper gap.

Assuming that the lap film thickness may vary from zero to (t) during final seat finishing, the resultant ball seat diameter is

$$D_{BS} \equiv D_L + t \pm t$$

$$\Delta D_{BSL} \equiv D_{BS} - D_L = t \pm t$$

where (D_L) is the final lapping ball diameter. In fabricating a seat, however, the only known quantities are poppet ball diameter and maximum allowable taper gap. A tolerance must be allowed for (D_L) to provide for lapping wear and also because an exact match is not possible. The equation for taper gap as defined in the Seating Analysis section is:

$$h = \frac{\Delta D\ L}{D \tan(\theta \pm \beta)} \equiv \frac{\Delta D}{\eta}$$

$$\beta = \frac{L}{D} \text{ (radians)}, \quad \eta \equiv \frac{\tan(\theta \pm \beta)}{\beta}$$

For bilateral tolerancing, ΔD, η, and h are defined as follows:

$$\Delta D \equiv D_{BS} \dot{-} D_P$$

$$D_{BS} > D_P \; : \; \beta \text{ is } (+); \; h_{BS} = \frac{\Delta D}{\eta_{BS}} \quad \text{and is } (+)$$

$$D_P > D_{BS} \; : \; \beta \text{ is } (-); \; h_P = \frac{\Delta D}{\eta_P} \quad \text{and is } (-)$$

In these analyses, the exact ball size is unimportant as only differentials between various ball diameters affect (h). Therefore, poppet ball diameter (D_P) is used as a datum with the lapping ball differential defined as:

$$\Delta D_L \equiv D_L - D_P$$

Combining preceding equations gives

$$\Delta D_L = (h\,\eta)_{BS} + (h\,\eta)_P - (t \pm t)$$

which basically allows a certain (±) gap variation to compensate for the unknown film thickness. In application of this equation, the bilateral (±) division of $(h\,\eta)_{BS} + (h\,\eta)_P$ must be greater than ($\pm$ t); and, ($\pm$ t) must be subtracted from ($\pm h\,\eta$).

As an example, consider the 1/2-inch ball, 19.95-degree seat with a 0.03-inch land (Fig. 73). Assuming a maximum desired gap of 5 microinches, the allowable (ΔD_L) and (t) must be weighed against each other as shown below:

$$\eta_{BS} = 7.21 \quad ; \quad \eta_P = 4.93$$

$$\Delta D_L = (5)(7.21) + (-5)(4.93) - t \mp t \quad \text{(microinches)}$$

$$\Delta D_L = -t + (36.0-t) - (t - 24.6)$$

For this case, the film thickness cannot exceed 24.6 microinches. Assuming a nominal grit size of 10 microinches (0- to 1/2-micron diamond) results in a lapping ball differential size of:

$$\Delta D_L = -10\,{}^{+26}_{-14.6} \text{ microinches}$$

A lapping ball must be selected within this range allowing for wear and measurement error. To check this results, (ΔD) is determined for the extreme limits of (ΔD_L) as follows:

$$\Delta D = \Delta D_L + \Delta D_{BS} = \Delta D_L + t \pm t$$

$$\Delta D = -10\,{}^{+26}_{-14.6} + 10 \pm 10$$

$$\Delta D = {}^{+36}_{-24.6} \text{ microinches}$$

$$h_{BS} = \frac{+\Delta D}{\eta_{BS}} = \frac{+36.}{7.21} = +5 \text{ microinches}$$

$$h_P = \frac{(-)\Delta D}{\eta_P} = \frac{-24.6}{4.93} = -5 \text{ microinches}$$

A number of 1/2-, 9/16-, and 5/8-inch 440C balls were obtained for lapping and poppet ball selection. A master ball was arbitrarily chosen from each size lot and differentials measured within about 2 microinches (as later described in model inspection procedures). Appropriate sized balls were then chosen for rough and final lapping and for the poppet.

General Finishing Procedures

The seat land was initially formed by diamond turning the heat-treated seat. Spherical geometry and land dimensions were obtained by rough lapping using 1200-grit aluminum oxide, followed by 1- to 5-micron diamond. The seat was turned at 250 rpm, while the lapping ball was finger-held socketed in the seat so that a natural angular turning occurred at a reduced speed.

For final finishing, short lengths of 1/4-inch-OD brass tubing were epoxied to the lapping balls. This allowed a better control of ball rotation and ensured minimum temperature differential between ball and seat. Lapping of model A_s seat is shown in Fig. 83. The circular lay lapping was accomplished as follows:

1. The initial lap ball was finger-coated with a thin film of 0- to 1-micron diamond compound. With the seat turning at 250 rpm, the seat ID hole was profusely sprayed with benzene and the ball immediately plunged into the seat.
2. To allow uniform lap wear while minimizing radial scratches, the lap stick was restrained to rotate at about 50 rpm with the axis angle varied from 0 to 60 degrees off the seat axis. The ball was lightly sprayed with benzene as required to prevent dry seizure. Lapping load was just enough to keep the ball in the socket.
3. A near-circular lay with minimum gap was obtained using the final ball and 0- to 1/2-micron diamond compound. During this operation, the ball was carefully located in the running seat as before, except the ball was not allowed to rotate. Angular feed (axis tilt) was varied slowly from about 45 to 10 degrees off the seat axis.
4. Sharp corners were broken and the land brightened by 15 seconds of finger-polishing while turning with 0- to 1-micron compound on wiping tissue.

Taper gap between matched poppet and seat was determined from temperature-stabilized differential measurements between poppets and respective 0- to 1/2-micron lap balls. The results are tabulated below, assuming an overall measurement error of ±5 microinches and t = 10 microinches.

Model	D, inch	L, inch	θ, degrees	η_{BS}	η_P	ΔD_L ±5, maximum, micro-inches	Δ D, maximum, micro-inches	h, maximum micro-inches
A_s	0.625	0.03	41.23	20.4	16.56	-10	-15	-0.91
B_s	0.5625	0.03	33.33	13.83	10.95	-25	-30	-2.7
C_s	0.5000	0.03	19.95	7.21	4.93	0	+25	+3.5
D_s	0.625	0.005	41.23	111.3	107.8	-10	-15	-0.135

It is evident from the above data that less gap results from: (1) a narrow land, (2) large seating angle (θ), and (3) with $D_{BS} > D_P$, since $\eta_{BS} > \eta_P$.

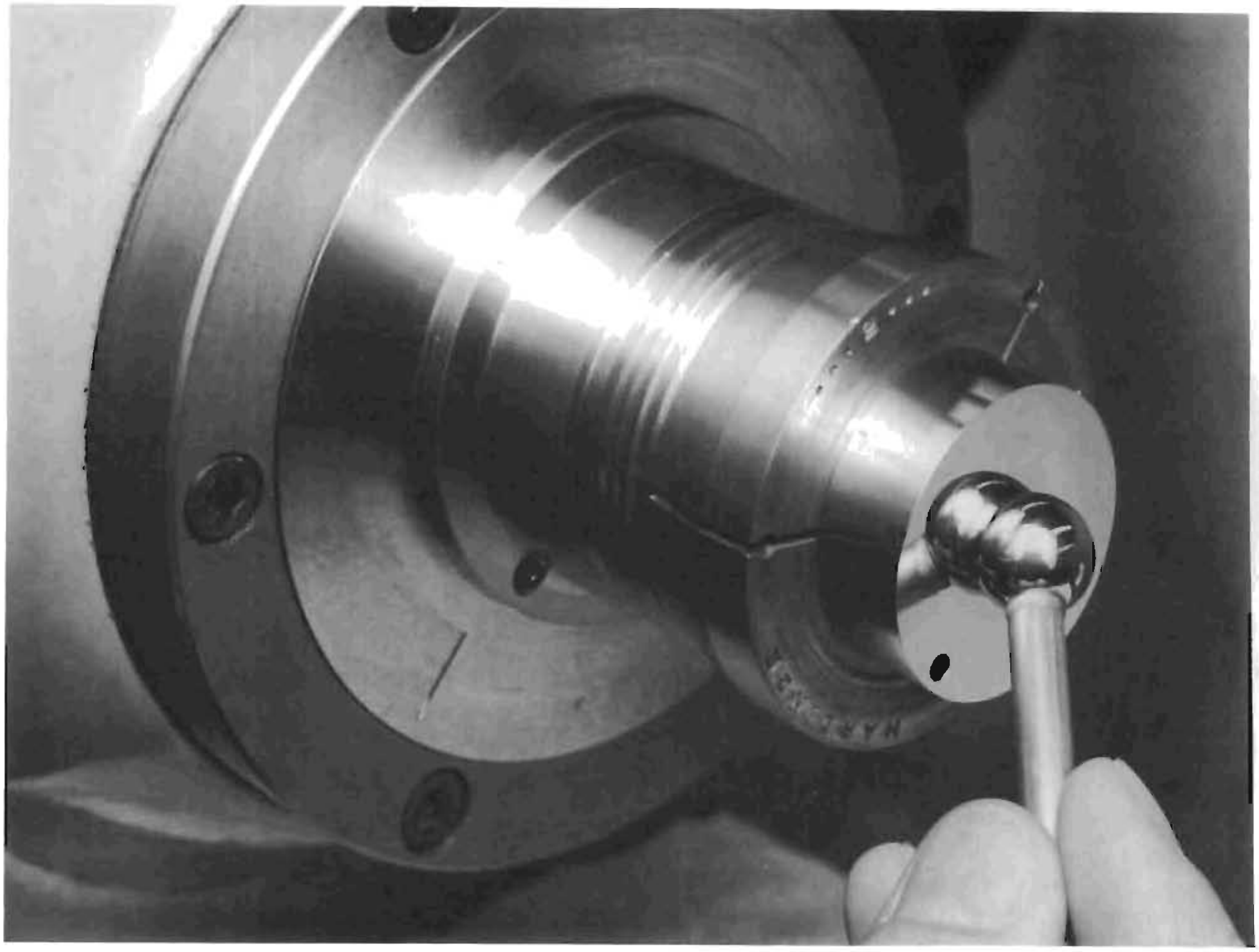

6AD41-3/16/66-C1D

Figure 83. Spherical Seat Lapping

MODEL INSPECTION EQUIPMENT, PROCEDURES, AND DATA

Poppet and seat model inspection data provide the measurements necessary to correlate configuration with test and analytical results. Because of the extremely small dimensions of surface profiles normally associated with metal-to-metal valve seating, no one piece of inspection equipment can provide a comprehensive definition of the surface in question. For example, only a small indication of the actual three-dimensional profile is obtained from a stylus instrument while optical devices give a three-dimensional view, but for measurement purposes, cover a very limited field. This results, to a degree, in a subjective interpretation of raw data from several instruments to arrive at a practical estimation of the parameters of interest.

Aside from normal inspection checks to indicate primary conformance with drawing requirements, additional parameters were considered to best define the seating surfaces and preclude erroneous test information input. These parameters were parallelism, flatness, roundness, concentricity, differential seating angle, seating land dimensions, surface texture (peak-to-valley parameter (h), average asperity angle (Φ), nodules, pits, and scratches), and surface hardness. To acquire this information, several types of optical, mechanical, and electromechanical measuring instruments were used. The following paragraphs describe this equipment and the procedures employed to obtain and interpret pertinent inspection information. A compilation of inspection data for each test model and the photographs and profile traces from which the bulk of this data was reduced is presented at the conclusion of this section.

MODEL INSPECTION EQUIPMENT

The inspection equipment used may roughly be categorized into four types--comparitor, stylus, optical, and indentation. Each has certain advantages and limitations, and the proper evaluation of these characteristics is necessary to place the measurements obtained in proper perspective.

Indicating Comparitors

One version of this type instrument uses a fixed anvil and vertically movable head to spot check height variations of a workpiece with reference to a precisely known dimension. In practice, one or a multiple stack of gage blocks is wrung to the anvil to provide the reference height for zero-setting the indicator. The reference stack is then replaced by the workpiece which is wrung to the anvil at discrete intervals under the indicator head and height differences noted. Such a device is particularly suitable for absolute height and parallel measurements within its accuracy capabilities. However, because the workpiece must be wrung to the anvil each time a new point is to be measured, a continuous indication of surface variation is not possible.

Another application of this type instrument is the measurement of differential heights relative to a common external datum. In this case, the indicating head rests on a precision reference plane and the workpiece is moved, on the same plane, under the indicator.

The two types of comparitor, mechanical and electronic, used in fabrication and inspection of the test models are shown in Fig. 84. The mechanical unit on the left is the Mikrokator made by the C. E. Johansson Gage Co., and is capable of difference measurements of about 2 microinches. This instrument was used for most model poppet and seat parallelism measurements.

For more precise parallelism inspection, the electronic comparitor shown at left center in Fig. 84 was used. This unit, the Micro-Ac, is made by the Cleveland Instrument Co. and can measure surface deviations down to 0.5 microinch, and is basically a reluctance-type position indicator coupled with a high-gain amplifier. For optimum results, this type indicator must be located in a temperature-controlled room and further isolated from drafts and operator body heat. Even the act of wringing small parts to the anvil adds sufficient heat to the workpiece to preclude instantaneous accurate measurement. During inspection of the test models, it was found that a 1.5- to 30-minute waiting period was required after initial workpiece setup to obtain consistent measurements to the nearest microinch.

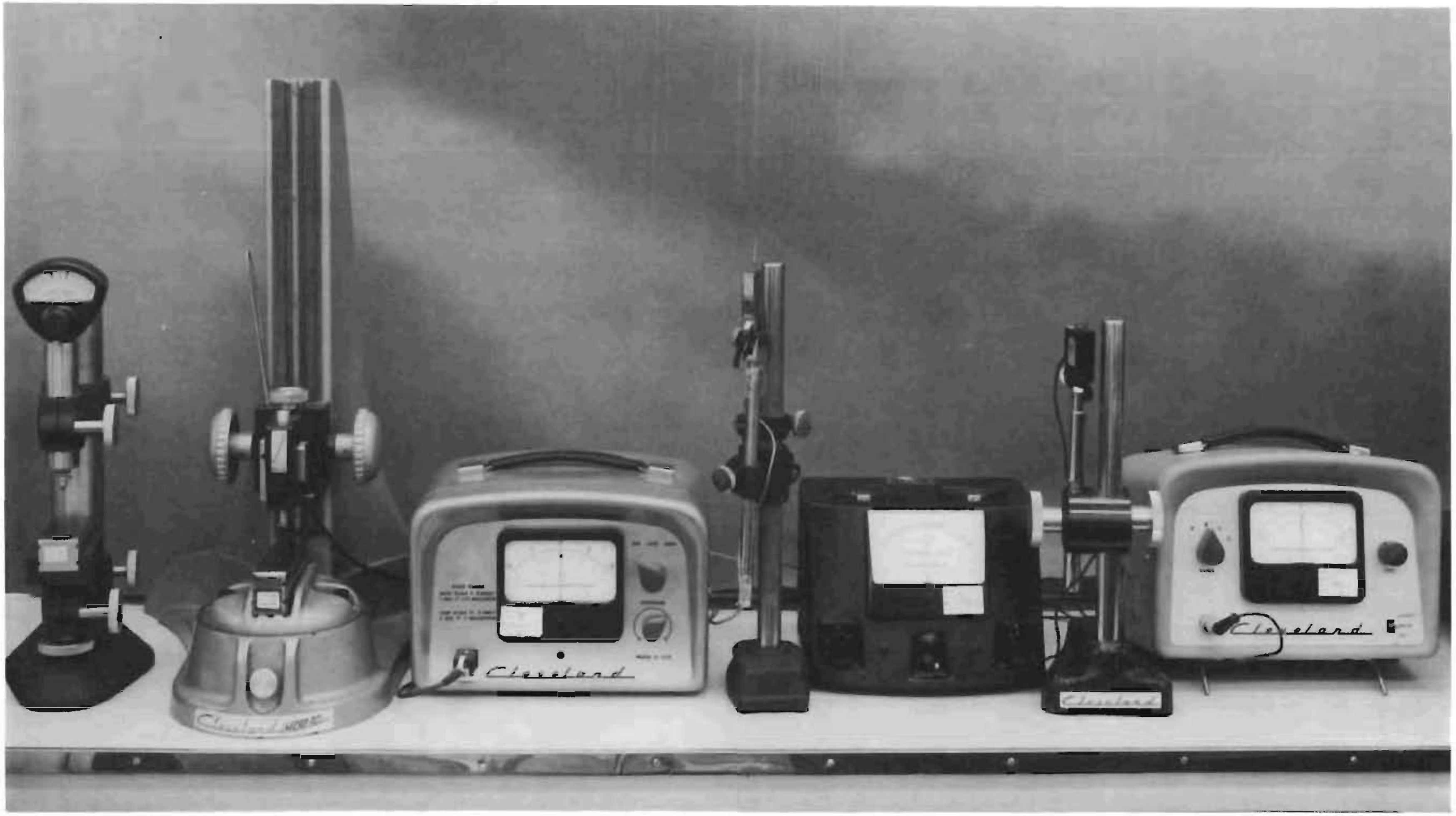

6AD41-3/16/66-C1C

Figure 84. Displacement Measuring Comparitors

The two instruments on the right in Fig. 84 are also electronic devices used for measurements relative to external reference planes. The unit at right center, made by the Merz Co., can resolve 2-microinch deviations while the recently introduced Cleveland Indi-Ac, at far right, can measure to the 1-microinch level. These instruments were used to determine tester-installed poppet and seat parallelism, near-seated test flow gaps and other similar measurements, where net deviation of a combination of parts was required.

Although the Micro-Ac due to its extreme resolving capabilities was most temperature sensitive, the measurement of dimensions on the order of a few microinches made temperature control precautions necessary in the use of all the noted instruments. However, because only differential measurements were taken, repetitive checking procedures reduced such errors near to the level of instrument sensitivity.

Stylus Instruments

Two types of stylus instrument were used in fabrication and inspection of the test models--the Profilometer and Proficorder, both manufactured by the Micrometrical Mfg. Co. The Profilometer (Fig. 85) is an electromechanical device incorporating a piloter or tracer arm, displacement head, and amplifier with meter output display. This unit, as well as the Proficorder uses a standard 0.0005-inch-radius stylus tip (supplied with a calibration plate), and a special 0.0001-inch-radius tip. The Profilometer output is readily switched between AA and rms and can be set for 0.003-, and 0.010-, and 0.030-inch roughness cutoff values. As the displacement head traverses the workpiece, the motion of the stylus generates a voltage proportional to the height of the measured surface irregularities, which is continuously averaged by the electronic system and displayed on the output meter. Therefore, the Profilometer shows the variations in average roughness height but does not indicate asperity configuration or wavelength variation greater than the set cutoff value.

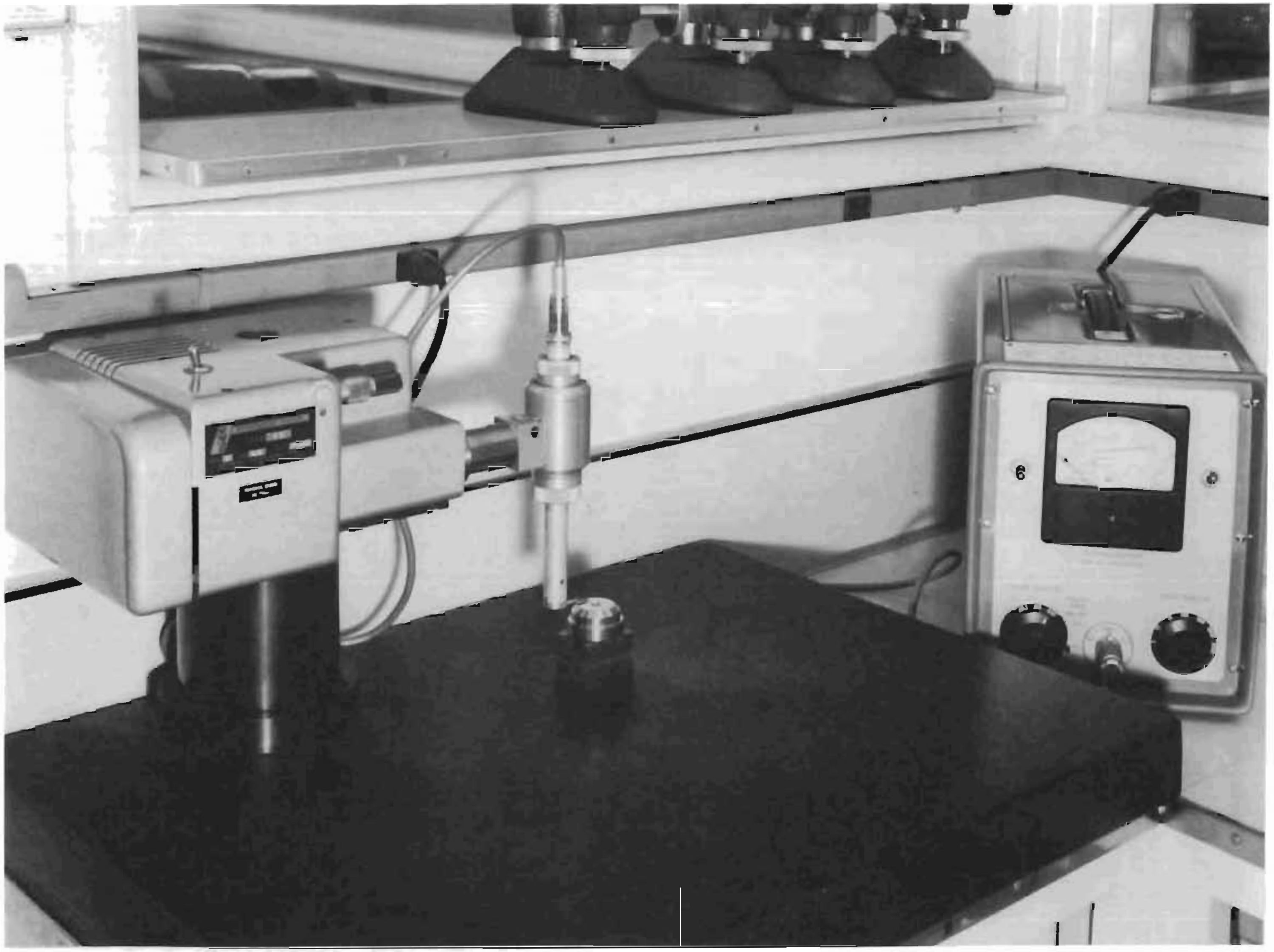

5AJ81-9/17/63-C1B

Figure 85. Profilometer and Test Poppet

For direct continuous surface irregularity measurement, including roughness, waviness, and asperity angle variations with permanent information display, the Proficorder was used. Figures 86, 87, and 88 show this instrument setup for typical measurements. The indicating head is similar to that of the Profilometer but the output is presented on a continuous strip chart permitting more discriminate evaluation of surface conditions. Unlike the Profilometer, the workpiece mounted on a rotating table moves relative to the indicating head, permitting the use of this instrument for flatness and parallelism measurements. Calibration of the Proficorder indicated a repeatable response to a 50-microinch step input accurate within 2 percent or 1 microinch. The precision spindle used in the rotary table runs true within 3 microinches.

In using the Profilometer and the Proficorder, several sources of error or extraneous inputs were encountered and evaluated. The first of these is vibration noise inherent in the instruments and from external sources. The latter problem is a function of shock mounting and isolation from ambient disturbances. Proficorder calibration checks indicated the total noise level resulting from internal and external vibration sources was less than 1 microinch.

For the particular Profilometer used during periods when nearby machinery was operating, an ambient-induced noise level of 0.7 to 0.8 microinch was noted. Accordingly, data were taken when ambient vibration was minimal. In addition, this Profilometer exhibited a peculiar vibration phenomenon apparently associated with the tracer system, which showed up particularly at the 0.030-inch cutoff level. The first indication of this problem was an observed difference between roughness values obtained on the extend and retract portions of the tracer cycle. To evaluate this condition, an optical flat was used as a test specimen and checked with the 0.0005-inch-radius tip stylus. The results, as tabulated at the top of page 266, were essentially verified by the 0.0001-inch tip stylus.

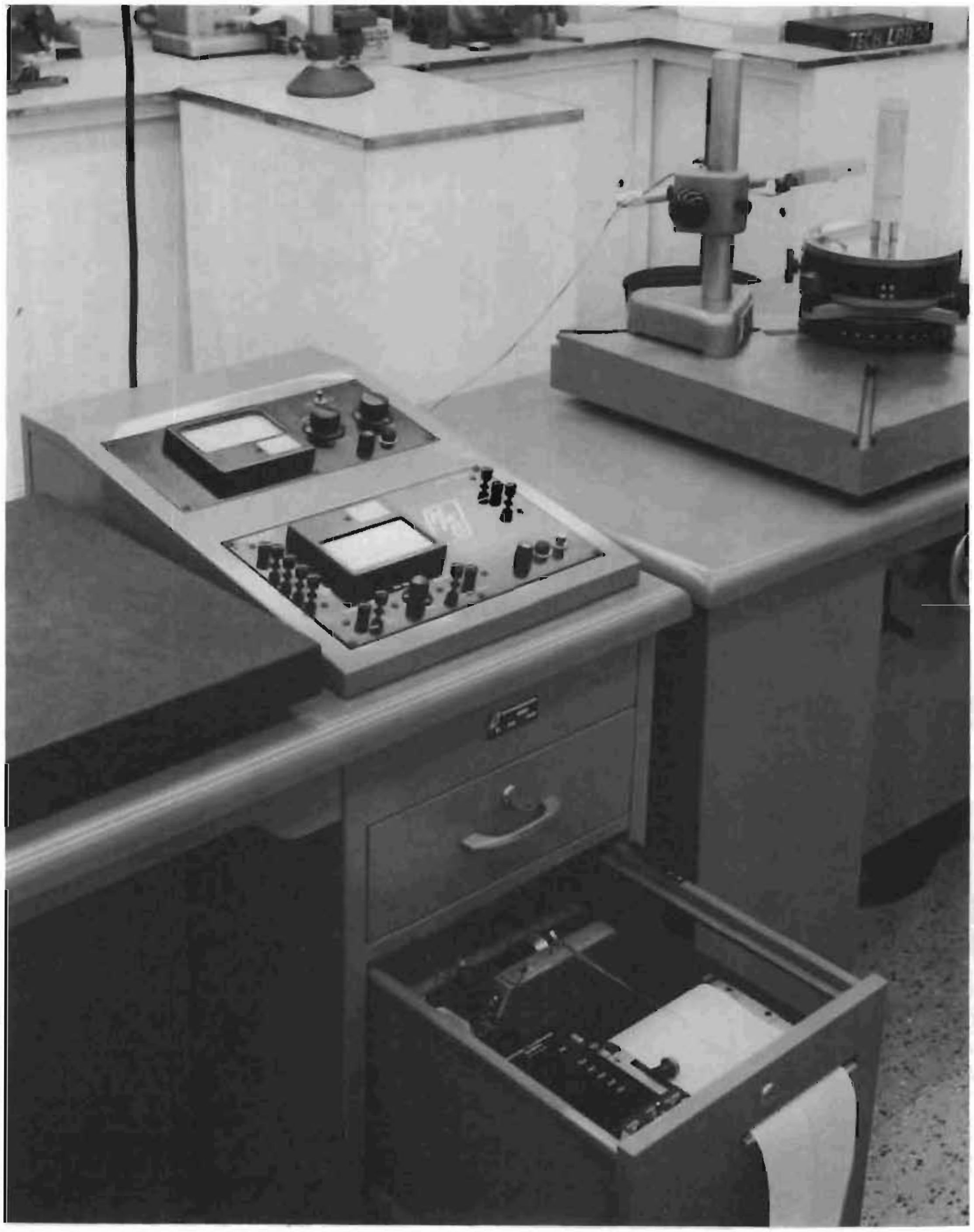

5AJ81-9/17/63-C1J

Figure 86. Proficorder Indicating Tester Piston

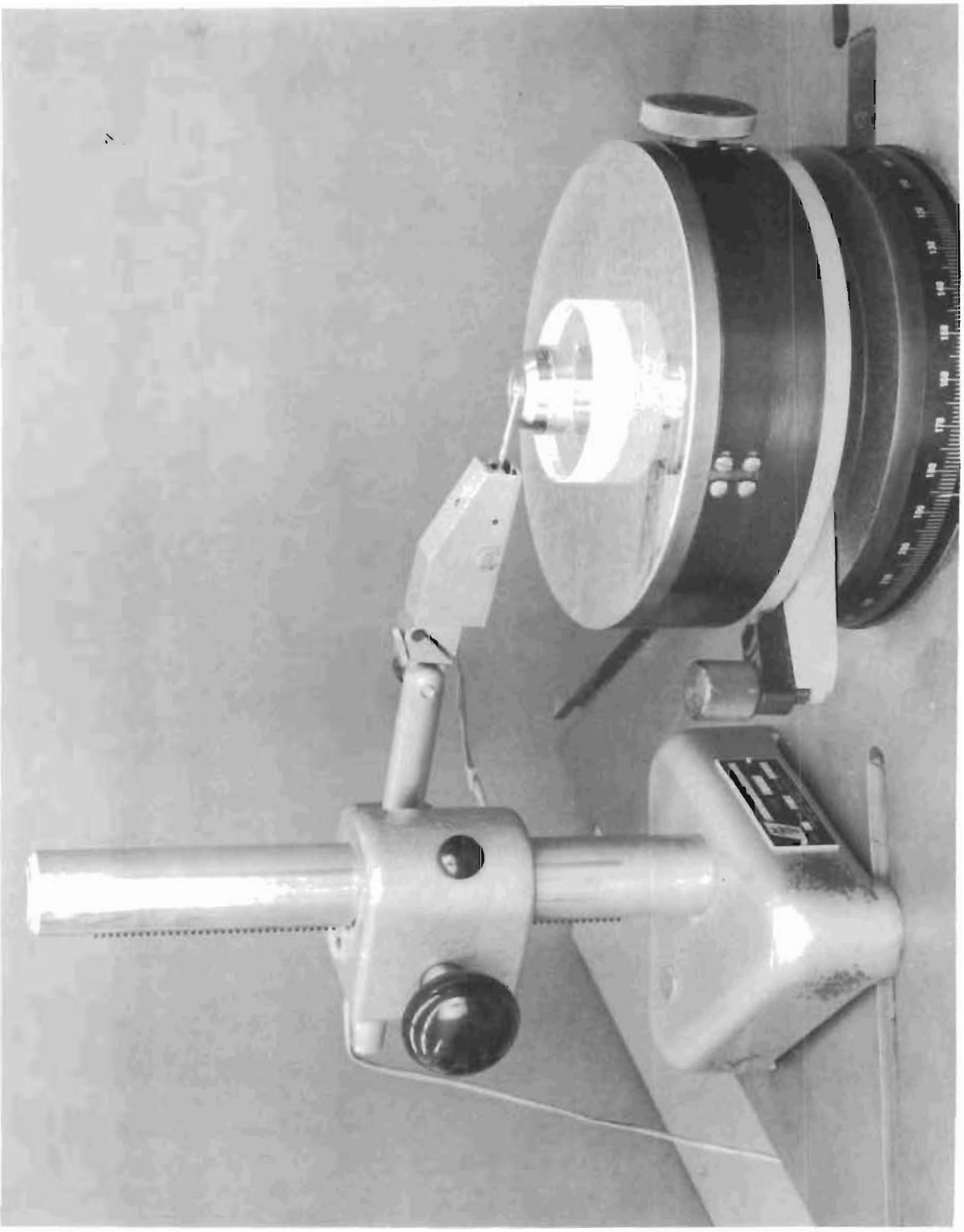

6AD41-3/16/66-C1A

Figure 87. Proficorder Indicating Test Poppet

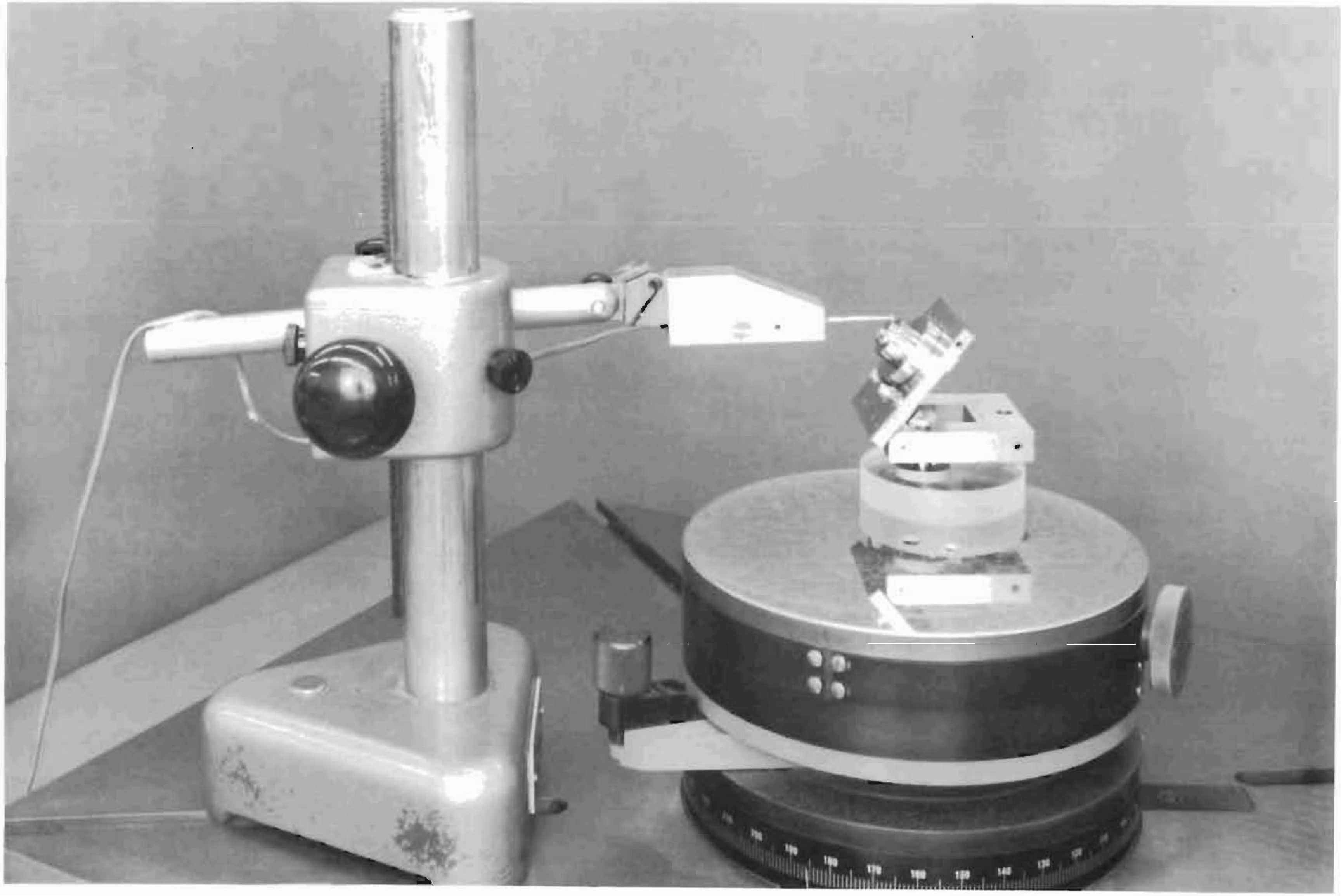

6AD41-3/16/66-C1B

Figure 88. Proficorder Indicating Conical Poppet Seating Land

AVERAGE PROFILE VALUES IN MICROINCHES AT CUTOFF NOTED				
Cutoff, inches		0.030	0.010	0.003
rms	Extend	1.7	0.40	0.25
	Retract	0.9	0.35	0.25
AA	Extend	1.7	0.35	0.25
	Retract	0.8	0.30	0.25
Ambient Vibration (AA)		0.25	0.25	0.20

Not only is there a marked difference in the extend and retract readings at a 0.030-inch cutoff, but the readings are much higher than at the other cutoff levels. The test optical flat surface profile was checked on the Proficorder and the interference microscope (Fig. 89).

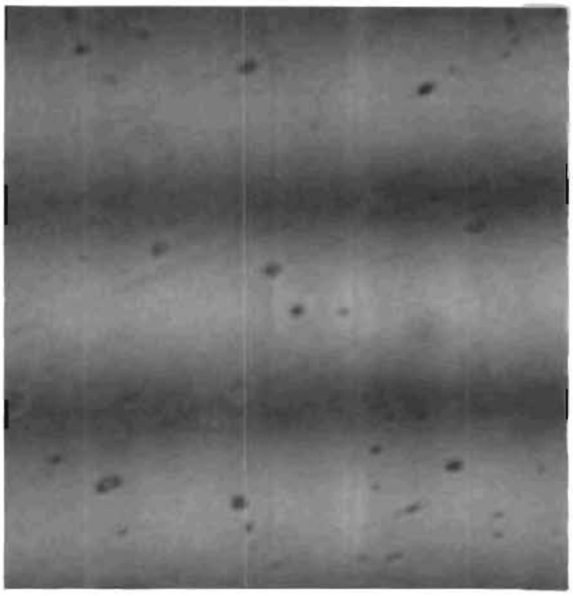

Figure 89. Optical Flat, 0.0065- x 0.0065-Inch Interference Photo (lines and dots are from optics flaws)

Both instruments indicated total surface deviation less than 1 microinch; therefore, the corresponding AA reading should be about 0.3 microinch or less. Based on this information (and the ambient vibration effect), it was concluded that readings below 1.0 microinch for the 0.030-inch cutoff and 0.3 microinch for the 0.010- and 0.003-inch cutoff were essentially meaningless for this particular Profilometer. Furthermore, only retract values were recorded for the inspection data.

The remaining errors considered apply to the stylus and include contact stress and influences of tip radius and wear on asperity depth measurements. An elastic stress analysis assuming Hertz contact shows that, for the instrument loads, stylus radii and metal surfaces under consideration, the surface will be plastically indented and plowed to some degree. The ASA standard (Ref. 1) requires a load-geometry relationship for stylus instruments as defined by the formula $P \text{ (grams)} < 10^{-5} R^2$, where R is the stylus tip radius in microinches. This requirement was met for the 0.0005-inch radius stylus, where the loads were nominally 1.5 grams for the Proficorder and 2.0 grams for the Profilometer. In the case of the 0.0001-inch radius stylus, the maximum load requirement of 0.1 gram was exceeded. The Proficorder load in this case remained at 1.5 grams whereas the Profilometer head with the smaller tip was reduced to 1.1 grams. It was therefore expected that excessive plowing might exist with the 0.0001-inch radius tip.

To consider these effects, a simple plastic analysis (after Bowden and Tabor, Ref. 6) was assumed where the bearing area is proportional to the surface hardness or plastic flow pressure. This is schematically shown in the sketch below.

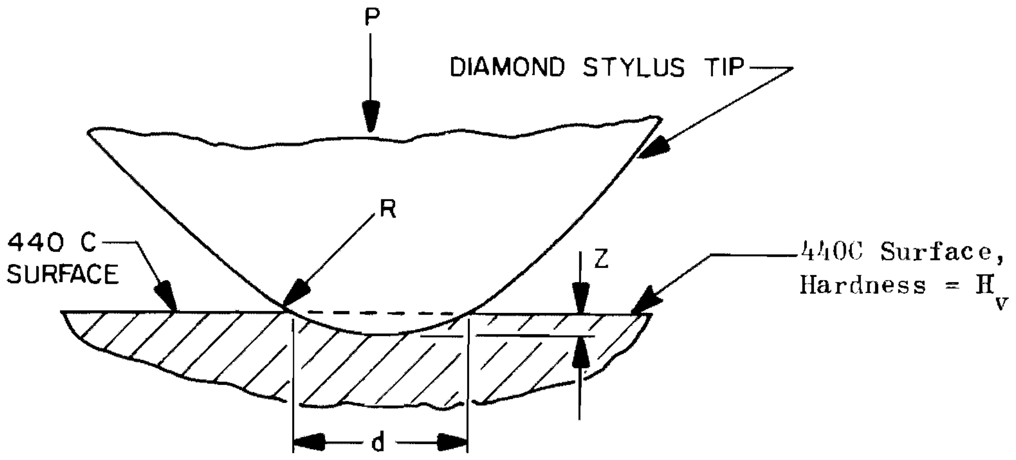

Equations relating indentation, tip geometry and hardness are:

$$Z = \frac{P}{2\pi R H_v}, \quad d = \sqrt{\frac{4P}{\pi H_v}}$$

Assuming a minimum surface hardness for 440C stainless steel of 700 kg/mm^2 (10^6 psi) results in the following table of data:

Pressure, grams	0.0005-Inch Radius		0.0001-Inch Radius	
	Z, microinches	d, microinches	Z, microinches	d, microinches
0.1	0.0704	16.8	0.352	16.8
1.0	0.704	53.0	3.52	53.0
1.5	1.05	64.9	5.27	64.9
2.0	1.41	75.1	7.04	75.1
2.5	1.76	84.0	8.80	84.0

Comparison of these data with typical stylus tracks indicates a close correlation. For example, an interference photo of Model F (presented subsequently in the Inspection Data section as Fig. 140) shows 0.0005-inch radius Profilometer tracks on a 440C surface having a width of about 75 microinches and depth on the order of 1 microinch. Additional comparisons may be made from photos of Model L_f (similarly presented under Inspection Data as Fig. 188 and 189) where the 0.0001-inch radius stylus plowed a track about 78 microinches wide and 2 microinches deep. The difference in track depths might be attributed to wear of the diamond tip radius. At these dimensions, variations from the pure radius could not be seen, even under high magnification.

While this analysis has shown that stylus tips can and do plow the surface a limited amount, it is concluded that the basic surface contour is followed by the stylus (except for deep pits) because of the relatively constant plastic flow depth noted in these instances. However, it is expected that large errors may result for some surfaces and particularly for the softer metals (Inspection Data section, Model K, Fig. 48).

Further analyses were performed to determine the bottoming errors resulting from stylus tip radius and wear. These errors are caused by the tip radius not being able to follow the asperity completely into the valley. The following sketch illustrates this condition.

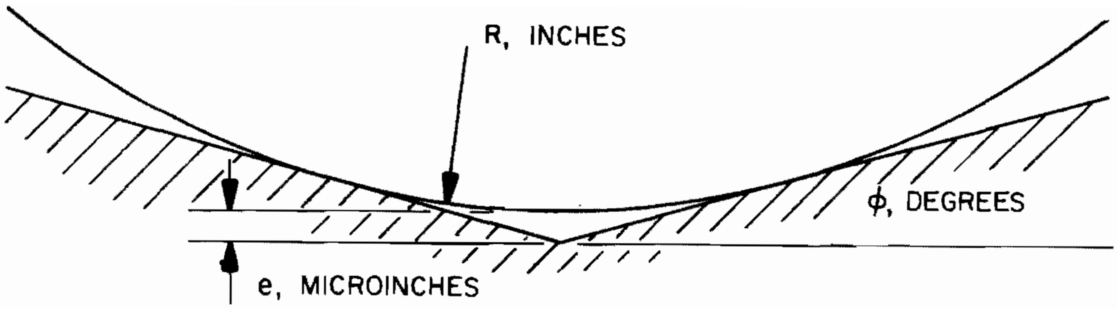

The bottoming errors (e) tabulated below have been computed using the equation

$$e = R\left(\frac{1}{\cos\Phi} - 1\right) \simeq \frac{R\,\Phi^2}{6560}$$

Angle, Φ degrees	Values of e, microinches	
	0.0005-Inch Radius	0.0001-Inch Radius
1	0.076	0.0152
2	0.306	0.0612
4	1.25	0.245
8	5.00	1.00
10	7.75	1.55

For the test models inspected, the relationship of Φ and the roughness height (h) are such that the errors tabulated above, though significant, are minimal. Obviously, the 0.0001-inch radius stylus results in greater accuracy and should be used when measuring fine or large slope angle surfaces.

A worn stylus limits the depth to which the tip can enter a valley. This can be seen from the sketch and calculated errors shown below. From the equation $e = d/2 \tan\Phi$, this error is independent of tip radius ($d > 2\,R\sin\Phi$).

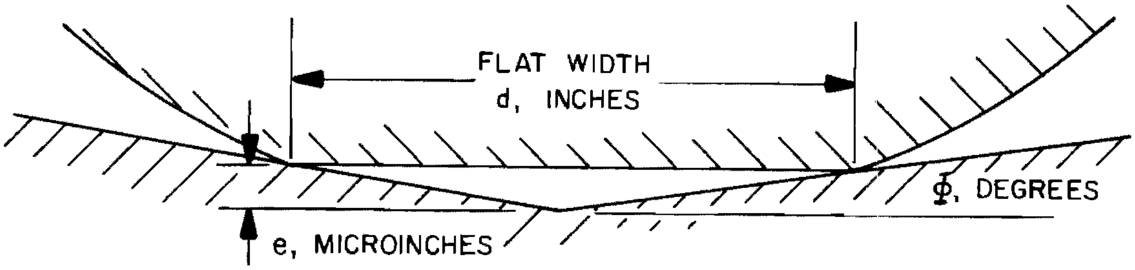

Angle Φ, degrees	Valves of *e*, microinches	
	$d = 50 \times 10^{-6}$, inches	$d = 100 \times 10^{-6}$, inches
1	0.436	0.872
4	1.75	3.50
8	3.50	7.00
12	5.30	10.00

Errors resulting from worn tips are appreciable, particularly at the greater angles. During the inspection of the scratch configuration (test Model G), a discrepancy was noted between the interference microphotograph and the Proficorder data. Based on the microphotograph, the scratch depth was 31 microinches while the Proficorder, with a 0.0001-inch radius tip, indicated 20 microinches. Because the 0.0001-inch radius stylus was used, this discrepancy was not caused by a bottoming error. However, it could have resulted from a worn tip because the scratch angle was 11 degrees. Microphotographs of tip stylii are shown in Fig. 90 through 92. While the large flat on the worn 0.0005-inch-radius tip is quite apparent, a 100-microinch flat with worn and faired edges would not be readily discernible on the 0.0001-inch tip and could account for the 10-microinch discrepancy noted above.

The Profilometer data taken were useful in interpretation of gross surface texture in lieu of explicit interference microscope information as in the case of relatively rough or nonuniform ground or multidirectional lapped surfaces. Its value, however, should not be discounted since, when used on surfaces of sufficient roughness to render insignificant the noted limitations, excellent correlation resulted.

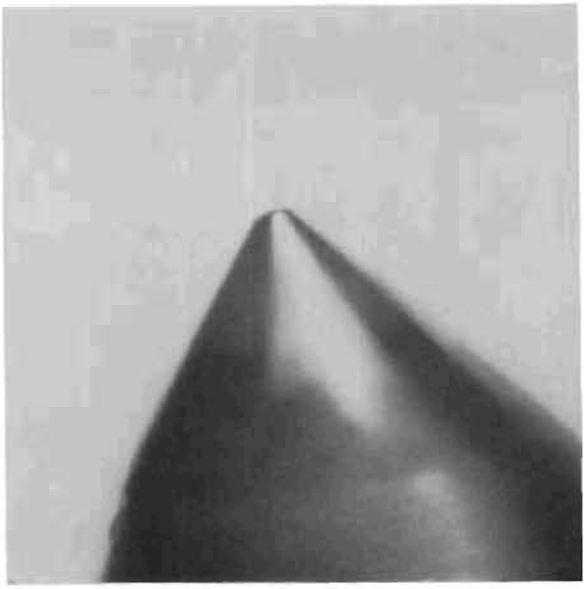

Figure 90. Profilometer Stylus, 0.0005-Inch Radius, 0.016- x 0.016-Inch Plain Photo

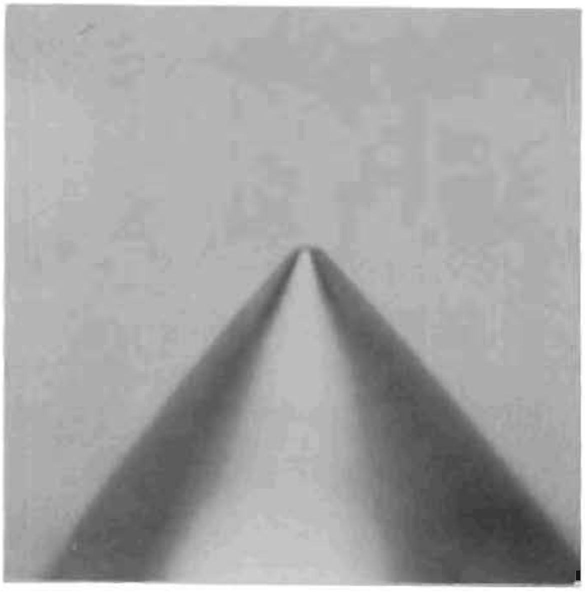

Figure 91. Proficorder Stylus, 0.0005-Inch Radius, 0.016- x 0.016-Inch Plain Photo

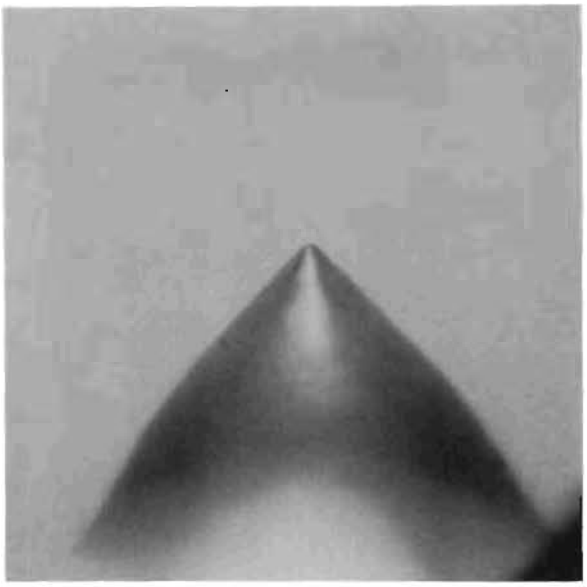

Figure 92. Proficorder Stylus, 0.0001-Inch Radius, 0.016- x 0.016-Inch Plain Photo

The Proficorder served a variety of purposes and, like the Profilometer, was particularly useful in aiding assessment of surface roughness. Geometrical information such as roundness, parallelism, waviness, and overall seating land profile was also determined from Proficorder data.

Optical Instruments

Several optical devices were used in the program for test model inspection and supplementary data. Included were the optical flat, interferometer, interference and plain microscopes, and optical comparitors.

The optical flat is used extensively for production operations where gross flatness measurements are required. It was used to verify overall flatness of flat poppets and seats and was particularly useful for rapidly measuring the cylindrical-shaped deviation of flat poppets used in the out-of-flat stress leakage tests (Models H and I). Figure 93 shows a typical use of the optical flat in measuring gross flatness.

Also used for flatness measurement, the interferometer utilizes isolated mirror reference planes to achieve light interference. The surface to be assessed is not contacted by the measurement device and potential surface damage is avoided. In its basic form, however, the interferometer employs 1:1 or even slight negative magnification; thus, like the optical flat, it is useful for only gross measurements.

A Leitz interference microscope was used for detailed assessment of seating land flatness, surface roughness, and certain geometrical irregularities. Figure 94 shows the unit with a Polaroid camera attachment for photographing test specimens. This device could be used for either plain or interference viewing with thallium (green) or white light at 100-, 200-, and 500-power magnifications. In addition to multiple magnification capabilities, the interference bands could be rotated 360 degrees and band-to-band spacing varied.

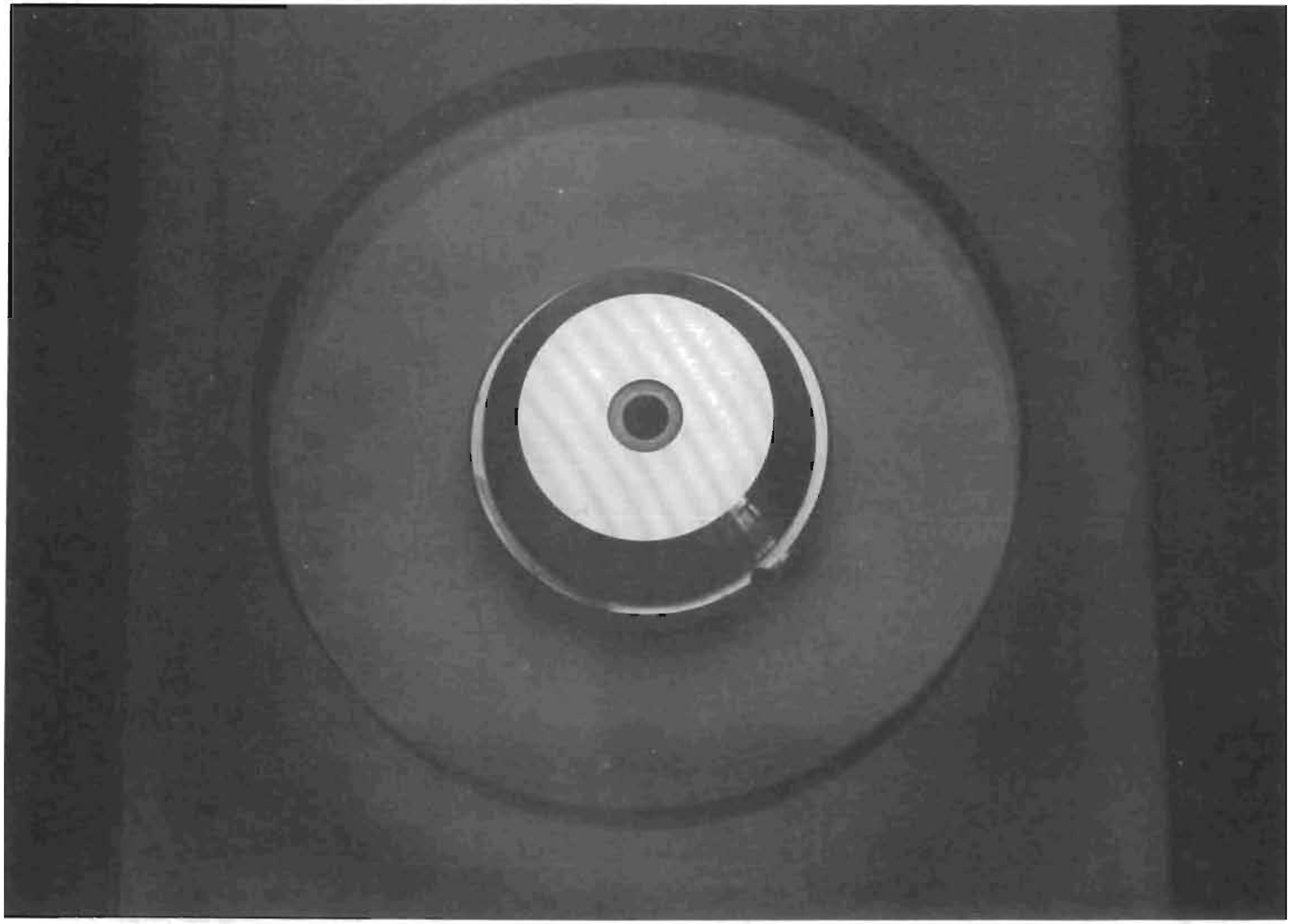

5AJ81-9/17/63-C1C

Figure 93. Optical Flat and Test Poppet Showing Helium Light Interference Bands

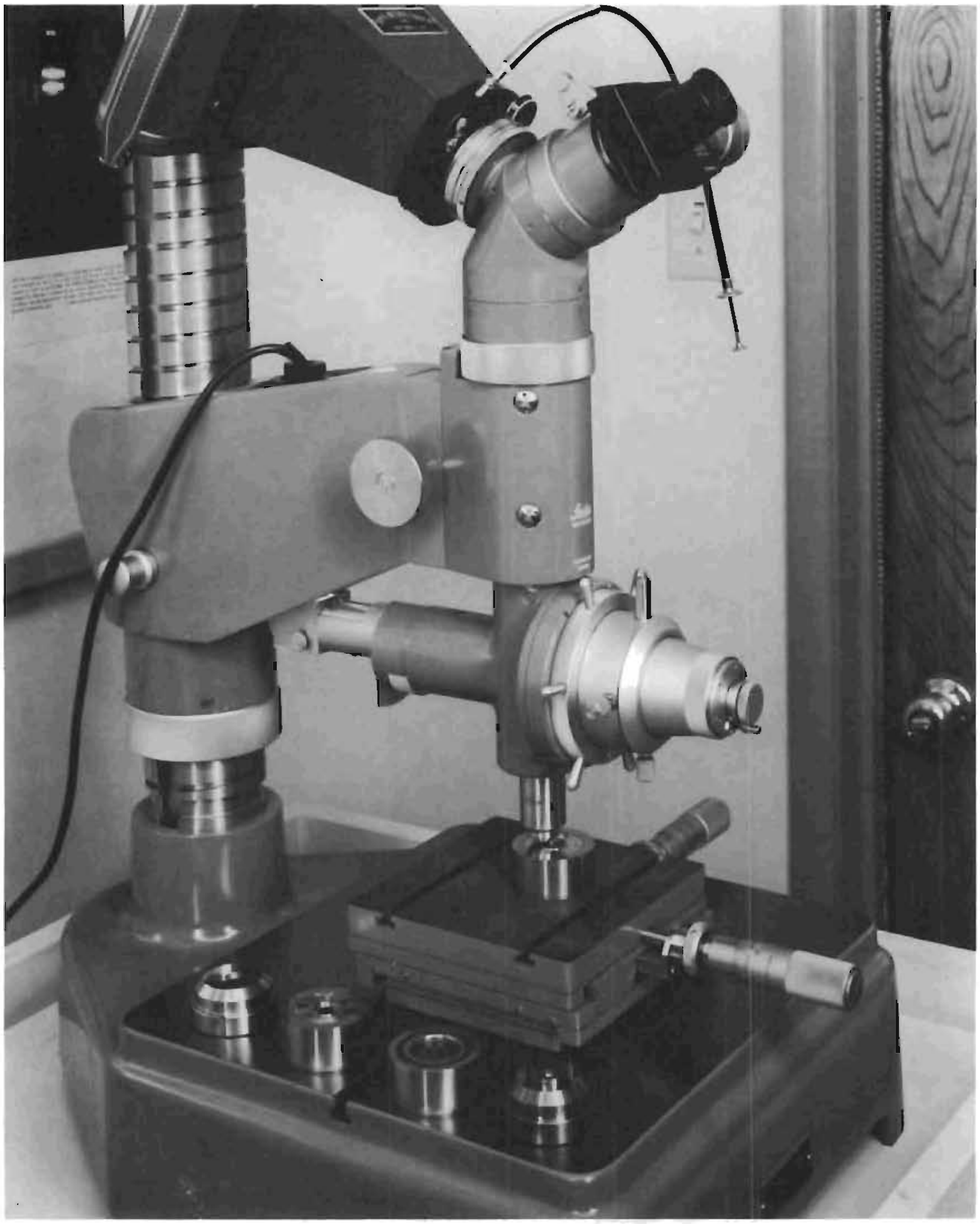

5AJ81-9/17/63-C1K

Figure 94. Leitz Interference Microscope With Flat Poppet and Seat Models

The interference microscope was used continually throughout the test program and, in fact, was the primary inspection tool employed. For evaluation of seating land gross geometry and edge conditions, 100-power magnification was used. Surface texture characteristics of all test surfaces were determined in full or in part with this instrument under 500-power viewing. Photographs were taken of all surfaces to form permanent records for detail study. Unless, otherwise noted, the interference bands are from green light of 10.4 microinches half wavelength. Representative photographs presented in this section have been cut to the definite calibrated size described in each figure so that they may be scaled to obtain specific dimensions. Approximate magnifications are:

1. 0.0065 x 0.0065 = 462X (50X objective lens)
2. 0.0089 x 0.011 = 462X (50X objective lens)
3. 0.016 x 0.016 = 187X (20X objective lens)
4. 0.033 x 0.033 = 91X (10X objective lens)
5. 0.045 x 0.056 = 91X (10X objective lens)

As discussed in subsequent paragraphs, conical and spherical model surfaces were primarily assessed with the interference microscope. Lacking the simple, parallel backface reference plane of the flat models, a means of precise, repeatable setup positioning for interference viewing was required. The precision leveling table shown in Fig. 95 was fabricated for this purpose. With the capability of gross angular setting and precision (120 pitch thread) three-point final adjustment, the optically flat table mounting surface provided an accurate intermediate reference plane.

Optical comparitors with various magnification capabilities were also used for certain relatively noncritical inspection tasks. The basic included angle of conical poppets, for instance, was determined in this manner with an estimated accuracy of ±2 minutes. (The important differential seating angle parameter was measured by other methods as discussed later in this section.)

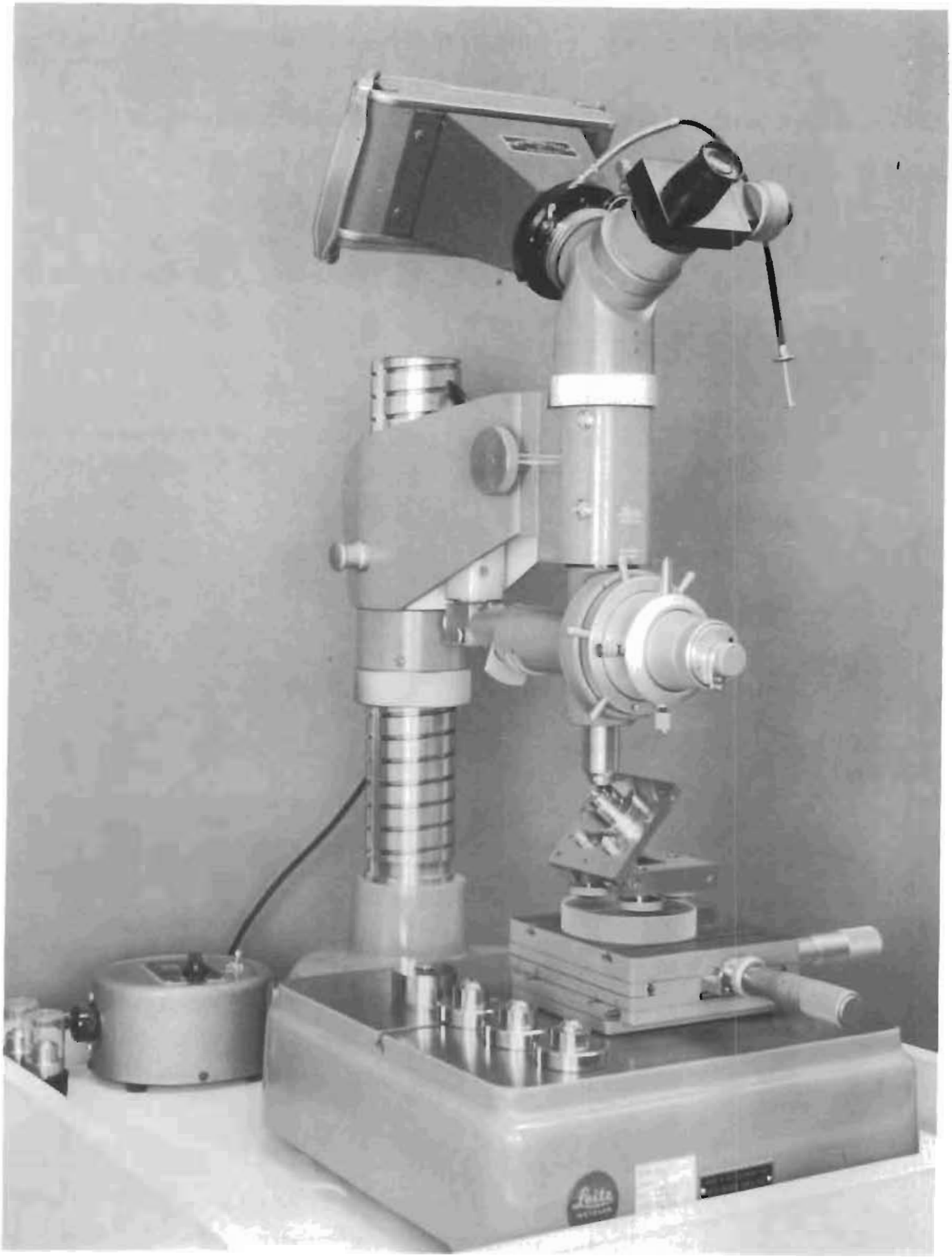

CAD41-3/16/66-C11

Figure 95. Leitz Interference Microscope With Conical Poppet on Leveling Table

For gross surface defect assessment and general low-power viewing, a 40-power Bausch and Lomb microscope was used. This unit provided excellent naked-eye assistance without complicating the viewed surface with minuscule defects and variations. Seating land corner condition and radii inspection was aided with this instrument which contained a 0.001-inch graduation reticle.

Indentation Instruments

Two indentation instruments were used to assess test model hardness properties. Conformance with basic model fabrication heat treat requirements was verified on a Rockwell hardness tester, using the C-scale test.

The more important test specimen surface hardness was determined by the Vickers test, using a Leitz microhardness tester (Fig. 96). This instrument is capable of making hardness measurements with loads from 15 to 1000 grams. A pyramidal shaped diamond indenter having a depth-to-diagonal ratio of 1:7 was used; diagonal identation width was directly measured through a self-contained, optical-recticle system.

Vickers diamond pyramid hardness number (DPH) is deined as the pressure distributed over the contact area of the identation. The mathematical expression is:

$$\mathrm{DPH} = \frac{P}{0.5393\ d^2} \quad \text{(or Hv)}$$

where

P = load, kilograms

d = diagonal distance, millimeters

Because only the surface hardness was of interest, the indentation loads used were 15 and 100 grams. The procedure used was to make two indentations and average the diagonal dimensions from each. Accurate measurements on the test surface profiles limit the minimum diagonal to

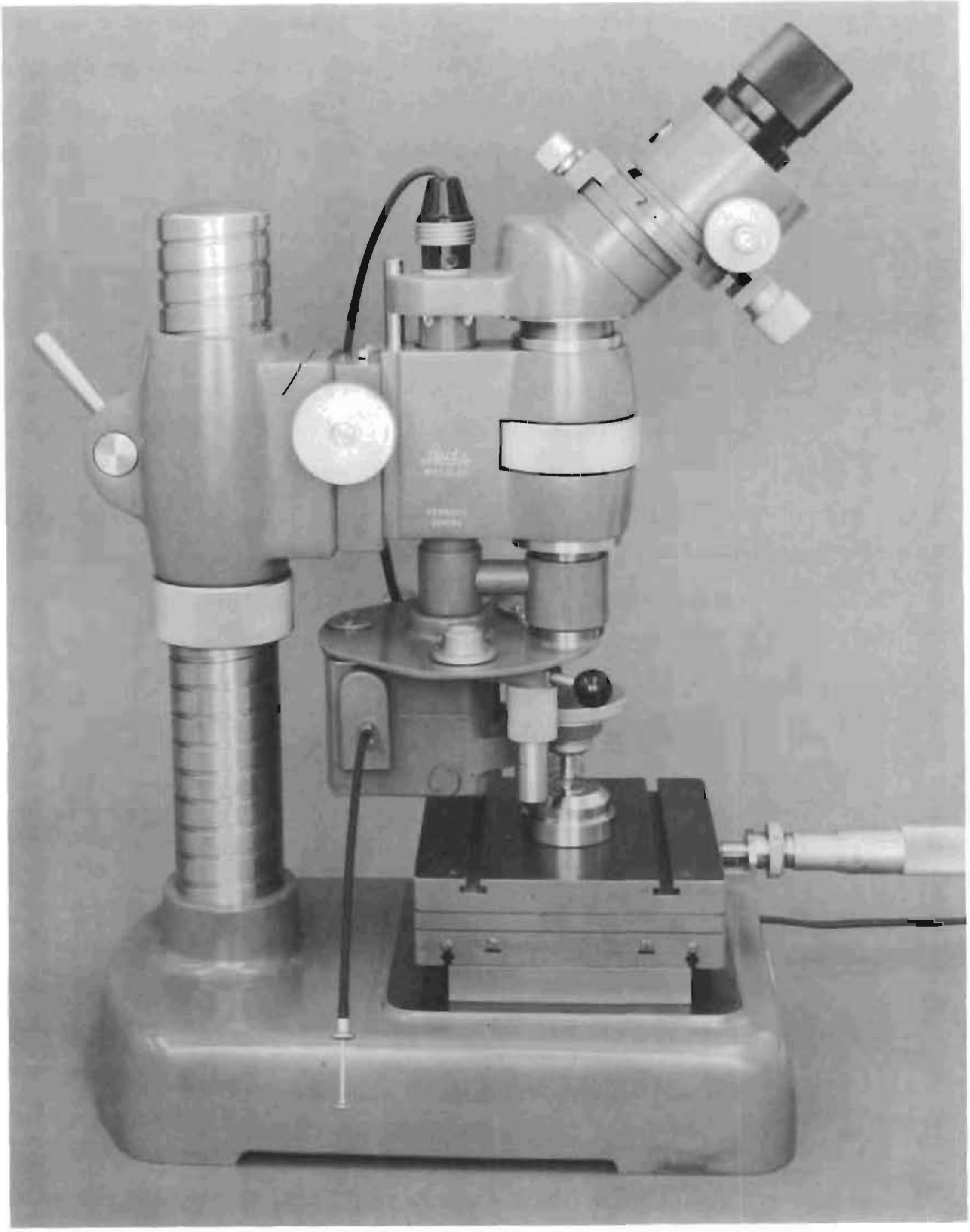

6AD41-3/16/66-C1L

Figure 96. Leitz Microhardness Tester and Test Poppet

approximately 10 microns (0.0004 inch); therefore, only the 100-gram data were measured on the steel and carbide parts. In the subsequently presented Inspection Data section, Fig. 105 and 107 (Model A) show interference photographs of indentations at both loads. Note roughness interference and also that the depth may be determined by counting interference bands but not as accurately as direct measurement because the exact edge cannot be precisely defined. Figure 188 and 189 also in the Inspection Data, section, Model L_f) show 100-gram indentations on a much smoother steel surface).

The hardness pressure may be used for an estimate of yield strengths. The plastic flow pressure for fully work-hardened metal is approximately 2.8 times the yield strength (Y) Ref. 6. Hardness values and approximate yield strengths for each of the test model materials are tabulated below:

Material	15-Gram Average Diagonal, Microns	100-Gram Average Diagonal, Microns	Vickers Hardness Number, Kg/mm^2	Yield Strength Criterion, psi x 10^3
440C Stainless Steel	--	15.2	800	406
6061-T651 Aluminum	15.5	40.0	123*	62.5*
Tungsten Carbide	--	11.8	1330	676

*Based on 15-gram load

INSPECTION AND INTERPRETATION PROCEDURES

In evaluating the inspection data, the following procedures and ground rules were practiced to obtain the most accurate and representative values.

Parallelism

Parallelism measurements were performed to define the deviation between representative seating and loading (backface) surface planes of flat models. The resultant dimension defined an overall trend, independent of localized waviness, flatness, depressions, or nodular conditions and was measured in several ways. Except for the turned surfaces, all models were finished with either an outer surface or land in a plane coincident with the seating land. Parallelism measurements relative to the mounting face were made from this external area to avoid damage to sealing surfaces. (The sealing surfaces of turned models were formed independent of existing outer lands and are subject to additional setup parallelism error. These models, however, were tested only with ball-joint loading where out-of-parallel effects are nullified.)

Merz, Cleveland, and Mikrokator indicating comparitors were variously used with occasional substantiation checks made on the Proficorder. In general, all flat model poppets and seats were parallel within less than 10 microinches over their respective 0.50-inch seating diameter.

The more difficult to define installed-parallelism between poppet and seat sealing surfaces was indicated by both Merz and Cleveland reference plane comparitors and experimental test data, as discussed in the Experimental Test Program section.

Flatness

The term flatness, as applied to test model inspection, was defined as errors of form occurring uniformly across the entire poppet or seat diameter. As such, it was a measure of overall concave, convex, or egg-shaped condition. Both Proficorder and optical flat measurement methods were used although the latter was continually employed during lapping operations. (The tendency of gross land duboff, attendant with lapping, was also monitored in this manner.)

Unless otherwise specified in the applicable test section, all models were flat within 3 microinches over the 0.50-inch seat diameter.

Diametral Differentials and Roundness

This error of form (defined as the surface deviation from a true circular plane) was a necessary inspection parameter for conical and spherical models. Two methods of inspection were employed.

Balls to be used for spherical model poppets were first checked with the Mikrokator, as shown in Fig. 97. The three close-coupled pins in the baseplate were centered under the indicator head, forming a retaining and self-aligning mount. Essentially a two-point measuring system, this permitted ball rotation and replacement without constant recentering. Diametral deviations from an arbitrarily selected "master" ball were determined in this manner (absolute size was not critical) within about 2 microinches.

It had been intended that the axis of deviation for alleged 50-, 100-, and 200-microinch out-of-round balls would also be established during this check. Inspection data indicated, however, that these balls were quite round but had local flat spots (change in radius) rather than true aspherical (ellipsoidal or lobed) configurations.

Roundness measurement of all conical and spherical models (balls were mounted in retainers to form spherical poppets) was performed on the Proficorder using a 1/16-inch ball stylus. An optical flat, wrung to the rotary table and running true within 5 microinches at a 2.0-inch diameter, was used as a reference plane. Conical poppets and seats and spherical seats were wrung to this surface, centered in best possible position and indicated normal to the seating surface at approximately mid-land (0.470-inch diameter). Having no geometrically defined seating land, spherical poppets required an additional setup step. The poppet ball was indicated at top dead center, and the resulting Proficorder stylus height transferred to a height gage. A differential height reduction, corresponding to the position of the seating land 0.470 nominal diameter, was then established

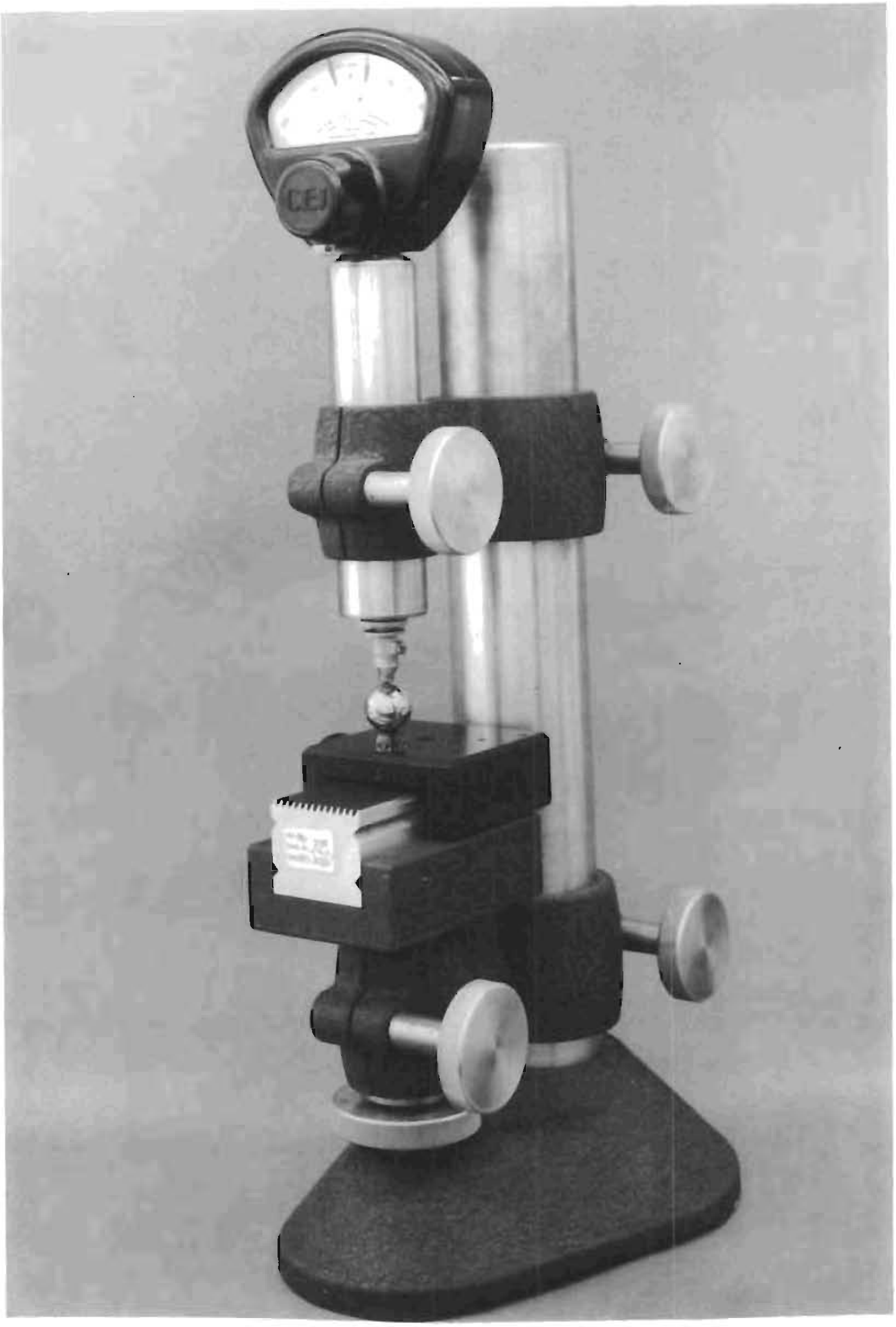

6AD41-3/16/66-C1K

Figure 97. Mikrokator Indicating Spherical Poppet Balls

on the gage. The Proficorder stylus was reindicated at this height, positioned on the ball, and the measurement made.

Roundness deviation of all spherical seats and the poppet of spherical Model C_s was less than 5 microinches. The remaining spherical poppets were round within 10 microinches. Conical model roundness varied as indicated later.

Concentricity

The only critical concentricity requirement encountered during the program could not be measured. This was the potential eccentricity of lapped circular roughness lay. Not fully appreciated during fabrication and test, later analysis indicated this parameter to have pronounced effect on the stress-leakage characteristic.

Positive definition of lay concentricity could not be established since no single 360-degree diamond particle cut was discernible. In retrospect, it appears that the only way to control this parameter reasonably is by precision fabrication setup. The models tested, however, were collet-chucked for surface finishing without precise runout measurements. Seats probably ran true within 0.0002-inch TIR but, in the same collet, the 0.0025-inch smaller OD poppets ran out about 0.001-inch TIR.

Differential Seating Angle

This parameter was computed from multiple inspection measurements which differed with model configuration. It defines the anticipated (excluding contaminant effects) tester-installed poppet and seat land angular mismatch.

For flat models, the differential seating angle was deduced from flatness and parallelism deviations. Establishment of this parameter for conical models, however, involved more elaborate inspection techniques.

The primary inspection tool for conical model differential angle assessment was the interference microscope. Two potential angular deviations were considered: (1) cone axis abnormal to loading face, and (2) a difference in basic included seat angle due to manufacturing error.

Microscopic evaluation of these deviations was performed in the same inspection setup. An optical flat was wrung to the microscope base to provide a reference plane. The test poppet was mounted on the precision leveling table which, in turn, was placed on the optical flat. A gage block stack, approximately the same height as the mounted poppet seating land-reference plane spacing, was wrung to the optical flat (Fig. 95). Interference bands were focused and set horizontal (with reference to the microscope reticle) on this reference surface which was then removed.

The leveling table was then adjusted until parallel interference bands were focused on the poppet seating land. (Minor vertical microscope adjustment was required but the mirror reference plane was not changed.) In this fashion, the precision of the optical flat reference plane was combined with the interference microscope to compare the seating land geometry with the optical flat.

Interference photographs of each poppet and seat having the same basic angle were taken at 90-degree rotation intervals without setup change. By comparing the interference band patterns on each set of photographs, angular deviation between cone and loading face (and hence come axis normality to the loading surface) could be assessed. All poppet and seat axes were true within an estimated 5 microinches over the 0.03-inch seating land.

By plotting surface profiles for a mating poppet and seat from these photographs, the contacting land basic seat angle difference could be computed. (In some instances, these data were further substantiated with Proficorder traces obtained in a similar, fixed-reference plane manner.)

The net differential angle specified in the test section represents the maximum potential deviation.

There was no method by which spherical model differential contact conditions could be directly measured. The poppet-seat mismatch gap specified in the applicable test model section is deduced from poppet and lapping ball differential diameters as described in the section on model fabrication.

Seating Land Dimensions

Model seating lands varied from flat to full crowned with edge conditions ranging from pronounced radii to corner discontinuities less than 50 microinches. Interference and 40X plain microscopes were used for land measurements. Linear dimensions (OD, ID, and land width) were determined from both microscope stage micrometer readings and scaled values from photographs of known magnification. Duboff, crown, and radius conditions were interferometrically assessed aided by 40X plain microscope viewing.

Flat Models. For lands flat over virtually the entire width, terminating in abrupt surface falloff, the flat land width was defined as extending to the point where the amount of duboff equalled the PTV surface roughness. Where definite radii are noted, the flat land width terminates at the point of tangency and the full radius has been specified. The defined radius, however, does not necessarily extend to the land edge due to its variability. Thus, for the majority of model seats, the flat land width is less than the total; seat area was calculated based on the projected flat width value.

Flat, crowned models have been defined in terms of the crown radius and list no flat land width. (Test stress calculations used a seat area assuming the total projected land width. These data were later supplemented by Hertz contact stress values from computed variable land widths based on a mean radius condition.) The crown curvature specified in that portion interpreted as a full radius and does not necessarily include the entire land.

Radii noted in the inspection data were computed using the simplified expression:

$$R \cong \frac{r^2}{2z}$$

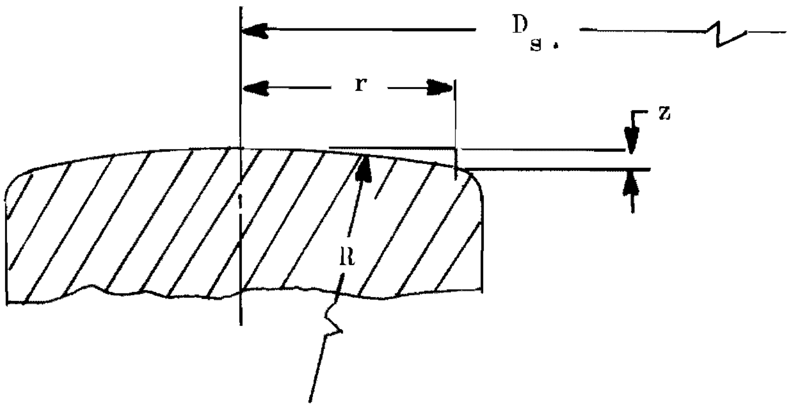

Conical Models. The conical model seat lands were dubbed, nonuniformly crowned, and had differential angle contact conditions. Land width for seat area calculations on these models was arbitrarily eatablished as the total projected width.

Spherical Models. Land curvature and corner break on these models was insignificant to area calculations. Thus, the total projected chordal width was employed for area determination.

Surface Texture

Of all the test model parameters measured, surface texture was the most complex. The full compliment of inspection tools available was utilized to aid interpretation of test surfaces.

A gross measure of average surface texture was obtained from Profilometer data. Recognizing that this information includes previously noted deviations of cutoff width, stylus configuration, and damage to the measured surface, Profilometer data are presented, as recorded. The readings are based on the arithmetic average (AA) which has supplanted the rms average. (Though not presented, many rms readings were taken and found to be 1.1 to 1.15 times greater than AA readings.) Information is tabulated for both the 0.0005- and 0.0001-inch radius tip stylii. In general, the 0.0001-inch radius tip indicated somewhat higher readings at all cutoff values because of the deeper penetration of the smaller tip. Generally, Profilometer readings were taken only for those models difficult to assess by other methods, and then usually after test since the stylus produced damaging scratches on all materials tested except tungsten carbide.

For more explicit surface texture definition, the surface was first cataloged by the type of lay (multidirectional, unidirectional, or circular). This was followed by further reduction into roughness, waviness, nodule, and scratch assessment categories. The resultant surface texture parameters presented (Model Inspection Data section) represent a composite reduction and interpretation of both Proficorder and interference microscope inspection data.

All Proficorder traces pertinent to surface roughness measurement were taken with a 0.0001-inch radius stylus tip across the prevailing lay if a defined lay existed. Unidirectional and multidirectional lay models were centered on the rotary table within 10 microinches. While indicating on the land or surface outside the seating area (1/16-inch-diameter ball stylus used for this setup operation), the surface to be measured was adjusted to run out less than 5 microinches over the 0.50-inch seating diameter. Multidirectional surfaces were then traced at any convenient area while the unidrectional lay models were indicated normal to the lay. Both readings were taken at approximately mid-land (0.470-inch diameter).

Circular lay models were setup eccentric such that the stylus traversed the land approximately normal to the lay. Pretracing surface runout adjustment and control was performed as noted above.

For best resolution and to minimize point to point stylus skip, the slowest possible table speed (approximately 0.02 rpm) was used. However, as table motion was rotary, the surface speed varied with the measured diameter, thus accounting for the different linear calibrations noted.

As with interferometrically obtained surface texture data discussed later in this section, evaluation of profile recorded roughness height involved subjective interpretation. The entire trace was considered and a PTV height representative of the average surface selected. The trace vertical scale provided the reference from which a numerical value was then established.

The Proficorder was also used on occasion to measure gross surface waviness, both radial (cross-land) and circumferential. Procedures were similar to those practiced for surface roughness measurements except that entire land width (radial measurements) and 360-degree circumferential traces were recorded. A 1/16-inch-diameter ball stylus was used for these measurements. From these data, surface waviness conditions were determined which, by their relatively gross nature, could not be observed through the limited microscopic field of view. The traces were viewed from an overall standpoint, average representative trends or cyclic patterns identified, and appropriate numerical values applied.

Interference microscope evaluation of unidirectional or circular lay surface texture with a PTV roughness dimension ranging from 1 to 10 microinches was performed from photographic data as illustrated by the following example taken with green light interference (Model F, seat).

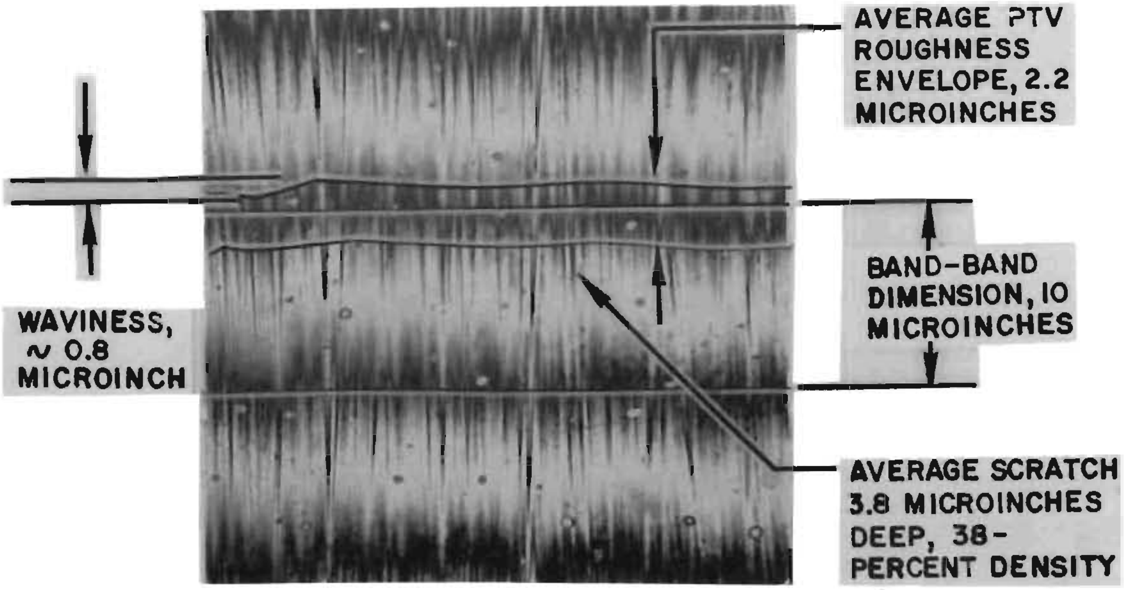
AVERAGE PTV ROUGHNESS ENVELOPE, 2.2 MICROINCHES
WAVINESS, ~ 0.8 MICROINCH
BAND-BAND DIMENSION, 10 MICROINCHES
AVERAGE SCRATCH 3.8 MICROINCHES DEEP, 38-PERCENT DENSITY

The band-to-band dimension was first established. This direct dimension, in inches, was equivalent to the half wavelength of the green monochromatic light used in the Leitz interference microscope. (Although the actual value was 10.4 microinches, 10 microinches was used for convenience. As later discussed, this assumption does not detract from reasonable surface evaluation.) An envelope was imagined which encompassed the bulk of the peak-to-valley roughness and within this envelope a representative (average) asperity or group of asperities was selected. Ratioing the directly measured height of this average deviation to the previously noted bandwidth dimension yielded an equivalent PTV height in microinches.

Scratches (pointing downward) were assessed in a similar manner with the selection of an average scratch and determination of its depth. From the width and number of scratches over a given portion of the surface being evaluated, an average scratch density was computed.

Localized waviness, as illustrated, was determined from the deviation of the imagined profile line and numerically evaluated as with roughness and scratches. Significant pits and nodules were assessed in like fashion and, if warranted, surface density computed.

It should be apparent that interpretation of surfaces as viewed through the interference microscope must be done on a gross or overall basis rather than limiting consideration to a small area. Even so, individual analysts can reasonably be expected to differ by as much as 50 percent in the application of numerical values to PTV dimension. As this dimension approaches 1 microinch, evaluation by two-beam interferometry becomes exceeding difficult. The resultant interference bands appear as a blurred gradation of dark to light areas, since the very small roughness wavelength attendant with such surfaces is virtually indiscernible, even at 500X magnification.

Multiple-beam interferometry, which produces sharper focused interference bands, aids the assessment of surface having PTV dimensions on the order of 1 microinch or less. Although not available for use during the program, a Johansson "Multimi" multiple beam interference microscope was used to compare results obtained on one model seat H_{f1} with two-beam interferometry. The subsequently presented (Model Inspection Data section, Model H_{f1}) comparative photos of Fig. 179, 180, and 181 illustrate the difference. While the PTV roughness height of Fig. 179 may be interpreted as approximately 1.5 microinches, the multiple beam photographs of Fig. 180 and 181 indicate a roughness level of about half that amount, or 0.8 microinch. Thus, the deduction of PTV roughness height for the finer surfaces where two-beam interference bands merge into a blur has been performed on a comparative basis using the data of Model H_{f1} (and similar evidence) for reference.

The asperity wavelength, even with the Multimi, was still poorly defined. An oil-immersion lens procedure, providing a means of additional horizontal magnification, may improve individual asperity resolution but was not evaluated.

The assessment of random nature or multidirectionally textured surfaces and certain discontinuities with two-beam interferometry requires additional techniques. Consider Fig. 98 through 101, which show a scratch on a 440C stainless surface diamond lapped to approximately 1-microinch AA.

Figure 98, with wide bands, looks like it has been inverted with the scratch direction upward. With narrower bands as in Fig. 99, the raised edges of the scratch are recognizable but depth assessment is still difficult. With the very narrow bands of Fig. 100 and 101, the scratch topography is plainly evident and may be accurately evaluated.

Similarly, assessment of a uniform multidirectional lay surface is greatly enhanced by gross reduction of interference band width. For example, Fig. 102 through 104 illustrate the surface of a 440C stainless-steel part which has been wet-slurry, aluminum-oxide lapped and polished. Figure 102 is a plain view of the surface, while Fig. 103 shows relatively wide interference bands. From Fig. 103, pits and knobs can be identified but the general surface profile is indistinct. When very narrow bands are employed (Fig. 104), the surface profile is resolved into one of round crested parabolic form (see Fig. 17, Seating Analysis Section.)

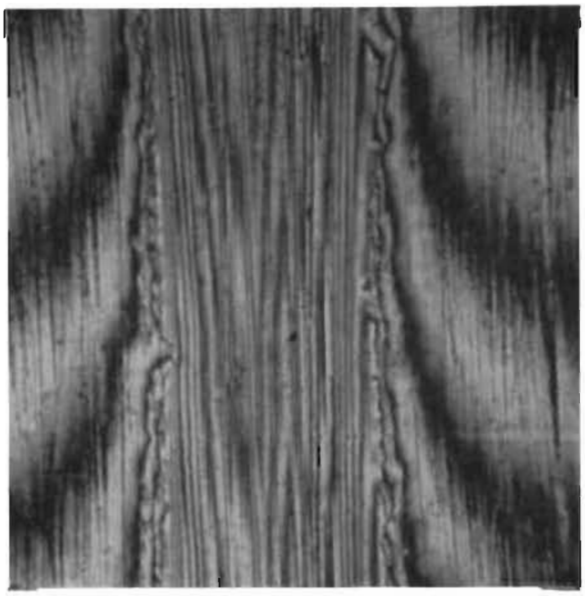

Figure 98. Sample Scratch, 0.0065- x 0.0065-Inch Interference Photo, Wide Bands

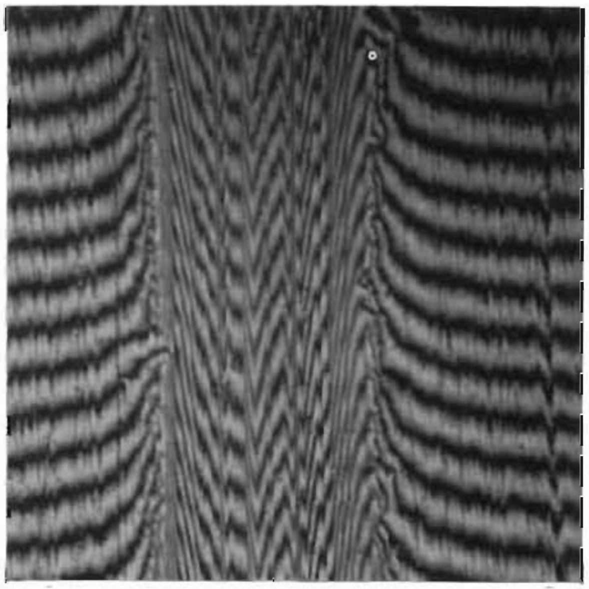

Figure 99. Sample Scratch, 0.0065- x 0.0065-Inch Interference Photo, Narrow Bands

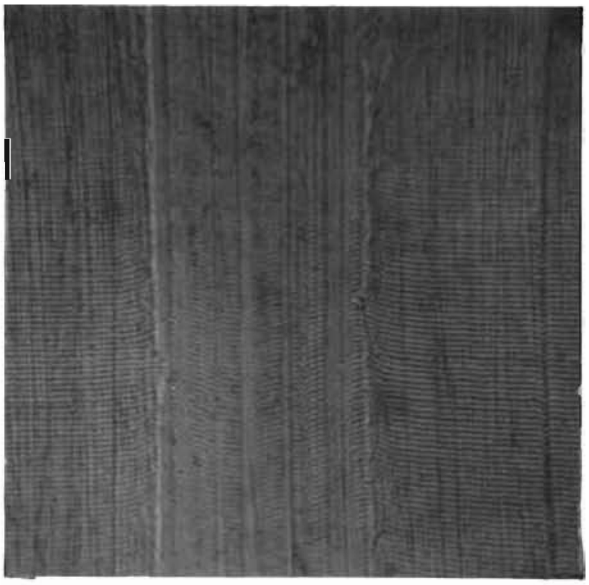

Figure 100. Sample Scratch, 0.0065- x 0.0065-Inch Interference Photo, Very Narrow Bands

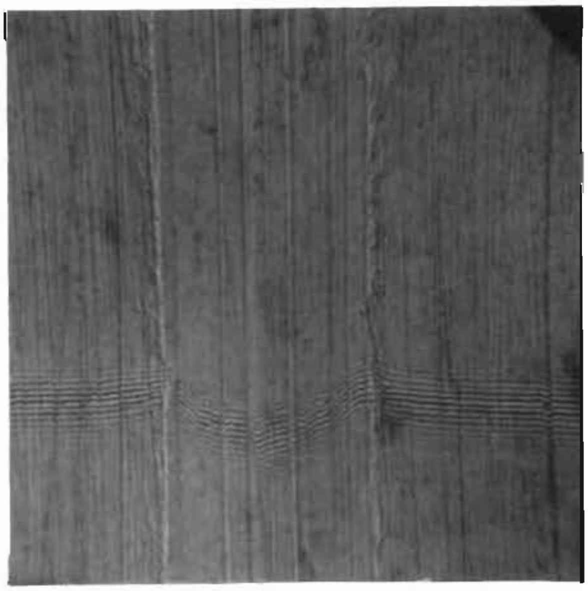

Figure 101. Sample Scratch, 0.0065- x 0.0065-Inch Interference Photo Very Narrow Bands, White Light

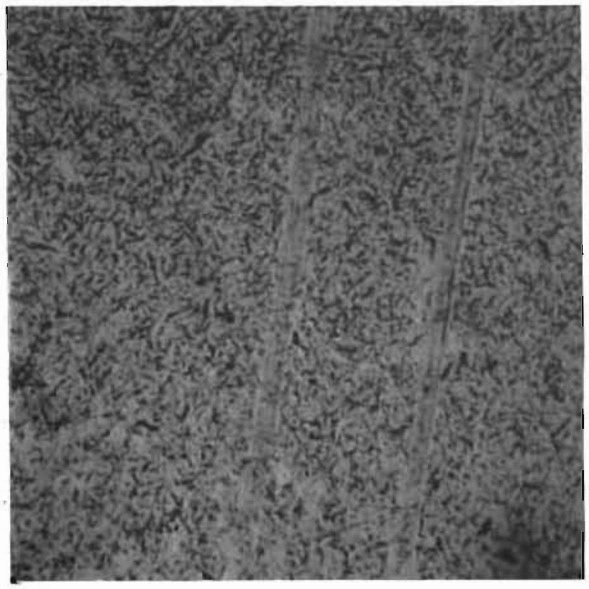

Figure 102. Sample Multidirectional Lay Surface, 0.0065- x 0.0065-Inch Plain Photo

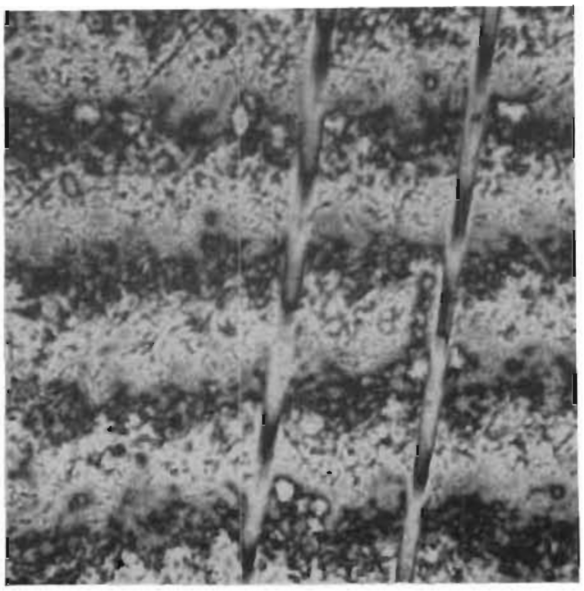

Figure 103. Sample Multidirectional Lay Surface, 0.0065- x 0.0065-Inch Interference Photo, Wide Bands

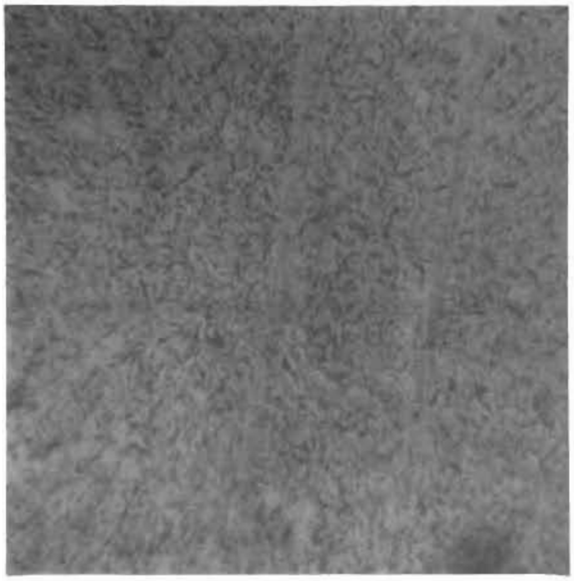

Figure 104. Sample Multidirectional Lay Surface, 0.0065- x 0.0065-Inch Interference Photo, Very Narrow Bands, White Light

The technique of using narrow bands to aid definition of surface features evolved during the experimental effort and was not used during the initial contract work. Thus, the photographs of multidirectional surfaces fabricated during that portion of the test effort were taken with wide bands, and Proficorder data were heavily relied upon to support evaluation of these surfaces.

To evaluate consistently the surface profile input data, the following distinct parameters and resolution limits were established:

1. Roughness

   h = 1.0 microinch and above

   φ = 0.1 degree and above

2. Waviness

   h = 1.0 microinch and above

   φ = 1.0 and below

3. Nodules

   h = 25 percent above the maximum peak-to-valley roughness (h)

   φ = no confines

   β = 1 percent and above

4. Scratches

   h = 1 microinch and greater which occur below level of surface roughness (or waviness)

   φ = no confines

   β = 1 percent and above

These ground rules were established for both Proficorder and two-beam interference microscope inspection data and, in general, reflect the practical limits of obtaining these data. For example, h values cannot be resolved any lower than 1.0 microinch on either instrument. An overlap is provided for roughness and waviness angles (φ) because these two categories merge into each other, and a finite division cannot be made.

MODEL INSPECTION DATA

A compilation of direct and reduced model inspection results and the raw data from which much of this information has been interpreted is presented on the following pages. In Table 4 data of specific nature, potentially applicable to all or groups of models, are given in tabular form. Thus, many blank areas exist where certain models by virtue of geometry, surface texture, or other reasons could not be as assessed or specific tabulated parameters were not applicable. Comments pertinent to isolated or random characteristics not ameanable to or warranting tabulation are listed adjacently.

The raw inspection data in the form of plain and interference photographs (Fig. 105 through 328) and profile traces (Fig. 329 through 374) are presented in groups according to model designation (cross referenced in Table 4 by figure numbers). These data include pretest basic model inspection information and, where significant test-incurred changes were observed, posttest comparative data as well.

Interference photographs and Proficorder traces have been oriented such that the top side of the interference bands or profile record represents the inspected surface profile. Scratches or surface indentations appear as downward pointing grooves.

A test model is defined as a poppet and seat pair forming a unique combination of sealing surfaces. Each model has been given a letter designation with a subscript denoting basic geometry, i.e., f (flat), c (conical), and s (spherical). When a minor rework or processing operations was performed on either or both model poppet and seat for comparison with original performance a numerical subscript was added to the basic designation. Thus, for example, flat model J_f, when subsequently passivated, became Model J_{f1}. This rework designation is additionally denoted in Table 4 by an applicable poppet or seat serial number suffix RW followed by a sequential rework number.

When an existing model surface was radically changed as, for example, rework from a multidirectional to unidirectional or circular lay, the basic model letter designation was changed. Similarly, the combination of a poppet from one model and the seat from a second called for new letter identification.

An exception to the above procedures are the models included herein but previously tested and reported in Ref. 37. For comparison purposes, these models (all flat configurations) are designated exactly as they originally appeared with no subscript. Rework of these models, however, is indicated by serial number suffix.

TABLE 4

MODEL POPPET AND SEAT INSPECTION DATA

Test Model Designation	Test Model Description							Seating Land Data										Profilometer Finish, microinches AA						Cross Lay Surface Texture Parameters (h = PVT Height, microinches; Φ = Average Asperity Angle, degrees; β = Density, in./in.)										Photograph Figure Number	Profile Record Figure Number	Miscellaneous Inspection Notations
	Part Number	Serial Number	Material	Crown Radius, inches	Predominant Surface Lay	Nominal Surface Finish, microinches AA	Seating Angle, degrees	ID, inches	OD, inches	Land Width (L), inches		Corner Duboff			Seat Area (A_{sp}), sq in.	Δ Seating Angle (Δθ), degrees	Mean Diameter (D_m), inches	0.0005-Inch-Radius Tip			0.0001-Inch-Radius Tip			Roughness		Waviness		Nodules			Scratches					
										Flat	Total	Radial Dimension, inches	Height, microinches	Equivalent Radius (R_o), inches				0.030-inch Cutoff	0.010-inch Cutoff	0.003-inch Cutoff	0.030-inch Cutoff	0.010-inch Cutoff	0.003-inch Cutoff	h	Φ	h	Φ	h	Φ	β	h	Φ	β			
NEAR SEATED TESTS																																				
A Poppet	28-5	02	Tungsten carbide (lapped)		Unidirec.	1			1.012		0.490							1.5	0.7	0.6	1.7	1.5	1.3	3.0	2.0	1.4	0.074				4.0	11.0	0.20	105-107	--	
A Seat	27-31	01	440 C steel (lapped)		Multidirec.	2			0.9995	0.0589	0.0597				0.174		0.9398	1.6	1.4	1.3	2.4	2.2	2.0	6.0	1.0			4.3	1.4	0.061						
SURFACE TEXTURE EVALUATION																																				
Flat Turned Models																																				
Q_f Poppet	28-7	02	17-4 PH steel			16			0.5314		0.1166					0.086		11.5	12.5	11.5	13.0	12.0	12.0	48.0	9.1									108-109	329-331	Q_f Poppet: 0.042-degree concave taper; circumferential waviness; two 20-microinch PTV waves with 180-degree period; 5-microinch PTV short period (0.047-inch) waves
Q_f Seat	29-7	02-HW1	17-4 PH steel			15			0.4998	0.0300	0.0310				0.0442		0.4698							45.0	7.5											Q_f Seat: 0.044-degree concave taper; two circumferential 20-microinch PTV waves with 180-degree period; no short-period waves; 9-microinch hump extending in 0.0036-inch from OD
N_f Poppet	28-7	01-HW1	17-4 PH steel			2.7			0.5440		0.1230					0.19		2.5	1.9	1.8	3.0	2.4	2.3	8.0	3.1									110-113	332-333	N_f Poppet: 0.077-degree concave taper; circumferential waviness; two 14-microinch PTV waves with 180-degree period; 3- to 5-microinch PTV short-period (~0.046-inch) waves
N_f Seat	29-7	01	17-4 PH steel			2.7			0.4967	0.0288	0.0291				0.0423		0.4679							8.0	2.9											N_f Seat: 0.114-degree concave taper; circumferential waviness; two 12-microinch PTV waves with 180-degree period; 2- to 5-microinch PTV short-period (~0.035-inch) waves; 12-microinch hump extending in 0.0037 inch from OD
R_f Poppet	28-5	02-HW1	Tungsten carbide		Unidirec.	0.3			1.012		0.490					0.012								1.0										114-116	—	R_f Poppet: Two pit densities noted—β = 0.18, h = 1.5; and β = 0.01, h = 4
R_f Seat	29-9	02-HW1	Aluminum			40			0.4955	0.0278	0.0279				0.0408		0.4677							120		10.0										R_f Seat: 0.012-degree concave taper; 12-microinch hump extending in 0.003 inch from OD
S_f Poppet	28-5	02-HW1	Tungsten carbide		Unidirec.	0.3		Same as Model R_f								0.019	Same as Model R_f																	117-119	—	
S_f Seat	29-9	01-HW1	Aluminum			3.0			0.4981	0.0291	0.0295				0.0428		0.4690							9.2	5.1											S_f Seat: 0.019-degree convex taper; 6- to 10-microinch PTV waves extending radially outward from center of land; 4- to 8-microinch hump extending in 0.003 inch from OD
Flat Ground Models																																				
D_f Poppet	28-3	01-HW1	440 C steel		Undirec.	2.0			1.012		0.490													6.0										120-126	334-337	D_f Poppet: 5-microinch PTV short-period (0.030- to 0.126-inch) waves
D_f Seat	29-3	01-HW1	440 C steel		Undirec.	2.7			0.4988	0.0296	0.0300				0.0436		0.4692	3.0	2.2	1.9	3.1	3.0	2.8	8.0												D_f Seat: Circumferential waviness;two 10- to 14-microinch PTV waves with 180-degree period; varied (5- to 10-microinch PTV average) short-period (0.025- to 0.084-inch) waves
A_f Poppet	28-3	02-HW1	440 C steel		Circular	2.3			1.012		0.490							3.2	2.5	2.3	3.2	3.0	2.5	7.0										127-128	338-341	A_f Poppet: Circumferential waviness; two 10-microinch PTV waves with 180-degree period; 12-to 15-microinch PTV short-period (~ 0.037-inch) waves
A_f Seat	29-3	02-HW1	440 C steel		Circular	2.3			0.4993	0.0298	0.0300				0.0439		0.4695	3.8	3.1	2.5	3.2	2.7	2.5	7.0												A_f Seat: Circumferential waviness; two 22- to 32-microinch PTV waves with 180-degree period; 10- to 15-microinch PTV short-period (~0.037-inch waves
Flat Lapped Models																																				
D Poppet	28-3	01	440 C steel		Multidirec.	6.3			1.012		0.490							5.5	5.0	4.0	9.5	8.5	7.0	19.0	3.5	5.0	0.15	5.2	2.9	0.044				129	342	
D Seat	29-3	01	440 C steel		Multidirec.	6.3			0.4986	0.0290	0.0291				0.0428		0.4695	5.0	4.3	3.5	8.5	8.0	7.0	Same as Model D Poppet												
C Poppet	28-3	02	440 C steel		Multidirec.	4.7			1.012		0.490							3.5	3.0	2.5	6.4	5.9	5.1	Same as Model C Seat										—	343	
C Seat	29-3	02	440 C steel		Multidirec.	4.7			0.4992	0.0295	0.0297				0.0436		0.4695	3.6	2.7	2.3	5.5	5.0	4.5	14.0	2.8	5.0	0.17	3.3	2.2	0.054						
B Poppet	28-3	03	440 C steel		Multidirec.	1.5			1.012		0.490							1.6	1.2	1.0	2.2	1.7	1.5	4.5	0.75			3.1	0.99	0.042				130-131	344-345	
B Seat	29-3	03	440 C steel		Multidirec.	2.2			0.4988	0.0284	0.0288				0.0419		0.4700	2.0	1.7	1.5	2.5	2.4	2.2	6.6	1.2			4.5	1.7	0.020						
J Poppet	28-7	01	17-4 PH steel		Multidirec.	2			1.012		0.490							1.5	1.3	1.1	2.0	1.8	1.6	Same as Model J Seat										132-134	346	
J Seat	29-7	02	17-4 PH steel		Multidirec.	2			0.5003	0.0292	0.0299				0.0431		0.4704	1.4	1.2	1.0	2.2	1.9	1.5	6.0	1.6											
K Poppet	28-9	01	Aluminum		Multidirec.	2			1.012		0.490							1.5	1.2	1.0	2.3	1.8	1.5	Same as Model K Seat										135-138	—	
K Seat	29-9	01	Aluminum		Multidirec.	2			0.4990	0.0286	0.0287				0.0408		0.4703	1.5	1.1	0.8	2.0	1.7	1.4	6.0	1.3	3.0	0.32				5.0	13.0	0.056			
F Poppet	28-3	04-HW1	440 C steel		Unidirec.	0.7			1.012		0.490															0.8	0.08				4.0	11.0	0.12	139-142	—	
F Seat	29-3	06	440 C steel		Unidirec.	0.7			0.4994	0.0284	0.0293				0.0419		0.4701	0.9	0.55	0.45	1.3	1.1	1.1	2.2	0.4	0.8	0.07				3.8	6.6	0.38			
G_f Poppet	28-3	03-HW1	440 C steel		Unidirec.	0.7			1.012		0.490							1.1	0.5	0.45	1.0	0.65	0.55	2.0	3.9									143-146	—	
G_f Seat	29-3	04	440 C steel		Unidirec.	0.8			0.4984	0.0294	0.0297				0.0433		0.4690	1.0	0.65	0.5	1.2	0.8	0.7	2.3	4.0	1.4	0.16									
G_{f1} Poppet	28-3	03-HW2	440 C steel		Unidirec.	0.6			1.012		0.490													1.8	3.2									147-157	—	
G_{f1} Seat	29-3	04-HW1	440 C steel		Unidirec.	0.6			0.4942	0.0254	0.0257	0.0004	3.0	0.026	0.0374		0.4688							1.7	3.0											
CC_f Poppet	28-5	01	Tungsten carbide		Circular	0.3			1.012		0.490													0.8	2.1									158-166	—	CC_f Poppet: Two pit densities noted—β = 0.18, h = 1.5; and β = 0.01, h = 4
CC_f Seat	29-3	06-HW1	440 C steel		Circular	0.2			0.4977	0.0290	0.0293				0.0427		0.4687							0.7	1.7											CC_f Seat: Two scratches 5 microinches deep by 65 microinches wide
B_f Poppet	28A-3	04-HW4	440 C steel		Circular	0.6			0.518	0.044	0.048													1.9	4.1									167-171	—	
B_f Seat	29-3	05-HW1	440 C steel		Circular	0.8			0.4982	0.0287	0.0288				0.0423		0.4695							2.5	2.6											
B_{f1} Poppet	28A-3	04-HW4	440 C steel		Circular	0.6		Same as Model B_f																												
B_{f1} Seat	29-3	05-HW2	440 C steel		Circular	0.5			0.4974	0.0277	0.0283				0.0408		0.4697							1.4	3.1									172-173	—	
H_f Poppet	28A-3	05-HW2	440 C steel		Circular	0.2			0.518		0.048													0.7	1.5									174-178	—	
H_f Seat	29-3	03-HW1	440 C steel		Circular	0.2			0.4982	0.0290	0.0292				0.0427		0.4692							0.7	1.5											
H_{f1} Poppet	28A-3	05-HW2	440 C steel		Circular	0.2		Same as Model H_f																										179-183	—	
H_{f1} Seat	29-3	03-HW2	440 C steel		Circular	0.3			0.4980	0.0286	0.0290				0.0422		0.4694							0.8	1.6											
L_f Poppet	28A-3	06	440 C steel		Unidirec.	0.3			0.518		0.048													0.8	1.8						2.5	14.3	0.00081	184-189	—	L_f Poppet: Six scratches averaging 4.3 microinches deep by 37 microinches wide
L_f Seat	29-3	07	440 C steel		Unidirec.	0.3			0.4966	0.0280	0.0284				0.0412		0.4686							0.8	1.8						2.5	9.5	0.0012			
BB_f Poppet	28-5	01	Tungsten carbide		Circular	0.3		Same as Model CC_f																												
BB_f Seat	29-3	03-HW2	440 C steel		Circular	0.3		Same as Model H_{f1}																												
M_f Poppet	28A-3	07	440 C steel		Circular	0.2																		0.7	1.8									190-192	—	
M_f Seat	29-3	08	440 C steel	5.4	Circular	0.1			0.4982	0.0	0.0290	0.0037	20.0	0.30	0.0427		0.4692							0.4												M_f Seat: Three scratches noted—3.6 microinches deep by 87 microinches wide, 4.6 microinches deep by 87 microinches wide, and 3.3 microinches deep by 43 microinches wide; center 0.010 inch of land pitted; pit density of β = 0.25, h = 1
M_{f1} Poppet	28A-3	07-HW1	440 C steel		Circular	0.2		Same as Model M_f																										193-196	—	
M_{f1} Seat	29-3	08-HW1	440 C steel	5.4	Circular	0.1		Same as Model M_f																												
AA_f Poppet	28-5	01	Tungsten carbide		Circular	0.3		Same as Model CC_f																												
AA_f Seat	29-3	06-HW2	440 C steel	12	Circular	0.2			0.4981	0.0	0.0290	0.0035	9.0	0.70	0.0427		0.4691							0.5										197-204	—	
CIRCULAR LAY ECCENTRICITY EVALUATION																																				
NN_f Poppet	28-7	01-HW2	17-4 PH steel (lathe turned)			2.0			0.4980	0.0270	0.0290				0.0398		0.4690							6.0										205-211	—	NN_f Poppet and Seat: Lay was eccentric to guide diameter by 0.001 inch (0.002-inch Total Indicator Reading); ~8-microinch hump extending in 0.0015 inch from OD
NN_f Seat	29-7	01-HW1	17-4 PH steel (lathe turned)			2.0			0.4996	0.0274	0.0294				0.0404		0.4702							6.0												
HH_f Poppet	28A-3	05-HW3	440 C steel (lapped)		Circular	0.4			0.518		0.048													1.1										212-216	—	HH_f Poppet: 1.5-microinch taper, extending out 0.0242 inch from ID (high end of taper at ID)
HH_f Seat	29-3	03-HW3	440 C steel (lapped)		Circular	0.5			0.4980	0.0288	0.0290				0.0424	0.002	0.4693							1.5												HH_f Seat: 2.4-microinch taper, extending across outer 0.0242-inch land width (high end of taper at OD)

TABLE 4
(Continued)

Test Model Designation	Test Model Description							Seating Land Data										Profilometer Finish, microinches AA						Cross Lay Surface Texture Parameters (h = PTV Height, microinches; Φ = Average Asperity Angle, degrees; β = Density, in./in.)										Photograph Figure Number	Profile Record Figure Number	Miscellaneous Inspection Notations
	Part Number	Serial Number	Material	Crown Radius, inches	Predominant Surface Lay	Nominal Surface Finish, microinches AA	Seating Angle, degrees	L', inches	O', inches	Land Width (L), inches		Corner Runoff			Seat Area (A_{sp}), sq in.	Δ Seating Angle (Δθ), degrees	Mean Diameter (D_s), inches	0.0005-Inch-Radius Tip			0.0001-Inch-Radius Tip			Roughness		Waviness		Nodules			Scratches					
										Flat	Total	Radial Dimension, inches	Height, microinches	Equivalent Radius (R_o), inches				0.030-inch Cutoff	0.010-inch Cutoff	0.003-inch Cutoff	0.030-inch Cutoff	0.010-inch Cutoff	0.003-inch Cutoff	h	Φ	h	Φ	h	Φ	β	h	Φ	β			
CONICAL AND SPHERICAL MODEL EVALUATION																																				
Conical																																				
A_c Poppet	82-6	01	440 C steel		Circular	1	41	0.4332	0.5113		0.0592						0.4722							3.0	4.8									217-219	347-350	A_c Poppet: Roundness—one 20-microinch PTV wave extending 0.32 inch; 6- to 10-microinch PTV deviations with periods varying from 0.1 to 0.2 inch
A_c Seat	81-6	01	440 C steel		Circular	1	41	0.4510	0.4893		0.0290				0.0281	0.050	0.4702							3.0		6.0	3.25									A_c Seat: Roundness—two average 20-microiugh PTV waves with 180-degree period; 5-microinch PTV short-period (0.024-inch) deviations
B_c Poppet	82-4	01	440 C steel		Circular	1	33	0.4337	0.5039		0.0638						0.4689							3.0										220-223	351-354	B_c Poppet: Roundness--basically four 15-microinch PTV waves with 90-degree period
B_c Seat	81-4	01	440 C steel		Circular	1	33	0.4539	0.4866		0.0297				0.0241	0.0094	0.4703							3.0												B_c Seat: Roundness--two 20-microinch PTV waves with 180-degree period; 5-microinch PTV short-period (0.019-inch) deviations
C_c Poppet	82-2	01	440 C steel		Circular	1	20	0.4441	0.4903		0.0682						0.4672							3.0										224	355-358	C_c Poppet: Roundness—two 20-microinch PTV waves with 180-degree period and trough at base of each wave; trough dimensions—25 microinches deep by 0.150 inch wide, and 45 microinches deep by 0.173 inch wide
C_c Seat	81-2	01	440 C steel		Circular	1	20	0.4598	0.4810		0.0314				0.0157	0.044	0.4704							3.0												C_c Seat: Roundness--two 18-microinch PTV waves with 180-degree period
D_c Poppet	82-6	01	440 C steel		Circular	1	41	← Same as Model A_c →																										225-227	359-360	
D_c Seat	81-5	01	440 C steel (0.005" land)		Circular	1	41	0.4665	0.4734		0.0046				0.0045	0.086	0.4704							4.0												D_c Seat: Roundness—two 17-microinch PTV waves with 180-degree period
E_c Poppet	82-6	03	440 C steel		Circular	1	41	0.4284	0.5103		0.062						0.4693							3.0										228-230	361-362	E_c Poppet: Roundness--3-microinch PTV short-period (0.11-inch) deviations
E_c Seat	81-6	03	440 C steel		Circular	1	41	0.4507	0.4904		0.0301				0.0293	<0.009	0.4706							3.0												E_c Seat: Roundess—two 15-microinch PTV waves with 180-degree period; 5-microinch PTV short-period (0.04-inch) deviations
F_c Poppet	82-6	02	440 C steel		Circular	1	41	0.4244	0.5098		0.0636						0.4671							3.0										231-232	363-364	F_c Poppet: Roundness—2-microinch PTV short-period (0.15-inch) deviations
F_c Seat	81-6	04	440 C steel		Circular	1	41	0.4504	0.4916		0.0313				0.0304	0.045	0.4710							3.0												F_c Seat: Roundness—two 24-microinch PTV waves with 180-degree period; 2-microinch PTV short-period (0.027-inch) deviations
G_c Poppet	82-6	04	440 C steel		Circular	1	41	0.4282	0.5104		0.0622						0.4693							3.0										233-235	365-366	G_c Poppet: Roundness--round within 3 microinches; six troughs noted; trough dimensions—6 to 10 microinches deep by 0.075 to 0.100 inch wide
G_c Seat	81-6	02	440 C steel		Circular	1	41	0.4503	0.4892		0.0295				0.0287	0.08	0.4698							4.0												G_c Seat: Roundness--two 24-microinch PTV waves with 180-degree period; 2-microinch PTV short-period (0.03-inch) deviations
Spherical																																				
A_s Poppet	80-6	01	440 C steel		Multidirec.	0.1	41																	<1.0				4.0	1.5	0.011				238-243	367-368	A_s Poppet: Round within 10 microinches; two pit densities noted—β = 0.022, h = 7; and β = 0.33, h = 2
A_s Seat	83-6	01	440 C steel		Circular	0.5	41	0.4500	0.4899	0.0301					0.0294	0.0017	0.4700							<1.0												A_s Seat: Round within 3 microinches
B_s Poppet	80-4	01	440 C steel		Multidirec.	0.1	33																	<1.0				4.0	0.16	0.024				244-247	369	B_s Poppet: Round within 10 microinches; pit density of β = 0.14, h ≈ 7
B_s Seat	83-4	01	440 C steel		Circular	0.5	33	0.4532	0.4859	0.0301					0.0241	0.0052	0.4695							<1.0												B_s Seat: Round within 6 microinches
C_s Poppet	80-2	01	440 C steel		Multidirec.	0.1	20																	<1.0				2.0	0.84	0.034				248-249	370	C_s Poppet: Round within 5 microinches; pit density of β = 0.022, h = 3
C_s Seat	83-2	01	440 C steel		Circular	0.5	20	0.4589	0.4795	0.0306					0.0152	0.0065	0.4692							<1.0												C_s Seat: Round within 6 microinches
D_s Poppet	80-6	01	440 C steel		Multidirec.	0.1	41	← Same as Model A_s →																										250	—	
D_s Seat	83-5	01	440 C steel (0.005" land)		Circular	0.5	41	0.4668	0.4750	0.00604					0.00605	0.0013	0.4709							<1.0												D_s Seat: Round within 5 microinches
Sphere on Cone																																				
D_{sc} Poppet	80-6	01	440 C steel (spherical)		Multidirec.	0.5	41	← Same as Model A_s →																												
D_{sc} Seat	81-5	01	440 C steel (conical)		Circular	1	41	← Same as Model D_c →																												
PROCESSED, PLATED, AND COATED MODEL EVALUATION																																				
Processed																																				
I_f Poppet	28A-3	09	440 C steel (lapped)		Unidirec.	0.6			0.519		0.050							1.5	0.6	0.5	1.5	0.6	0.5	1.7	4.0									251-252	—	
I_f Seat	29A-3	09	440 C steel (lapped)		Unidirec.	0.6			0.4998	0.0300	0.0303				0.0442		0.4698							1.9	3.4											
I_{f1} Poppet	28A-3	09-RW1	440 C steel (liquid honed)			6.0		← Same as Model I_f →										3.5	2.5	2.2	3.2	2.5	2.5											253-254	—	
I_{f1} Seat	29A-3	09-RW1	440 C steel (liquid honed)			6.0		← Same as Model I_f →										← Assumed Same as Model I_{f1} Poppet →																		
J_f Poppet	28A-3	010	440 C steel (lapped)		Unidirec.	0.6			0.5195		0.050													1.7	3.6									255-256	—	
J_f Seat	29A-3	010	440 C steel (lapped)		Unidirec.	0.6			0.4998	0.0301	0.0304				0.0444		0.4697							1.6	3.6											
J_{f1} Poppet	28A-3	010-RW1	440 C steel (passivated)		Unidirec.	0.6		← Same as Model J_f →																										257-258	—	
J_{f1} Seat	29A-3	010-RW1	440 C steel (passivated)		Unidirec.	0.6		← Same as Model J_f →																												
U_f Poppet	28-5	01	Tungsten carbide (lapped)		Circular	0.3		← Same as Model CC_f (SURFACE TEXTURE EVALUATION section) →																										259-262	371	
U_f Seat	29A-9	05	Aluminum (anodized)		Circular	1.0			0.4999	0.0248	0.0297	0.0013	10.0	0.08	0.0367		0.4702	1.7	1.2	0.9	1.7	1.2	0.9	3.0												
V_f Poppet	28-5	01	Tungsten carbide (lapped)		Circular	0.3		← Same as Model CC_f (SURFACE TEXTURE EVALUATION section) →																										263-265	372	
V_f Seat	29A-9	04	Aluminum (anodized)	5.6	Circular	0.7			0.5000	0.0	0.0295				0.0436		0.4705	1.6	0.8	0.5	1.4	0.9	0.7	2.0												
Plated																																				
W_f Poppet	28A-3	011-RW1	440C steel (lapped)		Unidirec.	0.5			0.5200		0.0493													1.6	4.3									266-267	—	
W_f Seat	29A-3	012-RW1	440C steel (lapped)		Unidirec.	0.6			0.5001	0.0284	0.0305	0.0012	10.0	0.07	0.0419		0.4696							1.8	3.9											
W_{f1} Poppet	28A-3	011-RW1	440 C steel (lapped)		Unidirec.	0.5		← Same as Model W_f →																										268-276	—	
W_{f1} Seat	29A-3	012-RW2	440 C steel (gold plate)						0.5001		0.0305				0.0419		0.4696																			W_{f1} Seat: 44-microinch gold plate
G_{c1} Poppet	82-6	04	440 C steel		Circular	1	41	← Same as Model G_c (CONICAL AND SPHERICAL MODEL EVALUATION section) →																										236-237	—	
G_{c1} Seat	81-6	02-RW1	440 C steel (gold plate)				41	0.4503	0.4892		0.0295				0.0287		0.4698																			G_{c1} Seat: 44-microinch gold plate
T_f Poppet	28A-3	010-RW2	440 C steel (polished)		Unidirec.	0.4			0.5195		0.0500													1.2	2.9									277-279	—	
T_f Seat	29A-3	010-RW2	440 C steel (polished)		Unidirec.	0.4			0.4999	0.0273	0.0301	0.0004	10.0	0.01	0.0403		0.4698							1.2	3.0											
T_{f1} Poppet	28A-3	010-RW2	440 C steel (polished)		Unidirec.	0.5		← Same as Model T_f →																										280-284	—	
T_{f1} Seat	29A-3	010-RW3	440 C steel (gold plate)						0.4999		0.0301				0.0444		0.4698																			T_{f1} Seat: 30-microinch gold plate

TABLE 4
(Concluded)

Test Model Designation	Test Model Description							Seating Land Data										Profilometer Finish, microinches AA						Cross Lay Surface Texture Parameters (h = PVT Height, microinches; Φ = Average Asperity Angle, degrees; β = Density, in./in.)										Photograph Figure Number	Profile Record Figure Number	Miscellaneous Inspection Notations
	Part Number	Serial Number	Material	Crown Radius, inches	Predominant Surface Lay	Nominal Surface Finish, microinches AA	Seating Angle, degrees	ID, inches	OD, inches	Land Width (L), inches		Corner Runoff			Seat Area (A_{sp}), sq in.	Δ Seating Angle (Δθ), degrees	Mean Diameter (D_s), inches	0.0005-Inch-Radius Tip			0.0001-Inch-Radius Tip			Roughness		Waviness		Nodules			Scratches					
										Flat	Total	Radial Dimension, inches	Height, microinches	Equivalent Radius (R_o), inches				0.030-inch Cutoff	0.010-inch Cutoff	0.003-inch Cutoff	0.030-inch Cutoff	0.010-inch Cutoff	0.003-inch Cutoff	h	Φ	h	Φ	h	Φ	β	h	Φ	β			
Coated																																				
AA_f Poppet	28-5	01	Tungsten carbide		Circular	0.3		← Same as Model AA_f (SURFACE TEXTURE EVALUATION section) →																												AA_f Poppet and Seat: Tested with Viscasil fluid
AA_f Seat	29-3	06-4W2	440 C steel	12	Circular	0.2		← Same as Model AA_f (SURFACE TEXTURE EVALUATION section) →																												
B_{f1} Poppet	28A-3	04-4W4	440 C steel		Circular	0.6		← Same as Model B_{f1} (SURFACE TEXTURE EVALUATION section) →																												B_{f1} Poppet and Seat: Tested with Oronite oil film and Viscasil, Versilube, and Drayco fluids
B_{f1} Seat	29-3	05-4W2	440 C steel		Circular	0.5		← Same as Model B_{f1} (SURFACE TEXTURE EVALUATION section) →																												
J_{f1} Poppet	28A-3	010-4W1	440 C steel (passivated)		Unidirec.	0.6		← Same as Model J_{f1} (SURFACE TEXTURE EVALUATION section) →																												J_{f1} Poppet and Seat: Tested with Viscasil fluid
J_{f1} Seat	29A-3	010-4W1	440 C steel (passivated)		Unidirec.	0.6		← Same as Model J_{f1} (SURFACE TEXTURE EVALUATION section) →																												
SEATING ERROR INVESTIGATION																																				
G Poppet	28-3	04-4W2	440 C steel (polished)		Multidirec.	0.25		← Similar to Model G below (S/N 04-4W3) but without test scratches →																										285-286	—	
G Poppet	28-3	04-4W3	440 C steel (polished)		Multidirec.	0.25			1.012		0.490							0.8	0.55	0.35	1.0	0.6	0.5					2.3	0.3	0.094	← See Discussion →					
G Seat	29-3	06	440 C steel (lapped)		Unidirec.	0.5		← Same as Model F (SURFACE TEXTURE EVALUATION section) →																												
H Poppet	28-3	05	440 C steel		Multidirec.	2.5			1.012		0.490							2.1	1.6	1.4				← Same as 29-3 S/N 05 →										287-288	373	H Poppet: 10 microinches out-of-flat
H Seat	29-3	05	440 C steel		Multidirec.	2.5			0.4990	0.0283	0.0287				0.0418		0.4703	2.0	1.7	1.5	2.5	2.3	2.1	7.4	1.2			4.4	1.1	0.046						
I Poppet	28-3	05-4W1	440 C steel		Multidirec.	2.6			1.012		0.490							2.1	1.8	1.6	2.7	2.4	2.1	7.9	1.3			4.7	1.1	0.05				289	374	I Poppet: 20 microinches out-of-flat
I Seat	29-3	05	440 C steel		Multidirec.	2.5		← Same as Model H →																												
B Poppet	28-3	03	440 C steel		Multidirec.	1.5		← Same as Model B (SURFACE TEXTURE EVALUATION section) →																												B Poppet: 125 microinches out-of-parallel
B Seat	29-3	03	440 C steel		Multidirec.	2.2		← Same as Model B (SURFACE TEXTURE EVALUATION section) →																												
E_c Poppet	82-6	03	440 C steel		Circular	1	41	← Same as Model E_c (CONICAL AND SPHERICAL MODEL EVALUATION section) →																												E_c Poppet: Cone axis tilted 0.313 and 0.215 degrees
E_c Seat	81-6	03	440 C steel		Circular	1	41	← Same as Model E_c (CONICAL AND SPHERICAL MODEL EVALUATION section) →																												
H_c Poppet	82-6	02	440 C steel		Circular	1	41	← Same as Model F_c (CONICAL AND SPHERICAL MODEL EVALUATION section) →																												H_c Poppet: Cone axis tilted 0.313 degrees
H_c Seat	81-5	01	440 C steel (0.005" land)		Circular	1	41	← Same as Model D_c (CONICAL AND SPHERICAL MODEL EVALUATION section) →																												
L Poppet	28-3	03	440 C steel		Multidirec.	1.5		← Same as Model H (SURFACE TEXTURE EVALUATION section) →																										290-295	—	
L Seat	27-3	01	440 C steel		Unidirec.	0.6			1.000	0.060	0.060				0.177		0.940							1.9												L Seat: Contaminated
CYCLE TESTS																																				
Preliminary																																				
D_f Poppet	28-3	01-4W1	440 C steel		Unidirec.	2.0		← Same as Model D_f (SURFACE TEXTURE EVALUATION section) →																												
D_f Seat	29-3	01-4W1	440 C steel		Unidirec.	2.7		← Same as Model D_f (SURFACE TEXTURE EVALUATION section) →																												
G_{f1} Poppet	28-3	03-4W1	440 C steel		Unidirec.	0.7		← Same as Model G_{f1} (SURFACE TEXTURE EVALUATION section) →																												
G_{f1} Seat	29-3	04-4W1	440 C steel		Unidirec.	0.7		← Same as Model G_{f1} (SURFACE TEXTURE EVALUATION section) →																												
B_{f1} Poppet	28A-3	04-4W4	440 C steel		Circular	0.6		← Same as Model B_{f1} (SURFACE TEXTURE EVALUATION section) →																												
B_{f1} Seat	29-3	05-4W2	440 C steel		Circular	0.5		← Same as Model B_{f1} (SURFACE TEXTURE EVALUATION section) →																												
B_c Poppet	82-4	01	440 C steel		Circular	1	33	← Same as Model B_c (CONICAL AND SPHERICAL MODEL EVALUATION section) →																												
B_c Seat	81-4	01	440 C steel		Circular	1	33	← Same as Model B_c (CONICAL AND SPHERICAL MODEL EVALUATION section) →																												
X_f Poppet	28A-3	08	440 C steel		Unidirec.	0.5			0.5195		0.0498													1.4	2.8									296-303	—	
X_f Seat	29A-3	011	440 C steel		Unidirec.	0.5			0.4995	0.0299	0.0301				0.0440		0.4696							1.5	3.2											
Performance Comparison																																				
Y_f Poppet	28A-3	011	440 C steel		Unidirec.	0.6			0.5200		0.0493													1.7	3.8									304-312	—	
Y_f Seat	29A-3	012	440 C steel		Unidirec.	0.7			0.5004	0.0303	0.0307	0.0009	5.0	0.08	0.0447		0.4697							2.0	2.9											
AA_f Poppet	28-5	01	Tungsten carbide		Circular	0.3		← Same as Model AA_f (SURFACE TEXTURE EVALUATION section) →																												
AA_f Seat	29-3	06-4W2	440 C steel	12	Circular	0.2		← Same as Model AA_f (SURFACE TEXTURE EVALUATION section) →																												AA_f Seat: Five scratches 5 microinches deep by 100 microinches wide; one scratch 3 microinches deep by 60 microinches wide
P_f Poppet	28A-3	09-4W2	440 C steel		Unidirec.	0.3			0.5008	0.0258	0.0306	0.0017	20.0	0.075	0.0381		0.4706							1.6	3.1									313-321	—	
P_f Seat	29A-3	09-4W2	440 C steel		Unidirec.	0.7			0.5002	0.0261	0.0301	0.002	10.0	0.20			0.4701							2.1	3.6											
Z_f Poppet	28A-3	09-4W3	440 C steel	16	Circular	0.4			0.5014	0.0	0.0310	0.007	25.0	1.0			0.4704							1.2	2.5									322-328	—	
Z_f Seat	29A-3	09-4W3	440 C steel	6.0	Circular	0.5			0.5007	0.0	0.0308	0.0035	20.0	0.30	0.0454		0.4699							1.5	2.0											Z_f Seat: Surface texture primarily elongated pits; pit density of β = 0.75, h = 1.5
A_s Poppet	80-6	01	440 C steel		Multidirec.	0.1	41	← Same as Model A_s (CONICAL AND SPHERICAL MODEL EVALUATION section) →																												
A_s Seat	83-6	01	440 C steel		Circular	0.5	41	← Same as Model A_s (CONICAL AND SPHERICAL MODEL EVALUATION section) →																												
T_{f1} Poppet	28A-3	010-4W2	440 C steel (polished)		Unidirec.	0.5		← Same as Model T_{f1} (PROCESSED, PLATED, AND COATED MODEL EVALUATION section) →																												
T_{f1} Seat	29A-3	010-4W3	440 C steel (gold plate)					← Same as Model T_{f1} (PROCESSED, PLATED, AND COATED MODEL EVALUATION section) →																												T_{f1} Seat: 30-microinch gold plate

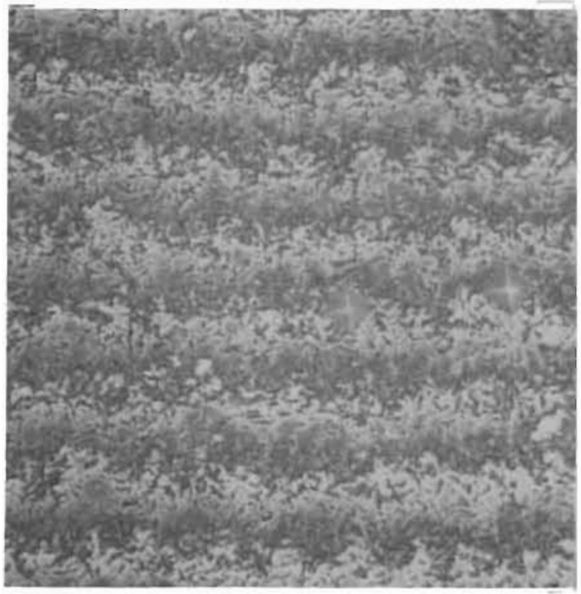

Figure 105. Test Model A, Seat, 0.0065- x 0.0065-Inch Interference Photo

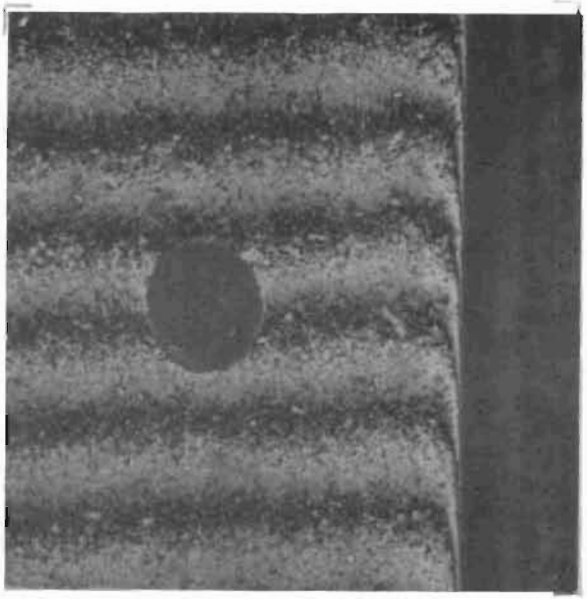

Figure 106. Test Model A, Seat, 0.033- x 0.033-Inch Interference Photo Showing Duboff and Pressure Tap

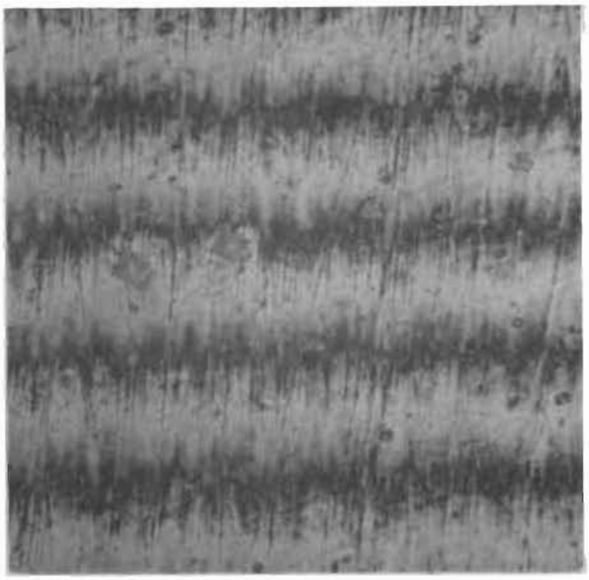

Figure 107. Test Model A, Poppet, 0.0065- x 0.0065-Inch Interference Photo, Cross Lay

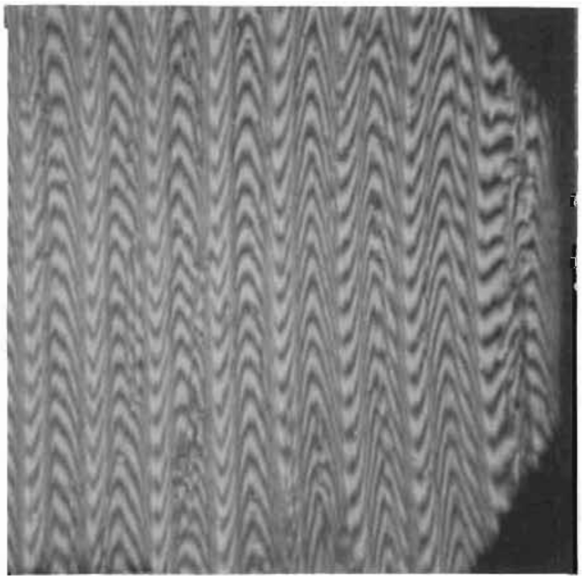

Figure 108. Test Model Q_f, Seat, 0.0065- x 0.0065-Inch Interference Photo, OD Plastic Deformation at Right

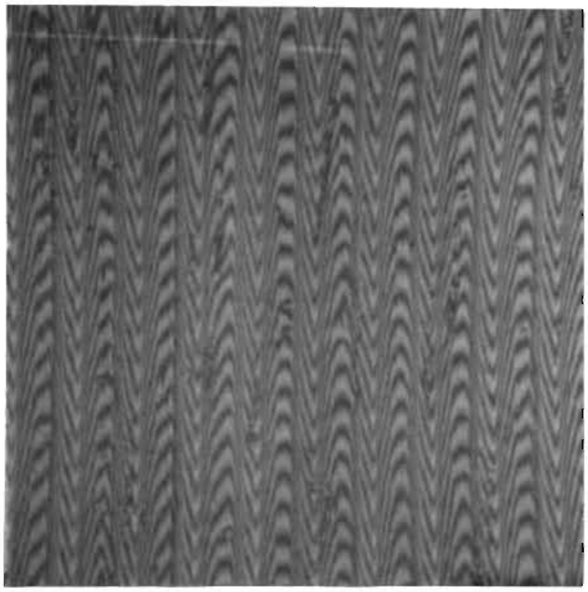

Figure 109. Test Model Q_f, Poppet, 0.0065- x 0.0065-Inch Interference Photo, Center Plastic Deformation Corresponds to Seat OD

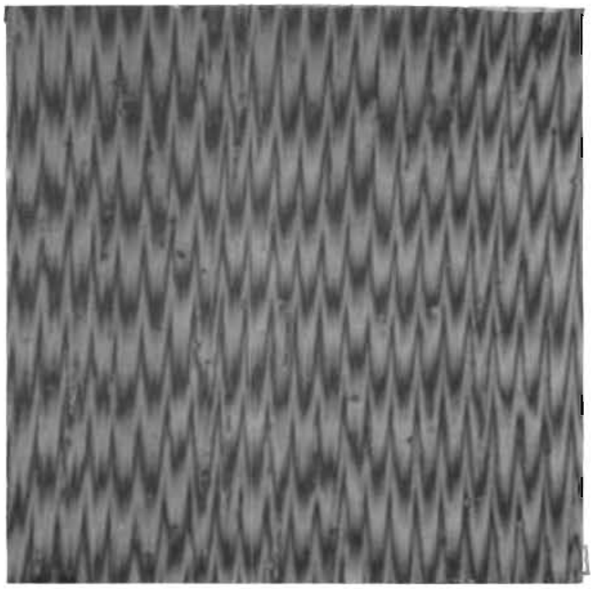

Figure 110. Test Model N_f, Seat, 0.0065- x 0.0065-Inch Interference Photo

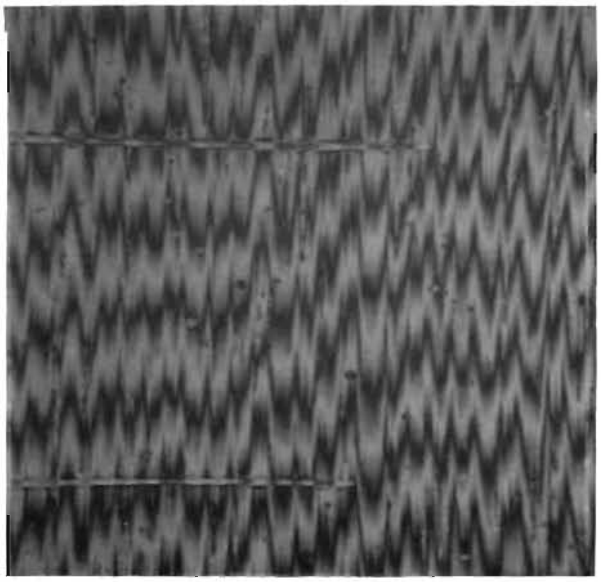

Figure 111. Test Model N_f, Poppet, 0.0065- x 0.0065-Inch Interference Photo (Tracks From 0.0001-Inch Profilometer Stylus)

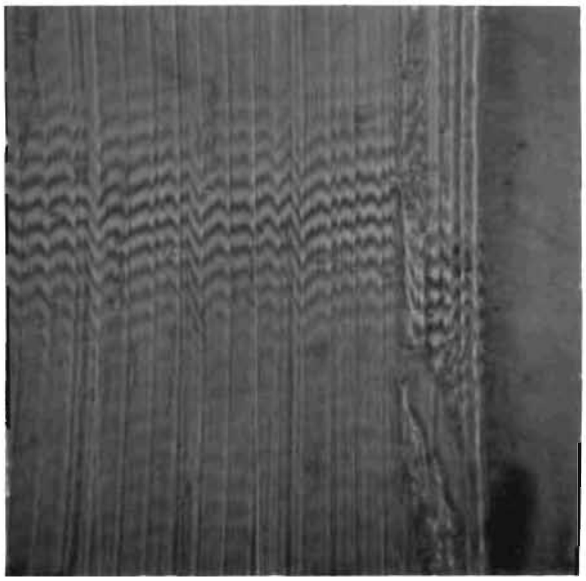

Figure 112. Test Model N_f, Seat, 0.0065- x 0.0065-Inch Interference Photo Showing OD Plastic Deformation, White Light

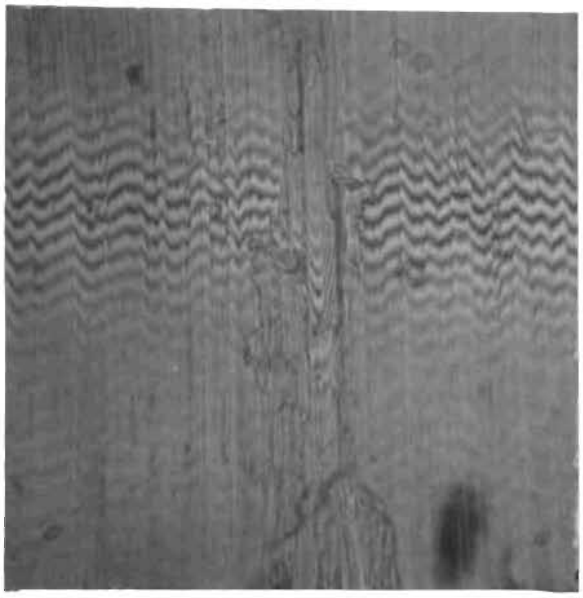

Figure 113. Test Model N_f, Poppet, 0.0065- x 0.0065-Inch Interference Photo Showing Plastic Deformation at Area of Seat Land OD Contact, White Light

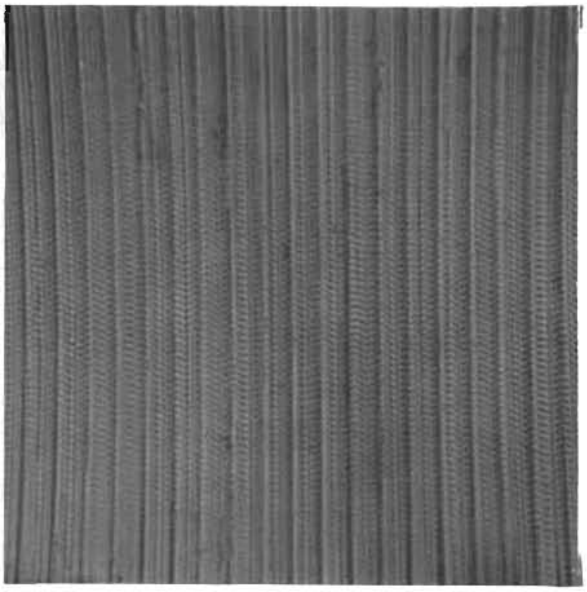

Figure 114. Test Model R_f, Seat, 0.0065- x 0.0065-Inch Interference Photo, Narrow Bands

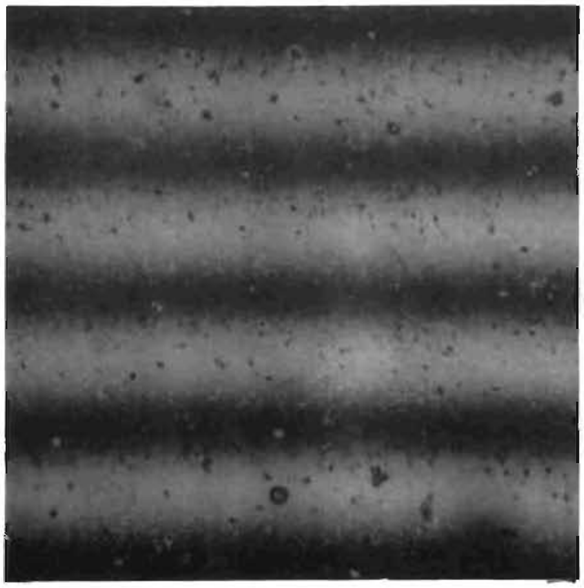

Figure 115. Test Model R_f and S_f, Poppet, 0.0065- x 0.0065-Inch Interference Photo

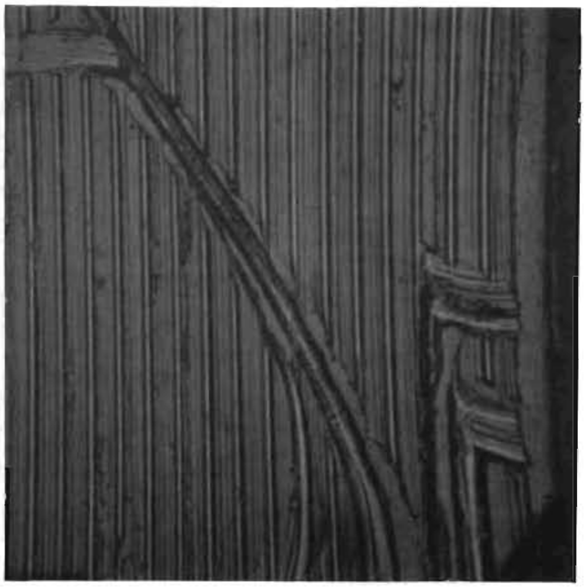

Figure 116. Test Model R_f, Seat, 0.0065- x 0.0065-Inch Plain Photo Showing OD Plastic Deformation at Right and Handling Scratch

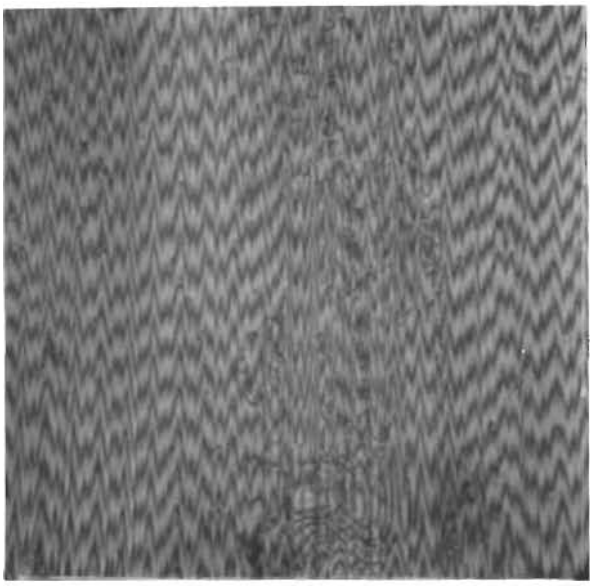

Figure 117. Test Model S_f, Seat, 0.0065- x 0.0065-Inch Interference Photo Showing Plastic Deformation

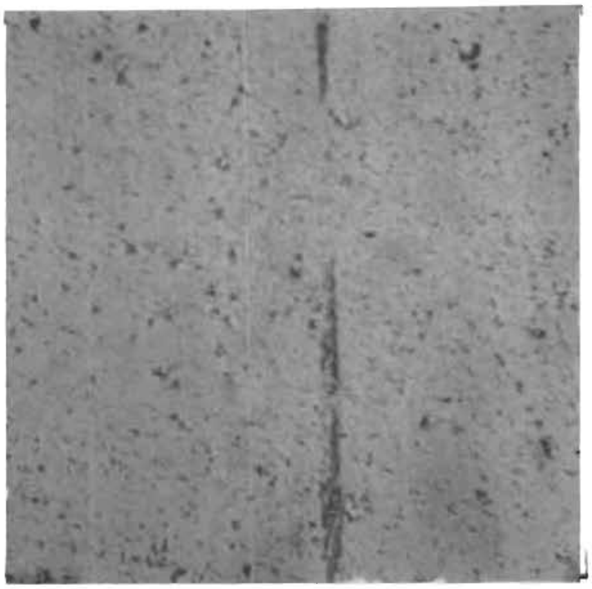

Figure 118. Test Model S_f and R_f, Poppet, 0.0065- x 0.0065-Inch Plain Photo Showing Metal Transfer

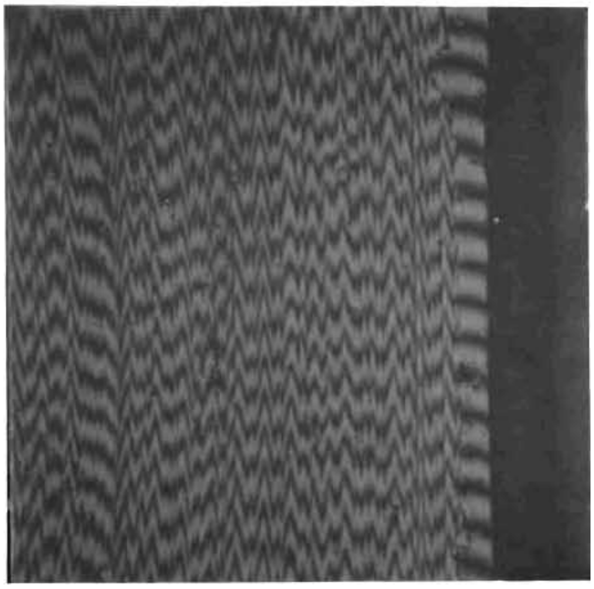

Figure 119. Test Model S_f, Seat, 0.0065- x 0.0065-Inch Interference Photo Showing OD Deformation

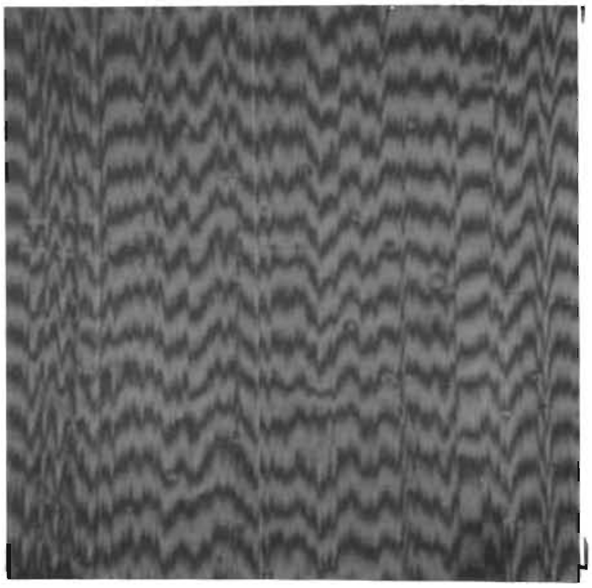

Figure 120. Test Model D_f, Poppet, 0.0065- x 0.0065-Inch Interference Photo, Tracks From 0.0001-Inch Radius Proficorder Stylus

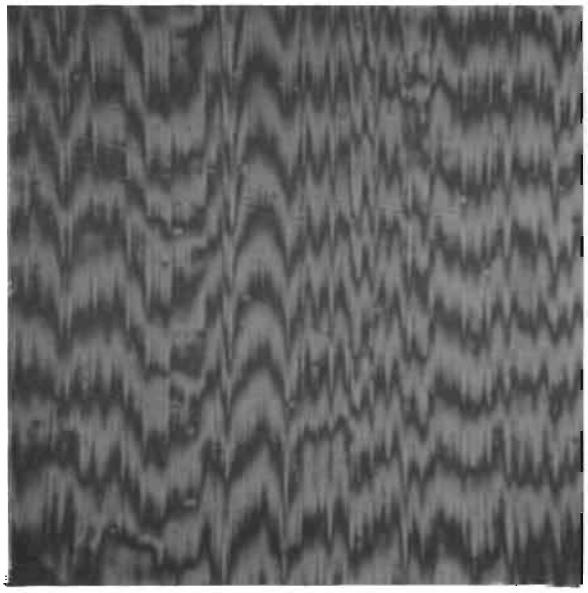

Figure 121. Test Model D_f, Seat, 0.0065- x 0.0065-Inch Interference Photo, Tracks From 0.0001-Inch Radius Proficorder Stylus

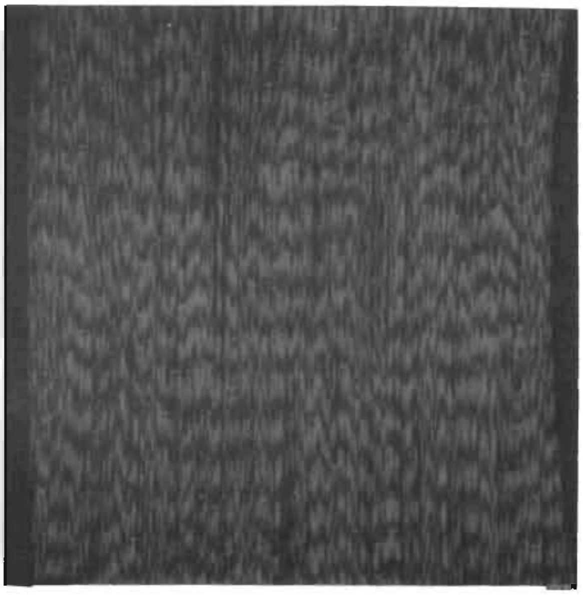

Figure 122. Test Model D_f, Seat, 0.033- x 0.033-Inch Interference Photo, Showing Cross-Land Waviness

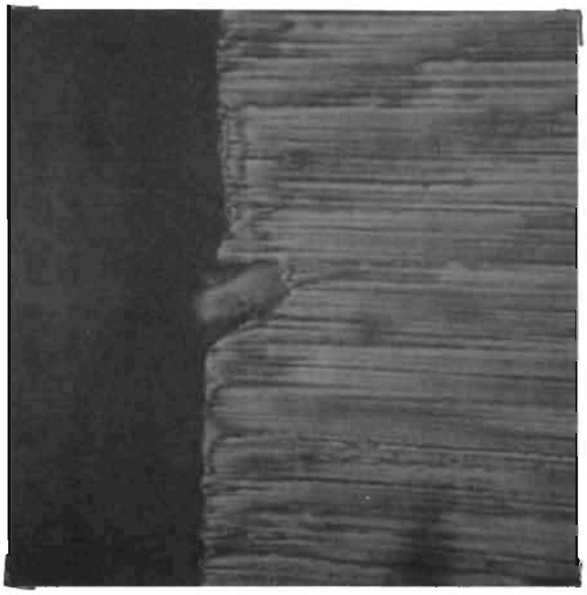

Figure 123. Test Model D_f, Seat, 0.0065- x 0.0065-Inch Interference Photo at OD Showing Fracture

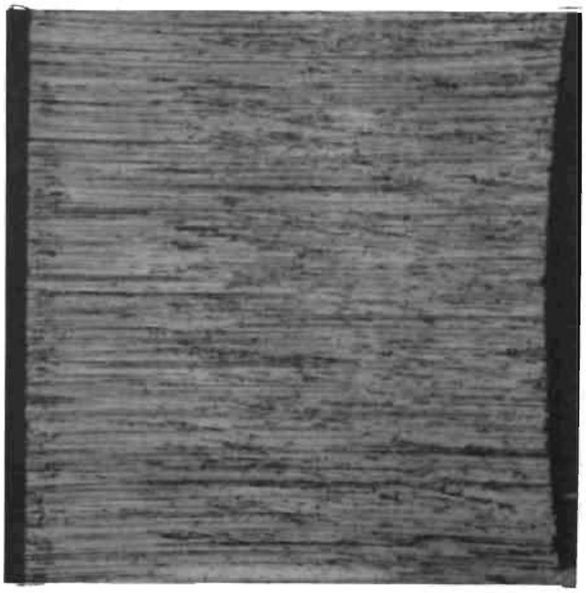

Figure 124. Test Model D_f, Seat, 0.033- x 0.033-Inch Plain Photo Showing Corrosion Fretting After 91,800-psi Cycle Test

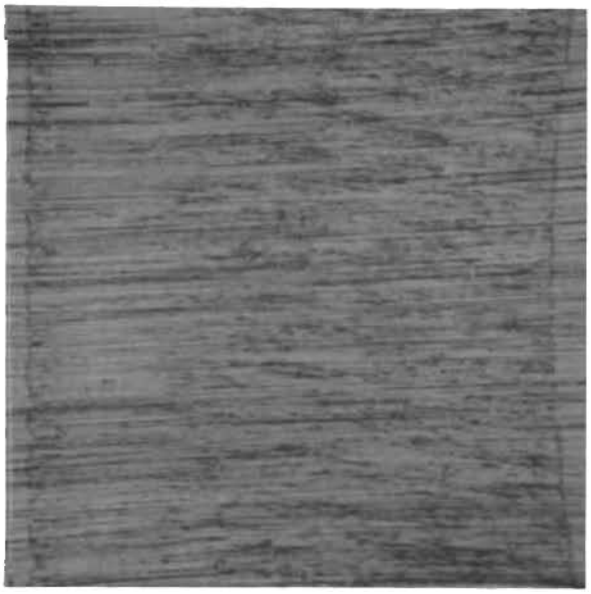

Figure 125. Test Model D_f, Poppet, 0.033- x 0.033-Inch Plain Photo Showing Corrosion Fretting After 91,800-psi Cycle Test

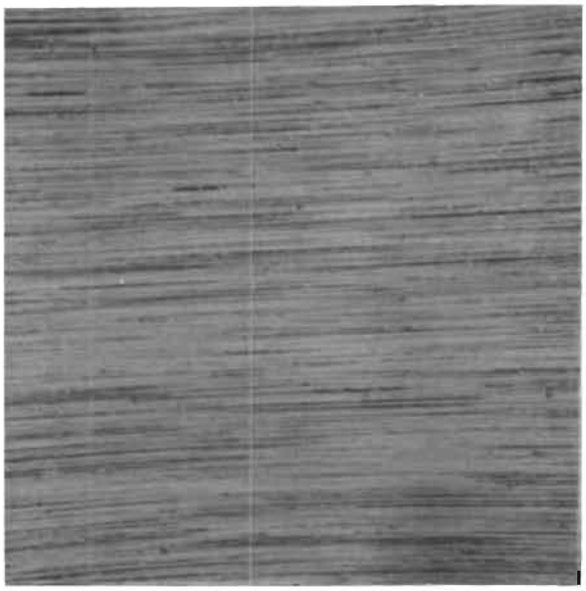

Figure 126. Test Model D_f, Poppet, 0.033- x 0.033-Inch Plain Photo, Same Location as Fig. 125 After Wiping

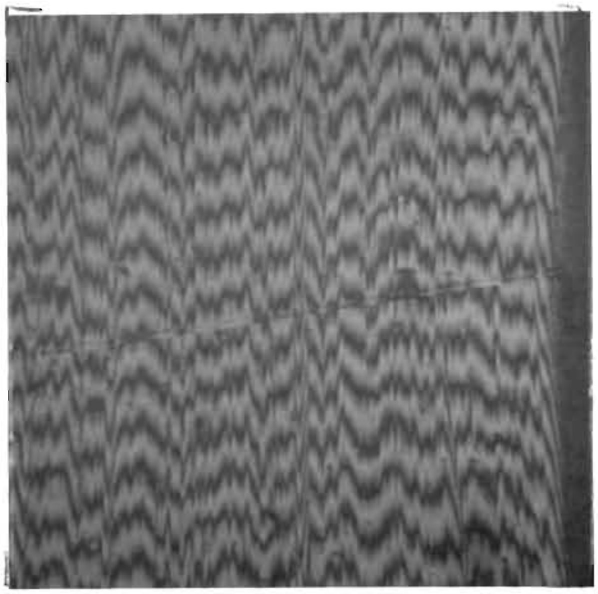

Figure 127. Test Model A_f, Seat, 0.0065- x 0.0065-Inch Interference Photo at ID, Track From 0.0001-Inch Radius Proficorder Stylus

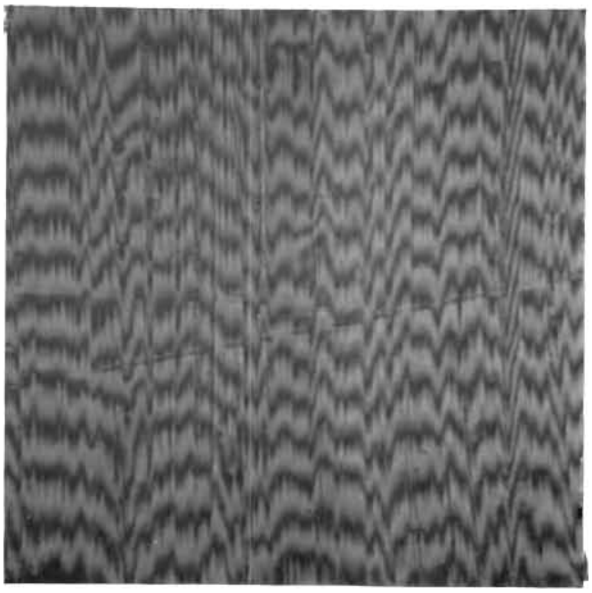

Figure 128. Test Model A_f, Poppet, 0.0065- x 0.0065-Inch Interference Photo, Tracks From 0.0001-Inch Radius Proficorder and Profilometer Stylii

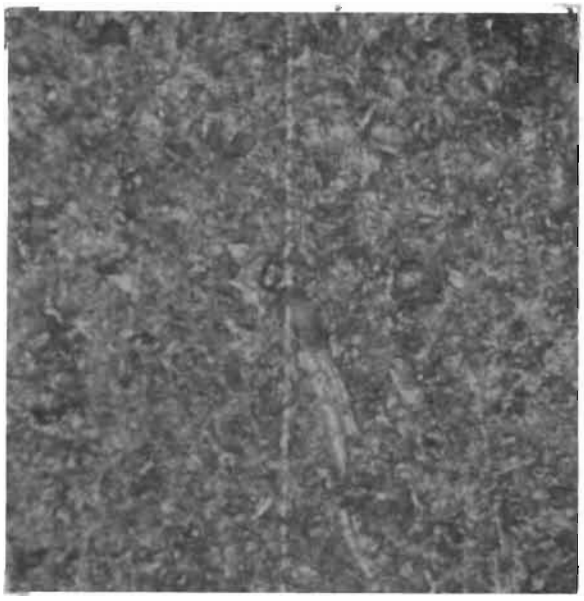

Figure 129. Test Model D, Poppet, 0.0065- x 0.0065-Inch Plain Photo Showing 0.0001-Inch Radius Proficorder Stylus Scratches

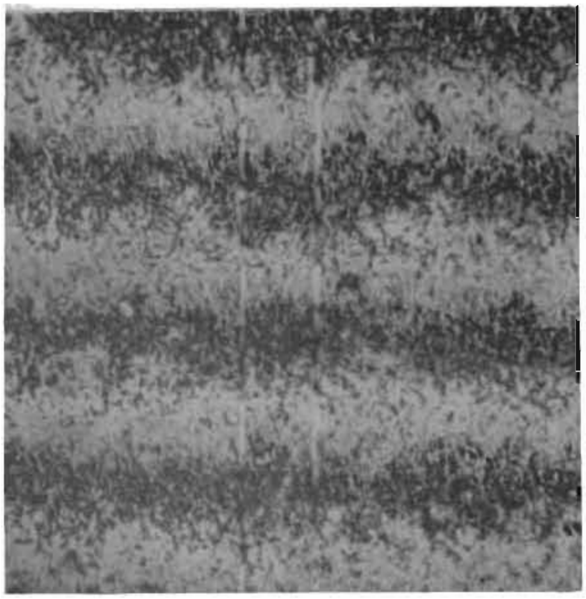

Figure 130. Test Model B, Poppet, 0.0065- x 0.0065-Inch Interference Photo Showing 0.0005-Inch Radius Profilometer Stylus Scratches

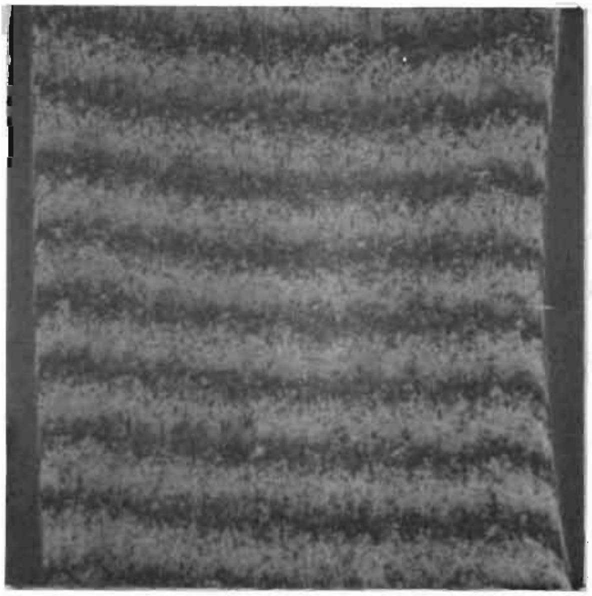

Figure 131. Test Model B, Seat, 0.033- x 0.033-Inch Interference Photo Showing Duboff

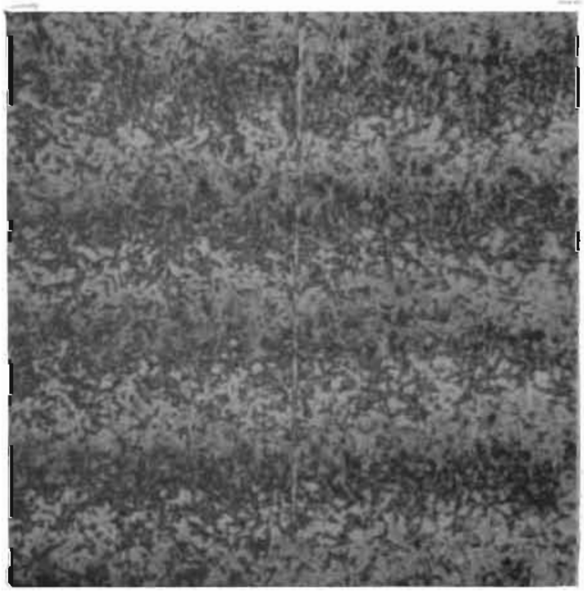

Figure 132. Test Model J, Poppet, 0.0065- x 0.0065-Inch Interference Photo Showing 0.0001-Inch Radius Proficorder Stylus Scratch

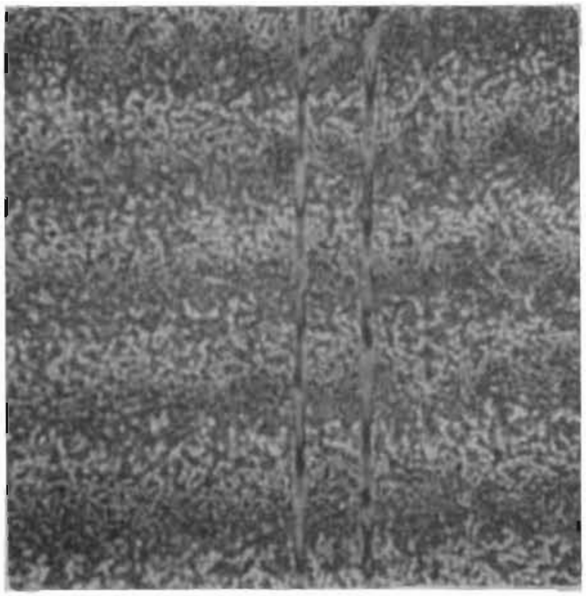

Figure 133. Test Model J, Poppet, 0.0065- x 0.0065-Inch Interference Photo Showing 0.0005-Inch Radius Profilometer Stylus Scratches

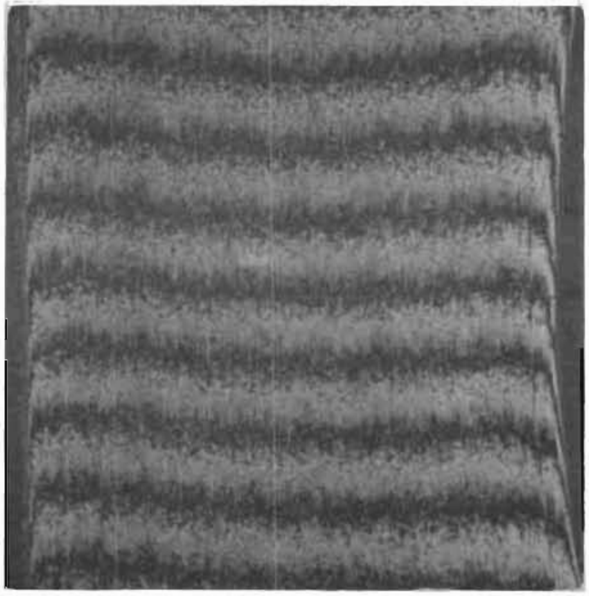

Figure 134. Test Model J, Seat, 0.033- x 0.033-Inch Interference Photo

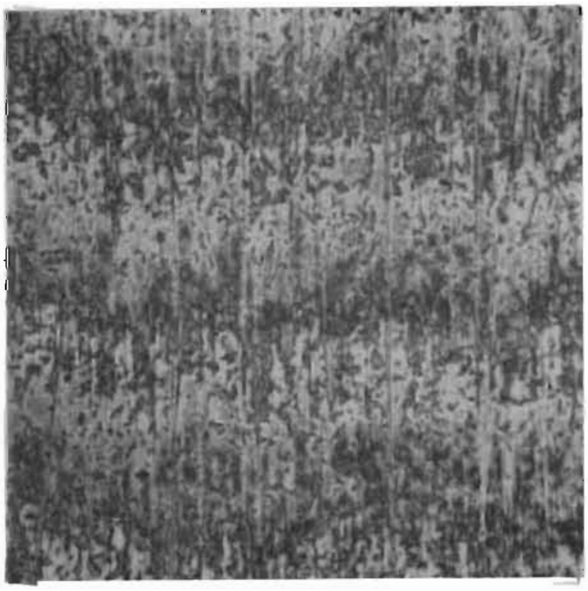

Figure 135. Test Model K, Seat, 0.0065- x 0.0065-Inch Interference Photo Across Circumferentially Polished Lay

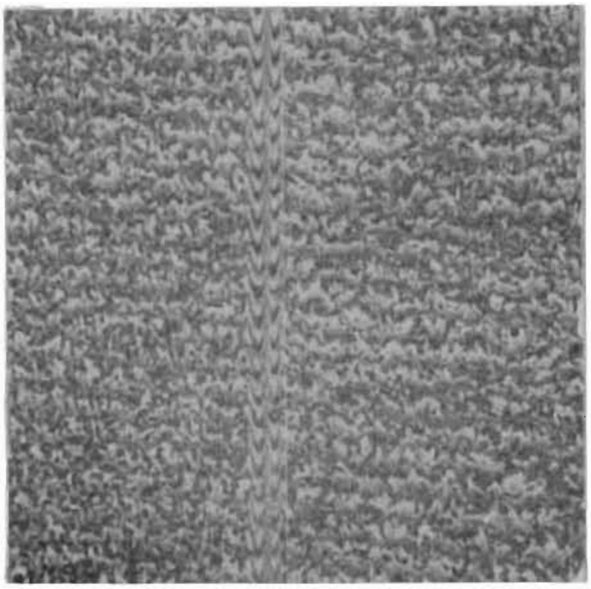

Figure 136. Test Model K, Seat, 0.0065- x 0.0065-Inch Interference Photo Showing 0.0005-Inch Radius Profilometer Stylus Scratches

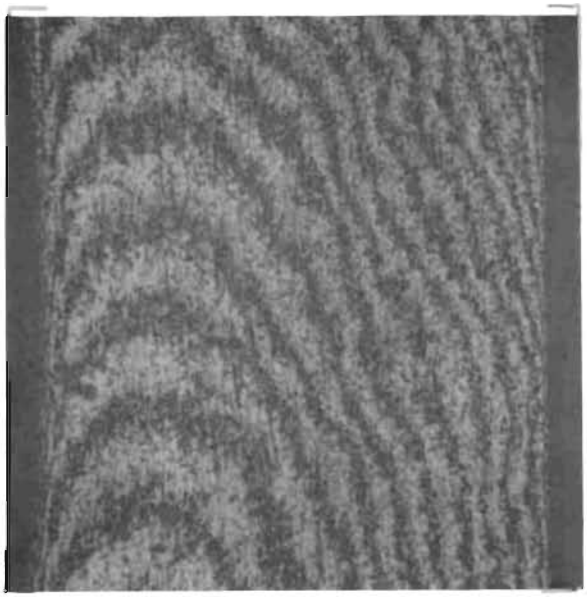

Figure 137. Test Model K, Seat, 0.033- x 0.033-Inch Interference Photo Showing OD Plastic Reformation Following Test 1

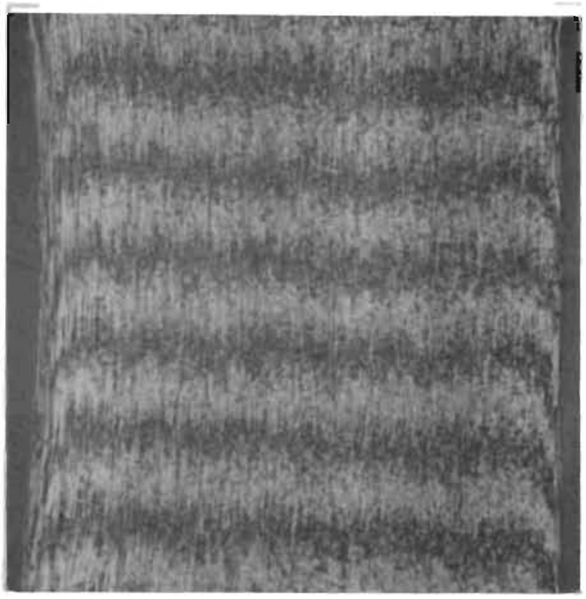

Figure 138. Test Model K, Seat, 0.033- x 0.033-Inch Interference Photo After Rework, Prior to Test 2

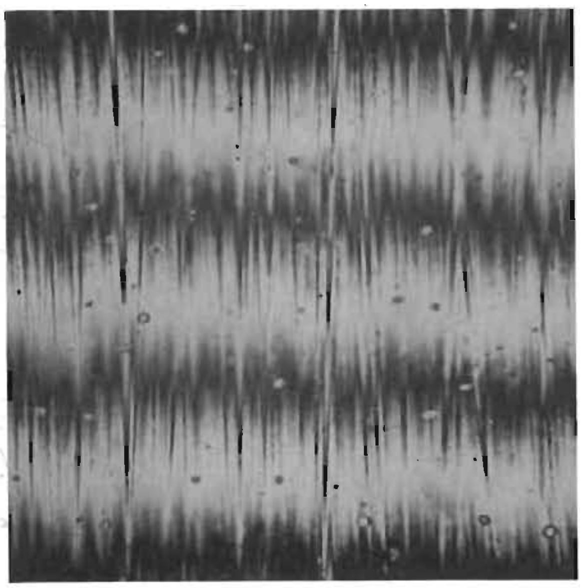

Figure 139. Test Model F, Seat, 0.0065- x 0.0065-Inch Interference Photo, Cross Lay (Dots on Reference Mirror)

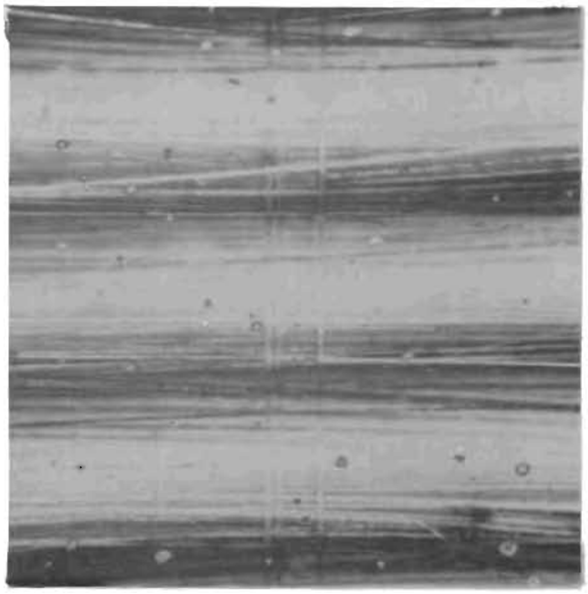

Figure 140. Test Model F, Seat, 0.0065- x 0.0065-Inch Interference Photo With-Lay Showing 0.0005-Inch Radius Profilometer Stylus Scratches

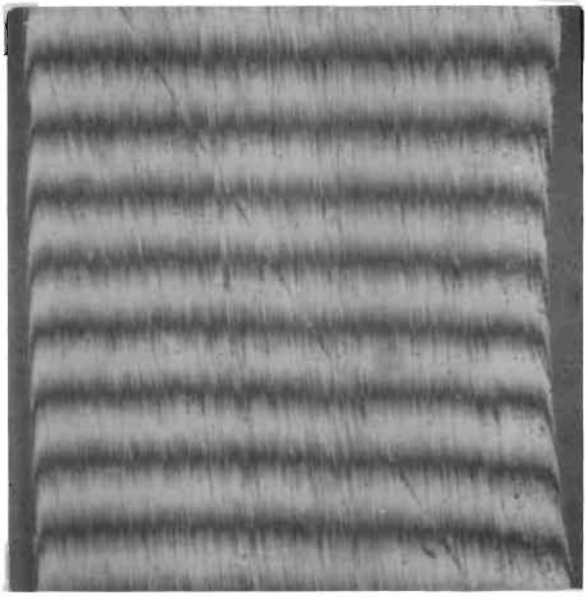

Figure 141. Test Model F, Seat, 0.033- x 0.033-Inch Interference Photo

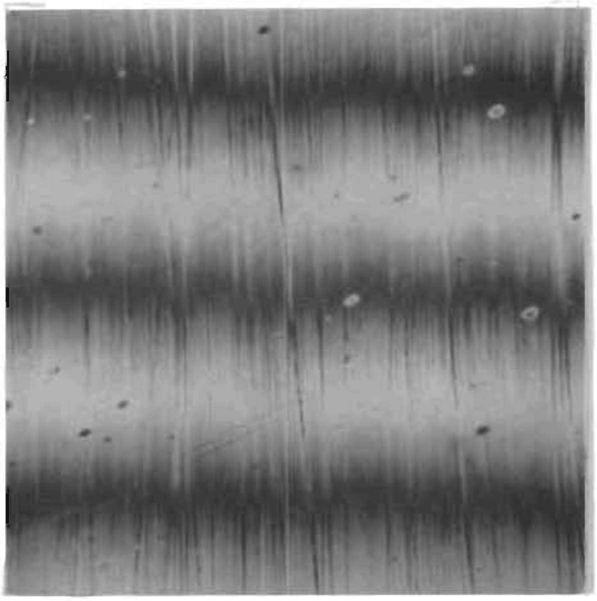

Figure 142. Test Model F, Poppet, 0.0065- x 0.0065-Inch Interference Photo, Cross Lay

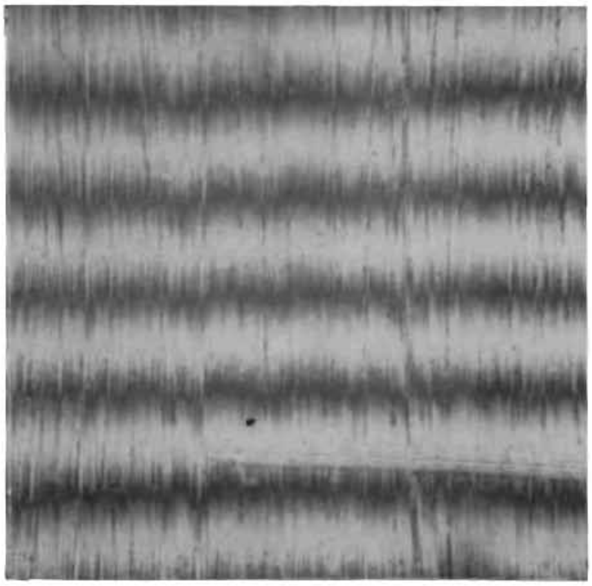

Figure 143. Test Model G_f, Poppet, 0.0065- x 0.0065-Inch Interference Photo, Tracks From 0.0005-Inch Radius Profilometer Stylus

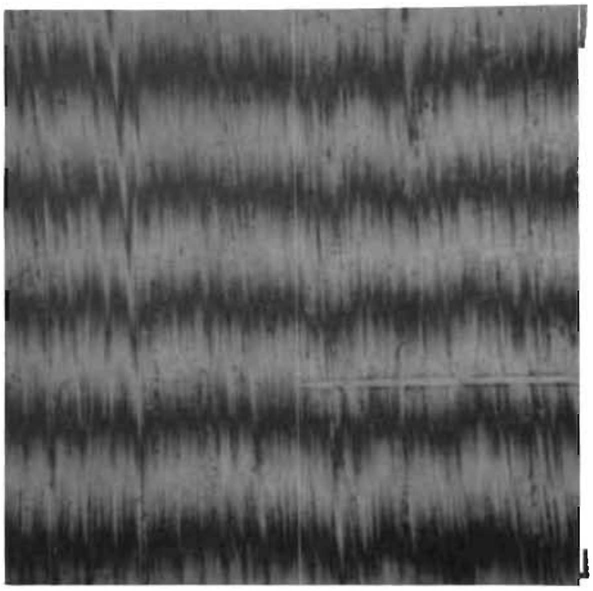

Figure 144. Test Model G_f, Seat, 0.0065- x 0.0065-Inch Interference Photo, Track From 0.0001-Inch Profilometer Stylus

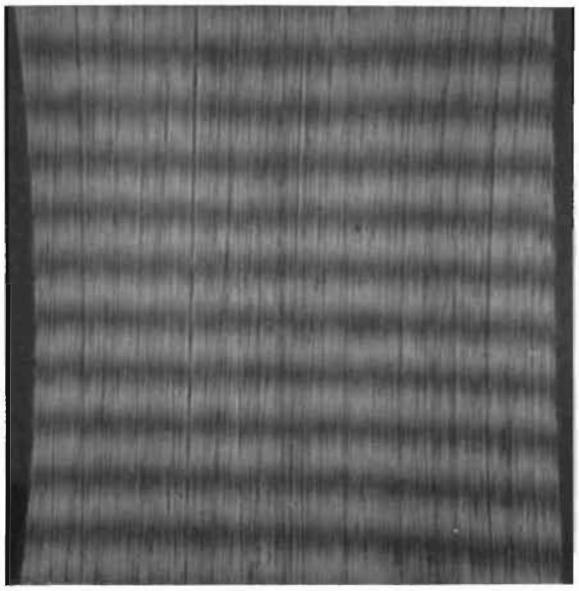

Figure 145. Test Model G_f, Seat, 0.033- x 0.033-Inch Interference Photo

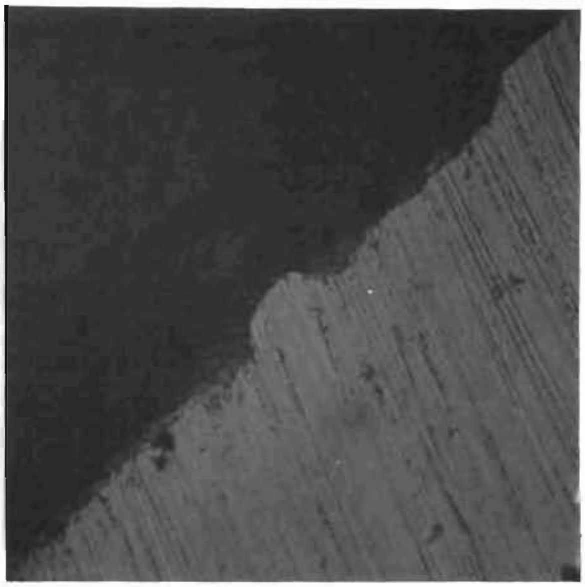

Figure 146. Test Model G_f, Seat, 0.0065- x 0.0065-Inch Plain Photo Showing Corner Fracture Damage (OD)

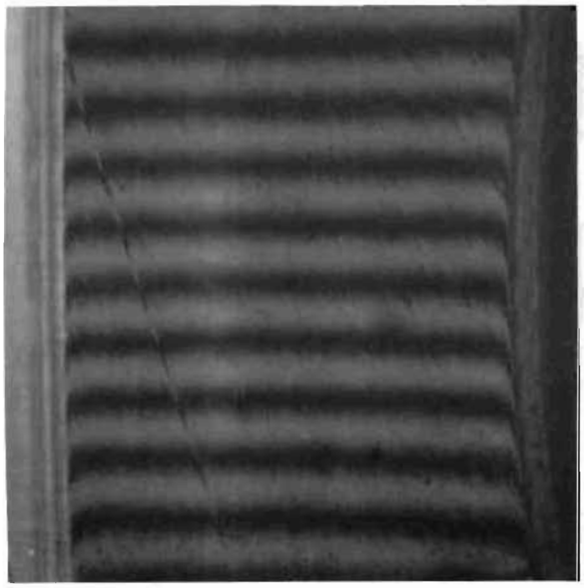

Figure 147. Test Model G_{f1}, Seat, 0.033- x 0.033-Inch Interference Photo

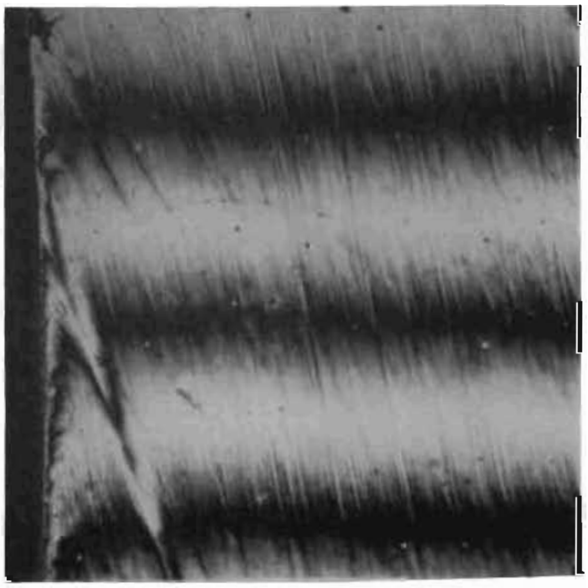

Figure 148. Test Model G_{f1}, Seat, 0.0065- x 0.0065-Inch Interference Photo, Same Location as Fig. 147

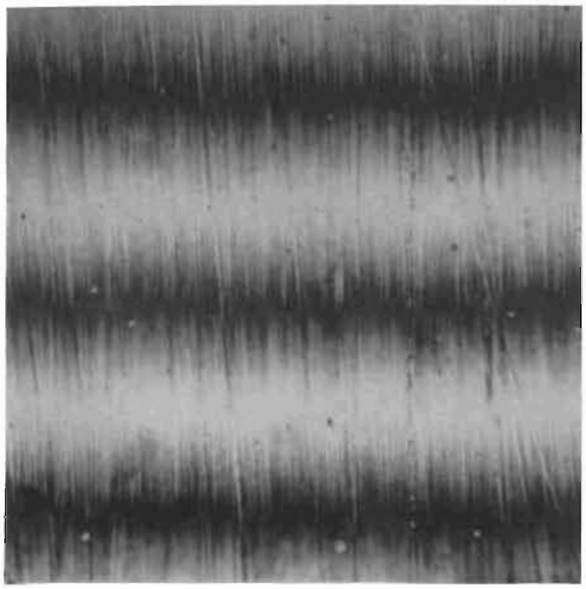

Figure 149. Test Model G_{f1}, Poppet, 0.0065- x 0.0065-Inch Interference Photo

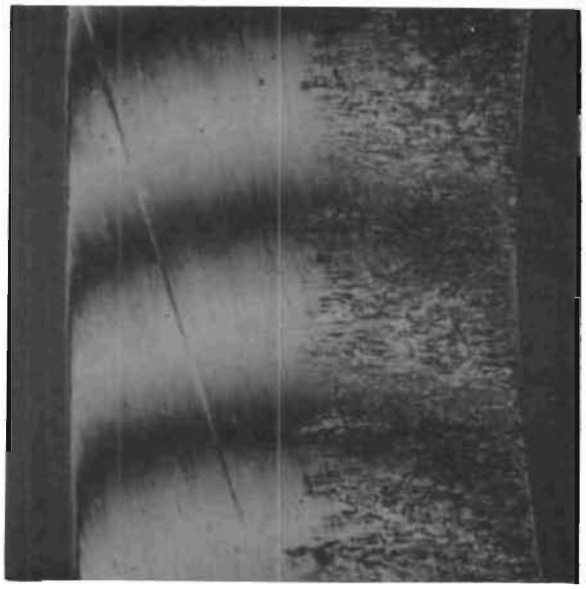

Figure 150. Test Model G_{f1}, Seat, 0.033- x 0.033-Inch Interference Photo, Same Location as Fig. 147

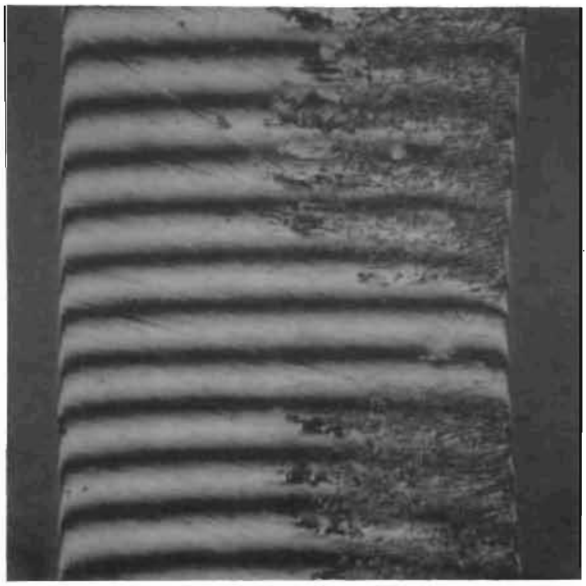

Figure 151. Test Model G_{f1}, Seat, 0.033- x 0.033-Inch Interference Photo Showing Corrosion Fretting Before Wiping

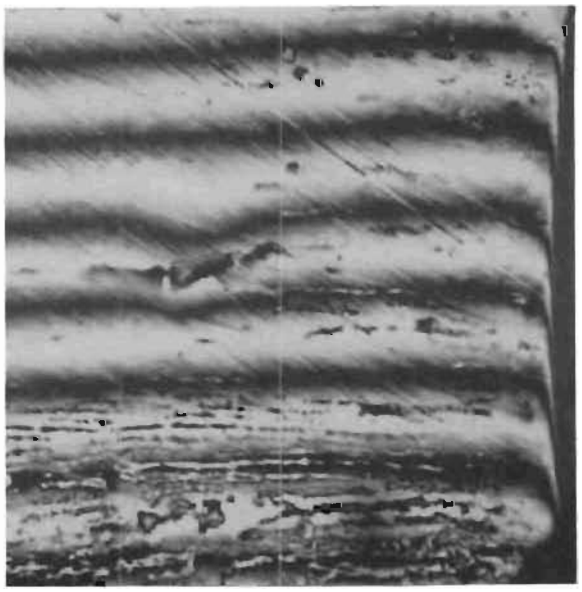

Figure 152. Test Model G_{f1}, Seat, 0.0065- x 0.0065-Inch Interference Photo, Same Location as Fig. 151 at ID

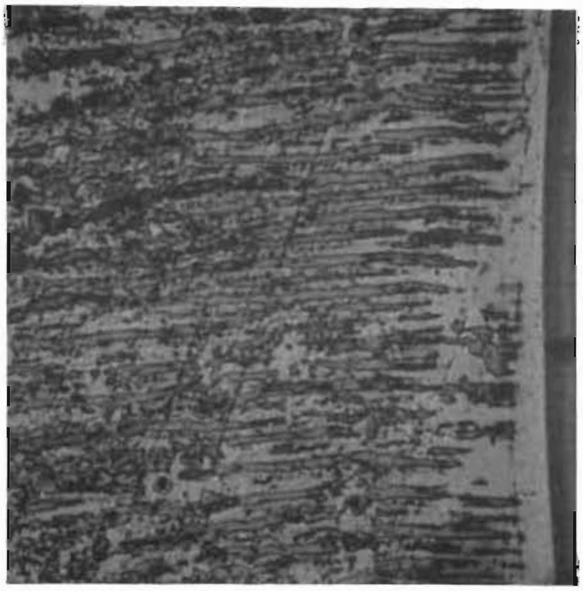

Figure 153. Test Model G_{f1}, Seat, 0.0065- x 0.0065-Inch Plain Photo Showing Corrosion Fretting Before Wiping at ID

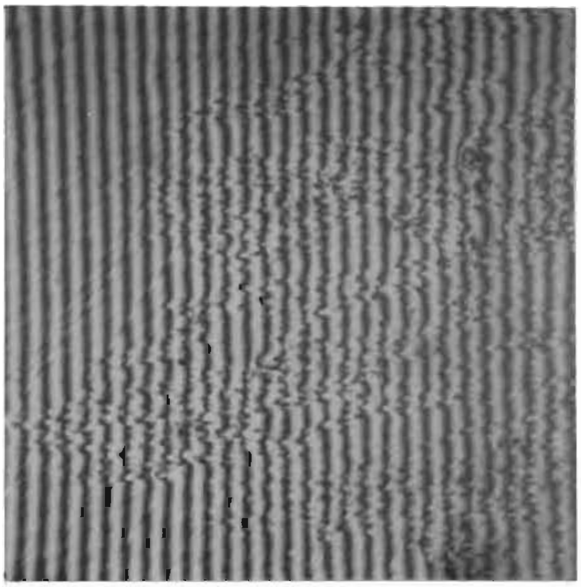

Figure 154. Test Model G_{f1}, Seat, 0.0065- x 0.0065-Inch Interference Photo Showing Fretted Surface After Polishing (ID Right)

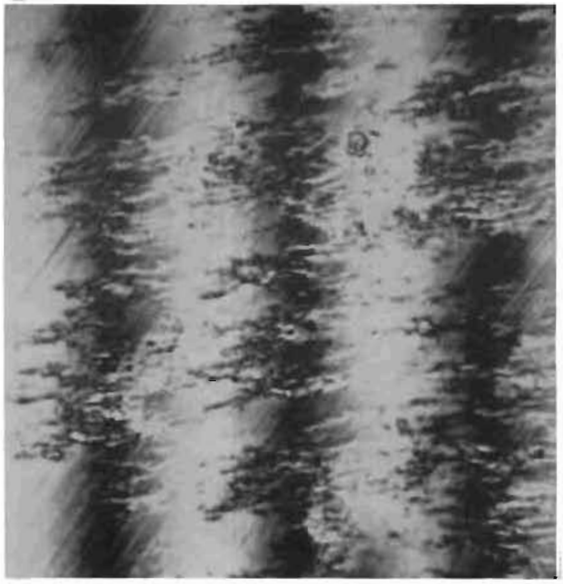

Figure 155. Test Model G_{f1}, Seat, 0.0065- x 0.0065-Inch Interference Photo, Same Location as Fig. 154

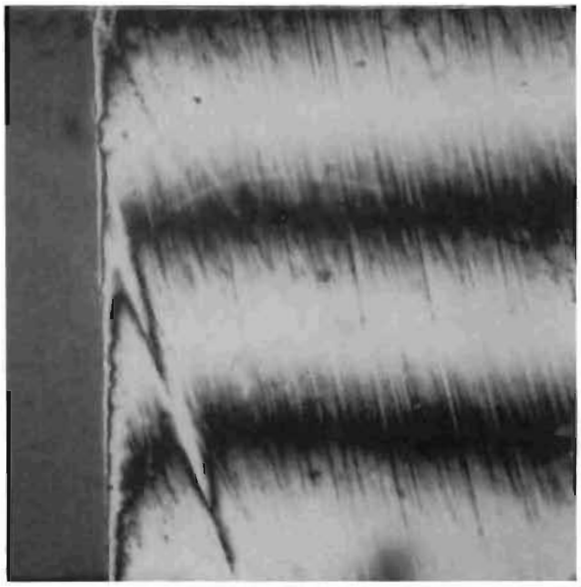

Figure 156. Test Model G_{f1}, Seat, 0.0065- x 0.0065-Inch Interference Photo, Same Location as Fig. 148

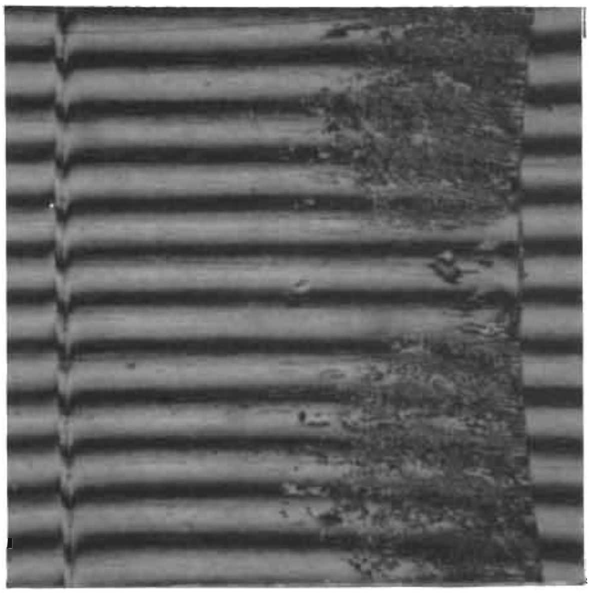

Figure 157. Test Model G_{f1}, Poppet, 0.033- x 0.033-Inch Interference Photo, Same Location as Fig. 151

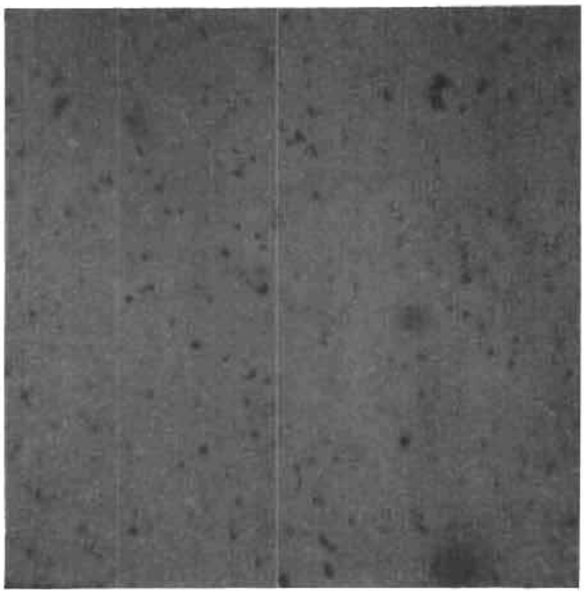

Figure 158. Test Model CC_f, Poppet, 0.0065- x 0.0065-Inch Plain Photo

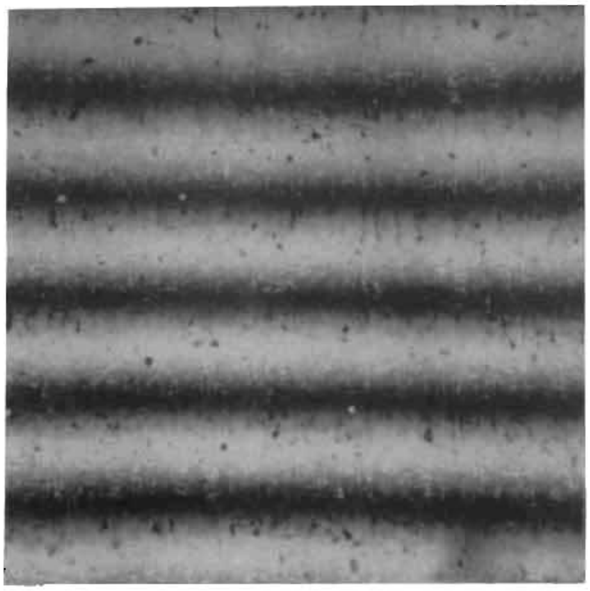

Figure 159. Test Model CC_f, Poppet, 0.0065- x 0.0065-Inch Interference Photo

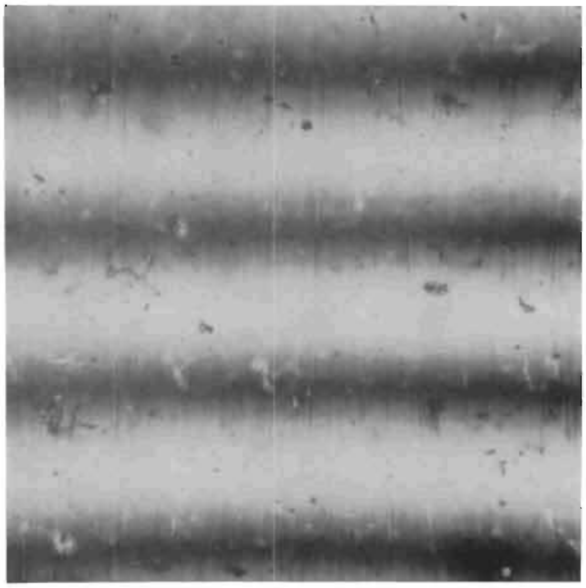

Figure 160. Webber "Chroblox" Master Gage Block, 0.0065- x 0.0065-Inch Interference Photo For Comparison With Fig. 159

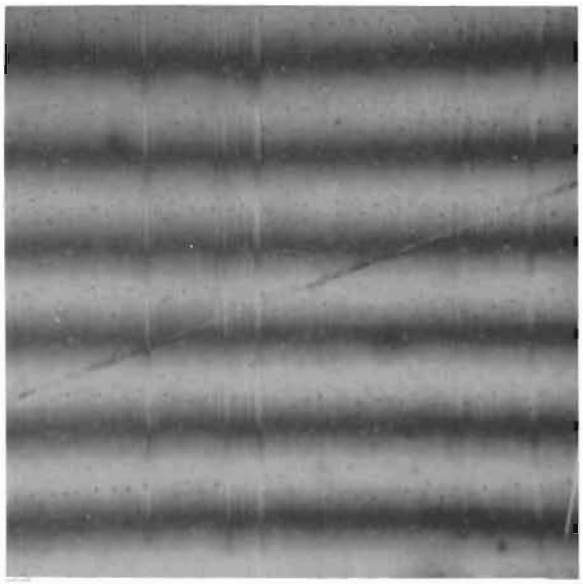

Figure 161. Test Model CC_f, Seat, 0.0065- x 0.0065-Inch Interference Photo Showing Surface Texture and Cross Lay Scratch (Dots on Reference Mirror)

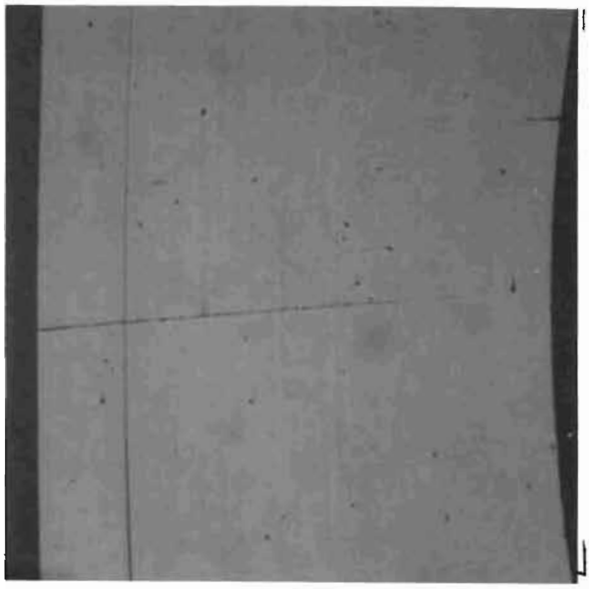

Figure 162. Test Model CC_f, Seat, 0.033- x 0.033-Inch Plain Photo Showing Scratch of Fig. 161

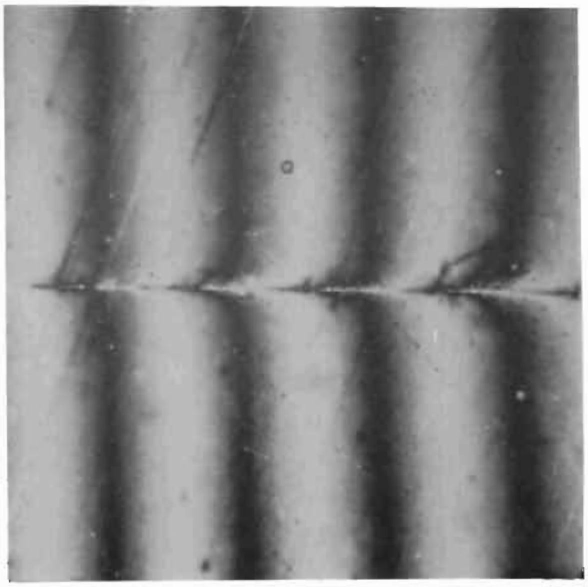

Figure 163. Test Model CC_f, Seat, 0.0065- x 0.0065-Inch Interference Photo Showing Scratch of Fig. 161 After Light Polish

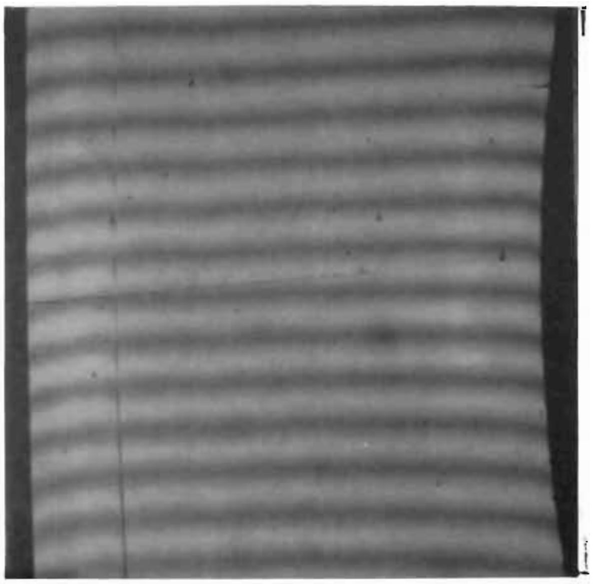

Figure 164. Test Model CC_f, Seat, 0.033- x 0.033-Inch Interference Photo Showing Plastically Dubbed Seat Corners

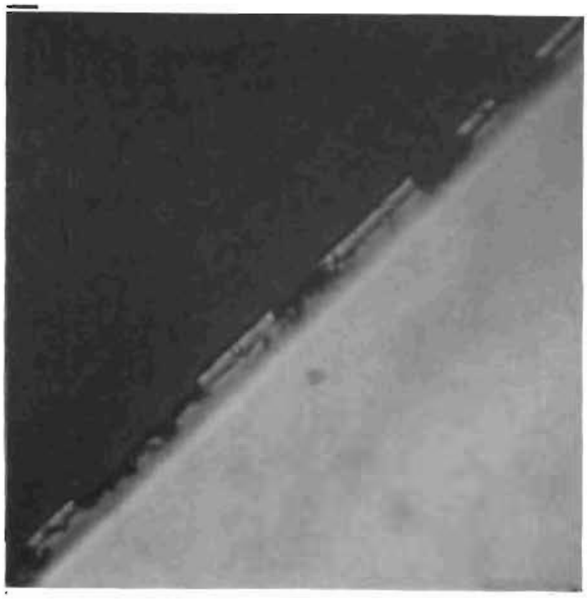

Figure 165. Test Model CC_f, Seat, 0.0065- x 0.0065-Inch Plain Photo Showing OD Corner Fractures

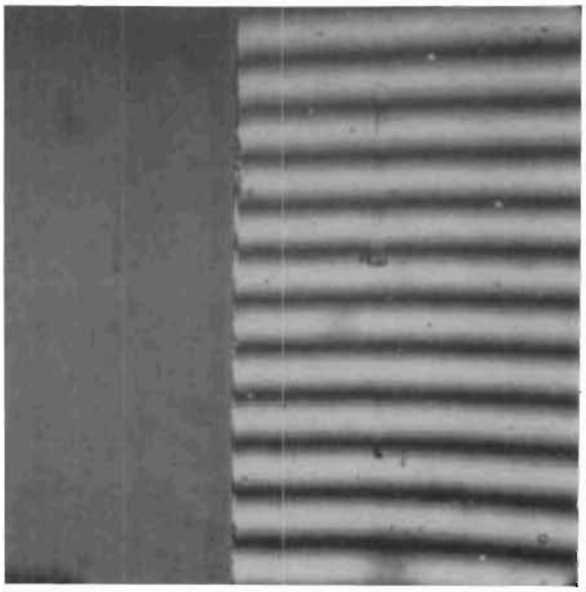

Figure 166. Test Model CC_f, Seat, 0.0065- x 0.0065-Inch Interference Photo Showing Raised Lip at OD

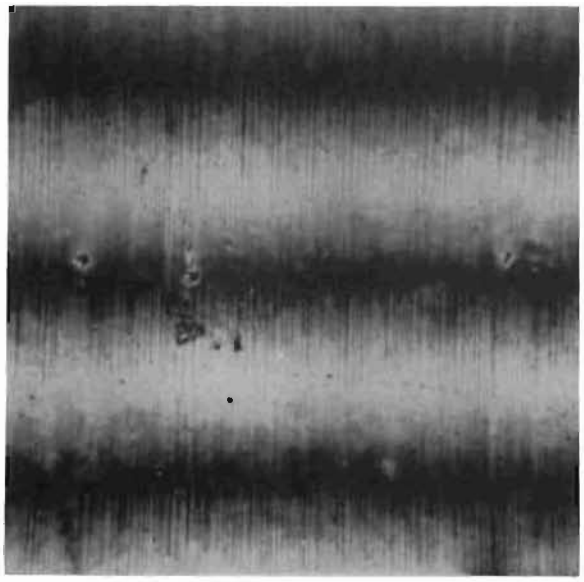

Figure 167. Test Model B_f, Poppet, 0.0065- x 0.0065-Inch Interference Photo

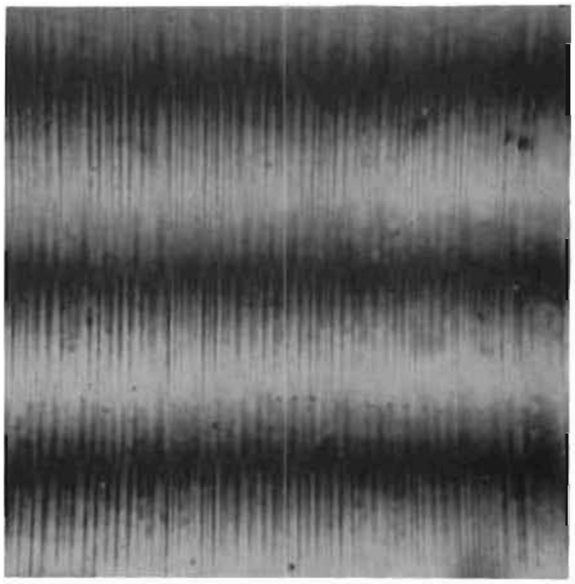

Figure 168. Test Model B_f, Seat, 0.0065- x 0.0065-Inch Interference Photo

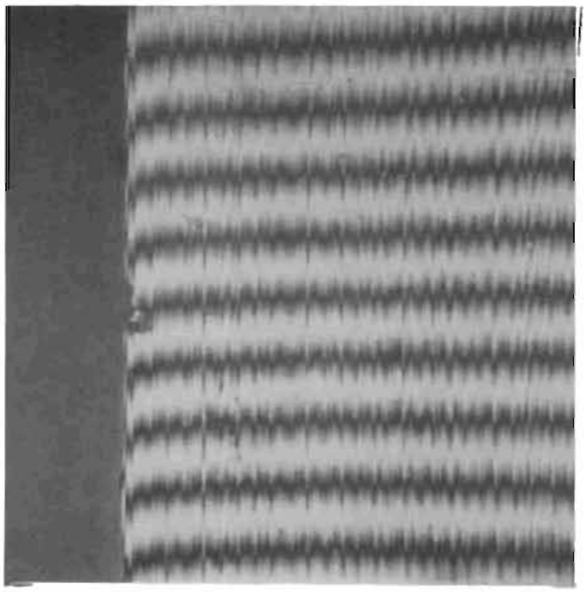

Figure 169. Test Model B_f, Seat, 0.0065- x 0.0065-Inch Interference Photo Showing OD Corner

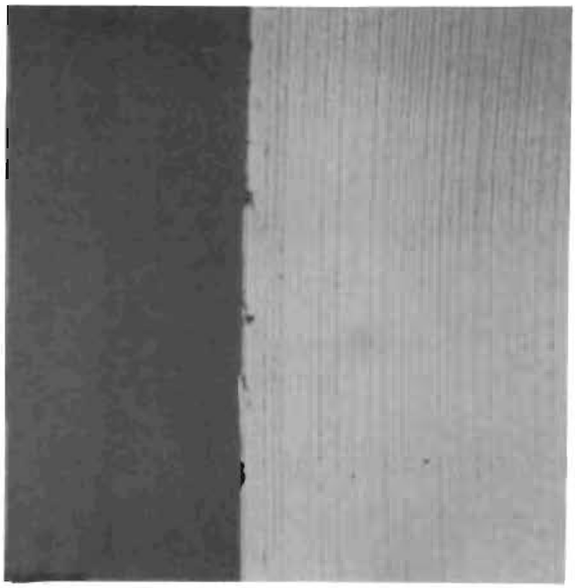

Figure 170. Test Model B_f, Seat, 0.0065- x 0.0065-Inch Plain Photo Showing OD Fractures and Cracks

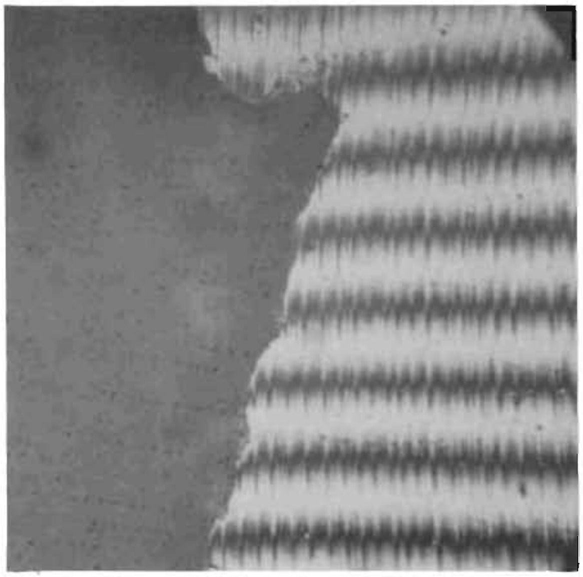

Figure 171. Test Model B_f, Seat, 0.0065- x 0.0065-Inch Interference Photo Showing Largest Fracture

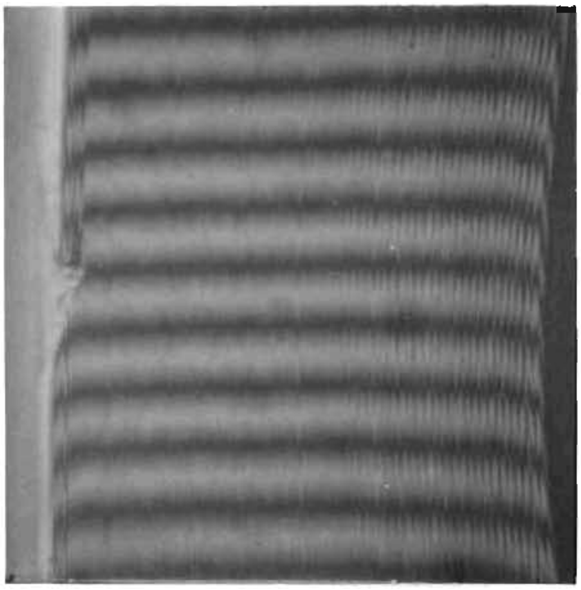

Figure 172. Test Model B_{f1}, Seat, 0.033- x 0.033-Inch Interference Photo, Fracture Same as Shown in Fig. 171

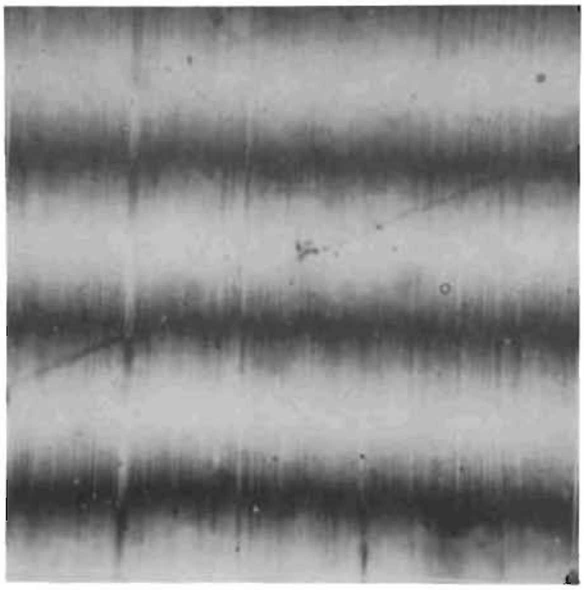

Figure 173. Test Model B_{f1}, Seat, 0.0065- x 0.0065-Inch Interference Photo

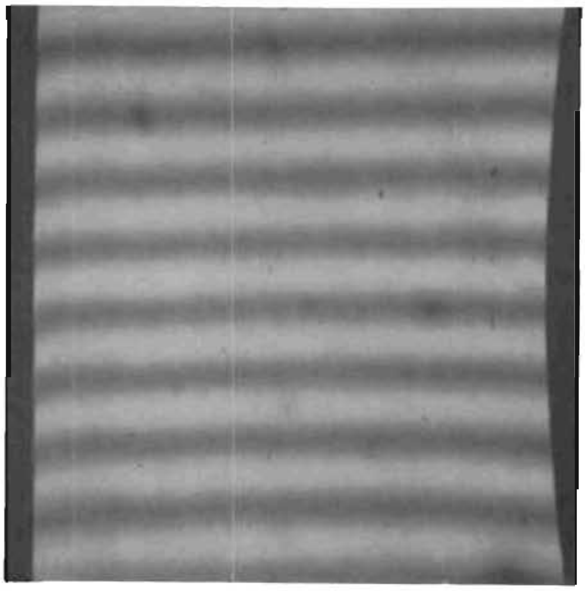

Figure 174. Test Model H_f, Seat, 0.033- x 0.033-Inch Interference Photo

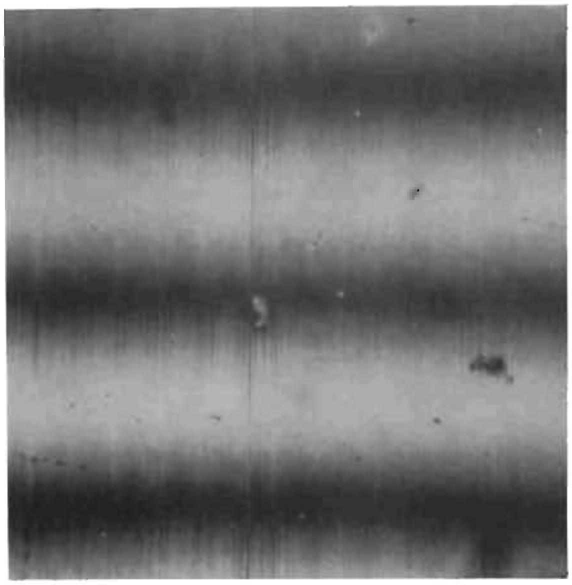

Figure 175. Test Model H_f, Seat, 0.0065- x 0.0065-Inch Interference Photo

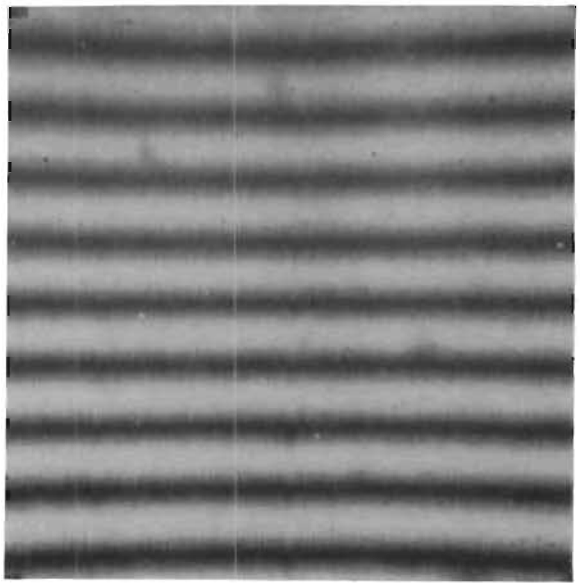

Figure 176. Test Model H_f, Poppet, 0.0065- x 0.0065-Inch Interference Photo

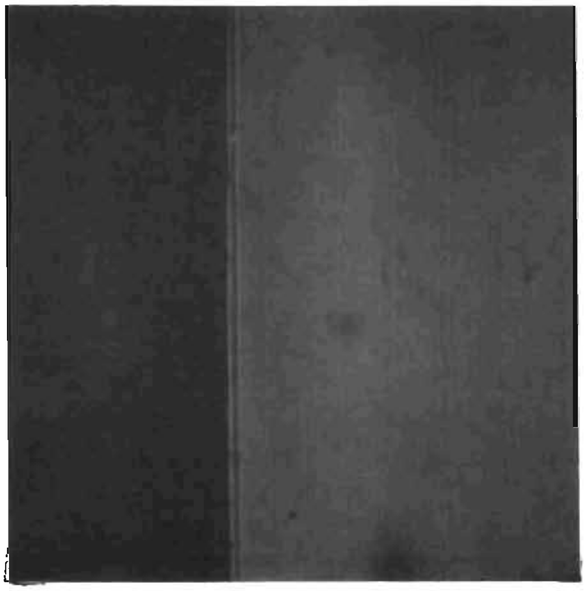

Figure 177. Test Model H_f, Seat, 0.0065- x 0.0065-Inch Plain Photo Showing OD Fracture and Metal Slip

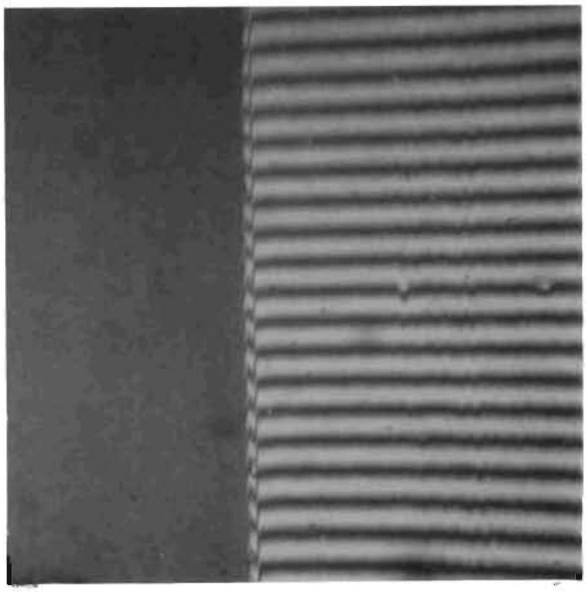

Figure 178. Test Model H_f, Seat, 0.0065- x 0.0065-Inch Interference Photo, Same Location as Fig. 177

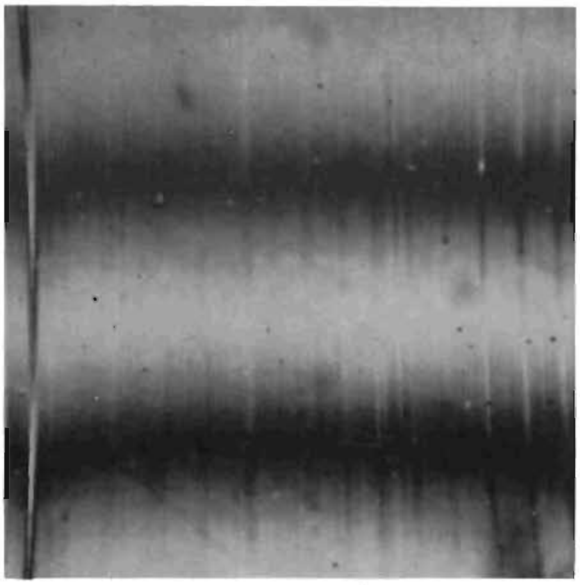

Figure 179. Test Model H_{f1}, Seat, 0.0065- x 0.0065-Inch Interference Photo

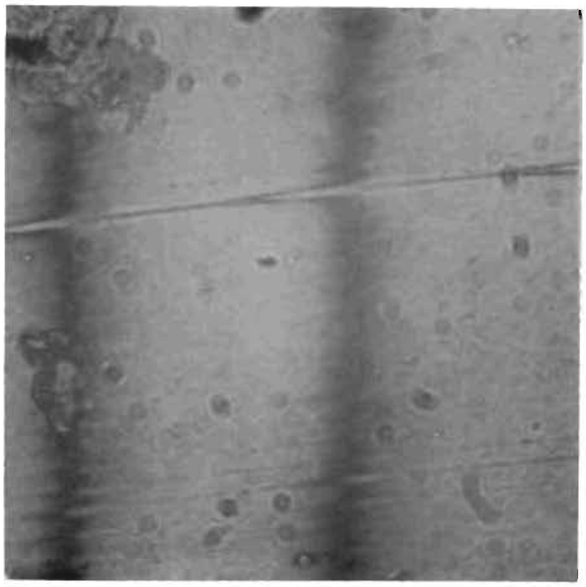

Figure 180. Test Model H_{f1}, Seat, 0.0065- x 0.0065-Inch Multiple Beam Interference Photo (Spots and Blemishes From Optics Contaminants)

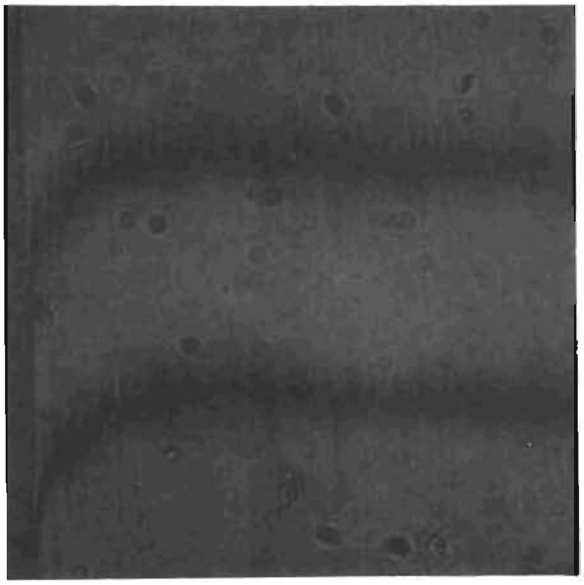

Figure 181. Test Model H_{f1}, Seat, 0.0065- x 0.0065-Inch Multiple Beam Interference Photo (Spots From Optics Contaminants)

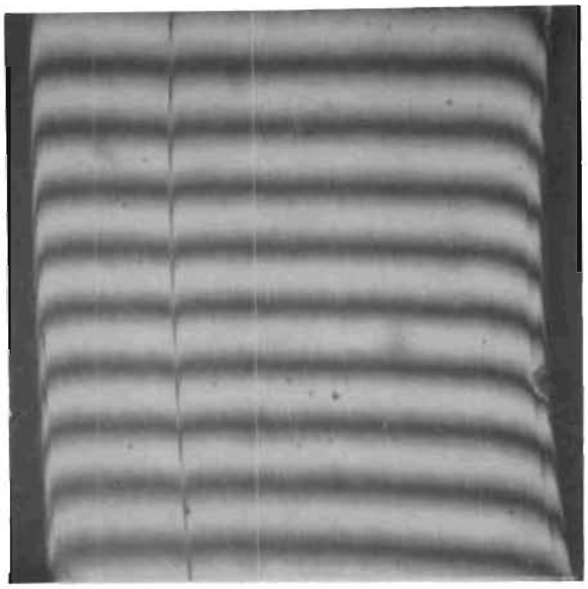

Figure 182. Test Model H_{f1}, Seat, 0.033- x 0.033-Inch Interference Photo

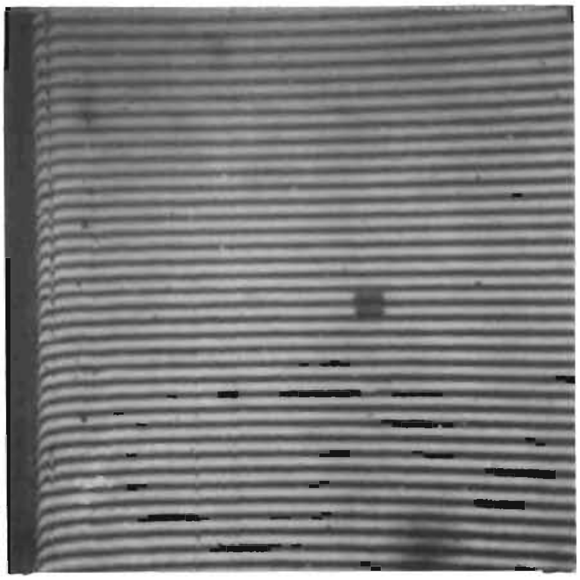

Figure 183. Test Model H_{f1}, Seat, 0.0065- x 0.0065-Inch Interference Photo Showing Embedded Contaminant From Finishing Process

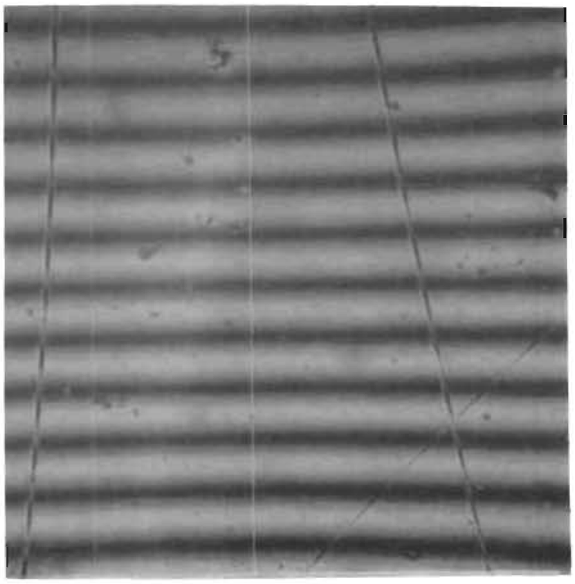

Figure 184. Test Model L_f, Poppet, 0.0065- x 0.0065-Inch Interference Photo Showing Finishing Scratches

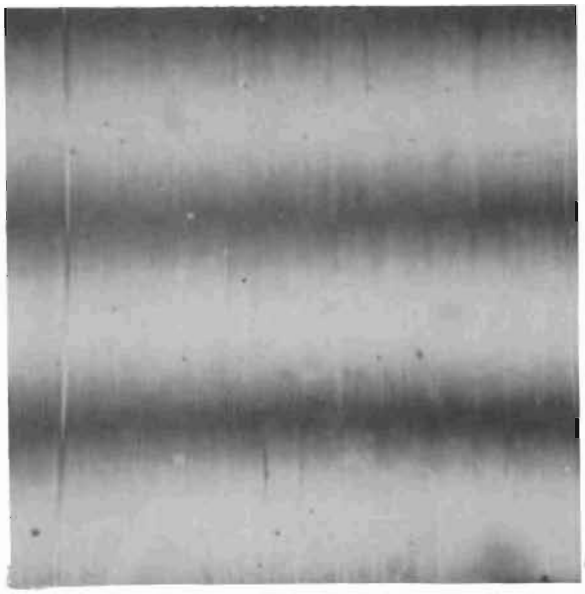

Figure 185. Test Model L_f, Seat, 0.0065- x 0.0065-Inch Interference Photo Showing Typical Surface Scratches

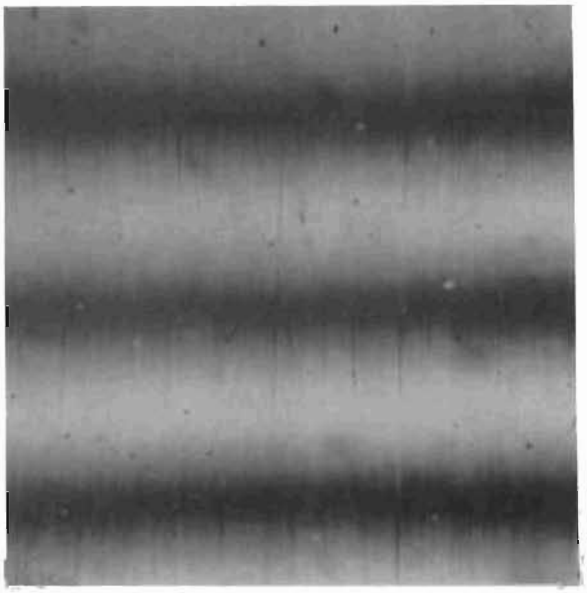

Figure 186. Test Model L_f, Poppet, 0.0065- x 0.0065-Inch Interference Photo

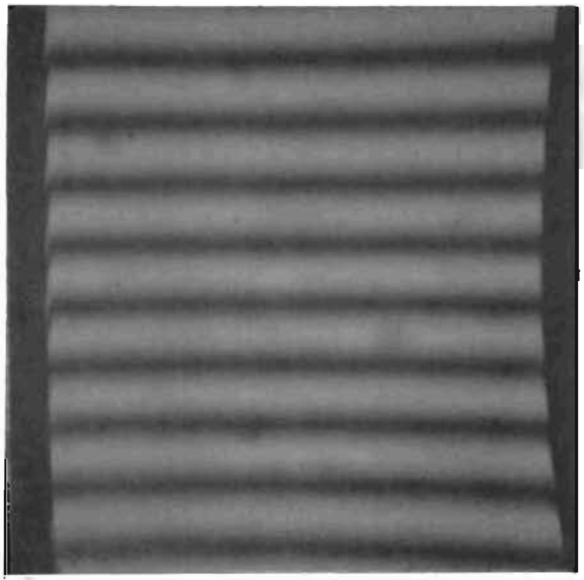

Figure 187. Test Model L_f, Seat, 0.033- x 0.033-Inch Interference Photo

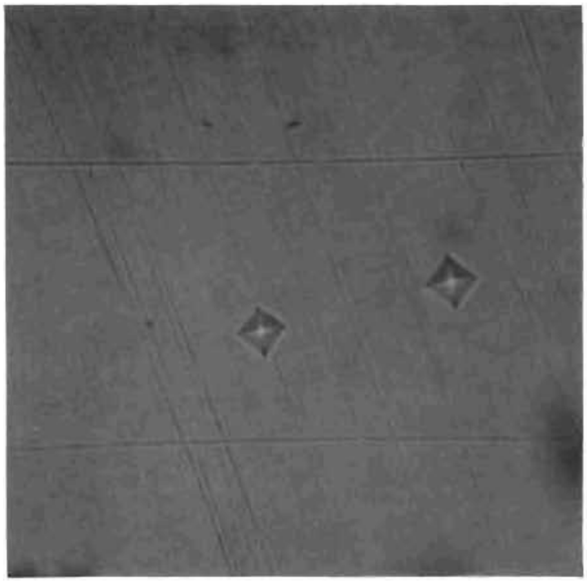

Figure 188. Test Model L_f, Seat, 0.0065- x 0.0065-Inch Plain Photo Showing 0.0001-Inch Radius Proficorder Tracks and Microhardness Test Indentations

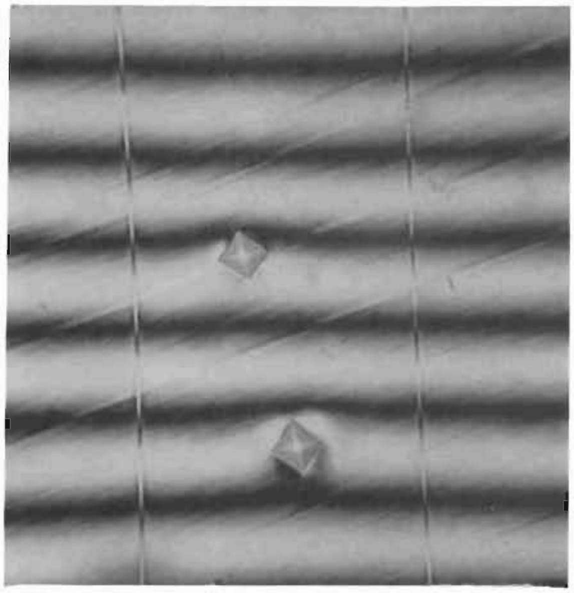

Figure 189. Test Model L_f, Seat, 0.0065- x 0.0065-Inch Interference Photo, Same Location as Fig. 188

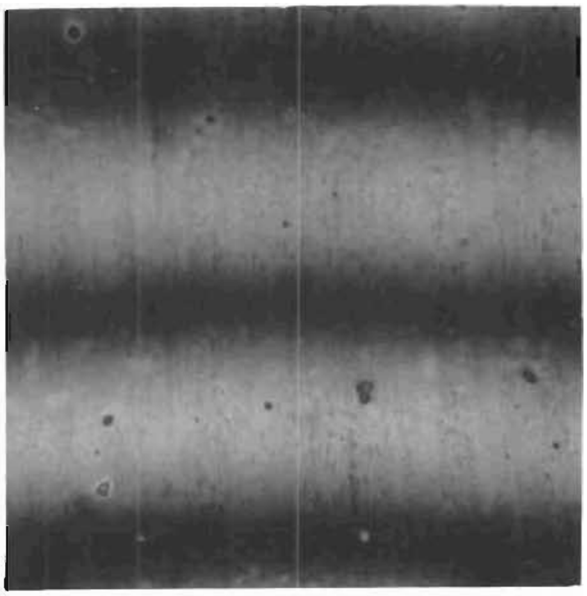

Figure 190. Test Model M_f, Seat, 0.0065- x 0.0065-Inch Interference Photo

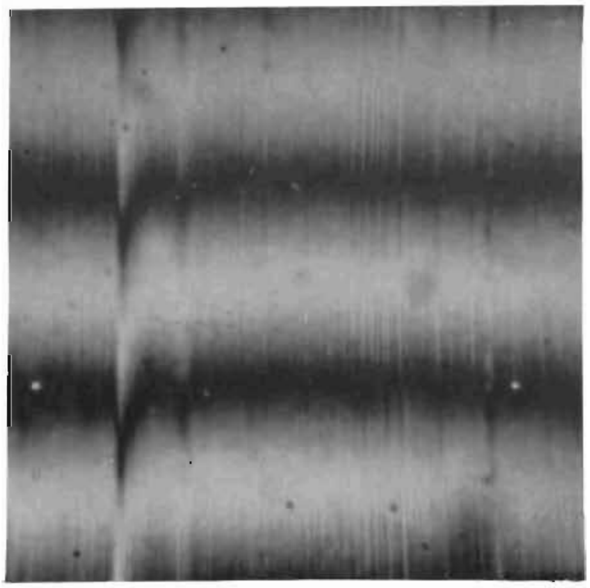

Figure 191. Test Model M_f, Poppet, 0.0065- x 0.0065-Inch Interference Photo

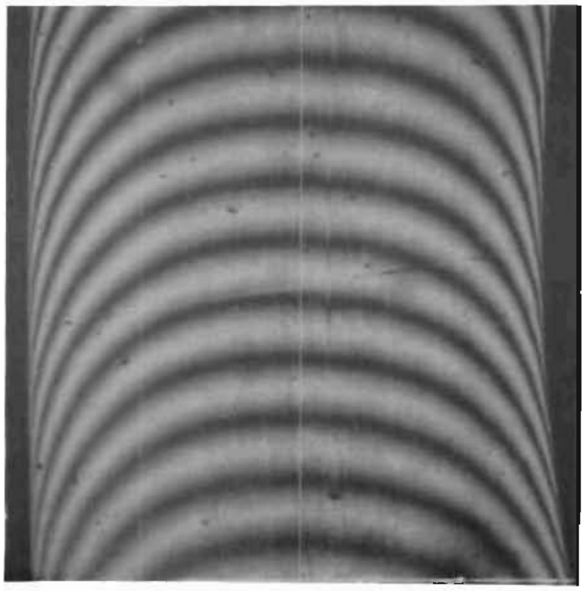

Figure 192. Test Model M_f, Seat, 0.033- x 0.033-Inch Interference Photo Showing Typical Cross Land Scratch

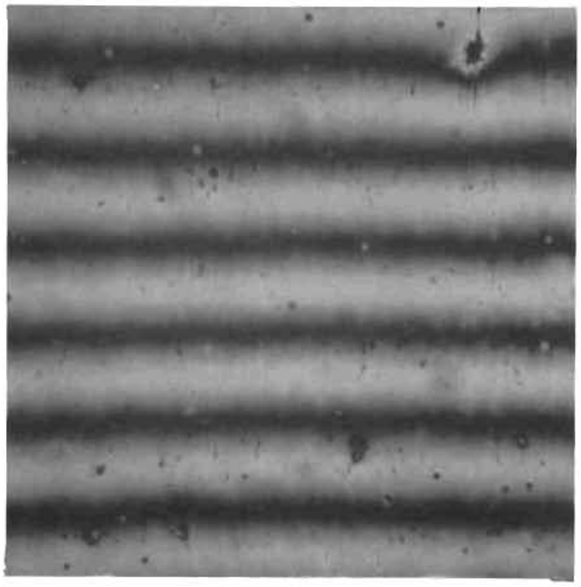

Figure 193. Test Model M_{f1}, Seat, 0.0065- x 0.0065-Inch Interference Photo, Same Location as Fig. 190

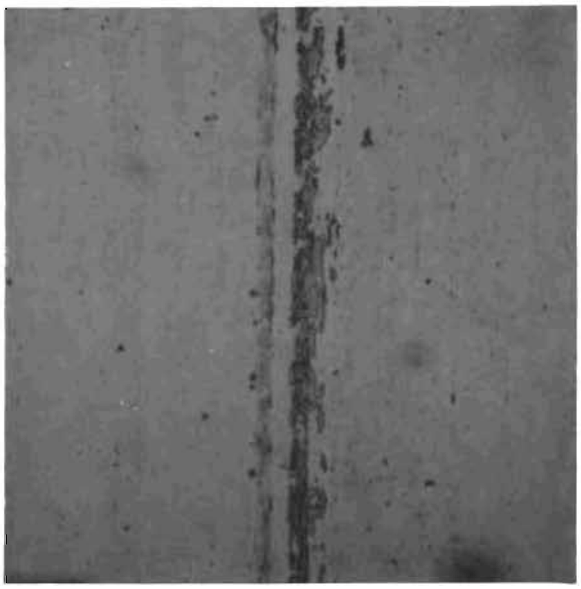

Figure 194. Test Model M_{f1}, Seat, 0.0065- x 0.0065-Inch Plain Photo Showing Galled Area

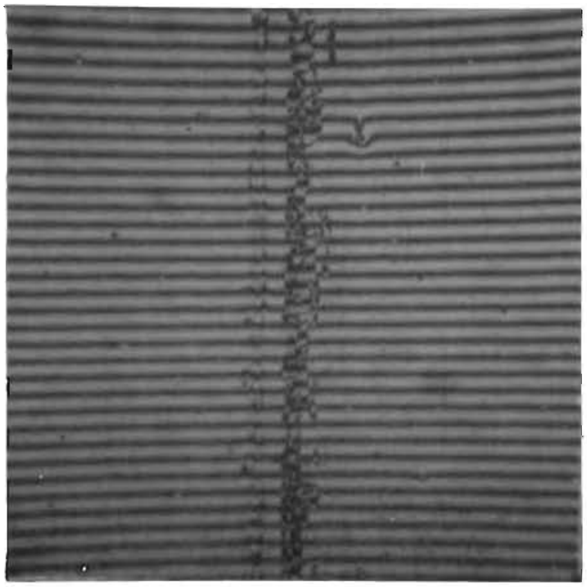

Figure 195. Test Model M_{f1}, Seat, 0.0065- x 0.0065-Inch Interference Photo, Same Location as Fig. 194

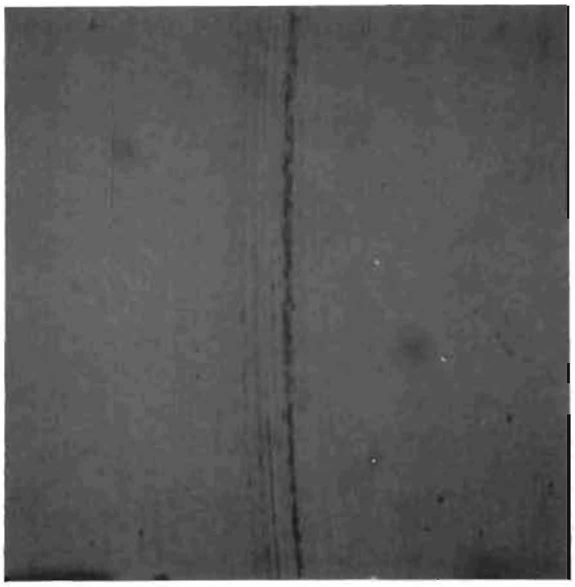

Figure 196. Test Model M_{f1}, Poppet, 0.033- x 0.033-Inch Plain Photo Showing Galled Area

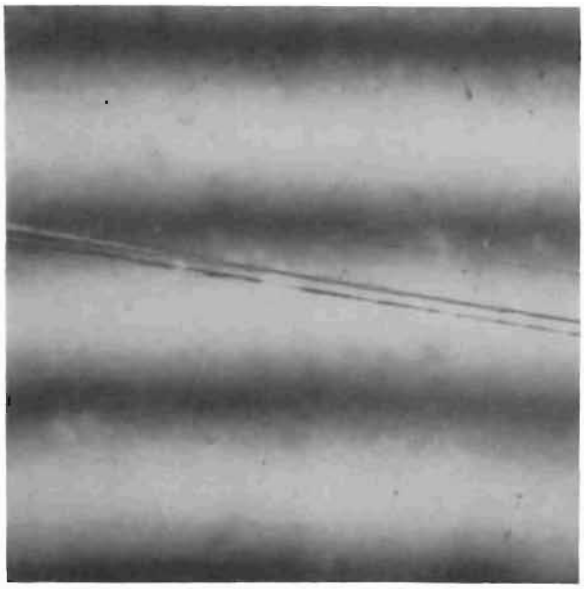

Figure 197. Test Model AA_f, Seat, 0.0065- x 0.0065-Inch Interference Photo

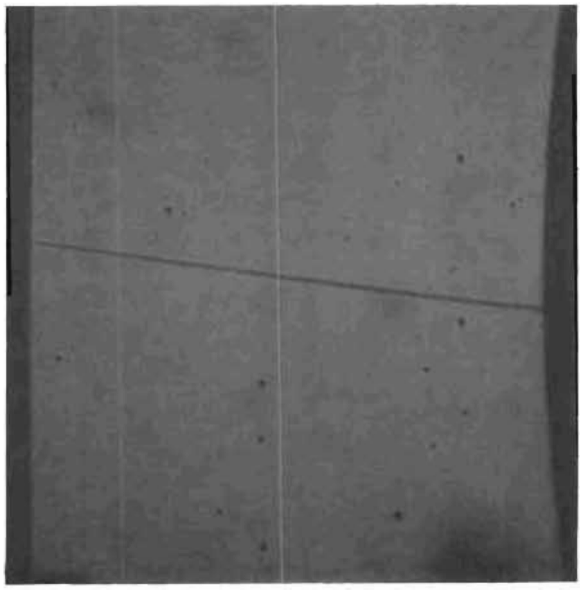

Figure 198. Test Model AA_f, Seat, 0.033- x 0.033-Inch Plain Photo Showing Typical Scratches

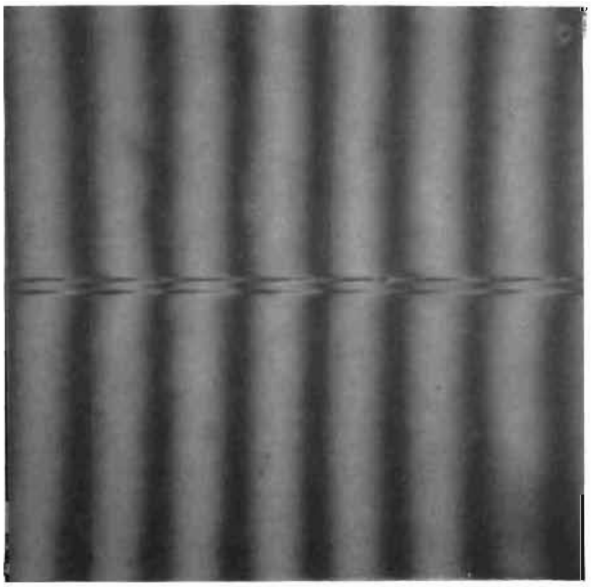

Figure 199. Test Model AA_f, Seat, 0.0065- x 0.0065-Inch Interference Photo Showing Typical Scratches, Same Location as Fig. 198

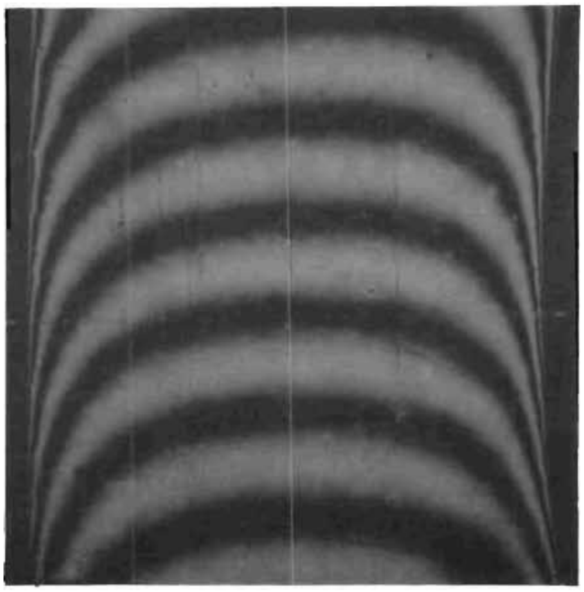

Figure 200. Test Model AA_f, Seat, 0.033- x 0.033-Inch Interference Photo Showing Crowned Land

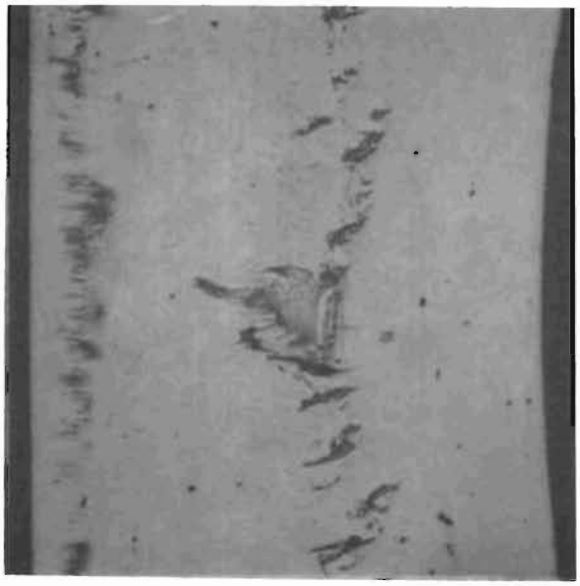

Figure 201. Test Model AA_f, Seat, 0.033- x 0.033-Inch Interference Photo Showing Corrosion Fretting

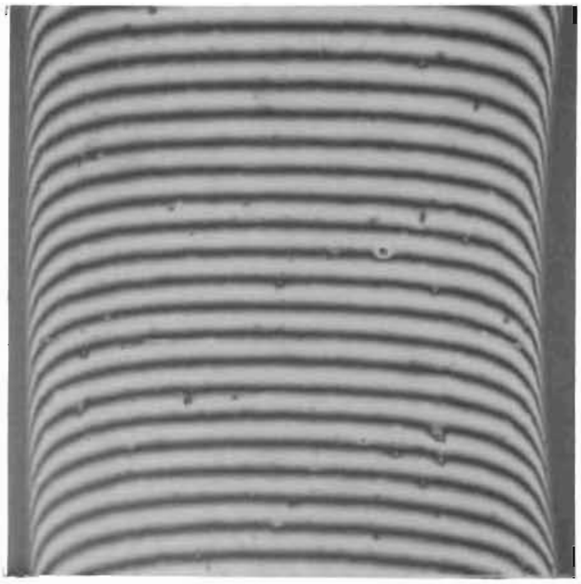

Figure 202. Test Model AA_f, Seat, 0.033- x 0.033-Inch Interference Photo, Same Location as Fig. 201 After Wiping

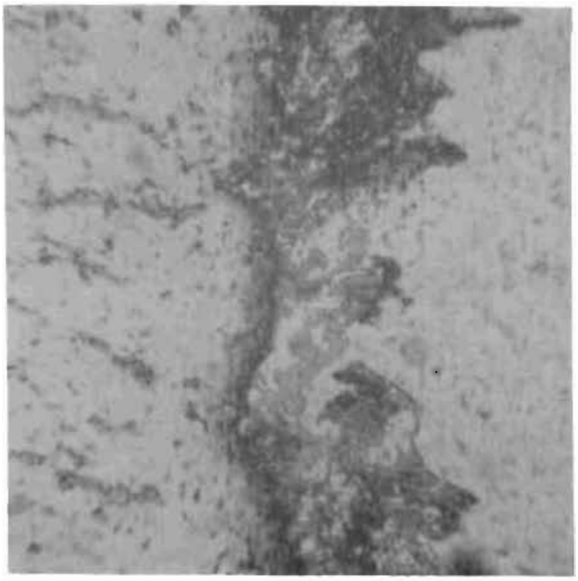

Figure 203. Test Model AA_f, Poppet (Ref. Fig. 64), 0.0065- x 0.0065-Inch Plain Photo Showing Corrosion Fretting Film at 0.458 to 0.460 Diameter

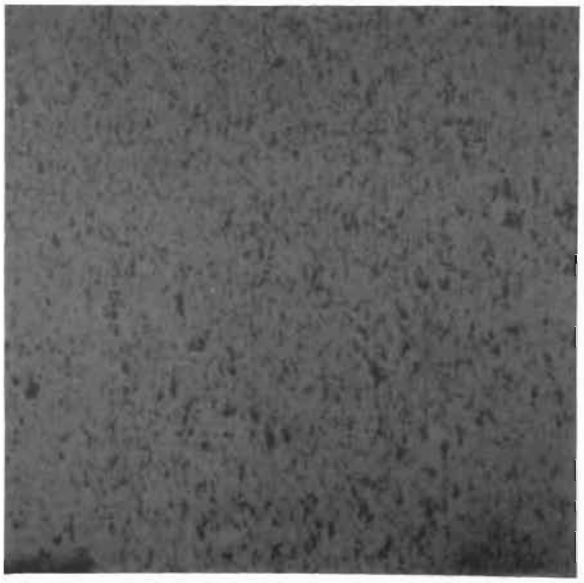

Figure 204. Test Model AA_f, Poppet, 0.0065- x 0.0065-Inch Plain Photo, Same Location as Fig. 203 After Wiping

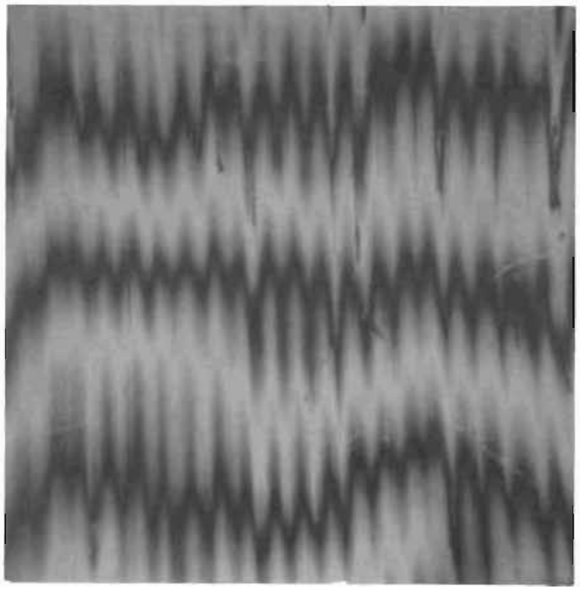

Figure 205. Test Model NN_f, Seat, 0.0065- x 0.0065-Inch Interference Photo

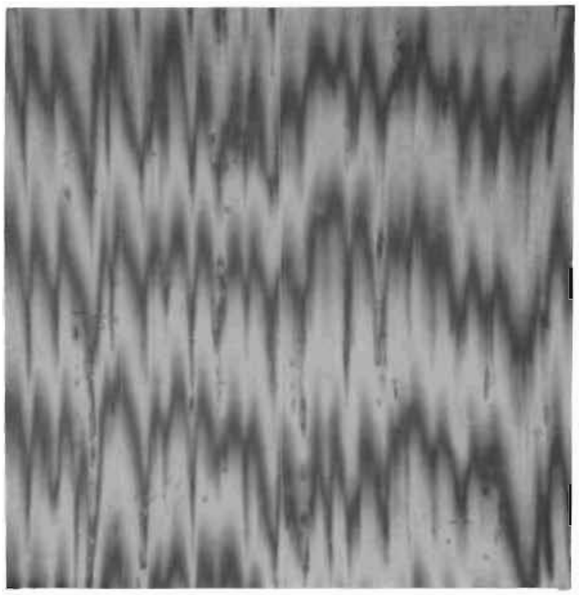

Figure 206. Test Model NN_f, Poppet, 0.0065- x 0.0065-Inch Interference Photo

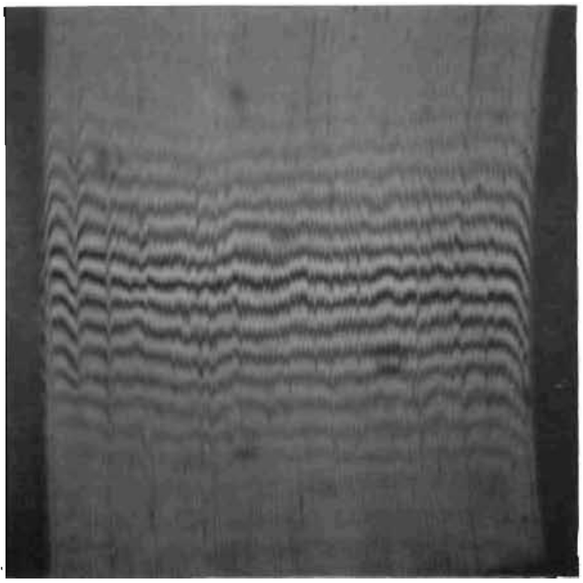

Figure 207. Test Model NN_f, Seat, 0.033- x 0.033-Inch Interference Photo, White Light

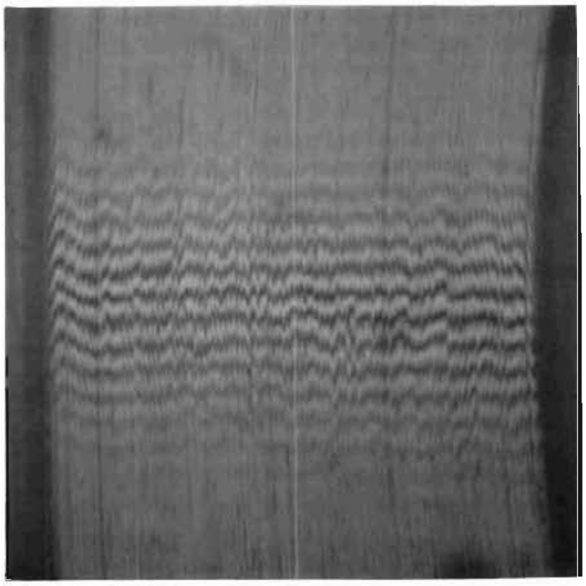

Figure 208. Test Model NN_f, Poppet, 0.033- x 0.033-Inch Interference Photo, White Light

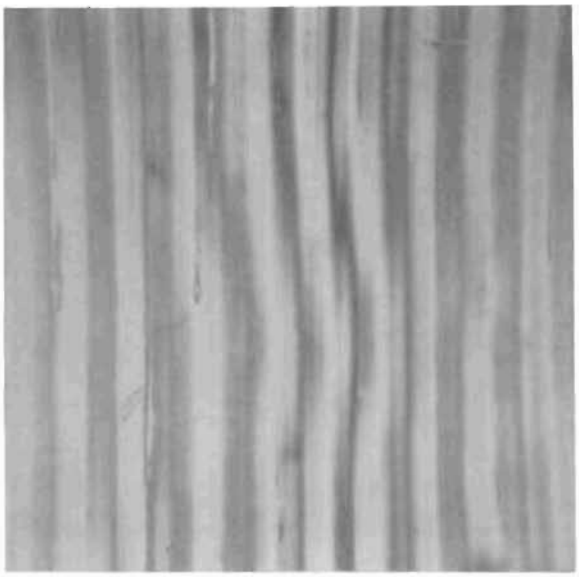

Figure 209. Test Model NN_f, Seat, 0.0065- x 0.0065-Inch Interference Photo, White Light, Bands Rotated to Show With-Lay Waviness, Same Location as Fig. 205

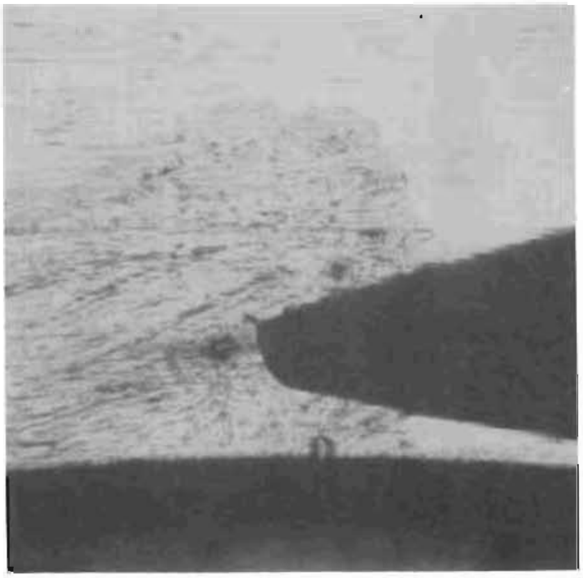

Figure 210. Test Model NN_f, Seat, 0.033- x 0.033-Inch Plain Photo Showing Contaminant Removal Lapping Method

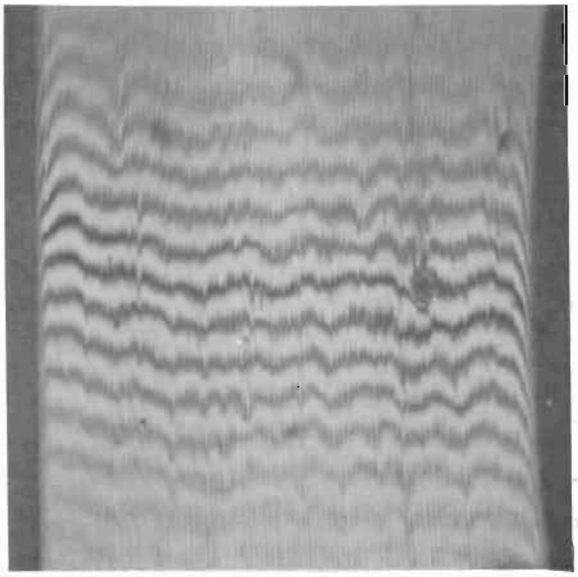

Figure 211. Test Model NN_f, Seat, 0.033- x 0.033-Inch Interference Photo, White Light, Showing Depression After Contaminant Removal

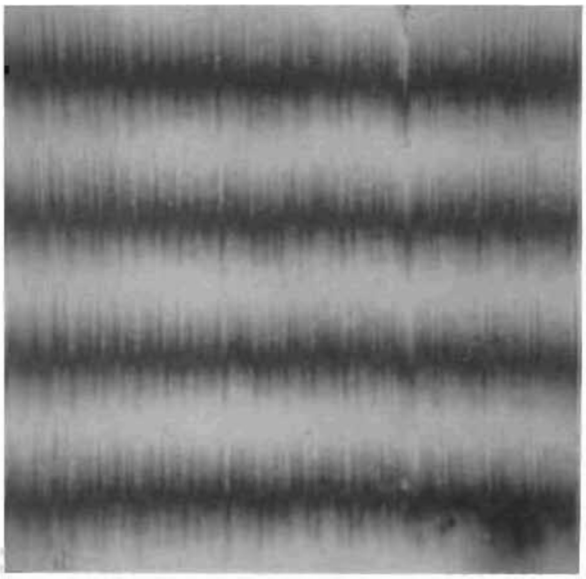

Figure 212. Test Model HH_f, Poppet, 0.0065- x 0.0065-Inch Interference Photo

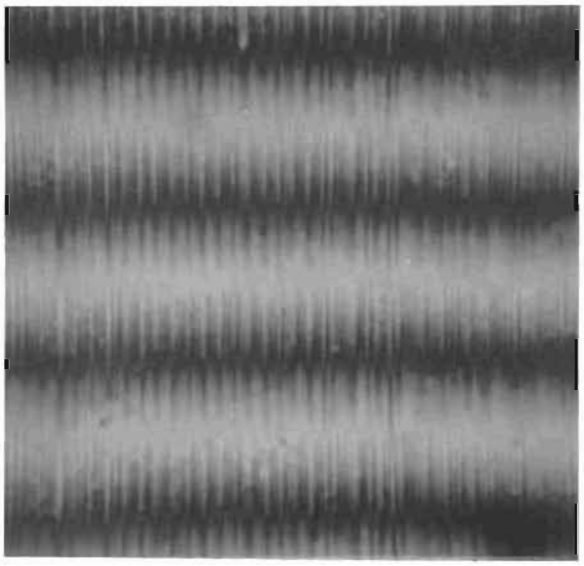

Figure 213. Test Model HH_f, Seat, 0.0065- x 0.0065-Inch Interference Photo

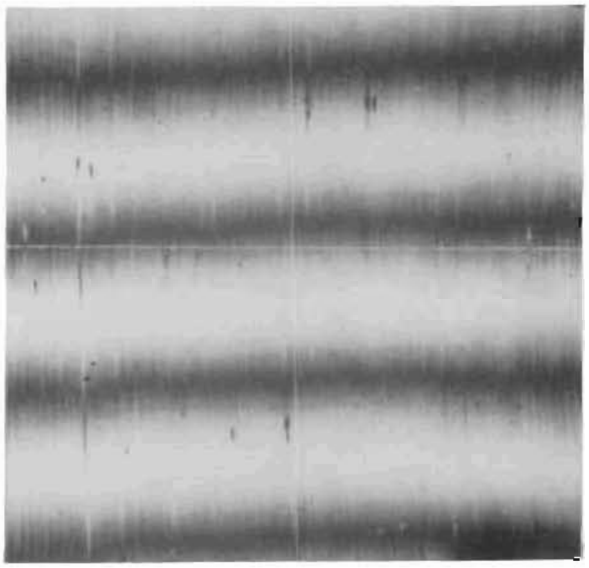

Figure 214. Test Model HH_f, Poppet, 0.033- x 0.033-Inch Interference Photo

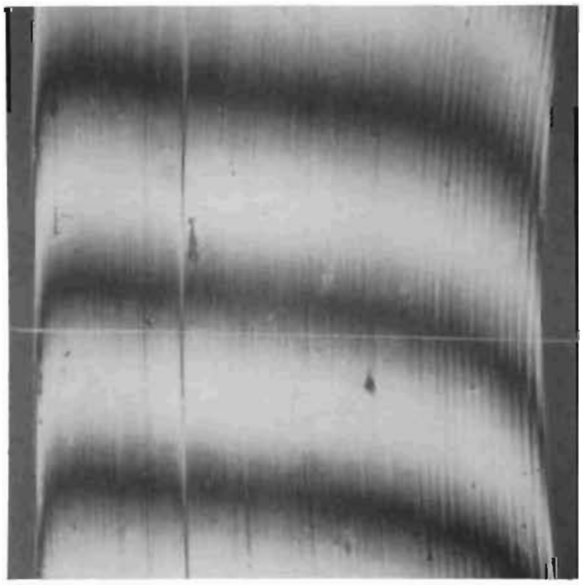

Figure 215. Test Model HH_f, Seat, 0.033- x 0.033-Inch Interference Photo

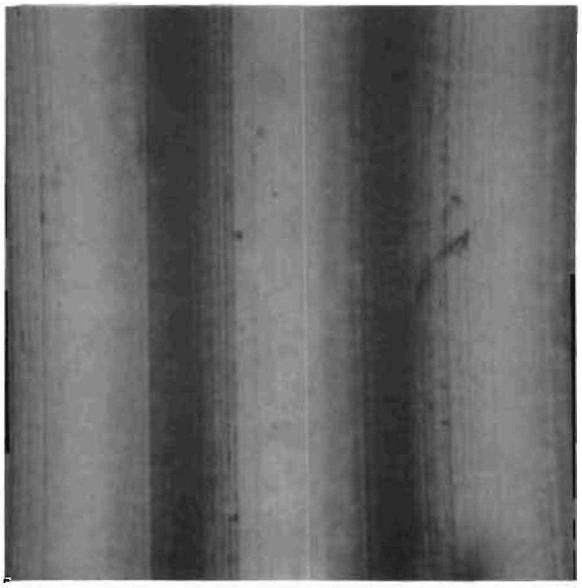

Figure 216. Test Model HH_f, Poppet, 0.0065- x 0.0065-Inch Interference Photo, With Lay

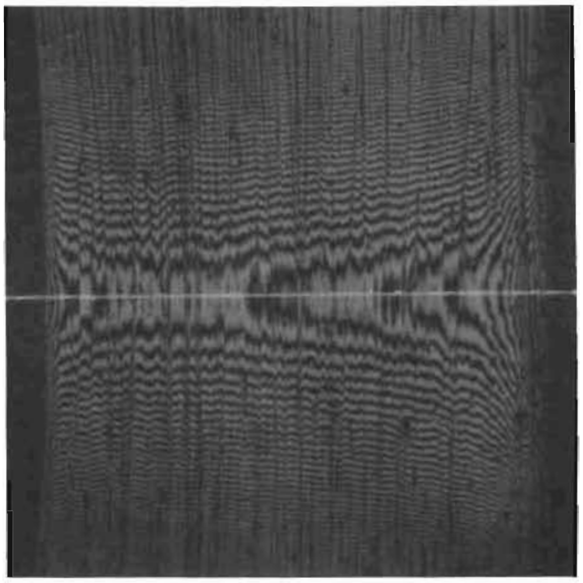

Figure 217. Test Model A_c, Seat, 0.033- x 0.033-Inch Interference Photo

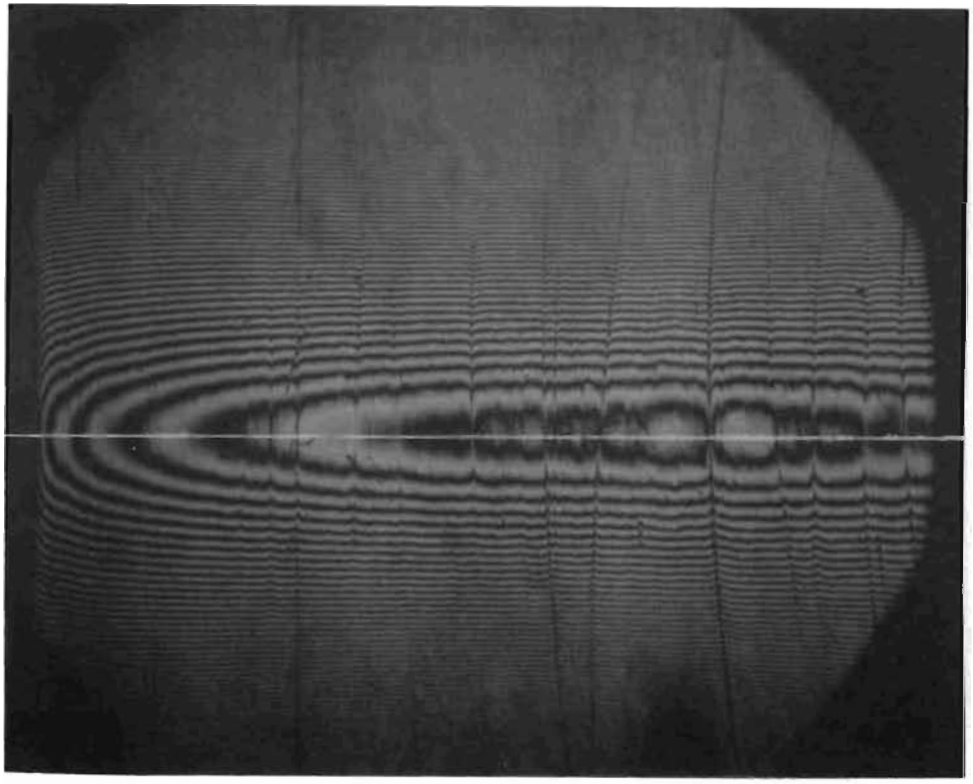

Figure 218. Test Model A_c, Poppet, 0.045- x 0.056-Inch Interference Photo, OD at Left

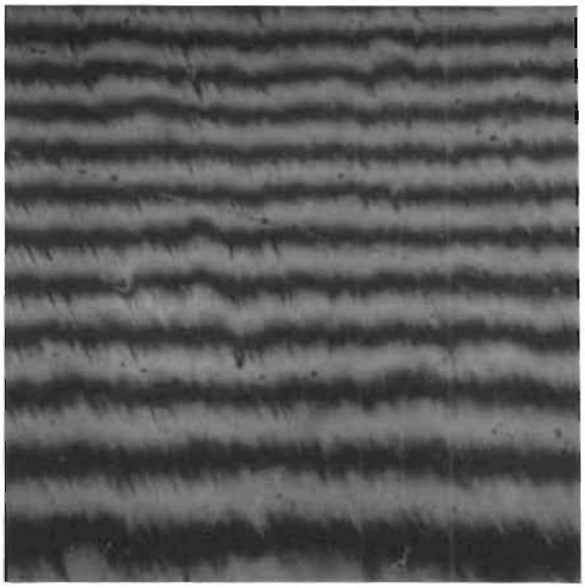

Figure 219. Test Model A_c, Poppet, 0.0065- x 0.0065-Inch Interference Photo

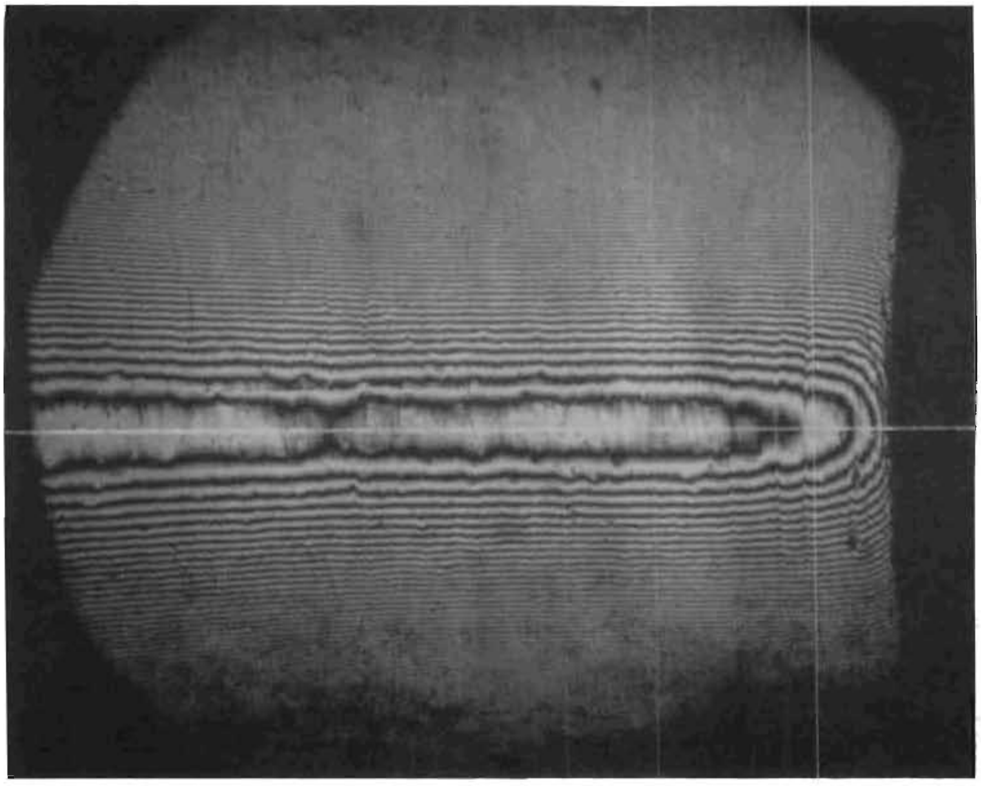

Figure 220. Test Model B_c, Poppet, 0.045- x 0.056-Inch Interference Photo, ID at Right

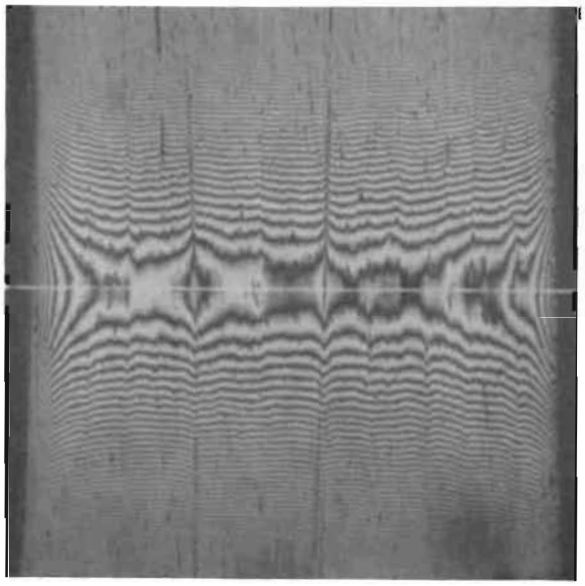

Figure 221. Test Model B_c, Seat, 0.033- x 0.033-Inch Interference Photo

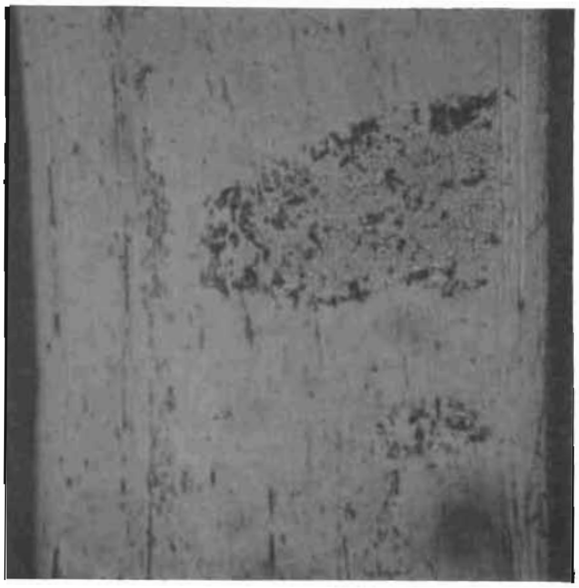

Figure 222. Test Model B_c, Seat, 0.033- x 0.033-Inch Plain Photo Showing Corrosion Fretting After Light Wipe

Figure 223. Test Model B_c, Poppet, 0.033- x 0.033-Inch Plain Photo, Same Location as Fig. 222

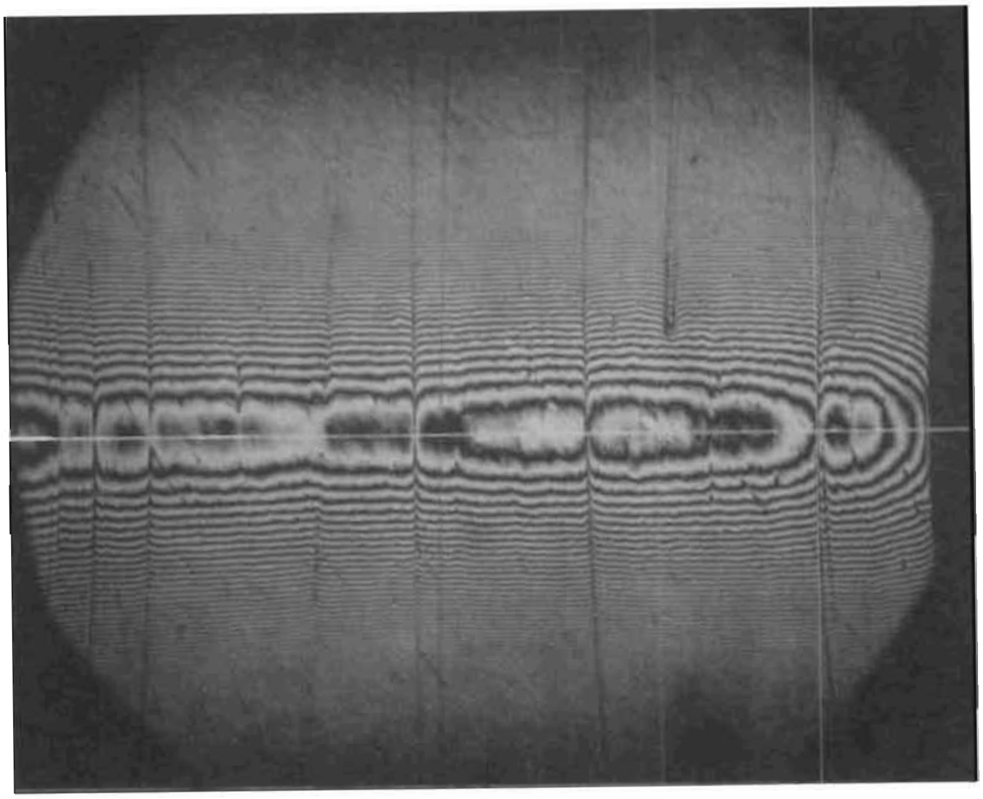

Figure 224. Test Model C_c, Poppet, 0.045- x 0.056-Inch Interference Photo at ID

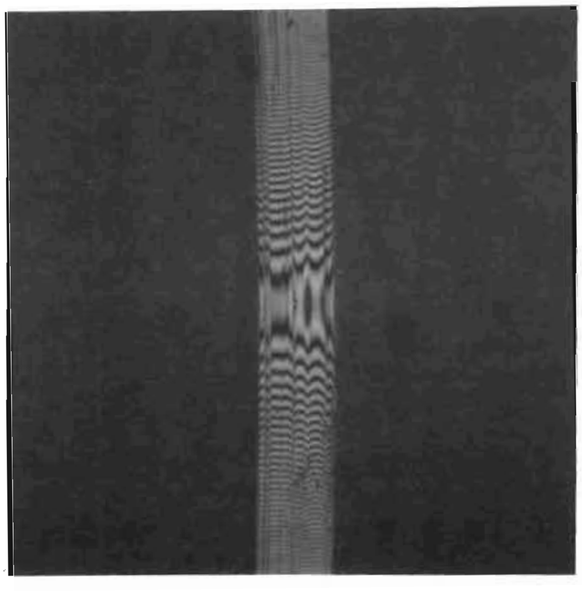

Figure 225. Test Model D_c, Seat, 0.033- x 0.033-Inch Interference Photo Showing Nominal Land Width Before Rework Lapping

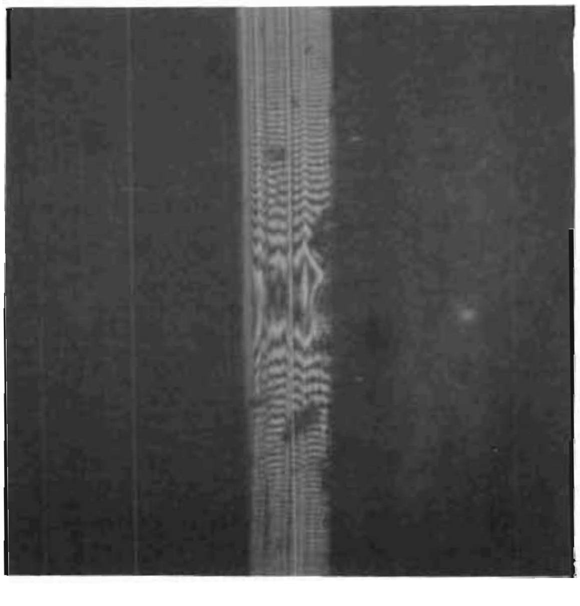

Figure 226. Test Model D_c, Seat, 0.033- x 0.033-Inch Interference Photo Showing Wide Land Width and Major Blemishes Before Rework Lapping

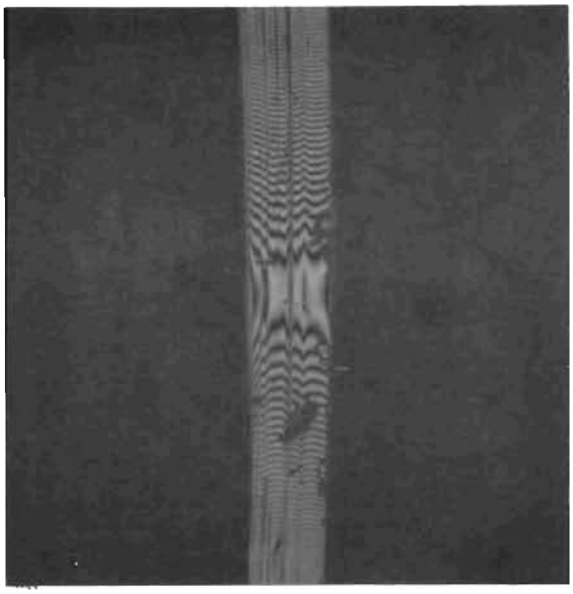

Figure 227. Test Model D_c, Seat, 0.033- x 0.033-Inch Interference Photo, Same Location as Fig. 226 After Rework Lapping

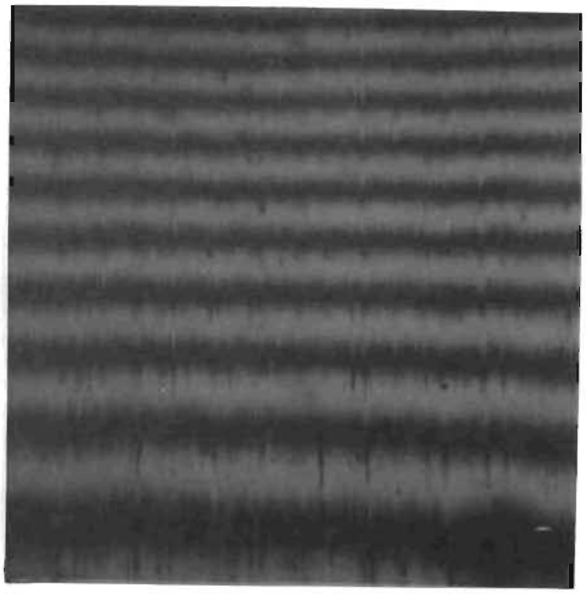

Figure 228. Test Model E_c, Poppet, 0.0065- x 0.0065-Inch Interference Photo

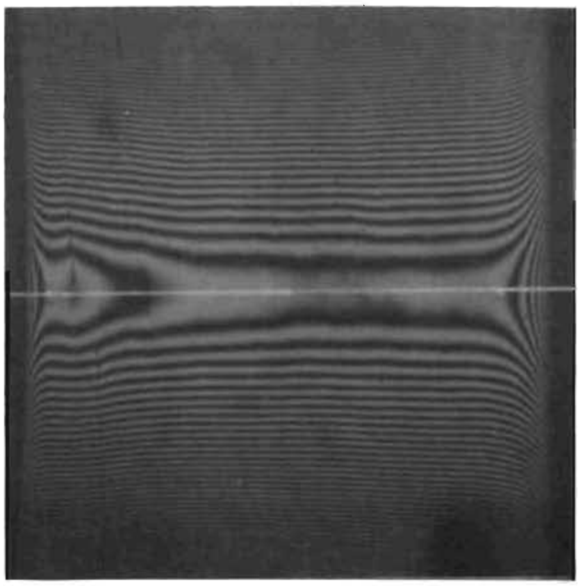

Figure 229. Test Model E_c, Seat, 0.033- x 0.033-Inch Interference Photo

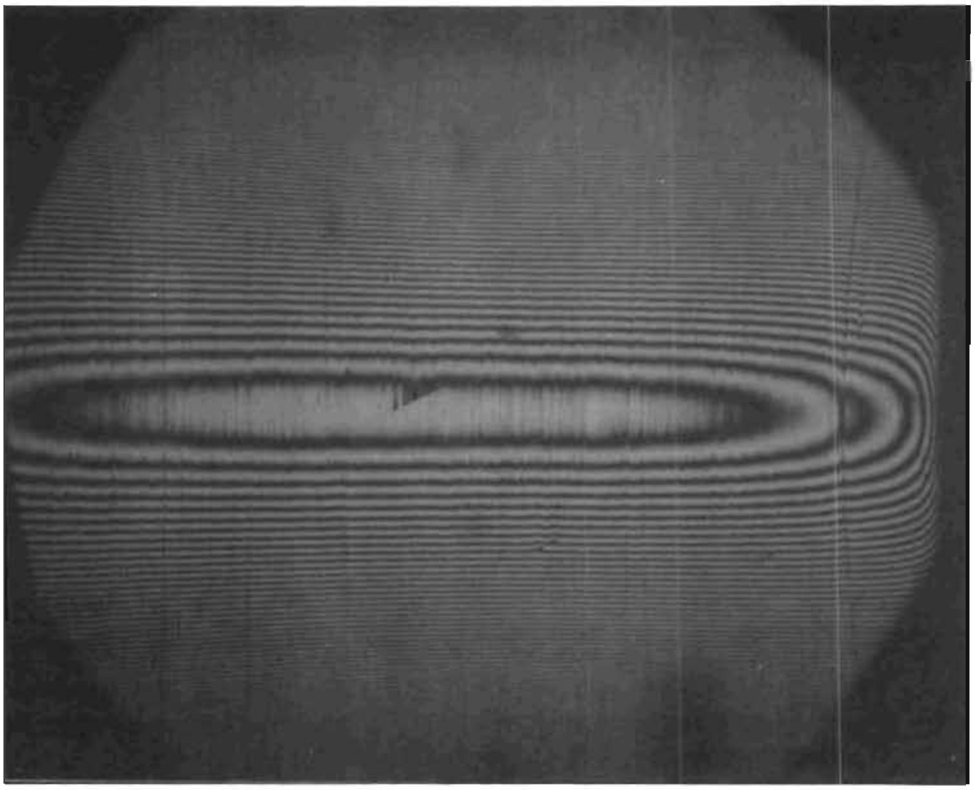

Figure 230. Test Model E_c, Poppet, 0.045- x 0.056-Inch Interference Photo, ID at Right

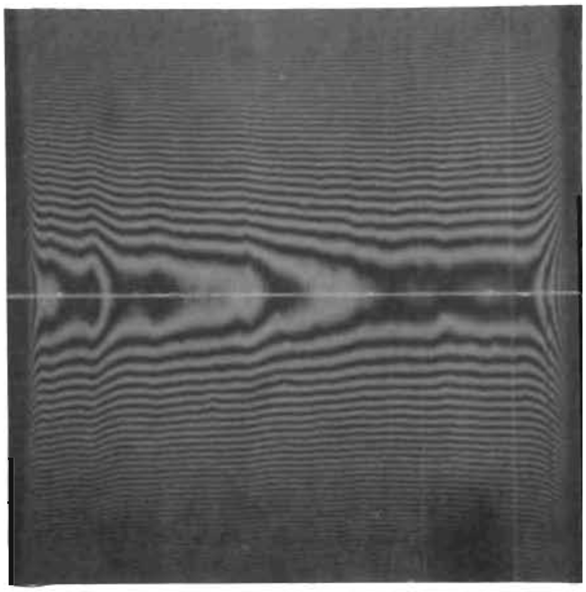

Figure 231. Test Model F_c, Seat, 0.033- x 0.033-Inch Interference Photo

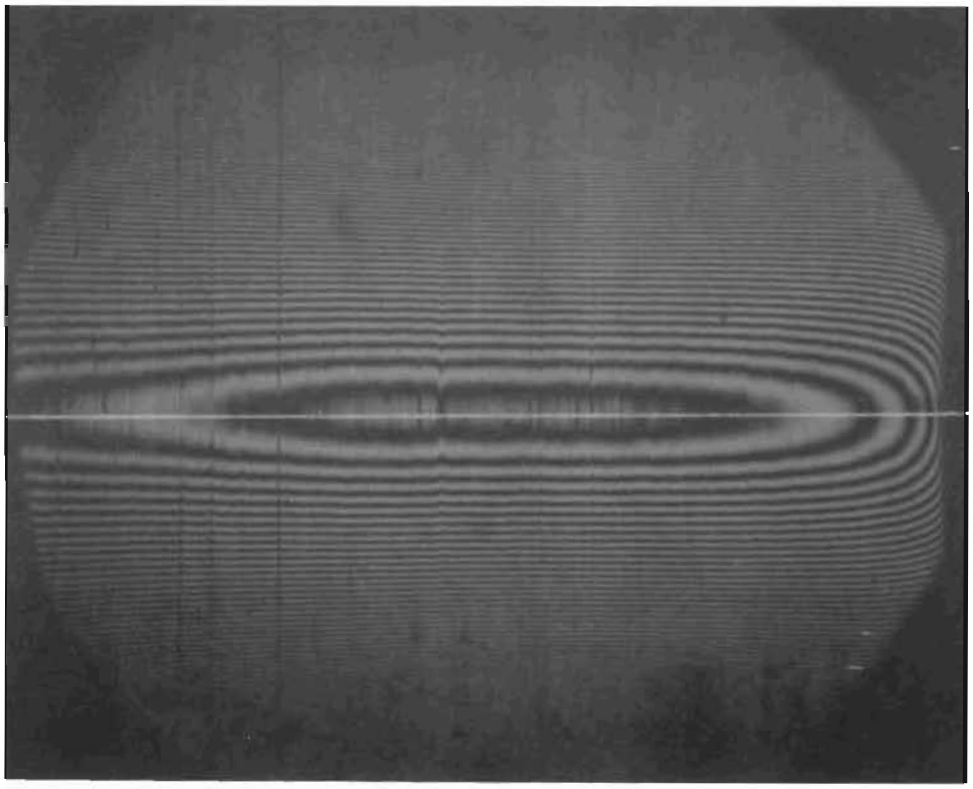

Figure 232. Test Model F_c, Poppet, 0.045- x 0.056-Inch Interference Photo, ID at Right

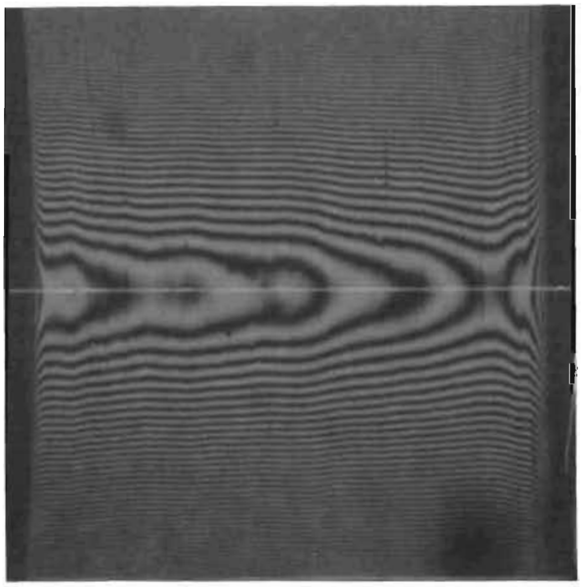

Figure 233. Test Model G_c, Seat, 0.033- x 0.033-Inch Interference Photo

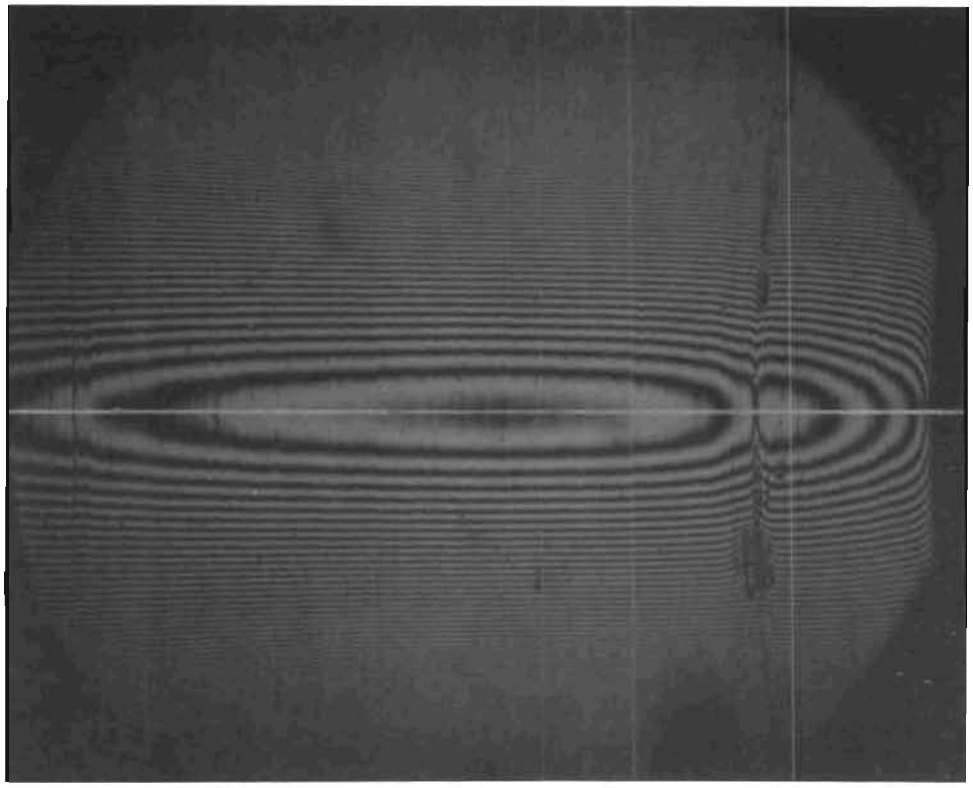

Figure 234. Test Model G_c, Poppet, 0.045- x 0.056-Inch Interference Photo,ID at Right

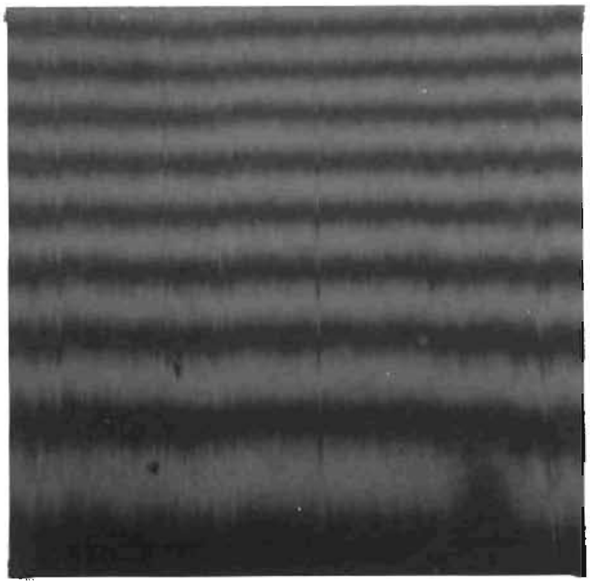

Figure 235. Test Model G_c, Poppet, 0.0065- x 0.0065-Inch Interference Photo

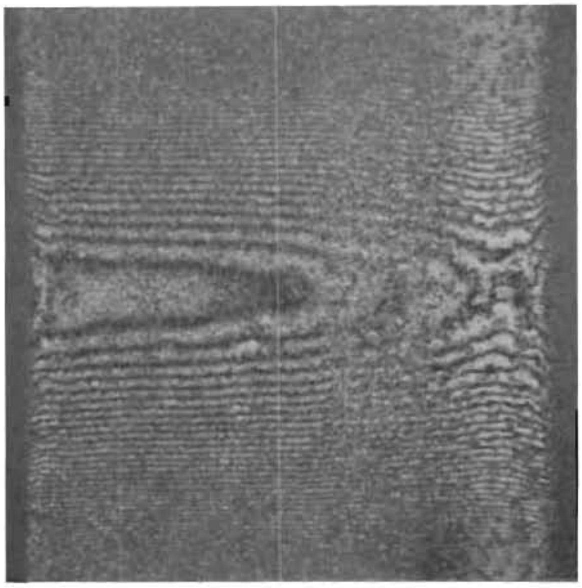

Figure 236. Test Model G_{c1}, Seat, 0.033- x 0.033-Inch Interference Photo Showing Plastic Deformation at ID And OD

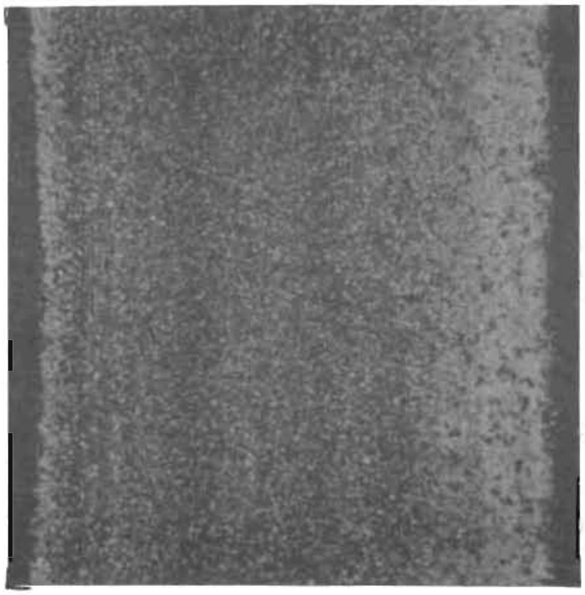

Figure 237. Test Model G_{c1}, Seat, 0.033- x 0.033-Inch Plain Photo Showing Plastic Deformation

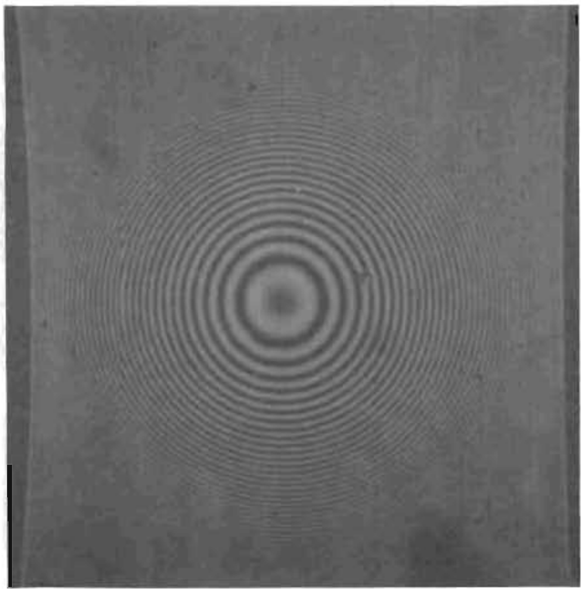

Figure 238. Test Model A_s, Seat, 0.033- x 0.033-Inch Interference Photo

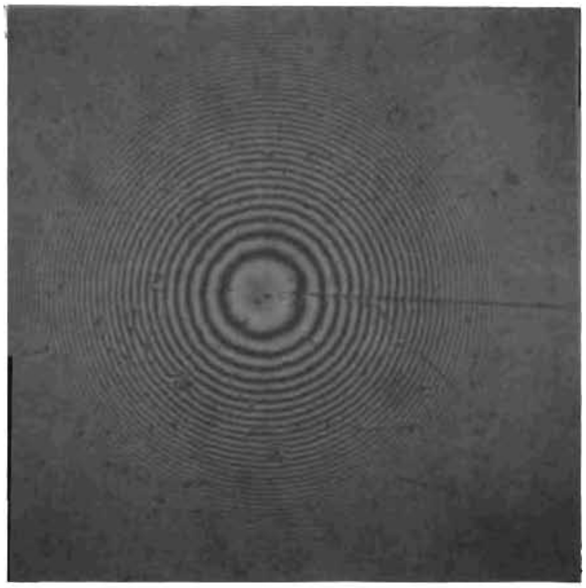

Figure 239. Test Model A_s, Poppet, 0.033- x 0.033-Inch Interference Photo Showing Typical Surface Defects at Midland

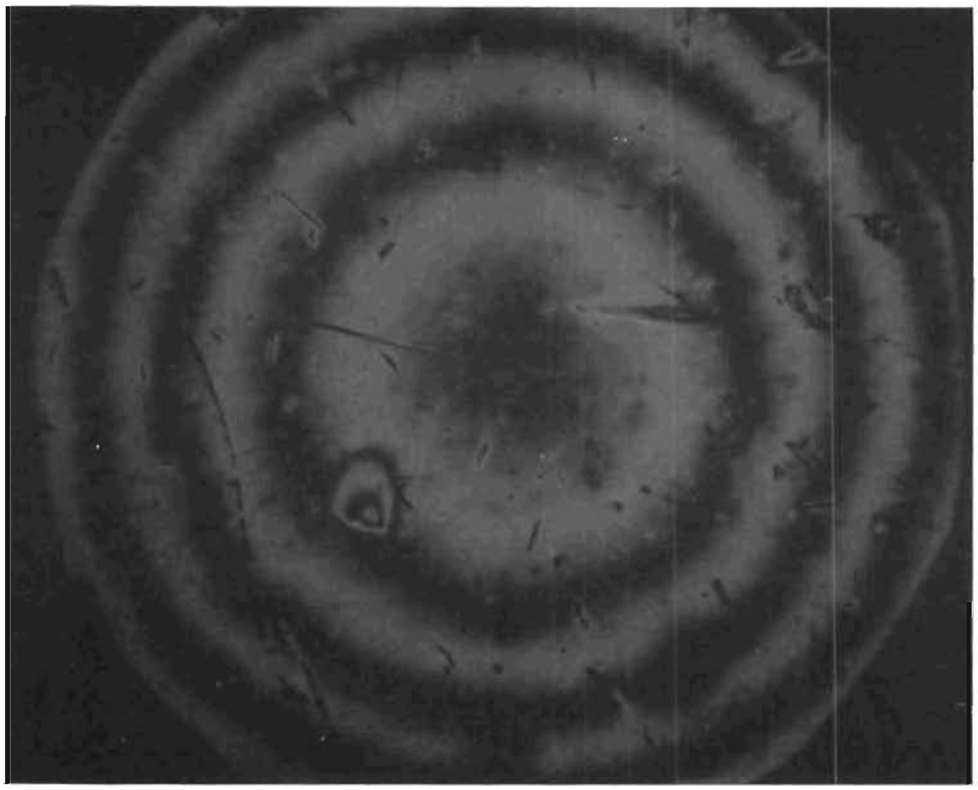

Figure 240. Test Model A_S, Poppet, 0.0089- x 0.0110-Inch Interference Photo at θ = 35 Degrees

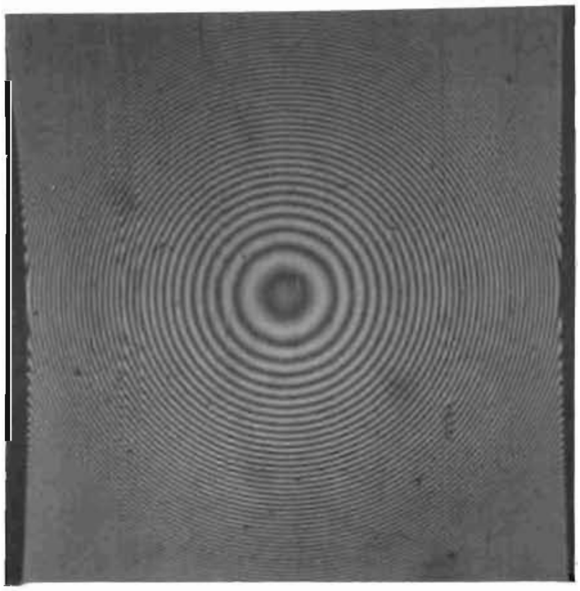

Figure 241. Test Model A_S, Seat, 0.033- x 0.033-Inch Interference Photo Showing Fretting Pits

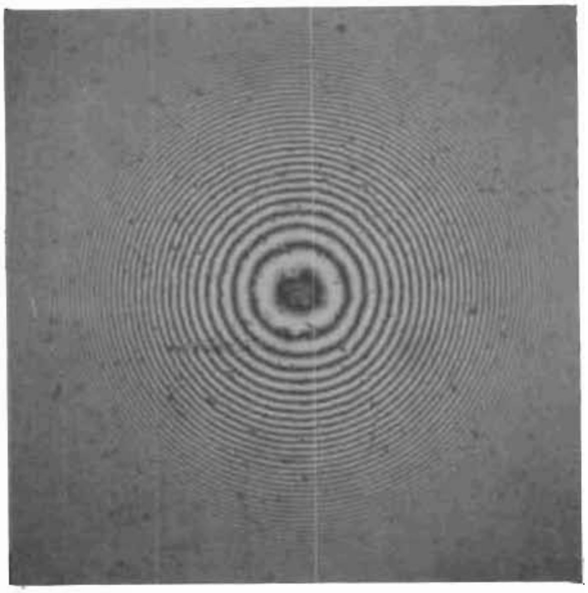

Figure 242. Test Model A_S, Poppet, 0.033- x 0.033-Inch Interference Photo Showing Fretting Pits

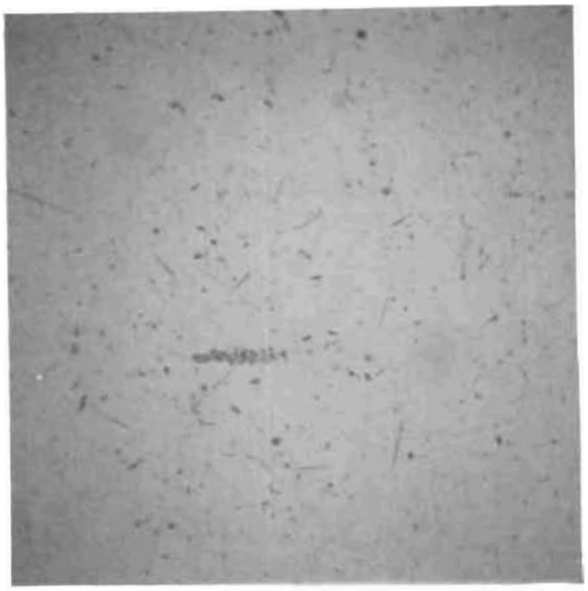

Figure 243. Test Model A_s, Poppet, 0.033- x 0.033-Inch Plain Photo, Same Location as Fig. 242

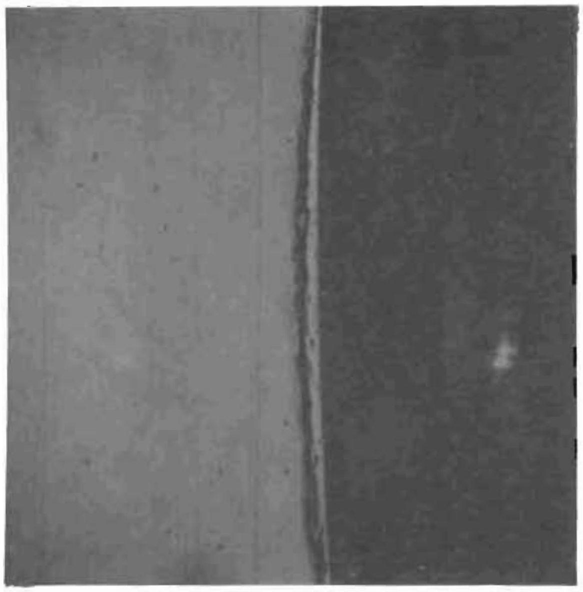

Figure 244. Test Model B_s, Seat, 0.033- x 0.033-Inch Plain Photo Showing Land OD Handling Damage

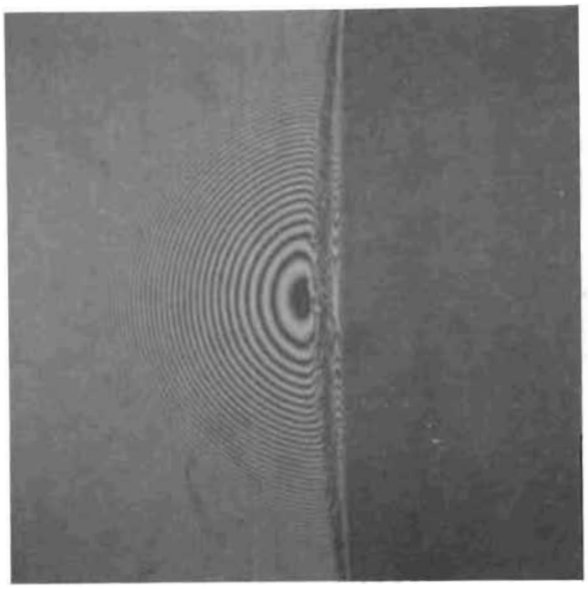

Figure 245. Test Model B_s, Seat, 0.033- x 0.033-Inch Interference Photo, Same Location as Fig. 244, Surface Tilted Slightly to Focus Bands on Damaged Area

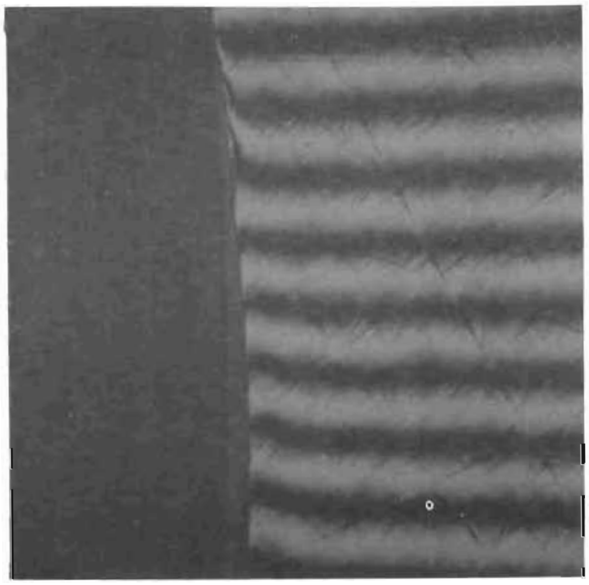

Figure 246. Test Model B_s, Seat, 0.033- x 0.033-Inch Interference Photo Normal to ID Showing Handling Damage

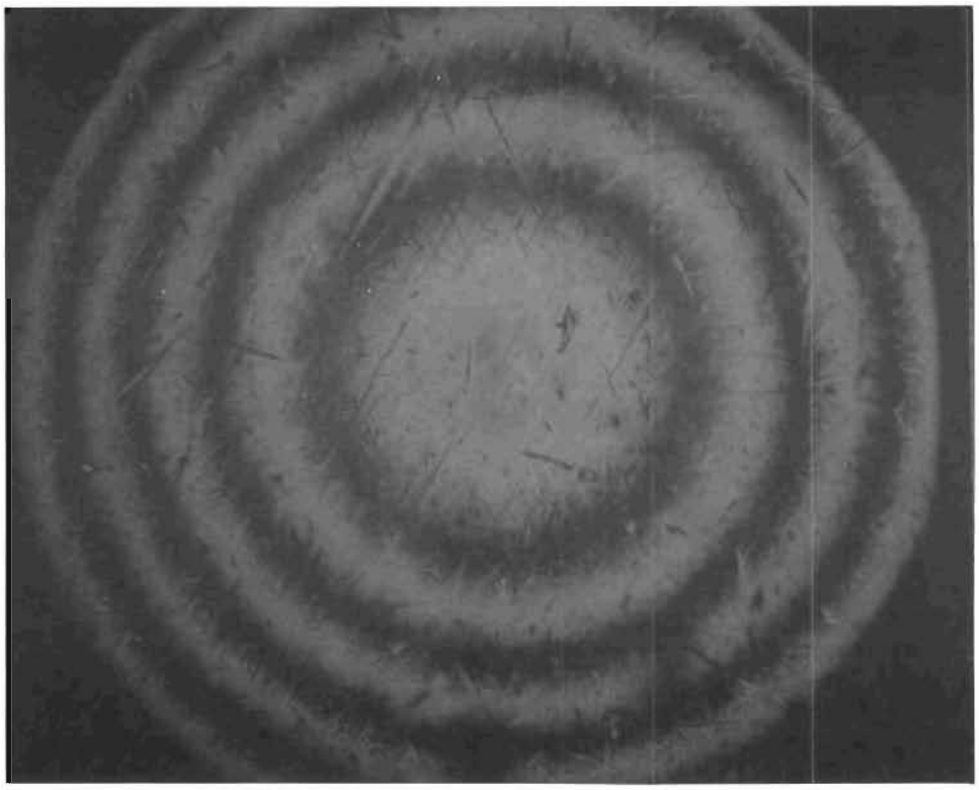

Figure 247. Test Model B_s, Poppet, 0.0089- x 0.0110-Inch Interference Photo at θ = 35 Degrees

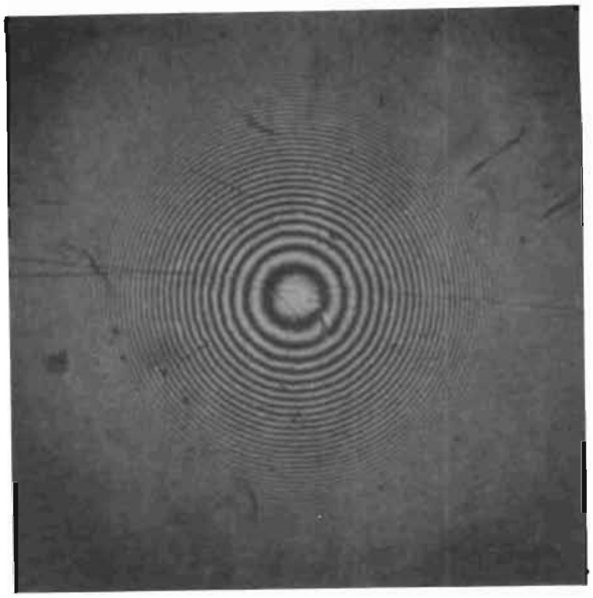

Figure 248. Test Model C_s, Poppet, 0.033- x 0.033-Inch Interference Photo at Midland

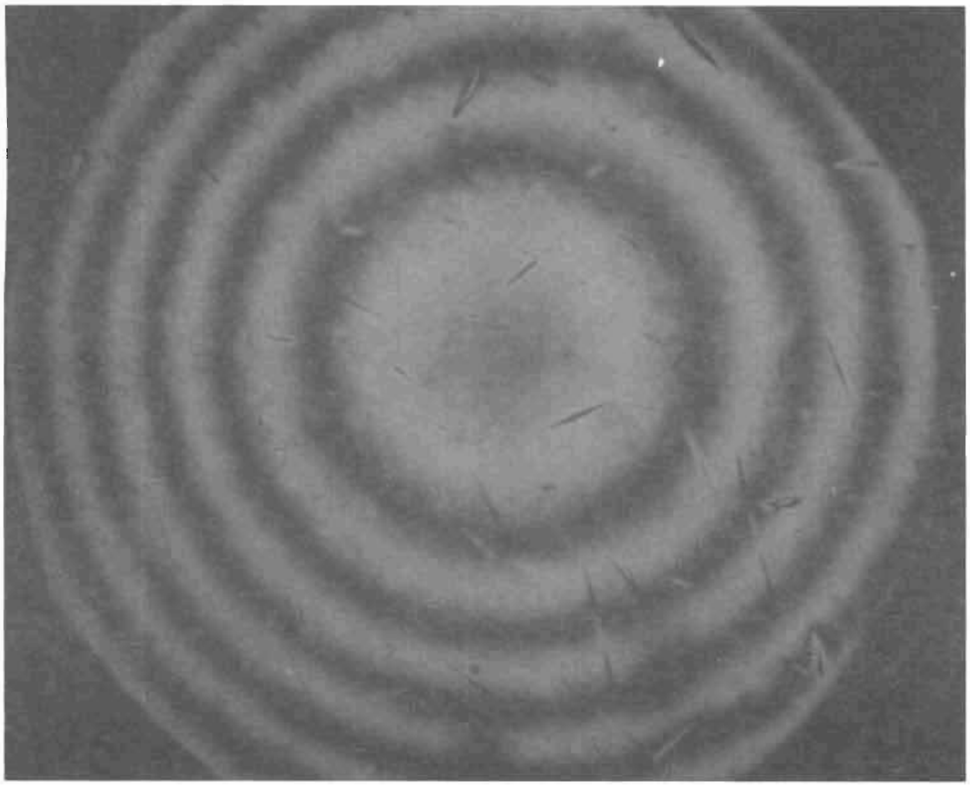

Figure 249. Test Model C_s, Poppet, 0.0089- x 0.0110-Inch Interference Photo at θ = 35 Degrees

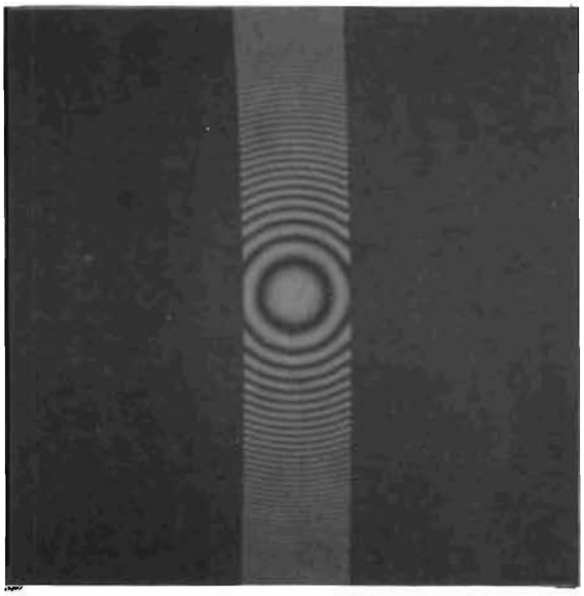

Figure 250. Test Model D_s, Seat, 0.033- x 0.033-Inch Interference Photo

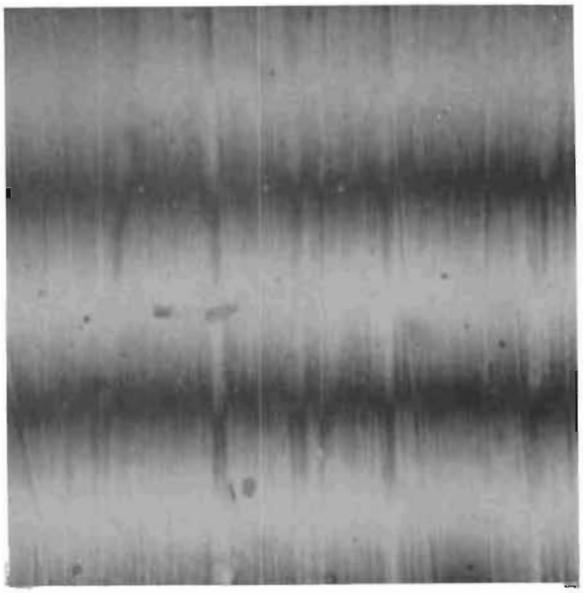

Figure 251. Test Model I_f, Poppet, 0.0065- x 0.0065-Inch Interference Photo

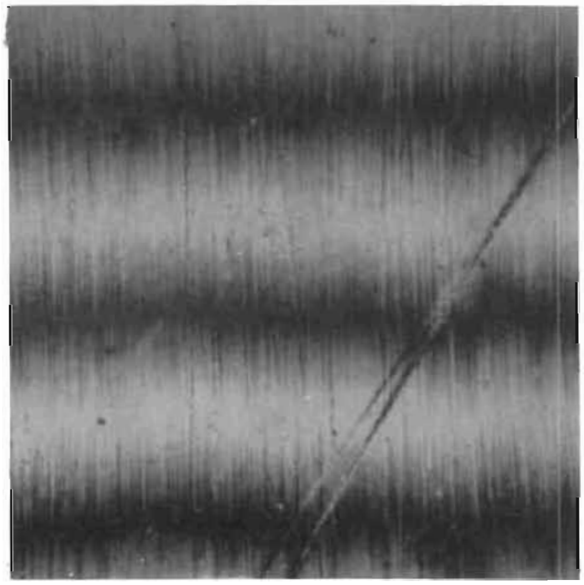

Figure 252. Test Model I_f, Seat, 0.0065- x 0.0065-Inch Interference Photo

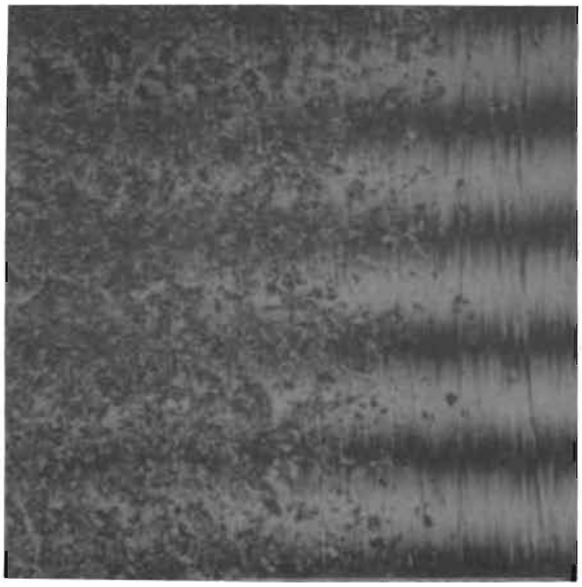

Figure 253. Test Model I_{f1}, Seat, 0.0065- x 0.0065-Inch Interference Photo Showing Transition From Lapped to Liquid Honed Surface

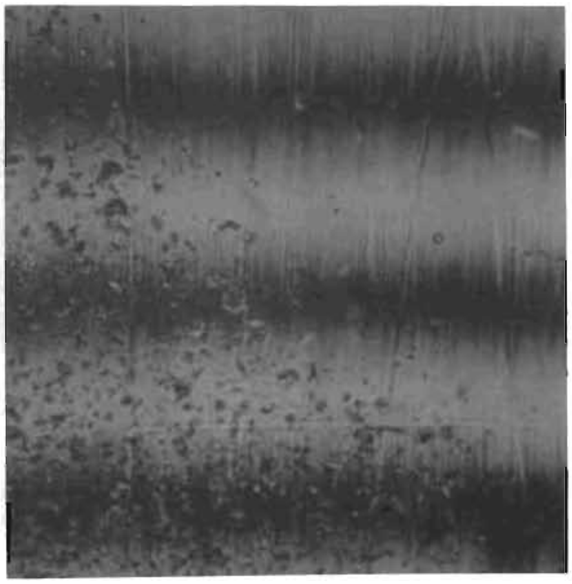

Figure 254. Test Model I_{f1}, Poppet, 0.0065- x 0.0065-Inch Interference Photo Showing Transition From Lapped to Liquid Honed Surface

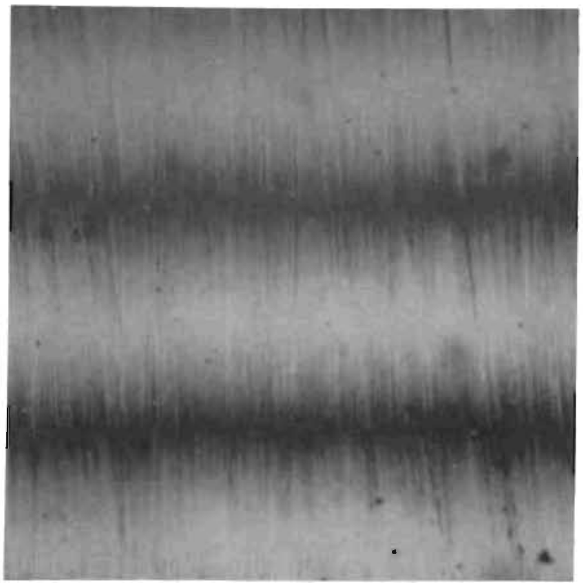

Figure 255. Test Model J_f, Seat, 0.0065- x 0.0065-Inch Interference Photo

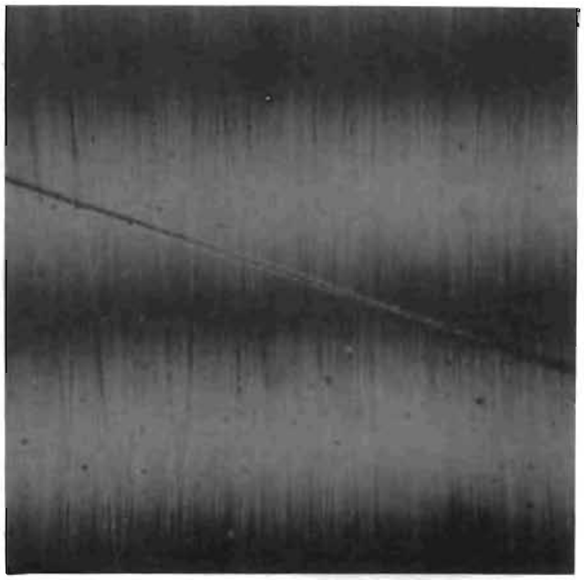

Figure 256. Test Model J_f, Poppet, 0.0065- x 0.0065-Inch Interference Photo

Figure 257. Test Model J_{f1}, Seat, 0.0065- x 0.0065-Inch Plain Photo, Same Location as Fig. 255 After Passivation

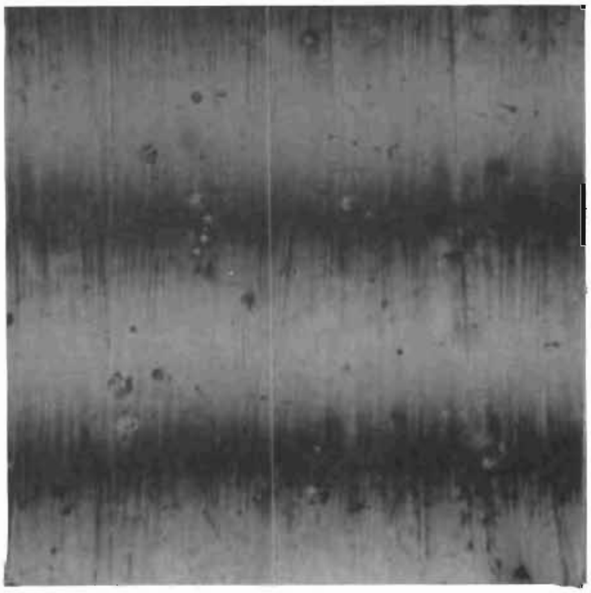

Figure 258. Test Model J_{f1}, Seat, 0.0065- x 0.0065-Inch Interference Photo, After Passivation, Same Location as Fig. 257

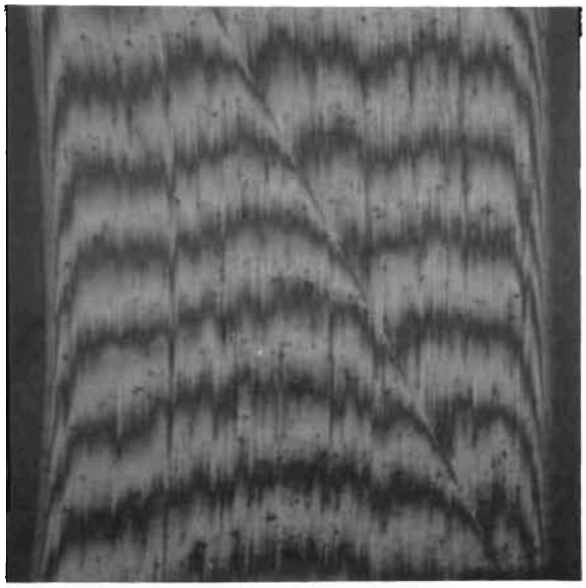

Figure 259. Test Model U_f, Seat, 0.033- x 0.033-Inch Interference Photo Prior to Anodizing

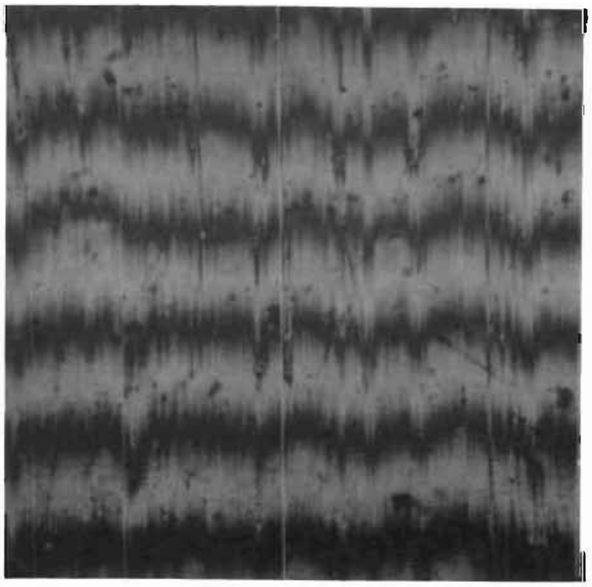

Figure 260. Test Model U_f, Seat, 0.0065- x 0.0065-Inch Interference Photo Prior to Anodizing

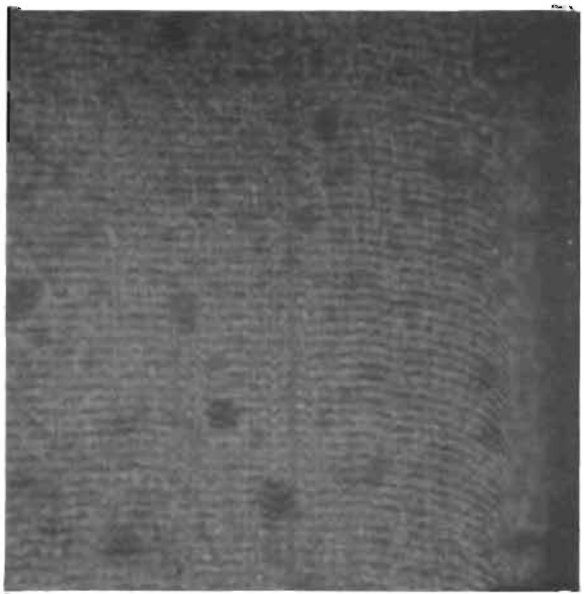

Figure 261. Test Model U_f, Seat, 0.0065- x 0.0065-Inch Interference Photo, Bands Focused on Anodized Surface

Figure 262. Test Model U_f, Seat, 0.0065- x 0.0065-Inch Interference Photo, Bands Focused Through Anodize, on Base-Metal Surface

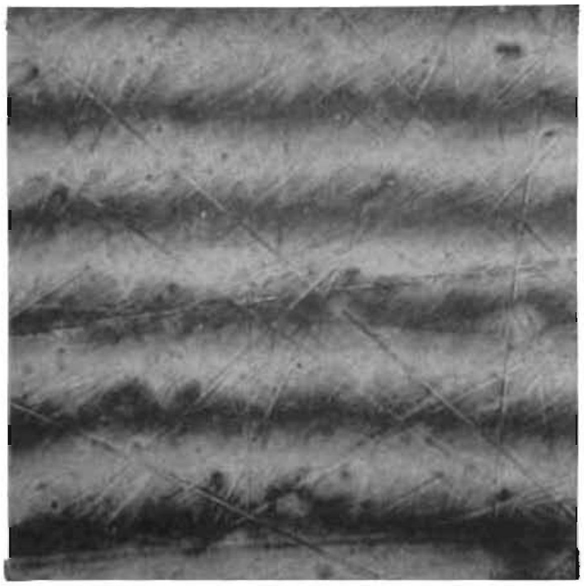

Figure 263. Test Model V_f, Seat, 0.0065- x 0.0065-Inch Interference Photo, Prior to Anodizing

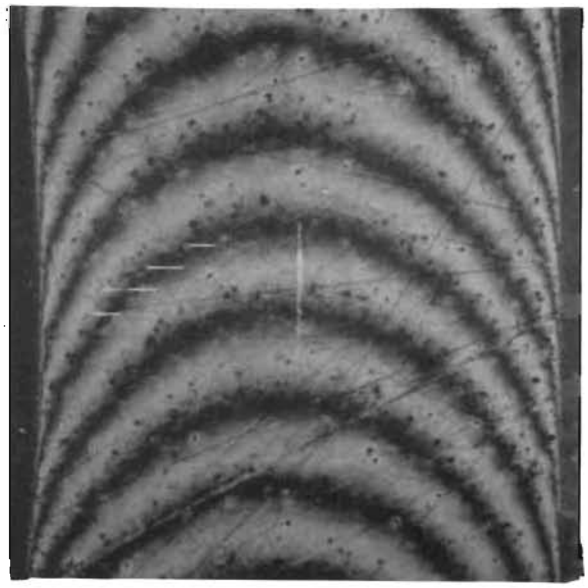

Figure 264. Test Model V_f, Seat, 0.033- x 0.033-Inch Interference Photo Prior to Anodizing

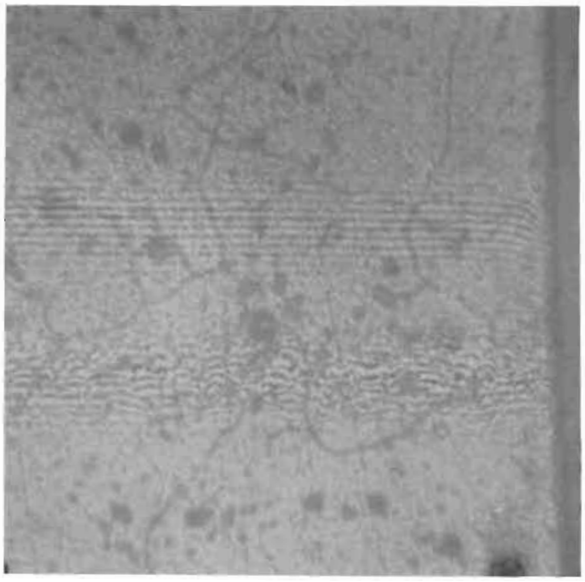

Figure 265. Test Model V_f, Seat, 0.0065- x 0.0065-Inch Interference Photo, White Light, Upper Bands Focused on Anodized Surface, Lower Bands on Base Metal

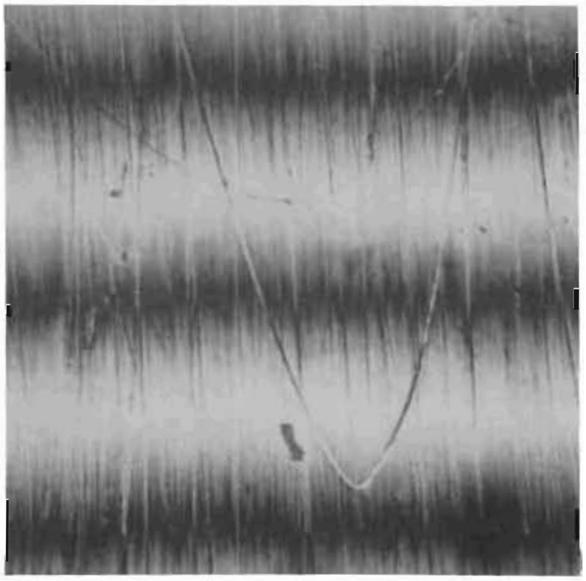

Figure 266. Test Model W_f, Poppet, 0.0065- x 0.0065-Inch Interference Photo

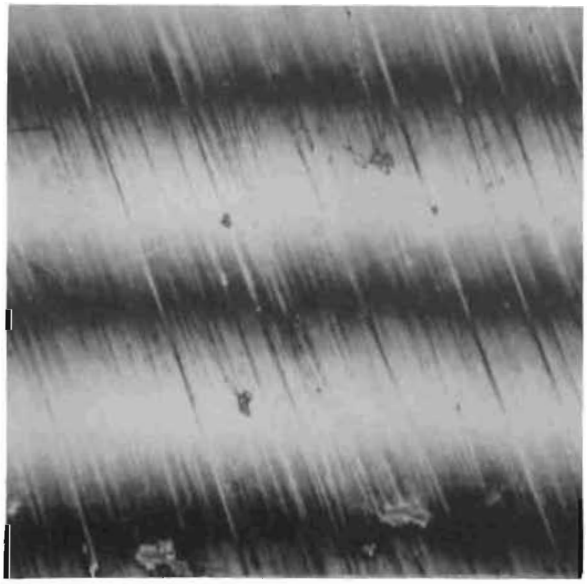

Figure 267. Test Model W_f, Seat, 0.0065- x 0.0065-Inch Interference Photo

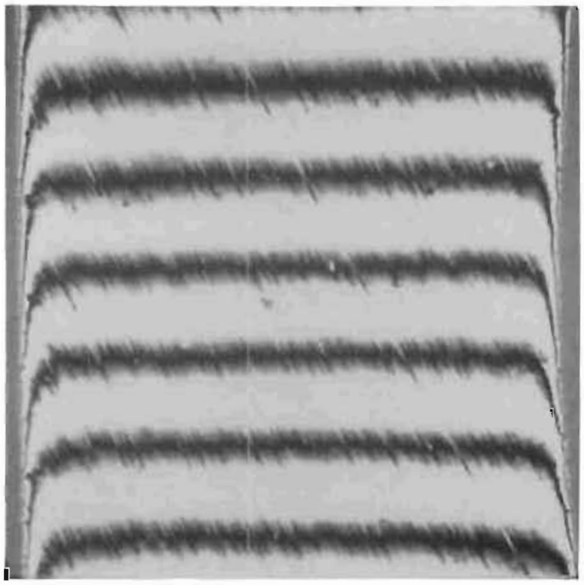

Figure 268. Test Model W_f, Seat, 0.033- x 0.033-Inch Interference Photo

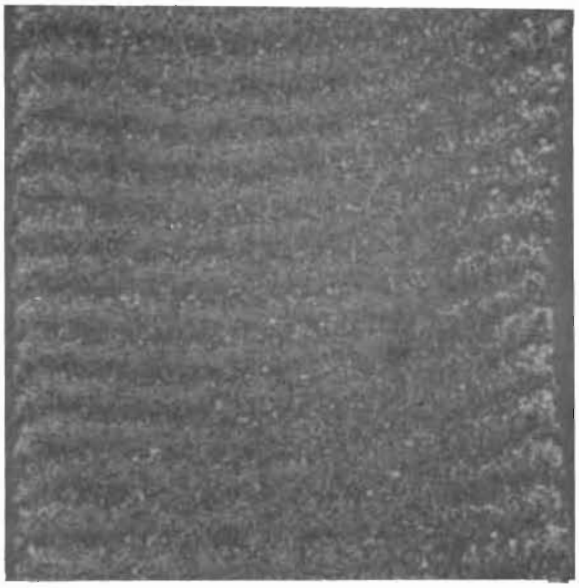

Figure 269. Test Model W_{f1}, Seat, 0.033- x 0.033-Inch Interference Photo Showing Plating Buildup at Corners (Posttest)

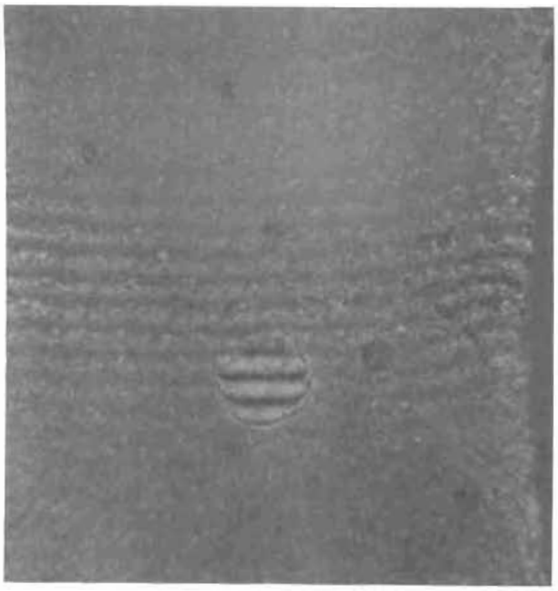

Figure 270. Test Model W_{f1}, Seat, 0.033- x 0.033-Inch Interference Photo Showing Plating Void, White Light (Posttest)

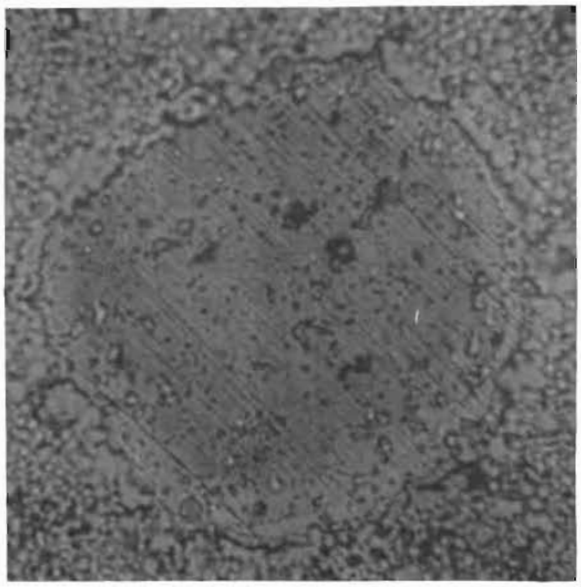

Figure 271. Test Model W_{f1}, Seat, 0.0065- x 0.0065-Inch Plain Photo Showing Plating Void (Preplate Finish Visible at Void Bottom)

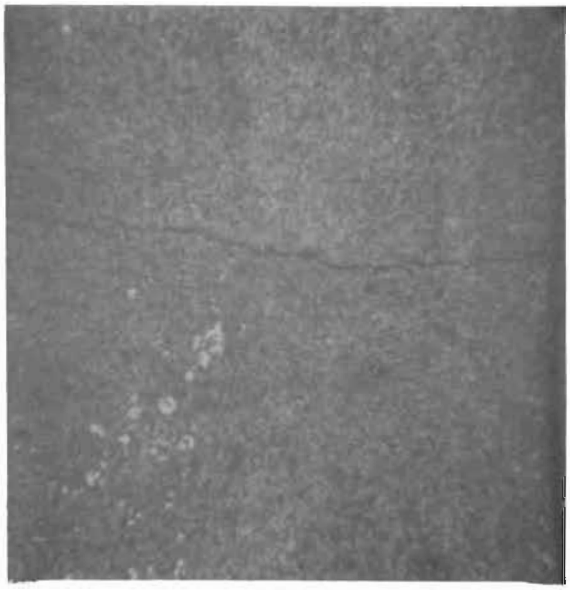

Figure 272. Test Model W_{f1}, Seat, 0.033- x 0.033-Inch Plain Photo Showing Ridged Crack in Plating

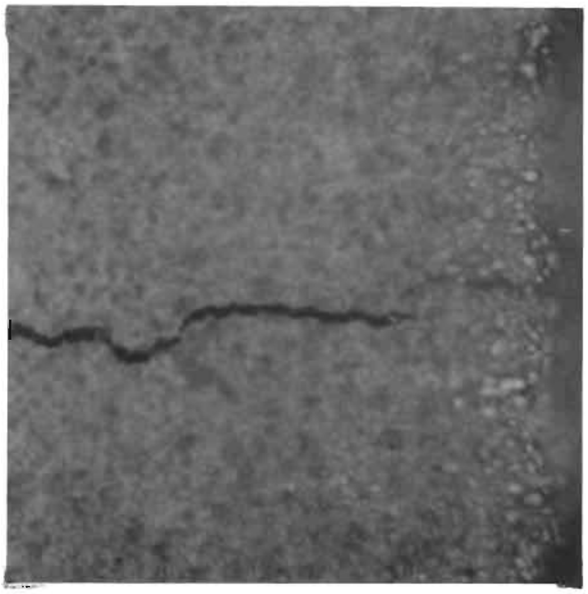

Figure 273. Test Model W_{f1}, Seat 0.0065- x 0.0065-Inch Plain Photo Showing ID Termination of Ridged Crack, Fig. 272

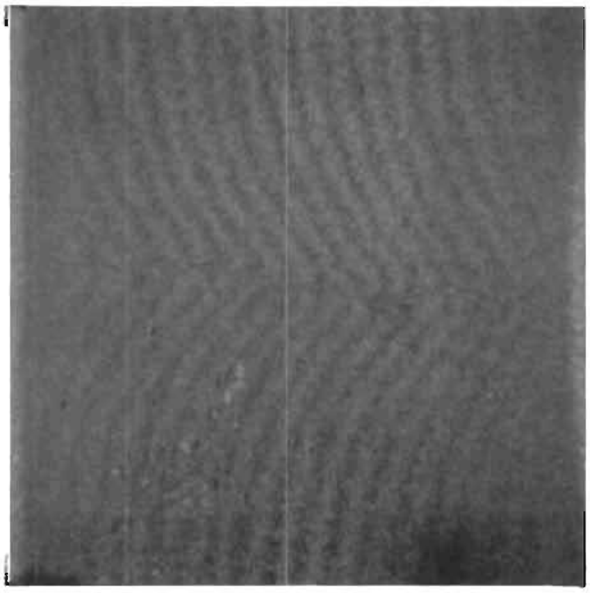

Figure 274. Test Model W_{f1}, Seat, 0.033- x 0.033-Inch Interference Photo, Bands Rotated to Illustrate Ridged Crack, Fig. 272

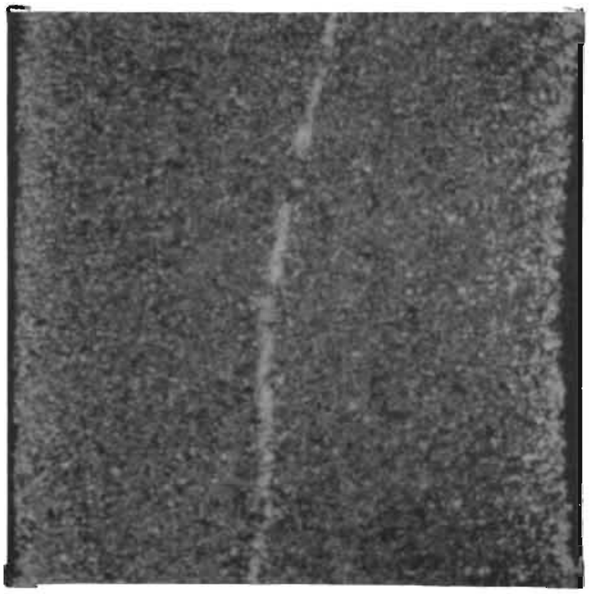

Figure 275. Test Model W_{f1}, Seat, 0.033- x 0.033-Inch Plain Photo Showing Plastic Deformation and Plating Void

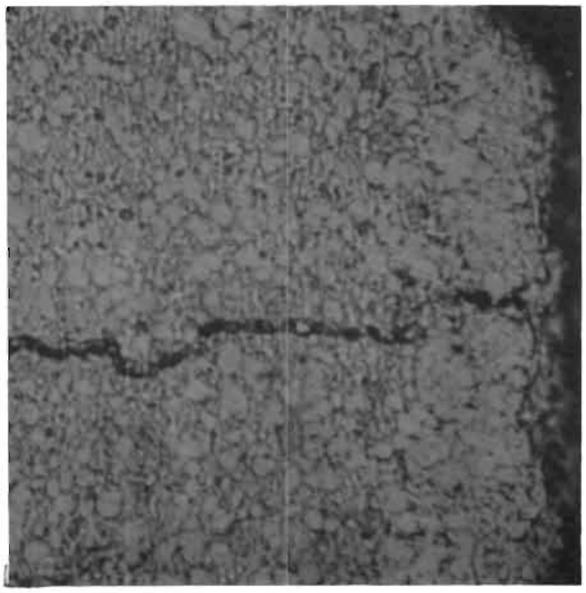

Figure 276. Test Model W_{f1}, Seat, 0.0065- x 0.0065-Inch Plain Photo Showing Plastic Deformation, Same Location as Fig. 273

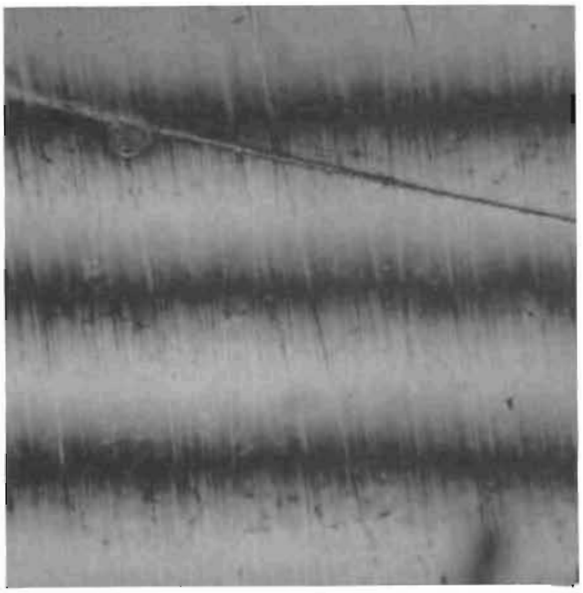

Figure 277. Test Model T_f, Poppet, 0.0065- x 0.0065-Inch Interference Photo

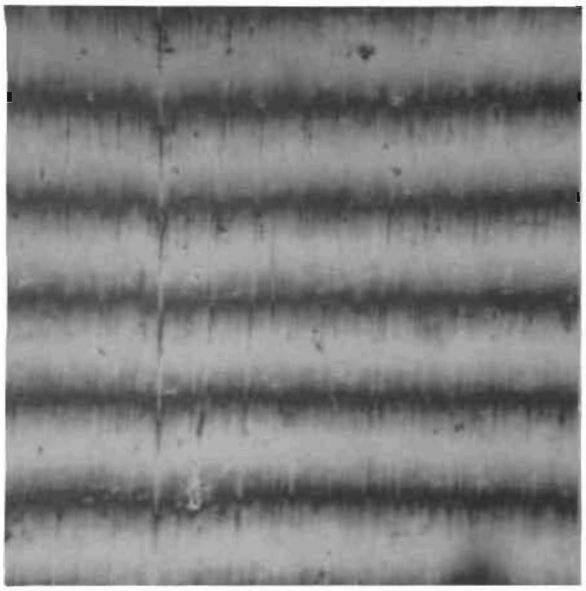

Figure 278. Test Model T_f, Seat, 0.0065- x 0.0065-Inch Interference Photo

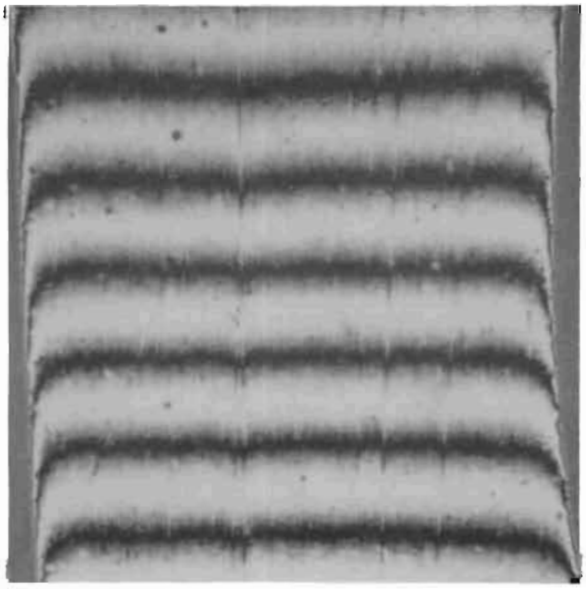

Figure 279. Test Model T_f, Seat, 0.033- x 0.033-Inch Interference Photo

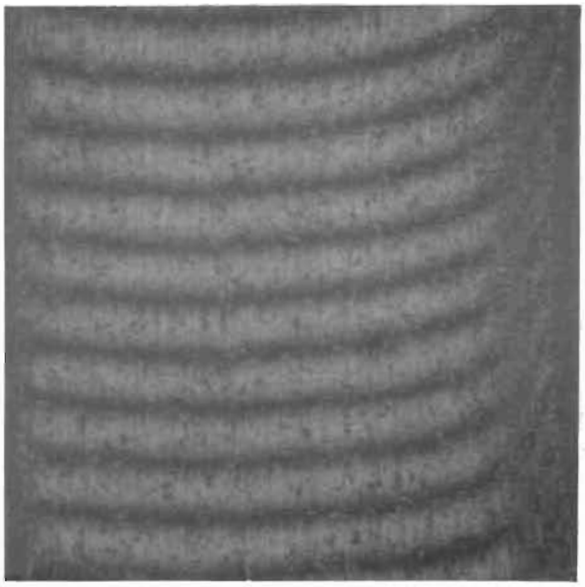

Figure 280. Test Model T_{f1}, Seat, 0.033- x 0.033-Inch Interference Photo

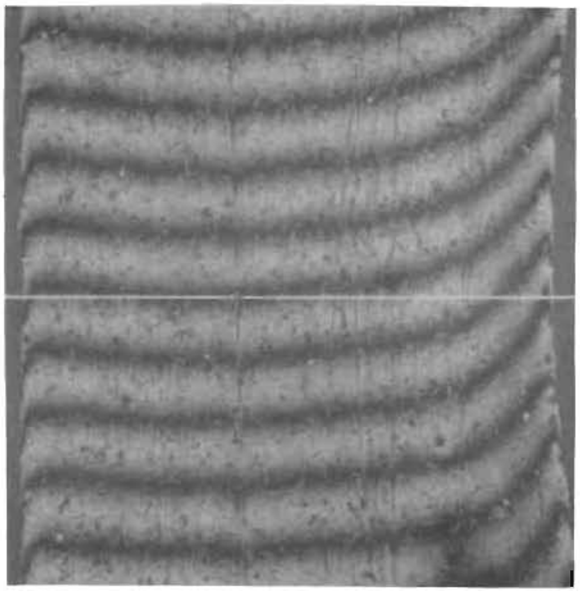

Figure 281. Test Model T_{f1}, Seat, 0.033- x 0.033-Inch Interference Photo, After Test 1, Same Location as Fig. 280

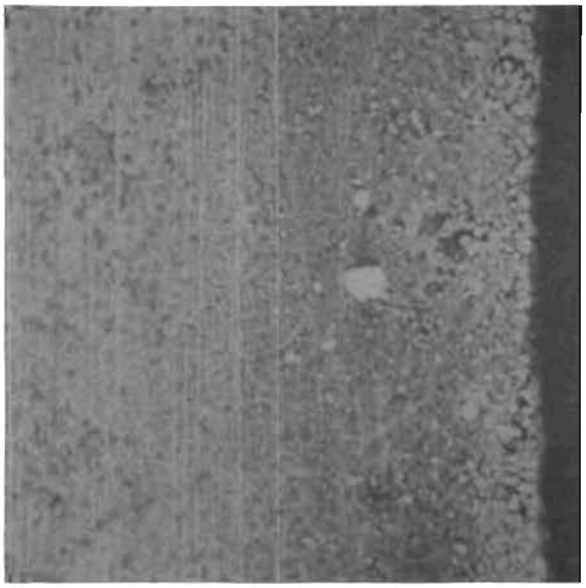

Figure 282. Test Model T_{f1}, Seat, 0.0065- x 0.0065-Inch Plain Photo Showing ID Plastic Deformation After Test 1

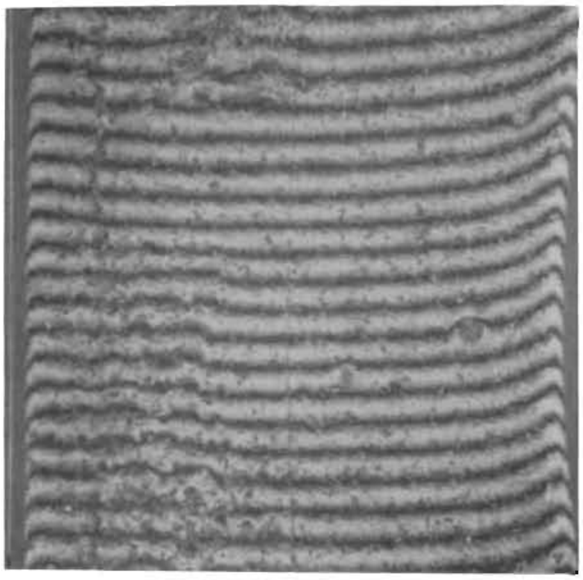

Figure 283. Test Model T_{f1}, Seat, 0.033- x 0.033-Inch Interference Photo Showing Gold-Plate Disruption

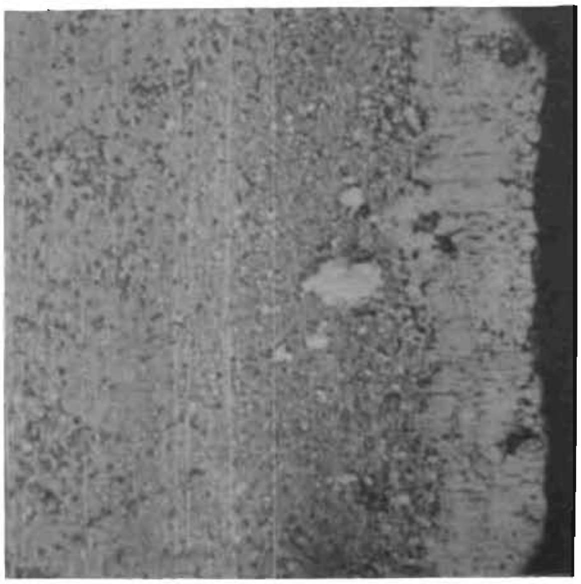

Figure 284. Test Model T_{f1}, Seat, 0.0065- x 0.0065-Inch Plain Photo Showing ID Plastic Flow After Cycling, Same Location as Fig. 282

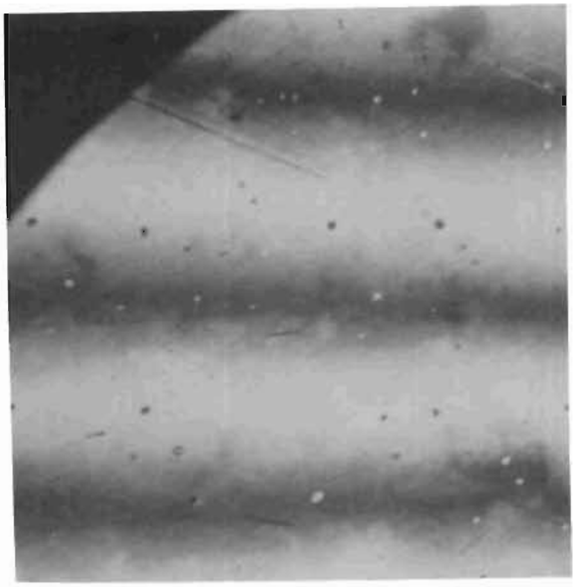

Figure 285. Test Model G, Poppet, 0.0065- x 0.0065-Inch Interference Photo, Wide Bandwidth

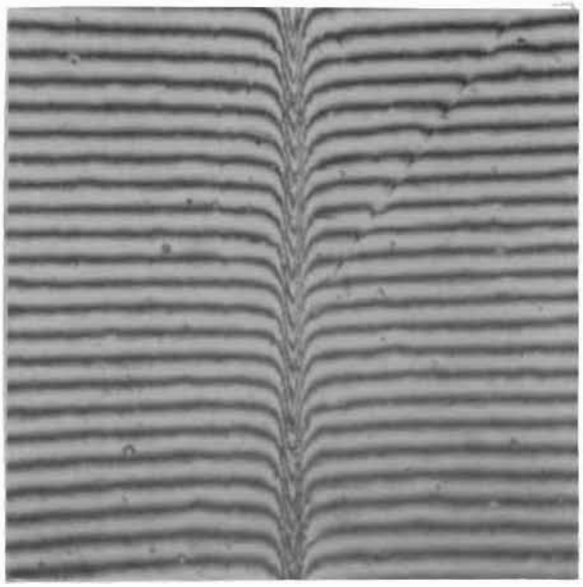

Figure 286. Test Model G, Poppet, 0.0065- x 0.0065-Inch Interference Photo, Narrow Bandwidth Showing Test Scratch

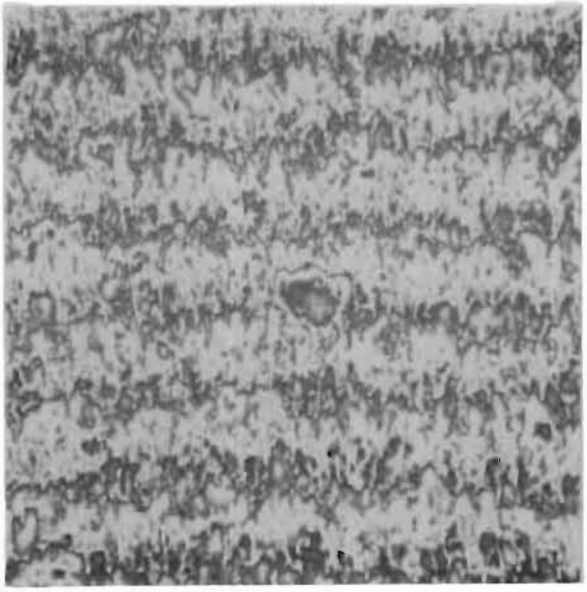

Figure 287. Test Model H, Poppet, 0.0065- x 0.0065-Inch Interference Photo

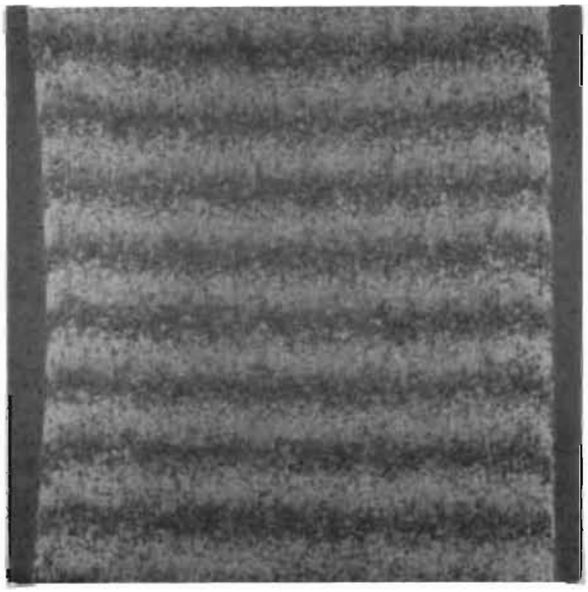

Figure 288. Test Model H, Seat, 0.033- x 0.033-Inch Interference Photo

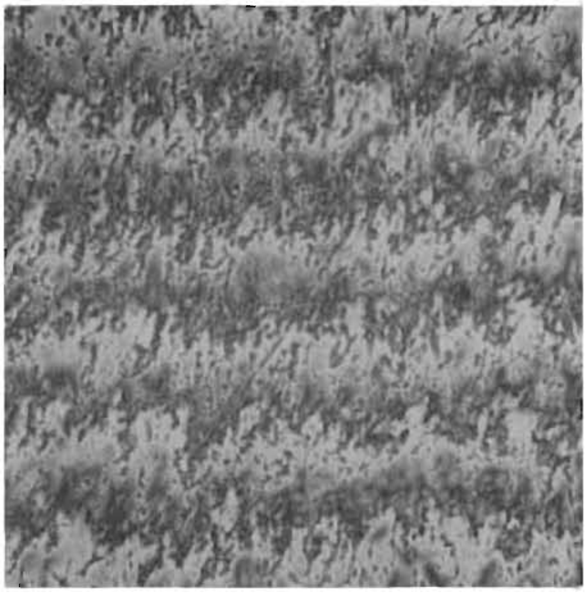

Figure 289. Test Model I, Poppet, 0.0065- x 0.0065-Inch Interference Photo

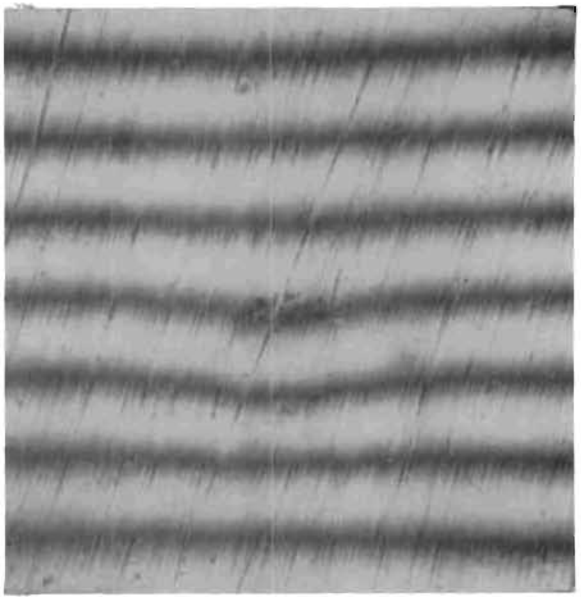

Figure 290. Test Model L, Seat, 0.033- x 0.033-Inch Interference Photo Showing Plastic Deformation at Area of Lead Particle 3

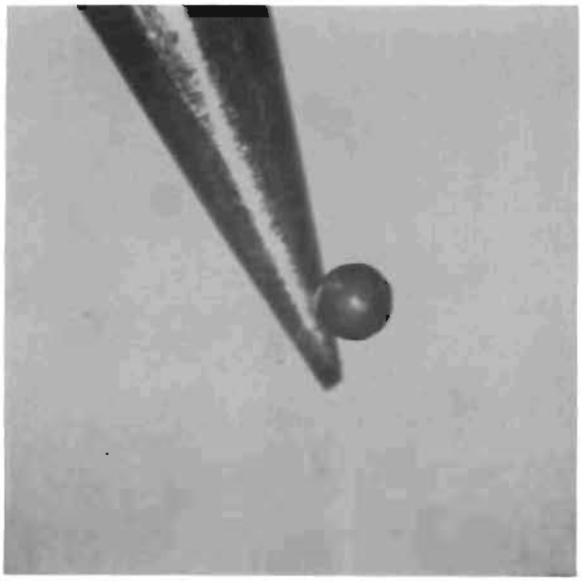

Figure 291. Handling Probe and Lead Particle 3, 0.033- x 0.033-Inch Plain Photo (Ref. Test Model L)

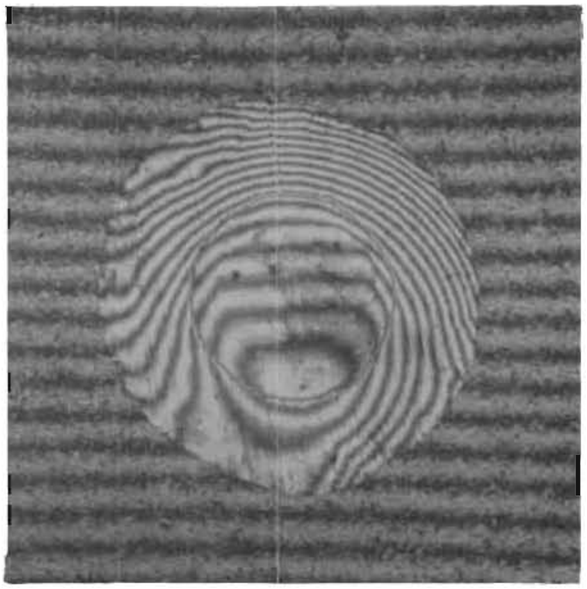

Figure 292. Test Model L, Poppet, 0.033- x 0.033-Inch Interference Photo Showing Flattened Lead Particle 3 (Note Lay of Opposing Surface)

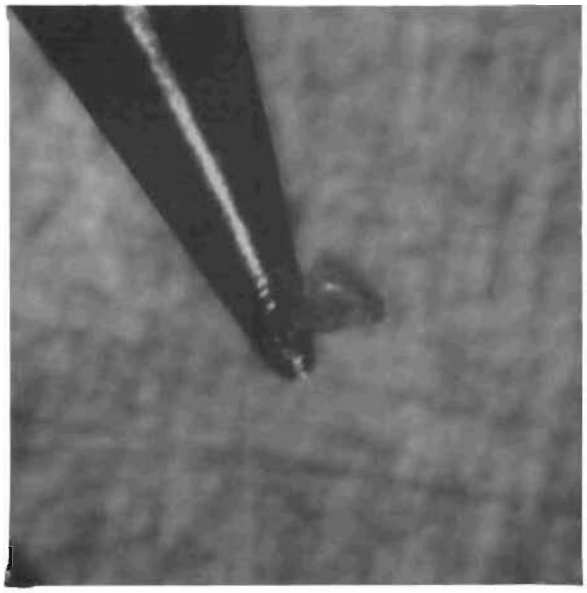

Figure 293. Handling Probe and Diamond Particle 2, 0.033- x 0.033-Inch Plain Photo (Ref. Test Model L)

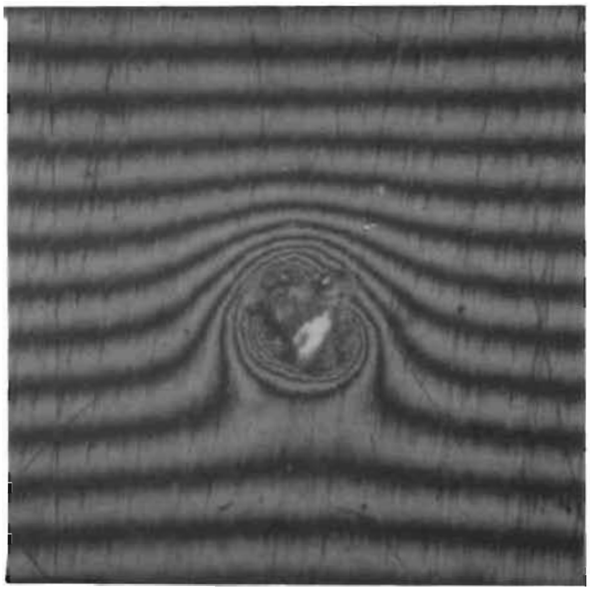

Figure 294. Test Model L, Seat, 0.033- x 0.033-Inch Interference Photo Showing Embedded Diamond Particle 3

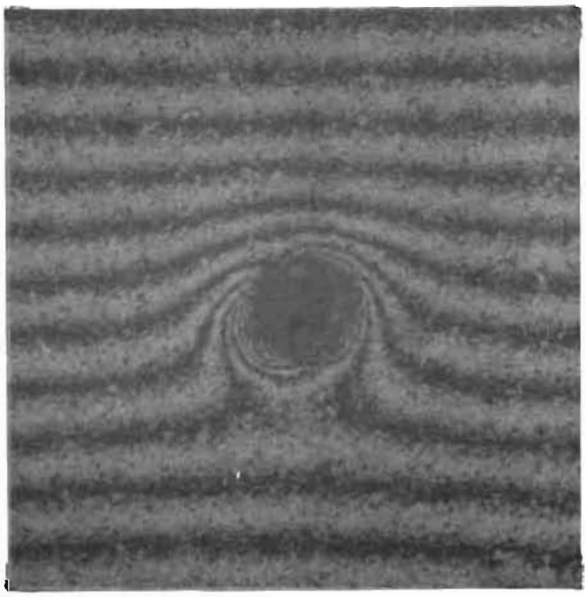

Figure 295. Test Model L, Poppet, 0.033- x 0.033-Inch Interference Photo Showing Plastic Deformation Caused by Diamond Particle 2

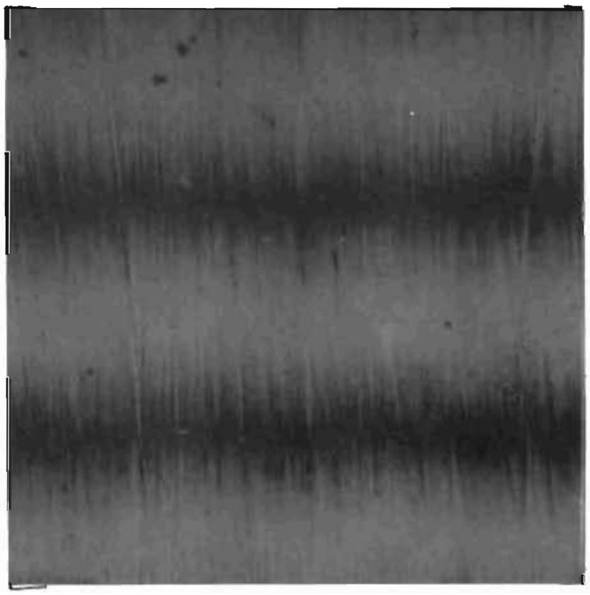

Figure 296. Test Model X_f, Seat, 0.0065- x 0.0065-Inch Interference Photo

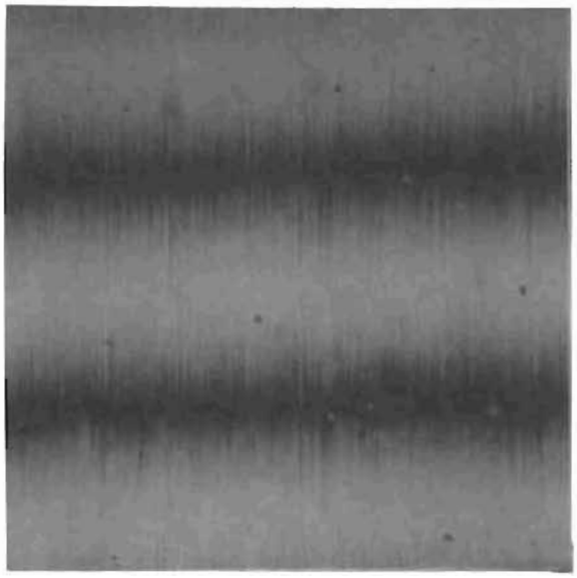

Figure 297. Test Model X_f, Poppet, 0.0065- x 0.0065-Inch Interference Photo

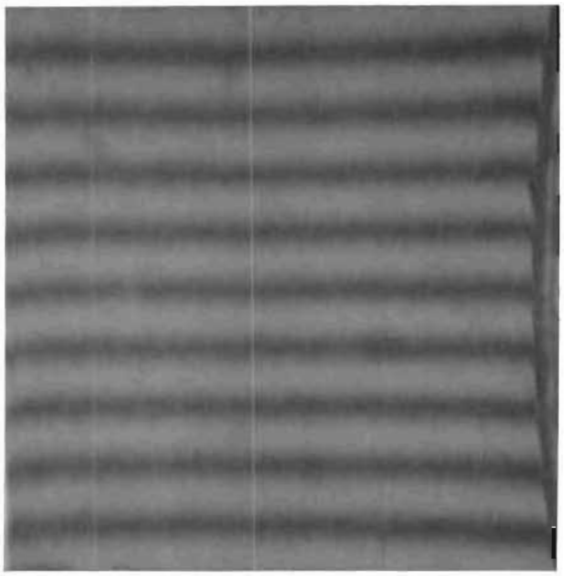

Figure 298. Test Model X_f, Seat, 0.033- x 0.033-Inch Interference Photo

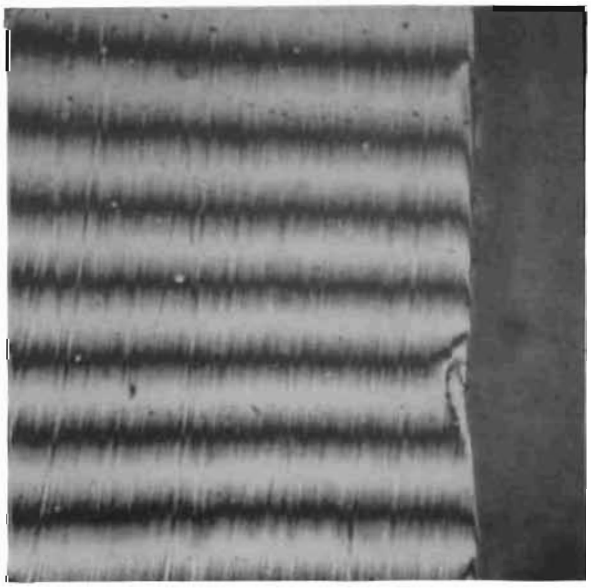

Figure 299. Test Model X_f, Seat, 0.0065- x 0.0065-Inch Interference Photo Showing Raised Nodule Posttest at ID

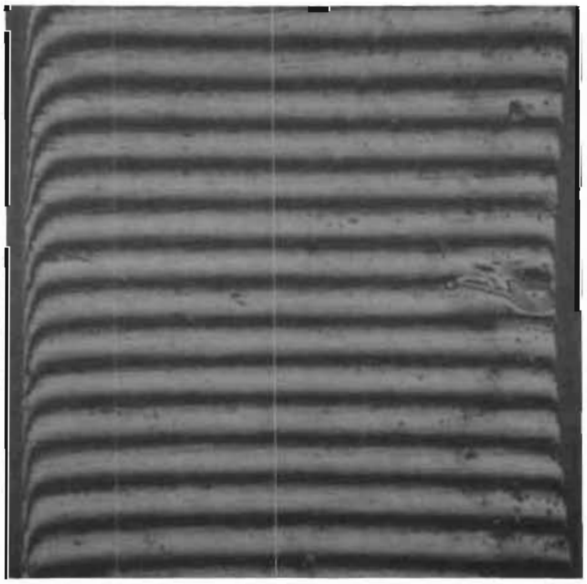

Figure 300. Test Model X_f, Seat, 0.033- x 0.033-Inch Interference Photo Showing Edge Plastic Flow and Corrosion Fretting

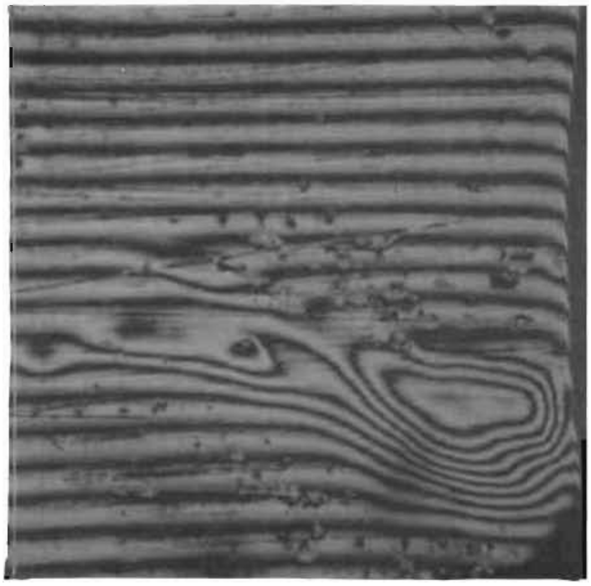

Figure 301. Test Model X_f, Seat, 0.0065- x 0.0065-Inch Interference Photo, Same Location as Fig. 300

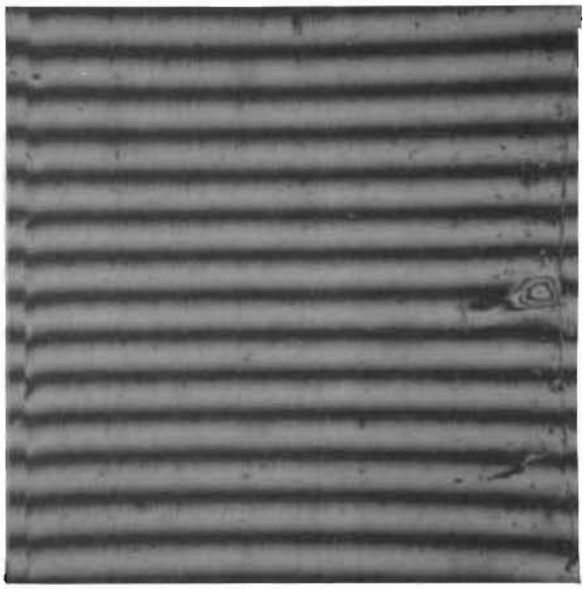

Figure 302. Test Model X_f, Poppet, 0.033- x 0.033-Inch Interference Photo, Same Location as Fig. 300

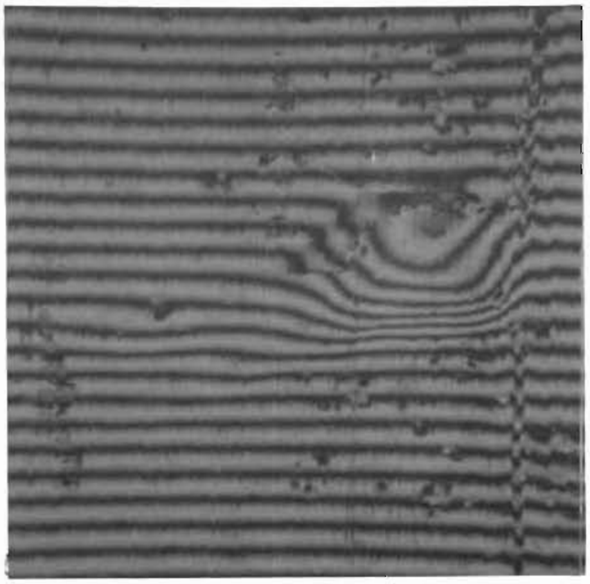

Figure 303. Test Model X_f, Poppet, 0.0065- x 0.0065-Inch Interference Photo, Same Location as Fig. 302

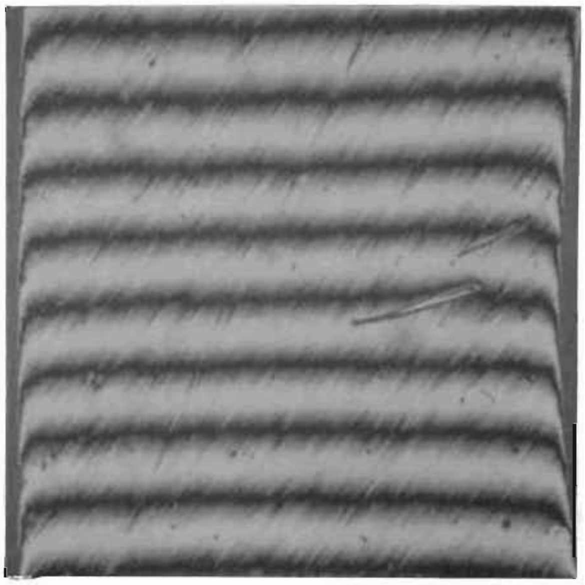

Figure 304. Test Model Y_f, Seat, 0.033- x 0.033-Inch Interference Photo Showing Lapping Scratch

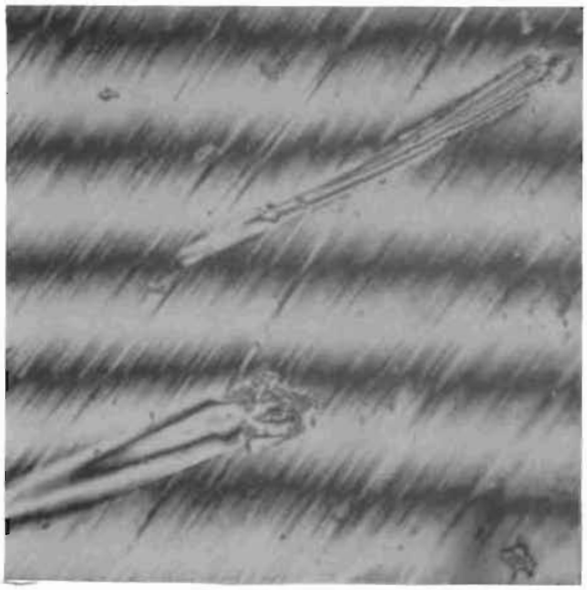

Figure 305. Test Model Y_f, Seat, 0.0065- x 0.0065-Inch Interference Photo, Same Location as Fig. 304

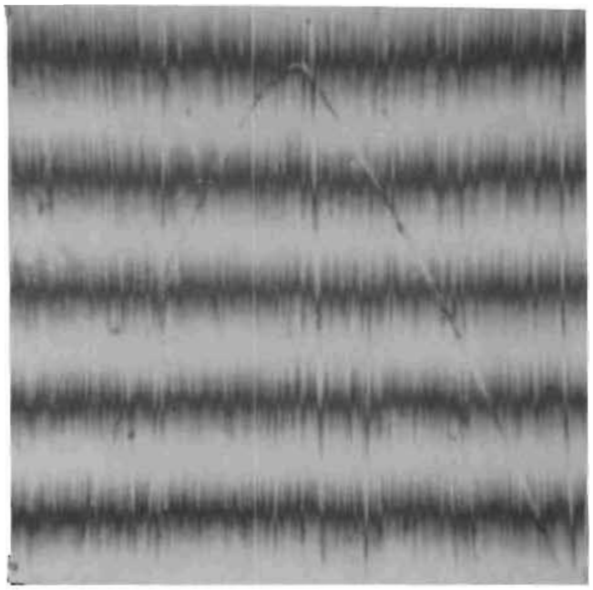

Figure 306. Test Model Y_f, Poppet, 0.0065- x 0.0065-Inch Interference Photo

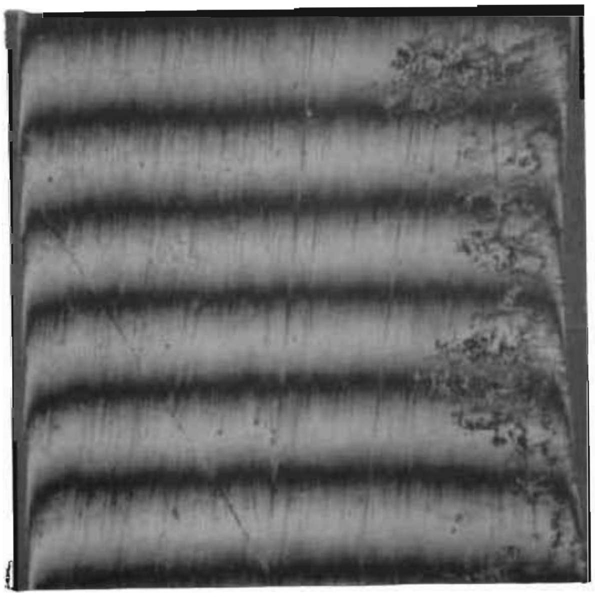

Figure 307. Test Model Y_f, Seat, 0.033- x 0.033-Inch Interference Photo Showing Fretting Corrosion at ID Before Wiping

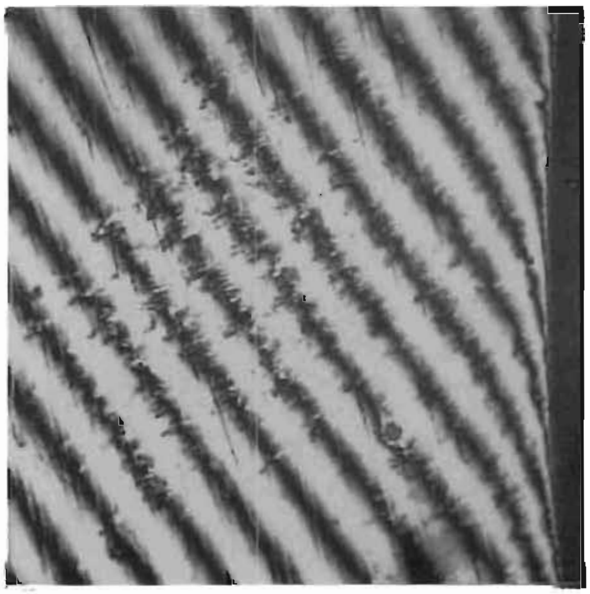

Figure 308. Test Model Y_f, Seat, 0.0065- x 0.0065-Inch Interference Photo Showing Fretting Wear at ID After Wiping

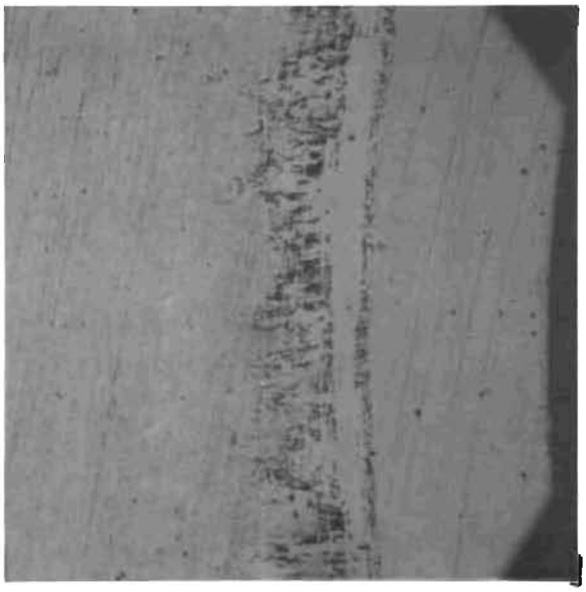

Figure 309. Test Model Y_f, Poppet, 0.033- x 0.033-Inch Plain Photo Showing Corrosion Fretting at ID After Wiping

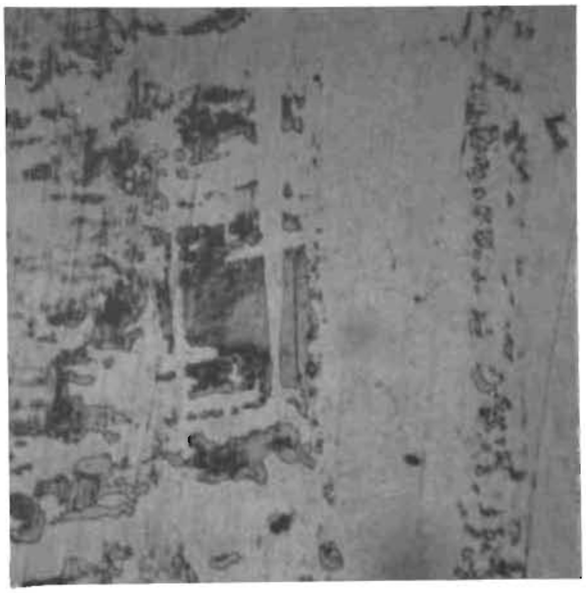

Figure 310. Test Model Y_f, Poppet, 0.0065- x 0.0065-Inch Plain Photo, Same Location as Fig. 309 at ID

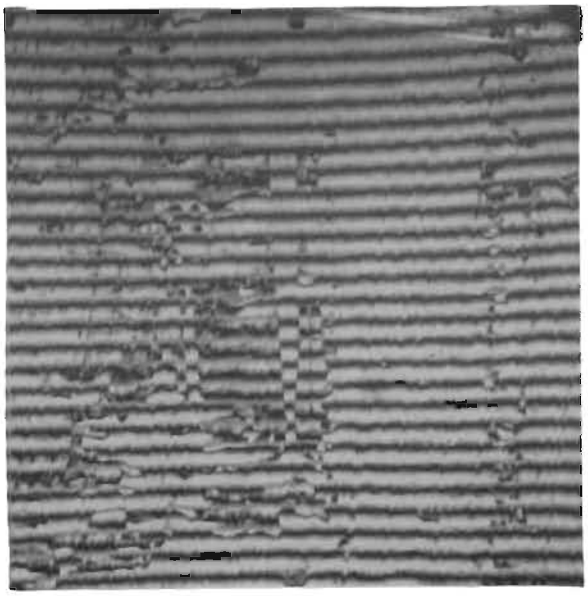

Figure 311. Test Model Y_f, Poppet, 0.0065- x 0.0065-Inch Interference Photo, Same Location as Fig. 310, Showing Corrosion Products

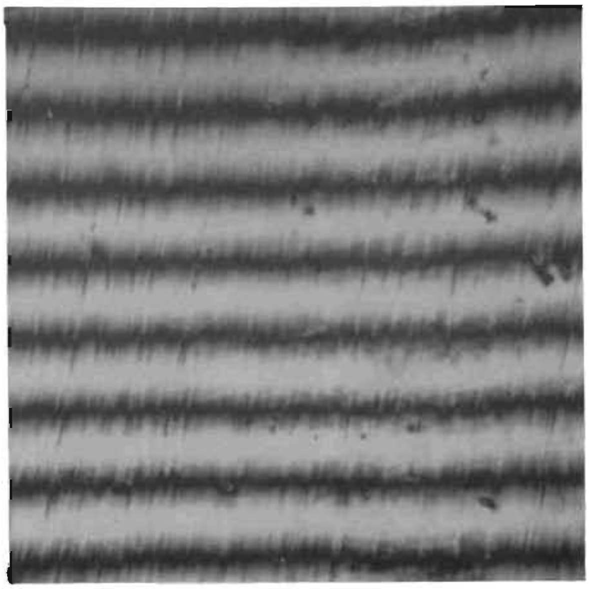

Figure 312. Test Model Y_f, Poppet, 0.0065- x 0.0065-Inch Interference Photo, Same Location as Fig. 311 After Light Polish

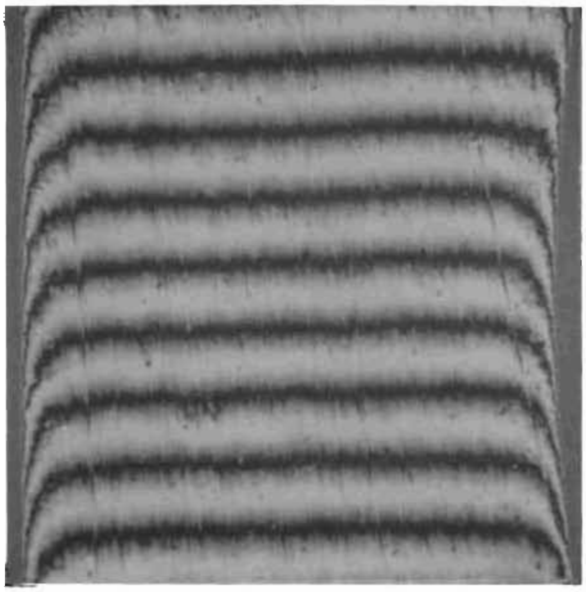

Figure 313. Test Model P_f, Seat, 0.033- x 0.033-Inch Interference Photo

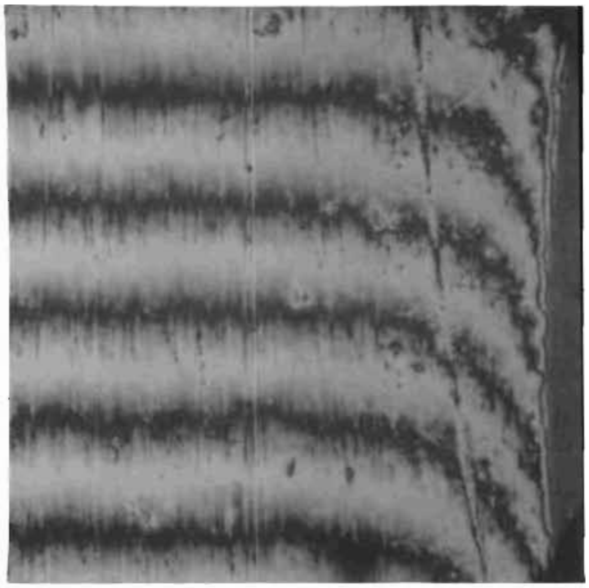

Figure 314. Test Model P_f, Seat, 0.0065- x 0.0065-Inch Interference Photo, Same Location as Fig. 313 at ID

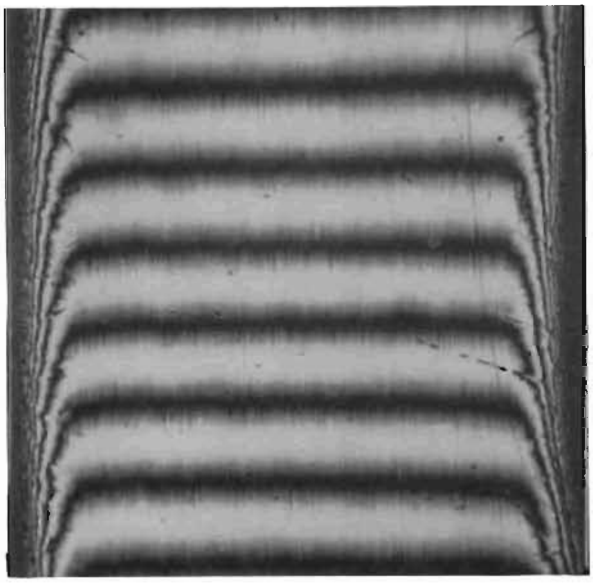

Figure 315. Test Model P_f, Poppet, 0.033- x 0.033-Inch Interference Photo

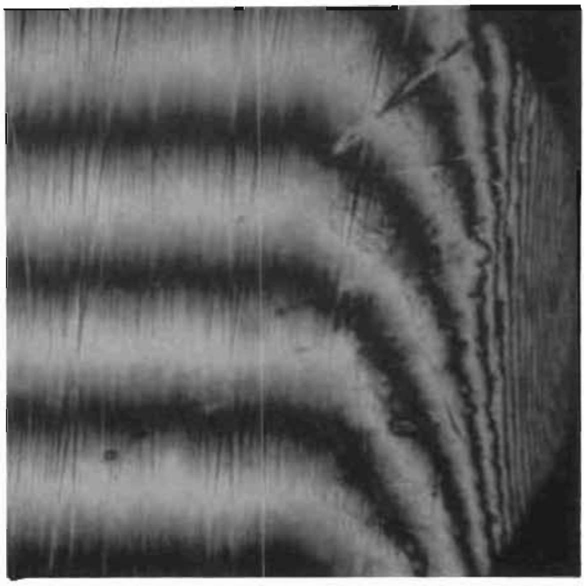

Figure 316. Test Model P_f, Poppet, 0.0065- x 0.0065-Inch Interference Photo, Same Location as Fig. 315 at ID

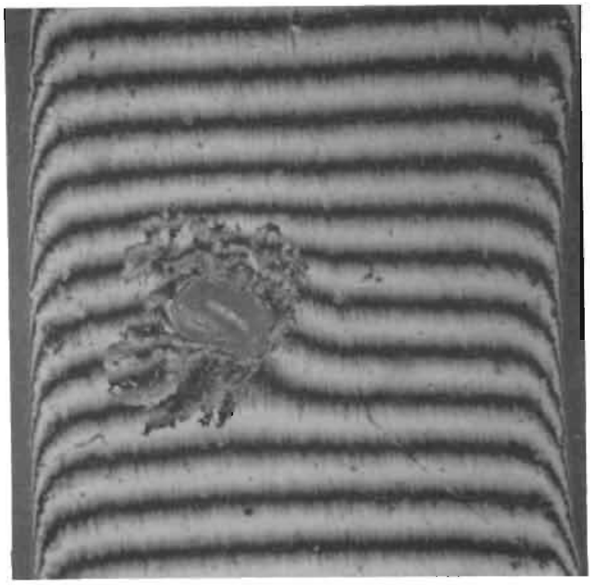

Figure 317. Test Model P_f, Seat, 0.033- x 0.033-Inch Interference Photo Showing Pit and Adherent Contaminant

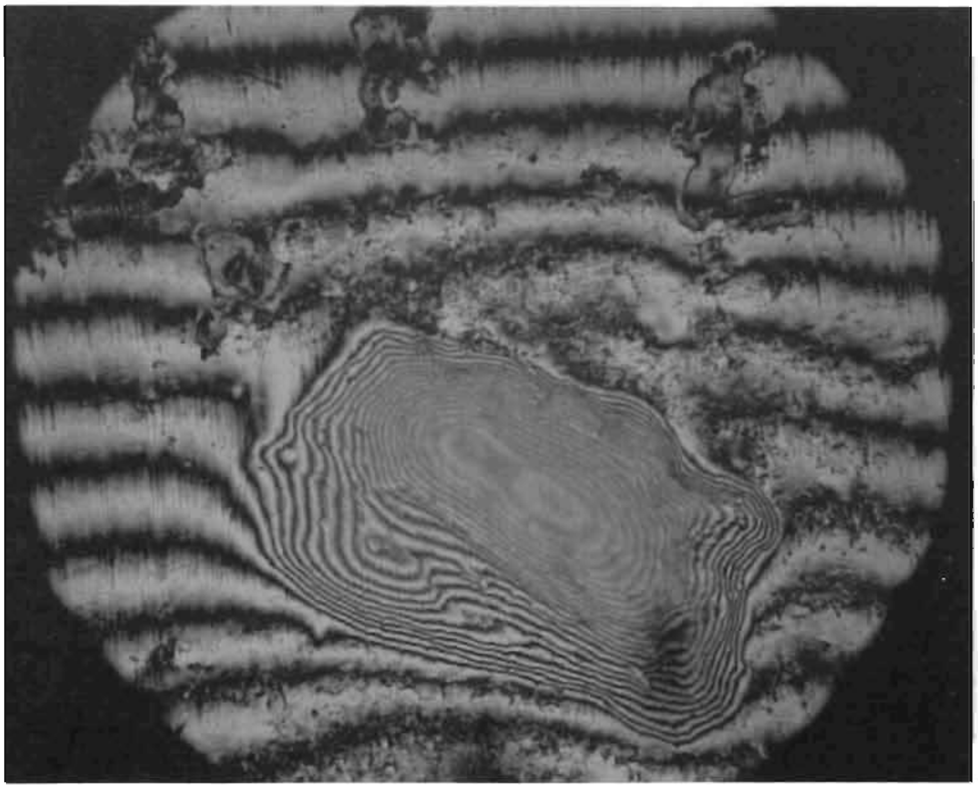

Figure 318. Test Model P_f, Seat, 0.0089- x 0.011-Inch Interference Photo, Same Location as Fig. 317 After Wiping

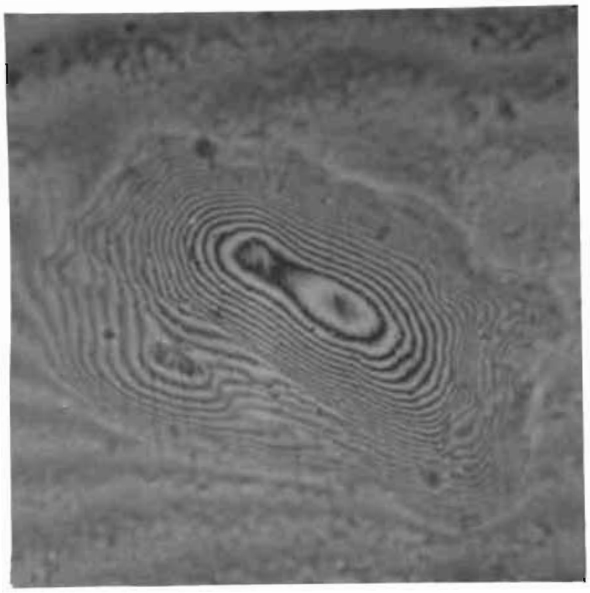

Figure 319. Test Model P_f, Seat, 0.0065- x 0.0065-Inch Interference Photo, Same Location as Fig. 318

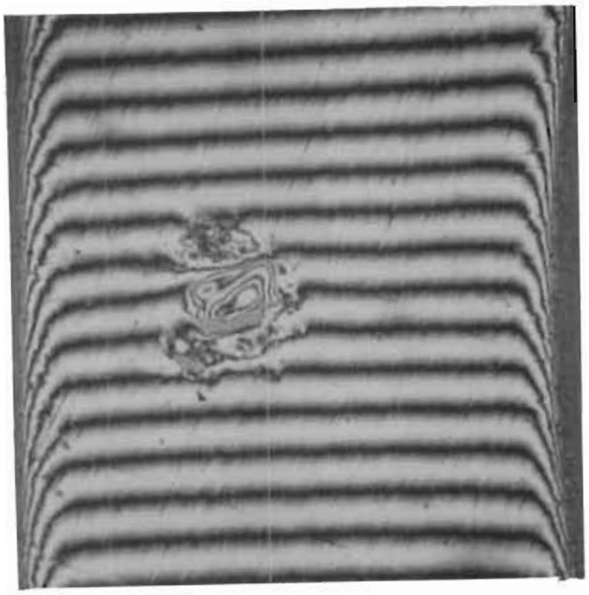

Figure 320. Test Model P_f, Poppet, 0.033- x 0.033-Inch Interference Photo, Same Location as Fig. 317

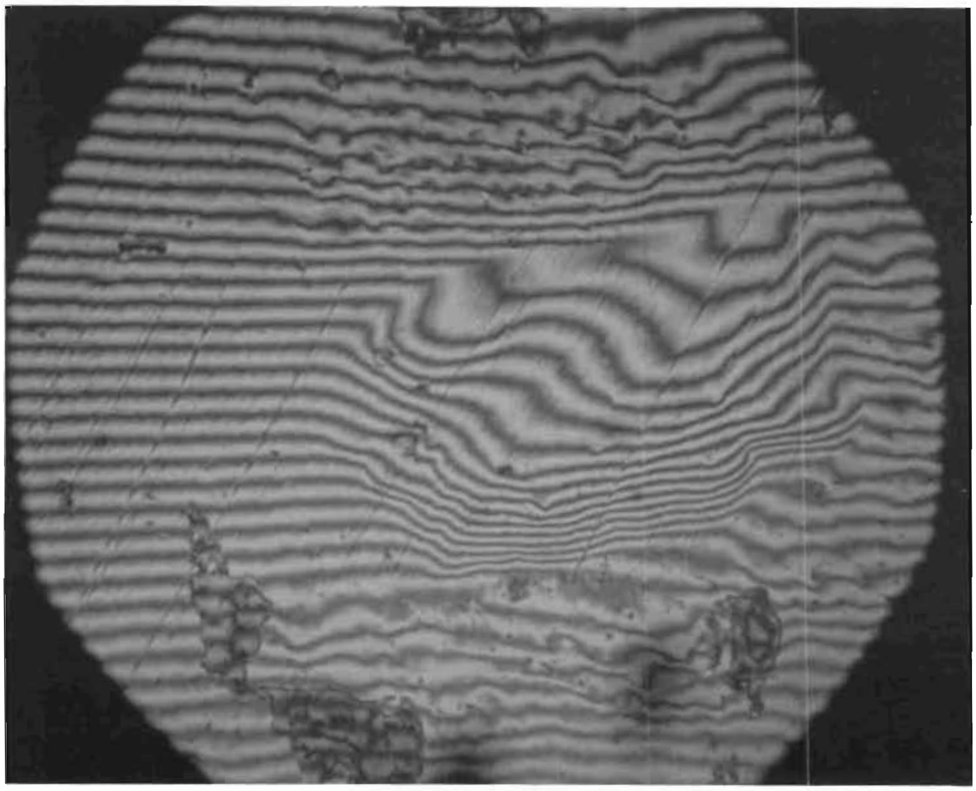

Figure 321. Test Model P_f, Poppet, 0.0089- x 0.011-Inch Interference Photo, Same Location as Fig. 320

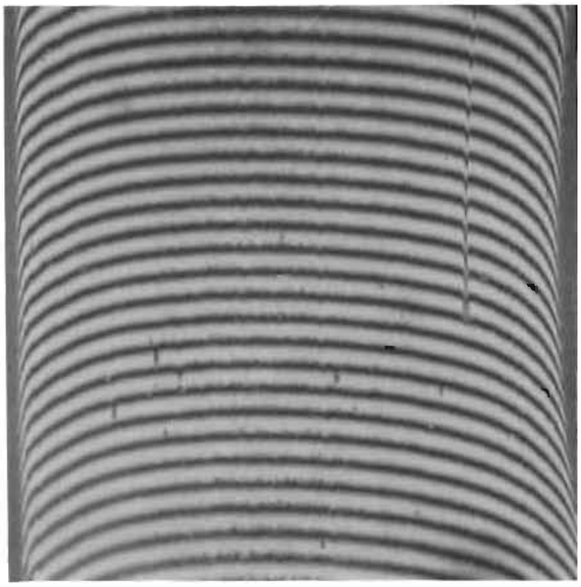

Figure 322. Test Model Z_f, Seat, 0.033- x 0.033-Inch Interference Photo

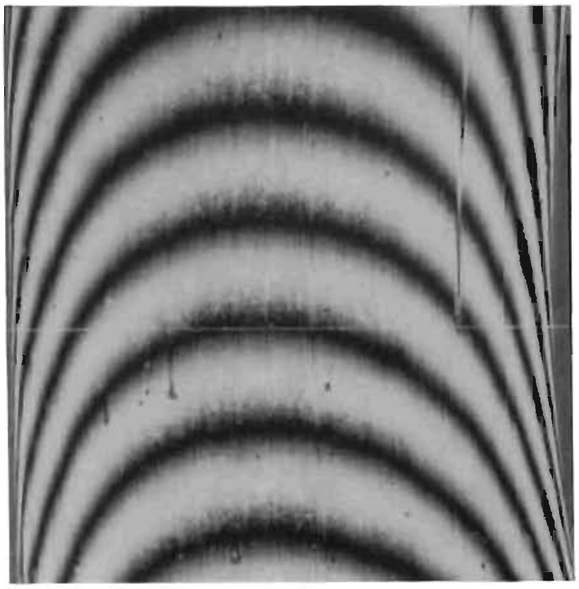

Figure 323. Test Model Z_f, Seat, 0.033- x 0.033-Inch Interference Photo, Same Location as Fig. 322

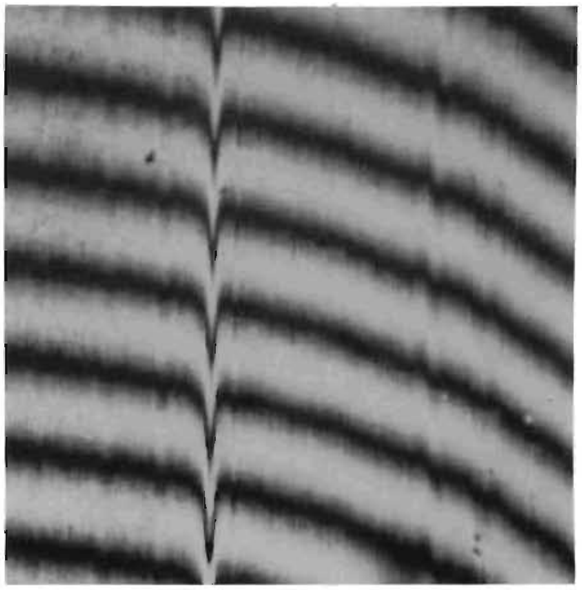

Figure 324. Test Model Z_f, Seat, 0.0065- x 0.0065-Inch Interference Photo, Same Location as Fig. 322 at ID

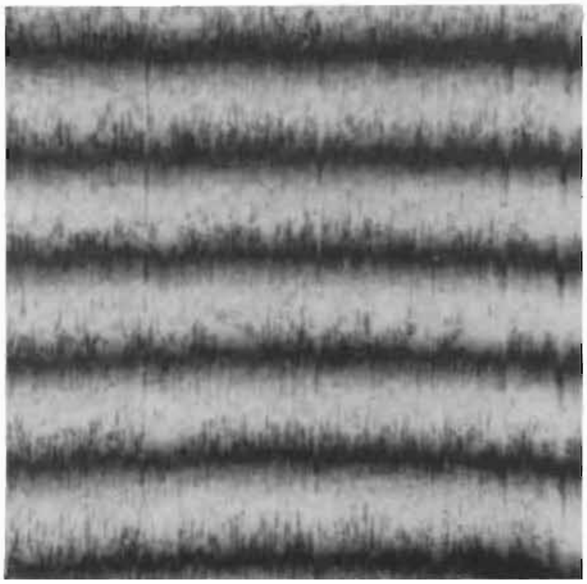

Figure 325. Test Model Z_f, Seat, 0.0065- x 0.0065-Inch Interference Photo, Same Location as Fig. 322 at Midland

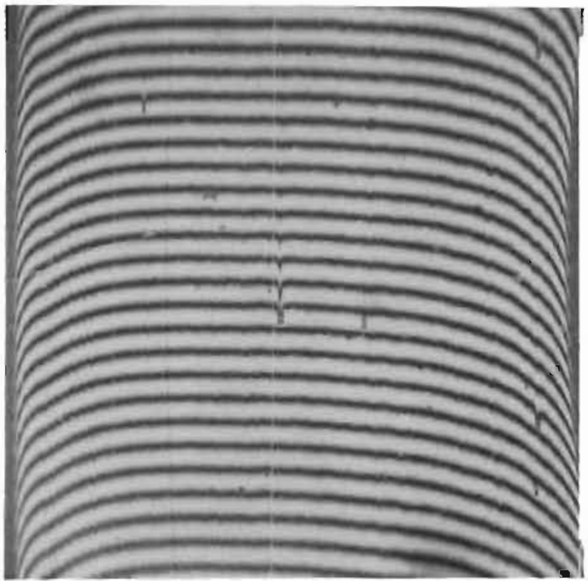

Figure 326. Test Model Z_f, Poppet, 0.033- x 0.033-Inch Interference Photo

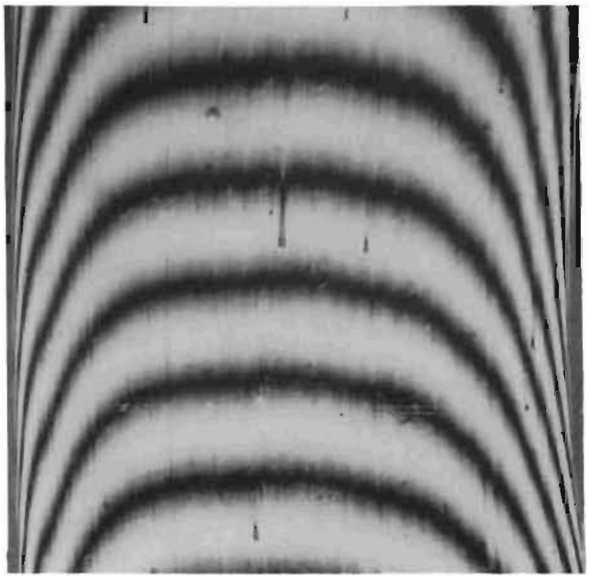

Figure 327. Test Model Z_f, Poppet, 0.033- x 0.033-Inch Interference Photo, Same Location as Fig. 326

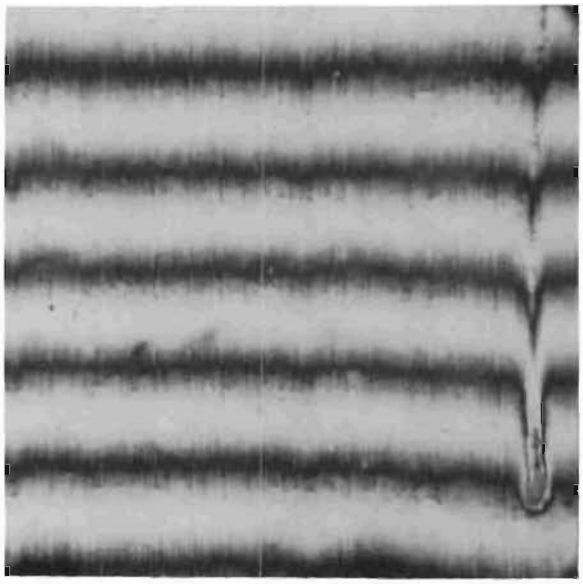

Figure 328. Test Model Z_f, Poppet, 0.0065- x 0.0065-Inch Interference Photo at Midland

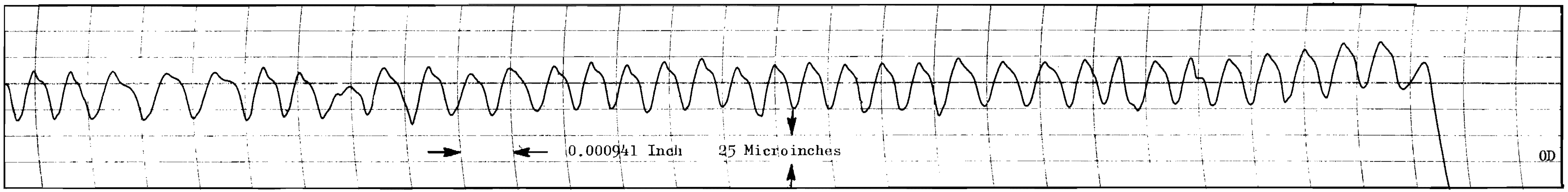

Figure 329. Test Model Q_f, Seat Cross Lay Roughness Profile Record, 0.0001-Inch Radius Stylus

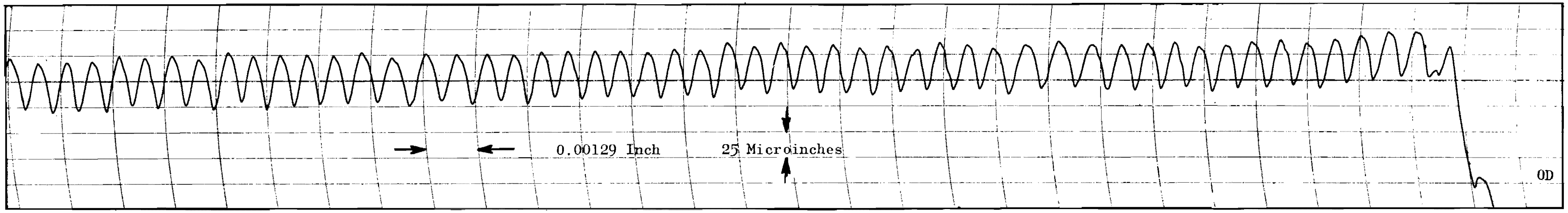

Figure 330. Test Model Q_f, Poppet Cross Lay Roughness Profile Record, 0.0001-Inch Radius Stylus

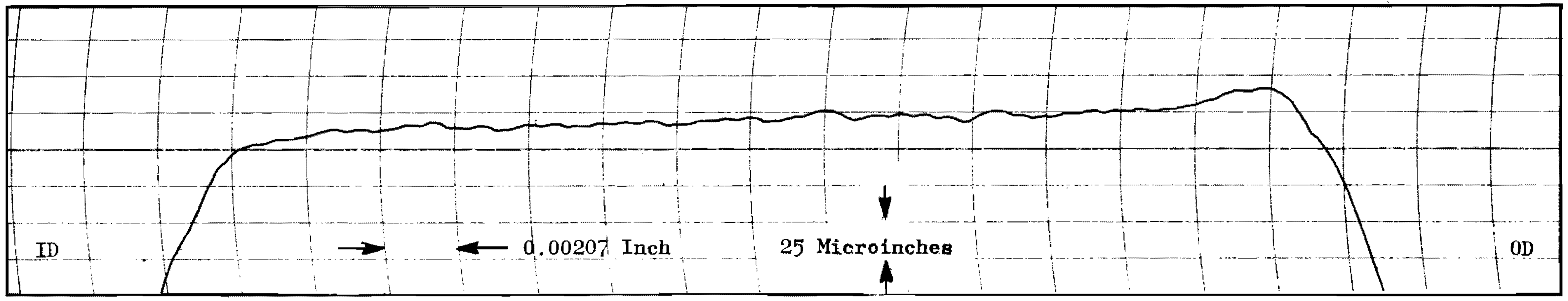

Figure 331. Test Model Q_f, Seat Cross Land Profile Record, 1/16-Inch Ball Stylus

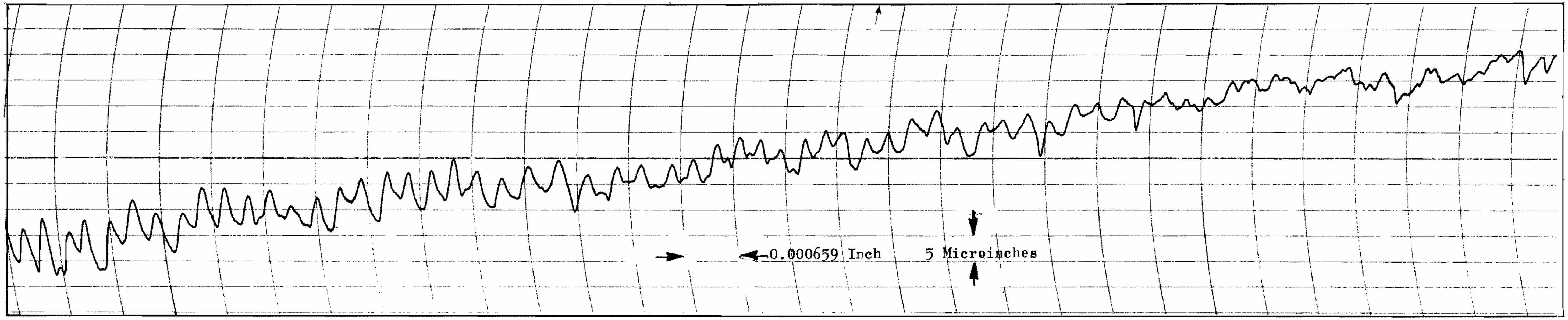

Figure 332. Test Model N_f, Seat Cross Lay Roughness Profile Record, 0.0001-Inch Radius Stylus

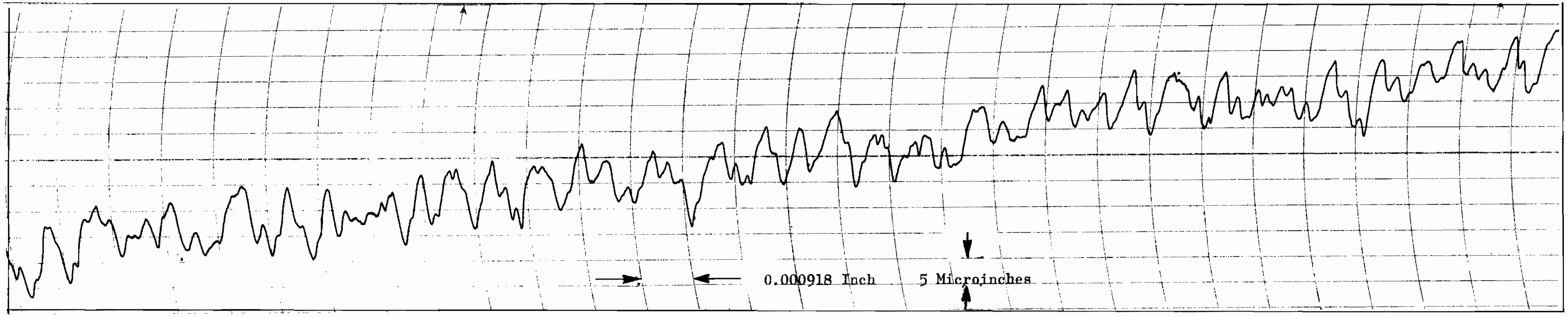

Figure 333. Test Model N_f, Poppet Cross Lay Roughness Profile Record, 0.0001-Inch Radius Stylus

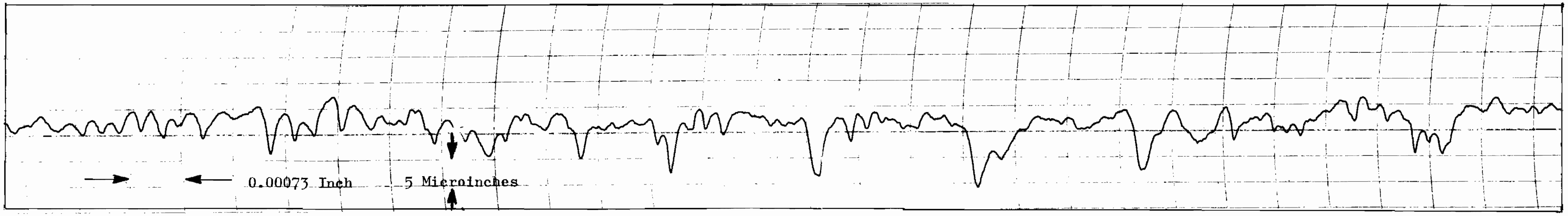

Figure 334. Test Model D_f, Poppet Roughness Profile Record, 0.0001-Inch Radius Stylus

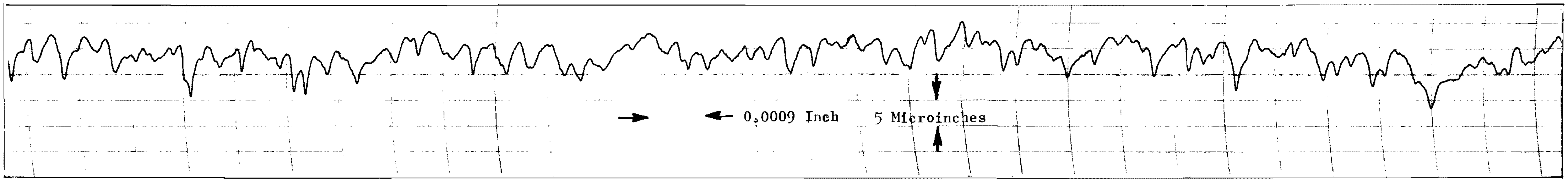

Figure 335. Test Model D_f, Seat Roughness Profile Record, 0.0001-Inch Radius Stylus

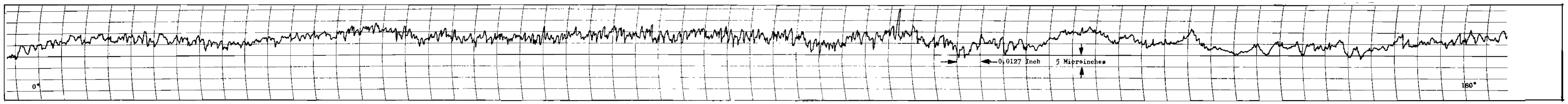

Figure 336. Test Model D_f, Poppet Circumferential Waviness Profile Record, Midland, 1/16-Inch Ball Stylus

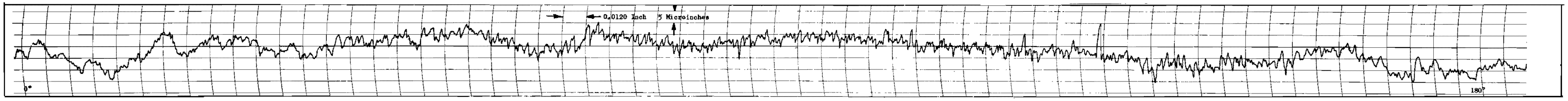

Figure 337. Test Model D_f, Seat Circumferential Waviness Profile Record, Midland, 1/16-Inch Ball Stylus

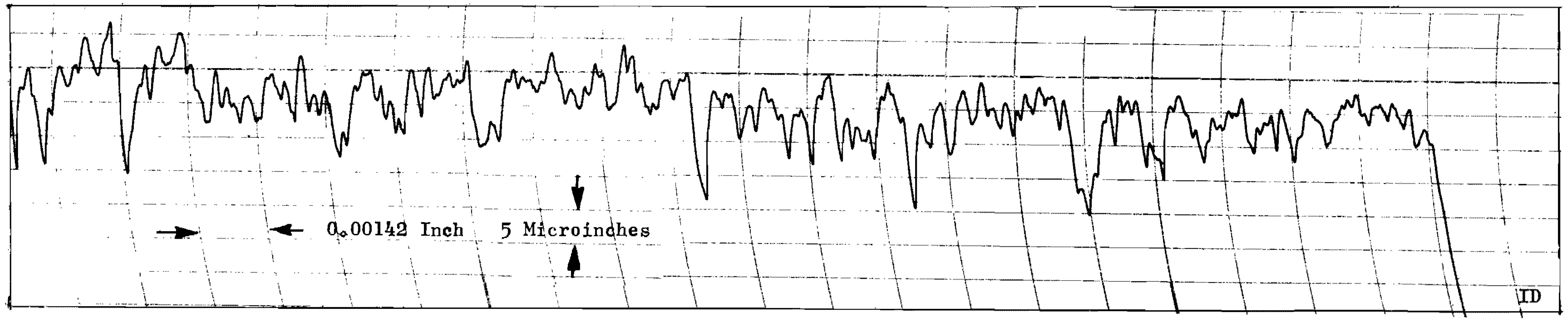

Figure 338. Test Model A_f, Seat Cross Lay Roughness Profile Record, 0.0001-Inch Radius Stylus

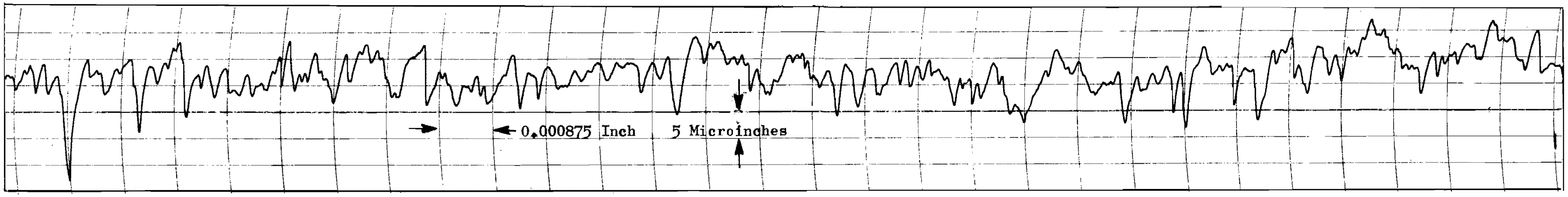

Figure 339. Test Model A_f, Poppet Cross Lay Roughness Profile Record, 0.0001-Inch Radius Stylus

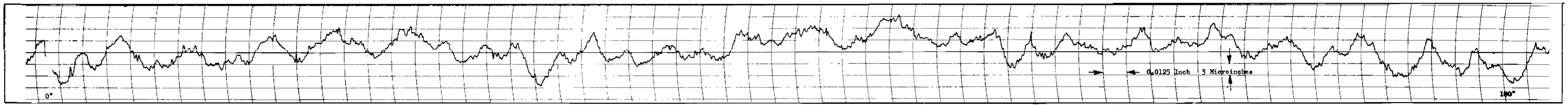

Figure 340. Test Model A_f, Poppet Circumferential Waviness Profile Record, Midland, 1/16-Inch Ball Stylus

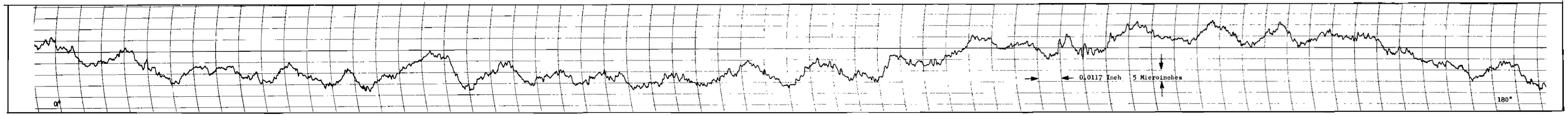

Figure 341. Test Model A_f, Seat Circumferential Waviness Profile Record, Midland, 1/16-Inch Ball Stylus

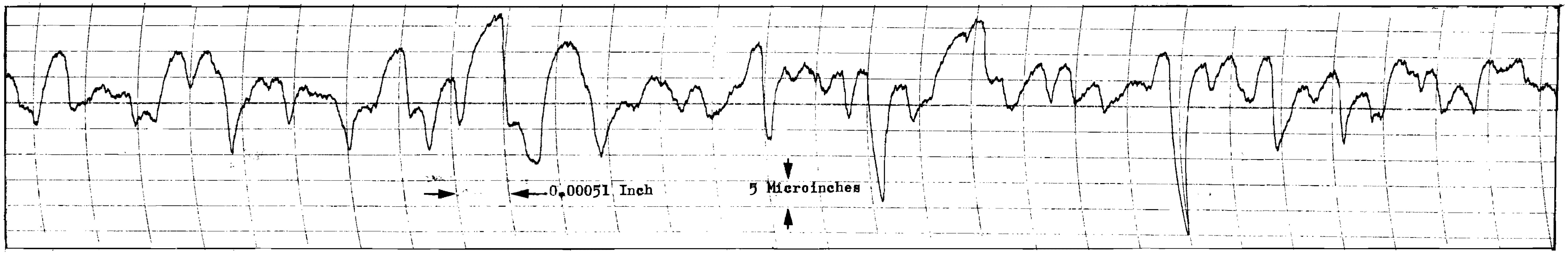

Figure 342. Test Model D, Poppet Roughness Profile Record, 0.0001-Inch Radius Stylus

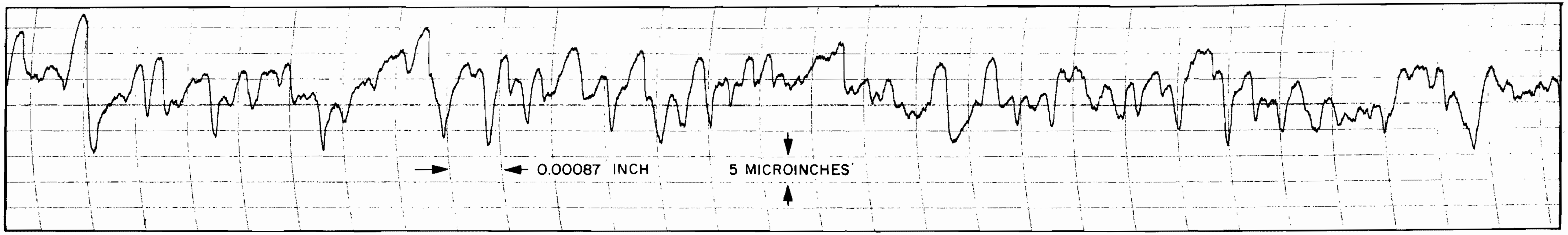

Figure 343. Test Model C, Poppet Roughness Profile Record, 0.0001-Inch Radius Stylus

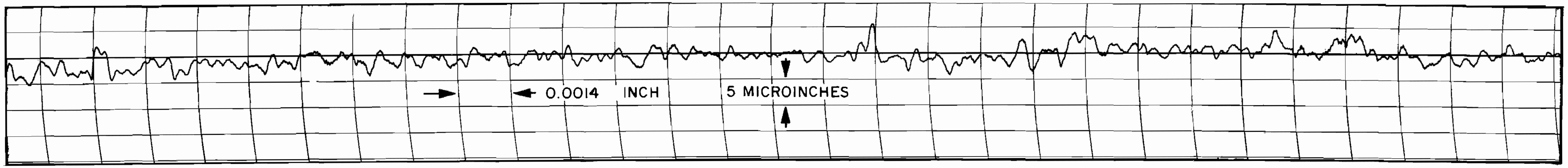

Figure 344. Test Model B, Poppet Roughness Profile Record, 0.0001-Inch Radius Stylus

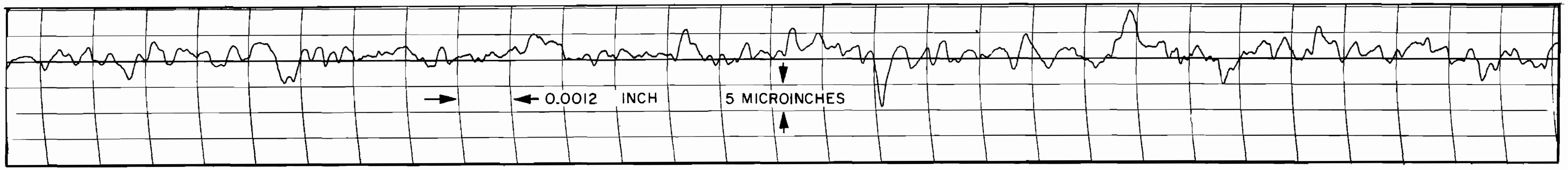

Figure 345. Test Model B, Seat Roughness Profile Record, 0.0001-Inch Radius Stylus

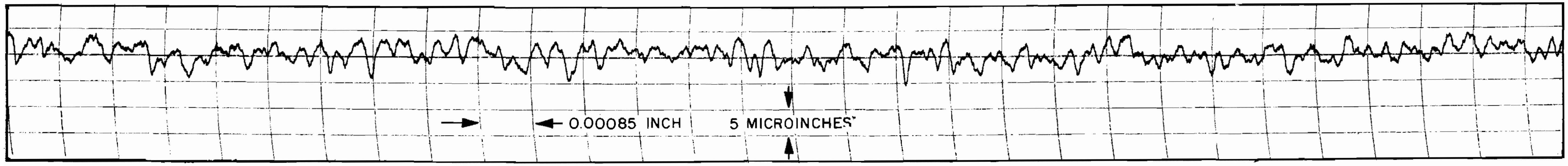

Figure 346. Test Model J, Poppet Roughness Profile Record, 0.0001-Inch Radius Stylus

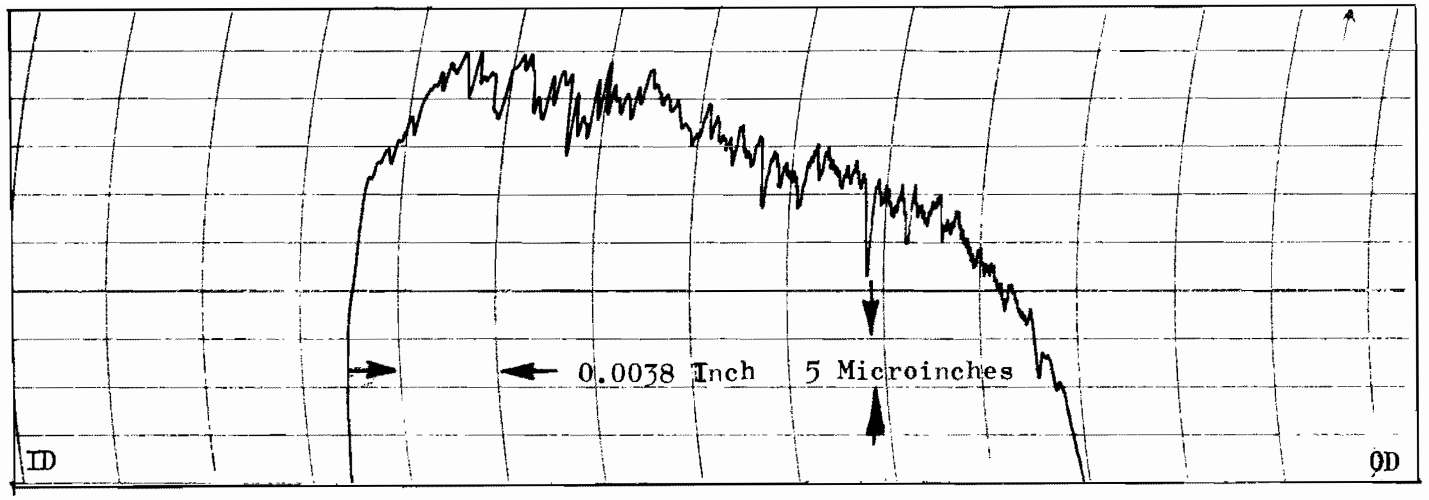

Figure 347. Test Model A_c, Seat Cross Land Roughness Profile Record, 0.0005-Inch Radius Stylus

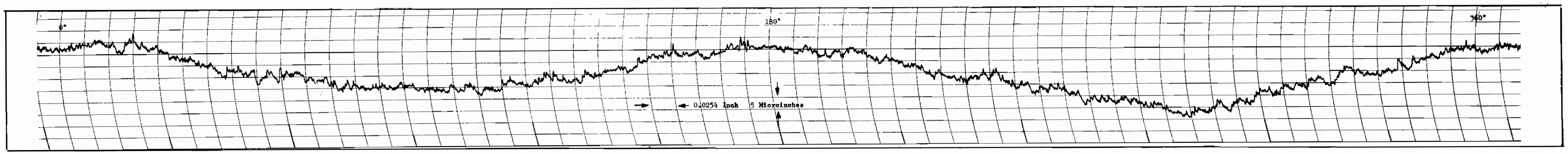

Figure 348. Test Model A_c, Seat Circumferential Roundness Profile Record, Midland, 1/16-Inch Ball Stylus

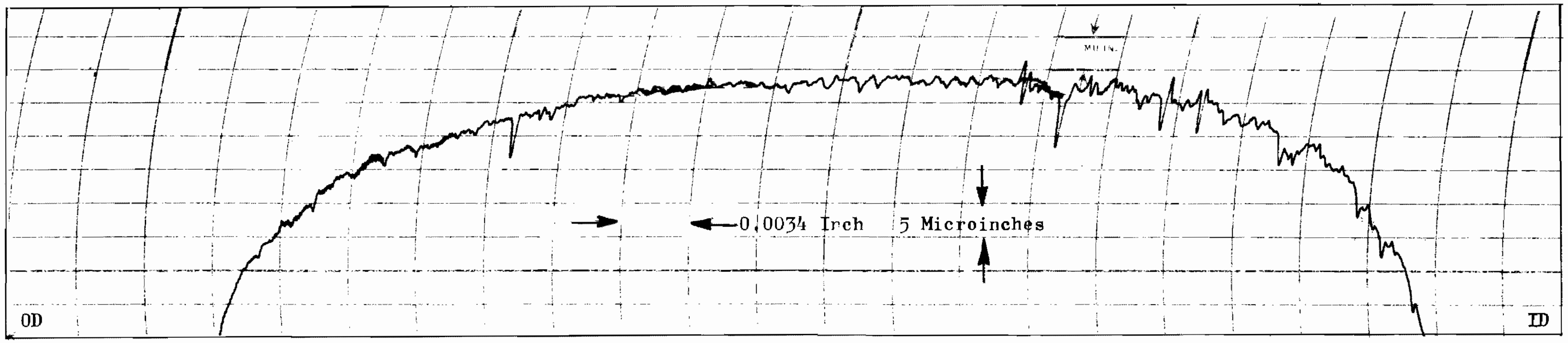

Figure 349. Test Model A_c, Poppet Cross Land Roughness Profile Record, 0.0005-Inch Radius Stylus

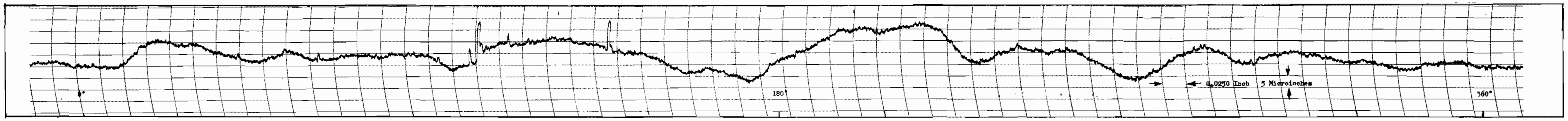

Figure 350. Test Model A_c, Poppet Circumferential Roundness Profile Record, Midland, 1/16-Inch Ball Stylus

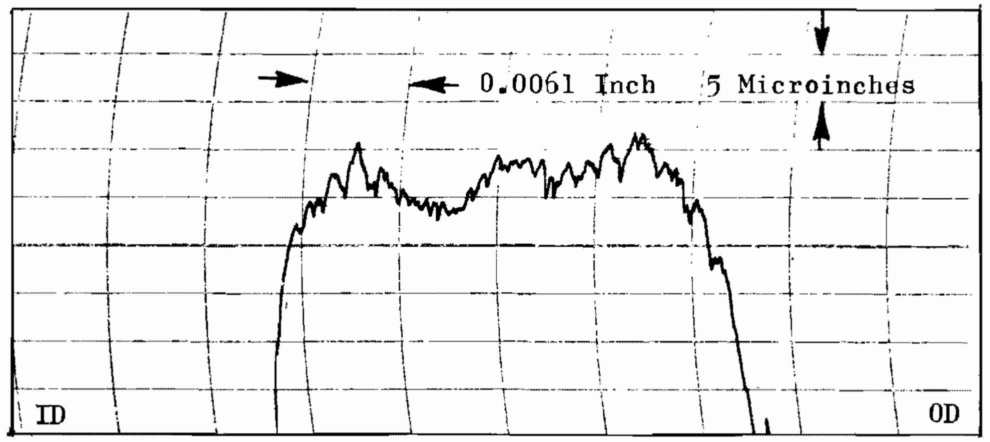

Figure 351. Test Model B_c, Seat Cross Land Roughness Profile Record, 0.0005-Inch Radius Stylus

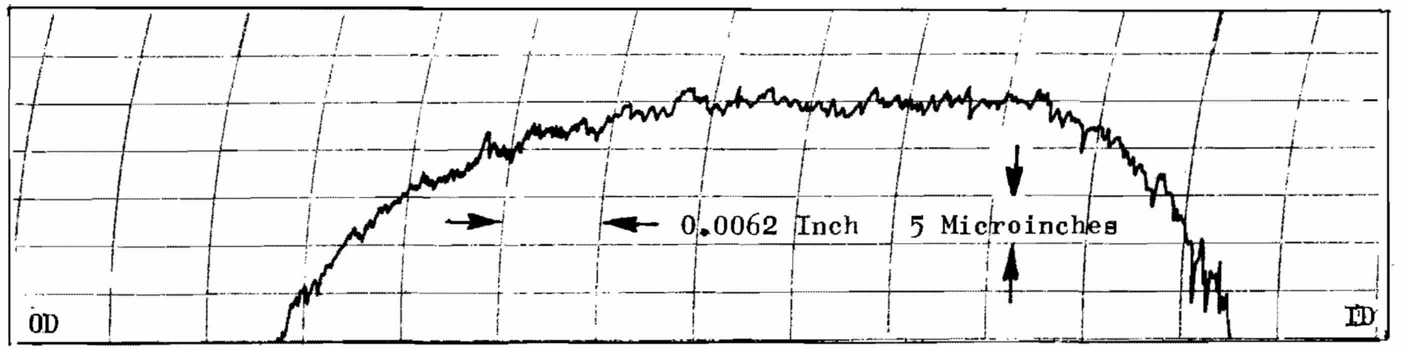

Figure 352. Test Model B_c, Poppet Cross Land Roughness Profile Record, 0.0005-Inch Radius Stylus

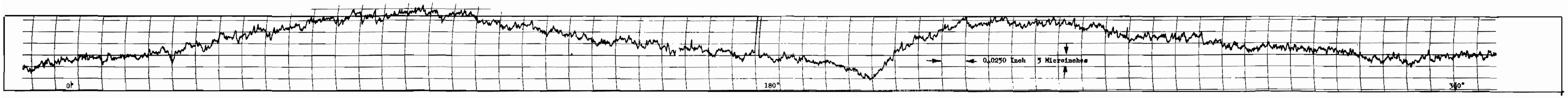

Figure 353. Test Model B_c, Seat Circumferential Roundness Profile Record, Midland, 1/16-Inch Ball Stylus

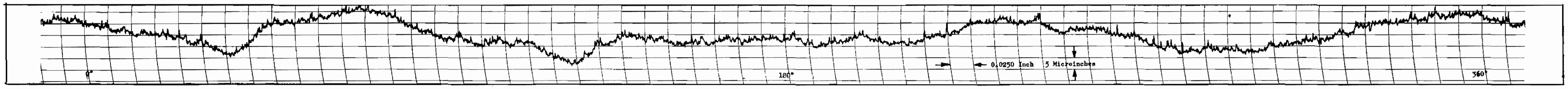

Figure 354. Test Model B_c, Poppet Circumferential Roundness Profile Record, Midland, 1/16-Inch Ball Stylus

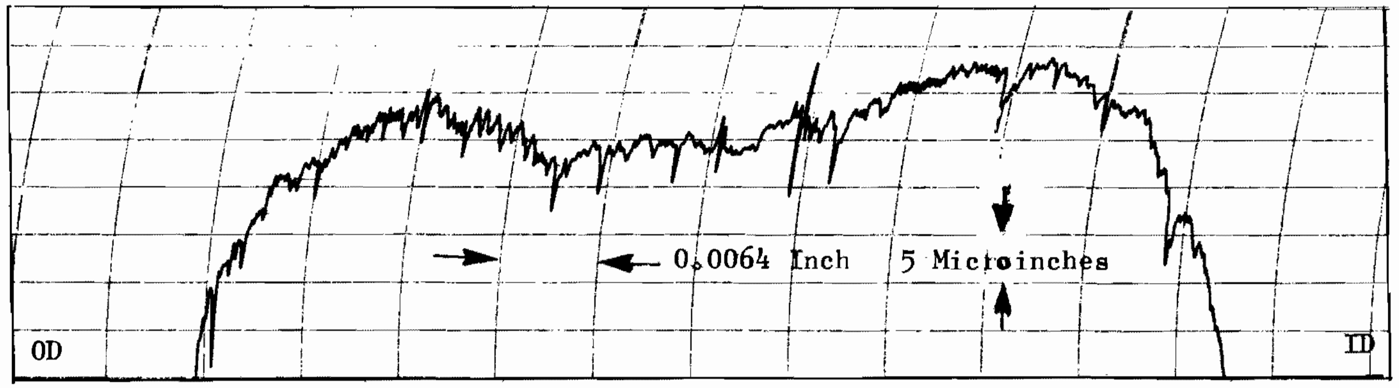

Figure 355. Test Model C_c, Poppet Cross Land Roughness Profile Trace, 0.0005-Inch Radius Stylus

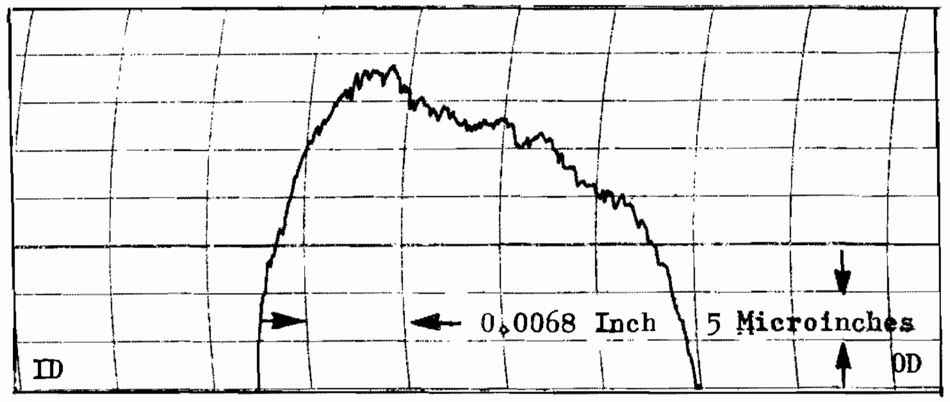

Figure 356. Test Model C_c, Seat Cross Land Roughness Profile Record, 0.0005-Inch Radius Stylus

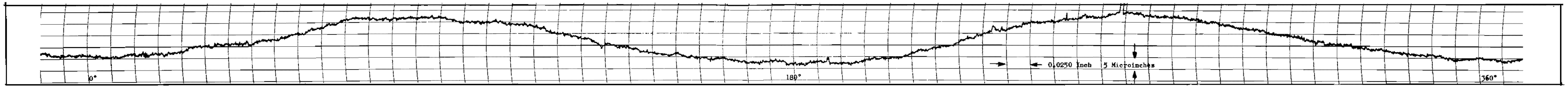

Figure 357. Test Model C_c, Seat Circumferential Roundness Profile Record, Midland, 1/16-Inch Ball Stylus

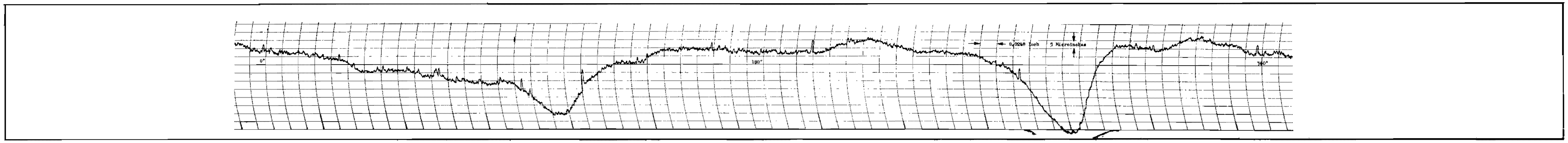

Figure 358. Test Model C_c, Poppet Circumferential Roundness Profile Record, Midland, 1/16-Inch Ball Stylus

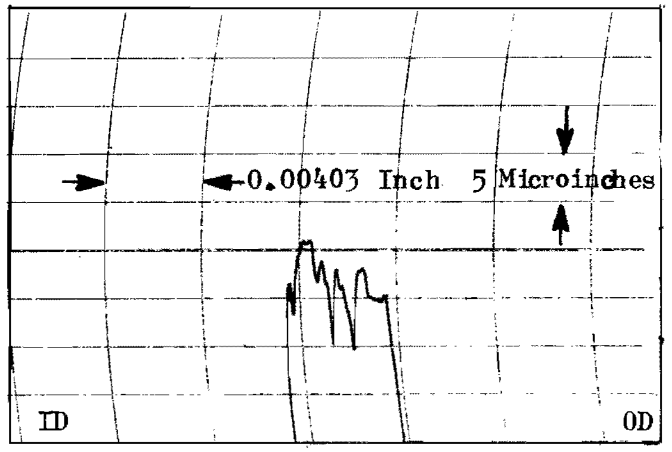

Figure 359. Test Model D_c, Seat Cross Land Profile Trace, 0.0005-Inch Radius Stylus

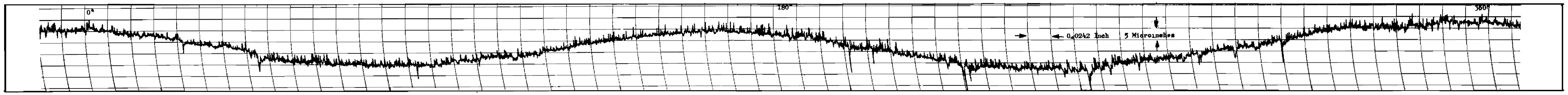

Figure 360. Test Model D_c, Seat Circumferential Roundness Profile Record, Midland, 0.0005-Inch Radius Stylus

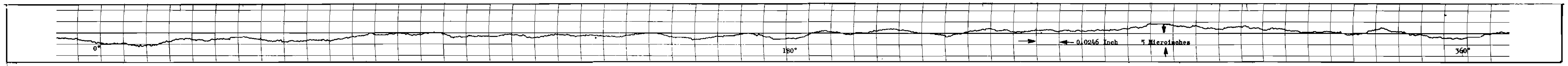

Figure 361. Test Model E_c, Poppet Circumferential Roundness Profile Record, Midland, 1/16-Inch Ball Stylus

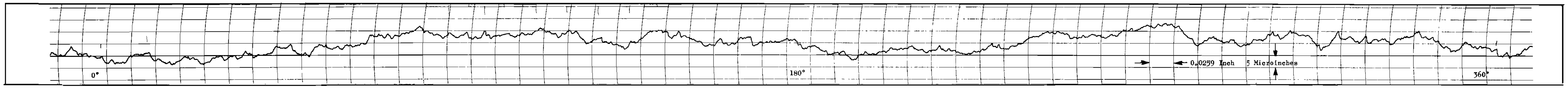

Figure 362. Test Model E_c, Seat Circumferential Roundness Profile Record, Midland, 1/16-Inch Ball Stylus

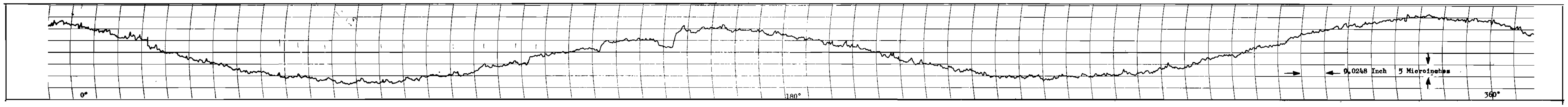

Figure 363. Test Model F_c, Seat Circumferential Roundness Profile Record, Midland, 1/16-Inch Ball Stylus

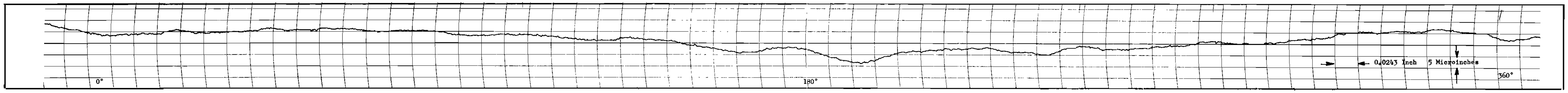

Figure 364. Test Model F_c, Poppet Circumferential Roundness Profile Record, Midland, 1/16-Inch Ball Stylus

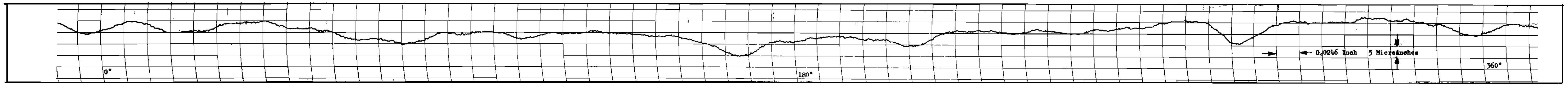

Figure 365. Test Model G_c, Poppet Circumferential Roundness Profile Record, Midland, 1/16-Inch Ball Stylus

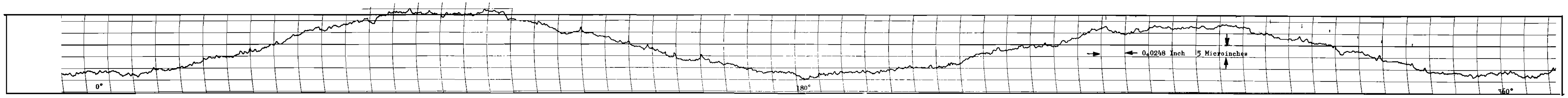

Figure 366. Test Model G_c, Seat Circumferential Roundness Profile Record, Midland, 1/16-Inch Ball Stylus

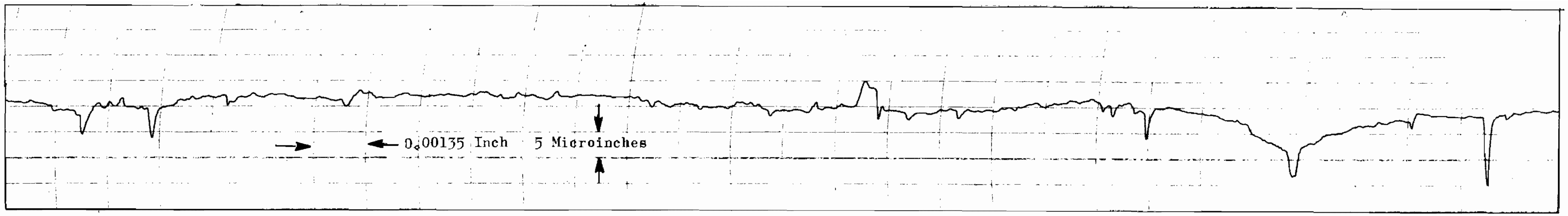

Figure 367. Test Model A_s, Poppet Roughness Profile Record, 0.0001-Inch Radius Stylus

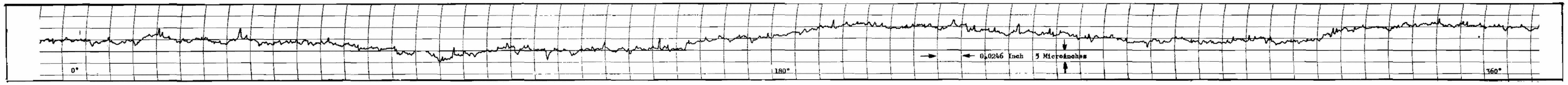

Figure 368. Test Model A_s, Poppet Circumferential Roundness Profile Record, 0.470-Inch Diameter, 1/16-Inch Ball Stylus

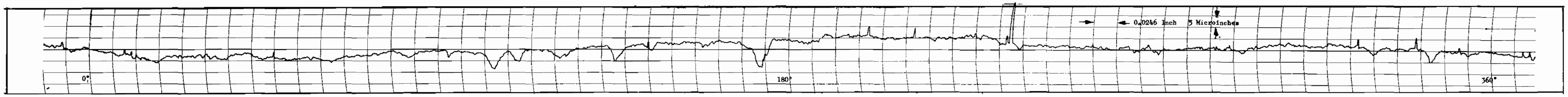

Figure 369. Test Model B_s, Poppet Circumferential Roundness Profile Record, 0.470-Inch Diameter, 1/16-Inch Ball Stylus

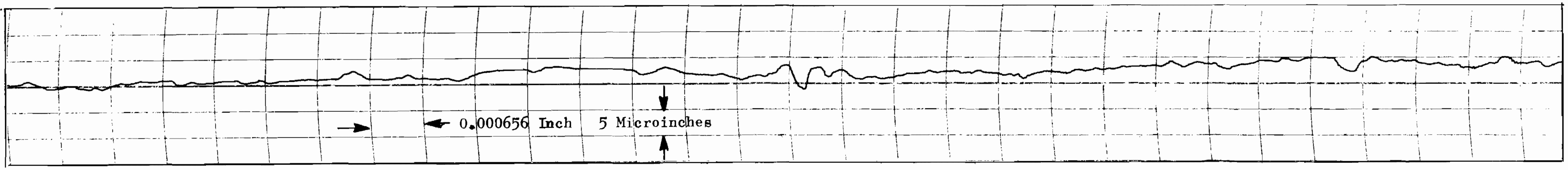

Figure 370. Test Model C_s, Poppet Cross Lay Roughness Profile Record, 0.0001-Inch Radius Stylus

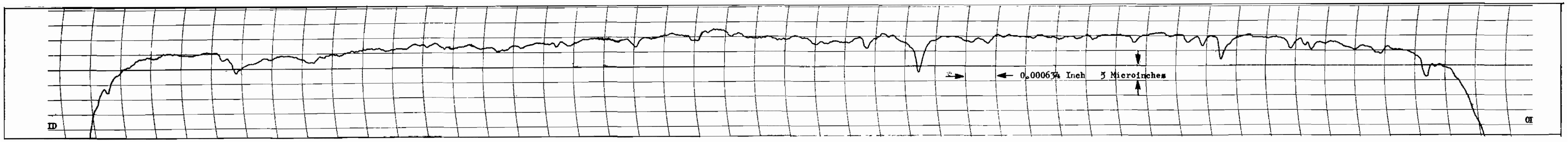

Figure 371. Test Model U_f, Seat Cross Land Roughness Profile Record, 0.0001-Inch Radius Stylus

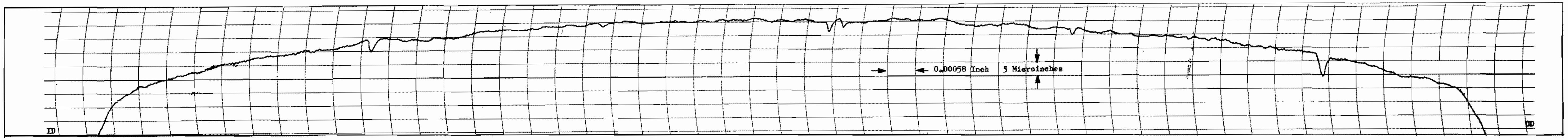

Figure 372. Test Model V_f, Seat Cross Land Roughness Profile Record, 0.0001-Inch Radius Stylus

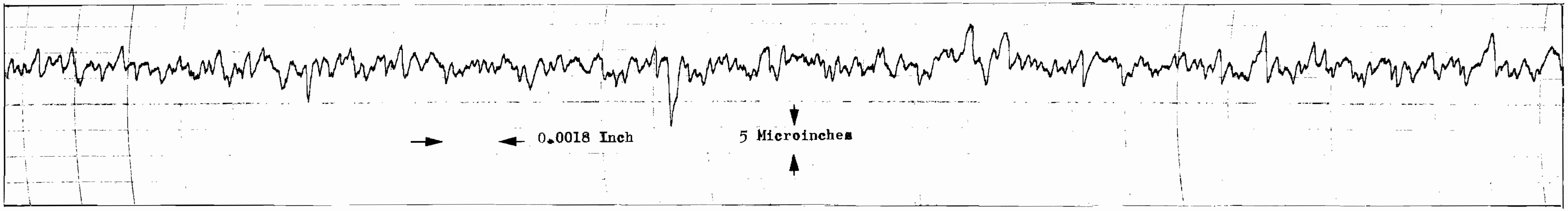

Figure 373. Test Model H, Seat Roughness Profile Record, 0.0001-Inch Radius Stylus

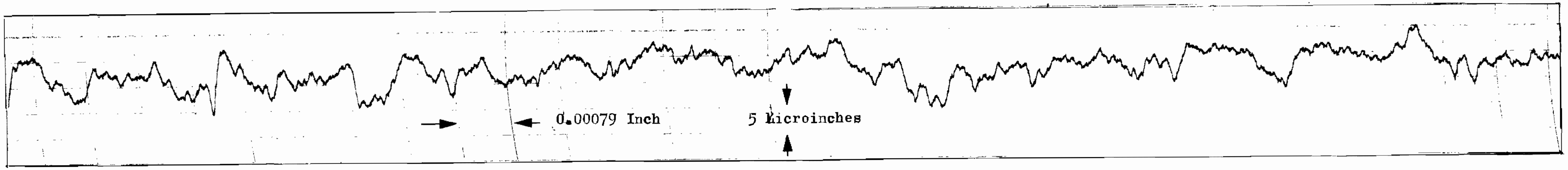

Figure 374. Test Model I, Poppet Roughness Profile Record, 0.0001-Inch Radius Stylus

EXPERIMENTAL TEST PROGRAM

The experimental program was designed to support leakage and seating analyses and to provide emperical model seating data where an analytical approach was not possible or feasible.

The experimental approach undertaken was to study initially near-seated valving parameters to verify leakage and pressure distribution analyses. The near-seated region was defined as that poppet-seat separation which encompassed a complete transition through the various flow regimes (see Leakage Flow Analysis). Following the near-seated tests, the characteristics and capabilities of the testers were determined and their influence on model seating defined or anticipated.

Within the program scope, detailed correlative study of each model tested was limited. This was due to the complexity of many models and also because the fabrication techniques employed resulted in a combination of variables which could not be separated or, in some cases, even identified. However, the inclusion of pertinent inspection records and data may be used by the designer to reach design decisions based upon personal study and supplemental information.

EXPERIMENTAL TEST SETUP

The poppet and seat testers were setup in an air-conditioned room containing all of the pressure-, flow-, dynamic- and linear- measurement devices necessary to the test effort and microscopes for visual surface inspection. Other surface inspection equipment was located nearby so that measurements could be conveniently made when necessary. Access to suitable surface inspection equipment was mandatory since a basic program objective was to identify and relate the various surface parameters controlling leakage for the specific model tested. Figures 375 and 376 show the testers and associated instrumentation. Schematic diagrams of the static and cycle test arrangements are shown in Fig. 377, 378, and 379.

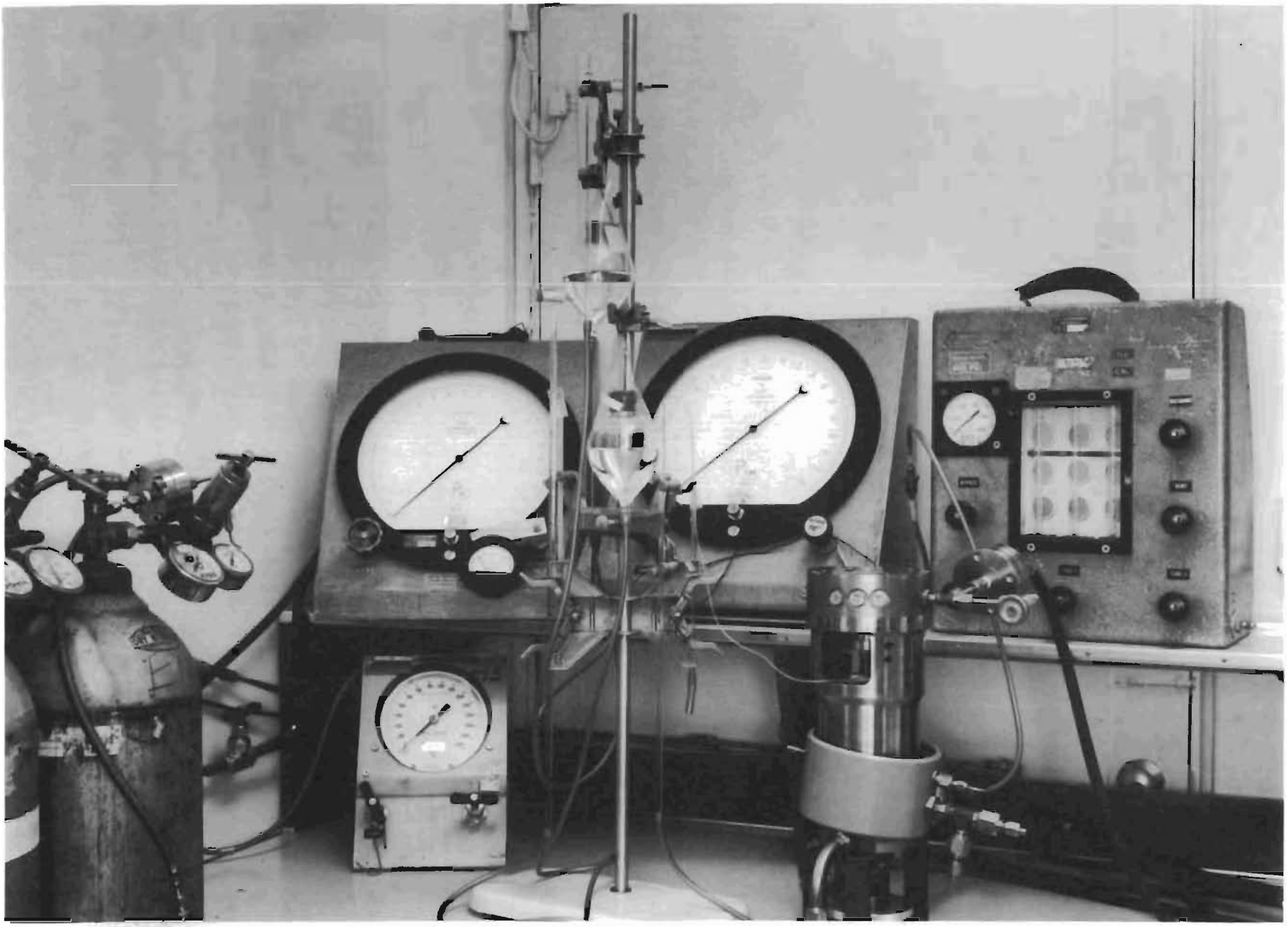

6AD41-2/16/66-C1G

Figure 375. Static Test Setup

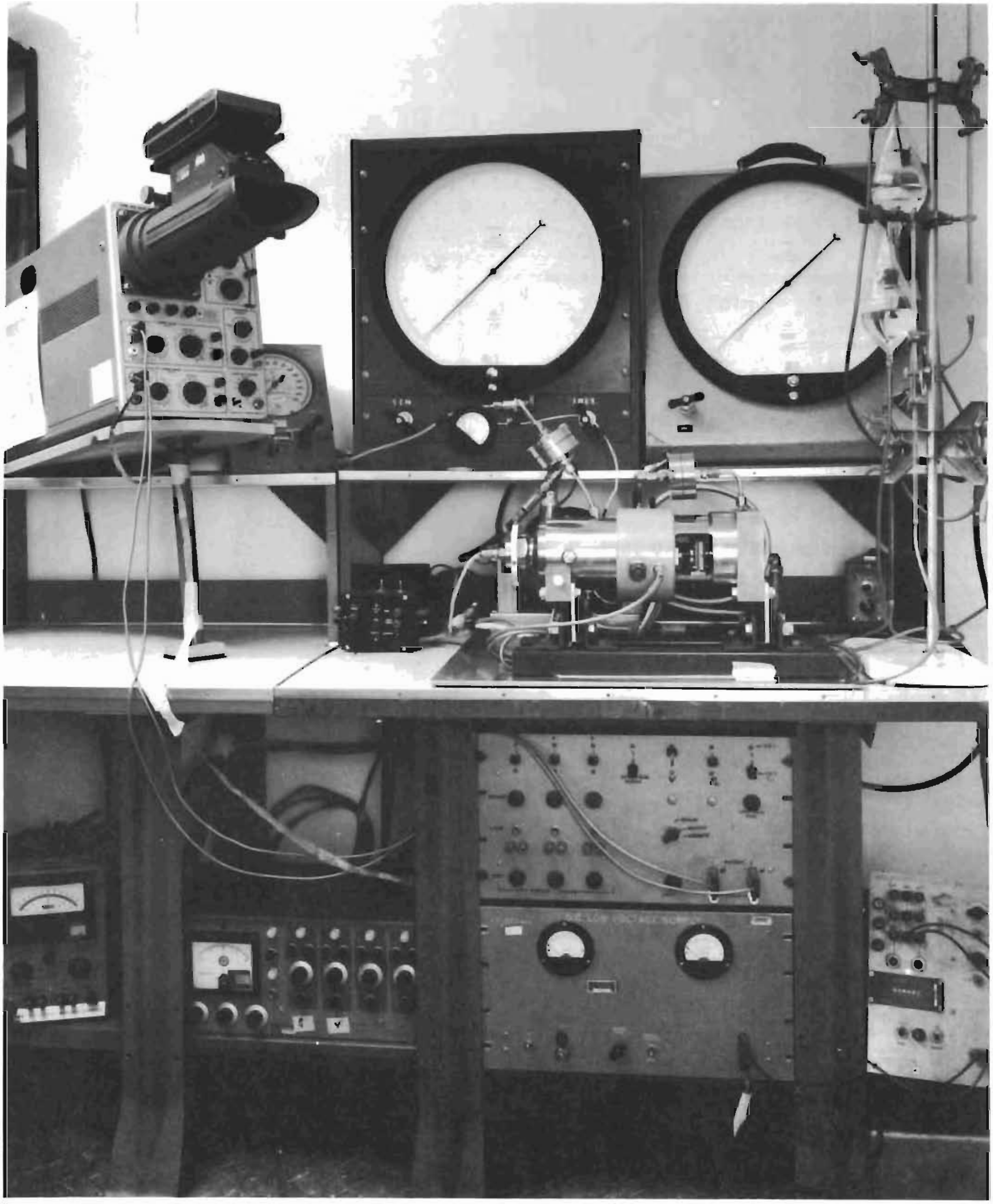

6AD41-3/16/66-C1H

Figure 376. Cycle Test Setup

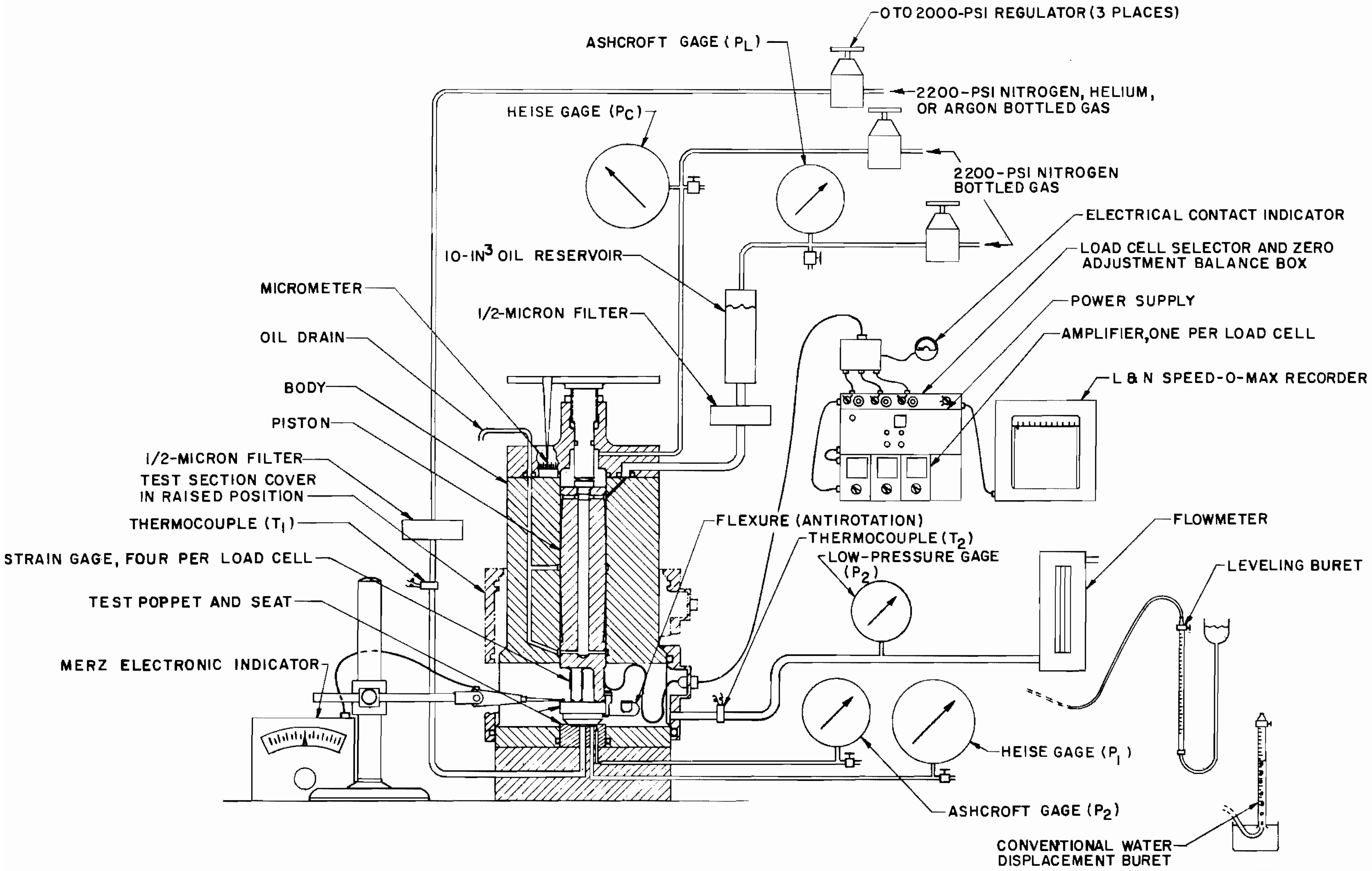
0 TO 2000-PSI REGULATOR (3 PLACES)
ASHCROFT GAGE (P_L)
2200-PSI NITROGEN, HELIUM, OR ARGON BOTTLED GAS
HEISE GAGE (P_C)
2200-PSI NITROGEN BOTTLED GAS
ELECTRICAL CONTACT INDICATOR
LOAD CELL SELECTOR AND ZERO ADJUSTMENT BALANCE BOX
10-IN^3 OIL RESERVOIR
MICROMETER
1/2-MICRON FILTER
POWER SUPPLY
AMPLIFIER, ONE PER LOAD CELL
OIL DRAIN
L & N SPEED-O-MAX RECORDER
BODY
PISTON
1/2-MICRON FILTER
TEST SECTION COVER IN RAISED POSITION
THERMOCOUPLE (T_1)
FLEXURE (ANTIROTATION)
FLOWMETER
THERMOCOUPLE (T_2)
LOW-PRESSURE GAGE (P_2)
STRAIN GAGE, FOUR PER LOAD CELL
LEVELING BURET
TEST POPPET AND SEAT
MERZ ELECTRONIC INDICATOR
HEISE GAGE (P_1)
ASHCROFT GAGE (P_2)
CONVENTIONAL WATER DISPLACEMENT BURET

Figure 377. Static Test Setup Schematic (Initial Contract Effort)

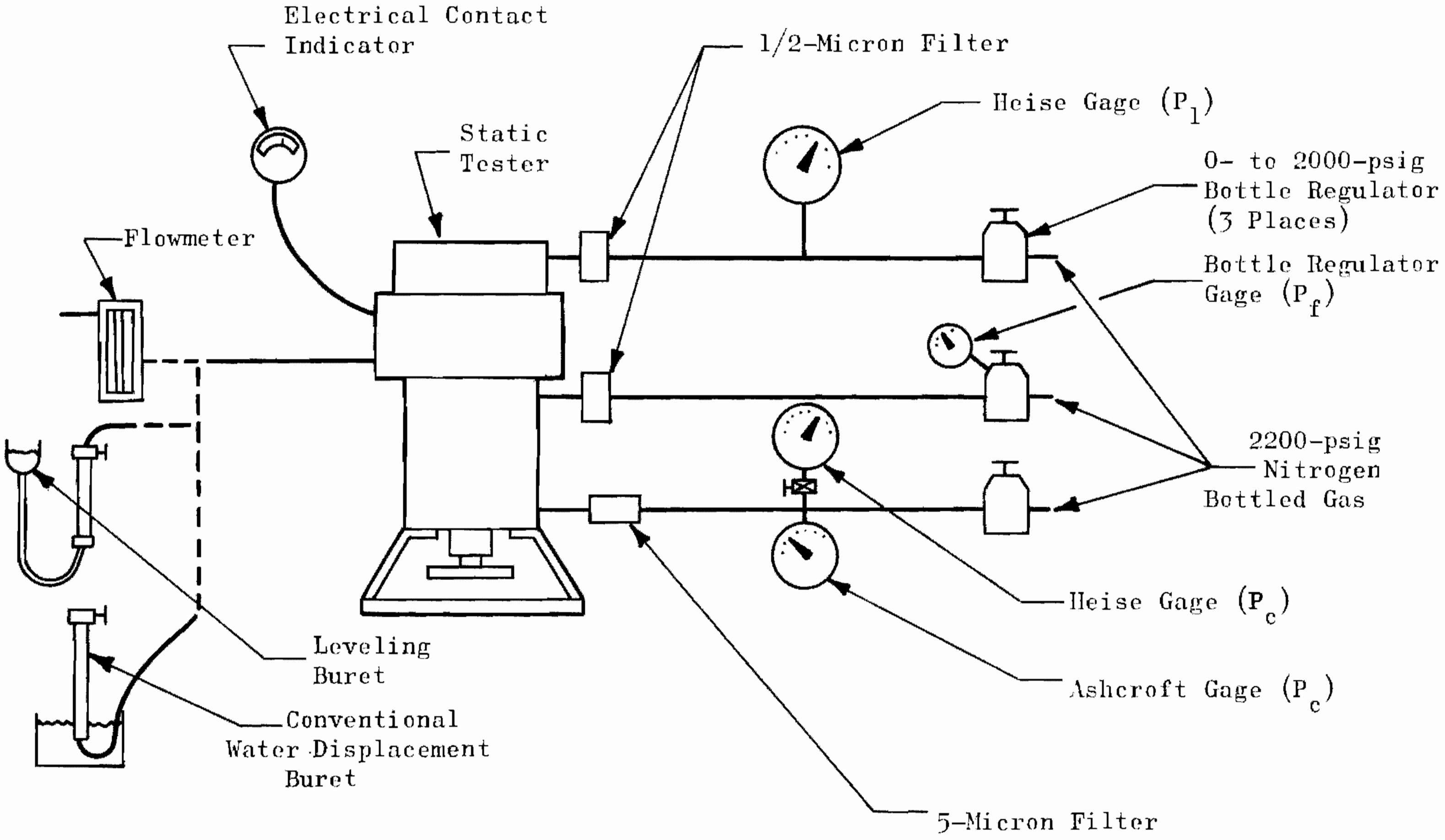
Electrical Contact Indicator
1/2-Micron Filter
Heise Gage (P_1)
Static Tester
0- to 2000-psig Bottle Regulator (3 Places)
Flowmeter
Bottle Regulator Gage (P_f)
2200-psig Nitrogen Bottled Gas
Heise Gage (P_c)
Leveling Buret
Ashcroft Gage (P_c)
Conventional Water Displacement Buret
5-Micron Filter

Figure 378. Static Test Setup Schematic (Follow-on Contract)

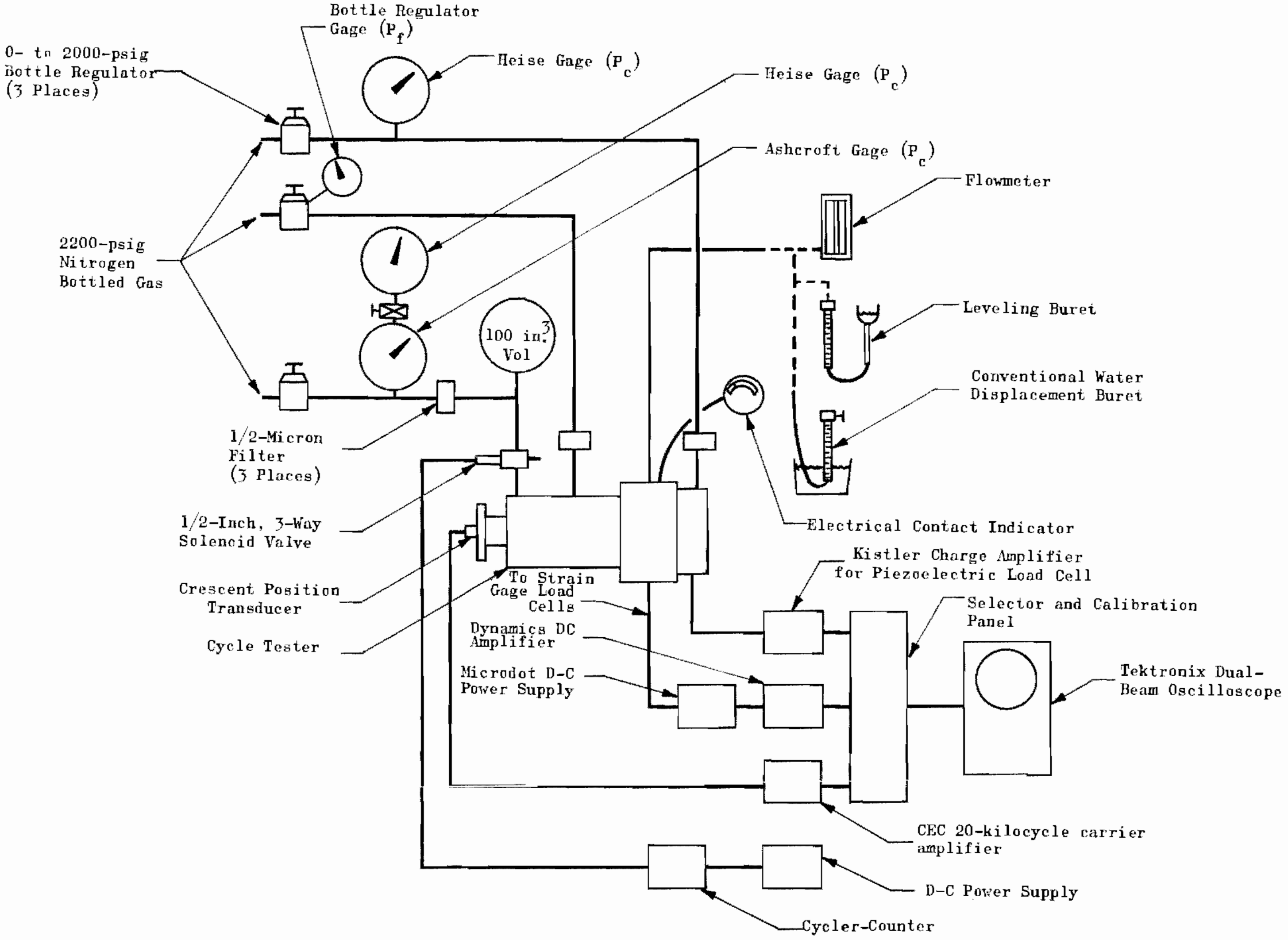
Bottle Regulator Gage (P_f)
Heise Gage (P_c)
0- to 2000-psig Bottle Regulator (3 Places)
Heise Gage (P_c)
Ashcroft Gage (P_c)
Flowmeter
2200-psig Nitrogen Bottled Gas
Leveling Buret
100 in.^{3} Vol
Conventional Water Displacement Buret
1/2-Micron Filter (3 Places)
1/2-Inch, 3-Way Solenoid Valve
Electrical Contact Indicator
Kistler Charge Amplifier for Piezoelectric Load Cell
To Strain Gage Load Cells
Crescent Position Transducer
Selector and Calibration Panel
Cycle Tester
Dynamics DC Amplifier
Microdot D-C Power Supply
Tektronix Dual-Beam Oscilloscope
CEC 20-kilocycle carrier amplifier
D-C Power Supply
Cycler-Counter

Figure 379. Cycle Test Setup Schematic

Test parameters, systems, and instruments bearing upon the accuracy and precision of the data are discussed below.

Gas Pressure Supply

Except for the variety of gases required for the near-seated tests, gaseous nitrogen (MIL-N-6011) at room temperature (70 ±5 F) was used for control and leak testing purposes. For all tests gas temperature was corrected as necessary to 70 F. Standard bottle regulators were utilized to hand control the 2200 psig gas from 0 to 1500 psig; pressures could be maintained within 0.2 psi for most applications. During cycle tests, however, the solenoid valve feed system demand was such that overpressurization was required. In this manner, pressure drop occurring during actuation of the control solenoid valve was recovered prior to initiation of the next cycle.

Inlet and piston centering film pressure gas was pressed through 0.5-micron (absolute) porous membrane filters close-coupled to the testers. Piston-loading control pressure was fed to the static tester through a 5-micron, wire-mesh filter. Because of pressure drop considerations, cycle tester control pressure was filtered upstream of the reservoir bottle; a 0.5-micron member filter was employed. The unavoidable wear and lubricant contaminants from the solenoid valve necessitated periodic cleaning of the cycle tester control cavity.

Pressure Measurement

The testers were connected to a complex of pressure gages to provide measurement of inlet and load control pressures. Heise gages, 0- to 500-, 0- to 600-(control) and 0- to 1000-(inlet) psig ranges, having 1-psi subdivisions and accurate to ±0.1-percent of full scale were used. For control pressures greater than 500 psig, 0 to 1500 psig ±0.25-percent Ashcroft gages were utilized and similar accuracy gages were employed for seat land pressure distribution and other tests. To permit accurate differential measurements, all gages were parallel-connected and calibrated against one Heise gage. The noncritical film pressures were set with the bottle regulator gages.

Temperature Measurement

All tests were performed at room temperature which was monitored with ordinary thermometers. Initially, static tester inlet and outlet (leakage) gas temperatures were indicated with thermocouples and an Alnore pyrometer, a necessity for high-volume, off-seat flow temperature corrections. This system was eventually discarded and, for leak testing, ordinary thermometers were employed, one monitoring adjacent room temperature and one close-coupled to the leak source. Only in rare cases did a significant differential requiring correction occur during a test run.

Piston Centering (Film Pressure) System

To achieve, essentialy, a frictionless loading member and to prevent abnormal or eccentric poppet-seat loading due to tester piston misalignment, both testers employed the hydrostatic air bearing principle. As noted in the Test Fixture section, the static tester piston with a 0.00012-inch body diametral clearance "floated" with a 105-in.-lb moment about the piston center and 450-psig film pressure. The cycle tester having 0.000050-inch diametral clearance, withstood in excess of a 150-in.-lb moment at 300-psig film pressure without diametral contact. To provide a safe-operating margin, both testers were operated at 600-psig film pressure. This was more than adequate since no evidence of out-of-parallelism approaching the 125-microinch test of the initial program (which produced only a 35-in.-lb moment) was encountered during the test effort.

Linear Measurements

Depending on the test, several linear measurement and positional control methods were employed. Both testers utilized a 40 pitch screw thread adjustment feature for piston position control. Together with the scale and pointer arrangement (see Test Fixture section), and assuming a ±0.001-inch scale reading resolution (interpolation of 0.01-inch scale subdivisions under 5X magnification), axial position accuracy of approximately ±2 microinches was possible under ideal conditions.

For near-seated tests, the static tester was located on a granite surface plate flat within 25 microinches over a 18- by 24-inch area. This surface was used as a reference datum for necessary height measurements. Poppet-seat gap was indicated by the tester screw thread arrangement with a Merz electronic indicator providing backup and calibration service. As the piston and poppet were electrically insulated from the seat, zero position or contact indication could be accomplished by an electrical short-circuit signal readout on a microammeter. A 1-1/2-volt battery in series with a 1.2-megohm resistor provided a source of electrical energy which did not visibly (500X) pit or burn the surfaces.

The electrical contact signal, in conjunction with simultaneously noted leakage rate, was also used in both testers to indicate an out-of-parallel condition or the presence of interfacial contamination. If leakage at electrical contact was significantly more than surface inspection data would indicate, a contamination or geometrical defect was generally noted.

Cycle tester dynamic piston displacement data were obtained from position transducer traces and, with known time bases, piston velocities were computed. Several calibration procedures were necessary to verify accuracy of the velocity parameter. The cycle tester screw thread was used to establish total piston stroke and calibrate position transducer linearity. The latter was accomplished by stepping in 0.025 ±0.00005-inch increments for a 0.10-inch stroke and noting incremental variations over 8 centimeter of oscilloscope screen traversement. A nonlinearity of 7.5 percent was noted for the initial 0.025 inch; thereafter, the incremental deviation was 2.5 percent of each 0.025 inch. Displacement values were appropriately corrected using these data.

Oscilloscope horizontal sweep times were calibrated against commercial 60 cps and the precisely known internal square wave frequency of 1258 cps. The time-base settings so calibrated (5 to 0.1 ms/cm) were accurate within 1.1 percent.

Oscilloscope vertical linearity was within trace resolution capability of approximately ±0.02 centimeter. Camera parallax and oscilloscope screen curvature potential errors were eliminated by setting data points through the camera viewer and producing the position trace in the center of the screen. With the application of pertinent corrections and necessary precautions the calculated velocity values are considered accurate within 5 percent.

Load Measurement

Static Loads. For initial contract effort, the 3-kilocycle energized strain gage load cells were employed for static load distribution evaluation and piston-area load measurement correlation. The pressure-area method was used for all stress-leakage testing, both in static and cycle testers. Additionally, this relationship was used for static calibration of the d-c energized strain gage load cell resistors and the piezoelectric load cell utilized in the cycle tester.

The following basic expressions were used to compute apparent seat stress from the piston area-control pressure loading relationship. The static tester was in an inverted position (piston end down), a convenience condition utilized for the majority of on-seat tests. The cycle tester was in a horizontal position where moving parts weight does not enter the computation and, under film pressurized conditions, the piston-body friction load is negligible. For the static tester:

$$S = \frac{F_1 + F_2 + F_3 - P_1 A_e}{A_s} = \frac{P_c A_{ps} - W - P_1 A_e}{A_s}$$

For the cycle tester:

$$S = \frac{F_1 + F_2 + F_3 - F_f - F_b - P_1 A_e}{A_s}$$

$$= \frac{P_c (A_{pc} - A_r) - F_f - F_b - P_1 A_e}{A_s}$$

where

A_e = effective seating area (see Leakage Flow Analysis section), sq in.

A_{pc} = cycle tester piston area, 1.762 sq in.

A_{ps} = static tester piston area, 1.767 sq in.

A_r = dashpot-piston connection rod area, 0.0756 sq in. ($A_{pc} - A_r = 1.687$ sq in.)

A_s = flat seat land normal projected area, sq in.

$F_{1,2,3}$ = strain gage force, cells 1, 2, and 3

F_b = bias spring force, 13.0 pounds

F_f = dashpot O-ring friction, approximately 4 pounds

P_c = piston control pressure, psig

S = apparent seat stress, psi

W = piston assembly weight, variable with poppet material and retaining method, pounds

The computation of apparent seat stress was simplified by a balance pressure test where inlet pressure and other extraneous forces are nullified. The balance, or null point was determined by positioning the poppet slightly off-seat (about 50 microinches) against inlet pressure (and other forces) with the manually controlled screw thread adjustment and gradually increasing control (P_c) pressure. The control pressure required to just override the manual loading force (as evidenced by electrical contact and/or an abrupt change in simultaneously monitored leakage) was defined as the P_c balance pressure. With all system forces in balance the apparent seat stress is then:

$$S = \frac{\Delta P_c A_p}{A_s}$$

Where (ΔP_c) is the increase in piston control pressure above the balance pressure. The balance pressure was also proved by computation with the above equations assuming a zero-stress condition. The error involved in determination and use of the balance pressure parameter as a means of computing seat stress may be considered as:

$$e = \frac{\Delta \Delta P_c A_p + P_1 A_e + \Delta F}{S A_s} \times 100$$

where

e = seat stress error, percent

$\Delta\Delta P_c$ = includes P_c balance definition or interpretation error estimated at ±0.2 psig and P_c gage reading error, ±0.1 psig

ΔP_1 = inlet pressure gage reading error and variation from set point during test, ±1 psig

ΔF = potential change in dashpot O-ring friction or static tester leak collector O-ring force subsequent to P_c balance test, estimated at ±0.1 pound maximum

A_s = seat area, nominally 0.0443 sq in.

Assuming a maximum error condition, seat stress computations are accurate within ±18.3 percent at 100 psi, ±9.2 percent at 200 psi and, with continually reducing error, ±1.8 percent at 1000-psi apparent stress. Figure 380 presents a typical model stress-leakage characteristic and illustrates the maximum calculated stress error band. As the stress-leakage information generally represents repetitive data, the probable experimental deviation is on the order of 70 percent of the noted errors.

Dynamic Loads. Both strain gage with d-c energization and piezoelectric load cell systems were used to measure dynamic (cycle) impact loads. While dynamic calibration was not possible, static calibration was performed prior to each test. The strain gage calibration resistors were used to set up this system and were periodically verified by the pressurized-piston load standard method. The piezoelectric load cell, having no intermediate calibration resistors, was directly calibrated with appropriate pressurized-piston loads. Static calibration accuracy of both systems was well within 5 percent.

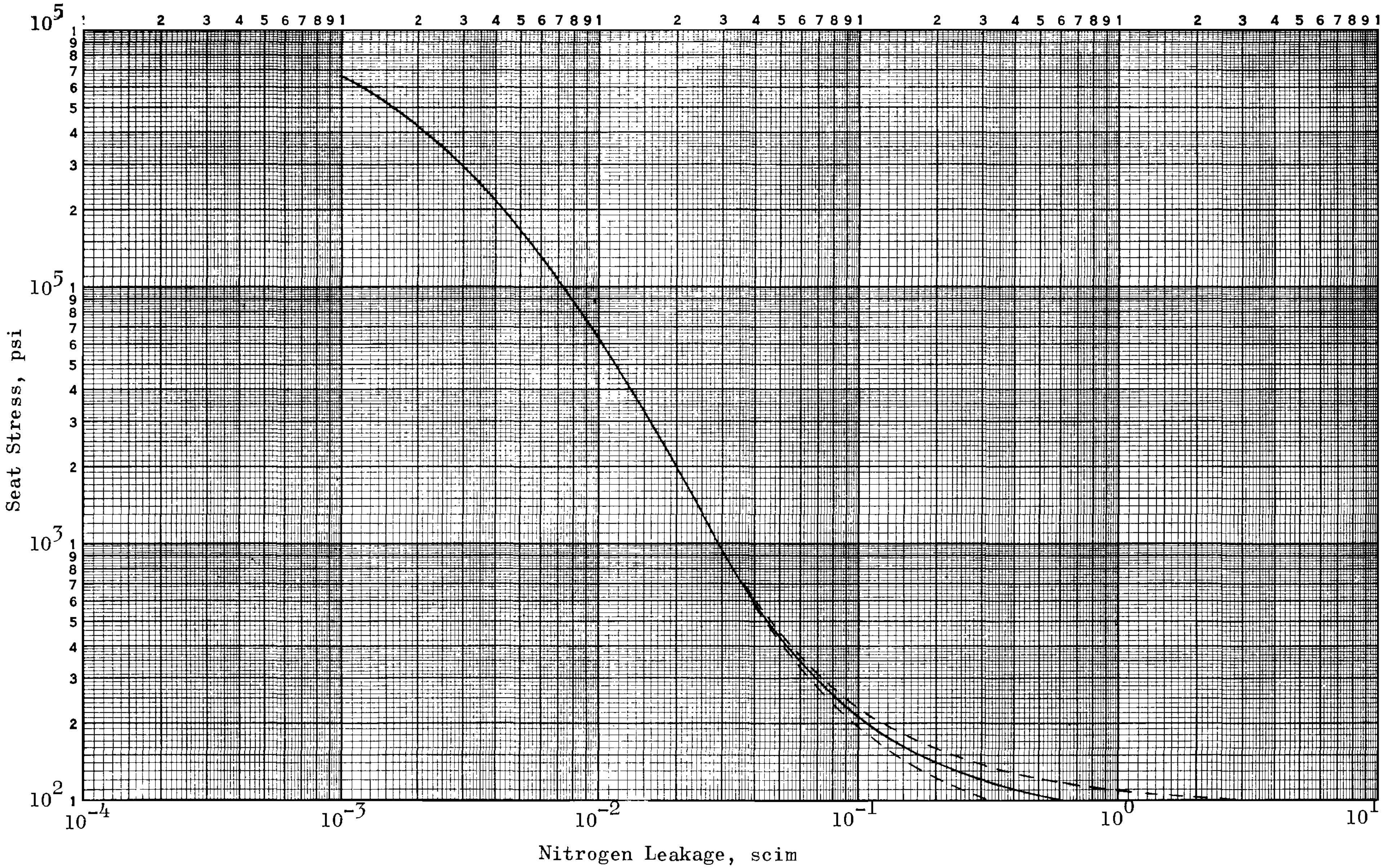

Figure 380. Error Band, Typical Stress-Leakage Curve

During the latter stages of the cycle test effort, the strain gage system signal-to-noise ratio progressively got worse making assessment of load traces difficult. Ultimately, one cell failed and the piezoelectric system was used for all further dynamic load measurements.

Leakage Measurement

Two basic leakage measuring methods were used in the experimental test program. For flowrates below 0.1 scim, positive-displacement burets were used whereas flows greater than 0.1 scim allowed the more versatile rate meters to be employed. All measurements were taken at essentially ambient conditions.

Brooks pyrex ball-float rotameters (tube numbers R-2-15-AAA; 3-15-4; 6-15-2) measured leakage from 0.05 to 110 scim. These devices were calibrated with burets and positive-displacement meters using nitrogen gas. For gas comparison tests, these meters were additionally calibrated for use with helium, argon, and hydrogen gases. Calibration precision was on the order of ±2 percent with an overall accuracy estimated at better than ±5 percent.

Brief mention should be made of the Brooks tube number R-2-15-AAA which exhibited phenomenal repeatability and precision. This is the smallest tube manufactured, having a range from its sensitivity level of 0.02 to 3.7 scim (sensitivity ratio of 185:1). Periodic calibration of this meter with burets over a 2-year span consistently indicated a repeatability of better than 0.01 scim from 0.02 scim up. Furthermore, the meter was relatively insensitive to tilt showing no reading deviation for angles up to 10 degrees. Calibration of this tube with several gases indicated that the mode of flow was laminar. For higher flows in which the larger tubes were employed a mixed laminar-turbulent flow was evident gradually transisting to a nozzle flow condition.

Considerable time was expended attempting to calibrate several Fisher and Porter minimum flow volume "Tri-Flat" tube and ball combinations for the cycle test program. These meters proved to have a low sensitivity ratio (15:1) with poor accuracy (up to 30-percent error). Errors were attributed to tilt sensitivity and electrostatic charges which even anti-stat fluid could not entirely correct. The problem appeared to result from the high rotational speed of the ball float which, in conjunction with a slight tilt angle (4 degrees), caused an inconsistent high reading. (The Brooks meter ball rotated slowly.)

For the higher flowrates encountered in near-seated testing (up to 14 scfm), plug-type rotameters were used. These meters were calibrated with positive-displacement gas meters to an accuracy of better than ±5 percent.

Calibration and leak measurement burets (Manostat Corp.) used were 100 milliliters for the conventional bubble under method and 10, 5, and 1 milliliters for leveling. The 5- and 1-milliliter tubes having graduations of 0.01 and 0.002 cc, respectively, were predominately used. The buret systems (Fig. 377) are described in detail below with correction equations and analysis of probable errors.

Leakage Collection. The 23-cu in. cavity enclosed by the tester covers (Fig. 36 and 37) proved suitable for rotameter levels of flow. Lower leakages, however, necessitated collection in a smaller container so that the leakage volume would not be submerged by pressure and temperature variations. This was accomplished in the initial program by placing a lubricated O-ring seal between the poppet and seat. A 0.04-inch-diameter brass tube was inserted through the seal and in turn, was connected to the leveling buret by 4 to 52 inches of 0.038-inch ID plastic tubing. For testing conical, spherical, and cycle test models, lapped aluminum collecting rings (Fig. 68) were located between the poppet and seat and sealed with center-point lube. Plastic tubing as above connected the ring to the buret.

Conventional Bubble Under Buret. Of the two positive-displacement systems evaluated in detail, the first was the conventional method of introducing the leak through water at the base of an inverted buret to displace a column of water. This proved satisfactory and accurate for larger flows; however, leakage measurements under 0.1 scim required small bore tubes to obtain readings in a reasonable time and, when used in the above manner, large gas bubbles tended to stick at the base of the tube. Reducing the diameter of the gas bubbles by a small-exit orifice helped to attain the measurement, but this caused back pressure on the leak which had to be overcome before a stable reading could be taken.

Leveling Bulb Buret. The second method which overcame these difficulties was successfully employed for low-rate leakage testing. The gas leak was introduced at the top of the buret rather than bubbling it through the water. A leveling bottle connected to the base of the buret provided control of both the level and internal pressure after introducing the leak. By dropping the height of the bottle to match (within approximately 0.06-inch negative head) the level in the buret as the leak volume increased, the pressure differential in the system was made negligibly small. However, in measuring small leaks, it was noted that slight positive or negative pressure differentials could cause extraneous leakage resulting in large errors. Therefore, the system was always leak checked by sealing off the inlet pressure and purposely creating up to a 1-foot negative head so that the buret level could be observed for change which would indicate an external leak.

Buret Flow Equation. Examination of the flow equations that correct for water head, vapor pressure, and ambient conditions for the conventional and leveling bottle systems show the advantage of the second method in requiring fewer corrections. These expressions assume a constant run temperature and pressure.

Conventional:

$$Q_s = \frac{3.66\ T_s}{T\ t\ P_s} \left[\rho_L\ V_1\ (h_1 - h_2) + \Delta V\ (P_a - \rho_L\ h_2 - P_v) \right]$$

Leveling:

$$Q_s = \frac{3.66\ \Delta V\ (P_a - P_v)\ T_s}{T\ t\ P_s}$$

where

h = water level head, inches

P_a = atmospheric pressure, psia

P_s = standard atmospheric pressure, psia

P_v = vapor pressure of water at temperature, psia

Q_s = leakage, scim

t = time, seconds

T = gas temperature (assumed equal to water temperature), R

T_s = standard atmospheric temperature, R

V_1 = initial volume in buret, cc

ρ_L = liquid density (with water used) lb/in.^{3}

ΔV = change in volume as a result of leakage, cc

Buret Flow Measurement Errors. The ultimate use of the flow data is to allow comparison of the performance capabilities of various seating configurations. Because the range of data spans several orders of magnitude, great accuracy is not required. However, consistency of point to point data and repeat hysteresis loops dictated the need for reasonable precision, i.e., about ±2 percent. To meet these requirements, the following measurement errors were evaluated.

Volumetric. Where leakage values were greater than 10^{-3} scim, volume and time errors were made small by obtaining suitably large buret displacements over a sufficient time interval. These intervals ranged from a minimum of 30 seconds to 1 hour for 10^{-5} scim. Where leakage was measured between 10^{-3} and 10^{-5} scim, a minimum volume of 0.01 cc was displaced from the 1.0-milliliter buret (five 0.002 cc divisions). Because burets have precision bore tubes, the significant source of error is in the reading accuracy of the displaced water levels at start and stop. For the minimum leak of 10^{-5}, the length of displaced water is 0.200 inch which, for an estimated

$\Delta h = 0.02$ inch (± 0.01 at each level), results in a maximum error of 10 percent. (The ± is dropped as an error is assumed to deviate from the perfect reading.)

Leveling. Errors in leveling cause the volume of gas being leaked into, as well as the leak volume, to be at a pressure other than atmospheric. Leveling errors stem from two sources:

1. Capillary action results in a differential height between the tube and bulb level. Variations in this height differential (due to film contamination of the glass) over a given span will result in pressure changes during a test run if a constant capillary height is assumed. This error was nullified by calibration over a specific span. (Proper detergent cleaning of the tubes and use of a few drops of ordinary bleach usually eliminated any noticeable error.)
2. Basic comparison reading errors of the levels in the bulb and buret

The equation for leakage error caused by pressure variations from variable head is:

$$\text{Error} = \frac{\rho_L \, \Delta h \, (V_L + \Delta V + V_1)}{(P_a - P_v + \rho_L \, \Delta h) \, \Delta V}$$

where Δh is the leveling head error, and V_L is the total leakage volume external from the buret. This relation indicates that within visual leveling capabilities there is a minimum leak volume, ΔV, which can be measured for a given error and total volume $(V_L + V_1)$. For the 23-cu in. volume enclosed by the tester cover, the minimum leak volume, ΔV, for a 5-percent error (0.02-inch Δh reading error assumed) is 0.023 cu in. or 0.38 cc. Thus, for a 1-minute test, the minimum rate for this large volume is 0.023 scim, or 1/1000 of the total volume. The volume of the collecting ring system, external to the buret, was less than 0.1 cu in.; thus, for a 50-percent error, only 1×10^{-4} cu in. or 0.00164 cc leakage need be captured.

This minimum volume was increased to 0.01 cc to compensate for reading and temperature errors. With this volume, it was concluded that basic leveling errors had negligible effect on leak measurement accuracy compared with other errors.

<u>Temperature</u>. Variations in air temperature surrounding the external leak volume and buret induced indeterminate changes in the final leak volume. Consequently, where timed runs were long for low leakage, a 4-inch section of 1.0-milliliter buret was taped and insulated directly to the tester base. (This had the added advantage of minimizing the tube length from leak collector ring to buret.) A thermometer was located next to the tube to measure any temperature change. The equation for leakage error caused by a change in system temperature is:

$$\text{Error} = \frac{V_L \, \Delta T}{\Delta V \, T}$$

where ΔT is the temperature variation, and T is the mean absolute temperature. Because temperature errors occurred only for long duration runs involving low leakage, only the low-volume system was affected. Temperature variations were estimated to be generally less than 1.0 R. Consequently, for a minimum leak of 0.01 cc (6.1×10^{-4} cu in.), maximum leak volume of 0.1 cu in. and mean temperature of 530 R, the maximum (calculated) error in leakage is 31 percent. For most measurements, the leakage volume was sufficiently large and time short enough so that temperature error was less than 5 percent.

<u>Summary of Errors</u>. From the previous discussion, it is evident that an accuracy of better than ±5 percent was probable for leakage values down to 10^{-3} scim. It should be noted that had human errors resulted in even a 10-percent deviation, little effect would be noted in the data presentation which can only be read to about this level. Between 10^{-3} and 10^{-5} scim, the possible error increases from the 5-percent level to a predicted 41 percent. Numerous repeats of data points did indicate, however, better precision than this, usually ±10 to ±30 percent. Overall data presentation

accuracy was improved by simultaneously reducing and plotting stress-leakage data during test; thus, nonrepeat points or those appearing in error could be rerun if required.

MODEL ASSEMBLY AND GENERAL TEST PROCEDURES

Operation of the testers and associated equipment required observance of a number of procedural steps to avoid damage to the seating and loading surfaces and ensure the validity of the test. Very often, tests were performed and theories evolved to explain the results only to later find that other variables, in addition to the one being evaluated, had influenced the experimental results. Consequently, many tests were performed more than once to ensure repeatability and allow a thorough definition of the test parameters.

Poppet and Seat Assembly

The primary consideration in assembly of poppets and seats into the testers was cleanliness. Cleaning procedures varied during the test effort with improvements being incorporated as test needs dictated.

Initially, parts were cleaned with trichlorethylene or benzene, seating surfaces wiped and tester installation performed under an inlet gas purge. A secondary benzene wipe was then followed by removal of lint particles with a fine brush while purging. Under bright edge-lighting, such particles were easily discernible on the reflective seating surfaces.

It was noted, however, that parts removed from the hot trichlorethylene vapor degreasing tank would "squeak" when rubbed with wiping paper while parts cleaned with cold trichlorethylene, benzene, or freon, would not. Apparently, even these well-filtered solvents retained some oil-like residue which adhered to test parts. Furthermore, while lint particles could be seen, electrostatic charge effects made their removal difficult. A radioactive element contained in a special brush(Staticmaster)was found to significantly reduce this latter difficulty.

A standardized cleaning procedure evolved which was utilized for the majority of the test effort. Poppets and seats were demagnetized followed by ultrasonic cleaning and vapor degreasing with hot trichlorethylene and transferred to the test area in a closed container. After cooling, the parts were dry-wiped with lint-free paper or foam plastic wiping material, passed under the antistatic device and blown off with high velocity nitrogen gas. Assembly into the tester followed under a heavy nitrogen purge. With the establishment of this cleaning process, contamination problems during assembly were virtually eliminated.

As originally conceived, the static tester was to stand upright on its baseplate. This arrangement, however, had some drawbacks. Installation of test seats was relatively simple requiring only slight OD lubrication to permit easy insertion down into the body cavity past the seal O-ring. With the seat in place, the locking bolt was torqued to about 100 pounds preload, drawing the seat firmly down on the baseplate. As an installation check, parallelism of the seat to the baseplate was measured with the Merz indicator. All seats so checked were parallel to the base within 10 microinches over the seating diameter.

Poppet installation was much more difficult since it had to be inserted into the tester and suspended above the seat. Extreme care was required so as not to touch the seating surfaces as any edge or rubbing contact would likely cause damage. In some cases, a thin sheet of polyethylene was inserted between poppet and seat to preclude contact during assembly. This arrangement protected the surfaces but often introduced contamination necessitating further cleaning and scrubbing. The tester was used in the noted position throughout the initial program effort. Prior to initiation of follow-on testing, however, a fixture was made to support the unit in an inverted position, baseplate up. This greatly simplified installation procedures since the seat, as the suspended part, was installed first and torqued in place. The poppet could then be conveniently installed. When clamped, the preload on all poppets was about 100 pounds.

The cycle tester, mounted in a horizontal position and having a larger access cavity, presented few installation difficulties. The seat was first installed and torqued. The poppet and clamping fixture were preassembled and inserted into the tester, where clamping fixture mounting brackets supported the subassembly while it was slipped onto the piston.

Three methods of poppet installation were used. The first (clamped condition), shown on the tester drawing (Fig. 36), incorporates a retainer, flexure spring, and clips for positively positioning the poppet relative to the seat. This arrangement was used for static tester near-seated and some on-seated tests and exclusively on the cycle tester. This necessitated that flat poppet and seat model parallelism be measured and the models oriented to produce the best parallel condition. Occasionally, rework of the back (loading face) of either poppet or seat was necessary to achieve this end. All flat models, as installed and tested, were parallel within less than 10 microinches over the seat diameter.

When it became apparent that even a slight out-of-parallel condition greatly influenced on-seat, low-stress test results, a second arrangement was employed. This method (Fig. 36, detail P) loads the poppet through a ball joint allowing it to conform with the seat. With this test method (ball loaded or ball joint tests), loads must be computed from piston control pressure readings since the strain gage load cells are isolated. Also, electrical contact tests could not be performed due to poppet tilt.

A third arrangement was used for static testing conical and spherical models. Unlike the flat models, both axial alignment (conical only) and concentricity were critical and unsufficiently controlled for normal clamped loading. Like the flat model ball joint, means had to be provided for self-centering so that the tester would have a minimal influence on the data.

Interfacial friction and small righting moments precluded angular alignment of the poppet cone with the ball-loading method. Furthermore, relative interfacial motion was undesirable due to potential surface damage.

To achieve the desired axial coincidence between conical and spherical poppets and seats with minimum sliding contact, the three piston "feet" were coated with a thin film of low-viscosity, E.P. oil on which the poppet rested. As the screw thread was advanced, the poppet entered the seat and, sliding on the oil film, was radially and axially aligned. For static testing, the poppet was completely unguided except for the seat, but cycle tests necessitated clamping as with the flat models using a special procedure.

Position,parallelism, and cleanliness integrity of a model installed in the clamped condition was indicated by leakage at electrical contact. The best flat model match achieved during the test program was an equivalent parallel plate gap of 11 to 12 microinches (Model M_f). More common equivalent gaps ranged up to 25 microinches for the better (lapped) models. Except for those models with known surface deviations commensurate with such results, indication of equivalent parallel plate gap in excess of 25 microinches was cause for disassembly and recleaning.

Even with these precautions, most models exhibited a relatively fast closure rate at initial low loads which, with the exception of circular lay or rapidly changing contact land width models, indicated:

1. An out-of-parallel condition (primarily clamped models)
2. Contamination (possible on both clamped or ball-loaded models though minimized by rigid cleaning procedures
3. The probability of random surface nodules, and the relative difficulty of producing a perfectly uniform surface. This effect would be most noticable on ball-loaded models where electrical contact tests were not possible but parallelism effects are virtually negligible.

Unless otherwise specified in the test section, all unidirectional lay models were tested with the lay approximately 90 degrees opposed. Circular lay models were installed with guide diameters eccentric a maximum of 0.0008 inch. The individual poppet and seat lay could have an additionally eccentricity of about 0.0006 inch due to fabrication (lathe) setup tolerance. The probable net poppet to seat lay eccentricity, however, was more likely something less than 0.001 inch.

Model Test Procedures

As with any responsible test effort, generation, and acquisition of repeatable, valid data requires adherence to certain methods and procedures which generally evolve through a learning period. The following procedures reflect such a learning period and represent practices followed for the majority of the test effort. The rules, however, are not inflexible and specific deviations to general practice have occurred. These deviations are noted under the applicable test model section.

Near-Seated Tests. The basic problem in this test series was to establish a datum or zero height point. The leakage at electrical contact provided this datum. Once correlated with the roughness and other geometrical parameters of the tests, it established a repeatable starting point for all tests. The value of this datum is apparent when it is considered that electrical contact is a no-load condition. If an electrical contact can be obtained at a level commensurate with the surface roughness profile being tested, it is reasonably assured that what is being tested is the profile and not some other variable such as a ridge, nodule or other protuberance, out-of-parallel face, or contaminant.

After a reasonable datum or electric contact leakage had been established, off-seat flow tests were performed. For these tests, the inlet pressure was measured directly adjacent to the seat interfaces from a 1/32-inch drill hole pressure tap provided in the seat (Fig. 60). Position control was maintained by the micrometer screw which also provided the necessary position reference.

Two critical problems encountered in the flow tests were the dependence of positional accuracy at low gaps on inlet pressure and at large gaps on temperature. Because the micrometer screw required a precision ball joint for loading, the variable deformation of the joint contact affected the flow gap as a function of inlet pressure changes. Calibration of the screw between 30- and 1000-psig inlet pressures showed it to be precise and repeatable; however, at gaps below 0.0001 inch, the inlet pressure had to be maintained within 1.0 psi to keep system loads and, thus position, essentially constant.

The second problem was caused by shrinkage of the poppet and seat interfaces because of temperature drops at high flowrates (nozzle regime). This required establishing a reference micrometer zero at electrical contact (with proper leakage) and rapidly obtaining a stabilized high flow reading.

In all cases, the correlation of leakage with the electrical contact provided a ready reference from which to collect the off-seat flow data, and the precision of the flow curves presented later is attributed to this reliable reference.

The pressure profile across the seat was measured by nine pressure taps located in the seat (Fig. 60). After determining that the profile did not vary around the seating diameter, only three radial taps were used. Initially, there was a problem with slow pressure rise time in the gage system. Readings below a 100-microinch seat spacing required more than 15 minutes to stabilize. This problem was partially allevaited by filling the gage and line with water which allowed readings to be obtained at 50 microinches off-seat within a 5-minute stabilization period.

On-Seat (Stress-Leakage) Tests. These tests comprised the bulk of the experimental effort and illustrate the relationship of leakage with increasing and decreasing load loops (or cycles) for variations of model surface texture and geometry. As used herein, a stress-leakage test is defined as one or more load loops obtained without seating surface separation. Two classes of stress-leakage tests were performed:

1. The initial test of a new model (one with poppet and seat surfaces having no former loading history or the combination of a poppet and seat not previously tested together). This test was

always conducted in the static tester and involved special care to obtain first load-cycle data and sufficient data points to define adequately the model characteristic. Additional load-cycles were generally performed to verify data repeatability.

2. A comparison test to verify establishment of or return to a previous test characteristic after seating surfaces were separated. This type of test, performed in both static and cycle testers, involved a lesser number of data points with no special concern for first cycle data. By definition it consisted of all tests subsequent to the initial test.

Initial Tests. When possible (clamped position or conical and spherical tests), the electrical contact check was performed first to verify geometric and cleanliness integrity. Pressures were then raised to the desired operating level. To ensure acquisition of first cycle data, the model interfaces were kept separated during this operation by maintaining an inlet pressure-piston control pressure force imbalance and assuming hand control (screw thread) of piston position. Simultaneously monitored leakage was held at a level commensurate with some positive poppet-seat gap during this process. When the desired inlet pressure level was attained, additional control pressure was slowly applied and the balance point noted as previously defined. Balance pressure was generally checked several times.

Following establishment of the balance point, control pressure was increased to initiate first cycle poppet-seat loading. The basic stress-leakage test consisted of increasing incremental load changes with steady-state leakage measurement at each load level until a maximum stress was reached. A return (decreasing load) series of data points was then taken until the load approached the balance point. A second (or more) stress-leakage loop (or cycle) was subsequently performed to verify data repeatability and model elasticity.

If a plastic deformation characteristic was anticipated, increasing load cycles were periodically reversed and return, decreasing-load data points obtained to a level near the balance point. Subsequent loops to increasingly higher maximum stress levels followed.

The maximum stress level attained was defined by: (1) practical loading limitations, <100,000 psi; (2) leak measurement limitation, $\sim 1 \times 10^{-5}$ scim; or (3) potential model damage.

An alternate procedure was employed for some early tests. Up to 300-psig inlet pressure, screw thread friction load was low enough to premit hand control of poppet position without the supplemental application of control pressure (P_c). Consequently, some models were tested first at 300 psig until a control pressure in excess of the anticipated 1000-psig balance pressure was reached. After completing the decreasing stress loop, P_c was raised to the previously attained level, inlet pressure increased to 1000 psig, and testing commenced again. In this manner, first cycle data was obtained while avoiding the tedious juggling of inlet and control pressures.

<u>Comparison Tests</u>. As first cycle data was not necessary, control pressure was increased to a level slightly above the balance point. Inlet pressure was then raised and control pressure reduced to measure balance pressure.

These tests, as performed in the cycle tester deviated somewhat from static tester procedures. Although dashpot O-ring friction change during a given stress-leakage tests was minimal, it did vary significantly with cycles. Consequently, balance pressure was measured prior to each stress-leakage test.

It was noted that when control pressure exceeded dashpot pressure for any length of time, as occured during stress-leakage tests, gas leakage into the dashpot followed with subsequent damping changes. To obviate this problem, the dashpot reservoir piston was additionally loaded to increase internal pressure. This was accomplished by threading in the adjustment screw to override spring load and bottom on the piston. Because the dashpot cap wall and bottom were thin enough to deform, the loading screw could be advanced several turns with relatively low torque. The amount of piston displacement (screw thread advancement) required to establish internal pressure in excess of specific control pressure values was calculated and such change made prior to each new control pressure setting. This additional dashpot adjustment was required when control pressure exceeded 190 psig.

Cycle Tests. As previously noted, flat models were installed at about 100 pounds preload in the tester parallel within 10 microinches over the 1/2 inch seat diameter. Conical and spherical model seating surfaces were lightly loaded for orientation and the poppets clamped in position while loaded. Verification of best possible installation position and/or contamination was determined by electrical contact test. Following these checks, a stress-leakage test was performed for comparison with previously obtained static tester data. Cycle testing was not begun until favorable electrical contact and stress-leakage correlation was obtained. Additional preparatory operations included adjustment of piston stroke and calibration of load cells and position transducer.

Cycle tests were performed at three nominal peak impact stress levels of 30,000, 92,000, and 159,000 psi, corresponding to nominal impact velocities of 7.6, 24, and 35 in./sec, respectively. For the majority of these tests, a solenoid valve, actuated by an electronically controlled cycler-counter with manual override, was used to apply piston control pressure; piston stroke was set at 0.10 inch. Cycle rate was established at 60 cpm with approximately equal on-off periods.

To avoid changing control pressure during test and preclude leakage into the dashpot, cycle control pressure was established at the spot leak-test-pressure (169 psi for flat models or approximately 20 psig less than minimum dashpot static pressure). Impact velocity was then varied by adjustment of the dashpot orifice. When a succeeding model was to be tested at a lower impact stress, piston velocity was readjusted to this level prior to removal of the previously tested model. In this manner, overstressing was avoided and only minor dashpot orifice adjustment was necessary when the succeeding model was prepared for test. If the following test was to be at a higher stress level, necessary velocity adjustment was accomplished on the high stress model. To eliminate external contamination, inlet pressure was orificed (No. 80 drill hole) to provide a nominal 100-scim bleed during cycling. With this low flow, inlet pressure at impact was essentially zero.

Spot leak checks were periodically performed during a cycle test at the cycle control pressure with an inlet pressure of 1000 psig, which yielded a static seat stress level between 2000 and 3000 psi. This stress was sufficiently high to submerge effects of contamination or geometrical (out-of-parallel or nodule) defects while fully contacting the roughness level yet low enough (reasonable leakage levels) to permit relatively fast leak measurement. Consequently, all spot leak checks were performed at this stress level without resetting control pressure.

Although spot checks were taken more frequently during initial tests, experience ultimately indicated that leakage change with cycles was a slow process and a less time-consuming procedure was adopted. A typical sequence of spot leak checks was 5, 200, 1000, 2000, 5000, 7500, and 10,000 cycles. At the conclusion of the cycle test, a final stress-leakage test was performed.

To permit rapid accumulation of a large number of cycles, a high-frequency cyclic procedure was devised. The dashpot was disconnected and 25-psig piston control pressure applied. Inlet pressure was set at approximately 950 psig and, with the No. 80 drill orifice immediately upstream of the seat face, a dynamically unstable condition similar to a chattering relief valve was established. Poppet stroke was approximately 0.010-inch impacting at nominally 214 cps. Accumulated cycles were computed on a timed-run basis. Typical high-frequency test leak check points were at 25,000, 100,000, and subsequent 100,000 cycle intervals concluding with 1,000,000 cycles. As with the low-cycle rate method, a final stress leakage test was performed when cycling was terminated.

MODEL DATA PRESENTATION

The presentation of experimental program data has been categorized by test type or objective. This section contains the detailed description of each applicable test by specific model designation and sequential test number.

Data pertinent to and generated during tests are presented in several forms. The primary purpose of these data is to describe the performance of a specific test model configuration under specific conditions and identify the parameters causing or contributing to this performance. The accumulated test, inspection, and descriptive information forms the resultant design data.

A summary or reference of fabrication method and pretest inspection data initiates each test model discussion. This information has been abstracted from detail data presented and compiled in either the Model Fabrication and Surface Preparation or Model Inspection Equipment Procedures and Data sections. Following this, additional pertinent inspection or fabrication details, a test description (if significantly differing from previously noted procedures) and specific test data are presented. Posttest inspection observations appear lastly with the discussion and correlation of test results and conclusions.

Because many models were tested under multiple test categories without metal surface texture change, some cross-referencing of inspection and performance data and descriptive redundancy has been unavoidable.

Except for the near-seated and leakage comparison experiments, all test data are presented as apparent seat stress vs leakage characteristic curves. Actual test data points are shown, and the interconnecting curves represent a best-fit plot of this information; no averaging procedures were employed. Arrows on the stress-leakage curves indicate the direction of recorded data (increasing or decreasing stress levels) similar to hysteresis loops. Unless otherwise specified, the circles, triangles, squares, and X's represent, respectively, first, second, third, and fourth cycles of increasing-decreasing load. (Except when noted by test number change, sealing surfaces were not separated between loading cycles.)

It will be noted in the inspection data compilation (Table 4) that model seating land contact geometry varied considerably. Conditions ranging from uniform, well-defined flat land areas to combinations of differential angles, crowning and gross duboff were encountered. Accordingly, alternate methods of computing seat stress data points were employed.

When a flat land width could be defined (as described in model inspection procedures) the projected seating area (A_{sp}) was computed using this land width. For models of load variable land geometry the total land width was used in presentation of apparent stress data on a comparative load basis. A supplemental Hertz contact average stress curve based upon actual contact land width is also presented for crowned models; this stress (σ_{avg}) is comparable to apparent stress (S) where a flat land width is defined.

In the case of conical models, combined land geometry involving taper, crowning, duboff, and various degrees of out-of-roundness preclude a meaningful stress comparison. Apparent stress for these models is presented on the basis of total projected land width. In reviewing these models, the indication of higher contact stress should be considered.

In general, repeatable stress-leakage curve hysteresis effects (when increasing and decreasing load low-stress leakage values are approximately the same) are attributed to internal material hysteresis and interfacial microslip friction with little plastic deformation. Gross plastic deformation is evidenced by failure of the return load cycle to return to the initial low-stress value on each of successively higher load loops.

NEAR-SEATED TESTS

Parametric test data were obtained for comparison with theoretically predicted flow and force balance characteristics of parallel plate poppet and seat models. These investigations included leakage measurement of nitrogen, helium, and argon gases for the nozzle, turbulent channel, laminar, and transition-molecular regimes of flow. For force-balance analysis, the pressure profile was determine in the nozzle, turbulent channel, and laminar flow regimes.

Flow and pressure-distribution tests were performed using the flat poppet and 1-inch seat configuration of Test Model A. Land dimensions for this model are nearly identical with those used for the sample calculation in the Leakage Flow Analysis section. Interpreted surface texture and land dimensions for Model A are presented in Table 4. The multidirectionally lapped texture of the seat is illustrated in Fig. 105. Seat corner conditions along with a typical pressure tap used in pressure distribution tests are shown in the microinterference photo (Fig. 106). The diamond-lapped and polished-poppet surface texture is shown in Fig. 107. These surfaces, having a combined average PTV roughness of less than 10 microinches, are thus suitable for correlation tests down to the electrical contact leakage nominal (h_p) value of 20 microinches.

NEAR-SEATED FLOW TESTS

Leakage flow from 10^{-1} to 10^{4} scim was measured for poppet stroke (h_p) ranging from approximately 20 microinches to 0.006 inch. Data were obtained at 30-, 100-, 300-, and 1000-psig inlet pressure levels with nitrogen and, for comparison, tests were also performed at 100 psig with helium and argon gases. All test results were corrected to standard conditions of 14.7 psia and 70 F.

The correlation of test and theoretical data is shown in Fig. 381 through 389 by an overlay of test data points on computed curves. Data for preparation of these curves were presented in the noted sample calculation.

Gas properties assumed are tabulated below; hydrogen gas has been included for correlation use in the next section. As gas viscosities do not change appreciably with pressure, the values shown are based upon 70 F and 500 psia which is the average for the 1000-psig inlet pressure test condition used predominantly in the test program.

Gas	K	R, in./R	μ, lb-min/in.^{2}	Figure Number
Nitrogen	1.4	663	4.40×10^{-11}	381, 382, and 383
Helium	1.66	4630	4.70×10^{-11}	384 and 385
Argon	1.67	464	5.66×10^{-11}	386 and 387
Hydrogen	1.4	9210	2.15×10^{-11}	388 and 389

To minimize confusion, the theoretical curves, computed from the equations outlined in the Leakage Flow Analysis section, are continuously plotted while the actual test data points are represented by symbols. Because the theoretical trend of the nozzle to the laminar transition (turbulent channel regime) is sufficiently shown by the 30- and 100-psig data of Fig. 381, these curves were not computed for the 300- and 1000-psig nitrogen tests nor for the other gases.

The reference used in all of the flow data is the point where electrical contact occurs. This position represents approximately 20 microinches height when equated to flow between two flat plates. The physical determination of this point in the test setup involves some error. Based on comparative measurement with the Merz (and other instruments), it was determined that the micrometer adjustment for position is sensitive to approximately ±2 microinches. In addition to this, there is a possible error because of an out-of-parallel condition between the poppet and seat; however, experiments have shown that this error can be controlled to less than 10 microinches. Contamination can also introduce error into the evaluation of electrical contact. Contamination is an elusive variable which is relatively easy to detect but extremely difficult to accurately evaluate. Generally, the test setup was torn down and the poppet and seat cleaned (or refinished) when contamination was detected. In summary,

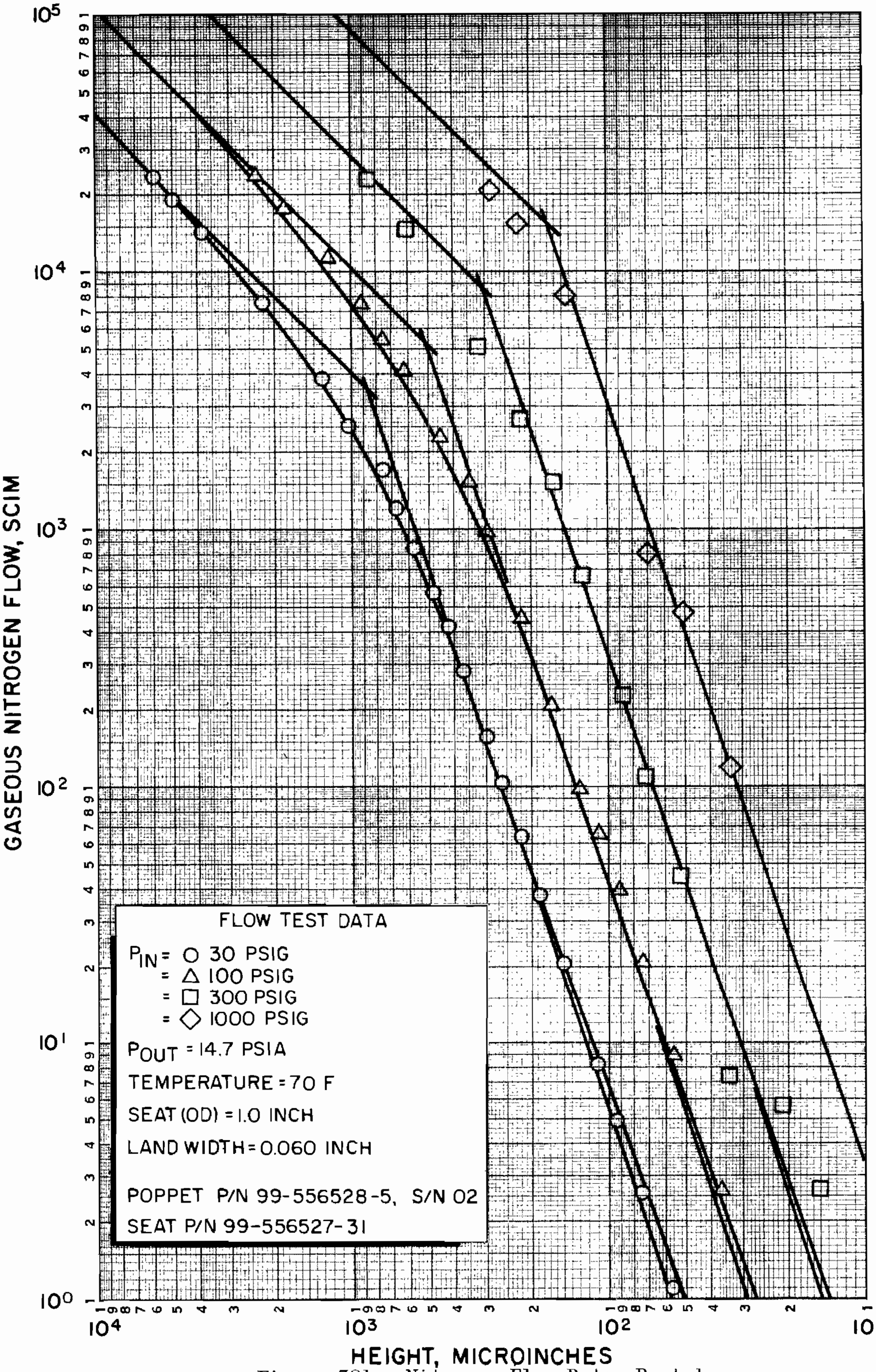

Figure 381. Nitrogen Flow Data, Part 1

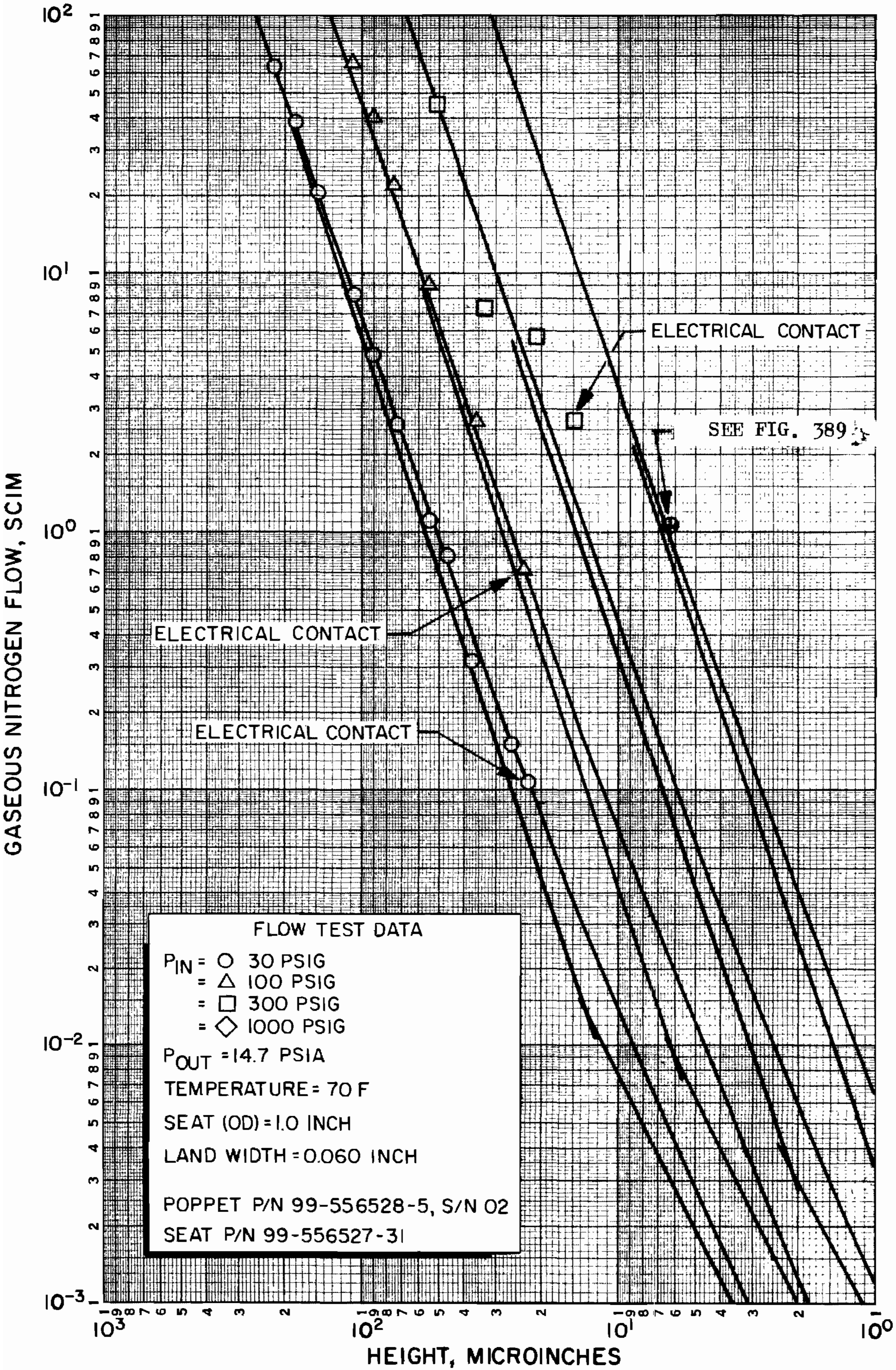

Figure 382. Nitrogen Flow Data, Part 2

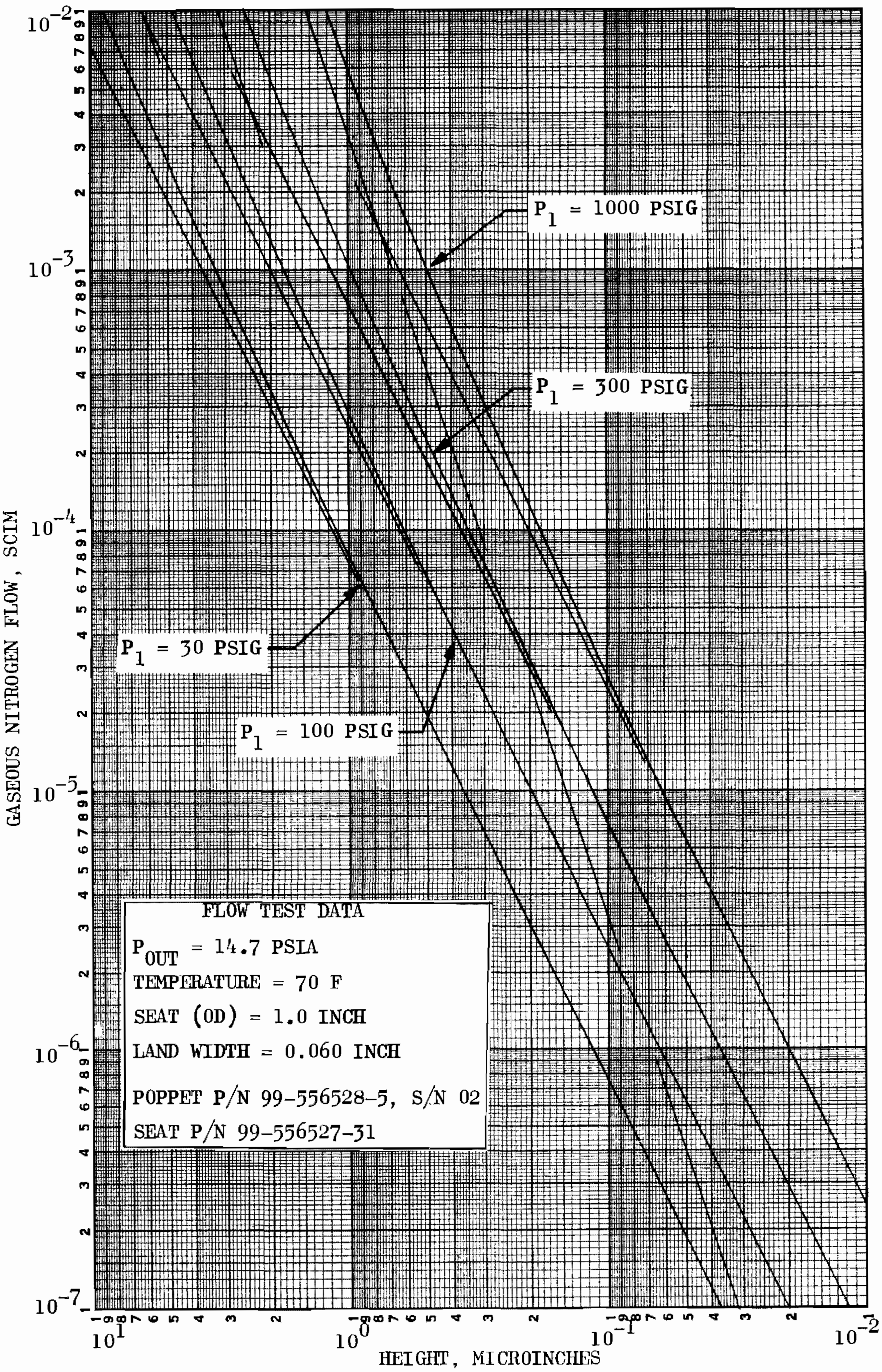

Figure 383. Nitrogen Flow Data, Part 3

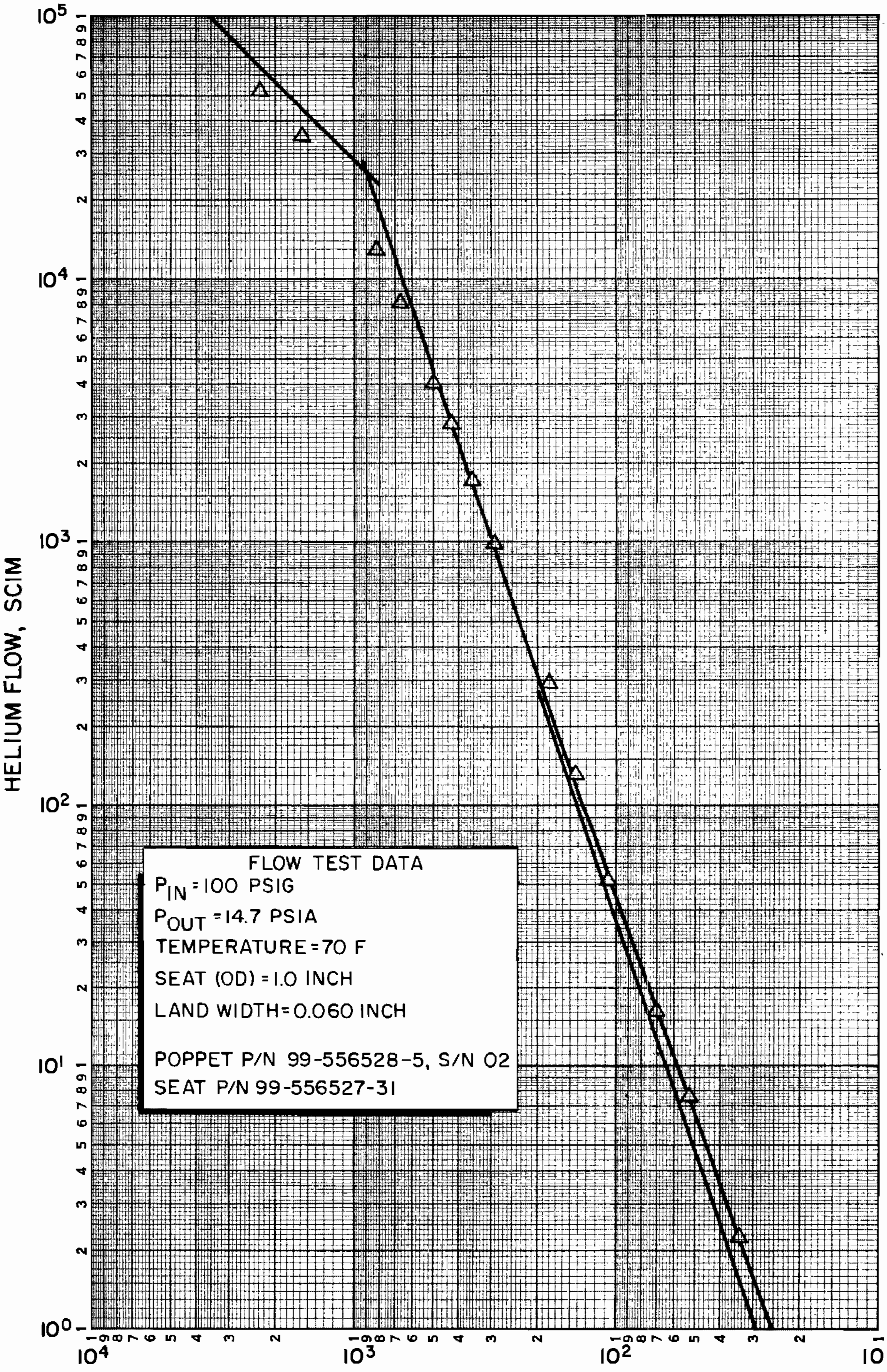

Figure 384. Helium Flow Data, Part 1

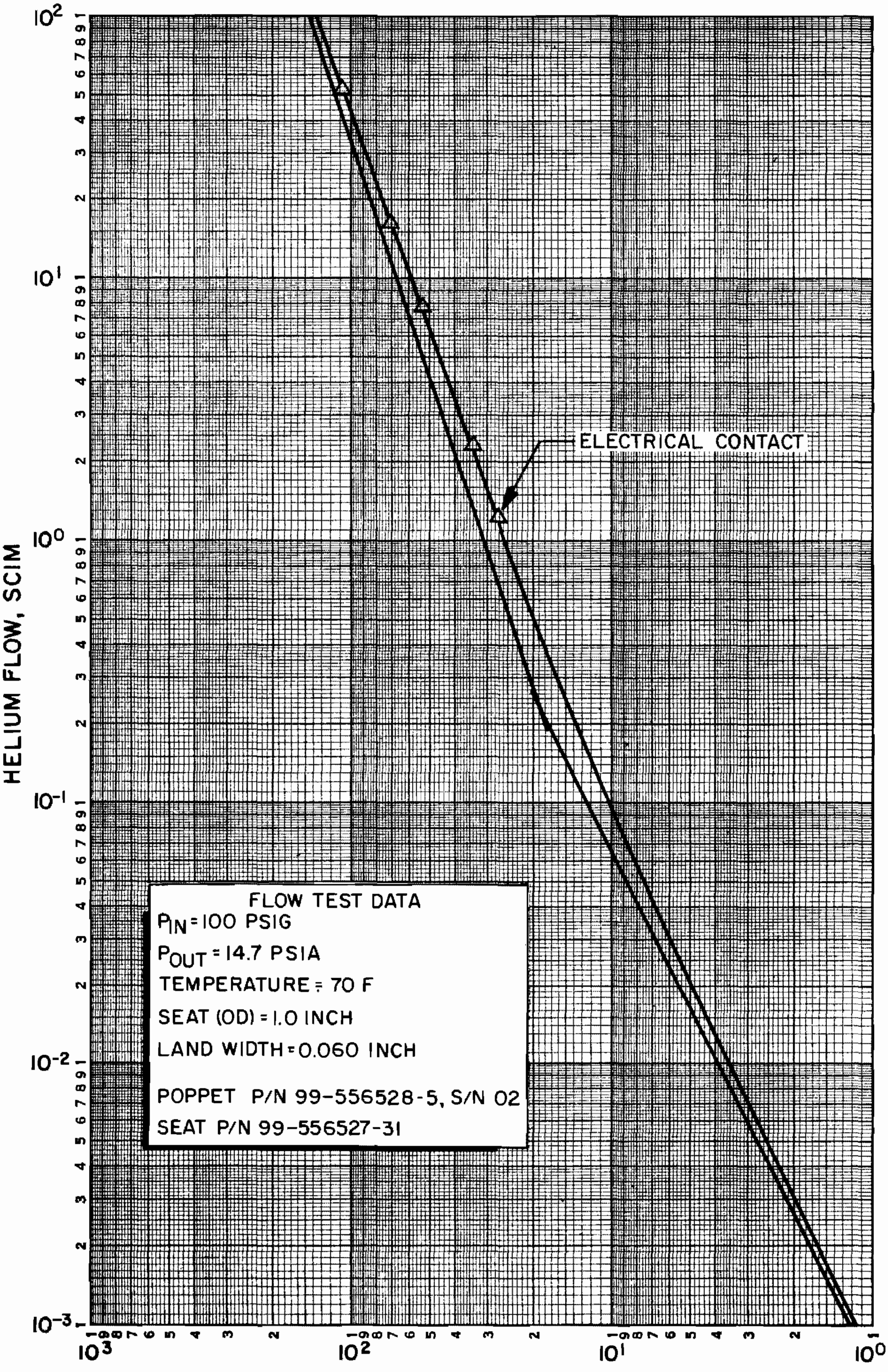

Figure 385. Helium Flow Data, Part 2

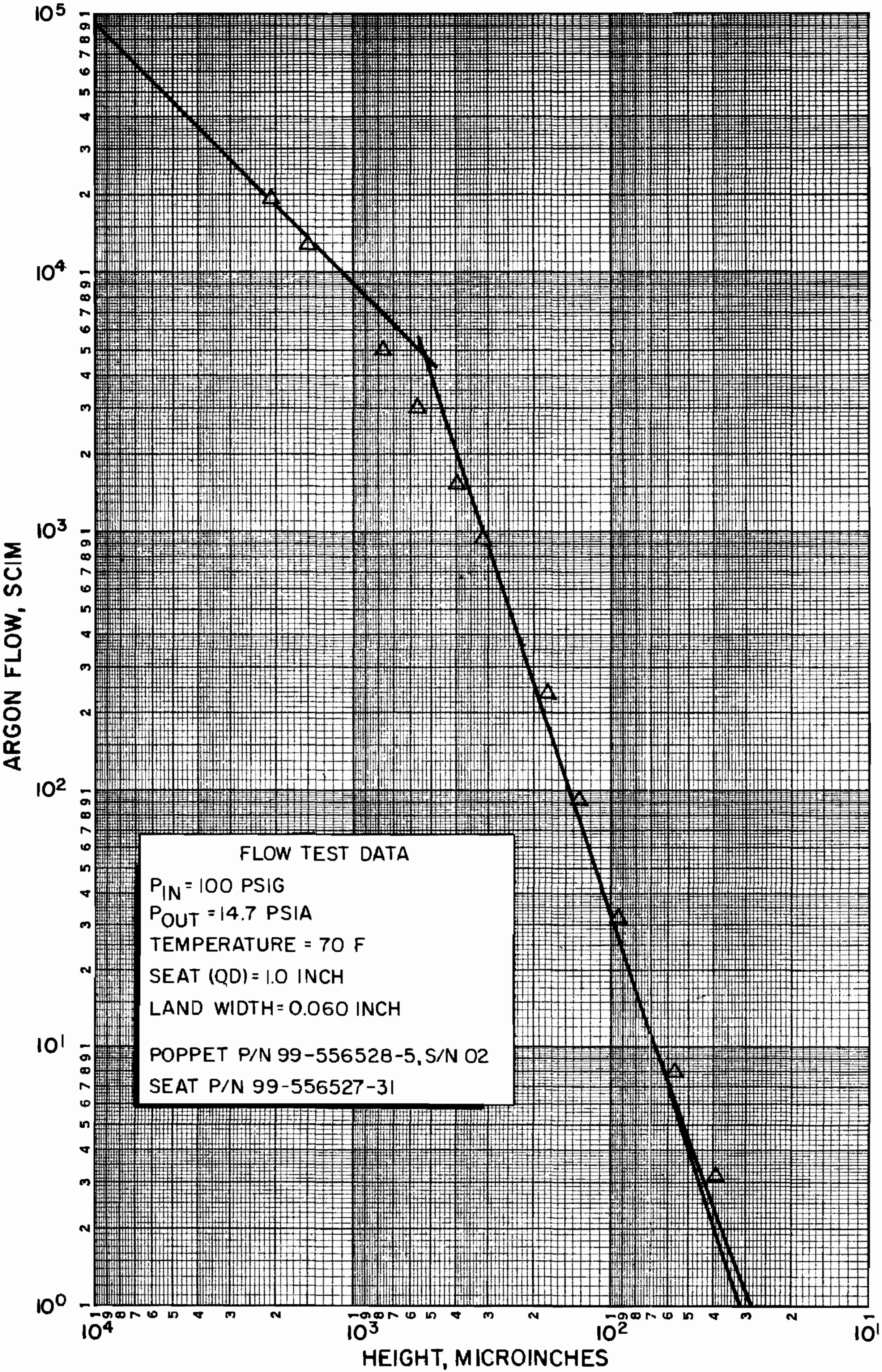

Figure 386. Argon Flow Data, Part 1

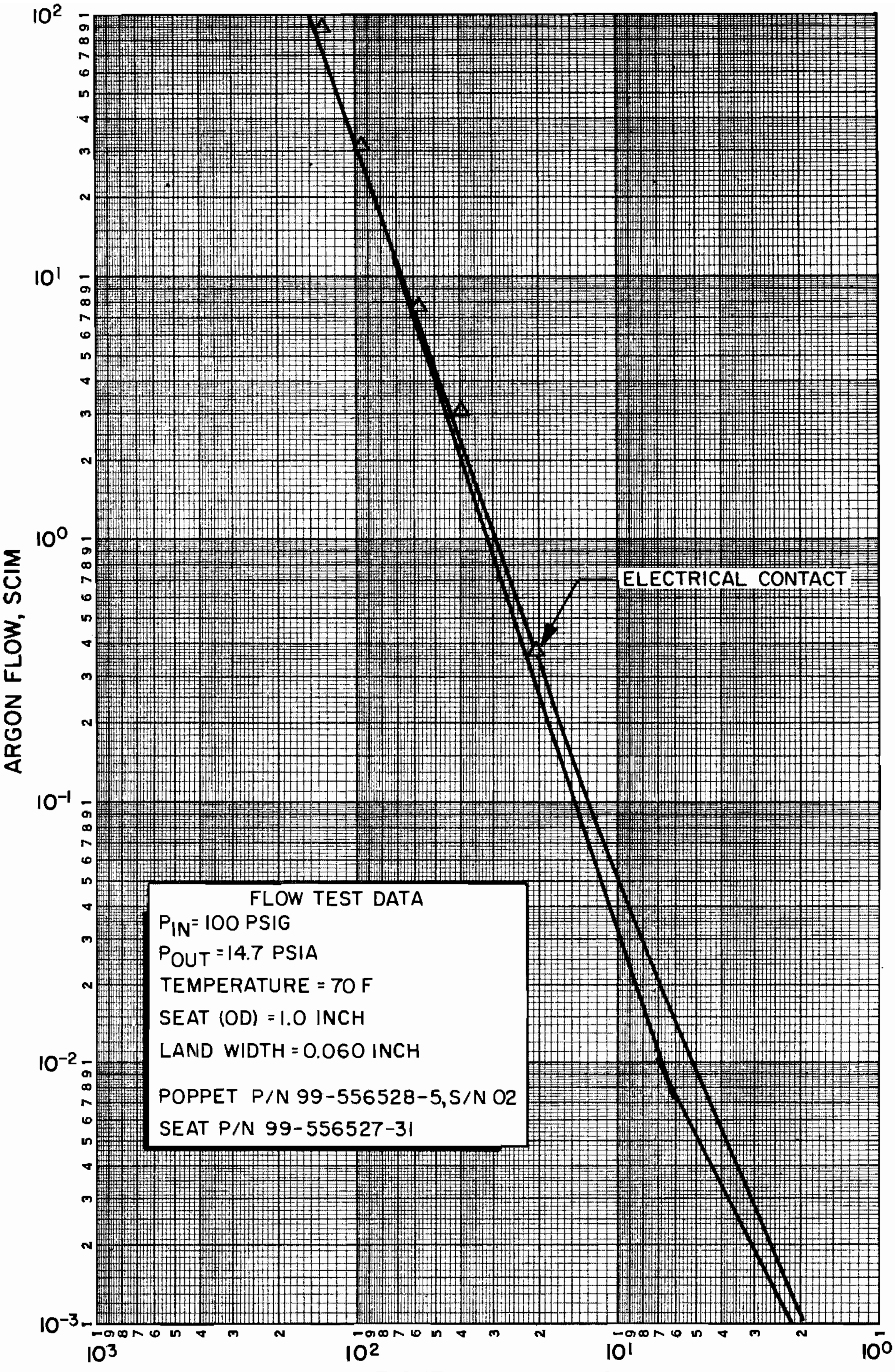

Figure 387. Argon Flow Data, Part 2

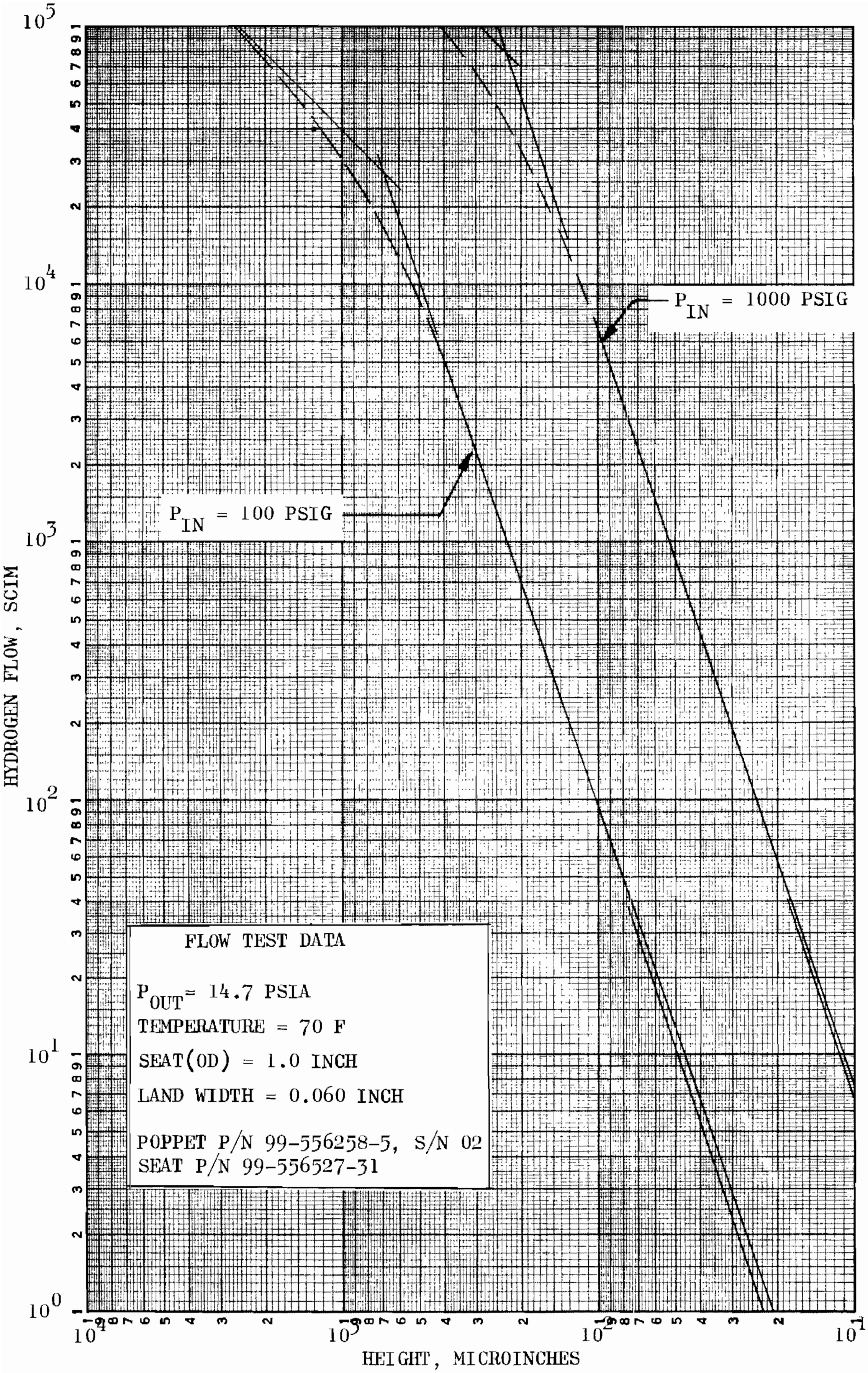

Figure 388. Hydrogen Flow Data, Part 1

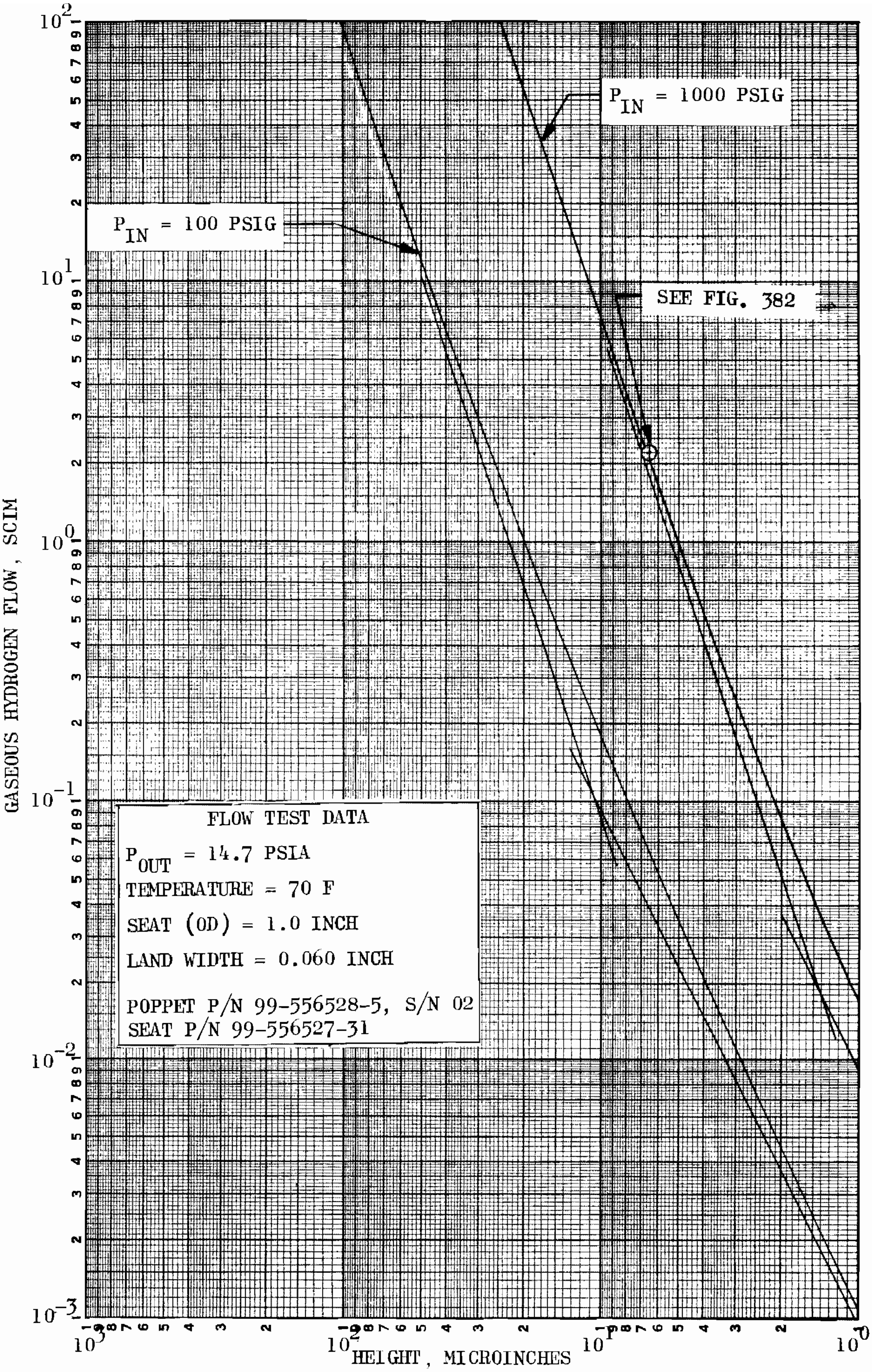

Figure 389. Hydrogen Flow Data, Part 2

it appears that the point of electrical contact could vary by as much as 10 microinches. An examination of the test data showed a range from 20 to 27 microinches. These data points were determined by placing the flow at electrical contact on the theoretical flow curve to establish the smooth plate height (h_p).

Except for the reference point of electrical contact, the experimental and theoretical flow data are plotted independent of each other. Within the 5-percent plot and test accuracy there is a high degree of correlation between experimental and theoretical data through several orders of magnitude of flow. The correlation was found throughout the pressure range and gas media investigated. The flow regimes covered include nozzle, turbulent channel, laminar, and approaching the region of molecular flow. (A detail examination of these flow regimes appears in the Leakage Flow Analysis section where a specific example, illustrating how each flow regime blends into the next to build the overall flow-leakage characteristic curve, is presented.) Some data scatter resulted at the high-pressure conditions (300 and 1000 psig) because of the difficulty in controlling poppet position with the micrometer head at these higher pressures and resultant loads. In the 1000-psig condition, control pressure was necessary to enable the adjustment of the micrometer. Consequently, no electrical contact point was established because of the difficulty in maintaining a sufficiently precise load balance.

If the near-seated test data are examined for the significant flow characteristic, laminar flow is selected as being the most representative regime. When the laminar flow curves are compared for each of the three gases, the flow does not vary by more than 30 percent for any given height (h_p). This is verified by the laminar equation for volumetric flow which shows that flow is a function of viscosity only. (Viscosity for the common gases varies by, at most, 2:1 for any given pressure and temperature.) The significance of this observation is that if leakage data are known for one particular gas, it will serve as an estimate for most any other gas of interest. As the predominant characteristic for system leakages is laminar flow, the rate of change of bottle storage pressure will be a function of gas viscosity and thus essentially the same for most gases.

SEAT LAND PRESSURE DISTRIBUTION

Evaluation of the gas pressure profile across the seating land was performed using the same poppet and 1-inch seat of Test Model A. The seat of this model was provided with three series of three pressure taps located across the land face (see Fig. 60). Data were obtained for nitrogen supply pressures of 30, 100, 300, and 1000 psig with the stroke (h_p) varied so that laminar, turbulent channel and nozzle flow regimes were covered. In addition, laminar regime data at 100 psig were taken with helium and argon.

Figure 390 shows pressure distribution across the test seat land in the laminar regime for various inlet pressure conditions. The pressure parameter is presented in nondimensional form so that the various levels can be compared on a common basis. Actual data points are represented by symbols, and the theoretical curves are continuously plotted, terminating at various pressure levels as a function of the back pressure-inlet pressure relationship. In general, the test data closely correlate with the theoretical. Within the accuracy of measurements, helium and argon test data at 100 psig were identical to the nitrogen, indicating that the pressure distribution characteristic is not a function of the particular gas involved for the laminar regime.

Figure 391 shows pressure distribution across the seat land for various poppet-seat heights. The range of heights was selected to cover the nozzle, turbulent channel, and well into the laminar flow regime. It can be seen from the curves that height has a definite effect on the shape of the pressure distribution profile. The 50- and 100-microinch data, being in the laminar flow regime, are identical and follow the parabolic laminar curve very closely. However, at heights above this point, the profile gradually changes with increasing height until it approaches that of a nozzle at h_p = 2500 microinches. Because pressure taps could not be located at the entrance and exit of the land, these points were computed. Entrance conditions were computed on the basis of isentropic gas flow. The dashed lines on the graph represent a best-fit curve of the data points indicated.

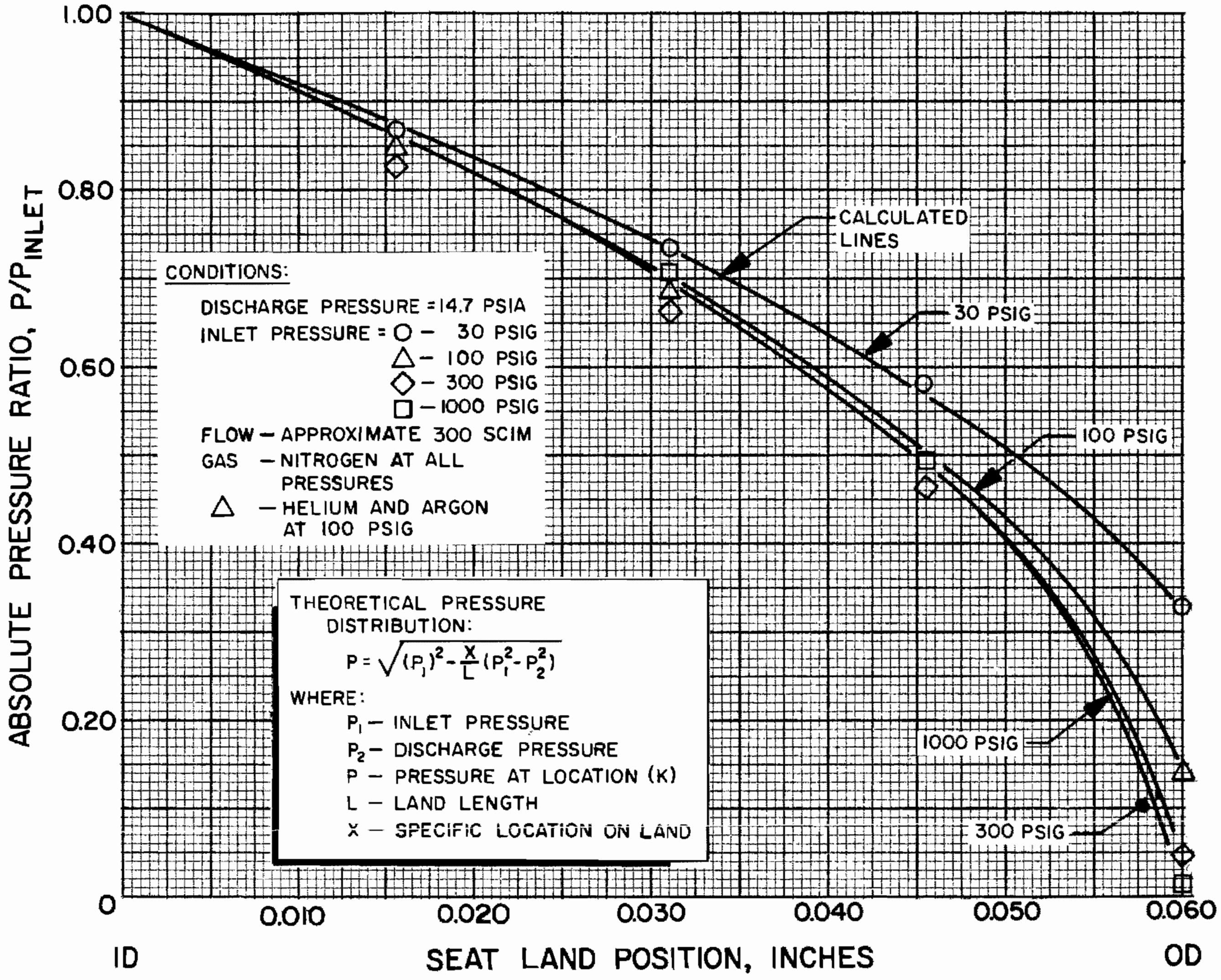

Figure 390. Laminar Pressure Distribution at Various Pressure Levels

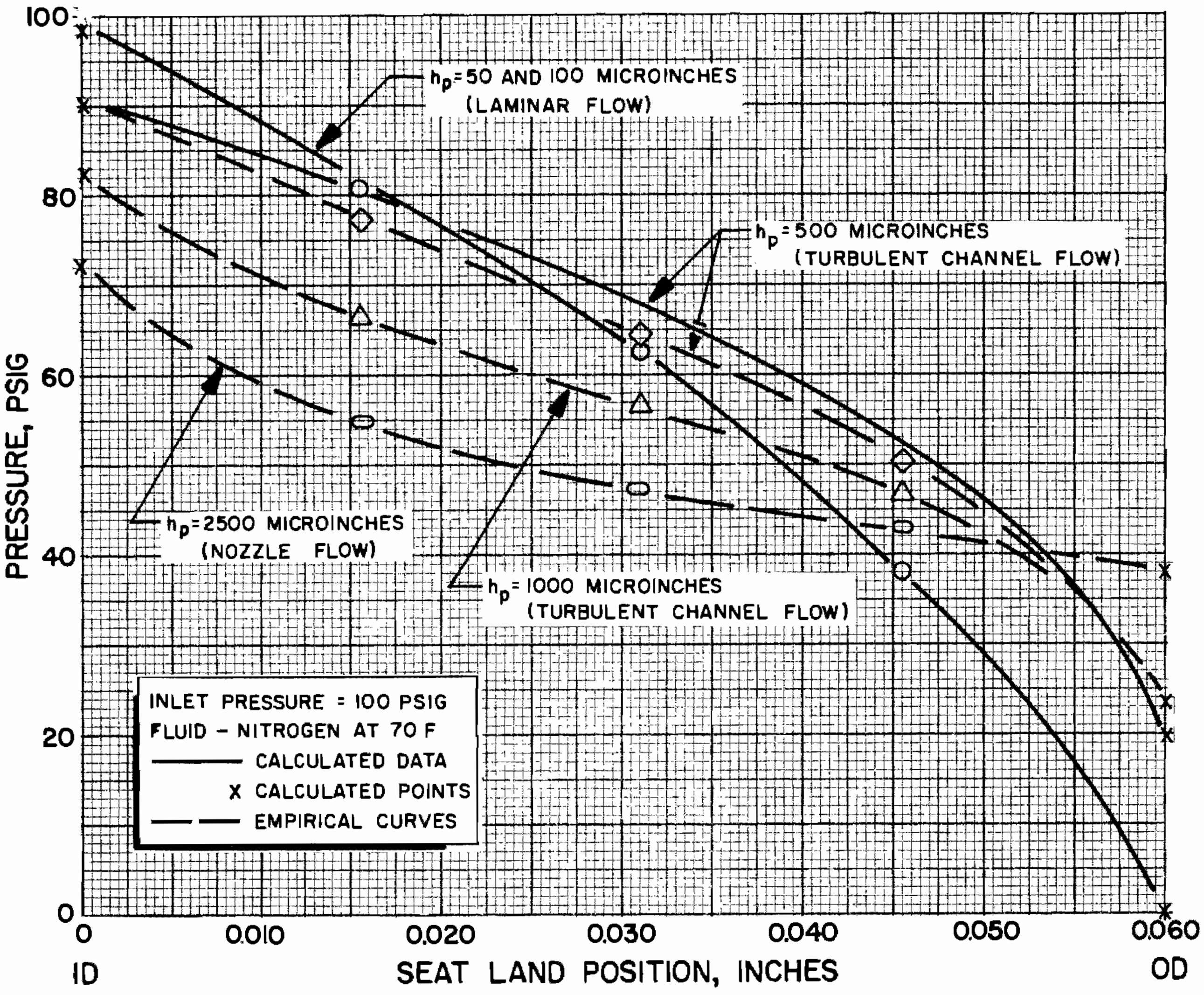

Figure 391. Pressure Distribution at Various Poppet-Seat Heights

The theory and test data correlation in the turbulent channel regime is shown in Fig. 391 for the 500-microinch height. Reasonable agreement was obtained. As the height was increased from 500 microinches, inlet conditions increasingly influence the pressure profile. Because of this and attendant analytical complexities, correlation analysis of the 1000- and 2500-microinch height was not attempted.

Because the pressure profile varies as a function of stroke, it will cause the effective seating diameter to vary also. For example, the effective diameter for the laminar regime is located at 2/3 across the land width in the direction of (P_2). However, as stroke increases such that flow is in the turbulent channel regime, the effective diameter decreases. When stroke becomes even greater so that flow is in the nozzle regime, the effective diameter is very near the land midpoint. Of potentially more drastic influence on the location of the effective diameter is the effect of land taper. Near contact the effective diameter may be located at ID or OD depending upon taper direction and subsequent increases in stroke will cause rapid changes. These variations in effective diameter are a contributory cause of valve instability in the near-seated position, particularly for valves having a relatively wide seat land.

FORCE-BALANCE CORRELATION

The effective seating area as determined by the pressure distribution profile analysis was checked during the initial contract effort by load cells and pressure force-balance measurements. These data were taken with the identical 1-inch poppet and seat used in the pressure distribution tests. The force-balance tests were performed by lifting the piston assembly with inlet pressure (P_1) while controlling the piston position at electrical contact with control pressure (P_c). Knowing the control piston area and weight of the piston assembly (W), the effective seat area (A_e) is compared using the following equation (for static tester upright):

$$A_e = \frac{1.767\ P_c + W}{P_1}$$

For the load cells, the following simple relationship was used for effective area and total load cell force (F). The weight term in the equation is the weight of the test poppet and ring clamp assembly only.

$$A_e = \frac{F + W}{P_1}$$

Based on the theoretical pressure profile for laminar flow (P_2 negligible), the effective area is computed as:

$$A_e = \frac{\pi}{4} (D_s + 1/3\ L)^2$$

The following table shows the computed effective area for the three test methods. All information was taken in the laminar flow regime (h_p < 0.0002 inch).

Computed Effective Area, in.^{2}		
Force-Balance	Load Cells	Pressure Profile
0.720	0.705	0.724

The various methods correlate within 2.8 percent which is reasonable in view of load cell resolution and the various gage and reading errors. However, considering the measurement variables involved, the pressure force-balance method is considerably more accurate and agrees very closely with the pressure profile analysis.

Additional verification of laminar flow effective area analysis was obtained from follow-on contract balance pressure test results. For all flat, conical, and spherical models having uniform, well-defined seat lands, the effective area was calculated as above from inspected dimensions. Using the force-balance equations given in the Experimental Test Program section (Load Measurement), balance pressures were computed for comparison with test results. Calculated and test values agreed within less than 1 percent.

LEAKAGE COMPARISON TESTS

A series of tests was performed directly comparing the leakage rates of nitrogen, helium, and hydrogen gases at 70 F. Test Model D_f (described later) provided a repeatable and stable leak for the tests. The test method consisted of performing repeated nitrogen leak tests (to atmosphere) at an inlet pressure of 1000 psig and 9840-psi seat stress. Between each test, pressures were reduced to zero and the poppet and seat separated. Seven such tests indicated a leak repeatability within 2 percent. The inlet system was then replumbed with helium, purged, and the model leakage obtained exactly as with nitrogen. The same procedure was followed using hydrogen gas, and then, as final proof of leak repeatability, with nitrogen. As before, the nitrogen leak repeated within 2 percent.

An additional comparison was made between nitrogen and hydrogen gases at low pressure (30 psig). The poppet and seat were manually controlled at a nominal gap of 0.00011 inch, and leak values obtained as above.

The 1000-psig nitrogen and hydrogen leakage data points above are plotted in Fig. 382 and 389 as a circled cross. For a more exact comparison, values of flow have been computed for the actual model geometry and gas parameters. As a computational starting point, the smooth plate gap (h_p) was calculated based upon the nitrogen test leakage. The applicability of the flow equations was established by correlation of h_p with the test model PTV roughness level and Reynolds number. This gap was then used to compute the leakage for the other gases. Gas viscosities are essentially the same for the 30- and 1000-psig conditions except for nitrogen where a viscosity of 4.3×10^{-11} lb.-min/in.^{2} was used for the 30-psig calculation. Theoretical and experimental data are presented for comparison in Table 5. Flow ratios computed from data in Table 5 are shown in Table 6.

The close correlation between theory and experiment indicated by Tables 5 and 6 provide additional verification of the flow equations. The applicability of the molecular component of flow is open to question, however, as the point of transition for the real model (D_f) is unknown.

TABLE 5

COMPARISON OF CALCULATED AND TEST LEAKAGE DATA FOR NITROGEN, HELIUM, AND HYDROGEN GASES

Gas	Inlet Pressure, P_1, psig	Calculated Gap, h_p, in.x10^6	Reynolds Number, Re	Calculated Leakage, scim			Q_M/Q	Test Leakage, scim
				Q_M	Q_L	Q		
N_2	1000	6.50	0.935	0.106	0.905	1.01	0.105	1.01
He	1000	6.50	0.132	0.281	0.848	1.13	0.250	1.06
H_2	1000	6.50	0.300	0.395	1.85	2.25	0.175	2.20
N_2	30	114.	8.99	0.98	8.74	9.72	0.101	9.70
H_2	30	114.	2.76	3.68	17.5	21.2	0.174	20.4

TABLE 6

COMPARISON OF CALCULATED AND TEST LEAKAGE RATIOS FOR NITROGEN, HELIUM, AND HYDROGEN GASES

Pressure, P_1, psig	Gas Ratio	Calculated Leak Ratios			Test Leak Ratio
		Q_M/Q_M	Q_L/Q_L	Q/Q	
1000	N_2/He	0.377	1.07	0.893	0.953
1000	H_2/N_2	3.72	2.04	2.22	2.18
1000	H_2/He	1.41	2.18	1.99	2.08
30	H_2/N_2	3.72	2.00	2.18	2.10

Work carried out by the General Electric Co. in investigation of superfinished metallic surfaces for sealing (Ref. 40) indicated that, for two optically polished, flat, annular-raised surfaces pressed together, the transition from laminar to molecular flow occurred rather sharply between 10^{-4} and 10^{-6} scim. These results were obtained for a constant seal load with inlet pressures between 500 and 1500 psig and discharge to a mass spectrometer for measuring leakage. The transition indication was provided by leak rate slope change from one (molecular) to two (laminar) on a leakage vs inlet pressure plot.

A possible explanation for the low transition may be that the leakage path of the General Electric specimens was not a parallel plate or even equivalent (sinusoidal) parallel plate model but rather composed of a few troughs or scratches. Because these leak paths would be relatively deeper than the equivalent height of the mating interfaces, the laminar regime of flow would be depressed to low values of leakage. Furthermore, the extremely smooth surfaces provided by optical finishing (see Fig. 89 for interference photo of an optical flat) with contact stresses between 4000 and 10,000 psi would indicate a large percentage of real contact area which would destroy the annular parallel plate separation model.

The consequence of a downward shift in transition would be to cause flows computed herein to be high. Considering the scope of data, however, this error loses significance. For example, from Fig. 383 at 1.4×10^{-3} scim, laminar and transitional flow ($Q_L + Q_M$) differ by a factor of 2.4. Assuming transition at 10^{-5} scim, the difference is a constant factor of 5.4 for the molecular component and decreases as the flow increases. Even if in error, the addition of the excess molecular component in considering model leakages provides a factor of safety where a large gap in very low leakage data indicates such is needed.

SURFACE TEXTURE EVALUATION TESTS

These tests relate the stress-leakage characteristic with surfaces resulting from specific fabrication processes and materials. The objective was to define the fabrication method,and the surfaces produced sufficiently well to permit analytical correlation between leakage and surface texture.

Included in this section are model surfaces produced by turning, grinding, and lapping procedures. Because of fabrication form errors, the turned and ground model complexities were such as to preclude correlation of test results. These models, however, serve as typical representations of the noted fabrication processes for comparison with the more uniform lapped surfaces.

Although not all were subjected to each fabrication method, poppet and seat materials evaluated were tungsten carbide, 440C and 17-4 PH stainless steels, and 6061 aluminum alloy. Data are presented by fabrication method category. In some instances, posttest inspection photographs are used to illustrate both unchanged before-test surface texture characteristics and local, after-test, damaged areas. Unless noted in model discussions, no visible damage was detected during posttest surface examination.

FLAT-TURNED MODELS

Four turned models, two 17-4PH stainless steel and two aluminum versions, were fabricated to evaluate both the "rough" and the best surfaces possible with available equipment. For the stainless models both poppet and seat were turned; the aluminum models were comprised of turned seats and a lapped tungsten carbide poppet.

From the inspection data of Table 4 it will be noted that the turned models (Q_f, N_f, R_f, and S_f) were out-of-flat, i.e., concave or convex tapered. In an investigation of this discrepancy, a flat ($<$ 3 microinch) tungsten carbide poppet was chucked in the Harding lathe used and indicated within

20 microinches runout. An indicator set up on the cross-feed carriage was traversed across the poppet's 1.5-inch diameter, indicating less than 0.0001 inch taper which was compatible with the Hardinge-designed concave taper of 0.0005 inch per 6 inches. Measurement of sample aluminum surfaces cut on this lathe, however, revealed that concave, convex, or crowned configurations could occur. This indicated that the dynamics of tool pressure, workpiece material, and lathe way surface variations and lubrication contributed to the noted model tapers. Later, however, it was found that the cross-feed gibs were improperly adjusted. After appropriate corrections, the taper-cutting problem appeared to be solved.

The turned surfaces, as fabricated, represented a considerable investment in fabrication and inspection time. Furthermore, they exhibited a characteristic probably common in the routine turning operation but of dimensions undetectable by normal inspection methods. Consequently, the models were tested as-fabricated. Additional testing was accomplished on a turned model in investigating the eccentric circular lay parameter. This is described in the Circular Lay Eccentricity Evaluation section.

Model Q_f, 16 AA 17-4PH Poppet and Seat

This model represents, from a valve-sealing standpoint, a relatively rough surface. Poppet and seat lands were turned from ID to OD in the same radial direction. Thus, the roughness lay with sealing surfaces mated was one of opposing fine pitch spirals.

Both poppet and seat were concave tapered approximately 22 microinches over a 0.030-inch land width for a net differential seating angle of about 0.086 degree. No significant cross-lay waviness was noted, but both parts had 20-microinch PTV, 180-degree circumferential waves. The poppet, in addition, exhibited 5-microinch PTV, 11-degree, short-period waviness.

As shown in the Proficorder traces of Fig. 329 and 330 and posttest interference photographs (Fig. 108 and 109), the turned surface texture was remarkably uniform with poppet and seat PTV roughness of 48 and 45 microinches, respectively. A 9- to 10-microinch hump extending in approximately 0.004 inch from the seat OD was noted. This land flatness deviation is shown in the cross-land profile trace of Fig. 331 which, in addition, illustrates the typical model land taper condition.

It will be noted in the data compilation of Table 4 that, assuming an h/AA ratio of 3, the Profilometer PTV height (0.0001-inch radius tip) for the poppet is approximately 36 microinches. This value is about 12 microinches less than interference microscope data indicated. However, interference photos showed that the Profilometer stylus plastically deformed the surface peaks to a depth of 8 to 12 microinches which, when added to the indicated reading, yields a PTV roughness height commensurate with other data.

Model Q_f stress-leakage data are presented in Fig. 392. (The initial 300-psig test was prematurely terminated due to a test system failure). It should be noted that the calculated stress values are predicated on two assumptions: (1) that full land width contact exists over the entire tested stress range and (2) that the pressure profile (hence balance pressure) remains constant with load. Neither are entirely correct because of the tapered contact condition.

The full land width is certainly not in contact at low stress levels. Although increased contact was developed at an elevated stress value, no known analytical method describing the deformation characteristic of this configuration exists. Accordingly, stress was based on total flat seat land area.

From the tapered contact pressure profile analysis (Leakage Flow Analysis section), it can be seen that the seat land effective pressure area increases with reduction in contact gap. This tends to reduce the computed apparent seat stress near the balance point. However, this change is minor compared with the potential effect of land width variation on calculated stress values.

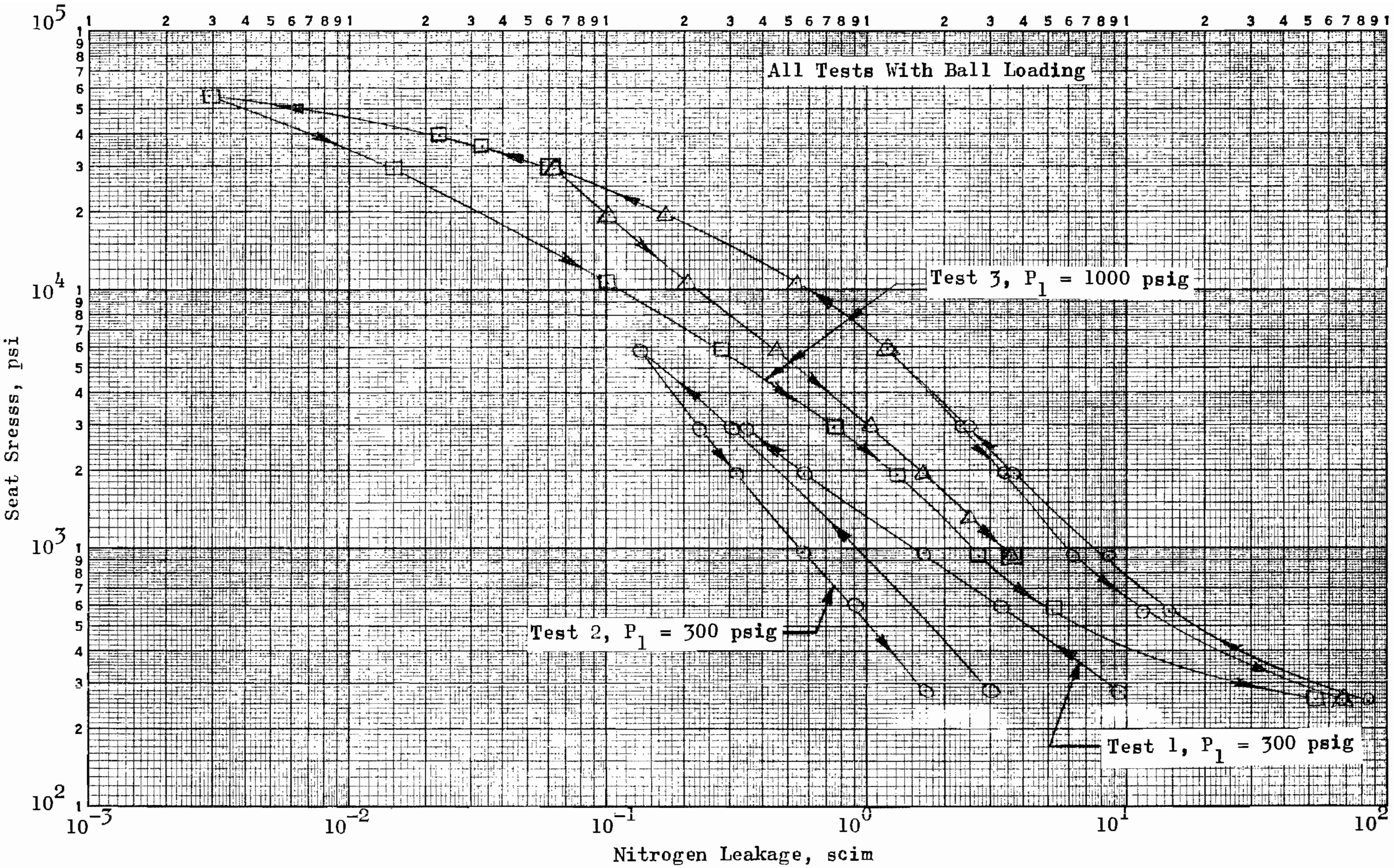

Figure 392. Stress-Leakage Data for Test Model Q_f, Tests 1, 2 and 3

Because of the tapered contact condition and circular lay, Model Q_f performance is difficult to assess. As evidenced by posttest inspection data, and stress-leakage results, slight plastic deformation occurred (as noted in Fig. 108 and 109) accounting for pronounced hysteresis effects).

Considering the very regular (0.00069-inch pitch) spiral finish of Model Q_f, it is probable that at low stress, most leakage is escaping through the spiral groove. Computing the effective laminar leakage path at the 1000-psi stress level for 3 scim indicates a spiral length of about 2.3 inches. The resultant land width establishing leakage is, correspondingly, about 0.001 inch. If this assumed model is correct, the real contact stress is undoubtedly near the material yield point(200,000 psi).

Assuming a contact yield condition, about 0.00014-inch width of real contact is required (approximately 20 percent of a single pitch) to support the 44.2-pound load for 1000-psi apparent stress.

Model N_f, 2.7 AA 17-4PH Poppet and Seat

In contrast with Model Q_f, this model represents a considerably finer turned 17-4 PH surface although the seating land concave taper condition was more pronounced. Over a 0.030-inch land width, seat deviation was 60 microinches while the poppet tapered 40 microinches for a net differential seating angle of approximately 0.19 degree. As with Model Q_f, mating lay was one of opposing fine-pitch spirals.

Both poppet and seat had 12- to 14-microinch, 180-degree circumferential waves with short period (~ 10 degrees) 2- to 5-microinch PTV superimposed waviness. A cross lay waviness deviation on the order of 5 microinches PTV was noted on both parts. Additionally, the seat had a 10-microinch hump extending in approximately 0.002 inch from the OD.

The surface texture was not as uniform as the rougher Model Q_f. However, as deduced from before test Proficorder traces (Fig. 332 and 333) and interference photographs (Fig. 110 and 111). a PTV roughness of approximately

8 microinches was achieved. Profilometer data (0.0001-inch radius tip, 0.003-inch cutoff and h/AA = 3) indicated a PTV value of about 7 microinches. Stylus-caused plastic deformation was on the order of 2 microinches; thus, Profilometer readings correlate well with other data.

Figure 393 presents the stress-leakage results obtained using the alternate 300- to 1000-psig transition test method. As with Model Q_f, the unknown tapered contact deformation characteristic led to the assumption of full land contact in computing seat stress. It will be noted that in both the 300-psig test and the first load cycle of the 1000-psig test, significant plastic deformation is indicated. The high closure rate evident is due to this deformation, occasioned by the relatively severe differential seating angle. Additionally, the tapered contact load compliance continually increases the sealing land width to reduce leakage even more.

Not only did plastic deformation occur at the seat land OD, but a more severe damage in the form of metal transfer from one sealing member to the other was evident in posttest inspection, as illustrated by Fig. 112 and 113. It is probable that this damage occurred during the second 1000-psig test stress cycle (triangles) since, after return to the 300-psi stress level, leakage was more than 10 times that of the previous cycle.

Significant hysteresis is also evident. Interim data points between conclusion of one load loop, and the high stress start of the next were not taken except for the fourth cycle (X's). The one applicable interim leakage point (3000-psi stress) is approximately twice the corresponding previous return cycle value, indicating nonplastic hysteresis.

Because of the tapered contact and relatively severe plastic deformation, correlation of surface texture with the resultant leakage characteristic is not possible. However, additional data are presented later for a similarly turned model which had less than 10 microinches taper (see Model NN_f).

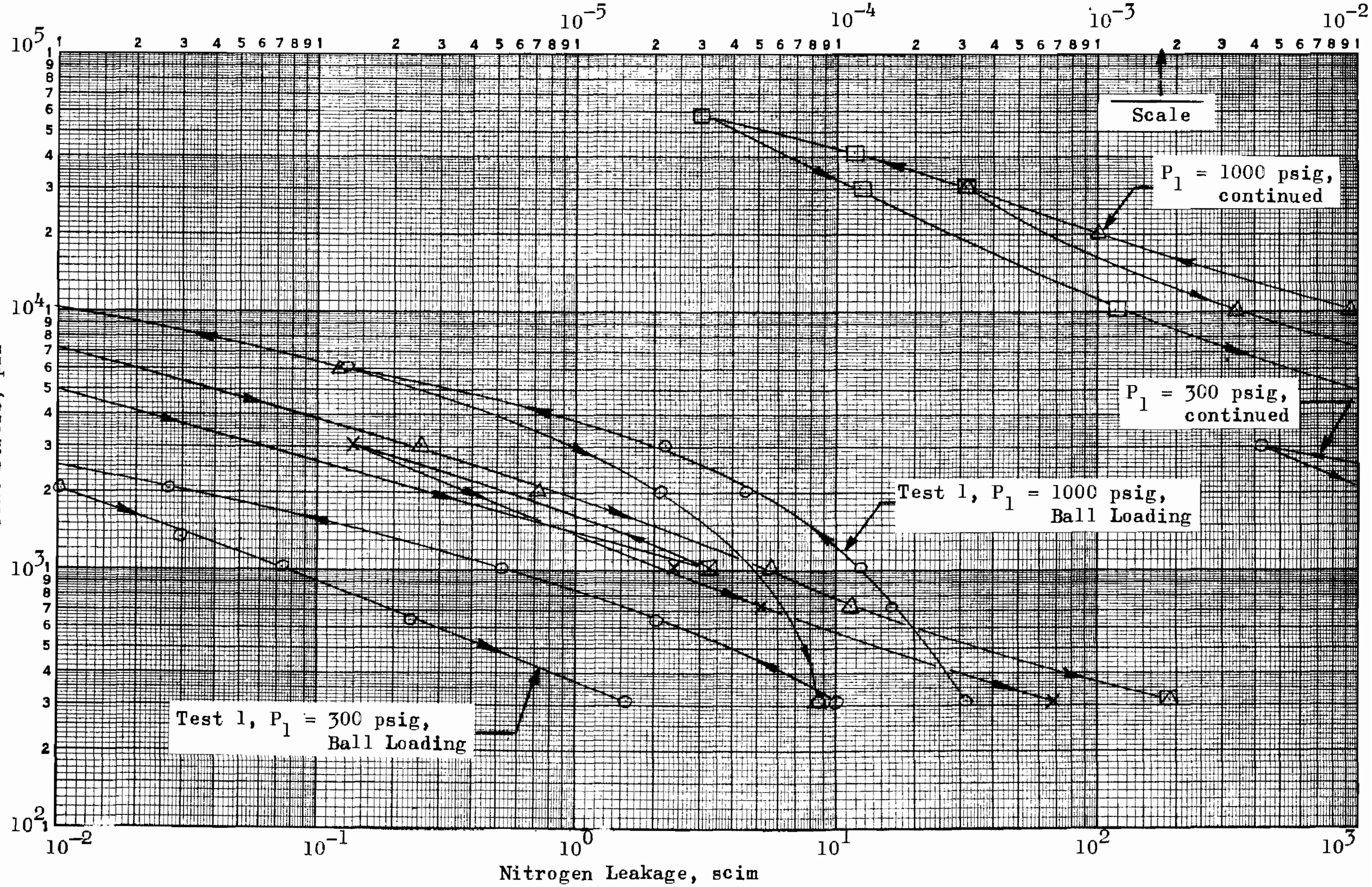

Figure 393. Stress-Leakage Data for Test Model N_f, Test 1

Model R_f, 40 AA Aluminum Seat and 0.3 AA Tungsten Carbide Poppet

In some valve applications, unanodized aluminum is used for fluid compatability reasons. Because of aluminum's poor resistance to abrasion, however, a different mating material is employed. For tests of turned aluminum models, the noted tungsten carbide poppet provided the mating material and, furthermore, represented the most perfect surface then available. Thus, it appeared that the sealing characteristics of the turned aluminum surface could be evaluated without mating member influence.

Model R_f seat roughness precluded assessment of the surface texture with interferometric methods (Fig. 114). Light-section microscopy inspection indicated a PTV dimension of 120 microinches, estimated accurate to ±20 microinches. The microscopically viewed surface correlated, comparatively, with that of a "Caliblock" certified as a 29- to 34-microinch AA finish.

While stylus instruments of small radii (0.0001 to 0.0005 inch) plow deep tracks in unanodized aluminum, a posttest Proficorder trace using a 1/32-inch radius tip was taken to evaluate seat taper condition. The part was concave tapered to a much lesser degree than previously described models with 6 microinches over the 0.028-inch land width (0.012 degree) noted. A 12-microinch hump over 0.003 inch at the land OD was also observed. Cross lay waviness was on the order of 10 microinches PTV.

An interference photograph of Model R_f poppet (also used with Model S_f) is shown in Fig. 115. Combined inspection data for this unidirectional lay and a second, similar finish but circumferential lay, tungsten carbide poppet (Model CC_f), indicates both surfaces to be significantly pitted. An 18-percent density of approximately 2-microinch-deep pits was estimated with an additional 1-percent of the surface comprised of 4-microinch pits.

Model R_f was tested using the alternate 300- to 1000-psig transition procedure, as illustrated in Fig. 394 and 395. Total land width contact is presumed in computing seat stress. The data of Fig. 394 indicate a

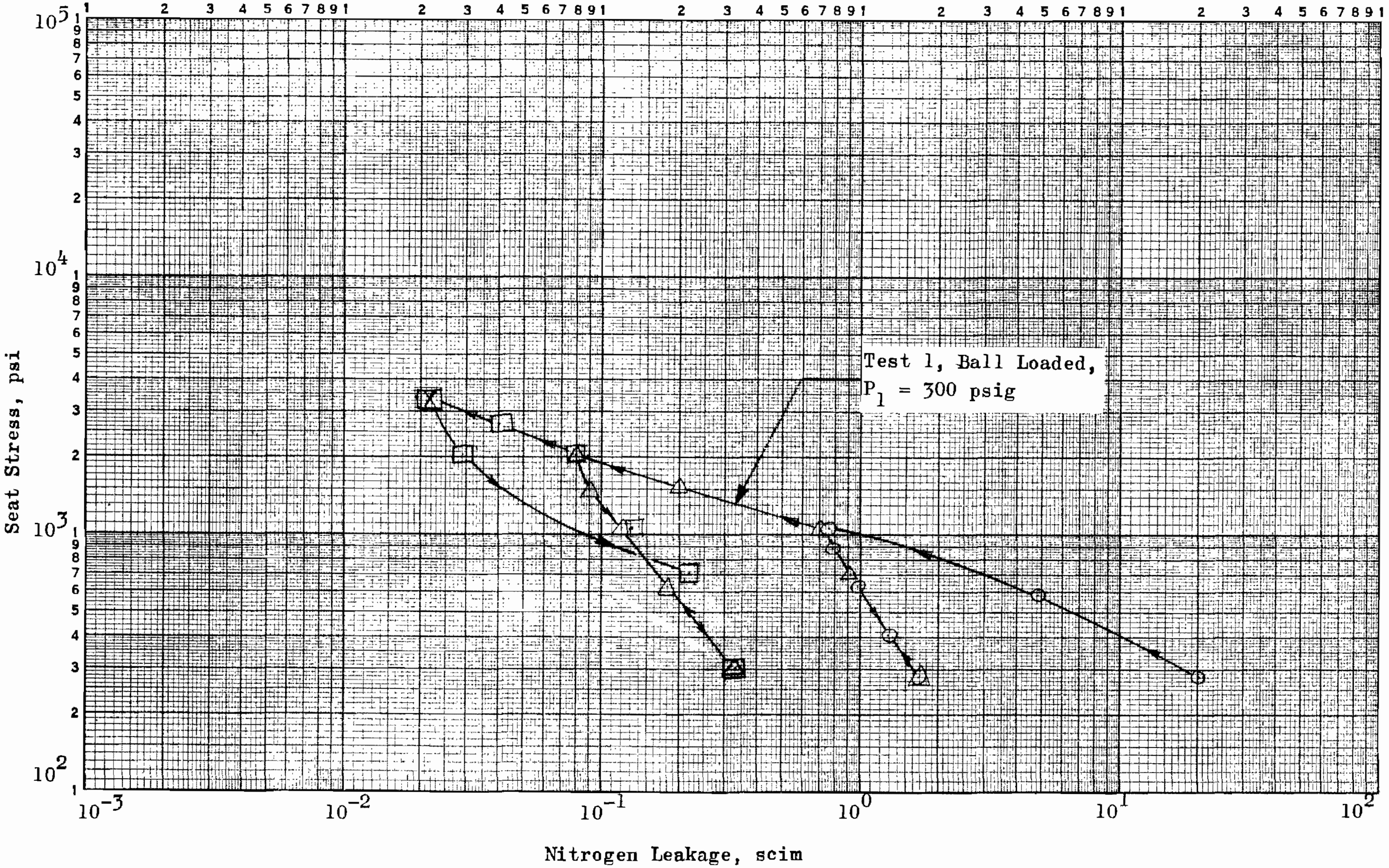

Figure 394. Stress-Leakage Data for Test Model R_f, Test 1

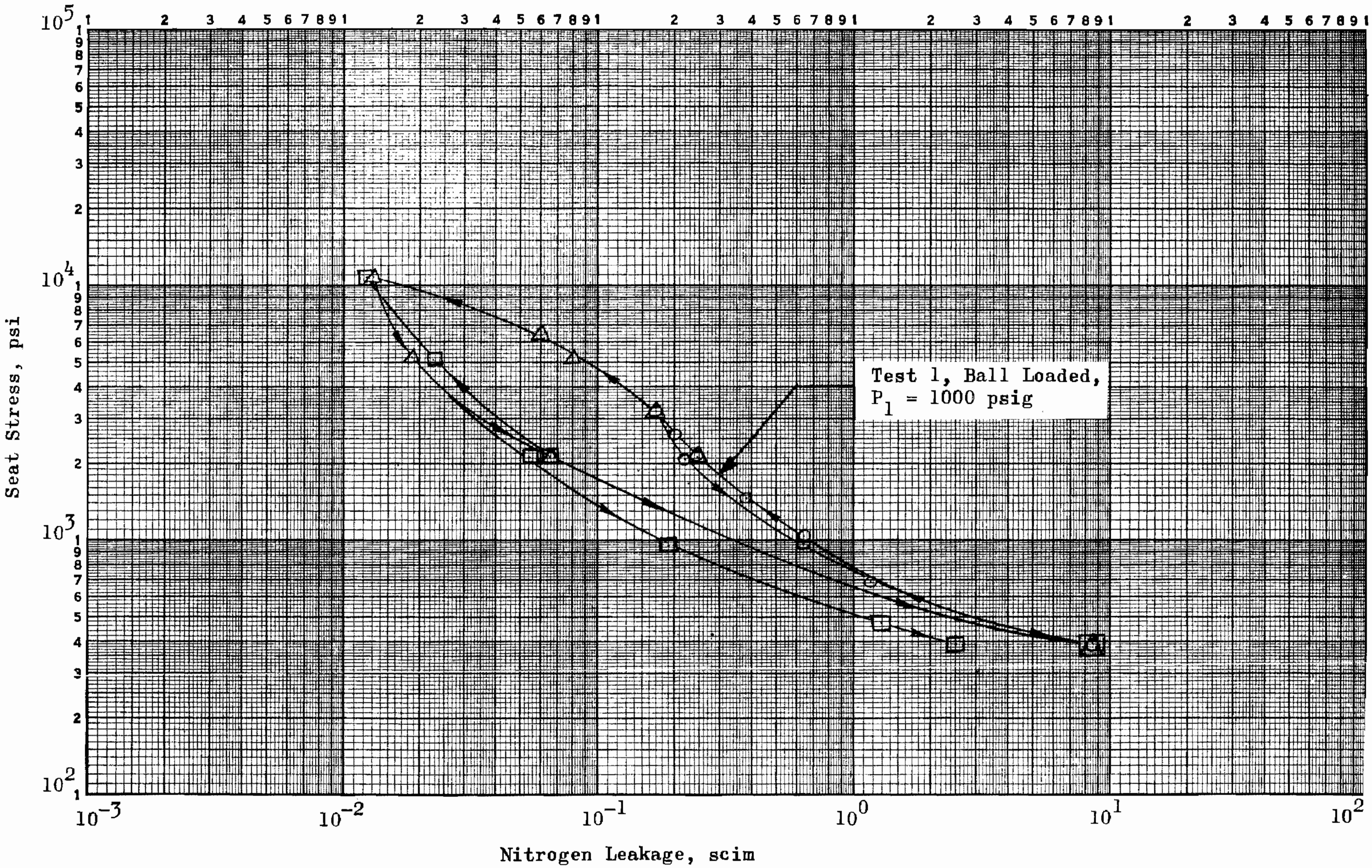

Figure 395. Stress-Leakage Data for Test Model R_f, Test 1 (Continued)

high closure rate and marked first-cycle plastic deformation. Elastic compliance following plastic flow, however, is evidenced by the repeatability of the succeeding increasing-load characteristic up to a previously stressed level. Figure 395, which shows the 1000-psig continuation of initial testing (seating surfaces not separated), reveals similar tendencies. The excellent repeatability of the initial 1000-psig test cycle to 3000-psi stress clearly shows the elastic compliance after a prestress cycle. (Seat stressed to 3000 psi maximum during 300-psig testing. Posttest inspection of Model R_f gave no real evidence of metal transfer but did reveal the presence of a 0.00035-inch-wide plastically deformed flat area at the seat OD (Fig. 116). As with previously reported models having a taper and/or ridged surface, it is probable that the majority of the sealing stress occurred at the land OD periphery where plastic flow occurred and surface texture-leakage correlation is not possible.

Model S_f, 3 AA Aluminum Seat and 0.3 AA Tungsten Carbide Poppet

Tested with the same poppet as rough Model R_f, this model represents the best turned aluminum surface fabricated. Unlike the previously described lathe-turned models, which exhibited full land taper conditions, the Model S_f seat had a composite deviation. Posttest Proficorder inspection indicated the general land profile to be high at the ID, convex tapering approximately 5 microinches over a radial distance of about 0.015 inch. From this mid-land point, three 6- to 10-microinch PTV waves extending to the OD were noted. The wave peaks were on the same general plane as the land tapered inner section, but a hump 4 to 8 microinches above this plane at the OD was evident. (This posttest inspection would not reveal plastically flowed areas.)

Roughness assessment by interference photos proved exceedingly difficult because of the profile sharpness. While PTV variations between rdiges are less than 10 microinches (Fig. 117), it is apparent that this roughness is superimposed upon a waviness of about 0.001-inch pitch which is up to 30 microinches PTV height. It is also likely that there were even higher ridges within the land and, although not microscopically observed before test, a burr certainly was raised in terminating the land OD as posttest inspection revealed.

Model S_f, was tested at 300- and 1000-psig supply pressures, as illustrated by the stress-leakage curves of Fig. 396 through 398. The alternate test procedure was used. In the plot of the 300-psig test (Fig. 396), considerable plastic deformation and hysteresis "sticking" is indicated by an extremely fast closure rate. At a 1000-psig inlet pressure (Fig. 397),first cycle data taken up to 3000 psi stress (maximum attained during 300-psig test) show evidence of hysteresis but with no sticking or appreciable plastic deformation. Leakage at 3000 psi stress is approximately 13 times greater than at the similar stress 300-psig test. This is commensurate with the leakage change to be expected from the increased inlet pressure.

However, on a second load cycle to the previously unattained stress of 10,000 psi, the sticking characteristic is again evident. Additional plastic deformation apparently occurred on subsequent load cycles as indicated by Fig. 398. From this plot and test 1 overlay, it can be seen that leakage on the order of 2×10^{-5} scim was achieved at only 3000 psi as compared with the 10,000-psi level necessary on the initial high-stress loop. The sticking phenomenon was due to metal transfer from seat to poppet as shown in Fig. 117 and 118. Apparently, the aluminum seat material flowed into and was retained by the pitted tungsten carbide surface at high ridge areas. This transfer occurred at approximately mid-land, where the aforementioned taper discontinuity existed. Some PTV reduction plastic deformation probably occurred here also. As shown in Fig. 119, the seat OD hump was also plastically deformed; this probably occurred during the initial 300-psig test and accounts for the pronounced closure rate previously noted and the very low leakage. No gross plastic deformation of the land occurred as shown by the profile records and comparison with lapped Model K.

The evidence established from this model indicates that unanodized aluminum should not be mated with the characteristic pitted surface of tungsten carbide for a cyclic requirement. Whether or not metal transfer to

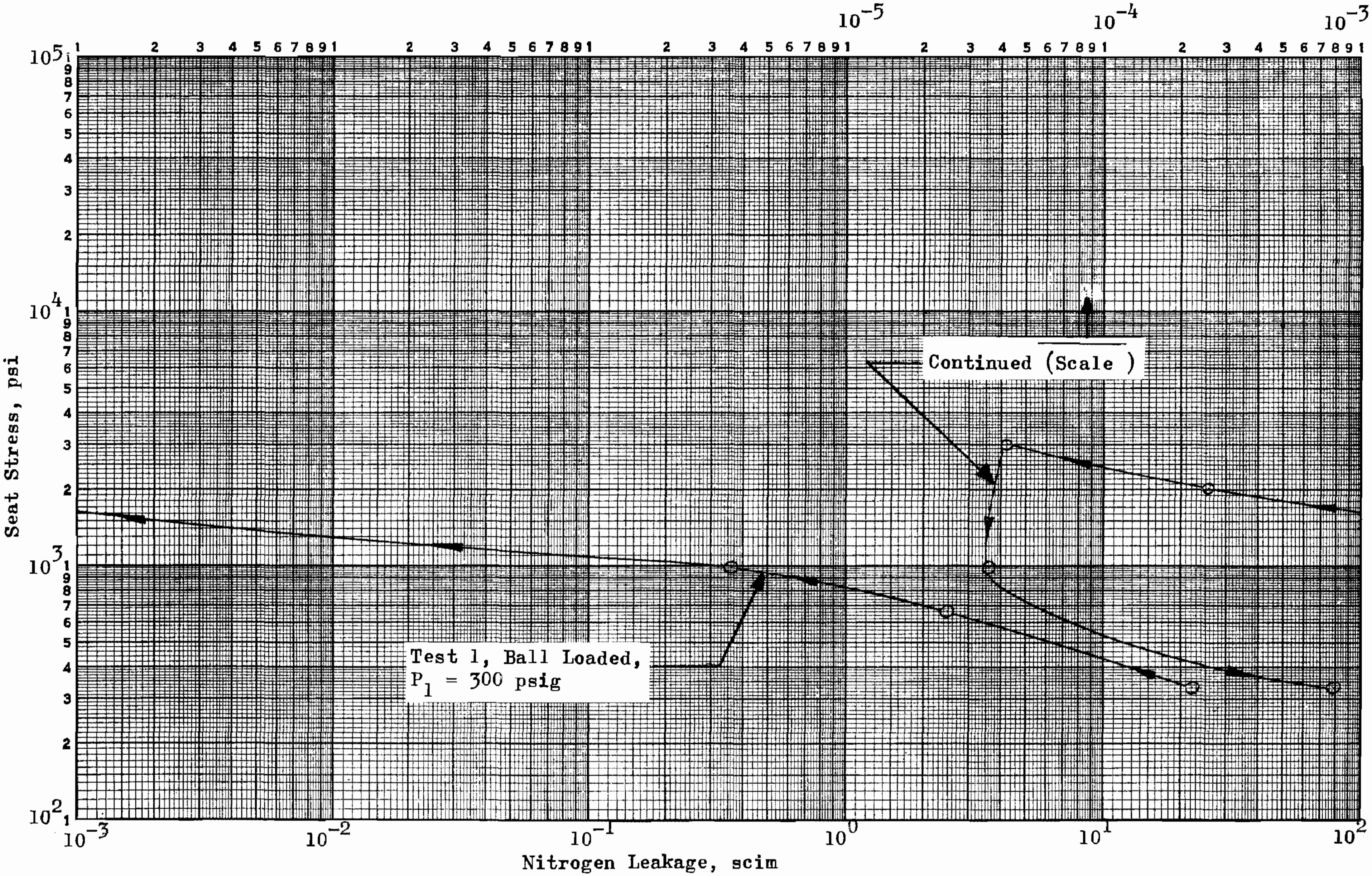

Figure 396. Stress-Leakage Data for Test Model S_f, Test 1

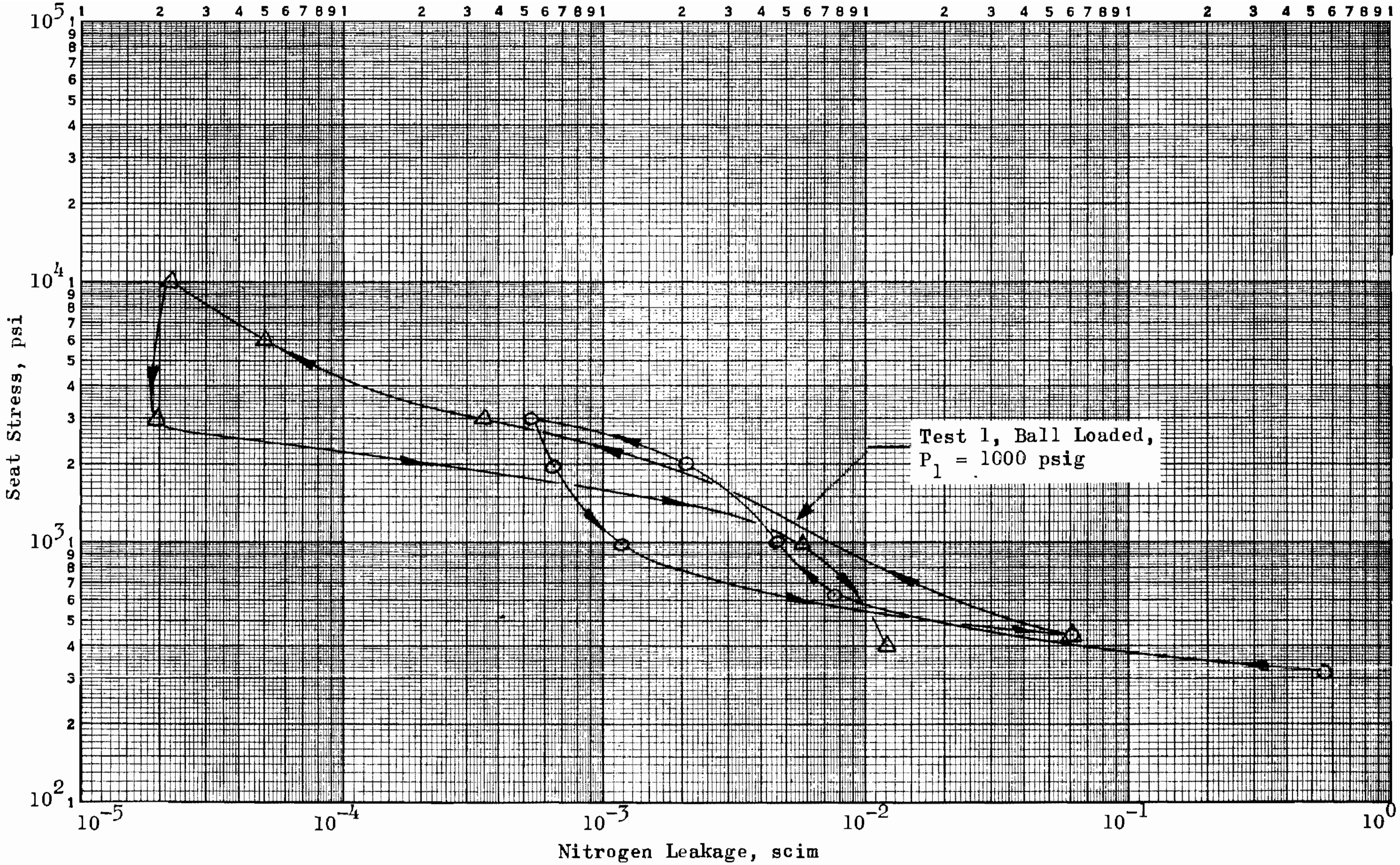

Figure 397. Stress-Leakage Data for Test Model S_f, Test 1 (Continued)

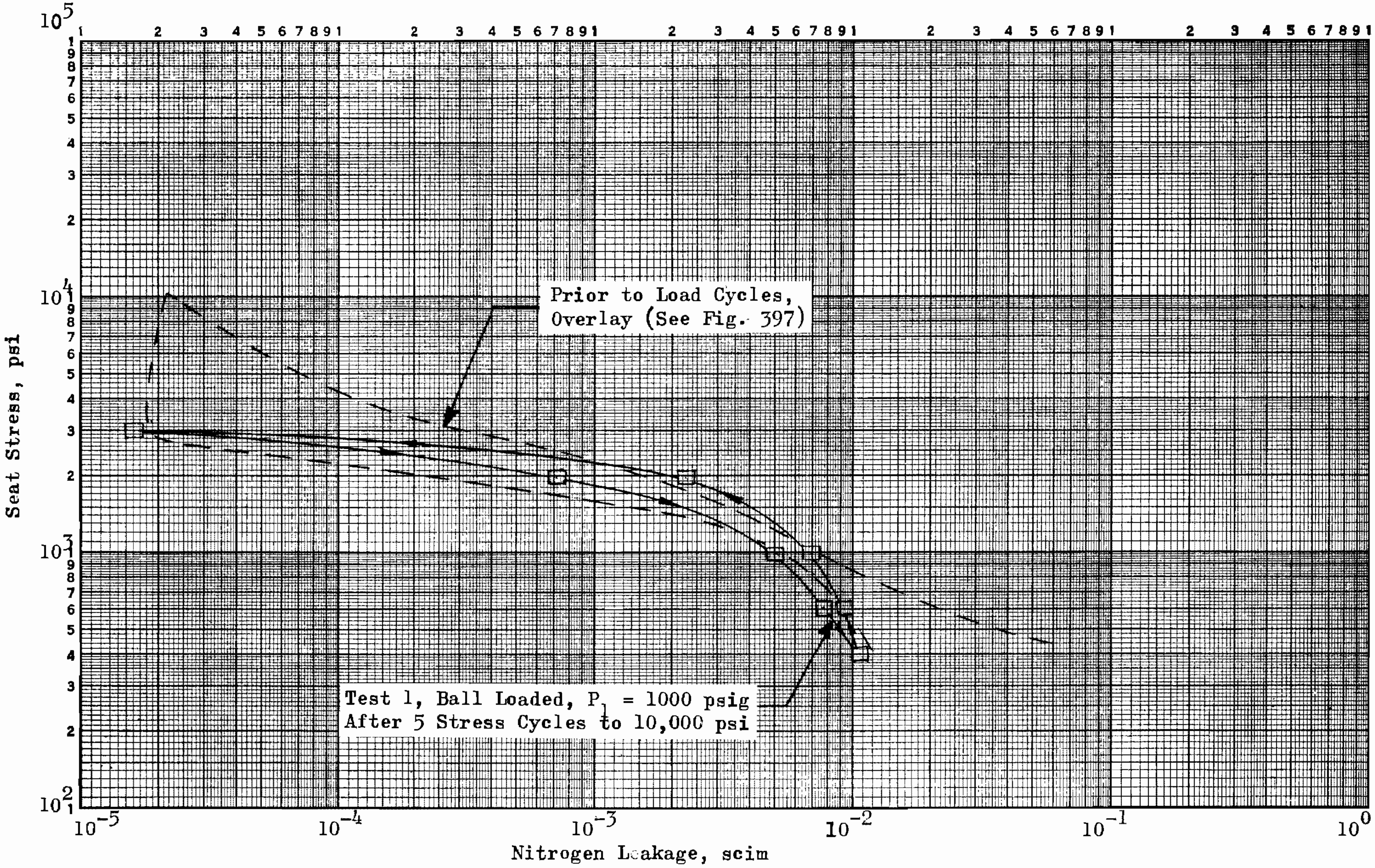

Figure 398. Stress-Leakage Data for Test Model S_f After Load Cycles, Test 1

a smooth, fine-finish, stainless-steel surface would occur has not been established. As discussed later (Plating and Coating Evaluation Tests), the anodized aluminum surfaces of Models U_f and V_f, though untapered, gave little indication of surface or substrata plastic deformation.

FLAT-GROUND MODELS

Two 440C steel models were fabricated for evaluation of surfaces ground to a roughness level comparable to lapped models. Model D_f was unidirectionally ground while Model A_f had an apparent circular lay. (As noted in the model fabrication section, the latter surface was comprised of a series of tangential cuts, discontinuous but in a circular direction.) The surface characteristic of both models was one of waviness in which a succession of ever-decreasing PTV height waves were superimposed on one another. Assessment of these surfaces was largely subjective (as with some lapped models), and Profilometer readings were utilized as a reference datum. The roughness PTV heights recorded in Table 4 represent average values over a 0.001- to 0.003-inch cutoff width.

Model D_f, 2.7 AA Unidirectional Lay 440C Poppet and Seat

The interference photographs of Fig. 120 through 122 and profile records of Fig. 334 and 335 typically illustrate Model D_f sealing surfaces. From these data, supported by Profilometer readings (presented in Table 4), poppet and seat roughness heights were estimated at 6.0 and 8.0 microinches PTV, respectively. Circumferential waviness varied depending on lay orientation (across or with lay). The poppet (Fig. 336) exhibited a 5-microinch PTV waviness height with wavelengths ranging from approximately 0.030-inch (cross lay) to 0.126-inch with lay. Similarly, the seat (Fig. 337 and 122) had 5-microinch PTV, 0.084-inch period with-lay waves, and 5- to 10-microinch PTV 0.025-inch wavelength cross-lay deviations. In addition, the seat evidenced two 180-degree period, 10- to 14-microinch PTV waves.

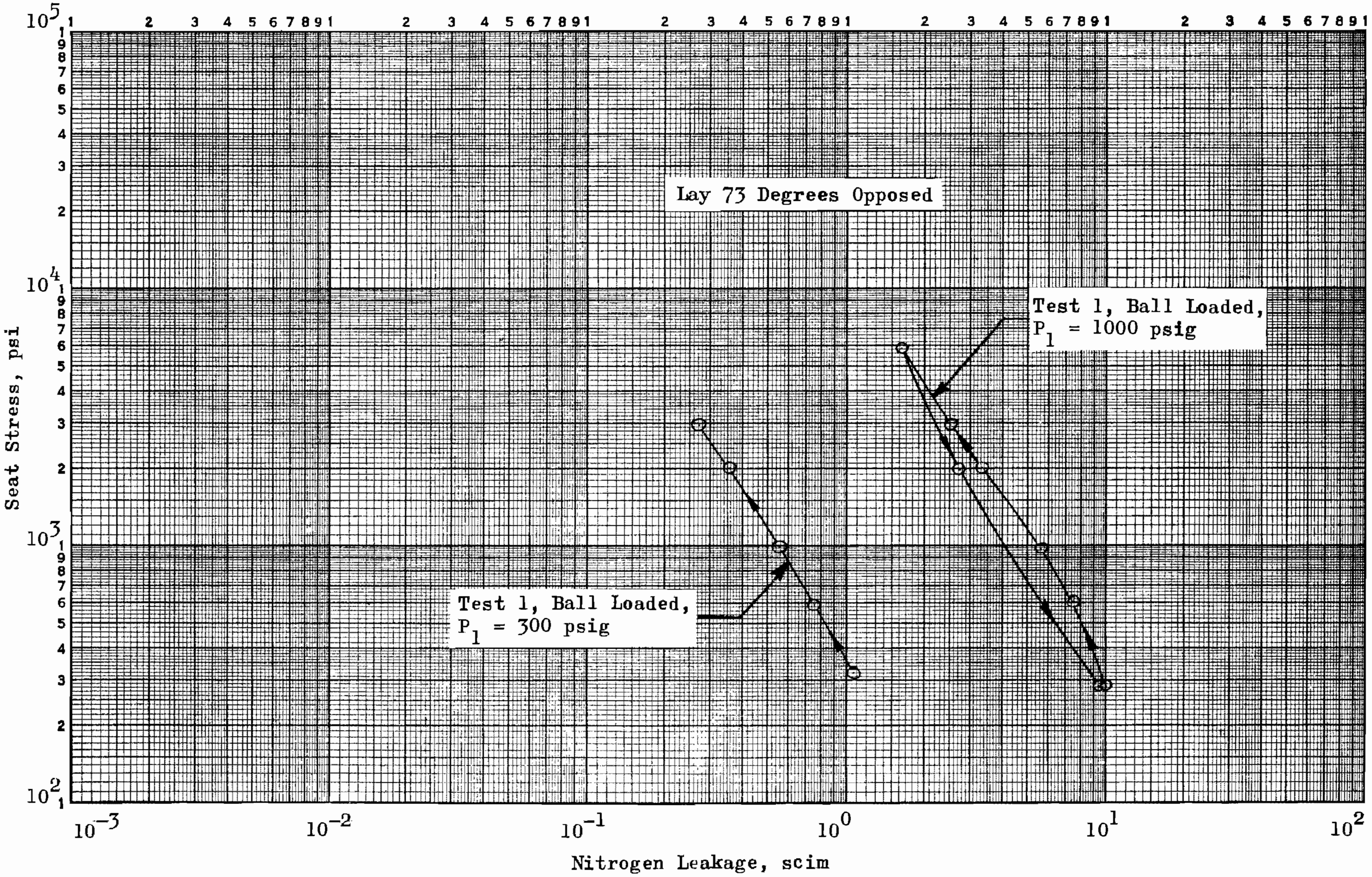

Figure 399. Stress–Leakage Data for Test Model D_f, Test 1

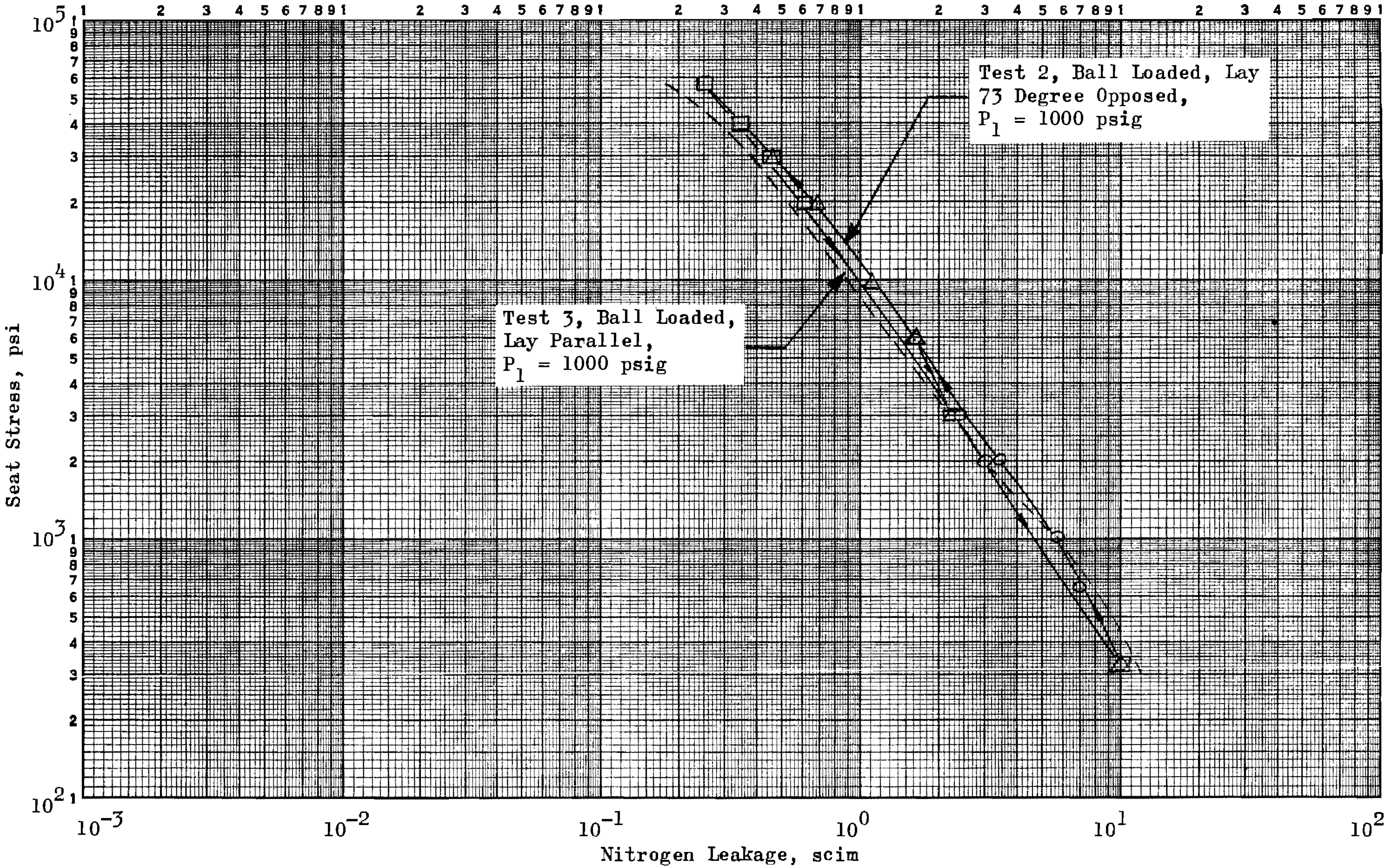

Figure 400. Stress-Leakage Data for Test Model D_f, Tests 2 and 3

Model D_f was tested three times, twice with the lay approximately 73 degrees opposed and once with near parallel lay as illustrated by Fig. 399 and 400. The initial test (Fig. 399) started with a 300-psig supply pressure and, after transition to 1000 psig (alternate test method), was continued at the elevated pressure. Due to low P_c bottle pressure, however, test 1 was terminated after reaching only 600 psi stress. Test 2 (sealing surfaces separated during bottle change) was subsequently performed and, as shown in Fig. 400, a stress of 56,000 psi was attained. The data were extremely repeatable with virtually no hysteresis evident. It is interesting to note that this model, straight from the grinder, leaked only 3 to 5 times more than the commonly employed 2 AA multidirectional lapped surface. (Refer to Model B, Test 4 discussed later).

After completion of test 2, the poppet was rotated to bring the two surface lays parallel within less than 5 degrees. Model D_f was then retested to the 56,000-psi stress level (Test 3, Fig. 400). The results were so similar that, for clarity, test 3 is represented only a dashed line without data point symbols. The lack of change may be attributed to: (1) surface waviness deviations, effective regardless of lay orientation, (2) cross-feed variations on the two parts during fabrication, causing different and nonuniform lay "pitch", and (3) the improbability of achieving perfect lay alignment. Even if the first two problems were solved, it is apparent that in the practical application, parallel lay orientation to reduce leakage offers little promise.

Model A_f, 2.3 AA Circular Lay 440C Poppet and Seat

Both Model A_f poppet and seat roughness heights at 0.001- to 0.003-inch cutoff were estimated at 7 microinches PTV. The interference photographs of Fig. 127 and 128 together with Fig. 338 and 339 roughness profile records were used for this assessment, substantiated, as with Model D_f, by Profilometer readings. Having circular lay, Model A_f did not give evidence of the variable circumferential waviness characteristic noted with D_f; significant waviness, however, was observed.

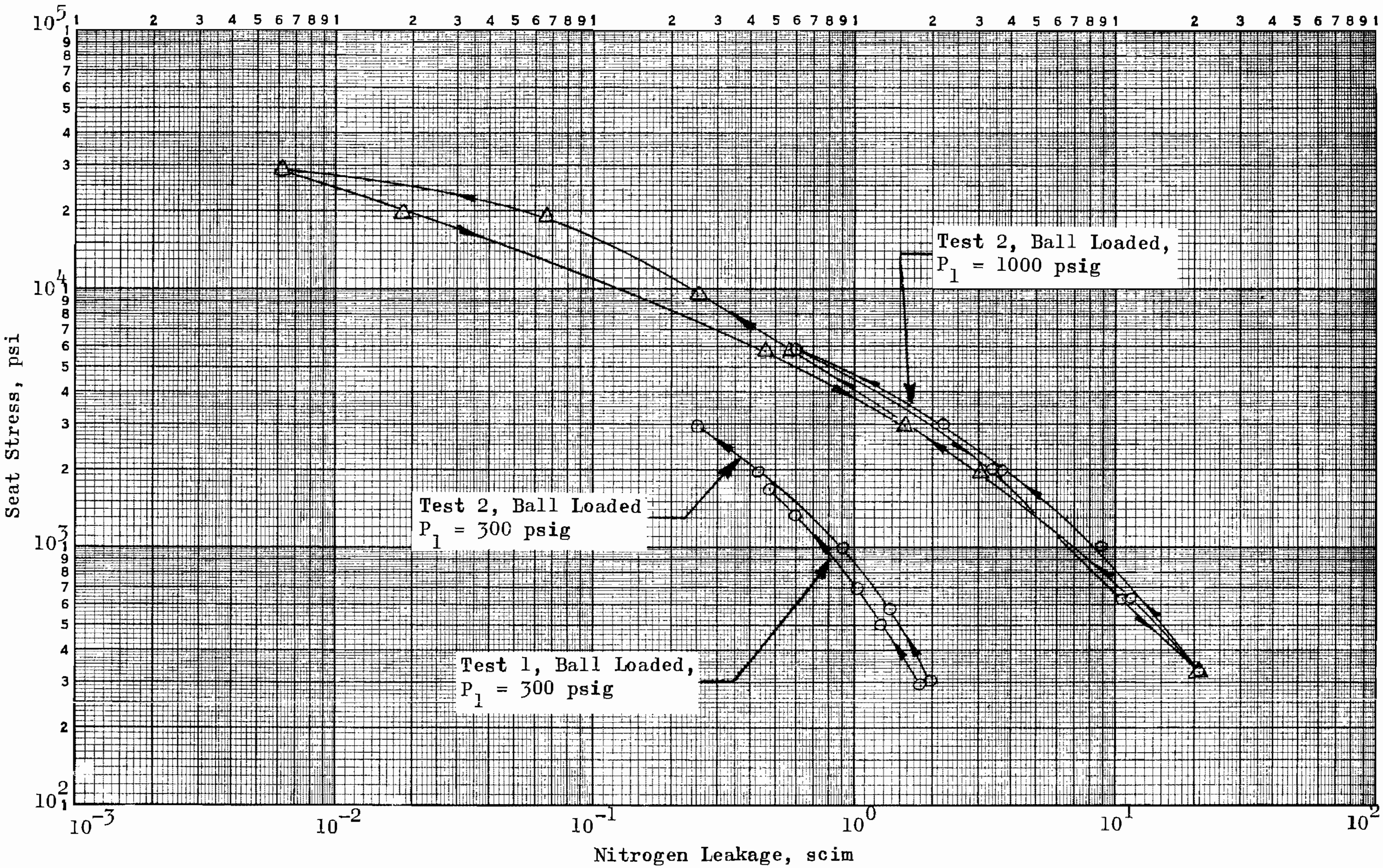

Figure 401. Stress-Leakage Data for Test Model A_f, Tests 1 and 2

From the circumferential waviness profile record of Fig. 340, Model A_f poppet had two 180-degree-period (only one-half shown because of long trace), 10-microinch PTV major deviations with 12- to 15-microinch PTV short wavelength (0.037-inch) superimposed waves. The seat (Fig. 341) short wave characteristic was about the same as the poppet's, but about 25 microinch PTV 180-degree-period waves (also one-half shown) were noted.

Two tests were performed on Model A_f, as illustrated by Fig. 401. Test 1, at a 300-psig supply pressure, was terminated prematurely because of facility problems. Using the alternate test method, test 2 was begun at 300 psig, followed by the transition to 1000 psig, and in two successive loops, a maximum stress of 29,000 psi was attained.

A comparison of Model A_f with its unidirectional lay counterpart, D_f (P_1 = 1000 psig) illustrates the superiority of the circular lay finish over attempts to align a unidirectional version. At stress levels up to 2000 psi, D_f by virtue of smaller waviness deviations, leaks slightly less than A_f. Above a 2000-psi stress, however, Model A_f exhibits the much faster shutoff rate characteristic of circular lay, as described in the seating analysis. Furthermore, by 2000-psi stress, the large radial troughs caused by circumferential waviness have been nearly closed. This is indicated by the sinusoidal model height of 13.7 microinches (correponding to 3.5 scim leakage at 2000 psi stress) compared with the assessed PTV roughness of 14 microinches. Had this waviness been avoided in fabrication (as with Model D_f), leakage at 2000 psi stress would be reduced by about a factor of 3.

FLAT-LAPPED MODELS

The bulk of surface texture evaluation was performed with lapped models for two basic reasons. First, the lapping process affords the only currently practical means of producing the ultralow leakage sealing surfaces required of advanced rocket engine valves. Secondly, considerable lapping technology, both in methods and materials, has been established.

In general, models are discussed in fabrication chronological order, thus reflecting improvements in finishing technique and geometrical consideration dictated by test results. Models reworked to eliminate damage or poor performance characteristics, but with approximately the same roughness level as their former configurations, are reported together.

The major problem necessitating rework was that of seat land corner damage caused by stress concentration at the edge discontinuity. This type of failure occurred on early diamond-lapped models fabricated with sharp edges commonly considered necessary by most lapping practitioners. As the contact pressure distribution analyses and experimental results indicated, the sharp-edged condition is undersirable. (Posttest inspection lagged the test operation somewhat; thus, four model seats incurred corner damage before the problem was fully recognized.)

Subsequently, all existing model seats were reworked by lapping 0.001- to 0.002-inch radii at OD and ID corners. New models employed a supporting 0.002-inch, 45-degree chamfer. Additionally, a succession of geometrical changes designed to obviate the problem were evaluated. Configurations from a flat with large tangential radii (dubbed) to the ultimately determined optimum geometry of a full-crowned land were fabricated and tested.

It is interesting to note that the dubbed corner condition occurs naturally with the lapping process and is often difficult to avoid, particularly in polishing and wet slurry multidirectional lay lapping. Thus, with the initial contract models so fabricated, a sufficient corner dub was generated to preclude land corner damage.

With leakage as the prime comparison parameter, lapped model surfaces were fabricated and tested to fulfill several purposes:

1. To compare the performance of several typical surfaces (as produced on various materials) currently employed in the valve industry. These represent the common machine or manual aluminum oxide wet slurry, multidirectional lapped surfaces

2. To investigate the more readily defined but less commonly used "dry" diamond-lapped surfaces for comparison with the wet slurry process noted above
3. With the diamond-lapped surface, evaluate the influence of lay orientation, i.e., parallel or perpendicular unidirectional lay and unidirectional vs circumferential
4. Evaluate the potential of geometrical configurations intended to obviate the aforementioned seat land corner damage
5. Investigate the performance reproducibility of several ~ 1 AA diamond-lapped, unidirectional lay surfaces adopted as a "standard" for concurrently performed cycle tests
6. Compare the basic effect of changing PTV roughness level
7. Identify the contribution of scratches to the leakage obtained at various surface textures

Model D, 6.3 AA Multidirectional Lay 440C Poppet and Seat

This model, in conjunction with Models C (4.7 AA) and B (2.2 AA) was formed to evaluate one of three levels of multidirectional lay surface roughness. As previously noted, assessment of this type of surface is most difficult with interferometric techniques. Even had very narrow bandwidth procedures been employed, it is doubtful that with so rough a surface (Fig. 129), definitive data could have been obtained. Thus, Profilometer and Proficorder information formed the basis for surface description.

Model D poppet exhibited both wavy and nodular characteristics in addition to an average roughness PTV height of 19 microinches as deduced from the poppet profile trace of Fig. 342. Waviness on the order of 5 microinches PTV was noted together with a 4.4-percent density of 5-microinch-high nodules. Although Profilometer data indicated a slightly rougher surface, the seat was similar to the poppet.

Model D was tested in the clamped condition at a 300-psig inlet pressure. As indicated by the test results of Fig. 402, two stress loops to 60,000

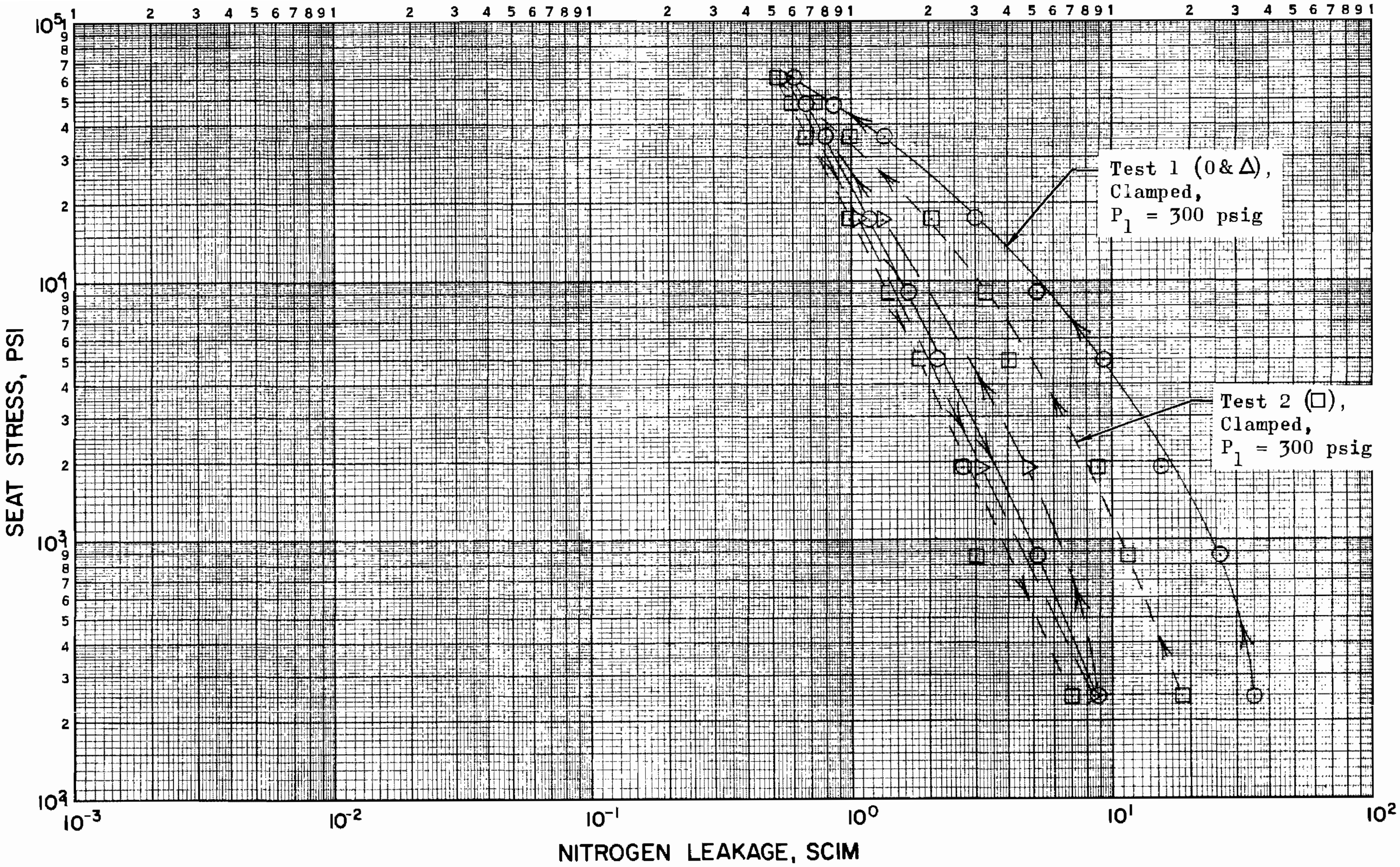

Figure 402. Stress-Leakage Data for Test Model D, Tests 1 and 2

psi were initially performed (test 1). The surfaces were separated and, without reorientation, were subjected to an additional two cycles to 60,000 psi (test 2).

The initial load cycle of test 1 shows considerable plastic deformation evidence which may be attributed to nodule compression. While some hysteresis is present in the second cycle, identical first- and second-cycle, low stress return points indicate general elastic compliance. The reappearance of the plastic characteristic on the first cycle of test 2 is indicative of surface disruption at separation.

Model C, 4.7 AA Multidirectional Lay 440C Poppet and Seat

Model C was the intermediate model in the series of multidirectional lay surface evaluation tests. Poppet and seat surfaces were similar with an average PTV roughness height of 14 microinches. Waviness on the order of 5 microinches PTV and a 5.4-percent density of approximately 3-microinch-high nodules was also noted. The Proficorder trace of Fig. 343 is representative of both surfaces.

Model C was tested in the clamped condition at both 300- (test 1) and 1000-psig inlet pressures (test 2). As indicated by the test results (Fig. 403), considerable plastic deformation occurred during the initial test 1 load cycle. Slight hysteresis and plastic deformation is evident on the following cycle, but the latter performance was, essentially, one of elastic compliance. Similarly, test 2 at 1000 psig shows, basically, an elastic characteristic.

Model B, 2.2 AA Multidirectional Lay 440C Poppet and Seat

Smoothest of the multidirectional lay series, Model B poppet and seat surfaces were not as similar as those of Models C and D. Examination of

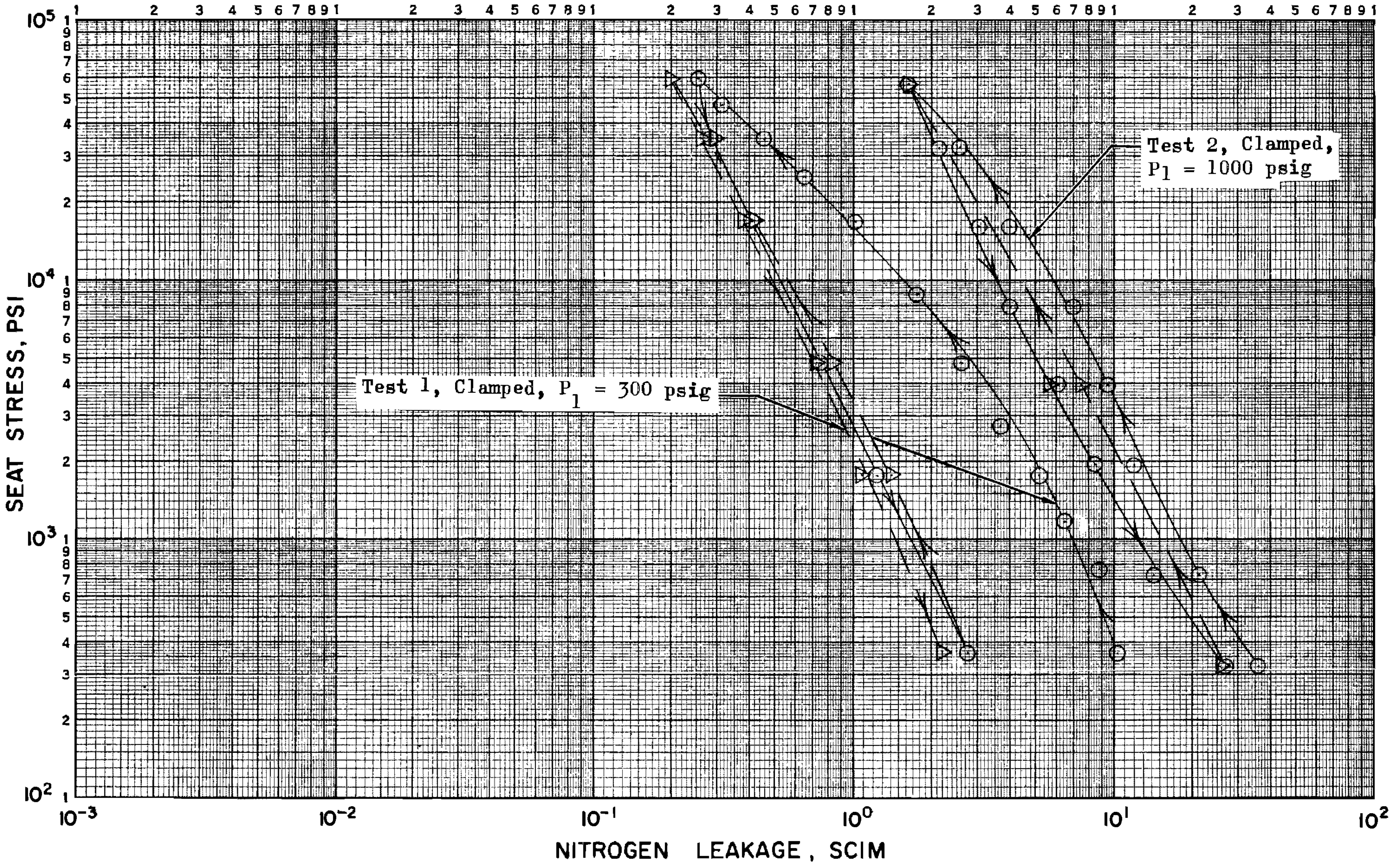

Figure 403. Stress-Leakage Data for Test Model C, Tests 1 and 2

the Proficorder trace and interference photo of Fig. 344 and 130, respectively, indicates a poppet surface roughness PTV height of 4.5 microinches. The seat was slightly rougher at 6.6 microinches, as deduced from the seat profile record (Fig. 345). As illustrated in the interference photo of Fig. 131, the seat land was concave some 2 to 3 microinches (an unusual condition). Both surfaces contained nodules 3 to 4.5 microinches high.

The first stress-leakage information obtained on Model B was run at 300 psig with the poppet in a clamped position. Test data for this configuration are shown as test 1 (Fig. 404), representing the first and second test loops and show that slight plastic flow had taken place in the first cycle.

Test 2 (Fig. 405) represents the sixth cycle on this test surface and was conducted at 1000 psig with the ball-loading device. To recheck the data of test 1, test 3 was conducted at a 300-psig inlet pressure with the ball-loading device. The results of test 3 are plotted along with an overlay of test 1 which indicates that the stress-leakage characteristic has not changed with cycles. The difference between the two curves at low-stress levels is attributed to the clamped vs unclamped (ball) loading methods. (Clamping the poppet to the piston results in a potential out-of-parallel condition which may be as much as 10 microinches over a 1/2-inch seat diameter.)

Model J, 2 AA Multidirectional Lay 17-4 PH Poppet and Seat

Model J and aluminum model K, to follow, were tested to evaluate the material parameter effect on sealing performance. The 17-4 PH steel has the same elastic modulus as 440C; however, its yield strength is approximately three-fourths that of 440C. Tests with 17-4 PH were performed to determine if decreased strength would have any effect on the stress-leakage characteristic. The aluminum model was included to investigate any changes resulting from a different modulus of elasticity. Both models were multidirectional finished to approximately 2 microinch AA for comparison with 440C Model B.

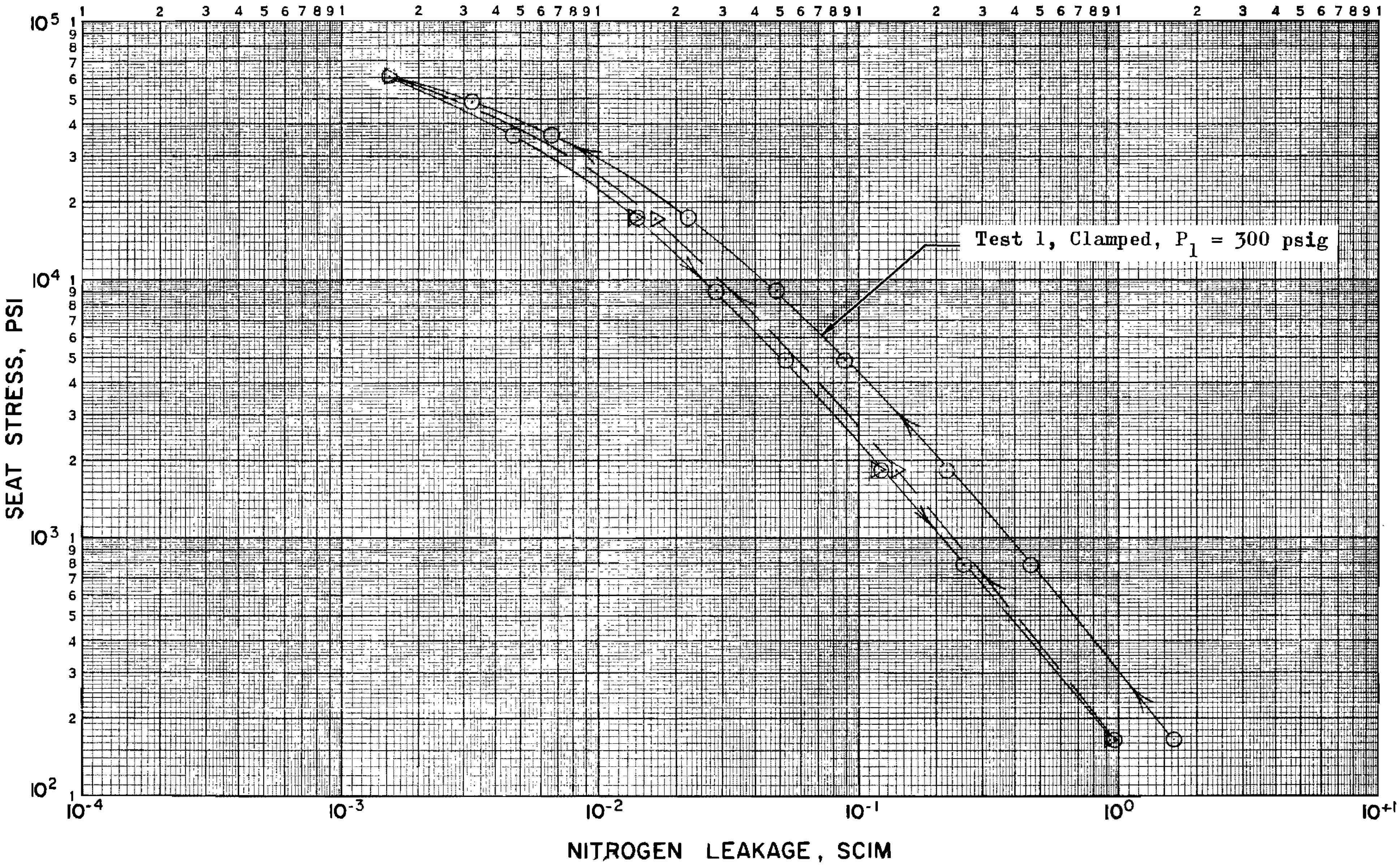

Figure 404. Stress-Leakage Data for Test Model B, Test 1

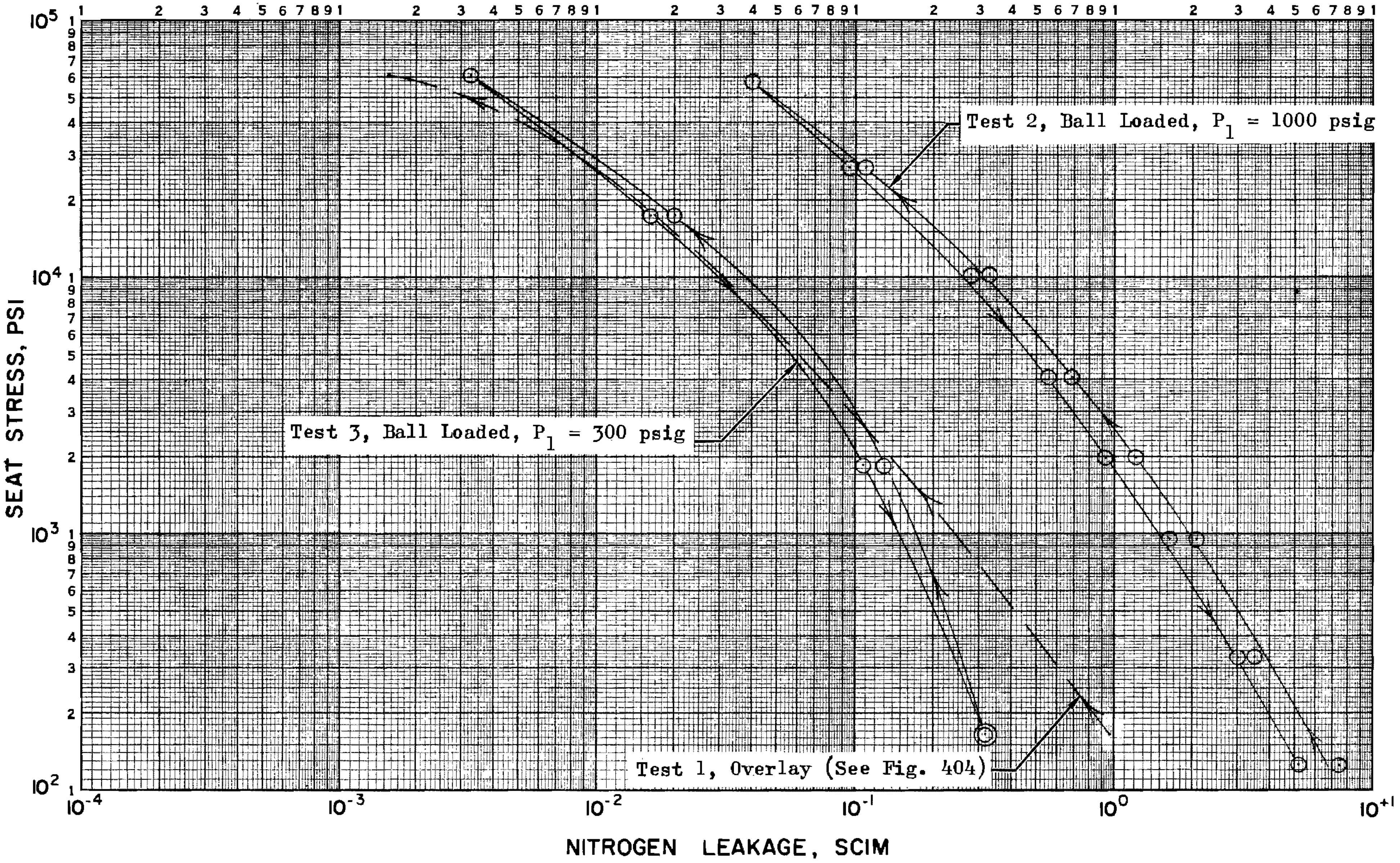

Figure 405. Stress-Leakage Data for Test Model B, Tests 1 through 3

Test Model J surface texture was very similar to Model B except that there were no nodules on J. Model J poppet and seat had essentially the same surface texture. The average asperity height was 6 microinches as measured by the Proficorder trace (Fig. 346) and the interference microphotographs of Fig. 132 through 134. While no sifnificant waviness or nodules were noted, the seat land was concave similar to Model B (about 2 microinch, Fig. 134).

Model J was tested twice at a 300-psig inlet pressure with the ball-loading device installed. As shown in Fig. 406, test 1 was the first cycle and test 2 was a repeat cycle after poppet-seat separation to check for contamination. The seat was carefully examined, and the system was purged with nitrogen; however, noting the high leakage at low stress for both tests, it must be concluded that the contamination was not removed. A comparison of Model J high-stress leakage data with those of test Model B (Fig. 405) shows very close correlation. It is concluded from this comparison that the two materials, 440C and 17-4PH essentially have the same stress-leakage characteristic, and that variations of yield strength do not influence these characteristics. However, it is presumed further that if the two materials had been tested into regions of gross plastic surface stress, significant differences would have resulted.

Model K, 2 AA Multidirectional Lay Aluminum Poppet and Seat

As with Model J, this model was multidirectional finished to approximately 2 microinches AA for comparison with 440C Model B.

Since stylus instruments cause gross plastic deformation on an unanodized aluminum surface, the interference photos of Fig. 135 and 136 were used to assess surface texture parameters for this model. The surface was very similar to that of Model B with a PTV roughness height estimated at 6 microinches. Unlike Model B, however, the aluminum model contained 5-microinch scratches over about 6 percent of the surface. (Several unsuccessful attempts were made during the lapping operation to eliminate

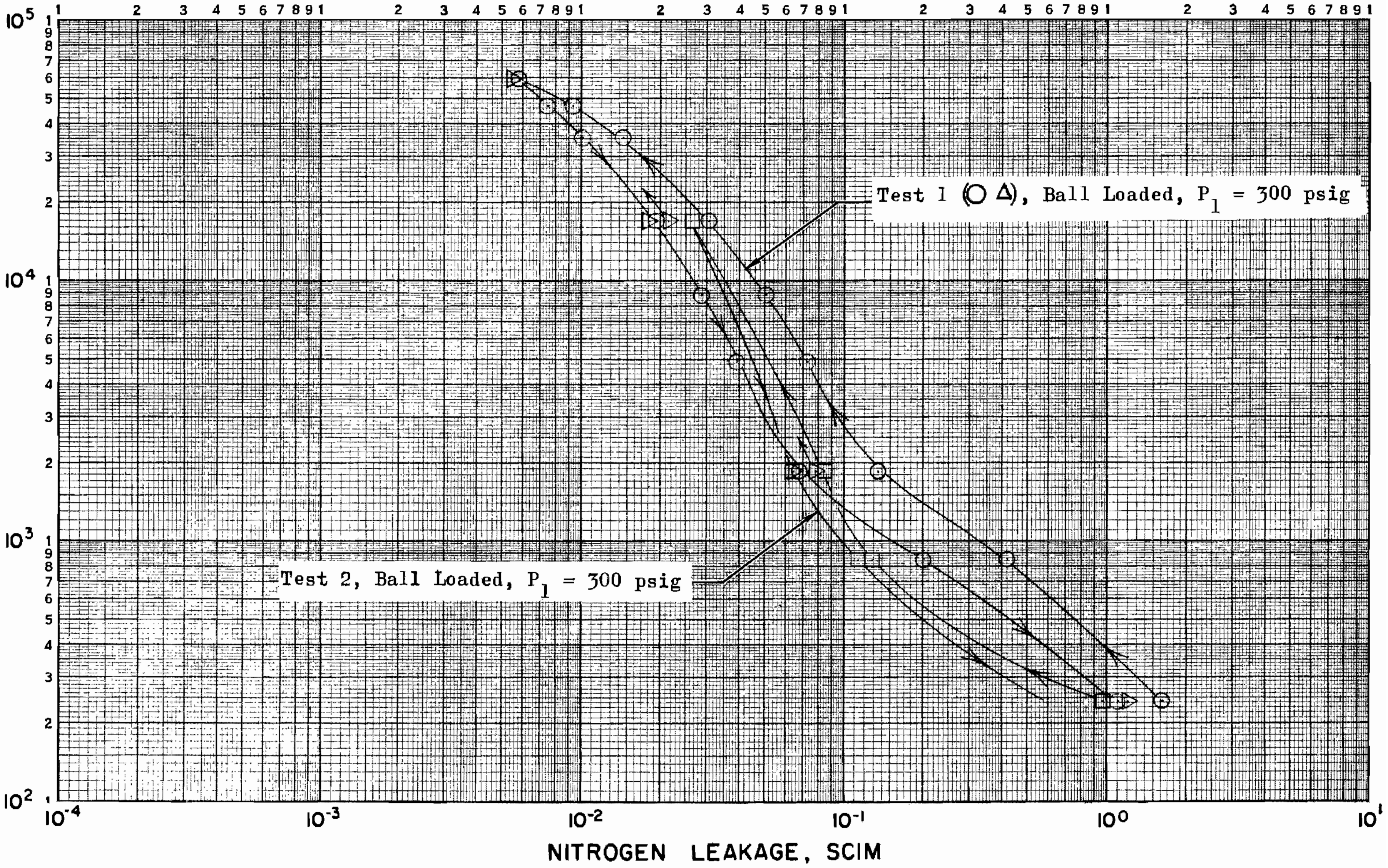

Figure 406. Stress-Leakage Data for Test Model J, Tests 1 and 2

these scratches.) Because of the small number of scratches, however, it was concluded that this model surface texture approximated the 2-microinch AA surface of Model B, so that the eleastic modulus factor could be viewed independently.

Model K was tested initially in the clamped condition with one load cycle to 50,000 psi (test 1, Fig. 407) nearly twice the aluminum bulk yield strength. Although not too evident from the test 1 curve, gross seat plastic deformation occurred as shown in the interference photo of Fig. 137. The falloff of approximately 95 microinches occurred primarily on the OD half of the land. The unequal deformation is attributed to the confinement characteristic of the ID relative to the OD; i.e., the metal cannot move inward without drastic change of shape. There is, however, little constrainment to outward deformation. On the other hand, the totally confined poppet showed only slight (less than 10 microinches) plastic flow.

Following rework, Model K was retested at 1000 psig, this time with ball loading and in a different loading sequence (Fig. 407). Test 2 represents a series of load cycles where the maximum stress was progressively increased with each cycle. The first (initial contact) was conducted from 350 to 2080 psi, the second from 350 to 2080 psi, and the third from 350 to 10,750 psi; the surfaces were not separated between tests. Before the data were recorded for each test group, the model was cycled five times (350 to 2080 psi; 350 to 5330 psi, and 350 to 10,750 psi) to ensure that the elastic characteristics were being measured. The test results (Fig. 407) indicate that plastic deformation took place with each successive increase in the level of operating stress. The dashed line indicates the estimated initial characteristic indicating progressive plasticity. It should be emphasized, however, that the three stress-leakage loops were elastic and thus repeatable. The bulk yield of the aluminum material (approximately 31,000 psi) was not reached in these tests, and it is concluded that the plastic deformation was taking place only at the asperity level. Posttest inspection revealed little visible evidence of damage; the seat was essentially unchanged from the pretest condition shown in Fig. 138 (which also represents the pretest 1 configuration).

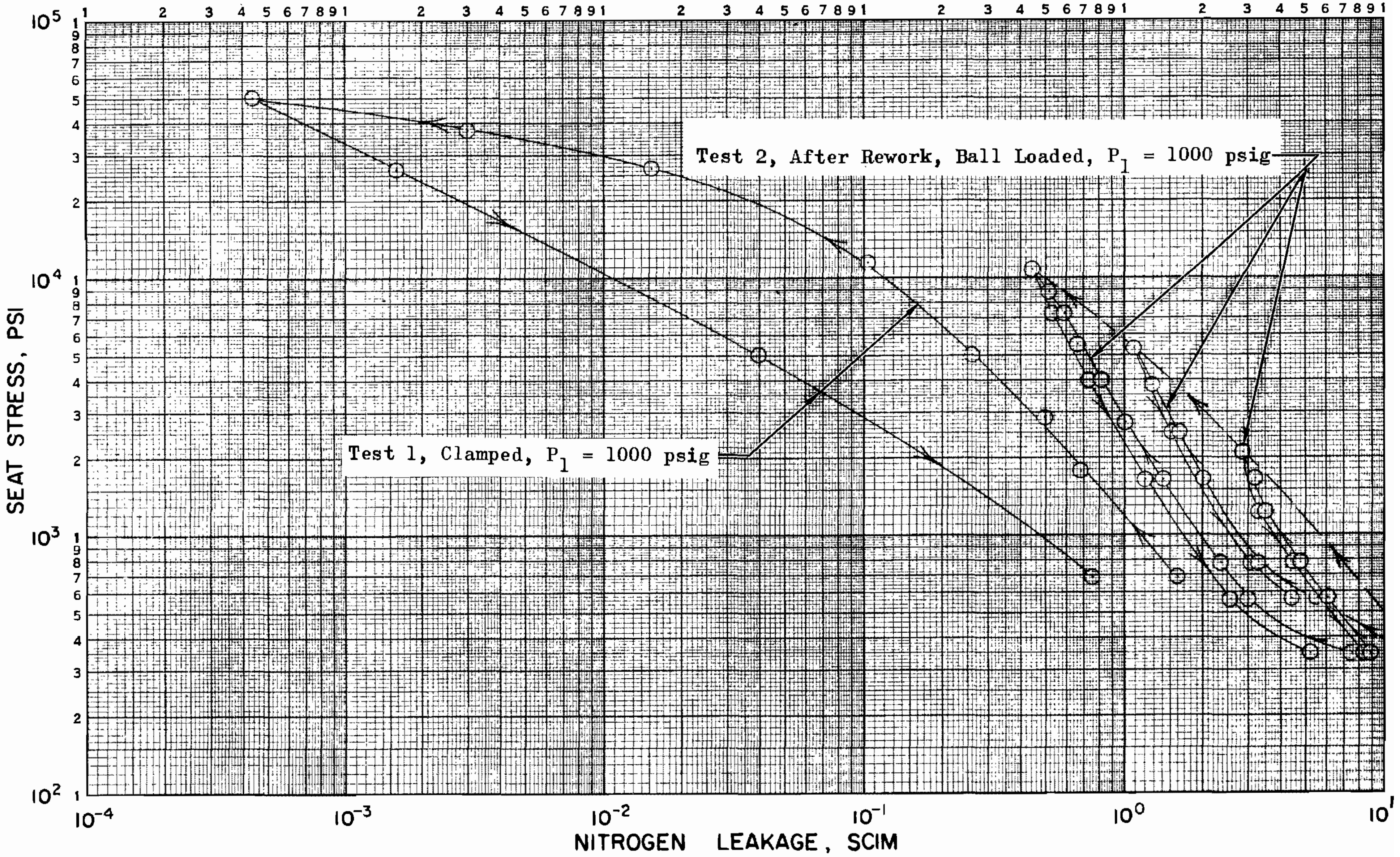

Figure 407. Stress-Leakage Data for Test Model K, Tests 1 and 2

Model F, 0.7 AA Unidirectional Lay 440C Poppet and Seat

Model F was one of the first diamond-lapped surfaces fabricated and was tested during the initial contract effort. This model, like unidirectional ground Model D_f described previously, was used to investigate stress-leakage characteristic differences between opposed and near-parallel lay orientation.

As shown in Fig. 139 through 141, Model F seat exhibited a relatively large scratch density. Approximately 38 percent of the surface was comprised of 3.8-microinch average depth scratches. The lightly polished surface texture PTV height was 2.2 microinches. The poppet, Fig. 142, had been polished considerably more than the seat and was interpreted as having essentially no significant roughness. Instead, the surface was comprised of a 12-percent density of 4-microinch-deep scratches and a waviness characteristic of approximately 0.8 microinch PTV.

Model F was initially tested through several stress-leakage cycles to a 60,000-psi stress with poppet and seat lay approximately 90 degree opposed. The results of the fourth cycle are shown in Fig. 408 as test 1. (The three previous load cycles matched the plotted loop within 5 percent.) Test 2 (Fig. 408) was performed with surface lays oriented in near-parallel fashion. The increased leakage in the low-stress region is attributed to contamination because, with the ball loading arrangement, out-of-parallel effects are negligible.

As with the results of Model D_f, there is virtually no difference between the crossed or parallel lay condition performance. In both models, the varied surface texture wavelengths caused by random spacing of the finishing abrasive make it extremely unlikely that an interlocking poppet and seat lay could exist even if it were possible to align the surfaces perfectly. Furthermore, the lapped version was formed in the relatively precise machine-controlled manner as the ground model. Thus, its lay is not exactly parallel but is comprised of scratches crossing one another at a slight angle, making a lay match impossible. It is concluded that

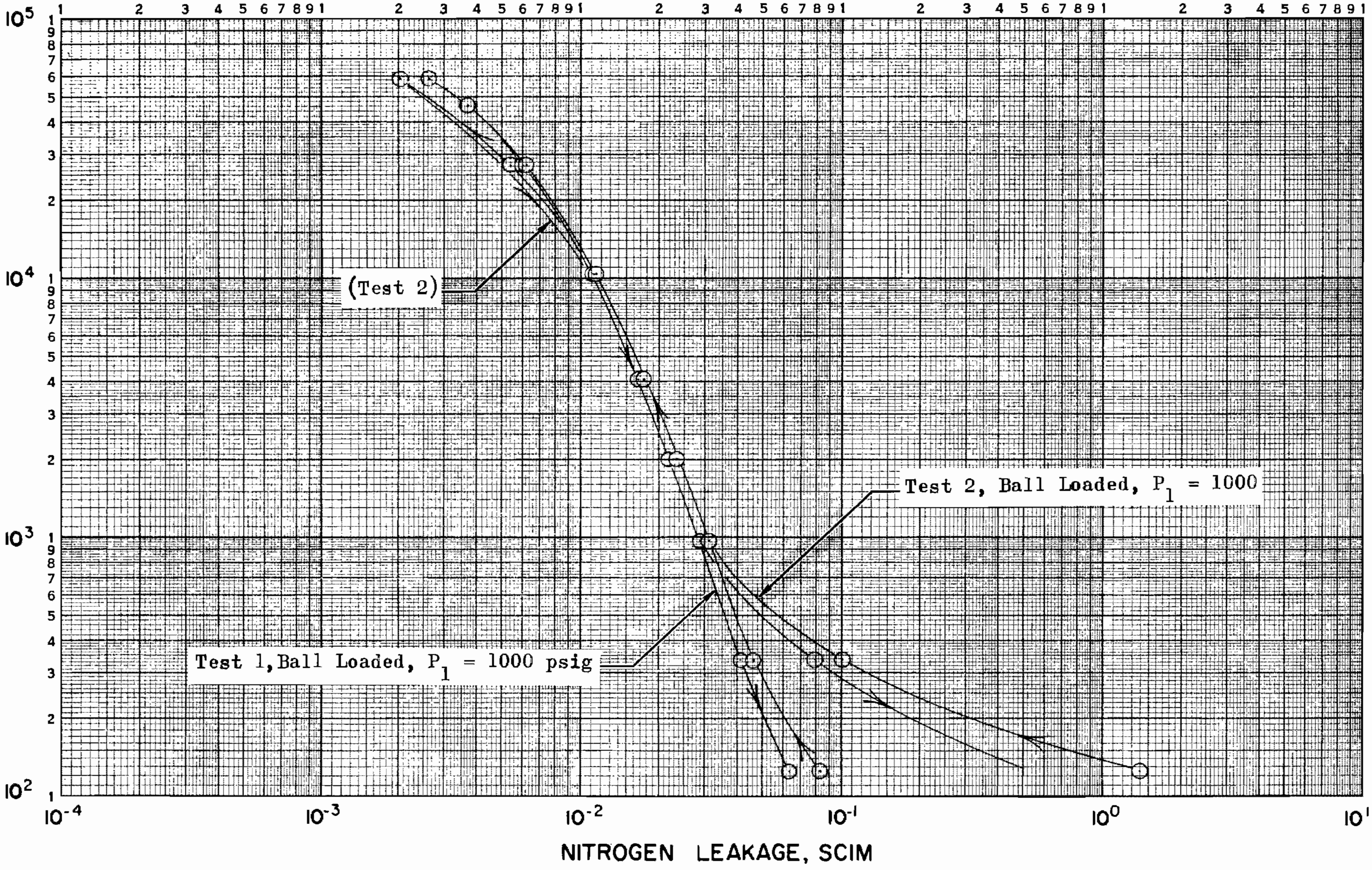

Figure 408. Stress-Leakage Data for Test Model F, Tests 1 and 2

parallel orientation of unidirectional surface lays formed as described herein will not significantly affect the stress-leakage characteristic.

Because the scratches in Model F comprise an appreciable percentage of the surface area, it is worth evaluating their effect in terms of leakage. Using the density relationship (β_s) previously defined, the leakage is given by the combined laminar-molecular flow equation:

$$Q = \beta \left\{ \frac{4.7 \, D_s \, (P_1^2 - P_2^2)}{\mu \, LT} \left[M_L h \right]^3 + \frac{1.4 \times 10^5 \, D_s \, (P_1 - P_2)}{L} \sqrt{\frac{R}{T}} \left[M_M h \right]^2 \right\}$$

By computing the scratch leakage and comparing it with relatively low-stress (1000-psi) test leakage, an estimate may be made of the controlling surface characteristics. For example, the sawtooth scratches of test Model F occupy a large percentage of the seating surfaces; therefore, significant leakage will result. For the seat, which has a scratch depth of 3.8 microinches and a density of 38 percent, the computed scratch flow is 2.2×10^{-2} scim. The corresponding poppet flow is 0.8×10^{-2} scim for a scratch depth of 4.0 microinches and a density of 12 percent. The total scratch flow of 3.0×10^{-2}, compared to 3.0×10^{-2} scim at a 1000-psi seat stress, indicates that virtually all leakage at this stress level is through the scratches. This analysis cannot be carried farther because a stress-leakage relationship has not been developed for the scratch configuration.

Models G_f and G_{f1}, 0.8 AA Unidirectional Lay 440C Poppet and Seat

This model was initially fabricated with "sharp" seat land corners which were damaged during test. Reworked Model G_{f1} seat with approximately a 0.001-inch radius at both ID and OD evidenced no similar damage either after static or subsequent cycle tests.

Model G_f surface roughness PTV height, as deduced from the interference photos of Fig. 143 and 144, was 2.0 and 2.3 microinches, respectively, for poppet and seat. Profilometer data agreed with this assessment and, as with the figures noted, indicated a 1- to 2-microinch PTV waviness characteristic.

Model G_f was tested at 1000 psig with four stress loops, two to 10,000 and two to 55,000 psi. As the results of Fig. 409 indicate, some evidence of plastic deformation on the first cycle is apparent. Subsequent cycles, however, show elastic compliance with minimal hysteresis.

Posttest inspection revealed evidence of extensive seat land corner fracturing. As indicated by Fig. 145, the seating land and total land width are virtually identical with little evidence of corner break. The resultant concentrated edge contact stress caused minute chipping of OD and ID material similar to the typical damage shown in Fig. 146. While the metal failure noted is indicative of improper seating geometry, the effect of the damage is not apparent from test results. If poppet and seat had been separated, it is probable that the disrupted seat surface would have caused an increase in low-stress leakage, particularly if a slight seating surface reorientation had occurred.

In subsequent rework to the Model G_{f1} configuration, a radius of about 0.001 inch was applied to both seat ID and OD. Metal upset from this operation necessitated surface refinishing; the poppet was also refinished. As shown in Table 4, a slight improvement in surface texture resulted with a roughness PTV height of 1.8 microinches (poppet) and 1.7 microinches (seat), and negligible waviness was noted. Figures 147 and 148 illustrate the seat corner condition and surface texture. The refinished poppet surface is shown in Fig. 149.

Model G_{f1} test results (Fig. 410) reflect the noted surface roughness improvement with leakage approximately one-fourth that of Model G_f. Although only one stress loop was performed, an elastic characteristic is evident. The increased low-stress leakage values are attributed to nodule or contaminant effects. No posttest damage or surface changes were noted.

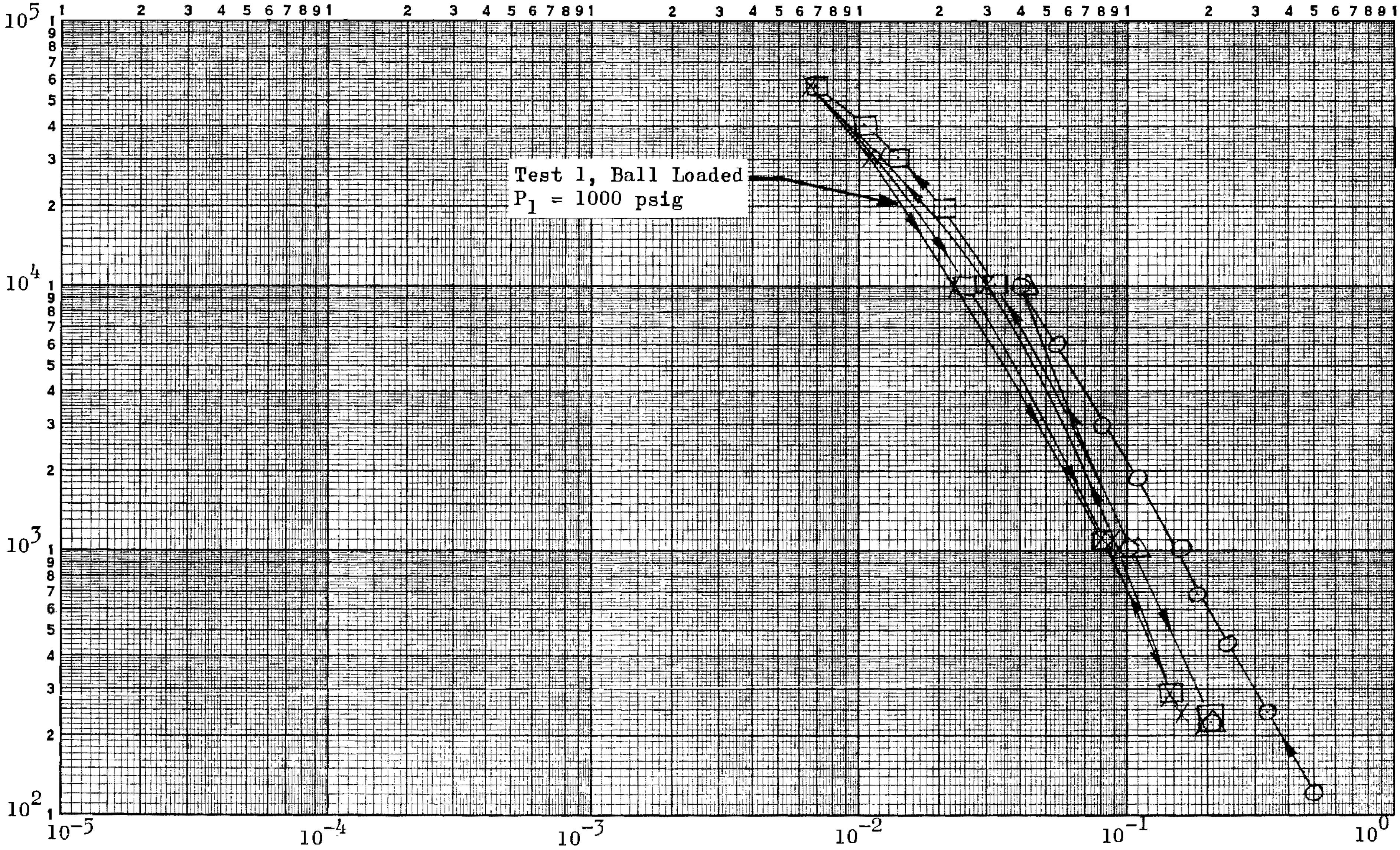

Figure 409. Stress-Leakage Data for Test Model G_f, Test 1

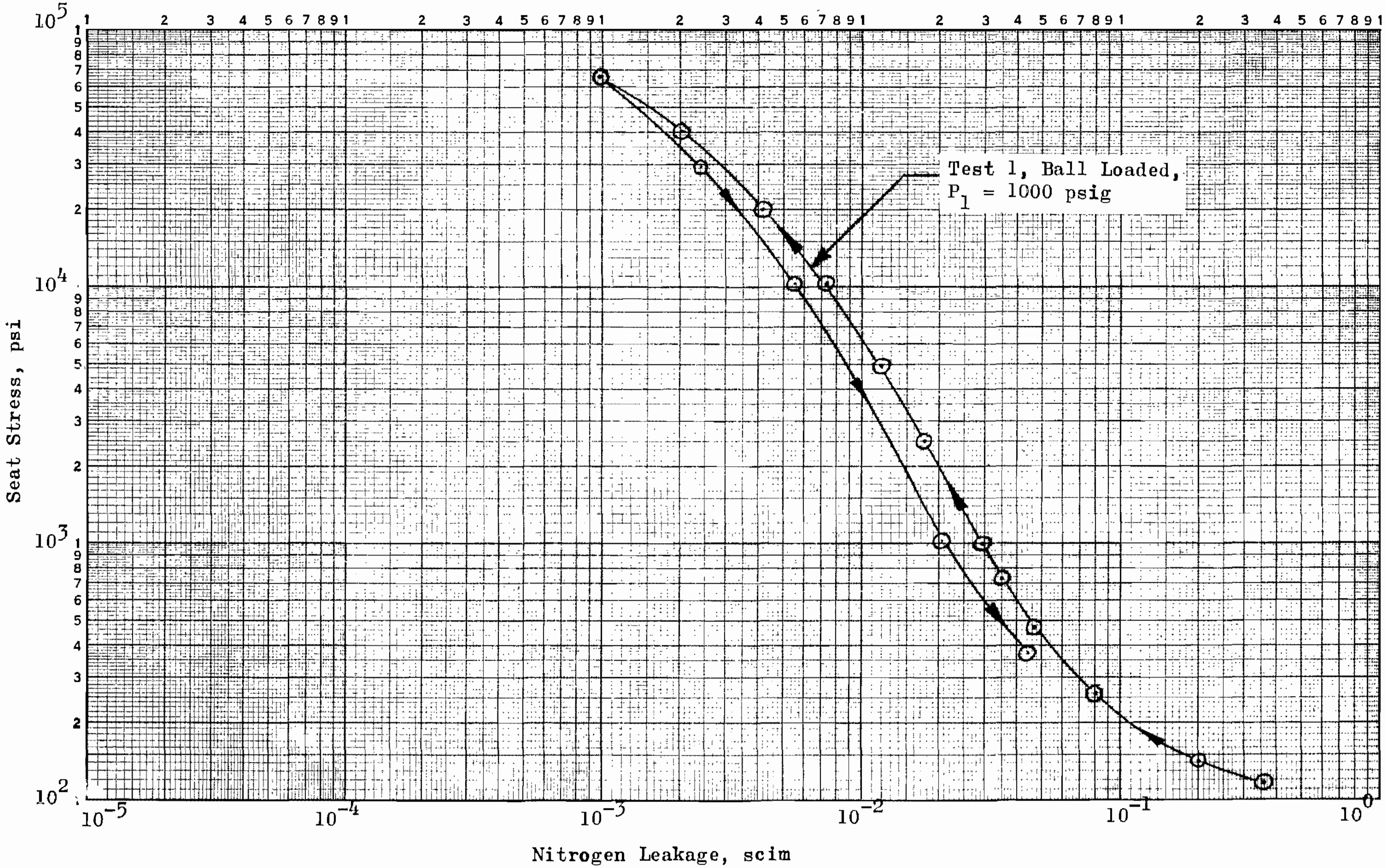

Figure 410. Stress-Leakage Data for Test Model G_{f1}, Test 1

Model CC_f, 0.3 AA Circular Lay Tungsten Carbide Poppet and 0.2 AA 440C Seat

Throughout the lapping experimentation portion of the program and in preparation of models for process evaluation (concurrent with surface texture evaluation models described in this section), it was virtually impossible to prepare a surface without occasional deep scratches. Furthermore, the unidirectional surfaces so fabricated consist solely of minute scratches, all crossing the sealing land. With circular lay, however, both texture and random, deeper scratches close in on themselves (or very nearly so), resulting in much longer leakage paths. This model represents the first surface fabricated for investigation of circular lay capabilities. Additionally, Model CC_f was tested for comparison with an all 440C version of similar finish. Thus, the best material for a reference poppet which would be used for further investigation of seat geometry and finishing techniques could be determined.

The poppet (Fig. 158 and 159) had a roughness height of 0.8 microinch PTV superimposed on a pitted surface. An 18-percent density of 1.5-microinch-deep pits with additional deeper pits (approximately 4 microinches) over 1 percent of the surface was noted. (For reference, Fig. 160 illustrates the surface texture of a new chromium carbide Webber "Croblox" master gage block. It would appear that chromium carbide was a more-dense structure than the K96 Kennametal tungsten carbide poppet, or the gage block was more completely finished.) The seat roughness height was approximately 0.7 microinch PTV as deduced from the interference photo of Fig. 161. Additionally, one scratch 5 microinches deep and 65 microinches wide extending diametrally across the land, was observed (Fig.161 and 162). This scratch was lightly polished out after test, as shown in Fig. 163, to allow a more accurate estimation of depth. From Fig. 18, these two scratches would contribute about 10^{-5} scim.

Two stress-leakage tests were performed on Model CC_f, which along with good leakage characteristics, revealed an odd phenomenom. On Fig. 411 (test 1), the circled data points represent the first cycle of increasing and decreasing load. The second cycle (triangles) was performed after an overnight

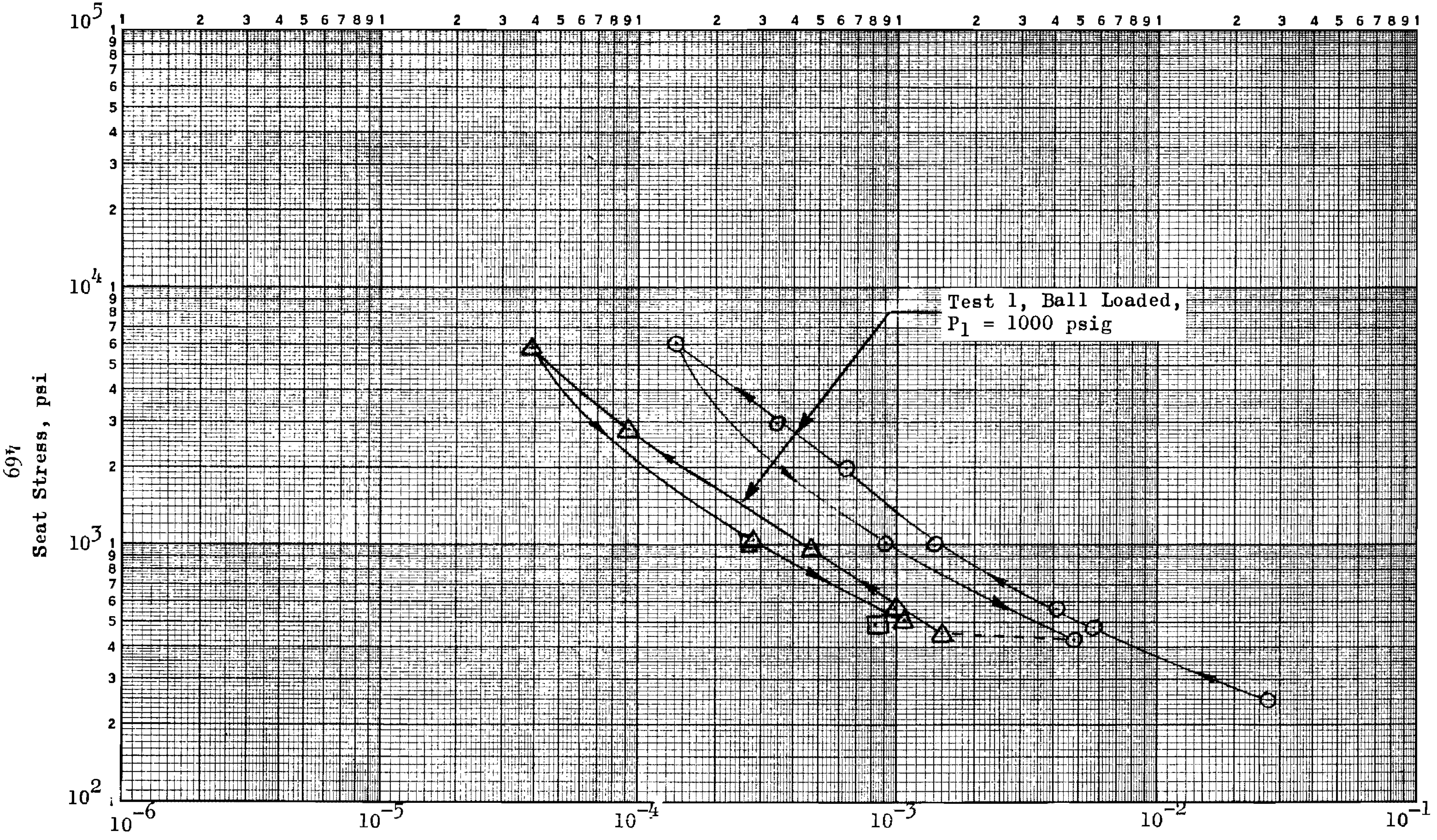

Figure 411. Stress-Leakage Data for Test Model CC_f, Test 1

wait at zero inlet pressure with less than 500-psi seat stress applied; the sealing surface had not been separated. The data indicate a time-dependent or creep condition existed. The model was disassembled and examined; no test-caused damage or contamination was observed although diamond embedment was suspected. It was decided to retest this model and determine if cycles to a higher stress level would reduce the leakage and hysteresis. The parts were reassembled in the tester, and the circled data points shown in Fig. 412 (test 2) were obtained. Again the time of day and test length precluded completion of a second cycle, so another overnight lapse ensued with less than 500-psi applied seat stress. The next cycle (triangles on Fig. 412) was taken the following morning and again showed a creep characteristic. It will be seen that the noted two cycles of Fig. 411 and 412 are nearly identical in leakage magnitude and "creep" characteristic although test 2 exhibited somewhat greater hysteresis. No explanation has been determined for the time-dependency factor. However, it is significant that a leakage ratio of up to 4:1 was obtained, representing a 60-percent decrease in h_e and thus PTV height, which should be considered in evaluation of metal-to-metal valve seats.

After completion of the initial two stress-leakage loops of test 2, 10 load cycles to 58,000 psi were applied, and the final stress-leakage cycle was performed. The data obtained on this cycle, represented by squares in Fig. 412, indicated sealing surface degradation had occurred. At this point, the test was terminated and the model disassembled for inspection.

As with previous sharp-edged models, seat corner damage had occurred. The OD was plastically dubbed about 4 microinches over the outer 0.003-inch around one-half of the periphery (Fig. 164). The ID was dubbed a lesser amount. OD fracture damage (Fig. 165) was also observed. In one area (Fig. 166), a raised lip 1 to 3 microinches high, was formed at the OD. No poppet damage was evident nor was there any evidence of contamination on poppet or seat.

Because of the more rigid and stronger poppet, the permanent deformation occurred in the seat land edge as would be expected from the seating analysis. The raised edge noted may have been caused by crystal

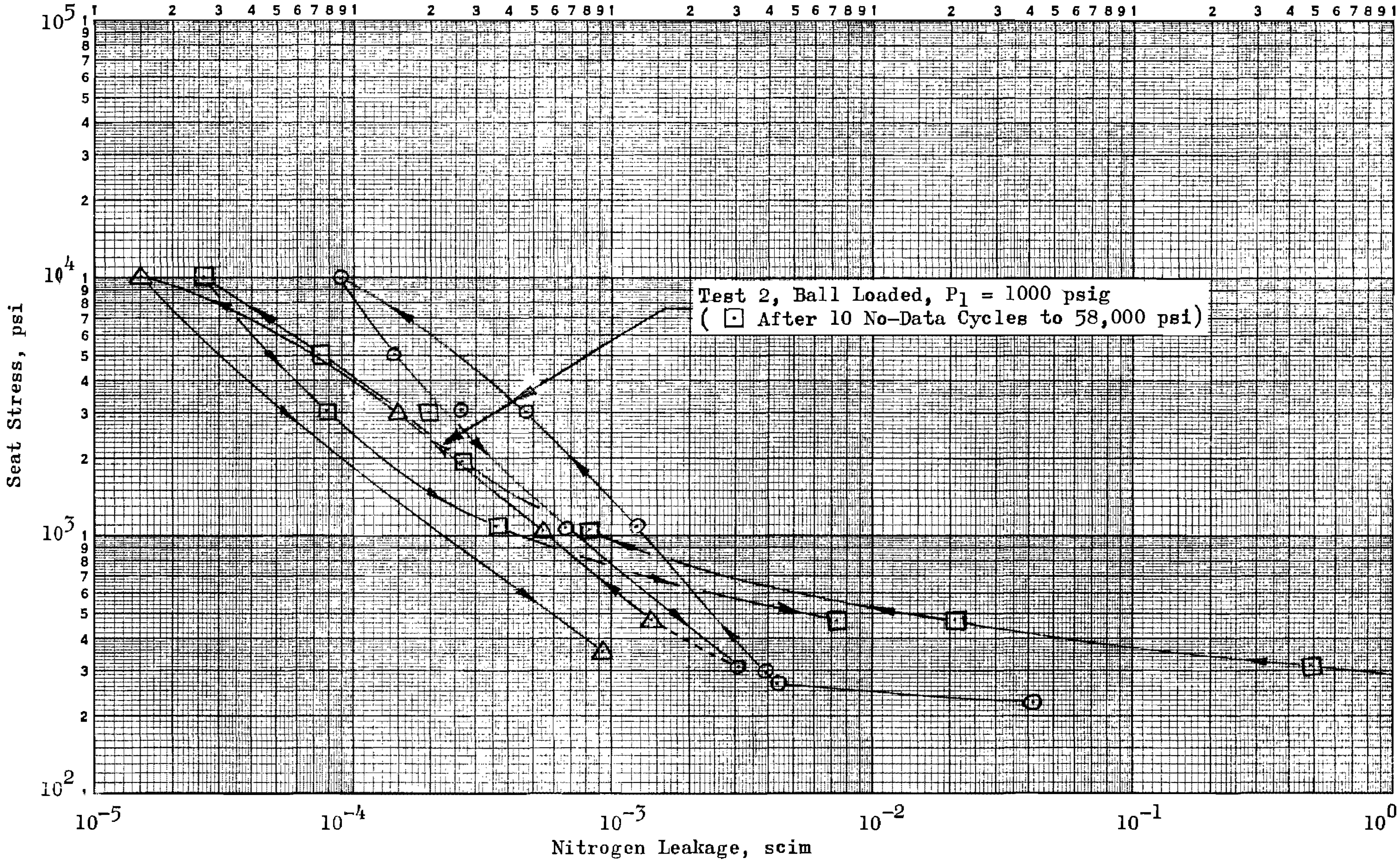

Figure 412. Stress-Leakage Data for Test Model CC_f, Test 2

reorientation after the high-stress loading cycles, and subsequently was responsible for the increased postcycle low-stress leakage; however, no proof of this was found.

A subsequent test (Model BB_f) continued the tungsten carbide poppet 440C seat evaluation, but no further tests were conducted with Model CC_f because of the problems noted. The seat was ultimately reworked to a different configuration.

Models B_f and B_{f1}, 0.8 AA
Circular Lay 440C Poppet and Seat

Circular lay test Model B_f was fabricated for comparison with the unidirectional lay (similar roughness PTV height) stress-leakage characteristic of Model G_f. As with Model G_f, seat land corner fracture occurred, necessitating rework and retest.

Model B_f poppet and seat surface roughness heights were 1.9 and 2.5 microinches PTV, respectively. The interference photos of Fig. 167 and 168 illustrate the surfaces, while the sharp-edged seat corner condition is shown in Fig. 169. Circumferential waviness deviation of both poppet and seat was less than 3 microinches, indicating the uniformity of the lathe-lapping process. No radial scratches were noted.

Figure 413 presents the stress-leakage test results for Model B_f. The sharp shutoff rate characteristic of the circular lay surface is evident. Slight evidence of low-rate contact is indicated by the slope change below 200-psi stress. The balance of the curve, however, shows minimal hysteresis with essentially elastic surface compliance.

Posttest inspection revealed the sharp-edged corners of Model B_f seat to be the most severely damaged of the models so fabricated. Approximately 160 fractures at the OD and 250 of the ID were noted. Several cracks about 0.0005-inch long, running inward from the OD at approximately 30-degrees, were also found. Figure 170 shows typical OD fracture cracks,

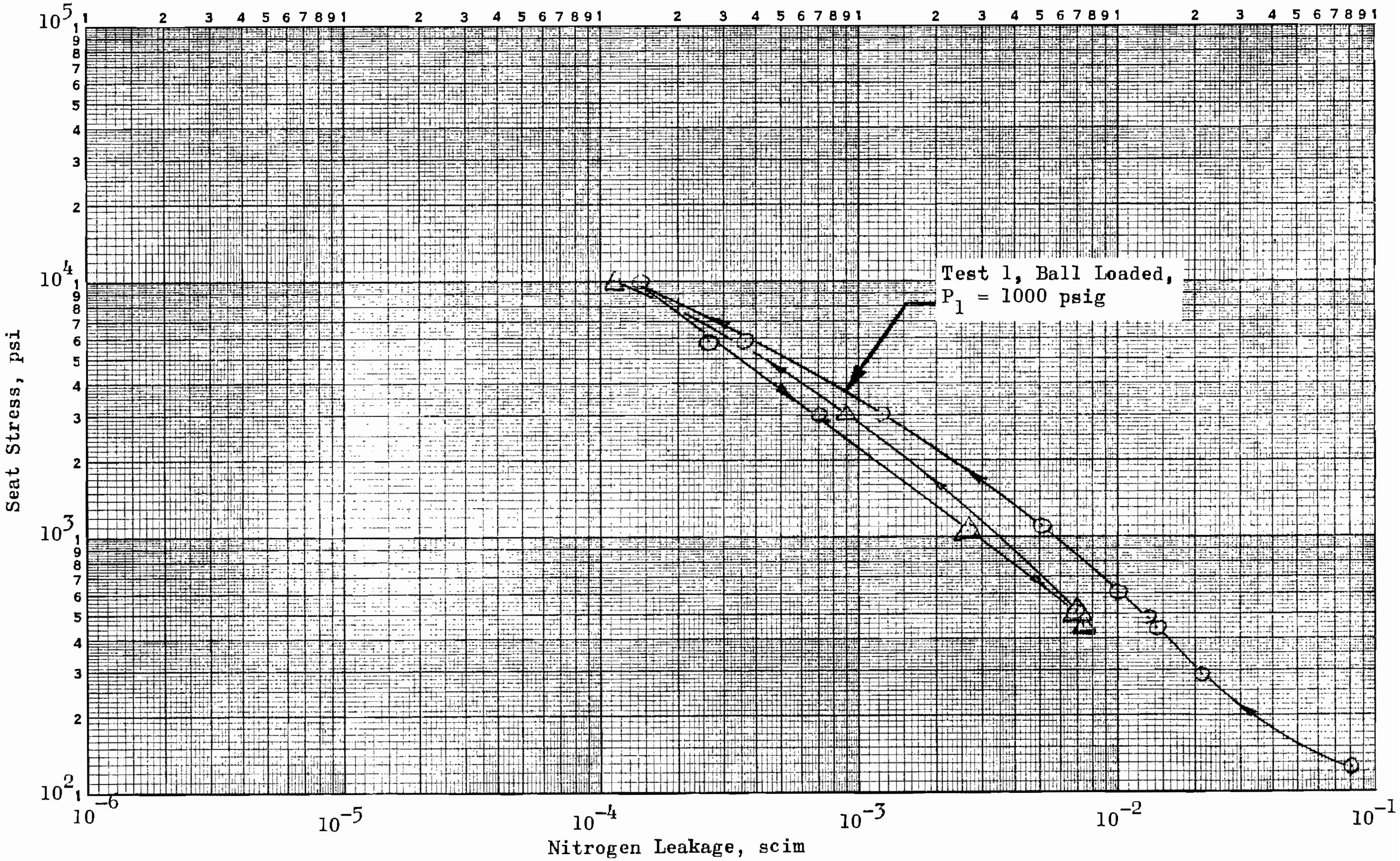

Figure 413. Stress-Leakage Data for Test Model B_f, Test 1

while the largest single failed area is illustrated by Fig. 171. One contaminant particle ~ 0.0004 inch in diameter and 3 microinches high was noted on the poppet.

In the subsequent rework to Model B_{f1} configuration, the seat corners were slightly broken and the surface dubbed at OD and ID as shown in Fig. 172. (The previously mentioned large fracture is also visible). A deeper circular scratch pattern occurred over the inner third of the seat land, but the net surface roughness was reduced from 2.5 to 1.4 microinches PTV (Fig. 173). The poppet was not refinished.

As shown by Fig. 414, test results for Model B_{f1} differed little from those of the initial configuration. Although the poppet was unchanged, the similar performance characteristic attests to the reproducibility of the circular lay surface. Posttest examination of the reworked model revealed no further evidence of seat land damage.

Models H_f and H_{f1}, 0.2 AA Circular Lay 440C Poppet and Seat

Model H_f was the last model to be finished with a sharp-edged seat and to incur corner fracture damage. It was fabricated for comparison with the tungsten carbide poppet version of similar lay and roughness level.

Figures 174 and 175 show seat edge condition and surface texture, respectively. Roughness height was approximately 0.7 microinch PTV for the seat and poppet; the latter is illustrated by Fig. 176. Neither poppet nor seat had any radial scratches extending over more than 25 percent of the sealing land.

Model H_f test results (Fig. 415) represented the best performance obtained at that time. Hysteresis was minimal although it appeared that the decreasing stress curve would cross the initial plot if stress had been reduced further. Disassembly inspection revealed heavy contamination of fiber-like particles, probably from the wiping paper used. (The improved

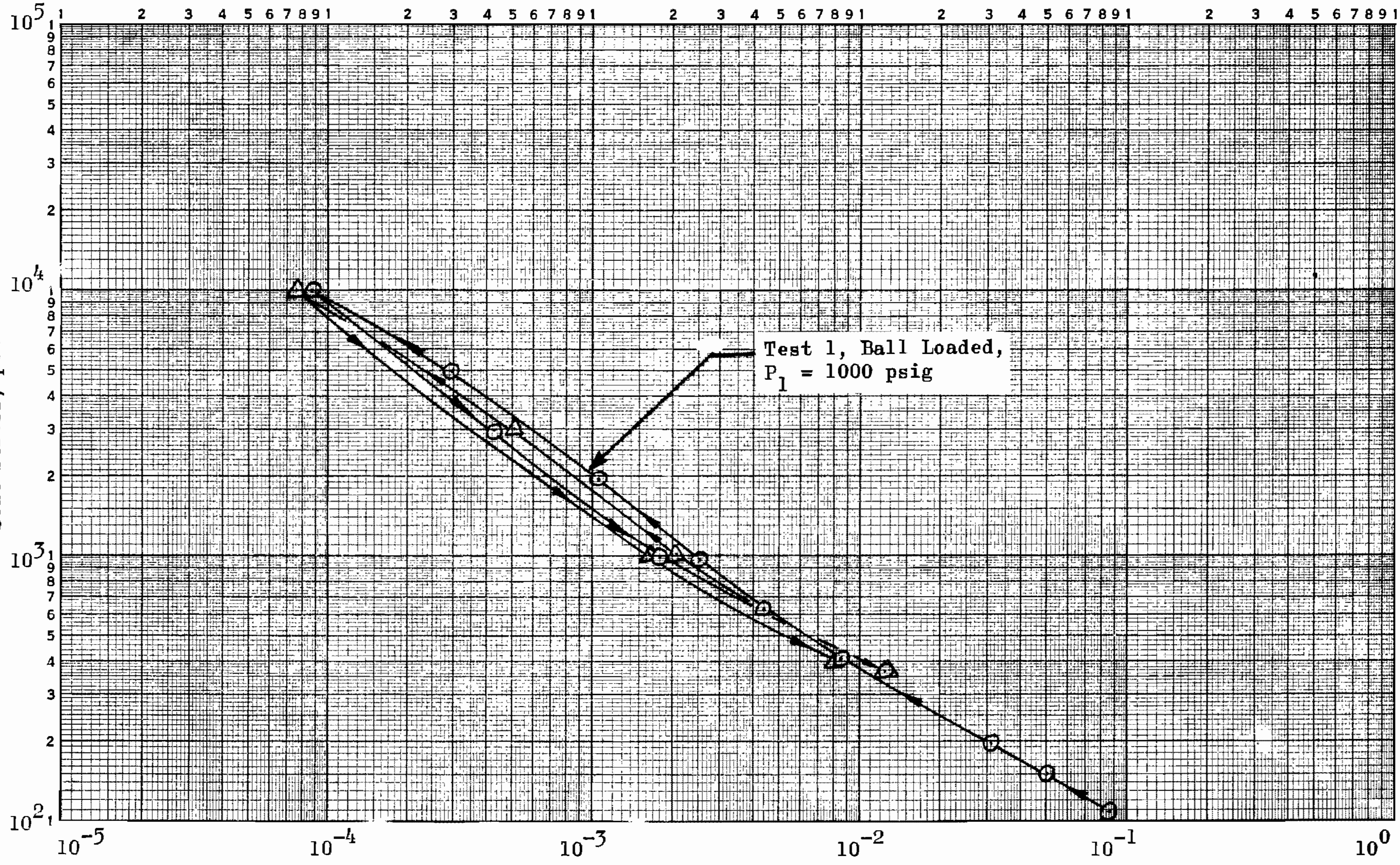

Figure 414. Stress-Leakage Data for Test Model B_{f1}, Test 1

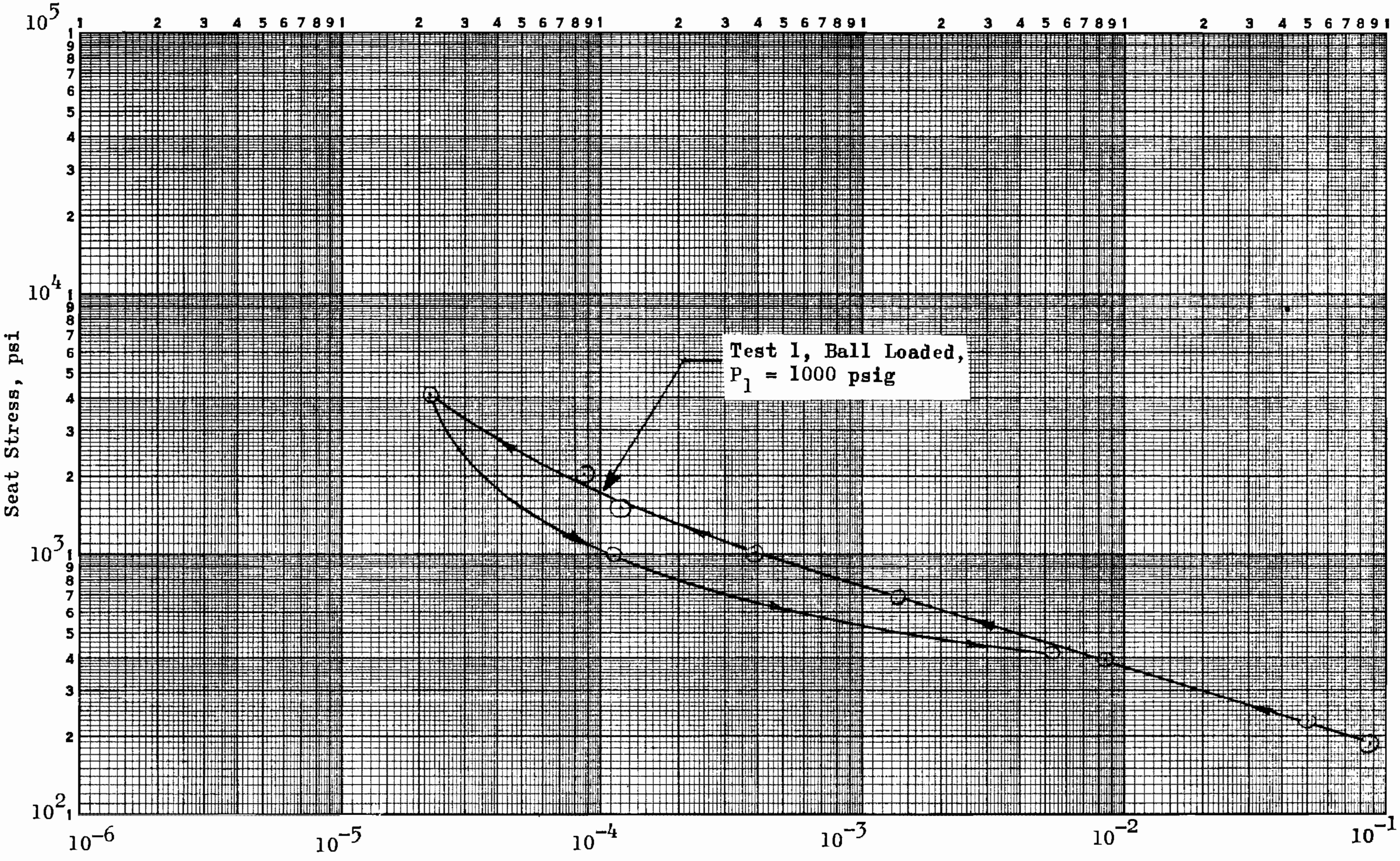

Figure 415. Stress-Leakage Data for Test Model H_f, Test 1

cleaning procedures noted in the Assembly and General Test Procedure subsection were initiated following Model H_f tests). Additionally, minor OD fractures were noted as well as a condition of metal slippage at the OD edge (Fig. 177 and 178).

Because this model had been tested to a maximum apparent stress of only 4000 psi, it is presumed that any similar surface having "sharp" edges would be liable to such deterioration. For this and damaged models previously noted, the extremely flat uniform surfaces, low PTV asperity height, and material characteristics probably contributed to the fracture problem. Corner fracturing, as noted herein, would probably not affect rougher or less brittle surfaces. Nevertheless, the test results support the edge-contact analysis (Seating Analysis section) and indicate that an adequate corner break is necessary for any metal seat having poppet overlap whether of flat, conical, or spherical configuration.

Model H_{f1} seat was reworked with land corner radii and refinished; no poppet rework was required. Seat roughness PTV height (Fig. 179, through 181, where the last two photos are from multiple beam interference) at 0.8 microinch was slightly rougher than the initial H_f version. Figure 182 illustrates corner condition. (The ID blemish is a handling-caused nick, not pertinent to test performance). Figure 183 shows a surface feature first noted with this model. Approximately 0.0003-inch square and 3 to 4 microinches high, this "contaminant" is typical of several found on Model H_{f1} poppet and seat as well as on later models. Although called contaminants, they could not be scrubbed off nor would light lapping remove them. Never positively identified, the contaminants are hypothesized to be either chrome carbide particles (inherent in 440C steel) or embedded metal "slag" from the lapping operation.

Figure 416 presents the data for the first stress-leakage cycle after seat rework and refinishing. As with Model H_f and other circular lay models, a relatively fast shutoff rate is noted. However, the presence of several 3- to 4-microinch-high contaminants probably accentuated this effect. For example, at 105 psi stress, the 0.59-scim leakage is commensurate with a 5.3-microinch parallel plate gap. This is much larger than surface roughness

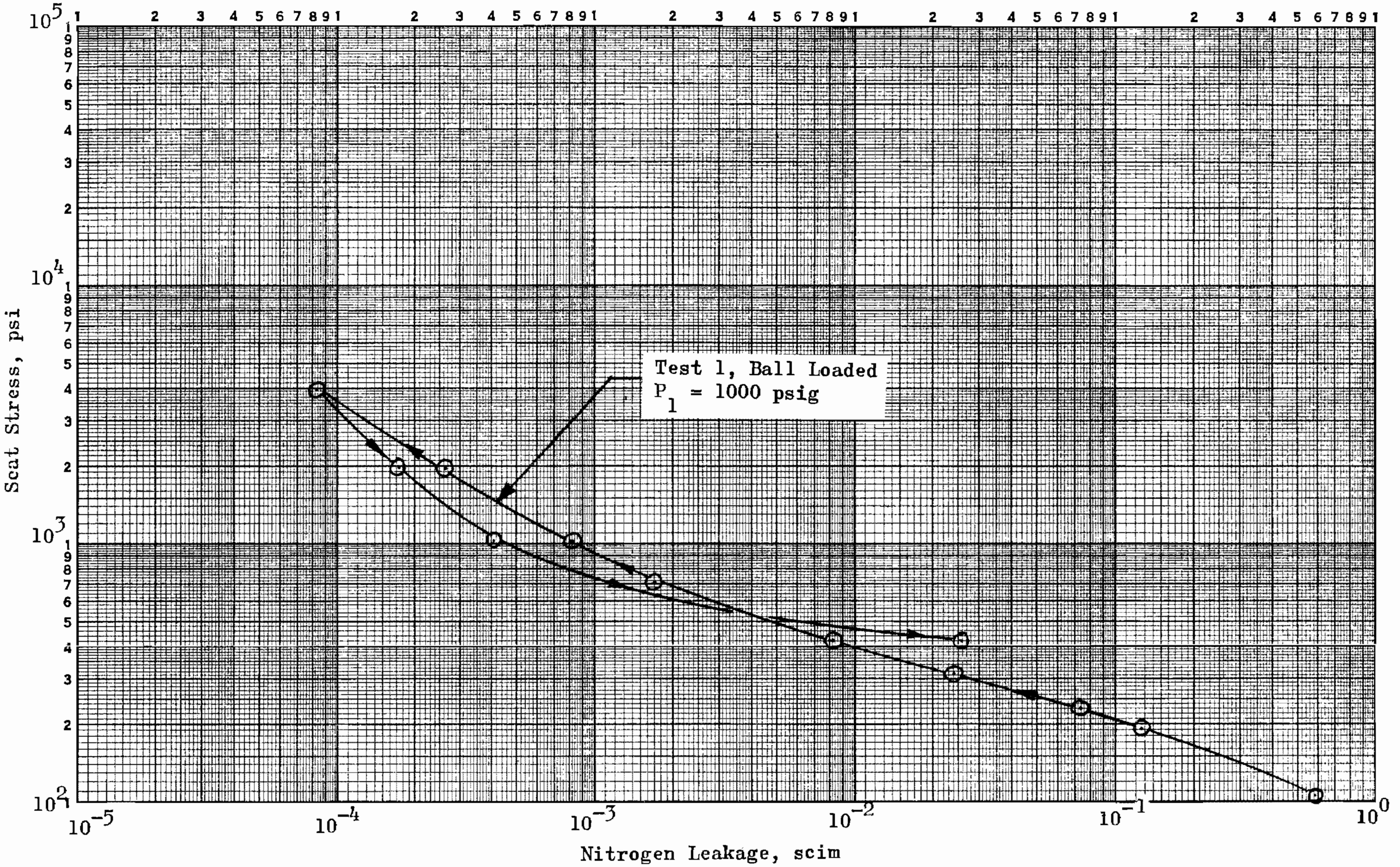

Figure 416. Stress-Leakage Data for Test Model H_{f1}, Test 1

level but agrees favorably with the noted contaminant height. Thus, at least a portion of the low-stress shutoff rate may be attributed to envelopment of a few contaminant particles.

Further comparison of Fig. 416 data with those of Model H_f reveal that above 1000-psi stress, the refinished version leaked 2 to 4 times as much as contaminated and damaged Model H_f. The model was removed from the tester and examined; no evidence of seat corner damage or sealing surface imperfections was found. However, on the supposition that some contaminant or blemish might not have been noticed, it was decided to "clean" the seat by relapping. Using 0-1 to 1-micron-grade diamond compound on a micarta lap, the seat was lathe lapped for 15 seconds. There was no change in the sealing surface finish visible under two beam interference viewing at 500 power following this rework.

Subsequent stress-leakage performance is shown in Fig. 417. Test 2 comprises the initial two load cycles. Prior to test 3, the sealing surfaces were separated and the poppet rotated slightly. These two tests represent the best bare metal sealing characteristic obtained during the test program with 2×10^{-5} scim leakage achieved at only a 1450-psi seat stress. (During fluid coating evaluation, discussed later, one model exhibited slightly less leakage at similar stress levels.) The pronounced improvement over Model H_f, H_{f1} (test 1) and other fine-finish models tested has not been completely explained. Two probabilities exist:

1. The relapping (cleaning) operation. While no change in surface roughness was detectable with the inspection equipment available, the removal of even 1/4 microinch from the seat surface asperities could be expected to reduce the already low leakage significantly.
2. Lay orientation. As discussed in the Seating Analysis section, concentric circular lay can greatly reduce leakage. While the potential individual poppet and seat lay eccentricity has been noted previously, it is possible that the parts were assembled so that near-concentric lays resulted. For this to have occurred, however, the results after poppet repositioning (test 2) are even

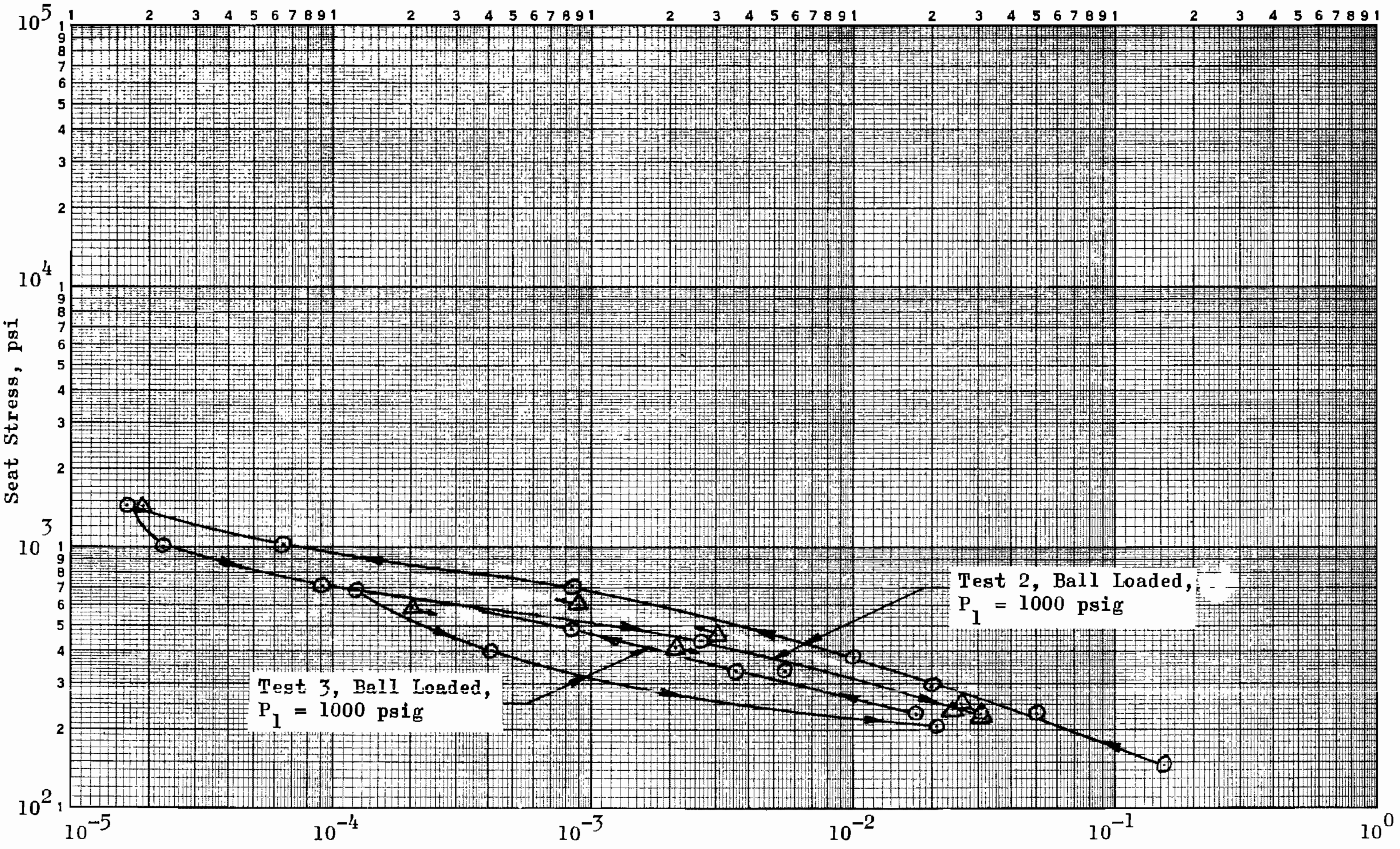

Figure 417. Stress-Leakage Data for Test Model H_{f1}, Tests 2 and 3

more extraordinary, indicating a fortuitous happening rather than setup precision.

In considering possible causes, the former is deemed most likely responsible for the results noted. Because the "cleaning" lapping operation did not remove the previously described contaminant nodules, the low-stress leakage level and closure rate were similar to those of Models H_f and H_{f1}, test 1.

Model L_f, 0.3 AA Unidirectional Lay 440C Poppet and Seat

This model, fabricated for comparison with similar roughness but circular lay Model H_{f1}, represents the best unidirectional lay surface achieved during the test program. Because of the problems encountered in finishing this model, it was concluded that a scratch-free surface could not be attained. Both poppet and seat had a sufficient number of with-lay scratches approximately 2.5 microinches deep to warrant scratch density (poppet β_s = 0.0012 and seat β_s = 0.0008) consideration. In addition, the poppet had six random scratches averaging slightly more than 4 microinches deep and 37 microinches wide which crossed the sealing land as shown (typical) in Fig. 184.

Both poppet and seat PTV roughness height was approximately 0.8 microinch (Fig. 185 and 186). Radii were formed on the seat corners to support edge loads although the sealing surface was not dubbed off as indicated by Fig. 187. While not photographically documented, both poppet and seat sealing surfaces had approximately 20 contaminant nodules 2 to 3 microinches high, similar to those noted in the description of Model H_{f1}. (The additional figures (Fig. 188 and 189) illustrate microhardness test indentations and 0.0001-inch radius tip Proficorder stylus tracks discussed in the Model Inspection Equipment, Procedures and Data section).

Model L_f was tested to a 60,000-psi stress, as shown by the test results of Fig. 418. The marked slope change at approximately a 1000-psi stress gives evidence of completion of contaminant nodule envelopment and initial surface contact. The 0.33-scim leakage at 130 psi stress is equivalent to that of a 4.3-microinch parallel plate gap which agrees favorably with the noted contaminant height. Leakage between 500 and 1000 psi stress is indicative of a net sinusoidal PTV gap of 1.8 to 1.2 microinches; thus, in this region, the basic poppet and seat surfaces have come in contact. The test data show minimal hysteresis, and therefore an extremely elastic condition.

Based on the test pressure of 1000 psig, the total scratch density and random scratch leakage (Fig. 18) is approximately 6×10^{-5} scim. This amount of scratch-attributable leakage has negligible effect on the stress-leakage curve shape until some 20,000-psi stress has been attained. Thus, the leakage from 1000 to 20,000 psi stress is directly related to the unidirectional lay surface roughness.

Above 1000-psi stress, Model L_f leaks an order of magnitude more than the the similar roughness but circular lay model H_{f1} (test 1) and cannot reasonably be compared with the "cleaned" results of Model H_{f1}, tests 2 and 3. Furthermore, Model L_f leakage is greater than that of circular lay Model B_{f1} (Fig. 414) even though the latter model PTV roughness height is more than twice that of L_f. Thus, the results of Model L_f testing more clearly than any other model demonstrate the superiority of the circular lay finish.

Model BB_f, 0.3 AA Circular Lay Tungsten-Carbide Poppet and 440C Seat

To complete the 440C vs tungsten-carbide poppet reference surface investigation begun with Model CC_f, this model used CC_f poppet and H_{f1} seat. Parts were identical to those used in final testing of the contributing models.

Figure 419 presents the test results. Two load cycles were performed initially (test 1). The surfaces were then separated, the poppet rotated

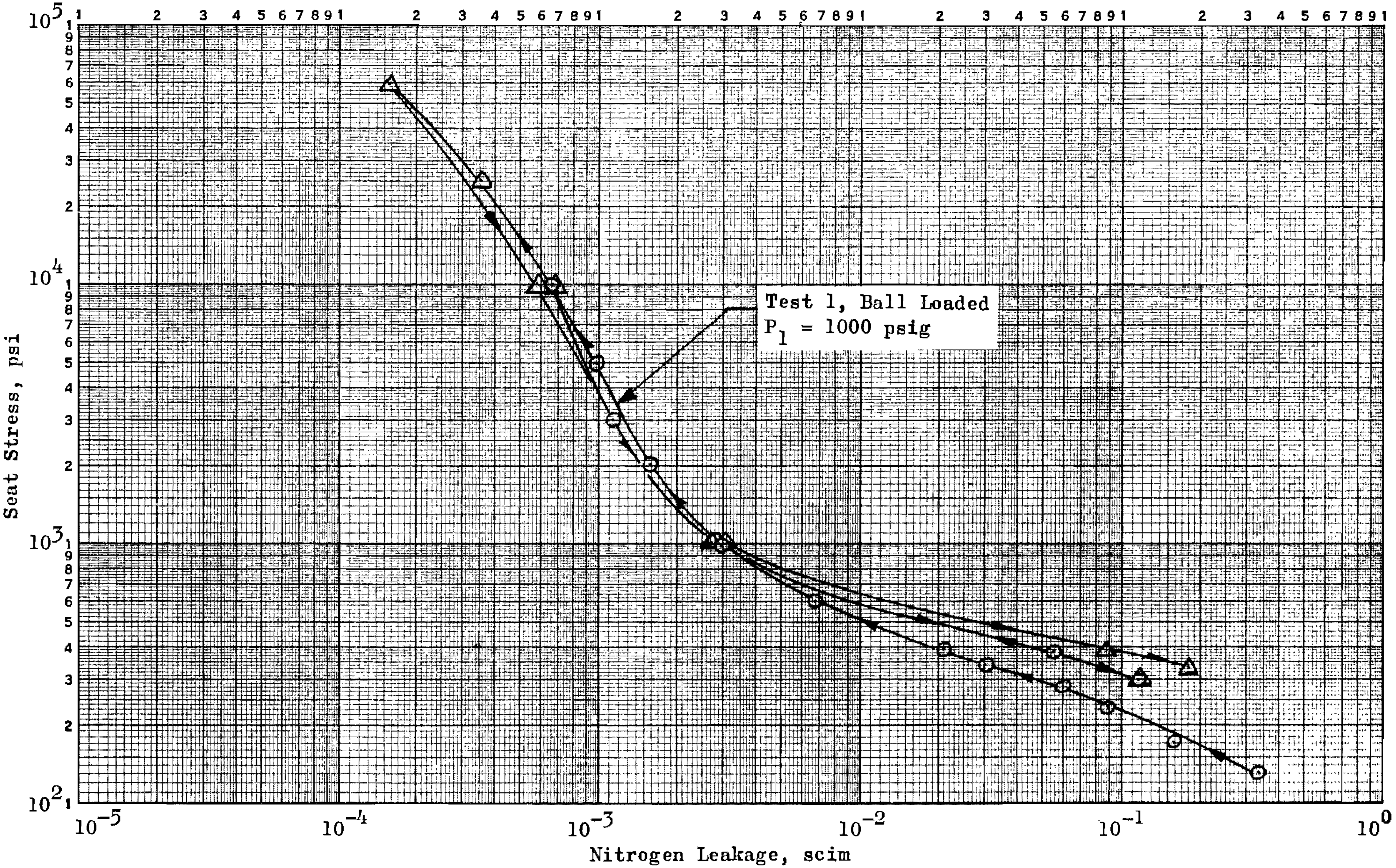

Figure 418. Stress-Leakage Data for Test Model L_f, Test 1

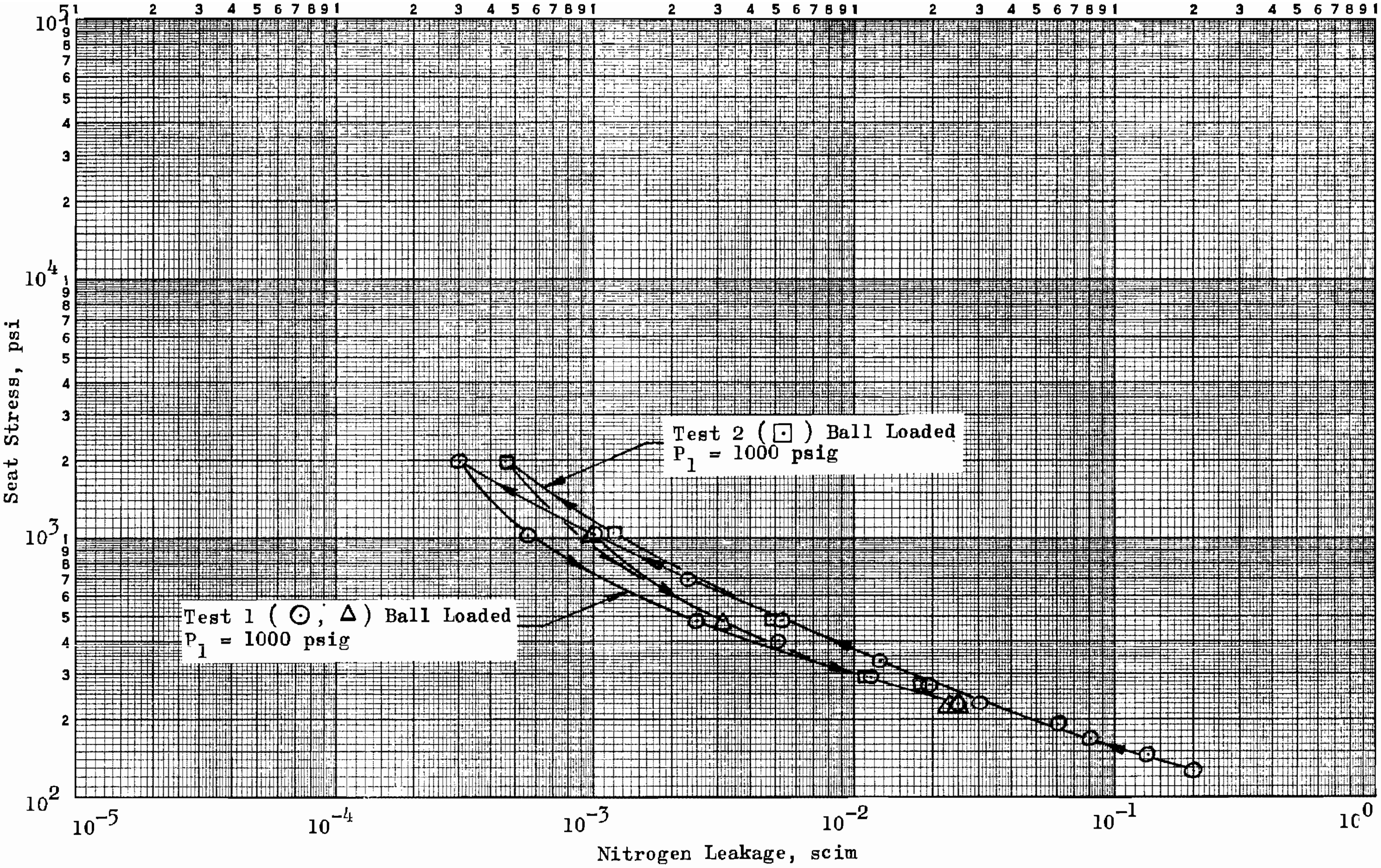

Figure 419. Stress-Leakage Data for Test Model BB_f, Tests 1 and 2

several degrees, and the data of test 2 taken. As shown, there is little difference between the two tests.

A comparison of tungsten-carbide poppet models (CC_f and BB_f) with the 440C poppet version (H_f and H_{fl}) is presented in Fig. 420. The data clearly indicate the superiority of the more homogenous (vacuum melt) 440C poppet over the minutely pitted tungsten-carbide material for similar basic surface roughness PTV height. The tungsten-carbide material used (Kennametal K96) was one of the most dense commercially available. While not an indication of porosity (as it is sometimes described), the pitted surface is characteristic of the material finish and may be due to grinding or lapping pits, or voids associated with the sintering process.

From these tests it was concluded that, for evaluation of very fine surfaces (roughness PTV height less than about 2 microinches), the 440C material was most suitable although a less-pitted carbide surface would undoubtedly reduce the noted difference.

Models M_f and M_{fl}, 0.2 AA Circular Lay 440C Poppet and Seat; 5.4-Inch Seat Crown Radius

Model M_f was fabricated to evaluate the stress-leakage characteristic of a crowned seat land. Surface roughness was similar to that of Model H_{fl}, permitting comparison with the latter circular lay, but uncrowned model. Additionally, the effect of ball vs clamped loading was investigated.

Model M_f seat roughness height was deduced as 0.4 microinch (Fig. 190), while the poppet was slightly rougher at 0.7 microinch (Fig. 191). From interference photographs similar to Fig. 192, the seat crown radius was interpreted as approximately 5.4 inches over the center 0.021-inch portion of the land with transition to approximately 0.7-inch corner radii. Also visible on Fig. 192 is one of three scratches crossing one side of the seat land due to incomplete cleanup of the pre-finish unidirectional lay surface. These scratches varied from 3.6 to 4.6 microinches deep and 43 to 87 microinches wide (Table 4). The poppet had no visible cross-land scratches.

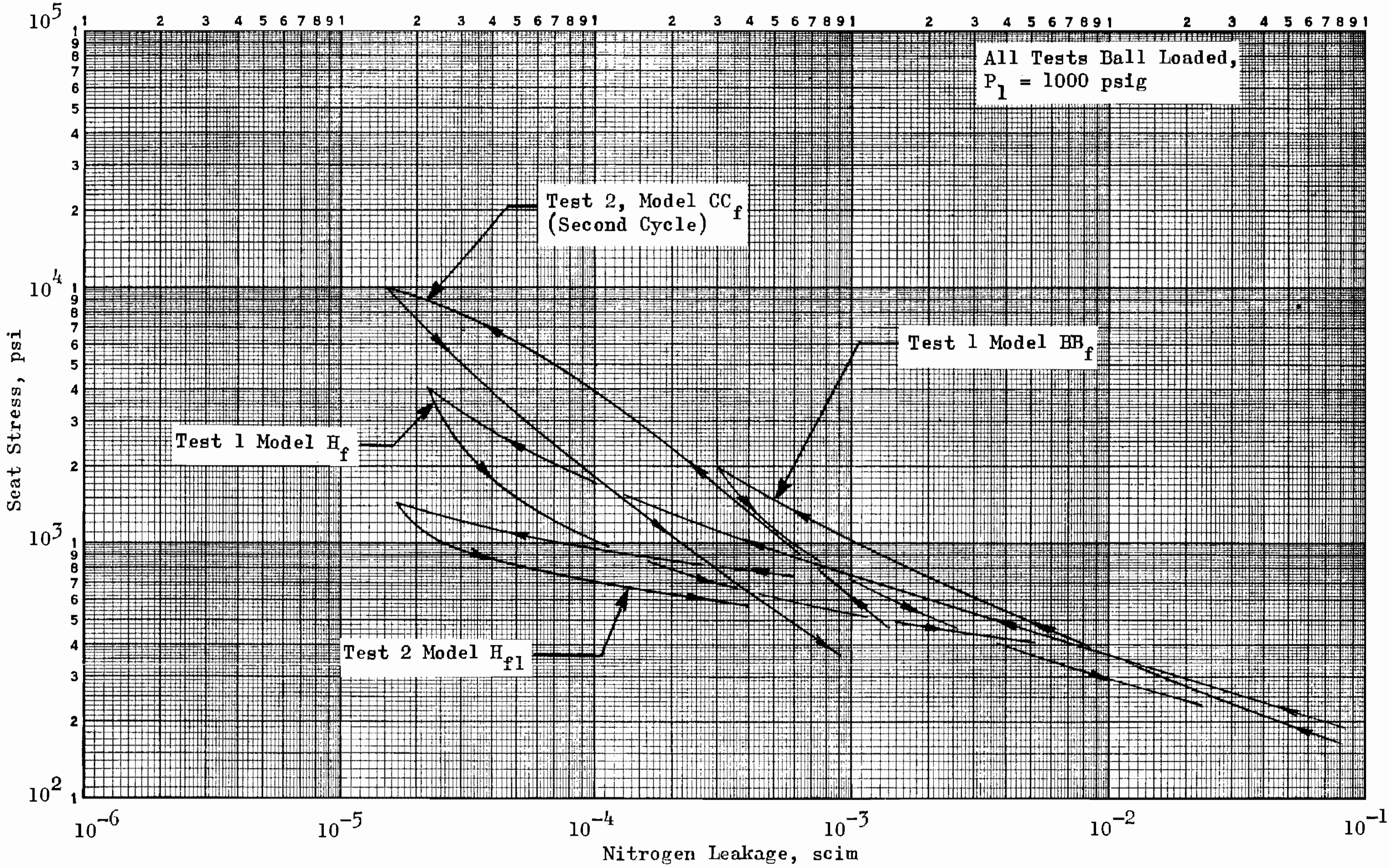

Figure 420. Stress-Leakage Data for Test Models BB_f, CC_f, H_f and H_{f1}

Model M_f was tested twice in the ball loaded condition as shown in Fig. 421. Between tests 1 and 2, sealing surfaces were separated and the poppet rotated approximately 10 degrees. Except for the very low stress portion of the decreasing load loop, test results were virtually identical. In addition to the "standard" stress-leakage plot (which is purely an indication of applied load since the entire projected land area is used in computing apparent stress) Fig. 421 also presents the stress-leakage characteristic of test 1 based on Hertz contact area. In this case, the average seat stress (σ_{avg}) which varies with surface deformation and, hence, the actual bearing contact land width is considered*. Maximum contact stress (σ_c) is $4/\pi$ times the values noted.

Model M_f leakage was sufficiently low for scratch flow to influence the high-stress portion of the stress-leakage characteristic ($Q < 3 \times 10^{-4}$ scim).

Considering the actual contacting land width and assuming no significant scratch deformation, net scratch leakage at 7200-psi Hertz stress was calculated at 2.4×10^{-5} scim, or approximately half the total leakage measured. If the stress-leakage curves were modified by subtraction of scratch flow, an even more pronounced high-stress closure rate would be evident.

As an indication of Model M_f performance capabilities, it may be compared with Model H_{f1}, test 2, on an apparent stress (load) basis. At 1000-psi stress (increasing load, no effect from scratches), Model M_f contact land width is calculated to be approximately 0.007 inch (Fig. 34, Seating Analysis section). When reduced by the M_f/H_{f1} land width ratio, Model M_f leakage was only about 1.5 times greater than that of H_{f1}. Thus, although actual contact stress was higher, from a valve sealing standpoint on a common load basis Model M_f compares very favorably with flat Model H_{f1}. In fact, the low-stress leakage characteristic was better than H_{f1} even without correction for land width difference, probably because of the previously

---

*This is not to be confused with the so called "real" contact area generated from the sum of asperity contacts which is less than the annular bearing area referred to.

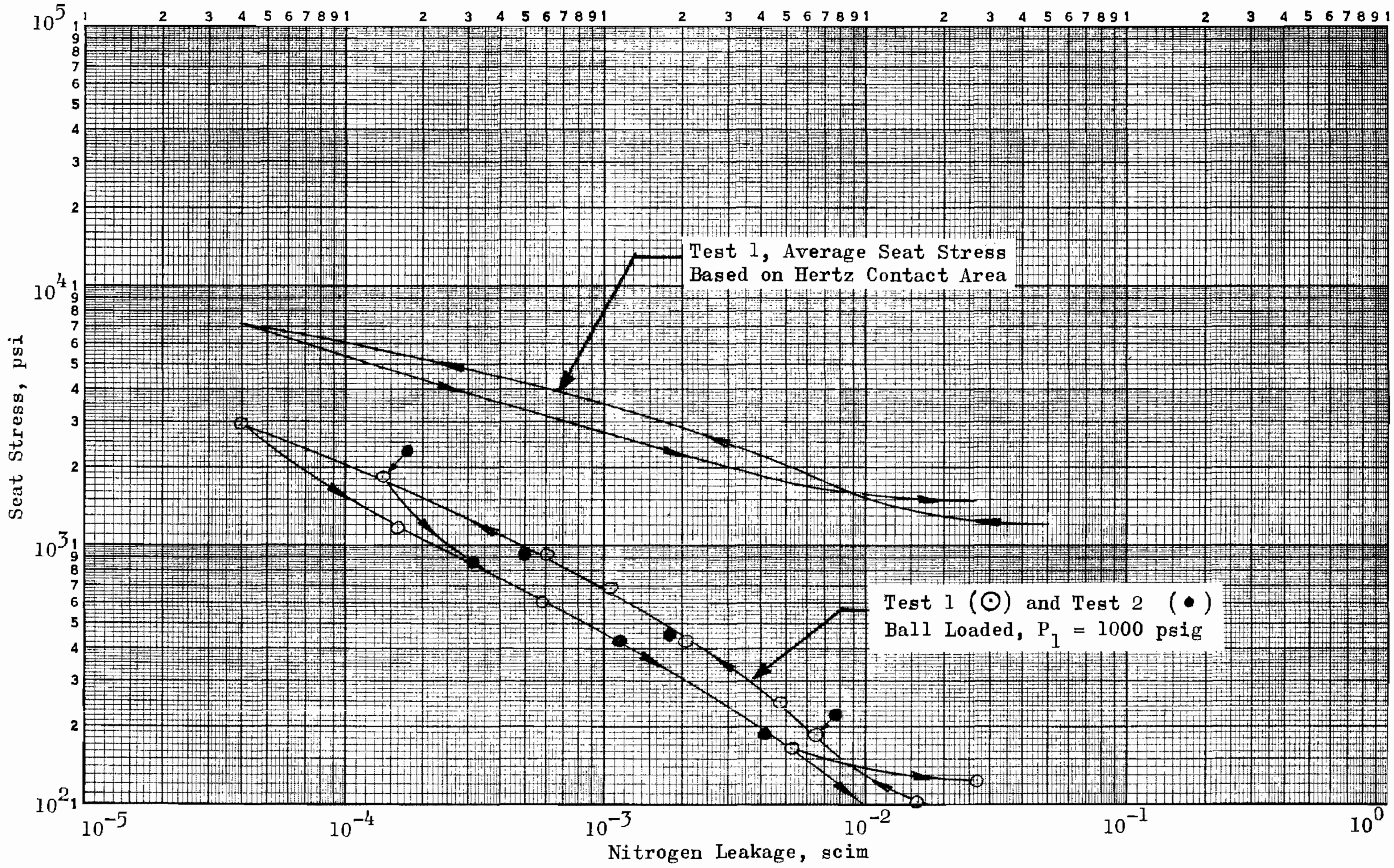

Figure 421. Stress-Leakage Data for Test Model M_f, Tests 1 and 2

noted nodules present on Model H_{f1} surfaces and lack of any high-stress corner contact. Furthermore, with the crowned surface, Model M_f could be expected to withstand cyclic loads in better fashion that flat Model H_{f1}.

On the seat inspection photos (Fig. 190 and 192), it will be noted that the surface is somewhat streaked through the center portion of the land. This effect was actually the indication of a multitude of minute elongated pits caused by "rolling" diamond lapping compound particles. Although tested in this condition, it was decided to attempt surface improvement. The seat was polished with 0- to 1/2-micron diamond compound on paper pressed onto the surface with rotary thumb pressure. The resulting surface is shown in Fig. 193 (taken at the same place as Fig. 190 but with more narrow bands). The majority of small pits were removed although, as Fig. 193 indicates, some of the larger pits were, by polishing, made more visible. The poppet was not reworked and the model was designated M_{f1}.

Model M_{f1} was tested first with ball loading and, in anticipation of cycle testing, subsequently in the clamped condition for comparison purposes. The results are shown in Fig. 422. The removal of pits bridging the narrow low-stress contact land width greatly reduced low-stress leakage (ball loaded test 1) as compared with the unpolished version (tests 1 and 2, Fig. 421).

As with Model M_f, scratch leakage correction would decrease the slope of M_{f1} stress-leakage characteristic since the polishing action did not significantly reduce scratch depth. It is apparent, however, that at elevated stress levels where Model M_f had developed sufficient contact land width to suppress the bridging pit effect, both models are similar. Exprapolation of both sets of data indicates Models M_f and M_{f1} leakage would be about the same at approximately 4000-psi apparent stress.

Following the ball loaded test, the poppet was clamped to the piston feet in preparation for a comparison clamped-loading test in simulation of the cycle test configuration. Using the electrical contact equivalent parallel plate leakage method, the poppet was determined to be parallel to the seat within 10 microinches. However, during this procedure the poppet was

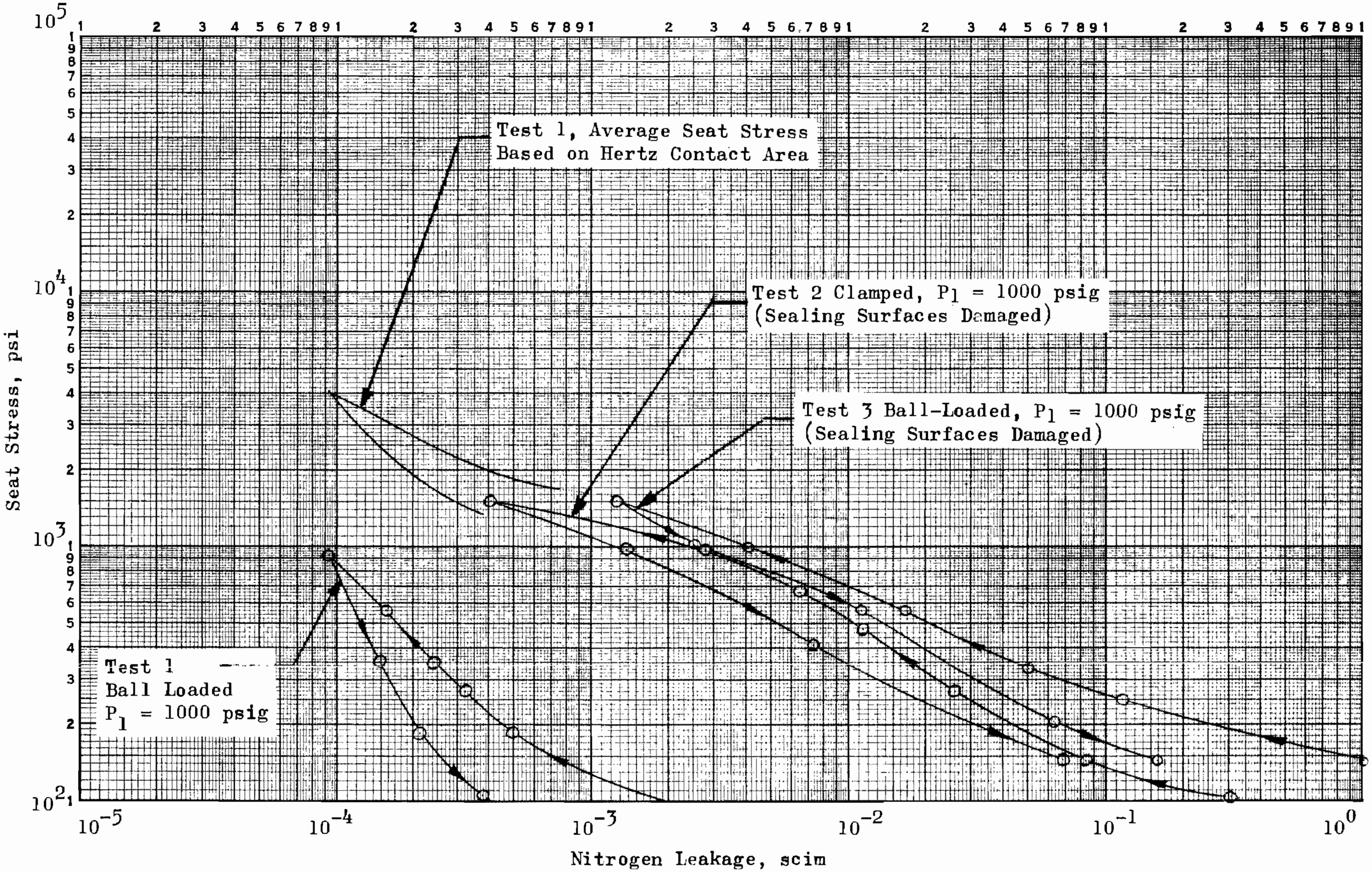

Figure 422. Stress-Leakage Data for Test Model M_{f1}, Test 1, 2 and 3

purposely rotated relative to the seat under what was thought to be an insignificant load (electrical contact test condition). This action, as higher than anticipated leakage and subsequent microscopic inspection revealed, galled both poppet and seat. The stress-leakage data (test 2 of Fig. 422), with one to two orders of magnitude increase in leakage over the ball loaded version, is indicative of such damage. However, extrapolation of test 2 data indicates potential envelopment of the damaged area with subsequent contact land deformation and increase in width. Disassembly inspection revealed both poppet and seat were galled in a circumferential streak of approximately 60 degrees by 0.001-inch wide and 2 to 3 microinches high as shown in Fig. 194, 195, and 196. Metal transfer from both parts had occurred.

Assuming both surfaces perfectly parallel, the Hertz deflection at 1/2 pound load is less than 1 microinch. Since these surfaces were out of parallel by several microinches, it is evident that the initial contact took place at essentially one spot, rupturing the protective oxide film. Once a wear particle was thrown up, the rolling action caused by the external rotation produced additional wear particles. As the interfacial distance was fixed by the piston adjustment screw, and the less than one microinch roughness provided no troughs to receive particles, the resultant wedging action tended to promote the wear process. Repositioning the screw literally mashed the minute particles down into the surface commensurate with the out-of-parallel dimension since the handwheel system is relatively insensitive to these light loads.

It is evident that failures of this type are precipitated by the mating surfaces being of the same material and hardness. Atomically clean steel surfaces readily weld to form bonds strong as the parent metal. It would appear that to avoid this type of failure, one of the mating surfaces should be made from a completely dissimilar material or a coating provided which readily shears leaving the base material intact. Even so, damage would have resulted probably from this type of contact loading.

In subsequent test 3, Model M_{f1} was retested in the ball loaded condition. The poppet was inadvertently reoriented such that the two galled areas were adjacent to one another rather than directly superimposed. Thus, while test 3 leakage is somewhat higher than test 2 it is probable that, if the damaged areas had been mated (PTV height approximately doubled), an even greater leakage rate than that noted would have occurred in the low-stress region.

Model AA_f, 0.3 AA Tungsten Carbide Poppet and 0.2 AA Crowned 440C Seat, Circular Lay

As the ball vs clamped loading tests of Model M_f proved inconclusive because of the aforementioned damage, Model AA_f was selected for continuation of this investigation. This model was comprised of the identical poppet and formerly damaged seat of Model CC_f.

The seat (Fig. 197, 198, and 199) was refinished to approximately 0.5-microinch PTV roughness, but had six cross-land scratches 3 to 5 microinches deep and 60 to 100 microinches wide. From Fig. 200 the crowned condition was assessed as 7.0 to 20.0-inch radius, with corner and crown radii dependent on the crowned land width assumed.

Model AA_f was initially tested in the ball loaded condition (test 1); Fig. 423 presents the test results. Also shown is the average Hertz stress curve based on an average crown radius of 12.0 inches. The poppet was then assembled in the clamped position, oriented to the seat such that a net out-of-parallel condition of 6.4 microinches PTV existed at the 0.500-inch seating diameter (1.1 microinches poppet and seat roughness, plus 5.3 microinches total measured individual part parallelism deviation). Electrical contact tests indicated an equivalent parallel plate gap of approximately 10 microinches. This value was indicative of excellent assembly and cleanliness conditions which, in fact, were sufficient to negate the primary test purpose. Stress leakage test data so closely matched the ball loaded results that, for clarity, they are not plotted in Fig. 423. (For evaluation of out-of-parallel clamping effects see Cycle Test Models G_{f1} and X_f.)

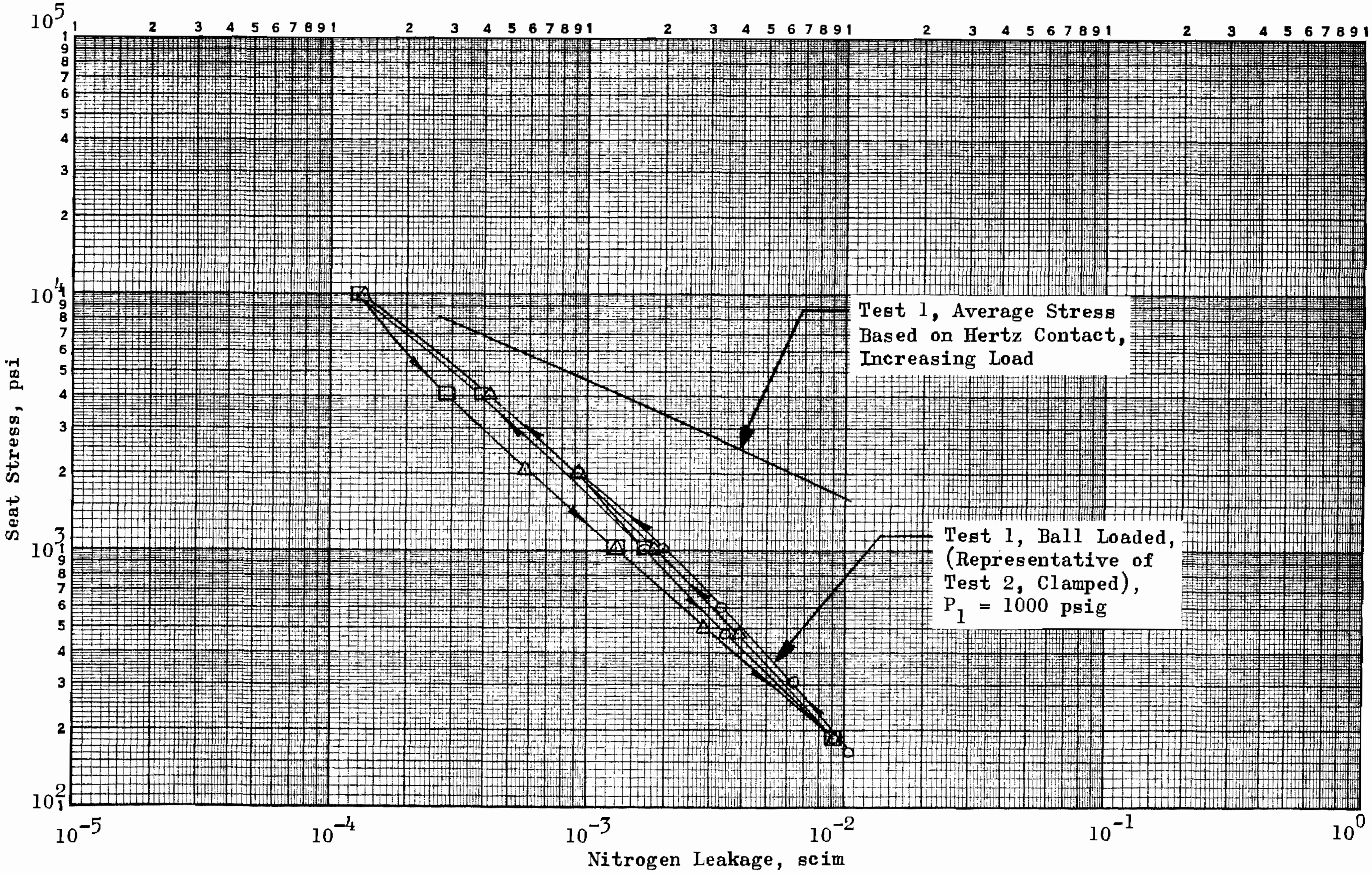

Test 1, Average Stress Based on Hertz Contact, Increasing Load

Test 1, Ball Loaded, (Representative of Test 2, Clamped), P_1 = 1000 psig

Figure 423. Stress-Leakage Data for Test Model AA_f, Test 1

As with other tungsten carbide poppet models, AA_f sealing capability was limited by the pitted poppet surface texture. This is illustrated by comparison with crowned Model M_f having similar texture (including a minor pitted condition as previously described). At 200-psi stress both models leak at nearly the same rate. However, as stress is increased, Model M_f evidence a faster closure rate even though it is less load compliant (crown radius smaller than that of AA_f), hence develops land width at a lesser rate than AA_f. At 2000 psi, Model M_f leaks on order of magnitude less than AA_f, and the difference increases even more with additional stress.

Conservatively assuming all seat scratches at 5 microinches deep and 100 microinches wide yields a scratch leakage at an apparent stress of 5580 psi of 7.5×10^5 scim (calculated land width of 0.020 inch, 12.0-inch crown radius). This represents approximately 28 percent of the total leakage measured and, if subtracted from the total, would influence the stress-leakage curve somewhat. However, the scratch leakage would assume much greater importance if the pitted poppet condition (causing relatively high leakage) did not exist.

Model AA_f seat configuration may be interpreted as having an average radius or a nearly flat center section with relatively large radius and dubbed, small radius outer (ID and OD) sections. Assessment of this composite geometry led in part to preparation of the parametric data presented in Fig. 34 and 35, Seating Analysis section. Figure 34 illustrates the Hertz contact analysis for a cylinder on a flat plate for a seat model of nominal dimensions as noted (sufficiently similar to AA_f seat for comparison).

From this data, contact land width as a function of radius can be obtained for any given model load (apparent stress). Figure 35 presents, in similar fashion, contact land width variations for a model having a center land flat of 0.010 inch. As previously noted, AA_f seat contact radii varied from about 20 inches, taken over a 0.010-inch center land section, to approximately 7 inches when nearly the whole land width was included. Assuming the center 0.010-inch section to be flat, the corner radius was determined to be 2.25 inches. From this information and the graphical data of Fig. 34 and 35, the following contact land width and stress values were computed (appropriate correction for material difference has been applied).

	Apparent Seat Stress, psi			
	300	1000	3000	10,000
Hertz Contact Land Width, inch				
R = 20	0.00603	0.0110		
R = 7			0.0114	0.0208
Hertz Contact Stress, psi				
σ ave	1490	2730	7889	14,400
σ max = σ_c	1900	3480	10,040	18,340
Flat Contact Land Width, inch	0.0110	0.0124	0.0144	0.0194
Flat Contact Stress, psi				
σ ave	818	2420	6250	15,460
σ max = σ_c		5020		
σ min		1790		

Consideration of the above data with respect to Model AA_f seat geometry indicates that the Hertz contact land width and stress values are correct probably up to the 3000-psi apparent stress level. Beyond this point the assumed center flat configuration yields the most meaningful data. There is, however, relatively good correlation between land width and stress values of both methods above the 1000-psi apparent stress level. The maximum-minimum contact stress values tabulated are based on the stress distribution pattern generated by the two analogies, i.e., semi-cylindrical shape for the Hertz contact and U-shaped (with peak stress at the edges of land contact) for the center flat assumption. Inasmuch as both methods yield reasonably close results, the Hertz contact condition (for an average 12.0-inch radius extending over the center 0.020-inch portion of the land with transition to OD and ID corner radii of about 0.7 inch) is shown in Fig. 423.

DATA COMPARISON AND CORRELATION

The flat model surface texture evaluation tests have demonstrated a general correlation with the simplified analyses of seat roughness closure over limited ranges of seat load. Because of the natural occurrence of a multiplicity of surface variables rather than a single geometry, it was further shown that absolute load is a significant parameter in establishing the overall leakage characteristic. This was evident in the case of low loads (below 1000-psi apparent stress, or 43 pounds) where waviness, taper, or nodules often influenced the leakage gap, and at high loads (above 10,000 psi, or 430 pounds) where radial scratches or pits sometimes comprised the significant leak path. The effect of load dependence must be considered in the application of the apparent seat stress parameter as very small or large seats could have large deviations from the results presented herein.

Although measurements were recorded for waviness and taper, the location of each nodule which might contribute to low-stress leakage was beyond the scope of the program inspection capabilities. Moreover, inacurracies inherent in limited surface texture measurements tend to relegate these measurements to a more or less comparative position. Consequently, the stress-leakage test is the sole accurate criterion of the composite interfacial gap characteristic. This applies to all surface textures including circular lay. The basic problem in interpreting stress-leakage data is the identification of the significant geometric characteristic over any given load range. For example, two quartz optical flats (near zero roughness) which literally weld if wrung together would require some load to obtain a closure when initially separated by contaminant particles. For this case, roughness or waviness measurements and apparent seating stress would be meaningless since the resultant gap would be a function of particle distribution and the local deformation characteristics. The same analogy exists with machined metal surfaces more or less depending upon the uniformity of the surface texture. Unfortunately, where the stress-leakage characteristic is significantly influenced by nodules or contamination, their identification by microscopic inspection methods is tedius and difficult since existing techniques normally view (at high magnification) only a small percentage of the total seating area. Moreover, if contamination is present, the elastic relaxation and separation of the interface may dislodge or move the particles changing the characteristic. In view of these observations, the stress-leakage curves must be considered as primary data defining the overall interfacial gap for each model. Inspection data, therefore, provides a means for comparing potential seating characteristics on a numerical basis but, perforce, only superficially. (Seating surfaces should never be accepted or rejected on the sole basis of either inspection or test data, but a combination of both.)

Comparison of the stress-leakage characteristics for all significant ball joint loaded flat models is shown in Fig. 424. These curves represent the final test increasing load condition. Since all models have nearly the same land width, and stress is based upon either the flat or total width, the stress ordinate also represents load. Overlayed on these curves is computed parallel plate model leakage curve (h_p) which may be employed as a dimensional reference to relative gaps. Also included with the surface texture evaluation model curves are those from flat models discussed later which offer significant contributions for empirical correlation; refer to Table 4 and the Table of Contents.

All initial turned models O_f, N_f, R_f, and S_f were tapered such that unknown land width variations with load occurred. Also, each model was loaded to a plastic flow condition at the seat OD. Consequently, these models cannot be directly compared with the other essentially flat models. It is significant to note, however, that the smoother of these models (N_f and S_f) reached leakages below 10^{-4} scim which indicates the potential of turned surfaces provided they can be made flat. As later described, Model NN_f (turned similar to N_f, but flat within 10 microinches) exhibited the same shutoff slope as lapped circular lay models. Even though 3 times rougher than typical 0.8-microinch AA unidirectional diamond lapped models, at 1000-psi stress Model NN_f leakage was comparable to the lapped models, and by 10,000 psi, was further reduced by a factor of 10.

Although of considerably rougher texture, ground models A_f and D_f offer similar comparisons. It can be seen that circular ground Model A_f is capable of achieving a nearly complete shutoff condition, whereas unidirectional ground Model D_f exhibits the usual stiff shutoff characteristic of all multidirectional and unidirectional lay surfaces.

Lapped models comprise the remainder of those shown in Fig. 424. Multidirectional lay Models C and D are undoubtedly rougher than would be encountered normally in practice, however, they are presented for basic correlation. Model B (also multidirectional) represents the typical 2-microinch AA matte finished surface used in many valves. With finer compounds, a reduced PTV roughness could be achieved as exemplified by machine optical polishing techniques. However, such methods are not employed commonly, whereas diamond lapping, as described herein, provides a relatively rapid method for achieving fine surfaces which are capable of lower leakage than the common multidirectional finishes. The basic parameter, however, is the PTV roughness. As indicated, circular lay surfaces have 10 to 1000 times less leakage than models of similar unidirectional lay roughness.

Model M_{f1} demonstrates the basic advantage of the crowned configuration in evenly concentrating the load in an area free from edge discontinuities. Where low loads are involved, proper edge radius and duboff offer significant advantage.

In view of the overriding influence of roughness, little effect of the material parameter was observed other than the physical resistance to plastic deformation. Where only elastic roughness deformation is involved, it is reasonably certain that tungsten carbide would require considerably more load to achieve a given leakage than aluminum. However, no such direct comparisons could be made and, therefore, the parametric data presented in the Seating Analysis section must serve as a comparative measure of this parameter. It should be noted, however, that unanodized aluminum may serve well in crush gasket applications, but for multiple seating it is entirely unsatisfactory because of low hardness and poor abrasion resistance.

Numerical comparison of the flat models is shown in Table 7. The purpose of this tabulation is to correlate the PTV parameter (H) with leakage;

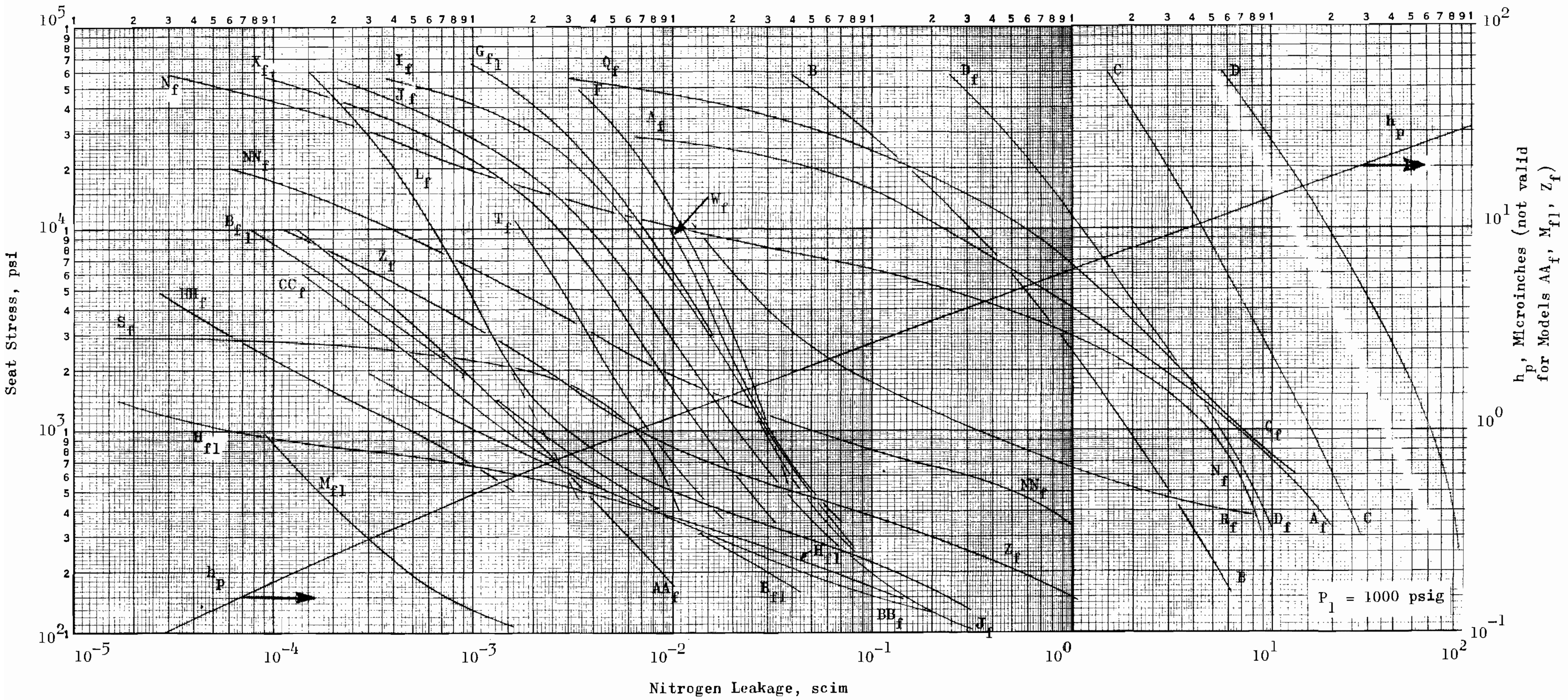

Figure 424. Stress-Leakage Data for Flat Test Models

therefore, models having crowned surfaces or significant pits are omitted. Roughness values (indicated as ϵ h) are taken from Table 4; as noted, circular lay values are halved in accordance with the analytical model described in the Seating Analysis section. Evaluation of the apparent stress level, corresponding to the sinusoidal model surface, is obtained next from the h_p curve of Fig. 424 with test leakages following. As shown, the measured roughness gap is reached for most models between 300 and 600 psi, indicating the relative level of nodule, waviness, and taper influence.

Empirical equations describing the multidirectional or crossed unidirection lay surfaces and the circular lay surfaces are based upon the laminar flow equation. Since leakage over a limited span follows a nearly constant inverse relationship with apparent stress,

$$Q \propto \frac{1}{S^n}$$

these relationships may be combined in a single equation for leakage between 500- and 20,000-psi apparent stress. For unidirectional lay surfaces

$$Q_u = \frac{100 \ P_s \ H^3 \ (P_1{}^2 - P_2{}^2)}{\mu \ LTS^{2/3}}$$

and for circular lay surfaces

$$Q_c = \frac{2 \times 10^4 \ D_s h^3 \ (P_1{}^2 - P_2{}^2)}{\mu \ LTS^{3/2}}$$

where the terms and units previously defined still apply. It should be noted that (H) represents the sum of the PTV dimensions for both poopet and seat, whereas (h) in the equation for (Q_c) is one-half of (H).

As shown in Table 7, these equations adequately describe a wide range of data within nearly a factor of 2. Exceptions exist primarily in the circular lay models where slopes in excess of 3/2 (Models H_f and NN_f) were obtained. Indepedent of test data these equations should be capable of

TABLE 7

EMPIRICAL CORRELATION OF SURFACE ROUGHNESS, LEAKAGE, AND SEAT STRESS

Test Model	Σh From Inspection Data, microinch	0.68 Σh = h_p, microinch	"S" Corresponding to h_p, psi	Test Q, scim at Stress, S, psi			Calculated Q, scim at Stress, S, psi		
				500	1000	10,000	500	1000	10,000
A_f	20 ***	13.6	760	14	6.8	0.23	10	3.6	0.11
D_f	14	17.7	320	8.1	5.5	1.1	3.1	2.0	0.42
B	11	7.5	1100	3.0	1.9	0.31	1.5	0.95	0.21
C	28	19	410	22	15.6	4.5	25	15.7	3.4
D	38	26	1200	76	62	19	63	39.4	8.5
B_{f1}	1.65*	1.1	340	6.0×10^{-3}	2.1×10^{-3}	7.7×10^{-5}	5.7×10^{-3}	2.0×10^{-3}	6.4×10^{-5}
G_{f1}	3.5	2.4	280	4.4×10^{-2}	2.9×10^{-2}	7.2×10^{-3}	4.9×10^{-2}	3.1×10^{-2}	6.6×10^{-3}
X_f	2.9	2.0	250	2.4×10^{-2}	1.4×10^{-2}	2.7×10^{-3}	2.8×10^{-2}	1.7×10^{-2}	3.8×10^{-3}
L_f	1.6	1.1	540	1.0×10^{-2}	3.0×10^{-3}	6.4×10^{-4}	4.7×10^{-3}	2.9×10^{-3}	6.4×10^{-4}
H_{f1}	0.75*	0.51	640	3.7×10^{-3}	6.2×10^{-5}	—	5.4×10^{-4}	1.9×10^{-4}	6.0×10^{-6}
I_f	3.6	2.4	300	4.9×10^{-2}	3.0×10^{-2}	6.4×10^{-3}	5.3×10^{-2}	3.3×10^{-2}	7.2×10^{-3}
J_f	3.3	2.2	310	3.7×10^{-2}	2.1×10^{-2}	3.8×10^{-3}	4.1×10^{-2}	2.6×10^{-2}	5.6×10^{-3}
T_f	2.4	1.6	280	1.3×10^{-2}	7.7×10^{-3}	1.7×10^{-3}	1.6×10^{-2}	9.9×10^{-3}	2.1×10^{-3}
W_f	3.4	2.3	390	5.1×10^{-2}	3.1×10^{-2}	9.6×10^{-3}	4.5×10^{-2}	2.8×10^{-2}	6.0×10^{-3}
NN_f	6.0*	4.1	600	0.50	5.1×10^{-2}	4.0×10^{-4}	0.50	1.8×10^{-1}	5.6×10^{-3}
HH_f	1.4*	0.95	450	1.6×10^{-3}	5.0×10^{-4}	1.0×10^{-5}	2.2×10^{-3}	7.8×10^{-4}	2.5×10^{-5}

*$\Sigma h/2$ for circular lay surfaces
**Average short period waviness added to roughness

predicting leakage within a factor of 10. With circular lay surfaces, indications are that much lower leakage than predicted may be obtained. With loads less than 43 pounds, the effects of nodules, waviness, and taper become increasingly important; therefore, the incidence of these variables may drastically affect the final results. Although unlikely that other regimes of flow will be encountered, the existance of laminar flow should be proved following the methods established in the Flow Analysis section. Due to the configuration of most surfaces, the transition to molecular flow will probably be below that noted herein. Considering the roughness of the empirical equations, omission of the molecular component causes negligible error. However, for flows below 10^{-5} scim, leakage may follow the molecular curve and, in which case, would be greater than predicted. Considering the overriding influence of PTV dimensions in controlling leakage, the performance of a test is the only way to determine accurately the stress-leakage characteristic for any given poppet and seat.

CIRCULAR LAY ECCENTRICITY EVALUATION

As previously shown, the stress-leakage performance of circularly finished models reflected a pronounced improvement over the unidirectional and multidirectional lay versions. However, while the circular lays were estimated concentric within 0.0010 inch as tested, the exact degree of eccentricity was unknown. Furthermore, both poppets and seats were finished in the same rotary and cross-feed direction with the resultant match (one of opposing, fine-pitch spirals, rather than a mirror image). To define precisely the potential performance capability of the circular finish and the effect of the lay eccentricity parameter on this performance, two additional models were fabricated and tested.

FABRICATION AND TEST PROCEDURES

One turned and one lapped model were used in the investigation. For these models, poppets and seats were finished in opposite directions such that, when assembled, a mirror-image lay match resulted. Additionally, both poppet and seat were fabricated with the lay eccentric to the OD or guide diameter by 0.001 inch nominal (0.002-inch TIR). Thus, the parts could be assembled in the tester and, by rotating poppet relative to seat, various degrees of eccentricity from 0 to 0.002 inch established. The following paragraphs delineate the fabrication and test procedures followed.

Model Fabrication

Prior to finishing, poppet and seat guide diameters were witness-marked with $\sim$ 0.0005-inch-wide scribe lines to permit setup of 0.001- and 0.002-inch lay eccentricities. The necessary angular relationship was determined in the following manner.

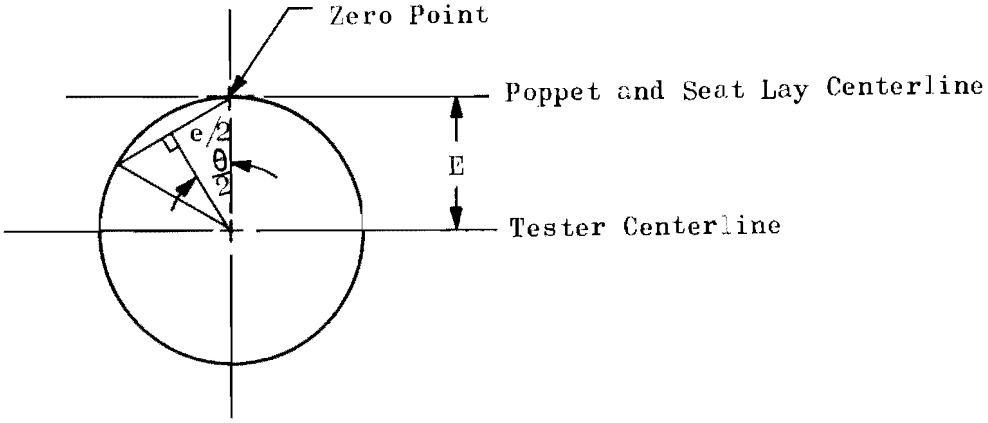

$e = 2E \sin \theta/2 \quad ; \quad \theta = 2 \arcsin e/2E$

Eccentricity e, inch	θ, degrees
0.001	60.00
0.002	180.00

Additional witness marks 90 degrees from the zero reference point were established for lathe setup purposes. All marks were accurate within 0.2 degree.

Parts were then set up in a Hardinge lathe. Using a Cleveland electronic indicator, the OD was made 0.001 inch eccentric (within ±10 microinches) to the lathe spindle centerline with the high and low points at the 0 and 180 degree marks, respectively. Similarly, the 90 degree points were adjusted to run true within ±5 microinches. Finishing operations were carried out with the rotation and feed directions shown below.

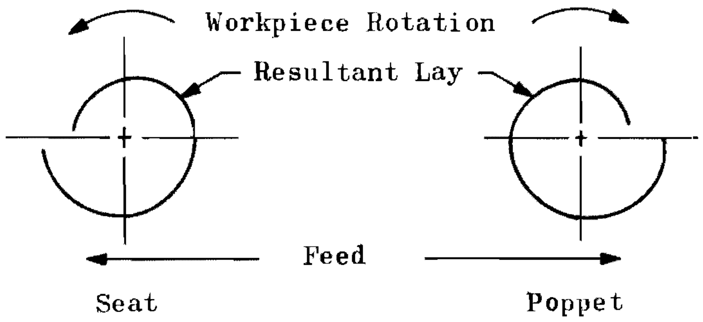

The turned version, Model NN_f, was a rework of former Model N_f, and was fabricated in the same general manner as the latter although NN_f lay pitch was smaller at 0.00031 inch. As with other turned models, the terminating burr at the OD proved difficult to eliminate. This burr, originally about 30 microinches high on Model NN_f, was reduced in two steps. A corner break was first applied with 600-grit sandpaper followed by a final radius operation using a micarta lap and 4- to 8-micron diamond compound. Additionally, poppet and seat were lightly polished with 0- to 1-micron diamond compound on Kleenex, while turning in the lathe. This improved reflectivity without changing the PTV dimensions.

The lapped model, HH_f (formerly H_{f1}) was refinished similar to Model B_f.

Test Setup and Procedures

Stress-leakage testing was initiated in the cycle tester which, with only 50 microinches piston-body diametral clearance, minimized this potential eccentricity error. The unit was set up in an inverted, upright position with the dashpot disconnected. As discussed later, however, a severe contamination problem was encountered and testing was shifted to the static tester. With the latter unit, low friction of the smaller handwheel screw permitted reasonably accurate low-stress testing (balance pressure to 100 psi). In this manner, contamination effects could be detected before the test model was damaged. All reported tests involved a 300-psig balance pressure check and at least one low-stress leakage point.

An alignment jig (Fig. 425) was made to locate poppet and seat witness marks relative to one another. Vertical misalignment between the jig pointers as installed on the tester was less than 0.0005 inch. Visual alignment of pointer and witness mark was accurate to 0.010 inch total.

Two basic errors contributing to potential deviations from the zero or concentric lay position were considered. The first was angular alignment which included electronic indicator sensitivity and witness mark location in both the lathe and tester. This total eccentric error was 1.95 degrees

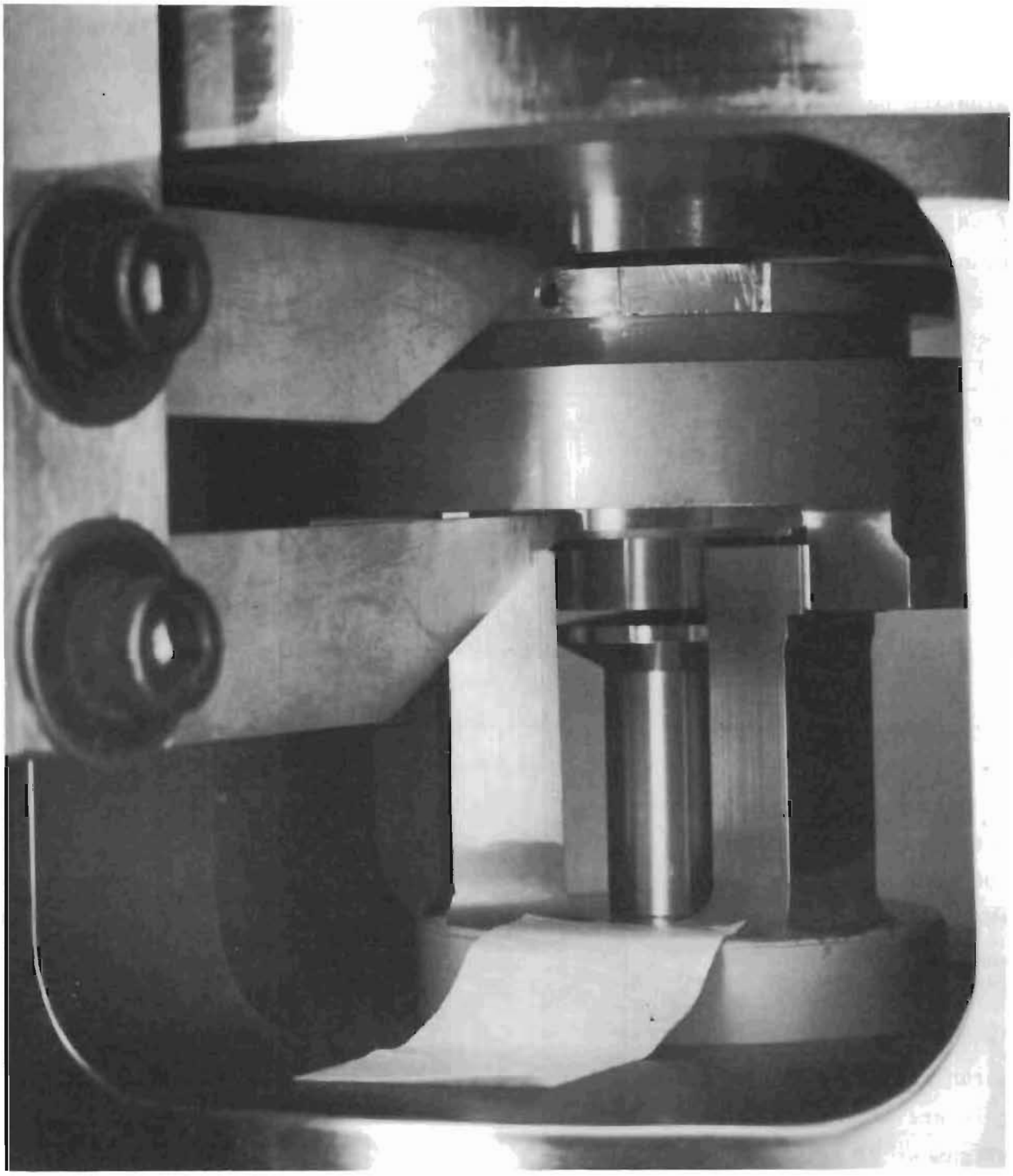

6AD41-3/16/66-C1J

Figure 425. Static Tester With Alignment Jig Setup

or only 35 microinches and was submerged by eccentricity allowed by tester and model parts diametral clearances. In the latter case, resultant eccentricity could be up to 0.0008 inch. Assuming that nodular asperities and the "floating-centering" motion applied during assembly precluded full diametral clearance shift, it is estimated that the zero position included a basic eccentricity error of 0.0001 to 0.0005 inch.

Test procedures deviated somewhat from previously described static testing. To minimize initial hysteresis effects, following the low-stress check points the models were load cycled to 20,000-psi stress three times prior to 1000-psig nitrogen pressure stress-leakage tests. The zero position was tested first, followed by sealing surface separation and poppet rotation to the 0.001- or 0.002-inch eccentric point with final return to the zero position.

TEST RESULTS

Initial test attempts in the cycle tester were invalid because of a metallic contamination problem heretofore unencountered. While schedule and fund commitments precluded determination of the contaminant source, it is suspected that pockets of accumulated debris were disturbed when the setup was moved and the tester inverted. Additionally, the nitrogen bottle first used to blow off sealing surfaces was found to be oil contaminated, a condition for which the 0.5-micron filter employed proved ineffective. As a consequence, the lapped-model sealing surface fabricated originally was destroyed, necessitating fabrication of a second model. The turned version, while damaged, was reworked by light rotary polishing with 1- to 5-micron diamond compound on Kleenex to remove embedded particles, and re-turning was not necessary. With the transfer of testing to the static tester and replacement-cleaning of the blowoff system, no further contamination problems occurred.

Model NN_f, 2 AA Lathe Turned 17-4 PH Poppet and Seat

Model NN_f surpassed all other turned models from a roughness and geometry consideration. Both poppet and seat exhibited a net PTV roughness level of approximately 6 microinches (Fig. 205 and 206) and, for the most part, were flat within 5 microinches. Figures 207 and 208, which show also nearly identical land widths, illustrate the OD hump of approximately 8 microinches remaining after corner burr polishing. With-lay waviness on the order of 5 to 10 microinches PTV was also evident (Fig. 209).

While the previously noted polishing removed the bulk of contamination incurred during initial testing, one large particle remained in the seat. This particle was selectively lapped and removed under 100-power magnification. A sharpened wire, attached to an adjustable stand and lowered onto the contaminated area, was used as a lap with the seat resting on the microscope micrometer stage. Using 1- to 5-micron diamond and reciprocating, with-lay stage motion, the particle was removed with minimum disturbance to adjacent areas. Figure 210 shows the lapping operation, while in Fig. 211 the resultant depression is visible.

Following the cleaning operation, Model NN_f was subjected to a series of stress-leakage tests shown in Fig. 426. The plots on this figure represent a departure from general procedures in that each series of symbols indicates an individual test (sealing surfaces separated). Test 1 established the zero-position characteristic and is plotted (circles) in its entirety. For clarity, only the increasing load points of subsequent tests are shown. These included checks at eccentricities of 0.0020, 0.0000 (repeat), 0.0010 and 0.0020 inch (repeat), noted as tests 2 through 5, respectively. As the 0.0020-inch eccentric test data so closely matched that of the zero position, only a check point was taken at the 0.0010-inch setting.

Since the limiting condition of 0.0020-inch eccentricity failed to demonstrate a significant eccentricity parameter up to 10,000-psi stress, tests 3 and 5 were performed. With 20,000-psi maximum stress check points, these tests (at 0.0000 and 0.0020 inch) also indicated little

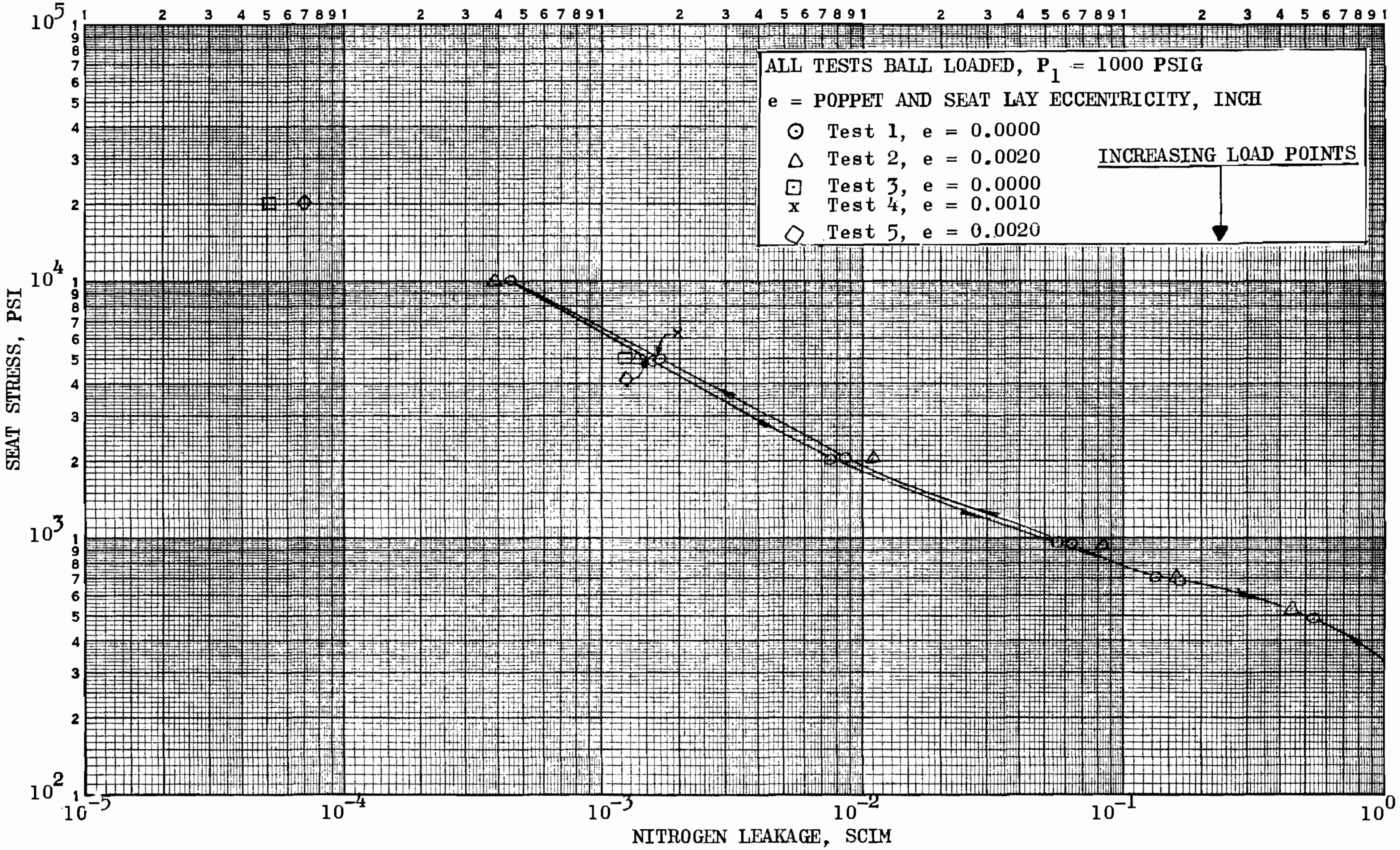

Figure 426. Stress-Leakage Data For Test Model NN_f
Tests 1 Through 5

difference in performance, although a slight increase in leakage was evident in the maximum eccentric position as shown in Fig. 426.

While an indication of eccentricity effects on sealing performance had been expected from Model NN_f, it is probable that any such effect was submerged by sealing surface deviations. Sealing stress was obviously concentrated at the OD because of the aforementioned raised hump on both poppet and seat. Furthermore, the with-lay waviness, particularly in depressed areas, provided radial leakage paths. Also, from Fig. 205 and 206, the spiral pitch is imperfect, possibly causing an irregular overlay of peaks.

From a general performance standpoint, however, Model NN_f reflected a significant improvement over its former configuration, N_f. Leakage at 10,000- and 1000-psi stress was approximately 1-1/2 and 2 orders of magnitude, respectively, better than N_f. Thus, while further manufacturing investigations would be necessary to develop consistent surface capability on a production basis, the turned surface offers considerable promise for valve seats.

Model HH_f, 0.5 AA 440C Poppet and Seat

Model HH_f poppet and seat were reworked from the Model H_{f1} configuration by directly eccentric circular lapping over the former surface without prefinishing. Poppet PTV roughness was 1.1 microinches (Fig. 212), while the seat (Fig. 213) was slightly rougher at 1.5 microinches. The poppet land width was not reduced to equal that of the seat.

As illustrated by Fig. 214 and 215, poppet and seat lands were slightly tapered with the seat OD and poppet ID high. A seating mismatch of approximately 1 microinch (0.002 degree) resulted. While this error was nearly canceled by the opposite direction tapers, the cause of the tapered condition is unknown. Some rolling compound pitting occurred and may be noted in the preceding figures. A more minute pitting characteristic is evident in the with-lay photograph (Fig. 216).

Figure 427 presents the test results obtained with Model HH_f. For clarity as with Model NN_f, the initial zero position stress-leakage curve is completely plotted. Only the increasing load points for the subsequent eccentric positions of 0.001 and 0.002 inch and the final zero return check are shown.

The resultant stress-leakage performance above 700-psi stress was surpassed only by Models H_{f1} and M_{f1}. Again, as with Model NN_f, there was no predominant lay eccentricity parameter evident, and it is possible that pitch irregularity combined with pitting roughness submerged any potential lay eccentricity parameter. With the basic tester assembly errors it is also possible that no test was performed with concentricity better than 0.0005 inch.

DATA ANALYSIS

It is apparent from the test results that parameters in addition to those normally recorded had a more predominant role in effecting closure than lay eccentricity. The repeat of zero position data ensured the validity of the test method and results, therefore, these data are considered reasonably conclusive for the models tested. This is not to say than an eccentricity parameter does not exist. It is obvious that for the perfectly flat and concentric model assumed to have zero roughness with-lay, the leakage for concentric circles would be zero. With mirror image spirals, leakage would result from the spiral scratch which, due to extreme length, would be negligibly small. As this hypothetical model was made eccentric, leakage would be expected to increase gradually for a fixed set of conditions; first, due to an opening of the sinusoidal gap, and second, because of increased contacts. Although the equations for load deformation were developed in the Seating Analysis section, parametric data for the 1/2-inch seat model was not computed; therefore the variation in deformation rate, (stiffness) with eccentricity is not known. Consequently, it is possible that the interrelationship between eccentricity and stiffness is such that for eccentricities greater than the radial roughness wavelength, the increase in number of contacts compensates the reduced stiffness of

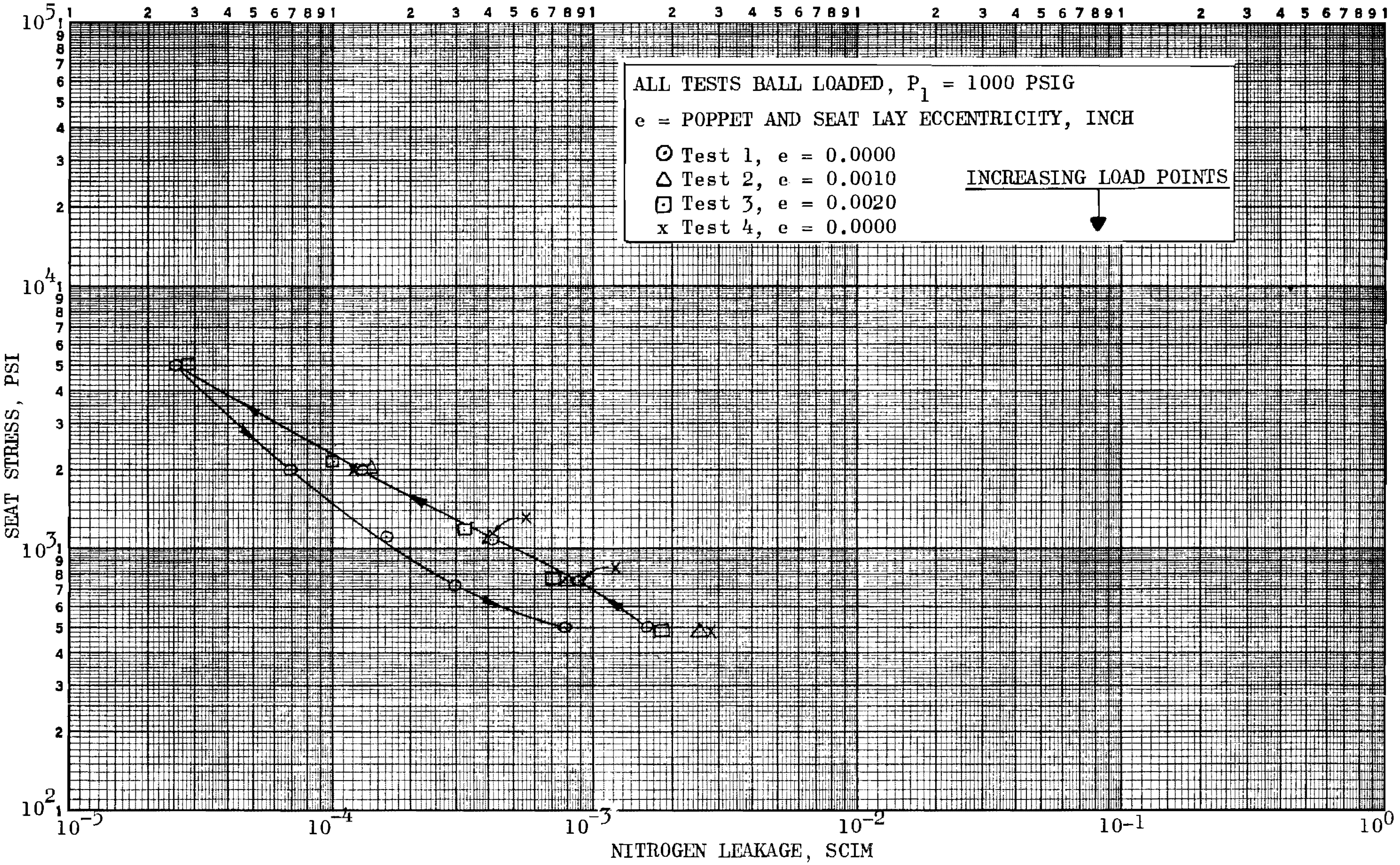

Figure 427. Stress-Leakage Data For Test Model HH_f
Tests 1 Through 4

individual contacts resulting from increased intersection angle. Such was the case in the comparison between the circular and crossed lay models where the much greater number of crossed lay contacts resulted in less deformation and thus, a greater leakage gap for a given load.

For the models evaluated, two conditions are hypothesized which could have obviated the lay parameter. As previously noted, zero-position eccentricity of up to 0.0008 inch was possible and thus, with eccentricity potentially greater than wavelength, the crest intermesh expected to give lower leakage might not have been tested.

Second, interference photos indicated both roughness (though very small) and waviness with lay, which may have submerged any benefits of lay concentricity. This is particularly true if the roughness with-lay was comprised of pits only a microinch deep, but of equally small diameter (say 10 microinches) which would not be detected by visible-light microscopic means. Examination of these surfaces by reflection electron microscopy techniques would answer possibly this last question.

In view of the results, however, it must be concluded that, for the model surfaces and degree of eccentricity investigated, circular lay mismatch causes no significant change in performance characteristics.

CONICAL AND SPHERICAL MODEL EVALUATION

This portion of the test program was devoted to investigation of the stress-leakage characteristics for commonly used cone and sphere seating geometries. For comparison purposes, all conical and spherical seats had, nominally, the same mean diameter as the flat models and, with two exceptions, the same land width as their flat counterparts. (One model seat of each type had a 0.005-inch land.) All models were made of 440C steel with surface roughness of approximately 1-microinch AA or less. Nominal seating angles of 20, 33, and 41 degrees for both conical and spherical models were tested. As noted in the general test procedures, poppets rested directly on the tester piston loading feet on an EP oil film to facilitate axial alignment. Otherwise, test procedures were identical to those employed for clamped flat model static testing, including the capability of electrical contact tests to indicate closure precision.

CONICAL MODELS

Two sets of conical models were made. The first group consisted of one poppet and 0.030-inch land seat pair for each of the three angles to be investigated (Models A_c, B_c, and C_c, with an additional 41-degree seat having a 0.005-inch land width (Model D_c). As noted in the Model Fabrication section, the machining sequence employed for these first models resulted in poor land geometry with significant out-of-roundness and duboff deviations. The subsequent parts, three pairs of 0.030-inch land, 41-degree models, were fabricated differently resulting in more uniform geometry. However, significant discrepancies still existed and these subsequently fabricated poppets and seats were matched in order of best mating conditions (Model E_c first, followed by F_c and G_c).

Because of lens clearance limitations, only the 41-degree poppets could be inspected at 500-power magnification and only a portion of the land could be observed. This and matching 100-power data was used as a reference for determining **surface** roughness on other models. Except for the slightly rougher (4 microinches PTV) Model D_c seat, all conical surfaces are estimated to be approximately 1 microinch AA (3 microinches PTV). As discussed in the Model Inspection Procedures section, 100-power interference photographs taken at 90-degree intervals were used to determine cone axis loading face normalcy. All poppets and seats were true within 5 microinches over 0.03-inch land width.

The bulk of seating geometry inspection data was derived from cross-land and circumferential Proficorder traces obtained as noted in the Model Inspection section. Cross-land data was taken with a 0.0005-inch radius tip stylus. Circumferential traces used a 1/16-inch-diameter ball stylus and are a measure of roundness deviations. These records, however, were recorded on linear charts and thus are shown as a plane surface (unwrapped).

Model A_c, 1 AA, 41-Degree Seating Angle

This model was the first 41-degree version fabricated and reflects virtually all of the dimensional and form errors encountered with the initial set of conical hardware. On the other hand, however, Model A_c represents probably a better geometry than most when compared with commonly fabricated parts.

Model A_c seat was both crowned and dubbed and formed at a slightly different included angle than the poppet. The interference photograph of Fig. 217 and the profile record (Fig. 347) illustrate cross-land geometry. Additionally, (from the profile record of Fig. 348) a 20-microinch average PTV, 180-degree period gross circumferential waviness (out of round) was evident, probably due to lathe runout. Superimposed on the basic wavy surface were smaller, 5-microinch PTV undulations with 0.024-inch average wavelength.

The poppet land was crowned slightly (Fig. 218 and 349). Circumferential roundness deviation (Fig. 350) was of more random nature than that of the seat and reflects the inability of light-cut diamond turning and stick lapping to remove original grinding waves. The major deviation was 20 microinches PTV with a 0.32-inch wavelength. Shorter period (0.1 to 0.2 inch) waves 6 to 10 microinches PTV were superimposed irregularly on the surface.

From Fig. 219, a poppet surface texture PTV height of 2 to 4 microinches was interpreted. Comparison of this 500-power and the 100-power photo of Fig. 218 with the seat indicated the latter to have similar roughness, in addition to a 6-microinch PTV waviness component.

Net poppet-seat differential seating angle was approximately 0.05 degree as illustrated by Fig. 428 which also shows the bellmouth condition typical on all conical model ID's. Additionally, the seating angle relationship of Model D_c (0.005-inch seat land and poppet of Model A_c) is pictured.

At 30-psig inlet pressure, Model A_c electrical contact leakage was 0.244 scim, which is equivalent to a parallel plate gap separation of 31 microinches (for a land width of 0.03-inch,Fig. 382). Assuming a somewhat reduced influence from the single large poppet wave, the average poppet circumferential waviness may be assessed at 15 microinches PTV. Thus, the apparent net poppet and seat sinusoidal gap is 35 microinches, or only 25 microinches equivalent parallel plate separation. However, the contacting lands are neither parallel nor a full 0.03 inch wide, which necessitates certain corrections before a model test comparison can be made.

From the combined profile records of Fig. 349 and 347, the basic tapered portion of the seat land is approximately 0.0175 inch wide. The taper height over this land width is about 15 microinches. From Fig. 12 (Seating Analysis section), the resultant h_p/h_o ratio of 1.6 (24/15) yields a tapered equivalent parallel plate factor (N_L) of about 0.78. For the 0.0175-inch land, the equivalent parallel plate height for combined poppet and seat is

$$
\begin{aligned}
h_e &= N_L(h_o+h_p) \\
&= 0.78\ (15 + 24) \\
&= 30 \text{ microinches}
\end{aligned}
$$

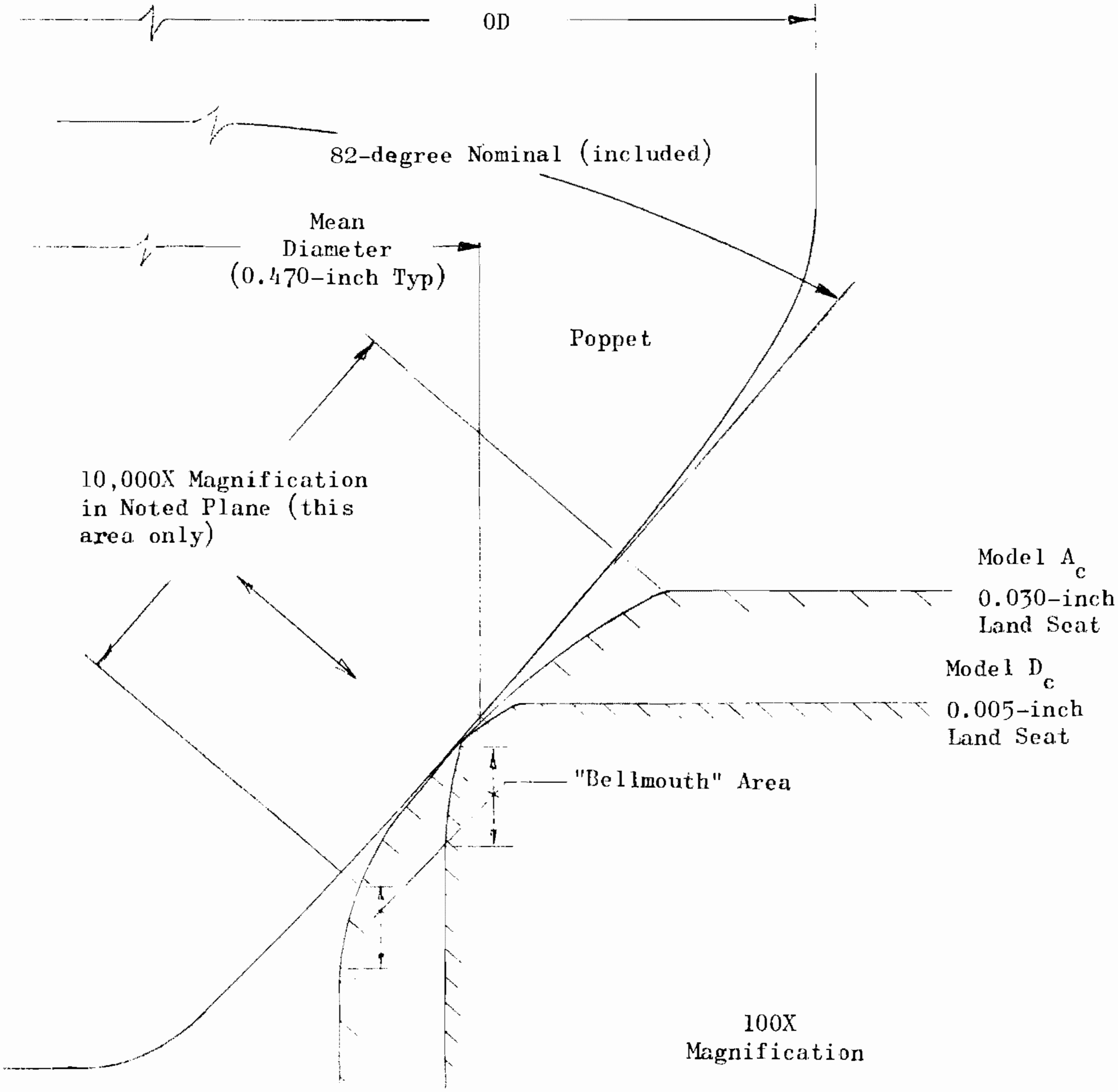
OD
82-degree Nominal (included)
Mean Diameter (0.470-inch Typ)
Poppet
10,000X Magnification in Noted Plane (this area only)
Model A_c
0.030-inch Land Seat
Model D_c
0.005-inch Land Seat
"Bellmouth" Area
100X Magnification

Figure 428. Seating Relationship of 41-Degree Conical Models A_c and D_c

Correcting for the reduced model effective land width,

$$h_e\ (L = 0.03) = 30\ \left(\frac{0.03}{0.0175}\right)^{1/3}$$

$$= 36 \text{ microinches}$$

Therefore, assessment of the actual model geometry equivalent parallel plate gap yields close agreement with the electrical contact test results of 31 microinches. Furthermore, this correlation indicates that abnormal cone axis and contaminant effects are minimal.

Two tests were performed on Model A_c. The results are shown in Fig. 429 where a comparison of both tests indicates excellent repeatability and elastic compliance. The relatively fast closure rate may be attributed to the effect of circular lay, but probably to a greater extent, the pressing out of successive levels of waviness and generation, with load, of increasing contact land width. Obviously, because of the noted geometrical discrepancies, the curve represents a load rather than a stress parameter. Posttest inspection revealed minor radial scuff marks but no significant test damage.

Model B_c, 1 AA 33-Degree Seating Angle

Conical Model B_c also had certain geometrical discrepancies caused by the fabrication method although not so severe as Model A_c. The seat land (Fig. 220 and 351) was scalloped radially and formed with the near flat poppet (in the contact region) a differential seating angle of 0.0094 degrees. (Poppet cross-land interference photograph and profile trace are shown as Fig. 221 and 352, respectively.)

The seat (Fig. 353) had 20-microinch PTV circumferential waves with a 180-degree wavelength on which was superimposed a 5-microinch PTV short period waviness characteristic with 0.019-inch average period. The poppet roundness-waviness characteristic was comprised, basically, of four 90-degree period, 15-microinch PTV waves (Fig. 354).

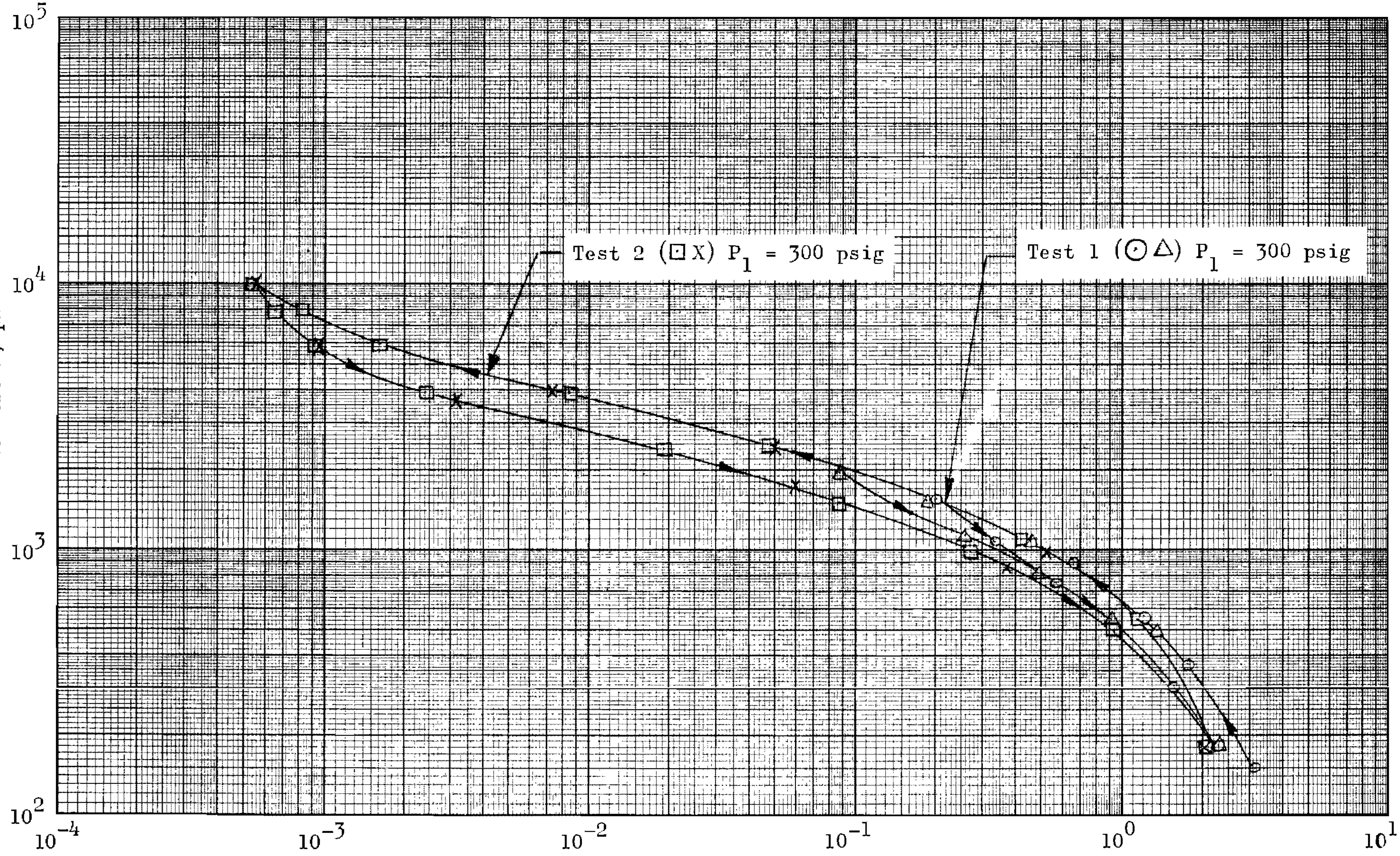

Figure 429. Stress-Leakage Data for Test Model A_c, Tests 1 and 2

Electrical contact leakage of 1.42 scim at 100-psig supply pressure indicated an equivalent parallel plate gap of 30 microinches. This was virtually identical with the net corrected seating geometry equivalent separation of 30.4 microinches. (The latter was derived as reported in Model A_c discussion except that the net waviness value was unweighted.)

Model B_c was tested at 1000 psig as shown in Fig. 430. The test data to various stress levels are repeatable and indicate no plastic deformation. However, it will be noted that hysteresis effects are more pronounced than those with Model A_c. This is attributed to the smaller seating angle with attendant increase in interfacial shear forces. Closure characteristics are similar to the 41-degree Model A_c, reflecting the effect of circular lay and successive deformation of fabrication waves. Some scuffing damage, apparently due to "feed in" of poppet to seat during initial closure, was noted in posttest examination, but no major damage occurred.

Model C_c, 1 AA 20-Degree Seating Angle

Because of microscope lens clearance proglems, Model C_c seat could not be viewed or photographed even at 100-power magnification. However, 40X plain microscope comparison viewing indicated a surface texture similar to other conical models. The poppet (Fig. 224) had approximately a 1-microinch AA finish with a scalloped condition. Evaluation of poppet and seat cross-land profile traces (Fig. 355 and 356, respectively) indicated an average net differential seating angle of approximately 0.044 degrees over an effective land width of 0.0183 inch.

Seat out-of-roundness deviations as shown in Fig. 357 were relatively uniform at 18 microinches PTV. The poppet (Fig. 358), however, evidenced a relatively constant surface with trough-like deviations. For comparison with electrical contact test results (predominantly laminar flow), this surface was assessed in the following manner.

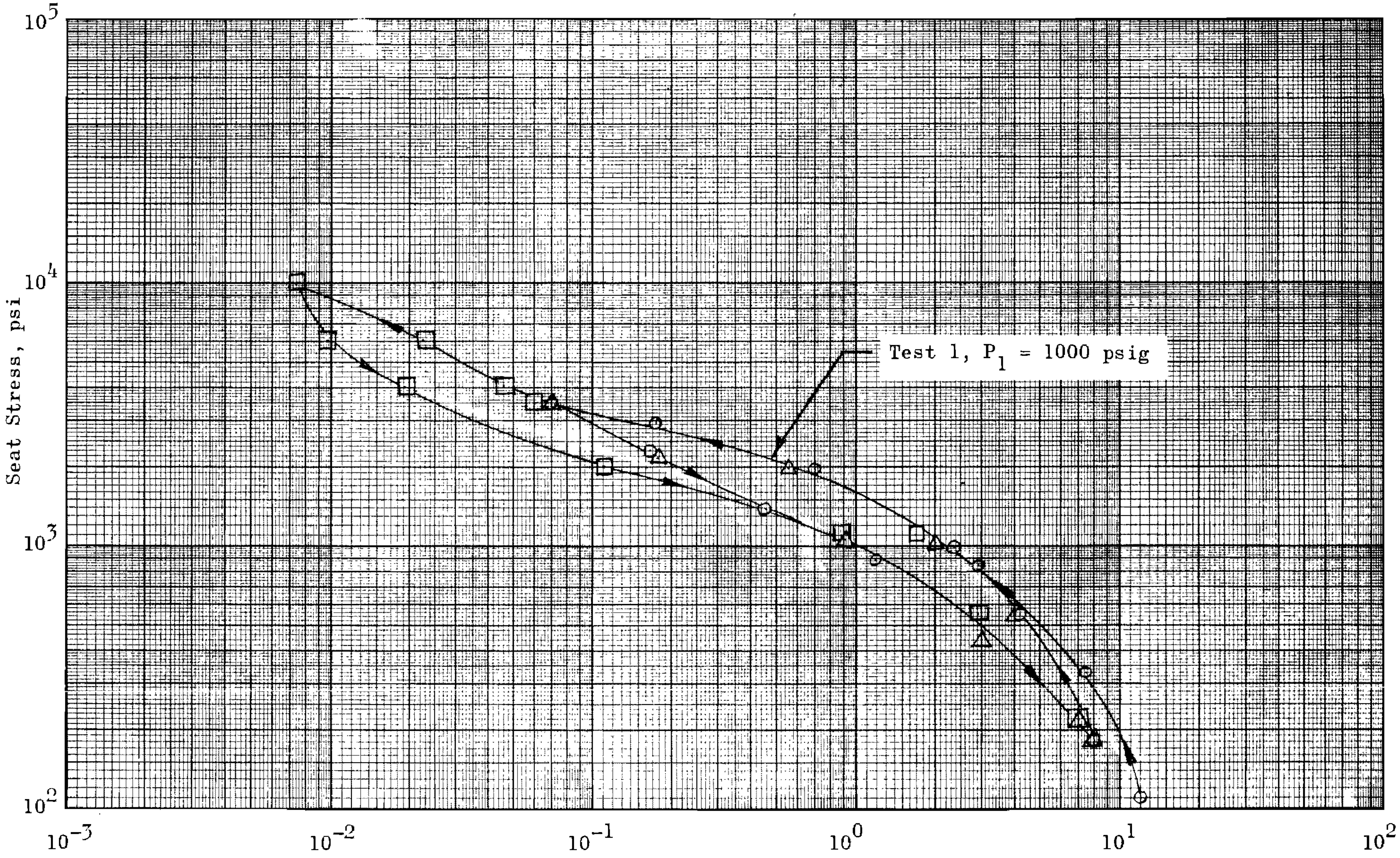

Figure 430. Stress-Leakage Data for Test **Model** B_c, Test 1

The portion from 0 to approximately 90 degrees was considered a triangular-shaped trough extending over a 0.372-inch peripheral distance with a PTV height maximum of 20 microinches. The two remaining troughs (sinusoidal) were assessed as 25 microinches PTV over 0.149 inch (110 degrees), and 45 microinches PTV with a 0.173-inch wavelength (290 degrees). The balance of the surface was considered uniform. Resolution of surface discrepancies into a representative equivalent parallel plate height was accomplished proportionally as shown below in the schematic profile.

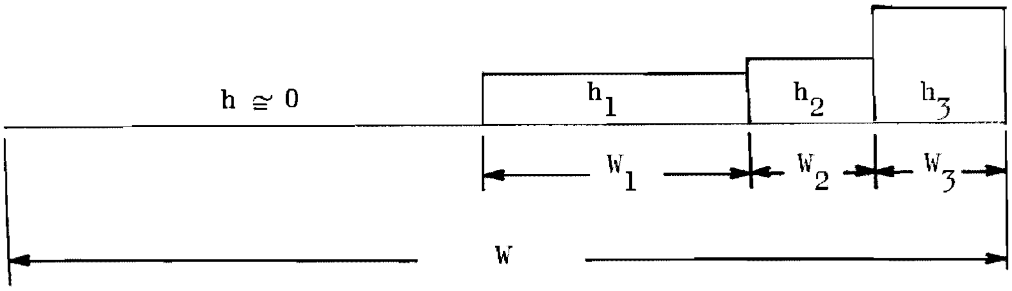

$$h_{e1} = 0.63 \times 20 \times 10^{-6} = 12.6 \text{ microinches (sawtooth factor)}$$

$$h_{e2} = 0.68 \times 25 \times 10^{-6} = 17.0 \text{ microinches (sinusoidal form)}$$

$$h_{e3} = 0.68 \times 45 \times 10^{-6} = 30.6 \text{ microinches (sinusoidal form)}$$

$$W = \pi D_s = \pi \times 0.470 = 1.475 \text{ inches}$$

$$W_1 = 0.372, \; W_2 = 0.149, \; W_3 = 0.173 \text{ inch}$$

Since

$$Q \sim W h_e^3$$

$$h_e = \left[\frac{1}{W}\left(W_1 h_{e1}^3 + W_2 h_{e2}^3 + W_3 h_{e3}^3\right)\right]^{1/3}$$

$$= 24.2 \text{ microinches}$$

The equivalent parallel plate height for the seat deviation (18 microinches PTV) is 12.2 microinches for a net contacting surface parallel gap of 36.4 microinches.

The taper height (h_o) over the effective seat land width (0.0183-inch) was assessed as 16 microinches. Again, as with previous models, using the procedure described in the Seating Analysis section, the equivalent tapered flow passage height was established as 43.5 microinches. Correcting to a 0.03-inch land width yields a final net contacting surface separation of 51.3 microinches. Electrical contact leakage test data resolved to a parallel plate gap of 40 to 47 microinches, which agrees reasonably well with the above considering the contact geometry complexity.

Model C_c was tested at 300 psig with three successively higher stress loops as illustrated by Fig. 431. The data indicate a repeatable elastic condition with considerable hysteresis. Interfacial shear effects accentuated by the smaller 20-degree seating angle make this condition more pronounced than with the 33- and 41-degree Models B_c and A_c. (From this data it would appear that, from a cyclic standpoint, as seating angles become smaller damage due to wear will be accelerated.)

Model C_c closure rate was much less than that of Models A_c and B_c. This characteristic is attributed to the aforementioned trough-like form errors present on the poppet. Unlike the approximate sinusoidal characteristic of the other conical parts, Model C_c poppet represents, essentially, a circular plane having two depressions occupying some 22 percent of the surface (neglecting the more compliant, triangularly assessed portion). The load to compress this plane sufficiently to displace the sub-surface voids is considerably greater than that required to depress a long wave sinusoidal sufface. This condition is analogous to the deformation of uniform sinusoidal surface texture where nodules are compressed and a portion of the material is displaced laterally, causing adjacent valleys to rise (Surface Analysis section). Scratches interspersed on a relatively flat (hence stiff) plane, however, are not so influenced. Thus Model C_c poppet voids were not reduced greatly over the stress range tested.

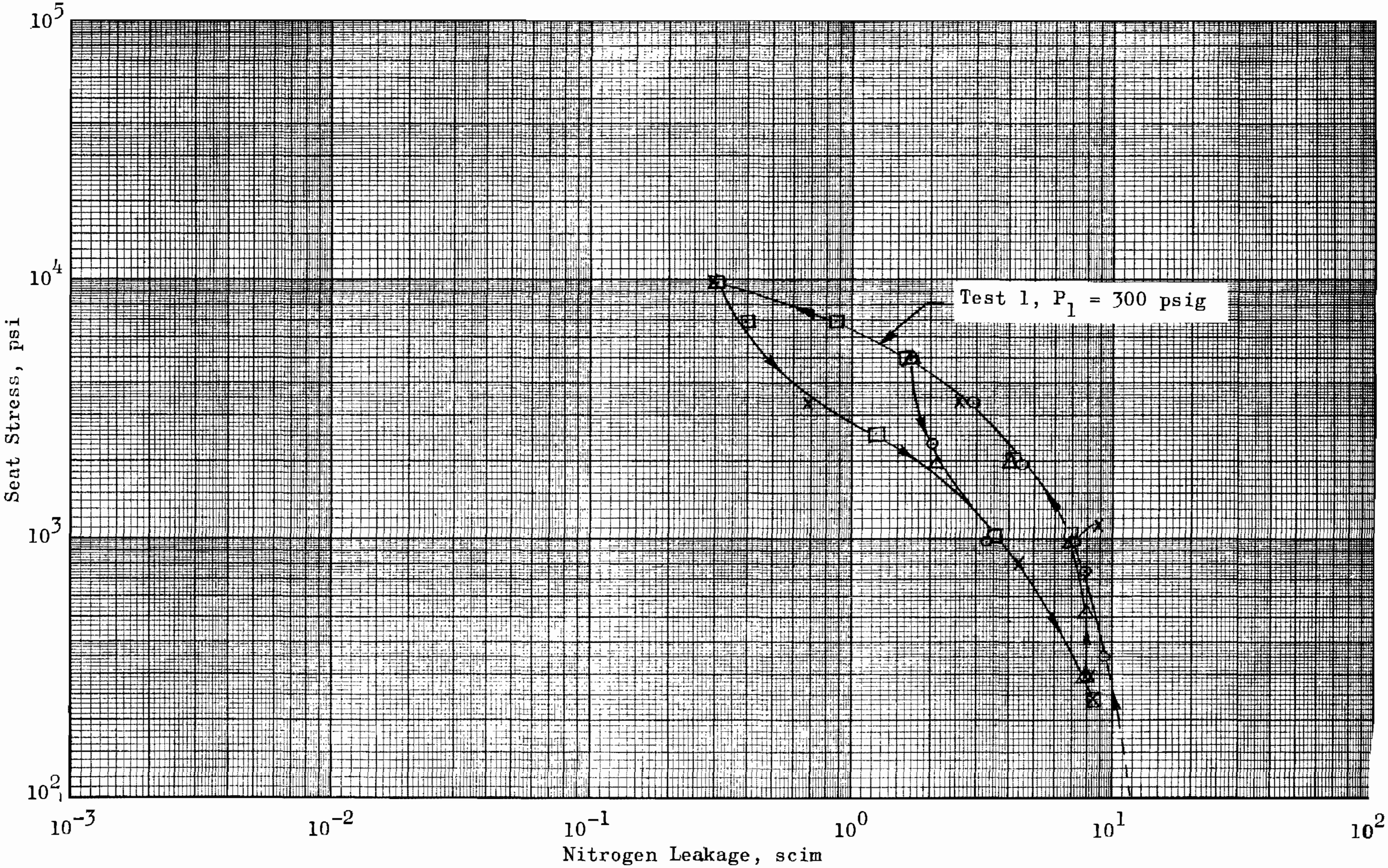

Figure 431. Stress-Leakage Data for Test Model C_c, Test 1

Model D_c, 1 AA 41-Degree Seating Angle, 0.005-Inch Land Width

This model, utilizing the poppet of Model A_c, also exhibited significant form and dimensional errors. Notable was the varied land width which ranged from 0.004 to 0.0051 inch. The value tabulated in Table 4 (0.0046 inch) represents the nominal, or predominant, width which is also illustrated by Fig. 225. The land was tapered (Fig. 359) with respect to the mating poppet, yielding a net differential seating angle of approximately 0.086 degree.

The circumferential profile record was obtained with a 0.0005-inch radius stylus which could be setup visually near the center of the small land more accurately than the ball stylus. Thus, the profile record of Fig. 360 shows evidence of minute waviness. It cannot be evaluated accurately, however, since (1) the horizontal scale is greatly compressed and (2) the relatively fast rotational speed employed for the circumferential profile trace undoubtedly caused stylus skip and perhaps vertical resonance. From this trace, however, the seat roundness deviation can be established at approximately 17 microinches PTV with two 180-degree period waves.

Initial electrical contact tests indicated a parallel plate separation on the order of 100 microinches, much greater than model geometry inspection data had indicated. The model was disassembled and recleaned twice with no significant improvement. Assuming the presence of random nodules or contaminants, a conical lap was made from 0.001-inch thick brass and positioned on the poppet with lanolin. With the model installed in the tester, the intermediate brass conical face was coated with 0- to 1-micron diamond and the seat lightly lapped. This operation improved general contact conditions and also reduced the PTV roughness slightly as the pre- and post-lap photographs of Fig. 226 and 227, respectively, show. (These two figures also illustrate, when compared with Fig. 225, the previously noted land width variation. In addition, the most severe blemish present in the form of three large pits is also evident.)

Electrical contact tests following seat lapping indicated a parallel plate gap of 56 microinches. Using the procedure outlined previously (with h_p = 21.7 microinches and h_o = 5 microinches over a 0.0036-inch land width), actual seating geometry equivalent parallel plate separation (L = 0.03 inch) was assessed at 48.5 microinches.

With reasonable correlation between inspection and test contact condition data established, Model D_c was stress-leakage tested at 300 psig supply pressure. The results as shown in Fig. 432 indicate, as with previous models, a repeatable elastic condition. The hysteresis component was comparable to that exhibited by the earlier 41-degree Model A_c. At 1000-psi stress, Model D_c leakage was approximately 10 times that of its counterpart, Model A_c, which is commensurate with the difference to be expected from the land width difference. However, land geometry complexity precludes a more explicit correlation of the two models.

Model E_c, 1 AA 41-Degree Seating Angle

This model (and subsequently discussed Models F_c and G_c) reflects the improvements achieved by the manufacturing procedure changes noted in the Model Fabrication section. While seating geometry deviations were less pronounced than with the first lot (Models A_c, B_c, C_c, and D_c) form and dimensional errors still existed.

Surface texture (from 500X poppet data, Fig. 228) was on the order of 1 microinch AA, but radially more uniform than that of the original models (Model A_c poppet, Fig. 219). As a comparison of 100-power interference photographs (Fig. 229 and 230) indicates, the seat was polished to a lesser roughness PTV height than the poppet.

Similarly, roundness deviations were improved, particularly for the poppets. Model E_c poppet (Fig. 361) exhibited a maximum deviation on the order of 7 microinches with 3-microinch PTV average undulations having approximately

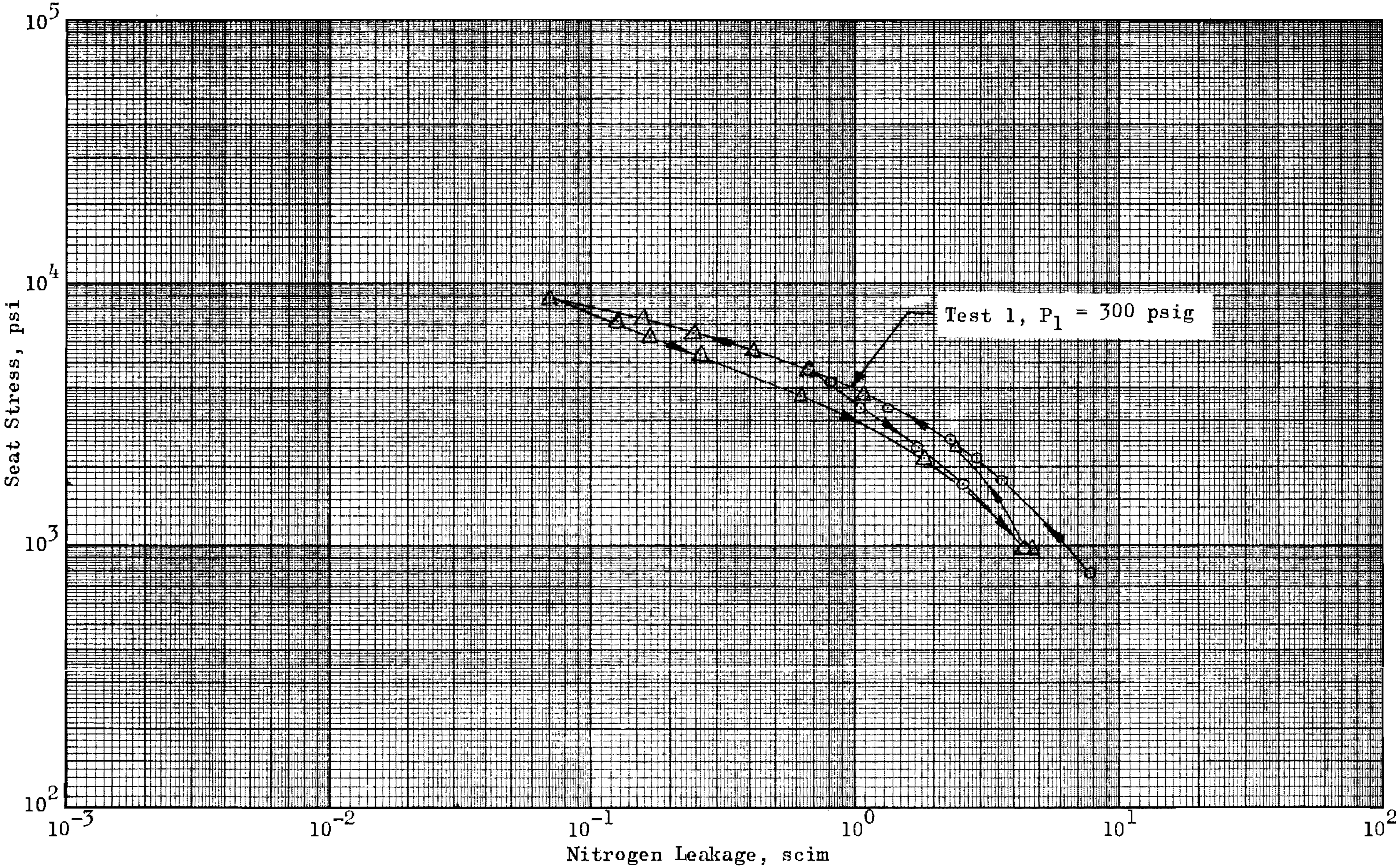

Figure 432. Stress-Leakage Data for Test Model D_c, Test 1

0.11-inch wavelength. Seat roundness error (Fig. 363) was more pronounced having two 180-degree period waves of 13 microinches PTV with shorter period (0.04 inch) 3-microinch PTV deviations. No cross-land profile records were obtained for this model (nor for Models F_c and G_c). Assessment of interference photographs, however, indicates seating differential angle is negligible, the contacting surfaces in essence forming a crown-on-crown condition.

Electrical contact tests indicated an equivalent parallel plate separation of approximately 17 microinches. Assuming a net poppet and seat PTV gap of 16 microinches (3 + 13) yields a parallel plate gap of about 11 microinches. Thus, the greater test value confirms inspection data assessment of crowned (less than full land) contact.

Model E_c was tested with two load cycles to 6000 psi. As the test results of Fig. 433 illustrate, some plastic deformation occurred on the first cycle; the second loop was repeatable. Hysteresis was more pronounced than with the first 41-degree Model A_c. This was due to (1) the increased interfacial shear forces attendant with the greater contact land width of Model E_c and (2) the lack of significant separation force from deformed differential angle contact and circumferential waviness.

Model F_c, 1 AA 41-Degree Seating Angle

This model did not match as well as Model E_c and exhibited a differential seating angle. From the interference photographs of Fig. 231 and 232 this angle was assessed as tapering approximately 0.045 degrees (7 microinches over 0.009-inch land width) to both OD and ID sides of the initial contact point. Seat roundness deviation (Fig. 363) was on the order of 24 microinches PTV with 180-degree periods. Superimposed on this out of round surface were 2 microinch PTV waves with short, 0.027-inch average wavelengths. From the poppet profile record of Fig. 364, a net deviation of approximately 6 microinches was deduced after correcting for some apparent inspection setup eccentricity (indicated by the single 360-degree wave).

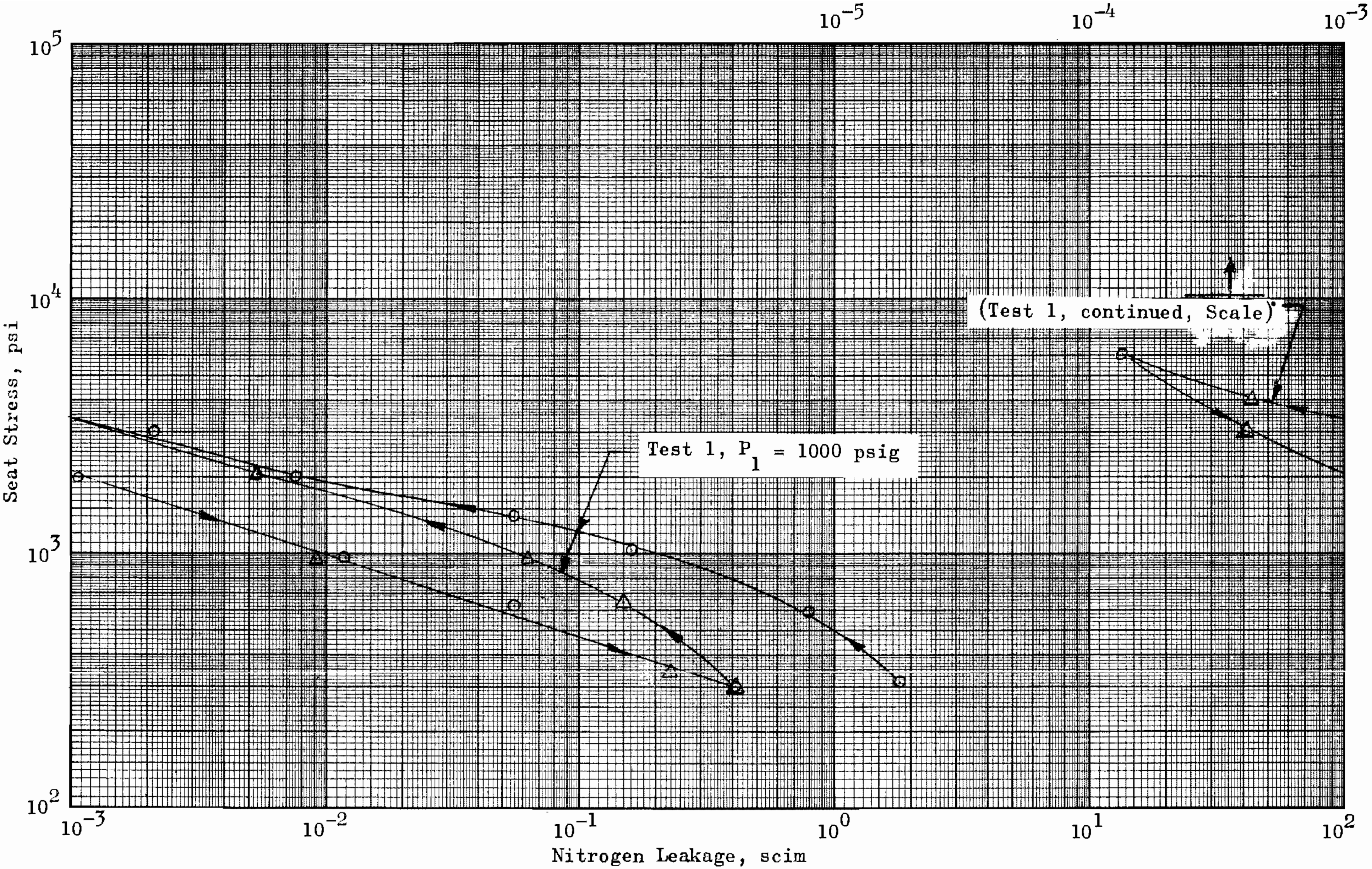

Figure 433. Stress-Leakage Data for Test Model E_c, Test 1

Some shorter wavelength ($\sim$ 0.015 inch) undulations about 2 microinches PTV were also evident. As with Model E_c, the seat surface roughness PTV height was somewhat less than that of the $\sim$ 1-microinch AA poppet.

The double angle contacting geometry precluded reasonable assessment of an equivalent parallel plate no-load gap. Electrical contact tests, however, indicated a separation of 31 microinches which was commensurate with values obtained for other models.

Test data for Model F_c is presented in Fig. 434. As with the previous Model E_c, some plastic deformation occurred on the first stress loop. At low seat stress (second loop, elastic condition), Model F_c leakage is more than an order of magnitude greater than that of Model E_c. This may be attributed to the effects of differential seating angle and the greater PTV out-of-roundness deviation exhibited by Model F_c. However, because of these defects (and for similar surface roughness), Model F_c contact geometry is more readily compliant than the former relatively large crown radii, no differential angle version. Thus, Model F_c evidences a faster closure rate and, ultimately, (4000-psi apparent stress) leaks less than E_c due to a greater peak contact stress. However, the additional interfacial shear stresses imposed in deformation of out-of-roundness and differential angle deviations make Model F_c a poor candidate for low-wear cyclic life.

Model G_c, 1 AA 41-Degree Seating Angle

Model G_c combines the poorest geometry additional poppets and seats fabricated, hence exhibits the greatest differential angle of the three. Evaluation of interference photographs (Fig. 233 and 234) indicates approximately 0.08 degrees mismatch (38 microinches over 0.0275-inch land width). Surface roughness was commensurate with that of the other additional models as indicated by the 500X photograph of Fig. 235 compared with Fig. 234 and 233. As before, the seat surface is somewhat smoother.

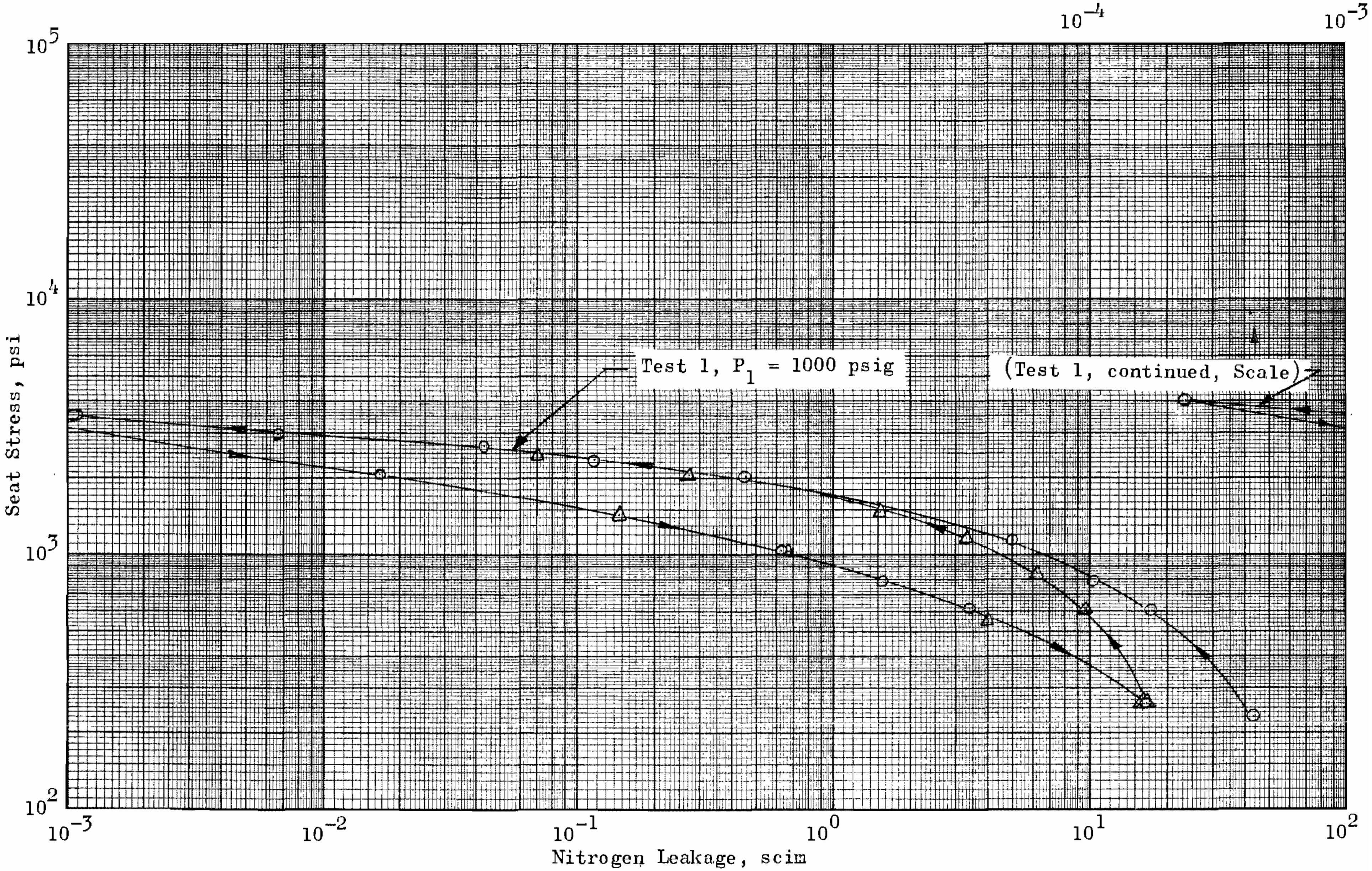

Figure 434. Stress-Leakage Data for Test Model F_c, Test 1

Similarly, as with Models E_c and F_c, the poppet of Model G_c was more round than the seat. Correcting for an apparent inspection setup eccentricity, Model G_c poppet net roundness deviation is about 3 microinches, but has six 6- to 10-microinch deep troughs with 0.075- to 0.100-inch wavelength (Fig. 365). The seat (Fig. 366) was out of round by 24 microinches PTV (180-degree period), with approximately 0.03-inch wavelength, 2-microinch PTV average undulations superimposed on the basic surface. An equivalent parallel plate gap of 31 microinches was deduced from evaluation of contact geometry (h_p = 18.3 and h_o = 28 microinches with an affected land width of 0.0225 inch). Electrical contact tests indicated 28 to 30 microinches.

Figure 435 presents Model G_c stress-leakage data. This model evidenced virtually no plastic deformation. Hysteresis effects were considerably less than with Models E_c and F_c, which is attributable to the deformed differential angle separation force. Although too complex to accurately evaluate, land-width development and resulting contact-stress characteristics for Model G_c and the preceding Model F_c were such that, above 2000-psi stress their performances were virtually identical.

SPHERICAL MODELS

Four spherical test models were fabricated. Models A_s, B_s, and C_s utilized 0.030-inch nominal seat land widths and tangential seating angles of 20, 33, and 41 degrees, respectively. As with the conical group, an 0.005-inch land, 41-degree seat was also made which, with the poppet of Model A_s, formed the final model D_s.

As described in the model fabrication section, all spherical seats were circular lay diamond lapped. Since no 500X seat interference photographs could be taken (insufficient lens clearance), these surfaces were assessed on a 100K magnification comparison basis as approximately 0.5 microinch AA.

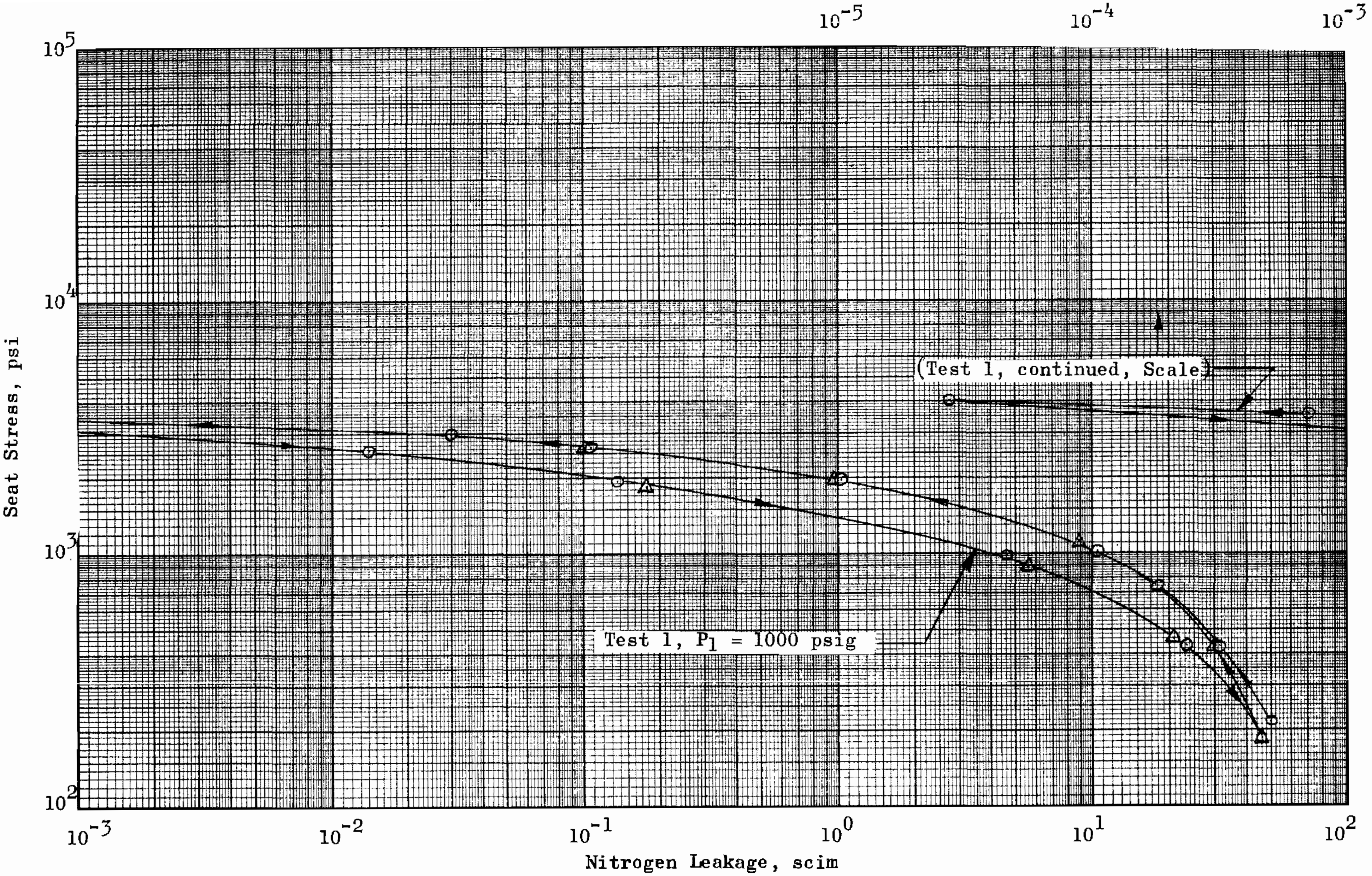

Figure 435. Stress-Leakage Data for Test Model G_c, Test 1

Poppet surface texture was assessed with 500X interference photos taken adjacent to the seat land because of lens clearance requirements. Poppet ball surface roughness was considerably less than 1-microinch PTV (bright mirror finish), but all balls evidenced scratched, pitted, and nodular characteristics as discussed in the applicable model section. Models A_s, B_s, and D_s used grade 25 balls (5/8- and 9/16-inch diameters). The only standard size grade 5 ball commercially available (1/2-inch diameter) was employed in Model C_s.

As tester setup angular misalignment was not critical for the spherical models, no cross-land profile records were taken. Contact taper angles resulting from poppet and lapping ball diameter differentials were computed from ball dimensions (Model Fabrication section). Roundness profile records were obtained, however, on linear charts as with the conical models.

Model A_s , 0.5 AA, 41-Degree Seating Angle

Model A_s seat (Fig. 238) is typical of all spherical model seats fabricated, in that a uniform, low PTV roughness surface without radial scratches was produced. As previously noted, surface texture was assessed at approximately 0.5 microinch AA. The commercially finished poppet ball, however, was a different matter.

Illustrated by Fig. 239, 240, and 367, Model A_s poppet evidenced virtually no surface roughness, but did have a myriad of pits, nodules, nicks, and scratches detrimental to sealing capabilities. From this inspection data, a nodule density (h = 4 microinches) of 1.1 percent was determined. In addition, two pit densities were evident, h = 7 microinches, β = 0.022 and h = 2 microinches, β = 0.33. As typically shown by Fig. 239, random scratches were present also though not assessed.

Model A_s seat was round within 3 microinches (the accuracy level of the Proficorder) and plotted virtually a straight line; thus, the profile record is not presented. The poppet roundness deviation (Fig. 368) was on the order of 10 microinches. A differential seating angle of 0.0017-degree (0.91 microinch over 0.0301-inch seat land width with $D_p > D_{BS}$) was calculated from poppet and lapping ball dimensions.

Stress-leakage test results for Model A_s are shown in Fig. 436. Plastic deformation on the first loop is indicated (nodule flattening), but hysteresis is minimal. Assessment of mating surface geometry indicated an equivalent parallel plate gap at initial contact of 13.3 microinches. (This assumes a net sinusoidal gap of 13 microinches, plus 4 microinches parallel separation due to nodules). Extrapolating the initial increasing-load curve to a low stress of 100 psi (3.0 scim) yields a parallel plate height of 9.5 microinches, which is commensurate with the assessed surface value.

Electrical contact data, on the other hand, indicated a separation of 25 microinches. It is suspected that this was caused by contamination or slight poppet eccentric shift during the electrical contact test. The latter case is most probable and could have occurred during conical testing also. However, the larger surface deviations of the conical models would have easily submerged small eccentricity effects.

Model B_S, 0.5 AA 33-Degree Seating Angle

During assembly into the tester, Model B_s poppet dinged the seat, upsetting the land OD corner approximately 0.00015-inch over a 0.030-inch circumferential length. Figures 244, 245 and 246 illustrate the damage. As the model had been completed and inspected, it was tested as-is, representing "minor" damage probably quite often accepted for valve use. It was intended that the seat be refinished and retested for comparison purposes. However, due to time limitations the rework was not accomplished.

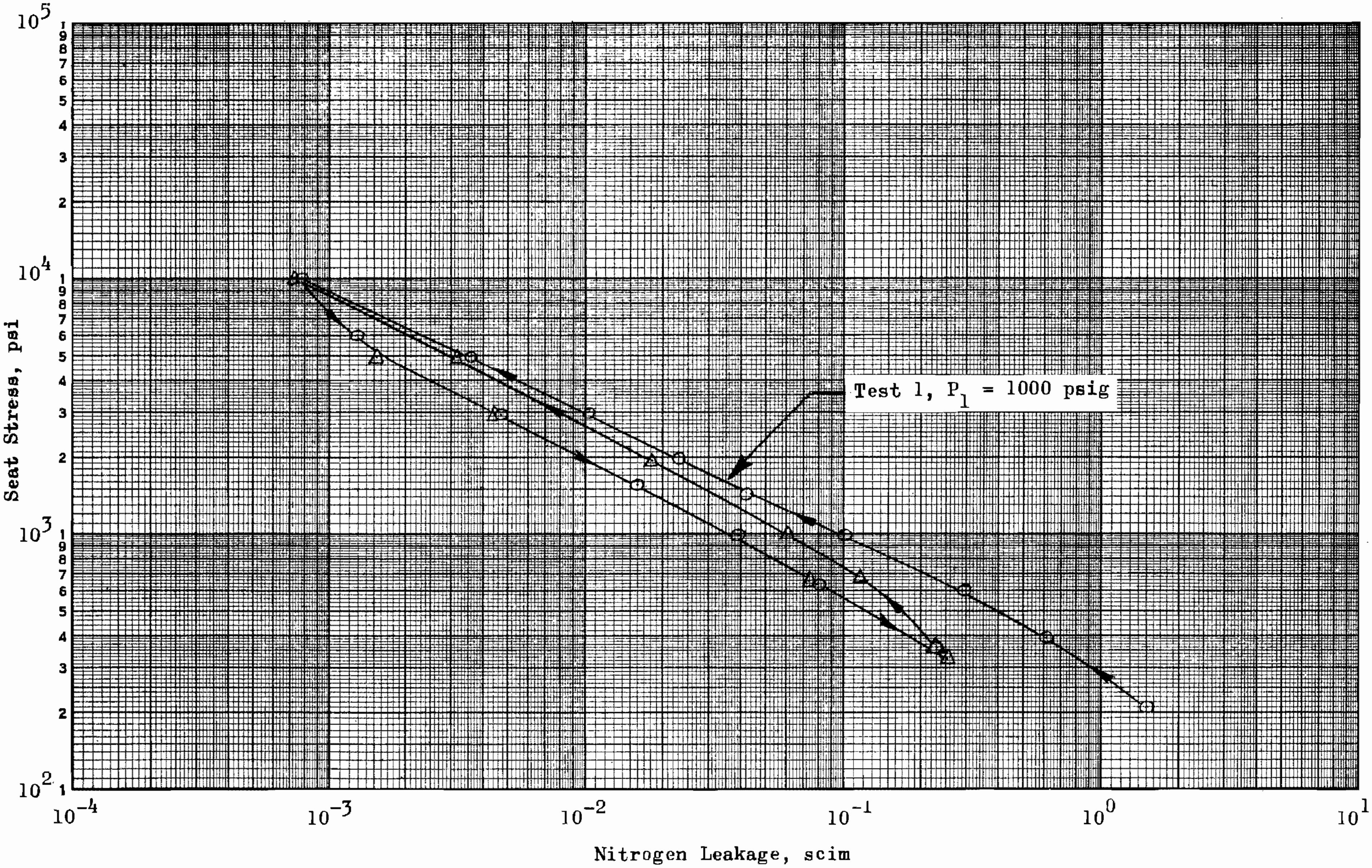

Test 1, P_1 = 1000 psig

Figure 436. Stress-Leakage Data for Test Model A_s, Test 1

Model B_s seat was round within 6 microinches. The poppet (Fig. 369)was round within 10 microinches, but had several trough-like discrepancies. Although a surface roughness profile record was not taken, from Fig. 369 and interference photograph (Fig. 247) assessment a nodule density (h = 4 microinches, β = 0.024) and pit density (h = 7 microinches, β = 0.14) was determined. As with Model A_s, the grade 25 ball was also randomly scratched with one major double scratch 5 microinches deep, approximately 200 microinches wide, and long enough to bridge the seat land.

Electrical contact data indicated an equivalent parallel plate gap of 107 microinches. Since it is probable that the poppet shifted radially, touching both at the upset area and diametrally opposite, the resultant flow path is analogous to an out-of-parallel flat model. Applying the sinusoidal averaging factor, the equivalent parallel plate separation due to the upset is 102 microinches. This value, plus the parallel plate equivalent of out of roundness (excluding knobs), 11 microinches (thus 113 microinches total), agreed reasonably with electrical contact test data.

The stress-leakage test data of Fig. 437 illustrates the effect of the damaged area. Neglecting the anticipated increased hysteresis effect because of a smaller seating angle, this model may be compared with 41-degree Model A_s since both have similar finish parts. Model B_s demonstrates a more rapid closure rate (upset area deformation) but, up to 1000-psi stress, leaks in excess of two orders of magnitude more than Model A_s. Even at 10,000 psi, Model B_s leakage is nearly six times greater, thus emphasizing the marked effect of the "minor" damage.

Posttest inspection revealed the poppet ball was plastically deformed 2 to 3 microinches in the area of contact with the seat defect. Both poppet and seat were slightly scuffed opposite the dinged area apparently because of seating closure motion, and a slight flattening of the seat upset area was noted.

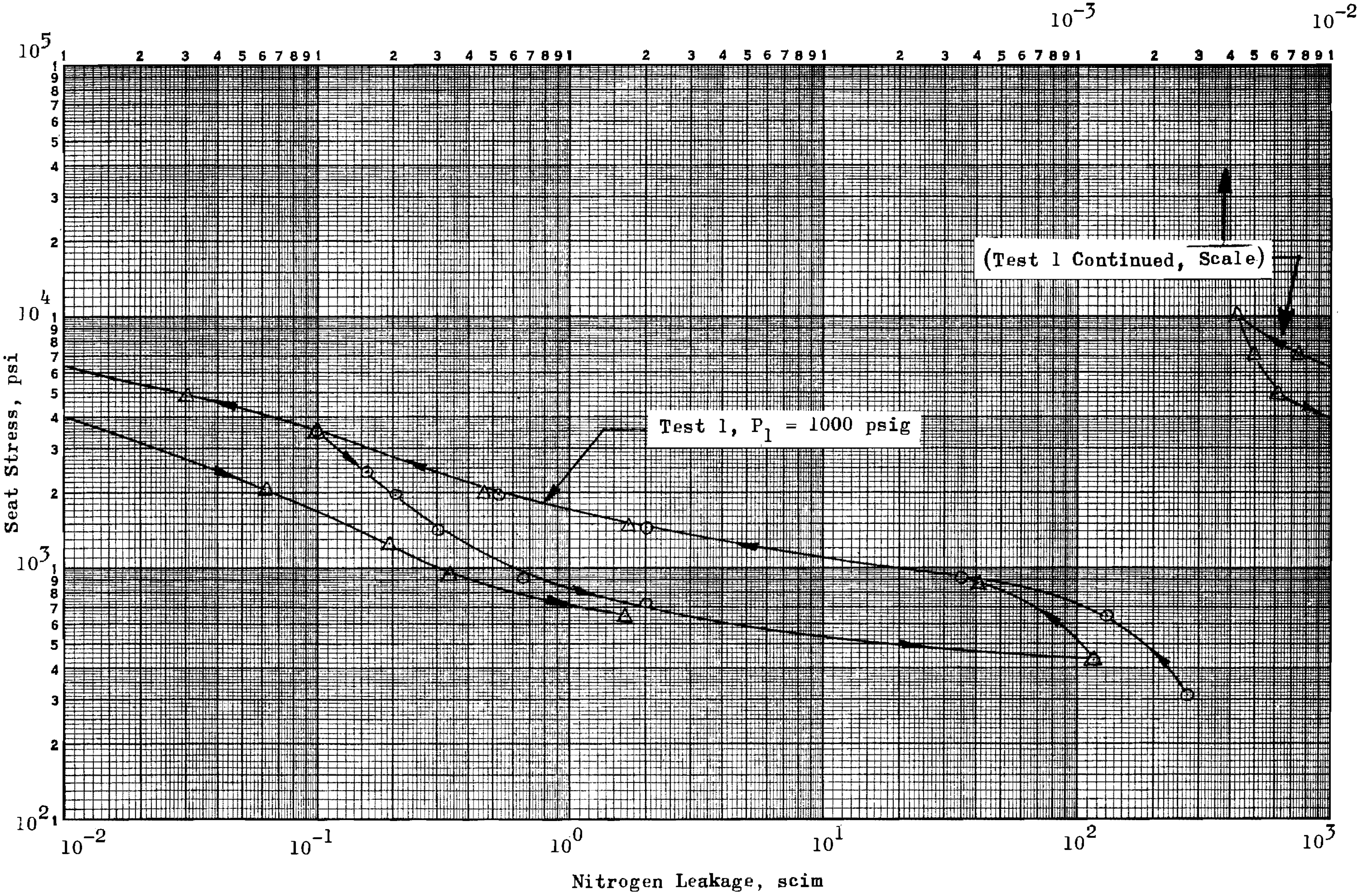

Figure 437. Stress-Leakage Data for Test Model B_s, Test 1

Model C_s, 0.5 AA 20-Degree Seating Angle

This model was the only spherical model to use a grade 5 poppet ball. The ball was round within 5 microinches and, as illustrated by Fig. 370, 248, and 249 exhibited a more uniform surface than the grade 25 ball of Model A_s (Fig. 367 and 240). Nevertheless, pits ($\beta = 0.022$, h = 3 microinches) and nodules ($\beta = 0.34$, h = 2 microinches) were evident and, as Fig. 248 shows, this ball was not free of long scratches and nicks.

The seat was round also within 5 microinches and, with the poppet, formed a calculated 0.0065-degree differential seating angle. Like the 20-degree angle conical model, microscope lens clearance limitations precluded even 100X interference inspection. The surface roughness by 40X comparison viewing, however, was similar to the other spherical seats.

Two stress-leakage tests were performed on Model C_s (Fig. 438). As expected, the small seating angle resulted in a more pronounced hysteresis effect than with 41-degree Model A_s (similar also to the difference noted between conical Models A_c and C_c). Model C_s leakage reflects a significant improvement over the less uniform ball, greater net roundness deviation Model A_s (Fig. 436). At 1000-psi stress, Model C_s leakage is an order of magnitude less and, at 10,000 psi, is still one-fourth that of Model A_s. In both cases, however, the scratched and pitted poppet surfaces detract from the circular lay seat sealing potential. Thus, for low-leakage valve applications, the use of commercial ball poppets, regardless of grade, can serve to limit performance capabilities.

These balls can be lapped to remove surface defects and, ultimately, produce circular lay commensurate with that possible on the seats. However, multiple match lapping operations are involved with special precautions required to maintain a differential angle gap (h_c) such that required flattening loads do not become excessive. (The problem is analogous to that of crowned surface deformation discussed in the Seating Analysis section.)

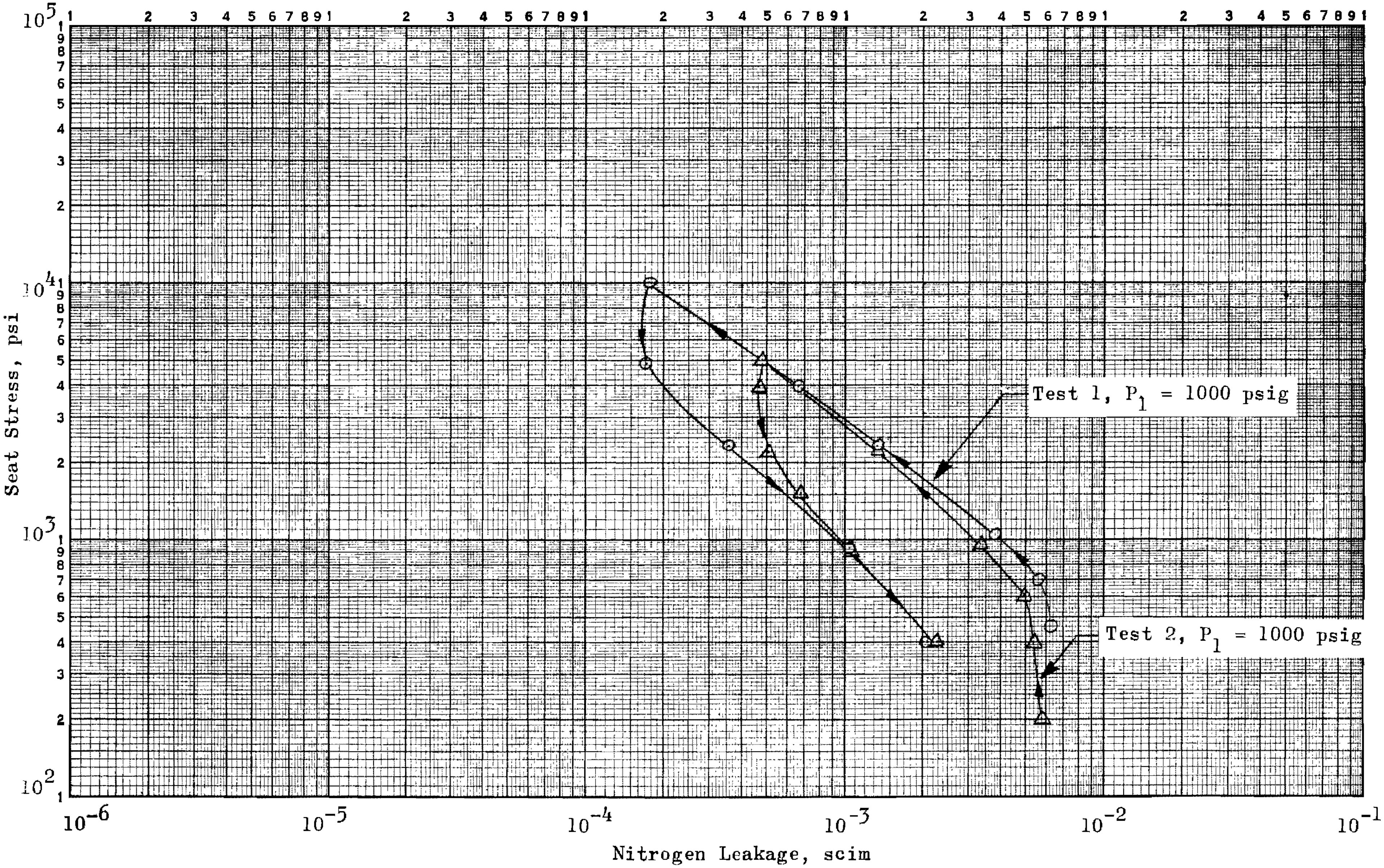

Figure 438. Stress-Leakage Data for Test Model C_s, Tests 1 and 2

Model D_s, 0.5 AA 41-Degree Seating Angle, 0.006-Inch Land Width

Model D_s used the grade 25 ball poppet of Model A_s on an 0.006-inch land width seat finished similar to the other spherical models. The seat (Fig. 250) was round within 6 microinches and, with A_s poppet, formed a 0.0013-degree differential seating angle. No significant seat surface blemishes were noted, but the poppet (Fig. 239) had several scratches (not fully documented) which could bridge the sealing land.

Evaluation of poppet and seat contact geometry from inspection data (h_p = 14.9 and h_o = 0.135 microinches) resulted in an equivalent 0.03-inch land parallel plate gap of 24.5 microinches. Electrical contact tests indicated a 36-microinch separation. The difference is caused probably by poppet eccentric shift during the test. (No evidence of contamination was found during posttest inspection.)

Stress-leakage test results are shown in Fig. 439. These data indicate a repeatable, elastic characteristic with a hysteresis component nearly the same as the initial 41-degree Model A_s. By virtue of land width differences, Model D_s should leak approximately five times as much as its larger land counterpart assuming full land uniform contact in both cases. A comparison of data, however, shows Model D_s leakage exceeds that of Model A_s by 50 times at 1000-psi stress, and by a factor of 10 at 10,000 psi.

When compared on a load basis, Model D_s leaks less generally than the wider land model A_s (above 35 pounds), as might be expected. This is certainly due to the higher concentrated stress of the narrower land. However, the much greater leakage of the narrow land model at equivalent stresses is attributed to the necessity for the land to deform itself and the ball in closing off form errors other than roughness. While not analytically assessable, it seems reasonable that a greater reduction gap will result in equal apparent contact stresses with the wider land seat due to greater

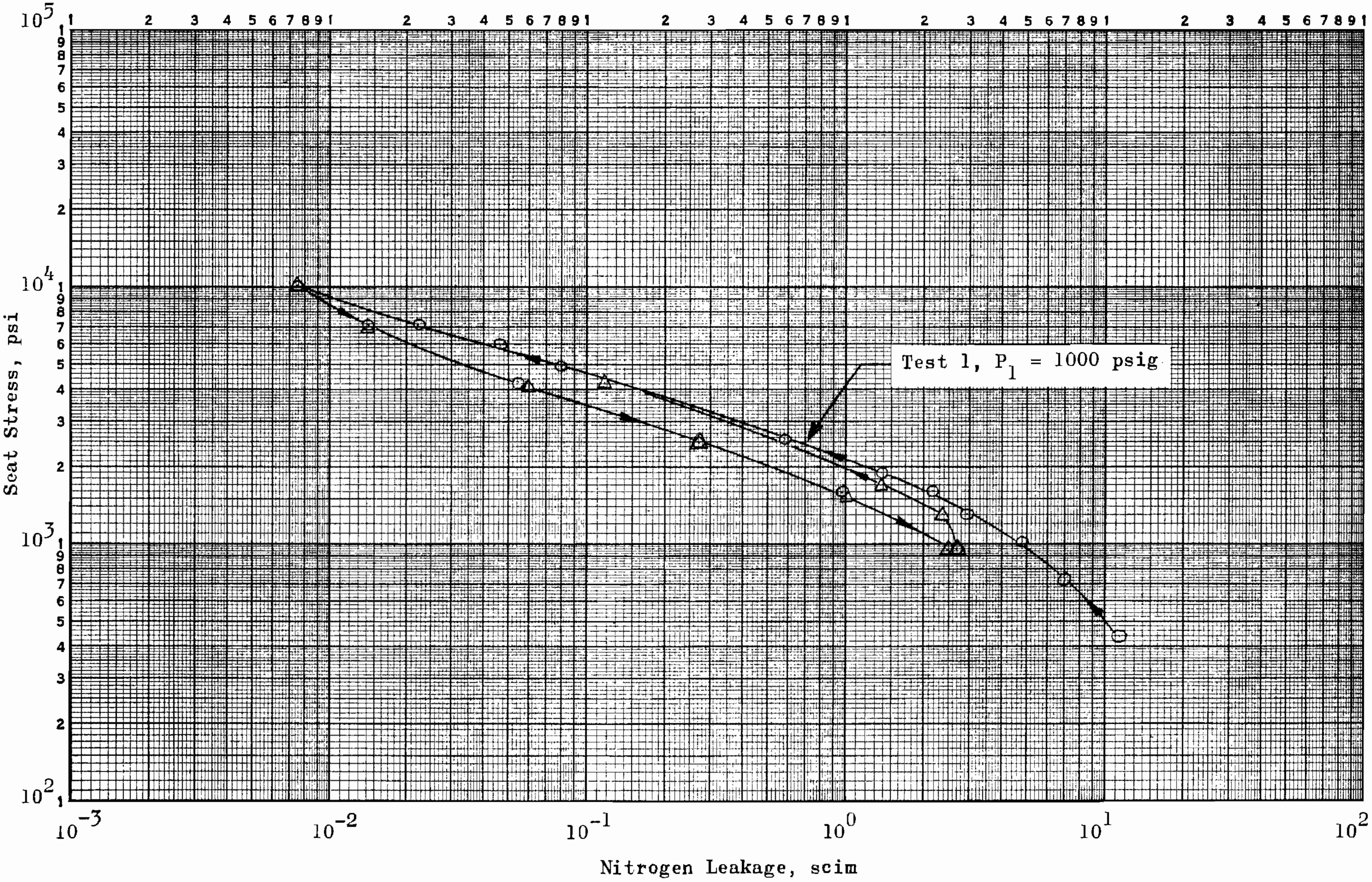

Figure 439. Stress-Leakage Data for Test Model D_s, Test 1

load, even though distributed over a wider area. This argument is supported by the relative equivalent parallel plate (h_e) dimensions associated with Model D_s (for its 0.00604-inch land) which vary from about 4 microinches at 2000-psi stress (12.1 pounds), to about 1.2 microinches at 5800 psi (35 pounds). On the other hand, Model A_s reaches a computed equivalent parallel plate gap of 2.0 microinches at only 1200-psi apparent contact stress (35 pounds), which results in the same leakage as Model D_s.

From these observations it would appear that where a seat land bears upon a much wider poppet land, the apparent stress criterion is not the basic measure of gap closure; this should be considered when changing the dimensions of a given seat.

Model H_{sc}, 0.5 AA Spherical Poppet, 1 AA 41-Degree Seating Angle Conical Seat

The purpose of this model was to evaluate the ball-in-cone seating geometry. The poppet and seat are from Models A_s and F_c, respectively. Since the actual contact land width for this geometry is very narrow, the leakage data are presented in terms of average Hertz stress and load. The seating geometry is shown below schematically with defining equations.

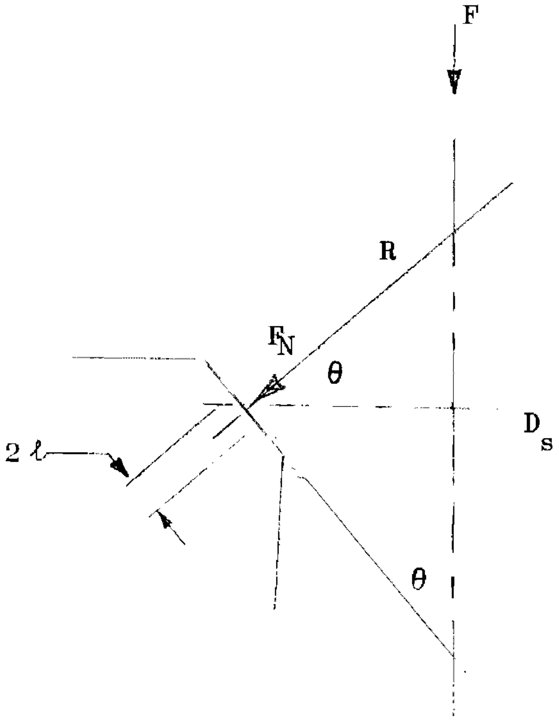

$$\sigma_{avg} = \frac{F_N}{2\,\pi\, D_s\, \ell} = \frac{F}{2\,\pi\, D_s\, \ell\, \sin\,\theta}$$

$$\ell = \sqrt{\frac{4\, F_N\, \alpha\, R}{\pi\, D_s}} = \sqrt{\frac{2\, F\, \alpha}{\pi^2\, \cos\,\theta\, \sin\,\theta}}$$

$$\sigma_{avg} = \sqrt{\frac{F}{8\, D_s^{\,2}\; \alpha\, \tan\,\theta}} = \frac{\pi}{4}\, \sigma_c$$

Maximum allowable average contact stress based on yield strength (Y) is given by

$$\sigma_{avg\ max} = \frac{3\pi}{8}\, Y\ \sin\ \theta$$

From the above equations it is interesting to note that the contact land width ($2\,\ell$) is independent of seat and ball diameter. For normal seating angles, the land width is relatively small because (F) is generally much less than (α).

Model H_{sc} seating angle is 41.27 degrees for a ball diameter of 0.6250 inch. The resultant means seat diameter is 0.470 inch. Introducing these parameters into the preceding relations gives the following equations for land width and average Hertz stress:

$$2\ell = 3.18 \times 10^{-4}\, F^{1/2}$$

$$\sigma_{avg} = 3.26 \times 10^{3}\, F^{1/2}$$

$$2\ell = 9.75 \times 10^{-8}\, \sigma_{avg}$$

Leakage data is presented in Fig. 440 for Hertz stress and actual load. From the constant relation between (ℓ) and (σ_{avg}) it can be seen that land width is exceedingly small at reasonable loads. At 44.3 pounds (σ_{avg} = 21,600 psi), comparable to 1000 psi for the 0.03-inch land flat model, the total land width is 0.00211 inch. Although the load-leakage change is quite large for this model, the narrow initial land width results in high leakage. Moreover, maximum contact stresses are very high at sealing levels comparable to formed land seats. This is shown by load curves for the subject model and Model A_s overlay.

Based upon the preceding data, it is concluded that for best performance a preload land should be generated. With many valve seats the ball is hammered into the seat, thus plastically forming a land. Although performance may be improved in some cases, this method cannot generally match results obtained through lapping.

DATA COMPARISON AND OBSERVATIONS

Conical and spherical valve seats differ from flat seats primarily in the manner of load delivery. Loads applied along the seating axis result in a normal acting seat force that is developed from the mechanical advantage inherent in the wedge. This force is accompanied by a frictional shearing force which, with the normal force component, resists axial motion. Elasticity of the opposing faces potentially allows axial entry, depending upon the friction coefficient, so that the effective contact seating stress is a complex function of these combined forces. Because of the frictional component, the maximum shearing stress is raised toward the contact surface with increasing friction coefficient and, when the coefficient is 1/10 or greater, is located at the surface (Ref. 29). Tangential friction forces also cause an increase in tensile stresses near the contact boundary (opposite to the direction of the frictional force), thus increase the possibility of pitting and wear. The significance of these factors on

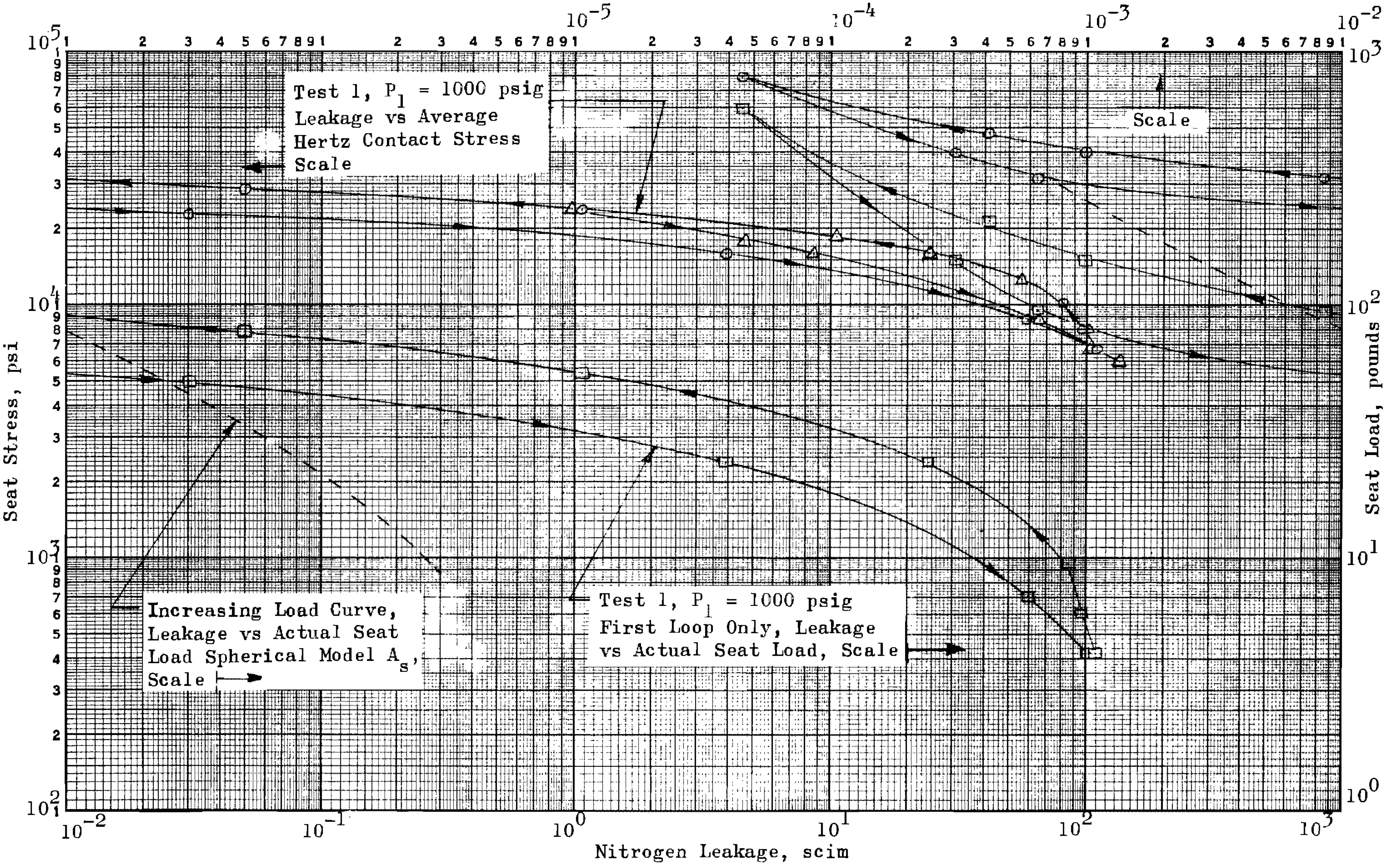

Figure 440. Stress-Leakage Data for Test Model H_{sc}, Test 1

leakage is a function of seating loads, angles and, because a wear consideration is involved, contact cycles. For a valve seat very nearly flat, the angular components are negligible, and the normal load is essentially the axial load. However, for the usual seating angles between 45 and 15 degrees, it is probable that some relative shearing motion takes place during loading. With light loads and larger angles this motion may be negligible although, as with tapered pins, sufficient load will result in significant motion and, thus, cause plastic flow and wear.

Comparison curves on a stress and load basis for conical and spherical models are presented in Fig. 441 and 442. For evaluation of equivalent parallel plate gaps, the (h_p) curve is overlayed on each graph for the 0.03-inch land models. To approximate the equivalent gap for a 0.005-inch land, the values read for (h_p) should be multiplied by 1.8. Where significant taper is involved (conical models), actual gaps are less than indicated.

Since all models except the spherical poppets had circular lay, the characteristic high shutoff rate is evident. Part of this high shutoff rate is due, at the lower loads, to the geometric errors inherent in most test models, particularly the conical versions. Unlike the majority of flat models where total land contact was obtained at relatively low loads, the conical models required additional load to flatten waviness and taper. Likewise, the spherical models had to flatten the nodules on commercial ball poppets before roughness seating was achieved.

The question of what stress or load level was necessary to obtain roughness sealing is difficult to answer because of the unpredictable effects of other geometric variables and the lack of an ideal comparison model. The conical models evaluated were the epitome of geometric error combining waviness, out-of-roundness, taper, and surface roughness in varying degrees. As a result, direct comparison between conical models of different seating angle and flat or spherical models on either an apparent stress or load basis is

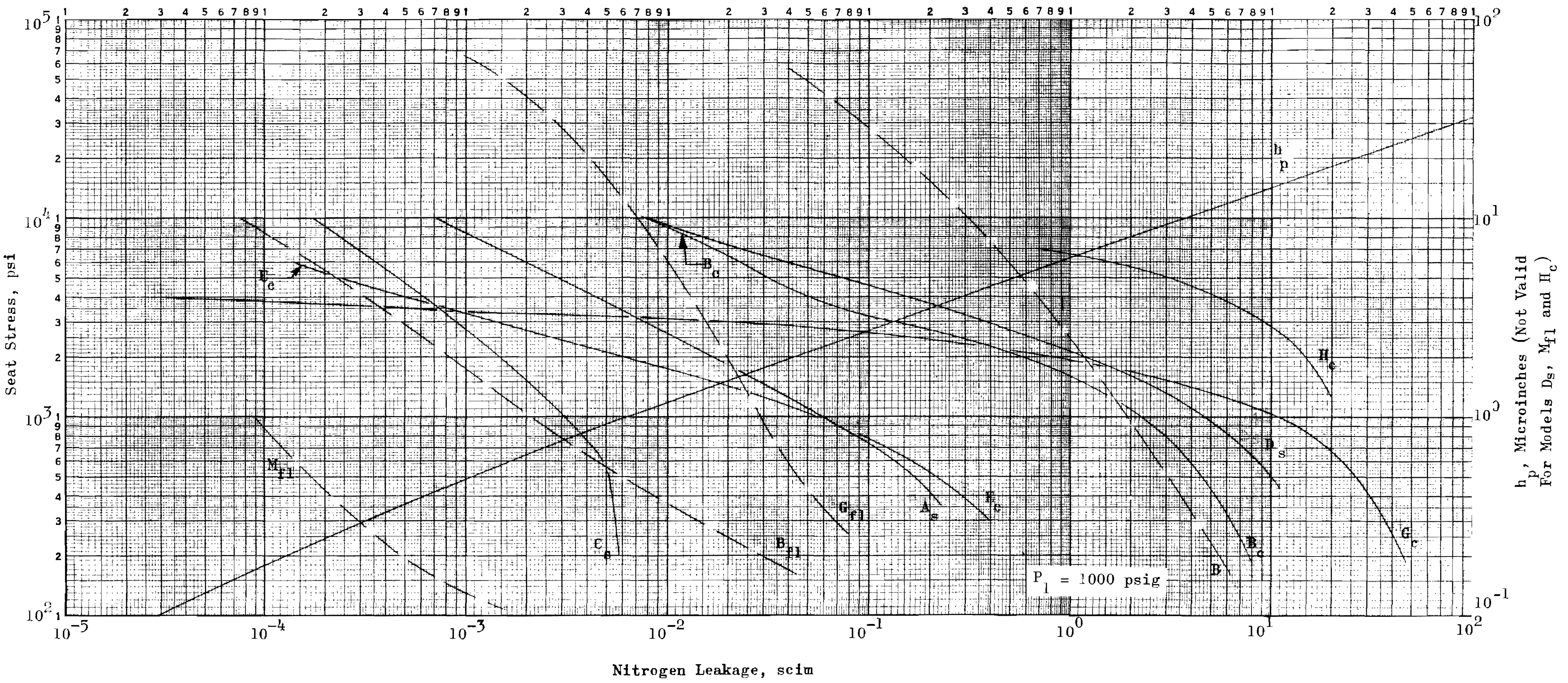

Figure 441. Stress-Leakage Data for Conical and Spherical Test Models

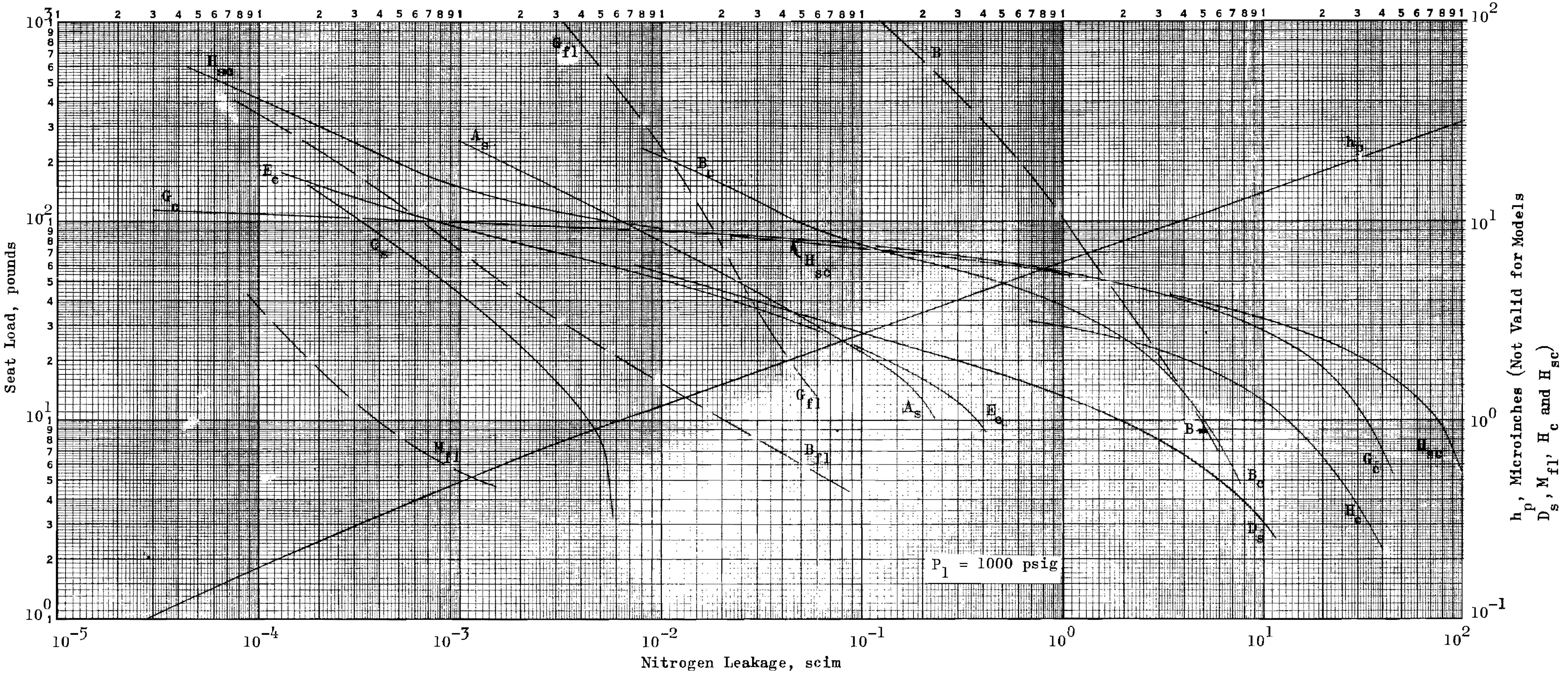

Figure 442. Load-Leakage Data for Conical and Spherical Test Models

not possible. Even had gross errors been avoided (as was accomplished with flat and spherical models), slight variations in roughness between models would have probably submerged any static effect of the seating angle parameter.

Model E_c was sufficiently accurate to provide some degree of comparison with flat Model B_{fl}. The effect of gross geometric errors was predominant in the conical model below 5000 psi (74 pounds), but above this stress the crown effect, augmented by slight taper, caused a higher shutoff rate than evident with the flat surface. Increased shutoff might be attributed to interfacial shear; however, this effect could not be isolated from other variables within the limited test scope. It is possible that, since frictional shear is only a component of normal load, the leakage reduction could be comparable, i.e., not too significant compared ith the geometric parameters, particularly roughness.

The effect of load concentration caused by taper is markedly shown by Model G_c. At low load, the contact land was narrow and leakage high due to some 30-microinch roundness error and 38-microinch taper. Increased load resulted in much greater contact stress than indicated by Fig. 441; therefore was considerably lower than with model E_c. Although this may appear to be an argument for tapered seating, it should be noted that high-stress concentrations accelerate wear roughening, which could destroy the low-leakage capability.

Only sphereical Model C_s provided a reasonable correlation with comparably finished flat Model B_{fl}. The 3:1 mechanical advantage effect on load is shown by the load curve (Fig. 442). Lower leakage obtained with Model C_s compared with Model A_s is attributed (unproved) to the better finished grade 5 ball poppet and not the seating angle difference.

Model D_s (0.006-inch land width) exemplifies the load dependency factor where variables other than roughness are involved. This model appears the same as Model A_s (0.03-inch land width) in roughness, and yet on a stress basis there is wide leakage divergence from the 5:1 land-width ratio. From Fig. 441 the curve directions are almost parallel indicating no convergence at higher loads. This might be attributed to the increased effectivity of poppet ball pits over the narrower land which are inherently stiff.

In summary, the conical and spherical models emphasize the need for a conformal match between poppet and seat interfaces measured in terms of a few millionths of an inch. This was achieved with the spherical seats, although the nodular protuberances on the spherical poppets caused poor low-load performance. With conical models, it is possible that improved low-load performance could be achieved with matched lapping of the poppet and seat.

PROCESSED, PLATED, AND COATED MODELS

In this portion of the test program, the effect of several common processes on the stress-leakage characteristic of previously tested surfaces was investigated. Additionally, oil-film coatings were applied to certain models to determine their effects and potential sealing capabilities.

In the processed category, liquid-honed, passivated, and chromic acid anodized surfaces were tested. (As previous data indicated poor performance characteristics from unanodized aluminum surfaces, the two aluminum models were not pretested prior to processing. For all other models, however, previous test history was known.)

Gold plating was evaluated by plating only the seats of one conical and two flat models. Two of the models were to have been plated 40 to 60 microinches thick, while the third was to receive a 10 to 20-microinch coating. A commercial plating process was used, which proved inadequate for sealing surfaces of the quality under consideration. Both inspection and subsequent stress-leakage data indicated the plating, rather than improving the basic seat, constituted a completely new surface having virtually no relationship with the preplated model condition. Furthermore, it appears in retrospect that the film thickness desired was too great and coatings of 2 to 15 microinches were probably more in order. (If the thinner coatings had been initially considered, a more precise plating operation would have been dictated to the overall benefit of this portion of the test program.)

Comparator measurements indicated two models were plated 44 to 45 microinches thick (satisfactory), but the third was 30 to 31 microinches, 10 microinches thicker than the maximum specified. Microscopic inspection revealed the following additional defects or discrepancies.

1. The plating was quite granular, particularly on the thicker versions.

2. A plating buildup of approximately 20 microinches occurred at the land ID's of all models. The majority of this buildup occurred in the last (inner) 0.005 inch, with the peak at the ID.

3. One model (W_{fl}) had a ridged crack across the seat land with numerous similar cracks on the non-critical outer land. The seat land deformity had a peak height of about 40 microinches, with a crack width of approximately 0.00015 inch and undetermined depth.

4. Also on Model (W_{fl}), an unplated area, approximately 0.005 inch in diameter at land center, was noted.

A discussion with the plater indicated that the granular effect may be reduced by increased process time and lower current. Higher current density at "sharp" edges causes the noted corner plating buildup. The pronounced ID buildup was probably due to location of the anode connection at the seat center (by way of a bolt screwed into the mounting threads). Anode relocation and a crowned land would alleviate this problem. A crack in the underlying nickel strike with high current density at the edges was believed to be the cause of the ridged crack. (This strike, 5 to 7 microinches thick was required as gold cannot be plated directly on 440C stainless steel.) The unplated area was attributed to an incomplete or oxide-contaminated nickel strike. Admittedly, the plater was unfamiliar with processing to the roughness-level and blemish-free requirements of the models submitted. The resultant parts represented a first-time, best-guess approach to the problem.

Since the gold-plated models represented a considerable investment in inspection, finishing and preplating test time, they were tested as-is. (Program schedule commitments and time limitations precluded refinishing and replating.) Test results from the gold-plated models left much to be desired. This, however, should not be taken as a blanket condemnation of gold plating, but rather an indication that the precision of this or any process must be established commensurate with the performance capabilities desired.

The coating investigation involved treatment of several surfaces with four available compounds. It represents only the briefest exploration of an approach which might be a significant advancement of both valve-sealing and cyclic-life capabilities. Tested were General Electric Corporation silicone fluids "Viscasil" (100,000 centistoke viscosity) and "Versilube" (70 centistoke), and "Brayco" NPT-5 diester EP oil. Finally, one part was treated with Oronite oil to deposit a film of zinc, phosphorous, and sulphur less than 1 microinch thick. (This process is used at Rocketdyne for turbopump gear lubrication.)

Except for the Oronite treatment, fluids were applied to poppet and seat with an applicator made of foam-plastic wiping cloth. All visible residue was removed by several hard scrubbing operations using clean applicators. In some instances, fluid application was performed external to the tester. In others, the poppet was removed while the seat remained installed. Similarly, cleaning with benzene and freon-saturated applicators (followed by dry scrubbing) was done wholly or in part external to the tester. High-velocity gas purging of contaminants prior to individual tests was accomplished by bringing the tester-installed poppet and seat surfaces close together (near electrical contact), and raising inlet pressure.

PROCESSED MODELS

Models I_f, 0.6 AA Unidirectional Lay 440C Poppet and Seat and I_{fl}, Liquid Honed

From the interference photographs of Fig. 251 and 252, Model I_f poppet and seat roughness height was assessed at 1.7 and 1.9 microinches PTV, respectively. The large scratch (Fig. 251) was the only significant blemish on the poppet, but did not bridge the sealing land width. The seat scratch (Fig. 252) was approximately 5 microinches deep and 87 microinches wide. However, 1000 psig leakage through this scratch was only 7.2×10^{-6} scim which, as subsequent test data indicates, did not influence the results.

Model I_f was tested twice to establish a reference performance capability. For clarity, the test data (Fig. 443) shows only the first and last load cycles.

Following this test, poppet and seat surfaces were liquid honed as described in the model fabrication section to form Model I_{f1}. The makeup of the resultant surface, however, created some inspection problems. Microscopic examination (Fig. 253 and 254) indicated the surface asperities were crater-like (depression with raised edges), and not as dense as on a multidirectional lapped surface (hence, they were not as well supported by adjacent asperities). Profilometer inspection indicated a surface roughness of approximately 2.5 AA and the Proficorder indicated even less. Apparently stylus pressure was flattening asperity peaks and yielding erroneously low surface roughness values. This conclusion was substantiated by the stress-leakage tests.

Figure 444 presents the stress-leakage data obtained from Model I_{f1}. It will be noted that three stress loops were initially performed with maximum stress values of 1000, 10,000, and 56,000 psi,respectively. The dashed envelope enscribes the results of the fourth through tenth cycles, each taken to 56,000 psi. Plastic deformation occurred, as evidenced by the hysteresis and successively reduced low-stress leakage apparent in the first through third cycles.

The equivalent parallel plate height at 1000 psi seat stress after maximum plastic deformation had occurred is 12.5 microinches, which yields an individual surface roughness of approximately 3.1 AA. This correlates reasonably well with the Profilometer value, and indicates that the stylus data reflected a plastically deformed condition. On the initial cycle, at the maximum stress of 1000 psi, the equivalent parallel plate height is 31 microinches which resolves to a surface roughness (per part) of 5.1 microinches AA. Furthermore, Model I_{f1} stress-leakage characteristic compares very well with that of the 6 AA multidirectional lapped surface, Model D (Fig. 402). Thus, Model I_{f1} surface roughness has been estimated at 6 AA from performance and comparison results.

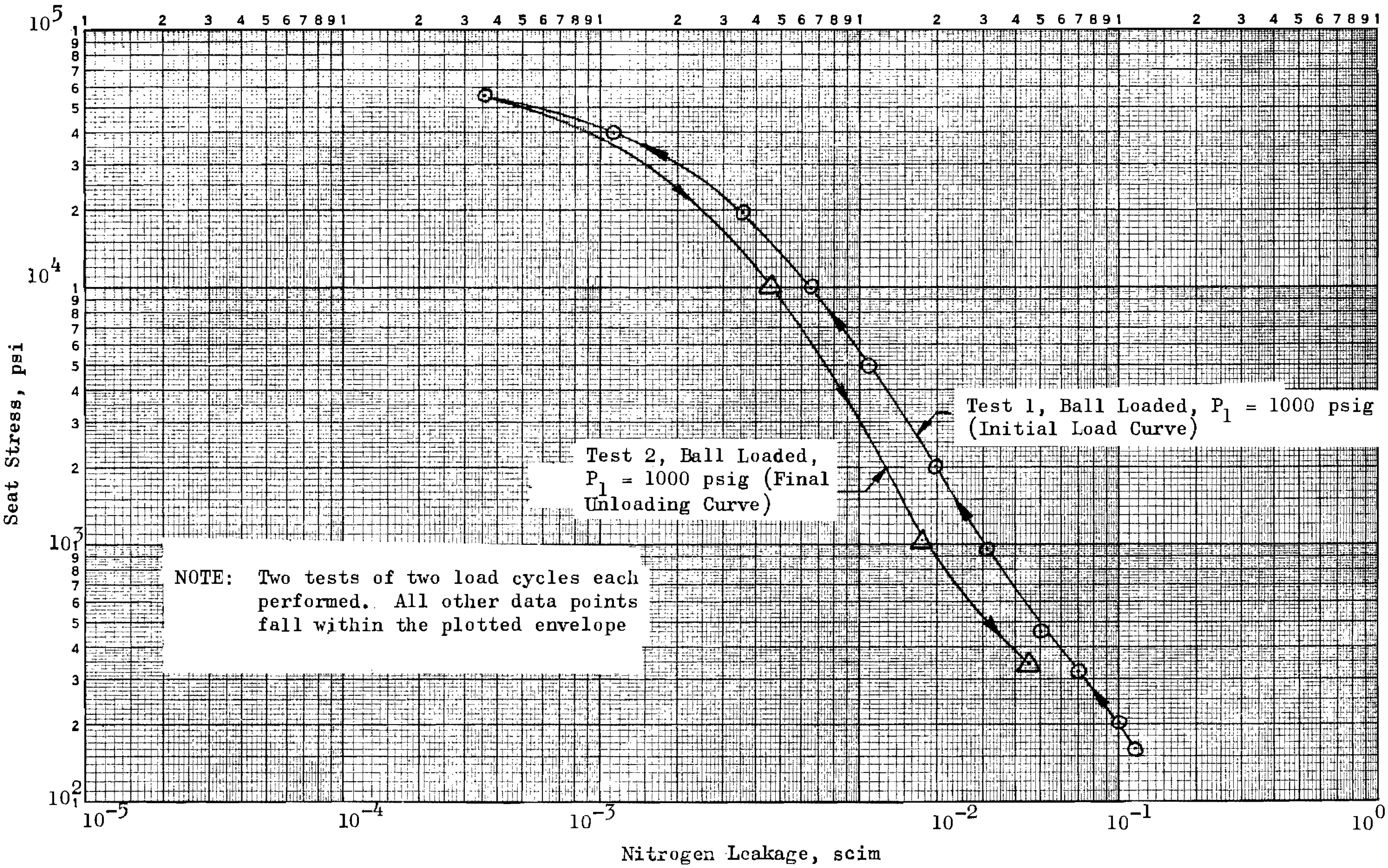

Test 1, Ball Loaded, P_1 = 1000 psig (Initial Load Curve)

Test 2, Ball Loaded, P_1 = 1000 psig (Final Unloading Curve)

NOTE: Two tests of two load cycles each performed. All other data points fall within the plotted envelope

Figure 443. Stress-Leakage Data for Test Model I_f, Tests 1 and 2

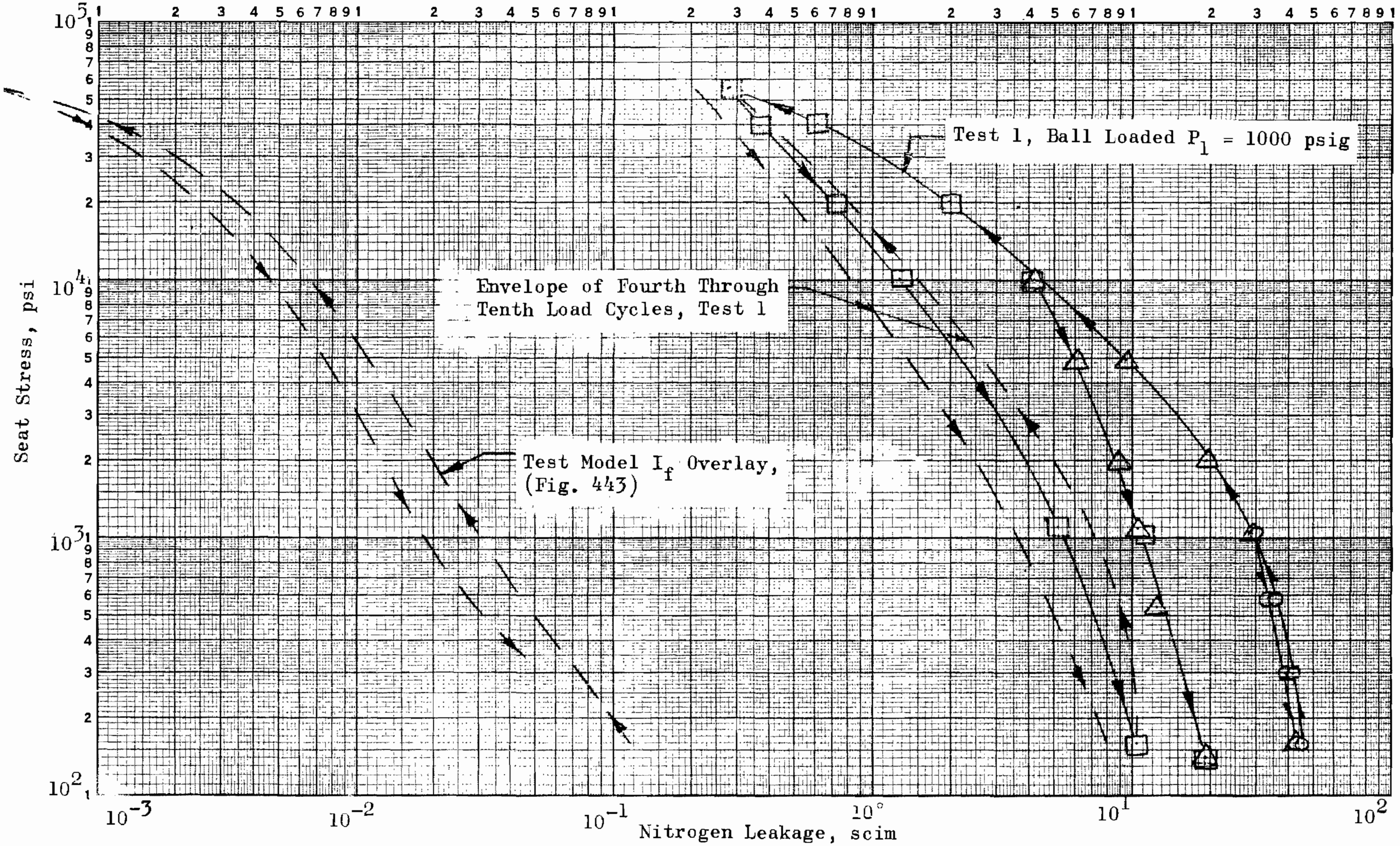

Figure 444. Stress-Leakage Data for Test Model I_{f1}, Test 1

Included as an overlay on Fig. 444 is the stress-leakage characteristic obtained from Model I_f prior to liquid-hone processing. A comparison of this data with the nominal (after load cycling) liquid-hone characteristic indicates the latter version leaked more than 200 times that of the 0.6 AA diamond-lapped surface over the 1000 to 10,000 psi stress range.

It may be argued that the 0.6 AA surface was perhaps an inappropriate one for the noted process evaluation inasmuch as its finish was better than that caused by the process. The processed finish, however, is considered a terminal one, or the best that can be achieved with the particles used. It is probable that a much rougher initial surface could be improved by suitable processing exposure time, approaching the same finish achieved during these investigations. In this case, then, the ultimate process finish was being evaluated.

From a valve-sealing standpoint, where very low leakage values are desired, it is unlikely that the liquid-hone process should even be considered. This is emphasized particularly by the relative ease of fabrication and duplicability of, for instance, the much better diamond-lapped surface as examplified by models I_f, G_f (surface texture evaluation), and subsequently discussed Models J_f and X_f. It is possible that continued investigation, using finer grit particles down to optical flour grades, may result in surface finish comparable to lapped versions, but such investigations were beyond the scope of this program.

Models J_f, 0.6 AA Unidirectional Lay 440C Poppet and Seat, and J_{f1}, Passivated

Model J_f surface texture was very similar to that of I_f with poppet and seat roughness heights of 1.9 and 1.7 microinches PTV, respectively. Figures 255 and 256 illustrate the surfaces. The poppet scratch shown in Fig. 256 was the only significant defect noted and was 10 microinches deep by 40 microinches wide. Its potential leakage at 1000 psig (2.5×10^{-5} scim, Fig. 18), however, made only minor (high-stress) difference in the test results.

Two reference tests were performed on Model J_f prior to passivation. Figure 445 presents the results; as with Model I_f, only the enveloping increasing and decreasing load curves are shown.

The poppet and seat were then passivated (model fabrication section), and the resultant model designated J_{f1}. The passivated surfaces, typically illustrated by the interference photographs of Fig. 257 and 258, were etched and pitted. (As these photographs were taken at the same place as Fig. 255, a direct before- and after-passivation comparison may be made.) The pitting noted may be due to preferential attack of certain impurities and constituents of the base metal. Such damage was by no means dense enough to be considered a large part of the total surface, but the appearance of raised crater-like edges on some pits indicated some leakage performance deterioration would result.

The above conclusion was substantiated by subsequent test results (Fig. 446). While leakage was not greatly increased, the surface degradation noted did influence the models sealing capability. The low-stress leakage increase is attributed to the raised-edge pits. At elevated stress levels, the noted difference may be due to the etched characteristic, or possibly, to slight differences in poppet and seat alignment after reassembly into the tester. It is probable that the passivation effects apparent with Model J_{f1} would be submerged by a more rough texture but accentuated on smoother surfaces.

Model U_f, 1 AA Dubbed, Anodized Seat and 0.3 AA Tungsten Carbide Poppet, Circular Lays

Model U_f seat was unidirectionally lapped with 0 to 1 micron chromimum oxide compound followed by light soft lap polishing to dub the land corners. The final pre-anodize finish treatment consisted of pressing Kleenex tissue, lightly coated with the same compound, into the surface with rotary thumb pressure to further dub the corners and produce a circular lay. The interference photographs (Fig. 259 and 260) illustrate

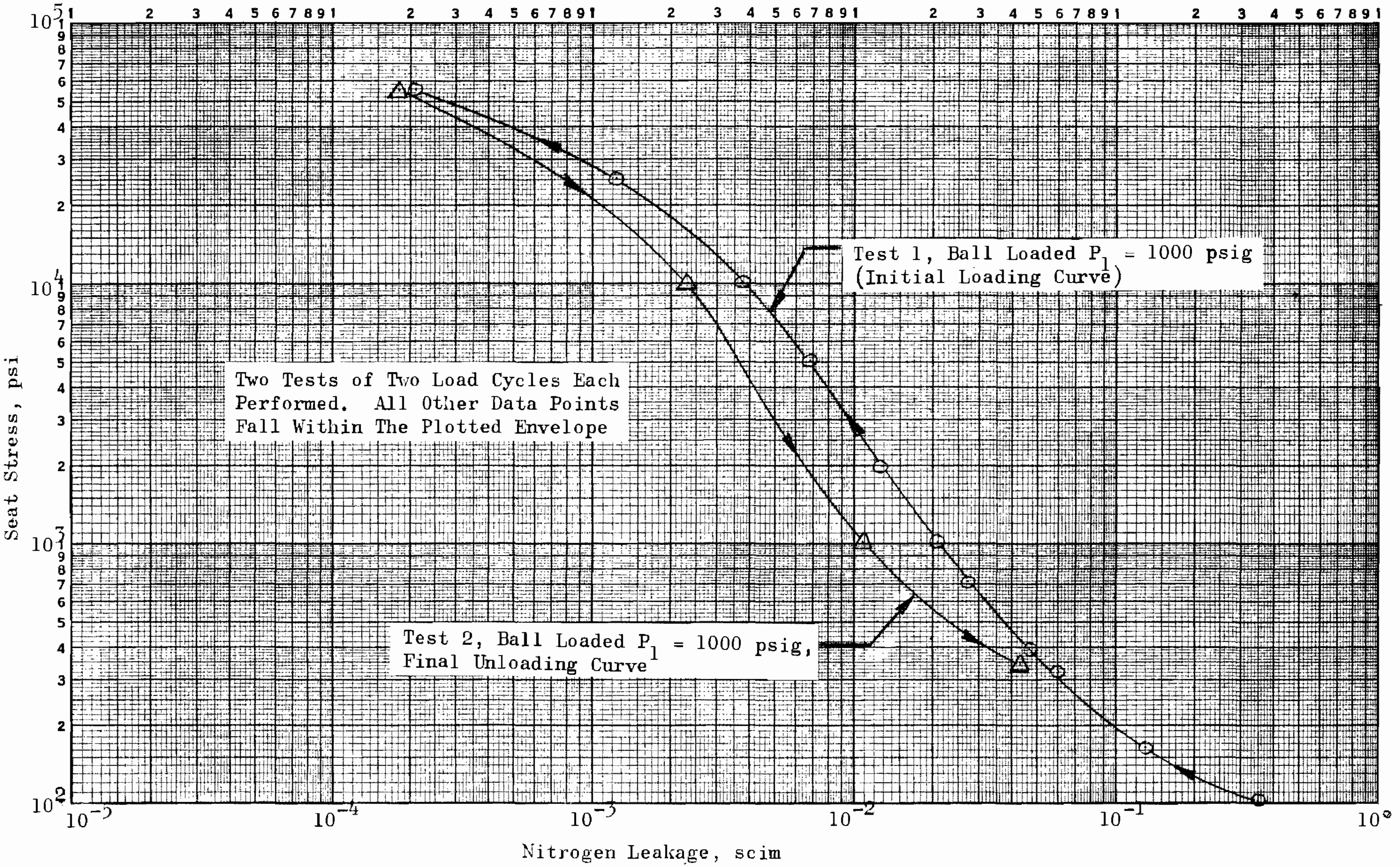

Figure 445. Stress-Leakage Data for Test Model J_f, Tests 1 and 2

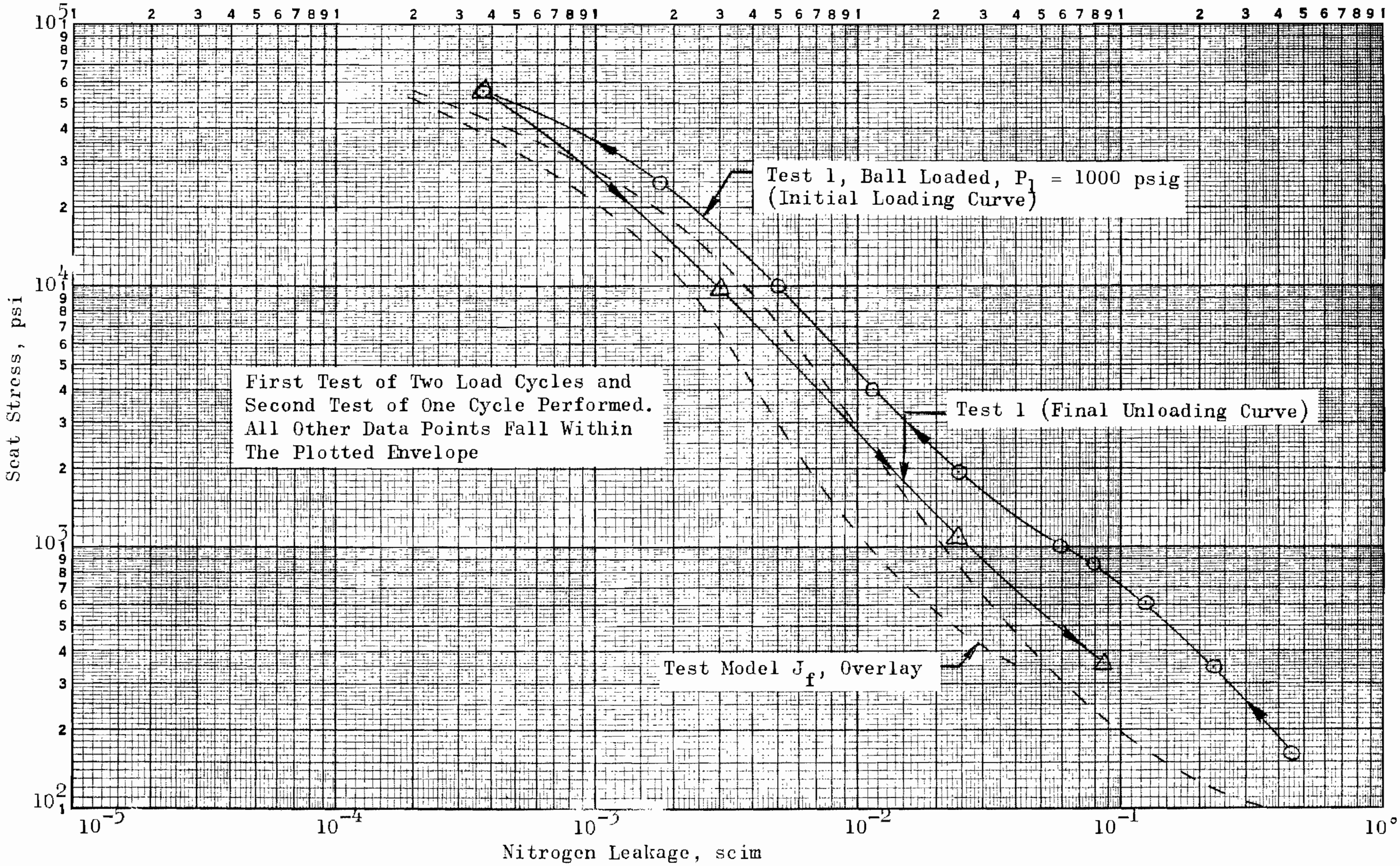

Figure 446. Stress-Leakage Data For Test Model J_{f1}, Tests 1 and 2

the resultant land and surface texture conditions. The scratch of Fig. 259 was the only significant cross-lay blemish.

The seat was anodized (model fabrication section) and circularly polished to somewhat improve the resultant matte, nodular surface characteristic of the anodize process. By focusing white and green light interference bands alternately on the anodized surface and then on the sublevel base metal, the anodize depth could be determined. (This top-and bottom viewing is illustrated in Fig. 261 and 262.) With this method, the anodize thickness was assessed at approximately 0.00019 inch.

Similar to the multidirectional lapped models, the anodized surface texture was difficult to assess. However, from a study of interference photographs and a posttest profile record (Fig. 371), Model U_f seat roughness was estimated at about 3 microinches PTV. A pitting characteristic (possibly accentuated by process preferential attack of prefinish pits) is also evident in the post-anodize inspection data. Model U_f tungsten-carbide poppet was formerly used with Model CC_f; surface characteristics are described under the latter heading.

Model U_f was tested twice; the first test was comprised of three successively increased maximum stress loops followed by 11 cycles to 12,000 psi. A second test (poppet rotated approximately 5 degrees) of two 12,000 psi load cycles followed, Figure 447 presents a composite plot of the resultant data. The square data points represent the decreasing load half of the first cycle to 12,000 psi, and indicate some surface degradation following this cycle. However, the stress-leakage data of the eleventh cycle to 12,000 psi fell within the enscribed envelope suggesting load-induced self-healing had occurred. No posttest damage was evident.

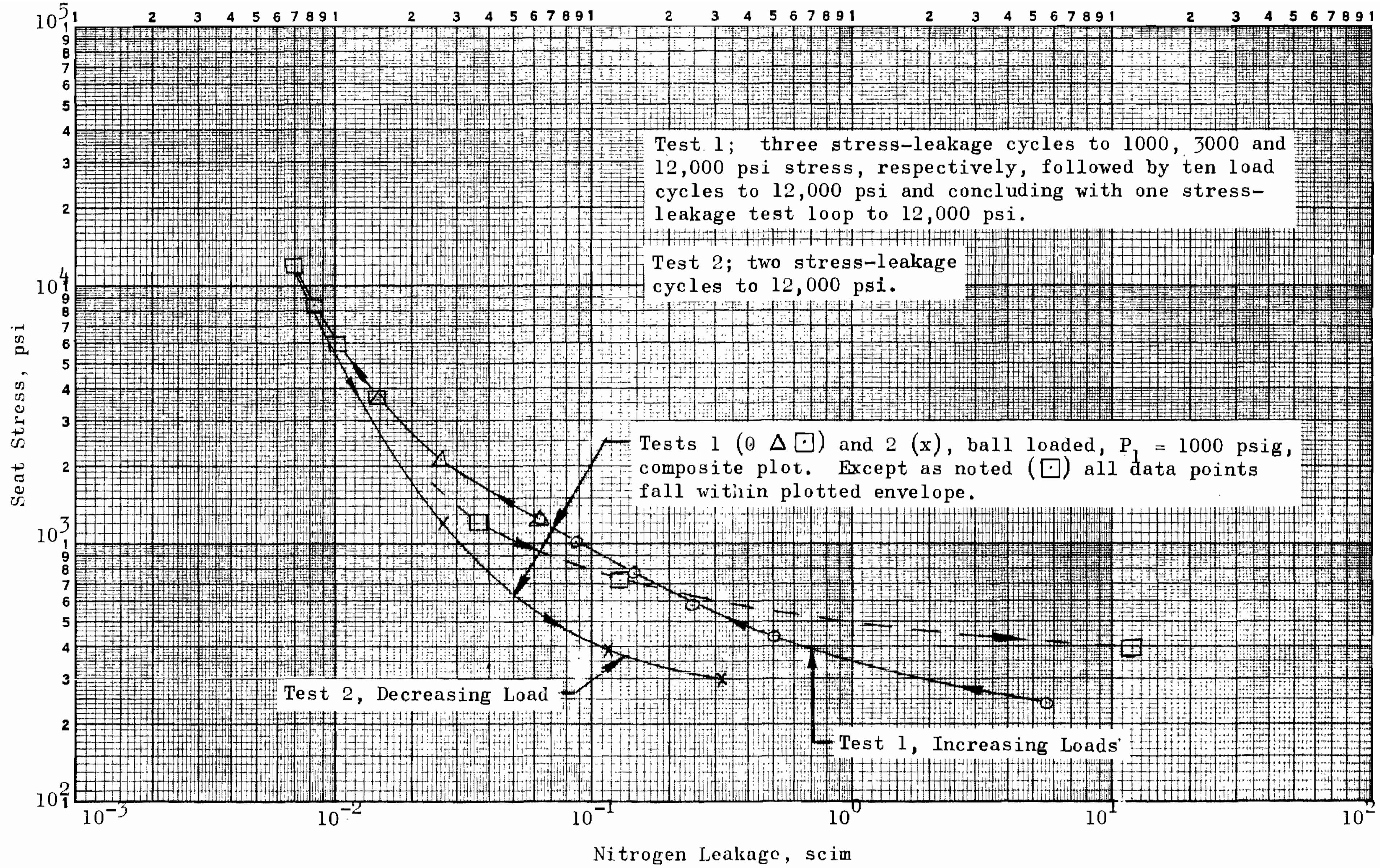

Test 1; three stress-leakage cycles to 1000, 3000 and 12,000 psi stress, respectively, followed by ten load cycles to 12,000 psi and concluding with one stress-leakage test loop to 12,000 psi.

Test 2; two stress-leakage cycles to 12,000 psi.

Tests 1 (0 Δ ⊡) and 2 (x), ball loaded, P_1 = 1000 psig, composite plot. Except as noted (⊡) all data points fall within plotted envelope.

Test 2, Decreasing Load

Test 1, Increasing Loads

Figure 447. Stress-Leakage Data for Test Model U_f, Tests 1 and 2

Model V_f, 0.7 AA Criss-Cross Lay, Anodized Seat (6.2-Inch Crown Radius) and 0.3 AA Circular-Lay Tungsten Carbide Poppet

Model V_f seat pre-anodize finish treatment was similar to that used for Model U_f except that a circular lay was not produced. The soft lap (bond paper mounted on a granite surface plate) polishing with 0- to 1-micron chromium oxide compound to achieve the crowned geometry left a criss-cross pattern of random scratches (Fig. 263). The resultant crown radius of 6.2 inches was interpreted from the interference photograph of Fig. 264.

The seat was anodized like that of U_f (model fabrication section), resulting in the same general characteristics, i.e., dull matte appearance with pitting. A light seat polishing with 0- to 1-micron chromium-oxide compound in rotary fashion, as with Model U_f, was also performed on V_f to somewhat improve the surface texture and make interference viewing possible. Anodize thickness was assessed at approximately 0.00019 inch using the double-band focus method made possible by the transparent (sapphire) aluminum-oxide coating. The interference photo of Fig.265 clearly illustrates this characteristic. (The number of 10-microinch bandwidths between darkest bands on the two surfaces defines the thickness.)

Evaluation of Fig. 265 (and similar interference photographs) and the profile record of Fig. 372 led to a surface texture PTV interpreted height of about 2 microinches, slightly better than that of Model U_f. The tungsten-carbide poppet of Model CC_f was used with Model V_f seat.

Stress-leakage tests were performed similar to those reported for Model U_f. Three successively increasing maximum stress laps to a final 10,000 psi level were followed by ten load cycles to 10,000 psi and a concluding stress-leakage loop. The poppet was rotated approximately 5 degrees, and a final (test 2) stress-leakage loop was performed. Figure 448 presents the test results in an envelope-curve arrangement for clarity. In addition, since the seat was crowned, Fig. 448 shows the increasing load characteristic

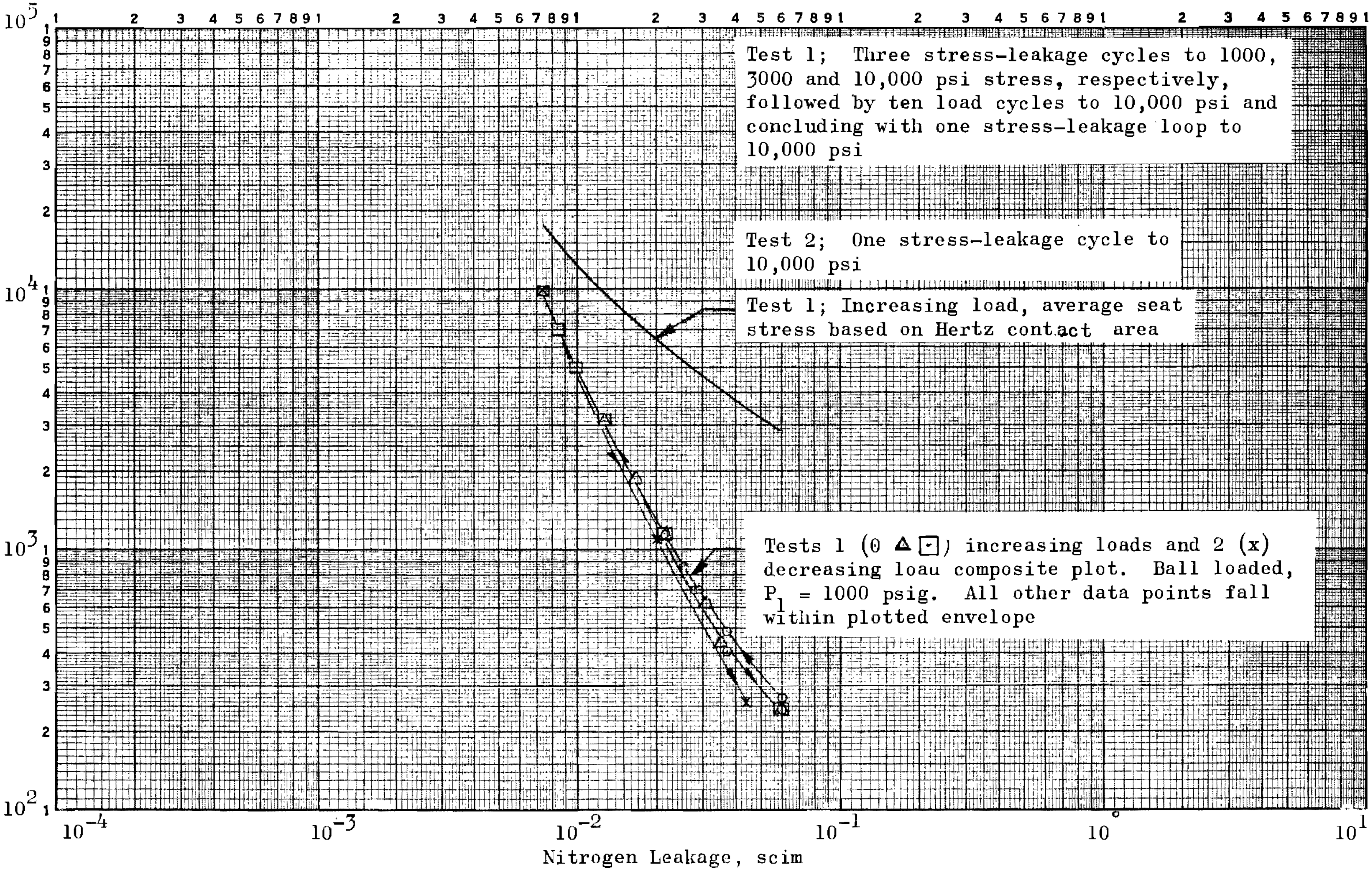

Test 1; Three stress-leakage cycles to 1000, 3000 and 10,000 psi stress, respectively, followed by ten load cycles to 10,000 psi and concluding with one stress-leakage loop to 10,000 psi

Test 2; One stress-leakage cycle to 10,000 psi

Test 1; Increasing load, average seat stress based on Hertz contact area

Tests 1 (○ △ ☐) increasing loads and 2 (x) decreasing load composite plot. Ball loaded, P_1 = 1000 psig. All other data points fall within plotted envelope

Figure 448. Stress-Leakage Data for Test Model V_f, Tests 1 and 2

based on average stress (σ_{avg}) Hertz analysis considering actual contact land width (2ℓ). For this analysis, the seat material was assumed to be aluminum oxide (sapphire) having a modulus of 46×10^6 psi. Over the span shown, the computed land width varies from 0.00271 to 0.0167 inch.

The advantage of the crown surface at low loads is apparent in this model where light loads may be concentrated at the land center to decrease the gap. Model U_f and V_f have the same leakage at 10,000 psi apparent stress indicating similar roughness levels; however, at low loads Model V_f leaks considerably less than U_f.

PLATED MODELS

Models W_f, 0.6 AA Unidirectional Lay 440C Poppet and Seat and W_{f1}, Gold-Plated Seat

The preplating reference surface of Model W_f (refinished from Model Y_f after cycle test presented later) represented a "standard," easily produced, unidirectional lay configuration similar to that of many models produced for the test program. Figures 266 and 267 typically illustrate surface texture which was assessed at 1.6 and 1.8 microinches PTV, respectively, for poppet and seat. The seat land corners were dubbed to approximately 0.07-inch radius as Fig. 268 shows. (The marked contrast of this photograph is due to a lighting variation; the evenly cropped bands are not indicative of the actual surface texture condition.) Figure 449 presents the results of the reference stress-leakage test.

Model W_{f2} seat was gold plated to a 44-microinch nominal thickness and probably exhibits most of the discrepancies possible in the process used. Corner buildup, assessed at something greater than 20 microinches, was difficult to resolve by interference bands due to the matte texture of the gold plate. Figure 269, illustrates the corner-plating buildup after test where some plastic flow has increased reflectively. Typical of all models,

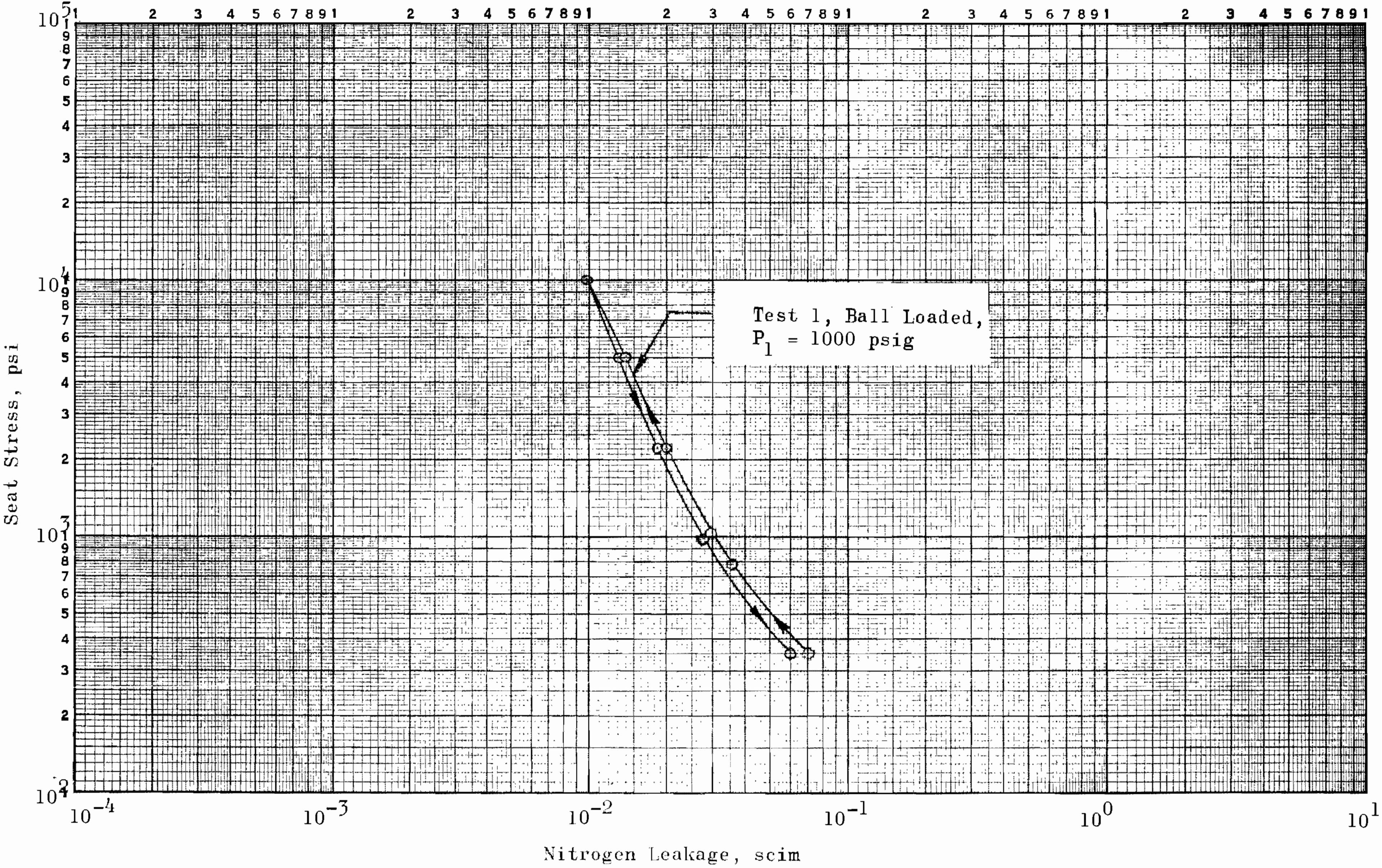

Figure 449. Stress-Leakage Data for Test Model W_f, Test 1

several microinches buildup at the land OD and approximately 20 microinches at the ID is evident. Thus, for all models, contacting landwidth is variable and undefined. Consequently, the resultant stress-leakage test results reflect a contact stress greater than indicated.

Figures 270 and 271 picture the plating-void defect. It is unknown whether this was caused by complete lack of a nickel strike in this area or a properly pre-plated but subsequently contaminated condition. Both noted photographs were taken after test, and Fig. 271 shows a greater plastic deformation characteristic adjacent to the void than in the surrounding area, indicating the presence of a raised edge. Thus, while the single void is not particularly detrimental to sealing, the raised portion, requiring additional flattening load, would be.

A similar, though more pronounced defect is pictured in Fig. 272 and 273. This crack (as with the circular void, a function of the nickel-strike condition) was approximately 0.00015 inch wide. Assuming a depth equal to the nominal plating thickness of 44 microinches, crack leakage at 1000 psig would be approximately 0.008 scim. More important, however, is the raised condition present at the crack edges (Fig. 274). Assessment of this defect indicates a peak height of some 40 microinches above the nominal surface. Neglecting the ID buildup, this defect would create an out-of-parallel condition equivalent to a parallel plate gap of 27 microinches, an intolerable condition if occurring on an otherwise blemish-free surface. Avoiding the complexities of a plastic-elastic deformation analysis, it is nevertheless apparent that the ridged characteristic would be far more detrimental to sealing capability than the initiating crack. Figure 274 also illustrates the granular plating composition typical of all models.

Model W_{f1} was tested initially with successively higher maximum stress-leakage loops of 3000, 10,000 and 30,000 psi. Following these initial loops to demonstrate plastic deformation characteristics, five 30,000-psi maximum stress load cycles were performed, concluding with a final stress-leakage loop. The results are shown in Fig. 450.

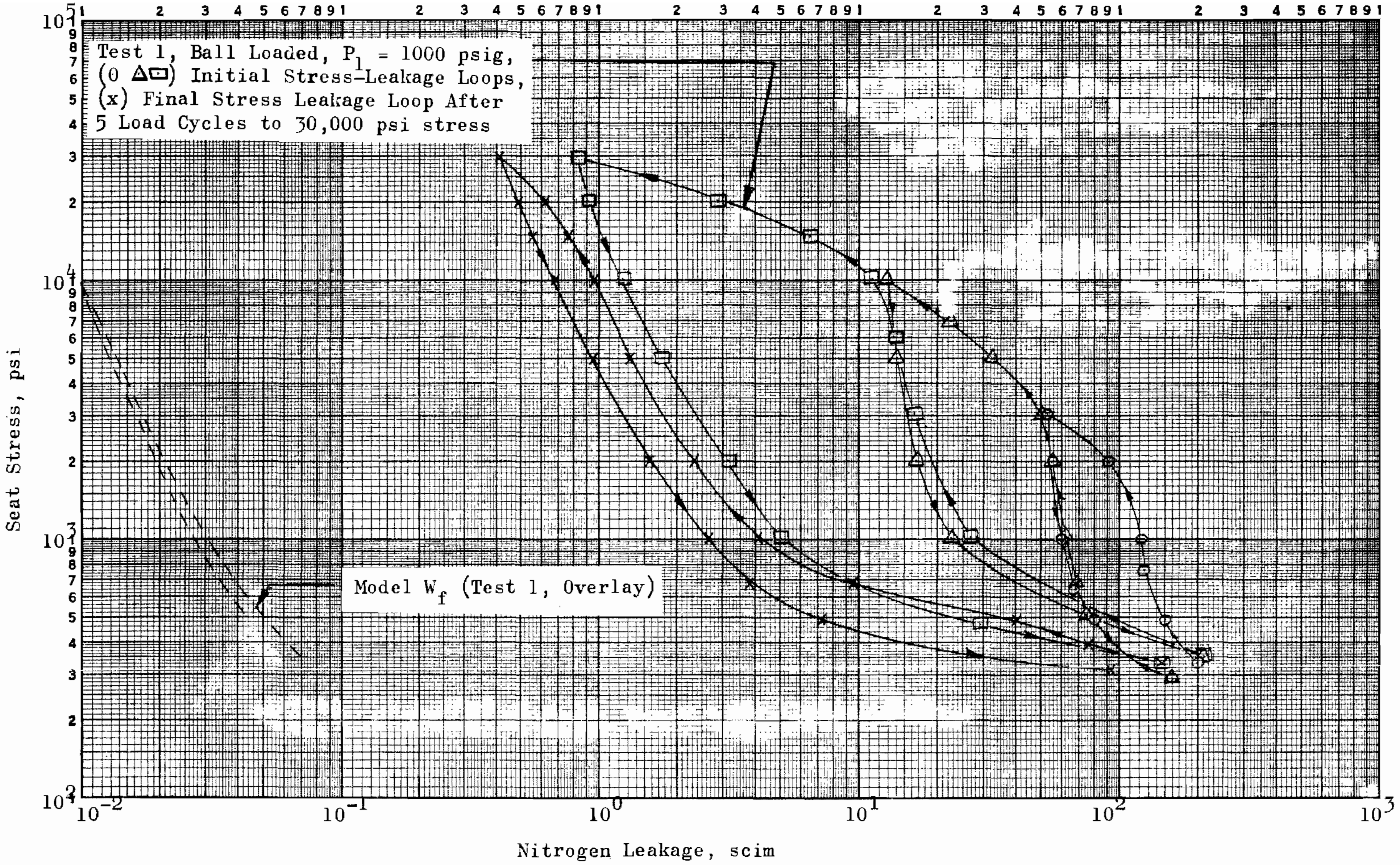

Figure 450. Stress-Leakage Data for Test Model W_{f1}, Test 1

With this model, the large hysteresis loops are indicative of localized nodular plastic deformation, thus reducing leakage at elevated stresses. The out-of-parallel effect is so pronounced, however, that all loops return to nearly the same low-stress level leakage giving a false indication of minimal plastic deformation. The abrupt slope change at 1000 psi stress probably indicates the point at which the ridged crack height has been elastically-plastically deformed to the level of the ID built-up area. (The majority of sealing undoubtedly took place at the ID.) Considerably more rigid, the ID hump prevented further significant ridged crack deformation at stresses above 1000 psi. Ridge elastic spring back, however, is effective at the lower stress levels causing the noted leakage increase in this region.

Figure 450 also presents an overlay of the Model W_f stress-leakage curve. Over the 1000 to 10,000 psi range, Model W_{f1} leaks approximately 100 times more than its preplated counterpart. The undefined contact landwidth of W_{f1} precludes explicit comparison, but between 1000 and 10,000 psi its performance is very similar to that of the 6 AA multidirectional-lapped Model D.

Posttest inspection photographs of resultant plastic deformation are shown as Fig. 275 and 276. The latter, taken at the same place as Fig. 273, shows the granular surface characteristic of the plated models; the poppet lay has been impressed on the more severely deformed nodules. Figure 275, at lesser magnification, illustrates the overall grainy structure and the more pronounced ID plastic deformation (built-up area). The center streak is void of plating similar to that shown in Fig. 271.

Model G_{c1}, 41-Degree Seating Angle, Gold-Plated Seat

This model is the plated-seat version of Model G_c, discussed in the conical and spherical model section. The poppet was unchanged, while the seat, like that of Model Y_{f2}, was plated 44 microinches thick. Model G_{c1} did not evidence all the defects noted on Y_{f2}, but did have the granular surface structure and ID buildup characteristic of the latter. Pretest photographs of the plated surface were indistinct due to the matte texture, and interference bands could not be resolved. Posttest inspection, however, indicated the general characteristic.

Model G_{c1} was tested twice. Test 1 was comprised of two stress-leakage loops to 3000- and 10,000-psi stress, respectively. A stress-leakage loop to 50,000 psi initiated test 2, followed by five load cycles to 50,000 psi, and a final stress-leakage loop. The results, together with an overlay of the Model G_c characteristic curve, are presented in Fig. 451.

Unlike Model Y_{f2}, some low-stress indications of plastic deformation are evident with G_{c1}. The large hysteresis loops are further evidence of nodular deformation. The final stress-leakage curve has about the same slope as the unplated version up to 4000-psi apparent stress since both models have a differential seating-angle condition with similar compliance characteristics. However, the ID plating buildup reduces the length of land over which the differential gap extends, and ultimately, the ID ridge is contacted, creating a stiffer bearing surface. The slope change at 4000 psi is indicative of this condition and the increased roughness of the gold plate.

It should be further noted that, due to the differential angle, Model G_{c1} contacting land is more highly stressed than that of Y_{f2}, thus accounting for the leakage-rate difference between the two. Furthermore, G_{c1} poppet has a circular lay which contributes to the reduced leakage. On the other hand, leakage difference between G_c and G_{c1} is not so much due to poor plating as to the excellence of the initial circularlay finish which was submerged by the plating operation.

As anticipated, posttest inspection revealed OD and ID plastic deformation. The differential-angle-caused initial contact was at the OD followed by subsequent ID contact as illustrated by Fig. 236 and 237. This evidence supports the observations made in discussing the stress-leakage test curves.

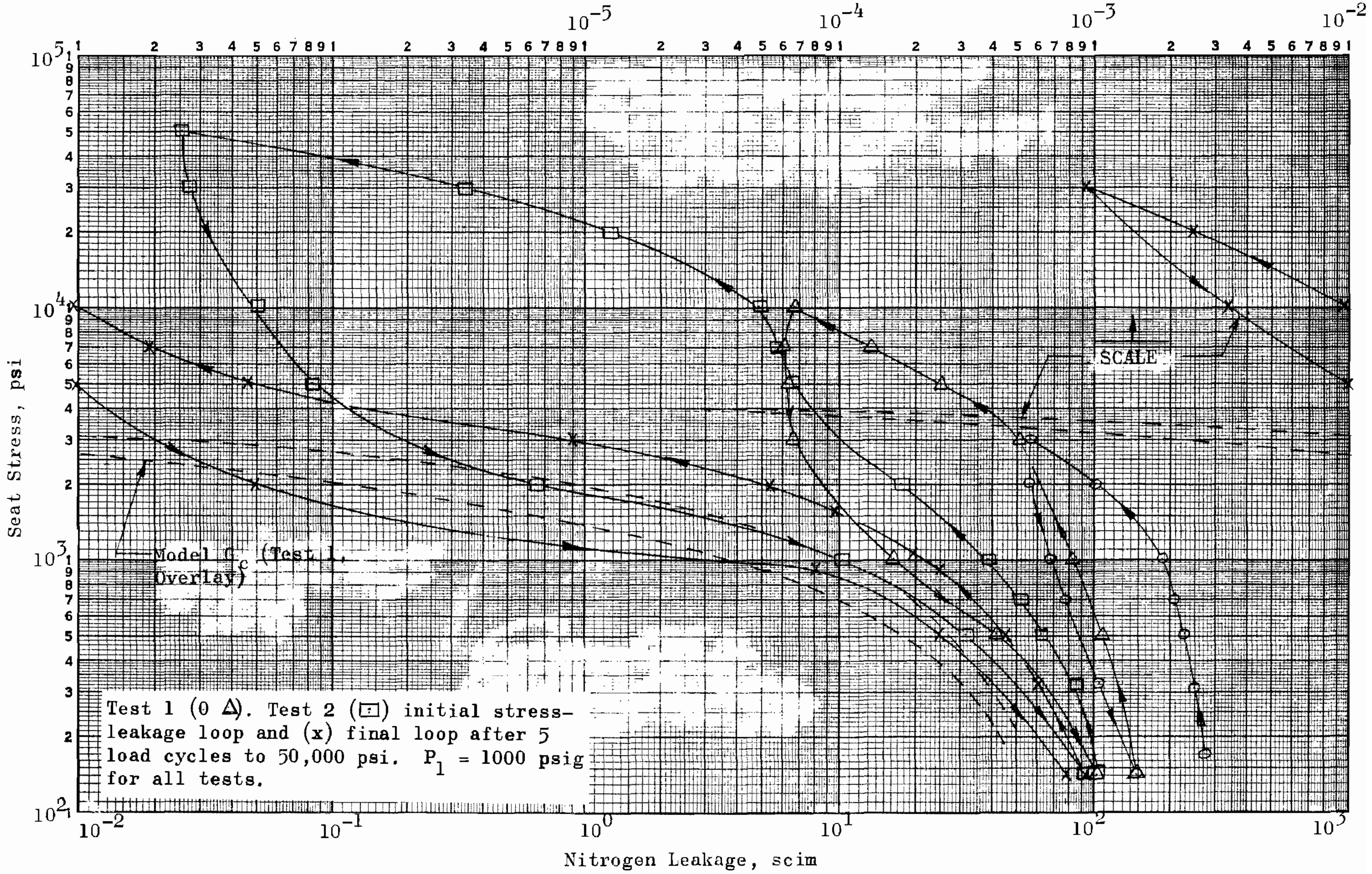

Figure 451. Stress-Leakage Data for Test Model G_{c1}, Tests 1 and 2

Models T_f, 0.6 AA Unidirectional Lay 440C Poppet and Seat and T_{f1}, Gold-Plated Seat

Model T_f was finished similar to Y_{f1} to provide a reference surface for gold-plating evaluation. Poppet and seat roughness PTV heights were both assessed at 1.2 microinches, respectively (Fig. 277 and 278). The seat corners (Fig. 279) were slightly dubbed.

One reference stress-leakage test was performed on Model T_f; Fig. 452 presents the results. Model Y_{f1}, by comparison (Fig. 449), leaked only 4 to 5 times more which indicates the reproducibility of the "standard" surface. The increase in low stress decreasing load leakage over the initial value is indicative of minor damage, although posttest inspection revealed no visible evidence of such damage.

Following reference surface tests, the seat was gold plated 30 to 31 microinches thick to form, with the unchanged poppet, Model T_{f1}. (The intended thickness had been 10 to 20 microinches.) The resultant surface, while evidencing corner buildup of 3 to 4 microinches (OD) and approximately 20 microinches at the ID (Fig. 280), was more uniform in appearance than the thicker coated models. (Plating granules were somewhat smaller.)

Similar to the other plated versions, Model T_{f1} was tested with three initial stress-leakage loops followed by six load cycles to establish a stable deformed condition, and finished with a final stress-leakage loop (Fig. 453). Plastic deformation is indicated by both hysteresis loops and successively reduced low-stress leakage. Since the seat geometry was relatively uniform, i.e., a 20-microinch circumferential ID hump, the final (x's) stress leakage loop reflects a continual flattening of the hump asperities and development of increasing land width.

The high contact stress attendant with the noted geometry and the uniform surface texture resulted in Model T_{f1} attaining the same leakage level as the non-plated reference version at 10,000 psi. Even at 1000 psi, plated-model leakage is only 15 times that of T_f. Nevertheless, the gold plating,

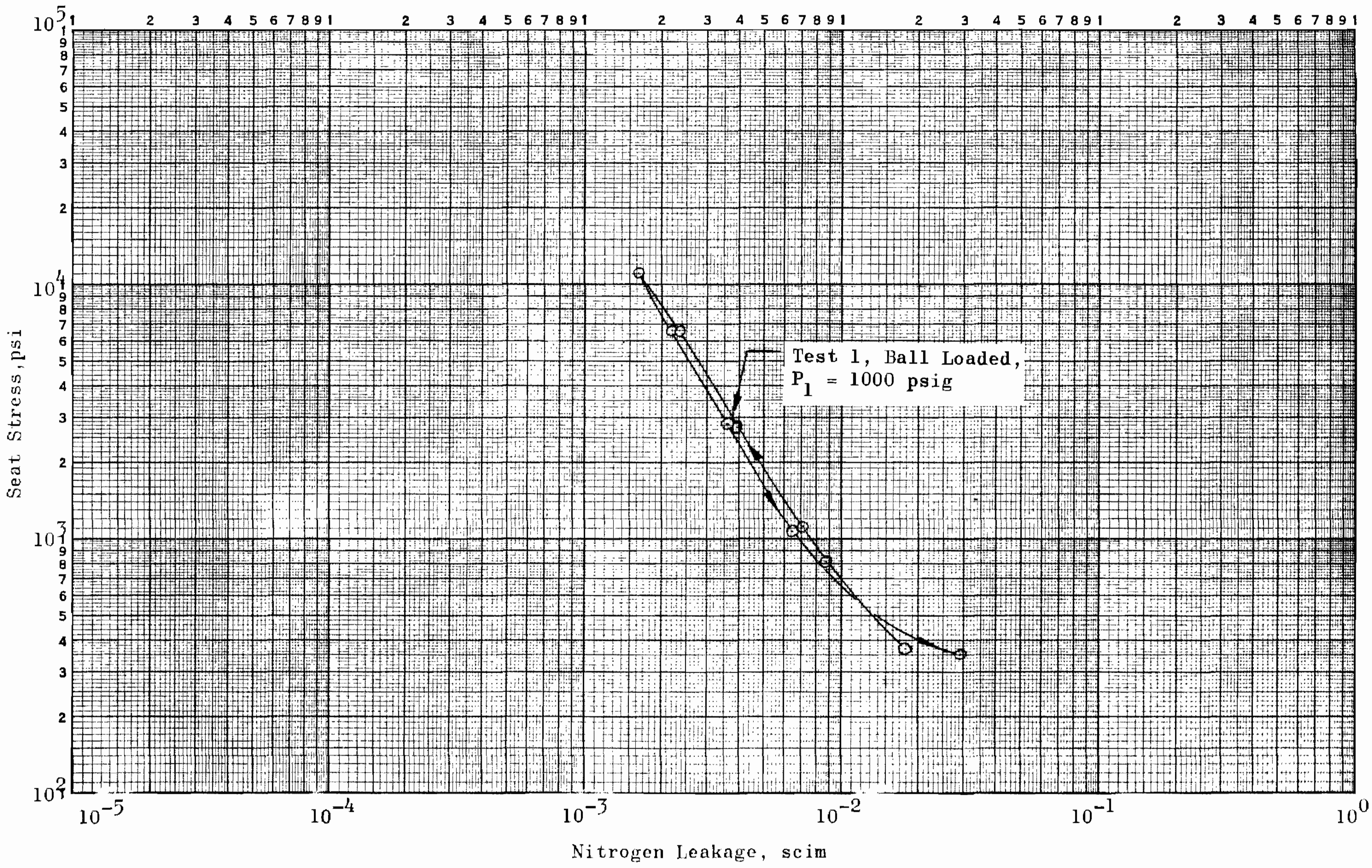

Figure 452. Stress-Leakage Data for Test Model T_f, Test 1

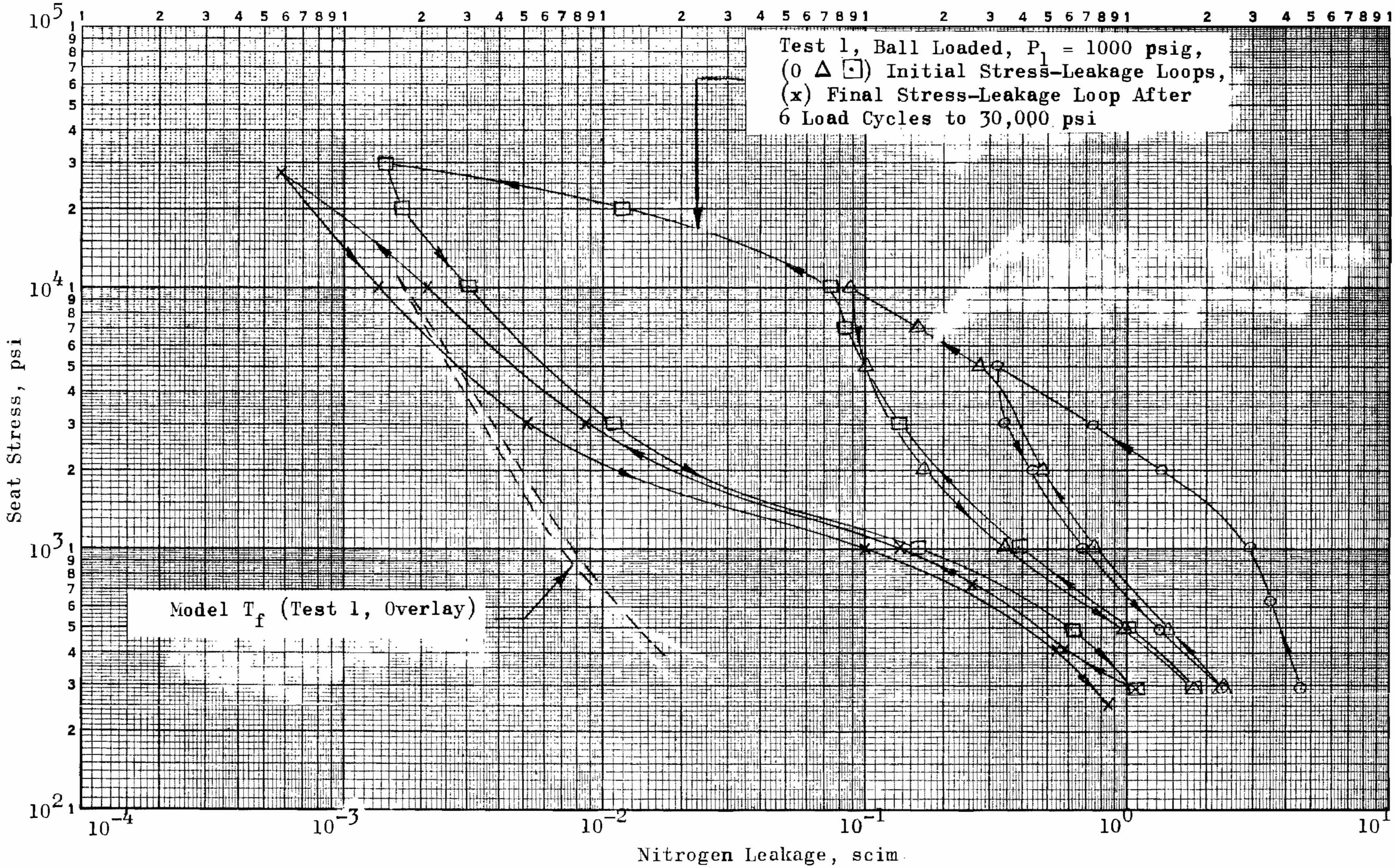

Figure 453. Stress-Leakage Data for Test Model T_{f1}, Test 1

as applied, resulted in a deterioriation of model performance. A detailed investigation of improved plating processes capable of producing a gold film with surface texture PTV height equal to or less than the model base metal was beyond the scope of the experimental effort.

Posttest inspection indicated that full land contact had been developed as a comparison of Fig. 280 with 281 illustrates. The improved reflectivity of Fig. 281 indicates some plastic deformation of nodules from ID to OD. However, as Fig. 282 shows, the bulk of the plastic deformation occurred at a very narrow ID land where the ridge hieght was reduced to about 9 microinches.

COATED MODELS

Model AA_f, 0.3 AA Tungsten Carbide Poppet, 0.2 AA Crowned 440C Seat, Circular Lays, Silicone Fluid Evaluation

Although finished with smooth circular lay surfaces, Model AA_f did not seal as well as expected due to the pitted condition of the poppet (Referenced in discussion of Surface Texture Evaluation section and Fig. 423) It thus represented a good model for evaluation of a fluid coating to improve leakage. The very viscous (100,000 centistoke) "Viscasil 100,000" silicone fluid was selected for this investigation which was initiated immediately after the above referenced tests. Figure 454 presents the results as discussed below.

Tests 3 through 5 were performed in the clamped condition (following ball-vs-clamped-loading comparison tests 1 and 2), while the subsequently performed test 6 was done with ball leading. As the stress-leakage curve overlay of tests 1 and 2 indicates, virtually no difference between the two loading methods was detected with the very parallel Model AA_f.

The results of the first "Viscasil" test (3) represent an unexplained phenomenom as no significant change was noted. However, test 4, after

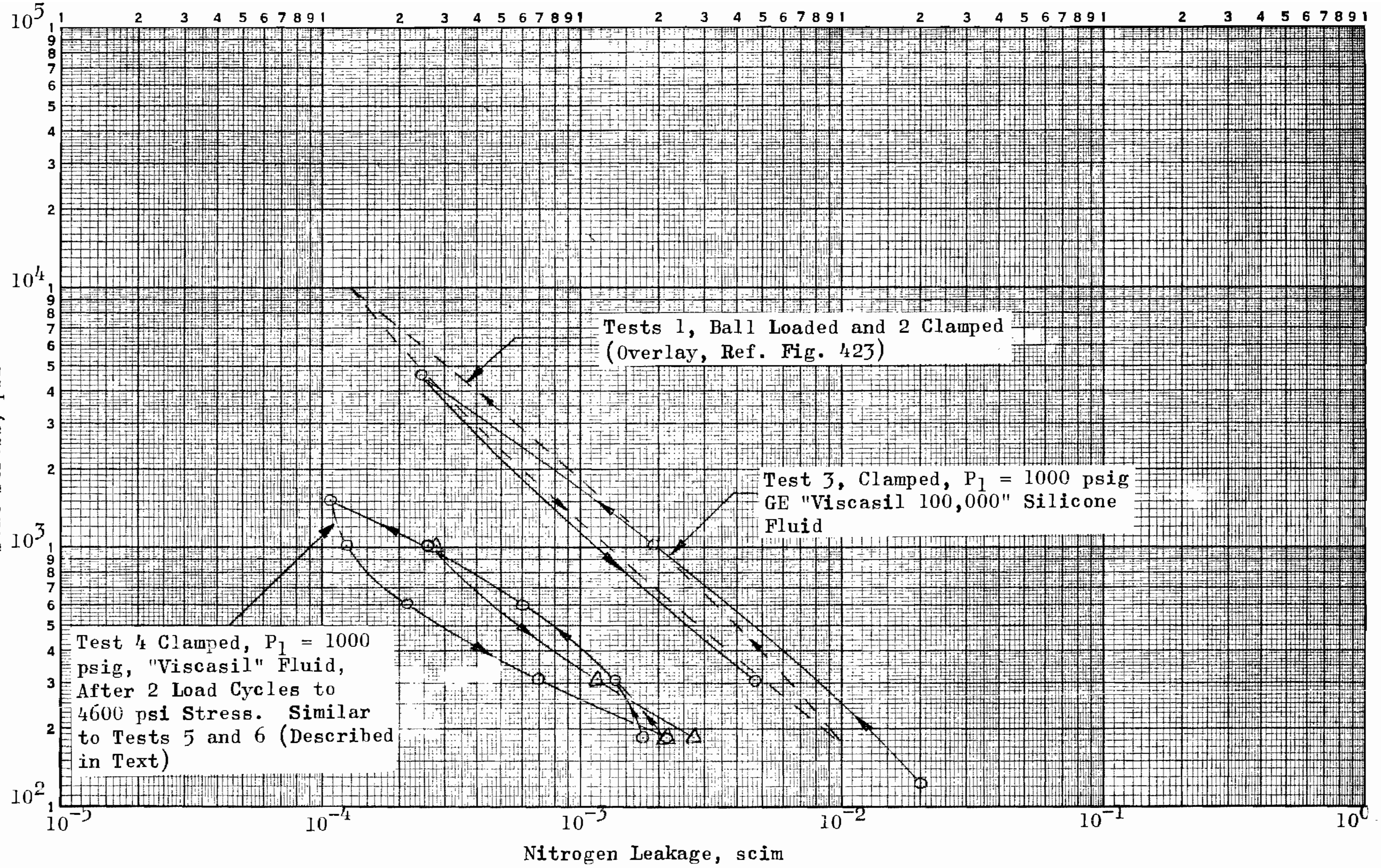

Figure 454. Stress-Leakage Data for Test Model AA_f, Tests 3 through 6

two 4500-psi stress cycles, reflects a marked sealing improvement. Test 5, performed 2 weeks later (assembled model was stored in the tester), yielded virtually the same results as test 4, and for clarity is not plotted. The model was disassembled and, without fluid-coating removal, stored. After two months, Model AA_f was dry wiped to remove contaminants and reassembled into the tester with ball loading. Initial checks indicated, as with test 3, leakage similar to the uncoated version. After four load cycles to approximately 4500 psi, however, the final data of test 6 duplicated the improved condition previously noted.

Following test 6 the model was disassembled, cleaned with freon and hot trichloroethylene, and reassembled in the tester. Stress-leakage checks indicated satisfactory return (factor of two higher) to the original, uncoated version.

From the results of Model AA_f tests, a significant performance improvement due to fluid coating was evident. This evidence, however, was somewhat tempered by the load cycling necessary in two cases to duplicate results. Accordingly, additional tests on other models were performed as subsequently discussed.

Model B_{fl}, 0.6 AA Circular Lay 440C Poppet and Seat, Fluid Coating Evaluation

In the continuation of fluid coating testing, Model B_{fl} was selected as a test vehicle representing a relatively easily produced circular lay finish. Furthermore, since the initial investigation with Model AA_f involved only one fluid, additional compounds were chosen for Model B_{fl} tests. These included retest of "Viscasil 100,000;" a second, less viscous silicone fluid, "Versilube F-50;" and an extreme pressure diester oil, "Brayco" NPT-5.

Finally, after tests of the above fluids, the seat (only) was Oronite treated. This simple process involved immersion of the 300 F preheated seat into 200 F Oronite oil for 4 hours. The part was cooled and residual Oronite removed by flushing in benzene (chlorinated solvents are not recommended). A final dry wipe to remove dust particles was performed prior to tester installation.

The stress-leakage curves of Fig. 455 summarize the results of Model B_{fl} fluid-coating tests. As might be expected, the "Viscasil 100,000" fluid caused the greatest change in leakage performance. The single data point obtained represents a five-hundredfold reduction in leakage at only 360 psi apparent stress. The dash-lined slope is assumed since leak measurement limitation precluded obtaining higher stress data, and with much lower loads, balance pressure measurement error affects calculated stress accuracy.

"Versilube F-50", was next in effectiveness. It was noted, however, that both "Viscasil" and "Versilube" were easily removed with benzene or freon wiping, with subsequent return to the clean or control-test condition. The "Brayco" and Oronite films, however, were more tenacious. Hand scrubbing with freon and benzene caused the "Brayco" version to return only halfway to the control-test level. Hot trichloroethylene sonic cleaning and vapor degreasing was required to remove the coating. Similarly, the Oronite film while producing the least effect, also achieved the most lasting. As the data of Fig. 455 shows, the Oronite version remained essentially unchanged after cleaning operations of benzene, freon, and hot trichloroethylene (the latter, as previously indicated, alleged to be detrimental to film adhesion). Furthermore, since only the seat was coated, it is probably that a fully treated model would yield a significantly greater leakage reduction.

Thus, the beneficial aspects of a few fluid film coatings were demonstrated with Model B_{fl}. Certainly, many other compounds could be investigated, not only from an initial sealing improvement standpoint, but for the cyclic wear-reduction potential. As previously noted, however, extensive evaluation of platings and coatings was beyond the scope of the program. Nevertheless, the approach appears to warrant further investigation.

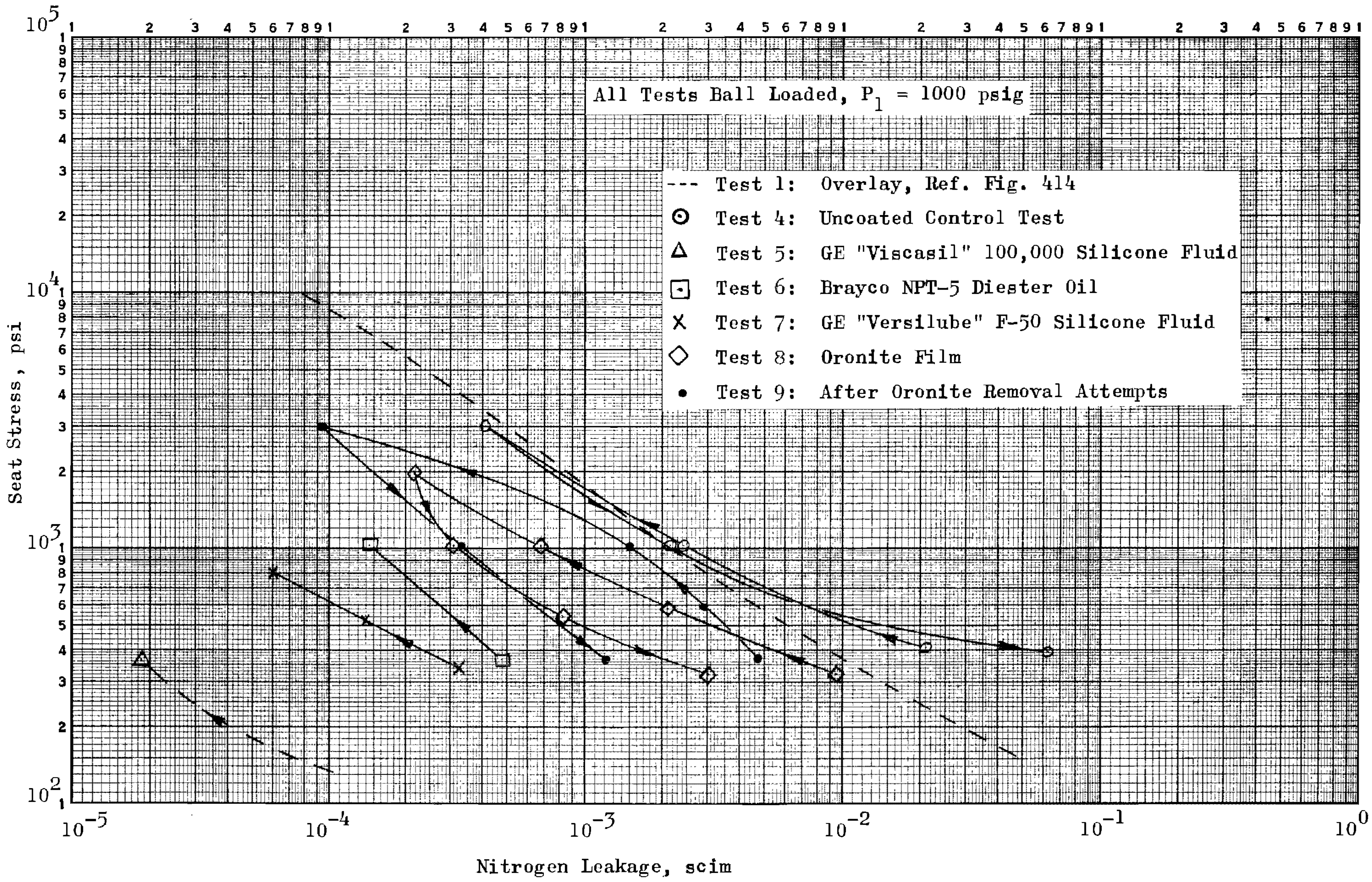

Figure 455. Stress-Leakage Data for Test Model B_{fl}, Tests 4 Through 9

The marked improvement in sealing capabilities demonstrated by Models AA_f and B_{fl} were achieved with circular lay surfaces. A disadvantage of the purely fluid coatings has been illustrated by the subsequently discussed unidrectional lay Model J_{fl}.

Model J_{fl}, 0.6 AA Unidirectional Lay 440C Poppet and Seat, Fluid-Coating Evaluation

The effect of "Viscasil 100,000" on the sealing characteristic of unidirectional lay surfaces was investigated with this model. The results are shown in Fig. 456. Although the surfaces had not been reworked (from the passivated condition), test 3 was performed for control purposes. The test results agreed with those previously established (Fig. 446, test 1).

Model J_{fl} poppet and seat were coated with "Viscasil" fluid and the data of test 4 obtained. It will be noted that the basic stress-leakage loop indicates a leakage reduction, though not of the magnitude achieved with models AA_f and B_{fl}. However, in two 1/2-hour hold periods at 600-psi stress (P_1 = 1000 psig), successive increases in leakage were observed. This characteristic was indicative of fluid (sealant) flow through the contacting surfaces. Posttest inspection verified this assumption as a ring of "Viscasil" was visible on the poppet at a diamter equivalent to the seat OD. It is probable that some sealant flow occurred on the much longer leak path, circular lay Model B_{fl}, but the time dependency factor is not known.

From the preceding evidence it may be concluded that the unidirectional lay surface does not lend itself to effective leakage suppression by fluid coatings unless the roughness PTV dimension approaches the molecular size of the fluid used. On the other hand, the more tenacious Oronite coating might prove effective on this type surface.

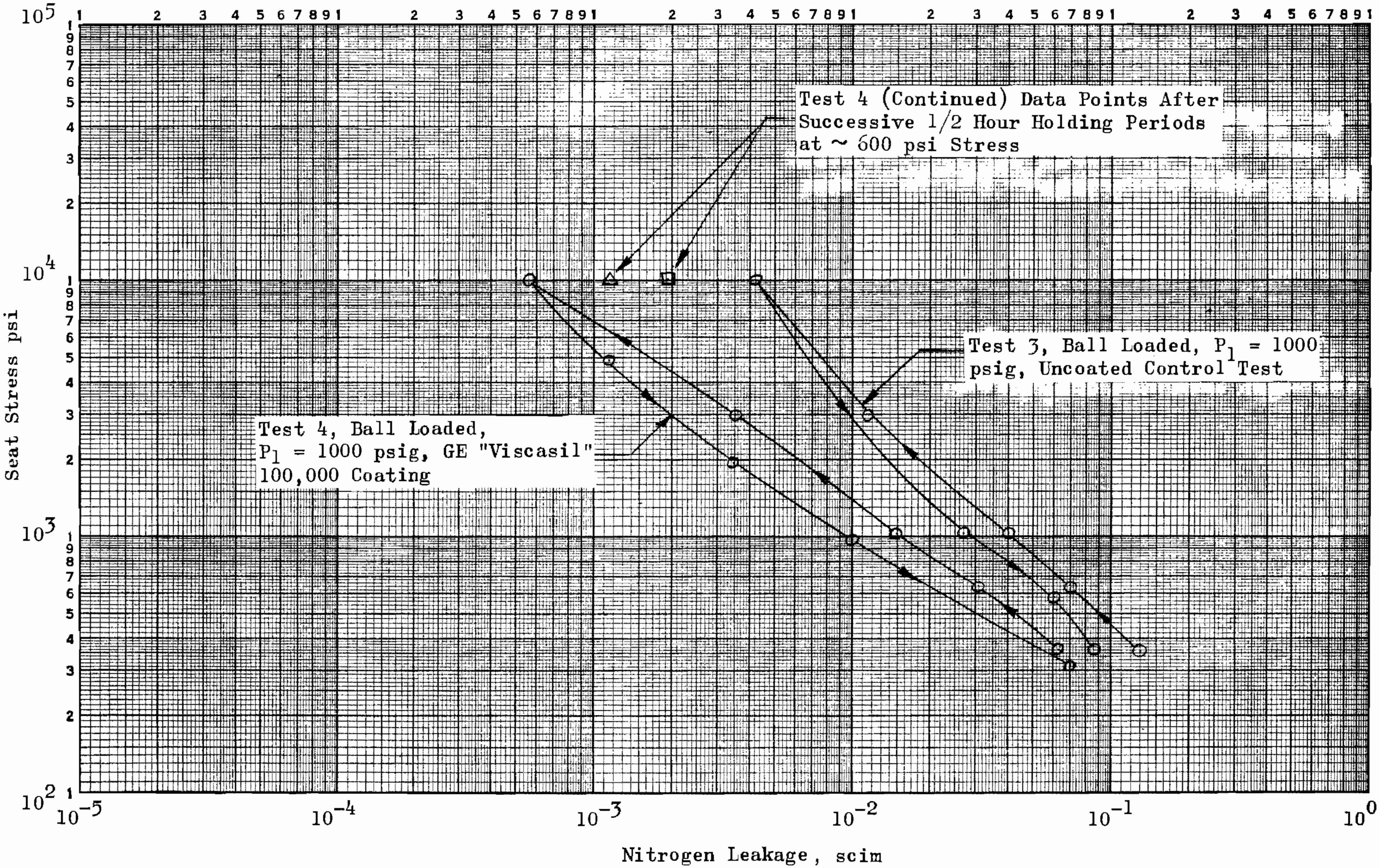

Figure 456. Stress-Leakage Data for Test Model J_{fl}, Tests 3 and 4

OBSERVATIONS

The processed plated and coated models investigated represent only a small part of the multitude of treatment and variations thereof possible. The intent, primarily, was to demonstrate the potentially good and adverse effects of such techniques. Thus, a frame of reference for specific conditions is eatablished from which further effort may be directed.

As previously stated, the liquid-hone approach holds little promise in the realm of low-leakage seals. Experiments with fine particles and flours may prove reasonably successful in producing surfaces of roughness level similar to the lapped texture. However, such surfaces probably would not be sufficiently uniform for low leakage applications because of the potential grading and contamination problem associated with a large volume of reused grits. Moreover, the inherent sharpness of the pitted profile results in a very poor closure characteristic.

The results obtained with Model J_{fl} indicate that, for fine finishes, the passivation technique employed was deleterious to performance. It is probable that experiments with different solutions and processing techniques would have led to a noninjurious procedure. However, the basic need for the process was not demonstrated by the numerous models utilized in the test program. No instance of surface deterioration due to fabrication contamination was noted on either the 440C or 17-4PH material over a 2-year period, and except for model J_{fl}, none were passivated. This lack of substantiation is not necessarily conclusive, but strongly indicates that the potentially adverse effects of the passivation process on sealing surfaces should be avoided.

The material handling and assembly of aluminum sealing surfaces present a constant damage hazard. Thus, except for noncompatible applications, anodizing is dictated. However, for optimum performance, the anodized surface must be refinished to remove pitting and sharp nodules caused by the process.

While the experiments using gold plating may be termed a failure, they do provide valuable data since the reasons for failure have been documented. This information may serve to explain the lack of improvement often noted when gold or other platings are employed to alleviate troublesome sealing problems. It further emphasizes the necessity for process control to the dimensional level associated with performance requirements.

The results of fluid-coating evaluations indicate this approach to leakage reduction offers great promise and should be explored in detail. The tests indicate that fluids retained primarily by surface tension are helpful only if circular lay surfaces are employed and then for an indeterminate period. For long-lived performance improvement, however, it appears that chemical compounds either transforming or bonding to the surface are required.

SEATING ERROR INVESTIGATION

Although some notable failures were experienced, the intent in fabrication of test models was to produce a sample surfaces, free of major discrepancies, with single-parameter variations. Thus, for example, the lapped models were formed with sufficient precision to permit surface texture evaluations without undue extraneous influence. In this portion of the experimental test effort, the following seating errors, avoided in normal test model fabrication and testing, but commonly present in actual valve applications, were deliberately exaggerated and evaluated.

SEATING ERRORS

1. Scratches (Model G). To correlate flow equations with test data, scratches, having width and depth large with respect to surface texture asperities, were formed on one model.
2. Out-of-flat (Models H and I). Two out-of-flat (solid cylindrical segment) conditions, 8 and 24 microinches total were tested.
3. Out-of-parallel (Model B). Poppet canted 125 microinches relative to the 0.500-inch seat diameter.
4. Tilted cone axes (Models E_c and H_c). Poppet-seat cone axis angular deviations were tested on both 0.005- and 0.030- inch land width models.
5. Contamination (Model L). The load required to envelope contaminants of known quantity and material was determined for lead and diamond particles.

TEST RESULTS

The test results, together with analytical correlation, are presented in the following model sections.

Model G, 0.5 AA Multidirectional Lapped 440C Poppet and Seat, Poppet Scratched

Model G poppet and seat were the same as used for test model F except that the poppet was reworked to a fine polished finish. Examination of the inspection data of Table 4 shows that the reworked Model G poppet has no measurable roughness or waviness, and contains only widely scattered nodules with an average height of 2.3 microinches. Figure 285 shows an interference photograph of this surface.

For the scratch evaluation, the polished poppet was scratched radially, using the diamond indenter from the Leitz microhardness tester. This indenter is the Vickers pyramid configuration which has a depth-to-diagonal ratio of 1:7. After four scratches located at 90-degree intervals were scribed on the surface, the poppet was polished to remove the feather edges along the scratch. Figure 286 shows a typical scratch (No. 2 in the following table) after the polishing operation. Each of the scratches were slightly different; the following table describes the average depth (h), width (λ), and angle (ϕ) for all four.

Scratch No.	Depth, microinches	Width, microinches	Angle, Degrees
1	31.8	522	7.0
2	31.8	391	9.3
3	42.4	391	12.4
4	37.1	435	9.4

Test 1 (Fig. 457) was performed to establish model stress-leakage characteristics before scratch application. The plotted curve represents the fourth cycle to a 60,000-psi stress conducted with the ball-loading device. The high leakage rate below the 1000-psi stress level is attributed to contamination.

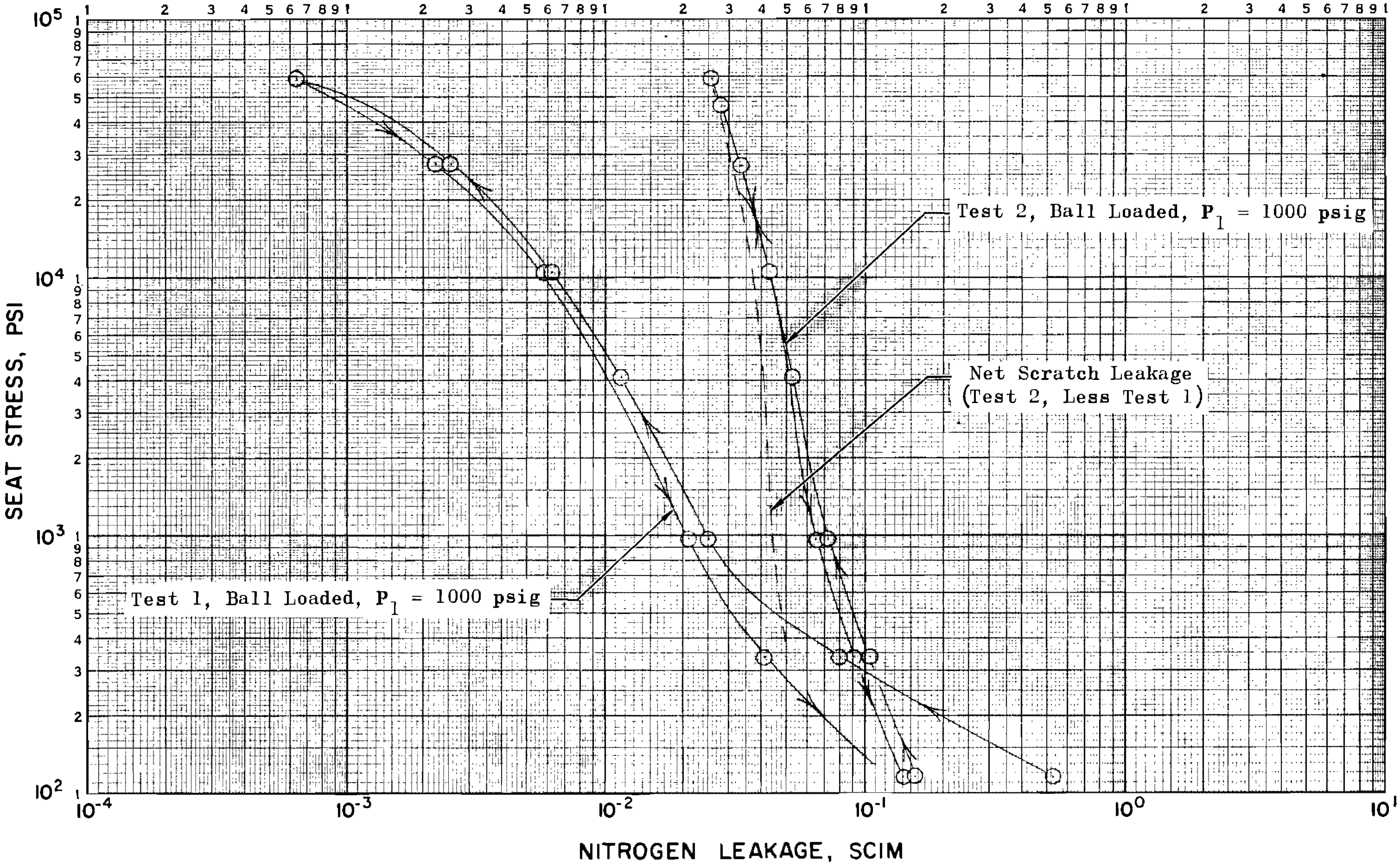

Figure 457. Stress-Leakage Data for Test Model G, Tests 1 and 2

Test 2 illustrates Model G leakage information after the scratches were scribed on the poppet. This curve represents the sum of surface-texture leakage and the leakage through the four scratches. To find the net scratch leakage, the data of test 1 was subtracted from that of test 2. This scratch leakage is shown as a dashed line in Fig. 457.

To correlate net scratch leakage with analytical data, the following equation was used:

$$Q = \frac{1.5\,(\lambda)\,(P_1^{\,2} - P_2^{\,2})}{\mu\, LT} \left[M_L h \right]^3 + \frac{4.5 \times 10^4\,(\lambda)\,(P_1 - P_2)}{L} \sqrt{\frac{R}{T}} \left[M_M h \right]^2$$

This basic equation was presented in the Seating Analysis section and has been modified by substituting scratch width (λ) for (πD_s) and eliminating the deflection term. M_L and M_M are the flat plate averaging factors for a saw tooth surface and are 0.63 for laminar flow (M_L) and 0.58 for molecular flow (M_M).

Because the four scratches are not identical, data were computed independently for each as follows:

Scratch No. 1 $Q = 0.975 \times 10^{-2}$ scim

Scratch No. 2 $Q = 0.730 \times 10^{-2}$ scim

Scratch No. 3 $Q = 1.740 \times 10^{-2}$ scim

Scratch No. 4 $Q = 1.294 \times 10^{-2}$ scim

$\Sigma \quad Q = 4.739 \times 10^{-2}$ scim

The flow correlates very well (8 percent at a 1000-psi stress) with the net scratch leakage of Fig. 457. A mathematical stress vs leakage model has not been developed for scratch flow, but it can be seen from the experimental results that the scratch leakage has been reduced by one-half at a 60,000-psi stress. Several more tests with scratches of varying depth should be performed before any conclusion can be reached as to the stress-leakage relationship for scratches.

Models H and I, 2.6 AA Multidirectional Lay 440C Poppet and Seat, Out-of-Flat Tests

The out-of-flat configuration consisted of curvature in one plane, i.e., a solid cylindrical segment. Of the two models fabricated, one had a chordal height of 8 microinches (H), the other 24 microinches (I). Both out-of-flat surfaces were formed on the poppet because it had a continuous surface which was measured easily. The common seat was flat within 3 microinches. Surface measurements were taken on the Proficorder, Cleveland height comparator, and an optical flat to ensure correct definition of the surface contour.

The intention was to keep the surface roughness of these test models the same as the 2-microinch AA Multidirectional surface of Model B. This surface texture was used as a datum to examine other variables such as gross geometry and material properties. Because of the variables in the lapping process, however, Models H and I were slightly rougher than Model B.

Model H poppet surface texture was the same as the seat which had a surface roughness PTV height of 7.4 microinches and an angle of 1.2 degrees. No waviness was noted, but 5 percent of the surface was composed of nodules with an average height of 4.4 microinches. These parameters were determined from the Proficorder trace (Fig. 373) and the interface photographs (Fig. 287 and 288).

The seat was common to Models H and I; however, Model H poppet was reworked after test to the Model I configuration. Model I poppet had a roughness PTV height of 7.9 microinches, an angle of 1.3 degrees, and widely scattered nodules 4.7 microinches in height. These parameters were determined from the Proficorder trace (Fig. 374) and interference photograph (Fig. 289). Even though the surface roughness of these models was close to 2.5 microinches AA, it was assumed that they approximated the datum roughness value (2 microinches AA); therefore, gross geometry flatness change could be viewed as an independent variable.

The test results of Models H and I are shown in Fig. 458. Tests 1 and 2 were conducted on the 8-microinch cylinder (Model H) at an inlet pressure of 1000 psig and stresses up to 60,000 psi. Test 1 was conducted with the poppet clamped, whereas test 2 was with the ball-loading device installed. The difference in leakage at the low-stress levels is attributed to the out-of-parallel condition caused by clamping the poppet to the piston. The stress-leakage curve for the 24-microinch cylinder (Model I, test 1) was conducted with the ball-loading device.

In examining the curves of Fig. 458 and comparing the curve shape with the test data obtained from Model B, it was concluded that the out-of-flat condition did not alter appreciably the stress-leakage characteristics. This conclusion is further substantiated by the similarity of the 8- and 24-microinch curves which were very close at high stresses and differed only by a factor of 2 to 3 at the low-stress levels.

A simplified deformation analysis based on Hertz contact of a cylinder on a flat plate can be made for these out-of-flat surfaces to support the above conclusions. The unwrapped, out-of-flat curve in the following sketch describes two cycles of a sine wave. An approximation of the load required to flatten each peak may be obtained by assuming the peaks are represented by two cylindrical segments having chordal distances of one-half the mean seat circumference. This results in a minimum deformation for a given load. It is assumed that the L/D_s and h/L ratios are small.

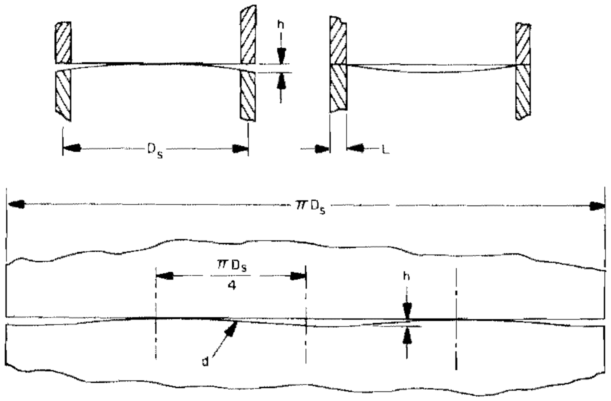

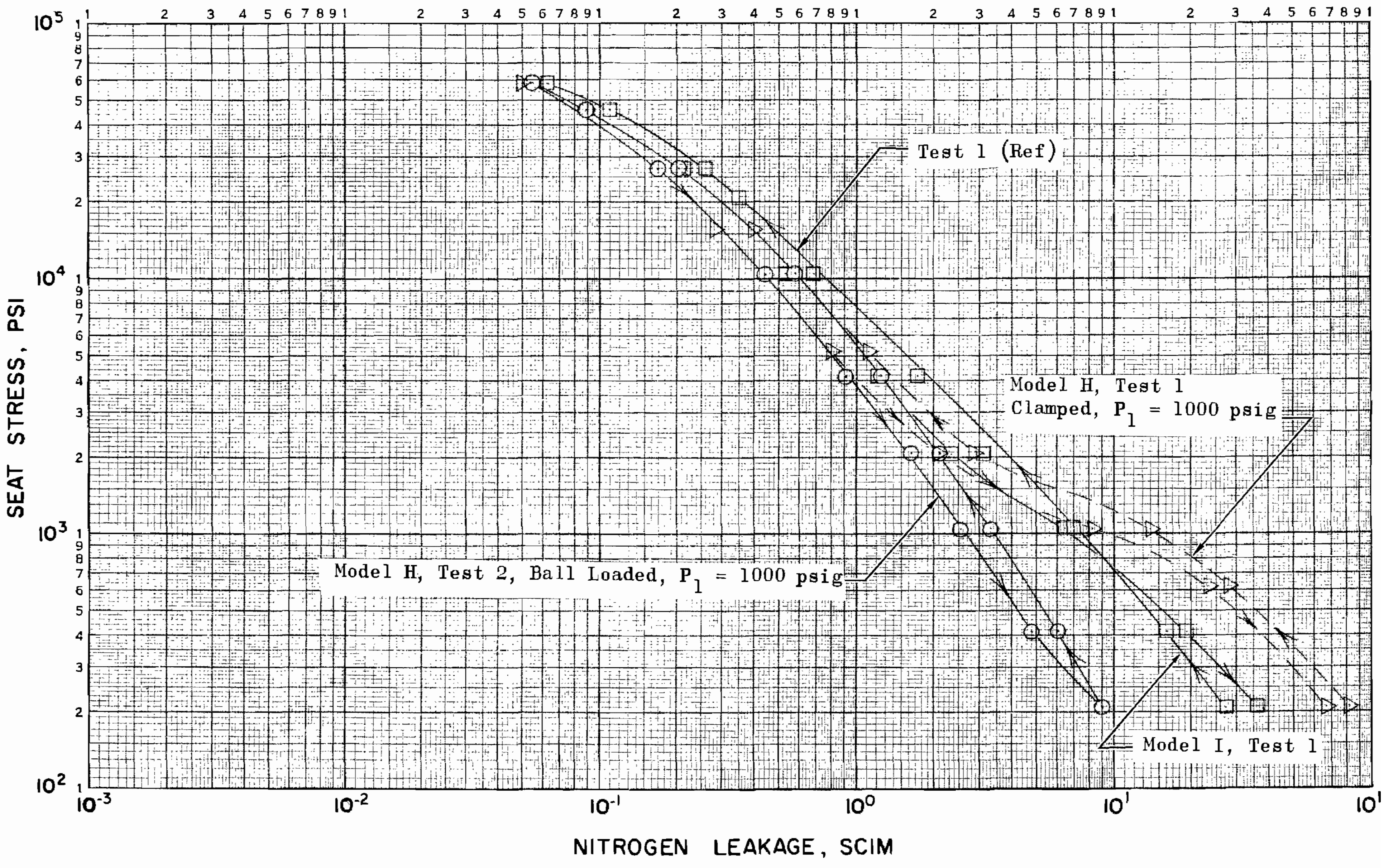

Figure 458. Stress-Leakage Data for Test Models H and I, Tests Noted

The assumed cylinder diameter may be expressed as:

$$d = \frac{\pi^2 D_s^2}{16h}$$

Describing the total seat load in terms of apparent seat stress the expression for deformation is:

$$\delta = \ln \left(\frac{4.4h}{D_s^3 S\alpha} \right)^{1.57 D_s S\alpha}$$

or in terms of total seat load, F,

$$\delta = \ln \left(\frac{13.8\ hL}{D_s^2\ F\alpha} \right)^{\frac{F\alpha}{2L}}$$

where

D_s = mean seat diameter, inches

F = total seat loads, pounds

h = peak-to-valley height, inches

L = land width, inches

S = apparent seat stress, psi

α = elastic constant for both materials, one/psi as previously defined

δ = peak deformation, inches

Introducing the test parameters into the stress-vs-deflection equation above for the 24-microinch curve, and solving (by trial and error) for stress required to flatten the curvature ($\delta = 24$ microinches) results in an indicated stress of 100 psi. While this approach is very approximate, the order of magnitude is a significant factor in these tests. This must not be taken as a general rule, however, because of the general independence of gross (substrata) deformation and surface deformation. For example, a very narrow seat land of typical corner construction could have very high unit surface loads (stresses) for a relatively small seat load. Therefore, deformation of the substrata would be small, and gross curvatures could be the significant parameter of the overall stress-leakage characteristic.

Model B, 2.2 AA Multidirectional Lay, 440C Poppet and Seat, Out-of-Parallel Tests

The poppet of previously tested Model B (surface texture evaluation) was reworked by lapping the back (loading) face out of parallel relative to its sealing surface. As measured on both Proficorder and Cleveland height comparator, the net deviation was 125 microinches over a 0.500-inch seating diameter. Poppet and seat sealing surfaces were unchanged from the originally tested condition.

Electrical contact tests for the out-of-parallel condition indicated an equivalent parallel plate separation (no-load) of 99 microinches. From inspection data, Model B net out-of-parallel PTV gap between mean roughness lines is the sum of the measured parallelism deviation, one-half the average poppet and seat roughness heights, and the total poppet and seat nodule height, or about 138 microinches. Applying the laminar sinusoidal weighting factor (M_L = 0.68) the computed equivalent parallel plate gap is 94 microinches which correlates reasonably with electrical contact data.

The out-of-parallel test consisted of six stress-leakage loops represented by test 5 in Fig. 459. The first increasing load loop is indicated by circles with the final decreasing load loop by squares. (Test 4 was a clamped-condition control test performed prior to poppet rework.) As the out-of-parallel model stress was increased above 2000 psi, the seating structure rapidly deformed until, from 15,000 psi on, the stress-leakage characteristic was nearly identical to the parallel version. It will be noted that the deformation characteristic is purely elastic and very repeatable.

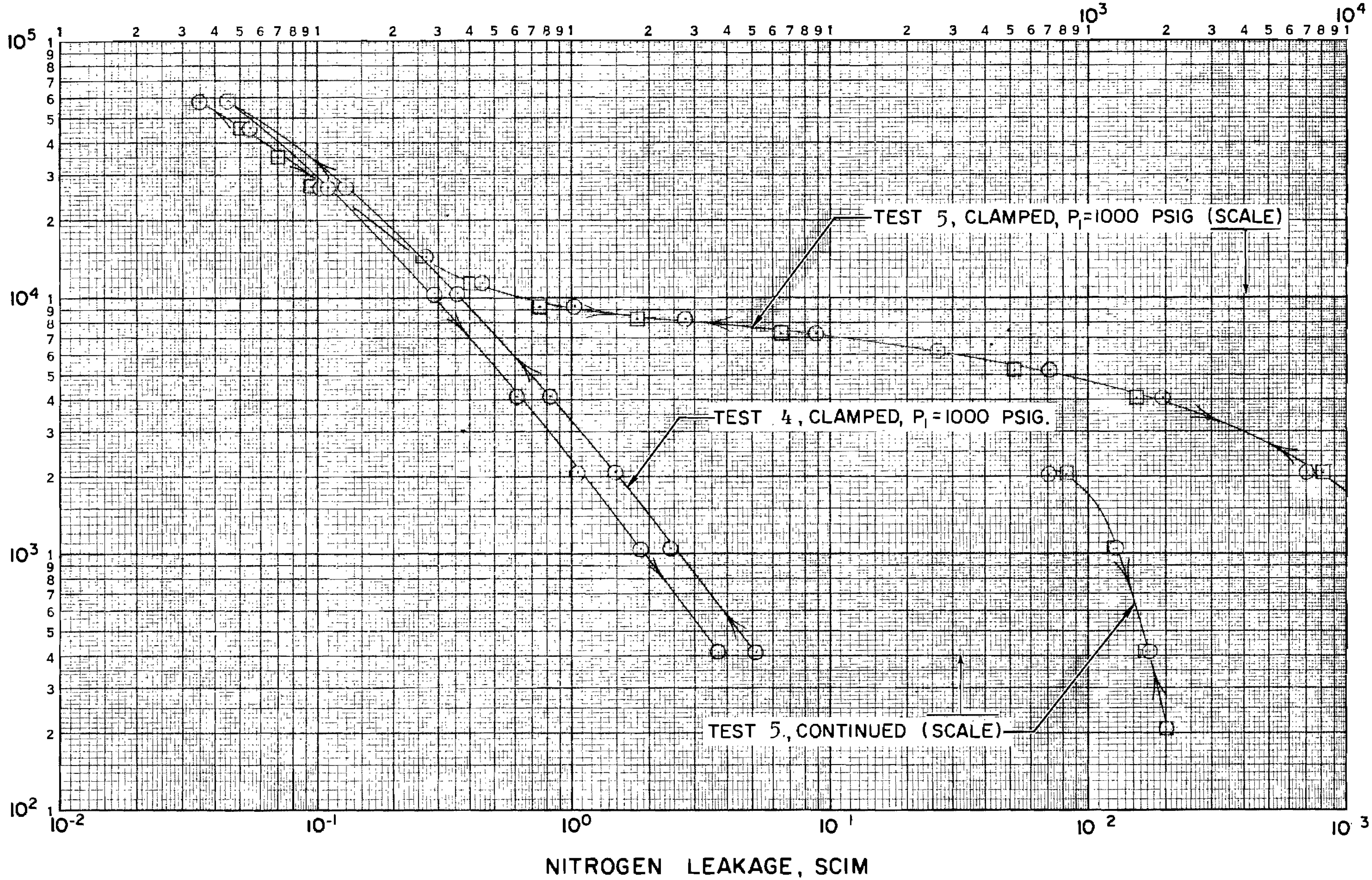

Figure 459. Stress-Leakage Data for Test Model B, Tests 4 and 5

The following analysis is presented to show where the various deflections occur which ultimately bring the two surfaces into a parallel and mating condition. The data recorded for the three most significant seat stresses are tabulated below from the piston pressure and load cells.

Net Piston Force, pounds	Apparent Seat Stress, psi	Load Cells, pounds			$\Sigma F = F_T$, pounds	Error, percent
		F_1	F_2	F_3		
224	1,040	79	72	60	211	6.2
669	11,430	258	187	193	638	4.9
2650	58,200	897	830	842	2570	3.1

The 125-microinch high point was located directly under cell No. 1. The variation in load between the three cells is not very large.

From the dimensions of load cells, poppet, and seat, an estimate of the deformation attributable to each of these parts may be made. The remainder, allowing for piston cocking, must be from interfacial deformation.

Load Cell Deformation (e_1, e_2, e_3).

$$e \cong \frac{FL}{EA} \cong \frac{1.0 \quad F}{30 \times 10^6 \times 0.313^2} \cong 0.34 \times 10^{-6} \ F$$

where

E = elastic modulus, psi

A = area, sq in.

L = length, inches

F = individual load cell force, pounds

e = deformation, inches

Poppet Deflection (e_p).

$$e_p = 0.0173 \times 10^{-6} F_T$$

Seat Deflection (e_s).

$$e_s = 0.014 \times 10^{-6} F_T$$

The deflections computed from the above expressions are summarized below for each of the previously noted seat-stress levels; all deflections are in microinches.

Apparent Seat Stress S, psi	e_1	Average e_2 and e_3	e_p	e_s	Δe
1,040	26.8	22.4	3.9	3.1	2.4
11,430	87.7	64.6	11.6	9.4	23.3
58,200	305.0	284.0	45.8	37.1	21.0

In the table, $\Delta e = e_1$-(average e_2 and e_3). The differential load cell deformation is approximately 22 microinches or 28 microinches across a 1-inch diameter, which reduces to 14 microinches across the 1/2-inch seat diameter. The righting allowed by piston clearance is approximately 20 microinches (initial contract static tester). Considering the relative stiffness of both the poppet and seat, probably very little differential deformation occurred within these parts. The difference between the 125-microinch out-of-parallel dimension and the 34-microinch (20 plus 14 inches) differential leaves 91 microinches for net interfacial deformation. From these figures, it is concluded that the deflection indicated by the large change in leakage at the 10,000-psi level is a result primarily of interfacial deformation.

Model E_c, 1 AA 41-Degree Seating Angle, Tilted Cone Axis

As discussed in the conical and spherical model section, Model E_c represented the best conical geomety fabricated. Consequently, it was the most suitable model for evaluation of angular misalignment effects.

As originally conceived, the tilted cone was to have been used to evaluate out-of-roundness effects. However, as initial tests and subsequent correlative analyses indicated, the major cause of seat gap was the poppet dislocation out of the seat caused by land width. Furthermore, as was shown in the Seating Analysis section (Fig. 14) the contribution of poppet ellipticity to the effective gap is negligible, except for unreasonably large tilt angles and narrow land widths.

Figure 69 (model fabrication section) illustrates the method of achieving the tilted cone axis condition. The tilting spacer (Fig. 67) was first wrung to the poppet. As with non-tilted tests, the poppet-spacer assembly then was set on the tester piston loading feet on drops of E.P. oil to permit radial self-alignment. Electrical contact tests were performed in the usual manner.

The initial test of Model E_c used the 0.313-degree, -8 spacer. As shown by Fig. 460 a hundredfold increase in low-stress leakage occurred. Extrapolating the test curves, it is estimated that 10,000-psi apparent stress would be required for the tilted condition leakage to match the coincident axes results. The reason for this is discussed in the following paragraphs.

For coincident test 1, electrical contact tests indicated an equivalent gap (h_e) of about 17 microinches (based on total land width), which agreed reasonably well with assessed geometry. Considering the effective land width reduced by the edge duboff shown in Fig. 228 (~ 50 microinches over 0.00253 inch) to 0.0244 inch, the above value for (h_e) is reduced to 16 microinches.

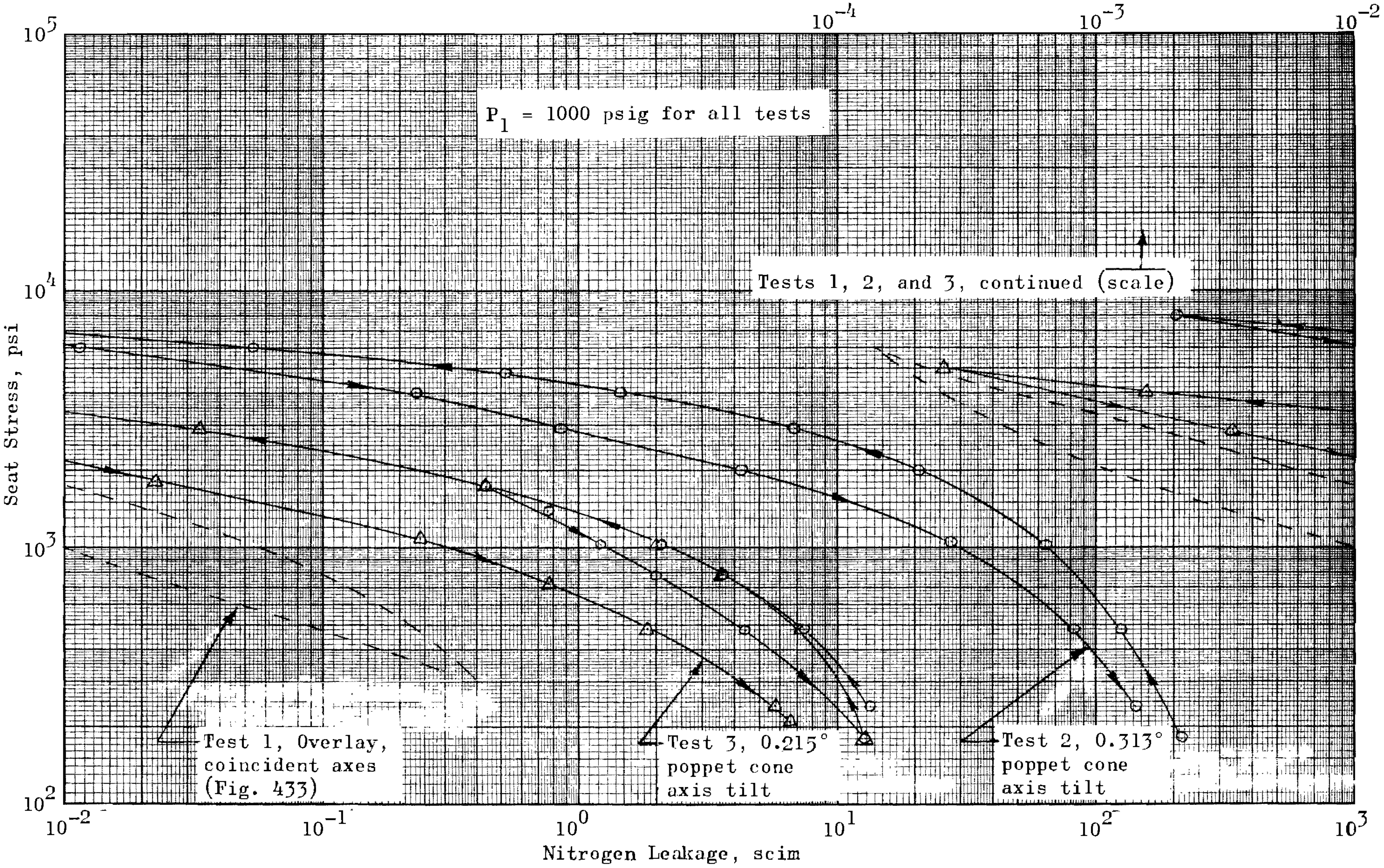

Figure 460. Stress-Leakage Data for Test Model E_c, Tests 2 and 3

Because of the dubbed condition, a like allowance for reduced land width must be made for consideration of the electrical contact results obtained with the preceding tilted cone. For analysis of the effective length and reduction in gap due to duboff, the following geometry is assumed for both seat edges contacted by the tilted cone.

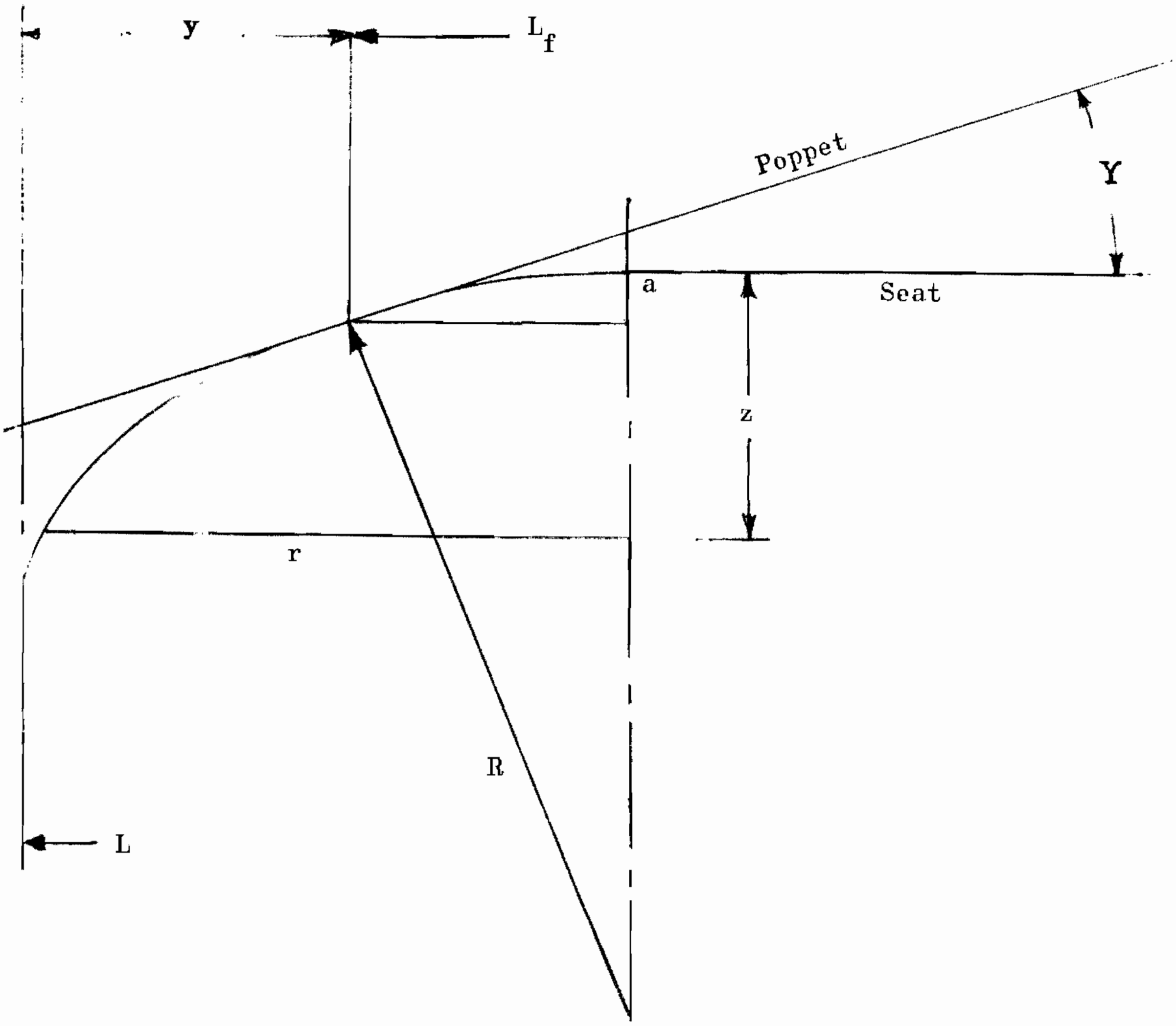

The effective flat land width is

$$L_f = L - 2y$$

where

$$y \cong r \left(1 - \frac{r\Upsilon}{2z}\right), \quad (\Upsilon \text{ in radians})$$

For Model E_c where $r \cong 0.00253$ inch and $z = 50$ microinches, L_f is 0.0257 inch.

From the Seating Analysis section, the taper gap in the plane of tilt at the contact points is LY; however this is reduced, as shown in the above sketch, by (2a); thus the taper gap is

$$h = L_f Y - 2a$$

where

$$a \cong \frac{r^2Y^2}{4z} \text{ , (Y in radians)}$$

For $Y = 0.313$ degrees $h \cong 140.8 - 1.92 \cong 139$ microinches.

Since the flow must split and recombine, the path is partially circumferential. The effective length is given by

$$L_e \cong \sqrt{L_f^2 + 0.132 D_f^2} = \sqrt{6.6 \times 10^{-4} + 292 \times 10^{-4}}$$

$$L_e \cong 0.1732 \text{ in.}$$

Based upon the sinusoidal gap shape and including 13 microinches out-of-roundness, the equivalent gap is

$$h_e = 0.68 \; (139 + 13) = 103.2 \text{ microinches}$$

For comparison with electrical-contact laminar-flow leakage data, the above equivalent gap for $L_e = 0.1732$ inch is ratioed to the standard 0.03-inch land as follows:

$$h_e \text{ (for } L = 0.03) = 103.2 \left(\frac{0.03}{0.1732}\right)^{1/3} = 57.6 \text{ microinches}$$

From electrical contact tests at P_1 = 30 psig, the equivalent parallel plate height was 56 microinches. The agreement between test and analysis is perhaps better than the analytical assumptions warrant. However, the important factor is that the dimensions measured and obtained from test do correlate sufficiently well to allow their use in defining design requirements. Also, it is apparent that the comparatively large gap caused by the 0.313-degree tilt (139 microinches) represents a considerable volume of material to be displaced in achieving closure and, therefore, explains the 10,000-psi stress required for the tilt condition leakage to match coincident test results.

Because of the relatively large change in leakage produced by the 0.313-degree tilt plate no further tests were performed with larger angles. To examine the effects of a smaller angle, the three available spacers were combined for a 0.215-degree tilt angle. As shown by Fig. 460 (test 3), this stress-leakage curve lies almost in the center of tests 1 and 2. Correlation of measured tilt gap and electrical contact tests did not agree as well as before. The computed gap (h_e) based on the standard 0.03-inch land is 42 microinches. Electrical contact test results, on the other hand, indicated (h_e) to be 29 microinches.

Although not indicated by interference inspection, it is probable that plastic deformation at the initial contact points was responsible for the change. (It should be noted that interference inspection of circumferential waves is not practical with conical surfaces due to band orientation. For an accurate estimate of plastic flow, before and after test profile records would be necessary.) Some evidence of surface degradation was indicated by a final coincident axis stress-leakage test (Fig. 461).

Model H_c, 1 AA 41-Degree Seating Angle, 0.005-Inch Land Width, Tilted Cone Axis

This model combined the nominal 0.005-inch land seat (D_c) with the improved poppet from F_c. From interference photos of the seat taken

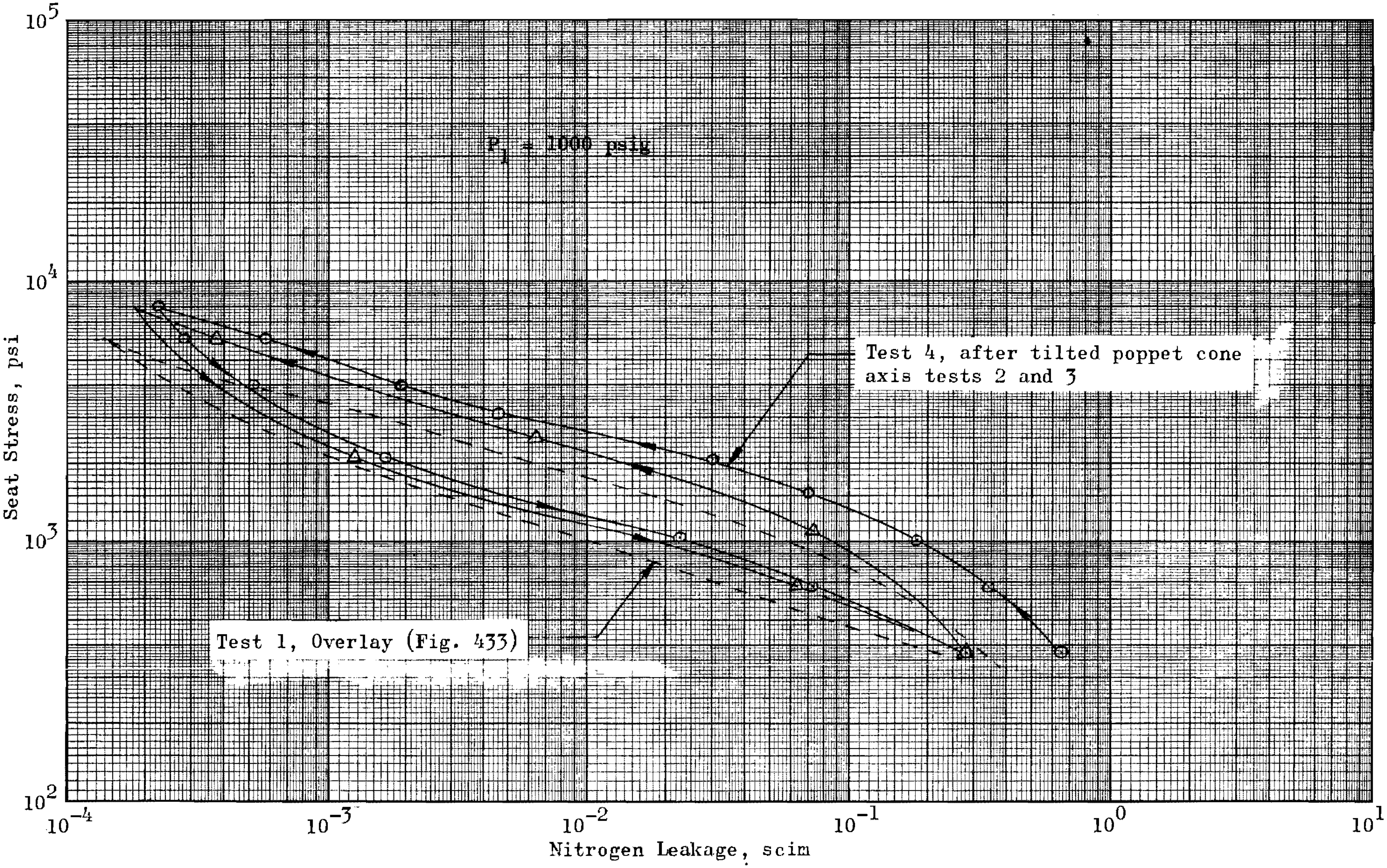

Figure 461. Stress-Leakage Data for Test Model E_c, Test 4

relative to the poppet, the center three-fourths of the seat tapers about 8 microinches. As previously indicated the seat also had 17 microinches out-of-roundness. The poppet had 6 microinches PTV waviness.

Figure 462 presents the stress-leakage test data for coincident axes as well as with the poppet tilted 0.313 degree. Electrical contact tests before tilt indicated a gap (h_e) of 27 microinches which agreed reasonably with assessed errors. After tilt h_e remained at about 27 microinches indicating the submergence of tilt effects by the above noted errors. As shown by Fig. 462, however, stress-leakage results reflected the increased gap. At 1000-psi increasing stress, the difference in equivalent gaps (h_e) based on the average 0.0046-inch land is about 6 microinches.

Although the test results could not be correlated with analyses due to the combination of errors, they do show the decreased effect of tilt angle with reduced land width.

Model L, 1.5 AA Multidirectional Lay 440C Poppet and 0.6 AA Unidirectional Lay 440C Seat, Contamination Tests

A series of tests were performed to define empirically the characteristics of hard and soft particle envelopment. The test vehicle, Model L, was comprised of the poppet of Model B and a 1.000-inch OD, 0.060-inch land width seat similar to that used for near seated tests (Model A), but without pressure taps. (The 0.060-inch land width permitted particle placement with less difficulty than a 0.500-inch OD, 0.030-inch land seat would have presented.) As previously described, the poppet had a surface roughness height of 4.5 microinches PTV and a 4.2-percent density of 3.1-microinch high nodules. The seat (illustrated by the post lead particle test photograph of Fig. 290) was diamond lapped with 1.9-microinch PTV roughness. Thus, the net PTV roughness was small enough with respect to the contaminant particles tested to have no effect on final test results.

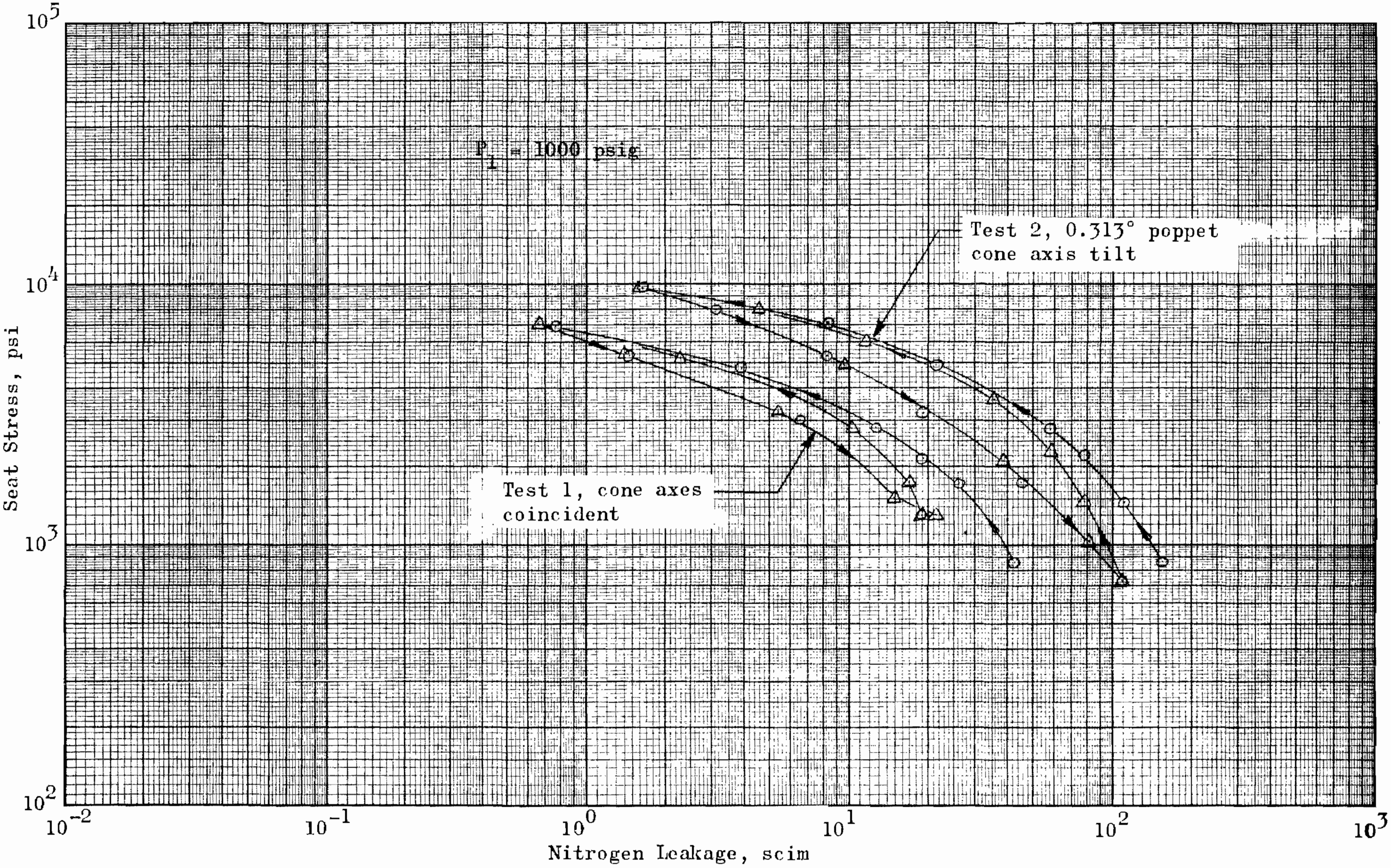

Figure 462. Stress-Leakage Data for Test Model H_c, Tests 1 and 2

As the particles had to be measured to determine size and volume, a reasonable geometrical shape was desired, preferably spherical. While the diamond specimens were not spherical, they were shaped so as to permit fairly accurate dimensional checks. The lead, however, posed a more difficult problem as it was only available in foil and granule form. The granules were highly irregular in shape and considerably larger than 0.020 inch. Because of the expected large increase in diameter due to flattening and a maximum available seat land width of 0.060 inch, the lead particle size desired was on the order of 0.004 inch. The problem was solved by forming lead spheres.

A chemically pure (99.95+ percent) lead foil, approximately 0.004 inch thick, was obtained from which particles were shredded with a clean (under microscopic examination) file and roughly graded in size. The particles were placed on a stainless-steel plate which had been rendered additionally non-wetting (for lead) by a heat-cured silicone fluid treatment. The plate was then covered by a pyrex funnel through which a continuous nitrogen purge was established to prevent oxidation. The particles were microscopically observed through the pyrex envelope while a torch heated the underside of the plate. As soon as the particles melted and formed into spherical shapes, the torch was removed and the plate rapidly cooled by a high-flow nitrogen purge. The resultant "near spheres" were then microscopically selected.

A probe was honed and lapped to a tip diameter less than 0.001 inch. Under 40-power magnification, the particles were readily seen and picked up with the probe. (Under bright light, a particle on the probe tip was easily distinguished with the naked eye.) The most difficult part of the procedure was removal of the specimen as static charges and slight plastic deformation tended to make the particles cling to the probe. Figure 291 illustrates the probe with a lead particle attached. This method of handling, while relatively simple, did have practical limits and, to ensure positive control, the contaminants used were selected at approximately 0.004 inch diameter. Final grading and dimensional checks of the contaminants were performed just prior to testing,at 100-power magnification.

The first tests performed were of a control nature to establish non-contaminated sealing capabilities. The stress-leakage characteristic was determined at 300-psig supply pressure up to an apparent seat stress of 9000 psi. Several stress cycles were run to prove repeatability. (The control characteristic, test 1, is shown in a subsequent discussed figure.)

Once the non-contaminated sealing characteristic had been obtained, the lead particles were selected and measured. The particle size, configuration, volume, and placement on the seat are indicated below:

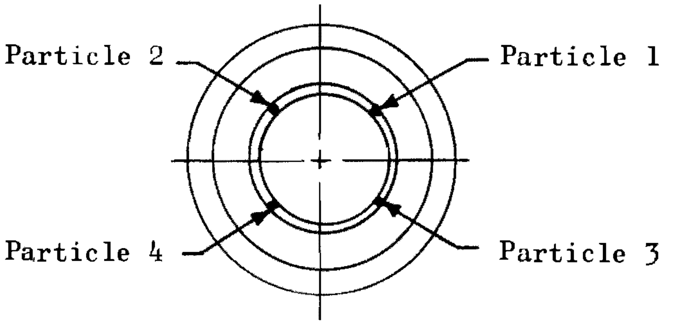

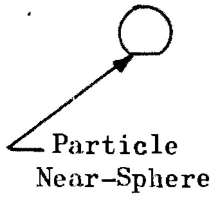

Particle	Configuration	Average Diameter, inch	Volume, cu in.
1	Near-Sphere	0.00386	29.8×10^{-9}
2	Near-Sphere	0.0043	40.2×10^{-9}
3	Sphere	0.00457	49.9×10^{-9}
4	Near-Sphere	0.00416	34.9×10^{-9}
			154.8×10^{-9}

After particle placement and at 30-psig inlet pressure, the poppet was pressure-loaded to incrementally increase apparent seat stress to 1000 psi and then reduced to a low-stress level. The resultant stress-leakage curve, test 2, is shown in Fig. 463. (A second stress cycle repeated on the lower, or return portion of the initial cycle.) Also plotted on this and succeeding figures is the equivalent laminar-flow parallel gap (h_e).

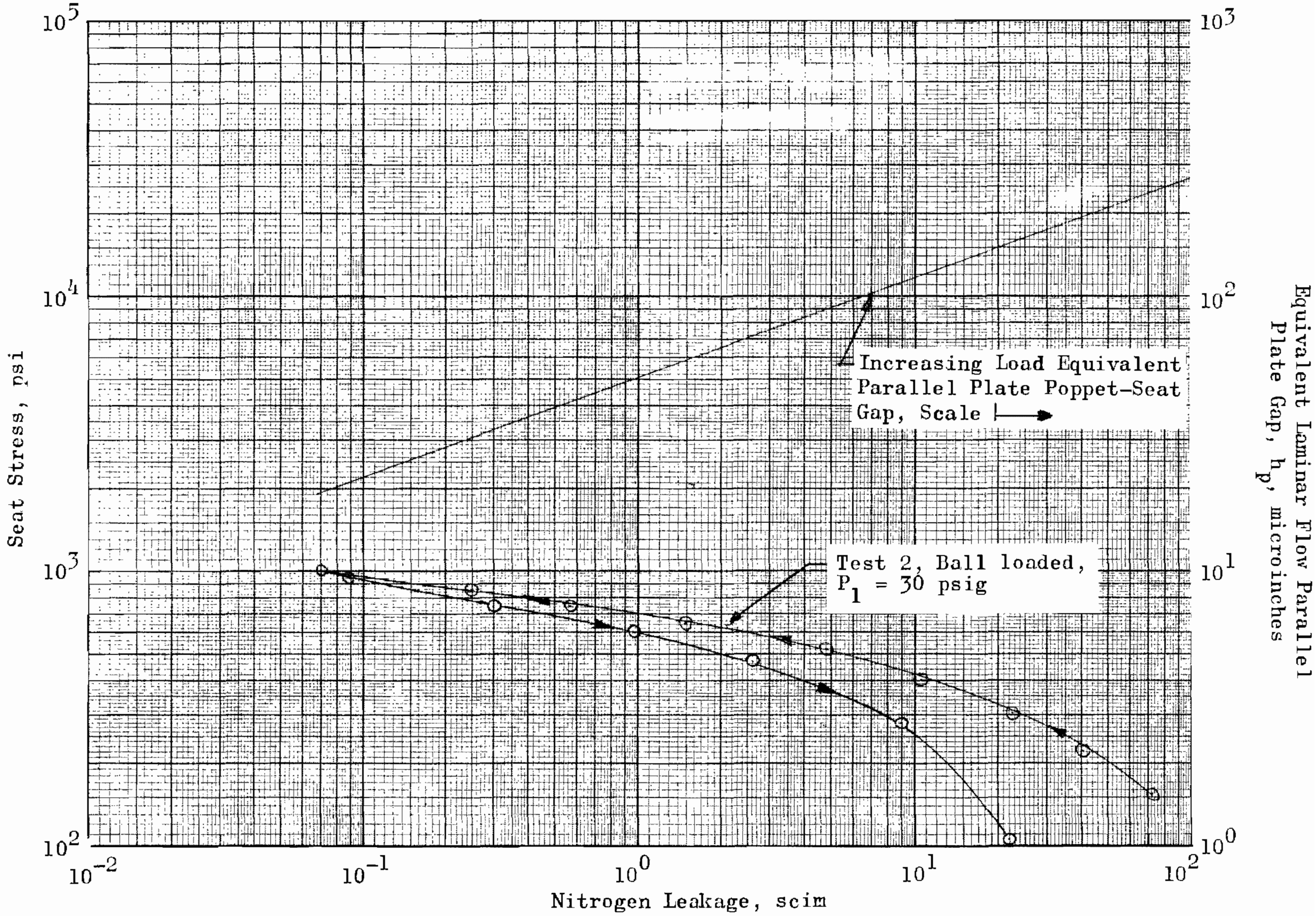

Figure 463. Stress-Leakage Data for Test Model L (Lead Contaminants), Test 2

Test 2 was continued at 300-psig supply pressure as shown in Fig. 464 (surfaces not separated). After seven stress cycles to 12,000 psi, the characteristic curve essentially followed the lower or return portion of the initial cycle. Also included in Fig. 464 is the original, non-contaminated stress-leakage curve for the test poppet and seat (test 1) which indicates potential particle envelopment at about 15,000 psi.

After completion of the noted tests, the poppet and seat were removed from the tester and microscopically examined. Three of the lead particles separated along with the poppet and seat at disassembly, but particle 3 stuck to the poppet in its entirety (Fig. 292). The flattened contaminant dimensions were determined as shown below (scale exaggerated for clarity):

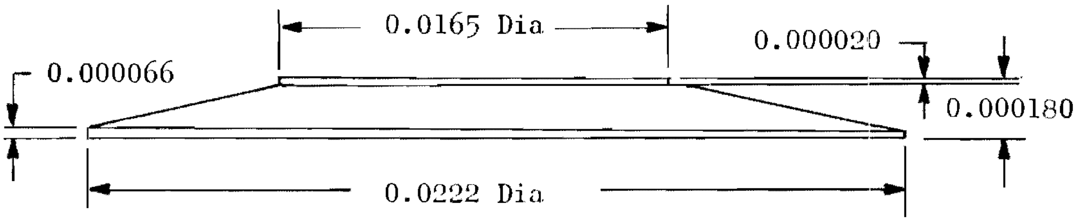

It is interesting to note that, although the unloaded particle height is 0.00018 inch, the seat had only approximately 3 microinches plastic set over about a 0.016-inch diameter (Fig. 290) and the poppet virtually none, indicating the elastic envelopment of the particle by poppet and seat.

After inspection the lead was removed. Approximately 90 percent could be wiped off with "Kimwipe"-type toweling; the balance was removed with a common pencil eraser. The 300-psig, no-contaminant stess-leakage test was then rerun indicating slightly lower leakage than noted prior to the lead contamination test. (For comparison, these data are plotted as the test 3 curve on Fig. 466, which presents diamond particle test data, subsequently discussed.)

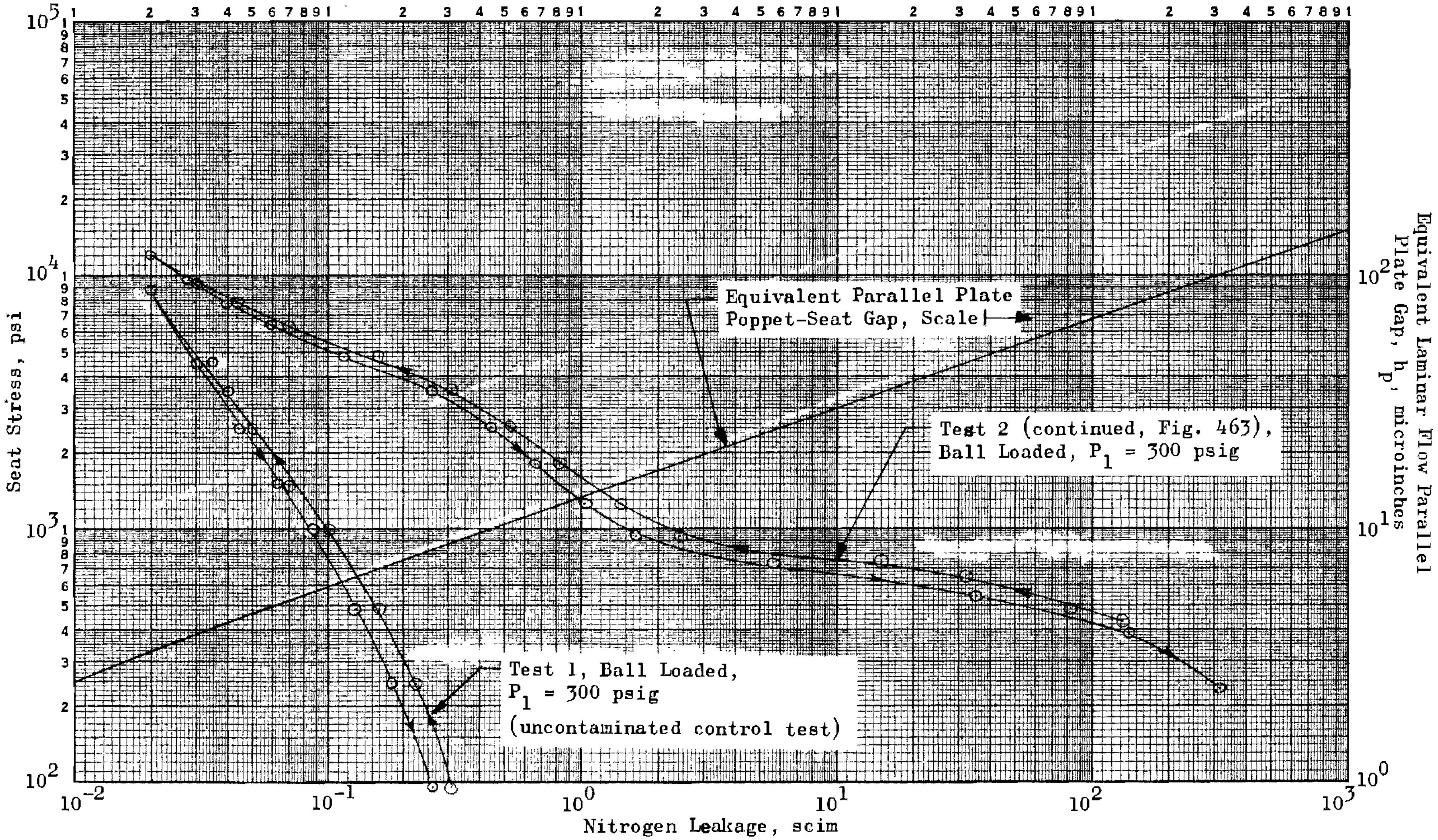

Figure 464. Stress-Leakage Data for Test Model L (Lead Contaminants), Tests 2 (continued) and 1

The diamond particles were then selected (Fig. 293 illustrates particle 2). Applicable dimensions and seat placement are shown in the sketch below.

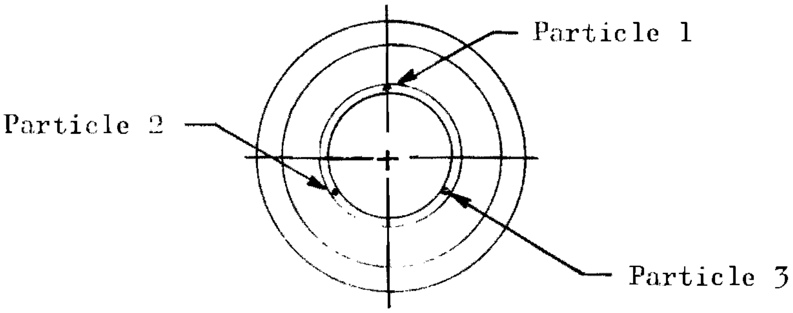

Particle	Approximate Configuration	Equivalent Spherical Diameter, inch	Volume, cu in.
1	Trapezoid With Uniform Thickness	0.00392	31.6×10^{-9}
2	Cone	0.00383	29.4×10^{-9}
3	Triangle With Uniform Thickness	0.00471	55.0×10^{-9}
			116.0×10^{-9}

As with the lead particles, a 30-psig load-deflection characteristic (test 4) was first obtained as shown in Fig. 465. The second stress cycle repeated the lower or return portion of the initial curve. Next, stress-leakage data at 300-psig supply pressure was obtained (Fig. 466, test 4 continued). The seat was then cycled to 10,000 psi five times; the last stress cycle followed the return portion of the initial curve so closely that it is not plotted.

The poppet and seat were removed from the tester and microscopically examined. Particle 1 had shattered over a large area, but particles 2 and 3 survived intact. Figures 294 and 295 show particle 2 embedded in the seat and the mating poppet deformation, respectively. The upward-shifting interference bands on these photos indicate a raised portion on the surface. Thus, a considerable upset of plastically flowed material above the surface is noted. As all of the particles were embedded in the seat, it was apparent that the poppet was the slightly harder of the two parts.

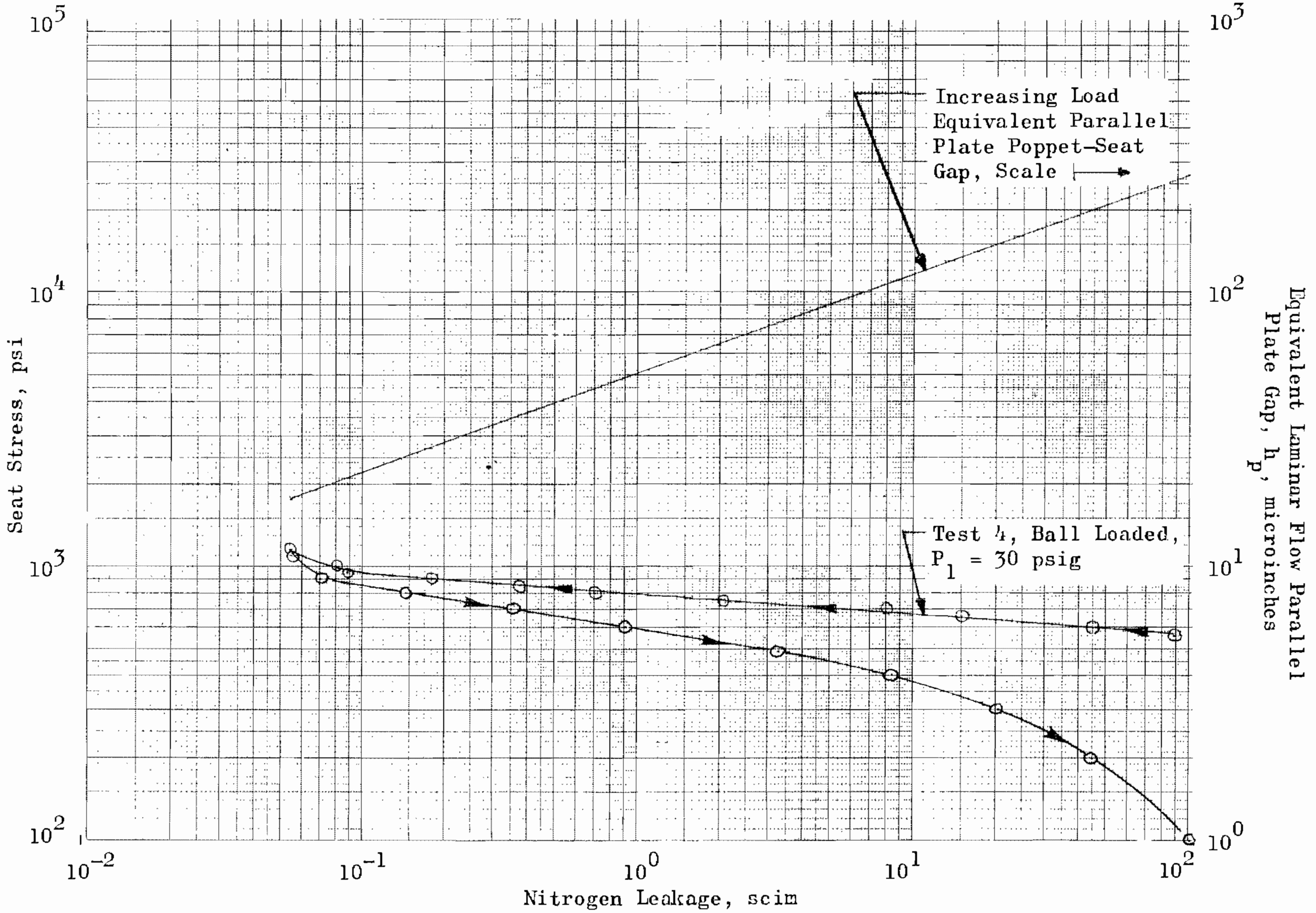

Figure 465. Stress-Leakage Data for Test Model L (Diamond Contaminants), Test 4

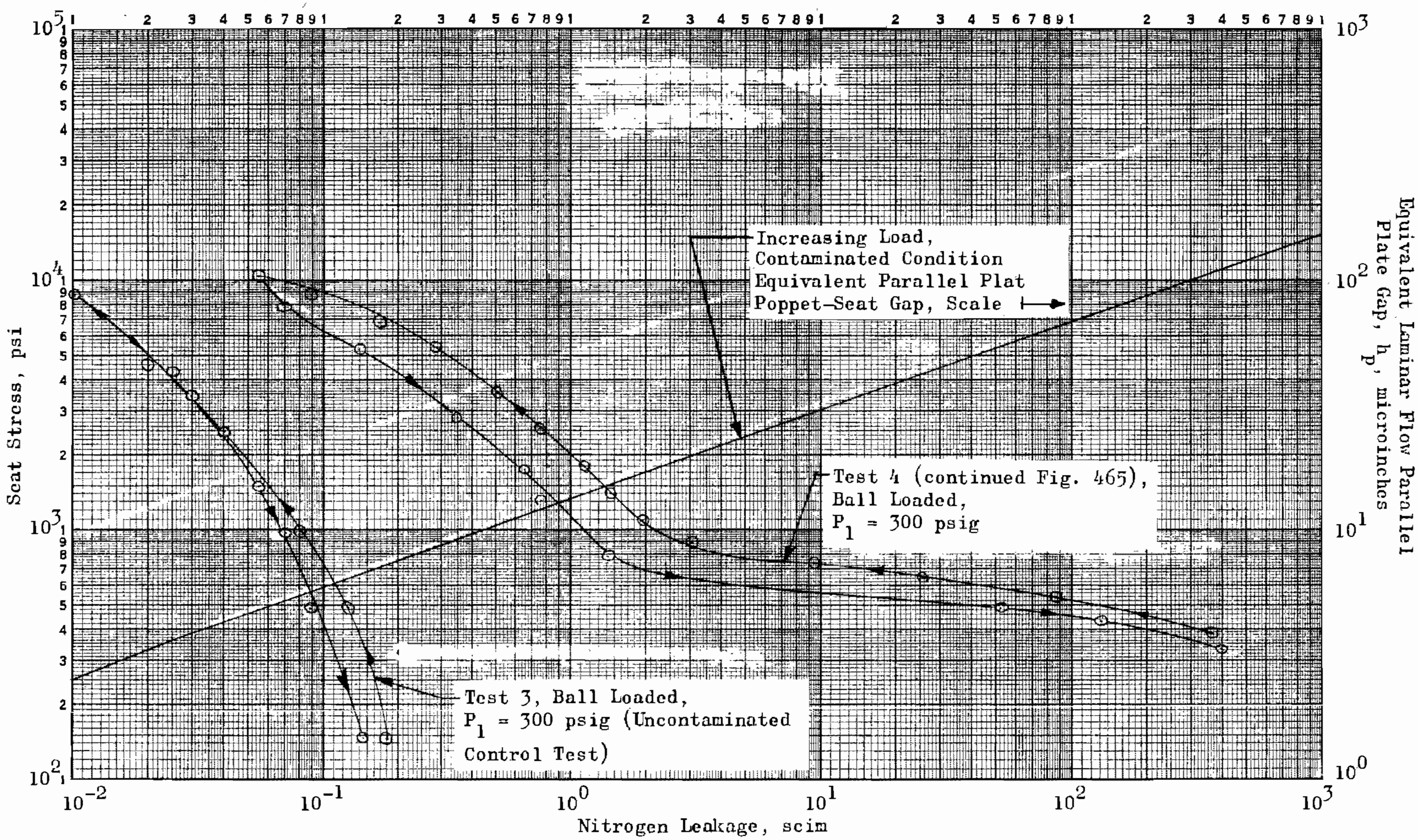

Figure 466. Stress-Leakage Data for Test Model L (Diamond Contaminants) Tests 4 (continued) and 3

It had been assumed that local elastic deformation of the 440C poppet and seat would compensate for the plastically displaced material. The photographs (Fig. 294 and 295) indicate this was not true, and a contact of upset material actually occurred as pictured below.

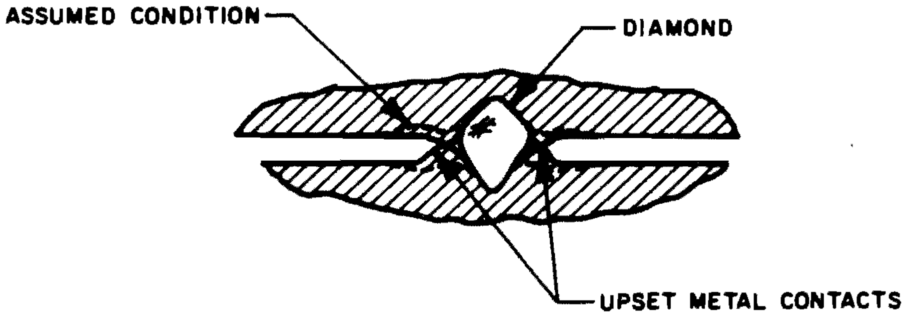

The abrupt knee of the test 4 stress-leakage curve at approximately 1000-psi stress (Fig. 466) is believed to be the initiation of this contact. From this point on, the additional rate of the severly cold-worked metal ridges must be overcome. While perhaps 60 to 80 microinches upset height can be observed (Fig. 294 and 295), the major bearing area is only 2 or 3 bands high. This compares favorably with the equivalent parallel plate height of approximately 23 microinches at the knee of the stress-leakage curve.

Extrapolation of test 3 and test 4 curves (Fig. 466) indicates the diamond particle envelopment stress would have been reached at about 15,000 psi or the same as for the lead contaminants. Considering the similar volumes, it would appear that a simple empirical particle diameter and volumetric relationship involving seating material parameters might exist for determining particle envelopment loads. However, these tests have served mainly to show the stress-leakage envelopment characteristics for the extremes of particle hardness.

OBSERVATIONS

The seating-error test series basically demonstrates various load-conformance characteristics at an exaggerated level. The data obtained are limited and insufficient for parameterization. However, they do provide a frame of reference for comparison with similar errors encountered in the test program and those likely in the construction and development of actual valves.

The scratch test was particularly significant in illustrating the poor compliance associated with subsurface voids. This characteristic was evident on all unidirectional models tested and emphasizes the advantage of the circular lay surface. Furthermore, the scratch influence is relatively constant over the entire stress range tested, and thus may be considered directly additive to total gap leakage regardless of load.

The remaining forms of seating error investigated, however, result in more drastic effects than the scratched surface, particularly at low-load levels. Unfortunately, the majority of small control or pilot valves are operated in this load region from 1 to perhaps 50 pounds of force. Even in their extreme, the reported tests, therefore, indicate that geometry and contamination control is vital to successful performance. This control must be exercised not only in fabrication detail, but more fundamentally in the design of the closure mechanism itself for the misaligned conical axis or cocked-poppet condition can obviate any improvements in surface roughness when available loads are limited. Moreover, these conditions result in contact stress concentration at the high points thus increasing the probability of cyclic damage.

CYCLE TEST

The Surface Studies section introduced the more conjectural aspects of cycling as viewed from considerations of metal plastic flow and wear. However, this study allowed few conclusions as to the effects of impact loading on surface structure. With the broad spectrum of static seating characteristics previously defined, the purpose of the cycle test effort was to investigate the cyclic impact effects on selected models with an aim toward defining and correcting modes of surface degradation.

With this objective, it was absolutely necessary that all cyclic variables be rigidly controlled and repeatable. The cycle tester provided this control through precise orientation of model surfaces and impact velocity. Thus, impact cycles were delivered axially to each model in the same manner without tangential motion, so that the only test variables were the impact velocity, number of cycles, and specific model properties. Also, with poppet and seat locked in position, and the gas-bearing centered piston restrained from rotation by the flexure, a repeat contact between poppet and seat was ensured within less than 10 microinches. Tester controls, dynamic analyses, and surface studies notwithstanding, the unknown elements inherent in cycle testing precluded anything but a cut-and-try approach.

A synopsis of pertinent parameters and results obtained in cycle testing is presented in Table 8. The models are listed in nearly chronological order tested, and thus reflect test developments and configuration improvements. Variations in peak impact stress and apparent static stress (established from steady-state control pressure) resulted from differences in seat land area, established impact velocity, and also by some revision in test approach as the program progressed. (It is recognized now that, for consistency, the peak impact stress should have been held constant for the two basic impact levels indicated in Table 8; i.e., impact stress levels, 26,500 to 30,700 and 96,000 to 91,300 psi. As will be seen, however, these variations had little affect on the results which were of a much more general nature.)

TABLE 8

CYCLE TEST MODELS AND PARAMETERS

Test Model, Lapped 440C Unless Otherwise Noted	Peak Impact Stress, psi	Peak Impact Load, pounds	Static Stress, psi	Impact Velocity, in./sec	Control Supply Pressure, psig	Basic Cycles	Impacts per Cycle	Total Impacts per Test	Leakage at 2000 psi Seat Stress, scim		~ h_e Change, Microinches
									Before Test	After Test	
D_f, 2 AA Ground Unidirectional Lay	26,500	1150	6190	7.60	169	10^4	2	2×10^4	3.7	2.8	0.97
G_{f1}, 0.7 AA Unidirectional Lay	30,700	~ 1150	7220	7.60	169	10^4	2	2×10^4	0.017	0.0062	0.42
B_{f1}, 0.6 AA Circular Lay	28,200	~ 1150	6610	7.60	169	10^4	2	2×10^4	4.4×10^{-4}	3.9×10^{-4}	0.014
B_c, 1 AA Circular Lay	27,000	650	9880	5.60	150	10^4	2	2×10^4	0.64	0.96	0.80
G_{f1}, Retest	2,340	87.5	2340	~ 0.7	54.	10^3	1	10^3	0.015	0.015	~ 0
G_{f1}, Retest	159,000	5960	7220	35.6	169	10^4	6	6×10^4	0.015	0.18	1.9
X_f, 0.8 AA Unidirectional Lay	26,600	1170	0	~ 7.7	25.	10^6	1	10^6	0.012	0.0027	0.50
Y_f, 0.8 AA Unidirectional Lay	91,700	4100	6040	~ 24.	169	10^4	5	5×10^4	0.019	0.015	0.11
D_f, Retest	91,800	4000	6190	~ 24.	169	10^4	6	6×10^4	4.1	2.3	1.8
AA_f, 0.3 AA Circular Lay, Tungsten Carbide Poppet, Crown Seat	96,000	4100	6320	-	169	10^4	6	6×10^4	0.013	0.0054	0.33
P_f, 0.6 AA Unidirectional Lay Identical Lands	106,000	4050	7090	~ 24.	169	10^4	5	5×10^4	0.028	0.023	0.11
Z_f, 0.5 AA Circular Lay Identical Crown Lands	30,400	1380	0	~ 9.1	25.	10^6	1	10^6	5.7×10^{-4}	4.6×10^{-4}	0.027
A_s, 0.5 AA Circular Lay	29,800	878	8540	~ 7.6	158	10^4	2	2×10^4	0.018	0.016	0.056
T_{f1}, 30 Microinches, Gold Plate Seat	30,000	1330	5920	~ 8.8	165	10^4	2	2×10^4	0.029	0.011	0.49

Peak impact stress was determined by dividing the peak impact load (measured by the piezoelectric load cell) by the apparent projected land area. Static stress was the steady-state stress level obtained after impulse stabilization and was controlled by the piston supply pressure (PS). Before and after cycle test leakage at 2000 psi, apparent (increasing) stress is given in Table 8 for comparison purposes. These values are obtained from the stress-leakage curves in which the model was not reoriented. The last column indicates the relative surface geometry change reflected by the accompanying leakages.

The impact level established for initial cycle tests was based upon evaluation of the flat 440C model used in calibration testing. Even though this model showed little leakage change throughout the calibration testing, a cautious approach was required with the more expensive inspected and static-tested models. Hence, initial 10,000-cycle tests were performed on representative rough and smooth models of flat (D_f, G_{fl}, B_{fl}) and conical (B_c) configurations at the lower stress levels noted in Table 8. Although having no measurable effect on flat models, some degradation in the surface texture and stress-leakage performance occurred with the conical model (B_c).

Following these initial tests, the effects of impact load level and total number of cycles were evaluated. As a control surface, the nominal 0.7 microinch AA roughness obtained from unidirectional diamond lapping was used. High and low impact levels were examined with Model G_{fl}. Low impacts at 2340-psi peak stress produced no change; however, 10,000 cycles at 159,000-psi peak stress caused considerable degradation in surface structure with increased leakage. The concluding test consisted of performing 1,000,000 high-frequency cycles with Model X_f at the lower stress level. This test also resulted in surface texture change, although not to the extent of Model G_{fl}.

With the preceding preliminary tests bracketing the results to be expected, performance comparison tests were performed on the remaining test models. Model Y_f was cycled at the intermediate level of 91,700 psi. Producing only moderate surface degradation, this impact level was employed then for evaluation of (1) impact on the rougher surface of Model D_f, tungsten carbide poppet on crowned seat (AA_f), and (2) the benefits to be obtained through identical land geometry (P_f). In comparison with Model P_f and X_f, 1,000,000 high-frequency cycles were performed with Model Z_f to evaluate the identical crowned land geometry. Concluding the cycle test effort, spherical Model A_s and gold-plated Model T_f were tested at the lower impact level.

Except for Models G_{f1}, B_c, AA_f and A_s, stress-leakage characteristics were improved by cyclic impacts. In cases where obvious surface degradation had occurred, decreased leakage was attributed to intermeshing of opposing surface textures and/or the submergence of degradation effects by undamaged land area. This was shown by subsequent reorientation model tests in the static tester with ball joint loading which resulted in increased leakage.

Unless otherwise noted, all cycle test stress-leakage curves are from tests performed in the cycle test fixture and, hence, obtained for a clamped loading condition.

PRELIMINARY TESTS

These tests explored the effect of a given impact stress on surface texture for flat and conical models. To bracket basic cyclic effects, the level of impact loading and number of cycles were evaluated also. Since the data is given by model designation, Model D_f, reported first in this section, contains the results of both preliminary and later performance comparison tests.

Model D_f, 2.7 AA Undirectional Ground 440C Poppet and Seat

Model D_f provided an ideal test specimen for the initial cycle test because leakage could be measured entirely on the flowmeter, facilitating repeat measurements as required. Electrical contact tests indicated an equivalent parallel plate separation of 36 microinches which correlated well with assessed roughness and waviness previously presented.

This initial exploratory 10,000-cycle test was performed at loading conditions shown in Table 8. Typical impact load displays per cycle are illustrated by Fig. 467 and 468.

Figure 469 presents the stress-leakage data before and after 10,000 cycles with an overlay from the static test program wherein the ball joint loading method was used (intermediate tests 5 and 6 fell between these two curves). As shown, the out-of-parallel condition is evident at the lower stresses. However, this is to a lesser degree because the roughness dimension is greater than the out-of-parallel condition. Spot leakage tests indicated a progressive decrease in leakage, eventually reaching the level indicated by the lower stress-leakage test.

Post cycle test examination of the poppet and seat revealed no evidence of surface texture change. Numerous OD and ID fractures were noted (Fig. 123), particularly in the area calculated to be the initial out-of-parallel contact point. Although the fracture shown in Fig. 123 is only about 0.00065 to 0.0009 inch wide by 0.0003 inch deep, it is indicative of an undesirable, and potentially dangerous condition correctable by adequate edge radii. Moreover, edge conditions such as this influence the low-stress region and, thus, could cause increased leakage in narrow land valves.

After evaluation of Models G_{fl}, B_{fl}, B_c, and X_f (following), the intermediate level impact test was established and Model D_f was, therefore, recycle-tested to determine the increased loading effect on a rough surface. Figures 470 and 471 display typical impact traces for peak load of approximately 4000 pounds.

Before and after cycle-test stress-leakage data is shown in Fig. 472. As before, intermediate spot tests indicated a continuous decrease in leakage with cycles.

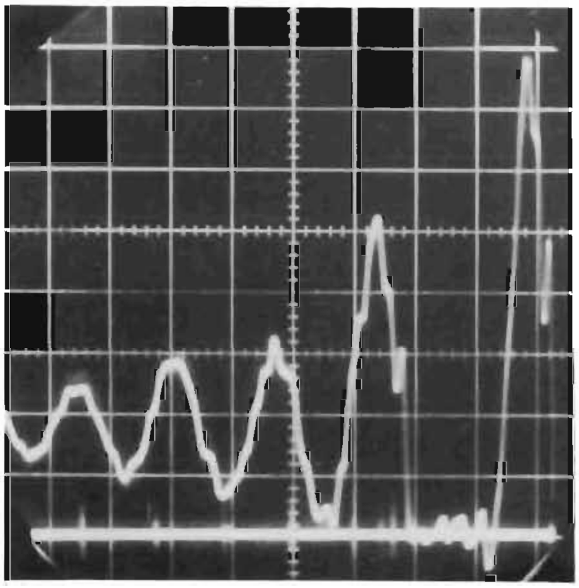

Figure 467. Test Model D_f, Piezoelectric Load Cell, 7.60 in./sec Impact Velocity, PS = 169 psig (149 lb/div.; 0.0002 sec/div.)

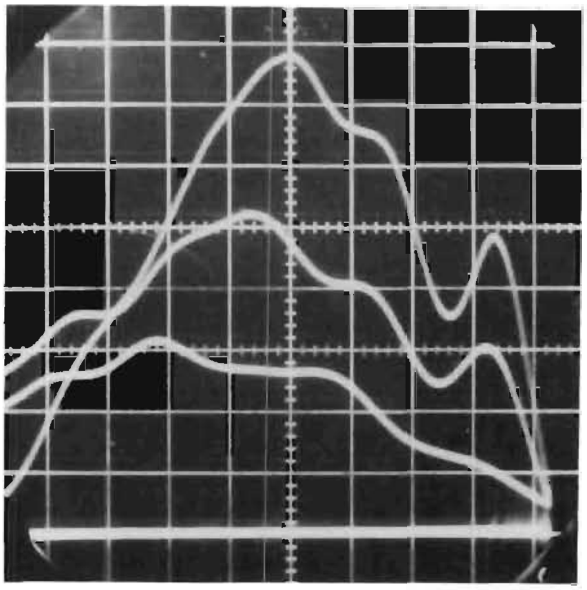

Figure 468. Test Model D_f, Piezoelectric Load Cell, 7.60 in./sec Impact Velocity, PS = 169 psig (149 lb/div.; 0.00002 sec/div.)

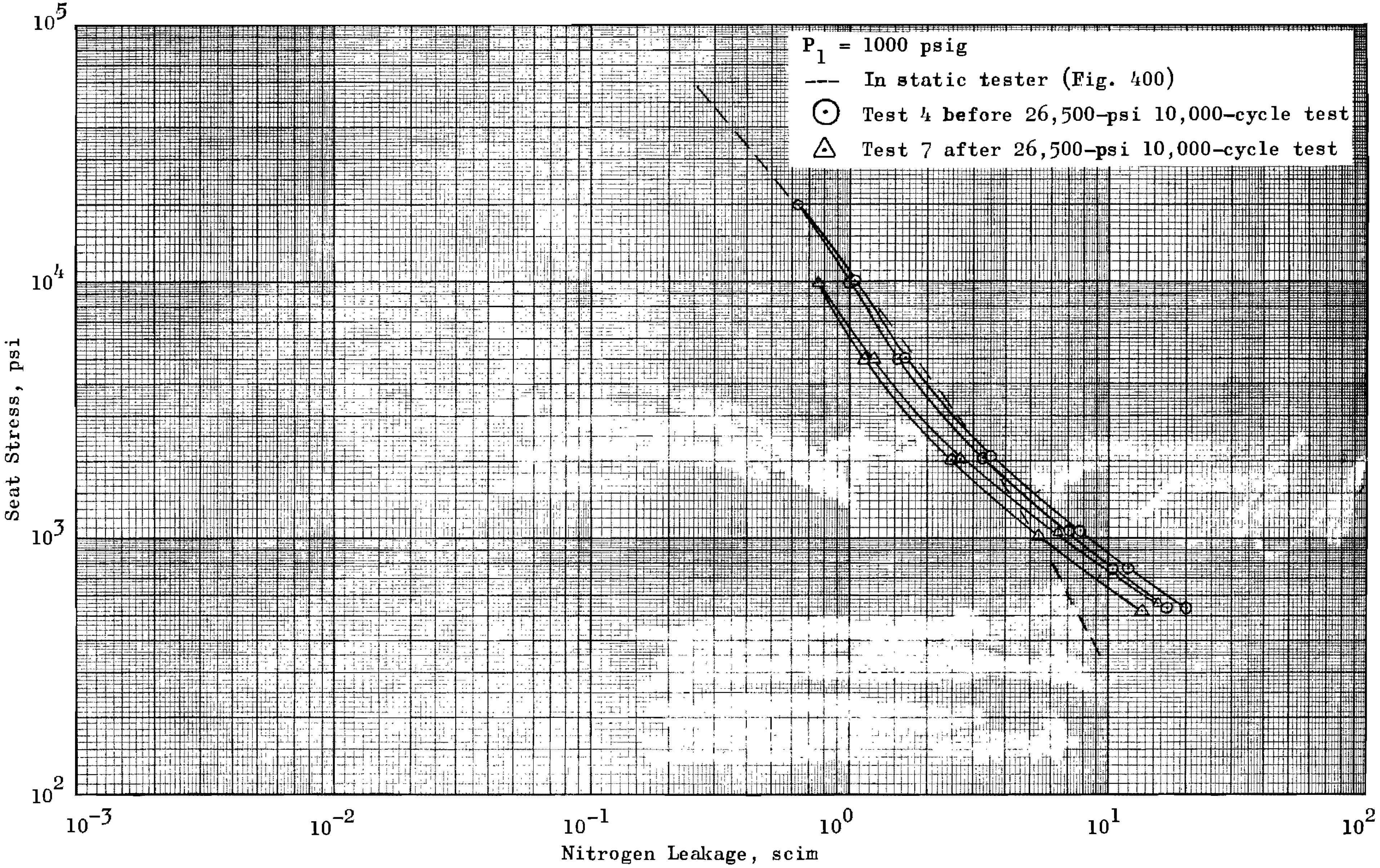

Figure 469. Stress-Leakage Data for Cycle Test Model D_f, Tests 4 and 7

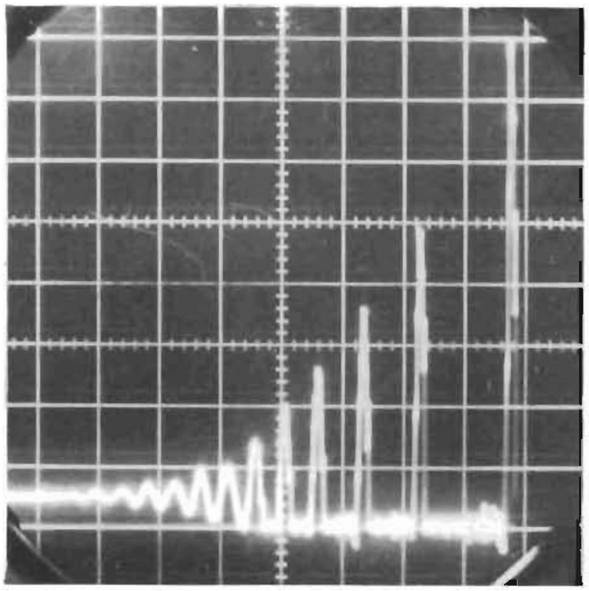

Figure 470. Test Model D_f, Piezoelectric Load Cell, 24 in./sec Impact Velocity, PS = 169 psig (500 lb/div.; 0.001 sec/div.)

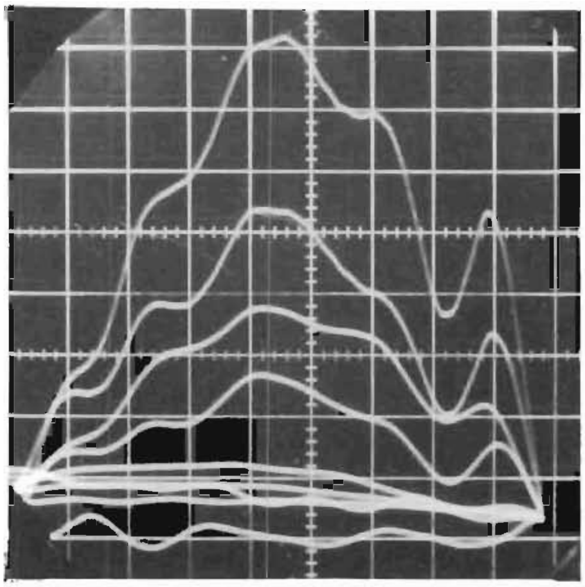

Figure 471. Test Model D_f, Piezoelectric Load Cell, 24 in./sec Impact Velocity, PS = 169 psig (500 lb/div.; 0.00002 sec/div.)

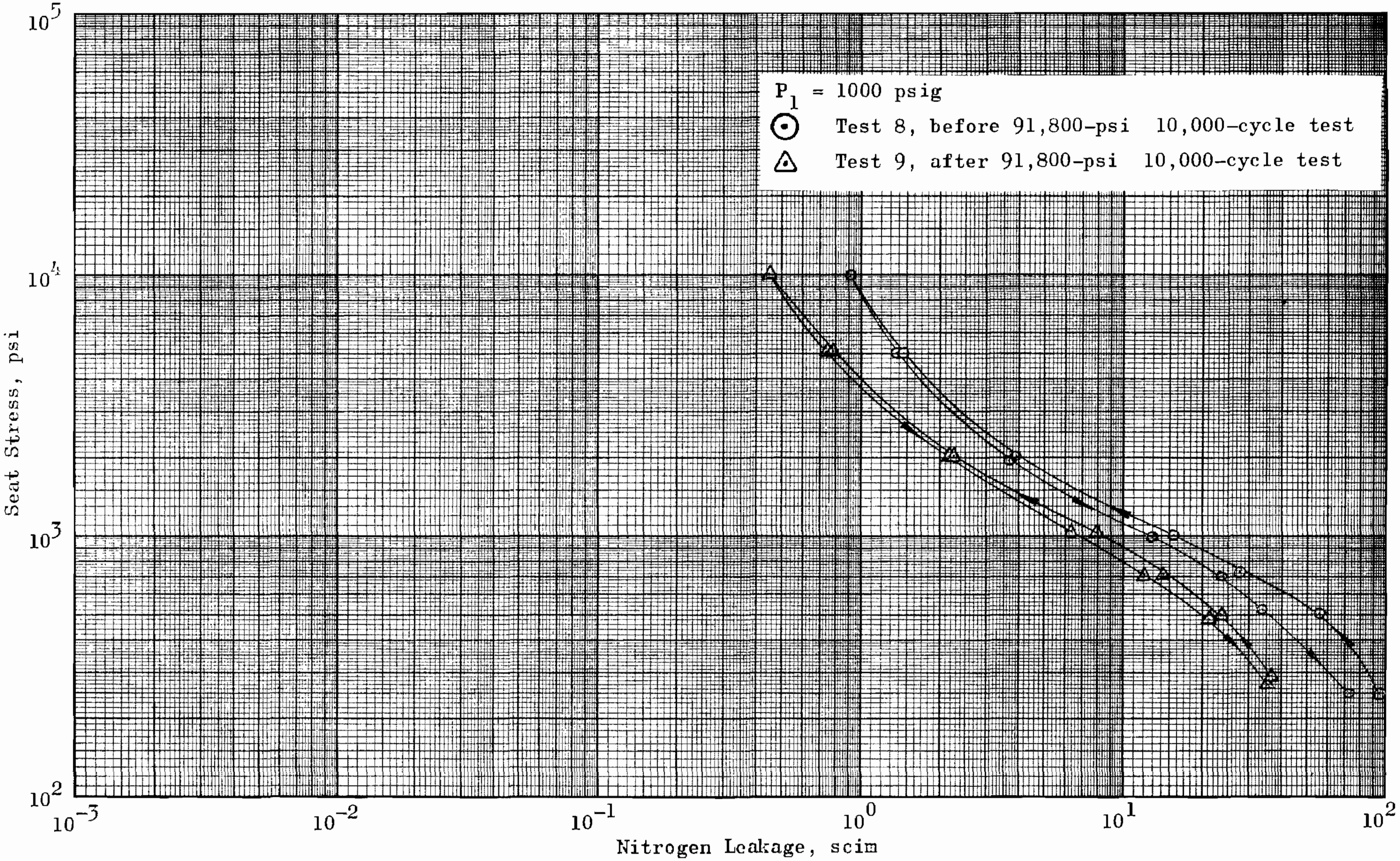

Figure 472. Stress Leakage Data for Cycle Test Model D_f, Tests 8 and 9

Posttest inspection revealed a fretting condition as with Model G_{fl} (discussed next); however, as shown by Fig. 124, 125, and 126, damage was limited to the asperity peaks. Moreover, damage was relatively slight as shown by the wiped poppet, Fig. 126 (seat appeared the same after wiping). Minimal damage is additionally reflected by the stress-leakage results at 2000-psi stress where the indicated change for (h_e) is only 0.97 microinches.

Model G_{fl}, 0.6 AA Unidirectional Lay 440C Poppet and Seat

Continuing the exploratory testing to determine potential cyclic effects on surface texture, Model G_{fl} provided the fine-finish standard with which other models would eventually be compared.

Electrical contact tests indicated a 17-microinch equivalent separation which was commensurate with physical dimensions. Cycle testing through 10,000 cycles was performed as with Model D_f. Since impact velocity settings were not changed, impact loading remained approximately the same.

Spot leakage tests showed a continual decrease in leakage with about one-half of the change indicated in Table 8 occurring in the first 1000 cycles.

Comparison of before-and-after cycling, stress-leakage results is shown in Fig. 473. The clamped condition before cycling curve (circles) indicates a definite out-of-parallel condition as reflected by the overlay data obtained in the static tester with ball joint. Out-of-parallelism is pronounced because of the relative model surface smoothness.

The effects of cycle testing are more evident at the lower stresses where impact loads were concentrated on the initially contacted edge. At 500 psi, the leakage decrease is about 10 to 1, indicating a dimensional decrease from (h_e) of 5.9 microinches to 2.6 microinches. At higher stresses, however, not only is the leakage decrease less, but the size of the dimensional change is much smaller. At 2000 psi, (h_e)before cycle test is about 1.45 microinches; after test (h_e) is reduced to about 1.03 microinches.

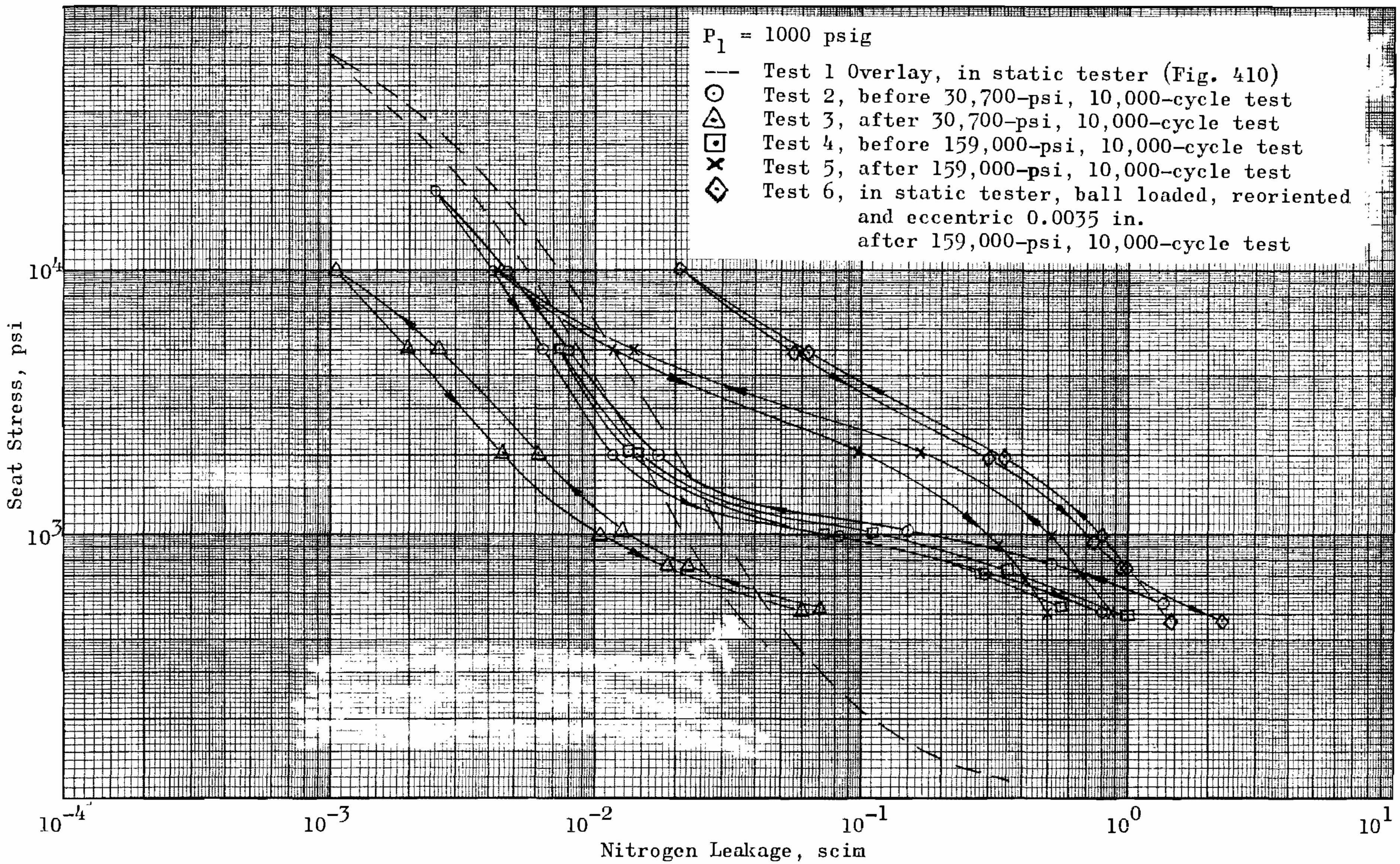

Figure 473. Stress-Leakage Data for Cycle Test Model G_{f1}, Tests 2 Through 6

In view of these small dimensional changes, it is not surprising that microscopic examination revealed no change in microstructure. It is apparent that the few higher asperities between poppet and seat had been plastically depressed. This contention is supported by the return to the original-condition leakage curve after reorientation in preparation for the next test.

In search for an answer to possible modes of impact degradation, it was hypothesized that the high impact loads were rehealing an otherwise (micro) ruptured surface with each impact. Since it was known that many static seals can only function through a few matings with no impact, the leakage just might increase as a function of plain contact. Consequently, the piston stroke was reduced to about 50 microinches (just off electrical contact) and the model was "zero impact" cycled 1000 times with nearly a square wave cyclic load variation zero to 87.5 pounds (2340 psi seat stress) with 0.5 seconds on-off time. No change was noted in leakage after 1000 cycles and the test was terminated. A brief stress leakage test verified the previous test results (squares on Fig. 473).

The cycle tester was next adjusted to give an impact velocity of about 35.6 in./sec for a peak impact load of 5960 pounds or 159,000 psi apparent seat stress. As shown by Fig. 474 and 475, dashpot damping allowed 4 to 5 progressively lower bounce cycles; therefore, a 10,000 cycle test actually represented about 60,000 contact cycles. Throughout the cycle test at the spot-leak test stress level of 2450 psi, the leakage remained nearly constant through 2000 cycles whereupon it progressively increased. The stress-leakage test data after cycling at 159,000 psi is indicated in Fig. 473 by the X's. As shown, there was little change in leakage at the low-stress level; however, between 1000- and 5000-psi stress, an order of magnitude increase is indicated. At 10,000-psi stress the leakage is again the same.

Disassembly inspection and microscopic examination provided explanation for the changed stress-leakage characteristics. After cycling, the poppet and seat were removed immediately from the tester. On both seating

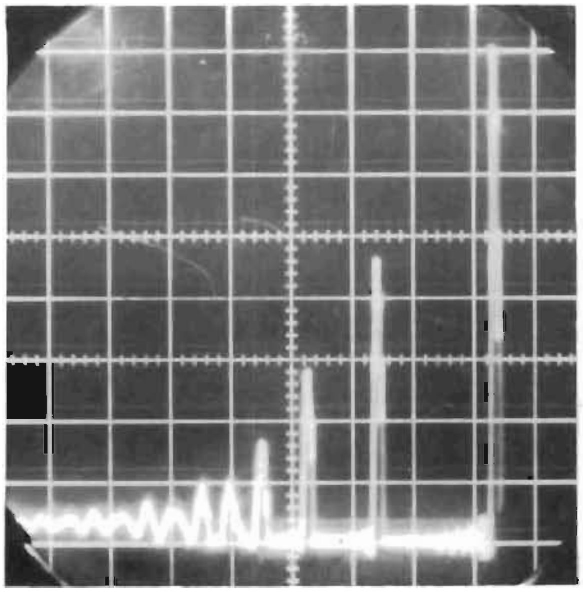

Figure 474. Test Model G_{f1}, Piezoelectric Load Cell, 35.6 in./sec Impact Velocity, PS = 169 psig (750 lb/div.; 0.001 sec/div.)

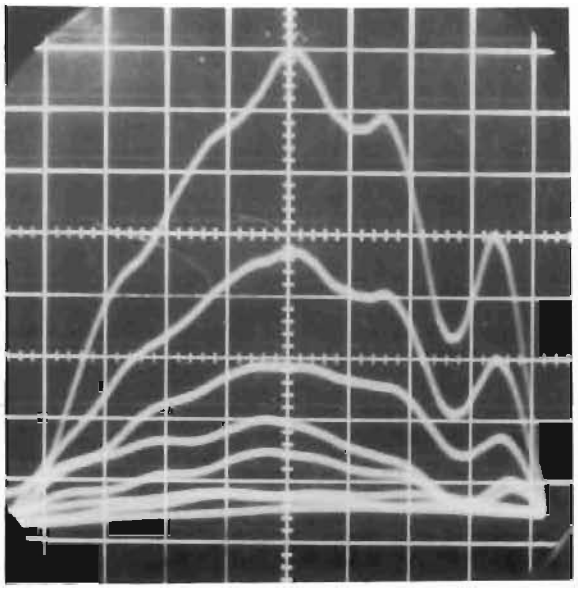

Figure 475. Test Model G_{f1}, Piezoelectric Load Cell, 35.6 in./sec Impact Velocity, PS = 169 psig (750 lb/div.; 0.00002 sec/div.)

surfaces there was observed a reddish-brown contaminant that appeared to be what is commonly described as "fretting corrosion." Figures 150, through 155 show the condition and other cyclic effects evident on the seat. Unlike the ID, the seat and poppet OD's did not show signs of fretting (Fig. 156 and 157) although the poppet was cut by the seat corners which also underwent slight plastic flow.

As shown by Fig. 150 and 151, the high-impact, load-induced corner stresses caused a 2.3-microinch crown in the seat. Taken in the same location as the seat, Fig. 157 illustrates the cutting effect the relatively sharp seat corners had on the poppet surface.

All of the noted photographs were taken before any cleaning had been done. However, even after vigorous wiping, much of the corrosion products were evident (as shown by Fig. 153), and not until the seat surface had been lightly polished with chromic oxide and tissue was the true character of the surface damage revealed. This is shown by Fig. 154 and 155 where narrow and wide band 500x interference photos, oriented tangent to the seat circumference and thus normal to fretting striations, clearly show the loss of material and attendant increased roughness.

The absence of fretting in the single location shown by Fig. 151 and 157 is assumed to be the last of several such areas that were gradually enveloped by the fretting condition during cycling. However, since no inspections were made during the test, this remains only an hypothesis.

Also notable is the protection afforded the seat corner by the slight corner dub as shown at the ID by Fig. 153.

In explanation of the stress-leakage characteristic after cycling, the undamaged portion of the land still provided a seal at both low and high stress. At the low-stress level, the crowned seat resulted in higher center contact stress, compensating for the nodular nature of the damage. At the intermediate-stress level where leakage had increased up to 10 times original, the crown was flattened and more of the damaged surface area was involved. At the high-stress level (10,000 psi), all nodules were flattened and the first-order effect of (lost) land width was completely submerged by the cubical peak-to-valley roughness parameter.

The fact that this model had exhibited such a relatively minor increase in leakage may be directly attributed to the precise control of the air-bearing piston and antirotation flexure. Had the poppet been allowed to move annularly and eccentrically, it is reasonably certain that the leakage would have increased after relatively few cycles. Some insight into this was gained by retesting this model in the static tester using the ball joint. The poppet was reoriented and set up 0.0035 inch eccentric to the seat thus assuring the damaged surfaces both contacted in different areas and undamaged areas overlapped damaged areas. As expected, the leakage increased over the original stress-leakage results as shown in Fig. 473 by the diamond data points.

As indicated in the Surface Studies section, fretting is caused by micromotions between two materials under a load. The different geometry of the poppet and seat results in different lateral expansion characteristics since the poppet surface is completely contained and the seat more easily deformed outwardly. It would appear, therefore, that the fretting should have occurred at the OD since this is the area undergoing the greatest relative motion. Two hypotheses are offered as to the experimental result. The first is that the ID fretting resulted primarily from interfacial movement under higher contact stresses at this location. Higher stress at the ID was indicated by Model K aluminum seat (Fig. 137) where the ID proved considerably stronger than OD. The second hypothesis discounts the high-stress idea because the parts are firmly mated under high loads. From the digital analysis it was shown that both poppet and seat would separate from their preloaded bearing surfaces under sufficiently high impacts. Evidence of this was shown after disassembly where the strain gage load cell bearing pads and mating poppet surfaces had fretted. The seat and piezoelectric load cell also had fretted, but to a much lesser extent. Considering the multiple impacts shown by Fig. 474, it is possible that the poppet and seat were in lateral motion at the instant of the second or third impacts. This would undoubtedly contribute to a fretting condition. Furthermore, since it has been shown that the OD plastically collapses more than the ID, there is some argument that the fretting took place at light loads because of its location only at the ID.

This does not explain, of course, why the fretting did not occur at the supposedly higher out-of-parallel OD. Before any firm conclusion could be reached, further tests would have to be performed. However, indications are that the first hypothesis is correct because cycle-tested models having nearly identical poppet and seat lands experienced almost no fretting.

Model B_{fl}, 0.6 AA Circular Lay 440C Poppet and Seat

This model had nearly the best surface produced in the program. Its less than 1-microinch AA roughness, combined with circular lay and ID and OD seat corners chamfered and dubbed (5 microinches over 0.0005 inch), was used to evaluate the cyclic capabilities of circular lay. Chronologically the model was tested following the initial 10,000 cycles on Model G_{fl}. Therefore, tester inputs were not changed where impact velocity was constant at 7.60 in./sec. Based upon seat-land area the peak impact stress was 28,200 psi.

Precycle electrical contact test indicated a 20-microinch equivalent parallel plate gap (h_e). With this result and comparison between ball joint and clamped precycle stress-leakage tests (Fig. 476), an out-of-parallel condition is indicated. Extrapolating the stress-leakage tests back to 100-psi stress (4 pounds load) the (h_e) difference indicated between clamped and ball loaded tests is 6.7 microinches. Allowing one-half of the total PTV roughness (1.8 microinches) for increased gap, the out-of-parallel height becomes

$$h = \frac{6.7 - 1.8}{0.68} = 7.2 \text{ microinches}$$

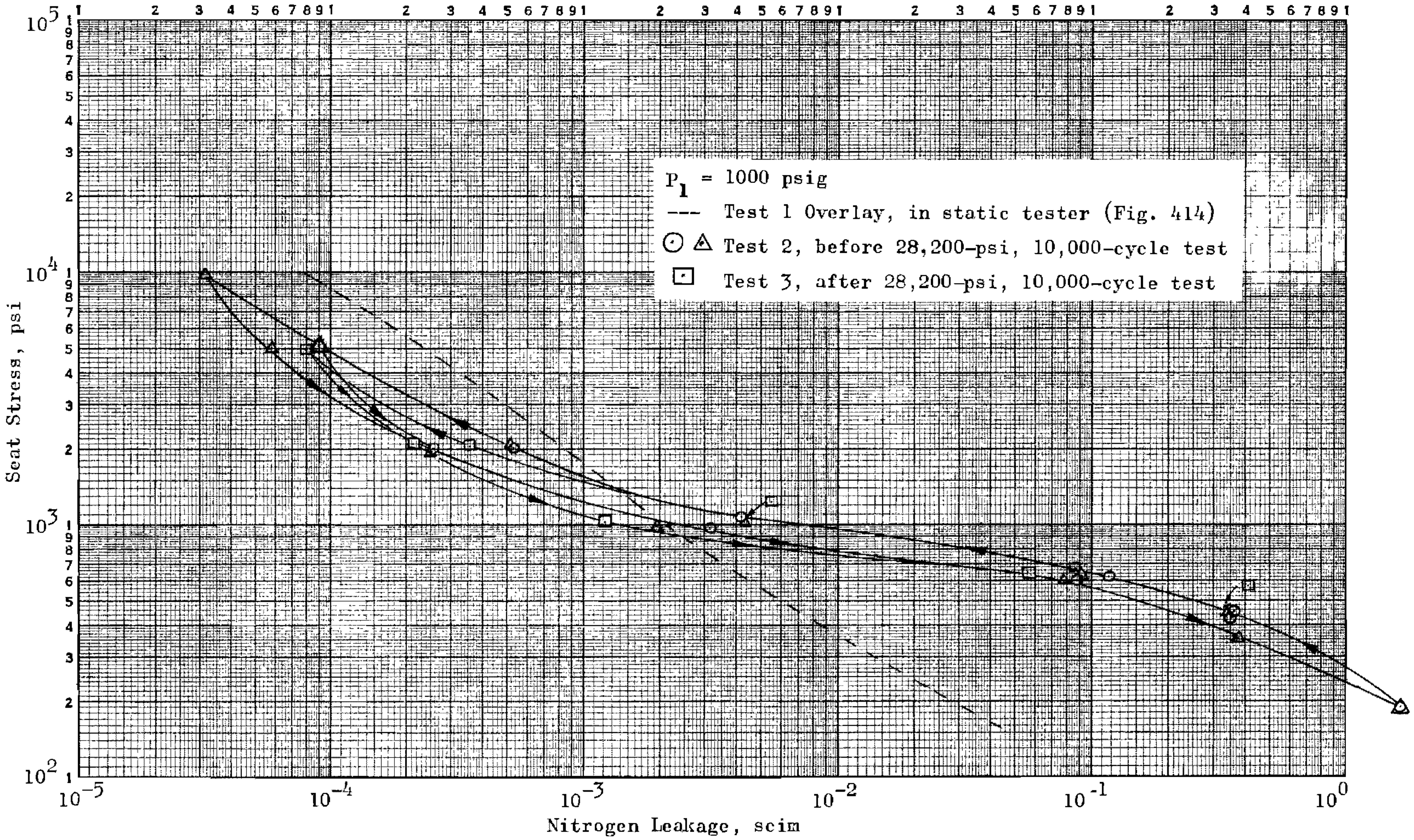

Figure 476. Stress-Leakage Data for Cycle Test Model B_{f1}, Tests 2 and 3

which is commensurate with measured dimensions. This example serves to show the relative influence of only slight parallelism errors on the stress-leakage characteristic where PTV roughness is small.

The reason for lower clamped condition leakage between 1000 and 10,000 psi, compared with ball joint results, might be explained by the concentration of load on one side of the seating interface which serves more to reduce the PTV height on this side than not reduce it on the other. The net result is decreased leakage. At these low leakage values, it should be noted that the difference in PTV height is very small. This condition was also evident on Model G_{fl}.

Throughout the 10,000-cycle test, little change in leakage occurred at the spot-test stress of 2210 psi. As shown by Fig. 476, before-and-after cycle stress-leakage tests indicate only slight decrease in leakage.

Microscopic examination of the poppet and seat revealed no evidence of surface deterioration or change in surface topography other than several obvious contaminant-caused depressions, 2 to 5 microinches deep, along with numerous smaller depressions.

Conical Model B_c, 1 AA 33-Degree Seating Angle

Having conical geometry with attendant wedging characteristics (as indicated by static stress-leakage hysteresis), it was expected that unavoidable rubbing at impact would result in surface texture change, even though previous flat models cycled at the lower impact level exhibited none.

Since apparent seat stress was based upon the axially projected apparent land area, the cycle test impact velocity was reduced to give a peak impact stress similar to the previous models. The calibration flat model was installed in the cycle tester and, from calibration results, an impact velocity of 4.4 in./sec was computed to give an impact stress of about 27,000 psi. However, upon installation of the conical model it was found that this velocity yielded an impact stress of only 19,000 psi. The velocity was then increased to 5.6 in./sec, resulting in 27,000 psi apparent seat stress. Based on a simple spring-mass system, the equivalent spring rate of the conical model was only 64 percent of the flat model. This was attributed partially to the pronounced surface waves of the conical poppet which acted as low-rate springs.

Figure 477 illustrates a typical impact trace which indicates two impacts per cycle, but with much of the high-frequency ringing evident with flat model impacts absent. This may also be attributed to the frictional damping provided by the conical wedge.

As cycling progressed, the leakage measured at the spot-test stress of 2520 psi dropped from about 0.3 to 0.2 scim within the first 5 cycles; additional decrease to 0.1 scim occurred within the next 200 cycles. Between 200 and 5000 cycles, leakage remained constant at about 0.05 to 0.08 scim; however, upon the conclusion of 10,000 cycles, leakage had increased to about 0.65 scim indicating surface degradation.

Comparison of before-and-after cycling stress-leakage data is shown by Fig. 478. Test repeatability from static to cycle tester is also shown by an overlay curve of data obtained in the static tester. Better (or corrective) poppet alignment was provided by the cycle tester as indicated by the 10,000-psi leak points.

The after 10,000-cycle test curve reflects surface degradation with considerably increased hysteresis. The reason for this is shown by posttest inspection photos (Fig. 222 and 223). Similar to Model G_{fl}, areas corresponding to peak waviness locations had what appeared to be corrosion fretted. A reddish-brown contaminant (visible as black areas in preceding figures) was evident without magnification. Interference measurements indicated the "worm-wood" like tracks to be about 2 to 4 microinches deep. It would seem reasonable that the increased hysteresis was caused by the interlocking action of obviously high areas. Had cycling taken place at

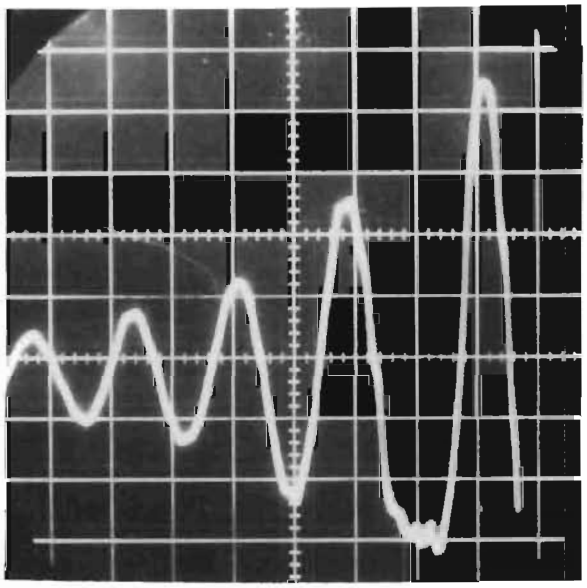

Figure 477. Test Model B_c, Piezoelectric Load Cell, 5.6 in./sec Impact Velocity, PS = 150 psig (87.5 lb/div.; 0.0002 sec/div.)

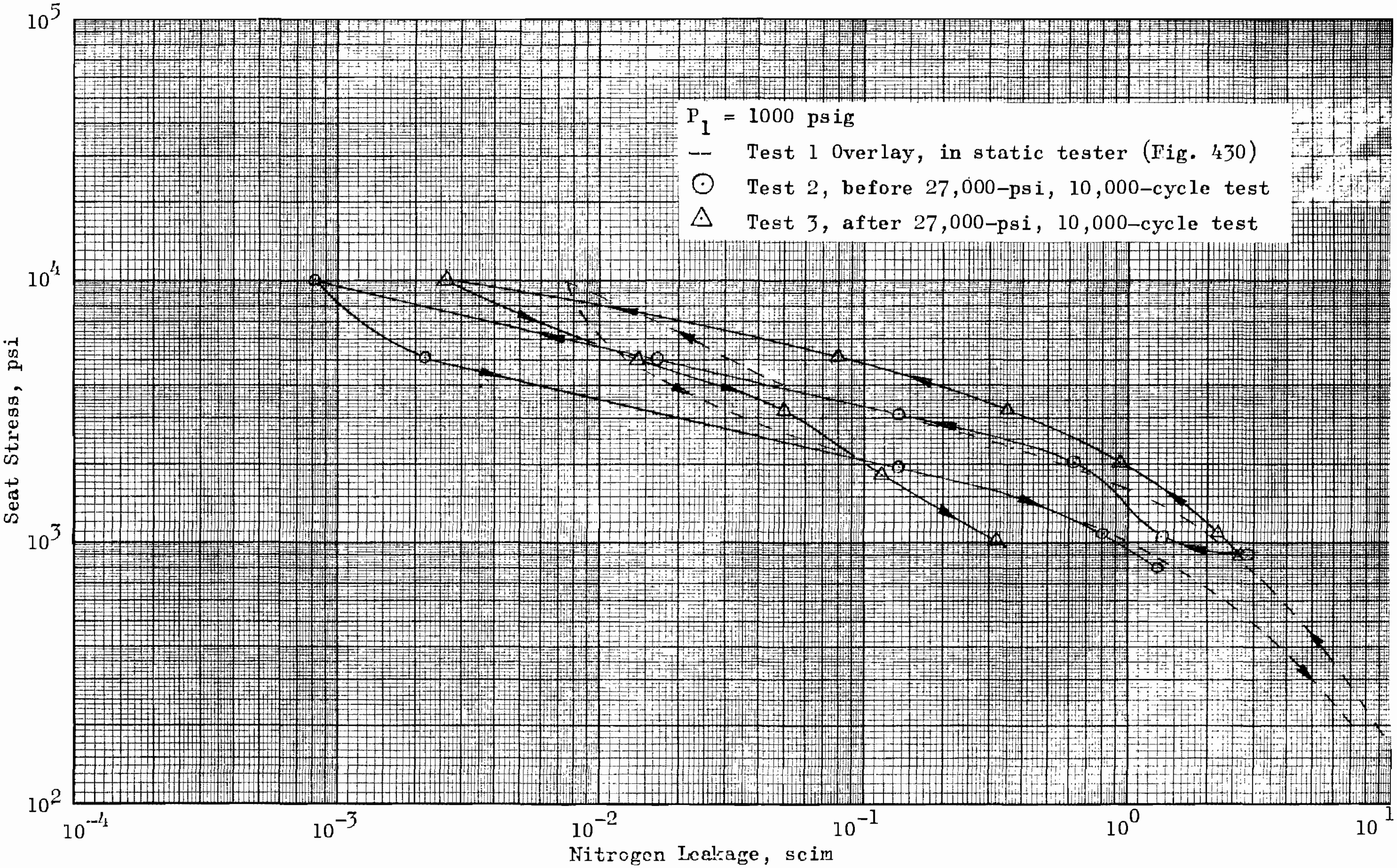

Figure 478. Stress-Leakage Data for Cycle Test Model B_c, Tests 2 and 3

higher impact loads or for additional cycles, the number and size of fretted areas would have increased likewise with attendant increased leakage degradation.

Model X_f, 0.5 AA Unidirectional Lay 440C Poppet and Seat

Having defined load and geometry variation effects, the remaining parameter to be investigated was the number of cycles. Model X_f, having geometry and texture very similar to Model G_{f1}, provided the necessary control.

Surface texture evaluation indicated Model X_f to have relatively uniform seating surfaces with no significant deep scratches. As deduced from the interference photos (Fig. 296 and 297), the seat roughness height was 1.5 microinches PTV with the poppet slightly less at 1.4 microinches PTV.

Model X_f was static tested to 56,000-psi stress as illustrated in Fig. 479. Some initial surface roughness plastic deformation is evident, but the second loading cycle demonstrated an extremely elastic condition. Post-test examination, however, revealed evidence of unique seat land edge damage. Figure 298 shows the seat land condition before static test. Although the land was made to the A change drawing (chamfered edges), it had no duboff with a rather sharp transition from flat to chamfer radius (shown by side lighting in Fig. 298). Figure 299 shows an ID area (typical of four such areas noted) where metal upset has occurred. The damage is not as severe as that noted on Model CC_f (Surface Texture Evaluation section) which may be attributed to the additional edge support offered by the corner chamfers. It does point out, however, that a rolled or dubbed land corner is necessary to preclude such damage.

As described in the test procedures section, Model X_f accumulated 1,000,000 single impact cycles at 214 cps. Figures 480, 481, and 482 illustrate the standing wave dynamics and typical impulse curve shape. Comparison between the impulse curve of Fig. 482, obtained while cycling at 214 cps, and an impulse of the same magnitude obtained statically indicated no discernable difference.

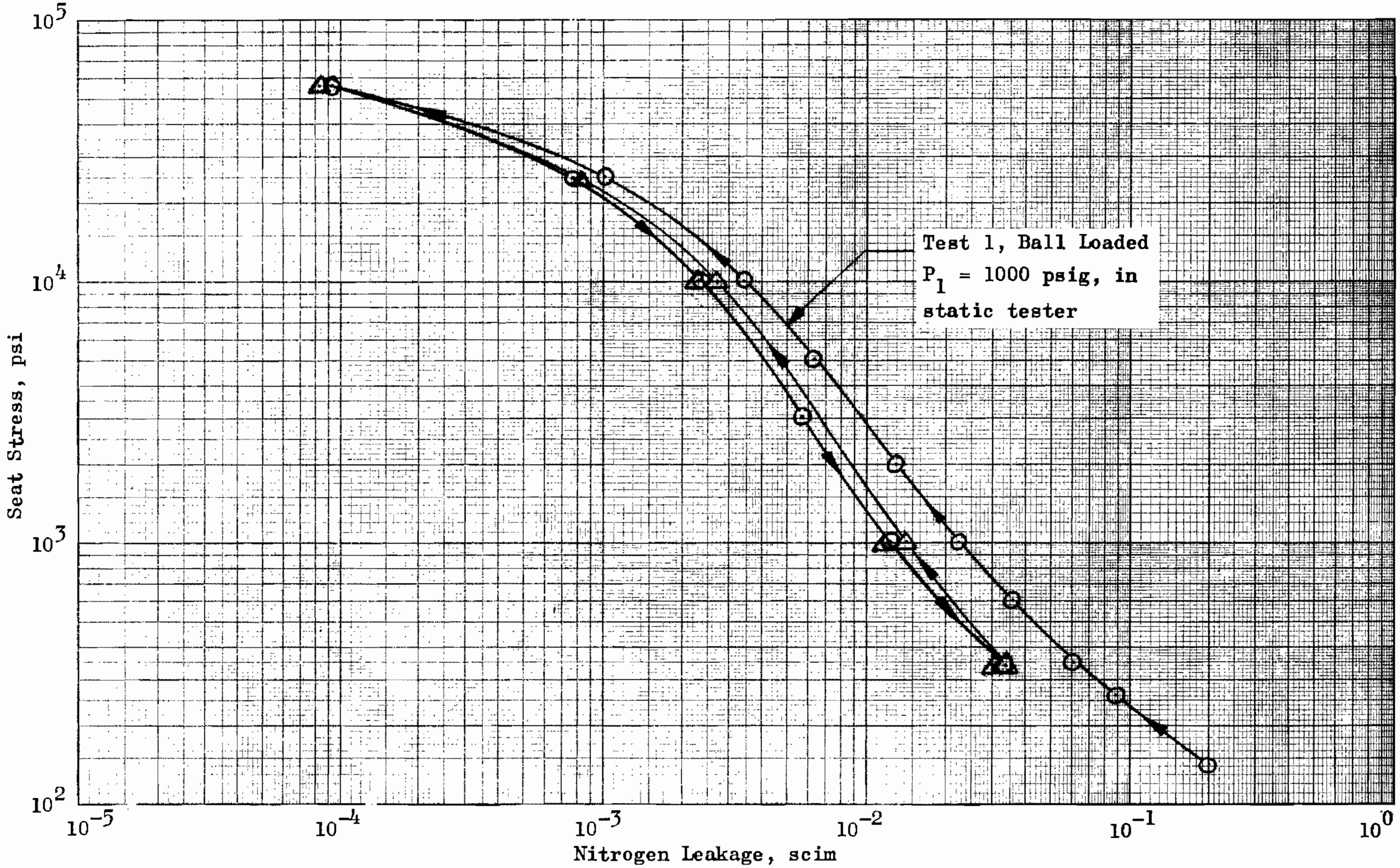

Figure 479. Stress-Leakage Data for Cycle Test Model X_f, Test 1

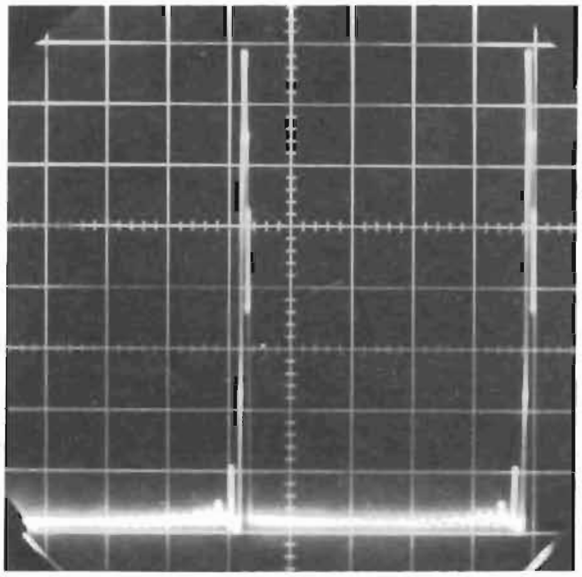

Figure 480. Test Model X_f, Piezoelectric Load Cell, ~ 7.7 in./sec Impact Velocity, PS = 25 psig (150 lb/div.; 0.001 sec/div.)

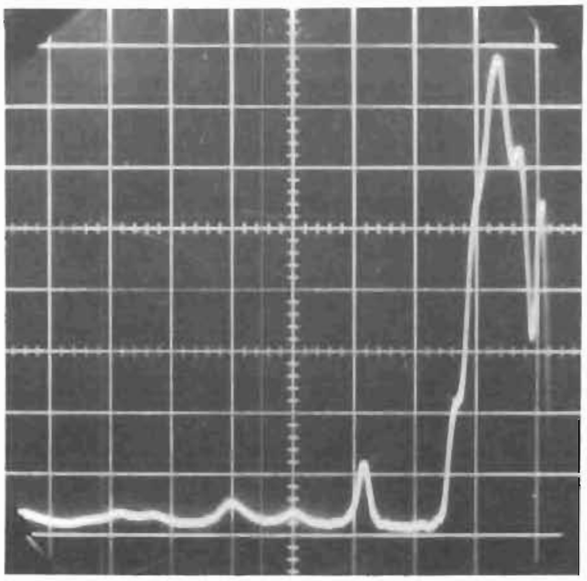

Figure 481. Test Model X_f, Piezoelectric Load Cell, ~ 7.7 in./sec Impact Velocity, PS = 25 psig (150 lb/div.; 0.0001 sec/div.)

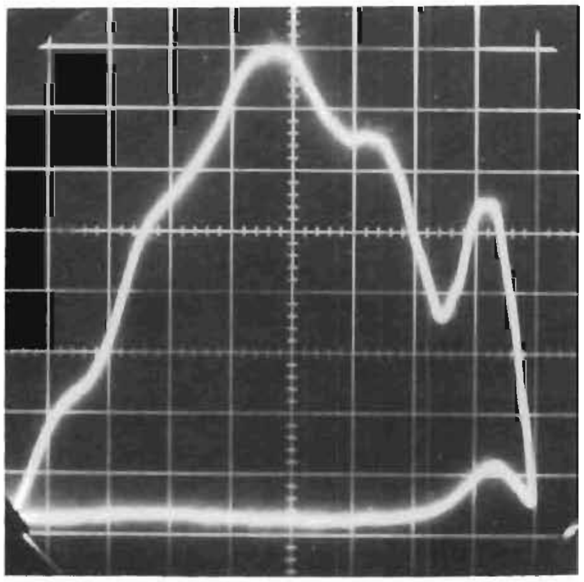

Figure 482. Test Model X_f, Piezoelectric Load Cell, ~ 7.7 in./sec Impact Velocity, PS = 25 psig (150 lb/div.; 0.00002 sec/div.)

The time between impacts (Fig. 480) was 4.67 milliseconds which was sufficient to permit cessation of piezoelectric load cell ringing before the subsequent impact. Thus, the integrity of each impact cycle was preserved to a greater degree than the multiple bounce condition of externally initiated cycles.

Although metal temperatures were not measured during cycling, it was assumed that the continuous bleed of gas between the seating surfaces, combined with the massive tester heat sink, maintained reasonably low interface temperatures. Finger contact indicated no heating from cyclic impacts. Moreover, since leakage was measured every 100,000 cycles, the continuous cycle time was limited to less than 8 minutes.

After the initial 25,000 cycles, leakage had changed from 0.011 scim (spot-test stress of 2010 psi) to 0.0049 scim. From this point, leakage gradually increased to a maximum of 0.0092 scim at 400,000 cycles and then gradually decreased to 0.0023 scim at 1,000,000 cycles. Before-and-after cycle stress-leakage results are shown in Fig. 483.

Although the relative decrease in leakage is significant (4/1 at 2000 psi stress) the change in equivalent height (h_e) is small (0.5 microinches) due to the fine finish of this model. The cause for this change is partially indicated by posttest interference photos.

Figures 300 and 301 show the seat land where the outer edges, particularly the OD, were plastically dubbed (compare with Fig. 298). The poppet (Fig. 302 and 303), taken in the same location, had similarly been plastically upset by the initially sharp corner condition. Evidence of corrosion fretting was also evident, but to a lesser degree than Models G_{f1} and B_c.

The plastically created pits illustrated by these photos are examples of several others of similar character. It was concluded that they originated from soft contaminants dislodged downstream of the supply pressure filter by the intense 214 cps vibration. The depression shown in Fig. 301 is,

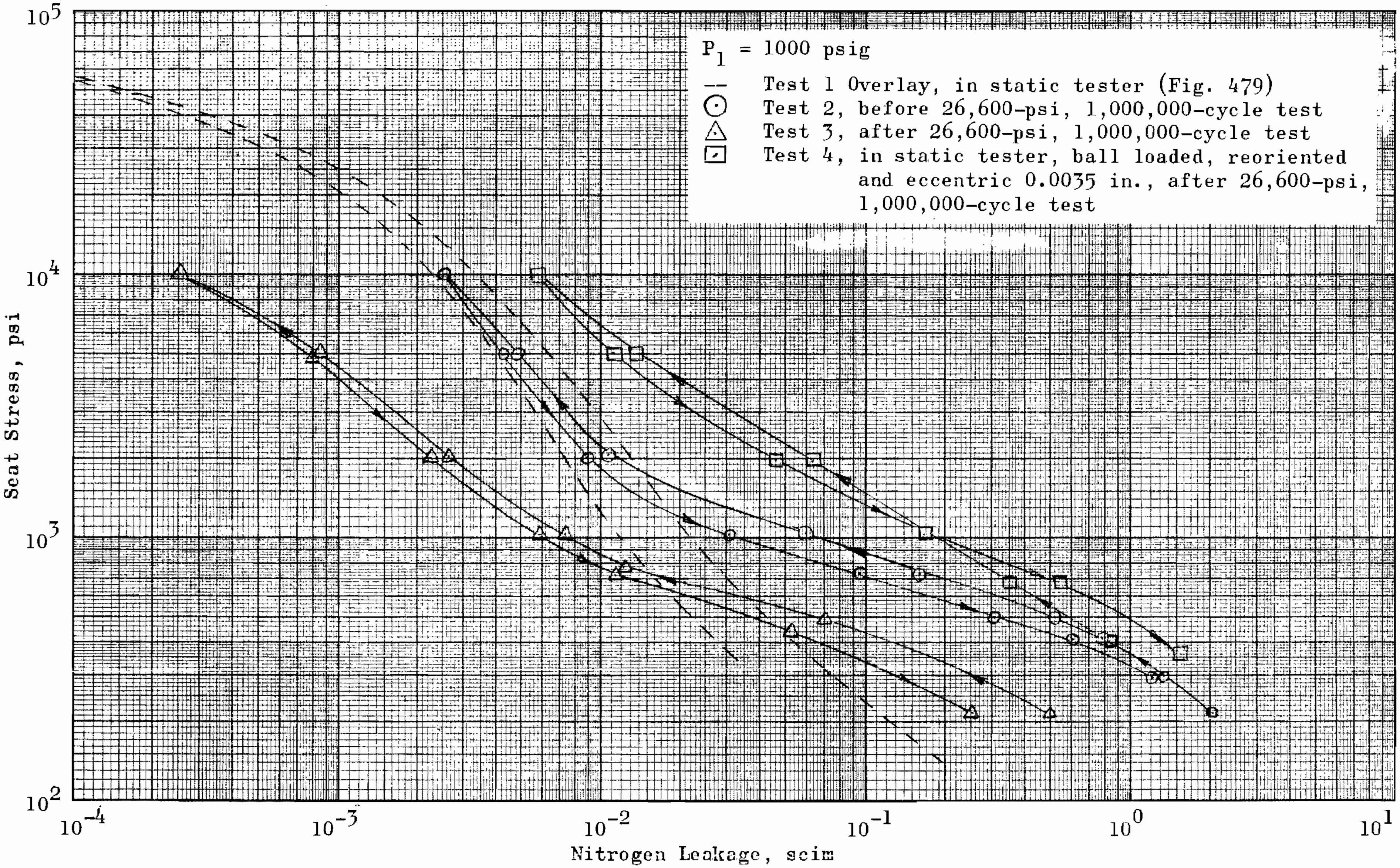

Figure 483. Stress-Leakage Data for Cycle Test Model X_f, Tests 2, 3, and 4

for example, about 50 microinches deep. Its counterpart on the poppet, however, is only about 20 microinches deep indicating it to be the harder of the two.

It is apparent from the above photos and stress leakage data that, although both surfaces had been plastically deformed, as with Model G_{f1}, the extreme position control provided by the tester allowed the interface to be pressed closer together for a given load. Furthermore, it is also likely that the plastic dubbing of the land edges allowed a more uniform distribution of contact stress, thus creating a smaller leakage gap. The extent of either of the two possibilities is, however, unknown.

Reorientation of the poppet and seat in the static tester after cleaning afforded a measure of the plastic surface damage. An increase in leakage resulted as shown by Fig. 483.

PERFORMANCE COMPARISON TESTS

With previous models establishing basic cyclic effects, additional models were cycle tested for performance comparison.

Model Y_f, 0.7 AA Unidirectional Lay 440C Poppet and Seat

As previously reported under Model D_f, the intermediate impact level cycle test was established as the median between those levels investigated with Model G_{f1}. This test level was evaluated with Model Y_f which had the same geometry as previous models to (1) provide a range of data on the fretting corrosion effect, and (2) reduce the level of fretting corrosion from that obtained with Model G_{f1} to something which might be eliminated by changes in contact geometry.

Model Y_f surface texture is shown by Fig 304, 305, and 306. The seat had been purposely predubbed prior to final finishing so that an edge roll-off remained. Assessed at 2.0 and 1.7 microinches PTV, the model surface roughnesses are representative of those previously cycled.

Used only as a relative control, this model was not tested with the ball joint loading method in the static tester. The model was assembled directly into the cycle tester and stress-leakage tested with the results shown in Fig. 484. As indicated by Table 8 and comparison with previous stress-leakage data, Model Y_f yielded data quite similar to Models G_{f1} and X_f.

With the dashpot adjusted to give an impact load of 4100 pounds (91,700 psi) Model Y_f was cycled 10,000 times. Typical impulse traces are shown in Fig. 485 and 486 which indicate five impacts per cycle. As expected, leakage continuously decreased with cycles, with the final result shown in Fig. 484.

Microscopic examination of model surfaces revealed a fretting condition between Model G_{f1} and X_f, however, there was no evidence of corner damage on either seat or poppet. Figures 307 and 308 show typical seat surface characteristics before and after wiping. As can be seen from Fig. 308, the wear pattern is extremely small and about 1 to 3 microinches deep.

Figures 309 through 312 show the deposit of corrosion products on the mating poppet face. Assessment of the film thickness with green and white light interference indicated it to be about 5 microinches and raised from the surface (Fig. 311). The interference patterns set up by two materials of different density and reflectivity is not known; therefore, this measurement is questionable. There is, however, conclusive proof from Fig. 312 that the corrosion products depressed the surface in the typical pattern about 1 microinch deep.

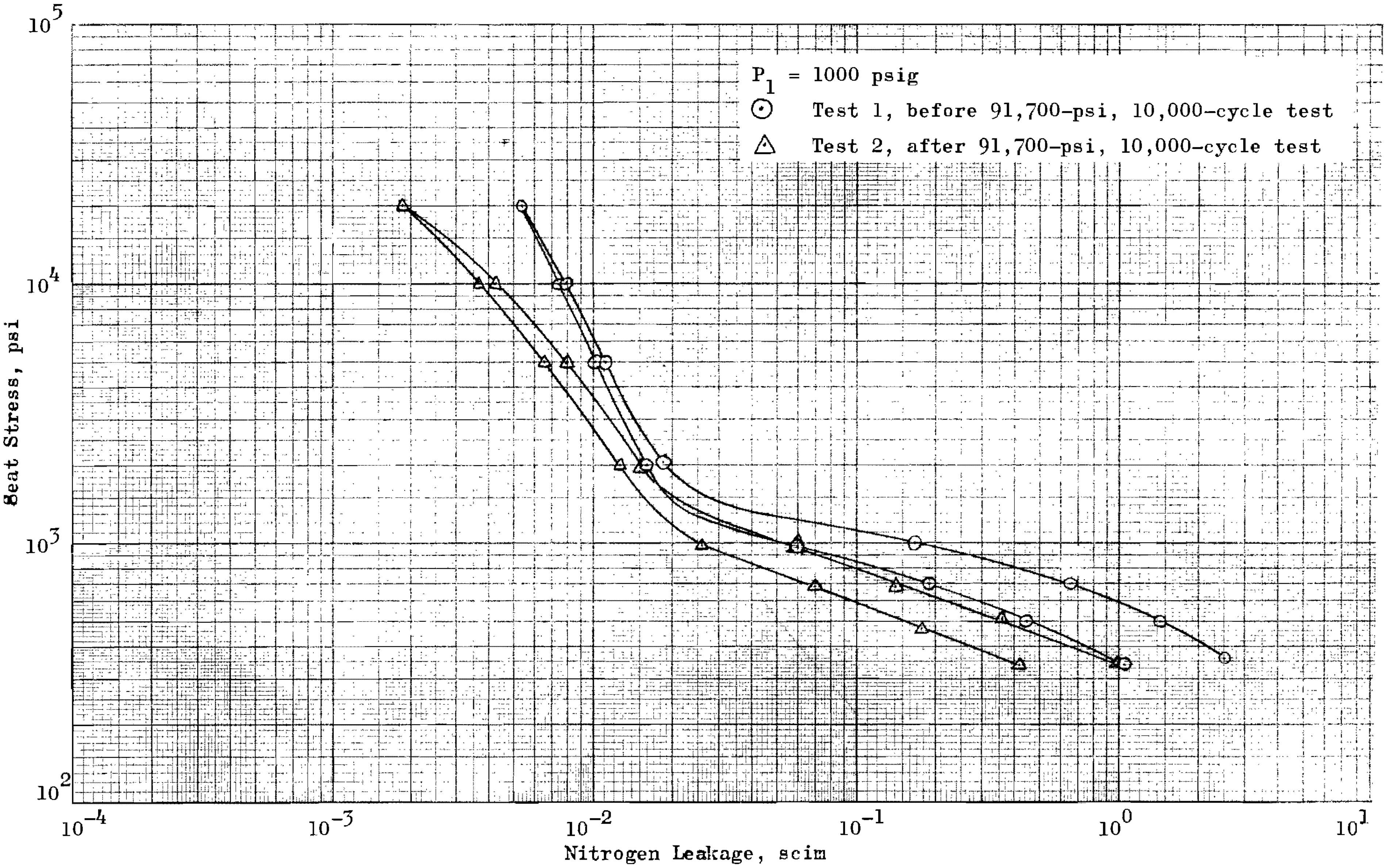

Figure 484. Stress-Leakage Data for Cycle Test Model Y_f, Tests 1 and 2

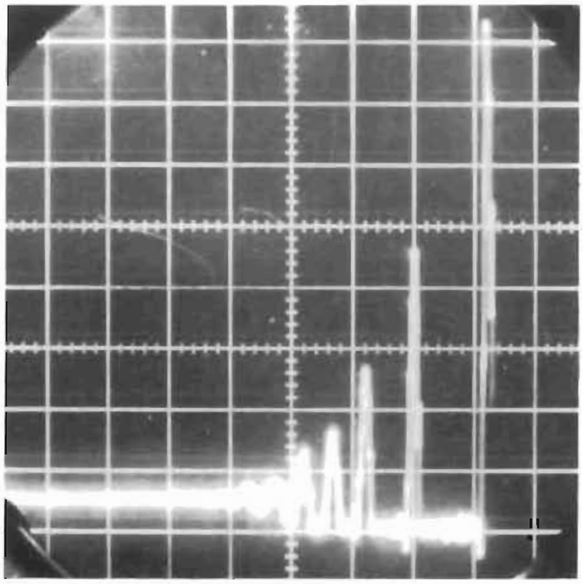

Figure 485. Test Model Y_f, Piezoelectric Load Cell, ~ 24 in./sec Impact Velocity, PS = 169 psig (500 lb/div.; 0.001 sec/div.)

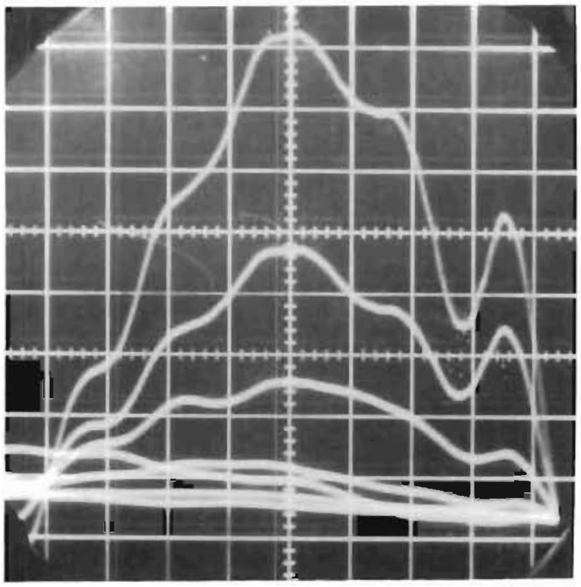

Figure 486. Test Model Y_f, Piezoelectric Load Cell, ~ 24 in./sec Impact Velocity, PS = 169 psig (500 lb/div.; 0.00002 sec/div.)

Model AA_f, 0.3 Tungsten Carbide Poppet and 0.2 AA Crowned 440C Seat, Circular Lay

Following Model D_f in line of test, the purpose of this model was to investigate the effect of impact between tungsten carbide and 440C. Having different moduli, it was expected that even with the crowned seat a fretting condition would result.

The 10,000-cycle test was performed the same as with Model Y_f, with peak impact load set at 4100 pounds. Typical impulse traces (Fig. 487 and 488) indicate the additional system stiffness caused by the carbide poppet. Impact velocity was not measured. Because of the unknown spring rate, calibration (F/V) values do not apply.

As shown in Fig. 489, the pretest stress-leakage characteristic does not blend into the static tester (ball-joint) curve until some 8000-psi seat stress has been developed. Electrical contact checks indicated a 21-microinch maximum parallelism deviation. Other cycle models with similar non-parallel conditions conformed with static test data by 2000-psi stress. It is probable that, because of the more rigid tungsten carbide poppet used, the seat had to deform more than those of previous tests hence, the higher conforming stress.

Leakage at the 2200-psi stress check point dropped from the initial value of 0.013 scim to 0.003 scim at 500 cycles, then steadily rose to 0.0052 scim at 7500 cycles after which it remained constant. The posttest stress-leakage curve (Fig. 489) revealed a low-stress improvement, but also the first instance of flat model high-stress sealing degradation noted during the program.

The low-stress improvement may be attributable to out-of-parallel corner and nodule flattening. Increased high-stress leakage was probably caused by a combination of corrosion-fretting contaminant film and increased density-of-carbide pits (Fig. 201 through 204). It is notable that the

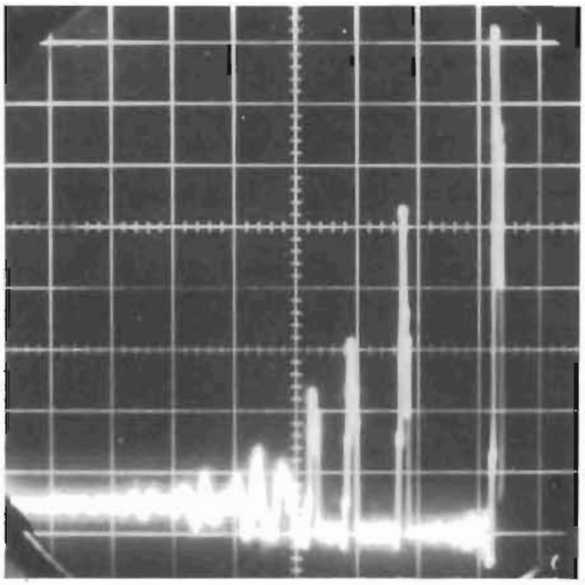

Figure 487. Test Model AA_f, Piezoelectric Load Cell, PS = 169 psig (500 lb/div.; 0.001 sec/div.)

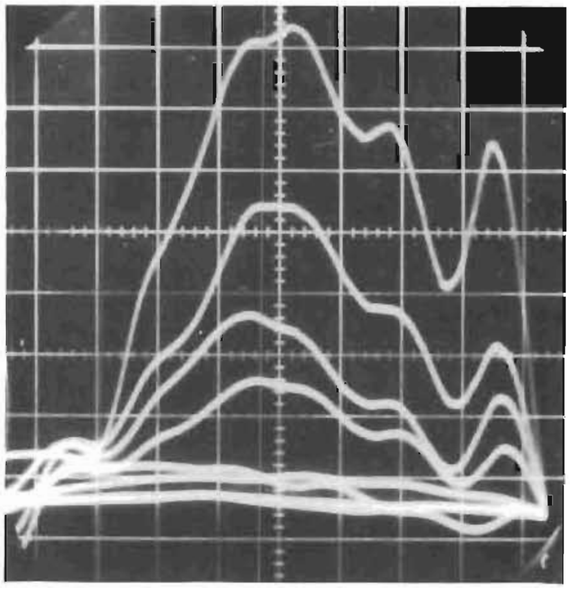

Figure 488. Test Model AA_f, Piezoelectric Load Cell, PS = 169 psig (500 lb/div.; 0.00002 sec/div.)

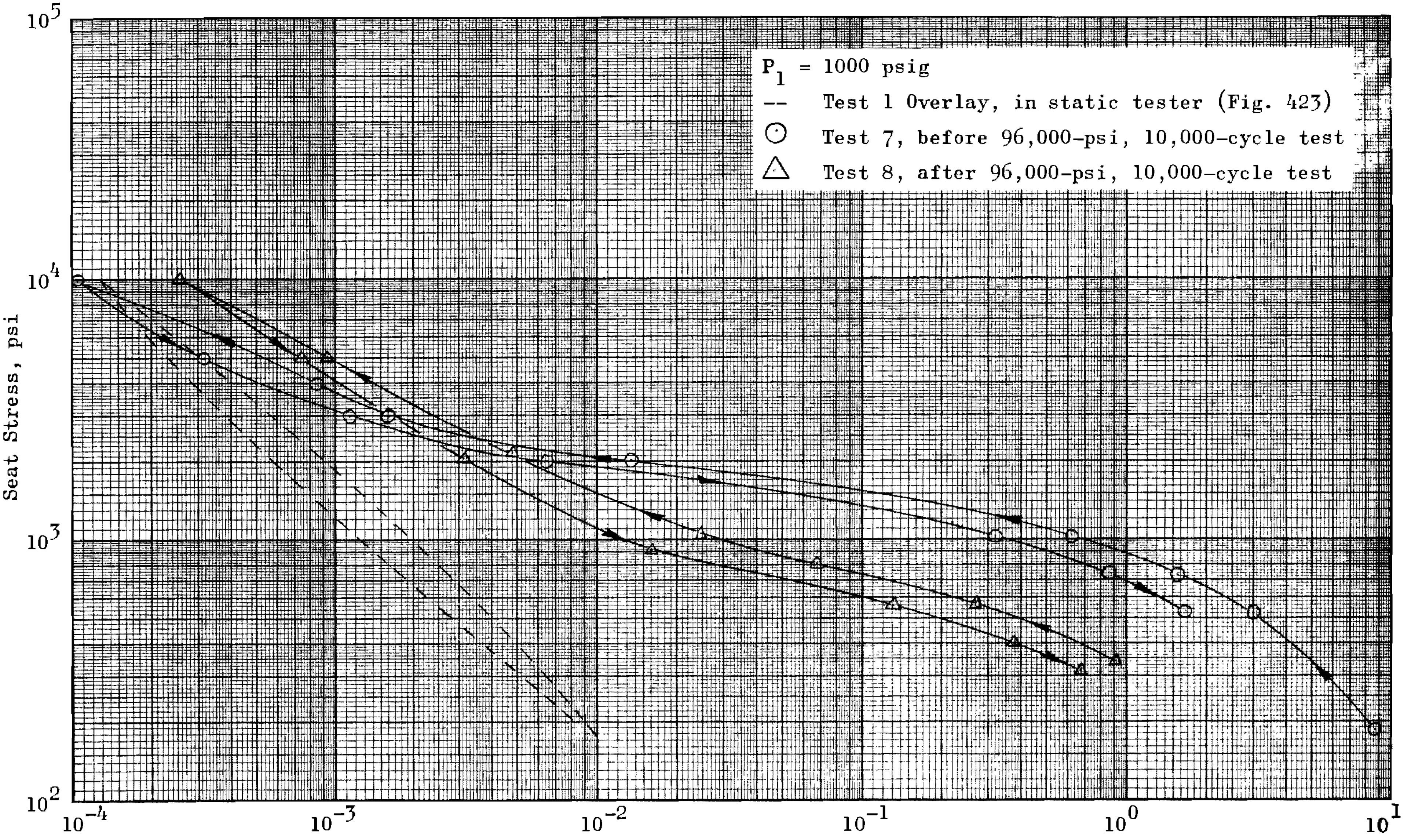

Figure 489. Stress-Leakage Data for Cycle Test Model AA_f, Tests 7 and 8

corrosion-wear products were not removed by light wiping with benzene-soaked cleaning tissue; as with previous models, vigorous rubbing was required.

As indicated by Fig. 201, the major wear area on the seat was slightly off-center toward the ID. This corresponds with the measured location of the contaminant shown on the poppet (Fig. 203). Although no damage was observed on the seat after cleaning, the poppet exhibited a marked increase in the density of pits evident after wiping (Fig. 204). While not changing the stress-leakage characteristic greatly, it is assumed from previous results that the high-stress leakage increase was due to increased carbide-pit density. In verification of this, a posttest Proficorder roughness trace was made using the 0.0001-inch radius tip. This trace, compared with one made before test, indicated a substantial increase in the average PTV dimension attributable to pits.

Although not conclusive, the results of this test indicate that the impact mating of materials having a large difference in elastic modules may precipitate an undesirable wear condition.

Re-evaluation of the seat crown radius from Fig. 202 did not indicate a radius change. Considering that much smaller corner radii of Model Y_f did not reflect any plastic flow, none would be expected of the lower stressed center of Model AA_f seat.

Model P_f, 0.7 AA Unidirectional Lay 440C Poppet and Seat

Based upon previous test results, it was concluded that fretting corrosion and corner damage was caused by the model geometry of a square-cornered seat pressed onto the overlapping poppet land. Corner damage could obviously be eliminated by suitable crowning of the seat which would preclude corner contact. However, by relieving the poppet to form a raised land similar to the seat, the poppet edge stiffness would be reduced also eliminating a corner problem. Furthermore, since the poppet and seat would have the same geometry and elastic properties, deformation should be nearly identical with minimal interfacial slip occurring during impact deformation.

Model P_f was fabricated to verify the above hypothesis. The poppet was diamond-turned to duplicate the mating seat land geometry as generally indicated by Fig. 63 (model fabrication section). Both poppet and seat were then unidirectional diamond-lapped with a heavy predub prior to achieving the final finish and land dimensions shown by Table 4. Eccentricity of poppet and seat lands relative to their respective guide diameters was within 0.0001 inch; thus total installed eccentricity between poppet and seat lands was probably within 0.0005 inch.

The before-test surface texture and land characteristics of the poppet and seat are typically shown in Fig. 313 through 316. Due to increased finishing time, the poppet roughness of 1.6 microinches PTV was less than the seat which was assessed at 2.1 microinches PTV. The minutely pitted seat surface structure (Fig. 314)was caused by a wet slurry of rolling-diamond compound not completely removed by finish unidirectional lapping. Because of greater poppet roughness, Model P_f, before cycling stress-leakage tests indicated slightly higher leakage than previous control surfaces. Other than this, before cycling, stress-leakage characteristics were similar to previous models.

With Model Y_f results as a reference, Model P_f was 10,000-cycle tested at 4050-pound impact load (106,000-psi apparent seat stress). Figures 490 and 491 illustrate typical impulse traces. The characteristic decrease in leakage with cycles was evident throughout the cycle test with results very similar to Model Y_f as shown by Fig. 492. Unlike Model Y_f, however, increased leakage below 1000 psi resulted.

Posttest microscopic examination of the seating surfaces revealed no evidence of fretting corrosion. The increased low stress leakage was caused by the embedment of a large metallic particle in both seat and poppet as

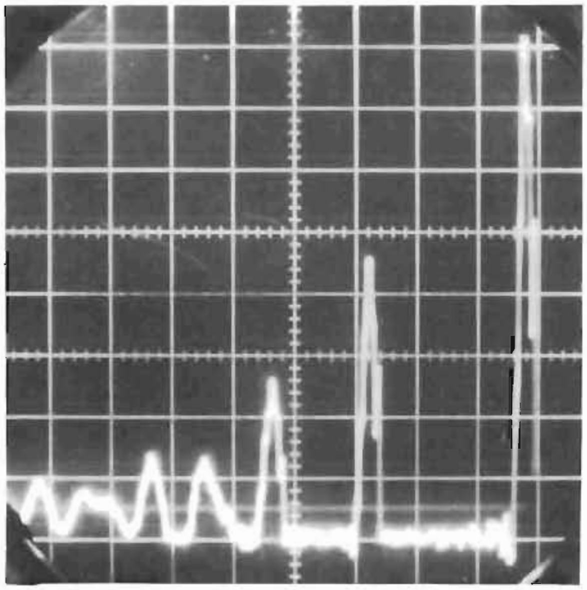

Figure 490. Test Model P_f, Piezoelectric Load Cell, ~ 24 in./sec Impact Velocity, PS = 169 psig (500 lb/div.; 0.0005 sec/div.)

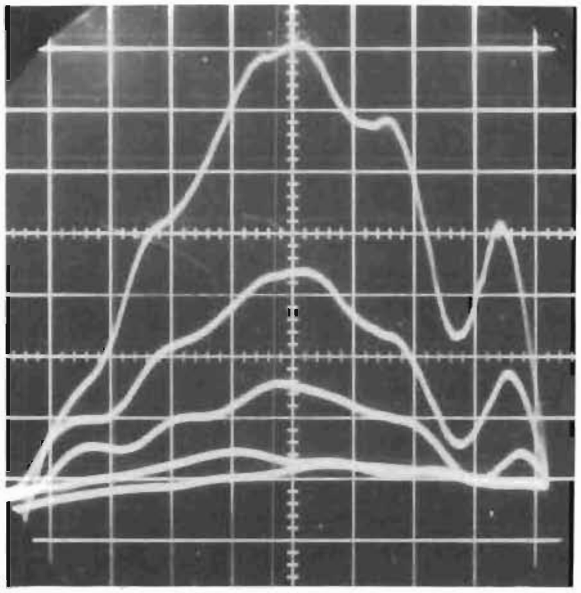

Figure 491. Test Model P_f, Piezoelectric Load Cell, ~ 24 in./sec Impact Velocity, PS = 169 psig (500 lb/div.; 0.00002 sec/div.)

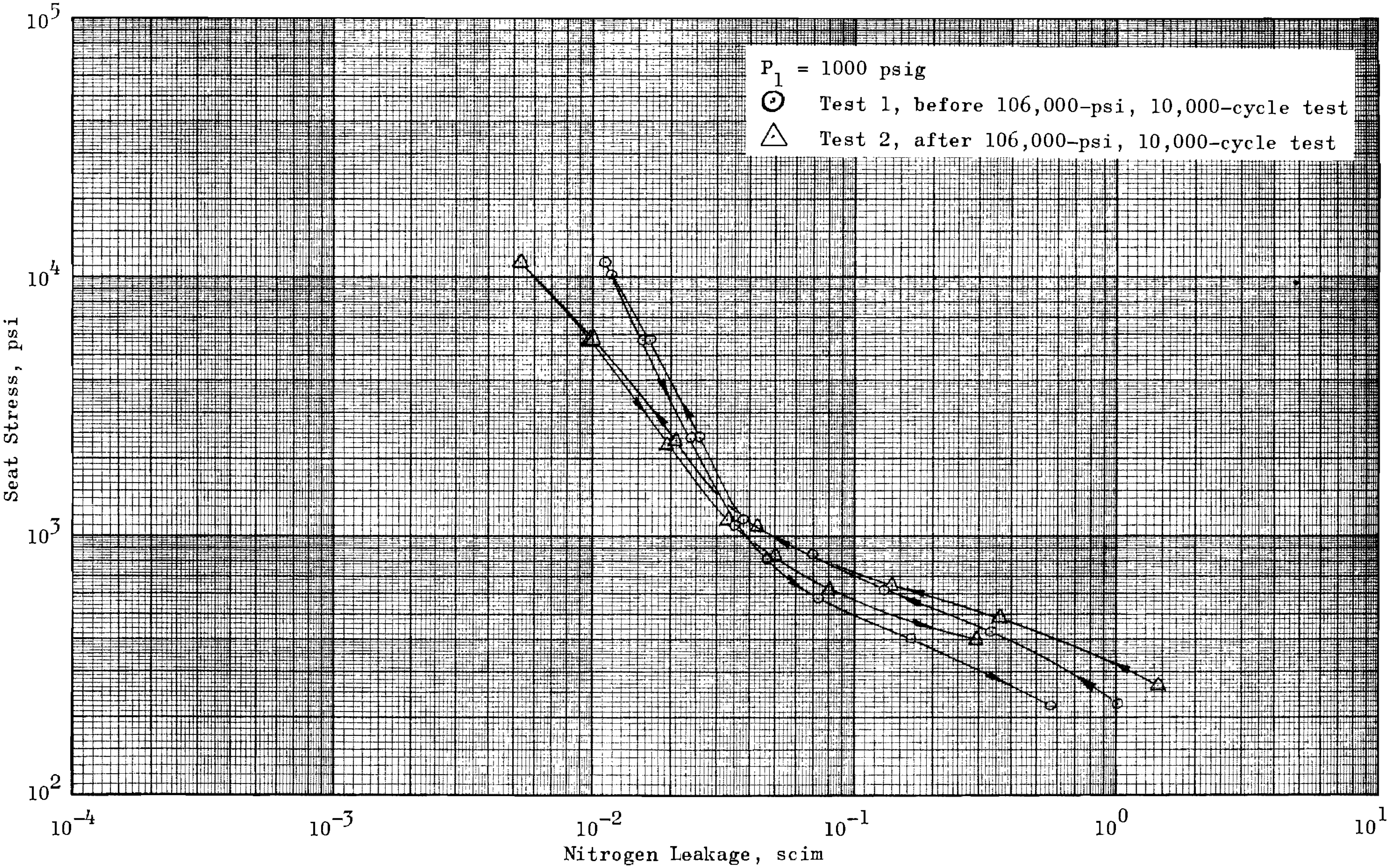

Figure 492. Stress-Leakage Data for Cycle Test Model P_f, Tests 1 and 2

shown by Fig. 317 through 321. The depression depth in the seat is indicated as 20 light bands, or about 0.0002 inch. The poppet, being slightly harder, was only depressed 40 microinches. White light interference measurements indicated the flattened particle height (Fig. 317) to be about 5 microinches.

Figures 319 and 321 show the surface texture at the bottom of the depression. Although the bands are quite narrow, the PTV roughness and lay characteristic has not been appreciably altered by the gross plastic deformation of substrate material. This further illustrates the extreme elastic strength and rigidity of the immediate surface. Furthermore, it indicates that the contaminant particle was softer than the R_c60 440C steel.

From the test results, it is concluded that identical poppet and seat land geometry is to be preferred over the bounded land design for cyclic endurance.

Model Z_f, 0.5 AA Circular Lay Crowned Poppet and Seat

Extending the identical poppet and seat geometry concept further, Model P_f was reworked to include crowning of both poppet and seat. During the final finishing operation, rolling-compound grit caused a minute pitting over the center portion of the seat land. As the primary purpose of the model was to determine cyclic effects upon surface texture, refinishing was not undertaken.

Seat-surface texture is shown in Fig. 322 through 325. The PTV roughness of this immediate surface was less than the assigned composite value of 1.5 microinch which included the noted pits. This is based upon the extreme pit density in the effective center section of the land. All cross lay scratches had been removed by circular finishing. From Fig. 322, the crown radius was computed as 6.0 inches over the center 0.0227-inch portion of the land ($Z \cong 10.8$ microinches).

Although finished with the same techniques, poppet geometry was slightly different than the seat (Fig. 326, 327, and 328). Having no pits, the PTV roughness was assessed at 1.2 microinches; also, there were no cross lay scratches. The poppet crown radius was larger than the seat because of less finishing time. Taken from Fig. 326 and 327, the radius computed over the central 0.0174-inch section (Z = 2 microinches) is 16 inches. Tangent to this large center radius are OD and ID dubboff radii computed at about 1.0 inch.

Model Z_f was static tested with the ball joint for two stress loops as shown in Fig. 493. Average Hertz contact stress (σ_{avg}) for the initial increasing load loop is also plotted. Due to the pitted texture of the seat this model approximates the results obtained with Model AA_f. However, low-stress leakage is considerably greater (than AA_f) due to the relative stiffness of the pitted surface which illustrates the detrimental effect of closely interspersed pits.

Precycle electrical contact evaluation indicated excellent assembly accuracy with an equivalent separation (h_e) based on a 0.03 land of about 9 microinches. Considering the crown condition, the actual equivalent gap was somewhat less than this. As with previous clamped models high-stress leakage was slightly less than that produced by the ball joint (Fig. 494). Low-stress results were nearly identical with those obtained in static testing. Cycle testing of Model Z_f was conducted using the high-frequency technique to accumulate 1,000,000 impact cycles. Figure 495 depicts a typical impulse trace. The cycles produced only minor change in leakage throughout the test with the final stress-leakage data indicating decreased leakage (Fig. 494).

Posttest microscopic examination showed the seating surfaces to be virtually free of the fretting contaminants evidenced by Model Y_f. However, the results were not of the excellence shown by Model P_f since four to seven wear spots of approximately 0.002-inch diameter were evident in the center of the seating surfaces. It is believed that this slight fretting was

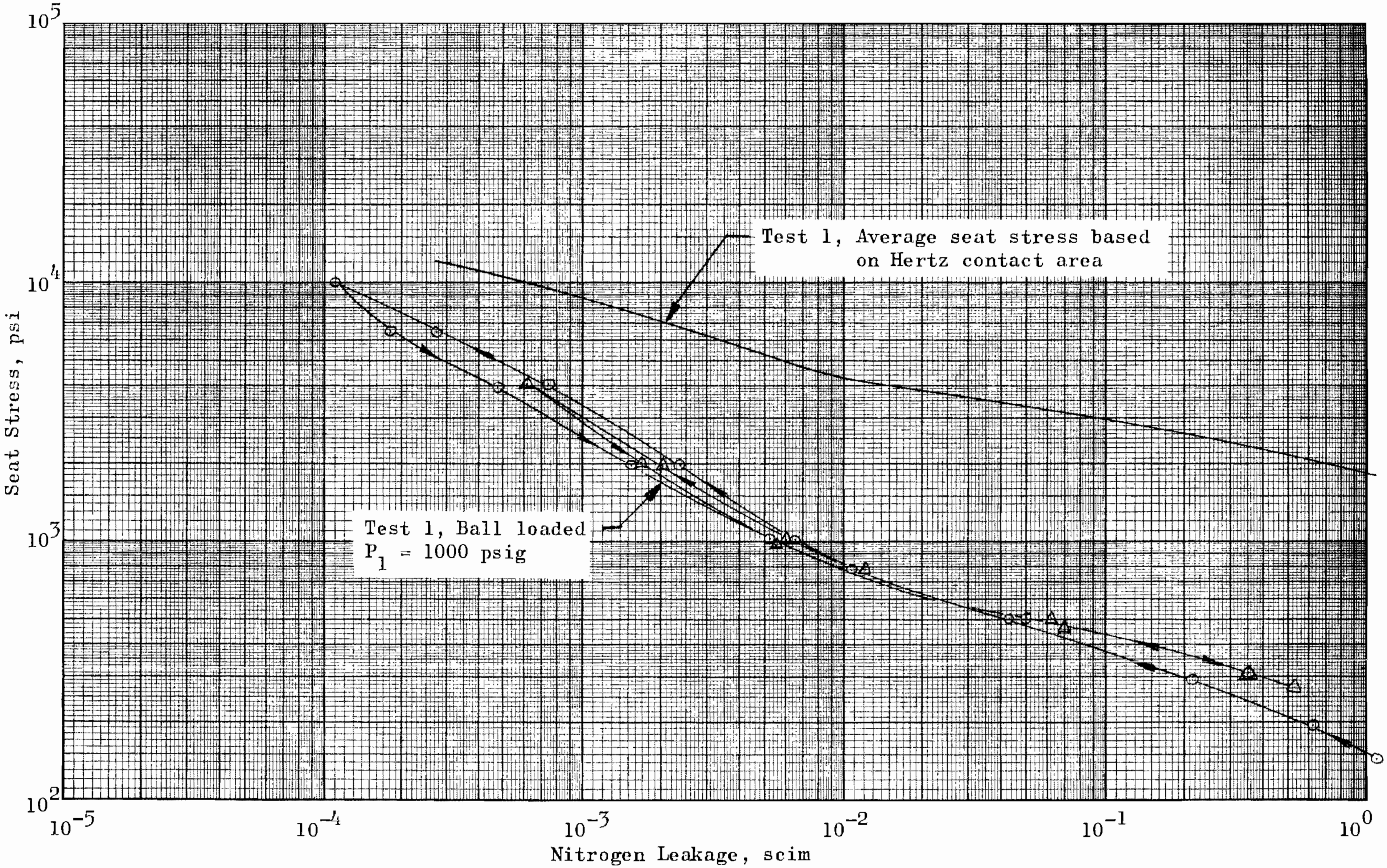

Figure 493. Stress-Leakage Data for Cycle Test Model Z_f, Test 1

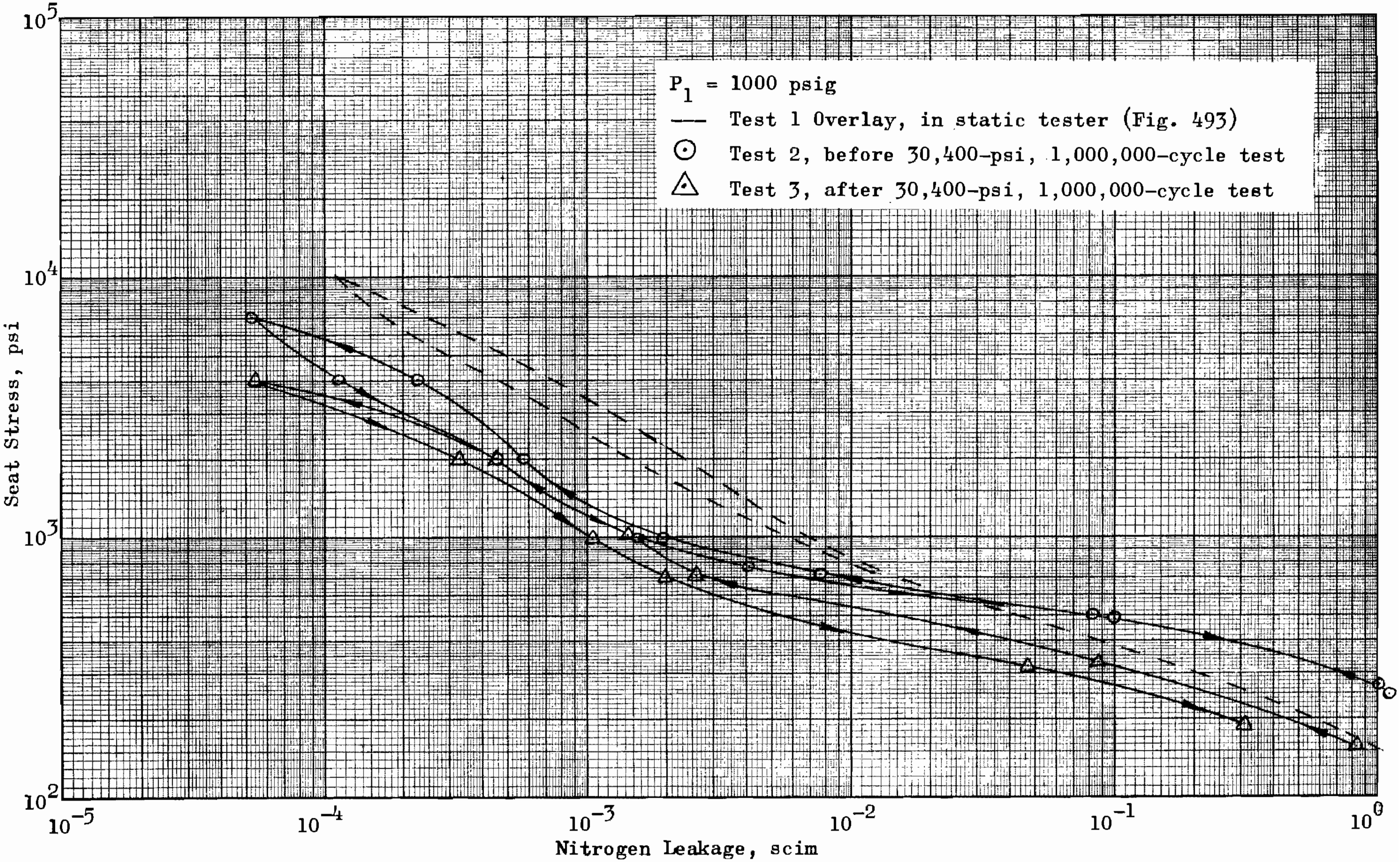

Figure 494. Stress-Leakage Data for Cycle Test Model Z_f, Test 2 and 3

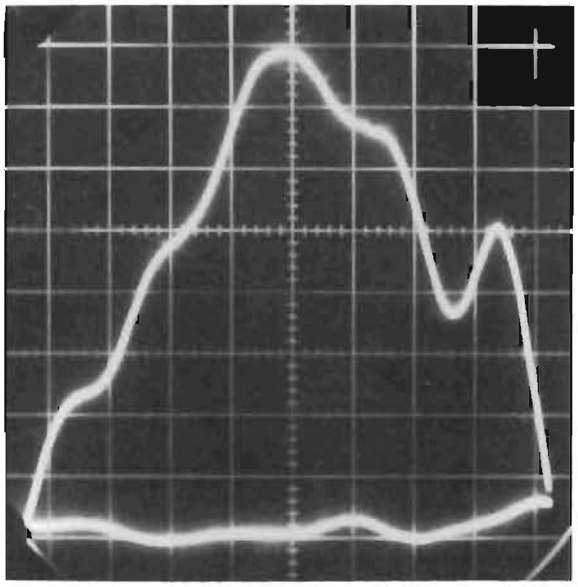

Figure 495. Test Model Z_f, Piezoelectric Load Cell, ~ 9.1 in./sec Impact Velocity, PS = 25 psig (175 lb/div.; 0.00002 sec/div.)

due primarily to the pitted seat which caused high-contact stresses on individual asperities. After removal of fretting products, no damage to the under surface was observed.

From these results it was concluded that the circular lay crowned geometry of identical poppet and seat land widths was an optimum configuration for metal-to-metal valve seating.

Spherical Model A_s, 0.5 AA 41-Degree Seating Angle

To investigate the cyclic characteristics of a spherical configuration, this model was cycled 10,000 times at 29,800 psi peak impact stress. As previously noted, Model A_s utilized a near-zero finish, but pitted grade 25 ball, and a spherically lapped 0.5 microinch AA circular lay finished seat. As shown in Fig. 496 the pretest stress-leakage curve closely conforms to the static tester data except for somewhat greater hysteresis. Unlike the flat models where parallelism is the prime factor, the spherical model requires precise axial alignment when installed in the cycle tester. The effect of taper or misalignment is increased hysteresis, as noted, since any slippage during poppet-seat loading results in added frictional holding forces.

To obtain the peak impact stress noted above, the dashpot was adjusted to the impact load of 878 pounds (Fig. 497). Cycle testing resulted in very slight change in leakage above 2000-psi seat stress. Below this level, however, a significant increase in increasing load leakage occurred.

Interference microscopic inspection revealed only about 10 small (0.002- to 0.011-inch long and less than 0.001-inch wide) fret areas comprised of minute pits up to 3 microinches deep. These are typically shown in Fig. 241, 242, and 243. The poppet photos also indicate (somewhat inconclusively) an increased nodule density compared with before-test photos. (Due to the low magnification and narrow band spread, 100-power interference photos of spherical surfaces are difficult to assess for textural changes.)

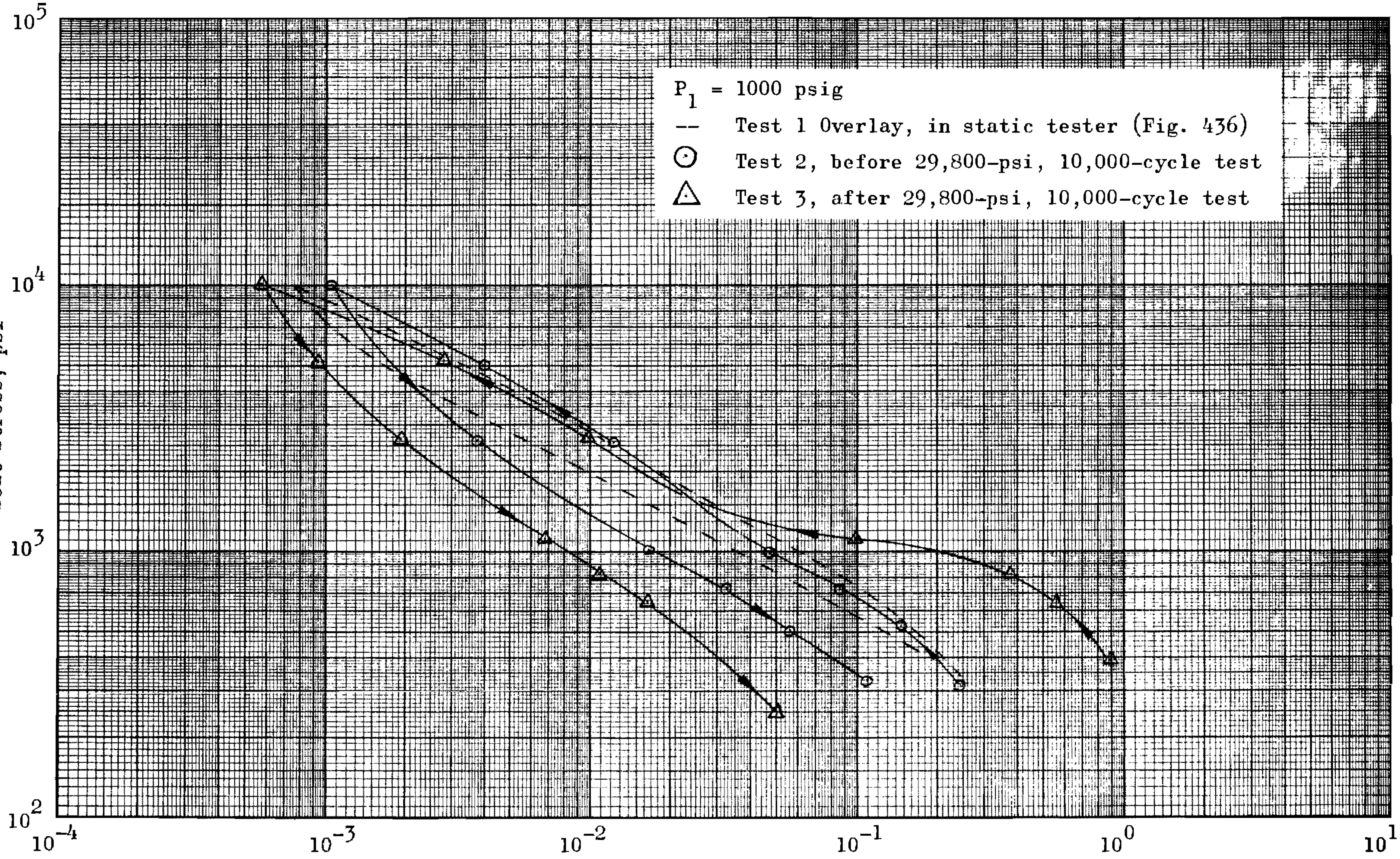

Figure 496. Stress-Leakage Data for Cycle Test Model A_s, Tests 2 and 3

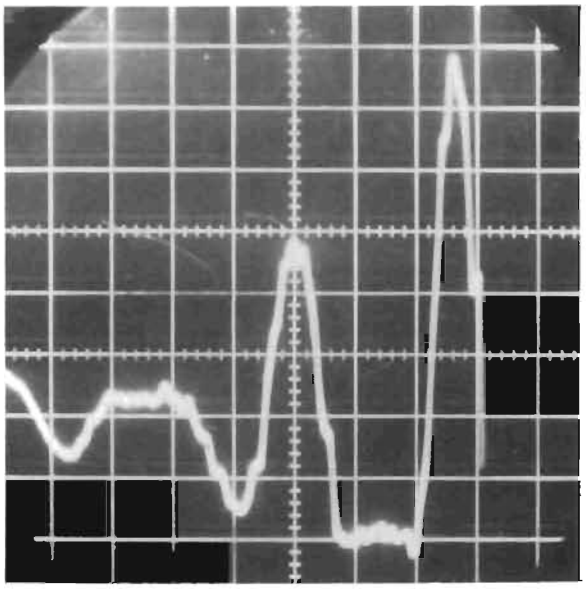

Figure 497. Test Model A_S, Piezoelectric Load Cell, ~ 7.6 in./sec Impact Velocity, PS = 158 psig (112.5 lb/div.; 0.0002 sec/div.)

It is also possible that the increased low-stress leakage, equivalent to a gap (h_e) change of about 2.5 microinches at 400 psi, is due to slight poppet radial position change during cycling, particularly because of the lower return-stress leakage.

The seat photo (Fig. 241) additionally shows the land edge condition which was not noticeably altered by cycling. Nor was there any noticeable plastic deformation of the poppet in the location of the seat corner.

Although inconclusive, the test results indicate the spherical configuration to have less resistance to fretting than equivalent flat models. Moreover, an additional test at the 90,000-psi impact-stress level would almost certainly have produced a wear condition that decreased seating angle would have aggravated.

Model T_{fl}, 0.6 AA Unidirectional Lay 440C Poppet, Gold-Plated Seat

Although of poor geometric and finish configuration, Model T_{fl} was, nonetheless, cycle tested to determine the general effects of impact loading ultra-thin gold plate. The flatness of the previously noted seat ID ridge was shown by electrical contact test before cycling by an indicated equivalent gap (h_e) of 21 microinches. As indicated by Fig. 498, stress-leakage data before cycling under clamped loading closely followed ball-joint static test results with any out-of-parallel submerged by the relatively rough gold surface texture.

With cycle test impact load set at 1330 pounds impact force, Model T_{fl} was cycled 10,000 times. Typical impulse characteristic is illustrated by Fig. 499, which indicates little change from the unplated versions. The peak impact stress of 30,000 psi was identical to the maximum value reached in the before-cycling stress-leakage evaluation. Consequently, any change in surface structure would, as with a valve seat, be due to only the effects of repeated cycles.

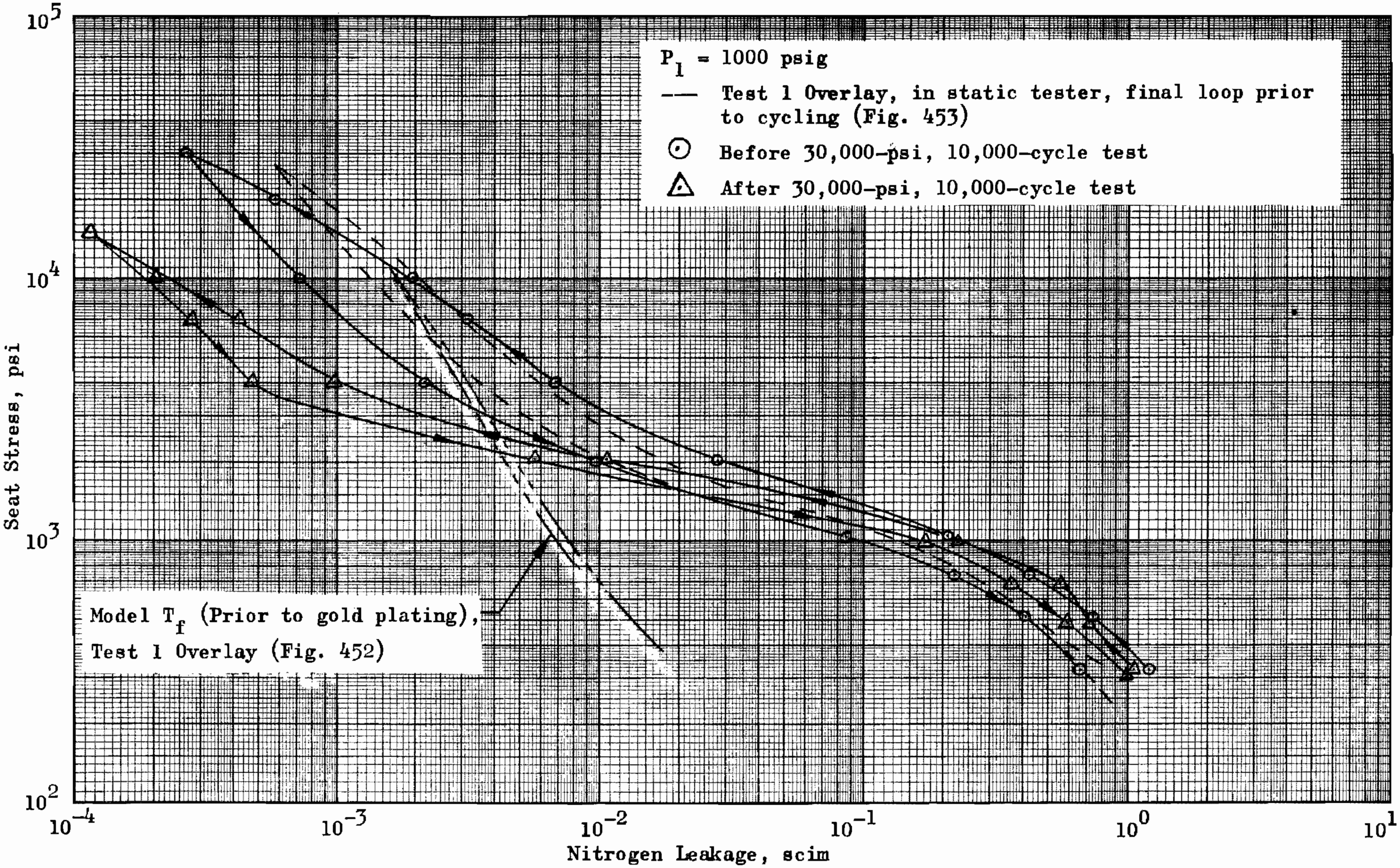

Figure 498. Stress-Leakage Data for Cycle Test Model T_{f1}, Tests 2 and 3

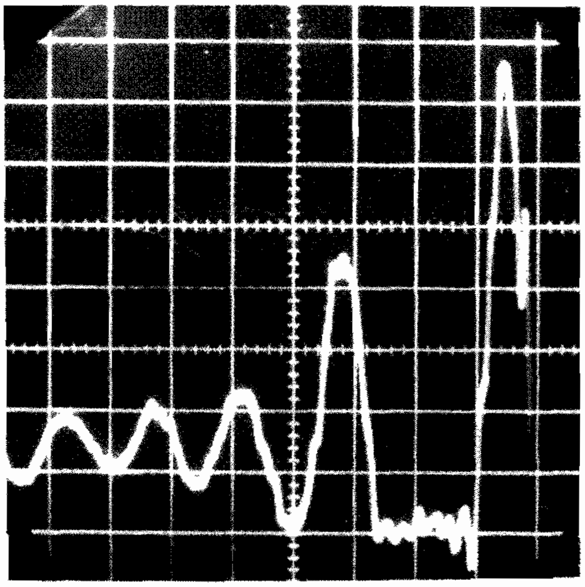

Figure 499. Test Model T_{f1}, Piezoelectric Load Cell, ~ 8.8 in./sec Impact Velocity, PS = 165 psig (175 lb/div.; 0.0002 sec/div.)

As shown by Fig. 498, the leakage after cycling was reduced above 1000-psi stress. Figures 283 and 284 illustrate typical seat conditions. Although the ID ridge width was slightly increased, its height above the average surface was not significantly changed from the before-test 9 microinches. Some disruption of the gold plate is evident toward the OD (Fig. 283) which, with a better geometry, might have increased leakage; however, this is not known. Microscopic inspection of the poppet revealed no substantial damage.

From these tests it is apparent that, for optimum results, the gold plate should have been applied over a crowned and thoroughly dubbed seat followed by finish lapping and polishing. However, program limitations did not permit further study.

OBSERVATIONS

Cycle testing has shown that seat degradation is closely related to the peak load and interfacial motion occurring during loading. With motions restricted to elastic differential deformation resulting from different poppet and seat geometries or elastic moduli, the basic wear mode was one of fretting. Wear particle size was probably much less than 1 microinch for the materials tested (440C, tungsten carbide). Attendant wear roughness was of a pitted nature having a PTV dimension of about 4 microinches. Leakage change was commensurate with the PTV roughness change. With the rougher models an improvement in leakage resulted as expected. The less than one microinch AA models also evidenced decreased leakage due to the fixed orientation of poppet and seat, however, reorientation testing revealed increased leakage.

Fretting was reduced significantly with flat poppet and seat lands of similar dimension and geometry. Elastic deformation of conical and spherical configurations caused interfacial slippage and thus greater fretting wear than the flat configuration. The limited scope of testing precluded any numerical correlations which might allow wear predictions at other conditions. Therefore, it should not be construed that conical or spherical configurations are unsuitable for any given application. This will depend upon loading, concentricity, impact velocity, interface spring rates, materials, and interface geometry.

The significance of the cycle test results lies in the positional and load control with which they were obtained. Few valves are constructed so that repeated interface contacts occur within the estimated 10-microinch variation maintained by the cycle tester. Also, most valves do not impact to produce the forces obtained herein. It is, therefore, reasonably certain that usual valve seat degradation and/or wear stems from gross interfacial sliding and contamination. Naturally, any plastic deformation due to edge contacts would likely further seat degradation.

Due to the inherent complexity of valve positional and impact relationships and many allied variables, there is no data on actual valves which might indicate a numerical basis from which to evaluate the cyclic seating phenomena. In this respect, the results presented herein provide a datum from which performance comparisons may be made. They also indicate the substantial benefits derived from fixed relationship seating as might be obtained by a flexure-mounted poppet.

There was considerable evidence of particle-caused deformation of greater than 50-microinch depth. However, the stress-leakage results were basically unaffected by this relative size contaminant particle. Moreover, as posttest inspection revealed, heavy impacts appeared to literally disintegrate most particles leaving only slight particle traces and the resultant depression in both surfaces. It is possible that the combination of high-impact forces and rigid positional control greatly reduced the potential deteriorating effects of contamination.

It would appear from the studies and results of this program that if the dynamic elastic deformations of impacted surfaces could be mathematically described, such relationships could be utilized with known impact forces to obtain a basic wear criterion. These relationships could then be employed to evaluate the material and lateral motion parameters typical of valve seating. Additional studies directed toward ascertaining terminal wear roughness levels for various materials and loading conditions would provide a basis for determining the resultant leakage variation with cycles.

CONCLUSIONS

Many conclusions have been reached from literature study, analyses, and model tests. These are noted throughout the report in view of the evidence presented. Some conclusions pertain to specific test data or a particular result. Such data cannot be generalized without conflicting with other found or anticipated results. On the other hand, data supported by the literature, analysis, and experimental evidence applicable to many seating configurations provide a firm basis for generalized conclusions which aid in delineating the basic mechanism of valve seating and leakage. These and supporting conclusions are summarized in the following paragraphs. Even these broader conclusions, however, must be reviewed within the limited scope of analysis and experiment from which they were originated. A case in point is the general conclusion adhered to by many researchers that metal-bearing area is developed by plastic asperity flow (Bowden and Tabor theory). It has been generally recognized that under certain conditions elasticity contributes significantly to bearing area under load. For hard smooth materials it has been conclusively demonstrated herein, that interfacial elasticity is the predominant mechanism of closure, although there are exceptions which must be recognized.

LEAKAGE

1. Established gas flow equations can be applied to valve seat leakage throughout the entire flow spectrum; for a given fluid and equivalent parallel plate closure, the established flow regimes are defined as:

    a. Nozzle: $Q \sim P_1 h$

    b. Turbulent channel: $Q \sim f(P_1, h, L, f, Re, \text{etc.})$

    c. Laminar: $Q \sim (P_1^2 - P_2^2)\, h^3/L$

    d. Transition: $Q \sim \left[(P_1^2 - P_2^2)\, h^3 + (P_1 - P_2)\, h^2\right]/L$

e. Molecular: $Q \sim (P_1-P_2)\ h^2/L$

f. Diffusion laws:

Although the applicable range for nozzle, turbulent channel, and laminar flows may be determined by established criteria for a measurable gap (h), the applicability of theoretical criteria for high-pressure transition and molecular flow is uncertain due to the very small gap. However, since the molecular component is theoretically indicated at higher flow levels than experimentally determined, it provides a factor of safety commensurate with the lack of data.

2. Examination of flow regime criteria will show that valve seat leakage is usually laminar. This is basically a function of the small gap (h) relative to land width (L) necessary in most valve seats for obtaining effective closure. The near impossibility of nozzle or orifice flow may be seen readily from Fig. 381 (1-inch flow test model) by extending the orifice curves to reasonable leakage levels (i.e., below 100 scim). For the case of P_1 = 100 psig, the orifice land width could not exceed about 0.0001 inch for Q = 100 scim or about 10 microinches for Q = 10 scim. Other practical considerations limit the probability of attaining pure molecular level of leakage with most metal-to-metal seating configurations.

3. Liquid leakage, although not evaluated herein, has been demonstrated in the literature to follow also a pattern similar to the above. At very low levels of leakage, the effects of surface tension may be a significant leakage limiting factor; however, no correlative data is available. Therefore, the application of gas-liquid conversions based on the laminar flow equation should provide a conservative prediction for liquid leakage.

4. Leakage flow comparison experiments with nitrogen, helium, argon, and hydrogen gases have proved the correlative accuracy of the laminar flow equation. Consequently, for volumetrically measured

leakage, viscosity is the controlling parameter. (It is probable that the disagreement obtained in valve testing with various gases is due to experimental error and gap variability.)

LEAKAGE PRESSURE PROFILE

Experiment and theory have demonstrated the variation in effective seat diameter within the near-seated region. From turbulent channel to laminar flow, the profile varies so that the effective seat diameter changes from near midland to two-thirds across the seat land width (in the flow direction). Where the land pressure force is a significant part of the total pressure force, pressure profile variations will contribute to instability (buzzing) in pressure sensitive devices because the transition between the flow regimes takes place normally within a few ten thousandths of an inch.

LEAKAGE PATH

1. The leakage path created by two opposed annular surfaces under a normal load is a function of the relative dimensions of various form and surface texture errors. Land crown, out-of-flatness, -parallel, or -roundness, and taper comprise the usual form errors. Surface texture errors are roughness, waviness, nodules, pits, and scratches. Under light loads the leakage gap will be controlled by errors causing material to protrude above some average plane. The partial load effect of each of these errors will be submerged in the total load in proportion to their relative size. At higher loads, the predominant flow path will be through roughness, scratches, and interconnecting pits.

   Approximation of these gap leakages may be determined by integration of height variation to determine equivalent parallel plate heights (h_e). Since the loading effects of composite form errors cannot be precisely separated, the assessment of leakage from test results for a known seat geometry and surface texture will allow a conclusion as to the probable cause for a given leakage level. This data should provide a sound basis for a practical compromise between geometry, surface texture, and leakage requirements.

2. Tests have shown that scratch leakage is relatively independent of load. Assuming a V-shaped scratch model, the equivalent laminar flow parallel plate height for this configuration is (0.63 h), where (h) is the scratch depth. Evaluation of numerous models has shown that all lapped surfaces have scratches, and scratch leakage can be calculated, providing accurate measurements are made of depth, width, length, and quantity. Many surfaces are remade due to visible but insignificant leakage contributing scratches. Application of suitable scratch criteria to engineering drawings based upon the parameters defined herein will reduce this waste.

3. With the lapped valve seat, the significant leakage path is usually through the minute interstices between contacting roughness asperities. (This is assuming that sufficient load exists to flatten nodules.) Where the surface roughness lay of opposed surfaces is multidirectional or a crossing of unidirectional scratches, the controlling leakage parameter is the sum of the average PTV heights for each surface.

   With circular lay opposed surfaces the leakage path is through the gap between intersections caused by lay irregularities and eccentricity. Since the PTV height sum (for both surfaces) adds only at each real contact intersection (which also blocks flow), the radial gap is only one-half of the PTV sum of the cross lay roughness heights between intersections. Consequently, circular lay surfaces under just enough load to contact the roughness level will have approximately one-eighth the leakage of similarly loaded unidirectional or multidirectional lay surfaces.

SURFACE TEXTURE DEFORMATION

1. Valve seating is essentially a totally elastic process of forcing two relatively flat surface textures into intimate contact. Plasticity may play an important role on the initial few contacts, particularly for the less hard metals; however, after the seat is set, very little plastic flow takes place on subsequent cycles.

   With some valves having relatively large geometric errors or very light loads, the situation of complete land contact may not be achieved. Other than the special cases presented herein, deformation analyses for errors such as land taper and conical poppet tilt have not been formulated due to their extreme complexity.

   Seat land taper which results in theoretical line contact at zero load is exceedingly difficult to assess because of the unknown contact width and stress variables. Below a certain load, taper is detrimental to closure compared with a full roughness land width contact. This is due to unavoidable edge roughness and waviness combined with the relatively narrow (real) contact land. As load is increased, closure occurs at a faster rate than the full contact land due to increased land width and higher contact stress at the initially contacted corner. The potential of edge plastic flow and cutting of the opposed surface (if overlapping) poses a danger to valve configurations having significant taper, due to the possibility of recontacting with the plastically raised metal edges overlapping. This situation is somewhat improved with seating structures that accurately control the axial and radial alignment of poppet and seat, or have the overlapping member substantially harder (> 20 percent) than the narrower land part.

2. From the test results it is concluded that all surface textures have a percentage of identifiable geometrical errors which affect the load-deformation characteristic. It would be an oversimplification to assume that the roughness parameter alone is the

significant topographical variable. The finest surface with insufficient load to flatten a waviness component would have excessive leakage compared with roughness expectations. Stress-leakage results have indicated that for most of the lapped models an apparent contact stress between 300 and 600 psi (13 to 26 pounds) was required to establish leakage equivalent to the sinusoidal analytical model idealized by the recorded PTV inspection data. Below this load level, the effects of waviness, nodules, and variable edge conditions predominate and, except in specific measured instances, their effect on the stress-leakage characteristic is undefined.

3. Roughness deformability is a function of the relative profile sharpness. The sharpness characteristic is broadly described by a PTV average slope angle. Similar to a corrugated tin roof, the sharper the angle, the more rigid the structure. Deformability is also controlled by the elastic material properties, modulus, and Poisson's ratio. It follows that under equal loading and test conditions, a "rough" surface of shallow profile could leak less than a "fine" surface having a sharp or pitted texture. Naturally, the rougher surface will leak more below a given load level.

4. Seating surfaces with nearly concentric circular lay roughness profiles are considerably more deformable than comparable multidirectional surfaces. This is best explained by the theoretically fewer real contacts and circumferential closure hypothesized in the analytical model analysis comparison (Seating Analysis section).

Increased deformability combined with a smaller effective radial flow gap (1/2 PTV sum of each surface) explains the observed reduced leakage with circular lay surfaces. Moreover, since radial scratches are either not generated or may be removed, closure continues at a high rate with increased load to lower levels than much finer unidirectional lay surfaces.

From comparisons of unidirectional and circular lay surfaces, it is concluded that comparable leakage rates may be obtained with circular lay surfaces having two times the roughness of unidirectional lay surfaces for apparent stress of 1000 psi, and four times for 10,000 psi. While these data are considered conservative for the models tested, it must be emphasized that the evaluation is only on a roughness basis and does not include other geometric variables.

CONTACT STRESS DISTRIBUTION

1. Valve seats are most often designed so that one seating surface overlaps the other. With small corner radii, edge-bearing stresses are much greater than apparent (stress). This effectively reduces the available load apportioned to the center of the land which, consequently, results in less asperity deformation in this area. In essence, the peripheral edges of the seat may become the predominant sealing areas with the land center acting as a trough. Under these conditions it may be hypothesized that edge radial scratches which do not bridge the land can conduct significant leakage. Furthermore, with sharp edges the maximum contact stress is developed in areas of minimum geometric regularity since discontinuities are more prevalent near machined boundaries (i.e., corners).
2. From the previous conclusion it follows that the crowned and/or edge-dubbed seat land configuration produces the optimum contact stress distribution for closure. This is evident particularly where sharp edge discontinuities may cause plastic deformation. A more subtle advantage lies in the distribution of effective load over a wider land width in the central land area where the finish is likely to be more uniform. Since the load is concentrated at the land center, edge scratches not bridging the land may be neglected.

3. Like flat surfaces, the spherical contour is easily obtained by lapping because of the constantly changing path between the lapping parts, which naturally generates a round surface at any section. Spherical seating, however, involves the additional radius parameter which can result in serious taper error if the seat and ball poppet radii are significantly different. The radius of a seat land cannot be measured with sufficient accuracy to determine this error. Therefore, analytical methods must be employed to ensure seating conformity.

   Where leakage requirements justify maximum accuracy, the ball poppet should be at least grade 5 to obtain a seating surface with the fewest pits and nodules. With very small valves or light-seating loads, a grade 1 ball may be well worth the additional expense in time saved in seat lapping.

   It is possible that accurate conformance between poppet and seat may be obtained by match lapping the ball poppet and seat with a suitably fine compound; however, this technique was not explored.

4. Unlike flat and spherical surfaces, the conical geometry is not self-generating and must be obtained through an external datum plane such as the ways of a lathe. Moreover, the difficulties attendant with measuring differential seating angle (taper) make this the least desirable geometry for most applications. Like spherical surfaces, accurate conformance may be obtained possibly by match lapping; however, the additional problems of poppet ridges and severe crowning due to axis wobble must be considered.

5. All metal seating surfaces should be polished following geometric finishing to remove what might be termed the roughness on the roughness. This process, accomplished at low speed with a soft lap such as paper, should remove no more than 10 percent of the PTV roughness. Polishing produces a specular surface which reveals surface flaws and scratches. It further reduces the sharpness of real asperity contacts yielding improved deformability and lower asperity stress. The result is less leakage and longer life.

3. Like flat surfaces, the spherical contour is easily obtained by lapping because of the constantly changing path between the lapping parts, which naturally generates a round surface at any section. Spherical seating, however, involves the additional radius parameter which can result in serious taper error if the seat and ball poppet radii are significantly different. The radius of a seat land cannot be measured with sufficient accuracy to determine this error. Therefore, analytical methods must be employed to ensure seating conformity.

   Where leakage requirements justify maximum accuracy, the ball poppet should be at least grade 5 to obtain a seating surface with the fewest pits and nodules. With very small valves or light-seating loads, a grade 1 ball may be well worth the additional expense in time saved in seat lapping.

   It is possible that accurate conformance between poppet and seat may be obtained by match lapping the ball poppet and seat with a suitably fine compound; however, this technique was not explored.

4. Unlike flat and spherical surfaces, the conical geometry is not self-generating and must be obtained through an external datum plane such as the ways of a lathe. Moreover, the difficulties attendant with measuring differential seating angle (taper) make this the least desirable geometry for most applications. Like spherical surfaces, accurate conformance may be obtained possibly by match lapping; however, the additional problems of poppet ridges and severe crowning due to axis wobble must be considered.

5. All metal seating surfaces should be polished following geometric finishing to remove what might be termed the roughness on the roughness. This process, accomplished at low speed with a soft lap such as paper, should remove no more than 10 percent of the PTV roughness. Polishing produces a specular surface which reveals surface flaws and scratches. It further reduces the sharpness of real asperity contacts yielding improved deformability and lower asperity stress. The result is less leakage and longer life.

SURFACE INSPECTION

1. The secret to fabricating fine surfaces lies in the ability to measure them. The interference microscope provides this capability down to about 1 microinch PTV. When the controlling parameters are defined and can be observed and measured, the correlation of cause (roughness) and effect (leakage) automatically points to the direction for improvement.

   The basic limitation in microinterferometric interpretation of surface texture is the horizontal resolving power of the ordinary microscope. When surface discontinuities (pits, scratches, etc.) become too narrow to follow a single interference band into and out of a given defect, the interference technique cannot be used for accurate depth measurement. With the Leitz instrument and Polaroid photos used in this effort, horizontal resolutions were made down to about 20 microinches. Unfortunately, with the finer valve seats much significant surface texture lies below optical resolution. For these cases the interference method may be used on a comparative basis (as with roughness comparison masters).

   Curved surfaces present an additional variable which must be considered when measuring surface texture variables with the interference microscope. Since interference band width depends upon a relatively small angle between a flat reference mirror and the viewed object, conical and spherical surfaces must be rotated to examine any given area. With conical surfaces, gross geometry may be measured along the cone axis. However, since spherical surfaces curve continuously, a similar comparison is not possible with a flat reference and only texture variables may be assessed.

2. With simple flat surfaces, the optical flat is most suitable for gross-geometry measurements. Where very small or complex shapes and combination of dimensions are involved the ultimate measuring system is comprised of the precision surface or spindle, electronic

gage, and profile data recorder. Supplemented by low-power interference and plain microscope measurements, seating geometry may be accurately assessed and correlated with leakage measurements.

MODEL TESTS

1. While indicating a general agreement with simplified seating analyses, the model tests have demonstrated the dependence of leakage at any given load upon the occurrence and distribution of a multiplicity of surface variables.

   The majority of tested flat models indicated that roughness and roughness lay were the significant load-leakage geometric parameters between 500- and 20,000-psi apparent seat stress.

   Analysis of these data has indicated that a correlation of the roughness PTV parameter and laminar flow equation is capable of predicting leakage change with load within a factor of about two over the noted stress range. This estimate is based upon the two empirical equations presented in the Surface Texture Evaluation section for 16 flat steel models. Leakage values computed directly from roughness measurements should be within a factor of 10, although circular lay surfaces may have much lower leakage than predicted due to the conservative slope employed in correlation. Combining the empirical equations for unidirectional lay roughness (h_u) leakage and circular lay roughness (h_c) leakage results in

   $$\frac{Q_u}{Q_c} = 0.04\ S^{5/6} \left(\frac{h_u}{h_c}\right)^3$$

   Thus, unidirectional lay leakage at light loads (500- to 1000-psi apparent stress, S) will be about eight times that for an equal circular lay surface. At 20,000 psi the ratio is approximately 150:1.

For a given leakage requirement, surfaces with circular lay may be considerably more rough than with unidirectional lay, depending upon the load as previously indicated.

2. Evaluation of circular lay eccentricity has led to the tentative conclusion that moderate amounts of lay eccentricity do not significantly affect leakage. Due to the small dimensions involved, numerical evaluation of this parameter was not possible. Therefore, the conclusion must be considered within the scope the models tested.

3. Because of the overriding influence of roughness, no direct comparison of the material parameter could be made. Where relatively large deformations take place to effect sealing, it is concluded that the more elastic material will require less load. The apparent flatten stress equation (based upon Hertz contact) indicates a direct relationship between flatten stress and elastic modulus (E). In view of many other factors, however, the selection of a material for seating should probably not be influenced by this parameter.

4. Combined with circular lay, the crowned land surface designed to develop an adequate land width is the optimum seating configuration. The advantage of this configuration is particularly evident at low loads where high-contact stresses are developed to decrease roughness height. In some cases, however, it may be determined that the load geometry relationship is such that crown dimensions cannot be measured (i.e., less than 1 microinch falloff) for the desired land width. The effect of adequate corner dub then becomes more critical and should be applied keeping the land essentially flat.

5. Selection of flat, conical, and spherical geometry must be based upon specific application requirements. This is best accomplished by a critical examination of advantages and disadvantages inherent in design, fabrication, inspection, and performance.

Conical or spherical seating has several basic advantages over the flat surface. The most apparent is the mechanical load advantage effect which allows a working contact stress to be developed with reduced loads. Since the land is developed from the intersection of right angle surfaces, a narrow width is easily obtainable. Once seated, the conical and spherical configurations have a force component which resists lateral motion due to vibration, often a serious disadvantage in flat seating since high-frequency vibration can cause failure in minutes.

An inherent disadvantage of conical and spherical geometry is the slippage which takes place during seating. Since conformance is measured in millionths of an inch, poppet and seat axes cannot be installed or guided with sufficient accuracy to avoid this wearing shear. Moreover, with large loads or small included angles, elastic entry of the poppet into the seat will add to the wear problem.

Spherical seats have the advantage of perfect alignment once seated. On the other hand, conical seating has the additional error of axis tilt. Alignment moments for the tilted cone are a complex function of the load application point and interfacial friction. Unless the seating load is applied below the seating line (toward the apex) and perfectly axial, conical seats are probably not self-aligning.

The conical configuration,therefore, must have generally a narrow land and higher seating loads to reduce the gap caused by axis tilt.

From a performance viewpoint the flat configuration is the natural choice for lowest leakage combined with maximum life. Spherical seating offers the load and lateral retention advantages, but with greater wear potential. Conical seating should probably be selected on an economical basis or where experience has indicated adequate performance.

6. Cycle testing has shown that seat degradation is closely related to the peak load and interfacial motion occurring during impact. The basic wear mode observed was one of fretting. Where the land was sharp, fracture and plastic flow occurred at the edge boundary. By making flat poppet and seat opposing surfaces of similar geometry and material, lateral differential deformation, and thus fretting, was greatly reduced. Edge damage was eliminated by land crowning and duboff.

   The poppets cycle tested herein experienced a 25-microinch maximum lateral axis motion relative to the seat. Under these conditions it was apparent from the results that a certain amount of impact was beneficial to seating. This was attributed to the plastic deformation of nodules, high asperities, and sharp edges which intermeshed with the matched opposing topography. The net effect was leakage reduction with cycles, even though surface roughness and contaminant induced flaws had increased. Combined with previous findings, it is concluded that optimum seating is provided by the flat dubbed or crowned configuration restrained to have only axial motion as might be obtained by a flexure mounted poppet.

GENERAL

1. Other than the gross-geometry parameters such as land width, seat diameter, and general configuration, valve closures are not designed in the full sense of the word. Engineering drawings do not, for the most part, specify the real controlling parameters, but only point the way toward a fabrication process. Few valve poppet and seat drawings specify the 1/4- to 4-microinch AA finishes, and 1- to 50-microinch flatness (or roundness) necessary to meet performance requirements. Scratches and pits are uncontrolled. Consequently, metal valve seats are being "developed" to meet leakage requirements.

The limitations of present inspection tools, combined with the prodigious amount of detail inspection required, preclude specifying exact surface profiles on engineering drawings. Nevertheless, in many instances the ultimate performance of a seat is dependent upon a fabrication process or control completely uncalled for by the drawing.

2. To control the reliability and performance of low-leakage components, all geometric parameters should be dimensionally specified to the level dictated by performance. Where such controls exceed measurement capabilities, or would be uneconomical to dimensionally prove, either the final or a comparative leakage test should be allowed in lieu of these controls. As shown herein, the leak test is cubically more sensitive to seating gap than are direct measurements. Therefore, with some dimensions measured to ensure basic geometry, the more difficult assessments as embodied in surface texture may be indirectly measured as a composite group. With the information provided, comparative tests may be established under a variety of conditions to ensure function in the final assembly. The most important aspect in defining such tests, would be to ensure loading and geometric similarity with the final assembly.

RECOMMENDATIONS FOR FUTURE EFFORT

Correlation of defined surface textures and geometrical errors with load and leakage has provided the data for a more systematic approach to valve seating design. The mechanism of metal-to-metal closure has been established over a working range of valve seats which extend from comparatively poor geometry to very low-leakage configurations. Due to the extreme complexity of real surfaces, exact mathematical descriptions are not possible. Consequently, analytical prediction of the load-leakage characteristic is limited to order of magnitude estimates. This is inherent in the cubical relationship between gap and leakage; i.e., $Q \propto (h-\delta)^3$. The role, therefore, of the analytical approach is to assist in defining the relative importance of the various geometric variables under a specific set of conditions. In this respect, the analyses and techniques described herein will assist the designer in establishing requirements with a greater assurance of success than previously possible.

As with most research efforts, the information obtained has furnished guide lines for the acquisition of much more data. Heretofore unimagined concepts and approaches to basic problems have been uncovered. Both the successes and failures documented in this report point the direction toward additional effort in solution of these problems which will enhance the capabilities of designers while contributing toward an "advanced art" (i.e., more science and less art). This effort is described in the following paragraphs.

LEAKAGE MEASUREMENT

Leakage measurement has always proved difficult and susceptible to large systematic errors. Methods of gas leakage measurement should be defined and correlated over the range from 100- to 10^{-8}-scim, under conditions which thoroughly define the transition between laminar and molecular flow for various leak paths. Analyses should be made which indicate probable measurement errors as a function of time, pressure, temperature, and other system variables. These analyses should be employed in comparison of the various methods for ease of measurement, reliability, accuracy, and precision.

CONTAMINATION

While a great deal is known about the more gross and obvious sources and characteristics of contaminant matter, very little data is available relative to its specific effect on valve seating. Moreover, the quantitative potential of contaminant sources is largely unknown. A basis research program is recommended to (1) define the sources, quantity, and sizes of contaminants and correlate this data with an analytical approach for its prediction, and (2) evaluate the effects of specific contaminants on valve closures. One approach to the latter is illustrated by the results obtained with Test Model L. An extension of this technique to a variety of contaminant materials and sizes would provide valuable data for establishing necessary seat loads and filtration requirements. Since contaminant load-envelopment evaluation is by nature a specifically defined test condition, each evaluation would be valuable.

Supplementing this effort, an analytical approach to load-deformation characteristics of single particles (both hard and soft) is recommended to allow extrapolation of contaminant effects into sizes and loads which cannot be practically measured.

SEATING ANALYSES

The contact stress distribution analysis of a dubbed seat has provided a basic approach to analysis of other similar configurations. Equations are needed to define the allowable limits of gross-geometry errors. While these problems are difficult to solve, solutions are feasible. Three areas of endeavor are recommended:

1. Flat land seat having small corner radii and poppet overlapping

2. Tapered flat seat land with poppet overlapping and with poppet identical to seat
3. Conical (or spherical) seat land with poppet overlapping, with and without friction

Parameterization of existing and any future analytical results should be performed covering a suitable range of data. This would be accomplished using a digital computer with tabulated and CRT output.

FABRICATION INVESTIGATION

The significant advancements achieved in surface fabrication are attributed directly to the correlation of method, inspection data, and test results. It is expected that much more can be achieved in the same manner. Areas recommended for investigation are noted below.

1. The question of optical finishing an extremely fine multidirectional texture vs circular lay for optimum sealing is pertinent and should be explored.
2. Basic lapping experiments on hard and soft laps would provide valuable data for meeting future requirements.
3. Conformal geometries, such as conical and spherical, may best be final finished by match lapping. Due to the problems associated with this technique, it is generally avoided in the industry.
4. Plastics occupy a prominent position in aerospace valving. However, inspection of geometry is difficult, and surface texture evaluation is not possible using stylus methods. It is likely that the inspection methods evolved herein for metals may be successfully applied to machined and lapped plastic surfaces. Surface finish may be assessed by interferometry through direct viewing or after vapor deposition of a reflective metal. It is recommended that this subject be explored, as proper finishing and control of plastics will usually provide more effective sealing than metal surfaces.

STATIC STRESS-LEAKAGE EVALUATION

Many areas have yet to be defined in relating seating geometry with load and leakage. A more precise separation of geometric variables is required to define experimentally the load parameter compared with apparent stress. To supplement the existing stress-leakage data for the flat 1/2-inch OD, 0.03-inch land models, a low-load evaluation of models one-tenth the size of the 1/2-inch models is recommended. The two additional parameters of land width and land standoff height should be investigated. These parameters could be evaluated on single models by removal of adjacent material without disturbing the original surface texture. Thus, the submergence of these parameters by roughness variations between models would be avoided.

Additional static testing of 1/2-inch OD models is recommended to evaluate (1) optically finished surfaces, (2) matched lapped conical and spherical surfaces (including balls), (3) optimum hand-lapped model, (4) land width and standoff height (as with one-tenth size model), and (5) plastic seat forming with hard poppet.

PARAMETRIC STUDY OF GEOMETRIC SEATING ERRORS

Attempts to evaluate the effect of gross geometric errors were largely unseccessful. This was due primarily to the inability to accurately control surface texture variation between models. The one and two band out-of-flat errors of Models H and I were completely submerged because of roughness variations. Out-of-roundness effects on spherical models were submerged by poppet nodules. The tilted cone evaluation was complicated by the out-of-roundness evident on both poppet and seat.

With many valve seating applications, gross-geometry errors cause the leakage gap. To ascertain the effects of these variables they must be separated so that only one parameter is significant. This could be accomplished by fabricating near geometrically perfect surfaces for establishing a datum reference. Variable geometric errors for a given surface roughness could then be evaluated by elastic deformation of a single seating surface through application of internal strain. This may be achieved by application of a variable load with screws or clamps remote from the seating surface. By this method, parametric data covering a wide range of conditions could be gathered using the unstrained condition to ensure repeatability precision.

It is recommended that the out-of-flat, out-of-round and taper conditions be evaluated for flat, conical, and spherical models. The positional errors of tilted cone and out-of-parallel flat should also be examined.

SEALING EFFICACY OF HARD METALS, CERAMICS, AND CERMETS

Little is known relative to the fabricability and sealing characteristics of the many hard metals, ceramics, and cermets used in seating. This is due largely to the unkown surface texture parameters controlling leakage. These materials should be comparatively evaluated for their textural characteristics by interference and profile inspection, and stress-leakage testing. The tungsten carbide model evaluated herein clearly did not have the sealing capability of comparable 440C surfaces. This was due to a significant pit density. The following materials are recommended for evaluation:

1. 440C (Control)
2. 17-4 PH
3. Stellite
4. Tungsten carbide (several grades from several manufacturers)
5. Tungsten-titanium carbide
6. Chrome carbide
7. Silicone carbide (KT)
8. Boron carbide

9. Sapphire (single crystal)
10. Alumina ceramic

CYCLE TESTING

Cyclic impact results in an interaction of many complex phenomena, few of which are very well understood. A great deal of careful experimentation is obviously required to provide the basic understanding necessary for a definition of the significant variables. An evaluation of several typical valves under controlled conditions is recommended to answer some of the basic questions. Certainly, the interaction of contamination is significant in valve failures as is vibration and sliding under impact. By employing test valves of suitable simplicity for separation and evaluation of individual variables, standard valve models could be developed from which to explore materials, coatings, platings, seating errors, etc., over a range of environmental conditions. As a further control, the cycle tester or a flexure device would provide a datum for evaluation of the maximum performance capabilities of any one variable.

REFERENCES

1. ASA B46.1-1962, Surface Texture, American Standards Association, American Society of Mechanical Engineers, New York.
2. ASA Sectional Committee B46, Minutes of Meeting of Subcommittee 5 at National Bureau of Standards, 15 May 1962.
3. Reason, R. E.: "Significance and Measurement of Surface Finish," Grinding and Finishing, Vol. 2, September, October, November 1956.
4. Bickel, Dr. Eng. E.: "Testing the Precision of Electric Instruments for the Measurement of Surface Roughness," Microtecnic, Vol. 14, No. 4, August 1960.
5. "Precision Measurements of Cylindrical Surface Elements Seminar," American Society of Tool and Manufacturing Engineers, Paper SP64-27 through -45 (nonconsecutive), January 1964.
6. Bowden, F. P. and D. Tabor: The Friction and Lubrication of Solids, Oxford University Press, London, Vol. 1, 1954, Vol. 2, 1964.
7. Tarasov, L. P.: "Relation of Surface-Roughness Readings to Actual Surface Profile," Trans. ASME, Vol. 67, April 1945.
8. Handbook 77, Precision Measurement and Calibration, Vol. 3, National Bureau of Standards, February 1961.
9. Sugg, Ronald E.: "An Interferometer for Examining Polished Surfaces," Mechanical Engineering, Vol. 75, No. 8, August 1953.
10. Tolansky, S.: "Surface Microtopography," International Science and Technology, Vol. 9, September 1962.
11. Bikerman, J. J.: Surface Chemistry, Academic Press Inc., New York, 1958.
12. Gress, S. J.: Surface Chemistry of Solids, Whitefriars Press Ltd., London, 1951.

13. Halliday, J. S.: "Surface Examination by Reflection Electron Microscopy," Proc. Inst. Mech. Engrs., London, Vol. 169, 1955.

14. Rabinowica, E.: Friction and Wear of Materials, John Wiley and Sons, New York, 1965.

15. Archard, J. F.: "Single Contacts and Multiple Encounters," Journal of Applied Physics, Vol. 32, No. 8, August 1961.

16. Ling, F. F.: "On Asperity Distributions of Metallic Surfaces," Journal of Applied Physics, Vol. 29, No. 8, August 1958.

17. Ling, F. F.: "Some Factors Influencing the Area-Load Characteristics for Semismooth Contiguous Surfaces Under Static Loading," Trans. ASME, Vol. 80, Peper No. 57 A-246, September 1957.

18. Rabinowicz, E.: "Influence of Surface Energy on Friction and Wear Phenomena," Journal of Applied Physics, Vol. 32, No. 8, August 1961.

19. Kragelsky, I. V. and N. B. Demkin: "Contact Area of Rough Surfaces," Wear, Vol. 3, May 1960.

20. Reason, R. E.: "Orderly Progress in Surface Measurement," Engineering, Vol. 189, February 1960.

21. Broadston, James A.: Control of Surface Quality, Surface Checking Gage Co., Hollywood, California, Report No. NA-8150, 1960.

22. Timoshenko, S. and J. N. Goodier: Theory of Elasticity, McGraw-Hill Book Co., New York, N. Y., 1951.

23. Dyson, J. and W. Hirst: "The True Contact Area Between Solids," Proc. Phys. Soc., London, B67, 1954, 309.

24. O'Conner, J. J. and K. Johnson: "The Role of Surface Asperities in Transmitting Tangential Forces Between Metals," ASME, Paper No. 62-Lubs-14 for meeting of June 1962.

25. D'yachenko, P. E.: "The Actual Contact Area Between Touching Surfaces," Inst. of Mech. Engrg., Academy of Sciences, Moscow, 1963 (Translation by Consultants Bureau, N. Y.).

26. Greenwood, J. A.: "On Area of Contact Between Rough Surfaces and Flats," Trans. ASME, Paper No. 65-Lub-10, October 1965.

27. Lipson, C. and L. V. Colwell: Handbook of Mechanical Wear, University of Michigan Press, Michigan, 1961.

28. Rothbard, H. A.: Mechanical Design and Systems Handbook, McGraw-Hill Book Co., Inc., New York, 1964.

29. Seeley, F. B.: Advanced Mechanics of Materials, John Wiley & Sons, New York, 1952.

30. "Advanced Valve Technology for Spacecraft Engines," 8651-6032-SU000 (Vol. 1), 8651-6033-SC000 (Vol. 2), TRW Space Technology Laboratories, July 1964.

31. Bauer, P.: "Investigation of Leakage and Sealing Parameters," AFRPL-TR-65-153, IIT Research Institute, Chicago, August 1965.

32. Comyn, R. H. and C. W. Furlani: "Fretting Corrosion, A Literature Survey," TR-1169, Harry Diamond Laboratories, U.S. Army Material Command, Washington D.C., December 1963.

33. Kennedy, N. G.: "Fatigue of Curved Surfaces in Contact Under Repeated Load Cycles," Proceedings of the International Conference on Fatigue of Metals.

34. Meacham, H. C.: "Laboratory Investigations of Fretting Corrosion in Antifriction Bearing Components, "ASME, Paper No. 64-WA/MD-18, December 1964.

35. Pittroff, H.: "Fretting Corrosion Caused by Vibration With Rolling Bearings Stationary," Trans. ASME, Journal of Basic Engineering, Paper No. 64-LUB-21, October 1964.

36. Goodman, L. E.: "Contact Stress Analysis of Normally Loaded Rough Spheres," Trans. ASME, Journal of Applied Mechanics, Paper No. 62-WA-19, November 1962.

37. RPL-TDR-64-68, Rocket Engine Valve Poppet and Seat Design Data, Rocketdyne, a Division of North American Aviation, Inc., Canoga Park, California, May 1964.

38. AFRPL-TR-65-93, Study, Design and Test of Functionally Integrated Pneumatic Components for Rocket Propulsion Systems, Bell Aerosystems Co., June 1965.

39. May, K. D.: Advanced Valve Technology, NASA SP-5019, Midwest Research Institute, February 1965.

40. Gitzendanner, L. G. and F. O. Rathbun,: Statistical Interface-Leakage Analysis and Feasibility of Superfinished Surfaces for Sealing, Contract NAS8-4012, General Electric Co., May 1965.

41. Howell, G. W.: Aerospace Fluid Component Designers' Handbook, RPL-TR-64-25 (Vol 1) TRW Space Technology Laboratories, May 1964.

42. "Machine Tools are Accurate to Millionths," Review of World Manufacturing literature, a digest, Machinery, August 1965.

43. "Tool Engineers Handbook, Second Edition," ASTE, McGraw-Hill Book Co., Inc., New York, 1959.

44. Hawxhurst, Stephen: "Lapping--A Skilled Art Becomes a Production Process," Machinery, Vol. 58, No. 8, April 1952.

45. Taylor, J.: "Tool Wear, Life and Surface Finish," International Research in Production Engineering, ASME, 1963

46. Chandiramani, K. L., and N. H. Cook: "Investigation on the Nature of Surface Finish and its Variation with Cutting Speed," ASME, Paper No. 63-WA-30 for meeting of November 1963.

47. Bickel, E.: "The Temperature on a Turning Tool," International Research in Production Engineering, ASME, 1963.

48. Trigger, R. J.: "Temperatures in Machining and Their Importance," International Research in Production Engineering, ASME, 1963.

49. Svahn, O.: "Wear of Cutting Tools and Tool Life," International Research in Production Engineering, ASME, 1963.

50. Tarasov, L. P.: "Grinding Fundamentals--I," International Research in Production Engineering, ASME, 1963.

51. Peklenik, J.: "Grinding Fundamentals--II," International Research in Production Engineering, ASME, 1963.

52. Williams, K. J.: The Embedment of Abrasive in Lapped Surfaces, Proceedings of the Conference of Lubrication and Wear, Institution of Mechanical Engineers, London, October 1957.

53. Lichtenberger, H.: "Analysis of the Lapping Process," Abstract, Tool Engineer, Vol. 35, August 1955.

54. Samuels, L. E.: "Modern Ideas on the Mechanical Polishing of Metals," Research Applied in Industry, Vol. 13, September 1960.

55. Samuels, L. E.: The Nature of Mechanically Polished Surfaces, Technical Proceedings of the American Electroplaters' Society, 1959.

56. "Microfinishing and Precision Lapping Compounds and Accessories," Spectrum Catalog, Penn Scientific Products Co., Abington, Penna., 1955.

57. Moody, L.F.: "Friction Factors for Pipe Flow," Trans. ASME, Vol. 66, 1948, 671.

58. Shapiro, A. H.: The Dynamics and Thermodynamics of Compressible Fluid Flow, Vol. 1, Ronald Press, New York, 1953.

59. Knudsen, J. G., et al: Fluid Dynamics and Heat Transfer, McGraw-Hill Book Co., Inc., New York, 1958.

60. Dushman, S., et al: Scientific Foundations of Vacuum Technique, John Wiley and Sons, New York, 1962.

61. Roark, R. J.: Formulas for Stress and Strain, McGraw-Hill Book Co., Inc., New York, 1954.

62. Muskhelishvili, N. I.: Some Basic Problems of the Mathematical Theory of Elasticity, Groningen, Holland, N.V.P. Noordhoff, 1953.

63. Dwight, H. D.: Tables of Integrals and Other Mathematical Data, 4th Ed. MacMillan, New York, 1961.

64. Blackburn, J. F., G. Reethof, and J. L. Shearer, Editors: Fluid Power Control, The Technology Press of M.I.T. and John Wiley and Sons, Inc., New York and London, 1960.

65. Absalom, J. G.: Digital Computer Analysis of Pneumatic Pressure Regulator Dynamics, Paper presented at Conference on Propellant Tank Pressurization and Stratification, George C. Marshall Space Flight Center, Huntsville, Alabama, January 1965.

66. AFRPL-TR-65-50, Development of a High Energy Pulse Throttled Microthrust Rocket Engine, Rocket Research Corp., January 1965.

APPENDIX A

CYCLE TESTER DIGITAL COMPUTER PROGRAM AND DATA

This appendix contains a listing of the cycle tester digital computer program. Sample input and output tabulated data follow the listing for a 1.87-in./sec impact velocity condition. See Fig. 52 and 53 for corresponding CRT plots.

VALVE SEAT DYNAMIC LOADING

```
C     VALVE SEAT DYNAMIC LOADING                                        00000200
C                                                                       00000300
C                                                                       00000400
C                                                                       00000500
C                           *********NOTES********                      00000600
C                                                                       00000610
C                TEST FIXTURE IN HORIZONTAL POSITION                    00000700
C                                                                       00000800
C                TEST FIXTURE BODY CLAMPED TO RIGID BASE                00001000
C                                                                       00001100
C                BODY CLAMP HAS FLEXIBILITY,DAMPING AND FRICTION        00001200
C                                                                       00001220
C                DASHPOT FLUID HAS COMPRESSIBILITY AND INTERNAL DAMPING 00001250
C                                                                       00001300
C                SEAT LOAD CELL INSTALLED WITH PRELOAD                  00001320
C                                                                       00001400
C                           **********************                      00001500
C                                                                       00001600
C                                                                       00001700
C                                                                       00001800
C                                                                       00001900
C                                                                       00002000
C                                                                       00002100
C                                                                       00002200
C                           *****NOMENCLATURE*****                      00002300
C                                                                       00002400
C     ADASH=DASHPOT PISTON CROSS-SECTIONAL AREA (IN. SQUARED)           00002420
C     AO1,AO2,AO3=ORIFICE EFFECTIVE FLOW AREAS (IN. SQUARED)            00002440
C     AP=PISTON CROSS-SECTIONAL AREA (IN. SQUARED)                      00002480
C     C1,C2,C3,C4,C5=CONSTANTS FOR PNEUMATIC FLOW COMPUTATIONS          00002490
C     COUNT=NUMBER OF ITERATIONS FOLLOWING A DATA PRINTOUT              00002500
C     COD=DASHPOT ORIFICE FLOW COEFFICIENT                              00002510
C     CRT=SUBROUTINE FOR CATHODE RAY TUBE DISPLAY OF OUTPUT DATA        00002518
C     CV=PNEUMATIC ORIFICE FLOW COEFFICIENT                             00002520
C     DAMP1,DAMP2,DAMP3=VISCOUS DAMPING COEFFICIENTS (LB.-SEC./IN.)     00002540
C     DB=INITIAL AXIAL DISTANCE FROM POPPET TO SEAT (INCHES)            00002560
C     DNEGB=VISCOUS DAMPING COEFFICIENT OF BODY CLAMP IN -XB DIRECTION  00002580
C     DO1,DO2,DO3=ORIFICE DIAMETERS (INCHES)                            00002600
C     DO4=VALVE SEAT DIAMETER (INCHES)                                  00002620
```

VALVE SEAT DYNAMIC LOADING

```
C     DPOSB=VISCOUS DAMPING COEFFICIENT OF BODY CLAMP IN +XB DIRECTION  00002640
C     DXY1,DXY2=CRT GRID INCREMENTS FOR THE ABSCISSAE (SEC.)            00002650
C     DYY1,DYY2=CRT GRID INCREMENTS FOR THE ORDINATES (LB. AND IN.)     00002655
C     F1,F2,F3,FB=SPRING FORCES (LB.)                                   00002660
C     F30=SEAT LOAD CELL PRELOAD (LB.)                                  00002670
C     FDASH=DASHPOT FORCE (LB.)                                         00002675
C     FFB=BODY CLAMP FRICTION FORCE (LB.)                               00002680
C     FINIS=PROGRAMMED END TIME FOR A COMPUTER RUN (SEC.)               00002700
C     FLIP=PROGRAMMED TIME FOR DEACTUATING PISTON (SEC.)                00002720
C     FLOW=SUBROUTINE FOR COMPUTING PNEUMATIC WEIGHT FLOW RATES         00002730
C     FR=FR2-FR1=BODY CLAMPING FORCE (LB.)                              00002740
C     G=GRAVITATIONAL CONSTANT (IN./SEC./SEC.)                          00002760
C     ORDY1,ORDY19=MIN. AND MAX. ORDINATES FOR CRT FRAME NO. 1 GRID (LB)00002770
C     ORDY2,ORDY29=MIN. AND MAX. ORDINATES FOR CRT FRAME NO. 2 GRID (IN)00002775
C     PA=AMBIENT PRESSURE (PSIA.)                                       00002780
C     PC=CYLINDER PRESSURE (PSIA.)                                      00002800
C     PCDOT,PDDOT=RATE OF CHANGE OF PRESSURE (PSI./SEC.)                00002820
C     PD=PRESSURE CONTROLLED BY VALVE POSITION (PSIA.)                  00002840
C     PQ=DASHPOT PISTON DIFFERENTIAL PRESSURE (PSI.)                    00002860
C     PRINT=PROGRAMMED TIME FOR START OF TABULATED DATA PRINTOUT (SEC.) 00002880
C     PS=SUPPLY PRESSURE FOR PISTON (PSIA.)                             00002900
C     PS1=SUPPLY PRESSURE FOR VALVE (PSIA.)                             00002920
C     QFLO=VOLUMETRIC FLOW THROUGH DASHPOT ORIFICE (IN. CUBED/SEC.)     00002930
C     R=SPECIFIC GAS CONSTANT (IN./DEGREE RANKINE)                      00002940
C     RESET=SWITCHING FUNCTION FOR CHANGE IN ITERATION TIME INTERVAL    00002960
C     RHO=SPECIFIC WEIGHT OF DASHPOT FLUID (LB./IN. CUBED)              00002970
C     STOP=PROGRAMMED TIME FOR END OF TABULATED DATA PRINTOUT (SEC.)    00002980
C     TAPE1,TAPE2=COMPUTER TAPE NUMBERS ASSIGNED FOR CRT DATA STORAGE   00003000
C     T=TIME INCREMENT PER ITERATION (SEC.)                             00003020
C     TEMP=GAS TEMPERATURE (DEGREES RANKINE)                            00003040
C     TIME=REAL TIME (SEC.)                                             00003060
C     VC=CYLINDER VOLUME (IN. CUBED)                                    00003080
C     VCO=CYL. VOL. WHEN X1=0. (IN. CUBED)                              00003100
C     VD=VOLUME BETWEEN A03 AND VALVE FLOW AREA (IN. CUBED)             00003120
C     W1,W2,W3,WB=WEIGHTS OF PARTS (LB.)                                00003140
C     WDOT1,WDOT2,ETC.=WEIGHT FLOW RATES (LB./SEC.)                     00003160
C     X0=X1=DASHPOT PISTON DISPLACEMENT (IN.)                           00003170
C     X1=PISTON DISPLACEMENT (IN.)                                      00003180
C     X1DOT,X2DOT,X3DOT=VELOCITIES (IN./SEC.)                           00003200
```

VALVE SEAT DYNAMIC LOADING

```
C     X1DDOT,X2DDOT,X3DDOT=ACCELERATIONS (IN./SEC./SEC.)                00003220
C     X1RB=X1 RELATIVE TO XB (IN.)                                      00003240
C     X2=POPPET DISPLACEMENT (IN.)                                      00003260
C     X2R1=X2 RELATIVE TO X1 (IN.)                                      00003280
C     X2RB=X2 RELATIVE TO XB (IN.)                                      00003300
C     X3=VALVE SEAT SURFACE DISPLACEMENT (IN.)                          00003320
C     X3RB=X3 RELATIVE TO XB (IN.)                                      00003340
C     XB=TEST FIXTURE BODY DISPLACEMENT (IN.)                           00003360
C     XDOT2B=POPPET VELOCITY RELATIVE TO BODY (IN./SEC.)                00003370
C     XIMBED=SEAT CONTACT COMPRESSION (IN.)                             00003380
C     XK=RATIO OF GAS SPECIFIC HEATS                                    00003400
C     XLIM=NUMBER OF ITERATIONS BETWEEN DATA PRINTOUTS                  00003420
C     XMASS1,XMASS2,XMASS3=MASSES OF PARTS (LB.-SEC. SQUARED/IN.)       00003440
C     XTIME=REAL TIME FROM RESET OF TIME INCREMENT TO END OF RUN (SEC.) 00003450
C     YDASH=DASHPOT EQUIVALENT SPRING RATE (LB./IN.)                    00003460
C     YR=BODY CLAMP COMBINED SPRING RATE=YRNEG+YRPOS (LB./IN.)          00003480
C     YRNEG=BODY CLAMP SPRING RATE IN -XB DIRECTION (LB./IN.)           00003500
C     YRPOS=BODY CLAMP SPRING RATE IN +XB DIRECTION (LB./IN.)           00003520
C     YS1,YS2,YS3,YSB=SPRING RATES (LB./IN.)                            00003540
C                                                                       00007600
C                                                                       00007700
      COMMON C1,C2,C3,C4,C5,RCR,SCR,DB                                  00007800
      COMMON ORDY1,ORDY19,DYY1,ORDY2,ORDY29,DYY2,DXY1,DXY2              00007810
C                                                                       00007850
      DIMENSION X(100),Y1(100,4),Y2(100,2)                              00007900
      DIMENSION ARRAY(360)                                              00007950
C                                                                       00008000
C     READ INPUT DATA FROM DATA CARDS                                   00008050
    1 READ INPUT TAPE 5,10,XK,R,TEMP,DO1,DO2,FLIP                       00008100
      READ INPUT TAPE 5,10,W1,W2,W3,YS1,YS2,YS3,DB,T,PRINT,STOP,FINIS   00008200
      READ INPUT TAPE 5,10,DAMP1,DAMP2,DAMP3,DAMPD,YDASH,YSB            00008300
      READ INPUT TAPE 5,10,DNEGB,DPOSB,YRNEG,YRPOS,WB,FFB               00008400
      READ INPUT TAPE 5,10,DO3,DO4,PS,PS1,F30,FBO                       00008500
      READ INPUT TAPE 5,10,RHO,COD,DOD,ADASH,XTIME                      00008600
C                                                                       00008700
C     READ INPUT DATA TO DEFINE CATHODE RAY TUBE DISPLAY GRID           00008710
      READ INPUT TAPE 5,10,ORDY1,ORDY19,DYY1,ORDY2,ORDY29,DYY2,DXY1,DXY200008715
C                                                                       00008720
C     LISTING OF FORMAT STATEMENTS                                      00008750
```

```
   10 FORMAT(6E12.5)                                                    00008800
   19 FORMAT(1H1 30H        ******INPUT DATA******//)                   00008900
   20 FORMAT(15X2HW1 15X2HW2 15X2HW3 14X3HYS1 14X3HYS2 14X3HYS3/6F17.3//00009000
     115X2HDB 16X1HT 12X5HPRINT 13X4HSTOP 12X5HFINIS/5F17.6//)          00009100
   22 FORMAT(/15X2HXK 16X1HR 13X4HTEMP 14X3HD01 14X3HD02 13X4HFLIP/6F17.00009200
     15//)                                                              00009300
   25 FORMAT(12X5HDAMP1 12X5HDAMP2 12X5HDAMP3 12X5HDAMPD 12X5HYDASH 14X300009400
     1HYSB/6F17.2//)                                                    00009500
   29 FORMAT(14X3HYSB 15X2HWB/2F17.2//)                                 00009600
   35 FORMAT(1H1 3X4HTIME 6X2HPC 6X2HPD 8X4HX1RB 8X4HX2R1 6X6HXIMBED 8X400009700
     1HX3RB 10X2HXB 6X2HF1 6X2HF2 6X2HF3 1X5HX2DOT 1X5HX3DOT)           00009800
   37 FORMAT(14X3HD03 14X3HD04 15X2HPS 14X3HPS1 14X3HF30 14X3HFB0/6F17.300009900
     1//)                                                               00009950
   40 FORMAT(F8.6,2F8.2,5F12.8,3F8.2,2F6.3)                             00010000
   43 FORMAT(12X5HDNEGB 12X5HDPOSB 12X5HYRNEG 12X5HYRPOS 15X2HWB 14X3HFF00010100
     1B/6F17.2//)                                                       00010200
   45 FORMAT(14X3HRHO 14X3HCOD 14X3HDOD 12X5HADASH 12X5HXTIME/5F17.4//) 00010210
   47 FORMAT(12X5HORDY1 11X6HORDY19 13X4HDYY1 12X5HORDY2 11X6HORDY29 13X00010220
     14HDYY2/6F17.3//13X4HDXY1 13X4HDXY2/2F17.4//)                      00010225
   65 FORMAT(1H1 4X4HTIME 6X2HPC 6X2HPD 6X2HPQ 8X4HX1RB 8X4HX2R1 6X6HXIM00010300
     1BED 8X4HX3RB 10X2HXB//(                                           00010310
     2F9.6,3F8.2,5F12.8))                                               00010312
   66 FORMAT(F9.6,5F8.2,5F8.3)                                          00010315
   67 FORMAT(1H1 4X4HTIME 3X5HFDASH 6X2HF1 6X2HF2 6X2HF3 6X2HFR 3X5HX1D000010317
     1T 3X5HX2DOT 3X5HX3DOT 3X5HXBDOT 2X6HXDOT2B//)                     00010318
C                                                                       00010400
C     PRINT INPUT DATA TABULATION                                       00010450
      WRITE OUTPUT TAPE 6,19                                            00010500
      WRITE OUTPUT TAPE 6,22,XK,R,TEMP,D01,D02,FLIP                     00010600
      WRITE OUTPUT TAPE 6,20,W1,W2,W3,YS1,YS2,YS3,DB,T,PRINT,STOP,FINIS 00010700
      WRITE OUTPUT TAPE 6,25,DAMP1,DAMP2,DAMP3,DAMPD,YDASH,YSB          00010800
      WRITE OUTPUT TAPE 6,43,DNEGB,DPOSB,YRNEG,YRPOS,WB,FFB             00010900
      WRITE OUTPUT TAPE 6,37,D03,D04,PS,PS1,F30,FB0                     00011000
      WRITE OUTPUT TAPE 6,45,RHO,COD,DOD,ADASH,XTIME                    00011010
      WRITE OUTPUT TAPE 6,47,ORDY1,ORDY19,DYY1,ORDY2,ORDY29,DYY2,DXY1,DX00011020
     1Y2                                                                00011025
C                                                                       00011100
C     SET INITIAL CONDITIONS FOR PROGRAM VARIABLES                      00011200
      TIME=0.                                                           00011300
      FDASH=0.                                                          00011350
      PA=14.7                                                           00011400
      PQ=1.                                                             00011410
      PQDOT=0.                                                          00011420
      PI=3.1415927                                                      00011500
      PI4=PI/4.                                                         00011600
      CV=.67                                                            00011700
      X0=0.                                                             00011750
      X1=0.                                                             00011800
      X1DOT=0.                                                          00011900
      X1DOT1=0.                                                         00012000
      X1DDOT=0.                                                         00012100
      XP=0.                                                             00012200
      XPDOT=0.                                                          00012300
      XPDOT1=0.                                                         00012400
      XPDDOT=0.                                                         00012500
      RESET=0.                                                          00012600
      XDEL=.0005                                                        00012700
      X2=0.                                                             00012800
      X2DOT=0.                                                          00012900
      X2DOT1=0.                                                         00013000
      X2DDOT=0.                                                         00013100
      XB=0.                                                             00013200
      XBDOT=0.                                                          00013300
      XBDOT1=0.                                                         00013400
      XBDDOT=0.                                                         00013500
      X3=0.                                                             00013600
      X3DOT=0.                                                          00013700
      X3DOT1=0.                                                         00013800
      X3DDOT=0.                                                         00013900
      WDOT1=0.                                                          00014000
      WDOT2=0.                                                          00014100
      WDOT3=0.                                                          00014200
      WDOT4=0.                                                          00014300
      QFLO=0.                                                           00014330
      QFLO1=0.                                                          00014335
      PC=PA                                                             00014400
      PCDOT=0.                                                          00014500
      PDDOT=0.                                                          00014600
      FBO=FBO-YSB*DB                                                    00014800
      FB=FBO                                                            00014900
      F2=0.                                                             00015000
      AP=1.687                                                          00015200
      AD=PI4*D04**2                                                     00015300
      A01=CV*PI4*D01**2                                                 00015400
      A02=CV*PI4*D02**2                                                 00015500
      A03=CV*PI4*D03**2                                                 00015600
      AOD=PI4*DOD**2                                                    00015650
      ACCEL1=0.                                                         00015700
      ACCEL2=0.                                                         00015800
      ACCEL3=0.                                                         00015900
      ACCELB=0.                                                         00016000
      VD=1.                                                             00016100
      VCO=1.39+1.58*DB                                                  00016200
      VC=VCO                                                            00016300
      AV=CV*PI*D04*(DB+X3-X2)                                           00016400
      AFLIP=0.                                                          00016500
      PD=PA                                                             00016600
      TFINIS=FINIS-T                                                    00016700
      F10=0.                                                            00016800
      F1=F10                                                            00016850
      F3=F30                                                            00016900
      FR=0.                                                             00017000
      YSR=YRNEG+YRPOS                                                   00017100
      DAMPB=DNEGB+DPOSB                                                 00017200
      X1RB=MAX1F(X1-XB,0.)                                              00017210
      X2RB=X2-XB                                                        00017215
      X2R1=X2-X1                                                        00017220
      XIMBED=X2-DB-X3                                                   00017230
      XIMBED=MAX1F(XIMBED,0.)                                           00017240
      X3RB=MAX1F(X3-XB,0.)                                              00017250
C                                                                       00017300
C     COMPUTE PROGRAM CONSTANTS                                         00017400
      G=386.                                                            00017500
      C1=2.*G/12.*XK/(XK-1.)                                            00017600
      C2=2./XK                                                          00017700
      C3=(XK+1.)/XK                                                     00017800
      C4=SQRTF(R/12.*TEMP)                                              00017900
      C5=XK                                                             00018000
      RCR=(2./(XK+1.))**(XK/(XK-1.))                                    00018100
      SCR=SQRTF(G/12.*XK*(2./(XK+1.))**((XK+1.)/(XK-1.)))               00018200
      RT=R*TEMP                                                         00018300
      C5RT=C5*RT                                                        00018400
      T2=T/2.                                                           00018500
      T22=T**2/2.                                                       00018600
      XMASS1=W1/G                                                       00019000
      XMASS2=W2/G                                                       00019100
      XMASS3=W3/G                                                       00019200
      XMASSB=WB/G                                                       00019300
      XMASSP=(W1+W2)/G                                                  00019400
C                                                                       00019500
C     SET INITIAL CONDITIONS FOR CRT AND PRINTOUT ROUTINES              00019600
      JQQ=10.                                                           00019650
      NN=0                                                              00019700
      I=0                                                               00019800
      IK=0                                                              00019850
      XN=0                                                              00019900
      M=1                                                               00020000
      TMIN=TIME                                                         00020100
      TMIN1=0.                                                          00020150
      TAPE1=8.                                                          00020200
      TAPE2=9.                                                          00020300
      IT1=TAPE1                                                         00020400
      IT2=TAPE2                                                         00020500
      REWIND IT1                                                        00020600
      REWIND IT2                                                        00020700
      XLIM=10.                                                          00020800
      STOP=MIN1F(STOP,FINIS-3.*T)                                       00020850
      COUNT=0.                                                          00020900
      WRITE OUTPUT TAPE 6,67                                            00021200
C                                                                       00021310
C                                                                       00021330
C                                                                       00021340
C     ITERATIVE COMPUTATION LOOP                                        00021370
C     ********* *********** ****                                        00021375
C                                                                       00021400
C     COMPUTE GAS FLOW RATES                                            00021500
```

VALVE SEAT DYNAMIC LOADING

```
  100 WDOT1=FLOW(PS,PC,A01)
      WDOT2=FLOW(PC,PA,AFLIP)
      WDOT3=FLOW(PS1,PD,A03)
      WDOT4=FLOW(PD,PA,AV)
C
C     COMPUTE PNEUMATIC PRESSURIZING COEFFICIENTS
      C5RTC=C5RT/VC
      C5RTD=C5RT/VD
C
C     COMPUTE RATES OF CHANGE OF PRESSURES
      PCDOT=C5RTC*(WDOT1-WDOT2-PC*AP*X1DOT/RT)
      PDDOT=C5RTD*(WDOT3-WDOT4)
C
C     COMPUTE PRESSURES
      PC=PC+PCDOT*T
      PD=PD+PDDOT*T
      PC=MIN1F(MAX1F(PC,0.),PS)
      PD=MIN1F(MAX1F(PD,PA),PS1)
C
C     COMPUTE COMBINED PISTON AND POPPET ACCELERATION,
C     VELOCITY AND DISPLACEMENT
      IF(RESET-0.9)111,212,212
  111 IF(X2RB-DB+XDEL)211,212,212
  211 XPDDOT=((PC-PA)*AP-FDASH-FB-(PD-PA)*AD-DAMPD*(XPDOT-XBDOT))/XMASSP
      XPDOT=MAX1F(XPDOT1+XPDDOT*T,0.)
      XP=MAX1F(XP+XPDOT1*T+XPDDOT*T22,XB)
      X1=XP
      X2=XP
      X1DOT=XPDOT
      X2DOT=XPDOT
      X1DDOT=XPDDOT
      X2DDOT=XPDDOT
      X3=XB
      X3DOT=XBDOT
      X3DDOT=XBDDOT
C
C     COMPUTE DASHPOT FLOW, PRESSURE AND FORCE
      QFLO=COD*ADD*SQRTF(2.*G*PQ/RHO)
      PQDOT=YDASH/ADASH*(X1DOT-XBDOT-QFLO/ADASH)
      PQ=MAX1F(1.,PQ+PQDOT*T)                                           00024470
      FDASH=PQ*ADASH                                                    00024472
      GO TO 215                                                         00024500
C                                                                       00024550
  212 RESET=RESET+1.                                                    00024600
      IF(RESET-1.1)213,213,214                                          00024700
  213 T=.0000001                                                        00024800
      T2=T/2.                                                           00024900
      T22=T**2/2.                                                       00025000
      XLIM=100.                                                         00025100
      TMIN1=TIME                                                        00025150
      FINIS=TIME+XTIME                                                  00025170
      STOP=MIN1F(STOP,FINIS-3.*T)                                       00025180
      TFINIS=FINIS-3.*T                                                 00025200
  214 RESET=MIN1F(RESET,2.)                                             00025300
C                                                                       00025400
C                                                                       00025410
C     COMPUTE PISTON ACCELERATION, VELOCITY AND DISPLACEMENT            00025450
      X1DDOT=((PC-PA)*AP-DAMP1*X1DOT+DAMP1*X2DOT-F1-FDASH-FB-DAMPD*(X1DO00025500
     1T-XBDOT))/XMASS1                                                  00025510
      X1DDOT=(X1DDOT+ACCEL1)/2.                                         00025700
      X1DOT=X1DOT1+X1DDOT*T                                             00025800
      X1=X1+X1DOT1*T+X1DDOT*T22                                         00025900
      X1=MAX1F(X1,XB)                                                   00026000
      IF(X1RB)103,103,108                                               00026100
  103 X1DOT=0.                                                          00026200
      X1DDOT=0.                                                         00026300
  108 CONTINUE                                                          00026400
C                                                                       00026410
C     COMPUTE DASHPOT FLOW, PRESSURE AND FORCE                          00026415
      QFLO=COD*AOD*SQRTF(2.*G*PQ/RHO)                                   00026440
      PQDOT=YDASH/ADASH*(X1DOT-XBDOT-QFLO/ADASH)                        00026460
      PQ=MAX1F(1.,PQ+PQDOT*T)                                           00026465
      FDASH=PQ*ADASH                                                    00026472
C                                                                       00026500
C     COMPUTE SPRING FORCES                                             00026550
      F1=F10+YS1*(X1-X2)                                                00026600
      FB=FB0+YSB*X1RB                                                   00026700
C                                                                       00026800
```

```
C     COMPUTE POPPET ACCELERATION, VELOCITY AND DISPLACEMENT            00026850
      X2DDOT=(F1-(PD-PA)*AD-DAMP1*X2DOT+DAMP1*X1DOT+F2/F2*(DAMP2*X3DOT-D00026900
     1AMP2*X2DOT)-F2)/XMASS2                                            00027000
      X2DDOT=(X2DDOT+ACCEL2)/2.                                         00027100
      X2DOT=X2DOT1+X2DDOT*T                                             00027200
      X2=X2+X2DOT1*T+X2DDOT*T22                                         00027300
C                                                                       00027400
C     COMPUTE SPRING FORCES                                             00027450
      F1=F10+YS1*(X1-X2)                                                00027500
      F2=YS2*(X2-DB-X3)                                                 00027600
      F2=MAX1F(F2,0.)                                                   00027700
C                                                                       00027800
C                                                                       00027900
C     COMPUTE SEAT ACCELERATION, VELOCITY AND DISPLACEMENT              00027950
      X3DDOT=(F2-F3-DAMP3*X3DOT+DAMP3*XBDOT-F2/F2*(DAMP2*X3DOT-DAMP2*X2D00028100
     1OT))/XMASS3                                                       00028200
      X3DDOT=(X3DDOT+ACCEL3)/2.                                         00028300
      X3DOT=X3DOT1+X3DDOT*T                                             00028400
      X3=X3+X3DOT1*T+X3DDOT*T22                                         00028500
  203 CONTINUE                                                          00029000
C                                                                       00029100
C     COMPUTE SPRING FORCES                                             00029150
      F3=F30+YS3*(X3-XB)                                                00029200
      F2=YS2*(X2-DB-X3)                                                 00029300
      F2=MAX1F(F2,0.)                                                   00029400
C                                                                       00029500
  215 X1RB=MAX1F(X1-XB,0.)                                              00029550
      FB=FB0+YSB*X1RB                                                   00029552
C                                                                       00029560
C     COMPUTE BODY ACCELERATION, VELOCITY AND DISPLACEMENT              00029600
      IF(X1RB)280,280,281                                               00029700
  280 XBDDOT=(F2-FR+(PD-PA)*AD-FFB*ABSF(XBDOT)/XBDOT+DAMP3*X3DOT-(DAMP3+00029800
     1DAMPB)*XBDOT+FDASH+DAMPD*(X1DOT-XBDOT))/XMASSB                    00029900
      GO TO 282                                                         00030000
  281 XBDDOT=(F2-FR+(PD-PA)*AD-FFB*ABSF(XBDOT)/XBDOT+DAMP3*X3DOT-(DAMP3+00030100
     1DAMPB)*XBDOT-(PC-PA)*AP+FB+FDASH+DAMPD*(X1DOT-XBDOT))/XMASSB      00030200
  282 CONTINUE                                                          00030300
      XBDDOT=(XBDDOT+ACCELB)/2.                                         00030400
      XBDOT=XBDOT1+XBDDOT*T                                             00030500
      XB=XB+XBDOT1*T+XBDDOT*T22                                         00030600
C                                                                       00030700
C     COMPUTE MISCELLANEOUS VARIABLES                                   00030750
      FR=YSR*XB                                                         00030800
      VC=VC0+AP*X1RB                                                    00031000
      AV=CV*PI*D04*(DB+X3-X2)                                           00031100
      X1RB=MAX1F(X1-XB,0.)                                              00031200
      FB=FB0+YSB*X1RB                                                   00031300
      X2RB=X2-XB                                                        00031400
      X2R1=X2-X1                                                        00031500
      XIMBED=X2-DB-X3                                                   00031600
      XIMBED=MAX1F(XIMBED,0.)                                           00031700
  217 X3RB=X3-XB                                                        00032450
      F3=F30+YS3*X3RB                                                   00032460
C                                                                       00032470
C     COMPUTE POPPET VELOCITY RELATIVE TO BODY                          00032480
      XDOT2B=X2DOT-XBDOT                                                00032485
C                                                                       00032500
C     REIDENTIFY AND STORE VELOCITY AND ACCELERATION VALUES             00032550
      X1DOT1=X1DOT                                                      00032600
      X2DOT1=X2DOT                                                      00032700
      X3DOT1=X3DOT                                                      00032800
      XBDOT1=XBDOT                                                      00032900
      XPDOT1=XPDOT                                                      00033000
      ACCEL1=X1DDOT                                                     00033100
      ACCEL2=X2DDOT                                                     00033200
      ACCEL3=X3DDOT                                                     00033300
      ACCELB=XBDDOT                                                     00033400
C                                                                       00033700
C     INCREMENT TIME                                                    00033800
      TIME=TIME+T                                                       00033850
C                                                                       00033860
C     STORE AND PRINT COMPUTED OUTPUT DATA                              00033900
      COUNT=COUNT+1.                                                    00034000
      X(M)=TIME                                                         00034150
      IF(XMODF(M,JQQ))551,552,551                                       00034200
  551 DO 5510 JJJJ=1,4                                                  00034300
 5510 Y1(M,JJJJ)=-1000                                                  00034400
      DO 5520 JJJJ=1,2                                                  00034500
 5520 Y2(M,JJJJ)=-1000                                                  00034600
      GO TO 553                                                         00034700
  552 CONTINUE                                                          00034800
      Y1(M,1)=F1                                                        00034900
      Y1(M,2)=F2                                                        00035000
      Y1(M,3)=F3-F30                                                    00035100
      Y1(M,4)=0.                                                        00035200
      Y2(M,1)=DB-X2RB                                                   00035300
      Y2(M,2)=XB                                                        00035400
  553 XN=XN+1.                                                          00035500
      IF(M-100)556,555,555                                              00035600
  555 WRITE TAPE IT1,X,Y1                                               00035700
C                                                                       00035800
      M=0                                                               00035900
      NN=NN+1                                                           00036000
      WRITE TAPE IT2,X,Y2                                               00036100
C                                                                       00036200
  556 M=M+1                                                             00036300
      IF(COUNT-XLIM)432,562,562                                         00036400
  562 COUNT=0.                                                          00036500
      IF(TIME-PRINT)432,560,560                                         00036600
  560 IF(TIME-STOP)558,432,432                                          00036700
  558 CONTINUE                                                          00036800
C                                                                       00037000
      I=I+1                                                             00037010
      IK=9*(I-1)+1                                                      00037020
      ARRAY(IK)=TIME                                                    00037030
      ARRAY(IK+1)=PC                                                    00037040
      ARRAY(IK+2)=PD                                                    00037050
      ARRAY(IK+3)=PQ                                                    00037060
      ARRAY(IK+4)=X1RB                                                  00037070
      ARRAY(IK+5)=X2R1                                                  00037080
      ARRAY(IK+6)=XIMBED                                                00037090
      ARRAY(IK+7)=X3RB                                                  00037100
      ARRAY(IK+8)=XB                                                    00037110
      WRITE OUTPUT TAPE 6,66,TIME,FDASH,F1,F2,F3,FR,X1DOT,X2DOT,X3DOT,XB00037180
     1DOT,XDOT2B                                                        00037182
C                                                                       00037190
  432 IF(TIME-FLIP)317,318,318                                          00037200
  317 AFLIP=0.                                                          00037300
      GO TO 319                                                         00037400
  318 AFLIP=AO2                                                         00037500
      AO1=0.                                                            00037600
C                                                                       00037700
C                                                                       00037750
  319 IF(TIME-TFINIS)489,434,434                                        00037800
C                                                                       00037810
  489 IF(I-40)100,487,487                                               00037820
C                                                                       00037825
  487 WRITE OUTPUT TAPE 6,65,ARRAY                                      00037830
      I=0                                                               00037840
      WRITE OUTPUT TAPE 6,67                                            00037845
      GO TO 100                                                         00037850
C                                                                       00037860
  434 WRITE TAPE IT1,X,Y1                                               00037900
      WRITE TAPE IT2,X,Y2                                               00038000
      END FILE IT1                                                      00038200
      END FILE IT2                                                      00038300
      CALL CRT(XN,NN,TIME,TMIN,TMIN1,Y1,Y2,IT1,IT2)                     00038400
      L=IK+8                                                            00038440
      WRITE OUTPUT TAPE 6,65,(ARRAY(I),I=1,L)                           00038450
      GO TO 1                                                           00038500
      END(1,0,0,0,0,0,1,0,0,1,0,0,0,0,0)
```

FUNCTION FOR SONIC OR SUBSONIC FLOW OF GAS THRU ORIFICES

```
C     FUNCTION FOR SONIC OR SUBSONIC FLOW OF GAS THRU ORIFICES           00070000
      FUNCTION FLOW(P1,P2,A)                                             00070100
      COMMON C1,C2,C3,C4,C5,RCR,SCR                                      00070200
      IF(A)325,325,330                                                   00070300
  325 FLOW=0.                                                            00070400
      RETURN                                                             00070500
  330 RR=MIN1F(P1,P2)/MAX1F(P1,P2)                                       00070600
      IF(RR-RCR)340,340,345                                              00070700
  345 S=SQRTF(C1*ABSF(RR**C2-RR**C3))                                    00070800
      GO TO 350                                                          00070900
  340 S=SCR                                                              00071000
  350 FLOW=SIGNF(A*MAX1F(P1,P2)*S/C4,(P1-P2))                            00071100
      RETURN                                                             00071200
      END(1,0,0,0,0,0,1,0,0,1,0,0,0,0,0)
      SUBROUTINE CRT(XN,NN,TIME,TMIN,TMIN1,Y1,Y2,IT1,IT2)                00054000
C                                                                        00054100
C                                                                        00054300
      DIMENSION X(100),Y1(100,4),Y2(100,2)                               00054400
C                                                                        00054500
      DIMENSION JCHAR(4)                                                 00054600
C                                                                        00054700
      COMMON C1,C2,C3,C4,C5,RCR,SCR,DB                                   00054800
      COMMON ORDY1,ORDY19,DYY1,ORDY2,ORDY29,DYY2,DXY1,DXY2               00054850
C                                                                        00055100
      II=100                                                             00055200
C                                                                        00055202
C                                                                        00055220
      TA1=IT1                                                            00055222
      TA2=IT2                                                            00055224
C                                                                        00055226
C                                                                        00055244
      CALL CAMRAV(9)                                                     00055300
      JCHAR(1)=42                                                        00055400
      JCHAR(2)=55                                                        00055500
      JCHAR(3)=38                                                        00055600
      JCHAR(4)=42                                                        00055650
C     JCHARS=DOT42,SQUARE63,CIRCLE38,CROSS55                             00055700
      REWIND IT1                                                         00055800
      REWIND IT2                                                         00055900
      CALL GRIDIV(1,TMIN1,TIME,ORDY1,ORDY19,DXY1,DYY1,0,2,-2,-2,5,4)     00056000
      NL=XN-FLOATF(NN*II)                                                00056100
      CALL APRNTV(0,-13,-11,11HFORCES, LB.,0,600)                        00056200
      CALL PRINTV(-13,13HTIME, SECONDS,450,0)                            00056300
      IF(NN)110,110,40                                                   00056400
   40 DO 100 I=1,NN                                                      00056500
      READ TAPE IT1,X,Y1                                                 00056600
      DO 50 J=1,4                                                        00056700
   50 CALL APLOTV(II,X,Y1(1,J),1,1,1,JCHAR(J),IERR)                      00056800
  100 CONTINUE                                                           00056900
  110 READ TAPE IT1,X,Y1                                                 00057000
      DO 150 J=1,4                                                       00057100
  150 CALL APLOTV(NL,X,Y1(1,J),1,1,1,JCHAR(J),IERR)                      00057200
      REWIND IT1                                                         00057300
      CALL GRID1V(1,TMIN,TIME,ORDY2,ORDY29,DXY2,DYY2,0,2,-2,-2,4,4)
      CALL LABLV(XN,800,1020,5,1,5)
      CALL PRINTV(6,6HPOINTS,850,1020)
      CALL APRNTV(0,-13,-18,18HDISPLACEMENTS, IN.,0,650)
      CALL PRINTV(-13,13HTIME, SECONDS,450,0)
      DO   200    I=1,NN
      READ TAPE IT2,X,Y2
      DO 200 J=1,2
  200 CALL APLOTV(II,X,Y2(1,J),1,1,1,JCHAR(J),IERR)
      READ TAPE IT2,X,Y2
      DO 300 J=1,2
  300 CALL APLOTV(NL,X,Y2(1,J),1,1,1,JCHAR(J),IERR)
      REWIND IT2
      RETURN
      END(1,0,0,0,0,0,1,0,0,1,0,0,0,0,0)
```

```
******INPUT DATA******


       XK             R             TEMP            D01             D02            FLIP
  1.40000     662.40000     530.00000        0.29700         0.20700         0.20000

       W1            W2               W3            YS1             YS2             YS3
    2.980         0.476            0.432    5040000.000     7000000.000    19300000.000

       DB             T            PRINT           STOP           FINIS
 0.010000      0.000005         0.000000        0.200000        0.200000

    DAMP1         DAMP2            DAMP3          DAMPD           YDASH             YSB
    12.00          5.57             7.15           5.00       155000.00           31.40

    DNEGB         DPOSB            YRNEG          YRPOS              WB             FFB
     3.68          3.68          1000.00        1000.00           65.00            1.00

      D03           D04               PS            PS1             F30             FBO
    0.014         0.446          156.000         20.000           0.000          13.000

      RHO           COD              DOD          ADASH           XTIME
   0.0313        0.6700           0.0266         0.5980          0.0030
```

```
     TIME    FDASH      F1       F2       F3       FR    X1DOT   X2DOT   X3DOT   XBDOT  XDOT2B

 0.000050     0.60     0.00     0.00    -0.00     0.00   0.000   0.000  -0.000   0.000  -0.000
 0.000100     0.60     0.00     0.00    -0.00     0.00   0.000   0.000  -0.000   0.000  -0.000
 0.000150     0.60     0.00     0.00     0.00     0.00   0.001   0.001  -0.000  -0.000   0.001
 0.000200     0.60     0.00     0.00     0.07    -0.00   0.023   0.023  -0.001  -0.001   0.024
 0.000250     0.60     0.00     0.00     0.26    -0.00   0.071   0.071  -0.003  -0.003   0.074
 0.000300     0.73     0.00     0.00     0.59    -0.00   0.144   0.144  -0.006  -0.006   0.150
 0.000350     1.34     0.00     0.00     1.03    -0.00   0.239   0.239  -0.010  -0.011   0.250
 0.000400     2.47     0.00     0.00     1.57    -0.00   0.354   0.354  -0.016  -0.017   0.371
 0.000450     4.17     0.00     0.00     2.19    -0.00   0.485   0.485  -0.022  -0.023   0.508
 0.000500     6.51     0.00     0.00     2.87    -0.01   0.628   0.628  -0.029  -0.030   0.658
 0.000550     9.54     0.00     0.00     3.59    -0.01   0.779   0.779  -0.037  -0.038   0.816
 0.000600    13.28     0.00     0.00     4.33    -0.02   0.933   0.933  -0.045  -0.045   0.979
 0.000650    17.73     0.00     0.00     5.07    -0.02   1.088   1.088  -0.052  -0.053   1.141
 0.000700    22.86     0.00     0.00     5.79    -0.03   1.238   1.238  -0.060  -0.060   1.298
 0.000750    28.63     0.00     0.00     6.47    -0.03   1.381   1.381  -0.067  -0.067   1.448
 0.000800    34.95     0.00     0.00     7.09    -0.04   1.513   1.513  -0.073  -0.074   1.587
 0.000850    41.75     0.00     0.00     7.65    -0.05   1.632   1.632  -0.079  -0.079   1.711
 0.000900    48.91     0.00     0.00     8.12    -0.05   1.735   1.735  -0.084  -0.084   1.820
 0.000950    56.33     0.00     0.00     8.51    -0.06   1.822   1.822  -0.088  -0.088   1.910
 0.001000    63.88     0.00     0.00     8.81    -0.07   1.892   1.892  -0.091  -0.091   1.983
 0.001050    71.46     0.00     0.00     9.02    -0.08   1.945   1.945  -0.093  -0.094   2.038
 0.001100    78.95     0.00     0.00     9.14    -0.09   1.981   1.981  -0.095  -0.095   2.075
 0.001150    86.24     0.00     0.00     9.19    -0.10   2.001   2.001  -0.095  -0.095   2.097
 0.001200    93.26     0.00     0.00     9.16    -0.11   2.009   2.009  -0.095  -0.095   2.104
 0.001250    99.94     0.00     0.00     9.08    -0.12   2.004   2.004  -0.094  -0.094   2.098
 0.001300   106.21     0.00     0.00     8.95    -0.13   1.991   1.991  -0.093  -0.093   2.083
 0.001350   112.04     0.00     0.00     8.78    -0.14   1.971   1.971  -0.091  -0.091   2.062
 0.001400   117.42     0.00     0.00     8.59    -0.15   1.946   1.946  -0.089  -0.089   2.035
 0.001450   122.36     0.00     0.00     8.39    -0.16   1.920   1.920  -0.087  -0.087   2.007
 0.001500   126.87     0.00     0.00     8.19    -0.16   1.895   1.895  -0.085  -0.085   1.980
 0.001550   130.98     0.00     0.00     8.01    -0.17   1.872   1.872  -0.083  -0.083   1.955
 0.001600   134.76     0.00     0.00     7.85    -0.18   1.854   1.854  -0.081  -0.081   1.935
 0.001650   138.25     0.00     0.00     7.72    -0.19   1.841   1.841  -0.080  -0.080   1.921
 0.001700   141.51     0.00     0.00     7.62    -0.20   1.834   1.834  -0.079  -0.079   1.913
 0.001750   144.62     0.00     0.00     7.56    -0.21   1.835   1.835  -0.078  -0.078   1.913
 0.001800   147.63     0.00     0.00     7.53    -0.21   1.842   1.842  -0.078  -0.078   1.920
 0.001850   150.61     0.00     0.00     7.54    -0.22   1.857   1.857  -0.078  -0.078   1.935
 0.001900   153.61     0.00     0.00     7.58    -0.23   1.877   1.877  -0.079  -0.079   1.956
 0.001950   156.68     0.00     0.00     7.65    -0.24   1.903   1.903  -0.079  -0.079   1.982
 0.002000   159.85     0.00     0.00     7.74    -0.24   1.933   1.933  -0.080  -0.080   2.013
```

```
   TIME       PC       PD       PQ        X1RB         X2R1        XIMBED        X3RB          XB

 0.000050    17.57    14.70     1.00   0.00000000   0.00000000   0.00000000  -0.00000000   0.00000000
 0.000100    20.45    14.70     1.00   0.00000000   0.00000000   0.00000000  -0.00000000   0.00000000
 0.000150    23.32    14.70     1.00   0.00000001   0.00000000   0.00000000   0.00000000   0.00000000
 0.000200    26.20    14.70     1.00   0.00000052   0.00000000   0.00000000   0.00000000  -0.00000001
 0.000250    29.07    14.70     1.00   0.00000284   0.00000000   0.00000000   0.00000001  -0.00000016
 0.000300    31.94    14.70     1.22   0.00000833   0.00000000   0.00000000   0.00000003  -0.00000032
 0.000350    34.82    14.70     2.25   0.00001824   0.00000000   0.00000000   0.00000005  -0.00000075
 0.000400    37.69    14.70     4.13   0.00003370   0.00000000   0.00000000   0.00000008  -0.00000143
 0.000450    40.56    14.70     6.98   0.00005563   0.00000000   0.00000000   0.00000011  -0.00000242
 0.000500    43.43    14.70    10.89   0.00008474   0.00000000   0.00000000   0.00000015  -0.00000374
 0.000550    46.31    14.70    15.96   0.00012158   0.00000000   0.00000000   0.00000019  -0.00000543
 0.000600    49.18    14.70    22.21   0.00016645   0.00000000   0.00000000   0.00000022  -0.00000751
 0.000650    52.04    14.70    29.65   0.00021944   0.00000000   0.00000000   0.00000026  -0.00000996
 0.000700    54.91    14.70    38.24   0.00028044   0.00000000   0.00000000   0.00000030  -0.00001281
 0.000750    57.78    14.70    47.87   0.00034914   0.00000000   0.00000000   0.00000034  -0.00001599
 0.000800    60.65    14.70    58.45   0.00042506   0.00000000   0.00000000   0.00000037  -0.00001953
 0.000850    63.51    14.70    69.81   0.00050757   0.00000000   0.00000000   0.00000040  -0.00002336
 0.000900    66.37    14.70    81.79   0.00059590   0.00000000   0.00000000   0.00000042  -0.00002746
 0.000950    69.23    14.70    94.19   0.00068923   0.00000000   0.00000000   0.00000044  -0.00003178
 0.001000    72.09    14.70   106.83   0.00078665   0.00000000   0.00000000   0.00000046  -0.00003628
 0.001050    74.95    14.70   119.49   0.00088726   0.00000000   0.00000000   0.00000047  -0.00004091
 0.001100    77.81    14.70   132.02   0.00099017   0.00000000   0.00000000   0.00000047  -0.00004562
 0.001150    80.67    14.70   144.22   0.00109453   0.00000000   0.00000000   0.00000048  -0.00005037
 0.001200    83.53    14.70   155.96   0.00119960   0.00000000   0.00000000   0.00000047  -0.00005513
 0.001250    86.38    14.70   167.12   0.00130469   0.00000000   0.00000000   0.00000047  -0.00005986
 0.001300    89.23    14.70   177.60   0.00140927   0.00000000   0.00000000   0.00000046  -0.00006452
 0.001350    92.06    14.70   187.36   0.00151292   0.00000000   0.00000000   0.00000045  -0.00006911
 0.001400    94.89    14.70   196.36   0.00161535   0.00000000   0.00000000   0.00000045  -0.00007361
 0.001450    97.69    14.70   204.61   0.00171641   0.00000000   0.00000000   0.00000043  -0.00007803
 0.001500   100.47    14.70   212.15   0.00181608   0.00000000   0.00000000   0.00000042  -0.00008229
 0.001550   103.22    14.70   219.04   0.00191444   0.00000000   0.00000000   0.00000042  -0.00008648
 0.001600   105.94    14.70   225.35   0.00201166   0.00000000   0.00000000   0.00000041  -0.00009059
 0.001650   108.63    14.70   231.18   0.00210802   0.00000000   0.00000000   0.00000040  -0.00009463
 0.001700   111.27    14.70   236.64   0.00220384   0.00000000   0.00000000   0.00000039  -0.00009859
 0.001750   113.87    14.70   241.84   0.00229946   0.00000000   0.00000000   0.00000039  -0.00010252
 0.001800   116.43    14.70   246.88   0.00239527   0.00000000   0.00000000   0.00000039  -0.00010643
 0.001850   118.93    14.70   251.86   0.00249163   0.00000000   0.00000000   0.00000039  -0.00011033
 0.001900   121.38    14.70   256.88   0.00258887   0.00000000   0.00000000   0.00000039  -0.00011425
 0.001950   123.77    14.70   262.01   0.00268731   0.00000000   0.00000000   0.00000040  -0.00011819
 0.002000   126.09    14.70   267.30   0.00278717   0.00000000   0.00000000   0.00000040  -0.00012218
```

```
   TIME     FDASH      F1       F2       F3       FR     X1DOT   X2DOT   X3DOT   X8DOT   XDOT28

0.002050   163.14    0.00     0.00     7.84    -0.25    1.965   1.965  -0.081  -0.081    2.046
0.002100   166.57    0.00     0.00     7.95    -0.26    1.999   1.999  -0.082  -0.082    2.081
0.002150   170.14    0.00     0.00     8.05    -0.27    2.032   2.032  -0.083  -0.084    2.115
0.002200   173.83    0.00     0.00     8.15    -0.28    2.063   2.063  -0.084  -0.085    2.148
0.002250   177.62    0.00     0.00     8.24    -0.29    2.092   2.092  -0.085  -0.085    2.178
0.002300   181.48    0.00     0.00     8.30    -0.29    2.117   2.117  -0.086  -0.086    2.203
0.002350   185.37    0.00     0.00     8.34    -0.30    2.136   2.136  -0.086  -0.086    2.223
0.002400   189.26    0.00     0.00     8.34    -0.31    2.150   2.150  -0.086  -0.086    2.236
0.002450   193.08    0.00     0.00     8.32    -0.32    2.157   2.157  -0.086  -0.086    2.243
0.002500   196.80    0.00     0.00     8.26    -0.33    2.158   2.158  -0.086  -0.086    2.244
0.002550   200.36    0.00     0.00     8.17    -0.34    2.153   2.153  -0.085  -0.085    2.237
0.002600   203.72    0.00     0.00     8.05    -0.35    2.141   2.141  -0.084  -0.083    2.224
0.002650   206.85    0.00     0.00     7.90    -0.35    2.123   2.123  -0.082  -0.082    2.205
0.002700   209.70    0.00     0.00     7.73    -0.36    2.101   2.101  -0.080  -0.080    2.181
0.002750   212.25    0.00     0.00     7.53    -0.37    2.074   2.074  -0.078  -0.078    2.152
0.002800   214.48    0.00     0.00     7.31    -0.38    2.044   2.044  -0.076  -0.076    2.119
0.002850   216.38    0.00     0.00     7.09    -0.39    2.011   2.011  -0.074  -0.073    2.084
0.002900   217.94    0.00     0.00     6.85    -0.39    1.977   1.977  -0.071  -0.071    2.048
0.002950   219.17    0.00     0.00     6.62    -0.40    1.942   1.942  -0.069  -0.068    2.010
0.003000   220.07    0.00     0.00     6.38    -0.41    1.908   1.908  -0.066  -0.066    1.974
0.003050   220.67    0.00     0.00     6.15    -0.41    1.874   1.874  -0.064  -0.064    1.938
0.003100   220.98    0.00     0.00     5.94    -0.42    1.842   1.842  -0.062  -0.061    1.904
0.003150   221.03    0.00     0.00     5.73    -0.42    1.813   1.813  -0.059  -0.059    1.872
0.003200   220.84    0.00     0.00     5.54    -0.43    1.786   1.786  -0.057  -0.057    1.843
0.003250   220.46    0.00     0.00     5.36    -0.44    1.761   1.761  -0.056  -0.055    1.817
0.003300   219.90    0.00     0.00     5.20    -0.44    1.741   1.741  -0.054  -0.054    1.794
0.003350   219.20    0.00     0.00     5.06    -0.45    1.724   1.724  -0.052  -0.052    1.776
0.003400   218.41    0.00     0.00     4.94    -0.45    1.712   1.712  -0.051  -0.051    1.763
0.003450   217.56    0.00     0.00     4.85    -0.46    1.704   1.704  -0.050  -0.050    1.754
0.003500   216.70    0.00     0.00     4.78    -0.46    1.702   1.702  -0.050  -0.050    1.751
0.003550   215.86    0.00     0.00     4.74    -0.47    1.704   1.704  -0.049  -0.049    1.753
0.003600   215.09    0.00     0.00     4.72    -0.47    1.711   1.711  -0.049  -0.049    1.760
0.003650   214.41    0.00     0.00     4.72    -0.48    1.721   1.721  -0.049  -0.049    1.770
0.003700   213.85    0.00     0.00     4.74    -0.48    1.735   1.735  -0.049  -0.049    1.784
0.003750   213.42    0.00     0.00     4.77    -0.49    1.751   1.751  -0.049  -0.049    1.801
0.003800   213.14    0.00     0.00     4.81    -0.49    1.769   1.769  -0.050  -0.050    1.819
0.003850   213.01    0.00     0.00     4.85    -0.50    1.787   1.787  -0.050  -0.050    1.837
0.003900   213.03    0.00     0.00     4.89    -0.50    1.805   1.805  -0.051  -0.051    1.856
0.003950   213.18    0.00     0.00     4.92    -0.51    1.822   1.822  -0.051  -0.051    1.873
0.004000   213.45    0.00     0.00     4.95    -0.51    1.838   1.838  -0.051  -0.051    1.889
```

```
  TIME       PC        PD      PQ        X1RB        X2R1        XIMBED        X3RB          XB

0.002050   128.35   14.70   272.81   0.00288864   0.00000000   0.00000000   0.00000041  -0.00012622
0.002100   130.54   14.70   278.55   0.00299182   0.00000000   0.00000000   0.00000041  -0.00013031
0.002150   132.65   14.7    284.51   0.00309673   0.00000000   0.00000000   0.00000042  -0.00013446
0.002200   134.69   14.70   290.68   0.00320333   0.00000000   0.00000000   0.00000042  -0.00013866
0.002250   136.65   14.70   297.02   0.00331148   0.00000000   0.00000000   0.00000043  -0.00014291
0.002300   138.53   14.70   303.48   0.00342101   0.00000000   0.00000000   0.00000043  -0.00014720
0.002350   140.32   14.70   309.99   0.00353167   0.00000000   0.00000000   0.00000043  -0.00015151
0.002400   142.03   14.70   316.48   0.00364317   0.00000000   0.00000000   0.00000043  -0.00015583
0.002450   143.64   14.70   322.88   0.00375519   0.00000000   0.00000000   0.00000043  -0.00016015
0.002500   145.17   14.70   329.09   0.00386740   0.00000000   0.00000000   0.00000043  -0.00016445
0.002550   146.60   14.70   335.05   0.00397945   0.00000000   0.00000000   0.00000042  -0.00016870
0.002600   147.93   14.70   340.68   0.00409101   0.00000000   0.00000000   0.00000042  -0.00017290
0.002650   149.16   14.70   345.90   0.00420177   0.00000000   0.00000000   0.00000041  -0.00017704
0.002700   150.30   14.70   350.67   0.00431144   0.00000000   0.00000000   0.00000040  -0.00018108
0.002750   151.33   14.70   354.94   0.00441977   0.00000000   0.00000000   0.00000039  -0.00018503
0.002800   152.27   14.70   358.67   0.00452656   0.00000000   0.00000000   0.00000038  -0.00018887
0.002850   153.09   14.70   361.84   0.00463166   0.00000000   0.00000000   0.00000037  -0.00019259
0.002900   153.82   14.70   364.45   0.00473496   0.00000000   0.00000000   0.00000036  -0.00019620
0.002950   154.44   14.70   366.50   0.00483642   0.00000000   0.00000000   0.00000034  -0.00019968
0.003000   154.95   14.70   368.01   0.00493602   0.00000000   0.00000000   0.00000033  -0.00020304
0.003050   155.36   14.70   369.01   0.00503379   0.00000000   0.00000000   0.00000032  -0.00020628
0.003100   155.67   14.70   369.52   0.00512982   0.00000000   0.00000000   0.00000031  -0.00020941
0.003150   155.87   14.70   369.61   0.00522420   0.00000000   0.00000000   0.00000030  -0.00021243
0.003200   155.97   14.70   369.30   0.00531706   0.00000000   0.00000000   0.00000029  -0.00021534
0.003250   156.00   14.70   368.65   0.00540855   0.00000000   0.00000000   0.00000028  -0.00021816
0.003300   156.00   14.70   367.72   0.00549881   0.00000000   0.00000000   0.00000027  -0.00022089
0.003350   156.00   14.70   366.56   0.00558805   0.00000000   0.00000000   0.00000026  -0.00022354
0.003400   156.00   14.70   365.23   0.00567650   0.00000000   0.00000000   0.00000026  -0.00022612
0.003450   156.00   14.70   363.82   0.00576441   0.00000000   0.00000000   0.00000025  -0.00022866
0.003500   156.00   14.70   362.38   0.00585202   0.00000000   0.00000000   0.00000025  -0.00023115
0.003550   156.00   14.70   360.98   0.00593961   0.00000000   0.00000000   0.00000025  -0.00023361
0.003600   156.00   14.70   359.68   0.00602742   0.00000000   0.00000000   0.00000024  -0.00023606
0.003650   156.00   14.7    358.54   0.00611565   0.00000000   0.00000000   0.00000024  -0.00023851
0.003700   156.00   14.70   357.60   0.00620450   0.00000000   0.00000000   0.00000025  -0.00024096
0.003750   156.00   14.7    356.89   0.00629412   0.00000000   0.00000000   0.00000025  -0.00024342
0.003800   156.00   14.70   356.42   0.00638460   0.00000000   0.00000000   0.00000025  -0.00024591
0.003850   156.00   14.70   356.20   0.00647600   0.00000000   0.00000000   0.00000025  -0.00024841
0.003900   156.00   14.70   356.23   0.00656834   0.00000000   0.00000000   0.00000025  -0.00025093
0.003950   156.00   14.70   356.49   0.00666158   0.00000000   0.00000000   0.00000025  -0.00025347
0.004000   156.00   14.70   356.95   0.00675565   0.00000000   0.00000000   0.00000026  -0.00025603
```

```
    TIME     FDASH       F1        F2        F3        FR    X1DOT    X2DOT    X3DOT    XBDOT  XDOT2B

  0.004050  213.83      0.00      0.00      4.96     -0.52    1.851    1.851   -0.051   -0.051    1.903
  0.004100  214.29      0.00      0.00      4.96     -0.52    1.862    1.862   -0.051   -0.051    1.913
  0.004150  214.80      0.00      0.00      4.95     -0.53    1.869    1.869   -0.051   -0.051    1.921
  0.004200  215.33      0.00      0.00      4.92     -0.53    1.874    1.874   -0.051   -0.051    1.925
  0.004250  215.87      0.00      0.00      4.87     -0.54    1.875    1.875   -0.050   -0.050    1.926
  0.004300  216.38      0.00      0.00      4.81     -0.54    1.874    1.874   -0.050   -0.050    1.924
  0.004350  216.85      0.00      0.00      4.73     -0.55    1.870    1.870   -0.049   -0.049    1.919
  0.004400  217.25      0.00      0.00      4.65     -0.55    1.863    1.863   -0.048   -0.048    1.911
  0.004450  217.57      0.00      0.00      4.55     -0.56    1.855    1.855   -0.047   -0.047    1.902
  0.004500  217.81      0.00      0.00      4.44     -0.56    1.845    1.845   -0.046   -0.046    1.891
  0.004550  217.95      0.00      0.00      4.34     -0.57    1.835    1.835   -0.045   -0.045    1.880
  0.004600  218.00      0.00      0.00      4.23     -0.57    1.824    1.824   -0.044   -0.044    1.868
  0.004650  217.96      0.00      0.00      4.12     -0.58    1.814    1.814   -0.043   -0.043    1.856
  0.004700  217.83      0.00      0.00      4.02     -0.58    1.804    1.804   -0.042   -0.042    1.845
  0.004750  217.63      0.00      0.00      3.92     -0.58    1.795    1.795   -0.041   -0.041    1.836
  0.004800  217.37      0.00      0.00      3.83     -0.59    1.788    1.788   -0.040   -0.040    1.828
  0.004850  217.07      0.00      0.00      3.75     -0.59    1.783    1.783   -0.039   -0.039    1.822
  0.004900  216.74      0.00      0.00      3.67     -0.60    1.780    1.780   -0.038   -0.038    1.818
  0.004950  216.39      0.00      0.00      3.61     -0.60    1.778    1.778   -0.037   -0.037    1.816
  0.005000  216.05      0.00      0.00      3.56     -0.60    1.779    1.779   -0.037   -0.037    1.816
  0.005050  215.73      0.00      0.00      3.52     -0.61    1.781    1.781   -0.036   -0.036    1.818
  0.005100  215.44      0.00      0.00      3.49     -0.61    1.785    1.785   -0.036   -0.036    1.821
  0.005150  215.20      0.00      0.00      3.46     -0.61    1.790    1.790   -0.036   -0.036    1.826
  0.005200  215.01      0.00      0.00      3.44     -0.62    1.797    1.797   -0.036   -0.036    1.833
  0.005250  214.87      0.00      0.00      3.42     -0.62    1.804    1.804   -0.035   -0.035    1.839
  0.005300  214.79      0.00      0.00      3.40     -0.62    1.812    1.812   -0.035   -0.035    1.847
  0.005350  214.78      0.00      0.00      3.39     -0.63    1.819    1.819   -0.035   -0.035    1.854
  0.005400  214.82      0.00      0.00      3.37     -0.63    1.826    1.826   -0.035   -0.035    1.861
  0.005450  214.91      0.00      0.00      3.35     -0.63    1.833    1.833   -0.035   -0.035    1.868
  0.005484  214.99     -0.12      0.00      1.12     -0.64    1.838    1.843   -0.056   -0.035    1.877
  0.005494  215.02     -0.47      0.00     -2.66     -0.64    1.839    1.847   -0.047   -0.035    1.882
  0.005504  215.06     -0.86      0.00     -2.41     -0.64    1.842    1.849   -0.029   -0.034    1.883
  0.005514  215.09     -1.07      0.00      1.34     -0.64    1.844    1.848   -0.016   -0.034    1.882
  0.005524  215.13     -1.09      0.00      2.98     -0.64    1.847    1.846   -0.039   -0.034    1.881
  0.005534  215.17     -0.93      0.00      0.19     -0.64    1.849    1.846   -0.055   -0.034    1.880
  0.005544  215.22     -0.73      0.00     -2.79     -0.64    1.851    1.847   -0.040   -0.034    1.881
  0.005554  215.27     -0.53      0.00     -1.58     -0.64    1.853    1.850   -0.018   -0.034    1.884
  0.005564  215.32     -0.44      0.00      1.88     -0.64    1.854    1.854   -0.020   -0.034    1.888
  0.005574  215.37     -0.47      0.00      2.45     -0.64    1.856    1.858   -0.043   -0.034    1.892
  0.005584  215.42     -0.61      0.00     -0.60     -0.64    1.857    1.861   -0.052   -0.034    1.894
```

```
   TIME        PC        PD       PQ          X1RB        X2R1        XIMBED        X3RB          XB

 0.004050   156.00    14.70   357.58   0.00685046  0.00000000  0.00000000  0.00000026 -0.00025860
 0.004100   156.00    14.70   358.34   0.00694587  0.00000000  0.00000000  0.00000026 -0.00026117
 0.004150   156.00    14.70   359.19   0.00704173  0.00000000  0.00000000  0.00000026 -0.00026374
 0.004200   156.00    14.71   360.09   0.00713788  0.00000000  0.00000000  0.00000025 -0.00026629
 0.004250   156.00    14.71   360.98   0.00723416  0.00000000  0.00000000  0.00000025 -0.00026883
 0.004300   156.00    14.71   361.84   0.00733041  0.00000000  0.00000000  0.00000025 -0.00027133
 0.004350   156.00    14.71   362.62   0.00742648  0.00000000  0.00000000  0.00000025 -0.00027380
 0.004400   156.00    14.71   363.29   0.00752223  0.00000000  0.00000000  0.00000024 -0.00027623
 0.004450   156.00    14.71   363.84   0.00761757  0.00000000  0.00000000  0.00000024 -0.00027861
 0.004500   156.00    14.71   364.23   0.00771240  0.00000000  0.00000000  0.00000023 -0.00028094
 0.004550   156.00    14.71   364.47   0.00780666  0.00000000  0.00000000  0.00000022 -0.00028321
 0.004600   156.00    14.71   364.55   0.00790035  0.00000000  0.00000000  0.00000022 -0.00028543
 0.004650   156.00    14.71   364.48   0.00799344  0.00000000  0.00000000  0.00000021 -0.00028759
 0.004700   156.00    14.71   364.27   0.00808597  0.00000000  0.00000000  0.00000021 -0.00028969
 0.004750   156.00    14.71   363.93   0.00817800  0.00000000  0.00000000  0.00000020 -0.00029174
 0.004800   156.00    14.71   363.50   0.00826958  0.00000000  0.00000000  0.00000020 -0.00029375
 0.004850   156.00    14.71   362.99   0.00836081  0.00000000  0.00000000  0.00000019 -0.00029570
 0.004900   156.00    14.71   362.43   0.00845179  0.00000000  0.00000000  0.00000019 -0.00029762
 0.004950   156.00    14.71   361.86   0.00854262  0.00000000  0.00000000  0.00000019 -0.00029951
 0.005000   156.00    14.71   361.29   0.00863339  0.00000000  0.00000000  0.00000018 -0.00030137
 0.005050   156.00    14.71   360.75   0.00872422  0.00000000  0.00000000  0.00000018 -0.00030320
 0.005100   156.00    14.71   360.27   0.00881518  0.00000000  0.00000000  0.00000018 -0.00030501
 0.005150   156.00    14.71   359.86   0.00890636  0.00000000  0.00000000  0.00000018 -0.00030681
 0.005200   156.00    14.71   359.54   0.00899783  0.00000000  0.00000000  0.00000018 -0.00030860
 0.005250   156.00    14.71   359.31   0.00908962  0.00000000  0.00000000  0.00000018 -0.00031037
 0.005300   156.00    14.71   359.19   0.00918178  0.00000000  0.00000000  0.00000018 -0.00031214
 0.005350   156.00    14.71   359.16   0.00927431  0.00000000  0.00000000  0.00000018 -0.00031390
 0.005400   156.00    14.71   359.22   0.00936720  0.00000001  0.00000000  0.00000017 -0.00031565
 0.005450   156.00    14.72   359.38   0.00946044  0.00000000  0.00000000  0.00000017 -0.00031745
-0.005484   156.00    14.72   359.52   0.00952495  0.00000002  0.00000000  0.00000006 -0.00031859
 0.005494   156.00    14.72   359.57   0.00954367  0.00000009  0.00000000 -0.00000014 -0.00031894
 0.005504   156.00    14.72   359.63   0.00956242  0.00000017  0.00000000 -0.00000012 -0.00031928
 0.005514   156.00    14.72   359.68   0.00958119  0.00000021  0.00000000  0.00000007 -0.00031962
 0.005524   156.00    14.72   359.75   0.00959998  0.00000022  0.00000000  0.00000015 -0.00031997
 0.005534   156.00    14.72   359.82   0.00961880  0.00000018  0.00000000  0.00000001 -0.00032031
 0.005544   156.00    14.72   359.90   0.00963763  0.00000014  0.00000000 -0.00000014 -0.00032065
 0.005554   156.00    14.72   359.98   0.00965649  0.00000011  0.00000000 -0.00000008 -0.00032099
 0.005564   156.00    14.72   360.06   0.00967536  0.00000009  0.00000000  0.00000010 -0.00032134
 0.005574   156.00    14.72   360.15   0.00969424  0.00000009  0.00000000  0.00000013 -0.00032168
 0.005584   156.00    14.72   360.24   0.00971314  0.00000012  0.00000000 -0.00000003 -0.00032201
```

```
   TIME     FDASH       F1        F2        F3        FR    X1DOT   X2DOT   X3DOT   XBDOT  XDOT2B


0.005594  215.48    -0.80      0.00     -2.67     -0.64    1.859   1.862  -0.034  -0.034   1.896
0.005604  215.53    -0.92      0.00     -0.77     -0.65    1.860   1.862  -0.017  -0.034   1.896
0.005614  215.59    -0.93      0.00      2.17     -0.65    1.862   1.862  -0.025  -0.034   1.896
0.005624  215.66    -0.89      0.00      1.81     -0.65    1.863   1.862  -0.046  -0.034   1.896
0.005634  215.72    -0.83      0.00     -1.22     -0.65    1.865   1.863  -0.048  -0.033   1.897
0.005644  215.78    -0.75      0.00     -2.36     -0.65    1.866   1.865  -0.029  -0.033   1.898
0.005654  215.85    -0.70      0.00     -0.04     -0.65    1.867   1.867  -0.017  -0.033   1.900
0.005664  215.91    -0.69      0.00      2.23     -0.65    1.868   1.868  -0.029  -0.033   1.902
0.005674  215.98    -0.75      0.00      1.13     -0.65    1.869   1.870  -0.047  -0.033   1.903
0.005684  216.05    -0.84      0.00     -1.60     -0.65    1.870   1.871  -0.043  -0.033   1.904
0.005694  216.12    -0.90      0.00     -1.91     -0.65    1.870   1.872  -0.025  -0.033   1.904
0.005704  216.19    -0.93      0.00      0.56     -0.65    1.871   1.872  -0.019  -0.033   1.904
0.005714  216.25    -0.93      0.00      2.13     -0.65    1.872   1.872  -0.033  -0.033   1.904
0.005724  216.32    -0.89      0.00      0.48     -0.65    1.873   1.872  -0.046  -0.032   1.905
0.005734  216.39    -0.89      0.00     -1.80     -0.65    1.873   1.873  -0.039  -0.032   1.905
0.005744  216.46     6.47     99.77     28.91     -0.65    1.869   1.445   0.415  -0.029   1.474
0.005754  216.49    46.18    129.35    157.50     -0.66    1.827   0.718   0.702  -0.022   0.740
0.005764  216.38   109.46    137.66    237.90     -0.66    1.709   0.397  -0.009  -0.013   0.410
0.005774  216.02   172.44    185.99    176.77     -0.66    1.508   0.349  -0.466  -0.004   0.353
0.005784  215.27   224.7     225.32    133.57     -0.66    1.238   0.350   0.141   0.008   0.342
0.005794  214.05   257.5     223.08    219.84     -0.66    0.920   0.555   0.639   0.021   0.534
0.005804  212.31   259.71    238.54    308.86     -0.65    0.592   0.836   0.234   0.034   0.801
0.005814  210.07   241.38    294.70    300.28     -0.65    0.288   0.658  -0.134   0.049   0.609
0.005824  207.38   231.51    321.05    282.21     -0.65    0.007  -0.012   0.123   0.067  -0.079
0.005834  204.24   240.92    283.69    308.79     -0.65   -0.273  -0.553   0.198   0.084  -0.637
0.005844  200.66   251.04    240.87    289.57     -0.65   -0.563  -0.619  -0.247   0.098  -0.716
0.005854  196.64   243.52    227.44    198.94     -0.65   -0.844  -0.495  -0.362   0.110  -0.605
0.005864  192.22   217.68    205.58    148.32     -0.65   -1.090  -0.430   0.106   0.120  -0.550
0.005874  187.48   177.66    159.63    174.15     -0.64   -1.282  -0.358   0.297   0.129  -0.487
0.005884  182.52   126.59    126.88    174.14     -0.64   -1.403  -0.342  -0.079   0.134  -0.476
0.005894  177.46    76.55    111.75    104.48     -0.64   -1.450  -0.583  -0.285   0.138  -0.721
0.005904  172.41    42.19     71.37     40.81     -0.63   -1.439  -0.933  -0.067   0.140  -1.072
0.005914  167.44    20.95      1.79     13.25     -0.63   -1.392  -0.991  -0.007   0.138  -1.129
0.005924  162.61     0.75      0.00    -16.58     -0.63   -1.312  -0.945   0.017   0.134  -1.079
0.005934  157.97   -13.32      0.00    -20.33     -0.63   -1.205  -1.033   0.212   0.130  -1.163
0.005944  153.55   -15.60      0.00      6.53     -0.62   -1.086  -1.168   0.279   0.125  -1.293
0.005954  149.36    -6.03      0.00     23.60     -0.62   -0.971  -1.250   0.118   0.120  -1.370
0.005964  145.37    10.21      0.00      6.30     -0.62   -0.870  -1.209  -0.034   0.115  -1.325
0.005974  141.57    25.65      0.00    -18.72     -0.62   -0.786  -1.036   0.038   0.110  -1.146
0.005984  137.93    33.82      0.00    -14.54     -0.61   -0.712  -0.777   0.212   0.105  -0.881
```

```
    TIME       PC        PD       PQ        X1RB        X2R1        XIMBED       X3RB         XB

0.005594  156.00    14.72  360.33  0.00973205  0.00000016  0.00000000 -0.00000014 -0.00032235
0.005604  156.00    14.72  360.43  0.00975098  0.00000018  0.00000000 -0.00000004 -0.00032269
0.005614  156.00    14.72  360.53  0.00976992  0.00000018  0.00000000  0.00000011 -0.00032303
0.005624  156.00    14.72  360.63  0.00978888  0.00000018  0.00000000  0.00000009 -0.00032336
0.005634  156.00    14.72  360.73  0.00980785  0.00000016  0.00000000 -0.00000006 -0.00032370
0.005644  156.00    14.72  360.84  0.00982683  0.00000015  0.00000000 -0.00000012 -0.00032403
0.005654  156.00    14.72  360.95  0.00984582  0.00000014  0.00000000 -0.00000005 -0.00032436
0.005664  156.00    14.72  361.06  0.00986482  0.00000014  0.00000000  0.00000012 -0.00032469
0.005674  156.00    14.72  361.17  0.00988383  0.00000015  0.00000000  0.00000006 -0.00032502
0.005684  156.00    14.72  361.26  0.00990284  0.00000017  0.00000000 -0.00000008 -0.00032535
0.005694  156.00    14.72  361.40  0.00992187  0.00000018  0.00000000 -0.00000010 -0.00032568
0.005704  156.00    14.72  361.51  0.00994090  0.00000018  0.00000000  0.00000003 -0.00032601
0.005714  156.00    14.72  361.63  0.00995993  0.00000018  0.00000000  0.00000011 -0.00032633
0.005724  156.00    14.72  361.75  0.00997897  0.00000018  0.00000000  0.00000003 -0.00032666
0.005734  156.00    14.72  361.86  0.00999801  0.00000018  0.00000000 -0.00000009 -0.00032698
0.005744  156.00    14.72  361.98  0.01001703 -0.00000128  0.00001425  0.00000150 -0.00032729
0.005754  156.00    14.72  362.02  0.01003580 -0.00000916  0.00001848  0.00000816 -0.00032755
0.005764  156.00    14.72  361.84  0.01005371 -0.00002172  0.00001967  0.00001233 -0.00032772
0.005774  156.00    14.72  361.23  0.01006994 -0.00003421  0.00002657  0.00000916 -0.00032781
0.005784  156.00    14.72  359.98  0.01008369 -0.00004458  0.00003219  0.00000692 -0.00032779
0.005794  156.00    14.72  357.94  0.01009435 -0.00005109  0.00003187  0.00001139 -0.00032764
0.005804  156.00    14.72  355.04  0.01010161 -0.00005153  0.00003408  0.00001600 -0.00032736
0.005814  156.00    14.72  351.29  0.01010555 -0.00004789  0.00004210  0.00001556 -0.00032695
0.005824  156.00    14.72  346.78  0.01010642 -0.00004593  0.00004586  0.00001462 -0.00032637
0.005834  156.00    14.72  341.54  0.01010433 -0.00004780  0.00004053  0.00001600 -0.00032561
0.005844  156.00    14.72  335.55  0.01009922 -0.00004981  0.00003441  0.00001500 -0.00032470
0.005854  156.00    14.72  328.83  0.01009112 -0.00004832  0.00003249  0.00001031 -0.00032366
0.005864  156.00    14.72  321.44  0.01008024 -0.00004319  0.00002937  0.00000768 -0.00032251
0.005874  156.00    14.72  313.51  0.01006708 -0.00003525  0.00002281  0.00000902 -0.00032126
0.005884  156.00    14.72  305.22  0.01005227 -0.00002512  0.00001813  0.00000902 -0.00031994
0.005894  156.00    14.72  296.75  0.01003657 -0.00001519  0.00001596  0.00000541 -0.00031858
0.005904  156.00    14.72  288.30  0.01002068 -0.00000837  0.00001020  0.00000211 -0.00031719
0.005914  156.00    14.72  279.99  0.01000510 -0.00000416  0.00000026  0.00000069 -0.00031580
0.005924  156.00    14.72  271.92  0.00999018 -0.00000015  0.00000000 -0.00000186 -0.00031444
0.005934  156.00    14.72  264.16  0.00997625  0.00000264  0.00000000 -0.00000105 -0.00031312
0.005944  156.00    14.72  256.77  0.00996350  0.00000309  0.00000000  0.00000034 -0.00031185
0.005954  156.00    14.72  249.76  0.00995199  0.00000120  0.00000000  0.00000122 -0.00031062
0.005964  156.00    14.73  243.10  0.00994161 -0.00000203  0.00000000  0.00000133 -0.00030944
0.005974  156.00    14.73  236.74  0.00993221 -0.00000509  0.00000000 -0.00000097 -0.00030832
0.005984  156.00    14.73  230.65  0.00992364 -0.00000671  0.00000000 -0.00000075 -0.00030725
```

APPENDIX B

DISTRIBUTION LIST

	Number of Copies
Air Force Rocket Propulsion Laboratory Edwards, California 93523 Attn: RPRP	1
AFRPL Edwards, Calif. 93523 Attn: RPRPD/J.R. Lawrence	10
Adel Products Division General Metals 10777 Vanowen Street Burbank, California Attn: B.R. Teree Chief Engineer	1
Aerojet-General Corporation Azusa, California Attn: T.R. Wallace Supervisor Engrg.	1
Aerojet-General Corporation P.O. Box 1947 Sacramento, Calif. Attn: H. Goldthorpe	1
Aeroquip Corporation Jackson, Michigan Attn: E. Robert Steinert Ch. Aircraft Devel. Engr.	1
AiResearch Manufacturing Company of Arizona 402 South 36th Street Phoenix, Arizona 85034 Attn: A.D. Stromme M/S 3570	2
The Annin Company P.O. Box 22081 Los Angeles 22, California Attn: R.D. Randall Chief Engineer	1

	Number of Copies
Battelle Memorial Institute Columbus, Ohio Attn: B. Goobich	1
Bell Aerosystems Company Buffalo 5, New York Attn: H.A. Ferullo Chief Engr., Rockets	1
Benbow Manufacturing Corporation 11920 Jefferson Blvd. Culver City, Calif. Attn: Frank Aikins, Ch. Engr.	1
The Bendix Corporation Bendix-Pacific Division North Hollywood, California Attn: Doublas M. Longyear, Jr. Chief Engineer	1
Calmac Manufacturing Corporation 5824 District Blvd. Los Angeles 22, Calif.	2
Clary Dynamics 408 Junipero Street San Gabriel, Calif. Attn: George F. Eas, Ch. Engr.	
Conoflow Corporation 2100 Arch Street Philadelphia 3, Penn. Attn: A.J. Hanseen, Ch. Engr.	1
Consolidated Controls Corporation 750 S. Isis Avenue Inglewood, Calif. Attn: James A. McBride, Ch. Engr.	1
Cryogenic Engineering Company 200 West 48th Avenue Denver 16, Colo. Attn: M.M. Reynolds Vice President - Sales	1

	Number of Copies
Douglas Aircraft Company Missile and Space Systems Division 3000 Ocean Park Blvd. Santa Monica, Calif. Attn: P. VanHorn, A2-260	1
Eckel Valve Company 1425 First Street San Fernando, Calif. Attn: H. Sutter	1
Fairchild Stratos 1800 Rosecrans Avenue Manhattan Beach, Calif. Attn: Library	2
Fox Valve Development Company, Inc. 84 Jackson Avenue Hackensack, New Jersey Attn: Mr. Zola Fox	1
Frebank Company 711 West Broadway Glendale, Calif. Attn: Director of Engrg.	1
Futurecraft Corporation 15430 Proctor Avenue Industry, California Attn: Murry Chilcoat, Chief Engineer	1
General Dynamics/Fort Worth P.O. Box 748 Fort Worth, Texas 76101 Attn: Library	2
General Electric Company General Engineering Laboratory Attn: J.A. Bain Schenectady, New York	1
Grumman Aircraft Engineering Corp. Bethpage, Long Island, New York Attn: Library	2

	Number of Copies
B. H. Hadley, Inc. P.O. Box 31 Pomona, California Attn: W. R. Brown, Director of Engrg.	1
Hannifin Pneumatic Division Attn: Z.J. Lansky, Manager 500 S. Wolf Road Des Plaines, Illinois	1
Homestead Valve Manufacturing Company Jenny Division Attn: D.M. Simmons, Jr. Chief Engineer Corapolis, Pennsylvania	1
Hughes Aircraft Company Aerospace Group Space Systems Division Culver City, California Attn: Library	1
Hydro-Aire Division of Crane Co. 3000 Winona Avenue Burbank, California	1
IIT Research Institute 10 West 35th Street Chicago 16, Illinois Attn: P.A. Bauer	1
Jamesbury Corporation 640 Lincoln Street Worcester, Massachusetts	1
James, Pond and Clark 2128 East Foothill Blvd. Pasadena, California	1
J. C. Carter 671 W. 17th Street Costa Mesa, California	1

	Number of Copies
Jet Propulsion Laboratory Propulsion Division 4800 Oak Grove Drive Pasadena, California 91103 Attn: R. Weiner	1
LTV Astronautics Division P.O. Box 6267 Dallas, Texas 75222	2
Marotta Valve Corporation Attn: Jon Janozur 2215 Standard Avenue Santa Ana, California	1
McDonnell Aircraft Corporation P.O. Box 516 St. Louis, Missouri 63166 Attn: Library	1
Minneapolis-Honeywell Regulator Company Valve Division 300 Gommers Drive Fort Washington, Pennsylvania	1
Minneapolis-Honeywell Regulator Company Aeronautical Division 2600 Ridgeway Road Minneapolis 40, Minnesota Attn: Mario Cardullo, Engrg.	1
Moog Servocontrols, Inc. Proner Airport East Aurora, New York	2
NASA Manned Spacecraft Center Houston, Texas 77058 Attn: J. Capps	1
National Waterlift Company 2220 Palmer Avenue Kalamazoo, Michigan	2

	Number of Copies
Parker Aircraft Company 5827 West Century Blvd. Los Angeles 45, California Attn: P. Brady	3
Pyronetics 11973 Slauson Santa Fe Springs, California Attn: H. Eckardt	1
Robertshaw Controls Company Santa Ana Freeway at Euclid Avenue Anaheim, California Attn: J.R. Tobias	2
Space Technology Laboratories, Inc. Space Technology Center One Space Park Redondo Beach, California Attn: T. Weathers	3
Sterer Engrg & Manufacturing Company 4690 Colorado Blvd. Los Angeles 30, California	2
Thompson Products Valve Division Thompson Ramo Wooldridge, Inc. Attn: J.M. Cherrie, Mgr. - Product Engrg. 1455 East 185th Street Cleveland 10, Ohio	1
Wallace O. Leonard, Inc. 373 Fair Oaks Avenue Pasadena, California	1
Walter Kidde Company 675 Main Street Belleville 9, New Jersey Attn: Library	2
The Weatherhead Company Attn: Richard C. Acker, Development Engr. 300 E. 131st Street Cleveland 8, Ohio	1

	Number of Copies
Weston Hydraulics Limited 7500 Tyrone Avenue Van Nuys, California	1
Whittaker Controls Division Telecomputing Corporation 915 North Citrus Avenue Los Angeles 38, California Attn: Ver Smith	3
U.S. Department of the Interior Bureau of Mines 4800 Forbes Avenue Pittsburgh, Pennsylvania 15213 Attn: M.M. Dolinar, Repts Librarian Explosives Research Center	1
Central Intelligence Agency 2430 E Street, N.W. Washington, D.C. 20505 Attn: OCD, Standard Dist.	1
Office of the Director of Defense Research & Engineering Washington, D.C. 20301 Attn: Dr. H.W. Schulz, Office of Asst. Dir. (Chem. Technology)	1
Nat'l Aeronautics & Space Admin. Lewis Research Center 21000 Brookpark Road Cleveland, Ohio 44135 Attn: Library	1
John F. Kennedy Space Center NASA Cocoa Beach, Florida 32931 Attn: Library	1
Nat'l Aeronautics & Space Admin. Manned Spacecraft Center P.O. Box 1537 Houston, Texas 77001 Attn: Library	1

	Number of Copies
Nat'l Aeronautics & Space Admin. Langley Research Center Langley Air Force Base Virginia 23365 Attn: Library	3
Nat'l Aeronautics & Space Admin. Washington, D.C. 20546 Attn: Office of Technical Information & Educational Programs, Code ETL	1
Scientific and Tech. Info. Facility P.O. Box 5700 Bethesda, Maryland 20014 Attn: NASA Representative	2
Nat'l Aeronautics & Space Admin. Washington, D.C. 20546 Attn: R.W. Ziem (RPS)	1
Nat'l Aeronautics & Space Admin. Goddard Space Flight Center Greenbelt, Maryland 20771 Attn: Library	1
Defense Documentation Center Cameron Station Alexandria, Virginia 22314	20
RTD (RTNP) Bolling AFB Washington, D.C. 20332	1
Arnold Eng. Development Center Attn: AEOIM Air Force Systems Command Tullahoma, Tennessee 37389	1
Hq. AFSC (SCTR) Andrews Air Force Base Washington, D.C. 20331	1
AFRPL (RPR) Edwards, California 93523	1

	Number of Copies
AFRPL (RPM) Edwards, California 93523	1
AFFTC (FTBPP-2) Attn: Technical Library Edwards AFB, California 93523	1
Office of Research Analyses (OAR) Attn: RRRT Holloman AFB, New Mexico 88330	1
Air Force Office of Scientific Research Washington, D.C. 20333 Attn: SREP, Dr. J.F. Masi	1
Wright-Patterson AFB, Ohio 45433 Attn: AFML (MAAE)	1
Commanding Officer Ballistic Research Laboratories Aberdeen Proving Ground, Maryland Attn: AMXBR-I 21005	1
Commanding Officer U.S. Army Research Office (Durham) Box CM, Duke Station Durham, North Carolina 27706	1
AFRPL (RPC) Edwards, California 93423	1
Commanding Officer Frankford Arsenal Philadelphia, Pennsylvania 19137 Attn: Propellant and Explosives Section, 1331	1
Commanding Officer Picatinny Arsenal Dover, New Jersey 07801 Attn: Library	1

	Number of Copies
Commanding Officer Picatinny Arsenal Liquid Rocket Propulsion Laboratory Dover, New Jersey 07801 Attn: Technical Library	2
U.S. Army Missile Command Redstone Scientific Info. Center Redstone Arsenal, Alabama 35808 Attn: Chief, Document Section	2
Commanding General White Sands Missile Range New Mexico 88002 Attn: Technical Library	1
Bureau of Naval Weapons Department of the Navy Washington, D.C. 20360 Attn: DLI-3	2
Bureau of Naval Weapons Department of the Navy Washington, D.C. 20360 Attn: RMMP-2	2
Bureau of Naval Weapons Department of the Navy Washington, D.C. 20360 Attn: RMMP-4	1
Bureau of Naval Weapons Department of the Navy Washington, D.C. 20360 Attn: RRRE-6	1
Commander U.S. Naval Missile Center Point Mugu, California 93041 Attn: Technical Library	2

	Number of Copies
Commander U.S. Naval Ordnance Laboratory White Oak Silver Spring, Maryland 20910 Attn: Library	2
Commander U.S. Naval Ordnance Test Station China Lake, California 93557 Attn: Code 45	2
Commander (Code 753) U.S. Naval Ordnance Test Station China Lake, California 93557 Attn: Technical Library	2
Superintendent U.S. Naval Postgraduate School Naval Academy Monterey, California 93900	1
Commanding Officer U.S. Naval Propellant Plant Indian Head, Maryland 20640 Attn: Technical Library	2
Commanding Officer Office of Naval Research 1030 E. Green Street Pasadena, California 91101	1
Department of the Navy Office of Naval Research Washington, D.C. 20360 Attn: Code 429	1
Director Special Project Office Department of the Navy Washington, D.C. 20360	1

	Number of Copies
Commanding Officer U.S. Naval Underwater Ordnance Station Newport, Rhode Island 02844 Attn: W.W. Bartlett	1
Aerojet-General Corporation P.O. Box 296 Azusa, California 91703 Attn: Librarian	2
Aerojet-General Corporation 11711 South Woodruff Avenue Downey, California 90241 Attn: F.M. West, Chief Librarian	1
Aerojet-General Corporation Attn: Tech. Library 2484-2015A P.O. Box 1947 Sacramento, California 95809	3
Aeronutronic Div. Philco Corporation Ford Road Newport Beach, California 92600 Attn: Dr. L.H. Linder, Manager Technical Information Dept.	1
Aeroprojects, Inc. 310 East Rosedale Avenue West Chester, Pennsylvania 19380 Attn: C.D. McKinney	1
Aerospace Corporation P.O. Box 95085 Los Angeles, California 90045 Attn: Library-Documents	2
Allied Chemical Corporation (General Chemical Division) Attn: Security Office P.O. Box 405 Morristown, New Jersey 07960	1

	Number of Copies
Northrop Carolina, Inc. Box 3049 Asheville, North Carolina 28802	1
American Cyanamid Company 1937 W. Main Street Stamford, Connecticut 06902 Attn: Security Officer	1
IIT Research Institute Technology Center Chicago, Illinois 60616 Attn: C.K. Hersh, Chemistry Div.	1
ARO, Inc. Arnold Engrg. Dev. Center Arnold AF Station, Tennessee 37389 Attn: Dr. B.H. Goethert Chief Scientist	1
Atlantic Research Corporation Shirley Highway and Edsall Road Alexandria, Virginia 22314 Attn: Security Office for Library	2
University of Denver Denver Research Inst. P.O. Box 10127 Attn: Security Office Denver, Colorado 80210	1
Battelle Memorial Institute 505 King Avenue Columbus, Ohio 43201 Attn: Report Library, Room 6A	1
Bell Aerosystems Box 1 Buffalo, New York 14205 Attn: Technical Library	1

	Number of Copies
The Boeing Company Aero Space Division P.O. Box 3707 Seattle, Washington 98124 Attn: Ruth E. Peerenboom, Library Processes Sup (1190)	2
Chemical Propulsion Information Agency Applied Physics Laboratory 8621 Georgia Avenue Silver Spring, Maryland 20910	2
Douglas Aircraft Co., Inc. Santa Monica Division 3000 Ocean Park Boulevard Santa Monica, California 90405 Attn: Library	3
The Dow Chemical Company Security Section Box 31 Midland, Michigan 48641 Attn: Dr. R.S. Karpiuk, 1710 Bldg.	1
E. I. duPont deNemours & Company Eastern Laboratory Gibbstown, New Jersey 08027 Attn: Mrs. Alice R. Steward	1
Esso Research and Engineering Co. Process Rsch. Div. P.O. Box 8 Linden New Jersey 07036 Attn: Dr. J.R. Lovett	1
General Dynamics/Astronautics P.O. Box 1128 San Diego, California 92112 Attn: Library and Information Services (128-00)	3

	Number of Copies
Hercules Powder Company Allegany Ballistics Laboratory P.O. Box 210 Cumberland, Maryland 21501 Attn: Library	1
Hercules Powder Company Research Center Wilmington, Delaware 19899 Attn: Dr. Herman Skolnik, Manager Technical Information Div.	1
Institute for Defense Analyses 400 Army-Navy Drive Arlington, Virginia 22202 Attn: Classified Library	1
Jet Propulsion Laboratory 4800 Oak Grove Drive Pasadena, California 91103	1
Lockheed Propulsion Company P.O. Box 111 Redlands, California 92374 Attn: Miss Belle Berlad, Librarian	1
Mardquardt Corp. 16555 Saticoy Street Box 2013 - South Annex Van Nuys, California 91404	1
Propulsion Engineering Div. D. 55-11 Lockheed Missiles & Space Co. 1111 Lockheed Way Sunnyvale, California 94087	1
Minnesota Mining & Manufacturing Co. 900 Bush Avenue St. Paul, Minnesota 55106 Attn: Code 0013 R&D VIA: H.C. Zeman, Security Administrator	2

	Number of Copies
North American Aviation, Inc. Space & Information Systems Div. 12214 Lakewood Boulevard Downey, California 90242 Attn: Technical Information Center D/096-722(AJ0I)	1
Rocket Research Corporation 520 South Portland Street Seattle, Washington 98108	1
Rohm and Haas Company Redstone Arsenal Research Division Huntsville, Alabama 35808 Attn: Librarian	1
TRW Systems 1 Space Park Redondo Beach, California 90200 Attn: STL Tech. Lib. Doc. Acquisitions	2
Texaco Experiment Incorporated P.O. Box 1-T Richmond, Virginia 23202 Attn: Librarian	1
Thiokol Chemical Corporation Alpha Division, Huntsville Plant Huntsville, Alabama 35800 Attn: Technical Director	1
Thiokol Chemical Corporation Elkton Division Elkton, Maryland 21921 Attn: Librarian	1
Thiokol Chemical Corporation Wasatch Division P.O. Box 524 Brigham City, Utah 84302 Attn: Library Section	2

	Number of Copies
United Aircraft Corporation Corporation Library 400 Main Street East Hartford, Connecticut 06118 Attn: Dr. David Rix	1
United Aircraft Corporation Pratt & Whitney Fla. Res. & Dev. Ctr. P.O. Box 2691 W. Palm Beach, Florida 33402 Attn: Library	1
United Aircraft Corporation United Technology Center P.O. Box 358 Sunnyvale, California 94088 Attn: Librarian	1
General Electric Company Apollo Support Department P.O. Box 2500 Daytona Beach, Florida 32015 Attn: C. Day	1
Stanford Research Institute Propulsion Sciences Division Menlo Park, California 94025 Attn: Document Custodian	1

DOCUMENT CONTROL DATA - R&D

(Security classification of title, body of abstract and indexing annotation must be entered when the overall report is classified)

1. ORIGINATING ACTIVITY *(Corporate author)*
Rockedyne, a Division of North American Aviation, Inc., 6633 Canoga Avenue, Canoga Park, California

2a. REPORT SECURITY CLASSIFICATION
UNCLASSIFIED

2b. GROUP

3. REPORT TITLE
POPPET AND SEAT DESIGN DATA FOR AEROSPACE VALVES

4. DESCRIPTIVE NOTES *(Type of report and inclusive dates)*
Final Report (April 1964 through February 1966)

5. AUTHOR(S) *(Last name, first name, initial)*
Tellier, G. F.

6. REPORT DATE
July 1966

7a. TOTAL NO. OF PAGES
761

7b. NO. OF REFS
66

8a. CONTRACT OR GRANT NO.
AF04(611)-9712

b. PROJECT NO.
6753

c.
Task No. 675304

d.

9a. ORIGINATOR'S REPORT NUMBER(S)
R-6472

9b. OTHER REPORT NO(S) *(Any other numbers that may be assigned this report)*
AFRPL-TR-66-147

10. AVAILABILITY/LIMITATION NOTICES ~~This document is subject to special export controls and each transmittal to foreign governments or foreign nationals may be made only with prior approval of AFRPL (RPRP), Edwards, California 93523.~~

11. SUPPLEMENTARY NOTES

12. SPONSORING MILITARY ACTIVITY
Air Force Rocket Propulsion Laboratory
Research and Technology Division
Edwards, California

13. ABSTRACT

Presented herein is a description of the work accomplished in providing fundamental sealing data on metal-to-metal seat and poppet valving elements. The reported effort supplements and updates initial results published as Technical Documentary Report No. RPL-TDR-64-68, "Rocket Engine Valve Poppet and Seat Design," dated May 1964. The program involved experimental and analytical studies of the detailed aspects of valve seating. Flat, conical, and spherical test models were fabricated with particular emphasis placed on documentation of fabrication methods and description of the resultant surfaces. Model stress-leakage characteristics, as a function of surface texture, geometry, coatings, and material variations, were experimentally investigated. The resulting information is presented in graphical form supported by inspection evidence from which test surface condition and features were deduced. Mathematical models relating surface texture and resulting deformation characteristics are formulated to provide understanding of the leakage path closure mechanism and extrapolation of experimental stress-leakage data. Additionally, cyclic effects on model sealing capabilities were investigated. A simplified analysis relating tester and model configuration with anticipated dynamic loading characteristics is developed and further extended by digital programming techniques. A high degree of correlation was obtained between the analytical predictions and the test results. From cycle tests of representative models at various impact levels, corrosion fretting was determined to be a fundamental mode of surface degradation and, from these results, an optimum seating configuration evolved.

14. KEY WORDS	LINK A		LINK B		LINK C	
	ROLE	WT	ROLE	WT	ROLE	WT
Valve poppets and seats						
Valve seating analyses						
Surface contact analyses						
Valve seat impact dynamics, analyses and tests						
Leakage (gases) analyses, measurements, and tests						
Surface texture and finish						
Interference, optical surface inspection						
Lapping and finishing						

INSTRUCTIONS

1. **ORIGINATING ACTIVITY:** Enter the name and address of the contractor, subcontractor, grantee, Department of Defense activity or other organization *(corporate author)* issuing the report.

2*a*. **REPORT SECURITY CLASSIFICATION:** Enter the overall security classification of the report. Indicate whether "Restricted Data" is included. Marking is to be in accordance with appropriate security regulations.

2*b*. **GROUP:** Automatic downgrading is specified in DoD Directive 5200.10 and Armed Forces Industrial Manual. Enter the group number. Also, when applicable, show that optional markings have been used for Group 3 and Group 4 as authorized.

3. **REPORT TITLE:** Enter the complete report title in all capital letters. Titles in all cases should be unclassified. If a meaningful title cannot be selected without classification, show title classification in all capitals in parenthesis immediately following the title.

4. **DESCRIPTIVE NOTES:** If appropriate, enter the type of report, e.g., interim, progress, summary, annual, or final. Give the inclusive dates when a specific reporting period is covered.

5. **AUTHOR(S):** Enter the name(s) of author(s) as shown on or in the report. Enter last name, first name, middle initial. If military, show rank and branch of service. The name of the principal author is an absolute minimum requirement.

6. **REPORT DATE:** Enter the date of the report as day, month, year; or month, year. If more than one date appears on the report, use date of publication.

7*a*. **TOTAL NUMBER OF PAGES:** The total page count should follow normal pagination procedures, i.e., enter the number of pages containing information.

7*b*. **NUMBER OF REFERENCES:** Enter the total number of references cited in the report.

8*a*. **CONTRACT OR GRANT NUMBER:** If appropriate, enter the applicable number of the contract or grant under which the report was written.

8*b*, 8*c*, & 8*d*. **PROJECT NUMBER:** Enter the appropriate military department identification, such as project number, subproject number, system numbers, task number, etc.

9*a*. **ORIGINATOR'S REPORT NUMBER(S):** Enter the official report number by which the document will be identified and controlled by the originating activity. This number must be unique to this report.

9*b*. **OTHER REPORT NUMBER(S):** If the report has been assigned any other report numbers *(either by the originator or by the sponsor)*, also enter this number(s).

10. **AVAILABILITY/LIMITATION NOTICES:** Enter any limitations on further dissemination of the report, other than those imposed by security classification, using standard statements such as:

(1) "Qualified requesters may obtain copies of this report from DDC."

(2) "Foreign announcement and dissemination of this report by DDC is not authorized."

(3) "U. S. Government agencies may obtain copies of this report directly from DDC. Other qualified DDC users shall request through
____ ."

(4) "U. S. military agencies may obtain copies of this report directly from DDC. Other qualified users shall request through
____ ."

(5) "All distribution of this report is controlled. Qualified DDC users shall request through
____ ."

If the report has been furnished to the Office of Technical Services, Department of Commerce, for sale to the public, indicate this fact and enter the price, if known.

11. **SUPPLEMENTARY NOTES:** Use for additional explanatory notes.

12. **SPONSORING MILITARY ACTIVITY:** Enter the name of the departmental project office or laboratory sponsoring *(paying for)* the research and development. Include address.

13. **ABSTRACT:** Enter an abstract giving a brief and factual summary of the document indicative of the report, even though it may also appear elsewhere in the body of the technical report. If additional space is required, a continuation sheet shall be attached.

It is highly desirable that the abstract of classified reports be unclassified. Each paragraph of the abstract shall end with an indication of the military security classification of the information in the paragraph, represented as *(TS)*, *(S)*, *(C)*, or *(U)*.

There is no limitation on the length of the abstract. However, the suggested length is from 150 to 225 words.

14. **KEY WORDS:** Key words are technically meaningful terms or short phrases that characterize a report and may be used as index entries for cataloging the report. Key words must be selected so that no security classification is required. Identifiers, such as equipment model designation, trade name, military project code name, geographic location, may be used as key words but will be followed by an indication of technical context. The assignment of links, rules, and weights is optional.